

Published in Journals: Biomedicines, Geriatrics,
International Journal of Molecular Sciences,
Pharmaceuticals and Brain Sciences

Topic Reprint

Emerging Translational Research in Neurological and Psychiatric Diseases

From In Vitro to In Vivo Models

Edited by
Masaru Tanaka and Lydia Giménez-Llort

mdpi.com/topics



Emerging Translational Research in Neurological and Psychiatric Diseases: From In Vitro to In Vivo Models

Emerging Translational Research in Neurological and Psychiatric Diseases: From In Vitro to In Vivo Models

Editors

Masaru Tanaka

Lydia Giménez-Llort



Basel • Beijing • Wuhan • Barcelona • Belgrade • Novi Sad • Cluj • Manchester

Editors

Masaru Tanaka
University of Szeged (MTA-SZTE)
Szeged, Hungary

Lydia Giménez-Llort
Universitat Autònoma de Barcelona
Cerdanyola del Vallès, Spain

Editorial Office

MDPI
St. Alban-Anlage 66
4052 Basel, Switzerland

This is a reprint of articles from the Topic published online in the open access journals *Biomedicines* (ISSN 2227-9059), *Geriatrics* (ISSN 2308-3417), *International Journal of Molecular Sciences* (ISSN 1422-0067), *Pharmaceuticals* (ISSN 1424-8247), and *Brain Sciences* (ISSN 2076-3425) (available at: <https://www.mdpi.com/topics/transl.res.neurol.psychiatr>).

For citation purposes, cite each article independently as indicated on the article page online and as indicated below:

Lastname, A.A.; Lastname, B.B. Article Title. <i>Journal Name</i> Year , <i>Volume Number</i> , Page Range.
--

ISBN 978-3-0365-9656-3 (Hbk)

ISBN 978-3-0365-9657-0 (PDF)

doi.org/10.3390/books978-3-0365-9657-0

© 2023 by the authors. Articles in this book are Open Access and distributed under the Creative Commons Attribution (CC BY) license. The book as a whole is distributed by MDPI under the terms and conditions of the Creative Commons Attribution-NonCommercial-NoDerivs (CC BY-NC-ND) license.

Contents

About the Editors	ix
Preface	xi
Masaru Tanaka, Ágnes Szabó, László Vécsei and Lydia Giménez-Llort Emerging Translational Research in Neurological and Psychiatric Diseases: From In Vitro to In Vivo Models Reprinted from: <i>Int. J. Mol. Sci.</i> 2023 , <i>24</i> , 15739, doi:10.3390/ijms242115739	1
Lidia Castillo-Mariqueo, M. José Pérez-García and Lydia Giménez-Llort Modeling Functional Limitations, Gait Impairments, and Muscle Pathology in Alzheimer’s Disease: Studies in the 3xTg-AD Mice Reprinted from: <i>Biomedicines</i> 2021 , <i>9</i> , 1365, doi:10.3390/biomedicines9101365	11
Mikel Santana-Santana, José-Ramón Bayascas and Lydia Giménez-Llort Sex-Dependent Signatures, Time Frames and Longitudinal Fine-Tuning of the Marble Burying Test in Normal and AD-Pathological Aging Mice Reprinted from: <i>Biomedicines</i> 2021 , <i>9</i> , 994, doi:10.3390/biomedicines9080994	33
Simon Lam, Nils Hartmann, Rui Benfeitas, Cheng Zhang, Muhammad Arif, Hasan Turkez, et al. Systems Analysis Reveals Ageing-Related Perturbations in Retinoids and Sex Hormones in Alzheimer’s and Parkinson’s Diseases Reprinted from: <i>Biomedicines</i> 2021 , <i>9</i> , 1310, doi:10.3390/biomedicines9101310	49
Dinko Mitrečić, Valentina Hribljan, Denis Jagečić, Jasmina Isaković, Federica Lamberto, Alex Horánszky, et al. Regenerative Neurology and Regenerative Cardiology: Shared Hurdles and Achievements Reprinted from: <i>Int. J. Mol. Sci.</i> 2022 , <i>23</i> , 855, doi:10.3390/ijms23020855	73
Yu Peng, Xuejiao Chang and Minglin Lang Iron Homeostasis Disorder and Alzheimer’s Disease Reprinted from: <i>Int. J. Mol. Sci.</i> 2021 , <i>22</i> , 12442, doi:10.3390/ijms222212442	93
Tracey E. Swingler, Lingzi Niu, Matthew G. Pontifex, David Vauzour and Ian M. Clark The microRNA-455 Null Mouse Has Memory Deficit and Increased Anxiety, Targeting Key Genes Involved in Alzheimer’s Disease Reprinted from: <i>Int. J. Mol. Sci.</i> 2022 , <i>23</i> , 554, doi:10.3390/ijms23010554	113
Abdullah Md. Sheikh, Yasuko Wada, Shatera Tabassum, Satoshi Inagaki, Shingo Mitaki, Shozo Yano and Atsushi Nagai Aggregation of Cystatin C Changes Its Inhibitory Functions on Protease Activities and Amyloid β Fibril Formation Reprinted from: <i>Int. J. Mol. Sci.</i> 2021 , <i>22</i> , 9682, doi:10.3390/ijms22189682	123
Tânia Fernandes, Rosa Resende, Diana F. Silva, Ana P. Marques, Armanda E. Santos, Sandra M. Cardoso, et al. Structural and Functional Alterations in Mitochondria-Associated Membranes (MAMs) and in Mitochondria Activate Stress Response Mechanisms in an In Vitro Model of Alzheimer’s Disease Reprinted from: <i>Biomedicines</i> 2021 , <i>9</i> , 881, doi:10.3390/biomedicines9080881	137

Yu-Show Fu, Chang-Ching Yeh, Pei-Ming Chu, Wen-Hsing Chang, Maan-Yuh Anya Lin and Yung-Yang Lin Xenograft of Human Umbilical Mesenchymal Stem Cells Promotes Recovery from Chronic Ischemic Stroke in Rats Reprinted from: <i>Int. J. Mol. Sci.</i> 2022 , <i>23</i> , 3149, doi:10.3390/ijms23063149	161
Amal Kassab, Nasser Rizk and Satya Prakash The Role of Systemic Filtrating Organs in Aging and Their Potential in Rejuvenation Strategies Reprinted from: <i>Int. J. Mol. Sci.</i> 2022 , <i>23</i> , 4338, doi:10.3390/ijms23084338	181
Yu-Ling Hsu, Huey-Shan Hung, Chia-Wen Tsai, Shih-Ping Liu, Yu-Ting Chiang, Yun-Hua Kuo, et al. Peiminine Reduces ARTS-Mediated Degradation of XIAP by Modulating the PINK1/Parkin Pathway to Ameliorate 6-Hydroxydopamine Toxicity and α -Synuclein Accumulation in Parkinson's Disease Models In Vivo and In Vitro Reprinted from: <i>Int. J. Mol. Sci.</i> 2021 , <i>22</i> , 10240, doi:10.3390/ijms221910240	201
Huey-Jen Tsay, Hui-Kang Liu, Yueh-Hsiung Kuo, Chuan-Sheng Chiu, Chih-Chiang Liang, Chen-Wei Chung, et al. EK100 and Antrodin C Improve Brain Amyloid Pathology in APP/PS1 Transgenic Mice by Promoting Microglial and Perivascular Clearance Pathways Reprinted from: <i>Int. J. Mol. Sci.</i> 2021 , <i>22</i> , 10413, doi:10.3390/ijms221910413	239
Hsing-Chun Kuo, Kam-Fai Lee, Shiou-Lan Chen, Shu-Chen Chiu, Li-Ya Lee, Wan-Ping Chen, et al. Neuron-Microglia Contacts Govern the PGE ₂ Tolerance through TLR4-Mediated de Novo Protein Synthesis Reprinted from: <i>Biomedicines</i> 2022 , <i>10</i> , 419, doi:10.3390/biomedicines10020419	263
Filipa Bezerra, Christoph Niemietz, Hartmut H. J. Schmidt, Andree Zibert, Shuling Guo, Brett P. Monia, et al. In Vitro and In Vivo Effects of SerpinA1 on the Modulation of Transthyretin Proteolysis Reprinted from: <i>Int. J. Mol. Sci.</i> 2021 , <i>22</i> , 9488, doi:10.3390/ijms22179488	277
Alfredo Bellon, Tuna Hasoglu, Mallory Peterson, Katherine Gao, Michael Chen, Elisabeta Blandin, et al. Optimization of Neurite Tracing and Further Characterization of Human Monocyte-Derived-Neuronal-like Cells Reprinted from: <i>Brain Sci.</i> 2021 , <i>11</i> , 1372, doi:10.3390/brainsci11111372	295
Won-Hyeong Jeong, Wang-In Kim, Jin-Won Lee, Hyeng-Kyu Park, Min-Keun Song, In-Sung Choi and Jae-Young Han Modulation of Long-Term Potentiation by Gamma Frequency Transcranial Alternating Current Stimulation in Transgenic Mouse Models of Alzheimer's Disease Reprinted from: <i>Brain Sci.</i> 2021 , <i>11</i> , 1532, doi:10.3390/brainsci11111532	311
Ying Chen, Jihong Lin, Andrea Schlotterer, Luke Kurowski, Sigrid Hoffmann, Seddik Hammad, et al. MicroRNA-124 Alleviates Retinal Vasoregression via Regulating Microglial Polarization Reprinted from: <i>Int. J. Mol. Sci.</i> 2021 , <i>22</i> , 11068, doi:10.3390/ijms222011068	321
Bibiana Quirant-Sánchez, María José Mansilla, Juan Navarro-Barruoso, Silvia Presas-Rodríguez, Aina Teniente-Serra, Federico Fondelli, et al. Combined Therapy of Vitamin D3-Tolerogenic Dendritic Cells and Interferon- β in a Preclinical Model of Multiple Sclerosis Reprinted from: <i>Biomedicines</i> 2021 , <i>9</i> , 1758, doi:10.3390/biomedicines9121758	343

Eleonóra Spekker, Masaru Tanaka, Ágnes Szabó and László Vécsei Neurogenic Inflammation: The Participant in Migraine and Recent Advancements in Translational Research Reprinted from: <i>Biomedicines</i> 2022 , <i>10</i> , 76, doi:10.3390/biomedicines10010076	359
Sylvain Lamoine, Mélissa Cumenal, David A. Barriere, Vanessa Pereira, Mathilde Fereyrolles, Laëtitia Prival, et al. The Class I HDAC Inhibitor, MS-275, Prevents Oxaliplatin-Induced Chronic Neuropathy and Potentiates Its Antiproliferative Activity in Mice Reprinted from: <i>Int. J. Mol. Sci.</i> 2022 , <i>23</i> , 98, doi:10.3390/ijms23010098	385
Mathieu Thabault, Valentine Turpin, Alexandre Maisterrena, Mohamed Jaber, Matthieu Egloff and Laurie Galvan Cerebellar and Striatal Implications in Autism Spectrum Disorders: From Clinical Observations to Animal Models Reprinted from: <i>Int. J. Mol. Sci.</i> 2022 , <i>23</i> , 2294, doi:10.3390/ijms23042294	409
Gilbert Aaron Lee, Yen-Kuang Lin, Jing-Huei Lai, Yu-Chun Lo, Yu-Chen S. H. Yang, Syuan-You Ye, et al. Maternal Immune Activation Causes Social Behavior Deficits and Hypomyelination in Male Rat Offspring with an Autism-Like Microbiota Profile Reprinted from: <i>Brain Sci.</i> 2021 , <i>11</i> , 1085, doi:10.3390/brainsci11081085	443
Sameera Abuaish, Norah M. Al-Otaibi, Turki S. Abujamel, Saleha Ahmad Alzahrani, Sohailah Masoud Alotaibi, Yasser A. AlShawakir, et al. Fecal Transplant and <i>Bifidobacterium</i> Treatments Modulate Gut <i>Clostridium</i> Bacteria and Rescue Social Impairment and Hippocampal BDNF Expression in a Rodent Model of Autism Reprinted from: <i>Brain Sci.</i> 2021 , <i>11</i> , 1038, doi:10.3390/brainsci11081038	459
Zhikui Wei, You Chen and Raghu P. Uppender Sleep Disturbance and Metabolic Dysfunction: The Roles of Adipokines Reprinted from: <i>Int. J. Mol. Sci.</i> 2022 , <i>23</i> , 1706, doi:10.3390/ijms23031706	477
Emilio Garro-Martínez, Maria Neus Fullana, Eva Florensa-Zanuy, Julia Senserrich, Verónica Paz, Esther Ruiz-Bronchal, et al. mTOR Knockdown in the Infralimbic Cortex Evokes A Depressive-like State in Mouse Reprinted from: <i>Int. J. Mol. Sci.</i> 2021 , <i>22</i> , 8671, doi:10.3390/ijms22168671	491

About the Editors

Masaru Tanaka

Masaru Tanaka, M.D., Ph.D., is a Senior Research Fellow in the Danube Neuroscience Research Laboratory, HUN-REN-SZTE Neuroscience Research Group, Hungarian Research Network, University of Szeged (HUN-REN-SZTE). His scientific interests include depression anxiety, dementia pain, their comorbid nature, and translational research in neurological diseases and psychiatric disorders. His current research focuses on the antidepressant, anxiolytic, and nootropic effects of neuropeptide, neurohormones and tryptophan metabolites and their analogues in the preclinical stages of neuropsychiatric diseases. He is an editorial board member of *Frontiers in Neuroscience*, *Frontiers in Psychiatry*, *Anesthesia Research*, the *Journal of Integrative Neuroscience*, *Advances in Clinical Experimental Medicine*, *Biology and Life Sciences*, and *Biomedicines*, among others. He obtained a PhD in Medicine and an MD in General Medicine from the University of Szeged and a bachelors' degree in Biophysics from the University of Illinois, Urbana-Champaign.

Lydia Giménez-Llort

Lydia Giménez-Llort, B.Sc., Ph.D. is a Full Professor in Psychiatry at the Autonomous University of Barcelona (UAB) and the Senior Research Fellow of Translational Behavioral Neuroscience group, Institut of Neuroscience, UAB. Her scientific and clinical interests include aging, neurodegenerative disorders (Alzheimer's disease, Parkinson's disease, multiple sclerosis), misophonia, grief, pain in dementia and gender medicine. Giménez-Llort holds a degree in Biology (University of Barcelona), Master in Biochemistry and Molecular Biology (UB), PhD in Anatomical Pathology (CSIC, Spanish Research Council and UB), Postdoc in Neuroscience (Karolinska Institute, Sweden), Postdoc in Psychiatry (UAB), Ramón y Cajal Tenure Track (UAB), and Masters in Psychology—Problem Solving Strategies and Advanced Problem Solving Strategies—SBT (CTs di Arezzo, Italy–Barcelona, Spain). She is an editorial board member of *Geriatrics*, *Behavioral Sciences* and Guest Associate Editor at *Frontiers in Neuropharmacology*, *Public Mental Health*, *Cognitive Neuroscience*, *Brain Disease Mechanisms*, *Alzheimer's Disease and Related Dementias* and Review Editor in *Cognitive Neuroscience*.

Preface

Translational research is required to uncover the underlying pathomechanisms of neurological and psychiatric disorders, search for new biomarkers, and develop novel therapeutics. Complex polygenic, multifactorial, and heterogeneous mechanisms have been elucidated using *in vivo* and *in vitro* preclinical models. Advanced disease models have recently revealed an intriguing interaction between sex/gender and aging in the pathogenesis and clinical manifestations of neuropsychiatric disorders. Despite these advances, much work remains to be carried out to fully understand the underlying pathology of these conditions and to develop treatments that can significantly improve the lives of those who suffer from them. The current challenge in the field of neurological and psychiatric disorders is the development of disease-modifying, effective treatments for these complex and long-term debilitating conditions with a high malady burden.

The first edition of this research topic, entitled 'Emerging Translational Research in Neurological and Psychiatric Diseases: From *In Vitro* to *In Vivo* Models', emphasizes the importance of translational research in bridging the gap between basic research and clinical applications. Furthermore, it provides a venue for researchers to share their findings and progress in translational research in this field. This new collection includes 25 papers that provide insights into the most recent advances in translational research as well as potential new treatment avenues. These papers cover a wide range of topics, including developing novel preclinical models, using *in vitro* and *in vivo* methods, and employing qualitative and quantitative research techniques.

Masaru Tanaka and Lydia Giménez-Llort

Editors



Editorial

Emerging Translational Research in Neurological and Psychiatric Diseases: From In Vitro to In Vivo Models

Masaru Tanaka ^{1,*}, Ágnes Szabó ^{2,3}, László Vécsei ^{1,2} and Lydia Giménez-Llort ^{4,5,*}

¹ Danube Neuroscience Research Laboratory, HUN-REN-SZTE Neuroscience Research Group, Hungarian Research Network, University of Szeged (HUN-REN-SZTE), Tisza Lajos krt. 113, H-6725 Szeged, Hungary; vecsei.laszlo@med.u-szeged.hu

² Department of Neurology, Albert Szent-Györgyi Medical School, University of Szeged, Semmelweis u. 6, H-6725 Szeged, Hungary; szabo.agnes.4@med.u-szeged.hu

³ Doctoral School of Clinical Medicine, University of Szeged, Korányi fasor 6, H-6720 Szeged, Hungary

⁴ Institut de Neurociències, Universitat Autònoma de Barcelona, Cerdanyola del Vallès, 08193 Barcelona, Spain

⁵ Department of Psychiatry & Forensic Medicine, Faculty of Medicine, Campus Bellaterra, Universitat Autònoma de Barcelona, Cerdanyola del Vallès, 08193 Barcelona, Spain

* Correspondence: tanaka.masaru.1@med.u-szeged.hu (M.T.); lidia.gimenez@uab.cat (L.G.-L.); Tel.: +36-62-342-847 (M.T.); +34-93-581-2378 (L.G.-L.)

† These authors contributed equally to this work.

1. Introduction

Revealing the underlying pathomechanisms of neurological and psychiatric disorders, searching for new biomarkers, and developing novel therapeutics all require translational research [1]. In vivo and in vitro models have been instrumental in elucidating complex polygenic, multifactorial, and heterogeneous mechanisms [2]. In recent years, advanced preclinical models have revealed the intriguing interaction of sex/gender and aging with the pathogenesis and clinical manifestations of neuropsychiatric disorders [3–5]. However, despite these advancements, a great deal of work remains to be undertaken to fully comprehend the underlying pathology of these conditions and to elaborate treatments that can significantly improve the lives of those who suffer from them. The current challenge in the field of neurological and psychiatric disorders is the development of disease-modifying, effective treatments for these complex and long-lasting debilitating conditions with a high burden of malady.

The first edition of this research topic, entitled ‘Emerging Translational Research in Neurological and Psychiatric Diseases: From In Vitro to In Vivo Models’, reinforces the notion that translational research plays a critical role in bridging the gap between basic research and clinical applications. In addition, it provides a platform for investigators to share their findings and advancements in translational research in this field. This new collection gathers 25 papers offering insights into the latest advancements in translational research and potential new avenues for treatments. These papers address a range of topics, including engineering novel preclinical models, utilizing in vitro and in vivo methods, and applying qualitative and quantitative research techniques.

2. Topic Articles

2.1. Neurological Disorders and Therapies

2.1.1. Pathophysiology

Understanding the pathogenesis of Alzheimer’s disease (AD) and elaborating suitable preclinical models are vital for research [6,7]. Castillo-Mariquero et al. devise a behavioral observation method to study gait and exploratory activity during AD progression and aging, adding motor symptoms to the classical cognitive perspective. Their work demonstrates pronounced functional impairment in 3× Tg-AD mice, underscoring the model’s applicative potential in AD research and therapeutic development [8]. This study contributes to

Citation: Tanaka, M.; Szabó, Á.; Vécsei, L.; Giménez-Llort, L. Emerging Translational Research in Neurological and Psychiatric Diseases: From In Vitro to In Vivo Models. *Int. J. Mol. Sci.* **2023**, *24*, 15739. <https://doi.org/10.3390/ijms242115739>

Received: 10 October 2023

Accepted: 13 October 2023

Published: 30 October 2023



Copyright: © 2023 by the authors. Licensee MDPI, Basel, Switzerland. This article is an open access article distributed under the terms and conditions of the Creative Commons Attribution (CC BY) license (<https://creativecommons.org/licenses/by/4.0/>).

our understanding of AD's complexities and potential treatment avenues, aligning with broader research in this field. Santana-Santana et al. investigate how the marble burying test outcomes differ between male and female mice, shedding light on potential sex-dependent variations in behavior relevant to aging and AD. The article also examines how these behaviors alter over time, providing insights into the progression of age- and AD-related behavioral changes in mice [9]. Furthermore, Lam et al. identify age-related disturbances in retinoids and sex hormones, particularly in the context of AD and Parkinson's disease (PD) [10]. The study suggests that these molecules may play a pivotal role in the pathogenesis and progression of these debilitating neurological conditions. These insights are valuable for advancing our knowledge of the mechanisms implicated in AD and PD, and potentially paving the way for innovative therapeutic approaches [11,12].

It is essential to burgeon novel therapeutic strategies for neurological and cardiovascular diseases, which are leading causes of morbidity and mortality worldwide. Additionally, non-invasive brain stimulation techniques have become an integral aspect of clinical research in mental illnesses [13,14]. Methods such as transcranial magnetic stimulation and transcranial direct current stimulation have been employed in preclinical models to investigate their potential therapeutic alternatives [15,16]. These techniques offer a unique opportunity to modulate neural activity in specific brain regions, mimicking the neuromodulatory effects observed in human studies [17–19]. Non-invasive brain stimulation in preclinical research allows scientists to explore the neural circuitry involved in neuropsychiatric conditions, providing valuable insights into the underlying pathology. It also facilitates the assessment of the safety and efficacy of these techniques before translating them into clinical applications. Mitrečić et al. discuss the potential of stem-cell-based therapies, tissue engineering, and regenerative medicine in augmenting effective treatments for these diseases, emphasizing the criticality of interdisciplinary collaboration and the need for an enhanced understanding of the underlying pathomechanisms of these conditions [20]. Revealing iron metabolism in AD is crucial due to its significant role in brain function and the development of AD-related pathologies. Peng et al. review the recent advances made regarding the relationship between iron and AD, highlighting the importance of iron in the brain for treating AD and discussing the potential of iron chelators as a therapeutic option for AD [21].

Three papers contribute to our knowledge regarding the pathophysiology of AD and reveal potential therapeutic targets for the disease. Swinger et al. investigate the role of microRNA-455 in AD-related memory deficits and anxiety, highlighting potential targets for therapeutic intervention [22]. Sheikh et al. discuss the aggregation of cystatin C and its effect on protease activities and the formation of amyloid beta fibrils, which are key pathogenesis in AD [23]. In an in vitro model of AD, Fernandes et al. investigate the structural and functional alterations in mitochondria-associated membranes and mitochondria, elucidating the stress response mechanisms activated by the disease [24]. These papers collectively provide valuable information regarding the underlying pathology of AD and its potential therapeutic targets, which could aid in elaborating novel treatments for the condition.

2.1.2. Therapies

Other researchers investigate the therapeutic potential of mesenchymal stem cells (MSCs) for neurological disorders. Fu et al. demonstrate that xenografts of human umbilical MSCs promote recovery after chronic ischemic stroke in rats [25]. The article highlights the potential of MSCs in treating chronic stroke and provides insights into the therapeutic benefits of the xenotransplantation of MSCs. Kassab et al. discuss the role of systemic filtering organs, particularly the kidney, in aging and rejuvenation from a systems biology perspective. It provides an overview of the major systemic causes of aging and identifies that the filtration system represents a clear gap in aging studies to date. The paper concludes by exploring possible rejuvenation avenues that must be developed in the future in order to address the complex topic of healthy aging [26]. These papers provide valuable information regarding the therapeutic potential of MSCs in treating neurological diseases and regenerative medicine, which can aid in elaborating novel therapeutic strategies for these conditions.

The common pathogenesis of neurodegeneration, such as inflammation, amyloid pathology, and microglial dysfunction, are explored in three articles that focus on AD and PD, two prevalent neurodegenerative diseases [27]. The articles also propose novel treatments that target these mechanisms. One article by Hsu et al. evaluates the effect of peiminine on PD by regulating the PINK1/Parkin pathway [28]. Another article by Tsay et al. assesses the effect of EK100 and Antradin C on AD by enhancing microglial and perivascular clearance pathways [29]. A third article by Kuo et al. examines the role of neuron–microglia contacts in controlling PGE2 tolerance and the effect of inhibiting TLR4-mediated de novo protein synthesis on neurodegeneration [30]. Bezerra et al. also investigate the possible role of SerpinA1 in modulating transthyretin proteolysis, a process involved in various neurodegenerative conditions, including AD and familial amyloid polyneuropathy [31]. These papers offer valuable insights into the potential application of new therapeutic strategies for neurodegenerative diseases, which can facilitate the development of effective treatments for these conditions.

Bellon et al. investigate the optimization of neurite tracing and the further characterization of neuronal-like cells derived from human monocytes [32]. Revealing the mechanisms underlying the differentiation of human circulating monocytes into neuronal-like cells is crucial for identifying novel therapeutic strategies for neurological conditions, as demonstrated by this study. The findings contribute to the growing body of research on the potential of circulating monocytes in human blood to be transdifferentiated into neuronal-like cells, which could lead to improved outcomes for patients with neurological disorders.

Transcranial alternating current stimulation (tACS) possesses the potential to reduce the symptoms of AD and improve cognitive function in those who have it. Jeong et al. examine the effects of tACS on long-term potentiation in transgenic mice with AD, which is an important process for learning and memory. The advantage of using tACS in this experiment is that its current can oscillate at a specific frequency and interact with the intrinsic oscillation of the brain [33]. The article highlights the applicative potential of tACS in treating AD-related cognitive impairments, which can aid in the development of novel therapeutic strategies for AD.

Chen et al. investigate the potential role of microRNA-124 in treating retinal vasoregression in neurodegenerative diseases [34]. The study highlights the significance of microRNA-124 in regulating microglial polarization, which is implicated in the retinal vasoregression. The findings contribute to our understanding of the potential of microRNA-124 in treating retinal vasoregression, aiding in searching novel therapeutic strategies for these conditions. The article also sheds light on the potential of microglial polarization as a therapeutic target for neurodegenerative diseases.

In a preclinical model of multiple sclerosis (MS), Quirant-Sánchez et al. investigate the application of a combined therapy approach involving vitamin D3-tolerogenic dendritic cells and interferon- β . The findings suggest that in a preclinical model, this combined treatment can effectively reduce the severity of MS symptoms and improve overall outcomes, potentially leading to the development of novel MS therapeutic strategies [35]. Thus, it is evident that the application of preclinical models has been instrumental in propelling research on MS forward [36]. These investigations have not only deepened our understanding of the intricate pathophysiology implicated in the condition, but have also been key in identifying potential biomarkers [37,38]. Furthermore, they have opened new avenues for the discovery of innovative treatments. Thus, the importance of these studies in shaping the future of MS research is undeniable.

2.2. Pain

Pain and mental illnesses are inextricably linked, and their comorbidities have been extensively investigated [39–41]. Neurogenic inflammation and neuropeptides have been implicated in the pathophysiology of various human diseases, including primary headache disorders and peripheral neuropathy [42]. These articles investigate the potential function of neurogenic inflammation and neuropeptides in the etiology and progression of a wide

range of illnesses, from primary headache disorders to peripheral neuropathy [43]. The article by Spekker et al. discusses the impact of neurogenic inflammation on migraines and reviews recent findings from translational research on the subject [44]. A better understanding of its role in migraines could have crucial implications for the clinical management of this neurological condition. Employing the Class I HDAC inhibitor MS-275, Lamoine et al. provide vital new information regarding the benefits of using this drug to prevent chronic neuropathy and enhance antiproliferative activity in mice. The study utilizes a systems biology approach, combining transcriptomic and bioinformatic analyses to identify the molecular mechanisms underlying the effects of MS-275 [45]. The article highlights the potential of systems biology approaches in identifying novel therapeutic targets and elaborating more effective treatments for various diseases.

2.3. *Psychiatric Disorders, Pathophysiology, Biomarkers, Therapies*

Five articles highlight the significance of revealing the pathomechanisms underlying various conditions, including autism, sleep disturbance, and metabolic dysfunction, in searching novel therapeutic strategies. The role of the cerebellum and striatum in autism spectrum disorders is investigated by Thabault et al. This study is valuable because it investigates the neurological aspects of autism spectrum disorder, elucidates potential pathophysiology, and provides a link between clinical observations and preclinical models [46]. Lee et al. investigate the influence of maternal immune activation on male rat offspring. In this study, maternal immune activation is associated with social behavior deficits and hypomyelination, a condition characterized by reduced myelin in the brain, according to the study. These effects are observed in male rat offspring, and the investigation suggests that they have an autism-like microbiota profile [47]. Abuaish et al. investigate the potential of fecal transplant and Bifidobacterium treatments in modulating gut Clostridium bacteria and rescuing social impairment and hippocampal brain-derived neurotrophic factor expression in a rodent model of autism [48]. The article highlights the significance of understanding the role of gut microbiota dysbiosis in the pathophysiology of autism and the potential of microbiota-based interventions in scrutinizing for novel therapeutic strategies for autism.

Sleep is an integral component of energy metabolism, and sleep disturbance has been implicated in a wide range of metabolic disorders. Wei et al. provide a balanced overview of adipokines and their role in sleep physiology and sleep disorders with reference to recent human and preclinical studies [49]. The significance of this review lies in its contribution to our understanding of the relationship among sleep disturbance, metabolic dysfunction, and adipokines, which can aid in identifying novel therapeutic strategies for metabolic disorders. Garro-Martínez et al. investigate the potential role of mTOR expression in the infralimbic cortex in the pathophysiology of depression [50]. The article highlights the significance of revealing the mechanisms underlying mTOR expression in the infralimbic cortex and its potential role in the development of depressive-like behaviors. The findings contribute to the growing body of research on the potential of mTOR as a therapeutic target for depression, potentially leading to improved outcomes for individuals with this condition.

3. Conclusions and Future Directions

In vitro- and in vivo-based preclinical research serves as a vital complement to human studies in understanding neuropsychiatric conditions [51–55]. These models enable researchers to simulate disease conditions and explore the intricate connections among genetics, environment, pharmacology, and comorbidities [56–60]. This study provides insights into the pathomechanisms underlying neurological and mental disorders, facilitates the testing of potential treatments, and evaluates therapeutic efficacy [61]. For instance, studies in translational research illustrate how preclinical models aid in translating findings from the lab to clinical applications. Preclinical models have also been crucial in exploring neurological and psychiatric conditions like AD and autism spectrum disorder, and shedding light on their underlying factors. Furthermore, this approach contributes to the elaboration of personalized medicine by enabling the application of tailored treatments for

mental disorders. It also enables the investigation of structural changes in the brain and the advancement of imaging techniques for clinical use. Preclinical research plays an essential role in unraveling the complexities of brain illnesses, offering valuable insights and testing treatments, and paving the way for innovative therapeutics and personalized medicine.

In this multidisciplinary endeavor, neuropharmacological research plays a pivotal role. The study of how drugs and compounds interact with the intricate neural networks present in preclinical models provides a deeper understanding of potential therapeutic agents [62–69]. These insights guide the future development of pharmacological interventions that can target the specific molecular pathways implicated in neuropsychiatric conditions. Researchers are exploring novel drug candidates, investigating their safety profiles, and assessing their efficacy in mitigating the symptoms of conditions like depression and anxiety, and the cognitive impairments associated with mental illnesses [70]. Advanced imaging techniques have significantly aided research on neuropsychiatric disorders. According to neuroimaging research, these conditions are associated with changes in brain structure and function [71–78]. These imaging methods can aid in the diagnosis of rare clinical cases and shed light on the underlying pathophysiology of the disorders being studied. Furthermore, neuropharmacological approach dovetails with the broader scope of preclinical investigations, facilitating a comprehensive exploration of the genetic, environmental, and pharmacological factors that influence mental health [66,68]. It expedites the identification of potential drug targets and the elaboration of personalized medicine approaches tailored to individuals' unique neurochemical profiles [79–81].

In summary, we aspire for this subject to act as a pivotal platform for the exploration of the neural foundations of neurological and psychiatric disorders. Researchers are attempting to open novel avenues for specialized treatment plans and preventive measures, with the ultimate aim of improving the quality of life of those suffering from these complex mental health conditions, by examining behavioral neuroscience from this perspective [82–88]. As our comprehension of the pathomechanisms underlying neuropsychiatry advances, we draw nearer to a future in which individuals can receive personalized care and support to conquer these challenging conditions.

This comprehensive and interdisciplinary approach is echoed in various academic works and research endeavors, and serves as a valuable resource when hoping to comprehend the etiological factors of neuropsychiatric disorders, search for biomarkers, achieve precision, and master their personalized treatment. Additionally, discussions regarding the quest for neuropsychiatric biomarkers and endophenotypes are ongoing in academia [89]. Philosophical perspectives on neuropsychiatric topics are also being investigated, thereby contributing to our philosophical comprehension of psychology [90]. Research in this area often involves the examination of abstracts and articles, as exemplified by the National Institutes of Health's database. This collective effort and interdisciplinary collaboration underscore the importance of advancing our understanding of mental illnesses and working towards enhanced treatments and support for affected individuals. We wish to express our heartfelt appreciation to all of those who contributed to this collection, and extend our gratitude to the reviewers for their invaluable feedback. We eagerly await future contributions that will further propel the fields of neurology and psychiatry, recognizing that your unwavering support and dedication play an indispensable role in shaping the progress and potential of this rapidly expanding domain.

Author Contributions: Conceptualization, M.T. and L.G.-L.; writing—original draft preparation, M.T.; writing—review and editing, M.T. and L.G.-L.; visualization, Á.S.; supervision, M.T., L.V. and L.G.-L.; funding acquisition, M.T., L.V. and L.G.-L. All authors have read and agreed to the published version of the manuscript.

Funding: This work was supported by the National Research, Development, and Innovation Office—NKFIH K138125, TUDFO/47138-1/2019-ITM, the HUN-REN Hungarian Research Network, and Universitat Autònoma de Barcelona, UAB-GE-260408.

Institutional Review Board Statement: Not applicable.

Informed Consent Statement: Not applicable.

Data Availability Statement: Data sharing is not applicable to this article.

Acknowledgments: The graphical abstract was created using BioRender.com.

Conflicts of Interest: The authors declare no conflict of interest.

Abbreviations

AD	Alzheimer's disease
MS	multiple sclerosis
MSCs	mesenchymal stem cells
PD	Parkinson's disease
tACS	Transcranial alternating current stimulation

References

1. Tanaka, M.; Szabó, Á.; Vécsei, L. Preclinical modeling in depression and anxiety: Current challenges and future research directions. *Adv. Clin. Exp. Med.* **2023**, *32*, 505–509. [CrossRef]
2. Tanaka, M.; Szabó, Á.; Vécsei, L. Integrating Armchair, Bench, and Bedside Research for Behavioral Neurology and Neuropsychiatry: Editorial. *Biomedicines* **2022**, *10*, 2999. [CrossRef] [PubMed]
3. Santana-Santana, M.; Bayascas, J.-R.; Giménez-Llort, L. Fine-Tuning the PI3K/Akt Signaling Pathway Intensity by Sex and Genotype-Load: Sex-Dependent Homozygotic Threshold for Somatic Growth but Feminization of Anxious Phenotype in Middle-Aged PDK1 K465E Knock-In and Heterozygous Mice. *Biomedicines* **2021**, *9*, 747. [CrossRef] [PubMed]
4. Giménez-Llort, L.; Marin-Pardo, D.; Marazuela, P.; Hernández-Guillamón, M. Survival Bias and Crosstalk between Chronological and Behavioral Age: Age- and Genotype-Sensitivity Tests Define Behavioral Signatures in Middle-Aged, Old, and Long-Lived Mice with Normal and AD-Associated Aging. *Biomedicines* **2021**, *9*, 636. [CrossRef]
5. Chen, W.-C.; Wang, T.-S.; Chang, F.-Y.; Chen, P.-A.; Chen, Y.-C. Age, Dose, and Locomotion: Decoding Vulnerability to Ketamine in C57BL/6J and BALB/c Mice. *Biomedicines* **2023**, *11*, 1821. [CrossRef]
6. Castillo-Mariqueo, L.; Giménez-Llort, L. Impact of Behavioral Assessment and Re-Test as Functional Trainings That Modify Survival, Anxiety and Functional Profile (Physical Endurance and Motor Learning) of Old Male and Female 3xTg-AD Mice and NTg Mice with Normal Aging. *Biomedicines* **2022**, *10*, 973. [CrossRef]
7. Muntsant, A.; Giménez-Llort, L. Genotype Load Modulates Amyloid Burden and Anxiety-Like Patterns in Male 3xTg-AD Survivors despite Similar Neuro-Immunoendocrine, Synaptic and Cognitive Impairments. *Biomedicines* **2021**, *9*, 715. [CrossRef]
8. Castillo-Mariqueo, L.; Pérez-García, M.J.; Giménez-Llort, L. Modeling Functional Limitations, Gait Impairments, and Muscle Pathology in Alzheimer's Disease: Studies in the 3xTg-AD Mice. *Biomedicines* **2021**, *9*, 1365. [CrossRef]
9. Santana-Santana, M.; Bayascas, J.-R.; Giménez-Llort, L. Sex-Dependent Signatures, Time Frames and Longitudinal Fine-Tuning of the Marble Burying Test in Normal and AD-Pathological Aging Mice. *Biomedicines* **2021**, *9*, 994. [CrossRef]
10. Lam, S.; Hartmann, N.; Benfeitas, R.; Zhang, C.; Arif, M.; Turkez, H.; Uhlén, M.; Englert, C.; Knight, R.; Mardinoglu, A. Systems Analysis Reveals Ageing-Related Perturbations in Retinoids and Sex Hormones in Alzheimer's and Parkinson's Diseases. *Biomedicines* **2021**, *9*, 1310. [CrossRef]
11. De Masi, R.; Orlando, S.; Toni, V.; Costa, M.C. Fluphenazine-Induced Neurotoxicity with Acute Almost Transient Parkinsonism and Permanent Memory Loss: Lessons from a Case Report. *Int. J. Mol. Sci.* **2023**, *24*, 2968. [CrossRef]
12. Török, N.; Maszlag-Török, R.; Molnár, K.; Szolnoki, Z.; Somogyvári, F.; Boda, K.; Tanaka, M.; Klivényi, P.; Vécsei, L. Single Nucleotide Polymorphisms of Indoleamine 2,3-Dioxygenase 1 Influenced the Age Onset of Parkinson's Disease. *Front. Biosci.* **2022**, *27*, 265. [CrossRef]
13. Chang, C.H.; Wang, W.L.; Shieh, Y.H.; Peng, H.Y.; Ho, C.S.; Tsai, H.C. Case Report: Low-Frequency Repetitive Transcranial Magnetic Stimulation to Dorsolateral Prefrontal Cortex and Auditory Cortex in a Patient With Tinnitus and Depression. *Front. Psychiatry* **2022**, *13*, 847618. [CrossRef] [PubMed]
14. de Albuquerque, L.L.; Pantovic, M.; Clingo, M.; Fischer, K.; Jalene, S.; Landers, M.; Mari, Z.; Poston, B. A Single Application of Cerebellar Transcranial Direct Current Stimulation Fails to Enhance Motor Skill Acquisition in Parkinson's Disease: A Pilot Study. *Biomedicines* **2023**, *11*, 2219. [CrossRef] [PubMed]
15. Vila-Merkle, H.; González-Martínez, A.; Campos-Jiménez, R.; Martínez-Ricós, J.; Teruel-Martí, V.; Blasco-Serra, A.; Lloret, A.; Celada, P.; Cervera-Ferri, A. The Oscillatory Profile Induced by the Anxiogenic Drug FG-7142 in the Amygdala-Hippocampal Network Is Reversed by Infralimbic Deep Brain Stimulation: Relevance for Mood Disorders. *Biomedicines* **2021**, *9*, 783. [CrossRef] [PubMed]
16. Ravache, T.T.; Batistuzzo, A.; Nunes, G.G.; Gomez, T.G.B.; Lorena, F.B.; Do Nascimento, B.P.P.; Bernardi, M.M.; Lima, E.R.R.; Martins, D.O.; Campos, A.C.P.; et al. Multisensory Stimulation Reverses Memory Impairment in Adr β_3 KO Male Mice. *Int. J. Mol. Sci.* **2023**, *24*, 10522. [CrossRef] [PubMed]
17. Battaglia, S.; Schmidt, A.; Hassel, S.; Tanaka, M. Editorial: Case reports in neuroimaging and stimulation. *Front. Psychiatry* **2023**, *14*, 1264669. [CrossRef]

18. Tanaka, M.; Diano, M.; Battaglia, S. Editorial: Insights into structural and functional organization of the brain: Evidence from neuroimaging and non-invasive brain stimulation techniques. *Front. Psychiatry* **2023**, *14*, 1225755. [CrossRef]
19. Borgomaneri, S.; Battaglia, S.; Sciamanna, G.; Tortora, F.; Laricchiuta, D. Memories are not written in stone: Re-writing fear memories by means of non-invasive brain stimulation and optogenetic manipulations. *Neurosci. Biobehav. Rev.* **2021**, *127*, 334–352. [CrossRef]
20. Mitrečić, D.; Hribljan, V.; Jagečić, D.; Isaković, J.; Lamberto, F.; Horánszky, A.; Zana, M.; Foldes, G.; Zavan, B.; Pivoriūnas, A.; et al. Regenerative Neurology and Regenerative Cardiology: Shared Hurdles and Achievements. *Int. J. Mol. Sci.* **2022**, *23*, 855. [CrossRef]
21. Peng, Y.; Chang, X.; Lang, M. Iron Homeostasis Disorder and Alzheimer’s Disease. *Int. J. Mol. Sci.* **2021**, *22*, 12442. [CrossRef] [PubMed]
22. Swingler, T.E.; Niu, L.; Pontifex, M.G.; Vauzour, D.; Clark, I.M. The microRNA-455 Null Mouse Has Memory Deficit and Increased Anxiety, Targeting Key Genes Involved in Alzheimer’s Disease. *Int. J. Mol. Sci.* **2022**, *23*, 554. [CrossRef] [PubMed]
23. Sheikh, A.M.; Wada, Y.; Tabassum, S.; Inagaki, S.; Mitaki, S.; Yano, S.; Nagai, A. Aggregation of Cystatin C Changes Its Inhibitory Functions on Protease Activities and Amyloid β Fibril Formation. *Int. J. Mol. Sci.* **2021**, *22*, 9682. [CrossRef] [PubMed]
24. Fernandes, T.; Resende, R.; Silva, D.F.; Marques, A.P.; Santos, A.E.; Cardoso, S.M.; Domingues, M.R.; Moreira, P.I.; Pereira, C.F. Structural and Functional Alterations in Mitochondria-Associated Membranes (MAMs) and in Mitochondria Activate Stress Response Mechanisms in an In Vitro Model of Alzheimer’s Disease. *Biomedicines* **2021**, *9*, 881. [CrossRef] [PubMed]
25. Fu, Y.-S.; Yeh, C.-C.; Chu, P.-M.; Chang, W.-H.; Lin, M.-Y.A.; Lin, Y.-Y. Xenograft of Human Umbilical Mesenchymal Stem Cells Promotes Recovery from Chronic Ischemic Stroke in Rats. *Int. J. Mol. Sci.* **2022**, *23*, 3149. [CrossRef]
26. Kassab, A.; Rizk, N.; Prakash, S. The Role of Systemic Filtrating Organs in Aging and Their Potential in Rejuvenation Strategies. *Int. J. Mol. Sci.* **2022**, *23*, 4338. [CrossRef]
27. Tanaka, M.; Toldi, J.; Vécsei, L. Exploring the Etiological Links behind Neurodegenerative Diseases: Inflammatory Cytokines and Bioactive Kynurenines. *Int. J. Mol. Sci.* **2020**, *21*, 2431. [CrossRef]
28. Hsu, Y.-L.; Hung, H.-S.; Tsai, C.-W.; Liu, S.-P.; Chiang, Y.-T.; Kuo, Y.-H.; Shyu, W.-C.; Lin, S.-Z.; Fu, R.-H. Peiminine Reduces ARTS-Mediated Degradation of XIAP by Modulating the PINK1/Parkin Pathway to Ameliorate 6-Hydroxydopamine Toxicity and α -Synuclein Accumulation in Parkinson’s Disease Models In Vivo and In Vitro. *Int. J. Mol. Sci.* **2021**, *22*, 10240. [CrossRef]
29. Tsay, H.-J.; Liu, H.-K.; Kuo, Y.-H.; Chiu, C.-S.; Liang, C.-C.; Chung, C.-W.; Chen, C.-C.; Chen, Y.-P.; Shiao, Y.-J. EK100 and Antrodin C Improve Brain Amyloid Pathology in APP/PS1 Transgenic Mice by Promoting Microglial and Perivascular Clearance Pathways. *Int. J. Mol. Sci.* **2021**, *22*, 10413. [CrossRef]
30. Kuo, H.-C.; Lee, K.-F.; Chen, S.-L.; Chiu, S.-C.; Lee, L.-Y.; Chen, W.-P.; Chen, C.-C.; Chu, C.-H. Neuron–Microglia Contacts Govern the PGE₂ Tolerance through TLR4-Mediated de Novo Protein Synthesis. *Biomedicines* **2022**, *10*, 419. [CrossRef]
31. Bezerra, F.; Niemietz, C.; Schmidt, H.H.J.; Zibert, A.; Guo, S.; Monia, B.P.; Gonçalves, P.; Saraiva, M.J.; Almeida, M.R. In Vitro and In Vivo Effects of SerpinA1 on the Modulation of Transhyretin Proteolysis. *Int. J. Mol. Sci.* **2021**, *22*, 9488. [CrossRef] [PubMed]
32. Bellon, A.; Hasoglu, T.; Peterson, M.; Gao, K.; Chen, M.; Blandin, E.; Cortez-Resendiz, A.; Clawson, G.A.; Hong, L.E. Optimization of Neurite Tracing and Further Characterization of Human Monocyte-Derived-Neuronal-like Cells. *Brain Sci.* **2021**, *11*, 1372. [CrossRef] [PubMed]
33. Jeong, W.-H.; Kim, W.-I.; Lee, J.-W.; Park, H.-K.; Song, M.-K.; Choi, I.-S.; Han, J.-Y. Modulation of Long-Term Potentiation by Gamma Frequency Transcranial Alternating Current Stimulation in Transgenic Mouse Models of Alzheimer’s Disease. *Brain Sci.* **2021**, *11*, 1532. [CrossRef] [PubMed]
34. Chen, Y.; Lin, J.; Schlotterer, A.; Kurowski, L.; Hoffmann, S.; Hammad, S.; Dooley, S.; Buchholz, M.; Hu, J.; Fleming, I.; et al. MicroRNA-124 Alleviates Retinal Vasoregression via Regulating Microglial Polarization. *Int. J. Mol. Sci.* **2021**, *22*, 11068. [CrossRef]
35. Quirant-Sánchez, B.; Mansilla, M.J.; Navarro-Barriuso, J.; Presas-Rodríguez, S.; Teniente-Serra, A.; Fondelli, F.; Ramo-Tello, C.; Martínez-Cáceres, E. Combined Therapy of Vitamin D3-Tolerogenic Dendritic Cells and Interferon- β in a Preclinical Model of Multiple Sclerosis. *Biomedicines* **2021**, *9*, 1758. [CrossRef] [PubMed]
36. Polyák, H.; Galla, Z.; Nánási, N.; Cseh, E.K.; Rajda, C.; Veres, G.; Spekker, E.; Szabó, Á.; Klivényi, P.; Tanaka, M.; et al. The Tryptophan-Kynurenine Metabolic System Is Suppressed in Cuprizone-Induced Model of Demyelination Simulating Progressive Multiple Sclerosis. *Biomedicines* **2023**, *11*, 945. [CrossRef]
37. Tanaka, M.; Vécsei, L. Monitoring the Redox Status in Multiple Sclerosis. *Biomedicines* **2020**, *8*, 406. [CrossRef]
38. de Oliveira, M.; Santinelli, F.B.; Lisboa-Filho, P.N.; Barbieri, F.A. The Blood Concentration of Metallic Nanoparticles Is Related to Cognitive Performance in People with Multiple Sclerosis: An Exploratory Analysis. *Biomedicines* **2023**, *11*, 1819. [CrossRef]
39. Parolini, F.; Goethel, M.; Becker, K.; Fernandes, C.; Fernandes, R.J.; Ervilha, U.F.; Santos, R.; Vilas-Boas, J.P. Breaking Barriers: Artificial Intelligence Interpreting the Interplay between Mental Illness and Pain as Defined by the International Association for the Study of Pain. *Biomedicines* **2023**, *11*, 2042. [CrossRef]
40. Liu, N.; Li, Y.; Hong, Y.; Huo, J.; Chang, T.; Wang, H.; Huang, Y.; Li, W.; Zhang, Y. Altered brain activities in mesocorticolimbic pathway in primary dysmenorrhea patients of long-term menstrual pain. *Front. Neurosci.* **2023**, *17*, 1098573. [CrossRef]
41. Crosstalk between Depression, Anxiety, Dementia, and Chronic Pain: Comorbidity in Behavioral Neurology and Neuropsychiatry 2.0. Available online: https://www.mdpi.com/journal/biomedicines/special_issues/neuropsychiatry_2 (accessed on 5 October 2023).
42. Tajti, J.; Szok, D.; Csáti, A.; Szabó, Á.; Tanaka, M.; Vécsei, L. Exploring Novel Therapeutic Targets in the Common Pathogenic Factors in Migraine and Neuropathic Pain. *Int. J. Mol. Sci.* **2023**, *24*, 4114. [CrossRef] [PubMed]
43. Leone, G.E.; Shields, D.C.; Haque, A.; Banik, N.L. Rehabilitation: Neurogenic Bone Loss after Spinal Cord Injury. *Biomedicines* **2023**, *11*, 2581. [CrossRef] [PubMed]

44. Spekker, E.; Tanaka, M.; Szabó, Á.; Vécsei, L. Neurogenic Inflammation: The Participant in Migraine and Recent Advancements in Translational Research. *Biomedicines* **2022**, *10*, 76. [CrossRef] [PubMed]
45. Lamoine, S.; Cumenal, M.; Barriere, D.A.; Pereira, V.; Fereyrolles, M.; Prival, L.; Barbier, J.; Boudieu, L.; Brassat, E.; Bertin, B.; et al. The Class I HDAC Inhibitor, MS-275, Prevents Oxaliplatin-Induced Chronic Neuropathy and Potentiates Its Antiproliferative Activity in Mice. *Int. J. Mol. Sci.* **2022**, *23*, 98. [CrossRef]
46. Thabault, M.; Turpin, V.; Maisterrena, A.; Jaber, M.; Egloff, M.; Galvan, L. Cerebellar and Striatal Implications in Autism Spectrum Disorders: From Clinical Observations to Animal Models. *Int. J. Mol. Sci.* **2022**, *23*, 2294. [CrossRef]
47. Lee, G.A.; Lin, Y.-K.; Lai, J.-H.; Lo, Y.-C.; Yang, Y.-C.S.H.; Ye, S.-Y.; Lee, C.-J.; Wang, C.-C.; Chiang, Y.-H.; Tseng, S.-H. Maternal Immune Activation Causes Social Behavior Deficits and Hypomyelination in Male Rat Offspring with an Autism-Like Microbiota Profile. *Brain Sci.* **2021**, *11*, 1085. [CrossRef]
48. Abuaish, S.; Al-Otaibi, N.M.; Abujaamel, T.S.; Alzahrani, S.A.; Alotaibi, S.M.; AlShawakir, Y.A.; Aabed, K.; El-Ansary, A. Fecal Transplant and *Bifidobacterium* Treatments Modulate Gut *Clostridium* Bacteria and Rescue Social Impairment and Hippocampal BDNF Expression in a Rodent Model of Autism. *Brain Sci.* **2021**, *11*, 1038. [CrossRef]
49. Wei, Z.; Chen, Y.; Upende, R.P. Sleep Disturbance and Metabolic Dysfunction: The Roles of Adipokines. *Int. J. Mol. Sci.* **2022**, *23*, 1706. [CrossRef]
50. Garro-Martínez, E.; Fullana, M.N.; Florensa-Zanuy, E.; Senserrich, J.; Paz, V.; Ruiz-Bronchal, E.; Adell, A.; Castro, E.; Díaz, Á.; Pazos, Á.; et al. mTOR Knockdown in the Infralimbic Cortex Evokes a Depressive-like State in Mouse. *Int. J. Mol. Sci.* **2021**, *22*, 8671. [CrossRef]
51. Palotai, M.; Telegdy, G.; Ekwerike, A.; Jászberényi, M. The action of orexin B on passive avoidance learning. *Involv. Neurotransm. Behav. Brain Res.* **2014**, *272*, 1–7. [CrossRef]
52. Palotai, M.; Telegdy, G.; Jászberényi, M. Orexin A-induced anxiety-like behavior is mediated through GABA-ergic, α - and β -adrenergic neurotransmissions in mice. *Peptides* **2014**, *57*, 129–134. [CrossRef] [PubMed]
53. Bagosi, Z.; Palotai, M.; Simon, B.; Bokor, P.; Buzás, A.; Balangó, B.; Pintér, D.; Jászberényi, M.; Csabafi, K.; Szabó, G. Selective CRF2 receptor agonists ameliorate the anxiety- and depression-like state developed during chronic nicotine treatment and consequent acute withdrawal in mice. *Brain Res.* **2016**, *1652*, 21–29. [CrossRef] [PubMed]
54. Bagosi, Z.; Csabafi, K.; Palotai, M.; Jászberényi, M.; Földesi, I.; Gardi, J.; Szabó, G.; Telegdy, G. The effect of urocortin I on the hypothalamic ACTH secretagogues and its impact on the hypothalamic-pituitary-adrenal axis. *Neuropeptides* **2014**, *48*, 15–20. [CrossRef] [PubMed]
55. Bagosi, Z.; Czébély-Lénárt, A.; Karasz, G.; Csabafi, K.; Jászberényi, M.; Telegdy, G. The effects of CRF and urocortins on the preference for social novelty of mice. *Behav. Brain Res.* **2017**, *324*, 146–154. [CrossRef]
56. Hakamata, Y.; Hori, H.; Mizukami, S.; Izawa, S.; Yoshida, F.; Moriguchi, Y.; Hanakawa, T.; Inoue, Y.; Tagaya, H. Blunted diurnal interleukin-6 rhythm is associated with amygdala emotional hyporeactivity and depression: A modulating role of gene-stressor interactions. *Front. Psychiatry* **2023**, *14*, 1196235. [CrossRef]
57. Salafutdinov, I.I.; Gatina, D.Z.; Markelova, M.I.; Garanina, E.E.; Malanin, S.Y.; Gazizov, I.M.; Izmailov, A.A.; Rizvanov, A.A.; Islamov, R.R.; Palotás, A.; et al. A Biosafety Study of Human Umbilical Cord Blood Mononuclear Cells Transduced with Adenoviral Vector Carrying Human Vascular Endothelial Growth Factor cDNA In Vitro. *Biomedicines* **2023**, *11*, 2020. [CrossRef]
58. Ikonnikova, A.; Anisimova, A.; Galkin, S.; Gunchenko, A.; Abdukhalikova, Z.; Filippova, M.; Surzhikov, S.; Selyaeva, L.; Shershov, V.; Zasedatelev, A.; et al. Genetic Association Study and Machine Learning to Investigate Differences in Platelet Reactivity in Patients with Acute Ischemic Stroke Treated with Aspirin. *Biomedicines* **2022**, *10*, 2564. [CrossRef]
59. Rajkumar, R.P. Comorbid depression and anxiety: Integration of insights from attachment theory and cognitive neuroscience, and their implications for research and treatment. *Front. Behav. Neurosci.* **2022**, *16*, 1104928. [CrossRef]
60. Ironside, M.; DeVille, D.C.; Kuplicki, R.T.; Burrows, K.P.; Smith, R.; Teed, A.R.; Paulus, M.P.; Khalsa, S.S. The unique face of comorbid anxiety and depression: Increased interoceptive fearfulness and reactivity. *Front. Behav. Neurosci.* **2023**, *16*, 1083357. [CrossRef]
61. Yoshimura, R.; Okamoto, N.; Chibaatar, E.; Natsuyama, T.; Ikenouchi, A. The Serum Brain-Derived Neurotrophic Factor Increases in Serotonin Reuptake Inhibitor Responders Patients with First-Episode, Drug-Naïve Major Depression. *Biomedicines* **2023**, *11*, 584. [CrossRef]
62. Tortora, F.; Battipour, A.L.; Battaglia, S.; Falzone, A.; Avenanti, A.; Vicario, C.M. The Role of Serotonin in Fear Learning and Memory: A Systematic Review of Human Studies. *Brain Sci.* **2023**, *13*, 1197. [CrossRef]
63. Battaglia, M.R.; Di Fazio, C.; Battaglia, S. Activated Tryptophan-Kynurenine metabolic system in the human brain is associated with learned fear. *Front. Mol. Neurosci.* **2023**, *16*, 1217090. [CrossRef] [PubMed]
64. Tanaka, M.; Török, N.; Vécsei, L. Novel Pharmaceutical Approaches in Dementia. In *NeuroPsychopharmacotherapy*; Riederer, P., Laux, G., Nagatsu, T., Le, W., Riederer, C., Eds.; Springer: Cham, Switzerland, 2021.
65. Battaglia, S.; Di Fazio, C.; Vicario, C.M.; Avenanti, A. Neuropharmacological Modulation of N-methyl-D-aspartate, Noradrenaline and Endocannabinoid Receptors in Fear Extinction Learning: Synaptic Transmission and Plasticity. *Int. J. Mol. Sci.* **2023**, *24*, 5926. [CrossRef] [PubMed]
66. Battaglia, S.; Nazzi, C.; Thayer, J.F. Heart's tale of trauma: Fear-conditioned heart rate changes in post-traumatic stress disorder. *Acta Psychiatr. Scand.* **2023**, *in press*. [CrossRef] [PubMed]
67. Di Gregorio, F.; Battaglia, S. Advances in EEG-based functional connectivity approaches to the study of the central nervous system in health and disease. *Adv. Clin. Exp. Med.* **2023**, *32*, 607–612. [CrossRef]

68. Battaglia, S.; Nazzi, C.; Thayer, J.F. Fear-induced bradycardia in mental disorders: Foundations, current advances, future perspectives. *Neurosci. Biobehav. Rev.* **2023**, *149*, 105163. [CrossRef]
69. Tanaka, M.; Chen, C. Editorial: Towards a mechanistic understanding of depression, anxiety, and their comorbidity: Perspectives from cognitive neuroscience. *Front. Behav. Neurosci.* **2023**, *17*, 1268156. [CrossRef]
70. Tanaka, M.; Bohár, Z.; Vécsei, L. Are Kynurenes Accomplices or Principal Villains in Dementia? Maintenance of Kynurenine Metabolism. *Molecules* **2020**, *25*, 564. [CrossRef]
71. Manuello, J.; Costa, T.; Cauda, F.; Liloia, D. Six actions to improve detection of critical features for neuroimaging coordinate-based meta-analysis preparation. *Neurosci. Biobehav. Rev.* **2022**, *137*, 104659. [CrossRef]
72. Nani, A.; Manuello, J.; Mancuso, L.; Liloia, D.; Costa, T.; Vercelli, A.; Duca, S.; Cauda, F. The pathoconnectivity network analysis of the insular cortex: A morphometric fingerprinting. *Neuroimage* **2021**, *225*, 117481. [CrossRef]
73. Liloia, D.; Crocetta, A.; Cauda, F.; Duca, S.; Costa, T.; Manuello, J. Seeking Overlapping Neuroanatomical Alterations between Dyslexia and Attention-Deficit/Hyperactivity Disorder: A Meta-Analytic Replication Study. *Brain Sci.* **2022**, *12*, 1367. [CrossRef] [PubMed]
74. Kim, B.H.; Kim, S.H.; Han, C.; Jeong, H.G.; Lee, M.S.; Kim, J. Antidepressant-induced mania in panic disorder: A single-case study of clinical and functional connectivity characteristics. *Front. Psychiatry* **2023**, *14*, 1205126. [CrossRef] [PubMed]
75. Zakia, H.; Iskandar, S. Case report: Depressive disorder with peripartum onset camouflages suspected intracranial tuberculoma. *Front. Psychiatry* **2022**, *13*, 932635. [CrossRef] [PubMed]
76. Liloia, D.; Cauda, F.; Uddin, L.Q.; Manuello, J.; Mancuso, L.; Keller, R.; Nani, A.; Costa, T. Revealing the Selectivity of Neuroanatomical Alteration in Autism Spectrum Disorder via Reverse Inference. *Biol. Psychiatry Cogn. Neurosci. Neuroimaging* **2022**. [CrossRef] [PubMed]
77. Zhou, J.; Cao, Y.; Deng, G.; Fang, J.; Qiu, C. Transient splenic lesion syndrome in bipolar-II disorder: A case report highlighting reversible brain changes during hypomanic episodes. *Front. Psychiatry* **2023**, *14*, 1219592. [CrossRef] [PubMed]
78. Liloia, D.; Brasso, C.; Cauda, F.; Mancuso, L.; Nani, A.; Manuello, J.; Costa, T.; Duca, S.; Rocca, P. Updating and characterizing neuroanatomical markers in high-risk subjects, recently diagnosed and chronic patients with schizophrenia: A revised coordinate-based meta-analysis. *Neurosci. Biobehav. Rev.* **2021**, *123*, 83–103. [CrossRef]
79. Ippolito, G.; Bertaccini, R.; Tarasi, L.; Di Gregorio, F.; Trajkovic, J.; Battaglia, S.; Romei, V. The Role of Alpha Oscillations among the Main Neuropsychiatric Disorders in the Adult and Developing Human Brain: Evidence from the Last 10 Years of Research. *Biomedicines* **2022**, *10*, 3189. [CrossRef]
80. Di Gregorio, F.; La Porta, F.; Petrone, V.; Battaglia, S.; Orlandi, S.; Ippolito, G.; Romei, V.; Piperno, R.; Lullini, G. Accuracy of EEG Biomarkers in the Detection of Clinical Outcome in Disorders of Consciousness after Severe Acquired Brain Injury: Preliminary Results of a Pilot Study Using a Machine Learning Approach. *Biomedicines* **2022**, *10*, 1897. [CrossRef]
81. Battaglia, S.; Cardelicchio, P.; Di Fazio, C.; Nazzi, C.; Fracasso, A.; Borgomaneri, S. The Influence of Vicarious Fear-Learning in “Infecting” Reactive Action Inhibition. *Front. Behav. Neurosci.* **2022**, *16*, 946263. [CrossRef]
82. Baliellias, D.E.M.; Barros, M.P.; Vardaris, C.V.; Guariroba, M.; Poppe, S.C.; Martins, M.F.; Pereira, Á.A.F.; Bondan, E.F. Propentofylline Improves Thiol-Based Antioxidant Defenses and Limits Lipid Peroxidation following Gliotoxic Injury in the Rat Brainstem. *Biomedicines* **2023**, *11*, 1652. [CrossRef]
83. Park, S.Y.; Lee, S.P.; Kim, D.; Kim, W.J. Gut Dysbiosis: A New Avenue for Stroke Prevention and Therapeutics. *Biomedicines* **2023**, *11*, 2352. [CrossRef] [PubMed]
84. Younes, R.; Issa, Y.; Jdaa, N.; Chouaib, B.; Brugiotti, V.; Challuau, D.; Raoul, C.; Scamps, F.; Cuisinier, F.; Hilaire, C. The Secretome of Human Dental Pulp Stem Cells and Its Components GDF15 and HB-EGF Protect Amyotrophic Lateral Sclerosis Motoneurons against Death. *Biomedicines* **2023**, *11*, 2152. [CrossRef] [PubMed]
85. Nasini, S.; Tidei, S.; Shkodra, A.; De Gregorio, D.; Cambiaghi, M.; Comai, S. Age-Related Effects of Exogenous Melatonin on Anxiety-like Behavior in C57/B6 Mice. *Biomedicines* **2023**, *11*, 1705. [CrossRef] [PubMed]
86. Chen, B.; Hasan, M.M.; Zhang, H.; Zhai, Q.; Waliullah, A.S.M.; Ping, Y.; Zhang, C.; Oyama, S.; Mimi, M.A.; Tomochika, Y.; et al. UBL3 Interacts with Alpha-Synuclein in Cells and the Interaction Is Downregulated by the EGFR Pathway Inhibitor Osimertinib. *Biomedicines* **2023**, *11*, 1685. [CrossRef]
87. Inoue, G.; Ohtaki, Y.; Satoh, K.; Odanaka, Y.; Katoh, A.; Suzuki, K.; Tomita, Y.; Eiraku, M.; Kikuchi, K.; Harano, K.; et al. Sedation Therapy in Intensive Care Units: Harnessing the Power of Antioxidants to Combat Oxidative Stress. *Biomedicines* **2023**, *11*, 2129. [CrossRef]
88. Li, J.; Li, C.; Subedi, P.; Tian, X.; Lu, X.; Miriyala, S.; Panchatcharam, M.; Sun, H. Light Alcohol Consumption Promotes Early Neurogenesis Following Ischemic Stroke in Adult C57BL/6J Mice. *Biomedicines* **2023**, *11*, 1074. [CrossRef]
89. Cremone, I.M.; Nardi, B.; Amatori, G.; Palego, L.; Baroni, D.; Casagrande, D.; Massimetti, E.; Betti, L.; Giannaccini, G.; Dell’Osso, L.; et al. Unlocking the Secrets: Exploring the Biochemical Correlates of Suicidal Thoughts and Behaviors in Adults with Autism Spectrum Conditions. *Biomedicines* **2023**, *11*, 1600. [CrossRef]
90. Balogh, L.; Tanaka, M.; Török, N.; Vécsei, L.; Taguchi, S. Crosstalk between Existential Phenomenological Psychotherapy and Neurological Sciences in Mood and Anxiety Disorders. *Biomedicines* **2021**, *9*, 340. [CrossRef]

Disclaimer/Publisher’s Note: The statements, opinions and data contained in all publications are solely those of the individual author(s) and contributor(s) and not of MDPI and/or the editor(s). MDPI and/or the editor(s) disclaim responsibility for any injury to people or property resulting from any ideas, methods, instructions or products referred to in the content.



Article

Modeling Functional Limitations, Gait Impairments, and Muscle Pathology in Alzheimer's Disease: Studies in the 3xTg-AD Mice

Lidia Castillo-Mariqueo^{1,2}, M. José Pérez-García³ and Lydia Giménez-Llort^{1,2,*}

¹ Institut de Neurociències, Universitat Autònoma de Barcelona, 08193 Barcelona, Spain; lidia.castillom@e-campus.uab.cat

² Department of Psychiatry and Forensic Medicine, School of Medicine, Universitat Autònoma de Barcelona, 08193 Barcelona, Spain

³ Department of Neuroscience, Vall d'Hebron Research Institute, 08035 Barcelona, Spain; maria.perez@vhir.org

* Correspondence: lidia.gimenez@uab.cat

Abstract: Gait impairments in Alzheimer's disease (AD) result from structural and functional deficiencies that generate limitations in the performance of activities and restrictions in individual's biopsychosocial participation. In a translational way, we have used the conceptual framework proposed by the International Classification of Disability and Health Functioning (ICF) to classify and describe the functioning and disability on gait and exploratory activity in the 3xTg-AD animal model. We developed a behavioral observation method that allows us to differentiate qualitative parameters of psychomotor performance in animals' gait, similar to the behavioral patterns observed in humans. The functional psychomotor evaluation allows measuring various dimensions of gait and exploratory activity at different stages of disease progression in dichotomy with aging. We included male 3xTg-AD mice and their non-transgenic counterpart (NTg) of 6, 12, and 16 months of age (n = 45). Here, we present the preliminary results. The 3xTg-AD mice show more significant functional impairment in gait and exploratory activity quantitative variables. The presence of movement limitations and muscle weakness mark the functional decline related to the disease severity stages that intensify with increasing age. Motor performance in 3xTg-AD is accompanied by a series of bizarre behaviors that interfere with the trajectory, which allows us to infer poor neurological control. Additionally, signs of physical frailty accompany the functional deterioration of these animals. The use of the ICF as a conceptual framework allows the functional status to be described, facilitating its interpretation and application in the rehabilitation of people with AD.

Citation: Castillo-Mariqueo, L.; Pérez-García, M.J.; Giménez-Llort, L. Modeling Functional Limitations, Gait Impairments, and Muscle Pathology in Alzheimer's Disease: Studies in the 3xTg-AD Mice. *Biomedicines* **2021**, *9*, 1365. <https://doi.org/10.3390/biomedicines9101365>

Academic Editor: Masaru Tanaka

Received: 14 August 2021

Accepted: 26 September 2021

Published: 1 October 2021

Keywords: translational neuroscience; Alzheimer's disease; gait; muscular strength; muscular endurance; motor performance; frailty

Publisher's Note: MDPI stays neutral with regard to jurisdictional claims in published maps and institutional affiliations.



Copyright: © 2021 by the authors. Licensee MDPI, Basel, Switzerland. This article is an open access article distributed under the terms and conditions of the Creative Commons Attribution (CC BY) license (<https://creativecommons.org/licenses/by/4.0/>).

1. Introduction

Alzheimer's disease (AD) is a complex and heterogeneous disorder with a distinctive clinical presentation [1,2]. Motor and sensory alterations are less frequent but can appear in intermediate and advanced stages of the disease [3]. Although the main signs of AD are cognitive impairment, motor disorders such as bradykinesia, rigidity, and gait disorders are of great importance due to the functional limitations and impairments that they cause during the disease [4,5]. In this sense, different studies have demonstrated different motor alterations during the last two decades, particularly those associated with walking and displacement [6–8]. Thus, gait disorders in AD patients have been described within the group of alterations known as “frontal gait” and, in particular, gait in AD has been defined as “cautious gait” [5,9,10]. This gait pattern is similar to that observed in the aging; there may be decrease in speed, stride length, and postural stability of gait, which is manifested more specifically in static and dynamic balance, with a widened base of support [11].

Walking (gait) constitutes a biological activity of the human being [12]. It is complex, learned, and begins with a voluntary act [13]. The mode of locomotion allows one to move in a vertical position without getting too tired; it is composed of three essential phases: support, double support, and swing [14,15]. It implies a dynamic balance, which is constantly lost and recovered each time a step is performed [9,14]. While the bodyweight is supported by one leg, the other swings forward to initiate the next support, this action being fluid, rhythmic, and automatically synchronized [16]. Achieving these steps makes it possible to reveal different patterns that can determine the healthy state of gait related to the physical health of individuals and, in particular, of older adults [17,18].

The gait pattern evolves through the different age groups; thus, in adolescents and young adults, it is characterized by a certain lightness, flexibility, and agility, qualities that will diminish as the years go by [19–21]. During aging, these parameters will change around 60 and 70 years of age, where the physiological process causes these changes to be progressive and of varying severity depending on the degree of alterations that may occur [20]. Even healthy people over the age of 65 show some decrease in performance on the timed walking test (TUG) and the 6 min walk test (6MWT) [22]. Lower mobility test scores in healthy older people have been shown to predict the development of future mobility limitations [23].

On the other hand, muscle strength is relevant to gait performance [24]. Some studies have reported that older adults' decreased muscle strength and gait speed were associated with poor cognition [25,26]. From the early stages of AD, a decrease in muscle strength can be observed even without loss of muscle mass, progressing to a loss of both in moderate stages [27]. However, optimal muscle strength and physical activity level are related to better performance on cognitive and learning tests in older adults with mild to moderate cognitive impairment who live in nursing homes [28].

In this way, sarcopenia is closely related to dementia, particularly AD, although few studies examine its prevalence and associated factors [27]. Poor muscle function, but not reduced lean muscle mass, drives the association of sarcopenia with cognitive decline in old age [29]. It needs more scientific studies that identify the characteristics of the muscular structure related to sarcopenia that identifies older adults at risk of cognitive deterioration in old age.

The present work proposes translating the International Classification of Functioning, Disability, and Health (ICF) conceptual framework to classify and describe functioning and disability in gait and exploratory activity in the 3xTg-AD animal model and its non-transgenic counterpart with normal aging. We developed a method for the characterization of qualitative parameters of psychomotor performance in the gait pattern of male mice in different stages of the disease: initial (6 months), advanced beta (12 months), and advanced beta-tau (16 months) in contrast with normal aging.

2. Materials and Methods

2.1. Animals

A total of forty-five homozygous 3xTg-AD ($n = 24$) and non-transgenic (NTg, $n = 21$) male mice of 6, 12, and 16 months of age in a C57BL/6J background (the transfer is accomplished by at least ten cycles of backcrossing) established at the Universitat Autònoma de Barcelona [30] were used in this study. As previously described, the 3xTg-AD mice harboring transgenes were genetically modified at the University of California at Irvine [31]. Animals were kept in groups of 3–4 mice per cage (Macrolon, $35 \times 35 \times 25$ cm, Panlab, SL, Barcelona, Spain) filled with 5 cm of clean wood cuttings (Ecopure, Chips6, Date Sand, UK; uniform cross-sectional wood granules with 2.8–1.0 mm chip size) and nesting materials (Kleenex, Art: 08834060, 21 cm \times 20 cm, White). In all cases, standard home cages covered with a metal grid allow the perception of olfactory and auditory stimuli from the rest of the colony. All animals were kept under standard laboratory conditions of food and water *ad libitum*, 20 ± 2 °C, 12 h light cycle: dark with lights on at 8:00 a.m. and 50–60% relative humidity. All procedures followed the Spanish legislation on "Protection of animals used

for experimental and other scientific purposes” and the EU Directive (2010/63/EU) on this issue. The study complies with the ARRIVE guidelines developed by the NC3Rs and aims to reduce the number of animals used [32].

2.2. Experimental Design

A cross-sectional study of 3 cohorts of 3xTg-AD and NTg male mice was carried out. The first group includes 6-month-old mice of both genotypes, the second 12-month-old, and the third 16-month-old. They were temporarily included in two batches once they reached the required study age. The evaluation of the gait and exploratory activity was carried out in two evaluation days.

2.3. Behavioral Assessments

In a translational approach, the concepts proposed in ICF have been incorporated to describe the factors that functionally intervene in spontaneous gait and exploratory activity. They have been included in this way: “Activity” describes the shape and quantification of the trajectory and displacement. “Body function” allows a description of the movement pattern and the associated muscular strength. Finally, “Body structure” gives an account of the state in which muscle groups and joints are found in our object of study. In the same way, we have included the concepts that account for disability in the assessed tasks, activity limitations, and body function and structure impairments (see Figure 1).

Behavioral evaluations were performed in two days. During the morning, the tests were carried out; 30 min were allowed to habituate the animals in the test room before starting the measurements. The evaluation protocol, bizarre behaviors registered, the physical phenotype of frailty, gait, and Rotarod used here were recently reported in Castillo-Mariqueo and Gimenez-Llort’s 2021 study [33]. In addition, videos of gait were taken for posterior analysis with KINOVEA version 0.8.15 free software.

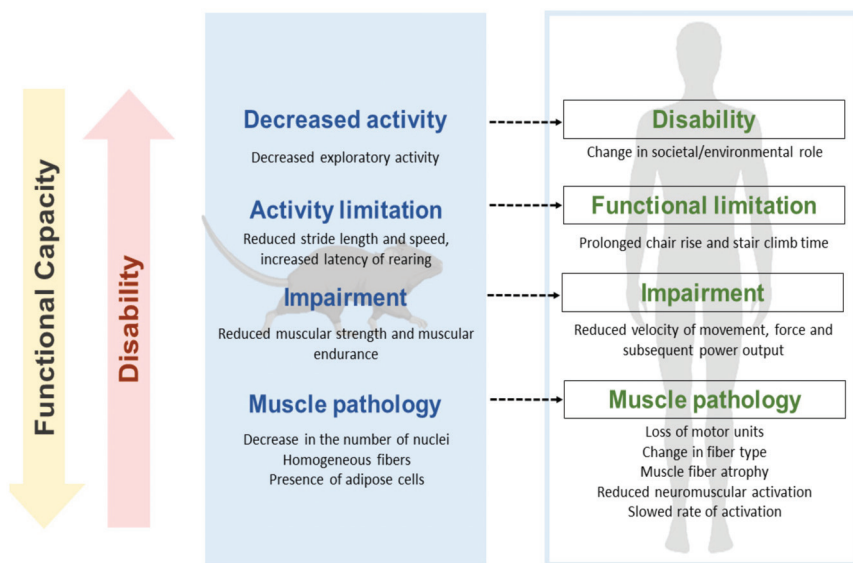


Figure 1. Proposal for a translational approach to motor dysfunction at different levels of disability. The figure details in a translational way the equivalence of the disability process from the 3xTg-AD mouse model to that expected in humans. It exemplifies a pathway that links pathology, deficiencies, functional limitations, and disability of gait and exploration (it has been adapted from Verbrugge and Jette, 1994; and Reid and Fielding, 2012) [34,35].

2.3.1. Activity—Spontaneous Gait and Exploration

The animals' spontaneous gait and exploratory activity were filmed from the undersurface [36] and a transverse plane that allowed the registration of the legs and the trajectory during the test. Each mouse was placed in a 27.5×9.5 cm transparent housing box, and gait performance was directly observed for one minute. The KINOVEA 8.15 software was used for the quantification and analysis of the gait trajectory.

Quantitative parameters of gait. The quantitative parameters were measured according to the Castillo-Mariqueo and Gimenez-Llort protocol 2021 [33]. Stride length, stride length variability, speed, and acceleration were included according to the methodology used by Wang et al. in 2017 [35].

Exploration includes body position, limb support, and moving around. The exploratory activity was recorded in parallel with spontaneous walking through video analysis and direct observation. For one minute, freezing or movement latency, the latency of the first rearing, the number of scans on the horizontal axis (corners visited), and scans on a vertical axis were recorded, taking the hind legs (rearings) as reference. During the tests, defecation and urination were also recorded.

2.3.2. Body Function—Mobility and Muscular Strength

General mobility includes bizarre gait patterns and freezing. For the discrimination of bizarre gait patterns, the trajectory of each route was differentiated according to the form of displacement, being able to be straight, scanning, backward, or circling. Then, the postural pattern of movement is differentiated: normal, shrink, or stretching. The movements were visually analyzed through videos and direct observation in the trajectory of the forward displacement in the transverse and sagittal planes. Their presence or absence was recorded for each one [33].

Forelimb grip strength-Hanger Test. The muscular strength of the forelimbs was measured using the hanger test, which is based on the tendency of a mouse to grasp a bar when suspended by the tail instinctively. We have replicated the methodology previously described by our group [33,37]. Muscle strength was measured on the second day of assessment.

2.3.3. Body Structure—Joints and Muscles

Joints to detect kyphosis. Kyphosis was differentiated into postural and structural, according to the analysis method established in previous research by our laboratory [38]. Kyphosis was measured during spontaneous locomotion and later confirmed in postural inspection (using joints and thoracic–lumbar structure as references), assigning a score from 0 to 2, where 0 indicates the absence of kyphosis, 1 indicates postural kyphosis, and 2 indicates structural kyphosis.

Muscles related to sarcopenia. The animals were sacrificed and subjected to necropsy to extract the quadriceps and triceps surae muscles, and these were subsequently weighed individually. The “sarcopenia index” [38] was applied to obtain an indirect measure of sarcopenia as a biological marker of frailty.

Morphological features of quadriceps and triceps surae. A qualitative evaluation of longitudinal sections of quadriceps and triceps surae stained with hematoxylin and eosin (H&E) was performed. The muscles were dissected and fixed with 10% formalin (Sigma-Aldrich, Saint Louis, MO, USA) for 24 h and then embedded in paraffin for further analysis. Histological sections of 5 μ m were stained with a standard H&E method. We used the standard protocol of the Laboratory of Microscopic Anatomy of the Department of Morphological Sciences of the Autonomous University of Barcelona. Sections were first rehydrated by passing them through decreasing concentrations of Ethanol (EtOH) (absolute and 96°). The sections were incubated in Harris hematoxylin (Merck-Sigma Aldrich, St. Louis, MO, USA) for 10 min and washed under running water for 5 min. Because Mayer Hematoxylin was used, a de-differentiation process was needed, with consecutively Et-OH-HCl (2.5%) and ammonia water (0.3%) solutions. After this, sections were incubated

in Eosin Y (Merck-Sigma Aldrich) for 5 min, previously acidified with glacial acetic acid. Finally, the sections were dehydrated by passing them through increasing concentrations of EtOH and cleared in Xylol, and mounted with DPX (PanReac AppliChem, ITW reagents, IL, USA). The images were taken with 20X objective on a Nikon Eclipse 80i microscope, using a digital camera running on the control software ACT-1 (ver2.70) (Nikon Instruments Inc., Tokyo, JP). Characteristics of location and number of nuclei, fibers' distribution and shape, and adipose tissue were identified. A generic description and qualifier of intensity were given with five levels represented by (+) for the quantity graduation.

2.3.4. Motor Performance, Geotaxis, and Hindlimb Claspings

Additionally, motor learning, physical endurance, geotaxis, and hindlimb claspings were evaluated to show functional impairment related to gait and exploratory activity, according to the protocol developed by Castillo-Mariquero, Giménez-Llort, 2021 [33]. In the present work, we have adopted the protocol combining learning and physical endurance. Thus, motor learning was evaluated in the constant mode and physical resistance in the accelerated mode of the Rotarod apparatus (Ugo basile[®], Mouse RotaRod NG). We recorded the number of trials until reaching over 60 s of permanence on the wheel to measure learning. Subsequently, after 2 min of rest, we carried out a single trial in the accelerated mode to assess physical endurance.

2.4. Statistics

Statistical analyses were performed using SPSS 15.0 software. Results were expressed as the mean \pm standard error of the mean (SEM) for each task and trial. Gait, exploration, forelimb grip strength, muscles (sarcopenia), motor performance, and geotaxis were analyzed with one-way ANOVA followed by post hoc Bonferroni. In addition, the effect of Genotype (G) and Age (A) in each of them was identified. The incidence and prevalence of body position, general mobility, kyphosis, and hindlimb claspings were analyzed using the Chi-square test or Fisher's exact test. Additionally, the relationship between activity limitation and restriction (presence/absence) with stride length, speed, and cadence was analyzed with the Point-Biserial Correlation. The horizontal and vertical exploration and rearing latency were also related to the deficiencies in exploration and gait. The survival curve of both genotypes was analyzed with the Kaplan–Meier test (Log Rank). In all cases, statistical significance was considered at $p < 0.05$.

3. Results

As shown in Table 1, we have proposed a translational approach for the interpretation of the results obtained in the measurement of gait and exploratory activity in the 3xTg-AD mouse model in different stages of the disease and its counterpart NTg of normal aging, according to the analysis and quantification parameters proposed by ICF.

3.1. Activity—Spontaneous Gait and Exploration

As illustrated in Figure 2, the quantitative parameters of gait show a tendency to increase stride length in 3xTg-AD animals, although they are not statistically significant (stride length (cm), NTg 6 months: 4.48 ± 0.20 ; NTg 12 months: 4.24 ± 0.95 ; NTg 16 months: 3.84 ± 0.68 ; 3xTg-AD 6 months: 1.92 ± 0.57 ; 3xTg-AD 12 months: 3.09 ± 0.54 ; 3xTg-AD 16 months: 4.36 ± 0.48). Although the differences between NTg ages do not reach statistical significance, we can observe that stride length remains relatively stable as age increases, while in the 3xTg-AD group they present differences between the ages since the 95% confidence interval does not overlap between 6 months, 12 months, and 16 months (6 months, $1.92 + 0.57 = 2.49$; 12 months, $3.09 - 0.57 = 2.52$; 16 months, $3.84 + 0.68 = 4.52$).

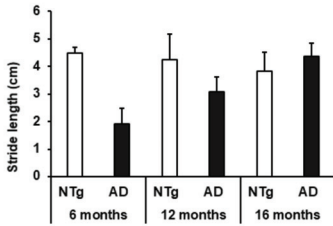
Table 1. Proposal to functional analysis to mimics capacities and disabilities from humans in mice.

Translational Functioning and Disability (ICF)						
<ul style="list-style-type: none"> ACTIVITY—Spontaneous gait and exploration 	NTg Mice			3xTg-AD Mice		
	6 Months	12 Months	16 Months	6 Months	12 Months	16 Months
1. Quantitative parameters of gait (see Figure 2)						
A. Stride length (cm)	ABSENT	MILD	MILD	MODERATE	MODERATE	MILD
B. Variability of stride length (%)	ABSENT	ABSENT	MILD	SEVERE	MODERATE	MODERATE
C. Speed (cm/s)	ABSENT	ABSENT	MILD	SEVERE	SEVERE	MODERATE
D. Cadence (steps/s)	ABSENT	ABSENT	ABSENT	SEVERE	MODERATE	MODERATE
2. Body position (see Figure 2)						
E. Maintaining body position (%)	ABSENT	ABSENT	ABSENT	ABSENT	ABSENT	MILD
3. Limb support						
F. Base of support (cm)	ABSENT	ABSENT	MILD	ABSENT	ABSENT	ABSENT
4. Exploration (see Figure 2)						
G. Vertical and horizontal activity (n episodes)	MILD	MILD	MILD	MODERATE	SEVERE	MILD
H. Rearing latency (s)	MILD	MODERATE	SEVERE	COMPLETE	SEVERE	MODERATE
BODY FUNCTION—mobility and forelimb grip strength						
1. General mobility (see Figure 3)						
A. Bizarre gait patterns (incidence %)	MILD	MODERATE	MILD	MODERATE	MODERATE	MILD
B. Freezing (movement latency)	ABSENT	MODERATE	MILD	MODERATE	MODERATE	MILD
C. Freezing—latency movement	ABSENT	MODERATE	MILD	MODERATE	MODERATE	MILD
2. Forelimb grip strength—Hanger Test (see Figure 3)						
D. Muscular Strength (latency)	ABSENT	MILD	MODERATE	MILD	MODERATE	MODERATE
E. Muscular Strength (distance)	ABSENT	MILD	SEVERE	MILD	SEVERE	MODERATE
F. Muscular Endurance (latency)	ABSENT	MODERATE	SEVERE	MILD	SEVERE	SEVERE
G. Muscular Endurance (distance)	ABSENT	MODERATE	SEVERE	MODERATE	SEVERE	SEVERE
BODY STRUCTURE—joints and muscles						
1. Joints (see Figure 4)						
A. Kyphosis prevalence	ABSENT	MODERATE	MODERATE	MILD	MILD	MILD
2. Muscles (see Figure 4)						
B. Quadriceps muscle (weight)	MILD	MILD	MILD	ABSENT	MILD	MODERATE
C. Triceps surae muscle (weight)	MILD	MILD	MILD	MILD	MILD	MODERATE
D. Sarcopenia index—Quadriceps	MILD	MILD	MILD	ABSENT	MILD	MODERATE
E. Sarcopenia index—Triceps	MILD	MILD	MILD	MILD	MILD	MODERATE
Qualifiers:	Generic qualifier with the negative scale used to indicate the extent or magnitude of an impairment: NO impairment, (absent) 0–4%; MILD impairment, (slight, low) 5–24%; MODERATE impairment, (medium, fair) 25–49%; SEVERE impairment, (high, extreme), 50–95%; COMPLETE impairment, (total) 96–100%—not specified in the ICF for humans. Activity limitations are difficulties an individual may have in executing activities: NO difficulty, (absent) 0–4%; MILD difficulty, (slight, low) 5–24%; MODERATE difficulty, (medium, fair) 25–49%; SEVERE difficulty, (high, extreme) 50–95%; COMPLETE difficulty, (total) 96–100%—not specified in the ICF for humans.					

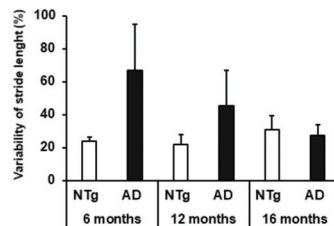
Table 1. Outcome measures that link gait and exploration impairments and limitations of male 3xTg-AD mice at different stages of AD progression to describe the functioning, according to qualifiers of ICF. Translational Functioning and Disability: ACTIVITY—spontaneous gait and exploration, BODY FUNCTION—mobility and forelimb grip strength, and BODY STRUCTURE—joints and muscles. Absent (green), Mild (light green), Moderate (yellow), Severe (orange), and Complete (red).

1. Quantitative parameters of gait

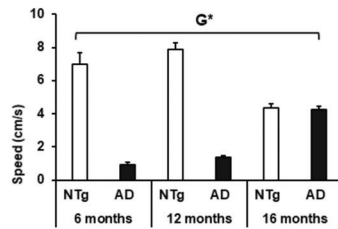
A. Stride length



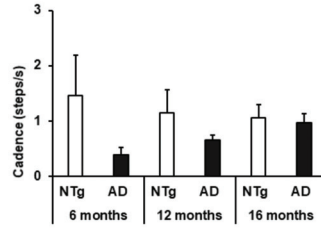
B. Variability of stride length



C. Speed

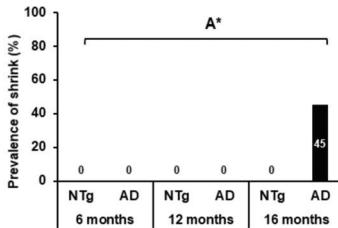


D. Cadence



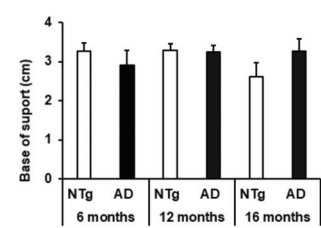
2. Body position

E. Maintaining body position



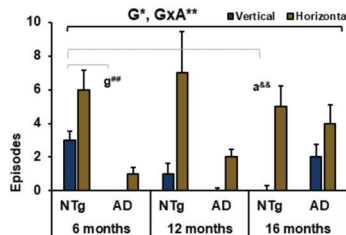
3. Limb support

F. Base of support



4. Exploration

G. Vertical and horizontal activity



H. Rearing latency

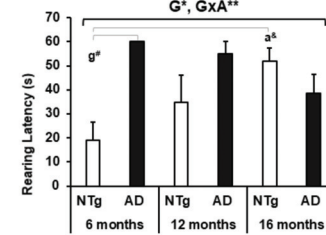


Figure 2. ACTIVITY: Spontaneous gait and exploration. 1. Quantitative parameters of gait; (A) stride length; (B) variability of stride length; (C) speed; (D) cadence. 3. Limb support. (F) Base of support. 4. Exploration. (G) Vertical and horizontal activity; (H) rearing latency. The results are expressed as mean ± SEM. Statistics: one-way ANOVA, Age effect expressed as (A); Genotype effect expressed as (G); Genotype and Age interaction effect is expressed as (GxA); * $p < 0.05$, ** $p < 0.01$ followed by post hoc Bonferroni test, * $p < 0.05$, ** $p < 0.01$; differences between NTg vs. 3xTg-AD are expressed (g): # $p < 0.05$, ### $p < 0.01$; differences between age in each group are expressed (a): & $p < 0.05$, && $p < 0.01$. 2. Body position; (E) maintaining body position, the results are expressed as prevalence (%). Statistics: Fisher’s exact test, Age effect are expressed as (A), Genotype effect are expressed as (G); Genotype and Age interaction effect are expressed as (GxA); * $p < 0.05$ and ** $p < 0.01$.

On the other hand, in the exploration, the animals differed in their performance in horizontal and vertical activity (horizontal activity, ANOVA $F(5,39) = 2.427, p = 0.050$; vertical activity, ANOVA $F(5,39) = 4.600, p = 0.002$). Genotype differences can be noted in each age group with a lower performance in 3xTg-AD animals (horizontal activity: genotype differences, ANOVA $F(1,44) = 9.548, p = 0.004$). Likewise, we can evidence a genotype difference in vertical activity (vertical activity: genotype differences, ANOVA $F(1,44) = 7.209, p = 0.011$) and a significant difference at the age of 6 months between the groups (Bonferroni post hoc: NTg 6 months vs. 3xTg-AD 6 months, $p = 0.004$). It was also detected that at an older age in the normal aging group there is a decrease in vertical activity (Bonferroni post hoc: NTg 6 months vs. NTg 16 months, $p = 0.012$). In turn, the genotype per age interaction (GxA) show the decrease in the vertical exploratory activity of NTg versus 3xTg-AD (GxA, ANOVA, $F(2,43) = 8.519, p = 0.001$), see Figure 2G (Exploration). The first time they perform vertical activity (latency of the first rearing) is also determined by the genotype and its interaction with age, highlighting that the group of 3xTg-AD mice at the age of 6 months did not register this activity and that in the animals NTg latency increases with age progressively (rearing latency, ANOVA $F(5,39) = 4120, p = 0.004$ post hoc NTg 6 months vs. 3xTg-AD 6 months, $p = 0.010$; NTg 6 months vs. NTg 16 months, $p = 0.026$. Genotype differences, ANOVA $F(1,44) = 6.443, p = 0.015$, GxA differences, $F(2,43) = 8330, p = 0.001$) (see Figure 2H (Exploration)).

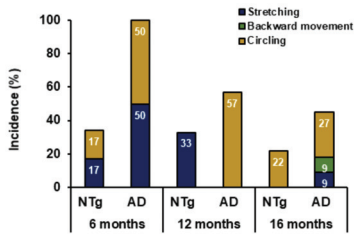
3.2. Body Function—Mobility and Muscular Strength

As shown in Figure 3, the animals exhibited a series of bizarre behaviors called bizarre gait patterns. There is a high incidence of circling in 3xTg-AD animals (3xTg-AD: 6 months 3/6 (50%), 12 months 4/7 (57%), 16 months 3/11 (27%)); despite not being statistically significant, its presence can modify performance in gait and exploration, which are described later (see Figure 5). It can also be seen that this behavior appears in NTg animals with a lower incidence (NTg: 6 months 1/6 (17%), 16 months 2/9 (22%)). Stretching (NTg: 6 months 1/6 (17%), 12 months 2/6 (33%)—3xTg-AD: 6 months 3/6 (50%), 16 months 1/11 (9%)), and in animals 3xTg-AD 16 months backward movement [1/11 (17%)], see Figure 3A. In addition, a high incidence of freezing was evidenced in which as age increases, its incidence decreases regardless of genotype (Fisher exact test, $p = 0.032$). It is also appreciated that the time invested in this behavior varies with age, being less at 16 months without genotype effect and higher at 12 months (ANOVA, $F(2,43) = 3.473, p = 0.041$), (see Figure 3B,C).

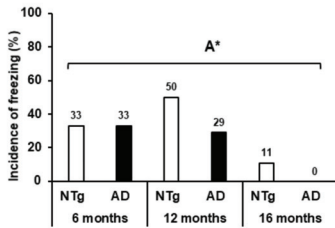
Additionally, we have detected a correlation between the incidence of these behaviors and performance in gait and exploration, as shown in Figure 4. Thus, the variables stride length, speed, and cadence negatively correlate with the presence of bizarre gait pattern, causing limitation in the displacement and trajectory of gait (stride length, Pearson: $r2 = (-) 0.294, p < 0.0001$. Speed, Pearson: $r2 = (-) 0.462, p < 0.0001$. Cadence, Pearson: $r2 = (-) 0.348, p < 0.0001$), see Figure 4A–C. While the horizontal and vertical exploration variables correlate negatively, rearing latency does so positively with the presence of bizarre gait pattern, which leads to a restriction to the performance of these behaviors (horizontal activity, Pearson $r2 = (-) 0.156, p = 0.008$. Vertical activity, Pearson: $r2 = (-) 0.118, p = 0.021$. Rearing latency, Pearson: $r2 = 0.098, p = 0.035$) (see Figure 4D–F).

1. General mobility

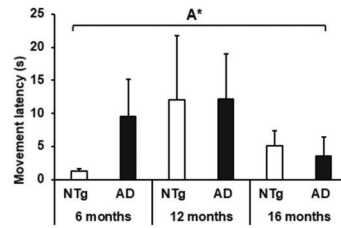
A. Bizarre gait patterns



B. Incidence of freezing

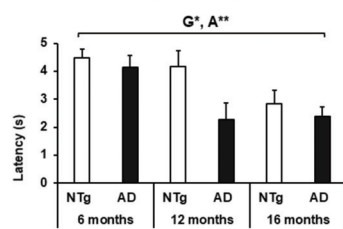


C. Freezing – latency movement

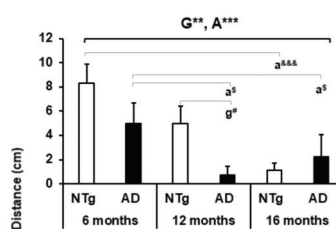


2. Forelimb grip strength – Hanger Test

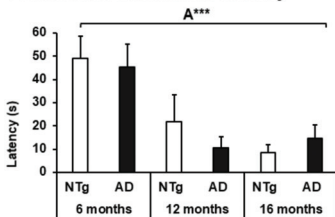
D. Muscular Strength–latency



E. Muscular Strength–distance



F. Muscular Endurance–latency



G. Muscular Endurance–distance

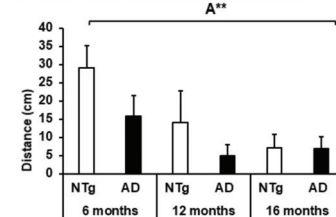


Figure 3. BODY FUNCTION—mobility and forelimb grip strength. 1. General mobility. (A) Bizarre gait patterns; (B) incidence of freezing; the results are expressed as incidence (%). Statistics: Fisher’s exact test, Age effect is expressed as (A); Genotype effect is expressed as (G); Genotype and Age interaction effect is expressed as (GxA); * $p < 0.05$, ** $p < 0.01$ and *** $p < 0.001$. (C) Freezing—latency movement; 2. Forelimb grip strength—Hanger Test. (D) Muscular Strength—latency; (E) Muscular Strength—distance; (F) Muscular Endurance—latency; (G) Muscular Endurance—distance, the results are expressed as mean \pm SEM. Statistics: one-way ANOVA, Age effect expressed as (A); Genotype effect expressed as (G); Genotype and Age interaction effect is expressed as (GxA). * $p < 0.05$, ** $p < 0.01$, and *** $p < 0.001$ followed by post hoc Bonferroni test, * $p < 0.05$, ** $p < 0.01$, and *** $p < 0.001$; differences between NTg vs. 3xTg-AD are expressed (g): # $p < 0.05$; differences between age in NTg group are expressed (a): & & $p < 0.001$, and for 3xTg-AD group are expressed (a): § $p < 0.01$.

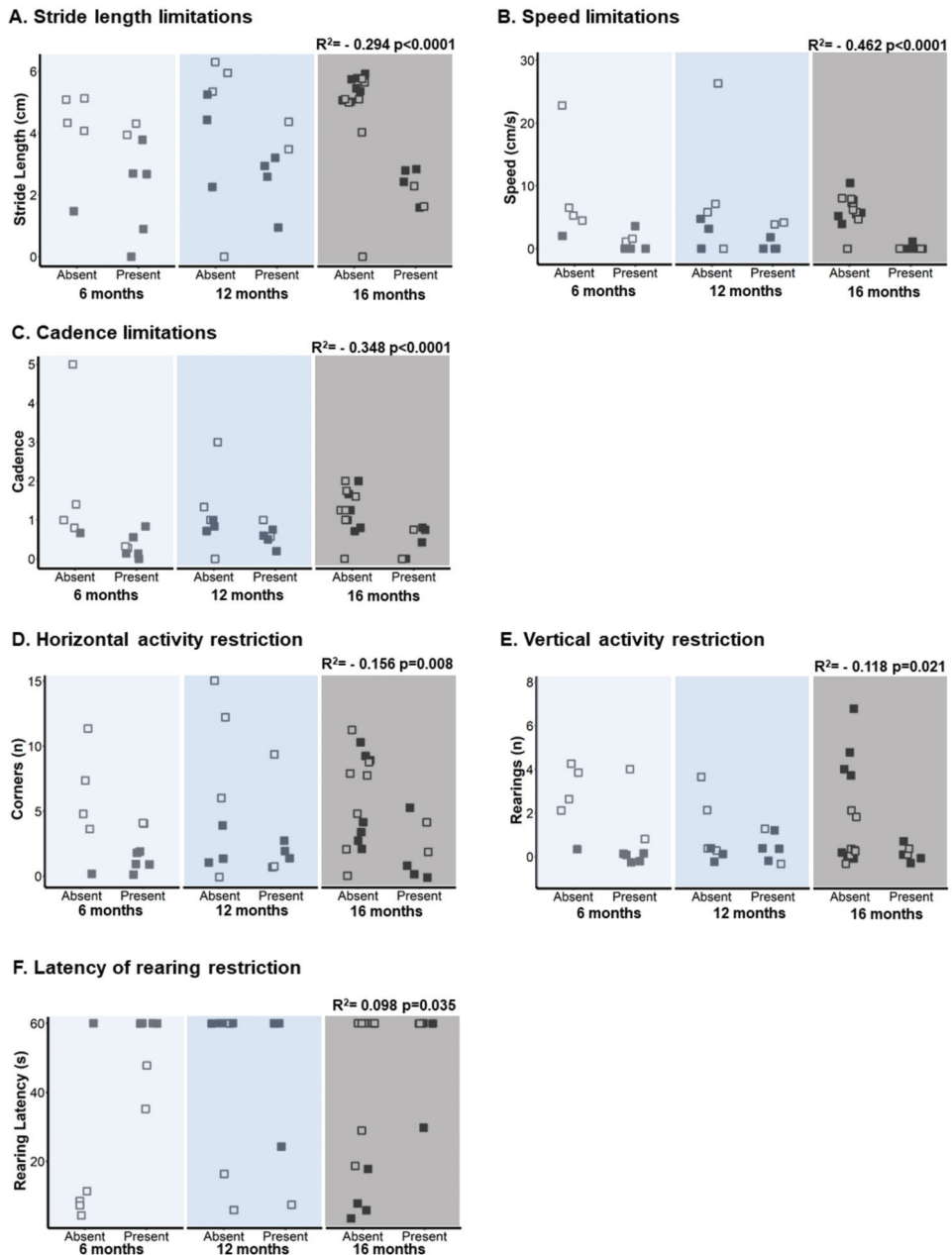


Figure 4. Activity limitations and restrictions of gait and exploration. (A) Stride length limitations, (B) speed limitations, (C) cadence limitations, (D) horizontal activity restriction, (E) vertical activity restriction, and (F) latency of rearing restriction. The NTg group has been represented by a white square and the 3xTg-AD group by a black square. According to the groups under study, it has been defined as “present/absent” the behaviors reported as bizarre gait patterns of each animal. The Point-Biserial Correlation has been applied to determine the relationship between the activity limitation and restriction (presence/absence) with stride length, speed, and cadence and exploration. Statistics: Pearson r^2 .

Muscle strength, on the other hand, was lower in older animals, and the transgenic genotype at each age was lower than the non-transgenic genotype at all ages (Muscular strength—latency: ANOVA $F(5,39) = 4.385, p = 0.003$; Age effect, $F(2, 43) = 5.702, p = 0.007$; Genotype effect, $F(1,44) = 5.895, p = 0.020$). In the same way, it can be noted that the distance reached when the animals move on the bar was less as age increases and the 3xTg-AD mice were lower than the NTg at 6 and 12 months; otherwise, it occurs at 16 months, but it is not statistically significant (muscular strength—distance: ANOVA $F(5,39) = 9.847, p < 0.0001$ post hoc NTg 6 months vs. NTg 16 months $p < 0.0001$; 3xTg-AD 6 months vs. 3xTg-AD 16 months $p = 0.023$; 3xTg-AD 6 months vs 3xTg-AD 12 months $p = 0.050$; NTg 12 months vs 3xTg-AD 12 months, $p = 0.045$). Age effect $F(2,43) = 17,320 p < 0.0001$. Genotype effect $F(1,44) = 11.786 p = 0.001$, see Figure 3D,E. At the same time, the muscular endurance and the distance of displacement was determined by the age of the animals decreasing as the age increases in both groups (muscular endurance—latency: ANOVA $F(5,39) = 3.296, p = 0.014$. Age effect, $F(2,43) = 8,154, p = 0.001$. Muscular endurance—distance ANOVA $F(5,39) = 3.394, p = 0.012$. Age effect, $F(2,43) = 7.295, p = 0.002$) (see Figure 3F,G).

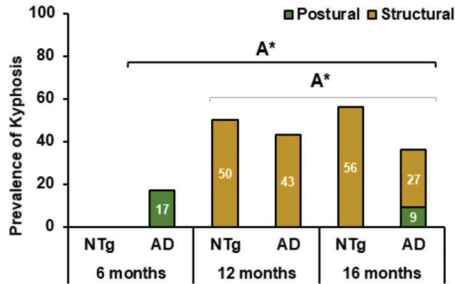
3.3. Body Structure—Joints and Muscles

The most prevalent postural alteration was kyphosis, with structural kyphosis having the highest incidence in older animals regardless of genotype (Kyphosis prevalence, age differences Fisher exact test $p = 0.025$. Structural kyphosis incidence, age differences $p = 0.016$), see Figure 5A. This joint deformation was observed at the thoracolumbar level.

At the level of muscle tissue, the quadriceps presented variations in weight, with a tendency to decrease with age determined by the GxA interaction and a significant decrease between the 3xTg-AD of 6 months versus 16 months (quadriceps, ANOVA $F(5, 39) = 4.314, p = 0.003$, post hoc 3xTg-AD 6 months vs. 3xTg-AD 16 months, $p = 0.001$. Age effect, $F(2,43) = 5.715, p = 0.007$. GxA effect, $F(2,43) = 4.291, p = 0.021$), see Figure 5B. In the triceps surae muscle, no statistically significant differences were detected; it can be seen that all groups, regardless of age, seem to maintain a similar weight range, see Figure 5C. When applying the indirect measure of sarcopenia, the differences in quadriceps were maintained (sarcopenia Index—quadriceps: ANOVA $F(5,39) = 6.705, p < 0.0001$, post hoc 3xTg-AD 6 months vs. 3xTg-AD 16 months $p < 0.0001$. Age effect $F(2,43) = 9.693, p < 0.0001$. GxA effect $F(2,43) = 5.623, p = 0.007$), see Figure 5D. On the other hand, when applying this method in the triceps sural muscle, it was possible to distinguish a GxA interaction effect, where at six months, the 3xTg-AD mice present greater weight and decrease with age, and in the case of the NTg, this is maintained stable (sarcopenia index—triceps surae: ANOVA $F(5,39) = 4.160 p = 0.004$ post hoc 3xTg-AD 6 months vs. 3xTg-AD 16 months $p = 0.010$. NTg 16 months vs. 3xTg-AD 16 months $p = 0.020$. GxA effect, $F(2,43) = 3.917 p = 0.028$), see Figure 5E. Figure 6A,B illustrates the morphological characteristics of the quadriceps and triceps surae. Table 2 depicts the characteristics of the nucleus, fiber, and adipose tissue.

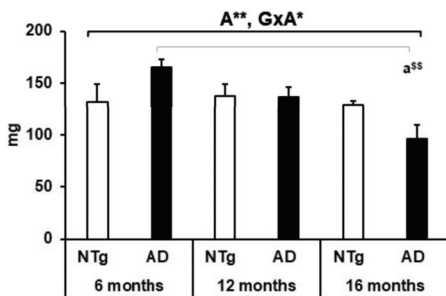
1. Joints (Kyphosis)

A. Kyphosis prevalence

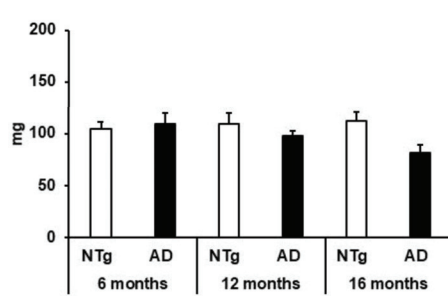


2. Muscles (sarcopenia)

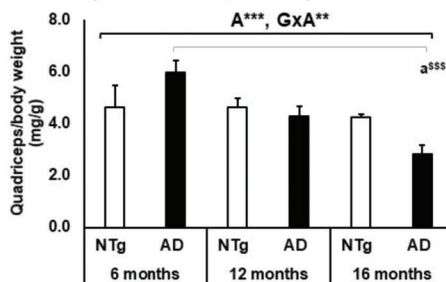
B. Quadriceps muscle (weight)



C. Triceps surae muscle (weight)



D. Sarcopenia index Quadriceps



E. Sarcopenia index Triceps surae

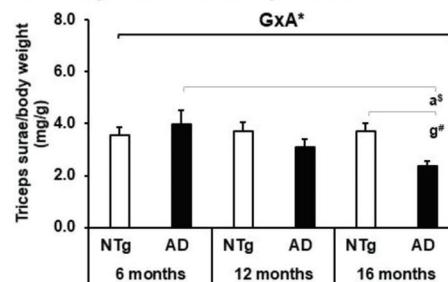


Figure 5. BODY STRUCTURE—joints and muscles. 1. Joints (Kyphosis), (A) kyphosis prevalence, the results are expressed as prevalence (%). Statistics: Fisher’s exact test; Age effect is expressed as (A); * $p < 0.05$. 2. Muscles (sarcopenia), (B) quadriceps muscle (weight); (C) triceps surae muscle (weight); (D) Sarcopenia index Quadriceps; (E) Sarcopenia index Triceps surae; the results are expressed as mean \pm SEM. Statistics: one-way ANOVA, Age effect expressed as (A); Genotype effect expressed as (G); Genotype and Age interaction effect is expressed as (GxA). * $p < 0.05$, ** $p < 0.01$ and *** $p < 0.001$ followed by post-hoc Bonferroni test, * $p < 0.05$, ** $p < 0.01$, and *** $p < 0.001$; differences between NTg vs. 3xTg-AD are expressed (g): # $p < 0.05$, differences between age in 3xTg-AD group are expressed (a): \$ $p < 0.01$, \$\$ $p < 0.01$, and \$\$\$ $p < 0.001$.

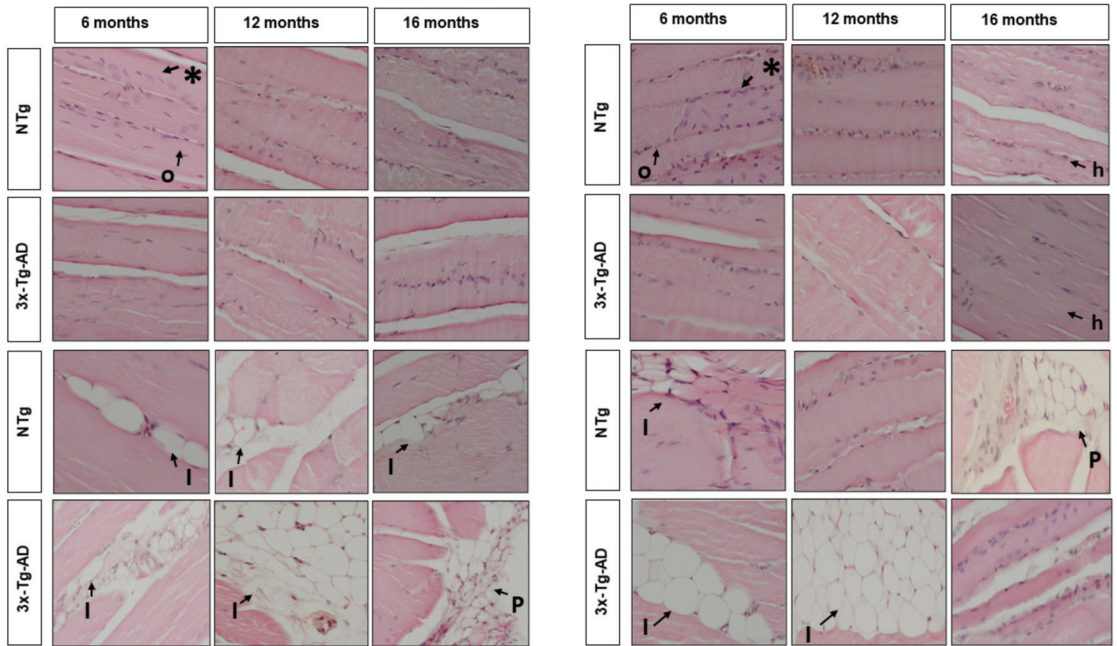
A. Quadriceps muscle**B. Triceps surae muscle**

Figure 6. Morphological comparison of muscle tissue in normal and AD-pathological aging. Hematoxylin and eosin-stained horizontal sections of muscles. (A) Quadriceps muscle; (B) Triceps surae muscle. Representative H&E images of longitudinal skeletal muscle at 6, 12, and 16 months. Symbols indicate the morphological features, as follows: *—Peripheral nuclei; o—homogeneous fibre distribution; h—heterogeneous fibre distribution; I—intramuscular adipose tissue; P—peripheral adipose tissue. The images were taken with 20× objective lens; the scale bar represents 0.32 μm.

3.4. Motor Performance, Geotaxis, and Hindlimb Clasping

Motor performance and physical performance were evaluated in other tests to obtain a complete analysis regarding the psychomotor abilities of the animals. Thus, motor learning showed an interaction between the genotype factor and GxA, highlighting a low performance in 3xTg-AD mice at the age of 6 and 16 months, concerning NTg of the same age (motor learning—latency, ANOVA $F(5.39) = 4.995$, $p = 0.001$ post hoc NTg 16 months vs. 3xTg-AD 16 months $p = 0.026$. Genotype effect $F(1.44) = 7.926$, $p = 0.008$. GxA effect $F(2, 43) = 5.184$, $p = 0.010$. Trials, ANOVA $F(5.39) = 3.953$, $p = 0.005$. GxA $F(2.43) = 5.454$, $p = 0.008$) (see Figure 7A,B). On the other hand, physical endurance decreases with age, with 16 months being the age with the lowest performance in both groups, but statistically significant in 3xTg-AD mice (physical endurance, ANOVA $F(5.39) = 5.189$, $p = 0.001$ post hoc 3xTg-AD 6 months vs. 3xTg-AD 16 months, $p = 0.017$; 3xTg-AD 12 months vs. 3xTg-AD 16 months, $p = 0.006$. Age effect $F(2.43) = 11.371$, $p < 0.0001$) (see Figure 7C). Geotaxis did not show statistical differences, but a higher latency was observed in the 3xTg-AD animals in each age group (see Figure 7D). In the hindlimb clasping test, we can highlight a significant genotype difference in each age group with a higher incidence of this sign in each 3xTg-AD mice (hindlimb clasping, Fisher exact test genotype = 0.007).

Table 2. Morphological features of quadriceps and triceps surae.

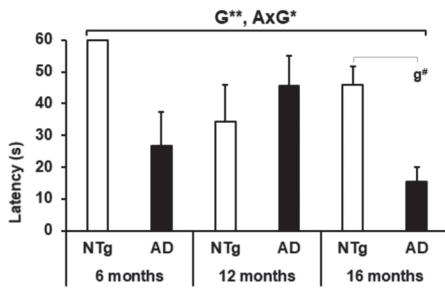
Morphological Features	NTg Mice			3xTg-AD Mice		
	6 Months	12 Months	16 Months	6 Months	12 Months	16 Months
Quadriceps						
1. Nuclei						
Localization	Peripheral nuclei	Peripheral nuclei	Peripheral nuclei	Peripheral nuclei	Peripheral nuclei	Peripheral nuclei
Number	++++	+++	+++	+++	++	+++
2. Fiber						
Distribution	Homogeneous	Homogeneous	Homogeneous	Homogeneous	Homogeneous	Homogeneous
3. Adipose tissue						
Localization	Intramuscular	Intramuscular	Intramuscular	Intramuscular	Intramuscular	Peripheral
Number	+	+	++	++	+	+
Triceps surae						
1. Nuclei						
Localization	Peripheral nuclei	Peripheral nuclei	Peripheral nuclei	Peripheral nuclei	Peripheral nuclei	Peripheral nuclei
Number	++++	+++	+++	+++	++	+++
2. Fiber						
Distribution	Homogeneous	Homogeneous	Heterogeneous	Homogeneous	Homogeneous	Heterogeneous
3. Adipose tissue						
Localization	Intramuscular		Peripheral	Intramuscular	Intramuscular	
Number	+		++++	+	++++	
Qualifier: 75–100% = +++++. 50–75% = +++. 25–50% = ++. 0–25% = +. 0% = -.						

Table 2. Morphological features of muscle tissue in 3xTg-AD mice: localization and number of nuclei, fiber distribution, and a number and localization adipose cells. Qualitative quantifier of intensity: (-) equal to 0%, (+) less to 25%, (++) less to 50%, (+++) less to 75%, and (++++) less or 100%.

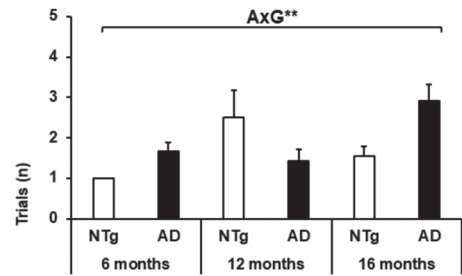
3.5. Survival, Kyphosis, and Frailty Phenotype

Table 3 shows the survival, kyphosis, and frailty phenotype of the mice at each age. For the survival analysis, we carried out a follow-up from birth to 16-month-old of the siblings of the sample included in the study, completing a cohort of 115 male mice. Logarithmic rank analysis shows a significant genotype-dependent difference ($\chi^2(1) = 8.045, p = 0.005$) with a higher mortality rate in NTg mice in each age group (6-month-old: NTg 3/15 (20%); 3xTg-AD 0/15. 12-month-old: NTg 3/9 (33.3%), 3xTg-AD 1/16 (6.2%). 16-month-old: NTg 20/40 (50%); 3xTg-AD 5/24 (20.8%)). On the other hand, kyphosis presents a higher incidence as age increases without genotype differences (Kyphosis (absent/present) Fisher exact test (5) = 10.694, $p = 0.052$. Age, Fisher exact test (2) = 10.070, $p = 0.007$. Genotype n.s). While postural kyphosis does not show significant differences between the groups, structural kyphosis increases its prevalence at ages 12 and 16 months of age independent of genotype (Fisher's exact test (2) = 8.464, $p = 0.016$). In the same way, body weight increases with age in the case of 3xTg-AD mice and is maintained in the case of NTg, with 3xTg-AD mice presenting greater weight at 16-month-old compared to NTg 16-month-old (Age effect, ANOVA F (2.44) = 3.268, $p = 0.049$; 3xTg-AD 12-month-old vs 16-month-old, $p = 0.037$). Regarding the physical conditions that the animals presented, no differences were detected in alopecia. On the other hand, body position, palpebral closure, and tail position were characteristics only present in the older group of 3xTg-AD mice (body position, Fisher's exact test (5) = 10.036, $p = 0.006$. Age effect, Fisher's exact test (2), $p = 0.046$. Palpebral closure, Fisher's exact test (5) = 7.493, $p = 0.037$. Tail position, Fisher's exact test (5) = 7.493, $p = 0.037$). Piloerection was present in NTg mice at the age of 12 and 16 months in contrast to 3xTg-AD mice, where its presentation appears at 16 months (Fisher (5) = 10.047, $p = 0.027$. Age effect, Fisher's exact test (2) = 8.338, $p = 0.010$).

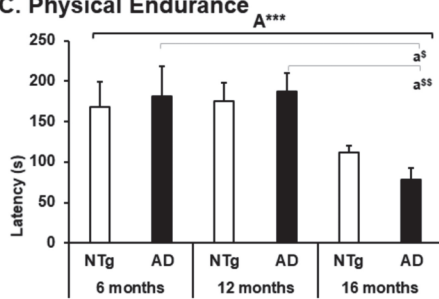
A. Motor learning—latency



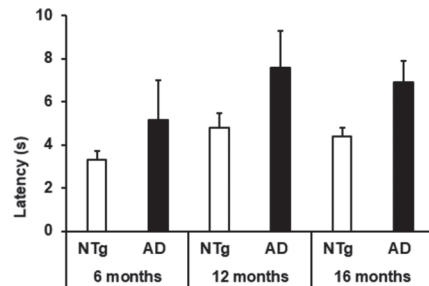
B. Trials



C. Physical Endurance



D. Geotaxis



E. Hindlimb claspings

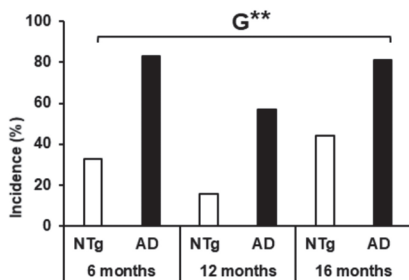


Figure 7. Motor performance, geotaxis and hindlimb claspings. (A) Motor learning—latency; (B) trials; (C) physical endurance; (D) geotaxis; the results are expressed as mean \pm SEM. Statistics: one-way ANOVA, Age effect expressed as (A); Genotype effect expressed as (G); Genotype and Age interaction effect are expressed as (GxA). * $p < 0.05$, ** $p < 0.01$, and *** $p < 0.001$ followed by post hoc Bonferroni test, # $p < 0.05$; differences between age in 3xTg-AD group are expressed (a): § $p < 0.01$, §§ $p < 0.01$. (E) Hindlimb claspings; the results are expressed as prevalence (%). Statistics: Fisher’s exact test; Age effect is expressed as (A); Genotype effect is expressed as (G); Genotype, * $p < 0.05$.

Table 3. Survival, kyphosis, and frailty phenotype.

Conditions	NTg Mice			3xTg-AD Mice			Statistics
	6 Months	12 Months	16 Months	6 Months	12 Months	16 Months	
1. Survival (mean + SEM days) (Mortality ratio)	329 + 25.26 3/15 (20%)	337 + 29.09 3/9 (33.3%)	350 + 15.60 20/40 (50%)	208 + 1.26 0/15 (0%)	395 + 9.63 1/16 (6.2%)	481 + 25.31 5/24 (20.8%)	S &&
2. Kyphosis (animals, %)	-	3/6 (50%)	5/9 (56%)	1/6 (17%)	3/7 (43%)	4/11 (36%)	A **
Postural	-	-	-	1/6 (17%)	-	1/11 (9%)	n.s.
Structural	-	3/6 (50%)	5/9 (56%)	-	3/7 (43%)	3/11 (27%)	A*
3. Physical conditions (animals, %)							
Body weight	30 g.	30 g.	30 g.	28 g.	33 g.	34g.	A *, a #
Alopecia	2/6 (33%)	4/6 (67%)	5/9 (56%)	1/6 (17%)	4/7 (57%)	4/11 (36%)	n.s.
Body position	-	-	-	-	-	5/11 (45%)	a #
Palpebral closure	-	-	-	-	-	4/11 (36%)	a #
Piloerection	-	1/6 (17%)	2/9 (22%)	-	-	6/11 (55%)	A *
Tail position	-	-	-	-	-	4/11 (36%)	a #
Tremor	-	1/6 (17%)	-	-	-	9/11 (82%)	A **, G *
Kaplan–Meier, Log Rank: S && $p < 0.01$. X ₂ , A: age, ** $p < 0.01$ * $p < 0.05$, G: genotype, * $p < 0.05$. n.s. $p > 0.05$. # $p < 0.05$.							

Table 3. Prevalence of physical conditions in male 3xTg-AD mice corresponding to the frailty phenotype. The progression of AD disease is contrasted with normal aging and the survival of the experimental lots included in the research.

Finally, tremor shows differences in genotype and age, presenting a high incidence at 16 months in 16-month-old mice (tremor, Fisher's exact test (5) = 23.346, $p < 0.0001$. Age effect, Fisher's exact test (2) = 10.170, $p = 0.005$. Genotype effect, χ^2 (1) = 6.945, $p = 0.012$).

4. Discussion

In contrast to the huge literature on the AD-associated hallmark impairment in cognitive domains, gait disorders in Alzheimer's disease are an emerging field. They result from structural and functional deficiencies that generate limitations in the performance of activities and also imply restrictions in the biopsychosocial participation of individuals [39–43]. Evidence suggests that AD has a long preclinical phase, during which its characteristic pathology accumulates, and the patient's function diminishes considerably [42,44]. Motor problems have been described as occurring early in the AD process, rather than being a feature exclusively related to end-stage AD pathology [45,46].

At the translational level, in animal models, we have recently described alterations in the trajectory and displacement that interfere with gait and exploratory activity have recently been reported in middle-aged (13-month-old) and old (16-month-old) male C57BL/6 and 3xTg-AD mice, which in the mutant corresponds to ages mimicking advanced and very advanced stages of the disease [33]. Furthermore, these alterations increase their incidence in endpoint situations at different ages regardless of the studied genotype [38,47,48]. In this report, we have expanded the study of functionality and disability described for humans to provide a translational proposal, which allows us to differentiate dysfunctions, gait disorders, and exploration in the 3xTg-AD model at different stages of disease progression

and as compared to C57BL/6 with normal aging. As shown in Figure 1, the functional limitations that we have detected are equivalent to the difficulties that an older adult typically faces when carrying out their activities of daily living and that we can consider as markers of functional health deterioration.

4.1. Activity—Spontaneous Gait and Exploration

Particularly in gait, the variable speed, as in humans [43,49], seems to be the variable with the highest sensitivity to detect impairments of displacement and locomotion. Furthermore, when bizarre gait patterns (circling, backward movement, stretching) are present, stride length, speed, and cadence decrease in performance regardless of age and genotype. On the other hand, 6-month-old 3xTg-AD mice have a shorter stride length that increases with age. This result may be related to the novelty situation, where we have detected a higher incidence of freezing (no movement) and higher episodes of bizarre gait patterns in this group. Furthermore, it has previously been reported that in 3xTg-AD mice aged from 10 to 14 months, the stride length is greater than that of control mice [49]. The authors point out that a possible explanation for this difference is the differences between species, where quadruped locomotion seems to have compensatory mechanisms that intervene even after injury at the brain level [50], mediating that the kinematic parameters can be preserved. In contrast, it can be inferred that older animals present a favorable indicator in their gait performance, and this may be related to survival and individual characteristics.

A study conducted in 3- and 24-month-old male C57BL/6 mice found that aged mice exhibited significantly lower cadence and decreased stride time variability [50]. They also reported that aging tended to alter footstep patterns, for which they associated with aging the alterations that occur in gait [50]. There are also technological devices and software to make possible the equivalence of some human signatures in mice, highlighting those related to gait disorders in Parkinson's disease [41,51–53]. However, studying whole body gait and posture in rodent models requires specialized methods and remains a challenge if other motivational or emotional response behavioral factors are integrated, which is the case of some Alzheimer's disease models where a noticeable neuropsychiatric-like pattern is exhibited. In this sense, in the face of novelty situations, 3xTg-AD mice respond with neophobia and anxiety-like behaviors [54,55], whereas in humans, they have been reported from initials stages of the disease [56]. Neophobia modifies the exploratory activity as age increases, accentuating the symptoms [57]. However, we have described that there's a relationship between bizarre gait patterns and horizontal and vertical components of exploratory activity. Thus, bizarre gait patterns limiting locomotion in 3xTg-AD mice do the same in NTg mice, which tends to increase with age. In 3xTg-AD mice, these behaviors are mainly related to psychiatric and neurological disorders [30,37,58]. However, bizarre behaviors can be heterogeneous and have a low incidence in males compared to females, as described by Baeta-Corral and Giménez-Llort, 2014 [30]. Therefore, in this sex, these behaviors emerge at early stages and progress with the disease similar to that observed in the bizarre swimming patterns in the Morris water maze, where we have described the presence of circling appears at early stages (6 months of age) [59] and worsens with age [60,61].

4.2. Body Function—Mobility and Muscular Strength

General mobility was interfered with by periods of freezing. We can distinguish that the 12-month-old animals presented several freezing episodes in both genotypes. At the age of 6 months, the group of 3xTg-AD mice presented a long freezing behavior, taking longer to perform the first movement, which can also influence the decrease in exploration and the quantitative parameters of the gait, similar to what happens in scenarios of social isolation [33].

At the level of muscle strength, in humans, it has been described that the decrease in strength in the initial stages of AD does not imply changes at the muscle fiber level [61–64]. However, in intermediate stages, it could be accompanied by a decrease in the number of

muscle fibers that in advanced stages are reflected in sarcopenia associated with loss of muscle strength [35,63]. Our results showed that the decrease in muscle strength would be associated with aging, as occurs with muscular endurance. Nevertheless, at the age of 12 months, there is a drop in grip strength in 3xTg-AD mice. It has also been reported that at six months, 3xTg-AD mice have a deficit in grip strength [65], but at 16 months, these results are not reproduced [66]. In isolation, the 3xTg-AD mice show a conserved strength at the age of 13 months over the mice that lived in groups [33]. These findings may point to the heterogeneity of aging and the stage of AD in which muscle strength is measured.

4.3. Body Structure—Joints and Muscles

At the same time, postural patterns such as shrinkage and structural changes at the joint level of the thoracolumbar spine accompany 3xTg-AD mice with a high incidence of structural kyphosis [33,38,48]. Our results show that both 3xTg-AD and C57BL/6 mice show an increase in the incidence of structural kyphosis after 12 months of age, which could explain, from a postural point of view, the decrease in exploration in both groups as age increases.

As the weight of the quadriceps muscle shows, there is a progressive decrease in 3xTg-AD mice that, unlike the C57BL/6 controls in which it appears to be attenuated, a higher weight range is preserved even in older animals. In contrast, both groups maintain a similar weight of triceps muscle at 12 and 16 months of age. A study in C57BL/6J females reported a progressive weight loss from 15 months in the quadriceps muscle, which is considerably accentuated at 24 months [66]. Similarly, a decrease in muscle weight over 25 months has been reported in male C57BL/6J mice in the gastrocnemius and soleus muscle [67].

Furthermore, we have applied an indirect measure of sarcopenia to verify its presence to investigate these findings further. In the quadriceps muscle, aging is related to sarcopenia, while in the transgenic group, sarcopenia appears at 16 months. Interestingly, the triceps surae muscle also indicates sarcopenia in 16-month-old 3xTg-AD mice. Using this measure, a study conducted in female C57BL/6J mice concluded that sarcopenia would be present at around 24 months in the quadriceps muscle [68]. However, in male C57BL/6J mice, it could occur at earlier ages, reporting 20 months as the age of most significant change in the gastrocnemius muscle [69].

In natural aging models of the C57BL/6J strain, it has been reported that the primary phenotype of sarcopenia is a decrease in muscle mass and a decrease in the cross-sectional area of muscle fibers [70–72]. The optimal age of study would be 25 months [67,72]. Thus, we found the fibers are distributed homogeneously, with differences between them, but maintain a similar distribution. However, a difference is observed in the number of nuclei in NTg control animals that seems higher than in 3xTg-AD, especially at 12 months. We also found the presence of adipose cells, which exhibited a different distribution for each muscle type. Thus, adipose cells were present to a lesser extent in quadriceps, independently of genotype and age, with an intramuscular predominance. Oppositely, adipose cells exhibited a peripheral or intramuscular localization according to the genotype and age in the triceps. Thus, in the NTg control group, adipose cells were found in more peripheral areas, with a more significant proportion at 16 months.

In contrast, in the 3xTg-AD group, the adipose cells were more intramuscular, and a higher proportion was found at 12 months. Interestingly, the NTg control mice had a similar weight at each age, while the weight of 3xTg-AD mice increased with age.

4.4. Motor Performance, Geotaxis, and Hindlimb Claspings

On the other hand, we have measured the animals' motor learning and physical resistance to obtain a global vision regarding their psychomotor performance. We have shown that in the advanced stage of the disease, 3xTg-AD mice have a lower-than-expected performance that is replicated in motor learning and physical endurance. Similarly, in C57BL/6 control animals, the observed changes are more attenuated due to aging. In the

case of geotaxis, an increase in turning latency was found in the 3xTg-AD group, which, although it did not present significant differences, could indicate a poor use of postural and balance strategies to regain the verticality of their body on the grille in which they are located. For its part, hindlimb clasp showed a higher incidence in the 3xTg-AD group without being associated with the stages of disease progression. This particular sign can indicate the severity of the motor impairment that the mice present [73–75].

4.5. Survival, Kyphosis, and Frailty Phenotype

Finally, we can point out that C57BL/6 control animals have a higher mortality ratio in all age groups regarding survival, consistent with previous studies [76]. As the frailty phenotype shows, some signs of deterioration are related to one group or another. In the case of 3xTg-AD mice, physical and postural conditions appear to be the highest incidence, and in their NTg counterparts, piloerection and tremor, which in both groups, were found similarly increased with age. These variables indicate the general state of the mice without interfering with their functional performance of the gait and exploration that we have reported.

5. Conclusions

According to the literature, this is the first report that comprehensively presents the gait disturbances and functional limitations in the exploratory activity of the 3xTg-AD mouse model and, as compared to C57BL/6 with normal aging, uses a conceptual model that allows translation to humans. The use of the ICF as a conceptual framework allows describing the functional state, facilitating its interpretation and application in the rehabilitation of people with AD.

In summary, the main conclusions are:

- (1) The 3xTg-AD mice show more significant functional impairment in gait and exploratory activity quantitative variables.
- (2) The presence of movement limitations and muscle weakness mark the functional decline related to the disease severity stages that intensify with increasing age.
- (3) Motor performance in 3xTg-AD is accompanied by a series of bizarre behaviors that interfere with the trajectory, which allows us to infer poor neurological control.
- (4) Signs of physical frailty accompany the functional deterioration of these animals.
- (5) Signs of sarcopenia are present in an advanced stage of AD, with differences in fibre distribution, number of cell nuclei, and presence of adipose tissue.

Author Contributions: Conceptualization, L.G.-L. and L.C.-M.; Behavioral performance, analysis, and statistics, L.C.-M.; Pathology: L.C.-M. and M.J.P.-G.; Illustrations: L.C.-M. and L.G.-L. Writing—original draft preparation, L.C.-M.; writing—review and editing, L.C.-M., L.G.-L. and M.J.P.-G.; Funding acquisition, L.G.-L. All authors have read and agreed to the published version of the manuscript.

Funding: This work was funded by 2017-SGR-1468 and UAB-GE-260408 to L.G.-L. The colony of 3xTg-AD mice is sustained by ArrestAD H2020 Fet-OPEN-1-2016-2017-737390, European Union's Horizon 2020 research and innovation program under grant agreement No 737390 to L.G.-L. It also received financial support from Memorial Mercedes Llorc Sender 2021/80/09241941.8.

Institutional Review Board Statement: The study was conducted according to the guidelines of the Declaration of Helsinki and approved by the Ethics Committee of Departament de Medi Ambient i Habitatge, Generalitat de Catalunya (CEEAH 3588/DMAH 9452) on the 8th of March 2019.

Informed Consent Statement: Not applicable.

Data Availability Statement: Not applicable.

Acknowledgments: We thank Frank M LaFerla Institute for Memory Impairments and Neurological Disorders, Department of Neurobiology and Behavior, University of California, Irvine, USA, for kindly providing the progenitors of the Spanish colonies of 3xTg-AD and NTg mice. LC-M is recipient of a CONICYT/BECAS CHILE/72180026 grant.

Conflicts of Interest: The authors declare no conflict of interest. The funders had no role in the study's design, in the collection, analyses, or interpretation of data; in the writing of the manuscript, or in the decision to publish the results.

References

- Goyal, D.; Tjandra, D.; Migrino, R.Q.; Giordani, B.; Syed, Z.; Wiens, J. Characterizing heterogeneity in the progression of Alzheimer's disease using longitudinal clinical and neuroimaging biomarkers. *Alzheimer's Dement. Diagn. Assess. Dis. Monit.* **2018**, *10*, 629–637. [CrossRef]
- Ryan, J.; Fransquet, P.; Wrigglesworth, J.; Lacaze, P. Phenotypic Heterogeneity in Dementia: A Challenge for Epidemiology and Biomarker Studies. *Front. Public Health* **2018**, *6*, 181. [CrossRef]
- Zidan, M.; ArCoverde, C.; BoM de Araújo, N.; Vasques, P.; Rios, A.; Laks, J.; Deslandes, A. Motor and functional changes in different stages of Alzheimer's disease. *Rev. Psiqu. Clín.* **2012**, *39*, 161–165. [CrossRef]
- Albers, M.W.; Gilmore, G.C.; Kaye, J.; Murphy, C.; Wingfield, A.; Bennett, D.A.; Boxer, A.L.; Buchman, A.S.; Cruickshanks, K.J.; Devanand, D.P.; et al. At the interface of sensory and motor dysfunctions and Alzheimer's Disease. *Alzheimer's Dement.* **2015**, *11*, 70. [CrossRef] [PubMed]
- Montero-Odasso, M.; Perry, G. Gait Disorders in Alzheimer's Disease and Other Dementias: There is Something in the Way You Walk. *J. Alzheimer's Dis.* **2019**, *71*, S1–S4. [CrossRef] [PubMed]
- Beauchet, O.; Allali, G.; Montero-Odasso, M.; Sejdic, E.; Fantino, B.; Annweiler, C. Motor phenotype of decline in cognitive performance among community-dwellers without dementia: Population-based study and meta-analysis. *PLoS ONE* **2014**, *9*, e99318. [CrossRef]
- Montero-Odasso, M.; Speechley, M. Falls in Cognitively Impaired Older Adults: Implications for Risk Assessment And Prevention. *J. Am. Geriatr. Soc.* **2018**, *66*, 367–375. [CrossRef] [PubMed]
- Muir, S.W.; Speechley, M.; Wells, J.; Borrie, M.; Gopaul, K.; Montero-Odasso, M. Gait assessment in mild cognitive impairment and Alzheimer's disease: The effect of dual-task challenges across the cognitive spectrum. *Gait Posture*. **2012**, *35*, 96–100. [CrossRef]
- Pirker, W.; Katzenschlager, R. Gait disorders in adults and the elderly: A clinical guide. *Wien. Klin. Wochenschr.* **2017**, *129*, 81. [CrossRef]
- Baker, J.M. Gait Disorders. *Am. J. Med.* **2018**, *131*, 602–607. [CrossRef]
- Scherder, E.; Eggermont, L.; Swaab, D.; van Heuvelen, M.; Kamsma, Y.; de Greef, M.; van Wijck, R.; Mulder, T. Gait in ageing and associated dementias; its relationship with cognition. *Neurosci. Biobehav. Rev.* **2007**, *31*, 485–497. [CrossRef] [PubMed]
- Valenti, G.; Bonomi, A.G.; Westerterp, K.R. Walking as a Contributor to Physical Activity in Healthy Older Adults: 2 Week Longitudinal Study Using Accelerometry and the Doubly Labeled Water Method. *JMIR Mhealth Uhealth* **2016**, *4*, e5445. [CrossRef]
- Leisman, G.; Moustafa, A.A.; Shafir, T. Thinking, Walking, Talking: Integratory Motor and Cognitive Brain Function. *Front. Public Health* **2016**, *4*, 4. [CrossRef]
- Taborri, J.; Palermo, E.; Rossi, S.; Cappa, P. Gait Partitioning Methods: A Systematic Review. *Sensor* **2016**, *16*, 66. [CrossRef] [PubMed]
- Umberger, B.R. Stance and swing phase costs in human walking. *J. R. Soc. Interface* **2010**, *7*, 1329. [CrossRef]
- Wert, D.M.; Brach, J.; Perera, S.; VanSwearingen, J.M. Gait Biomechanics, Spatial and Temporal Characteristics, and the Energy Cost of Walking in Older Adults With Impaired Mobility. *Phys. Ther.* **2010**, *90*, 977. [CrossRef]
- Gangliu, Y. Evaluación de la marcha en el adulto mayor. *Cart. Geriátrico Gerontológica* **2011**, *4*, 1–36.
- Salazar Pachón, J.D.; Ramírez Villada, J.F.; Chaparro, D.; León, H.H. Revisión Sistemática Sobre el Impacto de la Actividad Física en los Trastornos de la Marcha en el Adulto Mayor. *Apunt. Educ. Física Y Deport.* **2014**, *118*, 30–39. [CrossRef]
- Menz, H.B.; Lord, S.R.; Fitzpatrick, R.C. Age-related differences in walking stability. *Age Ageing* **2003**, *32*, 137–142. [CrossRef] [PubMed]
- Boyer, K.A.; Johnson, R.T.; Banks, J.J.; Jewell, C.; Hafer, J.F. Systematic review and meta-analysis of gait mechanics in young and older adults. *Exp. Gerontol.* **2017**, *95*, 63–70. [CrossRef]
- Ostrosky, K.M.; VanSwearingen, J.M.; Burdett, R.G.; Gee, Z. A comparison of gait characteristics in young and old subjects. *Phys. Ther.* **1994**, *74*, 637–646. [CrossRef]
- Montgomery, G.; McPhee, J.; Pääsuke, M.; Sipilä, S.; Maier, A.B.; Hogrel, J.-Y.; Degens, H. Determinants of Performance in the Timed up-and-go and Six-Minute Walk Tests in Young and Old Healthy Adults. *J. Clin. Med.* **2020**, *9*, 1561. [CrossRef] [PubMed]
- Guralnik, J.M.; Ferrucci, L.; Simonsick, E.M.; Salive, M.E.; Wallace, R.B. Lower-Extremity Function in Persons over the Age of 70 Years as a Predictor of Subsequent Disability. *N. Engl. J. Med.* **2009**, *332*, 556–561. [CrossRef] [PubMed]
- Bohannon, R.W. Relevance of Muscle Strength to Gait Performance in Patients with Neurologic Disability. *J. Neurol. Rehab.* **1989**, *3*, 97–100. [CrossRef]
- Boyle, P.A.; Buchman, A.S.; Wilson, R.S.; Leurgans, S.E.; Bennett, D.A. Association of muscle strength with the risk of Alzheimer disease and the rate of cognitive decline in community-dwelling older persons. *Arch. Neurol.* **2009**, *66*, 1339–1344. [CrossRef]
- Sui, S.X.; Holloway-Kew, K.L.; Hyde, N.K.; Williams, L.J.; Leach, S.; Pasco, J.A. Muscle strength and gait speed rather than lean mass are better indicators for poor cognitive function in older men. *Sci. Rep.* **2020**, *10*, 10367. [CrossRef] [PubMed]
- Ogawa, Y.; Kaneko, Y.; Sato, T.; Shimizu, S.; Kanetaka, H.; Hanyu, H. Sarcopenia and Muscle Functions at Various Stages of Alzheimer Disease. *Front. Neurol.* **2018**, *9*, 170. [CrossRef]

28. Arrieta, H.; Rezola-Pardo, C.; Echeverria, I.; Iturburu, M.; Gil, S.M.; Yanguas, J.J.; Irazusta, J.; Rodriguez-Larrad, A. Physical activity and fitness are associated with verbal memory, quality of life and depression among nursing home residents: Preliminary data of a randomized controlled trial. *BMC Geriatr.* **2018**, *18*, 80. [CrossRef]
29. Beeri, M.S.; Leugrants, S.E.; Delbono, O.; Bennett, D.A.; Buchman, A.S. Sarcopenia is associated with incident Alzheimer's dementia, mild cognitive impairment, and cognitive decline. *J. Am. Geriatr. Soc.* **2021**, *69*, 1826–1835. [CrossRef] [PubMed]
30. Baeta-Corral, R.; Giménez-Llort, L. Bizarre behaviors and risk assessment in 3xTg-AD mice at early stages of the disease. *Behav. Brain Res.* **2014**, *258*, 97–105. [CrossRef]
31. Kilkenny, C.; Browne, W.J.; Cuthill, I.C.; Emerson, M.; Altman, D.G. Improving Bioscience Research Reporting: The ARRIVE Guidelines for Reporting Animal Research. *PLoS Biol.* **2010**, *8*, e1000412. [CrossRef]
32. Castillo-Mariqueo, L.; Giménez-Llort, L. Translational Modeling of Psychomotor Function in Normal and AD-Pathological Aging With Special Concerns on the Effects of Social Isolation. *Front. Aging* **2021**, *2*, 648567. [CrossRef]
33. Verbrugge, L.M.; Jette, A.M. The disablement process. *Soc. Sci. Med.* **1994**, *38*, 1–14. [CrossRef]
34. Reid, K.F.; Fielding, R.A. Skeletal Muscle Power: A Critical Determinant of Physical Functioning In Older Adults. *Exerc. Sport Sci. Rev.* **2012**, *40*, 4. [CrossRef]
35. Wang, X.; Wang, Q.M.; Meng, Z.; Yin, Z.; Luo, X.; Yu, D. Gait disorder as a predictor of spatial learning and memory impairment in aged mice. *PeerJ* **2017**, *5*, e2854. [CrossRef] [PubMed]
36. Giménez-Llort, L.; Fernández-Teruel, A.; Escorihuela, R.M.; Fredholm, B.B.; Tobeña, A.; Pekny, M.; Johansson, B. Mice lacking the adenosine A1 receptor are anxious and aggressive, but are normal learners with reduced muscle strength and survival rate. *Eur. J. Neurosci.* **2002**, *16*, 547–550. [CrossRef] [PubMed]
37. Castillo Mariqueo, L.; Alveal-Mellado, D.; Gimenez-LLort, L. Hindlimb claspings, kyphosis and piloerection: Frailty markers from middle to very old ages in mice. *Eur. J. Neurol.* **2021**, *28*, 447.
38. Edström, E.; Ulfhake, B. Sarcopenia is not due to lack of regenerative drive in senescent skeletal muscle. *Aging Cell* **2005**, *4*, 65–77. [CrossRef] [PubMed]
39. Allan, L.M.; Ballard, C.G.; Burn, D.J.; Kenny, R.A. Prevalence and Severity of Gait Disorders in Alzheimer's and Non-Alzheimer's Dementias. *J. Am. Geriatr. Soc.* **2005**, *53*, 1681–1687. [CrossRef]
40. Broom, L.; Ellison, B.A.; Worley, A.; Wagenaar, L.; Sörberg, E.; Ashton, C.; Bennett, D.A.; Buchman, A.S.; Saper, C.B.; Shih, L.C.; et al. A translational approach to capture gait signatures of neurological disorders in mice and humans. *Sci. Rep.* **2017**, *7*, 3225. [CrossRef] [PubMed]
41. Buchman, A.S.; Bennett, D.A. Loss of motor function in preclinical Alzheimer's disease. *Expert Rev. Neurother.* **2011**, *11*, 665–676. [CrossRef] [PubMed]
42. Chiaramonte, R.; Cioni, M. Critical spatiotemporal gait parameters for individuals with dementia: A systematic review and meta-analysis. *Hong Kong Physiother. J.* **2021**, *41*, 1–14. [CrossRef]
43. Aggarwal, N.T.; Wilson, R.S.; Beck, T.L.; Bienias, J.L.; Bennett, D.A. Motor Dysfunction in Mild Cognitive Impairment and the Risk of Incident Alzheimer Disease. *Arch. Neurol.* **2006**, *63*, 1763–1769. [CrossRef]
44. Kurlan, R.; Richard, I.H.; Papka, M.; Marshall, F. Movement disorders in Alzheimer's disease: More rigidity of definitions is needed. *Mov. Disord.* **2000**, *15*, 24–29. [CrossRef]
45. Wirths, O.; Bayer, T.A. Motor impairment in Alzheimer's disease and transgenic Alzheimer's disease mouse models. *Genes Brain Behav.* **2008**, *7* (Suppl. 1), 1–5. [CrossRef]
46. Castillo Mariqueo, L.; Gimenez-LLort, L. Gait impairments and functional limitations in the exploratory activity in an animal model of Alzheimer's disease. *Eur. J. Neurol.* **2021**, *28*, 446.
47. Castillo Mariqueo, L.; Giménez Llort, L. Bizarre behaviors limit exploratory activity and impair spontaneous gait performance in aged mice with AD pathology. In *Behavioral Neuroscience, Proceedings of the 2nd International Electronic Conference on Brain Sciences, online, 15–20 July 2021*; MDPI: Basel, Switzerland, 2021. [CrossRef]
48. Coelho, F.G.; Stella, F.; de Andrade, L.P.; Barbieri, F.A.; Santos-Galduróz, R.F.; Gobbi, S.; Costa, J.L.; Gobbi, L.T. Gait and risk of falls associated with frontal cognitive functions at different stages of Alzheimer's disease. *Aging. Neuropsychol. Cogn.* **2012**, *19*, 644–656. [CrossRef] [PubMed]
49. Setogawa, S.; Yamaura, H.; Arasaki, T.; Endo, S.; Yanagihara, D. Deficits in memory-guided limb movements impair obstacle avoidance locomotion in Alzheimer's disease mouse model. *Sci. Rep.* **2014**, *41*, 7220. [CrossRef] [PubMed]
50. Aoki, S.; Sato, Y.; Yanagihara, D. Lesion in the lateral cerebellum specifically produces overshooting of the toe trajectory in leading forelimb during obstacle avoidance in the rat. *J. Neurophysiol.* **2013**, *110*, 1511–1524. [CrossRef]
51. Tarantini, S.; Yabluchanskiy, A.; Fülöp, G.A.; Kiss, T.; Perz, A.; O'Connor, D.; Johnson, E.; Sorond, F.; Ungvari, Z.I.; Csiszar, A. Age-Related Alterations in Gait Function in Freely Moving Male C57BL/6 Mice: Translational Relevance of Decreased Cadence and Increased Gait Variability. *J. Gerontol. Ser. A* **2019**, *74*, 1417. [CrossRef]
52. Akula, S.K.; McCullough, K.B.; Weichselbaum, C.; Dougherty, J.D.; Maloney, S.E. The trajectory of gait development in mice. *Brain Behav.* **2020**, *10*, e01636. [CrossRef]
53. Broom, L.; Worley, A.; Gao, F.; Hernandez, L.D.; Ashton, C.E.; Shih, L.C.; VanderHorst, V.G. Translational methods to detect asymmetries in temporal and spatial walking metrics in parkinsonian mouse models and human subjects with Parkinson's disease. *Sci. Rep.* **2019**, *9*, 2437. [CrossRef] [PubMed]

54. Sheppard, K.; Gardin, J.; Sabnis, G.; Peer, A.; Darrell, M.; Deats, S.; Geuther, B.; Lutz, C.M.; Kumar, V. Gait-level analysis of mouse open field behavior using deep learning-based pose estimation. *bioRxiv* **2020**. [CrossRef]
55. J España, J.; Giménez-Llort, L.; Valero, J.; Miñano, A.; Rábano, A.; Rodríguez-Alvarez, J.; LaFerla, F.M.; Saura, C.A. Intraneuronal β -Amyloid Accumulation in the Amygdala Enhances Fear and Anxiety in Alzheimer's Disease Transgenic Mice. *Biol. Psychiatry* **2010**, *67*, 513–521. [CrossRef] [PubMed]
56. Giménez-Llort, L.; Blázquez, G.; Cañete, T.; Johansson, B.; Oddo, S.; Tobeña, A.; LaFerla, F.M.; Fernández-Teruel, A.; Gimeez-Llort, L.; Blaquez, G.; et al. Modeling behavioral and neuronal symptoms of Alzheimer's disease in mice: A role for intraneuronal amyloid. *Neurosci. Biobehav. Rev.* **2007**, *31*, 125–147. [CrossRef] [PubMed]
57. Roda, A.R.; Esquerda-Canals, G.; Martí-Clúa, J.; Villegas, S. Cognitive Impairment in the 3xTg-AD Mouse Model of Alzheimer's Disease is Affected by A β -ImmunoTherapy and Cognitive Stimulation. *Pharmaceutics* **2020**, *12*, 944. [CrossRef]
58. Muntsant-Soria, A.; Gimenez-Llort, L. Impact of social isolation on the behavioral and functional profiles and hippocampal atrophy asymmetry in dementia in times of coronavirus pandemic (COVID-19): A translational neuroscience approach. *Front. Psychiatry* **2020**, *11*, 1126. [CrossRef]
59. Cerdón-Barris, L.; Pascual-Guiral, S.; Yang, S.; Giménez-Llort, L.; Lope-Piedrafita, S.; Niemeyer, C.; Claro, E.; Lizcano, J.M.; Bayascas, J.R. Mutation of the 3-Phosphoinositide-Dependent Protein Kinase 1 (PDK1) Substrate-Docking Site in the Developing Brain Causes Microcephaly with Abnormal Brain Morphogenesis Independently of Akt, Leading to Impaired Cognition and Disruptive Behaviors. *Mol. Cell. Biol.* **2016**, *36*, 2967–2982. [CrossRef]
60. Castillo-Mariqueo, L.; Giménez-Llort, L. Indexes for flotation and circling, two non-search behaviors in the water maze, sensitive to D-galactose-induced accelerated aging and Alzheimer's disease. *Behav. Brain Res.* **2019**, *377*, 112229. [CrossRef]
61. Baeta-Corral, R.; Giménez-Llort, L. Persistent hyperactivity and distinctive strategy features in the Morris water maze in 3xTg-AD mice at advanced stages of disease. *Behav. Neurosci.* **2015**, *129*, 129–137. [CrossRef]
62. Miljkovic, N.; Lim, J.Y.; Miljkovic, I.; Frontera, W.R. Aging of skeletal muscle fibers. *Ann. Rehabil. Med.* **2015**, *39*, 155–162. [CrossRef]
63. Larsson, L.; Degens, H.; Li, M.; Salvati, L.; Lee, Y.I.; Thompson, W.; Kirkland, J.L.; Sandri, M. Sarcopenia: Aging-Related Loss of Muscle Mass and Function. *Physiol. Rev.* **2019**, *99*, 427–511. [CrossRef] [PubMed]
64. Goodpaster, B.H.; Park, S.W.; Harris, T.B.; Kritchevsky, S.B.; Nevitt, M.; Schwartz, A.V.; Simonsick, E.M.; Tylavsky, F.A.; Visser, M.; Newman, A.B. The loss of skeletal muscle strength, mass, and quality in older adults: The health, aging and body composition study. *J. Gerontol. Ser. A Biol. Sci. Med. Sci.* **2006**, *61*, 1059–1064. [CrossRef]
65. Stover, K.R.; Campbell, M.A.; Van Winssen, C.M.; Brown, R.E. Analysis of motor function in 6-month-old male and female 3xTg-AD mice. *Behav. Brain Res.* **2015**, *281*, 16–23. [CrossRef] [PubMed]
66. Garvock-de Montbrun, T.; Fertan, E.; Stover, K.; Brown, R.E. Motor deficits in 16-month-old male and female 3xTg-AD mice. *Behav. Brain Res.* **2019**, *356*, 305–313. [CrossRef]
67. Shavlakadze, T.; McGeachie, J.; Grounds, M.D. Delayed but excellent myogenic stem cell response of regenerating geriatric skeletal muscles in mice. *Biogerontology* **2010**, *11*, 363–376. [CrossRef] [PubMed]
68. Van Dijk, M.; Nagel, J.; Dijk, F.J.; Salles, J.; Verlaan, S.; Walrand, S.; van Norren, K.; Luiking, Y. Sarcopenia in older mice is characterized by a decreased anabolic response to a protein meal. *Arch. Gerontol. Geriatr.* **2017**, *69*, 134–143. [CrossRef]
69. Sayer, A.A.; Robinson, S.M.; Patel, H.P.; Shavlakadze, T.; Cooper, C.; Grounds, M.D. New horizons in the pathogenesis, diagnosis and management of sarcopenia. *Age Ageing* **2013**, *42*, 1145–1150. [CrossRef] [PubMed]
70. Wang, H.; Listrat, A.; Meunier, B.; Gueugneau, M.; Coudy-Gandilhon, C.; Combaret, L.; Taillandier, D.; Polge, C.; Attaix, D.; Lethias, C.; et al. Apoptosis in capillary endothelial cells in ageing skeletal muscle. *Aging Cell* **2014**, *13*, 254–262. [CrossRef]
71. Mankhong, S.; Kim, S.; Moon, S.; Kwak, H.-B.; Park, D.-H.; Kang, J.-H. Experimental Models of Sarcopenia: Bridging Molecular Mechanism and Therapeutic Strategy. *Cells* **2020**, *9*, 1385. [CrossRef] [PubMed]
72. Kadoguchi, T.; Shimada, K.; Miyazaki, T.; Kitamura, K.; Kunimoto, M.; Aikawa, T.; Sugita, Y.; Ouchi, S.; Shiozawa, T.; Yokoyama-Nishitani, M.; et al. Promotion of oxidative stress is associated with mitochondrial dysfunction and muscle atrophy in aging mice. *Geriatr. Gerontol. Int.* **2020**, *20*, 78–84. [CrossRef] [PubMed]
73. Xie, W.; He, M.; Yu, D.; Wu, Y.; Wang, X.; Lv, S.; Xiao, W.; Li, Y. Mouse models of sarcopenia: Classification and evaluation. *J. Cachexia. Sarcopenia Muscle* **2021**, *12*, 538–554. [CrossRef]
74. Lalonde, R.; Strazielle, C. Brain regions and genes affecting limb-clasping responses. *Brain Res. Rev.* **2011**, *67*, 252–259. [CrossRef] [PubMed]
75. Lieu, C.A.; Chinta, S.J.; Rane, A.; Andersen, J.K. Age-related behavioral phenotype of an astrocytic monoamine oxidase-B transgenic mouse model of Parkinson's disease. *PLoS ONE* **2013**, *8*, e54200. [CrossRef] [PubMed]
76. Muntsant, A.; Jiménez-Altayó, F.; Puertas-Umbert, L.; Jiménez-Xarrie, E.; Vila, E.; Giménez-Llort, L. Sex-dependent end-of-life mental and vascular scenarios for compensatory mechanisms in mice with normal and ad-neurodegenerative aging. *Biomedicines* **2021**, *9*, 111. [CrossRef]



Article

Sex-Dependent Signatures, Time Frames and Longitudinal Fine-Tuning of the Marble Burying Test in Normal and AD-Pathological Aging Mice

Mikel Santana-Santana ^{1,2}, José-Ramón Bayascas ^{1,3} and Lydia Giménez-Llort ^{1,2,*}

¹ Institut de Neurociències, Universitat Autònoma de Barcelona, 08193 Barcelona, Spain; mikel.santana@e-campus.uab.cat (M.S.-S.); joseramon.bayascas@uab.cat (J.-R.B.)

² Department of Psychiatry and Forensic Medicine, School of Medicine, Universitat Autònoma de Barcelona, 08193 Barcelona, Spain

³ Department of Biochemistry and Molecular Biology, School of Medicine, Universitat Autònoma de Barcelona, 08193 Barcelona, Spain

* Correspondence: lidia.gimenez@uab.cat

Citation: Santana-Santana, M.; Bayascas, J.-R.; Giménez-Llort, L. Sex-Dependent Signatures, Time Frames and Longitudinal Fine-Tuning of the Marble Burying Test in Normal and AD-Pathological Aging Mice. *Biomedicines* **2021**, *9*, 994. <https://doi.org/10.3390/biomedicines9080994>

Academic Editor: Masaru Tanaka

Received: 9 July 2021

Accepted: 6 August 2021

Published: 11 August 2021

Publisher's Note: MDPI stays neutral with regard to jurisdictional claims in published maps and institutional affiliations.



Copyright: © 2021 by the authors. Licensee MDPI, Basel, Switzerland. This article is an open access article distributed under the terms and conditions of the Creative Commons Attribution (CC BY) license (<https://creativecommons.org/licenses/by/4.0/>).

Abstract: The marble burying (MB) test, a classical test based on the natural tendency of rodents to dig in diverse substrates and to bury small objects, is sensitive to some intrinsic and extrinsic factors. Here, under emerging neuroethological quantitative and qualitative analysis, the MB performance of 12-month-old male and female 3xTg-AD mice for Alzheimer's disease and age-matched counterparts of gold-standard C57BL6 strain with normal aging unveiled sex-dependent signatures. In addition, three temporal analyses, through the (1) time course of the performance, and (2) a repeated test schedule, identified the optimal time frames and schedules to detect sex- and genotype-dependent differences. Besides, a (3) longitudinal design from 12 to 16 months of age monitored the changes in the performance with aging, worsening in AD-mice, and modulation through the repeated test. In summary, the present results allow us to conclude that (1) the marble burying test is responsive to genotype, sex, aging, and its interactions; (2) the male sex was more sensitive to showing the AD-phenotype; (3) longitudinal assessment shows a reduction in females with AD pathology; (4) burying remains stable in repeated testing; (5) the time-course of marbles burying is useful; and (6) burying behavior most likely represents perseverative and/or stereotyped-like behavior rather than anxiety-like behavior in 3xTg-AD mice.

Keywords: neuroethology; behavioral neuroscience methodology; sexual differences; aging; Alzheimer's disease; comorbidities; phobia; anxiety; OCD (obsessive-compulsive symptoms)

1. Introduction

The behavioral and psychological symptoms associated with dementia (BPSD), including neuropsychiatric symptoms (NPS) such as anxiety and phobias, paranoia and delusion, hallucinations, stereotypes, and other disturbances, are comorbidities manifested in 50–90% of people with Alzheimer's disease (AD) [1]. These non-cognitive problems affect their quality of life [2], are an important source of distress for patients and caregivers [3], and frequently lead to premature institutionalization [4]. Furthermore, recent studies suggest a distinct distribution of NPS comorbidities among sexes, and therefore there is a need to characterize these differences, elucidate the underlying pathophysiology, and identify better treatment targets with a gender perspective [5]. At the translational level, the modeling of BPSD/NPS in basic and preclinical research of AD under the sex perspective is also needed to develop better pharmacological and non-pharmacological preventive/therapeutical interventions that could be effectively translated into clinical scenarios. In this context, natural species-typical behaviors representing active interaction with the environment are excellent ethological scenes to reflect the interplay of cognitive

and non-cognitive disturbances induced by normal and AD-pathological aging. In agreement with this, we have proven the validity of the 3xTg-AD mice to assess the impact of the disease on naturally occurring executive functions and daily life activities based on species-typical behaviors when interacting with the environment, such as burying behavior [6], and nest-building [7,8].

Burying behavior is commonly measured with the marble burying (MB) test [9], a classical behavioral test employed in rodents that exploit the tendency of these animals to dig in diverse substrates and to bury small objects, such as glass marbles, in a test cage with beddings [10]. Initially, this test was pharmacologically validated for its use to measure anxiety-related behaviors and screening for anxiolytic pharmacological drugs [11,12]. However, controversy exists regarding its specificity as it is also proposed as modeling meaningless repetitive and perseverative behaviors mimicking psychotic and obsessive-compulsive (OCD) symptoms [13]. Actually, some authors consider that for MB to be regarded as a reliable screening test for a specific assessment of a neuropsychological construct, the introduction of methodological changes or better experimental designs is needed [13–15]. Thus, two-zone configuration, repeated trials, and limitations inherent to MB score and ceiling/floor effects are among the experimental considerations discussed. Additionally, emerging neuroethological analysis of behavior, which integrates the sequence of behavioral events in an ethogram, may provide a better understanding of the functional role, its modulation, and underlying mechanisms than classical behavioral analysis.

Marble burying behavior is altered in the 3xTg-AD mice. Specifically, it is enhanced in 12-month-old 3xTg-AD male mice, an age mimicking advanced stages of the disease [16,17], can be reversed by risperidone, and be modulated by handling [6,18]. In addition, we have recently proven that at 15-months of age, just 2–3 months of naturalistic isolation, which occurs when congeners die, is enough to exacerbate this behavior despite social lives since they were born, modeling the worsening of OCD described in the current COVID-19 scenario [19]. However, there are still various unresolved questions regarding the effect of sex and age factors on marble burying behavior in normal and AD-pathological aging. First, as in the case in other fields with rodent experimentation [20], the inclusion of female mice in MB testing is not the most common choice [21]. The inclusion of females in animal studies of AD is relevant, even if similar incidence between sexes is found, since risk factors may differentially affect multiple pathways and evolve into different manifestations of NPS and comorbidities [5]. Second, how aging and AD-pathological processes affect burying behavior and the MB profile evolves in a long-term perspective. This is a significant concern due to the intrinsic nature of AD, in which cognitive and psychiatric symptoms are present in early stages and worsen over time as the disease progresses [22]. Hence, to increase the translational value of experimental designs, rather than a transversal comparison of the performance at different age stages, longitudinal studies allow monitoring of the progression of cognitive and non-cognitive deficits through an AD-pathological life-span.

Therefore, the present study aimed to explore further the contribution of sex and aging in the normal and AD-pathological brain in marble burying behavior. We used middle-aged 3xTg-AD mice through a longitudinal study including methodological modifications (two-zone configuration, repeated trials, and time-course counting of marbles buried) to have a better approach to the possible neuropsychiatric constructs involved in their alteration, and we compared them with those presented in their non-transgenic (NTg) counterparts with the gold-standard C57BL/6 strain genetic background.

2. Materials and Methods

2.1. Animals

A total number of forty-six 12-month-old male and female mice, homozygous 3xTg-AD (males $n = 15$, females $n = 8$) and non-transgenic (NTg, males $n = 10$, females $n = 13$) mice on a C57BL/6 background (after embryonic transfer and backcrossing at least 10 generations), established in the Universitat Autònoma de Barcelona [23] were used. The 3xTg-AD mice harboring transgenes were genetically engineered at the University of Cali-

fornia Irvine, as previously described [16]. Animals were maintained in groups of 3–4 mice per cage (Macrolon, 35 × 35 × 25 cm) filled with 5 cm thick layer of clean woodchips that were the same used for behavioral testing (Ecopure, Chips6, DateSand, UK; Uniform cross-cut wood granules with 2.8–1.0 mm chip size) and nesting materials (Kleenex, Art: 08834060, 21 × 20 cm, White). All animals were maintained under standard laboratory conditions of food and water ad libitum, 22 ± 2°C, 12 h light: dark cycle with lights on at 8:00 a.m., and relative humidity 50–60%.

2.2. Experimental Design

As illustrated in Figure 1, animals were behaviorally assessed at middle-age (12 months of age) and re-tested four months later when they reached old age (16 months of age). In the AD-genotype, these time points correspond to two different advanced stages of the disease with the progressive development of β A and tau pathologies [17].

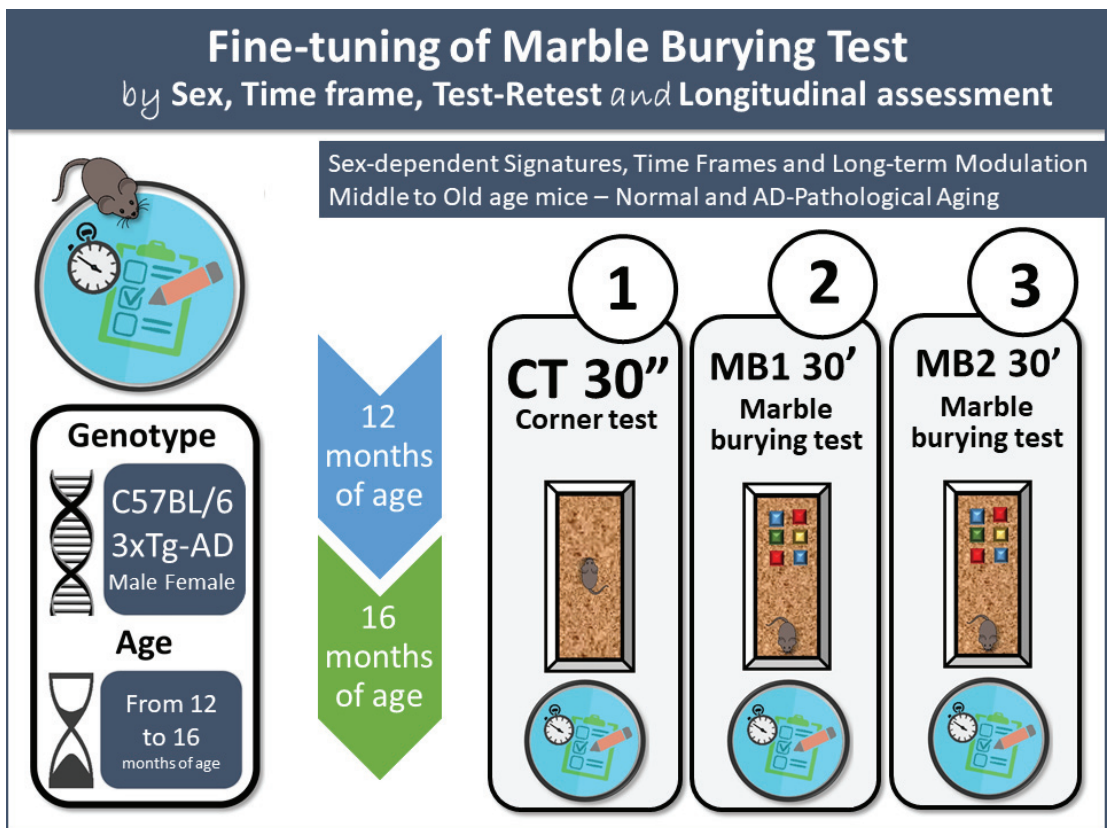


Figure 1. Fine-tuning of the marble burying test by sex, time frame, test–re-test, and longitudinal assessment. Experimental design: a 3-day battery of behavioral tests consisting of a corner test on day 1, a marble burying test on day 2 (MB1), and a repeated test on day 3 (MB2).

2.3. Behavioral Assessments

Behavioral assessments in the corner test and marble burying test under dim white light (20 lx) were conducted during the light phase of the light: dark cycle (from 10 a.m. to 1 p.m.). The tests were performed in a counterbalanced manner, by direct observation by a trained observer, blind to the genotype, and a camera's support. All procedures

were in accordance with the Spanish legislation on the “Protection of Animals Used for Experimental and Other Scientific Purposes” and the EU Directive (2010/63/UE) on this subject. The protocol CEEAH 3588/DMAH 9452 was approved the 8th of March 2019 by the Departament de Medi Ambient i Habitatge, Generalitat de Catalunya. The study complies with the ARRIVE guidelines developed by the NC3Rs and aims to reduce the number of animals used [24].

Day 1—Corner test (CT) was used to evaluate neophobia. The animal was placed in the center of a clean standard home cage filled with woodchip shave bedding and observed for 30 s. We measured the numbers of corners visited (CTc), the latency to perform the first rearing (CTlatR), and the number of rearings (CTr). The ratio of the number of visited corners and rearings variables (Ratio CTc/r) was calculated.

Days 2 and 3—Marble burying test (MB1) and re-test (MB2): Nine ceramic marbles were put in a standard home cage (Macrolon, $35 \times 35 \times 25 \text{ cm}^3$) with a 5 cm thick layer of clean woodchips. The marbles were placed evenly spaced (three rows of three) in one-quarter of the cage and allowing the mice to avoid interaction with the marbles. Then, the mouse was introduced in the zone without marbles facing the wall and left to interact with the cage freely. A picture of the cage was taken every 5 min to assess the buried marbles' progress. After 30 min the mice were gently removed from the cage, and the buried marbles were counted. Marbles were counted as buried when their surface was covered at least 90% with bedding material. The number of marbles buried was transformed in a percentage (MBx.y; x, day, y, time of measurement) for further statistical analysis. Twenty-four hours later, animals repeated the test under the same conditions.

2.4. Statistics

Statistical analyses were performed using SPSS 23.0 software. In the corner test, the variables recorded were analyzed by a split-plot design with the factors genotype (G), aging (A), sex (S), according to the experimental design $G(2) \times A(2) \times S(2)$. ANOVA split-plot designs analyzed the number of marbles buried with the factors time (T), genotype (G), aging (A), sex (S), and day (D), according to the experimental design $T(7) \times G(2) \times S(2) \times A(2) \times D(2)$. Post-hoc comparisons were run with Bonferroni corrections. Both the F and the degrees of freedom values were reported when it was possible. Spearman correlations were made to analyze behavioral correlates between the CT and the MB. Correlation coefficients (r) are indicated. A *p*-value < 0.05 was considered as statistically significant. Graphics were made with GraphPad Prism 6. Abbreviation: sexAgeMBday·minute (i.e, m12MB2.30, male at 12 months of age, re-test, 30 min).

3. Results

3.1. Corner Test for Neophobia

In the corner test (Figure 2), all the variables were sensitive to the aging factor, as the longitudinal analysis showed the reduction of the number of crossings (A, $F_{(1,42)} = 80.104$; $p < 0.001$), the number of rearings (A, $F_{(1,42)} = 24.564$; $p < 0.001$), the crossings/rearings ratio (A, $F_{(1,42)} = 23.903$; $p < 0.001$), and, conversely, the enhancement of the latency of rearing (A, $F_{(1,42)} = 18.085$; $p < 0.001$). Moreover, the crossings/rearings ratio was also sensitive to the genotype and aging interaction ($G \times A$, $F_{(1,42)} = 18.085$; $p < 0.001$).

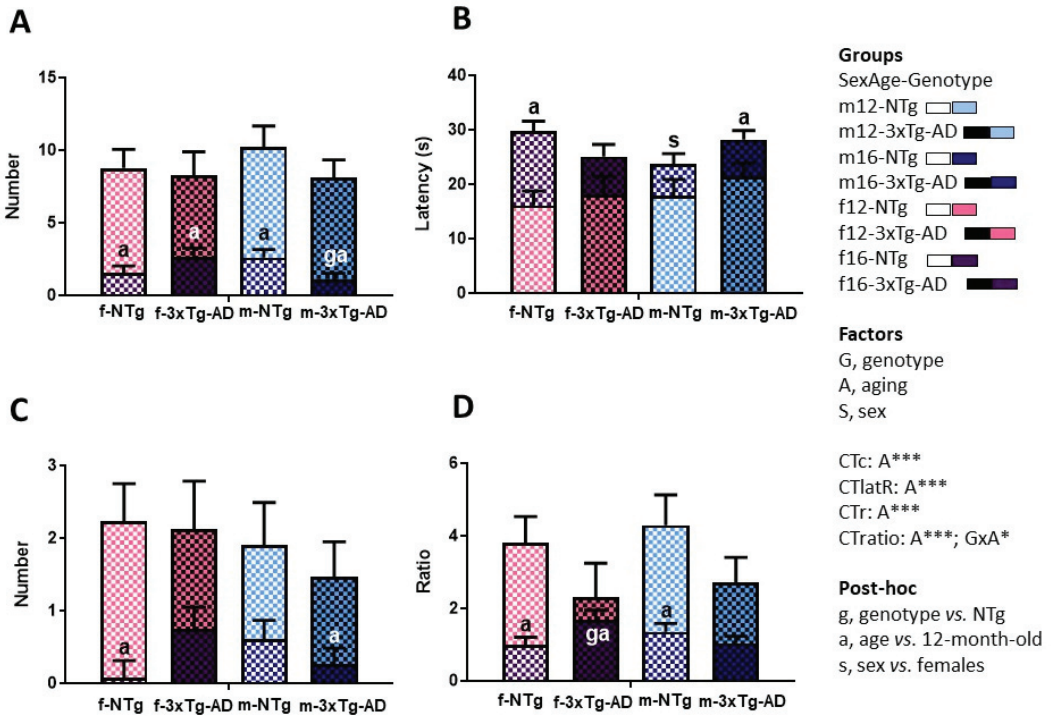


Figure 2. Sex and age effects in the longitudinal assessment in the corner test in mice with normal and AD-pathological aging. (A) Number of crossings (CTc); (B) Latency of rearing (CTlatR); (C) Number of rearings (CTr); (D) Ratio CTc/CTr (CTratio); Factorial analysis: G, genotype (NTg, 3xTg-AD mice); A, aging (12, 16 months of age); S, sex (male, female). * $p < 0.05$; *** $p < 0.001$.

The post-hoc analysis indicated meaningful differences as described hereinafter (see g, s, a at each variable in Figure 2). Thus, at 16 months, AD-males and AD-females exhibited a lower number of crossings (g, $F_{(1,42)} = 4.474$; $p = 0.040$) and higher crossings/rearings ratio (g, $F_{(1,42)} = 4.335$; $p = 0.043$), respectively, than their NTg counterparts. Regarding sex, NTg-males showed a lower latency of rearing than NTg-females at 16 months of age. With aging, all the groups manifested a reduction in the number of crossings (NTg-females: $p < 0.001$; AD-females: $p = 0.003$; NTg-males: $p < 0.001$; AD-males: $p < 0.001$). However, the rearing behavior only was affected in NTg-females (CTlatR: $p = 0.0001$; CTr: $p = 0.001$) and AD-males (CTlatR: $p = 0.048$; CTr: $p = 0.035$). At 16 months, these mice showed both a delayed elicitation of rearing and a lower number of total rearings. Finally, a reduction with aging in the ratio of crossings/rearings was also presented in NTg-females ($p = 0.001$), AD-males ($p = 0.021$) and WT-males ($p = 0.001$). The post-hoc analysis of these results is also depicted in Table 1.

Table 1. Post-hoc analysis of genotype, sex, and aging differences in the corner test.

Post-Hoc Analysis CORNER TEST	Genotype (vs. NTg Mice)		Sex (vs. Female Mice)		Aging (vs. 12-Month-Old Mice)	
	12 mo	16 mo	12 mo	16 mo	Each group	
CTc	All	Males	All	All	fNTg	$p < 0.001$
	n.s.	$p = 0.040$	n.s.	n.s.	f3xTg-AD	$p = 0.003$
					mNTg	$p < 0.001$
CTlatR	All	All	All	NTg	f3xTg-AD	$p < 0.001$
	n.s.	n.s.	n.s.	$p = 0.024$	mNTg	n.s.
					m3xTg-AD	$p = 0.048$
CTr	All	All	All	All	fNTg	$p = 0.001$
	n.s.	n.s.	n.s.	n.s.	f3xTg-AD	n.s.
					mNTg	n.s.
CTratio	All	Females	All	All	m3xTg-AD	$p = 0.035$
	n.s.	$p = 0.043$	n.s.	n.s.	fNTg	$p = 0.001$
					f3xTg-AD	n.s.
				mNTg	$p = 0.001$	
				m3xTgAD	$p = 0.021$	

Abbreviations: mo, months-old; CTc, number of crossings; CTlatR, latency of rearing; CTr, number of rearings; CTratio, CTc/CTr ratio; fNTg, female NTg mice; f3xTg-AD, female 3xTg-AD mice; mNTg, male NTg mice; m3xTg-AD, male 3xTg-AD mice; n.s., p -value value is not statistically significant.

3.2. Longitudinal Assessment of Marble Burying Test and Repeated Test

The marble burying test (Figure 3) was sensitive to the main factors genotype (G , $F_{(1,42)} = 4.212$; $p = 0.046$) and aging (A , $F_{(1,42)} = 4.325$; $p = 0.044$), while sex effects depended on the genotype ($G \times S$, $F_{(1,42)} = 12.768$; $p = 0.001$). The time-course analysis indicated that time (minute) (T , $F_{(2,373,99,681)} = 68.644$; $p < 0.001$) was determinant to detect genotype, sex, and age effects and interactions ($T \times G \times A \times S$, $F_{(3,234,135,830)} = 3.442$, $p = 0.016$; $T \times A$, $F_{(3,234,135,830)} = 3.385$; $p = 0.017$, $T \times G \times S$, $F_{(2,373,99,681)} = 5.589$; $p = 0.003$), while re-test 24 h later reduced the performances of 12-month-old animals in a lower/higher intensity manner depending on the genotype and sex ($G \times A \times S \times D$, $F_{(1,42)} = 5.598$; $p = 0.023$). In general, $T \times G \times A \times S \times D$ interactions effects were not statistically significant ($F_{(3,499,146,951)} = 5.400$; $p = 0.061$). The post-hoc analysis indicated meaningful differences as described hereinafter, providing evidence that the observation windows are critical (see g , a , s , d at each time point). The post-hoc analysis of these results is summarized in Table 2.

In the first MB testing, several meaningful differences between genotypes in the test performance were exhibited. At 12 months of age, post-hoc comparisons showed increased marble burying in AD-males compared to NTg-males (mMB5: $p = 0.010$; mMB10: $p = 0.013$; mMB15: $p = 0.009$; mMB20: $p = 0.014$), but no differences were found between females at this age.

However, when animals reached 16 months of age, the AD-phenotype was found up-regulated in males and down-regulated in females compared to their NTg counterparts. Thus, AD-males showed increased marble burying compared to NTg-males (m16MB1·10: $p = 0.016$; m16MB1·15: $p < 0.001$; m16MB1·20: $p < 0.001$; m16MB·25: $p = 0.001$), whereas AD-females buried less marbles than their NTg counterparts (f16MB1·15: $p = 0.046$; f16MB1·20: $p = 0.040$; f16MB1·25: $p = 0.011$; f16MB1·30: $p = 0.002$).

Table 2. Post-hoc analysis of genotype, sex, and aging differences in the marble test.

Post-Hoc Analysis MARBLE TEST	Genotype (vs. NTg Mice)		Sex (vs. Female Mice)		Aging (vs. 12 mo)	Repeated Test(vs. Day 1)
	12 mo	16 mo	12 mo	16 mo	Each group	Each group
Day 1 (MB1)						
MB1.5	Females <i>p</i> = 0.010	All n.s.	3xTg-AD <i>p</i> = 0.036	NTg <i>p</i> = 0.025	All n.s.	All n.s.
MB1.10	Females <i>p</i> = 0.013	Males <i>p</i> = 0.016	All n.s.	NTg <i>p</i> = 0.043	All n.s.	All n.s.
MB1.15	Females <i>p</i> = 0.009	Females <i>p</i> = 0.046 Males <i>p</i> = 0.000	All n.s.	NTg <i>p</i> = 0.002 3xTg-AD <i>p</i> = 0.011	All n.s.	All n.s.
MB1.20	Females <i>p</i> = 0.014	Females <i>p</i> = 0.040 Males <i>p</i> = 0.000	All n.s.	NTg <i>p</i> = 0.003 3xTg-AD <i>p</i> = 0.003	f3xTg-AD <i>p</i> = 0.043	All n.s.
MB1.25	All n.s.	Females <i>p</i> = 0.011 Males <i>p</i> = 0.001	All n.s.	NTg <i>p</i> = 0.004 3xTg-AD <i>p</i> = 0.003	f3xTg-AD <i>p</i> = 0.010	All n.s.
MB1.30	All n.s.	Females <i>p</i> = 0.002	All n.s.	NTg <i>p</i> = 0.012 3xTg-AD <i>p</i> = 0.007	f3xTg-AD <i>p</i> = 0.010	All n.s.
Day 2 (MB2)						
MB2.5	Males <i>p</i> = 0.005	Males <i>p</i> = 0.021	3xTg-AD <i>p</i> = 0.009	All n.s.	All n.s.	All n.s.
MB2.10	All n.s.	Males <i>p</i> = 0.024	3xTg-AD <i>p</i> = 0.045	All n.s.	All n.s.	All n.s.
MB2.15	Males <i>p</i> = 0.006	Males <i>p</i> = 0.008	All n.s.	All n.s.	All n.s.	All n.s.
MB2.20	Males <i>p</i> = 0.007	Males <i>p</i> = 0.004	All n.s.	3xTg-AD <i>p</i> = 0.012	All n.s.	All n.s.
MB2.25	Males <i>p</i> = 0.024	Males <i>p</i> = 0.020	All n.s.	3xTg-AD <i>p</i> = 0.039	All n.s.	All n.s.
MB2.30	All n.s.	Males <i>p</i> = 0.038	All n.s.	3xTg-AD <i>p</i> = 0.025	All n.s.	fNTg <i>p</i> = 0.005

Abbreviations: mo, months-old; (MBx.y), MB, Marble test; x, day; y, time (accumulated counts); fNTg, females NTg; n.s., *p*-value value is not statistically significant.

Besides, only the female sex exhibited longitudinal differences in the performance of the test. At 16 months of age, AD-female mice showed a lower percentage of marbles buried in the test's final minutes (f12-16MB1·20: *p* = 0.043; f12-16MB1·25: *p* = 0.010; f12-16MB1·30: *p* = 0.010) compared to their scores at 12 months of age.

Besides, several significant sex differences were found. At 12 months of age, significant post-hoc differences only appeared at the first five minutes of the test, where AD-males buried more marbles than AD-females (mf12MB1·5, *p* = 0.036). No differences were found between NTg mice at 12 months. Nevertheless, several meaningful differences were manifested by both AD-mice and NTg-mice at 16 months old. At this age, NTg-

males buried less marbles than NTg-females early in the test (mf16MB1·5: $p = 0.025$; mf16MB1·10: $p = 0.043$; mf16MB1·15: $p = 0.002$; mf16MB1·20: $p = 0.003$; mf16MB1·25: $p = 0.004$; mf16MB1·30: $p = 0.012$). Conversely, AD-males buried a higher percentage than AD-females (mf16MB1·15: $p = 0.011$; mf16MB1·20: $p = 0.003$; mf16MB1·25: $p = 0.003$; mf16MB1·30: $p = 0.007$).

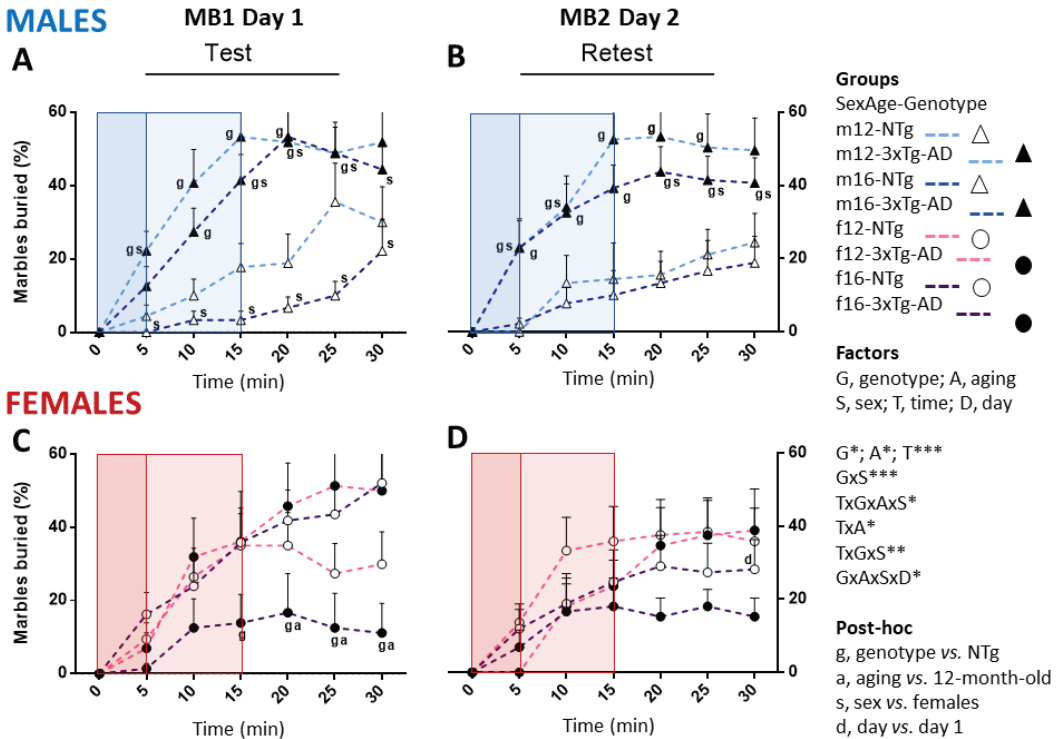


Figure 3. Sex, age, time, and day effects in the longitudinal assessment in the marble burying test and repeated test in mice with normal and AD-pathological aging. (A) Males marble burying test on day 1 (MB1 Day 1) and (B) re-test 24 h later (MB2 Day 2); (C) Females marble burying test on day 1 (MB1 Day 1) and (D) re-test 24 h later (MB2 Day 2); Factorial analysis: G, genotype (NTg, 3xTg-AD mice); A, aging (12, 16 months of age); S, sex (male, female); T, time (0–30 min); D, day (Day 1, Day 2). * $p < 0.05$; ** $p < 0.01$; *** $p < 0.001$.

In the re-test, 24 h later, 12-month-old AD-males buried more marbles than NTg-males at several time points of the test (m12MB2·5: $p = 0.005$; m12MB2·15: $p = 0.006$; m12MB2·20: $p = 0.007$; m12MB2·25: $p = 0.0024$). Conversely, there was an absence of differences between 12-month-old AD-females and NTg-females. When the animals reached 16 months of age, genotype differences still persisted between AD and NTg males (m16MB2·5: $p = 0.021$; m16MB2·10: $p = 0.024$; m16MB2·15: $p = 0.008$; m16MB2·20: $p = 0.004$; m16MB2·25: $p = 0.020$; m16MB2·30: $p = 0.038$), but those observed between females disappeared.

Regarding sex post-hoc differences in the re-test, they were clearly shown in the group of AD mice at both ages studied. Thus, 12-month-old AD-males buried a higher percentage of marbles than NTg-males at the beginning of the test (m12MB2·5: $p = 0.009$; m12MB2·10: $p = 0.0045$). Four months later, when they reached 16 months of age, AD-males showed very similar test and re-test patterns (m16MB2·20: $p = 0.012$; m16MB2·25: $p = 0.0039$; m16MB2·30: $p = 0.025$). However, at 16 months, differences between NTg-males and NTg-females were not found.

Finally, the percentage of marbles buried between the test and the re-test on the first and the second day of testing in all the time measures for all the groups were compared. At 12 months of age, no differences were found, while the performance of these animals at 16 months showed one difference: the NTg-females buried fewer marbles at the end time point of the second test (f16MB2-30: $p = 0.005$). Therefore, the time-course analysis is essential to unveil sex, aging, and re-test differences otherwise under-detected.

3.3. Corner Test and Marble Burying Test Correlations

In calculating these correlations, the variables genotype and sex were taken into account to generate the tables. The relationship between these tests was analyzed for the two ages studied. To simplify the analysis, we paid attention mainly to both the percentage of marbles buried at five and thirty minutes for the first marble test testing (MB1·5 and MB1·30, respectively).

At 12 months of age, correlations between the CT and the MB tests were only exhibited by female mice. For NTg-female mice, the number of rearings in the CT was positively correlated with the percentage of marbles buried at both five and thirty minutes (CTr © f12MB1·5, $r = 0.716$; $p = 0.006$; CTr © f12MB1·30, $r = 0.620$; $p = 0.024$). While for AD-female mice, the number of rearings in the CT were positively correlated with the percentage of marbles buried at five minutes (CTr © f12MB1·5, $r = 0.835$; $p = 0.010$), the latency of rearing was inversely correlated also with the percentage of marbles buried at five minutes (CTlatR © f12MB1·5, $r = -0.845$; $p = 0.008$). At 16 months of age, none of the groups exhibited correlations. Among others, all these results are summarized in Table 3.

Table 3. Corner test and marble burying test Spearman correlation analysis.

		CTc	CTlatR	CTr	CTratio
fNTg ($n = 13$) at 12 moa					
MB1.5	Spearman correlation Sig. (2-tailed)	n.s.	n.s.	0.716 ** 0.006	n.s.
MB1.10	Spearman correlation Sig. (2-tailed)	n.s.	n.s.	0.617 * 0.025	n.s.
MB1.15	Spearman correlation Sig. (2-tailed)	n.s.	n.s.	0.697 ** 0.008	n.s.
MB1.20	Spearman correlation Sig. (2-tailed)	n.s.	n.s.	0.631 * 0.021	n.s.
MB1.25	Spearman correlation Sig. (2-tailed)	n.s.	n.s.	n.s.	n.s.
MB1.30	Spearman correlation Sig. (2-tailed)	n.s.	n.s.	0.620 * 0.024	n.s.
fNTg at 16 moa					
MB1.25	Spearman correlation Sig. (2-tailed)	0.568 * 0.043	n.s.	n.s.	n.s.
f3xTg-AD ($n = 8$) at 12 moa					
MB1.5	Spearman correlation Sig. (2-tailed)	n.s.	-0.845 ** 0.008	0.0835 ** 0.010	n.s.
All the other groups					
MB1.all	Spearman correlation Sig. (2-tailed)	n.s.	n.s.	n.s.	n.s.

Only statistically significant correlations are indicated. Abbreviations: fNTg, females NTg; f3xTg-AD, females 3xTg-AD mice; moa, months of age; (MBx.y) MB, marble test; x, day; y, time (accumulated counts); fNTg Sig., significant; **, correlation significant at the 0.01 level (2-tailed), *, correlation significant at the 0.05 level (2-tailed).

4. Discussion

In the present work, we corroborate the previously described higher burying of marbles in 3xTg-AD male mice at 12 months of age [6,18], and we demonstrate the complexity of factor interplay in the performance of the MB test. For the first time, we show that the higher performance in 3xT-AD male mice is also observed in the female sex, albeit statistically significant genotype differences in females are only reached at 16 months. Moreover, the longitudinal design allows the monitoring of changes in the performance with worsening of the disease only in AD-female mice, and normal aging in NTg mice, from 12 to 16 months of age, and its modulation through the repeated test. Most importantly, the time-course analysis provides a tool to discriminate the best temporal windows of observation depending on these factors.

4.1. New Insight of Burying Behavior in 3xTg-AD Mice

We provide evidence that the higher burying of the AD-male mice than NTg mice over 30 min [6,19] is a phenomenon sustained throughout the test and could also be scored since the beginning. For the first time, the inclusion of 3xTg-AD female mice in MB testing is reported. In contrast, despite AD-females showing higher percentages than their NTg counterparts at the end of the test, these differences did not reach statistical significance. Sexual differences were present in the AD-phenotype at the beginning of the test at 12 months old. However, with aging, these differences were exhibited in the second half of the test. In both stances, AD-female mice presented the lower percentage of marbles buried. Although it is known that the estrous cycle can affect burying activity [25–27], comparative studies between sexes are scarce. Those available do not find differences [28], and if they do, they are dependent on the menstrual cycle [28]. Therefore, this finding represents a step forward in the exploration of sex differences in burying behavior.

In addition, for the first time, the longitudinal design showed that pathological aging influenced MB performance. At 16 months of age, males did not show any significant difference in performance compared to their assessment at 12 months. In contrast, the performance of AD-females was lower at 16 months through all the tests, although statistical significance was reached from minute 20, and the performance of NTg-females was relatively similar at both ages. In normal aging, NTg-males showed significantly lower MB compared to NTg-females of the same age. Also, the genotype differences between male mice persisted at this age through the MB test. Therefore, we found a differential influence of how normal and AD-pathological aging affects MB performance. Firstly, aging has a differentiated response, whether accompanied by pathology or not, as shown by the fact that NTg animals do not undergo percentage changes. However, in addition, the aging of 3xTg-AD mice produced a sex-dependent differential response in their behavior, with significant differences between 16-month-old AD-females and AD-males in the second half of the MB test.

Several authors advocate for repeated trials as necessary for using MB as a model of neophobia/anxiety or OCD [13]. Following these recommendations, at both ages, we applied two consecutive days of MB testing. When the time-course of the test and re-test of all groups was compared, the standard pattern was the absence of differences in their performance at both ages, although NTg-females showed significantly lower performance at min 30 in the re-test performed at 16 months of age. As can be seen, these variations are not large enough to generate significant changes concerning their performance on the previous day. At 16 months of age, the lower performance of NTg-females eliminates both the genotype and sexual differences with AD-females and NTg-males, respectively. Moreover, the reduction of the performance of marbles buried in AD-females at 12 months suggests that aging differences with respect to AD-females at 16 months did not show up, and caused the temporal amplification of sexual differences at the beginning of the test regarding AD-males. For the rest, genetic and sexual differences manifested by AD-males at both ages were still conserved. Although slight variations are exhibited in some measures, they do not change their manifested behavioral phenotype interpretation.

4.2. Corner Test and Its Relationship with Marble Burying Test in 3xTg-AD Mice

In the present work, we did not find genotype differences in neophobia, contrary to what occurred on other occasions [6,19]. However, we did observe a reduction in mouse activity and a slowdown of latency due to aging. This occurs in all variables, although it does not always occur in all groups in a statistically significant way, although a tendency can be appreciated.

The relationship between the burrowing percentage in the MB and the CT variables could be described as inconsistent and poor. To simplify its interpretation, we focused our attention on the first measure, which should be more sensitive to neophobia, and the last one, for comparative purposes. If we hypothesize that the higher percentage of buried marbles is due to anxiety, a clear relationship should be visible between the two tests, especially for AD-males. However, correlations only appeared in both NTg and AD female mice. To summarize, these results would be in line with the poor relationship showed between the MB and other tests for assessing anxiety-like behavior in other studies [29–31].

4.3. Marble Test as a Model of Anxiety-Like or OCD-Like Behavior in 3xTg-AD Mice?

With all of the previously discussed, the modeling of anxiety-like behavior in the burying behavior of this animal model is certainly questionable. First of all, due to the utilization of the two-zone configuration, the animals can avoid the marbles, so we can assume that the interaction with the marbles is, to some extent, voluntary. Then, it would be expected that AD-mice would show passive avoidance of marbles, which is not the case. These results would be consistent with those shown by other studies using a two-zone configuration [11,14,31–34]. Furthermore, in the re-testing, no change would indicate that habituation to a stressful situation is produced, either assuming two different fight-to-flight scenarios: a case where the animals were so frightened of the marbles that they buried as a defensive strategy (AD-mice), or they would avoid their interaction with them (NTg mice). However, they interact as well, but to a lesser extent. Moreover, although there are no clear genotype differences in neophobia, measured through CT, differences still appeared in burying behavior in MB. Finally, correlations between the burying percentages and the CT variables are scarce and inconsistent. A possible hypothesis to support the anxiety-like modeling of burying behavior could be that the inherited anxiety trait of these mice could make their response to marbles resistant to habituation [35,36] and thereby invoking either active burying or passive avoidance behavior as coping strategies [36–41]. Since 3xTg-AD mice present higher baseline anxiety [23], which produces differentiated anxious responses depending on the test [18], the previous hypothesis is still possible. Interestingly, we already reported that other animal models for anxiety, such as the A1 receptor knock out mice, also show reduced habituation [42]. Moreover, in our precedent Gimenez-Llort and Alveal-Mellado's work [19], 3xTg-AD mice showed a higher freezing behavior in the open-field test accompanied with higher amounts of marble burying, contrary to NTg-mice. Therefore, although the modeling of anxious-like behavior is questionable, with the methodology employed it is not completely discardable.

It seems pretty clear that regardless of whether they bury more or fewer marbles, their performance in this test is persistent and stable over time, in concordance with other studies with repeated MB application [28,31,32,43–45]. This event would support the current practice of using burying behavior as an indication of OCD-like behavior, although this approach also has certain validity concerns [13,45,46]. While OCD may be a risk factor for developing AD [47,48], it is unlikely to be the construct modeled in the 3xTg-AD mice. Due to the repetitive and perseverative nature of burying activity, this behavior could represent NPS such as perseverative behavior and/or stereotyped behavior. Both are NPS usually present in patients with Alzheimer's and other dementias [49–51]. In addition, 3xTg-AD mice have been shown to present more significant errors due to perseverative behavioral hopelessness paradigms [52] and attentional tasks [53], and greater presence of stereotyped behaviors at early stages of the disease [23]. Therefore, it is quite possible that burying behavior in 3xTg-AD mice reflects perseverative and/or stereotyped-like

behavior rather than anxiety-like behavior. However, this is not necessarily denying that anxiety may influence the performance on the marble test, mainly through differentiated coping strategies.

Far from discussions about which pathology models the test in our animal model, what remains clear is that the burying behavior is stable and resistant to repetition, regardless of the group or whether the animals show high or low percentages. Therefore another way of interpreting the results would be to look at them with a neuroethological perspective, in which burying is an inherent behavior of the animal [13], in this case, sensitive to AD-pathology and with differentiated response depending on sex, aging, and their interactions. Considering that burying represents the application of digging [13], defined as the displacement of a substrate mainly using forepaws [54], to a more complex task, it would be expected that digging was the sensitive behavior to the AD pathology. Thus, 3xTg-AD mice should show a similar profile in other tests involving digging behavior shown in the MB. Therefore, further research is needed to confirm this hypothesis.

4.4. Integrating Our New Findings into Our Previous Knowledge of The Burying Behavior of 3xTg-AD Mice

The inter-test stability in the burying behavior also has important implications for supporting the conclusions developed in previous works of our research group with the 3xTg-AD mice. In Torres-Lista's previous studies [6,18], chronic administration of risperidone reduced the number of marbles buried compared to their pre-treatment testing for both AD-male and NTg-male mice. Moreover, this number was modulated in saline groups, albeit presenting a different pattern depending on the genotype. In AD-mice, as happened with risperidone, the number of marbles buried was reduced, whereas for NTg-males, this number was higher. These changes in the marble activity were attributed to an effect of the repetitive handling for the administration of the saline compounds. The results obtained in the present study would support that conclusion since, without the handling, the animal's burying behavior should have been unaltered in the resetting. We attributed the reduction of marble activity in the AD saline group to the anxiolytic effect of handling [55–57], and the increase in marble activity in NTg-males with an increase in their emotional state. However, this claim remains unclear partly for our present results and partly because burying behavior can be enhanced in mice by stressing the animal through non-pharmacological intervention [58–60]. Thus, it may have been possible that the repetitive subcutaneous administration of the saline compound acted as a stressor affecting the inherited burying behavior of each group and thereby either increasing or decreasing it depending on their inherited pattern.

4.5. Benefits of Implementing the Time-Course of Marble Buried

This is the first time that time-course of marbles buried by 3xTg-AD mice in MB was studied as a methodological novelty. As we previously explained in the method, it consisted of counting the number of marbles buried at five minute intervals until the end of the test. Although we have already commented on their results in the previous section, we would like to make some remarks to promote its use. First of all, its application is easy and affordable. It can be done through photography or video, not interfering in the normal development of the test. Moreover, the intervals can be easily adapted to the needs of the study, although it would be advisable to include at least one measurement in the middle of the test. The reason for this is that, at least in our model, differences usually appear at 10–15 min, and the score at that time does not differ significantly from the score obtained at 30 min (analysis not shown). To us, the most important reason for its use is that it gives us valuable information about the behavioral pattern of the animal throughout the test, helping us to establish a more accurate profile of the animal and the possible differences between them. This may be especially important in pharmacological and non-pharmacological interventions as well, as such interventions could modify the pattern of the animal and not just the final test score. Concerning the latter, time-course could save many nightmares to researchers using the MB. If we consider only the final

measurement, we could erroneously conclude that there are significant differences (false positive) or not (false negative) between the two groups when in fact, throughout the test, this was not the case. In our experiment, we can see an example of each. As a false positive in the final measurement, we have that the 16-month-old AD-females burying percentage is significantly different regarding their score on the previous testing, but only in that score. While as a false negative, we see that in the last measurement of the re-test, the significant difference between AD-males and NTg-males at 12 months disappears when there have been significant differences in all the previous scores. In addition, although the counting of marbles through the test has existed for a long time [43], its use is not widespread. It is difficult to find examples of its use in the literature, although they certainly exist [59,61]. As in our experiment, the differences found at the end of the test are usually manifested from the first measurements and are relatively stable over the time course. Considering the foregoing, we consider that the advantages of its application far outweigh the costs of its implementation.

4.6. Methodological Limitations of the Study

Although, in our view, the data support the above discussions, certain methodological limitations may influence the degree of certainty of our conclusions. Here, we'll discuss them to warn the reader regarding the possible impact of these limitations on interpretability and, consequently, the conclusions drawn.

First, it is necessary to discuss the statistical analysis employed. MB is commonly analyzed using linear models, such as the *t*-test and ANOVA. In our case, we have also employed a split-plot ANOVA. However, as Lazic [15] points out, this type of analysis may be inadequate because, as the number of marbles is a counted data, it does not meet the requirements of this type of analysis, leading to 95% confidence intervals that include impossible values (less than zero or greater than the number of marbles present), misleading *p*-values, and impossible predictions. There are other more appropriate (non-parametric) types of analysis. However, in our case, we decided to use the analysis for several reasons: 1) to be in line with our previous studies, 2) to use the most commonly used method in the literature, and 3) the complexity of the experimental design made it very difficult to use non-parametric analysis techniques.

On the other hand, there are several limitations in ascertaining which construct the MB test relates to or models. In the case of anxiety, there are more classical tests than the CT for measuring anxiety-like behavior (e.g., open field, elevated plus maze). We used the CT because in our previous studies [6], there were correlations concerning the MB. However, as mentioned above, other studies have explored the relationship between anxiety tests and the MB and obtained relatively poor results [29–31], so it is unlikely that this would be any different in our case. In perseverative behavior, we also do not have an alternative behavior (e.g., grooming) in the MB or another test to validate this hypothesis. However, in this case, the design relies on the resistance to habituation of the marble test, as is the case in other experimental tests e.g., [31]. The main intention of this paper is not to conclude what behavior models the MB in the 3xTg-AD model, although we do hypothesize, based on the data obtained, that it could be due to the previous points of the discussion.

All in all, it is clear that more research is needed to explore these questions further and overcome the limitations present in this study.

5. Conclusions

In summary, the present results allow us to conclude that (1) the marble test is responsive to genotype, sex, aging, and its interactions; (2) the male sex was more sensitive to showing the AD-phenotype; (3) longitudinal study shows a reduction of burying in females with AD pathology; (4) burying remains stable in repeated testing; (5) the time-course of marbles buried is a useful methodological modification; and (6) burying behavior in the MB test most likely represents perseverative and/or stereotyped-like behavior rather than anxiety-like behavior in 3xTg-AD mice. More research is needed in the 3xTg-AD mice to

approach further the modeling of perseverative and stereotyped-like behavior in MB and to be able to verify if the profile shown in the MB test is transferable to other tests that imply digging behavior.

Author Contributions: Conceptualization, L.G.-L. and M.S.-S.; Behavioral performance, analysis, statistics, M.S.-S.; Illustrations: M.S.-S. and L.G.-L. Writing—original draft preparation, M.S.-S.; writing—review and editing, M.S.-S., L.G.-L. and J.-R.B.; Funding acquisition, L.G.-L. All authors have read and agreed to the published version of the manuscript.

Funding: This work was funded by UAB-GE-260408 to L.G.-L. The colony of 3xTg-AD mice is sustained by ArrestAD H2020 Fet-OPEN-1-2016-2017-737390, European Union’s Horizon 2020 research and innovation program under grant agreement No 737390 to L.G.-L. It also received financial support from Memorial Mercedes Llorc Sender 2021/80/09241941.6.

Institutional Review Board Statement: The study was conducted according to the guidelines of the Declaration of Helsinki, and approved by the Ethics Committee of Departament de Medi Ambient i Habitatge, Generalitat de Catalunya (CEEAH 3588/DMAH 9452) on the 8th of March 2019.

Informed Consent Statement: Not applicable.

Data Availability Statement: Not applicable.

Acknowledgments: We thank Frank M. LaFerla, Institute for Memory Impairments and Neurological Disorders, University of California Irvine, CA, USA, for kindly providing the progenitors of the Spanish colonies of homozygous 3xTg-AD and NTg mice.

Conflicts of Interest: The authors declare no conflict of interest. The funders had no role in the study’s design; in the collection, analyses, or interpretation of data; in the writing of the manuscript; or in the decision to publish the results.

References

- Ballard, C.; Corbett, A. Management of neuropsychiatric symptoms in people with dementia. *CNS Drugs* **2010**, *24*, 729–739. [CrossRef] [PubMed]
- Shin, I.S.; Carter, M.; Masterman, D.; Fairbanks, L.; Cummings, J.L. Neuropsychiatric symptoms and quality of life in Alzheimer disease. *Am. J. Geriatr. Psychiatry* **2005**, *13*, 469–474. [CrossRef] [PubMed]
- Tan, L.L.; Wong, H.B.; Allen, H. The impact of neuropsychiatric symptoms of dementia on distress in family and professional caregivers in Singapore. *Int. Psychogeriatr.* **2005**, *17*, 253–263. [CrossRef]
- Hope, T.; Keene, J.; Gedling, k.; Fairburn, C.G.; Jacoby, R. Predictors of institutionalization for people with dementia living at home with a carer. *Int. J. Geriatr. Psychiatry* **1998**, *13*, 682–690. [CrossRef]
- Mielke, M.M. Sex and Gender Differences in Alzheimer’s Disease Dementia. *Psychiatr. Times* **2018**, *35*, 14–17. [PubMed]
- Torres-Lista, V.; López-Pousa, S.; Giménez-Llort, L. Marble-burying is enhanced in 3xTg-AD mice, can be reversed by risperidone and it is modulable by handling. *Behav. Process.* **2015**, *116*, 69–74. [CrossRef]
- Torres-Lista, V.; Giménez-Llort, L. Impairment of nesting behaviour in 3xTg-AD mice. *Behav. Brain Res.* **2013**, *247*, 153–157. [CrossRef] [PubMed]
- Giménez-Llort, L.; Torres-Lista, V. Social Nesting, Animal Welfare, and Disease Monitoring. *Animals* **2021**, *11*, 1079. [CrossRef]
- Deacon, R.M. Digging and marble burying in mice: Simple methods for in vivo identification of biological impacts. *Nat. Protoc.* **2006**, *1*, 122–124. [CrossRef] [PubMed]
- Pinel, J.P.J.; Treit, D. Burying as a defensive response in rats. *J. Comp. Physiol. Psychol.* **1978**, *92*, 708–712. [CrossRef]
- Broekkamp, C.L.; Rijk, H.W.; Joly-Gelouin, D.; Lloyd, K.L. Major tranquillizers can be distinguished from minor tranquillizers on the basis of effects on marble burying and swim-induced grooming in mice. *Eur. J. Pharmacol.* **1986**, *126*, 223–229. [CrossRef]
- Njung’e, K.; Handley, S.L. Effects of 5-HT uptake inhibitors, agonists and antagonists on the burying of harmless objects by mice; a putative test for anxiolytic agents. *Br. J. Pharmacol.* **1991**, *104*, 105–112. [CrossRef] [PubMed]
- de Brouwer, G.; Fick, A.; Harvey, B.H.; Wolmarans, W. A critical inquiry into marble-burying as a preclinical screening paradigm of relevance for anxiety and obsessive-compulsive disorder: Mapping the way forward. *Cogn. Affect. Behav. Neurosci.* **2019**, *19*, 1–39. [CrossRef] [PubMed]
- de Brouwer, G.; Wolmarans, W. Back to basics: A methodological perspective on marble-burying behavior as a screening test for psychiatric illness. *Behav. Process.* **2018**, *157*, 590–600. [CrossRef]
- Lazic, S.E. Analytical strategies for the marble burying test: Avoiding impossible predictions and invalid *p*-values. *BMC Res. Notes* **2015**, *8*, 1–10. [CrossRef] [PubMed]

16. Oddo, S.; Caccamo, A.; Shepherd, J.D.; Murphy, M.P.; Golde, T.E.; Kaye, R.; Metherate, R.; Mattson, M.P.; Akbari, Y.; LaFerla, F.M. Triple-transgenic model of Alzheimer's disease with plaques and tangles: Intracellular Abeta and synaptic dysfunction. *Neuron* **2003**, *39*, 409–421. [CrossRef]
17. Belfiore, R.; Rodin, A.; Ferreira, E.; Velazquez, R.; Branca, C.; Caccamo, A.; Oddo, S. Temporal and regional progression of Alzheimer's disease-like pathology in 3xTg-AD mice. *Aging Cell* **2019**, *18*, e12873. [CrossRef]
18. Torres-Lista, V.; López-Pousa, S.; Giménez-Llort, L. Impact of Chronic Risperidone Use on Behavior and Survival of 3xTg-AD Mice Model of Alzheimer's Disease and Mice With Normal Aging. *Front. Pharmacol.* **2019**, *10*, 1061. [CrossRef]
19. Gimenez-Llort, L.; Alveal-Mellado, D. Digging Signatures in 13-Month-Old 3xTg-AD Mice for Alzheimer's Disease and Its Disruption by Isolation Despite Social Life Since They Were Born. *Front. Behav. Neurosci.* **2021**, *19*. [CrossRef]
20. Zucker, I.; Beery, A.K. Males still dominate animal studies. *Nature* **2010**, *465*, 690. [CrossRef]
21. Çalışkan, H.; Şentunalı, B.; Özden, F.M.; Cihan, K.H.; Uzunkulaoglu, M.; Çakan, O.; Kankal, S.; Zaloğlu, N. Marble burying test analysis in terms of biological and non-biological factors. *J. Appl. Biol. Sci.* **2017**, *11*, 54–57.
22. Giménez-Llort, L.; Blázquez, G.; Cañete, T.; ohansson, B.; Oddo, S.; Tobeña, A.; LaFerla, F.M.; Fernández-Teruel, A. Modeling behavioral and neuronal symptoms of Alzheimer's disease in mice: A role for intraneuronal amyloid. *Neurosci. Biobehav. Rev.* **2007**, *31*, 125–147. [CrossRef]
23. Baeta-Corral, R.; Giménez-Llort, L. Bizarre behaviors and risk assessment in 3xTg-AD mice at early stages of the disease. *Behav. Brain Res.* **2014**, *258*, 97–105. [CrossRef]
24. Kilkenny, C.; Browne, W.J.; Cuthill, I.C.; Emerson, M.; Altman, D.G. Improving bioscience research reporting: The ARRIVE guidelines for reporting animal research. *PLoS Biol.* **2010**, *24*. [CrossRef]
25. Schneider, T.; Popik, P. Attenuation of estrous cycle-dependent marble burying in female rats by acute treatment with progesterone and antidepressants. *Psychoneuroendocrinology* **2007**, *32*, 651–659. [CrossRef] [PubMed]
26. Llaneza, D.C.; Frye, C.A. Progestogens and estrogen influence impulsive burying and avoidant freezing behavior of naturally cycling and ovariectomized rats. *Pharmacol. Biochem. Behav.* **2009**, *93*, 337–342. [CrossRef] [PubMed]
27. Mitra, S.; Bastos, C.P.; Chesworth, S.; Frye, C.; Bult-Ito, A. Strain and sex based characterization of behavioral expressions in non-induced compulsive-like mice. *Physiol. Behav.* **2017**, *168*, 103–111. [CrossRef] [PubMed]
28. Taylor, G.T.; Lerch, S.; Chourbaji, S. Marble burying as compulsive behaviors in male and female mice. *Acta Neurobiol. Exp. (Wars)* **2017**, *77*, 254–260. [CrossRef] [PubMed]
29. Sanathara, N.M.; Garau, C.; Alachkar, A.; Wang, L.; Wang, Z.; Nishimori, K.; Xu, X.; Civelli, O. Melanin concentrating hormone modulates oxytocin-mediated marble burying. *Neuropharmacology* **2018**, *128*, 22–32. [CrossRef] [PubMed]
30. Savy, C.Y.; Fitchett, A.E.; McQuade, R.; Gartside, S.E.; Morris, C.M.; Blain, P.G.; Judge, S.J. Low-level repeated exposure to diazinon and chlorpyrifos decrease anxiety-like behaviour in adult male rats as assessed by marble burying behaviour. *Neurotoxicology* **2015**, *50*, 149–156. [CrossRef]
31. Thomas, A.; Burant, A.; Bui, N.; Graham, D.; Yuva-Paylor, L.A.; Paylor, R. Marble burying reflects a repetitive and perseverative behavior more than novelty-induced anxiety. *Psychopharmacology* **2009**, *204*, 361–373. [CrossRef]
32. Njung'e, K.; Handley, S.L. Evaluation of marble-burying behavior as a model of anxiety. *Pharmacol. Biochem. Behav.* **1991**, *38*, 63–67. [CrossRef]
33. Kaehler, S.T.; Singewald, N.; Sinner, C.; Philippu, A. Nitric oxide modulates the release of serotonin in the rat hypothalamus. *Brain Res.* **1999**, *835*, 346–349. [CrossRef]
34. Nicolas, L.B.; Kolb, Y.; Prinszen, E.P. A combined marble burying-locomotor activity test in mice: A practical screening test with sensitivity to different classes of anxiolytics and antidepressants. *Eur. J. Pharmacol.* **2006**, *547*, 106–115. [CrossRef] [PubMed]
35. Stein, D.J.; Bouwer, C. A neuro-evolutionary approach to the anxiety disorders. *J. Anxiety Disord.* **1997**, *11*, 409–429. [CrossRef]
36. Steimer, T. Animal models of anxiety disorders in rats and mice: Some conceptual issues. *Dialogues Clin. Neurosci.* **2011**, *13*, 495–506. [CrossRef]
37. Koolhaas, J.M.; Everts, H.; de Ruiter, A.J.; de Boer, S.F.; Bohus, B. Coping with stress in rats and mice: Differential peptidergic modulation of the amygdala-lateral septum complex. *Prog. Brain Res.* **1998**, *119*, 437–448. [CrossRef]
38. Koolhaas, J.M.; de Boer, S.F.; Buwalda, B.; van Reenen, K. Individual variation in coping with stress: A multidimensional approach of ultimate and proximate mechanisms. *Brain Behav. Evol.* **2007**, *70*, 218–226. [CrossRef] [PubMed]
39. Bruins Slot, L.A.; Bardin, L.; Auclair, A.L.; Depoortere, R.; Newman-Tancredi, A. Effects of antipsychotics and reference monoaminergic ligands on marble burying behavior in mice. *Behav. Pharmacol.* **2008**, *19*, 145–152. [CrossRef] [PubMed]
40. Coppens, C.M.; de Boer, S.F.; Koolhaas, J.M. Coping styles and behavioural flexibility: Towards underlying mechanisms. *Philos. Trans. R. Soc. B Biol. Sci.* **2010**, *365*, 4021–4028. [CrossRef]
41. Kinsey, S.G.; O'Neal, S.T.; Long, J.Z.; Cravatt, B.F.; Lichtman, A.H. Inhibition of endocannabinoid catabolic enzymes elicits anxiolytic-like effects in the marble burying assay. *Pharmacol. Biochem. Behav.* **2011**, *98*, 21–27. [CrossRef] [PubMed]
42. Giménez-Llort, L.; Masino, S.A.; Diao, L.; Fernández-Teruel, A.; Tobeña, A.; Halldner, L.; Fredholm, B.B. Mice lacking the adenosine A1 receptor have normal spatial learning and plasticity in the CA1 region of the hippocampus, but they habituate more slowly. *Synapse* **2005**, *57*, 8–16. [CrossRef]
43. Gyertyán, I. Analysis of the marble burying response: Marbles serve to measure digging rather than evoke burying. *Behav. Pharmacol.* **1995**, *6*, 24–31.

44. Poling, A.; Cleary, J.; Monaghan, M. Burying by rats in response to aversive and nonaversive stimuli. *J. Exp. Anal. Behav.* **1981**, *35*, 31–44. [CrossRef] [PubMed]
45. Wolmarans de, W.; Stein, D.J.; Harvey, B.H. Of mice and marbles: Novel perspectives on burying behavior as a screening test for psychiatric illness. *Cogn. Affect. Behav. Neurosci.* **2016**, *16*, 551–560. [CrossRef]
46. de Boer, S.F.; Koolhaas, J.M. Defensive burying in rodents: Ethology, neurobiology and psychopharmacology. *Eur. J. Pharmacol.* **2003**, *463*, 145–161. [CrossRef]
47. Mrabet Khiari, H.; Achouri, A.; Ben Ali, N.; Cherif, A.; Batti, H.; Messaoud, T.; Mrabet, A. Obsessive-compulsive disorder: A new risk factor for Alzheimer disease? *Neurol Sci.* **2011**, *32*, 959–962. [CrossRef]
48. Dondu, A.; Sevincoka, L.; Akyol, A.; Tataroglu, C. Is obsessive-compulsive symptomatology a risk factor for Alzheimer-type dementia? *Psychiatry Res.* **2015**, *225*, 381–386. [CrossRef]
49. Pekkala, S.; Albert, M.L.; Spiro, A., 3rd; Erkinjuntti, T. Perseveration in Alzheimer’s disease. *Dement. Geriatr. Cogn. Disord.* **2008**, *25*, 109–114. [CrossRef]
50. Dearthoff, W.J.; Grossberg, G.T. Behavioral and psychological symptoms in Alzheimer’s dementia and vascular dementia. *Handb. Clin. Neurol.* **2019**, *165*, 5–32. [CrossRef]
51. Cipriani, G.; Vedovello, M.; Ulivi, M.; Nuti, A.; Lucetti, C. Repetitive and stereotypic phenomena and dementia. *Am. J. Alzheimers Dis Other Demen.* **2013**, *28*, 223–227. [CrossRef]
52. Torres-Lista, V.; Giménez-Llort, L. Persistence of behaviours in the Forced Swim Test in 3xTg-AD mice at advanced stages of disease. *Behav. Processes* **2014**, *106*, 118–121. [CrossRef] [PubMed]
53. Romberg, C.; Mattson, M.P.; Mughal, M.R.; Bussey, T.J.; Saksida, L.M. Impaired attention in the 3xTgAD mouse model of Alzheimer’s disease: Rescue by donepezil (Aricept). *J. Neurosci.* **2011**, *31*, 3500–3507. [CrossRef]
54. Layne, J.N.; Ehrhart, L.M. Digging behavior of four species of deer mice (*Peromyscus*). In *American Museum Novitates*; American Museum of Natural History: Washington, DC, USA, 1970; p. 2429.
55. Boix, F.; Fernandez-Terula, A.; Tobeña, A. The anxiolytic action of benzodiazepines is not present in handling-habituated rats. *Pharmacol. Biochem. Behav.* **1988**, *31*, 541–546. [CrossRef]
56. Cañete, T.; Blázquez, G.; Tobeña, A.; Giménez-Llort, L.; Fernández-Teruel, A. Cognitive and emotional alterations in young Alzheimer’s disease (3xTgAD) mice: Effects of neonatal handling stimulation and sexual dimorphism. *Behav. Brain Res.* **2015**, *281*, 156–171. [CrossRef]
57. Gouveia, K.; Hurst, J.L. Improving the practicality of using non-aversive handling methods to reduce background stress and anxiety in laboratory mice. *Sci. Rep.* **2019**, *9*, 20305. [CrossRef] [PubMed]
58. Barnum, C.J.; Pace, T.W.; Hu, F.; Neigh, G.N.; Tansey, M.G. Psychological stress in adolescent and adult mice increases neuroinflammation and attenuates the response to LPS challenge. *J. Neuroinflamm.* **2012**, *9*, 9. [CrossRef]
59. Kedia, S.; Chattarji, S. Marble burying as a test of the delayed anxiogenic effects of acute immobilisation stress in mice. *J. Neurosci Methods.* **2014**, *233*, 150–154. [CrossRef] [PubMed]
60. Yohn, N.L.; Blendy, J.A. Adolescent Chronic Unpredictable Stress Exposure Is a Sensitive Window for Long-Term Changes in Adult Behavior in Mice. *Neuropsychopharmacology* **2017**, *42*, 1670–1678. [CrossRef]
61. Sugimoto, Y.; Tagawa, N.; Kobayashi, Y.; Hotta, Y.; Yamada, J. Effects of the serotonin and noradrenaline reuptake inhibitor (SNRI) milnacipran on marble burying behavior in mice. *Biol. Pharm. Bull.* **2007**, *30*, 2399–2401. [CrossRef]



Article

Systems Analysis Reveals Ageing-Related Perturbations in Retinoids and Sex Hormones in Alzheimer's and Parkinson's Diseases

Simon Lam ¹, Nils Hartmann ^{2,†}, Rui Benfeitas ³, Cheng Zhang ⁴, Muhammad Arif ⁴, Hasan Turkez ⁵, Mathias Uhlén ⁴, Christoph Englert ^{2,6}, Robert Knight ^{1,*} and Adil Mardinoglu ^{1,4,*}

- ¹ Faculty of Dentistry, Oral and Craniofacial Sciences, King's College London, London SE1 9RT, UK; simon.1.lam@kcl.ac.uk
- ² Leibniz Institute on Aging-Fritz Lipmann Institute, 07745 Jena, Germany; nils.hartmann@unimedizin-mainz.de (N.H.); christoph.englert@leibniz-ffi.de (C.E.)
- ³ National Bioinformatics Infrastructure Sweden (NBIS), Science for Life Laboratory, Department of Biochemistry and Biophysics, Stockholm University, SE-17121 Stockholm, Sweden; rui.benfeitas@scilifelab.se
- ⁴ Science for Life Laboratory, KTH—Royal Institute of Technology, SE-17121 Stockholm, Sweden; cheng.zhang@scilifelab.se (C.Z.); muhammad.arif@scilifelab.se (M.A.); mathias.uhlen@scilifelab.se (M.U.)
- ⁵ Department of Medical Biology, Faculty of Medicine, Atatürk University, 25240 Erzurum, Turkey; hasanturkez@gmail.com
- ⁶ Institute of Biochemistry and Biophysics, Freidrich-Schiller-University Jena, 07745 Jena, Germany
- * Correspondence: robert.knight@kcl.ac.uk (R.K.); adilm@scilifelab.se (A.M.)
- † Present address: Institute for Pathology, University Medical Center, 55131 Mainz, Germany.

Citation: Lam, S.; Hartmann, N.; Benfeitas, R.; Zhang, C.; Arif, M.; Turkez, H.; Uhlén, M.; Englert, C.; Knight, R.; Mardinoglu, A. Systems Analysis Reveals Ageing-Related Perturbations in Retinoids and Sex Hormones in Alzheimer's and Parkinson's Diseases. *Biomedicines* **2021**, *9*, 1310. <https://doi.org/10.3390/biomedicines9101310>

Academic Editor: Masaru Tanaka

Received: 28 July 2021

Accepted: 22 September 2021

Published: 24 September 2021

Publisher's Note: MDPI stays neutral with regard to jurisdictional claims in published maps and institutional affiliations.



Copyright: © 2021 by the authors. Licensee MDPI, Basel, Switzerland. This article is an open access article distributed under the terms and conditions of the Creative Commons Attribution (CC BY) license (<https://creativecommons.org/licenses/by/4.0/>).

Abstract: Neurodegenerative diseases, including Alzheimer's (AD) and Parkinson's diseases (PD), are complex heterogeneous diseases with highly variable patient responses to treatment. Due to the growing evidence for ageing-related clinical and pathological commonalities between AD and PD, these diseases have recently been studied in tandem. In this study, we analysed transcriptomic data from AD and PD patients, and stratified these patients into three subclasses with distinct gene expression and metabolic profiles. Through integrating transcriptomic data with a genome-scale metabolic model and validating our findings by network exploration and co-analysis using a zebrafish ageing model, we identified retinoids as a key ageing-related feature in all subclasses of AD and PD. We also demonstrated that the dysregulation of androgen metabolism by three different independent mechanisms is a source of heterogeneity in AD and PD. Taken together, our work highlights the need for stratification of AD/PD patients and development of personalised and precision medicine approaches based on the detailed characterisation of these subclasses.

Keywords: neurodegeneration; Alzheimer's; Parkinson's; ageing; systems biology

1. Introduction

Neurodegenerative diseases, including Alzheimer's (AD) and Parkinson's diseases (PD), cause years of a healthy life to be lost. Much previous AD and PD research has focused on the causative neurotoxicity agents, namely, amyloid β and α -synuclein, respectively. The current front-line therapies for AD and PD are cholinesterase inhibition and dopamine repletion, respectively, which are considered gold standards. Unfortunately, these therapies are not capable of reversing neurodegeneration [1,2], thus necessitating potentially lifelong dependence on the drug and risking drug-associated complications. Moreover, AD and PD are complex multifactorial diseases with heterogeneous underlying molecular mechanisms involved in their progression [3–5]. This variability can explain the differences in patient response to other treatments such as oestrogen replacement therapy [6,7] and statin treatment [8,9]. Hence, we observed that there are distinct disease

classes affecting specific cellular processes. Therefore, there is a need for the development of personalised treatment regimens.

In this study, we propose a holistic view of the mechanisms underlying the development of AD and PD rather than focusing on amyloid β and α -synuclein [10]. To date, complex diseases including liver disorders and certain cancers have been well studied through the use of metabolic modelling. This enabled the integration of multiple omics data for stratification of patients, discovery of diagnostic markers, identification of drug targets, and proposing of personalised or class-specific treatment strategies [11–14]. A similar approach may be applied for AD and PD since there is already a wealth of data from AD and PD patients from post-mortem brain tissues and blood transcriptomics.

AD and PD share multiple clinical and pathological similarities, including comorbidities [15,16], inverse associations with cancer [17,18], and ageing as a risk factor [19,20]. One type of ageing is telomeric ageing, which is associated with the loss of telomeres, protein/nucleic acid structures that protect chromosome ends from degradation [21]. The enzyme telomerase is necessary for the maintenance of telomeres. In adults, telomerase activity is mostly limited to progenitor tissues such as in the ovaries, testes, and bone marrow. Loss of telomerase activity leads to telomere shortening, loss of sequences due to end-replication, and eventual degradation of sequences within coding regions, leading to telomeric ageing. Considering AD and PD as products of ageing, we can use an ageing model organism to study its effects on the brain. In our study, we used zebrafish (*Danio rerio*) as a model organism since it has been used extensively used to study vertebrate ageing [22]. For example, a zebrafish ageing model can harbour a nonsense mutation in the *tert* gene, which encodes the catalytic subunit of telomerase, and exhibit faster-than-normal ageing [23,24].

In our study, we first analysed post-mortem brain gene expression data and protein–protein interaction data from the Genotype-Tissue Expression (GTEx) database [25], Functional Annotation of the Mammalian Genome 5 (FANTOM5) database [26–29], Human Reference Protein Interactome (HuRI) database [30], and Human Protein Atlas (HPA) (<http://www.proteinatlas.org>, accessed on 9 March 2021) [31] for characterization of normal brain tissue (Figure 1A). Secondly, we analysed transcriptomic data from the Religious Orders Study and Rush Memory Aging Project (ROSMAP) [32–34] with published expression data from anterior cingulate cortices and dorsolateral prefrontal cortices of PD and Lewy body dementia patients, hereafter referred to as the Rajkumar dataset [35], and from putamina, substantiae nigrae, and prefrontal cortices from patients with PD, hereafter referred to as the Zhang/Zheng dataset [36,37]. On these data, we conducted differential gene expression and functional analysis, and then constructed biological networks to further explore coordinated patterns of gene expression. Next, we performed global metabolic analyses using genome-scale metabolic modelling. Alongside these analyses, we also leveraged zebrafish *tert* mutants to test the hypothesis that the identified changes may be associated with telomeric ageing. Finally, on the basis of our integrative systems analysis, we defined three distinct disease subclasses within AD and PD and identified retinoids as a common feature of all three subclasses, being likely to be perturbed through ageing. We revealed subclass-specific perturbations at three separate processes in the androgen biosynthesis and metabolism pathway, namely, oestradiol metabolism, cholesterol biosynthesis, and testosterone metabolism.

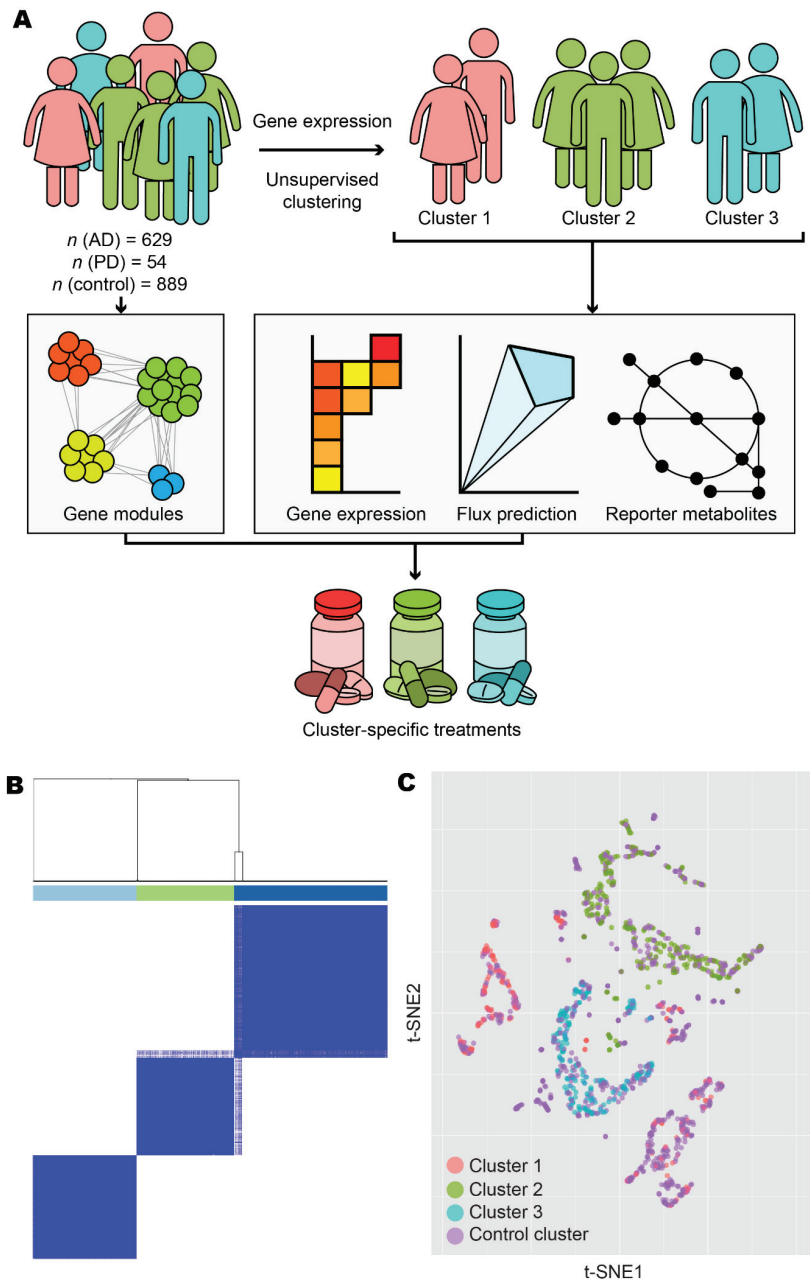


Figure 1. Overview and exploratory data analysis. (A) Workflow for the analysis of human AD and PD samples. (B) AD and PD samples were clustered into k clusters without supervision on the basis of normalised expression counts. Results are shown for $k = 3$ and 1000 bootstrap replicates. Colour bars indicate cluster identity for each sample. For $2 \leq k \leq 7$, refer to Figure S1. (C) Normalised expression data from AD, PD, and control samples were projected onto 2-D space using t-distributed stochastic neighbour embedding (t-SNE). Points are coloured according to cluster assignment by unsupervised clustering. For further data visualisation, refer to Figure S2.

2. Materials and Methods

2.1. Data Acquisition and Processing

Gene expression values of protein-coding genes from the ROSMAP dataset were determined using kallisto (version 0.46.1, Pachter Lab, Berkeley, CA, USA) [38] by aligning raw RNA sequencing reads to the *Homo sapiens* genome in Ensembl release 96 [39]. Raw single-cell RNA sequencing reads from ROSMAP were converted to counts in Cell Ranger (version 4.0, 10x Genomics, Pleasanton, CA, USA, <https://support.10xgenomics.com/single-cell-gene-expression/software/pipelines/latest/installation>; accessed on 24 July 2020), and aligned to the Cell Ranger *Homo sapiens* reference transcriptome version 2020-A. Single-cell expression values were compiled into pseudo-bulk expression profiles for each sample.

Expression values of protein-coding genes from brain samples of the ROSMAP dataset [32–34], GTEx database version 8 [25], FANTOM5 database [26–28] via Regulatory Circuits Network Compendium 1.0 [29], HPA database [31], Rajkumar dataset [35], and Zhang/Zheng dataset [36,37] were then combined. Genes from GTEx and FANTOM5 brain samples were filtered such that only genes whose products are known to participate in a protein–protein interaction described in the HuRI database [30] were included. Expression values were scaled and TMM normalised per sample, Pareto scaled per gene, and batch effects removed with the *removeBatchEffect* function from the limma (version 3.42.0, The Walter and Eliza Hall Institute of Medical Research, Parkville, Australia) [40] R package. After quality control and normalisation, a total of 64,794 genes and 2055 samples resulted. As the data also included samples from patients with neurological conditions other than AD or PD, we then removed those samples and finally accepted 1572 samples corresponding to AD, PD, or control for further analysis.

Projections onto 2-D space by PCA, t-SNE [41], and UMAP [42] methods were generated on data after missing value imputation with data diffusion [43]. t-SNE projections were generated with perplexity 20 and 1000 iterations. All other parameters were kept default. PCA and UMAP projections were generated using all default parameters.

2.2. Transcriptome Analysis

Using normalised, imputed expression values, AD and PD samples were then arranged into clusters without supervision using ConsensusClusterPlus (version 1.50.0, University of North Carolina at Chapel Hill, Chapel Hill, NC, USA) [44] with maxK = 20 and rep = 1000. All other parameters were kept default. Clustering by $k = 3$ clusters was selected for downstream analysis. A fourth cluster containing only control samples was artificially added to the analysis.

For differential gene expression analysis, normalised, non-imputed counts were used. Genes were removed if expression values were missing in 40% or more of samples or were zero in all samples. Differential expression was then performed using DESeq2 (version 1.26.0, European Molecular Biology Laboratory, Heidelberg, Germany) [45] with uniform size factors and all other parameters set to default. Genes with a Benjamini–Hochberg adjusted p -value at or below a cut-off of 1×10^{-10} were determined significantly differentially expressed genes.

Gene set enrichment analysis was performed using piano (version 2.2.0, Chalmers University of Technology, Göteborg, Sweden) [46] using all default parameters. GO term lists were obtained from Ensembl Biomart (<https://www.ensembl.org/biomart/martview>, accessed on 9 March 2021) and were used as gene set collections. Enrichment of GO terms was determined by analysing GO terms of genes differentially expressed genes detected by DESeq2 as well as the parents of those GO terms. GO terms with an adjusted p -value at or below 0.05 for distinct-directional and/or mixed-directional methods were determined statistically significant.

2.3. Metabolic Analysis

For each cluster, consensus gene expression values were determined by taking the arithmetic mean of normalised expression counts across all samples within each cluster.

A reference GEM was created by modifying the gene associations of all reactions within the adipocyte-specific GEM *iAdipocytes1850* [47] to match those within the generic human GEM HMR3 [48]. The resulting GEM was designated *iBrain2845*. Cluster-specific GEMs were reconstructed using the RAVEN Toolbox (version 2.0, Chalmers University of Technology, Göteborg, Sweden) [49] tINIT algorithm [50,51], with *iBrain2845* as the reference GEM.

FBA was conducted on each cluster-specific GEM using the *solveLP* function from the RAVEN Toolbox with previously reported constraints [52] and defining ATP synthesis (*iBrain2845*: HMR_6916) as the objective function. All constraints were applied with the exception of the following reaction IDs, which were excluded: EX_ac[e] (*iBrain2845*: HMR_9086) and EX_etoh[e] (*iBrain2845*: HMR_9099).

Reporter metabolite analysis was conducted using the *reporterMetabolites* function [53] from the RAVEN Toolbox, using *iBrain2845* as the reference model.

2.4. Network Analysis

To generate gene networks, we took normalised, non-imputed expression values from AD and PD samples. Control samples and samples from blood were excluded. One network was generated each for AD and PD. For the AD network, all male samples were included, and 171 female samples were chosen at random and included. For the PD network, all samples were included. Genes with any missing values were dropped. Genes with the 15% lowest expression or 15% lowest variance were disregarded from further analysis. Spearman correlations were calculated for each pair of genes, and the top 1% of significant correlations were used to generate gene co-expression networks. Random Erdős–Rényi models were created for the AD and PD networks, with the same numbers of nodes and edges to act as null networks, and compared against their respective networks in terms of centrality distributions. Community analyses were performed through the Leiden algorithm [54] by optimising CPMVertexPartition, after a resolution scan of 10,000 points between 10^{-3} and 10. The scan showed global maxima at resolutions = 0.077526 and 0.089074 for AD and PD networks, respectively, which were used for optimisation. Enrichment analysis was performed on modules with >30 nodes using enrichr (<https://maayanlab.cloud/Enrichr>, accessed on 5 March 2021) [55,56] using GO Biological Process, KEGG, and Online Mendelian Inheritance in Man libraries and was explored using Revigo (<http://revigo.irb.hr>, accessed on 5 March 2021) [57].

2.5. Zebrafish Data Acquisition and Analysis

The *tert* mutant zebrafish line (*tert*^{hu3430}) was obtained from Miguel Godhino Ferreira [24]. Fish maintenance, RNA isolation, processing, and sequencing were conducted as described previously [58].

From $n = 5$ wild-type (*tert*^{+/+}), $n = 5$ heterozygous mutant (*tert*^{+/-}), and $n = 3$ homozygous mutant (*tert*^{-/-}), expression values were determined from RNA sequencing reads using kallisto by aligning to the *Danio rerio* genome in Ensembl release 96 [39]. Expression values were generated for each extracted tissue as well as ‘pseudo-whole animal’, containing combined values across all tissues.

A reference zebrafish GEM was manually curated by modifying the existing *ZebraGEM2* model and was designated *ZebraGEM2.1*.

Differential expression analysis, gene set enrichment analysis, GEM reconstruction, FBA, and reporter metabolite analysis were conducted on *tert*^{-/-} and *tert*^{+/-} animals against a *tert*^{+/+} reference using DESeq2, piano, and RAVEN Toolbox 2.0 with default parameters. Reporter metabolite analysis was conducted with *ZebraGEM2.1* as the reference GEM.

FBA was attempted as described for the human GEMs with the exception that the following metabolic constraints were excluded: r1391, HMR_0482 (*ZebraGEM2.1*: G3PDm), EX_ile_L[e] (*ZebraGEM2.1*: EX_ile_e), EX_val_L[e] (*ZebraGEM2.1*: EX_val_e), EX_lys_L[e] (*ZebraGEM2.1*: EX_lys_e), EX_phe_L[e] (*ZebraGEM2.1*: EX_phe_e), GLC1r, EX_thr_L[e] (*ZebraGEM2.1*: EX_thr_e), EX_met_L[e] (*ZebraGEM2.1*: EX_met_L_e), EX_arg_L[e] (*ZebraGEM2.1*: EX_arg_e), EX_his_L[e] (*ZebraGEM2.1*: EX_his_L_e), EX_leu_L[e] (*ZebraGEM2.1*: EX_leu_e), and EX_o2[e] (*ZebraGEM2.1*: EX_o2_e). The objective function was defined as ATP synthesis (*ZebraGEM2.1*: ATPS4m). FBA results for zebrafish are not presented.

2.6. Data and Code Accessibility

All original computer code, models, and author-curated data files have been released under a Creative Commons Attribution ShareAlike 4.0 International Licence (<https://creativecommons.org/licenses/by-sa/4.0/>; accessed on 29 March 2021) and are freely available for download from <<https://github.com/SimonLammam/ad-pd-retinoid>>; accessed on 29 March 2021.

Zebrafish *tert* mutant sequencing data have been deposited in the NCBI Gene Expression Omnibus (GEO) and are accessible through GEO Series accession numbers GSE102426, GSE102429, GSE102431, and GSE102434.

2.7. Ethics Statement

Zebrafish were housed in the fish facility of the Leibniz Institute on Aging—Fritz Lipmann Institute (FLI) under standard conditions and a 14 h light and 10 h dark cycle. All animal procedures were performed in accordance with the German animal welfare guidelines and approved by the Landesamt für Verbraucherschutz Thüringen (TLV), Germany.

3. Results

3.1. Stratification of Patients Revealed Three Distinct Disease Classes

We retrieved gene expression and protein–protein interaction data from GTEx, FANTOM5, HuRI, HPA, and ROSMAP databases and integrated these data with the published datasets by Rajkumar and Zhang/Zheng. After performing quality control and normalisation (as outlined in the Materials and Methods), we included a total of 629 AD samples, 54 PD samples, and 889 control samples in the analysis (Table 1). To reveal transcriptomic differences between AD/PD samples compared to healthy controls, we identified differentially expressed genes (DEGs) and performed gene set enrichment (GSE) analyses. However, since AD and PD are complex diseases with no single cure, it is likely that multiple gene expression profiling exist, manifesting in numerous disease classes requiring distinct treatment strategies. We therefore used unsupervised clustering to elucidate these expression profiles and stratify the AD and PD patients on the basis of the underlying molecular mechanisms involved in the disease occurrence.

Table 1. Summary of expression data sources.

Source	AD Samples	PD Samples	Control Samples
GTEx/FANTOM5	0	0	67
HPA	0	0	52
Rajkumar	0	14	13
ROSMAP	629	0	704
Zhang/Zheng	0	40	53
Total	629	54	889

Expression data from AD and PD samples were obtained from the Genotype-Tissue Expression (GTEx) database, Functional Annotation of the Mammalian Genome 5 (FANTOM5) database, Human Protein Atlas (HPA), Religious Orders Study and Rush Memory Aging Project (ROSMAP), Rajkumar dataset, and Zhang/Zheng dataset.

Following unsupervised clustering with ConsensusClusterPlus [44], we separated AD and PD samples into three clusters (Figures 1B and S1). Clusters 1 and 2 contained samples from Zhang/Zheng and Rajkumar datasets, respectively, in addition to sam-

ples in the ROSMAP dataset, and consisted of 127 and 186 samples from female donors, respectively, and 73 and 95 samples from male donors, respectively. Cluster 2 also contained 14 samples with sex not recorded. Cluster 3 contained only ROSMAP samples and consisted of 114 female and 74 male samples. Clusters did not form firmly along lines of sex, age, or brain tissues or brain subregion (Figure S2). Samples from non-diseased individuals were artificially added as a fourth, control cluster, consisting of 495 female samples, 262 male samples, 13 samples with sex not recorded, and 119 samples derived from aggregate sources.

By differential expression analysis using DESeq2 [45], we then characterised the distinct transcriptomic profiles within our disease clusters (Figure 2A). Cluster 1 showed mixed up- and downregulation of genes compared to control, whereas cluster 2 showed more downregulation and cluster 3 showed vast downregulation of genes compared to control.

To infer the functional differences between the subclasses, we performed GSE analysis using piano [46] (Figure 2B, Supplementary Data S1). Globally, DEGs in any cluster 1–3 were enriched in upregulated Gene Ontology (GO) terms for immune response, olfaction, retinoid function, and apoptosis, but downregulated for copper ion transport and telomere organisation, compared to the control cluster. Considering individual clusters, cluster 1 DEGs were enriched in upregulated GO terms associated with immune signalling, cell signalling, and visual perception. We also found downregulation of GO terms associated with olfactory signalling and cytoskeleton. DEGs in cluster 2 were found to be enriched in downregulated GO terms associated with the cytoskeleton, organ development, cell differentiation, retinoid metabolism and response, DNA damage repair, inflammatory response, telomere maintenance, unfolded protein response, and acetylcholine biosynthesis and binding. On the other hand, we did not find any significantly enriched upregulated GO terms. In cluster 3, we found that DEGs were enriched in upregulated GO terms associated with neuron function, olfaction, cell motility, and immune system. DEGs in cluster 3 were found to be enriched in downregulated GO terms associated with DNA damage response, ageing, and retinoid metabolism and response.

The difference in expression profiles illustrate highly heterogeneous transcriptomics in AD and PD and that there are notable commonalities and differences between the subclasses of AD or PD samples. Interestingly, we found retinoid metabolism or function to be a common altered GO term in all subclasses. This was upregulated in cluster 1 but downregulated in clusters 2 and 3. We therefore observed that retinoid dysregulation appears to be a common ageing-related hallmark in AD and PD.

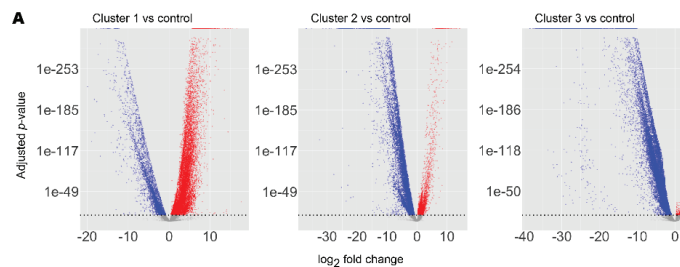


Figure 2. Cont.

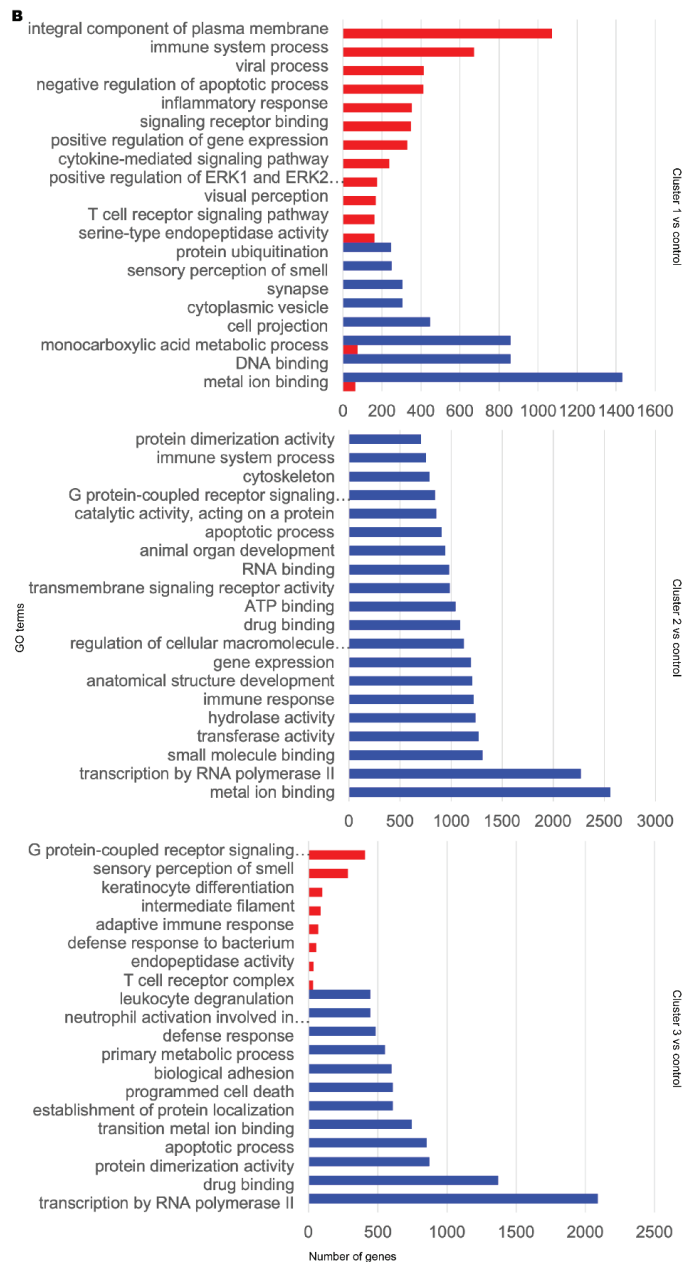


Figure 2. Transcriptomic and functional characterisation of AD and PD subclasses. Differentially expressed gene (DEG) analysis and gene set enrichment (GSE) analysis were performed for AD and PD and control samples for each disease cluster, using the control cluster as reference. (A) DEG results. Significant DEGs were determined as those with a Benjamini–Hochberg adjusted p -value at or below a cut-off of 1×10^{-10} . Upregulated significant DEGs are coloured red. Downregulated significant DEGs are coloured blue. Non-significant DEGs are coloured grey. (B) Selected significantly enriched GO terms by number of genes as determined by GSE analysis. Red bars indicate upregulated GO terms. Blue bars indicate downregulated GO terms. For full data, refer to Supplementary Data S1.

3.2. Metabolic Analysis Revealed Retinoids and Sex Hormones as Significantly Dysregulated in AD and PD

On the basis of clustering and GSE analysis, we identified distinct expression profiles, but these alone could not offer insights into metabolic activities of brain in AD and PD. To determine metabolic changes in the clusters compared to controls, we performed constraint-based genome-scale metabolic modelling. We reconstructed a brain-specific genome-scale metabolic model (GEM) based on the well-studied HMR2.0 [47] reference GEM by overlaying transcriptomic data from each cluster and applying brain-specific constraints as described previously [52] using the tINIT algorithm [50,51] within the RAVEN Toolbox 2.0 [49]. We generated a brain-specific GEM (*iBrain2845*) (Supplementary File S1) and used it as the reference GEM for reconstruction of cluster-specific GEMs in turn. We constructed the resulting context-specific *iADPD* series GEMs *iADPD1*, *iADPD2*, *iADPD3*, and *iADPDControl*, corresponding to cluster 1, cluster 2, cluster 3, and the control cluster, respectively (Supplementary File S2).

We conducted flux balance analysis (FBA) by defining maximisation of ATP synthesis as the objective function. *iADPD1* and *iADPD2* both showed upregulation of fluxes in reactions involved in cholesterol biosynthesis and downregulation in O-glycan metabolism, with reaction flux changes being more pronounced in *iADPD2* than in *iADPD1* (Table 2, Supplementary Data S2). We found that the fluxes in *iADPD1* were uniquely upregulated in oestrogen metabolism and the Kandustch–Russell pathway. *iADPD2* was uniquely upregulated in cholesterol metabolism, whereas *iADPD3* uniquely displayed roughly equal parts upregulation and downregulation in several pathways, including aminoacyl-tRNA biosynthesis; androgen metabolism; arginine and proline metabolism; cholesterol biosynthesis; galactose metabolism; glycine, serine, and threonine metabolism; and N-glycan metabolism.

Table 2. Flux balance analysis of *iADPD1*, *iADPD2*, and *iADPD3* versus *iADPDControl*.

Subsystem	<i>iADPD1</i>	<i>iADPD2</i>	<i>iADPD3</i>
Acyl-CoA hydrolysis	−0.001	0.001	0.000
Alanine, aspartate, and glutamate metabolism	−0.148	0.014	0.000
Aminoacyl-tRNA biosynthesis	4.698	4.698	0.000
Androgen metabolism	−1.426	−0.399	−0.001
Arachidonic acid metabolism	−0.098	0.010	0.000
Arginine and proline metabolism	−0.182	−0.327	0.000
Beta oxidation of branched-chain fatty acids (mitochondrial)	−0.049	−0.049	−0.049
Beta oxidation of di-unsaturated fatty acids (n-6) (mitochondrial)	−0.636	0.002	−0.001
Beta oxidation of odd-chain fatty acids (mitochondrial)	0.001	−0.002	−0.002
Beta oxidation of poly-unsaturated fatty acids (mitochondrial)	0.709	0.024	0.000
Beta oxidation of unsaturated fatty acids (n-7) (mitochondrial)	−0.016	0.001	−0.003
Beta oxidation of unsaturated fatty acids (n-9) (mitochondrial)	0.011	0.000	0.007
Carnitine shuttle (cytosolic)	0.012	0.000	−0.001
Carnitine shuttle (mitochondrial)	0.003	0.000	0.002
Cholesterol biosynthesis 1 (Bloch pathway)	0.076	−0.983	0.001
Cholesterol biosynthesis 2	2.501	4.472	0.000

Table 2. Cont.

Subsystem	<i>iADPD1</i>	<i>iADPD2</i>	<i>iADPD3</i>
Cholesterol biosynthesis 3 (Kandustch–Russell pathway)	1.699	0.000	0.000
Cholesterol metabolism	0.067	4.482	0.000
Estrogen metabolism	2.085	0.000	0.000
Fatty acid activation (endoplasmic reticular)	0.000	0.000	0.000
Fatty acid biosynthesis (even-chain)	0.000	0.000	0.000
Fatty acid desaturation (even-chain)	0.785	0.000	0.000
Fatty acid elongation (odd-chain)	−0.042	−0.024	0.000
Formation and hydrolysis of cholesterol esters	−0.382	0.004	0.000
Fructose and mannose metabolism	−0.211	−0.007	0.000
Galactose metabolism	−0.008	0.035	0.000
Glycine, serine, and threonine metabolism	0.276	0.557	0.000
Glycolysis/gluconeogenesis	−0.213	0.022	0.033
Histidine metabolism	0.000	0.000	0.000
Leukotriene metabolism	−0.032	0.000	0.000
Lysine metabolism	0.000	0.000	0.000
N-glycan metabolism	−0.784	0.016	0.000
Nitrogen metabolism	0.000	0.000	0.000
Nucleotide metabolism	0.027	−0.028	0.000
O-glycan metabolism	−2.346	−4.738	0.000
Pentose phosphate pathway	0.127	0.000	0.000
Propanoate metabolism	−0.116	0.020	0.091
Protein degradation	0.000	0.000	0.000
Purine metabolism	0.112	−0.013	0.000
Pyrimidine metabolism	−0.071	−0.010	−0.001
Pyruvate metabolism	−0.183	−0.004	−0.077
Starch and sucrose metabolism	0.000	0.000	0.000
Steroid metabolism	−0.097	−0.295	0.003
Terpenoid backbone biosynthesis	0.398	0.187	0.020
Valine, leucine, and isoleucine degradation	0.127	0.000	0.000

Flux balance analysis was performed for each *iADPD*-series GEM, and the predicted fluxes for the three disease cluster GEMs were compared against the predicted fluxes for the control cluster GEM. Reactions are grouped by subsystem and flux difference values are expressed as mean flux difference between disease clusters and the control cluster across all changed reactions within a subsystem. For full results, refer to Supplementary Data S2.

In particular, we observed increased positive fluxes through reactions HMR_2055 and HMR_2059 in *iADPD1*, which convert oestrone to 2-hydroxyoestrone and then to 2-methoxyoestrone (Figure 3). In *iADPDControl*, these reactions carried zero flux. In *iADPD2*, we observed increased positive fluxes through HMR_1457 and HMR_1533, which produce geranyl pyrophosphate and lathosterol, respectively. Both of these molecules are precursors to cholesterol, and while we did not see a proportionate increase in the production of other molecules along the pathway (namely, farnesyl pyrophosphate and squalene), we did observe a general increase in fluxes through the androgen biosynthesis and metabolism pathway. Finally, we observed that *iADPD3* displayed a decreased production of testosterone from 4-androstene-3,17-dione via HMR_1974, despite an increase in production of 4-androstene-3,17-dione via HMR_1971.

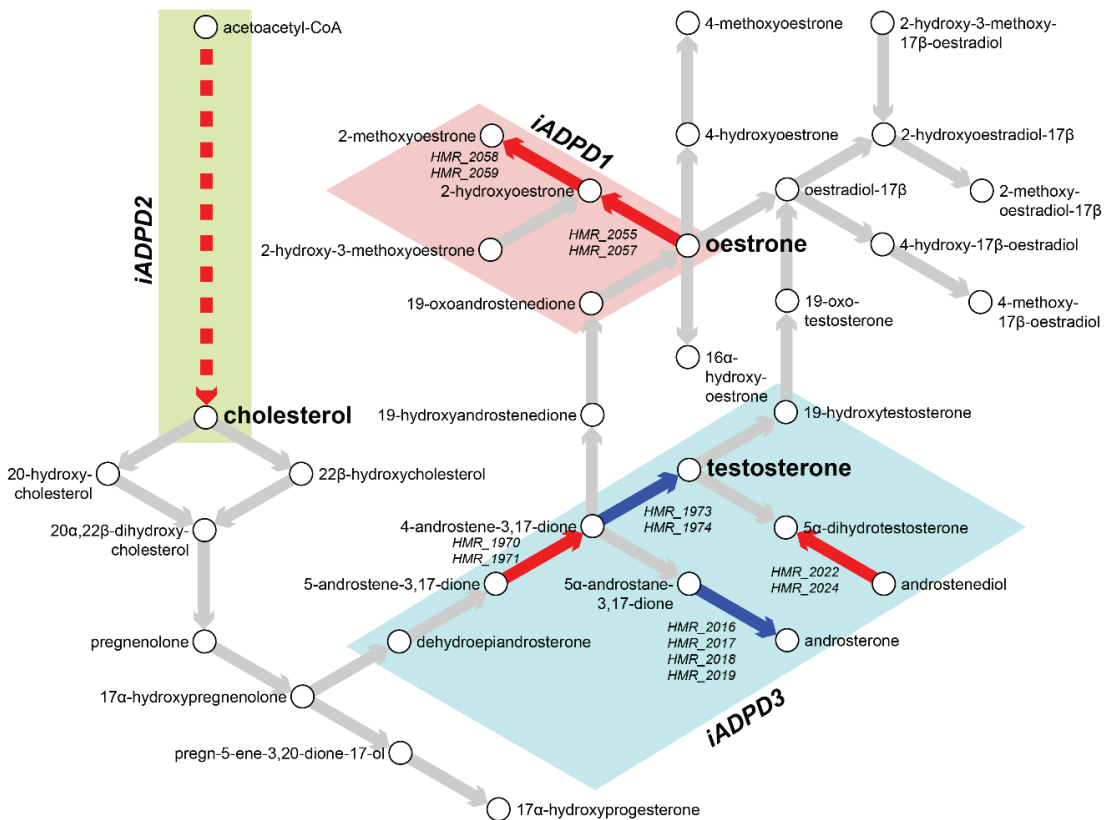


Figure 3. Metabolic characterisation of AD and PD subclasses. Flux balance analysis (FBA) was performed on *iADPD1-3* genome-scale metabolic models (GEMs), and flux values were compared with those of *iADPDControl*. Key metabolites and reactions within the androgen metabolism pathway are shown and key dysregulations are displayed as coloured arrows: red indicates increased flux compared to *iADPDControl*; blue indicates decreased flux compared to *iADPDControl*. Dysregulations associated to each GEM are shown in coloured boxes. The dashed line indicates multiple reactions are involved. Human Metabolic Reactions (HMR) identifiers are shown for androgen metabolism reactions with dysregulated fluxes. For full data, refer to Supplementary Data S2.

Taken together, the obtained results indicate the existence of three distinct metabolic dysregulation profiles in AD and PD, with dysregulation being most pronounced in cluster 2 patients and least pronounced in cluster 3 patients. Furthermore, we found that all three clusters show dysregulations in or around sex hormone biosynthesis and metabolism, which might explain the heterogeneity in responses to sex hormone replacement therapy in AD and PD patients as extensively reported previously [6,59–61]. We also confirmed that dysregulations through sex hormone pathways in the *iADPD* series GEMs were not due to differences in relative frequencies between sexes in the main clusters 1–3 (Fisher’s exact test, $p = 0.4700$).

In addition to metabolic inference and FBA, we performed reporter metabolite analysis [53] by overlaying DEG analysis results onto the reference GEM to identify hotspots of metabolism (Table 3, Supplementary Data S3). In short, we uniquely identified oestrone as a reporter metabolite in cluster 1, and lipids such as acylglycerol and dolichol in cluster 2. No notable reporter metabolites were identified as significantly changed in cluster 3 only. In common to all clusters 1–3, retinoids, and sex hormones such as androstosterone

and pregnanediol were identified as significantly changed reporter metabolites, which are generally in line with GSE and FBA results.

Table 3. Reporter metabolite analysis of AD and PD subclasses.

Reporter Metabolite	Z-Score	p-Value
Cluster 1		
O2	6.111	4.95×10^{-10}
Estrone	5.4557	2.44×10^{-8}
Retinoate	5.3943	3.44×10^{-8}
NADP+	5.3667	4.01×10^{-8}
Arachidonate	5.2822	6.38×10^{-8}
2-Hydroxyestradiol-17beta	5.0999	1.70×10^{-7}
Linoleate	5.0622	2.07×10^{-7}
10-HETE	5.0454	2.26×10^{-7}
11,12,15-THETA	5.0454	2.26×10^{-7}
11,14,15-Theta	5.0454	2.26×10^{-7}
Cluster 2		
1-Acylglycerol-3P-LD-PC pool	4.3322	7.38×10^{-6}
Acyl-CoA-LD-PI pool	4.143	1.71×10^{-5}
Phosphatidate-CL pool	4.0973	2.09×10^{-5}
Thymidine	3.5852	0.00016843
Uridine	3.5852	0.00016843
Prostaglandin D2	3.2144	0.00065348
G10596	3.1354	0.0008581
G10597	3.1354	0.0008581
D-Myo-inositol-1,4,5-trisphosphate	2.9988	0.0013552
Dolichyl-phosphate	2.9655	0.001511
Cluster 3		
D-Myo-inositol-1,4,5-trisphosphate	2.6543	0.0039734
13-cis-Retinal	2.6537	0.0039806
Heparan sulfate, precursor 9	2.5915	0.0047772
sn-Glycerol-3-phosphate	2.578	0.0049682
DHAP	2.5353	0.0056173
Porphobilinogen	2.4987	0.0062333
ATP	2.4838	0.0064998
L-Glutamate 5-semialdehyde	2.4576	0.006994
Prostaglandin D2	2.451	0.0071221
ribose	2.4133	0.0079045

Reporter metabolite analysis was performed for each AD/PD subclass by overlaying differential expression results onto *iBrain2845*. Top 10 unique reporter metabolites by *p*-value for each cluster compared to the control cluster are shown. For full results, refer to Supplementary Data S3.

3.3. Network Analysis Supported Retinoid and Androgen Dysregulation and Suggests Transcriptomic Similarity between AD and PD

To further explore the gene expression patterns shown across AD and PD patients, we took expression data and constructed a weighted gene co-expression network for each group (Spearman $\rho > 0.9$, FDR $< 10^{-9}$; see the Materials and Methods section). Each network was compared against equivalent randomly generated networks acting as null models. After quality control, the AD network contained 4861 nodes (genes) and $\approx 397,000$ edges (significant correlations), and the PD network contained 5857 nodes and $\approx 394,000$ edges (Figure 4A,B, Table 4). A community analysis to identify modules of highly co-expressed genes [54] highlighted 9 and 15 communities with significant functional enrichment in AD and PD, respectively.

In the AD network, gene module C3 was enriched for genes involved with neuron and synapse development, similar to patient cluster 3; C4 for genes involved with mRNA splicing, similar to patient cluster 2; and C5 for genes involved with the mitochondrial

electron transport chain (Figure 4C, Supplementary Data S4). C1 and C2 were the gene modules with the largest number of genes. C1 was enriched for gene expression quality control genes and development and morphogenesis genes, mirroring patient cluster 2, whereas C2 contained cytoskeleton-related genes, similar to patient cluster 1.

In the PD network, C1 was enriched for genes involved with retinoid metabolism, glucuronidation, and cytokine signalling. Since androgens are major targets of glucuronidation [62], these results are in line with our main findings. Further, C2 contained DNA damage response and gene regulation genes, similar to patient cluster 2; C3 contained nuclear protein regulation genes; and C4 contained mRNA splicing genes, again similar to patient cluster 2.

Further, the two networks share a large number of enriched terms in common, and there is high similarity between the major gene modules, highlighting the similarity between AD and PD. In addition to this, enrichment analysis for KEGG terms was unable to assign “Alzheimer disease” and “Parkinson disease” to the correct gene modules from the respective networks, and additional neurological disease terms such as “Huntington disease” and “amyotrophic lateral sclerosis” were also identified by the analysis, further suggesting the transcriptomic similarity between neurological diseases. We found that AD C1 and PD C2 were frequently annotated with these disease terms, and these gene modules are also highly similar. Therefore, this gene module could constitute a core set of dysregulated genes in neurodegeneration.

Taken together, the network analysis supports our GSE findings. The functional consequences of differential expression in the patient clusters could be explained by differential modulation of gene modules identified in our network analysis together with dysregulation of a core set of genes implicated in both AD and PD.

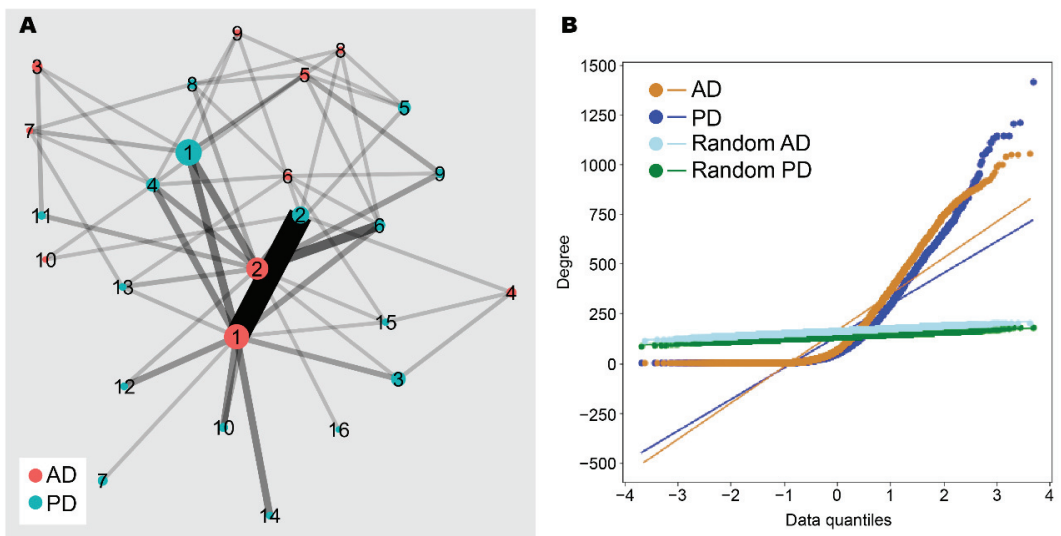


Figure 4. Cont.

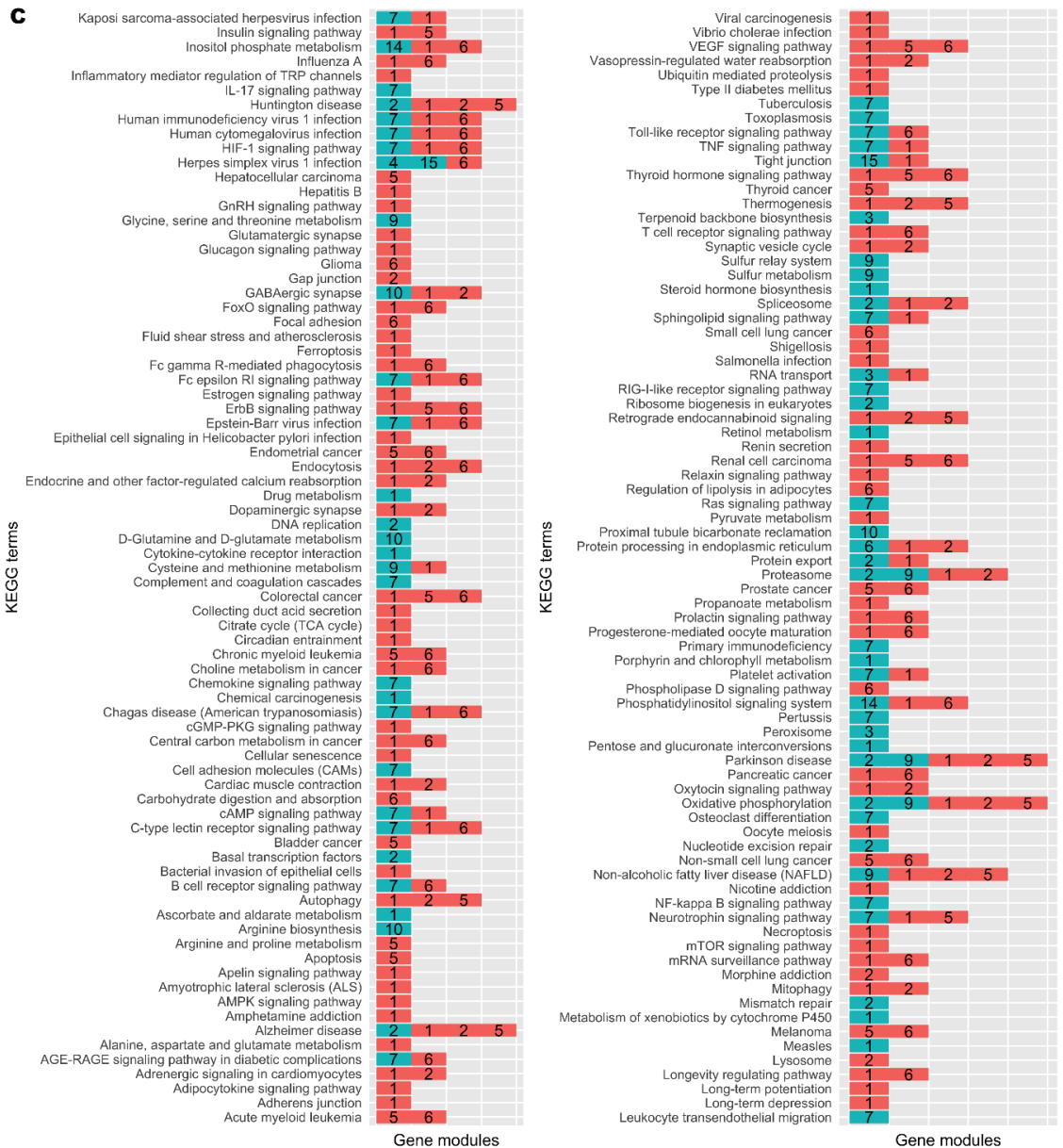


Figure 4. Network analysis of AD and PD gene co-expression modules. (A) Gene co-expression networks were constructed from transcriptomic data from AD and PD samples. Community analysis was used to identify gene modules (see the Materials and Methods section). Modules with at least 30 genes are shown as nodes. Node size indicates number of genes. Nodes are coloured by network of origin and numbered in descending order of module size. Shared genes between modules are shown as edges. Edge weight indicates number of shared genes. (B) Degree distribution of AD, PD, and random networks. (C) Enrichment analysis was performed on gene modules containing at least 30 genes using the KEGG database (see the Materials and Methods section). Significantly enriched gene modules are shown as coloured, numbered blocks. Colour and number keys are as in (A).

Table 4. AD and PD network properties.

	Nodes	Edges	Diameter	Average Path Length	Density	Clustering Coefficient	Connected Network?	Minimum Cut
AD	4861	396,985	11	3.004	0.034	0.443	No	-
PD	5857	394,405	18	3.598	0.023	0.397	No	-
Random AD	4861	396,985	3	1.970	0.034	0.034	Yes	114
Random PD	5857	394,405	3	2.021	0.023	0.023	Yes	89

Gene co-expression networks were generated for AD and PD samples. AD, PD, and random networks are shown.

3.4. Zebrafish Transcriptomic and Metabolic Investigations Suggest an Association between Brain Ageing and Retinoid Dysregulation

To further validate our findings regarding the differences between clusters of human AD and PD samples, we analysed transcriptomic data from *tert* mutant zebrafish and reconstructed tissue-specific GEMs (Figure 5A). To ascertain that these effects of ageing were limited to the brain, we analysed the brain, liver, muscle, and skin of zebrafish as well as the whole animal.

We first repeated DEG and GSE analyses in the *tert* mutants using brain transcriptomic data. We found significant enrichment of GO terms associated with retinoid metabolism as well as eye development and light sensing, in which retinoids act as signalling molecules [63] (Figures 5B and S3, Supplementary Data S5). To further support our findings, we then reconstructed mutant- and genotype-specific GEMs by overlaying zebrafish *tert* mutant transcriptomic data onto a modified generic *ZebraGEM2* GEM [64]. We designated the modified GEM *ZebraGEM2.1* (Supplementary File S3) and used it as the reference GEM. We also generated zebrafish organ-specific GEMs and provided them to the interested reader (Supplementary File S4).

We then repeated reporter metabolite analysis using the transcriptomic data from zebrafish tissue-specific GEMs and found that retinoids were identified as significant reporter metabolites in *tert*^{+/-} zebrafish ($p = 0.045$) but not in *tert*^{-/-}, where evidence was marginal ($p = 0.084$) (Figure 5C, Table 5, Supplementary Data S6). We also observed this result in the skin of *tert*^{-/-} mutants, where evidence was significant ($p = 0.017$). This result can be explained due to the susceptibility of skin as an organ to photoageing, for which topical application of retinol is a widely used treatment [65]. However, we did not find evidence for significant changes in pregnanediol, and androsterone was significant only in the skin of *tert*^{-/-} zebrafish ($p = 0.017$). This would suggest that either change in sex hormones are not ageing-related with regards AD and PD, or the changes were outside the scope of the zebrafish model that we used.

Taken together, these results indicated that ageing can largely explain alterations in retinoid metabolism in the brain but not alterations in sex hormone metabolism. These results also suggest that ageing has a differential effect on different organs, implying that metabolic changes due to ageing in the brain are associated with neurological disorders.

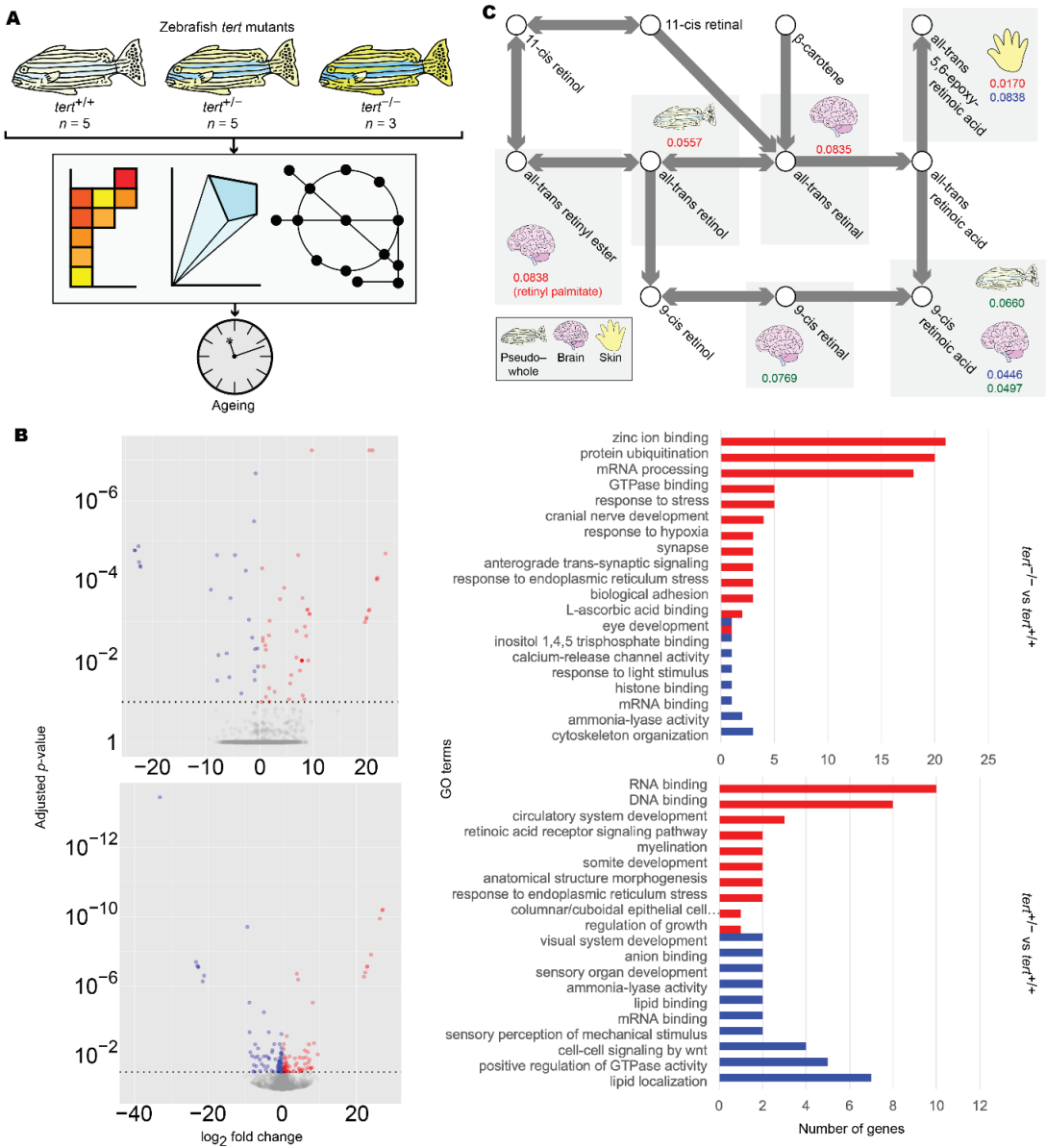


Figure 5. Summary of zebrafish *tert* mutant analysis. **(A)** Workflow for the analysis of zebrafish *tert* mutants. **(B)** Differentially expressed gene (DEG) (left panels) and gene set enrichment (GSE) analysis (right panels) of zebrafish brain samples. DEG and GSE analyses were performed on zebrafish *tert* mutant brain expression data for *tert*^{-/-} (upper panels) and *tert*^{+/-} (lower panels), using *tert*^{+/+} as a reference. Methods and colour keys are as in Figure 2. For muscle, liver, skin, and pseudo-whole animal analyses, refer to Figure S3. For full data, refer to Supplementary Data S5. **(C)** Reporter metabolite analysis of zebrafish samples. DEG data were overlaid on *ZebraGEM2.1* to determine reporter metabolites. Shown are reporter metabolites with *p* < 0.1 within the retinoic acid metabolic pathway. Red numbers indicate *p*-values in *tert*^{-/-} compared to *tert*^{+/+}. Blue numbers indicate *p*-values in *tert*^{+/-} compared to *tert*^{+/+}. Green numbers indicate *p*-values in *tert*^{-/-} compared to *tert*^{+/-}. Tissues are indicated with icons. For full data, refer to Supplementary Data S6.

Table 5. Reporter metabolite analysis of zebrafish *tert* mutants.

Reporter Metabolite	Z-Score	p-Value
<i>tert</i> ^{-/-}		
H+	3.911	4.60 × 10 ⁻⁵
H2O	3.0672	0.0010804
L-Lysine	2.8564	0.0021424
Biocyt c	2.8564	0.0021424
Ubiquinone	2.5742	0.0050241
Nicotinamide adenine dinucleotide—reduced	2.3946	0.0083183
Phosphate	2.0562	0.019883
Superoxide anion	2.0365	0.020851
Sodium	1.9228	0.027254
TRNA (Glu)	1.8752	0.030381
Thiosulfate	1.7684	0.038493
Selenate	1.7684	0.038493
Reduced glutathione	1.7184	0.042862
ADP	1.6716	0.047305
L-Lysine	1.6625	0.04821
Benzo[a]pyrene-4,5-oxide	1.6042	0.054333
Formaldehyde	1.5955	0.055302
L-Glutamate	1.4622	0.071837
(1R,2S)-Naphthalene epoxide	1.4518	0.073276
Aflatoxin B1 exo-8,9-epoxide	1.4518	0.073276
<i>tert</i> ^{+/-}		
H+	4.9585	3.55 × 10 ⁻⁷
Ubiquinol	3.9938	3.25 × 10 ⁻⁵
H2O	3.2078	0.00066883
Nicotinamide adenine dinucleotide—reduced	3.029	0.0012268
Superoxide anion	2.0908	0.018274
L-Lactate	2.0752	0.018983
O2	1.9958	0.022976
Lnlnco c	1.9628	0.024834
Succinate	1.9449	0.025895
Ferricytochrome c	1.8352	0.033237
Phosphatidylinositol-3,4,5-trisphosphate	1.7494	0.040109
9-cis-Retinoic acid	1.7	0.044567
[(Gal)2 (GlcNAc)4 (LFuc)1 (Man)3 (Asn)1']	1.6672	0.047739
O-Phospho-L-serine	1.6601	0.048451
[(Glc)3 (GlcNAc)2 (Man)9 (Asn)1']	1.6276	0.051802
Protein serine	1.6078	0.053937
[(GlcNAc)1 (Ser/Thr)1']	1.6078	0.053937
Geranyl diphosphate	1.5912	0.055785
CTP	1.5625	0.059088
[(Gal)2 (GlcNAc)4 (LFuc)1 (Man)3 (Neu5Ac)2 (Asn)1']	1.5367	0.062179

Reporter metabolite analysis was performed for the brains of zebrafish *tert* mutant by overlaying differential expression results onto *ZebraGEM2.1*. Top 20 unique reporter metabolites by *p*-value for each cluster compared to wild-type *tert*^{+/+} zebrafish are shown. For full results, refer to Supplementary Data S6.

4. Discussion

In this work, we integrated gene expression data across diverse sources into context-specific GEMs and sought to identify and characterise disease subclasses of AD and PD. We used unsupervised clustering to identify AD/PD subclasses and employed DEG and GSE analysis to functionally characterise them. We used network exploration, constraint-based metabolic modelling, and reporter metabolite analysis to characterise flux and metabolic perturbations within basal metabolic functions and pathways. We then leveraged expression data from zebrafish ageing mutants to validate our findings that these perturbations might be explained by ageing. Our analysis concluded with the identification and characterisation of three AD/PD subclasses, each with distinct functional characteristics and

metabolic profiles. All three subclasses showed depletion of retinoids by an ageing-related mechanism as a common characteristic.

We believe that a combined analysis that integrates AD and PD data is necessary to elucidate common attributes between the two diseases. However, we realised that such an analysis will likely obscure AD- and PD-specific factors, such as amyloid β and α -synuclein, but should aid the discovery of any factors in common. Since AD and PD share numerous risk factors and comorbidities such as old age, diabetes, and cancer risk, we believe that an AD/PD combined analysis can identify factors in common to both diseases and prove valuable for the identification of treatment strategies that might be effective in the treatment of both diseases.

GSE analysis highlighted significant changes related to retinoid function or visual system function, in which retinol and retinal act as signalling molecules [63], in all clusters (Figure 2, Supplementary Data S1). Together with the identification of multiple retinol derivatives as significant reporter metabolites in *iBrain2845* (Table 3, Supplementary Data S3), we hypothesised that retinoids are a commonly dysregulated class of molecules in both AD and PD, and that this may be due to an ageing mechanism. Indeed, in our investigation with zebrafish telomerase mutants, we again found alterations in retinoid and visual system function in GSE analysis (Figures 5B and S3, Supplementary Data S5) and reporter metabolite analysis (Figure 5C, Table 5, Supplementary Data S6).

Retinoids were identified as a reporter metabolite in all three clusters of patients in this study. Further, our zebrafish analysis highlighted the importance of retinoids in ageing of the brain and the skin (Figure 5C, Table 5, Supplementary Data S6). Retinol, its derivatives, and its analogues are already used as topical anti-ageing therapies for aged skin [65], and there is a growing body of evidence suggesting its efficacy for the treatment of AD [66–69]. We add to the body of evidence with this *in silico* investigation involving zebrafish telomerase mutants, suggesting that the source of retinoid depletion in AD and PD is ageing-related. Interestingly, regarding our finding for skin ageing in zebrafish, lipid biomarkers have been proposed in a recent skin sebum metabolomics study in PD patients [70]. This could be interpreted as co-ageing in brain and skin tissues, possibly allowing for cheap, non-invasive prognostic testing for PD.

In addition to retinoids, we found evidence for subclass-specific dysregulation within the androgen metabolism pathway in each of the three clusters in FBA (Table 2, Supplementary Data S2) and reporter metabolite analysis (Table 3, Supplementary Data S3). We found that *iADPD1* displayed increased oestrone conversion to the less potent [71] 2-methoxyoestrone, *iADPD2* displayed increased production of the cholesterol precursor molecules geranyl pyrophosphate and lathosterol and increased androgen biosynthesis, and *iADPD3* displayed decreased conversion of 4-androstene-3,17-dione to testosterone. However, there was no definitive evidence to suggest an ageing-related basis for these observations on the basis of our zebrafish study, but this may be due to the diverse functional roles that sex hormones have, limitations within the *ZebraGEM2.1* model, or absence of an actual biological link between sex hormones and ageing of the brain. Despite this, given the widely reported variability in responses to sex hormone replacement therapy in AD and PD [6,8,60,61], we believe that this observation represents a possible explanation for the heterogeneity. Our observation regarding the dysregulation of the androgen pathway at three separate points suggests that dysregulation at other points might also be linked to AD and PD, thus implying that androgen metabolism dysregulation in general might be important for the development of AD and PD. Our finding via network community analysis of a gene module associated with glucuronidation activity points to a possible therapeutic strategy to combat androgen dysregulation. In our study, the limitation of our dataset that some samples were aggregate samples or did not record the donor's sex meant that we were unable to assess in detail the sex-dependency of our results. However, as has been extensively studied in the AD model mouse [72–74], this remains an important question, and more work is needed to elucidate the importance of sex hormones and glucuronidation regarding AD and PD.

Identification of subclasses is desirable to address the heterogeneity in disease with regards transcriptomic profile and treatment response, but patients must be stratified in order to be diagnosed with the correct disease subclass and therefore administer the appropriate treatment. To this end, we used GSE analysis to functionally characterise the AD/PD subclasses (Figure 2, Supplementary Data S1). Cluster 2, which was associated with a decreased immune and stress response, appeared to be most severe disease subclass, whereas cluster 3, which was associated with an increased sensory perception of smell, reduced haemostasis, and reduced immune and DNA damage response, seemed to be the least severe. Meanwhile, cluster 1 was associated with an increased immune and inflammatory responses and reduced sensory perception of smell. The functional terms are supported by community analysis of our AD and PD gene co-expression networks, which identified gene modules that roughly align with the GSE results (Figure 4, Supplementary Data S4). The proposed severity ratings are supported by FBA findings, which show *iADPD2* as having the highest total flux dysregulation compared to control, and *iADPD3* as having the least (Table 2, Supplementary Data S2). Although we did not attempt to characterise for stratifying and diagnosing patients in our study, our findings clearly show that such stratification is possible.

In this work, we leveraged samples from zebrafish telomerase mutants and insights from the *ZebraGEM2.1* metabolic model. These models were utilised in order to test the hypothesis that the observations we made in the human subjects could be explained by telomeric ageing in a way where we could control the 'dosage' of ageing, i.e., *tert*^{+/-} and *tert*^{-/-} mutants. However, it is important to acknowledge the limitations of such models. Although zebrafish are a widely used model organism to study vertebrate ageing [22], most neurons of the brain do not divide and are therefore not likely to be subject to the direct effects of telomeric ageing. Therefore, we cannot conclude that the dysregulations we observed in AD and PD were caused by ageing of neurons per se, but rather correlations exist between telomeric ageing in zebrafish and AD and PD in humans, and these correlations may act via an indirect mechanism affecting multiple systems of the ageing organism. Due to these limitations, more data and more studies are required to support the link between ageing and neuronal degeneration in AD and PD. The basic requirement of such studies would be brain tissue from donors of a wide range of ages. In our study, we utilised datasets containing aggregated samples, where age cannot be assigned, and samples from age-matched donors, meaning that younger donors were poorly represented in our data, making it unsuitable for an ageing analysis.

In conclusion, we report three distinct subclasses of AD and PD. The first subclass was identified as being associated with increased immune response, inflammatory response, and reduced sensory perception of smell, according to GSE results. We observed that this subclass exhibited increased oestradiol turnover, according to FBA results. The second subclass was linked with increased cholesterol biosynthesis and general increased flux through the androgen biosynthesis and metabolism pathway. This subclass was characterised by reduced immune response. The third subclass was characterised by enrichment of GO terms indicating increased sensory perception of smell, reduced haemostasis, and reduced immune and DNA damage response. This subclass also exhibited reduced testosterone biosynthesis from androstenedione, as determined by FBA. All subclasses exhibited dysregulation within the retinoid metabolism pathway. For all subclasses of AD and PD, more investigation is required to verify the effectiveness of these stratification methods and to aid prediction of effective precision therapies. To our knowledge, this is the first meta-analysis at this scale highlighting the potential significance of retinoids, oestradiol, and testosterone in AD and PD by studying the two diseases in combination. We observed that the existence of disease subclasses demands precision or personalised medicine and explains the heterogeneity in AD and PD response to single-factor treatments.

Supplementary Materials: The following are available online at <https://www.mdpi.com/article/10.3390/biomedicines9101310/s1>, Figure S1: Unsupervised clustering of AD and PD samples, Figure S2: Visualisation of AD and PD samples, Figure S3: Transcriptomic and functional characterisation of zebrafish *tert* mutants, Supplementary File S1: *iBrain2845* genome-scale metabolic model, Supplementary File S2: *iADPD*-series context-specific genome-scale metabolic models, Supplementary File S3: *ZebraGEM2.1* genome-scale metabolic model, Supplementary File S4: Zebrafish context-specific genome-scale metabolic models, Supplementary Data S1: Gene set enrichment analysis results for AD and PD subclasses, Supplementary Data S2: Flux balance analysis results for *iADPD*-series genome-scale metabolic models, Supplementary Data SS3: Reporter metabolite analysis results for AD and PD subclasses, Supplementary Data S4: Network analysis results for AD and PD samples, Supplementary Data S5: Gene set enrichment analysis results for zebrafish *tert* mutants, Supplementary Data S6: Reporter metabolite analysis results for zebrafish *tert* mutants.

Author Contributions: A.M. and M.U. supervised the study and designed the study on human data. R.K. and C.E. designed the study on zebrafish. N.H. performed the zebrafish RNA sequencing and generated the raw counts. With the exception of the network analysis, S.L. performed all in silico analysis and M.A., R.B. and C.Z. provided technical consultation. R.B. performed the network analysis. S.L. analysed all the results. S.L. wrote the manuscript with input from H.T. and the rest of the authors. All authors have read and agreed to the published version of the manuscript.

Funding: This work was supported by the German Ministry for Education and Research within the framework of the GerontoSys initiative (research core JenAge, funding code BMBF 0315581) to C.E.; and the Knut and Alice Wallenberg Foundation (grant number 2017.0303) to A.M.

Institutional Review Board Statement: All animal procedures were performed in accordance with the German animal welfare guidelines and approved by the Landesamt für Verbraucherschutz Thüringen (TLV), Germany.

Informed Consent Statement: Not applicable.

Data Availability Statement: All original computer code, models, and author-curated data files have been released under a Creative Commons Attribution ShareAlike 4.0 International Licence (<https://creativecommons.org/licenses/by-sa/4.0/>) and are freely available for download from <https://github.com/SimonLammmm/ad-pd-retinoid>. Zebrafish *tert* mutant sequencing data have been deposited in the NCBI Gene Expression Omnibus (GEO) and are accessible through GEO Series accession numbers GSE102426, GSE102429, GSE102431, and GSE102434.

Acknowledgments: We are grateful to Catarina Henriques and Miguel Godinho Ferreira for sharing the *tert* mutant zebrafish line. We also thank Ivonne Heinze, Ivonne Görlich, and Marco Groth from the FLI sequencing facility for sequencing the zebrafish samples. The authors acknowledge use of the research computing facility at King's College London, *Rosalind* (<https://rosalind.kcl.ac.uk>; accessed on 17 July 2019). The Genotype-Tissue Expression (GTEx) Project was supported by the Common Fund of the Office of the Director of the National Institutes of Health, and by NCI, NHGRI, NHLBI, NIDA, NIMH, and NINDS. The data used for the analyses described in this manuscript were obtained from the GTEx Portal on 6 December 2019. The results published here are in part based on data obtained from the AD Knowledge Portal (<https://adknowledgeportal.synapse.org>; accessed on 1 October 2020). Study data were provided by the Rush Alzheimer's Disease Center, Rush University Medical Center, Chicago. Data collection was supported through funding by NIA grants P30AG10161 (ROS), R01AG15819 (ROSMAP; genomics and RNAseq), R01AG17917 (MAP), R01AG30146, R01AG36042 (5hC methylation, ATACseq), RC2AG036547 (H3K9Ac), R01AG36836 (RNAseq), R01AG48015 (monocyte RNAseq), RF1AG57473 (single nucleus RNAseq), U01AG32984 (genomic and whole exome sequencing), U01AG46152 (ROSMAP AMP-AD, targeted proteomics), U01AG46161 (TMT proteomics), U01AG61356 (whole genome sequencing, targeted proteomics, ROSMAP AMP-AD), the Illinois Department of Public Health (ROSMAP), and the Translational Genomics Research Institute (genomic). Additional phenotypic data can be requested at www.radc.rush.edu; accessed on 1 October 2020). We thank the patients and their families for their selfless donation to further understanding Alzheimer's disease. This project was supported by funding from the National Institute on Aging (AG034504 and AG041232). Many data and biomaterials were collected from several National Institute on Aging (NIA) and National Alzheimer's Coordinating Center (NACC, grant #U01 AG016976) funded sites. Amanda J. Myers, PhD (University of Miami, Department of Psychiatry), prepared the series. The directors, pathologist and technicians involved

include Rush University Medical Center; Rush Alzheimer’s Disease Center (NIH #AG10161); David A. Bennett, M.D.; Julie A. Schneider, MD, MS; Karen Skish, MS, PA (ASCP) MT; Wayne T Longman. The Rush portion of this study was supported by National Institutes of Health grants P30AG10161, R01AG15819, R01AG17917, R01AG36042, R01AG36836, U01AG46152, R01AG34374, R01NS78009, U18NS82140, R01AG42210, and R01AG39478, and the Illinois Department of Public Health. Quality control checks and preparation of the gene expression data was provided by the National Institute on Aging Alzheimer’s Disease Data Storage Site (NIAGADS, U24AG041689) at the University of Pennsylvania.

Conflicts of Interest: The authors declare no competing financial interests.

Abbreviations

AD, Alzheimer’s disease; DEG, differentially expressed gene; FANTOM5, Functional Annotation of the Mammalian Genome 5; FBA, flux balance analysis; GEM, genome-scale metabolic model; GO, Gene Ontology; GSE, gene set enrichment; GTE_x, Genotype-Tissue Expression; HuRI, Human Reference Protein Interactome; HPA, Human Protein Atlas; PD, Parkinson’s disease; ROSMAP, Religious Orders Study and Rush Memory Aging Project.

References

1. Liberini, P.; Valerio, A.; Memo, M.; Spano, P.F. Lewy-Body Dementia and Responsiveness to Cholinesterase Inhibitors: A Paradigm for Heterogeneity of Alzheimer’s Disease? *Trends Pharmacol. Sci.* **1996**, *17*, 155–160. [CrossRef]
2. Wijemanne, S.; Jankovic, J. Dopa-Responsive Dystonia—Clinical and Genetic Heterogeneity. *Nat. Rev. Neurol.* **2015**, *11*, 414–424. [CrossRef] [PubMed]
3. Long, J.M.; Holtzman, D.M. Alzheimer Disease: An Update on Pathobiology and Treatment Strategies. *Cell* **2019**, *179*, 312–339. [CrossRef] [PubMed]
4. Greenland, J.C.; Williams-Gray, C.H.; Barker, R.A. The Clinical Heterogeneity of Parkinson’s Disease and Its Therapeutic Implications. *Eur. J. Neurosci.* **2019**, *49*, 328–338. [CrossRef]
5. Tanaka, M.; Toldi, J.; Vécsei, L. Exploring the Etiological Links behind Neurodegenerative Diseases: Inflammatory Cytokines and Bioactive Kynurenes. *Int. J. Mol. Sci.* **2020**, *21*, 2431. [CrossRef]
6. Baum, L.W. Sex, Hormones, and Alzheimer’s Disease. *J. Gerontol. Ser. A Biol. Sci. Med. Sci.* **2005**, *60*, 736–743. [CrossRef] [PubMed]
7. Meoni, S.; Macerollo, A.; Moro, E. Sex Differences in Movement Disorders. *Nat. Rev. Neurol.* **2020**, *16*, 84–96. [CrossRef]
8. Shepardson, N.E.; Shankar, G.M.; Selkoe, D.J. Cholesterol Level and Statin Use in Alzheimer Disease: I. Review of Epidemiological and Preclinical Studies. *Arch. Neurol.* **2011**, *68*, 1239–1244. [CrossRef]
9. Jeong, S.M.; Jang, W.; Shin, D.W. Association of Statin Use with Parkinson’s Disease: Dose–Response Relationship. *Mov. Disord.* **2019**, *34*, 1014–1021. [CrossRef]
10. Lam, S.; Bayraktar, A.; Zhang, C.; Turkez, H.; Nielsen, J.; Boren, J.; Shoae, S.; Uhlen, M.; Mardinoglu, A. A Systems Biology Approach for Studying Neurodegenerative Diseases. *Drug Discov. Today* **2020**, *25*, 1146–1159. [CrossRef]
11. Mardinoglu, A.; Boren, J.; Smith, U.; Uhlen, M.; Nielsen, J. Systems Biology in Hepatology: Approaches and Applications. *Nat. Rev. Gastroenterol. Hepatol.* **2018**, *15*, 365–377. [CrossRef]
12. Lam, S.; Doran, S.; Yuksel, H.H.; Altay, O.; Turkez, H.; Nielsen, J.; Boren, J.; Uhlen, M.; Mardinoglu, A. Addressing the Heterogeneity in Liver Diseases Using Biological Networks. *Brief. Bioinform.* **2021**, *22*, 1751–1766. [CrossRef]
13. Altay, O.; Nielsen, J.; Uhlen, M.; Boren, J.; Mardinoglu, A. Systems Biology Perspective for Studying the Gut Microbiota in Human Physiology and Liver Diseases. *EBioMedicine* **2019**, *49*, 364–373. [CrossRef]
14. Joshi, A.; Rienks, M.; Theofilatos, K.; Mayr, M. Systems Biology in Cardiovascular Disease: A Multiomics Approach. *Nat. Rev. Cardiol.* **2020**, *18*, 313–330. [CrossRef]
15. De La Monte, S.M.; Wands, J.R. Alzheimer’s Disease Is Type 3 Diabetes—Evidence Reviewed. *J. Diabetes Sci. Technol.* **2008**, *2*, 1101–1113. [CrossRef]
16. Stampfer, M.J. Cardiovascular Disease and Alzheimer’s Disease: Common Links. *J. Intern. Med.* **2006**, *260*, 211–223. [CrossRef]
17. Driver, J.A.; Beiser, A.; Au, R.; Kreger, B.E.; Splansky, G.L.; Kurth, T.; Kiel, D.P.; Lu, K.P.; Seshadri, S.; Wolf, P.A. Inverse Association between Cancer and Alzheimer’s Disease: Results from the Framingham Heart Study. *BMJ (Online)* **2012**, *344*, e1442. [CrossRef]
18. Bajaj, A.; Driver, J.A.; Schernhammer, E.S. Parkinson’s Disease and Cancer Risk: A Systematic Review and Meta-Analysis. *Cancer Causes Control* **2010**, *21*, 697–707. [CrossRef]
19. Sengoku, R. Aging and Alzheimer’s Disease Pathology. *Neuropathology* **2020**, *40*, 22–29. [CrossRef]
20. Hindle, J.V. Ageing, Neurodegeneration and Parkinson’s Disease. *Age Ageing* **2010**, *39*, 156–161. [CrossRef]
21. Chakravarti, D.; LaBella, K.A.; DePinho, R.A. Telomeres: History, Health, and Hallmarks of Aging. *Cell* **2021**, *184*, 306–322. [CrossRef]
22. Carneiro, M.C.; De Castro, I.P.; Ferreira, M.G. Telomeres in Aging and Disease: Lessons from Zebrafish. *DMM Dis. Models Mech.* **2016**, *9*, 737–748. [CrossRef]

23. Anchelin, M.; Alcaraz-Pérez, F.; Martínez, C.M.; Bernabé-García, M.; Mulero, V.; Cayuela, M.L. Premature Aging in Telomerase-Deficient Zebrafish. *DMM Dis. Models Mech.* **2013**, *6*, 1101–1112. [CrossRef] [PubMed]
24. Henriques, C.M.; Carneiro, M.C.; Tenente, I.M.; Jacinto, A.; Ferreira, M.G. Telomerase Is Required for Zebrafish Lifespan. *PLoS Genet.* **2013**, *9*, 1003214. [CrossRef]
25. Lonsdale, J.; Thomas, J.; Salvatore, M.; Phillips, R.; Lo, E.; Shad, S.; Hasz, R.; Walters, G.; Garcia, F.; Young, N.; et al. GTEx Consortium The Genotype-Tissue Expression (GTEx) Project. *Nat. Genet.* **2013**, *45*, 580–585. [CrossRef] [PubMed]
26. Forrest, A.R.R.; Kawaji, H.; Rehli, M.; Baillie, J.K.; De Hoon, M.J.L.; Haberle, V.; Lassmann, T.; Kulakovskiy, I.V.; Lizio, M.; Itoh, M.; et al. A Promoter-Level Mammalian Expression Atlas. *Nature* **2014**, *507*, 462–470. [CrossRef] [PubMed]
27. Lizio, M.; Harshbarger, J.; Shimoji, H.; Severin, J.; Kasukawa, T.; Sahin, S.; Abugessaisa, I.; Fukuda, S.; Hori, F.; Ishikawa-Kato, S.; et al. Gateways to the FANTOM5 Promoter Level Mammalian Expression Atlas. *Genome Biol.* **2015**, *16*, 22. [CrossRef]
28. Lizio, M.; Abugessaisa, I.; Noguchi, S.; Kondo, A.; Hasegawa, A.; Hon, C.C.; De Hoon, M.; Severin, J.; Oki, S.; Hayashizaki, Y.; et al. Update of the FANTOM Web Resource: Expansion to Provide Additional Transcriptome Atlases. *Nucleic Acids Res.* **2019**, *47*, D752–D758. [CrossRef]
29. Marbach, D.; Lamparter, D.; Quon, G.; Kellis, M.; Kutalik, Z.; Bergmann, S. Tissue-Specific Regulatory Circuits Reveal Variable Modular Perturbations across Complex Diseases. *Nat. Methods* **2016**, *13*, 366–370. [CrossRef]
30. Luck, K.; Kim, D.-K.; Lambourne, L.; Spirohn, K.; Begg, B.E.; Bian, W.; Brignall, R.; Cafarelli, T.; Campos-Laborie, F.J.; Charloteaux, B.; et al. A Reference Map of the Human Protein Interactome. *bioRxiv* **2019**. [CrossRef]
31. Uhlén, M.; Fagerberg, L.; Hallström, B.M.; Lindskog, C.; Oksvold, P.; Mardinoglu, A.; Sivertsson, Å.; Kampf, C.; Sjöstedt, E.; Asplund, A.; et al. Tissue-Based Map of the Human Proteome. *Science* **2015**, *347*, 1260419. [CrossRef]
32. Mostafavi, S.; Gaiteri, C.; Sullivan, S.E.; White, C.C.; Tasaki, S.; Xu, J.; Taga, M.; Klein, H.U.; Patrick, E.; Komashko, V.; et al. A Molecular Network of the Aging Human Brain Provides Insights into the Pathology and Cognitive Decline of Alzheimer’s Disease. *Nat. Neurosci.* **2018**, *21*, 811–819. [CrossRef]
33. Myers, A.J.; Gibbs, J.R.; Webster, J.A.; Rohrer, K.; Zhao, A.; Marlowe, L.; Kaleem, M.; Leung, D.; Bryden, L.; Nath, P.; et al. A Survey of Genetic Human Cortical Gene Expression. *Nat. Genet.* **2007**, *39*, 1494–1499. [CrossRef] [PubMed]
34. Webster, J.A.; Gibbs, J.R.; Clarke, J.; Ray, M.; Zhang, W.; Holmans, P.; Rohrer, K.; Zhao, A.; Marlowe, L.; Kaleem, M.; et al. Genetic Control of Human Brain Transcript Expression in Alzheimer Disease. *Am. J. Hum. Genet.* **2009**, *84*, 445–458. [CrossRef] [PubMed]
35. Rajkumar, A.P.; Bidkhorji, G.; Shoaie, S.; Clarke, E.; Morrin, H.; Hye, A.; Williams, G.; Ballard, C.; Francis, P.; Aarsland, D. Postmortem Cortical Transcriptomics of Lewy Body Dementia Reveal Mitochondrial Dysfunction and Lack of Neuroinflammation. *Am. J. Geriatr. Psychiatry* **2020**, *28*, 75–86. [CrossRef]
36. Zhang, Y.; James, M.; Middleton, F.A.; Davis, R.L. Transcriptional Analysis of Multiple Brain Regions in Parkinson’s Disease Supports the Involvement of Specific Protein Processing, Energy Metabolism, and Signaling Pathways, and Suggests Novel Disease Mechanisms. *Am. J. Med. Genet. Neuropsychiatr. Genet.* **2005**, *137 B*, 5–16. [CrossRef]
37. Zheng, B.; Liao, Z.; Locascio, J.J.; Lesniak, K.A.; Roderick, S.S.; Watt, M.L.; Eklund, A.C.; Zhang-James, Y.; Kim, P.D.; Hauser, M.A.; et al. PGC-1 α , a Potential Therapeutic Target for Early Intervention in Parkinson’s Disease. *Sci. Transl. Med.* **2010**, *2*, 52ra73. [CrossRef]
38. Bray, N.L.; Pimentel, H.; Melsted, P.; Pachter, L. Near-Optimal Probabilistic RNA-Seq Quantification. *Nat. Biotechnol.* **2016**, *34*, 525–527. [CrossRef]
39. Yates, A.D.; Achuthan, P.; Akanni, W.; Allen, J.; Allen, J.; Alvarez-Jarreta, J.; Amode, M.R.; Armean, I.M.; Azov, A.G.; Bennett, R.; et al. Ensembl 2020. *Nucleic Acids Res.* **2020**, *48*, D682–D688. [CrossRef]
40. Ritchie, M.E.; Phipson, B.; Wu, D.; Hu, Y.; Law, C.W.; Shi, W.; Smyth, G.K. Limma Powers Differential Expression Analyses for RNA-Sequencing and Microarray Studies. *Nucleic Acids Res.* **2015**, *43*, e47. [CrossRef]
41. Van Der Maaten, L.; Hinton, G. Visualizing Data Using T-SNE. *J. Mach. Learn. Res.* **2008**, *9*, 2579–2625.
42. McInnes, L.; Healy, J.; Saul, N.; Großberger, L. UMAP: Uniform Manifold Approximation and Projection. *J. Open Source Softw.* **2018**, *3*, 861. [CrossRef]
43. van Dijk, D.; Sharma, R.; Nainys, J.; Yim, K.; Kathail, P.; Carr, A.J.; Burdziak, C.; Moon, K.R.; Chaffer, C.L.; Pattabiraman, D.; et al. Recovering Gene Interactions from Single-Cell Data Using Data Diffusion. *Cell* **2018**, *174*, 716–729.e27. [CrossRef] [PubMed]
44. Wilkerson, M.D.; Hayes, D.N. ConsensusClusterPlus: A Class Discovery Tool with Confidence Assessments and Item Tracking. *Bioinformatics* **2010**, *26*, 1572–1573. [CrossRef]
45. Love, M.I.; Huber, W.; Anders, S. Moderated Estimation of Fold Change and Dispersion for RNA-Seq Data with DESeq2. *Genome Biol.* **2014**, *15*, 550. [CrossRef] [PubMed]
46. Våremo, L.; Nielsen, J.; Nookaew, I. Enriching the Gene Set Analysis of Genome-Wide Data by Incorporating Directionality of Gene Expression and Combining Statistical Hypotheses and Methods. *Nucleic Acids Res.* **2013**, *41*, 4378–4391. [CrossRef] [PubMed]
47. Mardinoglu, A.; Agren, R.; Kampf, C.; Asplund, A.; Nookaew, I.; Jacobson, P.; Walley, A.J.; Froguel, P.; Carlsson, L.M.; Uhlen, M.; et al. Integration of Clinical Data with a Genome-Scale Metabolic Model of the Human Adipocyte. *Mol. Syst. Biol.* **2013**, *9*, 649. [CrossRef]
48. Mardinoglu, A.; Agren, R.; Kampf, C.; Asplund, A.; Uhlen, M.; Nielsen, J. Genome-Scale Metabolic Modelling of Hepatocytes Reveals Serine Deficiency in Patients with Non-Alcoholic Fatty Liver Disease. *Nat. Commun.* **2014**, *5*, 3083. [CrossRef]

49. Wang, H.; Marcišauskas, S.; Sánchez, B.J.; Domenzain, I.; Hermansson, D.; Agren, R.; Nielsen, J.; Kerkhoven, E.J. RAVEN 2.0: A Versatile Toolbox for Metabolic Network Reconstruction and a Case Study on *Streptomyces Coelicolor*. *PLoS Comput. Biol.* **2018**, *14*, e1006541. [CrossRef] [PubMed]
50. Agren, R.; Bordel, S.; Mardinoglu, A.; Pornputtapong, N.; Nookaew, I.; Nielsen, J. Reconstruction of Genome-Scale Active Metabolic Networks for 69 Human Cell Types and 16 Cancer Types Using INIT. *PLoS Comput. Biol.* **2012**, *8*, e1002518. [CrossRef]
51. Agren, R.; Mardinoglu, A.; Asplund, A.; Kampf, C.; Uhlen, M.; Nielsen, J. Identification of Anticancer Drugs for Hepatocellular Carcinoma through Personalized Genome-Scale Metabolic Modeling. *Mol. Syst. Biol.* **2014**, *10*, 721. [CrossRef]
52. Baloni, P.; Funk, C.C.; Yan, J.; Yurkovich, J.T.; Kueider-Paisley, A.; Nho, K.; Heinken, A.; Jia, W.; Mahmoudiandehkordi, S.; Louie, G.; et al. Metabolic Network Analysis Reveals Altered Bile Acid Synthesis and Metabolism in Alzheimer's Disease. *Cell Rep. Med.* **2020**, *1*, 100138. [CrossRef]
53. Patil, K.R.; Nielsen, J. Uncovering Transcriptional Regulation of Metabolism by Using Metabolic Network Topology. *Proc. Natl. Acad. Sci. USA* **2005**, *102*, 2685–2689. [CrossRef] [PubMed]
54. Traag, V.A.; Waltman, L.; van Eck, N.J. From Louvain to Leiden: Guaranteeing Well-Connected Communities. *Sci. Rep.* **2019**, *9*, 1–12. [CrossRef]
55. Chen, E.Y.; Tan, C.M.; Kou, Y.; Duan, Q.; Wang, Z.; Meirelles, G.V.; Clark, N.R.; Ma'ayan, A. Enrichr: Interactive and Collaborative HTML5 Gene List Enrichment Analysis Tool. *BMC Bioinform.* **2013**, *14*, 128. [CrossRef] [PubMed]
56. Kuleshov, M.V.; Jones, M.R.; Rouillard, A.D.; Fernandez, N.F.; Duan, Q.; Wang, Z.; Koplev, S.; Jenkins, S.L.; Jagodnik, K.M.; Lachmann, A.; et al. Enrichr: A Comprehensive Gene Set Enrichment Analysis Web Server 2016 Update. *Nucleic Acids Res.* **2016**, *44*, W90–W97. [CrossRef] [PubMed]
57. Supek, F.; Bošnjak, M.; Škunca, N.; Šmuc, T. Revigo Summarizes and Visualizes Long Lists of Gene Ontology Terms. *PLoS ONE* **2011**, *6*, e21800. [CrossRef]
58. Aramillo Irizar, P.; Schäuble, S.; Esser, D.; Groth, M.; Frahm, C.; Priebe, S.; Baumgart, M.; Hartmann, N.; Marthandan, S.; Menzel, U.; et al. Transcriptomic Alterations during Ageing Reflect the Shift from Cancer to Degenerative Diseases in the Elderly. *Nat. Commun.* **2018**, *9*, 327. [CrossRef]
59. Rajsombath, M.M.; Nam, A.Y.; Ericsson, M.; Nuber, S. Female Sex and Brain-Selective Estrogen Benefit α -Synuclein Tetramerization and the PD-like Motor Syndrome in 3K Transgenic Mice. *J. Neurosci. Off. J. Soc. Neurosci.* **2019**, *39*, 7628–7640. [CrossRef] [PubMed]
60. Resnick, S.M.; Matsumoto, A.M.; Stephens-Shields, A.J.; Ellenberg, S.S.; Gill, T.M.; Shumaker, S.A.; Pleasants, D.D.; Barrett-Connor, E.; Bhasin, S.; Cauley, J.A.; et al. Testosterone Treatment and Cognitive Function in Older Men with Low Testosterone and Age-Associated Memory Impairment. *JAMA J. Am. Med. Assoc.* **2017**, *317*, 717–727. [CrossRef]
61. Wahjoepramono, E.J.; Asih, P.R.; Aniwiyanti, V.; Taddei, K.; Dhaliwal, S.S.; Fuller, S.J.; Foster, J.; Carruthers, M.; Verdile, G.; Sohrabi, H.R.; et al. The Effects of Testosterone Supplementation on Cognitive Functioning in Older Men. *CNS Neurol. Disord. Drug Targets* **2016**, *15*, 337–343. [CrossRef] [PubMed]
62. Grosse, L.; Pâquet, S.; Caron, P.; Fazli, L.; Rennie, P.S.; Bélanger, A.; Barbier, O. Androgen Glucuronidation: An Unexpected Target for Androgen Deprivation Therapy, with Prognosis and Diagnostic Implications. *Cancer Res.* **2013**, *73*, 6963–6971. [CrossRef] [PubMed]
63. Blomhoff, R.; Blomhoff, H.K. Overview of Retinoid Metabolism and Function. *J. Neurobiol.* **2006**, *66*, 606–630. [CrossRef] [PubMed]
64. Van Steijn, L.; Verbeek, F.J.; Spaink, H.P.; Merks, R.M.H. Predicting Metabolism from Gene Expression in an Improved Whole-Genome Metabolic Network Model of *Danio Rerio*. *Zebrafish* **2019**, *16*, 348–362. [CrossRef]
65. Riahi, R.R.; Bush, A.E.; Cohen, P.R. Topical Retinoids: Therapeutic Mechanisms in the Treatment of Photodamaged Skin. *Am. J. Clin. Dermatol.* **2016**, *17*, 265–276. [CrossRef] [PubMed]
66. Das, B.; Dasgupta, S.; Ray, S. Potential Therapeutic Roles of Retinoids for Prevention of Neuroinflammation and Neurodegeneration in Alzheimer's Disease. *Neural Regen. Res.* **2019**, *14*, 1880–1892. [PubMed]
67. Shudo, K.; Fukasawa, H.; Nakagomi, M.; Yamagata, N. Towards Retinoid Therapy for Alzheimers Disease. *Curr. Alzheimer Res.* **2009**, *6*, 302–311. [CrossRef]
68. Fukasawa, H.; Nakagomi, M.; Yamagata, N.; Katsuki, H.; Kawahara, K.; Kitaoka, K.; Miki, T.; Shudo, K. Tamibarotene: A Candidate Retinoid Drug for Alzheimer's Disease. *Biol. Pharm. Bull.* **2012**, *35*, 1206–1212. [CrossRef]
69. Fitz, N.F.; Nam, K.N.; Koldamova, R.; Lefterov, I. Therapeutic Targeting of Nuclear Receptors, Liver X and Retinoid X Receptors, for Alzheimer's Disease. *Br. J. Pharmacol.* **2019**, *176*, 3599–3610. [CrossRef]
70. Sinclair, E.; Trivedi, D.K.; Sarkar, D.; Walton-Doyle, C.; Milne, J.; Kunath, T.; Rijs, A.M.; de Bie, R.M.A.; Goodacre, R.; Silverdale, M.; et al. Metabolomics of Sebum Reveals Lipid Dysregulation in Parkinson's Disease. *Nat. Commun.* **2021**, *12*, 1–9. [CrossRef]
71. Martucci, C.P. The Role of 2-Methoxyestrone in Estrogen Action. *J. Steroid Biochem.* **1983**, *19*, 635–638. [CrossRef]
72. Santana-Santana, M.; Bayascas, J.-R.; Giménez-Llort, L. Fine-Tuning the PI3K/Akt Signaling Pathway Intensity by Sex and Genotype-Load: Sex-Dependent Homozygotic Threshold for Somatic Growth but Feminization of Anxious Phenotype in Middle-Aged PDK1 K465E Knock-In and Heterozygous Mice. *Biomedicines* **2021**, *9*, 747. [CrossRef] [PubMed]
73. Santana-Santana, M.; Bayascas, J.-R.; Giménez-Llort, L. Sex-Dependent Signatures, Time Frames and Longitudinal Fine-Tuning of the Marble Burying Test in Normal and AD-Pathological Aging Mice. *Biomedicines* **2021**, *9*, 994. [CrossRef] [PubMed]
74. Muntsant, A.; Jiménez-Altayó, F.; Puertas-Umbert, L.; Jiménez-Xarrie, E.; Vila, E.; Giménez-Llort, L. Sex-Dependent End-of-Life Mental and Vascular Scenarios for Umbert Mechanisms in Mice with Normal and AD-Neurodegenerative Aging. *Biomedicines* **2021**, *9*, 111. [CrossRef] [PubMed]



Review

Regenerative Neurology and Regenerative Cardiology: Shared Hurdles and Achievements

Dinko Mitrečić^{1,2,*}, Valentina Hribljan^{1,2}, Denis Jagečić^{1,2}, Jasmina Isaković³, Federica Lamberto^{4,5}, Alex Horánszky^{4,5}, Melinda Zana⁴, Gabor Foldes^{6,7}, Barbara Zavan⁸, Augustas Pivoriūnas⁹, Salvador Martínez¹⁰, Letizia Mazzini¹¹, Lidija Radenovic¹², Jelena Milasin¹³, Juan Carlos Chachques¹⁴, Leonora Buzanska¹⁵, Min Suk Song³ and András Dinnyes^{4,5,16,17}

- ¹ Laboratory for Stem Cells, Croatian Institute for Brain Research, University of Zagreb School of Medicine, 10000 Zagreb, Croatia; valentina.hribljan@mef.hr (V.H.); denis.jagecic@mef.hr (D.J.)
 - ² Department of Histology and Embryology, University of Zagreb School of Medicine, 10000 Zagreb, Croatia
 - ³ Omnion Research International Ltd., 10000 Zagreb, Croatia; jasmina.isakovic@omnion-research.com (J.I.); min.suk.song@omnion-research.com (M.S.S.)
 - ⁴ BioTalentum Ltd., Aulich Lajos Str. 26, 2100 Gordillo, Hungary; federica.lamberto@biotalentum.hu (F.L.); alex.horanszky@biotalentum.hu (A.H.); melinda.zana@biotalentum.hu (M.Z.); andras.dinnyes@biotalentum.hu (A.D.)
 - ⁵ Department of Physiology and Animal Health, Institute of Physiology and Animal Health, Hungarian University of Agriculture and Life Sciences, Páter Károly Str. 1, 2100 Godollo, Hungary
 - ⁶ Heart and Vascular Center, Semmelweis University, 1122 Budapest, Hungary; foldes.gabor@med.semmelweis-univ.hu
 - ⁷ National Heart and Lung Institute, Imperial College London, London W12 0NN, UK
 - ⁸ Department of Translational Medicine, University of Ferrara, 44121 Ferrara, Italy; barbara.zavan@unipd.it
 - ⁹ Department of Stem Cell Biology, State Research Institute Centre for Innovative Medicine, LT-01102 Vilnius, Lithuania; augustas.pivoriunas@imcentras.lt
 - ¹⁰ Instituto de Neurociencias UMH-CSIC, 03550 San Juan de Alicante, Spain; smartinez@umh.es
 - ¹¹ ALS Center, Department of Neurology, Maggiore della Carità Hospital, University of Piemonte Orientale, 28100 Novara, Italy; letizia.mazzini@uniupo.it
 - ¹² Center for Laser Microscopy, Faculty of Biology, University of Belgrade, 11000 Belgrade, Serbia; lidijar@bio.bg.ac.rs
 - ¹³ Laboratory for Stem Cell Research, School of Dental Medicine, University of Belgrade, 11000 Belgrade, Serbia; jelena.milasin@stomf.bg.ac.rs
 - ¹⁴ Laboratory of Biosurgical Research, Pompidou Hospital, University of Paris, 75006 Paris, France; j.chachques-ext@aphp.fr
 - ¹⁵ Department of Stem Cell Bioengineering, Mossakowski Medical Research Institute Polish Academy of Sciences, 02-106 Warsaw, Poland; buzanska@imdik.pan.pl
 - ¹⁶ HCEMM-USZ Stem Cell Research Group, Department of Cell Biology and Molecular Medicine, University of Szeged, 6720 Szeged, Hungary
 - ¹⁷ College of Life Sciences, Sichuan University, Chengdu 610064, China
- * Correspondence: dinko.mitreccic@mef.hr

Citation: Mitrečić, D.; Hribljan, V.; Jagečić, D.; Isaković, J.; Lamberto, F.; Horánszky, A.; Zana, M.; Foldes, G.; Zavan, B.; Pivoriūnas, A.; et al. Regenerative Neurology and Regenerative Cardiology: Shared Hurdles and Achievements. *Int. J. Mol. Sci.* **2022**, *23*, 855. <https://doi.org/10.3390/ijms23020855>

Academic Editors: Masaru Tanaka and Lydia Giménez-Llort

Received: 7 November 2021

Accepted: 9 January 2022

Published: 13 January 2022

Publisher's Note: MDPI stays neutral with regard to jurisdictional claims in published maps and institutional affiliations.



Copyright: © 2022 by the authors. Licensee MDPI, Basel, Switzerland. This article is an open access article distributed under the terms and conditions of the Creative Commons Attribution (CC BY) license (<https://creativecommons.org/licenses/by/4.0/>).

Abstract: From the first success in cultivation of cells in vitro, it became clear that developing cell and/or tissue specific cultures would open a myriad of new opportunities for medical research. Expertise in various in vitro models has been developing over decades, so nowadays we benefit from highly specific in vitro systems imitating every organ of the human body. Moreover, obtaining sufficient number of standardized cells allows for cell transplantation approach with the goal of improving the regeneration of injured/disease affected tissue. However, different cell types bring different needs and place various types of hurdles on the path of regenerative neurology and regenerative cardiology. In this review, written by European experts gathered in Cost European action dedicated to neurology and cardiology-Bioneca, we present the experience acquired by working on two rather different organs: the brain and the heart. When taken into account that diseases of these two organs, mostly ischemic in their nature (stroke and heart infarction), bring by far the largest burden of the medical systems around Europe, it is not surprising that in vitro models of nervous and heart muscle tissue were in the focus of biomedical research in the last decades. In this review we describe and discuss hurdles which still impair further progress of regenerative neurology and cardiology and we detect those ones which are common to both fields and some, which are

field-specific. With the goal to elucidate strategies which might be shared between regenerative neurology and cardiology we discuss methodological solutions which can help each of the fields to accelerate their development.

Keywords: stem cells; regenerative neuroscience; brain regeneration; neurology; cardiology; myocardial regeneration; clinical trials

1. Introduction

Regenerative medicine aims at replacing human cells, tissues or organs damaged by disease or aging and restoring their normal functions. Among some of the most promising approaches in regenerative medicine are stem cell-based therapies, which may provide unparalleled possibilities in the treatment of various conditions, including brain and heart diseases [1]. The therapeutic effect, i.e., restoration of function in the damaged tissue, is attained through direct cell replacement, stimulation of endogenous regeneration/repair systems, establishment of a supportive environment for the remaining cells, or a combination of these mechanisms [2]. Besides the progenitor cells from the affected nervous or cardiac muscle tissue, stem cells of most diverse origins have also proved to be candidates with great potential for translation towards clinical trials. Human embryonic stem cells (hESCs) show the highest differentiation potential, yet their use is hampered by numerous ethical controversies, and alternative sources are sought for [3]. Multipotency of mesenchymal stem cells (MSCs), their presence in almost all adult tissues, the fact that they are usually easily accessible and that they can be differentiated into neural and myocardial lineages makes them very appealing in cell-based therapies [4,5]. Lately, great expectations have also been placed on induced pluripotent stem cells (iPSCs) generated from somatic cells that have undergone genetic reprogramming resulting in pluripotency. Most of cell types are easily obtainable and expanded, usually with no need for immunosuppression following transplantation [6]. Over the past two decades a large number of trials have been conducted, and many are currently underway, including those related to demyelinating diseases and spinal cord injuries, amyotrophic lateral sclerosis, stroke, Parkinson's disease, macular degeneration, as well as acute myocardial infarction, ischemic cardiomyopathy, refractory angina and many others [1]. Although different clinical trials in the fields of neurology and cardiology have reported promising benefits of stem cell-based therapies, many challenges still remain.

This review outlines various types of stem cells that are currently available in neurological and cardiovascular regenerative medicine and reports current state of the art in attempts to introduce those procedures in every day practice. Moreover, we analyse the signalling pathways and mechanisms of their action and examine the outcomes that have been reached with their application. In addition, we discuss the use of novel biomaterials as support for 2D and 3D cell growth, as well as the emerging role of exosomes and their cargos in tissue regeneration. Finally, an overview of the main obstacles, some shared between these two fields, and some field-specific, which we have yet to overcome are given.

2. Induced Pluripotent Stem Cells–Flying Start to Boosting In Vitro Models of the Nervous System and the Heart

The pioneer studies of Yamanaka and his group yielded protocols for obtaining induced pluripotent stem cells (iPSCs), thus providing the opportunity of dedifferentiating any cell to pluripotent state and, equally important, to obtain autologous, patient-specific cells [7,8]. iPSCs are generated from somatic cells, which have been reprogrammed to acquire pluripotency and have the unique capabilities of self-renewal, proliferation, and differentiation [9]. Since iPSCs can give rise to virtually any cellular lineage, an important application of iPSC technology is the in vitro differentiation of specialized cells, like neurons and cardiomyocytes (Figure 1). This can then be used for investigation of a specific tissue,

including both fully differentiated cells and their precursors. Such an approach paved the way for promising advances in patient-specific disease modelling, drug screening, and cell-based therapies without the risk of immune rejection [9–12].

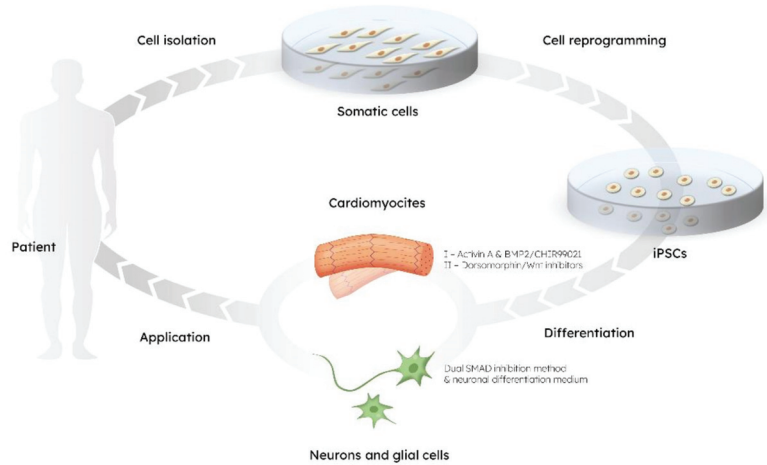


Figure 1. The circle of stem cells-based technology: from cell isolation to application.

3. iPSC-Derived Cardiomyocytes

The course of cardiomyocytes differentiation is validated using molecular markers for different stages of development, as well as investigating their beating capacity, electrophysiology and metabolism [13–15]. Most importantly, we developed methods to differentiate iPSC in cardiomyocytes, with the goal to generate a mixed population of cardiac cells, as ventricular-, atrial- and pacemaker-like cardiomyocytes [16]. That protocol consists of two major steps: firstly, growth factors (e.g., activin A, BMP2) or small molecules (e.g., CHIR99021) activate the Wnt signalling, allowing the mesoderm (*Nkx2.5+*, *Gata4+*, *Mesp1+*) induction [14,17–19]. Secondly, small molecules (e.g., dorsomorphin) or Wnt inhibitors (e.g., IWR-1, IWP-2) are used to enhance the cardiac lineage specification and differentiation (*cTnT+*, *Myh6+*, *Tnni3+*) [17,19,20]. Under these conditions, ventricular-like cardiomyocytes (*Hey2+*, *Mlc2v+*) are predominant than other cardiac cell types [14,21–23]. However, depending on the research aim, there are also methods to purify and isolate an atrial-like cell population (*Kcnj3+*, *Kcnj5+*, *Cacna1d+*), for example using retinoic acid or BMP antagonist (e.g., Noggin, Gremlin 2), by upregulating atrial-specific genes. [14,23–27]. On the other hand, the pacemaker-like cardiomyocytes are still difficult to obtain *in vitro*. So far, the inhibition of neuregulin1 β /ErbB signalling seems the most efficient way to enrich the sinoatrial node cells population (*Hcn4+*, *Tbx3+*, *Tbx18+*), and only recently it has been hypothesized that modulating the Wnt signalling through Nodal inhibition may promote the pacemaker cells fate [28–30].

4. Specific Requirements for In Vitro Heart Muscle Model

The iPSC-derived cardiomyocytes correspond to the foetal-like state concerning their functional and physiological characteristics [31]. A very specific challenge is to obtain more mature cardiomyocytes, and several methods are currently available [32]. Compared to immature counterparts, these adult-like cardiomyocytes metabolise fatty acids, display a high mitochondrial mass, well-arranged sarcomeres, and higher contraction force. Therefore, cardiomyocytes maturation can be achieved by providing fatty acids to the culture medium [33], using mechanical and electrical stimulation [34] or developing a 3D cellular model [21]. Interestingly, iPSCs obtained from cardiac sources suggest an improved differentiation capacity *in vitro* and possibly a higher degree of maturation of

cardiomyocytes. In this regard, the epigenetic memory of somatic cell source may play a fundamental role [35,36]. When the current state of the art is taken in account, the most promising approach is cultivating cardiomyocytes in 3D form (Figure 2). It comes very close to heart's unique cytoarchitectural arrangement and to an even higher level of similarity to the original tissue, with the ultimate goal to establish a heart-on-a-chip model [21,37]. This scaffold-based approach can mimic the patient-specific anatomical microstructure and composition of the human heart and vessels as well as generate responsive constructs to study intact tissue-level cardiovascular physiology. The interaction between cells and the cardiovascular extracellular niche and matrix constituents leads to activation of physiological underlying mechanisms and responsiveness to mechanical, electrical and pharmacological cues. Thus, multicellular microtissue may prove useful for many cell-based applications, like cardiotoxicity assessment and modelling myocardial infarction in a dish [38]. However, comparing structural, mechanical, and biological properties of these structures head-to-head with perfused intact tissues like myocardial and vascular slices and wedges is still warranted.

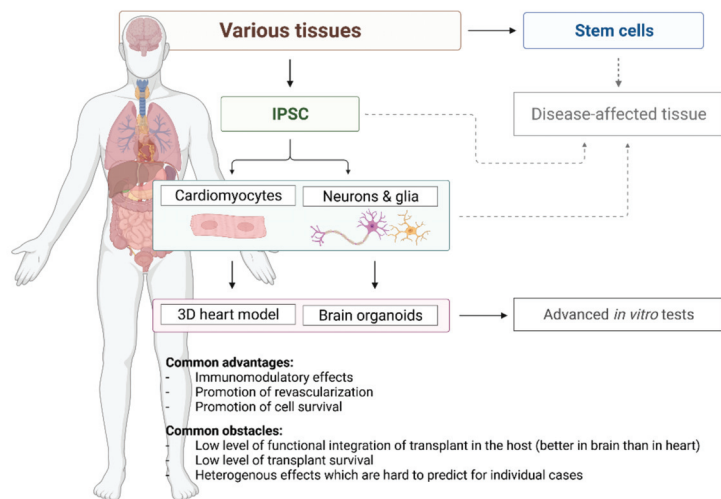


Figure 2. Current options offered by stem cell-based technology for regenerative cardiology and neurology.

Another critical cell subtype of the cardiovascular system is those forming the organotypic vasculature [39]. The generation of these endothelial cells should also rely on organ-specific differentiation protocols, where functional readouts can validate the efficacy and quality of the production. Their specific function comprises barrier-forming continuous layers, a specific vasoactive and growth factor secretion profile and thrombogenic properties [39,40]. Most importantly, being more than a passive conduit, prevascularisation by these endothelial cells can support the long-term survival and instruct the contractility and other functions of adjacent cardiomyocytes within the *in vitro* generated multicellular constructs. To establish vascularisation, pluripotent stem cell-derived endothelial cells show a remarkable capacity to self-organise into functional microvasculature, like cardiac capillaries, thereby providing sufficient perfusion throughout the cell constructs with a substantial thickness [41].

5. iPSC-Derived Neurons

The human brain is comprised of a combination of distinct cellular subtypes with a diverse range of specialized functions such as electrical communication, axonal ensheating

and metabolic coupling [42]. These include, but are not limited to neurons, which are the primary functional cells of the brain classified via their associated neurotransmitters, and glial cells, such as astrocytes, microglia and oligodendrocytes, which are all critical for maintaining homeostasis and working function in the CNS [43]. iPSCs can be differentiated into several of these specialized cellular subtypes with functional characteristics that are representative of those found in the brain, such as dopaminergic neurons, cortical neurons and the aforementioned neuroglia [44].

The *in vitro* neuroectodermal induction of iPSCs, initiated via the dual SMAD inhibition method, results in the efficient generation of neural rosettes comprised of neuronal stem cells (NSCs) (Sox1+, Nestin+) that represent a cross-section of the neural tube (Figure 1). These NSCs can then be passaged, producing neural progenitor cells (NPCs) which can be stably maintained in culture [45]. A neuronal differentiation medium can then be applied to NPCs, which can be plated and further differentiated into more mature neuronal (Map2+, TH+, SLC18A3+) and glial cultures, including astrocytes (AQP4+, s100β+) and oligodendrocytes (NG2, Olig1/2, NBP) [46,47].

Neuronal differentiation of iPSCs provides patient-specific cells of neural lineage, opening possibilities for developing therapeutics, analysing drugs, and studying the underlying mechanisms of neurological pathologies. This is done by differentiating iPSCs into NSCs in a 2D setting which includes primitive and neural rosette-type NSCs [48,49]. Conventional 2D *in vitro* neural models have enabled vast knowledge enhancements regarding brain cellular subtypes, such as adhesive and migratory cellular attachment sites, formation of spontaneous networks, cell type-specific resting membrane potentials and mechanisms underlying axonal guidance [50].

On the other hand, neural differentiation of iPSCs can also be undertaken in a 3D settings. This can involve the generation of neurospheres, floating 3D NSC cultures that have been widely utilized for in-depth NPC analysis and more closely resemble the *in vivo* setting than 2D cultures [51,52].

Other 3D methods can utilize artificial scaffolding or extra-cellular matrix (ECM) materials that are continuously under optimization to recapitulate the anatomical organisation of the brain [53,54]. 3D neural culture models involving cell growth using a hydrogel matrix or synthetic scaffolds are highly desirable, offering systems with intricate and easily calculable architecture with specific functional characteristics. Even though the reproducibility of these 3D models is a current challenge, newer methods that involve laser fabrication and bioprinting offer promising avenues for producing accurate and reproducible 3D *in vitro* neural cultures. Therefore, iPSCs have been, and will continue to be, utilized for advanced microstructured 3D scaffolds for *in vitro* disease modelling and for the study of neuronal function [55–58].

Persistent advances in the methodology used to obtain *in vitro* brain tissue from iPSCs led to the development of 3D brain-organoids from embryoid bodies [59]. These organoids have been demonstrated to consist of several distinctive brain regions and heterogeneous tissue that can mimic the sophisticated architecture of the central nervous system [60,61]. It is worth noting, however, that as the complexity of these 3D cultures improves, so does their variability and heterogeneity. Therefore, improved methods of high content analysis will be required to determine the phenotypic characteristics of these cultures with multidimensional readouts [62].

There are many issues being investigated concerning the source, quality, stability, safety and scalability of human iPSC and derivative cell production for a variety of uses. Concerning the somatic cell source, pre-existing mutations acquired during the lifetime of the donor are more frequent in skin samples than in bone marrow. This means that very early life stage sources, for example those from umbilical cord blood banks, exhibit these potentially adverse events to a much lesser degree [63–66]. However, during the reprogramming, maintenance and scaling-up of iPSC cultures further mutations, including chromosomal rearrangements, can happen. These need to be monitored, especially in case of further clinical use [67–69]. The process of adaptation to the *in vitro* culture conditions

favours some chromosomal rearrangements occurring more frequently [70]. Development of culture conditions occurrence, as well as advanced quality control methods, are an important direction of stem cell banking and the key towards clinical applicability. Major public and private entities have created human pluripotent stem cell banks with many cell lines originating from patients of different ethnic groups, yet many of them have not been consented for industrial use, and most of them have not been optimized for clinical grade applications—these are all potential hurdles to overcome if clinical applications are to be considered. The distribution of existing cell lines among ethnic groups is unbalanced, but since more nations are developing their own stem cell banks, we are gradually overcoming this ambiguity.

6. Specific Requirements for the In Vitro Nervous Tissue Model

While the heart muscle is a rather uniformly structured tissue, generally independent of the microanatomic region, nervous tissue brings inherent complexity stemming from the existence of various regions with a variety of cell subtypes and a multitude of functions. Thus, when cultivating cells of the nervous system in vitro, one can distinguish many types of cultures, existing in a range from mixed spontaneously differentiated and heterogeneous cultures to those ones in which selection of one subtype of cells is preferred (e.g., motoric neurons, cholinergic neurons, mixed glia-neuronal cultures, astrocytes, sensoric neurons, etc). Sometimes those experiments even include chimeric interspecies cultures [71]. Another important question which brings this complexity to the next level is whether the nervous system can, if at all, be investigated focusing only on one specific cell type or region, e.g., the cerebral cortex. This is a crucial point to consider since the main function of the nervous system is to achieve a well coordinated interaction between its various regions through receiving and transmission of electrical and chemical signals.

Thus, since the physiology of the brain is rather different than that of the heart muscle, it is crucial to address all the advantages and limitations prior to starting any further development. Two dimensional cultures of nervous tissue brought numerous pioneering discoveries on cellular level, but their value in understanding higher order cellular coordination is very limited. Thus, even more than in the heart muscle, 3D cultures of nervous tissue are required for all the research aiming to elucidate physiological and pathological events occurring in interaction between cells.

7. Brain Organoids

While stem cells platforms based on 2D culture are being successfully used for modeling of human development and disease at cellular and molecular levels, they lack the conditions imitating spatial and temporal signaling as well as the interactions of the cells in their natural niche. These limitations of in vitro culture might be resolved by the application of biomimetic 3D solutions, especially by combining microenvironmental bioengineering with the intrinsic capacity of pluripotent stem cells to build up 3D structures [72]. This intrinsic ability of pluripotent stem cells to self-organize under 3D in vitro culture conditions into highly structured tissue patterns, opened the era of “brain organoids” [60,73]. Yoshiki Sasai and colleagues were the first to obtain highly patterned neural structures resembling multi-layered brain cortex in vitro from human pluripotent stem cells, using SFEBq (serum-free floating culture of EB-like aggregates with quick re-aggregation) protocol [73]. Further developments from the Jougen Knoblich group brought advanced brain-like 3D in vitro structures with identified regions of cerebral cortex, retina, meninges and chordoid plexus. These 3D structures all exhibit the major stages of prenatal human brain development with functional nervous tissue cell types and cortical layer architecture, thus offering an unprecedented model for investigating human neurodevelopmental and neurodegenerative diseases [74]. Multimodal Single-Cell Analysis (single cell RT-qPCR and functional-microfluidic linked single cell RT-qPCR) of cerebral organoids cultured for more than nine months revealed a high level of neuronal and glial cell diversity as

well as confirmed their functionality with identified cell-type specific responsiveness to neurotransmitters and spontaneous action potential activity [75].

Brain organoid systems appeared feasible to model early human neurodevelopment and its pathology, however they have anatomical and functional limitations which are impairing their use for studying the later developmental stages due to the lack of the correct neuronal network connectivity and vascularization. Much work in the field has been addressed towards overcoming these limitations with two parallel, but interdependent, directions: the first is focused on developing new protocols for generating replicas of multiple brain regions (development of “directed”, region specific organoids), while the second is based on constricting regulatory control of the system through bioengineering approaches.

Apart from diseases modeling, brain organoid technology can be personalized for diagnostic or therapeutic purposes if patient-specific hiPSC are applied (Figure 2) [76,77]. Whole brain (cerebral) patient-derived organoids were used to model microcephaly, macrocephaly (Sandhoff disease), periventricular heteroplasia, schizophrenia, Alzheimer Disease and other neural disorders [76,78,79]. Brain region specific organoids, e.g., forebrain to study autism spectrum disorders, or midbrain to study sporadic or idiopathic form of Parkinson’s Disease have been already obtained [80,81]. In addition, those methods are combined with a gene-editing approach with the goal to obtain “healthy/repared” organoids by producing isogenic CRISPER/CAS9 engineered patient-derived iPSCs, as was shown for Sandhoff disease [82].

8. Sources of Cells for Transplantation into Nervous and Heart Tissue

Cellular therapy refers to the use of cells as medical product to treat human disorders for which other modalities of therapy either does not exist (e.g., stroke) or they are not efficient (e.g., ALS, heart decompensation). Thus, stem cell therapy has a high measurable potential in the treatment of brain and heart diseases through cell replacement and stimulation of the endogenous repair systems. Stem cells of diverse origins (embryonic stem cells, mesenchymal stem cells, induced pluripotent etc.) are all viable candidates with great potential for translation. Here we focus on two most often used stem cell types for the diseases of the brain and the heart: neural and mesenchymal stem cells.

Neural stem cells are a pluripotent cell population, expressing markers nestin and Nop2 [83], and are, thus, already inclined towards differentiation into neurons and glia. Process of forming adult cells of the nervous system, neurogenesis is a process in which neurons are generated through the division of neuronal precursors cells (NPCs) and their differentiation into neuron-specific progenitors. NPCs subsequently, over various stages of precursors, develop into fully functional and mature neurons which integrate into, and modify, existing neuronal networks. In gliogenesis, NPCs differentiate into glial progenitors, which differentiate into astrocytes, oligodendrocytes and ependymal cells.

Mesenchymal stem cells (MSC) are defined as a heterogeneous subset of stromal cells that can be easily isolated from many adult tissues and possess multilineage potential, i.e., ability to differentiate into cells of the mesodermal lineage, such as adipocytes, osteocytes, chondrocytes, and myocytes [84]. Actually, the multilineage potential of MSCs allows them to differentiate into neuron-like cells, which exhibit molecular and cellular characteristics of neurons. MSCs can give rise to derivatives of both ectodermal and mesodermal lineages. For example, MSCs derived from dental ligament can easily be differentiated into neurons and cardiomyocytes, opening up possibilities in treatment of neuromuscular diseases by tackling different aspects of such a complex pathophysiology [85–89].

9. Extracellular Vesicles–Desired Cellular Product on a Way towards Clinical Application

Extracellular vesicles (EVs) represent a modality for intercellular communication by acting as plasma membrane enclosed containers for a wide array of signalling molecules and ensuring transfer of biological information over long distances throughout the organism [90,91]. EVs are secreted by all types of cells and their molecular cargo reflects origin and physiological (or pathological) state of the producing cell [92–94]. This dichotomy

is most apparent in the central nervous system (CNS), where EVs are involved in the propagation and spread of several neurodegenerative diseases [94,95]. At the same time, EVs isolated from different types of, healthy" cells can act as effective suppressors of pathological processes [93,96–98]. Since these particles bring therapeutic potential, it is important to develop methods for their effective labelling and follow up. Direct labelling is the simplest and most preferable method for the experiments addressing the effects of external EVs, whereas precise monitoring of behaviour and fate of cell-specific EVs within heterogeneous and 3D cultures requires more sophisticated indirect labelling techniques. We refer the readers to excellent and comprehensive reviews that provide an in depth coverage of the topic [99–101]. Direct EV labelling is most often performed with lipophilic dyes by inserting lipid-anchored fluorophores into the EV membranes. Many commercial dyes such as PKH26, PKH67, DiI, DiD, DiR have been developed and extensively used for EV labelling and tracking in vitro by fluorescence imaging. However, lipophilic fluorophores have several important limitations. First of all, most EV preparations isolated from different sources such as serum, or cell culture supernatants, are contaminated with lipoproteins that can also incorporate lipophilic dyes, thus leading to misinterpretation of EV uptake experiments [102]. Some lipophilic dyes also tend to aggregate, forming nanoparticles with similar size to the EVs (100 nm), that also can be taken up by the cells [102]. In addition, PKH dyes can increase EV size by enhancing clustering and aggregation [103]. These limitations can be, at least partially, overcome with the use of recently introduced Mem lipophilic dyes that did not aggregate or change the size of EVs [104]. In conclusion, although simple and straightforward, direct EV labelling with lipophilic dyes has important limitations and therefore requires careful interpretation to avoid misleading results. Indirect labelling can be achieved by CFSE (carboxyfluorescein diacetate succinimidyl ester) fluorescent dye. It is activated by esterases and covalently binds to free amines inside the cells, or vesicles. Interestingly, after indirect labelling of cells, CFSE-positive EVs were detected only in the pellets after $10,000 \times g$ centrifugation (corresponding to microvesicular fraction originating from plasma membrane) indicating that indirect CFSE labelling may help to distinguish between microvesicular and exosomal fractions [105]. However, large concentrations of CFSE could be necessary to obtain vesicles with sufficient fluorescence and such high dye concentrations can be detrimental to the EV-producing cells [106]. Another promising study recently used hydrophobic insertion of maleimide (Mal) into the EV membranes [107]. Other strategies are focused on RNA imaging using chemical dyes that are selective for RNA that do not require conjugation, such as including E36, Styryl-TO and SYTORNAselect [108].

When coming to the topic of application of EVs, the major advantage they possess is that they can easily cross the blood brain barrier (BBB) and enter into the brain [109]. However, pharmacokinetic studies in vivo have shown that EVs can be very quickly removed from the bloodstream, with a majority of them being = entrapped in the liver and the lungs [110]. Accordingly, several groups investigated alternative delivery via minimally invasive intranasal route [111,112]. The EVs secreted by mouse macrophages were permeabilized, loaded with antioxidant enzyme catalase and applied intranasally to 6-hydroxydopamine (6-OHDA) mice [113]. Study demonstrates that EVs associated with microglia cells reduced their inflammatory activity and improved the apomorphin test results [113]. Another study compared how EVs stained with lipophilic dyes, or labelled with gold nanoparticles, distribute in the CNS after intranasal application [114]. Gold nanoparticles-marked EVs allow live observation of particle distribution in the brain by using accurate computer tomography methods. Interestingly, another study demonstrated similar distribution patterns of EVs labelled by both methods [9,114]. More importantly, EVs selectively accumulated in the affected areas of the brain. For example, after intranasal application to the 6-OHDA-treated mice (PD model), exosomes selectively accumulated in the damaged striatum areas even up to 96 h [114]. These findings confirm the potential of EVs as a therapeutic tool against various diseases and disorders of the CNS.

10. Cell Transplantation for Heart Ischemia

Heart failure and its direct consequences represent the leading cause of death worldwide [115]. Although heart transplantation developed substantially in the last decades, there are not enough donors which would satisfy the existing needs. Moreover, heart transplantation is a very complex and expensive procedure that afterwards require life-long immunosuppression. The mechanism by which transplantation of stem cells into the infarcted heart leads to health improvement is not yet completely understood. The most straightforward expectation would be that transplanted stem cells form new myocardial cells with the capability to contract. However, preclinical and clinical trials revealed at least two obstacles in this theoretically simple approach: first, transplanted cells survive very briefly, so differentiation into myocardial cells is not sufficient. Second, if maturation occurs, coupling with the host myocardium is not successful. As a result, arrhythmia is a very common side effect of such an approach [116].

Preclinical studies focusing on acute infarction, e.g., with interventions within 4 weeks after the incident, reported beneficial effects [117]. On the other hand, studies which were aiming to improve condition several months after the ischemic incident were not so successful [118]. With that being said, recently, the attention has shifted from the potential of transplanted stem cell to differentiate into cardiomyocytes towards secreting factors that improve the condition of damaged myocardium [119]. Reported mechanisms include immune modulation which promotes endogenous cardiac repair [120]. Additionally, it has been shown that stem cells transplanted into the heart secrete cytokines, with rather significant anti-apoptotic effect. One of the most positive effects observed after myocardial infarction is achieved by IL-10, which improves survival and function of myocardial muscle [121].

There are many clinical trials which assessed the efficiency of stem cells for acute myocardial infarction. However, their results are rather heterogenous. Those which focused on myocardial contractility and ventricular remodeling did not find statistically significant improvement. However, significant improvements were found when a longer follow-up was taken into account, ranging from one to three years [122,123]. Most importantly, ejection fraction was regularly improved and even ventricular remodeling was shifted in a positive direction.

Even after the transplanted cells disappear, beneficial effects can be followed for months and years. Thus reduced inflammation and stimulated vascularization can be detected for a long period, reaching up to few years [124]. Thus, it became clear that, unlike pharmacologic and surgical approaches, cell therapy can stimulate endogenous tissue regeneration to reverse worsening cardiac dysfunction. Some of the most commonly reported benefits of stem cells based clinical trials are listed in the Table 1.

Table 1. Overview of pathological entities and reported beneficial effects of cells.

Diagnoses	Requirements from Cells
Ischemic heart disease	Reduces myocardial necrosis, promotes myogenesis [119–121,124] Prevents apoptosis
Diabetic Cardiomyopathy	Reduces myocardial fibrosis Improves overall cardiac function [125,126] Stimulates cell attachment and migration
Cardiac Tissue Engineering	Source of biochemical factors [127]
Stroke	Reduce damage, improve recovery [128–137]
Amyotrophic lateral sclerosis	Support survival of motoric neurons [138,139]
Multiple sclerosis	Immunomodulation and decrease in demyelination [140]
Parkinson disease	Production of dopamine, reduces symptoms [141]
Spinal cord damage	Opposes anti-regenerative action of glial scar and promotes axon growth [142]

11. Specific Requirements for Further Improvement of Cell-Based Therapy of Heart Diseases

Future developments needed to boost cell-based therapy of heart diseases include nanotechnologies and bioengineered platforms, where stem cells are preconditioned to resist their implantation into a highly stressed myocardial tissue. Basically this approach consists of the development of bioactive membranes made of two integrated materials: (a) one nanofiber matrix made out of self-assembling peptides with molecule-release capacity (for growth factors such as VEGF and FGF), and (b) contained in a microscale elastomeric scaffold that provides the mechanical framework (elastic, loading) that will match the cardiac tissue mechanics. Both are essential to promote local angiogenesis in a necrotic affected tissue as well as its regeneration.

In many congenital heart diseases neonatal ventricles demonstrate a number of intrinsic pathologic modifications, including relative immaturity of the extra-cellular matrix, inappropriately low transcription factor expression and increased myocyte apoptosis, this should open the way for the evaluation of treatments associating tissue engineering with cells implants. The main mechanisms by which cell transplantation and tissue engineering can bring functional benefits in myocardial diseases is the combination of cells and scaffolds, which limit the spread of the pathologic area, preventing excessive remodeling and dilatation of the ventricle [143–146].

Emerging biomimetic technologies include 3D printing and additive manufacturing [147]. For heart healing applications, 3D-printed porous poly-caprolactone (PCL) elastomeric scaffolds represent a promising material functionalized with bio-additives such as stem cells, exosomes and angiogenic growth factors. Cardiopatch and Cardiowrap ventricular support bioprostheses were able to integrate in the damaged myocardium and the adjacent healthy heart, becoming artificial extracellular matrix that offers adequate cell niches for the homing of stem cells. These approaches contribute to the generation of Bioartificial Myocardium, offering possibility that the need for heart transplantation in the future will be reduced [127,148].

12. Cell Transplantation for Diseases of the Nervous System

The limited neurogenesis capacity in the brain makes neurological conditions difficult to treat. That's why cell transplantation approach is intensively being tested for neurological diseases.

Post-ischemic acute brain injury typically peaks within 24 h of the insult, and reaches its highest point within 48 h [149]. Due to this quick onset and short duration of acute brain injury, potential neuroprotective therapies need to be administered early, i.e., within 3–6 h of the onset. This has proven to be challenging in the clinical practice. Any treatment outside of the 48 h window will offer limited neuroprotection, and could instead be mainly restorative, targeting angiogenesis, vasculogenesis, neurogenesis, and synaptogenesis [128,150]. Finding a therapeutic approach that would delay the progressive secondary neurodegeneration will also benefit stroke survivors. To date, most cell transplantation studies have been conducted on animals during acute phase of post-ischemic injury, leaving chronic time points understudied. It has already been shown that in addition to anti-inflammatory, anti-oxidative and anti-apoptotic effects, transplanted cells also secrete various factors acting neurotrophically exhibiting neuroregenerative effects [130,151].

Upon optimized dose regime and the route of administration, the use of stem cells shows benefits in both the acute and subacute phase, as well as in the chronic phase of cerebral ischemia [131,132]. Similar has been observed in other diseases with neuroinflammatory component, like amyotrophic lateral sclerosis or multiple sclerosis. Since a higher degree of neuroinflammation is present in the acute and subacute phase of cerebral ischemia, in these phases it is necessary to use higher doses (10–1200 million cells) and to choose less invasive ways of stem cell application, such as intravenous, intra-arterial, intranasal and intraperitoneal [131,133,134]. In these phases, various stem cells have shown positive effects so far. In the acute phase (1–3 days after stroke): mesenchymal stem cells (MSCs) and

human mononuclear cells (MNCs), human embryonic stem cells (hESCs), human neural stem cells (hNSCs), and multipotent adult progenitor cells (MAPC) were used [131,152,153]. In the subacute phase (7 days after stroke): autologous CD34+ stem/progenitor cells and bone marrow stem cells (BMSCs) were used [131,154]. In the chronic phase (weeks, months, years) after stroke the smaller doses of stem cells were used (1–5 million cells), albeit with more invasive application methods (intracerebral and intraventricular) in order to allow greater bioavailability of injected cells near the affected brain region [128,155].

In the last two decades more than 70 clinical trials with stem cells for brain diseases have been successfully finished, but no definitive efficacy trials have been concluded. As such, there is currently still no approved cell therapy for neurological diseases. When talking about stroke, as the most common disease of the brain, various approaches have been taken thus far. Not entering into details of various type of stem cells and routes of cell delivery, all trials of Phase 1 and 2 reported safety and visibility. It is interesting to mention that one of the very first trials performed in 2005 in South Korea with 30 patients with cerebral infarct, who received IV infusion of autologous MSCs, reported a significant reduction in mortality within five years of stroke incidence compared to patients who did not receive MSC transplantation [135]. In clinical settings, the recipients of allogeneic MSCs demonstrated long-lasting or transient neurological improvement. Additionally, allogeneic MSCs infusion was associated with a short term decrease in circulating T cells and inflammatory cytokines [136]. The implantation of SB623 to the sites surrounding the subcortical stroke region was safe and accompanied by improvements in neurological recovery in 12 patients in a 2-year study [137]. At this stage, clinically confirmed beneficial effects were shown by CTX0E03 cells (hNSCs), administered one month after cerebral ischemia (a single intracerebral dose of up to 20 million cells), and SB623 (allogeneic MSCs), administered several times with 2.5, 5, and 10 million cells for a period of 6–60 months after stroke [129,131]. As the systemic inflammatory response is a major pathological component in secondary post-ischemic cell death [156], including some specific types of death, like necroptosis [157], stem cell transplantation should to be the therapy of choice to reduce neuroinflammatory effects and help stroke outcomes. Considerable numbers of clinical trials with stem cell therapy for stroke are currently underway. Clinical trials should include patient's co-morbidities which also can affect the efficacy and effectiveness of cell therapy.

MSCs are a population of cells which can be safely harvested from patients. Due to their low immunogenicity and reported benefits, they are already being recognized as approved therapeutic product in some countries [158]. Additionally, MSCs are capable of migrating towards lesioned areas upon receiving attraction signals by certain chemokines, suggesting their potential use as vehicles for therapeutic agent's delivery [159]. Therefore, as therapeutic agents, MSCs have multiple modes of action, including cell replacement, immunologic and metabolic properties; showing a pleiotropic activity that modify the tissues response to injuries and activate restorative mechanisms that improve organ function. Intense interchange of active cellular products between MSCs and resident cells have been proven, demonstrating the potential of MSCs secretome to achieve various paracrine effects, including immunomodulation [160]. Moreover, organelle interchange has been proven, including vesicular traffic (exosomes, microvesicles, etc), where, in addition to the vesicular cargo, MSCs inject membrane (carrying protein membrane complexes, receptors, ion channels, etc.) into host cells [161].

MSCs from the bone marrow had been widely used in clinical trials for neurological diseases. They were demonstrated to be safe but their effects were not always consistent, as preclinical studies suggested. This may be due to poor survival in disease environments and/or because inappropriate therapeutic dosage and route of delivery or inconsistent trial design [162–165].

In some studies, ALS patients treated with MSCs displayed a slight and transient decline in disease progression [138]. Interestingly, postmortem evaluation of ALS patients treated with MSCs showed that a more significant number of motor neurons were preserved at the location in the spinal cord where the cells were administered, compared to other

spinal sites [139]. Some of the most commonly reported benefits of stem cells based clinical trials are listed in the Table 1.

13. Specific Requirements for Further Improvement of Cell-Based Therapy of Brain Diseases

More than 300 papers have been published in the last 20 years reporting transplantation of cells in animal models and more than 70 clinical trials have been conducted in humans with neurological diseases with some common breakthroughs and some common obstacles. First of all, dogma that transplanted cells need to integrate and survive for a longer period is not only seen as obsolete, but in some cases is even overly stressed. Therefore, one needs to focus on cell products which are, nevertheless, being secreted in large quantities by many cell types. In addition, modification of these products can be achieved by genetic modifications of the stem cells [166]. Secreted growth factors, short sequences of RNA in various forms and still yet to be discovered components, often packed in the form of extracellular vesicles, obviously have a very strong and beneficial influence. So, it became clear that we need to focus on recognizing those beneficial products, to discover mechanism by which they improve regeneration, and then on methods how to deliver them in sufficient quantities. Apart from direct transplantation, intravascular delivery, based on positive results, deserves our attention [167]. Moreover many methodological gaps in clinical translation must be recognized. Well-designed, biomarker oriented endpoints and comparative trials are needed to address specific issues such as type of cells, cell doses, responsive phenotypes and time window of efficacy.

When thinking about side effects of cellular therapy, it is important to notice that transplantation of stem cells into brain tissue very rarely brings any significant obstacles from that side. Probably the most well defined are those linked to dyskinesia, mostly observed in transplantation to patients suffering from Parkinson's disease. However, methods to predict which patients are more prone to those side effects have been already developed. It is interesting to notice that no serious effects coming from uncontrolled electrical activity (e.g., partial or generalized seizures) of such cells have been reported. On the other hand, common obstacles observed are a limited period of activity of such cells, with very time-limited secretion of needed molecules. Thus, the main focus is in securing longer and more substantial effects of the secretome.

14. Conclusions Remarks

In this review we gathered experience from the last few decades dealing with attempts to treat diseases of the heart and the brain (primarily ischemic in its nature) by using stem cells and their products (Figure 2). When we make a general overview of what has been achieved with these replacement strategies, i.e., the approach in which transplanted cells will replace lost ones in the host tissue, results are rather limited. Nevertheless, replacement therapy seems to be very promising in the case where a very specific subpopulation of neurons, in limited regions, are involved. This can be seen in positive, albeit transient, results in clinical trials including patients with Parkinson's disease [141]. In all other cases, especially in brain ischemia (stroke) and myocardial infarction, transplanted cells can still hardly replace what has been lost. It is very interesting to notice that we expected probably much more from this approach in the heart tissue, which is, in theory, much less complex, than the neural one. However, cells which succeeded to survive in the cardiac muscle for a longer period, could hardly coordinate their activity with the rest of the healthy muscle and, most interestingly, often cause problematic arrhythmias. It is important to notice that arrhythmias in the heart muscle are a much more common problem of stem cell transplantation than uncontrolled electric activity of the transplant in the brain. In the same time, several decades of stem cells - based attempts to treat those diseases brought a huge progress in understanding of complexity of the tissue affected by pathological process. Although the ultimate goal is to discover and launch new drugs and/or procedures for human diseases, fragments of knowledge which we are collecting are without doubts constantly improving medicine.

When we take a look into the effects transplanted cells achieved with their secretome, and considering the experience in treating both the heart and the brain, this strategy emerges as a promising one. This idea has been boosted even further by the discovery of several types of extracellular vesicles which carry short sequences of RNA, peptides, growth factors, etc. In both organs, products of transplanted cells clearly influence inflammation and, in most of the cases, decrease damage with measurable effects. This is the case with neurodegenerative diseases such as ALS [168] or Alzheimer's disease [169]. One of the probably most surprising observations, again seen in both the heart and the brain, is that those effects are often more pronounced in chronic than in acute phases. Thus, overall survival and improvement in major parameters demonstrate statistically significant differences when patients are followed after 6, 12 or 48 months [122,123,137]. How is this possible if majority of cells disappear within a few weeks after transplantation? We can think of two possible explanations: first, those cells which remain, although in small numbers, are naturally selected as those which succeed to achieve substantial positive effects. So here we obviously have an example of supreme quality ruling over quantity. Another element adding to this explanation might be that a combination of positive effects achieved by all cells, before they disappear within a few weeks after transplantation, triggers a positive chain of events which requires a lot of time to pass the threshold which is then recognized as a positive therapeutic effect. Another common point where research into the brain and the heart yielded mutual benefits for both fields is a piece of knowledge about the need for standardization of products secreted by stem cells. Standardization is not only needed in order to cause more comparable results, but also to better define routes of delivery. When this will be achieved, and many efforts are currently being undertaken in that direction, one can imagine repetitive injection of solutions with extracellular vesicles, which will improve regeneration of either neural or cardiac muscle tissue. This review could not cover all parts of this complex field, so, for example, here we did not take in consideration numerous options of genetic engineering, which offers advantages of genetically modified cells. In addition, bioengineering field based on biomaterials is progressing even faster than stem cells. By taking all this in consideration, one of the factors which slow down the progress is complexity of all these elements which requires truly multidisciplinary approach. A very wide and multidimensional perspective is needed in order to pass the threshold of success in clinical trials. To conclude, the major advice we can get from the experience collected thus far is that more standardized methods of transplantation, either with well defined populations of cells or with extracellular vesicles are needed. In addition, transplanted cells need time to bring positive effects. Clinical trials need to plan prolonged follow up of the patients and, whenever possible, account for repeated therapeutic procedures based on cells and/or their products. When such a protocol enters routine practice, we will be witnessing the final confirmation of the value of regenerative medicine in the treatment of major human diseases.

Funding: DM research is funded by Croatian Science Foundation project Orastem (IP-16-6-9451) and by European Union through the European Regional Development Fund, as the Scientific Centre of Excellence for Basic, Clinical and Translational Neuroscience under Grant Agreement No. KK.01.1.1.01.0007, project "Experimental and clinical research of hypoxic-ischemic damage in perinatal and adult brain". VH and DJ are supported by PhD grants by Croatian Science Foundation. LM research is partly funded by the AGING Project for Department of Excellence at the Department of Translational Medicine (DIMET), Università del Piemonte Orientale, Novara, Italy. LR and JM research is supported by Grants no 451-03-68/2020-14/200178 and no 451-03-9/2021-14/200129 of the Ministry of Education, Science and Technological Development of Republic of Serbia. GF was supported by Medical Research Council [MR/R025002/1], NIHR Imperial Biomedical Research Centre and the Hungarian National Research, Development and Innovation Fund [2020-1.1.6-JÖVŐ-2021-00013 and K128369]. A.H, F.L., A.D were supported by EU Horizon 2020 Marie Skłodowska-Curie grant agreement No 812660 (DohART-NET) and Grant Agreement No. 739593 (HCEMM) (for A.D) and Chinese-Hungarian Bilateral Project (2018-2.1.14-TÉT-CN-2018-00011, Chinese No. 8-4 (for A.D). SM is founded by Spanish State Research Agency SAF2017-83702-R and the TERCEL (Instituto de Salud Carlos III (RD16/001/0010 and PID2020-11817RB-100). LB is supported by National Science Centre, Poland, grant # 2019/35/B/NZ3/04383.

Institutional Review Board Statement: Not applicable.

Informed Consent Statement: Not applicable.

Data Availability Statement: Not applicable.

Acknowledgments: The authors acknowledge support within the framework of COST Action BIONECA CA 16122—Biomaterials and Advanced Physical Techniques for Regenerative Cardiology and Neurology.

Conflicts of Interest: The authors declare no conflict of interest.

References

1. Chen, J.; Luo, L.; Tian, R.; Yu, C. A Review and Update for Registered Clinical Studies of Stem Cells for Non-Tumorous and Non-Hematological Diseases. *Regen. Ther.* **2021**, *18*, 355–362. [CrossRef]
2. Borlongan, M.C.; Farooq, J.; Sadanandan, N.; Wang, Z.J.; Cozene, B.; Lee, J.Y.; Steinberg, G.K. Stem Cells for Aging-Related Disorders. *Stem Cell Rev. Rep.* **2021**, *17*, 2054–2058. [CrossRef]
3. Ilic, D.; Ogilvie, C. Concise Review: Human Embryonic Stem Cells—What Have We Done? What Are We Doing? Where Are We Going? *Stem Cells* **2017**, *35*, 17–25. [CrossRef]
4. Andrzejewska, A.; Dabrowska, S.; Lukomska, B.; Janowski, M. Mesenchymal Stem Cells for Neurological Disorders. *Adv. Sci.* **2021**, *8*, 2002944. [CrossRef]
5. Gupta, S.; Sharma, A.; Archana, S.; Verma, R.S. Mesenchymal Stem Cells for Cardiac Regeneration: From Differentiation to Cell Delivery. *Stem Cell Rev. Rep.* **2021**, *17*, 1666–1694. [CrossRef]
6. Monti, M.; Perotti, C.; del Fante, C.; Cervio, M.; Redi, C.A. Stem Cells: Sources and Therapies. *Biol. Res.* **2012**, *45*, 207–214. [CrossRef] [PubMed]
7. Takahashi, K.; Tanabe, K.; Ohnuki, M.; Narita, M.; Ichisaka, T.; Tomoda, K.; Yamanaka, S. Induction of Pluripotent Stem Cells from Adult Human Fibroblasts by Defined Factors. *Cell* **2007**, *131*, 861–872. [CrossRef] [PubMed]
8. Takahashi, K.; Yamanaka, S. Induction of Pluripotent Stem Cells from Mouse Embryonic and Adult Fibroblast Cultures by Defined Factors. *Cell* **2006**, *126*, 663–676. [CrossRef]
9. Shi, Y.; Inoue, H.; Wu, J.C.; Yamanaka, S. Induced Pluripotent Stem Cell Technology: A Decade of Progress. *Nat. Rev. Drug Discov.* **2016**, *16*, 115–130. [CrossRef]
10. Doss, M.X.; Sachinidis, A. Current Challenges of iPSC-Based Disease Modeling and Therapeutic Implications. *Cells* **2019**, *8*, 403. [CrossRef]
11. Rowe, R.G.; Daley, G.Q. Induced Pluripotent Stem Cells in Disease Modelling and Drug Discovery. *Nat. Rev. Genet.* **2019**, *20*, 377–388. [CrossRef]
12. Singh, V.K.; Kalsan, M.; Kumar, N.; Saini, A.; Chandra, R. Induced Pluripotent Stem Cells: Applications in Regenerative Medicine, Disease Modeling, and Drug Discovery. *Front. Cell Dev. Biol.* **2015**. [CrossRef]
13. Bekhite, M.M.; González Delgado, A.; Menz, F.; Kretzschmar, T.; Wu, J.M.F.; Bekfani, T.; Nietzsche, S.; Wartenberg, M.; Westermann, M.; Greber, B.; et al. Longitudinal Metabolic Profiling of Cardiomyocytes Derived from Human-Induced Pluripotent Stem Cells. *Basic Res. Cardiol.* **2020**, *115*, 1–15. [CrossRef]
14. Burridge, P.W.; Matsa, E.; Shukla, P.; Lin, Z.C.; Churko, J.M.; Ebert, A.D.; Lan, F.; Diecke, S.; Huber, B.; Mordwinkin, N.M.; et al. Chemically Defined Generation of Human Cardiomyocytes. *Nat. Methods* **2014**, *11*, 855–860. [CrossRef]
15. Cyganek, L.; Tiburcy, M.; Sekeres, K.; Gerstenberg, K.; Bohnenberger, H.; Lenz, C.; Henze, S.; Stauske, M.; Salinas, G.; Zimmermann, W.-H.; et al. Deep Phenotyping of Human Induced Pluripotent Stem Cell–Derived Atrial and Ventricular Cardiomyocytes. *JCI Insight* **2018**, *3*, 12. [CrossRef] [PubMed]
16. Kolanowski, T.J.; Antos, C.L.; Guan, K. Making Human Cardiomyocytes up to Date: Derivation, Maturation State and Perspectives. *Int. J. Cardiol.* **2017**, *241*, 379–386. [CrossRef]
17. Burridge, P.W.; Keller, G.; Gold, J.D.; Wu, J.C. Production of De Novo Cardiomyocytes: Human Pluripotent Stem Cell Differentiation and Direct Reprogramming. *Cell Stem Cell* **2012**, *10*, 16–28. [CrossRef] [PubMed]
18. Jha, R.; Xu, R.-H.; Xu, C. Efficient Differentiation of Cardiomyocytes from Human Pluripotent Stem Cells with Growth Factors. *Cardiomyocytes Methods Protoc.* **2015**, 115–131. [CrossRef]
19. Lian, X.; Zhang, J.; Azarin, S.M.; Zhu, K.; Hazeltine, L.B.; Bao, X.; Hsiao, C.; Kamp, T.J.; Palecek, S.P. Directed Cardiomyocyte Differentiation from Human Pluripotent Stem Cells by Modulating Wnt/ β -Catenin Signaling under Fully Defined Conditions. *Nat. Protoc.* **2012**, *8*, 162–175. [CrossRef]
20. Kattman, S.J.; Witty, A.D.; Gagliardi, M.; Dubois, N.C.; Niapour, M.; Hotta, A.; Ellis, J.; Keller, G. Stage-Specific Optimization of Activin/Nodal and BMP Signaling Promotes Cardiac Differentiation of Mouse and Human Pluripotent Stem Cell Lines. *Cell Stem Cell* **2011**, *8*, 228–240. [CrossRef]
21. Hamad, S.; Derichsweiler, D.; Papadopoulos, S.; Nguemo, F.; Šarić, T.; Sachinidis, A.; Brockmeier, K.; Hescheler, J.; Boukens, B.J.; Pfannkuche, K. Generation of Human Induced Pluripotent Stem Cell–Derived Cardiomyocytes in 2D Monolayer and Scalable 3D Suspension Bioreactor Cultures with Reduced Batch-to-Batch Variations. *Theranostics* **2019**, *9*, 7222–7238. [CrossRef] [PubMed]

22. Lian, X.; Hsiao, C.; Wilson, G.; Zhu, K.; Hazeltine, L.B.; Azarin, S.M.; Raval, K.K.; Zhang, J.; Kamp, T.J.; Palecek, S.P. Robust Cardiomyocyte Differentiation from Human Pluripotent Stem Cells via Temporal Modulation of Canonical Wnt Signaling. *Proc. Natl. Acad. Sci. USA* **2012**, *109*, E1848–E1857. [CrossRef]
23. Weng, Z.; Kong, C.-W.; Ren, L.; Karakikes, I.; Geng, L.; Jiaozi, H.; Ying, C.Z.; Fai, M.; Keung, W.; Chow, H.; et al. A Simple, Cost-Effective but Highly Efficient System for Deriving Ventricular Cardiomyocytes from Human Pluripotent Stem Cells. *Stem Cells Dev.* **2014**, *23*, 1704–1716. [CrossRef]
24. Devalla, H.D.; Schwach, V.; Ford, J.W.; Milnes, J.T.; El-Haou, S.; Jackson, C.; Gkatzis, K.; Elliott, D.A.; Lopes, S.M.C.d.S.; Mummery, C.L.; et al. Atrial-like Cardiomyocytes from Human Pluripotent Stem Cells Are a Robust Preclinical Model for Assessing Atrial-Selective Pharmacology. *EMBO Mol. Med.* **2015**, *7*, 394–410. [CrossRef]
25. Goldfracht, I.; Protze, S.; Shiti, A.; Setter, N.; Gruber, A.; Shaheen, N.; Nartiss, Y.; Keller, G.; Gepstein, L. Generating Ring-Shaped Engineered Heart Tissues from Ventricular and Atrial Human Pluripotent Stem Cell-Derived Cardiomyocytes. *Nat. Commun.* **2020**, *11*, 75. [CrossRef]
26. Tanwar, V.; Bylund, J.B.; Hu, J.; Yan, J.; Walthall, J.M.; Mukherjee, A.; Heaton, W.H.; Wang, W.-D.; Potet, F.; Rai, M.; et al. Gremlin 2 Promotes Differentiation of Embryonic Stem Cells to Atrial Fate by Activation of the JNK Signaling Pathway. *Stem Cells* **2014**, *32*, 1774–1788. [CrossRef]
27. Zhang, Q.; Jiang, J.; Han, P.; Yuan, Q.; Zhang, J.; Zhang, X.; Xu, Y.; Cao, H.; Meng, Q.; Chen, L.; et al. Direct Differentiation of Atrial and Ventricular Myocytes from Human Embryonic Stem Cells by Alternating Retinoid Signals. *Cell Res.* **2010**, *21*, 579–587. [CrossRef]
28. Zhu, W.-Z.; Xie, Y.; Moyes, K.W.; Gold, J.D.; Askari, B.; Laflamme, M.A. Neuregulin/ErbB Signaling Regulates Cardiac Subtype Specification in Differentiating Human Embryonic Stem Cells. *Circ. Res.* **2010**, *107*, 776–786. [CrossRef]
29. Liang, W.; Han, P.; Kim, E.H.; Mak, J.; Zhang, R.; Torrente, A.G.; Goldhaber, J.I.; Marbán, E.; Cho, H.C. Canonical Wnt Signaling Promotes Pacemaker Cell Specification of Cardiac Mesodermal Cells Derived from Mouse and Human Embryonic Stem Cells. *Stem Cells* **2020**, *38*, 352–368. [CrossRef]
30. Yechikov, S.; Kao, H.K.J.; Chang, C.W.; Pretto, D.; Zhang, X.D.; Sun, Y.H.; Smithers, R.; Sirish, P.; Nolte, J.A.; Chan, J.W.; et al. NODAL Inhibition Promotes Differentiation of Pacemaker-like Cardiomyocytes from Human Induced Pluripotent Stem Cells. *Stem Cell Res.* **2020**, *49*, 102043. [CrossRef]
31. Scuderi, G.J.; Butcher, J. Naturally Engineered Maturation of Cardiomyocytes. *Front. Cell Dev. Biol.* **2017**, *5*, 50. [CrossRef]
32. Ahmed, R.E.; Anzai, T.; Chanthra, N.; Uosaki, H. A Brief Review of Current Maturation Methods for Human Induced Pluripotent Stem Cells-Derived Cardiomyocytes. *Front. Cell Dev. Biol.* **2020**, *8*, 178. [CrossRef]
33. Yang, X.; Rodriguez, M.L.; Leonard, A.; Sun, L.; Fischer, K.A.; Wang, Y.; Ritterhoff, J.; Zhao, L.; Kolwicz, S.C.; Pabon, L.; et al. Fatty Acids Enhance the Maturation of Cardiomyocytes Derived from Human Pluripotent Stem Cells. *Stem Cell Rep.* **2019**, *13*, 657–668. [CrossRef]
34. Ruan, J.L.; Tulloch, N.L.; Razumova, M.V.; Saiget, M.; Muskheli, V.; Pabon, L.; Reinecke, H.; Regnier, M.; Murry, C.E. Mechanical Stress Conditioning and Electrical Stimulation Promote Contractility and Force Maturation of Induced Pluripotent Stem Cell-Derived Human Cardiac Tissue. *Circulation* **2016**, *134*, 1557–1567. [CrossRef]
35. Pianezzi, E.; Altomare, C.; Bolis, S.; Balbi, C.; Torre, T.; Rinaldi, A.; Camici, G.G.; Barile, L.; Vassalli, G. Role of Somatic Cell Sources in the Maturation Degree of Human Induced Pluripotent Stem Cell-Derived Cardiomyocytes. *Biochim. Biophys. Acta-Mol. Cell Res.* **2020**, *1867*, 118538. [CrossRef]
36. Sanchez-Freire, V.; Lee, A.S.; Hu, S.; Abilez, O.J.; Liang, P.; Lan, F.; Huber, B.C.; Ong, S.G.; Hong, W.X.; Huang, M.; et al. Effect of Human Donor Cell Source on Differentiation and Function of Cardiac Induced Pluripotent Stem Cells. *J. Am. Coll. Cardiol.* **2014**, *64*, 436–448. [CrossRef]
37. Abulaiti, M.; Yalikul, Y.; Murata, K.; Sato, A.; Sami, M.M.; Sasaki, Y.; Fujiwara, Y.; Minatoya, K.; Shiba, Y.; Tanaka, Y.; et al. Establishment of a Heart-on-a-Chip Microdevice Based on Human IPS Cells for the Evaluation of Human Heart Tissue Function. *Sci. Rep.* **2020**, *10*, 1–12. [CrossRef]
38. Richards, D.J.; Li, Y.; Kerr, C.M.; Yao, J.; Beeson, G.C.; Coyle, R.C.; Chen, X.; Jia, J.; Damon, B.; Wilson, R.; et al. Human Cardiac Organoids for the Modelling of Myocardial Infarction and Drug Cardiotoxicity. *Nat. Biomed. Eng.* **2020**, *4*, 446–462. [CrossRef]
39. Augustin, H.G.; Koh, G.Y. Organotypic Vasculature: From Descriptive Heterogeneity to Functional Pathophysiology. *Science* **2017**, *357*, eaal2379. [CrossRef]
40. Rafii, S.; Butler, J.M.; Ding, B.-S. Angiocrine Functions of Organ-Specific Endothelial Cells. *Nature* **2016**, *529*, 316–325. [CrossRef]
41. Wimmer, R.A.; Leopoldi, A.; Aichinger, M.; Kerjaschki, D.; Penninger, J.M. Generation of Blood Vessel Organoids from Human Pluripotent Stem Cells. *Nat. Protoc.* **2019**, *14*, 3082–3100. [CrossRef]
42. Tremblay, M.É. A Diversity of Cell Types, Subtypes and Phenotypes in the Central Nervous System: The Importance of Studying Their Complex Relationships. *Front. Cell. Neurosci.* **2020**, *14*, 424. [CrossRef]
43. McKenzie, A.T.; Wang, M.; Hauberg, M.E.; Fullard, J.F.; Kozlenkov, A.; Keenan, A.; Hurd, Y.L.; Dracheva, S.; Casaccia, P.; Roussos, P.; et al. Brain Cell Type Specific Gene Expression and Co-Expression Network Architectures. *Sci. Rep.* **2018**, *8*, 8868. [CrossRef]
44. Tao, Y.; Zhang, S.C. Neural Subtype Specification from Human Pluripotent Stem Cells. *Cell Stem Cell* **2016**, *19*, 573–586. [CrossRef]
45. Shi, Y.; Kirwan, P.; Livesey, F.J. Directed Differentiation of Human Pluripotent Stem Cells to Cerebral Cortex Neurons and Neural Networks. *Nat. Protoc.* **2012**, *7*, 1836–1846. [CrossRef]

46. Bell, S.; Hettige, N.; Silveira, H.; Peng, H.; Wu, H.; Jefri, M.; Antonyan, L.; Zhang, Y.; Zhang, X.; Ernst, C. Differentiation of Human Induced Pluripotent Stem Cells (iPSCs) into an Effective Model of Forebrain Neural Progenitor Cells and Mature Neurons. *Bio-protocols* **2019**, *9*, e3188. [CrossRef]
47. Zheng, W.; Li, Q.; Zhao, C.; Da, Y.; Zhang, H.-L.; Chen, Z. Differentiation of Glial Cells from hiPSCs: Potential Applications in Neurological Diseases and Cell Replacement Therapy. *Front. Cell. Neurosci.* **2018**, *12*, 239. [CrossRef]
48. Yan, Y.; Shin, S.; Jha, B.S.; Liu, Q.; Sheng, J.; Li, F.; Zhan, M.; Davis, J.; Bharti, K.; Zeng, X.; et al. Efficient and Rapid Derivation of Primitive Neural Stem Cells and Generation of Brain Subtype Neurons from Human Pluripotent Stem Cells. *Stem Cells Transl. Med.* **2013**, *2*, 862–870. [CrossRef]
49. Chandrasekaran, A.; Avci, H.X.; Ochalek, A.; Rosingh, L.N.; Molnár, K.; László, L.; Bellák, T.; Téglási, A.; Pesti, K.; Mike, A.; et al. Comparison of 2D and 3D Neural Induction Methods for the Generation of Neural Progenitor Cells from Human Induced Pluripotent Stem Cells. *Stem Cell Res.* **2017**, *25*, 139–151. [CrossRef]
50. Hopkins, A.M.; DeSimone, E.; Chwalek, K.; Kaplan, D.L. 3D in Vitro Modeling of the Central Nervous System. *Prog. Neurobiol.* **2015**, *125*, 1–25. [CrossRef]
51. Hofrichter, M.; Nimtz, L.; Tigges, J.; Kabiri, Y.; Schröter, F.; Royer-Pokora, B.; Hildebrandt, B.; Schmuck, M.; Epanchintsev, A.; Theiss, S.; et al. Comparative Performance Analysis of Human iPSC-Derived and Primary Neural Progenitor Cells (NPC) Grown as Neurospheres in Vitro. *Stem Cell Res.* **2017**, *25*, 72–82. [CrossRef]
52. Gregory, P.M.; Brent, A.R.; Eric, D. Laywell. Using the Neurosphere Assay to Quantify Neural Stem Cells in Vivo. *Curr. Pharm. Biotechnol.* **2007**, *8*, 141–145. [CrossRef] [PubMed]
53. Brännvall, K.; Bergman, K.; Wallenquist, U.; Svahn, S.; Bowden, T.; Hilborn, J.; Forsberg-Nilsson, K. Enhanced Neuronal Differentiation in a Three-Dimensional Collagen-Hyaluronan Matrix. *J. Neurosci. Res.* **2007**, *85*, 2138–2146. [CrossRef] [PubMed]
54. Murphy, A.R.; Haynes, J.M.; Laslett, A.L.; Cameron, N.R.; O'Brien, C.M. Three-Dimensional Differentiation of Human Pluripotent Stem Cell-Derived Neural Precursor Cells Using Tailored Porous Polymer Scaffolds. *Acta Biomater.* **2020**, *101*, 102–116. [CrossRef] [PubMed]
55. Koroleva, A.; Deiwick, A.; El-Tamer, A.; Koch, L.; Shi, Y.; Estévez-Priego, E.; Ludl, A.A.; Soriano, J.; Guseva, D.; Ponimaskin, E.; et al. In Vitro Development of Human iPSC-Derived Functional Neuronal Networks on Laser-Fabricated 3D Scaffolds. *ACS Appl. Mater. Interfaces* **2021**, *13*, 7839–7853. [CrossRef] [PubMed]
56. Bolognin, S.; Fossépré, M.; Qing, X.; Jarazo, J.; Ščančar, J.; Moreno, E.L.; Nickels, S.L.; Wasner, K.; Ouzren, N.; Walter, J.; et al. 3D Cultures of Parkinson's Disease-Specific Dopaminergic Neurons for High Content Phenotyping and Drug Testing. *Adv. Sci.* **2019**, *6*, 1800927. [CrossRef]
57. Rouleau, N.; Cantley, W.L.; Liaudanskaya, V.; Berk, A.; Du, C.; Rusk, W.; Peirent, E.; Koester, C.; Nieland, T.J.F.; Kaplan, D.L. A Long-Living Bioengineered Neural Tissue Platform to Study Neurodegeneration. *Macromol. Biosci.* **2020**, *20*, e2000004. [CrossRef]
58. Zhang, Z.N.; Freitas, B.C.; Qian, H.; Lux, J.; Acab, A.; Trujillo, C.A.; Herai, R.H.; Huu, V.A.N.; Wen, J.H.; Joshi-Barr, S.; et al. Layered Hydrogels Accelerate iPSC-Derived Neuronal Maturation and Reveal Migration Defects Caused by MeCP2 Dysfunction. *Proc. Natl. Acad. Sci. USA* **2016**, *113*, 3185–3190. [CrossRef]
59. Sutcliffe, M.; Lancaster, M.A. A Simple Method of Generating 3D Brain Organoids Using Standard Laboratory Equipment. *Methods Mol. Biol.* **2017**, *1576*, 1–12. [CrossRef]
60. Lancaster, M.A.; Renner, M.; Martin, C.-A.; Wenzel, D.; Bicknell, L.S.; Hurler, M.E.; Homfray, T.; Penninger, J.M.; Jackson, A.P.; Knoblich, J.A. Cerebral Organoids Model Human Brain Development and Microcephaly. *Nature* **2013**, *501*, 373–379. [CrossRef]
61. Velasco, S.; Paulsen, B.; Arlotta, P. 3D Brain Organoids: Studying Brain Development and Disease Outside the Embryo. *Annu. Rev. Neurosci.* **2020**, *43*, 375–389. [CrossRef] [PubMed]
62. Tomov, M.L.; O'Neil, A.; Abbasi, H.S.; Cimini, B.A.; Carpenter, A.E.; Rubin, L.L.; Bathe, M. Resolving Cell State in iPSC-Derived Human Neural Samples with Multiplexed Fluorescence Imaging. *Commun. Biol.* **2021**, *4*, 786. [CrossRef]
63. Mohamed, A.; Chow, T.; Whiteley, J.; Fantin, A.; Sorra, K.; Hicks, R.; Rogers, I.M. Umbilical Cord Tissue as a Source of Young Cells for the Derivation of Induced Pluripotent Stem Cells Using Non-Integrating Episomal Vectors and Feeder-Free Conditions. *Cells* **2020**, *10*, 49. [CrossRef] [PubMed]
64. Ray, A.; Joshi, J.M.; Sundaravadivelu, P.K.; Raina, K.; Lenka, N.; Kaveeshwar, V.; Thummer, R.P. An Overview on Promising Somatic Cell Sources Utilized for the Efficient Generation of Induced Pluripotent Stem Cells. *Stem Cell Rev. Rep.* **2021**, *17*, 1954–1974. [CrossRef]
65. Strässler, E.T.; Aalto-Setälä, K.; Kiamehr, M.; Landmesser, U.; Kränkel, N. Age Is Relative—Impact of Donor Age on Induced Pluripotent Stem Cell-Derived Cell Functionality. *Front. Cardiovasc. Med.* **2018**, *5*, 4. [CrossRef]
66. Zhou, H.; Rao, M.S. Can Cord Blood Banks Transform into Induced Pluripotent Stem Cell Banks? *Cytotherapy* **2015**, *17*, 756–764. [CrossRef] [PubMed]
67. Perrera, V.; Martello, G. How Does Reprogramming to Pluripotency Affect Genomic Imprinting? *Front. Cell Dev. Biol.* **2019**, *7*, 76. [CrossRef] [PubMed]
68. Turinetto, V.; Orlando, L.; Giachino, C. Induced Pluripotent Stem Cells: Advances in the Quest for Genetic Stability during Reprogramming Process. *Int. J. Mol. Sci.* **2017**, *18*, 1952. [CrossRef]
69. Yoshihara, M.; Hayashizaki, Y.; Murakawa, Y. Genomic Instability of iPSCs: Challenges Towards Their Clinical Applications. *Stem Cell Rev. Rep.* **2016**, *13*, 7–16. [CrossRef] [PubMed]

70. Thompson, O.; von Meyenn, F.; Hewitt, Z.; Alexander, J.; Wood, A.; Weightman, R.; Gregory, S.; Krueger, F.; Andrews, S.; Barbaric, I.; et al. Low Rates of Mutation in Clinical Grade Human Pluripotent Stem Cells under Different Culture Conditions. *Nat. Commun.* **2020**, *11*, 1528. [CrossRef]
71. Alajbeg, I.; Alić, I.; Andabak-Rogulj, A.; Brailo, V.; Mitrečić, D. Human- and Mouse-Derived Neurons Can Be Simultaneously Obtained by Co-Cultures of Human Oral Mucosal Stem Cells and Mouse Neural Stem Cells. *Oral Dis.* **2018**, *24*, 5–10. [CrossRef]
72. Del Dosso, A.; Urenda, J.P.; Nguyen, T.; Quadrato, G. Upgrading the Physiological Relevance of Human Brain Organoids. *Neuron* **2020**, *107*, 1014–1028. [CrossRef] [PubMed]
73. Eiraku, M.; Watanabe, K.; Matsuo-Takasaki, M.; Kawada, M.; Yonemura, S.; Matsumura, M.; Wataya, T.; Nishiyama, A.; Muguruma, K.; Sasai, Y. Self-Organized Formation of Polarized Cortical Tissues from ESCs and Its Active Manipulation by Extrinsic Signals. *Cell Stem Cell* **2008**, *3*, 519–532. [CrossRef]
74. Khakipoor, S.; Crouch, E.E.; Mayer, S. Human Organoids to Model the Developing Human Neocortex in Health and Disease. *Brain Res.* **2020**, *1742*, 146803. [CrossRef] [PubMed]
75. Mayer, S.; Chen, J.; Velmeshev, D.; Mayer, A.; Eze, U.C.; Bhaduri, A.; Cunha, C.E.; Jung, D.; Arjun, A.; Li, E.; et al. Multimodal Single-Cell Analysis Reveals Physiological Maturation in the Developing Human Neocortex. *Neuron* **2019**, *102*, 143.e7–158.e7. [CrossRef] [PubMed]
76. Lancaster, M.A.; Huch, M. Disease Modelling in Human Organoids. *Dis. Model. Mech.* **2019**, *12*, dmm039347. [CrossRef]
77. Baldassari, S.; Musante, I.; Iacomino, M.; Zara, F.; Salpietro, V.; Scudieri, P. Brain Organoids as Model Systems for Genetic Neurodevelopmental Disorders. *Front. Cell Dev. Biol.* **2020**, *8*, 590119. [CrossRef]
78. Stachowiak, E.K.; Benson, C.A.; Narla, S.T.; Dimitri, A.; Chuye, L.E.B.; Dhiman, S.; Harikrishnan, K.; Elahi, S.; Freedman, D.; Brennand, K.J.; et al. Cerebral Organoids Reveal Early Cortical Maldevelopment in Schizophrenia—Computational Anatomy and Genomics, Role of FGFR1. *Transl. Psychiatry* **2017**, *7*, 6. [CrossRef] [PubMed]
79. Alić, I.; Goh, P.A.; Murray, A.; Portelius, E.; Gkanatsiou, E.; Gough, G.; Mok, K.Y.; Koschut, D.; Brunmeir, R.; Yeap, Y.J.; et al. Patient-Specific Alzheimer-like Pathology in Trisomy 21 Cerebral Organoids Reveals BACE2 as a Gene Dose-Sensitive AD Suppressor in Human Brain. *Mol. Psychiatry* **2020**, *4*, 1–23. [CrossRef]
80. Smits, L.M.; Reinhardt, L.; Reinhardt, P.; Glatza, M.; Monzel, A.S.; Stanslowsky, N.; Rosato-Siri, M.D.; Zanon, A.; Antony, P.M.; Bellmann, J.; et al. Modeling Parkinson's Disease in Midbrain-Like Organoids. *npj Park. Dis.* **2019**, *5*, 5. [CrossRef] [PubMed]
81. Chlebanowska, P.; Tejchman, A.; Sułkowski, M.; Skrzypek, K.; Majka, M. Use of 3D Organoids as a Model to Study Idiopathic Form of Parkinson's Disease. *Int. J. Mol. Sci.* **2020**, *21*, 694. [CrossRef] [PubMed]
82. Allende, M.L.; Cook, E.K.; Larman, B.C.; Nugent, A.; Brady, J.M.; Golebiowski, D.; Sena-Esteves, M.; Tiffet, C.J.; Proia, R.L. Cerebral Organoids Derived from Sandhoff Disease-Induced Pluripotent Stem Cells Exhibit Impaired Neurodifferentiation. *J. Lipid Res.* **2018**, *59*, 550. [CrossRef] [PubMed]
83. Kosi, N.; Alić, I.; Kolačević, M.; Vrsaljko, N.; Jovanov Milošević, N.; Sobol, M.; Philimonenko, A.; Hozák, P.; Gajović, S.; Pochet, R.; et al. Nop2 Is Expressed during Proliferation of Neural Stem Cells and in Adult Mouse and Human Brain. *Brain Res.* **2015**, *1597*, 65–76. [CrossRef] [PubMed]
84. Pittenger, M.F.; Mackay, A.M.; Beck, S.C.; Jaiswal, R.K.; Douglas, R.; Mosca, J.D.; Moorman, M.A.; Simonetti, D.W.; Craig, S.; Marshak, D.R. Multilineage Potential of Adult Human Mesenchymal Stem Cells. *Science* **1999**, *284*, 143–147. [CrossRef]
85. Bueno, C.; Ramirez, C.; Rodríguez-Lozano, F.J.; Tabarés-Seisdedos, R.; Rodenas, M.; Moraleda, J.M.; Jones, J.R.; Martinez, S. Human Adult Periodontal Ligament-Derived Cells Integrate and Differentiate after Implantation into the Adult Mammalian Brain. *Cell Transplant.* **2013**, *22*, 2017–2028. [CrossRef]
86. Bueno, C.; Martínez-Morga, M.; Martínez, S. Non-Proliferative Neurogenesis in Human Periodontal Ligament Stem Cells. *Sci. Rep.* **2019**, *9*, 18038. [CrossRef]
87. Bueno, C.; Martínez-Morga, M.; García-Bernal, D.; Moraleda, J.M.; Martínez, S. Differentiation of Human Adult-Derived Stem Cells towards a Neural Lineage Involves a Dedifferentiation Event Prior to Differentiation to Neural Phenotypes. *Sci. Rep.* **2021**, *11*, 12034. [CrossRef]
88. Simonović, J.; Toljić, B.; Rašković, B.; Jovanović, V.; Lazarević, M.; Milošević, M.; Nikolić, N.; Panajotović, R.; Milašin, J. Raman Microspectroscopy: Toward a Better Distinction and Profiling of Different Populations of Dental Stem Cells. *Croat. Med. J.* **2019**, *60*, 78–86. [CrossRef]
89. Simonovic, J.; Toljic, B.; Nikolic, N.; Peric, M.; Vujin, J.; Panajotovic, R.; Gajic, R.; Bekyarova, E.; Cataldi, A.; Parpura, V.; et al. Differentiation of Stem Cells from Apical Papilla into Neural Lineage Using Graphene Dispersion and Single Walled Carbon Nanotubes. *J. Biomed. Mater. Res. A* **2018**, *106*, 2653–2661. [CrossRef]
90. Mathieu, M.; Martin-Jaular, L.; Lavieu, G.; Théry, C. Specificities of Secretion and Uptake of Exosomes and Other Extracellular Vesicles for Cell-to-Cell Communication. *Nat. Cell Biol.* **2019**, *21*, 9–17. [CrossRef]
91. Tkach, M.; Théry, C. Communication by Extracellular Vesicles: Where We Are and Where We Need to Go. *Cell* **2016**, *164*, 1226–1232. [CrossRef] [PubMed]
92. Stahl, P.D.; Raposo, G. Exosomes and Extracellular Vesicles: The Path Forward. *Essays Biochem.* **2018**, *62*, 119–124. [CrossRef]
93. Jarmalavičiūtė, A.; Pivoriūnas, A. Exosomes as a Potential Novel Therapeutic Tools against Neurodegenerative Diseases. *Pharmacol. Res.* **2016**, *113* (Pt. B), 816–822. [CrossRef] [PubMed]
94. Pegtel, D.M.; Peferoen, L.; Amor, S. Extracellular Vesicles as Modulators of Cell-to-Cell Communication in the Healthy and Diseased Brain. *Philos. Trans. R. Soc. B Biol. Sci.* **2014**, *369*, 20130516. [CrossRef] [PubMed]

95. Stykel, M.G.; Humphries, K.M.; Kamski-Hennekam, E.; Buchner-Duby, B.; Porte-Trachsel, N.; Ryan, T.; Coackley, C.L.; Bamm, V.V.; Harauz, G.; Ryan, S.D. α -Synuclein Mutation Impairs Processing of Endomembrane Compartments and Promotes Exocytosis and Seeding of α -Synuclein Pathology. *Cell Rep.* **2021**, *35*, 109099. [CrossRef] [PubMed]
96. Narbutė, K.; Pilipenko, V.; Pupure, J.; Klinovičs, T.; Auders, J.; Jonavičė, U.; Kriaučiūnaitė, K.; Pivoriūnas, A.; Kluša, V. Time-Dependent Memory and Gait Improvement by Intranasally-Administered Extracellular Vesicles in Parkinson's Disease Model Rats. *Cell. Mol. Neurobiol.* **2020**, *41*, 605–613. [CrossRef] [PubMed]
97. Reed, S.L.; Escayg, A. Extracellular Vesicles in the Treatment of Neurological Disorders. *Neurobiol. Dis.* **2021**, *157*. [CrossRef] [PubMed]
98. Andjus, P.; Kosanović, M.; Miličević, K.; Gautam, M.; Vainio, S.J.; Jagečić, D.; Kozlova, E.N.; Pivoriūnas, A.; Chachques, J.C.; Sakaj, M.; et al. Extracellular Vesicles as Innovative Tool for Diagnosis, Regeneration and Protection against Neurological Damage. *Int. J. Mol. Sci.* **2020**, *21*, 6859. [CrossRef] [PubMed]
99. Li, Y.J.; Wu, J.Y.; Wang, J.M.; Hu, X.B.; Xiang, D.X. Emerging Strategies for Labeling and Tracking of Extracellular Vesicles. *J. Control. Release* **2020**, *328*, 141–159. [CrossRef]
100. Gao, Y.; Chu, C.; Jablonska, A.; Bulte, J.W.M.; Walczak, P.; Janowski, M. Imaging as a Tool to Accelerate the Translation of Extracellular Vesicle-Based Therapies for Central Nervous System Diseases. *Wiley Interdiscip. Rev. Nanomed. Nanobiotechnol.* **2021**, *13*, e1688. [CrossRef]
101. Choi, H.; Choi, Y.; Yim, H.Y.; Mirzaaghasi, A.; Yoo, J.-K.; Choi, C. Biodistribution of Exosomes and Engineering Strategies for Targeted Delivery of Therapeutic Exosomes. *Tissue Eng. Regen. Med.* **2021**, *18*, 499–511. [CrossRef]
102. Simonsen, J.B. Pitfalls Associated with Lipophilic Fluorophore Staining of Extracellular Vesicles for Uptake Studies. *J. Extracell. Vesicles* **2019**, *8*, 1582237. [CrossRef]
103. Dehghani, M.; Gulvin, S.M.; Flax, J.; Gaborski, T.R. Systematic Evaluation of PKH Labelling on Extracellular Vesicle Size by Nanoparticle Tracking Analysis. *Sci. Rep.* **2020**, *10*, 1–10. [CrossRef] [PubMed]
104. Shimomura, T.; Seino, R.; Umezaki, K.; Shimoda, A.; Ezoe, T.; Ishiyama, M.; Akiyoshi, K. New Lipophilic Fluorescent Dyes for Labeling Extracellular Vesicles: Characterization and Monitoring of Cellular Uptake. *Bioconjugate Chem.* **2021**, *32*, 680–684. [CrossRef] [PubMed]
105. Ender, F.; Zamzow, P.; von Bubnoff, N.; Gieseler, F. Detection and Quantification of Extracellular Vesicles via FACS: Membrane Labeling Matters! *Int. J. Mol. Sci.* **2020**, *21*, 291. [CrossRef]
106. Van der Vlist, E.J.; Nolte-'t Hoen, E.N.M.; Stoorvogel, W.; Arkesteijn, G.J.A.; Wauben, M.H.M. Fluorescent Labeling of Nano-Sized Vesicles Released by Cells and Subsequent Quantitative and Qualitative Analysis by High-Resolution Flow Cytometry. *Nat. Protoc.* **2012**, *7*, 1311–1326. [CrossRef] [PubMed]
107. Di, H.; Zeng, E.; Zhang, P.; Liu, X.; Zhang, C.; Yang, J.; Liu, D. General Approach to Engineering Extracellular Vesicles for Biomedical Analysis. *Anal. Chem.* **2019**, *91*, 12752–12759. [CrossRef]
108. Lu, Y.-J.; Deng, Q.; Hu, D.-P.; Wang, Z.-Y.; Huang, B.-H.; Du, Z.-Y.; Fang, Y.-X.; Wong, W.-L.; Zhang, K.; Chow, C.-F. A Molecular Fluorescent Dye for Specific Staining and Imaging of RNA in Live Cells: A Novel Ligand Integration from Classical Thiazole Orange and Styryl Compounds. *Chem. Commun.* **2015**, *51*, 15241–15244. [CrossRef] [PubMed]
109. Alvarez-Erviti, L.; Seow, Y.; Yin, H.; Betts, C.; Likhali, S.; Wood, M.J.A. Delivery of siRNA to the Mouse Brain by Systemic Injection of Targeted Exosomes. *Nat. Biotechnol.* **2011**, *29*, 341–345. [CrossRef] [PubMed]
110. Takahashi, Y.; Nishikawa, M.; Shinotsuka, H.; Matsui, Y.; Ohara, S.; Imai, T.; Takakura, Y. Visualization and in Vivo Tracking of the Exosomes of Murine Melanoma B16-BL6 Cells in Mice after Intravenous Injection. *J. Biotechnol.* **2013**, *165*, 77–84. [CrossRef] [PubMed]
111. Narbutė, K.; Pilipenko, V.; Pupure, J.; Dzirkale, Z.; Jonavičė, U.; Tunaitis, V.; Kriaučiūnaitė, K.; Jarmalavičiūtė, A.; Jansone, B.; Kluša, V.; et al. Intranasal Administration of Extracellular Vesicles Derived from Human Teeth Stem Cells Improves Motor Symptoms and Normalizes Tyrosine Hydroxylase Expression in the Substantia Nigra and Striatum of the 6-Hydroxydopamine-Treated Rats. *Stem Cells Transl. Med.* **2019**, *8*, 490–499. [CrossRef] [PubMed]
112. Herman, S.; Fishel, I.; Offen, D. Intranasal Delivery of Mesenchymal Stem Cells-Derived Extracellular Vesicles for the Treatment of Neurological Diseases. *Stem Cells* **2021**, *39*, 1589–1600. [CrossRef]
113. Haney, M.J.; Klyachko, N.L.; Zhao, Y.; Gupta, R.; Plotnikova, E.G.; He, Z.; Patel, T.; Piroyan, A.; Sokolsky, M.; Kabanov, A.V.; et al. Exosomes as Drug Delivery Vehicles for Parkinson's Disease Therapy. *J. Control. Release* **2015**, *207*, 18–30. [CrossRef] [PubMed]
114. Perets, N.; Betzer, O.; Shapira, R.; Brenstein, S.; Angel, A.; Sadan, T.; Ashery, U.; Popovtzer, R.; Offen, D. Golden Exosomes Selectively Target Brain Pathologies in Neurodegenerative and Neurodevelopmental Disorders. *Nano Lett.* **2019**, *19*, 3422–3431. [CrossRef]
115. Chan, D.Z.L.; Kerr, A.J.; Doughty, R.N. Temporal Trends in the Burden of Heart Failure. *Intern. Med. J.* **2021**, *51*, 1212–1218. [CrossRef] [PubMed]
116. Kadota, S.; Tanaka, Y.; Shiba, Y. Heart Regeneration Using Pluripotent Stem Cells. *J. Cardiol.* **2020**, *76*, 459–463. [CrossRef]
117. Gao, L.; Gregorich, Z.R.; Zhu, W.; Mattapally, S.; Oduk, Y.; Lou, X.; Kannappan, R.; Borovjagin, A.V.; Walcott, G.P.; Pollard, A.E.; et al. Large Cardiac Muscle Patches Engineered from Human Induced-Pluripotent Stem Cell-Derived Cardiac Cells Improve Recovery from Myocardial Infarction in Swine. *Circulation* **2018**, *137*, 1712–1730. [CrossRef]

118. Fernandes, S.; Naumova, A.V.; Zhu, W.Z.; Laflamme, M.A.; Gold, J.; Murry, C.E. Human Embryonic Stem Cell-Derived Cardiomyocytes Engraft but Do Not Alter Cardiac Remodeling after Chronic Infarction in Rats. *J. Mol. Cell. Cardiol.* **2010**, *49*, 941–949. [CrossRef] [PubMed]
119. Lima Correa, B.; El Harane, N.; Gomez, I.; Rachid Hocine, H.; Vilar, J.; Desgres, M.; Bellamy, V.; Keirththana, K.; Guillas, C.; Perotto, M.; et al. Extracellular Vesicles from Human Cardiovascular Progenitors Trigger a Reparative Immune Response in Infarcted Hearts. *Cardiovasc. Res.* **2021**, *117*, 292–307. [CrossRef] [PubMed]
120. Hume, R.D.; Chong, J.J.H. The Cardiac Injury Immune Response as a Target for Regenerative and Cellular Therapies. *Clin. Ther.* **2020**, *42*, 1923–1943. [CrossRef]
121. Yue, Y.; Wang, C.; Benedict, C.; Huang, G.; Truongcao, M.; Roy, R.; Cimini, M.; Garikipati, V.N.S.; Cheng, Z.; Koch, W.J.; et al. Interleukin-10 Deficiency Alters Endothelial Progenitor Cell-Derived Exosome Reparative Effect on Myocardial Repair via Integrin-Linked Kinase Enrichment. *Circ. Res.* **2020**, *126*, 315–329. [CrossRef]
122. Cong, X.Q.; Li, Y.; Zhao, X.; Dai, Y.J.; Liu, Y. Short-Term Effect of Autologous Bone Marrow Stem Cells to Treat Acute Myocardial Infarction: A Meta-Analysis of Randomized Controlled Clinical Trials. *J. Cardiovasc. Transl. Res.* **2015**, *8*, 221–231. [CrossRef]
123. Henry, T.D.; Pepine, C.J.; Lambert, C.R.; Traverse, J.H.; Schatz, R.; Costa, M.; Povsic, T.J.; David Anderson, R.; Willerson, J.T.; Kesten, S.; et al. The Athena Trials: Autologous Adipose-Derived Regenerative Cells for Refractory Chronic Myocardial Ischemia with Left Ventricular Dysfunction. *Catheter. Cardiovasc. Interv.* **2017**, *89*, 169–177. [CrossRef] [PubMed]
124. Baraniak, P.R.; McDevitt, T.C. Stem Cell Paracrine Actions and Tissue Regeneration. *Regen. Med.* **2010**, *5*, 121–143. [CrossRef]
125. Jin, L.; Zhang, J.; Deng, Z.; Liu, J.; Han, W.; Chen, G.; Si, Y.; Ye, P. Mesenchymal Stem Cells Ameliorate Myocardial Fibrosis in Diabetic Cardiomyopathy via the Secretion of Prostaglandin E2. *Stem Cell Res. Ther.* **2020**, *11*, 122. [CrossRef]
126. Liu, M.; Chen, H.; Jiang, J.; Zhang, Z.; Wang, C.; Zhang, N.; Dong, L.; Hu, X.; Zhu, W.; Yu, H.; et al. Stem Cells and Diabetic Cardiomyopathy: From Pathology to Therapy. *Heart Fail. Rev.* **2016**, *21*, 723–736. [CrossRef] [PubMed]
127. Copeland, J.; Langford, S.; Giampietro, J.; Arancio, J.; Arabia, F. Total Artificial Heart Update. *Surg. Technol. Int.* **2021**, *39*, 545–557. [CrossRef]
128. Baker, E.W.; Kinder, H.A.; West, F.D. Neural Stem Cell Therapy for Stroke: A Multimechanistic Approach to Restoring Neurological Function. *Brain Behav.* **2019**, *9*, e01214. [CrossRef] [PubMed]
129. Suda, S.; Nito, C.; Yokobori, S.; Sakamoto, Y.; Nakajima, M.; Sowa, K.; Obinata, H.; Sasaki, K.; Savitz, S.I.; Kimura, K. Recent Advances in Cell-Based Therapies for Ischemic Stroke. *Int. J. Mol. Sci.* **2020**, *21*, 1–24. [CrossRef] [PubMed]
130. Yasuhara, T.; Kawauchi, S.; Kin, K.; Morimoto, J.; Kameda, M.; Sasaki, T.; Bonsack, B.; Kingsbury, C.; Tajiri, N.; Borlongan, C.V.; et al. Cell Therapy for Central Nervous System Disorders: Current Obstacles to Progress. *CNS Neurosci. Ther.* **2020**, *26*, 595–602. [CrossRef] [PubMed]
131. Tuazon, J.P.; Castelli, V.; Borlongan, C.V. Drug-like Delivery Methods of Stem Cells as Biologics for Stroke. *Expert Opin. Drug Deliv.* **2019**, *16*, 823–833. [CrossRef] [PubMed]
132. Kawabori, M.; Shichinohe, H.; Kuroda, S.; Houkin, K. Clinical Trials of Stem Cell Therapy for Cerebral Ischemic Stroke. *Int. J. Mol. Sci.* **2020**, *21*, 7380. [CrossRef] [PubMed]
133. Mitrečić, D.; Nicaise, C.; Gajović, S.; Pochet, R. Distribution, Differentiation, and Survival of Intravenously Administered Neural Stem Cells in a Rat Model of Amyotrophic Lateral Sclerosis. *Cell Transplant.* **2010**, *19*, 537–548. [CrossRef] [PubMed]
134. Boltze, J.; Jolkkonen, J. Safety Evaluation of Intra-Arterial Cell Delivery in Stroke Patients—a Framework for Future Trials. *Ann. Transl. Med.* **2019**, *7*, S271. [CrossRef] [PubMed]
135. Bang, O.Y.; Lee, J.S.; Lee, P.H.; Lee, G. Autologous Mesenchymal Stem Cell Transplantation in Stroke Patients. *Ann. Neurol.* **2005**, *57*, 874–882. [CrossRef]
136. Hess, D.C.; Wechsler, L.R.; Clark, W.M.; Savitz, S.I.; Ford, G.A.; Chiu, D.; Yavagal, D.R.; Uchino, K.; Liebeskind, D.S.; Auchus, A.P.; et al. Safety and Efficacy of Multipotent Adult Progenitor Cells in Acute Ischaemic Stroke (MASTERS): A Randomised, Double-Blind, Placebo-Controlled, Phase 2 Trial. *Lancet Neurol.* **2017**, *16*, 360–368. [CrossRef]
137. Steinberg, G.K.; Kondziolka, D.; Wechsler, L.R.; Dade Lunsford, L.; Kim, A.S.; Johnson, J.N.; Bates, D.; Poggio, G.; Case, C.; McGrogan, M.; et al. Two-Year Safety and Clinical Outcomes in Chronic Ischemic Stroke Patients after Implantation of Modified Bone Marrow-Derived Mesenchymal Stem Cells (SB623): A Phase 1/2a Study. *J. Neurosurg.* **2019**, *131*, 1462–1472. [CrossRef] [PubMed]
138. Oh, K.W.; Noh, M.Y.; Kwon, M.S.; Kim, H.Y.; Oh, S.I.; Park, J.; Kim, H.J.; Ki, C.S.; Kim, S.H. Repeated Intrathecal Mesenchymal Stem Cells for Amyotrophic Lateral Sclerosis. *Ann. Neurol.* **2018**, *84*, 361–373. [CrossRef] [PubMed]
139. Blanquer, M.; Moraleda, J.M.; Iniesta, F.; Gómez-Espuch, J.; Meca-Lallana, J.; Villaverde, R.; Pérez-Espejo, M.Á.; Ruiz-López, F.J.; Santos, J.M.G.; Bleda, P.; et al. Neurotrophic Bone Marrow Cellular Nests Prevent Spinal Motoneuron Degeneration in Amyotrophic Lateral Sclerosis Patients: A Pilot Safety Study. *Stem Cells* **2012**, *30*, 1277–1285. [CrossRef]
140. Shroff, G. A Review on Stem Cell Therapy for Multiple Sclerosis: Special Focus on Human Embryonic Stem Cells. *Stem Cells Cloning* **2018**, *11*, 1–11. [CrossRef] [PubMed]
141. Liu, Z.; Cheung, H.H. Stem Cell-Based Therapies for Parkinson Disease. *Int. J. Mol. Sci.* **2020**, *21*, 7927. [CrossRef] [PubMed]
142. Shao, A.; Tu, S.; Lu, J.; Zhang, J. Crosstalk between Stem Cell and Spinal Cord Injury: Pathophysiology and Treatment Strategies. *Stem Cell Res. Ther.* **2019**, *10*, 238. [CrossRef] [PubMed]

143. Monguió-Tortajada, M.; Prat-Vidal, C.; Moron-Font, M.; Clos-Sansalvador, M.; Calle, A.; Gastelurrutia, P.; Cserkoova, A.; Morancho, A.; Ramírez, M.Á.; Rosell, A.; et al. Local Administration of Porcine Immunomodulatory, Chemotactic and Angiogenic Extracellular Vesicles Using Engineered Cardiac Scaffolds for Myocardial Infarction. *Bioact. Mater.* **2021**, *6*, 3314–3327. [CrossRef] [PubMed]
144. Chachques, J.C.; Gardin, C.; Lila, N.; Ferroni, L.; Migonney, V.; Falentin-Daudre, C.; Zanotti, F.; Trentini, M.; Brunello, G.; Rocca, T.; et al. Elastomeric Cardiowrap Scaffolds Functionalized with Mesenchymal Stem Cells-Derived Exosomes Induce a Positive Modulation in the Inflammatory and Wound Healing Response of Mesenchymal Stem Cell and Macrophage. *Biomedicines* **2021**, *9*, 824. [CrossRef]
145. Chachques, J.C.; Lila, N.; Soler-Botija, C.; Martinez-Ramos, C.; Valles, A.; Autret, G.; Perier, M.C.; Mirochnik, N.; Monleon-Pradas, M.; Bayes-Genis, A.; et al. Elastomeric Cardiopatch Scaffold for Myocardial Repair and Ventricular Support. *Eur. J. Cardio-Thoracic. Surg.* **2020**, *57*, 545–555. [CrossRef]
146. Bellin, G.; Gardin, C.; Ferroni, L.; Chachques, J.; Rogante, M.; Mitrečić, D.; Ferrari, R.; Zavan, B. Exosome in Cardiovascular Diseases: A Complex World Full of Hope. *Cells* **2019**, *8*, 166. [CrossRef]
147. Yan, Y.; Chen, H.; Zhang, H.; Guo, C.; Yang, K.; Chen, K.; Cheng, R.; Qian, N.; Sandler, N.; Zhang, Y.S.; et al. Vascularized 3D Printed Scaffolds for Promoting Bone Regeneration. *Biomaterials* **2019**, *190*, 97–110. [CrossRef]
148. Chachques, J.C.; Trainini, J.C.; Lago, N.; Masoli, O.H.; Barisani, J.L.; Cortes-Morichetti, M.; Schussler, O.; Carpentier, A. Myocardial Assistance by Grafting a New Bioartificial Upgraded Myocardium (MAGNUM Clinical Trial): One Year Follow-Up. *Cell Transplant.* **2007**, *16*, 927–934. [CrossRef]
149. Wu, C.C.; Chen, B. Sen. Key Immune Events of the Pathomechanisms of Early Cardioembolic Stroke: Multi-Database Mining and Systems Biology Approach. *Int. J. Mol. Sci.* **2016**, *17*. [CrossRef]
150. Tajiri, N.; Staples, M.; Acosta, S.; Pabon, M.; Dailey, T.; Kaneko, Y.; Borlongan, C.V. Stem Cell Therapies in Neurology. In *Adult Stem Cell Therapies: Alternatives to Plasticity*; Springer: Berlin/Heidelberg, Germany, 2014; pp. 117–136. [CrossRef]
151. Schimmel, S.; Acosta, S.; Lozano, D. Neuroinflammation in Traumatic Brain Injury: A Chronic Response to an Acute Injury. *Brain Circ.* **2017**, *3*, 135. [CrossRef]
152. Dailey, T.; Metcalf, C.; Mosley, Y.; Sullivan, R.; Shinozuka, K.; Tajiri, N.; Pabon, M.; Acosta, S.; Kaneko, Y.; Loveren, H.; et al. An Update on Translating Stem Cell Therapy for Stroke from Bench to Bedside. *J. Clin. Med.* **2013**, *2*, 220–241. [CrossRef] [PubMed]
153. Hao, L.; Zou, Z.; Tian, H.; Zhang, Y.; Zhou, H.; Liu, L. Stem Cell-Based Therapies for Ischemic Stroke. *BioMed Res. Int.* **2014**, *2014*, 468748. [CrossRef]
154. Toyoshima, A.; Yasuhara, T.; Date, I. Mesenchymal Stem Cell Therapy for Ischemic Stroke. *Acta Med. Okayama* **2017**, *71*, 263–268. [CrossRef]
155. Kenmuir, C.L.; Wechsler, L.R. Update on Cell Therapy for Stroke. *Stroke Vasc. Neurol.* **2017**, *2*, 59–64. [CrossRef]
156. Marcet, P.; Santos, N.; Borlongan, C.V. When Friend Turns Foe: Central and Peripheral Neuroinflammation in Central Nervous System Injury. *Neuroimmunol. Neuroinflamm.* **2017**, *4*, 82. [CrossRef]
157. Hribljan, V.; Lisjak, D.; Petrović, D.J.; Mitrečić, D. Necroptosis Is One of the Modalities of Cell Death Accompanying Ischemic Brain Stroke: From Pathogenesis to Therapeutic Possibilities. *Croat. Med. J.* **2019**, *60*, 121–126. [CrossRef]
158. Aggarwal, S.; Pittenger, M.F. Human Mesenchymal Stem Cells Modulate Allogeneic Immune Cell Responses. *Blood* **2005**, *105*, 1815–1822. [CrossRef] [PubMed]
159. Yao, P.; Zhou, L.; Zhu, L.; Zhou, B.; Yu, Q. Mesenchymal Stem Cells: A Potential Therapeutic Strategy for Neurodegenerative Diseases. *Eur. Neurol.* **2020**, *83*, 235–241. [CrossRef] [PubMed]
160. Fan, X.L.; Zhang, Y.; Li, X.; Fu, Q.L. Mechanisms Underlying the Protective Effects of Mesenchymal Stem Cell-Based Therapy. *Cell. Mol. Life Sci.* **2020**, *77*, 2771–2794. [CrossRef]
161. Yin, K.; Wang, S.; Zhao, R.C. Exosomes from Mesenchymal Stem/Stromal Cells: A New Therapeutic Paradigm. *Biomark. Res.* **2019**, *7*, 1–8. [CrossRef]
162. Kabat, M.; Bobkov, I.; Kumar, S.; Grumet, M. Trends in Mesenchymal Stem Cell Clinical Trials 2004–2018: Is Efficacy Optimal in a Narrow Dose Range? *Stem Cells Transl. Med.* **2020**, *9*, 17–27. [CrossRef]
163. Ritfeld, G.; Oudega, M. Bone Marrow-Derived Mesenchymal Stem Cell Transplant Survival in the Injured Rodent Spinal Cord. *J. Bone Marrow Res.* **2014**, *2*, 2–9. [CrossRef]
164. Shariati, A.; Nemati, R.; Sadeghipour, Y.; Yaghoobi, Y.; Baghban, R.; Javidi, K.; Zamani, M.; Hassanzadeh, A. Mesenchymal Stromal Cells (MSCs) for Neurodegenerative Disease: A Promising Frontier. *Eur. J. Cell Biol.* **2020**, *99*, 151097. [CrossRef]
165. Appelt, P.A.; Comella, K.; de Souza, L.A.P.S.; Luvizutto, G.J. Effect of Stem Cell Treatment on Functional Recovery of Spinocerebellar Ataxia: Systematic Review and Meta-Analysis. *Cerebellum Ataxias* **2021**, *8*, 8. [CrossRef]
166. Mitrecic, D. Genetically Modified Stem Cells for the Treatment of Neurological Diseases. *Front. Biosci.* **2012**, *E4*, 1170. [CrossRef]
167. Mitrečić, D. Current Advances in Intravascular Administration of Stem Cells for Neurological Diseases: A New Dose of Rejuvenation Injected. *Rejuvenation Res.* **2011**, *14*, 553–555. [CrossRef]
168. Morata-Tarifa, C.; Azkona, G.; Glass, J.; Mazzini, L.; Sanchez-Pernaute, R. Looking Backward to Move Forward: A Meta-Analysis of Stem Cell Therapy in Amyotrophic Lateral Sclerosis. *npj Regen. Med.* **2021**, *6*, 1–10. [CrossRef] [PubMed]
169. Chan, H.J.; Yanshree; Roy, J.; Tipoe, G.L.; Fung, M.L.; Lim, L.W. Therapeutic Potential of Human Stem Cell Implantation in Alzheimer's Disease. *Int. J. Mol. Sci.* **2021**, *22*, 10151. [CrossRef] [PubMed]



Review

Iron Homeostasis Disorder and Alzheimer's Disease

Yu Peng¹, Xuejiao Chang¹ and Minglin Lang^{1,2,*}

¹ CAS Center for Excellence in Biotic Interactions, College of Life Science, University of Chinese Academy of Sciences, Beijing 100049, China; pengyu18@mailsucas.ac.cn (Y.P.); changxuejiao20@mailsucas.ac.cn (X.C.)

² College of Life Science, Agricultural University of Hebei, Baoding 071000, China

* Correspondence: langml@ucas.ac.cn; Tel.: +86-10-6967-2639

Abstract: Iron is an essential trace metal for almost all organisms, including human; however, oxidative stress can easily be caused when iron is in excess, producing toxicity to the human body due to its capability to be both an electron donor and an electron acceptor. Although there is a strict regulation mechanism for iron homeostasis in the human body and brain, it is usually inevitably disturbed by genetic and environmental factors, or disordered with aging, which leads to iron metabolism diseases, including many neurodegenerative diseases such as Alzheimer's disease (AD). AD is one of the most common degenerative diseases of the central nervous system (CNS) threatening human health. However, the precise pathogenesis of AD is still unclear, which seriously restricts the design of interventions and treatment drugs based on the pathogenesis of AD. Many studies have observed abnormal iron accumulation in different regions of the AD brain, resulting in cognitive, memory, motor and other nerve damages. Understanding the metabolic balance mechanism of iron in the brain is crucial for the treatment of AD, which would provide new cures for the disease. This paper reviews the recent progress in the relationship between iron and AD from the aspects of iron absorption in intestinal cells, storage and regulation of iron in cells and organs, especially for the regulation of iron homeostasis in the human brain and prospects the future directions for AD treatments.

Keywords: Alzheimer's disease; iron homeostasis disorder; iron homeostasis regulators; β -amyloid; tau; APP; central nervous system; oxidative stress; pathogenesis; genetic intervention

Citation: Peng, Y.; Chang, X.; Lang, M. Iron Homeostasis Disorder and Alzheimer's Disease. *Int. J. Mol. Sci.* **2021**, *22*, 12442. <https://doi.org/10.3390/ijms222212442>

Academic Editor: Masaru Tanaka

Received: 16 October 2021

Accepted: 10 November 2021

Published: 18 November 2021

Publisher's Note: MDPI stays neutral with regard to jurisdictional claims in published maps and institutional affiliations.



Copyright: © 2021 by the authors. Licensee MDPI, Basel, Switzerland. This article is an open access article distributed under the terms and conditions of the Creative Commons Attribution (CC BY) license (<https://creativecommons.org/licenses/by/4.0/>).

1. Introduction

The transition metal element iron is the second most abundant metal element in the earth's crust behind, aluminum. It is also an essential trace element and an important component of metalloprotein for human body [1,2]. Due to its unique chemical reaction characteristics, it plays an important role in maintaining normal physiological function and metabolism, such as oxygen transport, DNA synthesis, iron sulfur cluster synthesis, neurotransmitter synthesis and electron transfer in respiratory chain [3–5]. The adult human body contains 3–5 g of iron [2]. In the normal metabolism of the human body, iron ions are absorbed into the blood through the small intestine and transported to the parts of the body requiring iron. Although the body strictly regulates the regulation of iron metabolism, changes with age, genetics and the environment will lead to iron metabolism disorders [6]. The disorder of iron metabolism in the body will catalyze the formation of reactive oxygen species (ROS) through Fenton and other chemical reactions, attack DNA, protein and lipid molecules, and lead to cell damage [7,8]. In recent years, more and more research teams on the pathogenesis of Alzheimer's disease (AD) have shown that the oxidative stress induced by iron metabolism disorder and the production of ROS are related to the pathological process of AD [7,9]. Alzheimer's disease is an age-related neurodegenerative disease with clinical symptoms of memory decline, cognitive impairment and learning impairment [10–12]. With the increasing human life span, the incidence rate of AD is also increasing, and has become one of the most important fatal diseases [5,13,14]. The pathological features of AD in the brain are the extracellular deposition of A β proteins forming

insoluble senile plaques and the intracellular accumulation of hyperphosphorylated tau proteins forming neurofibrillary tangles (NFTs), which result in a large degree of neuronal cell death [11,15,16]. Thus far, the main causes and pathogenesis of AD have not been fully clarified. Many research teams have found that there is regional deposition of iron in the brain of AD patients [17–19]; treatment with an iron chelator can effectively alleviate the symptoms of AD [9], suggesting that iron metabolism disorder has a close relationship with AD.

This paper reviews the relevant research progress in the field of iron and AD in recent years, focusing on the oxidative stresses induced by normal iron metabolism and its metabolic disorders, especially for abnormal expression of the iron transporters, transferrin receptors, divalent metal transporters, and their relationships with the AD pathological mark proteins, such as A β and tau proteins. Relevant contemporary AD treatment measures have also been discussed and prospected. The iron homeostasis on AD provides a theoretical basis for the prevention and treatment of neurodegenerative diseases and an effective drug screening target.

2. Physiological Function and Metabolic Process of Systemic Iron

2.1. Physiological Function of System Iron

Iron is an essential trace metal element and an important component of metalloprotein [2]. Due to its unique chemical reaction characteristics, iron plays an important role in oxygen transport, DNA synthesis and repair, energy generation and enzyme function, such as the formation of a variety of coordination compounds with organic ligands and redox reactions by the mutual conversion of divalent iron and trivalent iron [3,6,8,20].

2.2. Metabolic Process of System Iron

2.2.1. System Iron Absorption

As we know, the adult human body contains about 3–5 g of iron [2], for individuals without blood transfusion, a part of the iron in the system comes from intestinal cells absorbed from food, and the other part comes from macrophages [6,21]. As shown in Figure 1, the absorption of iron from food is Fe³⁺, which is reverted to Fe²⁺ by DCYTB (duodenal cytochrome-b-like protein); then, the divalent metal transporter 1 (DMT1) on the surface of the intestinal cell membrane combines the ferrous iron and transports it into the intestinal epithelial cells [20]. The ferrous iron entering intestinal epithelial cells can be transported to mitochondria for heme molecule synthesis, or oxidized to ferric iron and stored in ferritins [22,23]. Excess Fe²⁺ is released into plasma by FPN (ferroportin) which is located on the basal intestinal cell membrane where it is again oxidated to Fe³⁺ by the same situated hephaestin [24–26].

As shown in Figure 2, Fe³⁺ in plasma can bind to transferrin (TF), which is transported through blood in the form of TF-Fe complex. The complex then bind to transferrin receptor 1 (TfR1) that highly expressed on the surface of iron demanding cell membrane, and it enters iron demanding cells through clathrin-mediated endocytosis [27,28]. Fe³⁺ in endocytic vesicles is reduced to Fe²⁺ by STEAP (six-transmembrane epithelial antigen of prostate) and released into cells by divalent metal ion transporter DMT1 after separation in low pH environment of endocytic vesicles [29–32]. In addition, ZIP14 (member of the Zrt/IRT family) was initially identified as a transporter of Zn. In subsequent studies, it was found to be involved in the transport of ferrous iron released from endocytic vesicles into the cytoplasm [1,28,33]. TF and TfR1 separated from Fe³⁺ enter the plasma and are redistributed to the surface of cell membrane to participate in iron transport and the next round of iron absorption, respectively [1]. Fe³⁺ in plasma can also combine with citrate, ATP and ascorbate to form small-molecule complexes [6].

2.2.2. Storage and Loss of System Iron

In the body, iron is mainly stored in liver cells and macrophages. Macrophages phagocytize the aging red blood cells and release the iron ions inside red blood cells; then,

the released irons are stored in ferritin proteins in the macrophages [34]. When the body is in a state of iron demand, macrophages secrete ferritin protein into the serum circulatory system; therefore, the concentration of ferritin protein in serum can reflect the state of iron content in the body [35]. Ferritin protein plays an important role in iron storage and antioxidation in cells [36]. Ferritin protein contains two subunits of H-ferritin and L-ferritin, which exhibit ferrous oxidase activity and iron storage function, respectively [37]. Fe^{2+} in cells is oxidized by H-ferritin and stored in L-ferritin. Each ferritin protein can store 4500 iron atoms, which can considerably reduce the cell level of free iron ions and prevent the damage caused by free-iron-induced oxidative stresses; thus, it has antioxidant effects [38]. When the concentration of iron in cells decreases, ferritin protein is decomposed into hemoxanthin by lysosomes. Hemoxanthin and ferritin protein can be detected by Prussian blue staining [39]. In addition to ferritin protein, iron entering the cell can enter mitochondria to synthesize heme, as well as the iron sulfur cluster, and participate in the process of aerobic respiration as a cofactor of mitochondrial respiratory chain protein. It can also combine with some small molecular substances in the cell, such as citric acid, ATP, AMP and pyrophosphate to form an intracellular free iron pool [6,8,40]. The amount of pooled free iron can reflect the change in iron content in cells, which can be detected by some fluorescence techniques [8]. Increasing the pool content will produce harmful substances through redox reactions, causing damage to cells, which could even lead to cell death when it is serious [8,41,42]. Iron entering the blood can also be ingested and utilized by iron cells and iron storage cells. Most of the iron in the blood is used by red blood cells to participate in the transport of oxygen. About 20–30% of the iron is stored in the liver and macrophages, and some iron is involved in the formation of myoglobin, cytochrome and iron-containing enzymes [8].

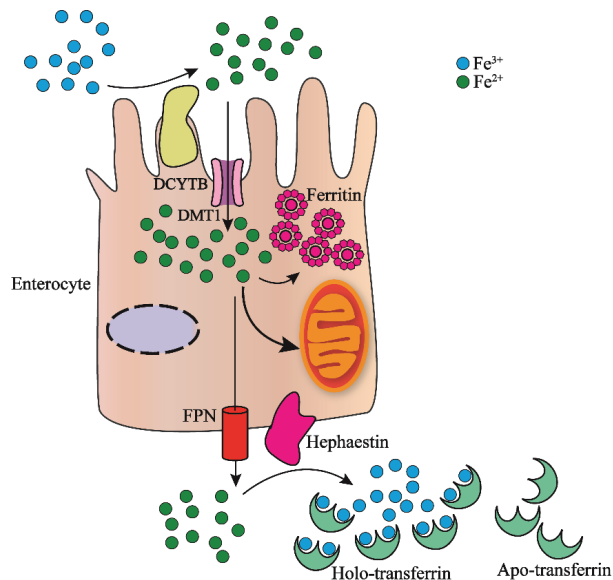


Figure 1. Nonheme iron intestinal absorption and transport by intestinal cells. Food Fe^{3+} is reduced to Fe^{2+} by DCYTB, which binds to the divalent metal transporter DMT1 on the surface of the intestinal cell membrane and transported into the intestinal epithelial cells. The Fe^{2+} that enters the intestinal cells can enter the mitochondria for the synthesis of heme. It can also be oxidized to Fe^{3+} and then stored in ferritin. The excess Fe^{2+} is released from FPN into the plasma and then oxidized to Fe^{3+} by hephaestin. Each molecule of Apo-transferrin in the plasma combines with two Fe^{3+} ions to form Holo-transferrin-Fe. The complex transports iron in the blood to the organs in the body that require iron.

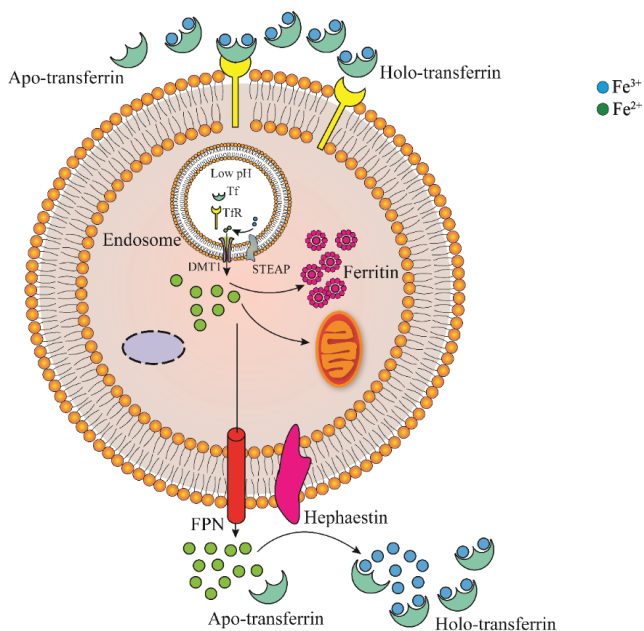


Figure 2. Somatic cell absorption and the transport of iron ions. Fe^{3+} in plasma can bind to Apo-transferrin (Tf), which forms a Tf-Fe complex; then, it is transported through the blood to bind to the transferrin receptor (TfR1) that requires high expression on the surface of iron cell membranes, which enters the iron-requiring cells through endocytosis mediated by clathrin. In the endocytic vesicles, Fe^{3+} is reduced to Fe^{2+} by the six-transmembrane epithelial antigen of prostate (STEAP). After separation in a low-pH environment, Fe^{2+} is released into the cell by the divalent metal ion transporter DMT1. The iron ions in the cell can enter the mitochondria to participate in the redox reaction and can also be stored in the ferritin protein. When the body is in a state of iron limiting, Fe^{2+} can be transported to the outside of the cell through FPN and oxidized by hephaestin to Fe^{3+} , and combines with Apo-transferrin to form Holo-transferrin.

The normal human body loses about 1–2 mg of iron every day [36,43]. Iron in the body is mainly excreted from intestinal mucosa, skin cells, sweat and urine [4,30,44].

2.2.3. Regulation of Iron in Cells

Iron regulatory proteins (IRPs) combine with iron regulatory elements (IREs) in the 3' or 5' untranslated region of mRNA transcripts of iron-metabolism-related genes to regulate the iron concentration in cells [43,45,46]. The IRE region contains a loop of 5'-cagugn-3' folded by 30 nucleotides (in which the hydrogen bond formed between G and C stabilizes its structure), without pairing to form hydrogen bonds which will destroy this structure [8,46–48]. As shown in Figure 3, IREs are located at the 3'-UTR and 5'-UTR areas of TfR1 and DMT1 mRNAs, and ferroportin and ferritin mRNAs, respectively, although the binding of IRPs to IREs could finely regulate the iron concentration in cells [49]. When the concentration of iron ions in cells is too high, on the one hand, it will induce conformation changes in the untranslated region of TfR1 and DMT1 mRNAs, so that IRPs cannot bind to the IRE region, and those mRNAs are degraded, whereas the expression levels of ferroportin and ferritin proteins are increased; on the other hand, iron ions can bind to IRP1, forming iron sulfur clusters in IRP1 that exhibit cytoplasmic aconitase activity. In contrast, when the concentration of iron ions decreases, the binding ability between IRP and IRE is enhanced, the expression level of ferroportin and ferritin proteins will decrease, and the expression level of TfR1 and DMT1 will increase [48,50–52].

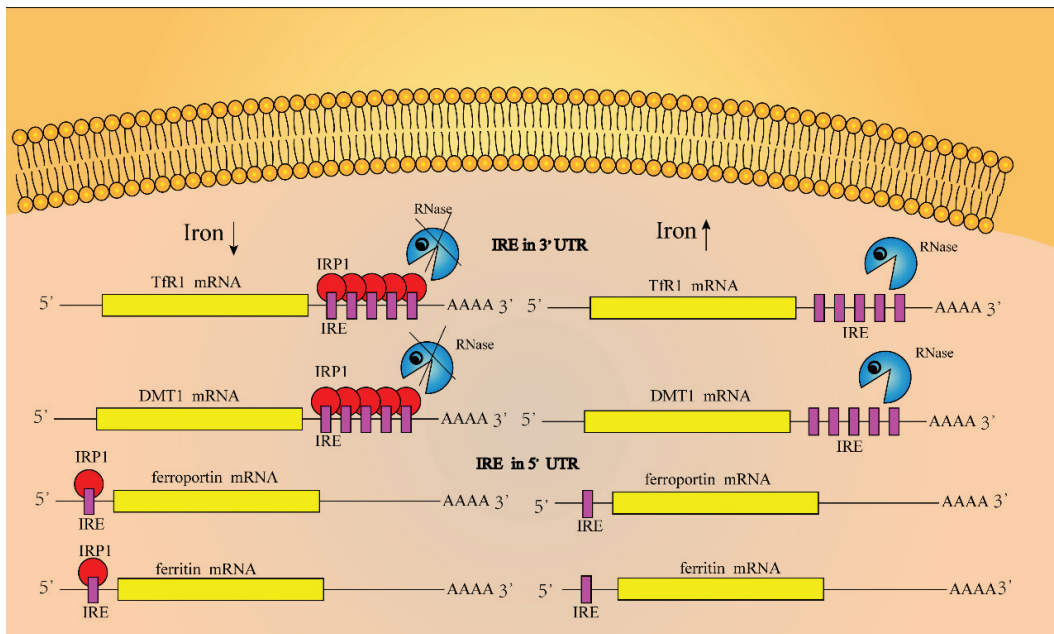


Figure 3. Regulation of iron homeostasis in cells. IREs are located in the 3'-UTR region of TfR1 and DMT1 mRNAs, whereas they are located in the 5'-UTR region of ferroportin and ferritin mRNAs. The combination of IRP and IRE regulates the iron ion concentration in the cell. When the iron ion concentration in the cell is too high, it will induce conformation changes in the untranslated region of mRNAs, making IRPs unable to bind to the IRE region; then, mRNAs of TfR1 and DMT1 are degraded, and the expression level of ferroportin and ferritin increases. On the other hand, iron ions bind to IRP1, and can form iron–sulfur clusters in IRP1 that exhibit cytoplasmic aconitase activity. In contrast, when the iron concentration in the cell decreases, the binding ability of IRP and IRE is enhanced, which leads to a decreased expression of ferroportin and ferritin proteins, and an increased expression of TfR1 and DMT1.

Iron regulatory proteins IRP1 and IRP2 are intracellular iron sensors. These are two proteins that are homologous proteins and belong to the iron–sulfur cluster isomerase family [53]. IRP1 can form a cis-aconitase-type iron sulfur cluster (4Fe-4S), which not only determines its functional mode, but also serves as an important regulatory site. IRP1 forms an iron sulfur cluster only when cells are rich in iron, in which IRP1 can display cis-aconitase activity in cytoplasm; however, it reduces the ability of IRP1 to bind to IRE. Low concentrations of iron in cells induce the depolymerization of iron sulfur clusters in IRP1 and enhance the ability of IRP1 to bind to IRE, although the mechanism of iron sulfur cluster depolymerization in IRP1 has not been fully illuminated. In addition, the increase in NO and H₂O₂ concentration in cells will activate the activity of IRP1 and promote its binding to IRE [38].

Iron ions and oxygen regulate the synthesis of IRP2 in cells through post-translational mechanisms. IRP2 has lost the activity of aconitase in the process of evolution. The decrease in intracellular iron ions and oxygen concentration promote the synthesis of IRP2 and maintain its stable state. In contrast, the increase in iron ion and oxygen concentration will accelerate the degradation of IRP2. The N-terminal 73 amino acid sequence of IRP2 is characteristic of IRP2. This highly conserved 73 amino acids is encoded by a determined exon and is related to the iron-dependent degradation of IRP2 [8].

2.2.4. Regulation of Iron in the System

Iron ions exported from the intestine are absorbed by the iron-demanding tissues and organs of the body through blood circulation. The liver is the main organ for the regulation

of iron balance, which plays an important role in the regulation of whole-body iron balances [34]. The liver produces and secretes the hepcidin hormone [25,54], which is a short polypeptide composed of an 84 amino acid sequence encoded by the HAMP gene and a 25 amino acid sequence hydrolyzed by basic amino acid protein hydrolase [30,34,42,55–58]. When the iron in the body is in a high-concentration state, hepcidin combines with FPN protein and JAK2 on the intestinal epidermal cell membrane to form a complex, which is phosphorylated before the endocytosis of FPN. FPN is endocytosed into the cell and degraded in the lysosome after ubiquitination to reduce the concentration of iron in the blood [30,46,55,59]. In contrast, when the body is in a state of iron deficiency, hypoxia, inflammation and erythrocyte synthesis, the expression of hepcidin decreases. Some studies have shown that hepcidin can also be produced by other organs and tissue cells, such as the heart, alveolar macrophages and spleen macrophages [42,60–62]. In addition to the liver, red blood cells and macrophages participate in the iron metabolism of the body. For example, iron in red blood cells participates in the synthesis of hemoglobin, and macrophages can phagocytize aging red blood cells to release iron; therefore, macrophages could participate in iron circulation when the body is in a state of low iron concentration [42,63].

2.3. Roles of Microbiota in Iron Homeostasis and Neurodegenerative Diseases

In mammals, iron ions are absorbed mainly through the duodenum, and there is a strict regulation mechanism for iron ion absorption. Iron ions that are not absorbed into the duodenum end up in the colon cavity, which is home to a host of microbes called the gut microbiome. Iron plays an important role in the growth of intestinal micro-organisms because it plays an important role as a ferritin cofactor in redox reactions, metabolic pathways and electron transport chains of microorganisms. Therefore, the content of iron ions in the colonic lumen will affect the composition, growth and living status of intestinal microbes, and conversely, the changes of intestinal microbes will also affect the health status of the host [64]. A growing number of studies have shown that the gastrointestinal tract and the central nervous system interact through the gut-brain axis, including neuronal, immune and metabolite-mediated pathways. Preclinical and clinical studies have shown that gut microbiome plays a key role in the gut-brain interaction, and that disturbances in the composition of gut microbiota are associated with the pathogenesis of neurological diseases, especially the neurodegenerative diseases [65]. Maternal immune activation (MIA) increases the risk of autism spectrum disorder (ASD) in offspring. Dysregulation of microorganisms is associated with ASD symptoms. In lipopolysaccharide (LIP)-induced MIA progenies, MIA progenies exhibited an abnormal brain-gut-microbiome axis compared with that of the control progenies, which were characterized by social behavioral deficits, anxiety-like and repetitive behaviors, low myelination, and ASD-like microbiome [66]. Studies have shown a potential link between host microbiome (such as gut and oral bacteria), neuroinflammation, and dementia, which may be caused by bacterial invasion of the brain due to barrier leakage, toxin and inflammation factor production, or indirectly by modulating immune responses, and moreover, the composition of microbiota affected the deposition level of A β in the cerebral cortex of APP/PS1 mice [67], suggesting a critical role of iron in these processes.

3. Brain Iron Metabolism

3.1. Brain Iron Absorption

The brain is composed of neurons and glia. Ferritin is also the main iron storage protein in neurons, and neuromelanin has been found to store iron ions for a long time. In glial cells, astrocytes and microglia synthesize L-ferritin to store iron ions, and L- and H-ferritin are expressed in oligodendrocytes [68]. Cells in the CNS are not in direct contact with nutrients, including iron ions. The blood–brain barrier (BBB) and blood–brain spinal cord barrier (BBSCB) separate the CNS from the system circulation. BBB is a special structure, which is composed of auxiliary feet of capillary endothelial cells, peripheral skin cells and astrocytes, and it strictly regulates the substances entering the CNS [69,70].

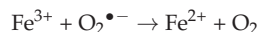
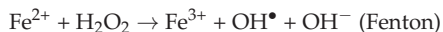
The hydrophobic BBB prevents the hydrophilic holo-TF from entering the nervous system. Holo-TF must pass across the BBB through the brain capillary endothelial cells. Holo-TF in the blood circulation binds to the TF receptor TfR1 on the luminal surface of the brain capillary endothelial cells and enters the cells. The FPN on the abluminal surface transports ferrous iron out of the capillary endothelial cells, where Fe^{2+} are oxidized to Fe^{3+} by ceruloplasmin (CP) [71,72]. CP is expressed in astrocytes and promotes the transport of FPN-exported ferrous iron [24,73]. The binding of iron ions into intercellular fluid and cerebrospinal fluid is secreted by nerve cells, especially TF, synthesized and secreted by oligodendrocytes, and choroid plexus cells, which diffuse through brain parenchymal tissue and bind to the TfR1 receptor on the surface of nerve cell membranes. After releasing iron ions, apo-TF enters the blood circulation through arachnoid villi [71,74]. FPN is regulated by hepcidin in the system, although the source of hepcidin in the brain is unknown. It may enter the brain across the BBB for iron metabolism regulation [68].

3.2. Brain Iron Regulation

The regulation of brain iron homeostasis at the cellular level involves IRPs regulating the expression of related proteins [9,75,76]. The decrease in the IRP2 expression level will lead to the imbalance of brain iron, but it has little effect on myelin iron. Mutations in genes controlling brain iron homeostasis will lead to the disorder of brain iron metabolism and affect the synthesis of myelin. It is unclear whether hepcidin plays a key role in the mediation of brain iron metabolism; whether hepcidin is synthesized in the brain or passes through the BBB after its synthesis in the liver has not been revealed. Recent results show that inflammation activates microglia and promotes the release of hepcidin by astrocytes in the model of signal cascade between inflammatory cells; this signal prevents the release of iron ions in neurons and eventually leads to neuronal death. At the same time, it will also lead to the release of anti-inflammatory and pro-inflammatory factors. Normal human microglia are not activated, and there is no intercellular signal cascade [36,72,77].

3.3. Brain Iron Accumulation and Toxicity

Iron ions accumulate in the brain with age [9,78,79]. Iron ions mainly bind to ferritin protein and substantia nigra [80–82]. The accumulation of iron ions can induce neurotoxicity through different mechanisms. The excessive accumulation of iron ions will increase the permeability of the BBB, induce inflammation, affect the redistribution of iron ions in the brain, and then change brain iron metabolism [47]. Iron ions can act as both electron acceptors and electron donors; therefore, when iron ions accumulate in the brain, they will produce reactive oxygen free radicals through Fenton and Haber–Weiss chemical reactions [41,83,84]. Free radicals are highly active substances, which may promote protein oxidation, membrane lipid peroxidation and nucleic acid modification. When the levels of ROS exceed the antioxidant capacity of organelles, this will induce oxidative stress and damage neurons [38,85,86], leading to tissue degradation in severe cases.



4. Iron Metabolism and AD

4.1. Effect of Iron Metabolism Disorder on AD

AD is the most common cause of dementia, which is characterized by impaired cognitive function and decreased ability of learning, memory and reasoning [24,87]. It was originally described by Dr. Alois Alzheimer, a German doctor. Patients with this kind of disease exhibit strange behavioral symptoms, memory loss and motor loss. Its histopathological characteristics are amyloid plaques deposited outside the cells, and the excessive phosphorylation of tau protein related to the cytoskeleton which forms

neurofibrillary tangles in the cells [88–90]. With the increase in age, iron ions in the brain tend to accumulate, especially in the cortex, globus pallidus, red nucleus, dentate nucleus and substantia nigra; however, the related molecular mechanisms are not clear at present [9,74,79]. The emerging evidence shows that iron with high redox activity is related to the deposition of amyloid plaques and the formation of nerve fiber tangles, suggesting it may be one of the main causes of AD [91–94].

The postmortem brain anatomy of AD patients showed that there was more A β deposition and neurofibrillary tangles in the hippocampal region of the patients [95–97]. Moreover, by detecting the level of antioxidant protein in the hippocampus and amygdala, the level of oxidative stress in these two regions was found to be much higher than other regions. Moreover, the oxidative stress caused by iron accumulation will enhance the activity of IRP1, resulting in the enhancement of iron absorption through TfR1 and the increase in intracellular free iron level by reducing the concentration of ferritin-H and ferritin-L, which further enhances intracellular oxidative stress [93,98]. Based on magnetic resonance imaging (MRI) technology [99], it was found that iron accumulation may further lead to the deposition of A β amyloid and the formation of neurofibrillary tangles in the brain of AD patients. Considerable studies have shown that iron metabolism disorder can affect A β misfolding and tau hyperphosphorylation, and the resultant oxidative stress and metal toxicity of iron ions may lead to AD [100–103].

Even more evidence supports a key role of ROS and RNS (reactive nitrogen species) in leading to AD, which are toxic and related to the formation of oxidative stress in the brain of AD patients [104]. The oxidative stress was more obvious with the increase in iron concentration, and the oxidation of protein, lipid and DNA in A β aggregation area was more significant [105,106]. The free radicals produced at regions of A β aggregation will destroy the adjacent neurons, resulting in a decline in cognitive and memory functions. The accumulation of tau protein in neurofibrillary tangles is also related to the induction of heme oxygenase-1 (HO-1). Overexpression of HO-1 can lead to the increase in iron content and accumulation of tau proteins in the mouse brain. In AD patients or patients with slight cognitive impairment, the concentration of HO-1 in the hippocampus and frontal cortex increased [86,107,108]. Increased levels of iron-bound melanin transfer protein were detected in the serum of AD patients, indicating that there may be abnormal binding of iron in the brain of AD patients. It was also found that iron ions accumulated in regions of A β deposition and neurofibrillary tangles formed by hyperphosphorylation of tau protein, and which were distributed in hippocampus, parietal cortex and motor cortex [93,106,109–112]. The A β amyloid is a segment of amyloid precursor protein (APP) cleaved by secretory enzymes [113]. APP is a transmembrane protein mainly expressed in the nervous system. At present, the physiological function of APP is not fully understood, and it may play a role in brain development, memory and synaptic plasticity [114]. In nerve cells, the concentration of iron ions regulates expression of the APP gene. The mechanism is shown in Figure 4. There is a loop ring formed by 11 bases in the 5'-UTR region of APP mRNA, which is called IRE. IRPs combine with IRE to regulate the synthesis of APP. High concentrations of iron in cells will combine with IRP1 to form iron sulfur clusters; at the same time, high concentrations of iron will also induce conformational changes in the IRE region of APP mRNA, increasing the expression of APP. In contrast, when the cell iron concentration is at a low level, IRP1 will bind to IRE and the expression of APP will decrease [97,106,115]. Under the action of different secretory enzymes in nerve cells, APP can undergo two different cleaving pathways, including the amyloidosis pathway and non-amyloidosis pathway. In the normal physiological state, APP is cleaved through the non-amyloidosis pathway, in which APP is firstly cleaved by α secretase enzyme, producing a segment called sA β PP α ; then, the fragments undergo β and γ secretase cleavage to form non-toxic fragments of P3, A β ₁₆ and A β _{17–40/42}, respectively. The high concentrations of iron in cells promote the cleaving of APP through amyloidosis pathway, in which APP undergoes β and γ secretases cleavage to form A β _{1–40} and A β _{1–42} fragments. The A β _{1–42} fragment is precipitated by Ile41, and the three histidines at its N-terminal

can combine with Fe^{2+} to induce oxidative stress, resulting in $A\beta_{1-42}$ damage to cells at deposition [93,106,109–111,115].

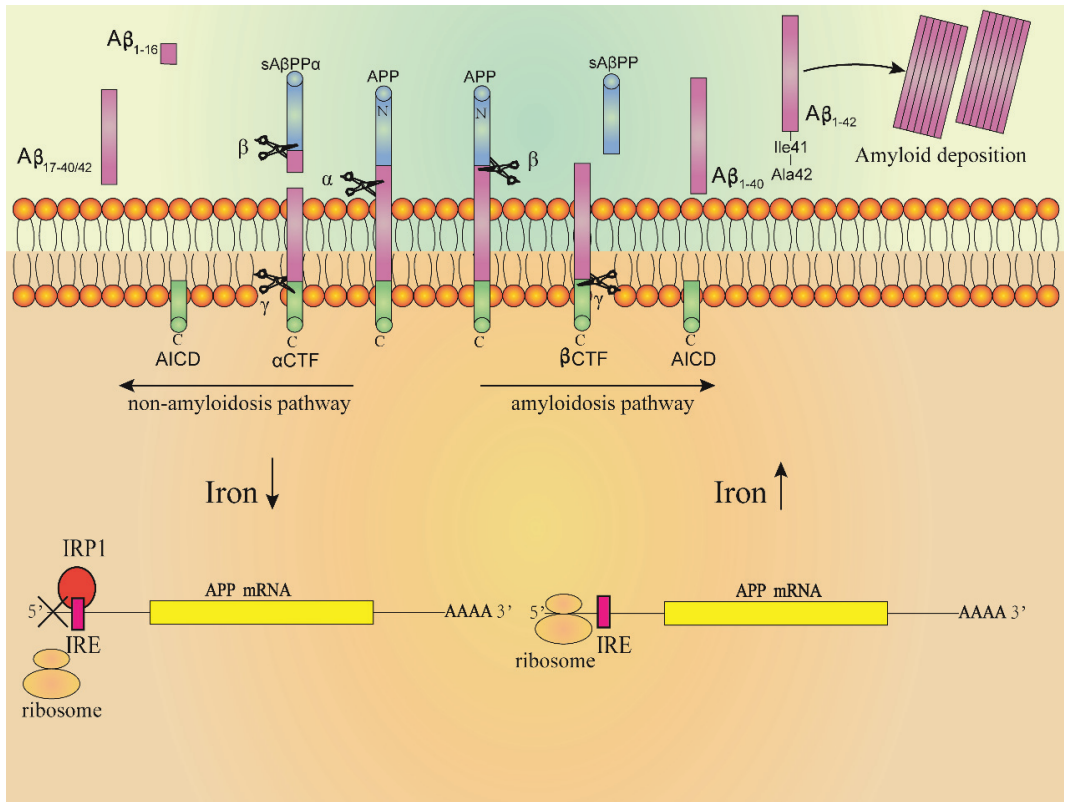


Figure 4. High concentrations of iron in neurons induce $A\beta$ formation. The 5'-UTR region of APP mRNA has an 11-base loop called IRE. The combination of IRPs and IRE regulates the synthesis of APP. The high concentration of iron in the cell will combine with IRP1 to form iron–sulfur clusters, and make IRP1 lose the ability to bind to IRE. At the same time, high concentrations of iron will also induce conformational changes in the IRE region of APP mRNA, which increases the expression of APP; in contrast, when the iron concentration in the cell is at a low level, IRP1 will bind to the IRE of APP mRNA, resulting in the decreased production of $A\beta_{42}$. $A\beta_{1-42}$ aggregates to form amyloid plaques.

In addition, the deposition of $A\beta_{1-42}$ can induce the hyperphosphorylation of tau protein, although the specific mechanism is not clear. At the same time, it can also lead to the disorder of energy metabolism, the activation of immune cells and the disorder of normal function of nerve cells, resulting in cell damage and death [50]. NFTs formed by the hyperphosphorylation of tau proteins and the combination of cytoskeleton mean that the cells are unable to maintain their normal structure. Many neurons in AD patients are affected by NFTs. A large number of NFTs were found in the hippocampus of patients with AD, and the hippocampus participates in the processing of experience and precedes the storage of permanent memory. In the early stages of AD, the clinical manifestations are the decline of learning ability, the ability to form new memory and the memory storage ability. At the same time, the basal forebrain, which provides the innervation activity of cholinergic neurons for the cortex, will also be affected, resulting in the reduction in cholinergic neurotransmitters. Generally, cholinergic enzyme inhibitors can be used to treat the reduction in cholinergic neurotransmitters. A Canadian butylcholinesterase inhibitor exhibited good performance for the treatment of AD symptoms. In clinical treatment, it

has been shown that this drug is suitable for the improvement of mild and moderate AD symptoms [116].

4.2. Relationship between Iron-Homeostasis-Related Proteins and AD

Oxidative stress can lead to neuronal damage; it has been observed that the disorder of iron metabolism and the expressional change in iron regulatory proteins in the iron metabolism pathway could lead to the accumulation of iron ions in the brain and induce oxidative stress, resulting in the damage of neurons [107]. Many experimental results have showed that iron accumulation in the brain of AD patients is one of the sources of brain oxidative stress, and this has a close relationship with the disorder of brain iron metabolism and some key iron homeostasis regulators, such as ferritin protein, transferrin protein, FPN, etc. [100].

4.2.1. Apolipoprotein E and AD

Apolipoprotein E (ApoE) is involved in the transport of cholesterol and other substances from the brain to the blood, including the discharge of A β protein from the brain to the blood. ApoE has three different conformations, which are encoded by *ApoE2*, *ApoE3* and *ApoE4* genes [117]. These three conformations are due to the differences in amino acid composition, resulting in differences in the structure, binding properties and multiple functions of lipoproteins. Among the three conformations, ApoE4 can lead to AD [18,118–122]. It can be seen from the extant literature that high concentrations of iron in cells will induce oxidative stress and cause damage to lipids, proteins and nucleic acids. Among them, lipid peroxidation will induce the production of 4-hydroxynonenal (4-HNE) molecules with high activity and neurotoxicity. It can combine with cysteine residues, lysine residues and histidine residues to reduce its damage to other molecules. Compared with ApoE2 and ApoE3, ApoE4 lacks cysteine amino acid and cannot clear HNE, resulting in the oxidative modification of proteins in neurons and neuronal death, increasing the risk of AD [123,124].

4.2.2. Ferroptosis and AD

Ferroptosis is an iron-dependent programmed cell death, which can lead to many diseases [125]. Ferroptosis was first described by Dixon in 2012, and is characterized by the accumulation of lipid reactive oxygen species. The experimental results show that GPX4 knockout mice exhibit neuronal necrosis, which will become more serious due to the lack of vitamin E (iron death inhibitor) in food. In contrast, inhibiting iron death can effectively improve the symptoms of AD. GPX4 is an anti-peroxidase that inhibits lipid peroxidation [101,126]. Moreover, lipid peroxidation products and 4-HNE in the AD brain have been significantly increased, indicating that ferroptosis will increase the risk of AD [127–129]. Iron induces oxidative stress, directly affecting lipids, DNA and proteins. Lipid peroxidation and iron metabolism disorder and accumulation in AD brain are also necessary conditions for ferroptosis [130]. In addition, iron ions interact with A β and Tau to induce ROS, which also leads to ferroptosis [101,129].

4.2.3. Iron Homeostasis Key Regulators and AD

Through the utilization of Western blot technology, researchers have found that in comparison with ferritin protein in the normal brain, the expression levels of ferritin protein in the brains of AD patients were increased significantly, including L-ferritin and H-ferritin proteins [36]. The ELISA results showed that the concentrations of H-ferritin and L-ferritin in the hippocampus of AD patients were three times higher than those in normal human brains. Moreover, the increases in H-ferritin and L-ferritin protein concentrations were not consistent with the increase in iron concentration, which was about 50% of the increase in iron concentration. Compared with the normal brain, the expression levels of ferrous oxidase CP increased significantly [131]. Results obtained from immunohistochemical experiments showed that the expression levels of transferrin proteins in the AD brains were also found to be increased compared with those in the normal brain [100].

However, by using Weston blot technology, it was found that the expression levels of DMT1 and FPN decreased in the AD brains compared with those of normal human brains. Due to the abnormal expression of genes related to iron metabolism, iron accumulates in AD brain and induces oxidative stress, which may damage brain neurons [36,131].

4.2.4. Furin and AD

Furin is associated with iron and A β metabolism [132]. Low concentrations of iron enhance furin enzyme activity, whereas high concentrations of iron reduce furin enzyme activity. Furin can enhance the activity of α secretory enzymes, and high concentrations of iron in cells reduce furin enzyme activity, leading to the amyloidosis pathway of APP cleaving. Recent experimental results also showed that the expression levels of furin mRNA in the brain of AD patients are lower than those of normal human brains [9,110,133].

5. Strategies for Treating AD

5.1. Iron Chelation in the Treatment of AD

Iron chelation strategy is the most direct method for limiting and redistributing iron in the system. At present, the most commonly used chelating agents are deferoxamine, deferrone and ferrite [2,134,135]. Deferoxamine is a chelating agent, recently found to exhibit good clinical manifestations. Although these chelating agents can improve the symptoms of AD caused by iron excess to a certain extent, they can also have toxic effects on the human body, such as allergic reactions, liver and kidney failure, etc. [1,136].

5.2. Regulating Iron Metabolism Pathway Proteins to Improve AD Symptoms

Fursultiamine is a small molecular substance called thiamine tetrahydrofuran disulfide, which can bind to cys326 amino acid residues of brain FPN and protect hepcidin from the endocytosis of FPN, thus improving the efflux of brain iron through this ferrous transporter. However, fursultiamine has limited functions in the body, because it can be quickly converted to ammonium sulfate, resulting in reduced iron contents in the body [137].

The anti-ferroportin antibody ly2928057 was successfully tested *in vitro*, and it has also been tested for its potential to effectively reduce iron concentrations *in vivo* by interfering with the potential regulatory mechanism of hepcidin. The specific mechanism is to regulate the BMP6 (bone morphogenetic protein 6)–SMAD signal pathway and prevent the binding of BMP6 to its receptor BMP6R [1,138]. Another way is to block the phosphorylation of SAMD with doxomorphine, so as to reduce the production of hepcidin induced by BMP6R [139]. The body has its own regulatory mechanism; therefore, the treatment of FPN or hepcidin interference is a great challenge, which is not conducive to long-term treatment.

Similar to glutathione peroxidase, ebselene, a drug containing selenium, also exhibits antioxidant effects. This drug can inhibit the absorption of iron ions through DMT1; however, it can cause cardiomyopathy [140]. Recent studies have shown that pyrazole derivatives and benzyl isothiourea have inhibitory effects on DMT1 both *in vitro* and *in vivo* [141].

5.3. Antioxidant Therapy Improves AD Symptoms

Brain iron excess induces oxidative stress through Fenton chemical reactions, which cause damage to protein, lipid and DNA [7], and lead to ryanodine-receptor-mediated calcium release under the stress, resulting in neurotoxicity [105]. Small molecular substances have been designed for ROS scavenging at fixed sites. These kinds of antioxidants enter the mitochondrial matrix driven by the mitochondrial intimal potential to scavenge active free radicals in the matrix [142]. In addition, antioxidants in food, such as tea polyphenols, can effectively improve AD symptoms through scavenging oxygen free radicals, chelating iron ions and their anti-inflammatory effects [143–145]. Other native neuroprotective compounds or species include resveratrol, curcumin, pinocembrin, caffeine, the combination of Panax ginseng, ginkgo biloba, crocus sativus [146–150]. The anti-inflammatory and

antioxidant properties of catechins in tea have been reported *in vivo* and *in vitro*, with potential for the prevention of AD symptoms [151].

Acetylcholinesterase inhibitors (AChEIs) have also been found to exhibit antioxidant effects. In 2010, Sinem et al. showed that AChEIs can reduce the levels of lipid oxidation, blood markers and nitric oxide in AD patients [152]. AChEI is the main drug for the treatment of AD, but it also has certain limitations [153].

6. Conclusions and Prospect

Iron is a rich metal element in the earth's crust. The unique redox properties of iron allow for efficient electron transfer, which is beneficial to many diverse biological reactions [154]. However, when iron metabolism in the body is unbalanced, such reactive properties of iron may also promote the generation of ROS, which will lead to the excessive accumulation of iron ions in the body [155,156]. As a result, there are fine regulatory mechanisms for iron absorption, storage and distribution in organisms. The excessive accumulation of iron induces oxidative stress reactions, which, in large doses, can be damaging to intracellular systems, including the tissues and organs of the body. Moreover, iron plays an important role in the formation of a myelin sheath in the brain and aerobic respiration in mitochondria. When brain iron metabolism is disordered, iron will be enriched in different regions of the brain, and the enriched iron will cause oxidative stress, mediate APP undergoing the amyloidosis pathway, and finally lead to the development of AD. In AD, oxidative stress caused by brain iron accumulation promotes the deposition of amyloid protein and the hyperphosphorylation of tau, which causes damage to neurons, resulting in declines in motor, cognitive and memory functions, etc. [133]. Although using iron-chelating strategies has achieved some positive results for improving the symptoms of AD, there is still much research needed in order to translate the research into practice for the clinical treatment of AD.

Nevertheless, there have been few studies on iron-reducing strategies in AD patients through genetic methods, and excessive emphasis has been put on the amyloid-reducing strategies, which have been disappointing thus far. Given that more and more iron-chelating compounds have potential disease-improving effects, as well as the availability of biomarkers of iron load in MRI and cerebrospinal fluid, there is considerable room for exploring this type of treatment to avoid its side effects as far as possible. In addition, genetic studies on the regulation of some key genes in iron homeostasis in model animals have shown potential for more effective and precise treatment [14,157].

Furthermore, AD is characterized by the progressive dysfunction and death of the cortical and hippocampal neurons; the main hypothetical mechanisms are the hyperphosphorylation of tau protein to form NFTs and the deposition of A β protein to form SPs [158,159]. However, a large number of clinical trials of drugs based on these two hypotheses all over the world have ended in failure; there is currently no effective treatment method. In addition, these two assumptions are facing increasing challenges [160,161]. In fact, the involvement of iron in the pathogenesis of AD has been widely accepted. Iron not only aggravates the accumulation of toxic A β and hyperphosphorylated tau, but also directly induces neuronal oxidative damage [162]. Considering the particularity and importance of iron role in the process of ferroptosis, it is essential to uncover how does ferroptosis play in the molecular pathophysiology of AD in the future research, which may provide new insights into the disease [163,164] and new ideas for the treatment [101]. Combining with the recent finding of a potential link among iron, host microbiome and AD, therefore, by deeply studying the mechanism of iron metabolism in the body and brain, it is expected to find new effective targets and therapeutic measures to improve or cure the disease.

Author Contributions: Concept and design: M.L. Writing, review of manuscript: Y.P. and M.L. Revision of manuscript: M.L., Y.P. and X.C. Display item design: Y.P. All authors have read and agreed to the published version of the manuscript.

Funding: This work was supported by the Fundamental Research Funds for the Central Universities, Beijing Municipal Natural Science Foundation (7202129), the Class B Breeding Program of Special Projects for Leading Science and Technology of the Chinese Academy of Sciences (XDPB16), the National Natural Science Foundation of China (31571042), the Key Basic Research Project of Applied Basic Research Program of Hebei Province (18966315D), and One Hundred Outstanding Creative Talents Support Program of Hebei (BR2-218).

Institutional Review Board Statement: Not applicable.

Informed Consent Statement: Not applicable.

Data Availability Statement: Not applicable.

Conflicts of Interest: The authors declare no conflict of interest.

Abbreviations

AD	Alzheimer's disease
CNS	central nervous system
ROS	reactive oxygen species
NFTs	neurofibrillary tangles
DCYTB	duodenal cytochrome-b-like protein
DMT1	divalent metal transporter1
FPN	ferroportin
TF	transferrin
TfR1	transferrin receptor 1
STEAP	six-transmembrane epithelial antigen of prostate
IRPs	iron regulatory proteins
IRE	iron regulatory element
BBB	blood–brain barrier
BBSCB	blood–brain spinal cord barrier
CP	ceruloplasmin
MRI	magnetic resonance imaging
RNS	reactive nitrogen species
HO-1	heme oxygenase-1
APP	amyloid precursor protein
ApoE	apolipoprotein E
4-HNE	4-hydroxynonenal
BMP6	bone morphogenetic protein 6
AChEI	acetylcholinesterase inhibitor

References

1. Galaris, D.; Barbouti, A.; Pantopoulos, K. Iron homeostasis and oxidative stress: An intimate relationship. *Biochim. Biophys. Acta Mol. Cell Res.* **2019**, *1866*, 118535. [CrossRef] [PubMed]
2. Evstatiev, R.; Gasche, C. Iron sensing and signalling. *Gut* **2012**, *61*, 933–952. [CrossRef] [PubMed]
3. Conway, D.; Henderson, M.A. Iron metabolism. *Anaesth. Intensive Care Med.* **2019**, *20*, 175–177. [CrossRef]
4. Lane, D.J.R.; Ayton, S.; Bush, A.I. Iron and Alzheimer's Disease: An Update on Emerging Mechanisms. *J. Alzheimers Dis.* **2018**, *64*, S379–S395. [CrossRef] [PubMed]
5. Ashraf, A.; Clark, M.; So, P.W. The Aging of Iron Man. *Front. Aging Neurosci.* **2018**, *10*, 65. [CrossRef] [PubMed]
6. Jomova, K.; Valko, M. Advances in metal-induced oxidative stress and human disease. *Toxicology* **2011**, *283*, 65–87. [CrossRef]
7. Papanikolaou, G.; Pantopoulos, K. Iron metabolism and toxicity. *Toxicol. Appl. Pharmacol.* **2005**, *202*, 199–211. [CrossRef]
8. Ward, R.J.; Zucca, F.A.; Duyn, J.H.; Crichton, R.R.; Zecca, L. The role of iron in brain ageing and neurodegenerative disorders. *Lancet Neurol.* **2014**, *13*, 1045–1060. [CrossRef]
9. Cassidy, L.; Fernandez, F.; Johnson, J.B.; Naiker, M.; Owoola, A.G.; Broszczak, D.A. Oxidative stress in alzheimer's disease: A review on emergent natural polyphenolic therapeutics. *Complement. Ther. Med.* **2020**, *49*, 102294. [CrossRef]
10. Oboudiyat, C.; Glazer, H.; Seifan, A.; Greer, C.; Isaacson, R.S. Alzheimer's disease. *Semin. Neurol.* **2013**, *33*, 313–329. [CrossRef]
11. Jalili-Baleh, L.; Babaei, E.; Abdpour, S.; Nasir Abbas Bukhari, S.; Foroumadi, A.; Ramazani, A.; Sharifzadeh, M.; Abdollahi, M.; Khoobi, M. A review on flavonoid-based scaffolds as multi-target-directed ligands (MTDLs) for Alzheimer's disease. *Eur. J. Med. Chem.* **2018**, *152*, 570–589. [CrossRef]
12. Brody, H. Alzheimer's disease. *Nature* **2011**, *475*, S1. [CrossRef] [PubMed]

13. Power, R.; Prado-Cabrero, A.; Mulcahy, R.; Howard, A.; Nolan, J.M. The Role of Nutrition for the Aging Population: Implications for Cognition and Alzheimer's Disease. *Annu. Rev. Food Sci. Technol.* **2019**, *10*, 619–639. [CrossRef] [PubMed]
14. Ranasinghe, K.G.; Cha, J.; Iaccarino, L.; Hinkley, L.B.; Beagle, A.J.; Pham, J.; Jagust, W.J.; Miller, B.L.; Rankin, K.P.; Rabinovici, G.D.; et al. Neurophysiological signatures in Alzheimer's disease are distinctly associated with TAU, amyloid-beta accumulation, and cognitive decline. *Sci. Transl. Med.* **2020**, *12*, 534. [CrossRef]
15. Briggs, R.; Kennelly, S.P.; O'Neill, D. Drug treatments in Alzheimer's disease. *Clin. Med.* **2016**, *16*, 247–253. [CrossRef] [PubMed]
16. Mandel, S.; Amit, T.; Bar-Am, O.; Youdim, M.B. Iron dysregulation in Alzheimer's disease: Multimodal brain permeable iron chelating drugs, possessing neuroprotective-neurorescue and amyloid precursor protein-processing regulatory activities as therapeutic agents. *Prog. Neurobiol.* **2007**, *82*, 348–360. [CrossRef] [PubMed]
17. Belaidi, A.A.; Bush, A.I. Iron neurochemistry in Alzheimer's disease and Parkinson's disease: Targets for therapeutics. *J. Neurochem.* **2016**, *139* (Suppl. S1), 179–197. [CrossRef]
18. Bush, A.I. The metallobiology of Alzheimer's disease. *Trends Neurosci.* **2003**, *26*, 207–214. [CrossRef]
19. Andrews, N.C. *Iron Metabolism*, in *Principles of Molecular Medicine*; Runge, M.S., Patterson, C., Eds.; Humana Press: Totowa, NJ, USA, 2006; pp. 848–853.
20. Ganz, T. Systemic iron homeostasis. *Physiol. Rev.* **2013**, *93*, 1721–1741. [CrossRef]
21. Arosio, P.; Levi, S. Cytosolic and mitochondrial ferritins in the regulation of cellular iron homeostasis and oxidative damage. *Biochim. Biophys. Acta* **2010**, *1800*, 783–792. [CrossRef]
22. Theil, E.C. Ferritin: At the crossroads of iron and oxygen metabolism. *J. Nutr.* **2003**, *133* (Suppl. S1), 1549S–1553S. [CrossRef] [PubMed]
23. Oshiro, S.; Morioka, M.S.; Kikuchi, M. Dysregulation of iron metabolism in Alzheimer's disease, Parkinson's disease, and amyotrophic lateral sclerosis. *Adv. Pharmacol. Sci.* **2011**, *2011*, 378278. [CrossRef]
24. Nemeth, E.; Tuttle, M.S.; Powelson, J.; Vaughn, M.B.; Donovan, A.; Ward, D.M.; Ganz, T.; Kaplan, J. Hepcidin regulates cellular iron efflux by binding to ferroportin and inducing its internalization. *Science* **2004**, *306*, 2090–2093. [CrossRef]
25. Ganz, T. Cellular iron: Ferroportin is the only way out. *Cell Metab.* **2005**, *1*, 155–157. [CrossRef] [PubMed]
26. Mayle, K.M.; Le, A.M.; Kamei, D.T. The intracellular trafficking pathway of transferrin. *Biochim. Biophys. Acta* **2012**, *1820*, 264–281. [CrossRef] [PubMed]
27. Lane, D.J.; Merlot, A.M.; Huang, M.L.; Bae, D.H.; Jansson, P.J.; Sahni, S.; Kalinowski, D.S.; Richardson, D.R. Cellular iron uptake, trafficking and metabolism: Key molecules and mechanisms and their roles in disease. *Biochim. Biophys. Acta* **2015**, *1853*, 1130–1144. [CrossRef]
28. Zhou, Z.D.; Tan, E.K. Iron regulatory protein (IRP)-iron responsive element (IRE) signaling pathway in human neurodegenerative diseases. *Mol. Neurodegener.* **2017**, *12*, 75. [CrossRef] [PubMed]
29. Hentze, M.W.; Muckenthaler, M.U.; Galy, B.; Camaschella, C. Two to tango: Regulation of Mammalian iron metabolism. *Cell* **2010**, *142*, 24–38. [CrossRef]
30. Knutson, M.D. Steap proteins: Implications for iron and copper metabolism. *Nutr. Rev.* **2007**, *65*, 335–340.
31. Sendamarai, A.K.; Ohgami, R.S.; Fleming, M.D.; Lawrence, C.M. Structure of the membrane proximal oxidoreductase domain of human Steap3, the dominant ferrireductase of the erythroid transferrin cycle. *Proc. Natl. Acad. Sci. USA* **2008**, *105*, 7410–7415. [CrossRef]
32. Crielaard, B.J.; Lammers, T.; Rivella, S. Targeting iron metabolism in drug discovery and delivery. *Nat. Rev. Drug Discov.* **2017**, *16*, 400–423. [CrossRef] [PubMed]
33. Upadhyay, M.; Agarwal, S. Ironing the mitochondria: Relevance to its dynamics. *Mitochondrion* **2020**, *50*, 82–87. [CrossRef]
34. Ganz, T.; Nemeth, E. Hepcidin and iron homeostasis. *Biochim. Biophys. Acta* **2012**, *1823*, 1434–1443. [CrossRef]
35. Cohen, L.A.; Gutierrez, L.; Weiss, A.; Leichtmann-Bardoogo, Y.; Zhang, D.L.; Crooks, D.R.; Sougrat, R.; Morgenstern, A.; Galy, B.; Hentze, M.W.; et al. Serum ferritin is derived primarily from macrophages through a nonclassical secretory pathway. *Blood* **2010**, *116*, 1574–1584. [CrossRef] [PubMed]
36. Zecca, L.; Youdim, M.B.; Riederer, P.; Connor, J.R.; Crichton, R.R. Iron, brain ageing and neurodegenerative disorders. *Nat. Rev. Neurosci.* **2004**, *5*, 863–873. [CrossRef]
37. Liu, Z.; Shen, H.C.; Lian, T.H.; Mao, L.; Tang, S.X.; Sun, L.; Huang, X.Y.; Guo, P.; Cao, C.J.; Yu, S.Y.; et al. Iron deposition in substantia nigra: Abnormal iron metabolism, neuroinflammatory mechanism and clinical relevance. *Sci. Rep.* **2017**, *7*, 14973. [CrossRef] [PubMed]
38. Meneghini, R. Iron Homeostasis, Oxidative Stress, and DNA Damage. *Free. Radic. Biol. Med.* **1997**, *23*, 783–792. [CrossRef]
39. Andrews, N.C. Molecular control of iron metabolism. *Best Pract. Res. Clin. Haematol.* **2005**, *18*, 159–169. [CrossRef] [PubMed]
40. Patel, S.J.; Frey, A.G.; Palenchar, D.J.; Achar, S.; Bullough, K.Z.; Vashisht, A.; Wohlschlegel, J.A.; Philpott, C.C. A PCBP1-BolA2 chaperone complex delivers iron for cytosolic [2Fe-2S] cluster assembly. *Nat. Chem. Biol.* **2019**, *15*, 872–881. [CrossRef] [PubMed]
41. Valko, M.; Leibfritz, D.; Moncol, J.; Cronin, M.T.; Mazur, M.; Telser, J. Free radicals and antioxidants in normal physiological functions and human disease. *Int. J. Biochem. Cell Biol.* **2007**, *39*, 44–84. [CrossRef]
42. Rishi, G.; Subramaniam, V.N. The liver in regulation of iron homeostasis. *Am. J. Physiol. Gastrointest. Liver Physiol.* **2017**, *313*, G157–G165. [CrossRef] [PubMed]
43. van Swelm, R.P.L.; Wetzels, J.F.M.; Swinkels, D.W. The multifaceted role of iron in renal health and disease. *Nat. Rev. Nephrol.* **2020**, *16*, 77–98. [CrossRef]

44. Stankiewicz, J.M.; Neema, M.; Ceccarelli, A. Iron and multiple sclerosis. *Neurobiol. Aging* **2014**, *35* (Suppl. S2), S51–S58. [CrossRef] [PubMed]
45. Leipuviene, R.; Theil, E.C. The family of iron responsive RNA structures regulated by changes in cellular iron and oxygen. *Cell Mol. Life Sci.* **2007**, *64*, 2945–2955. [CrossRef] [PubMed]
46. Pantopoulos, K.; Porwal, S.K.; Tartakoff, A.; Devireddy, L. Mechanisms of mammalian iron homeostasis. *Biochemistry* **2012**, *51*, 5705–5724. [CrossRef]
47. Sousa, L.; Oliveira, M.M.; Pessôa, M.T.C.; Barbosa, L.A. Iron overload: Effects on cellular biochemistry. *Clin. Chim. Acta* **2020**, *504*, 180–189. [CrossRef]
48. Pantopoulos, K. Iron metabolism and the IRE/IRP regulatory system: An update. *Ann. N. Y. Acad. Sci.* **2004**, *1012*, 1–13. [CrossRef]
49. Hin, N.; Newman, M.; Pederson, S.; Lardelli, M. Iron Responsive Element (IRE)-mediated responses to iron dyshomeostasis in Alzheimer's disease. *bioRxiv* **2021**. [CrossRef]
50. Everett, J.; Céspedes, E.; Shelford, L.R.; Exley, C.; Collingwood, J.F.; Dobson, J.; van der Laan, G.; Jenkins, C.A.; Arenholz, E.; Telling, N.D. Ferrous iron formation following the co-aggregation of ferric iron and the Alzheimer's disease peptide beta-amyloid (1–42). *J. R. Soc. Interface* **2014**, *11*, 20140165. [CrossRef]
51. Kuhn, L.C. Iron regulatory proteins and their role in controlling iron metabolism. *Metallomics* **2015**, *7*, 232–243. [CrossRef]
52. Thomson, A.M.; Rogers, J.T.; Leedman, P.J. Iron-regulatory proteins, iron-responsive elements and ferritin mRNA translation. *Int. J. Biochem. Cell Biol.* **1999**, *31*, 1139–1152. [CrossRef]
53. Rouault, T.A. The role of iron regulatory proteins in mammalian iron homeostasis and disease. *Nat. Chem. Biol.* **2006**, *2*, 406–414. [CrossRef] [PubMed]
54. Wang, L.; Liu, X.; You, L.H.; Ci, Y.Z.; Chang, S.; Yu, P.; Gao, G.; Chang, Y.Z. Heparin and iron regulatory proteins coordinately regulate ferroportin 1 expression in the brain of mice. *J. Cell. Physiol.* **2019**, *234*, 7600–7607. [CrossRef]
55. Ganz, T. Heparin, a key regulator of iron metabolism and mediator of anemia of inflammation. *Blood* **2003**, *102*, 783–788. [CrossRef]
56. Knutson, M.D. Iron-sensing proteins that regulate hepcidin and enteric iron absorption. *Annu. Rev. Nutr.* **2010**, *30*, 149–171. [CrossRef]
57. Oates, P.S. The role of hepcidin and ferroportin in iron absorption. *Histol. Histopathol.* **2007**, *22*, 791–804. [PubMed]
58. Hunter, H.N.; Fulton, D.B.; Ganz, T.; Vogel, H.J. The solution structure of human hepcidin, a peptide hormone with antimicrobial activity that is involved in iron uptake and hereditary hemochromatosis. *J. Biol. Chem.* **2002**, *277*, 37597–37603. [CrossRef] [PubMed]
59. Qiao, B.; Sugianto, P.; Fung, E.; Del-Castillo-Rueda, A.; Moran-Jimenez, M.J.; Ganz, T.; Nemeth, E. Heparin-induced endocytosis of ferroportin is dependent on ferroportin ubiquitination. *Cell Metab.* **2012**, *15*, 918–924. [CrossRef] [PubMed]
60. Liu, X.B.; Nguyen, N.B.; Marquess, K.D.; Yang, F.; Haile, D.J. Regulation of hepcidin and ferroportin expression by lipopolysaccharide in splenic macrophages. *Blood Cells Mol. Dis.* **2005**, *35*, 47–56. [CrossRef] [PubMed]
61. Merle, U.; Fein, E.; Gehrke, S.G.; Stremmel, W.; Kulaksiz, H. The iron regulatory peptide hepcidin is expressed in the heart and regulated by hypoxia and inflammation. *Endocrinology* **2007**, *148*, 2663–2668. [CrossRef]
62. Nguyen, N.B.; Callaghan, K.D.; Ghio, A.J.; Haile, D.J.; Yang, F. Heparin expression and iron transport in alveolar macrophages. *Am. J. Physiol. Lung Cell. Mol. Physiol.* **2006**, *291*, L417–L425. [CrossRef]
63. Ganz, T.; Nemeth, E. Iron homeostasis in host defence and inflammation. *Nat. Rev. Immunol.* **2015**, *15*, 500–510. [CrossRef] [PubMed]
64. Seyoum, Y.; Baye, K.; Humblot, C. Iron homeostasis in host and gut bacteria—A complex interrelationship. *Gut Microbes.* **2021**, *13*, 1–19. [CrossRef]
65. Sun, P.; Sun, P.; Su, L.; Zhu, H.; Li, X.; Guo, Y.; Du, X.; Zhang, L.; Qin, C. Gut Microbiota Regulation and Their Implication in the Development of Neurodegenerative Disease. *Microorganisms* **2021**, *9*, 11. [CrossRef]
66. Lee, G.A.; Lin, Y.K.; Lai, J.H.; Lo, Y.C.; Yang, Y.S.H.; Ye, S.Y.; Lee, C.J.; Wang, C.C.; Chiang, Y.H.; Tseng, S.H. Maternal Immune Activation Causes Social Behavior Deficits and Hypomyelination in Male Rat Offspring with an Autism-Like Microbiota Profile. *Brain Sci.* **2021**, *11*, 8. [CrossRef] [PubMed]
67. Gonzalez-Sanmiguel, J.; Schuh, C.; Muñoz-Montesino, C.; Contreras-Kallens, P.; Aguayo, L.G.; Aguayo, S. Complex Interaction between Resident Microbiota and Misfolded Proteins: Role in Neuroinflammation and Neurodegeneration. *Cells* **2020**, *9*, 11. [CrossRef]
68. Ndayisaba, A.; Kaindlstorfer, C.; Wenning, G.K. Iron in Neurodegeneration—Cause or Consequence? *Front. Neurosci.* **2019**, *13*, 180. [CrossRef] [PubMed]
69. Daneman, R.; Prat, A. The blood-brain barrier. *Cold Spring Harb. Perspect. Biol.* **2015**, *7*, a020412. [CrossRef]
70. Camandola, S.; Mattson, M.P. Brain metabolism in health, aging, and neurodegeneration. *EMBO J.* **2017**, *36*, 1474–1492. [CrossRef]
71. Rouault, T.A. Iron metabolism in the CNS: Implications for neurodegenerative diseases. *Nat. Rev. Neurosci.* **2013**, *14*, 551–564. [CrossRef]
72. Rouault, T.A.; Cooperman, S. Brain iron metabolism. *Semin. Pediatr. Neurol.* **2006**, *13*, 142–148. [CrossRef] [PubMed]
73. Patel, B.N.; Dunn, R.J.; Jeong, S.Y.; Zhu, Q.; Julien, J.P.; David, S. Ceruloplasmin Regulates Iron Levels in the CNS and Prevents Free Radical Injury. *J. Neurosci.* **2002**, *22*, 6578–6586. [CrossRef] [PubMed]

74. Chiou, B.; Neal, E.H.; Bowman, A.B.; Lippmann, E.S.; Simpson, I.A.; Connor, J.R. Endothelial cells are critical regulators of iron transport in a model of the human blood-brain barrier. *J. Cereb. Blood Flow Metab.* **2019**, *39*, 2117–2131. [CrossRef]
75. Rouault, T.A. Post-transcriptional regulation of human iron metabolism by iron regulatory proteins. *Blood Cells Mol. Dis.* **2002**, *29*, 309–314. [CrossRef] [PubMed]
76. Meyron-Holtz, E.G.; Ghosh, M.C.; Iwai, K.; LaVaute, T.; Brazzolotto, X.; Berger, U.V.; Land, W.; Ollivierre-Wilson, H.; Grinberg, A.; Love, P.; et al. Genetic ablations of iron regulatory proteins 1 and 2 reveal why iron regulatory protein 2 dominates iron homeostasis. *EMBO J.* **2004**, *23*, 386–395. [CrossRef]
77. Gerlach, M.; Ben-Shachar, D.; Riederer, P.; Youdim, M.B. Altered brain metabolism of iron as a cause of neurodegenerative diseases? *J. Neurochem.* **1994**, *63*, 793–807. [CrossRef] [PubMed]
78. Ayton, S.; Lei, P. Nigral iron elevation is an invariable feature of Parkinson’s disease and is a sufficient cause of neurodegeneration. *BioMed Res. Int.* **2014**, *2014*, 581256. [CrossRef] [PubMed]
79. Xiong, H.; Tuo, Q.Z.; Guo, Y.J.; Lei, P. Diagnostics and Treatments of Iron-Related CNS Diseases. *Adv. Exp. Med. Biol.* **2019**, *1173*, 179–194.
80. Zecca, L.; Pietra, R.; Goj, C.; Mecacci, C.; Radice, D.; Sabbioni, E. Iron and other metals in neuromelanin, substantia nigra, and putamen of human brain. *J. Neurochem.* **1994**, *62*, 1097–1101. [CrossRef]
81. Zecca, L.; Shima, T.; Stroppolo, A.; Goj, C.; Battiston, G.A.; Gerbasi, R.; Sarna, T.; Swartz, H.M. Interaction of neuromelanin and iron in substantia nigra and other areas of human brain. *Neuroscience* **1996**, *73*, 407–415. [CrossRef]
82. Zecca, L.; Gallorini, M.; Schünemann, V.; Trautwein, A.X.; Gerlach, M.; Riederer, P.; Vezzoni, P.; Tampellini, D. Iron, neuromelanin and ferritin content in the substantia nigra of normal subjects at different ages: Consequences for iron storage and neurodegenerative processes. *J. Neurochem.* **2001**, *76*, 1766–1773. [CrossRef]
83. Minotti, G.; Aust, S.D. Redox cycling of iron and lipid-peroxidation. *Lipids* **1992**, *27*, 219–226. [CrossRef]
84. Leitao, E.F.V.; Ventura, E.; de Souza, M.A.F.; Riveros, J.M.; do Monte, S.A. Spin-Forbidden Branching in the Mechanism of the Intrinsic Haber-Weiss Reaction. *ChemistryOpen* **2017**, *6*, 360–363. [CrossRef]
85. Farina, M.; Avila, D.S.; da Rocha, J.B.; Aschner, M. Metals, oxidative stress and neurodegeneration: A focus on iron, manganese and mercury. *Neurochem. Int.* **2013**, *62*, 575–594. [CrossRef]
86. Pham-Huy, L.A.; He, H.; Pham-Huy, C. Free radicals, antioxidants in disease and health. *Int. J. Biomed. Sci. IJBS* **2008**, *4*, 89. [PubMed]
87. Kent, S.A.; Spire-Jones, T.L.; Durrant, C.S. The physiological roles of tau and Aβeta: Implications for Alzheimer’s disease pathology and therapeutics. *Acta Neuropathol.* **2020**, *140*, 417–447. [CrossRef] [PubMed]
88. Skovronsky, D.M.; Lee, V.M.; Trojanowski, J.Q. Neurodegenerative diseases: New concepts of pathogenesis and their therapeutic implications. *Annu. Rev. Pathol.* **2006**, *1*, 151–170. [CrossRef] [PubMed]
89. McKhann, G.; Drachman, D.; Folstein, M.; Katzman, R.; Price, D.; Stadlan, E.M. Clinical diagnosis of Alzheimer’s disease: Report of the NINCDS-ADRDA Work Group under the auspices of Department of Health and Human Services Task Force on Alzheimer’s Disease. *Neurology* **1984**, *34*, 939–944. [CrossRef]
90. Frisoni, G.B.; Boccardi, M.; Barkhof, F.; Blennow, K.; Cappa, S.; Chiotis, K.; Démonet, J.F.; Garibotto, V.; Giannakopoulos, P.; Gietl, A.; et al. Strategic roadmap for an early diagnosis of Alzheimer’s disease based on biomarkers. *Lancet Neurol.* **2017**, *16*, 661–676. [CrossRef]
91. Long, J.M.; Maloney, B.; Rogers, J.T.; Lahiri, D.K. Novel upregulation of amyloid-beta precursor protein (APP) by microRNA-346 via targeting of APP mRNA 5'-untranslated region: Implications in Alzheimer’s disease. *Mol. Psychiatry* **2019**, *24*, 345–363. [CrossRef] [PubMed]
92. Smith, M.A.; Harris, P.L.; Sayre, L.M.; Perry, G. Iron accumulation in Alzheimer disease is a source of redox-generated free radicals. *Proc. Natl. Acad. Sci. USA* **1997**, *94*, 9866–9868. [CrossRef]
93. Altamura, S.; Muckenthaler, M.U. Iron toxicity in diseases of aging: Alzheimer’s disease, Parkinson’s disease and atherosclerosis. *J. Alzheimers Dis.* **2009**, *16*, 879–895. [CrossRef]
94. Hare, D.; Ayton, S.; Bush, A.; Lei, P. A delicate balance: Iron metabolism and diseases of the brain. *Front. Aging Neurosci.* **2013**, *5*, 34. [CrossRef]
95. Sengoku, R. Aging and Alzheimer’s disease pathology. *Neuropathology* **2020**, *40*, 22–29. [CrossRef]
96. Ashrafian, H.; Zadeh, E.H.; Khan, R.H. Review on Alzheimer’s disease: Inhibition of amyloid beta and tau tangle formation. *Int. J. Biol. Macromol.* **2021**, *167*, 382–394. [CrossRef]
97. Kozlov, S.; Afonin, A.; Evsyukov, I.; Bondarenko, A. Alzheimer’s disease: As it was in the beginning. *Rev. Neurosci.* **2017**, *28*, 825–843. [CrossRef] [PubMed]
98. Cogswell, P.M.; Wiste, H.J.; Senjem, M.L.; Gunter, J.L.; Weigand, S.D.; Schwarz, C.G.; Arani, A.; Therneau, T.M.; Lowe, V.J.; Knopman, D.S.; et al. Associations of quantitative susceptibility mapping with Alzheimer’s disease clinical and imaging markers. *NeuroImage* **2021**, *224*, 117433. [CrossRef] [PubMed]
99. Gong, N.J.; Dibb, R.; Bulk, M.; van der Weerd, L.; Liu, C. Imaging beta amyloid aggregation and iron accumulation in Alzheimer’s disease using quantitative susceptibility mapping MRI. *NeuroImage* **2019**, *191*, 176–185. [CrossRef]
100. Connor, J.R.; Menzies, S.L.; St Martin, S.M.; Mufson, E.J. A histochemical study of iron, transferrin, and ferritin in Alzheimer’s diseased brains. *J. Neurosci. Res.* **1992**, *31*, 75–83. [CrossRef] [PubMed]

101. Yan, N.; Zhang, J. Iron Metabolism, Ferroptosis, and the Links With Alzheimer's Disease. *Front. Neurosci.* **2019**, *13*, 1443. [CrossRef]
102. Spotorno, N.; Acosta-Cabrero, J.; Stomrud, E.; Lampinen, B.; Strandberg, O.T.; van Westen, D.; Hansson, O. Relationship between cortical iron and tau aggregation in Alzheimer's disease. *Brain* **2020**, *143*, 1341–1349. [CrossRef] [PubMed]
103. Borthakur, A.; Gur, T.; Wheaton, A.J.; Corbo, M.; Trojanowski, J.Q.; Lee, V.M.; Reddy, R. In vivo measurement of plaque burden in a mouse model of Alzheimer's disease. *J. Magn. Reson. Imaging* **2006**, *24*, 1011–1017. [CrossRef] [PubMed]
104. Agostinho, P.; Cunha, R.A.; Oliveira, C. Neuroinflammation, oxidative stress and the pathogenesis of Alzheimer's disease. *Curr. Pharm. Des.* **2010**, *16*, 2766–2778. [CrossRef] [PubMed]
105. Lee, D.G.; Kam, M.K.; Lee, S.R.; Lee, H.J.; Lee, D.S. Peroxiredoxin 5 deficiency exacerbates iron overload-induced neuronal death via ER-mediated mitochondrial fission in mouse hippocampus. *Cell Death Dis.* **2020**, *11*, 204. [CrossRef]
106. Bandyopadhyay, S.; Rogers, J.T. Alzheimer's disease therapeutics targeted to the control of amyloid precursor protein translation: Maintenance of brain iron homeostasis. *Biochem. Pharmacol.* **2014**, *88*, 486–494. [CrossRef]
107. Cheignon, C.; Tomas, M.; Bonnefont-Rousselot, D.; Faller, P.; Hureau, C.; Collin, F. Oxidative stress and the amyloid beta peptide in Alzheimer's disease. *Redox Biol.* **2018**, *14*, 450–464. [CrossRef]
108. Grundkeiqlbal, I.; Fleming, J.; Tung, Y.C.; Lassmann, H.; Iqbal, K.; Joshi, J.G. Ferritin is a component of the neuritic (senile) plaque in Alzheimer dementia. *Acta Neuropathol.* **1990**, *81*, 105–110. [CrossRef] [PubMed]
109. Boopathi, S.; Kolandaivel, P. Fe²⁺ binding on amyloid beta-peptide promotes aggregation. *Proteins* **2016**, *84*, 1257–1274. [CrossRef]
110. Guillemot, J.; Canuel, M.; Essalmani, R.; Prat, A.; Seidah, N.G. Implication of the proprotein convertases in iron homeostasis: Proprotein convertase 7 sheds human transferrin receptor 1 and furin activates hepcidin. *Hepatology* **2013**, *57*, 2514–2524. [CrossRef]
111. Prasanna, G.; Jing, P. Self-assembly of N-terminal Alzheimer's beta-amyloid and its inhibition. *Biochem. Biophys. Res. Commun.* **2021**, *534*, 950–956. [CrossRef]
112. Rogers, J.T.; Bush, A.I.; Cho, H.H.; Smith, D.H.; Thomson, A.M.; Friedlich, A.L.; Lahiri, D.K.; Leedman, P.J.; Huang, X.; Cahill, C.M. Iron and the translation of the amyloid precursor protein (APP) and ferritin mRNAs: Riboregulation against neural oxidative damage in Alzheimer's disease. *Biochem. Soc. Trans.* **2008**, *36 Pt 6*, 1282–1287. [CrossRef] [PubMed]
113. Wilkins, H.M.; Swerdlow, R.H. Amyloid precursor protein processing and bioenergetics. *Brain Res. Bull.* **2017**, *133*, 71–79. [CrossRef] [PubMed]
114. Dawkins, E.; Small, D.H. Insights into the physiological function of the beta-amyloid precursor protein: Beyond Alzheimer's disease. *J. Neurochem.* **2014**, *129*, 756–769. [CrossRef] [PubMed]
115. Rogers, J.T.; Venkataramani, V.; Washburn, C.; Liu, Y.; Tummala, V.; Jiang, H.; Smith, A.; Cahill, C.M. A role for amyloid precursor protein translation to restore iron homeostasis and ameliorate lead (Pb) neurotoxicity. *J. Neurochem.* **2016**, *138*, 479–494. [CrossRef] [PubMed]
116. Munoz, D.G.; Feldman, H. Causes of Alzheimer's disease. *CMAJ* **2000**, *162*, 65–72.
117. Alzheimer's, A. 2016 Alzheimer's disease facts and figures. *Alzheimers Dement.* **2016**, *12*, 459–509. [CrossRef]
118. Yamazaki, Y.; Zhao, N.; Caulfield, T.R.; Liu, C.C.; Bu, G. Apolipoprotein E and Alzheimer disease: Pathobiology and targeting strategies. *Nat. Rev. Neurol.* **2019**, *15*, 501–518. [CrossRef] [PubMed]
119. Corder, E.H.; Saunders, A.M.; Strittmatter, W.J.; Schmechel, D.E.; Gaskell, P.C.; Small, G.W.; Roses, A.D.; Haines, J.L.; Pericak-Vance, M.A. Gene dose of apolipoprotein E type 4 allele and the risk of Alzheimer's disease in late onset families. *Science* **1993**, *261*, 921–923. [CrossRef]
120. Saunders, A.M.; Strittmatter, W.J.; Schmechel, D.; George-Hyslop, P.H.; Pericak-Vance, M.A.; Joo, S.H.; Rosi, B.L.; Gusella, J.F.; Crapper-MacLachlan, D.R.; Alberts, M.J.; et al. Association of apolipoprotein E allele epsilon 4 with late-onset familial and sporadic Alzheimer's disease. *Neurology* **1993**, *43*, 1467–1472. [CrossRef]
121. Reiman, E.M.; Chen, K.; Liu, X.; Bandy, D.; Yu, M.; Lee, W.; Ayutyanont, N.; Keppler, J.; Reeder, S.A.; Langbaum, J.B.; et al. Fibrillar amyloid-beta burden in cognitively normal people at 3 levels of genetic risk for Alzheimer's disease. *Proc. Natl. Acad. Sci. USA* **2009**, *106*, 6820–6825. [CrossRef]
122. Aytun, S.; Faux, N.G.; Bush, A.I. Ferritin levels in the cerebrospinal fluid predict Alzheimer's disease outcomes and are regulated by APOE. *Nat. Commun.* **2015**, *6*, 6760. [CrossRef]
123. Butterfield, D.A.; Mattson, M.P. Apolipoprotein E and oxidative stress in brain with relevance to Alzheimer's disease. *Neurobiol. Dis.* **2020**, *138*, 104795. [CrossRef]
124. The Need for Early Detection and Treatment in Alzheimer's Disease. *EBioMedicine* **2016**, *9*, 1–2. [CrossRef]
125. Dixon, S.J.; Lemberg, K.M.; Lamprecht, M.R.; Skouta, R.; Zaitsev, E.M.; Gleason, C.E.; Patel, D.N.; Bauer, A.J.; Cantley, A.M.; Yang, W.S.; et al. Ferroptosis: An iron-dependent form of nonapoptotic cell death. *Cell* **2012**, *149*, 1060–1072. [CrossRef]
126. Cozza, G.; Rossetto, M.; Bosello-Travain, V.; Maiorino, M.; Roveri, A.; Toppo, S.; Zaccarin, M.; Zennaro, L.; Ursini, F. Glutathione peroxidase 4-catalyzed reduction of lipid hydroperoxides in membranes: The polar head of membrane phospholipids binds the enzyme and addresses the fatty acid hydroperoxide group toward the redox center. *Free Radic. Biol. Med.* **2017**, *112*, 1–11. [CrossRef] [PubMed]
127. Li, J.; Cao, F.; Yin, H.L.; Huang, Z.J.; Lin, Z.T.; Mao, N.; Sun, B.; Wang, G. Ferroptosis: Past, present and future. *Cell Death Dis.* **2020**, *11*, 88. [CrossRef]

128. Chen, X.; Li, J.; Kang, R.; Klionsky, D.J.; Tang, D. Ferroptosis: Machinery and regulation. *Autophagy* **2021**, *17*, 2054–2081. [CrossRef] [PubMed]
129. Derry, P.J.; Hegde, M.L.; Jackson, G.R.; Kaye, R.; Tour, J.M.; Tsai, A.L.; Kent, T.A. Revisiting the intersection of amyloid, pathologically modified tau and iron in Alzheimer’s disease from a ferroptosis perspective. *Prog. Neurobiol.* **2020**, *184*, 101716. [CrossRef]
130. Weiland, A.; Wang, Y.; Wu, W.; Lan, X.; Han, X.; Li, Q.; Wang, J. Ferroptosis and Its Role in Diverse Brain Diseases. *Mol. Neurobiol.* **2019**, *56*, 4880–4893. [CrossRef] [PubMed]
131. Ashraf, A.; Jeandriens, J.; Parkes, H.G.; So, P.W. Iron dyshomeostasis, lipid peroxidation and perturbed expression of cystine/glutamate antiporter in Alzheimer’s disease: Evidence of ferroptosis. *Redox Biol.* **2020**, *32*, 101494. [CrossRef]
132. Silvestri, L.; Camaschella, C. A potential pathogenetic role of iron in Alzheimer’s disease. *J. Cell. Mol. Med.* **2008**, *12*, 1548–1550. [CrossRef] [PubMed]
133. Choi, D.H.; Kwon, K.C.; Hwang, D.J.; Koo, J.H.; Um, H.S.; Song, H.S.; Kim, J.S.; Jang, Y.; Cho, J.Y. Treadmill Exercise Alleviates Brain Iron Dyshomeostasis Accelerating Neuronal Amyloid-beta Production, Neuronal Cell Death, and Cognitive Impairment in Transgenic Mice Model of Alzheimer’s Disease. *Mol. Neurobiol.* **2021**, *58*, 3208–3223. [CrossRef]
134. Amit, T.; Avramovich-Tirosh, Y.; Youdim, M.B.; Mandel, S. Targeting multiple Alzheimer’s disease etiologies with multimodal neuroprotective and neurorestorative iron chelators. *FASEB J.* **2008**, *22*, 1296–1305. [CrossRef]
135. Robert, A.; Liu, Y.; Nguyen, M.; Meunier, B. Regulation of copper and iron homeostasis by metal chelators: A possible chemotherapy for Alzheimer’s disease. *Acc. Chem. Res.* **2015**, *48*, 1332–1339. [CrossRef]
136. Kontoghiorghes, C.N.; Kontoghiorghes, G.J. New developments and controversies in iron metabolism and iron chelation therapy. *World J. Methodol.* **2016**, *6*, 1–19. [CrossRef] [PubMed]
137. Sebastiani, G.; Wilkinson, N.; Pantopoulos, K. Pharmacological Targeting of the Hepcidin/Ferroportin Axis. *Front. Pharmacol.* **2016**, *7*, 160. [CrossRef] [PubMed]
138. Witcher, D.R.; Leung, D.; Hill, K.A.; De Rosa, D.C.; Xu, J.; Manetta, J.; Wroblewski, V.J.; Benschop, R.J. LY2928057, An Antibody Targeting Ferroportin, Is a Potent Inhibitor Of Hepcidin Activity and Increases Iron Mobilization In Normal Cynomolgus Monkeys. *Blood* **2013**, *122*, 3433. [CrossRef]
139. Sheetz, M.; Barrington, P.; Callies, S.; Berg, P.H.; McColm, J.; Marbury, T.; Decker, B.; Dyas, G.L.; Truhlar, S.M.E.; Benschop, R.; et al. Targeting the hepcidin-ferroportin pathway in anemia of chronic kidney disease. *Br. J. Clin. Pharmacol.* **2019**, *85*, 935–948. [CrossRef]
140. Xie, Y.; Tan, Y.; Zheng, Y.; Du, X.; Liu, Q. Ebselen ameliorates beta-amyloid pathology, tau pathology, and cognitive impairment in triple-transgenic Alzheimer’s disease mice. *J. Biol. Inorg. Chem.* **2017**, *22*, 851–865. [CrossRef] [PubMed]
141. Zhang, Z.; Kodumuru, V.; Sviridov, S.; Liu, S.; Chafeev, M.; Chowdhury, S.; Chakka, N.; Sun, J.; Gauthier, S.J.; Mattice, M.; et al. Discovery of benzylisothioureas as potent divalent metal transporter 1 (DMT1) inhibitors. *Bioorg. Med. Chem. Lett.* **2012**, *22*, 5108–5113. [CrossRef]
142. Dixon, S.J.; Stockwell, B.R. The role of iron and reactive oxygen species in cell death. *Nat. Chem. Biol.* **2014**, *10*, 9–17. [CrossRef] [PubMed]
143. Mandel, S.; Youdim, M.B. Catechin polyphenols: Neurodegeneration and neuroprotection in neurodegenerative diseases. *Free Radic. Biol. Med.* **2004**, *37*, 304–317. [CrossRef]
144. Fernando, W.; Somaratne, G.; Goozee, K.G.; Williams, S.; Singh, H.; Martins, R.N. Diabetes and Alzheimer’s Disease: Can Tea Phytochemicals Play a Role in Prevention? *J. Alzheimers Dis.* **2017**, *59*, 481–501. [CrossRef]
145. Mazumder, M.K.; Choudhury, S. Tea polyphenols as multi-target therapeutics for Alzheimer’s disease: An in silico study. *Med. Hypotheses* **2019**, *125*, 94–99. [CrossRef]
146. Zhao, H.F.; Li, N.; Wang, Q.; Cheng, X.J.; Li, X.M.; Liu, T.T. Resveratrol decreases the insoluble Abeta1-42 level in hippocampus and protects the integrity of the blood-brain barrier in AD rats. *Neuroscience* **2015**, *310*, 641–649. [CrossRef]
147. Cox, K.H.; Pipingas, A.; Scholey, A.B. Investigation of the effects of solid lipid curcumin on cognition and mood in a healthy older population. *J. Psychopharmacol.* **2015**, *29*, 642–651. [CrossRef] [PubMed]
148. Saad, M.A.; Abdel Salam, R.M.; Kenawy, S.A.; Attia, A.S. Pinocembrin attenuates hippocampal inflammation, oxidative perturbations and apoptosis in a rat model of global cerebral ischemia reperfusion. *Pharmacol. Rep.* **2015**, *67*, 115–122. [CrossRef]
149. Chen, X.; Gawryluk, J.W.; Wagener, J.F.; Ghribi, O.; Geiger, J.D. Caffeine blocks disruption of blood brain barrier in a rabbit model of Alzheimer’s disease. *J. Neuroinflamm.* **2008**, *5*, 12. [CrossRef] [PubMed]
150. Cascella, M.; Bimonte, S.; Muzio, M.R.; Schiavone, V.; Cuomo, A. The efficacy of Epigallocatechin-3-gallate (green tea) in the treatment of Alzheimer’s disease: An overview of pre-clinical studies and translational perspectives in clinical practice. *Infect. Agent Cancer* **2017**, *12*, 36. [CrossRef]
151. Ide, K.; Matsuoka, N.; Yamada, H.; Furushima, D.; Kawakami, K. Effects of Tea Catechins on Alzheimer’s Disease: Recent Updates and Perspectives. *Molecules* **2018**, *23*, 2357. [CrossRef] [PubMed]
152. Jiang, T.; Sun, Q.; Chen, S. Oxidative stress: A major pathogenesis and potential therapeutic target of antioxidative agents in Parkinson’s disease and Alzheimer’s disease. *Prog. Neurobiol.* **2016**, *147*, 1–19. [CrossRef]
153. Anand, P.; Singh, B. A review on cholinesterase inhibitors for Alzheimer’s disease. *Arch. Pharm. Res.* **2013**, *36*, 375–399. [CrossRef]
154. Ghosh, M.C.; Zhang, D.L.; Rouault, T.A. Iron misregulation and neurodegenerative disease in mouse models that lack iron regulatory proteins. *Neurobiol. Dis.* **2015**, *81*, 66–75. [CrossRef]

155. Hower, V.; Mendes, P.; Torti, F.M.; Laubenbacher, R.; Akman, S.; Shulaev, V.; Torti, S.V. A general map of iron metabolism and tissue-specific subnetworks. *Mol. Biosyst.* **2009**, *5*, 422–443. [CrossRef] [PubMed]
156. Lieu, P.T.; Heiskala, M.; Peterson, P.A.; Yang, Y. The roles of iron in health and disease. *Mol. Asp. Med.* **2001**, *22*, 1–87. [CrossRef]
157. Seeley, W.W.; Crawford, R.K.; Zhou, J.; Miller, B.L.; Greicius, M.D. Neurodegenerative diseases target large-scale human brain networks. *Neuron* **2009**, *62*, 42–52. [CrossRef] [PubMed]
158. Dugger, B.N.; Dickson, D.W. Pathology of Neurodegenerative Diseases. *Cold Spring Harb. Perspect. Biol.* **2017**, *9*, 7. [CrossRef] [PubMed]
159. Roubroeks, J.A.Y.; Smith, R.G.; van den Hove, D.L.A.; Lunnon, K. Epigenetics and DNA methylomic profiling in Alzheimer’s disease and other neurodegenerative diseases. *J. Neurochem.* **2017**, *143*, 158–170. [CrossRef] [PubMed]
160. Liu, Y.; Nguyen, M.; Robert, A.; Meunier, B. Metal Ions in Alzheimer’s Disease: A Key Role or Not? *Acc. Chem. Res.* **2019**, *52*, 2026–2035. [CrossRef]
161. Nikseresht, S.; Bush, A.I.; Ayton, S. Treating Alzheimer’s disease by targeting iron. *Br. J. Pharmacol.* **2019**, *176*, 3622–3635. [CrossRef]
162. Thirupathi, A.; Chang, Y.Z. Brain Iron Metabolism and CNS Diseases. *Adv. Exp. Med. Biol.* **2019**, *1173*, 1–19. [PubMed]
163. Morris, G.; Berk, M.; Carvalho, A.F.; Maes, M.; Walker, A.J.; Puri, B.K. Why should neuroscientists worry about iron? The emerging role of ferroptosis in the pathophysiology of neuroprogressive diseases. *Behav. Brain Res.* **2018**, *341*, 154–175. [CrossRef] [PubMed]
164. Leong, Y.Q.; Ng, K.Y.; Chye, S.M.; Ling, A.P.K.; Koh, R.Y. Mechanisms of action of amyloid-beta and its precursor protein in neuronal cell death. *Metab. Brain Dis.* **2020**, *35*, 11–30. [CrossRef] [PubMed]



Article

The microRNA-455 Null Mouse Has Memory Deficit and Increased Anxiety, Targeting Key Genes Involved in Alzheimer's Disease

Tracey E. Swingler¹, Lingzi Niu¹, Matthew G. Pontifex², David Vauzour^{2,*},† and Ian M. Clark^{1,*},†

¹ School of Biological Sciences, University of East Anglia, Norwich NR4 7TJ, UK; t.swingler@uea.ac.uk (T.E.S.); l.niu@uea.ac.uk (L.N.)

² Norwich Medical School, University of East Anglia, Norwich NR4 7TJ, UK; m.pontifex@uea.ac.uk

* Correspondence: d.vauzour@uea.ac.uk (D.V.); i.clark@uea.ac.uk (I.M.C.); Tel.: +44-1603-592760 (I.M.C.)

† These authors contributed equally to this work.

Abstract: The complete molecular mechanisms underlying the pathophysiology of Alzheimer's disease (AD) remain to be elucidated. Recently, microRNA-455-3p has been identified as a circulating biomarker of early AD, with increased expression in post-mortem brain tissue of AD patients. MicroRNA-455-3p also directly targets and down-regulates APP, with the overexpression of miR-455-3p suppressing its toxic effects. Here, we show that miR-455-3p expression decreases with age in the brains of wild-type mice. We generated a miR-455 null mouse utilising CRISPR-Cas9 to explore its function further. Loss of miR-455 resulted in increased weight gain, potentially indicative of metabolic disturbances. Furthermore, performance on the novel object recognition task diminished significantly in miR-455 null mice ($p = 0.004$), indicating deficits in recognition memory. A slight increase in anxiety was also captured on the open field test. *BACE1* and *TAU* were identified as new direct targets for miR-455-3p, with overexpression of miR-455-3p leading to a reduction in the expression of *APP*, *BACE1* and *TAU* in neuroblastoma cells. In the hippocampus of miR-455 null mice at 14 months of age, the levels of protein for *APP*, *BACE1* and *TAU* were all increased. Such findings reinforce the involvement of miR-455 in AD progression and demonstrate its action on cognitive performance.

Keywords: Alzheimer's disease; microRNA; miR-455; knockout; *APP*; *TAU*; *BACE1*; novel object recognition; memory; anxiety

Citation: Swingler, T.E.; Niu, L.; Pontifex, M.G.; Vauzour, D.; Clark, I.M. The microRNA-455 Null Mouse Has Memory Deficit and Increased Anxiety, Targeting Key Genes Involved in Alzheimer's Disease. *Int. J. Mol. Sci.* **2022**, *23*, 554. <https://doi.org/10.3390/ijms23010554>

Academic Editors: Masaru Tanaka and Lydia Giménez-Llort

Received: 10 November 2021

Accepted: 30 December 2021

Published: 5 January 2022

Publisher's Note: MDPI stays neutral with regard to jurisdictional claims in published maps and institutional affiliations.



Copyright: © 2022 by the authors. Licensee MDPI, Basel, Switzerland. This article is an open access article distributed under the terms and conditions of the Creative Commons Attribution (CC BY) license (<https://creativecommons.org/licenses/by/4.0/>).

1. Introduction

There are approximately 50 million people worldwide currently living with dementia, and this figure is predicted to rise considerably over the next three decades [1,2]. Alzheimer's disease (AD) is the most common form of dementia accounting for approximately two thirds of dementia cases [3]. The progressive and debilitating nature of the disease make it a major cause of disability and mortality in later life, with no disease modifying treatment currently available [4]. The classic hallmarks of AD consist of cognitive decline and the presence of amyloid plaques and neurofibrillary tangles (NFT) [5]. According to the amyloid hypothesis [6], pathological conditions lead to altered/increased metabolism of the amyloid precursor protein (APP), under the actions of the β -secretase, *BACE1* and γ -secretases, presenilin 1 and 2 (*PSEN1* and *PSEN2*). APP cleavage leads to the production and aggregation of the amyloid β peptide ($A\beta$) and the formation of amyloid plaques, resulting in neurotoxicity and eventual death of the neuron [7,8]. On the other hand, the *TAU* (microtubule-associated protein tau) hypothesis [9] emphasises the importance of aberrant *TAU* phosphorylation and subsequent NFT formation, which undermines microtubule integrity resulting in structural and transport deficits in the neurons [10,11]. Further processes such as neuroinflammation have also been proposed to

explain the mechanistic basis of the disease, with proinflammatory cytokines elevated in the brains and serum of AD patients [12,13]. Mitochondrial dysfunction and oxidative stress (increased production of reactive oxygen species) are also seen [14]. AD is likely attributable to a combination of processes, adding to its complexity, and as a result, the overall molecular pathogenesis remains poorly understood.

Small non-coding RNAs known as microRNAs (miRNAs) are important regulators of gene expression in human cells [15]. MicroRNAs are transcribed as primary transcripts (pri-miRNA) and processed to short stem-loop structures (pre-miRNA) in the nucleus. The pre-miRNA is then processed by the ribonuclease, DICER, forming two complementary short RNA molecules one of which (the guide strand) is integrated into the RNA-induced silencing complex (RISC), the other of which (the passenger strand) is degraded. After integration into RISC, miRNAs base pair with their complementary mRNA targets, usually in the 3'UTR [16] to degrade mRNA or repress translation. A number of miRNAs have been shown to have roles in regulating AD associated proteins, targeting processes that contribute to β -amyloid production (e.g., *BACE1* and *APP*), TAU phosphorylation and mitochondrial dysfunction (reviewed in [17,18]). MicroRNAs and their target genes act in regulatory networks which are disrupted in disease [19]. Key miRNAs may act as biomarkers of pathology or even be targets for therapeutic intervention [18].

MicroRNA-455 is genomically located in an intron of the collagen type XXVII alpha 1 chain gene (*COL27A1*) and has previously been implicated in cartilage biology [20], with roles in the TGF β signalling pathway [20,21]. A number of studies have shown miR-455 to be dysregulated in a variety of pathologies including cancers and cardiovascular disease [22]. Recently, microRNA-455-3p was identified as a circulating biomarker in early AD [23] with levels of miR-455-3p upregulated in patients with mild cognitive impairment (MCI) and AD. Furthermore, miR-455-3p expression is increased in the post-mortem brain tissue and cells derived from AD patients when compared to healthy controls, [24]. MicroRNA-455-3p has also been shown to directly target and down-regulate APP, with the overexpression of miR-455 suppressing APP toxicity [25] providing a mechanistic explanation for its increased expression in AD.

In order to determine the function of miR-455 in vivo, we utilised a miR-455 null mouse, constructed using CrispR/Cas9. Behavioural tests of cognition and in vitro molecular analyses were employed to further delineate miR-455 function within the brain.

2. Results

2.1. MicroRNA-455-3p Expression Decreases with Age and Is Absent in the Null Mouse Model

The miR-455 null mouse was made by the Genome Editing Unit, University of Manchester, UK. Microinjection of one-day single cell C57/BL6 mouse embryos used in vitro transcribed sgRNA and recombinant Cas9 protein (<https://sites.manchester.ac.uk/genome-editing-unit/publications/>, accessed on 15 October 2021). Sequencing of genomic DNA from founder mice revealed a number of deletions within the targeted pre-miR-455 locus. One of these was identified as a 35-base deletion, removing part of both miR-455-5p and miR-455-3p mature sequences, as well as the intervening hairpin sequence (Figure 1A). This mouse was bred with a wild-type C57/BL6 and heterozygote offspring bred together to give homozygous null mice; these were maintained alongside wild-type littermates as parallel colonies. Deletion was confirmed by sequencing of genomic DNA.

Expression of miR-455 was absent in all tissues tested, with Figure 1B showing expression in the brain at 3 months of age. At 14 months of age, miR-455 null mice were significantly larger than the wild-type comparators (Figure 1C). Expression of miR-455-3p in the brain decreased across 3 weeks to 12 months of age in wild-type mice ($p = 0.04$, Figure 1D).

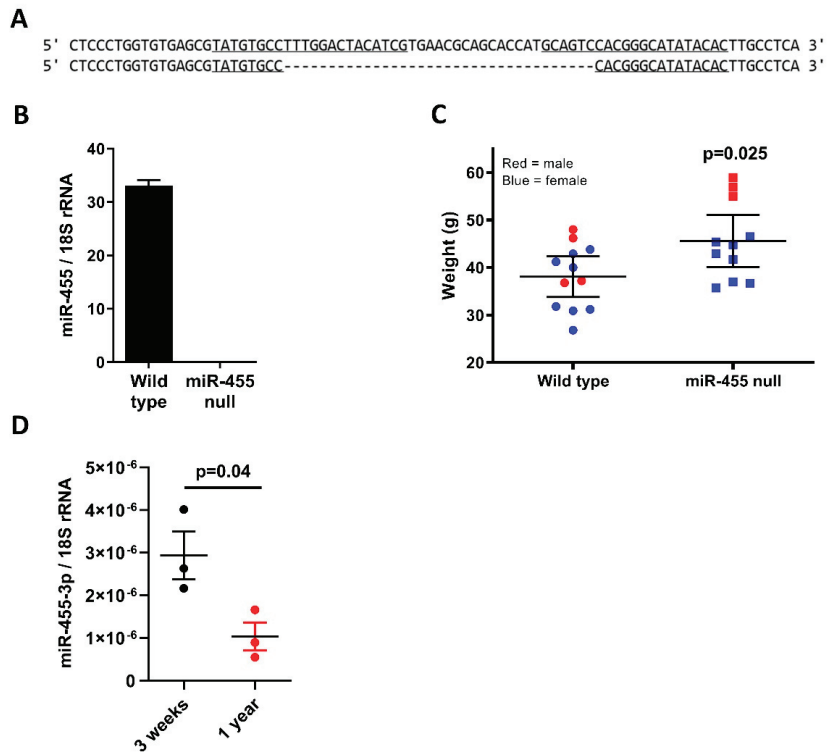


Figure 1. The miR-455 null mouse and the expression of miR-455-3p across age. (A) Deletion of miR-455 in mice. Sequencing of miR-455 null founder mouse shows a 35-base deletion, deleting both miR-455-5p and miR-455-3p mature sequences, as well as the intervening hairpin sequence. (B) Expression of miR-455-3p in 3-month-old mouse brain tissue. RNA was extracted from brain tissue and qRT-PCR performed; the miR-455 null mouse shows complete loss of miR-455-3p expression. (C) MiR-455 null mice show increased weight gain with age. Mice were weighed each month and showed that at 14 months of age, miR-455 null mice ($n = 13$) were significantly heavier than wild-type litter mates ($n = 11$). (D) MiR-455 expression decreases with age in wild-type mice. RNA was extracted from brain tissue at 3 weeks and 12 months of age and qRT-PCR performed ($n = 3$). Mean \pm SEM.

2.2. Recognition Memory Is Impaired in miR-455 Null Mice

We compared wild-type with miR-455 null mice at 14 months of age in both novel object recognition and the open field test. In object recognition, miR-455 null mice showed significantly impaired recognition memory compared to wild-type controls ($p = 0.004$, Figure 2A). In the open field test, miR-455 null mice displayed a slight increase in anxiety overall spending less time in the centre of the arena ($p = 0.09$, Figure 2B), with no alteration in motor function (Figure 2C).

2.3. BACE1 and TAU Are Direct Targets of miR-455-3p

APP has previously been identified as a direct target for miR-455-3p [25]. Here, we also identified *BACE1* and *TAU* as other targets. Expression of luciferase controlled by the 3'UTR of either the *BACE1* or *TAU* genes shows that miR-455-3p reduces this expression and that this is rescued by mutation of the miR-455-3p seed site in each UTR (Figure 3A,B). Expression of *APP*, *BACE1* and *TAU* were all decreased after overexpression of miR-455-3p in SH SY5Y neuroblastoma cells (Figure 3C,D).

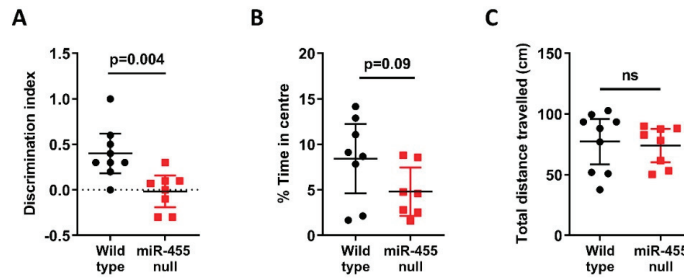


Figure 2. Behavioural studies comparing the miR-455 null mouse vs. wild-type. (A) 14-month-old miR-455 null ($n = 9$) mice and wild type mice ($n = 8$) were tested for recognition memory using the novel object recognition test (NOR); miR-455 null mice have significant recognition memory deficit as indicated by a decreased discrimination index. (B) Anxiety behaviour was tested using the open field test. MiR-455 null mice display an increase in anxiety with (C) no difference in overall locomotion. Bars show the mean \pm SEM.

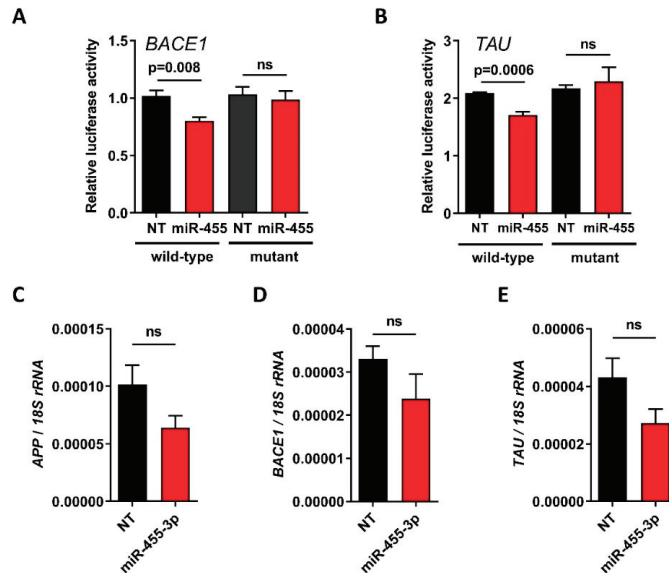


Figure 3. miR-455-3p directly targets *BACE1* and *TAU*. Cells (DF1 fibroblasts) were transfected with the 3'-untranslated region of *BACE1* (A), *TAU* (B) or the corresponding seed site mutants, cloned into pmiR-GLO \pm non-targeting control (NT) or miR-455-3p mimic (miR-455) and incubated for 24 h. Relative light units were normalized to Renilla activity. Bars show the mean \pm SEM; $n = 4$. SH SY5Y neuroblastoma cells were transfected with miR-455-3p mimic or non-targeting control (NT) for 48 h prior to measurement of *APP* (C), *BACE1* (D) and *TAU* (E) by qRT-PCR. Bars show the mean \pm SEM, $n = 3$.

2.4. The Levels of APP, BACE1 and TAU Proteins Are Increased in miR-455 Null Mouse Hippocampus

Both RNA and proteins were extracted from the hippocampus of wild-type vs. miR-455 null mice at 14 months of age. The level of both *App* and *Bace1* gene expression were not significantly different between groups (Figure 4A,B), although *Tau* expression was significantly increased in the miR-455 null mice ($p = 0.046$, Figure 4C). However, Western blot showed a significant increase in APP ($p = 0.0013$) and BACE1 ($p = 0.0447$)

protein levels in miR-455 null mice compared to wild-type (Figure 4D,E). Although it did not reach significance, protein levels of TAU were higher in miR-455 null vs. wild type mice (Figure 4F).

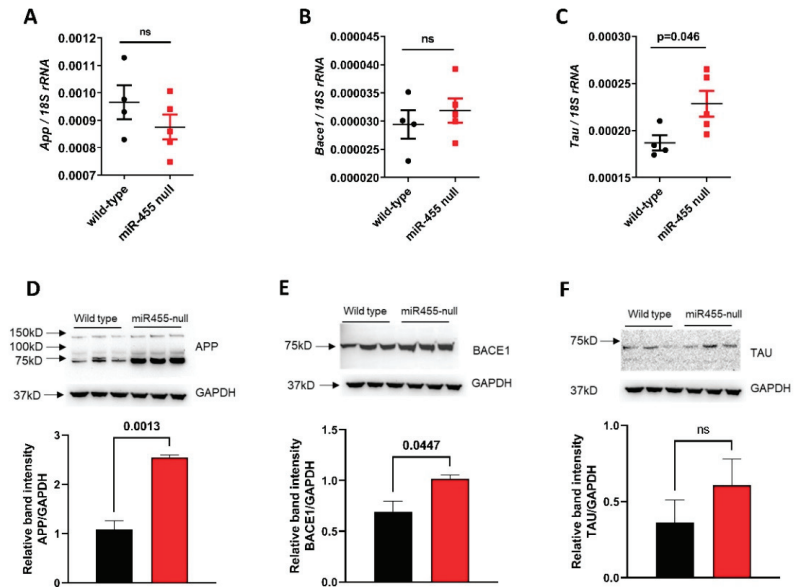


Figure 4. Expression of *App*, *Bace1* and *Tau* in the mouse hippocampus. RNA and proteins were extracted from the hippocampus of wild-type vs. miR-455 null mice at 14 months of age. Levels of *App*, *Bace1* and *Tau* were measured by qRT-PCR (A–C) and Western blot and densitometric analyses (D–F). Results are presented as mean \pm SEM, $n = 4$ wild type and $n = 5$ miR-455 null for RNA levels and $n = 3$ for both wild type and miR-455 null for protein levels.

3. Discussion

MicroRNA-455 has been described as a circulating biomarker of AD and is increased in the brains of AD patients [22–24]. Additionally, miR-455-3p has known roles in APP processing and abrogates the impact of mutant APP in vitro [25]. After revealing a decrease of miR-455-3p expression in ageing wild type mice, CrispR-Cas9 microinjection was used to create a miR-455 null mouse in order to determine its function in vivo. Behavioural assessment revealed deficits in recognition memory and increased anxiety in null mice. *BACE1* and *TAU* genes were shown to be direct targets for miR-455-3p. The use of homologous recombination was precluded because of the proximity of miR-455 to the downstream exon of the *COL27A1* gene. The deletion of 35 bases across the 5p and 3p sequences within the pre-miRNA hairpin was sufficient to prevent processing and no mature miR-455 was detected. A second deletion in founder mice was also bred forwards and no difference in phenotype of these mice has been detected (data not shown).

Expression of miR-455-3p decreased with age in the mouse brain across 12 months (Figure 1D). The expression of all microRNAs in mouse brain with ageing has previously been examined using RNA-Seq analysis [26,27], however n numbers were small and the read number of miR-455 using this technique was too small for analyses. The expression of a number of microRNAs both increase and decrease in the brain significantly across age. Roles for miRNAs in the brain are diverse, including modulation of synaptic plasticity, cognition, inflammation, neuroprotection, lipid metabolism and mitochondrial function [28,29]. MicroRNA-455 null mice were significantly heavier than their wild-type counterparts at 14 months of age (Figure 1C) and this divergence starts around 6 months of age (Supplementary Figure S1). Although the role of obesity as a risk factor for AD remains

uncertain [30,31] alterations in energy metabolism are now considered a prerequisite in AD progression [32–35].

Loss of miR-455 influenced recognition memory with null mice performing significantly worse on the novel object recognition task compared to the wild-type controls (Figure 2A). A slight increase in anxiety, was also noted (Figure 2B). Correlation analyses of NOR discrimination index with open field percentage time in centre or travelled distance showed no significant interaction indicating that anxiety did not impact on the NOR output (see Supplementary Figure S2). Several microRNAs implicated in AD have also been shown to impact these outcomes, including miR-9 [36], miR-124 [37], miR-101 [38], miR-153 [39], miR-132/212 [40] and miR-181a [41,42].

MicroRNA-455 has been shown to directly target and downregulate APP [25], suppressing its toxic effects. We extended this to demonstrate that both human *BACE1* and *TAU* are also direct targets for miR-455-3p (Figure 3A,B) with *APP*, *BACE1* and *TAU* expression suppressed by the overexpression of miR-455-3p (Figure 3C–E). In the miR-455 null mouse hippocampus, the protein levels of APP, BACE1 and TAU are all increased, though for APP and BACE1, this does not correlate with mRNA levels. In part this may be due to a small *n* number, but post-transcriptional mechanisms may also contribute. This clearly has potential to add to the pathology of AD via the amyloid or *Tau* axis. Although *APP*, *BACE1* and *TAU* have been implicated in impaired recognition memory [43–46] we have not demonstrated that this is the mechanism of action of miR-455.

In addition to our current findings, we have preliminary evidence to suggest miR-455 may also target components of the core clock machinery and likely impacts the upon circadian rhythm (Swingler et al., unpublished observations). This may provide another link to AD [47].

The main limitations to the current study are the future need to compare the miR-455 null mouse with a transgenic mouse overexpressing miR-455-3p. A greater suite of behavioural studies across age would identify the age of onset for the phenotype and enable targeted molecular studies to address mechanism further.

Altogether, the findings here suggest that miR-455-3p is neuroprotective, with loss of miR-455 across age leading to increased AD related gene expression and subsequent cognitive deficits. However, the knowledge that miR-455-3p [22] is increased in AD complicates this narrative. We hypothesize that the AD associated increase may represent a futile attempt to control pathology and is ultimately overwhelmed. Increasing research is warranted to further detail the interaction of miR-455 with brain physiology and pathology.

4. Materials and Methods

4.1. MiR-455 Null Mouse

MiR-455 mice were made using CRISPR-Cas9 by the Transgenic Unit, University of Manchester (<https://sites.manchester.ac.uk/genome-editing-unit/>, accessed 15 October 2021). Mice were maintained in a controlled environment under the Home Office Code of Practice (21 ± 2 °C, humidity 55 ± 10%, 12-h light/dark cycles (lights on at 07:00 h and off at 19:00 h), HEPA filtered air) and fed ad libitum on a standard chow diet (RM3-P; Special Diet Services, Essex, UK) for the duration of the experiments.

4.2. Behavioural Assessment

Behavioural tests were performed as previously described [48,49] on mice aged to 14 months old. Objects and arenas were cleaned with 70% (*v/v*) ethanol in between each trial. To evaluate anxiety behaviour and locomotion open field test was performed. Briefly, mice were placed in a house built 50 cm × 50 cm × 50 cm apparatus illuminated with low lux (100 lux) lighting and could move freely. Recognition memory was assessed using novel object recognition task (NOR) [50]. The open field test (Day 1) was used as the acclimatisation phase for the NOR experiment. On day 2, mice were placed into the same arena containing two identical objects and allowed to explore for 15 min. The mice were returned to their cages for a period of 1 h. Animals were again placed into their respective

arenas for a final time, the arena contained one original object and one novel object, and the mouse was free to explore either for a 10-min period. Mice were included in the analysis that explored objects for a period of 10 secs or greater. Videos were analysed for the full the 10-min period and time spent with each object was determined. Discrimination index (DI) was calculated using the following formula $DI = (TN - TF)/(TN + TF)$ where TN is time exploring the novel object and TF is time spent exploring the familiar object.

4.3. Overexpression of miR-455-3p

SH SY5Y neuroblastoma cells were plated in 96-well plate wells at a density of 7×10^4 cells/mL in 100 μ L and grown to 80–90% confluence. MicroRNA-455-3p mimic (50 nM) or non-targeting control (50 nM) were transfected in using Lipofectamine 3000 (Thermo Fisher Scientific, Paisley, UK), according to manufacturer's instructions for 48 h. Total RNA was extracted using Trizol (ThermoFisher Scientific, Paisley, UK) according to the manufacturer's instructions).

4.4. RNA and Protein Extraction from Mouse Brains

Mice were euthanized and the brains were immediately removed and dissected for the cerebral cortex, and hippocampus. Brain tissue was snap frozen and ground in liquid nitrogen. Total RNA was extracted from 20 mg tissue using Trizol (ThermoFisher Scientific, Paisley, UK) according to the manufacturer's instructions. Protein was extracted using NE-PER reagents (ThermoFisher Scientific, Paisley, UK) according to the manufacturer's instructions.

4.5. Quantitative Real-Time PCR

Complementary DNA was synthesized from 300 ng RNA using SuperScript II reverse transcriptase (Invitrogen, Paisley, UK) and either random hexamers or miRNA-specific primers (Applied Biosystems, Paisley, UK) according to the manufacturer's instructions. 18S rRNA was used as the housekeeping gene. Complementary DNA was stored at -20°C . The relative quantitation of gene expression was performed using an ABI Prism 7700 Sequence Detection System (Applied Biosystems, Paisley, UK), following the manufacturer's protocol.

4.6. Luciferase Assay

The 3'UTR of mRNAs containing the predicted binding site of miR-455-3p were subcloned into pmirGLO (Promega, Chilworth, UK), using QuikChange II XL site-directed mutagenesis kit (Agilent, Stockport, UK) to introduce mutations. Constructs were sequence verified (Source Bioscience, Nottingham, UK). DF1 fibroblast cells were seeded into 96-well plate wells at 5×10^4 cells/mL in 100 μ L medium overnight and transiently transfected with 100 ng reporter plasmid, 30nM miR-455-3p mimic (Qiagen, Manchester, UK) or non-targeting control (AllStars, Qiagen, Manchester, UK) using Lipofectamine 3000 (Thermo Fisher Scientific, Paisley, UK), according to manufacturer's instructions for 24 h. Cell lysates were assayed for luciferase using the Dual Luciferase Reporter Assay Kit (Promega, Chilworth, UK), read with an EnVision 2103 Multilabel plate reader (Perkin Elmer, Beaconsfield, UK). Relative luciferase activity was the ratio of firefly luciferase to Renilla luciferase activity

4.7. Western Blot

Samples were separated on reducing SDS-PAGE, transferred to PVDF membrane and probed overnight at 4°C . Antibodies against APP (A87840), BACE1 (A80396) and TAU (A98434) were all from antibodies.com (Cambridge, UK). The antibody against GAPDH (#2118) was from Cell Signalling Technology (London, UK). All antibodies were used at recommended concentrations and were detected using HRP-conjugated secondary antibodies (DAKO, Stockport, UK), visualised using Pierce™ ECL Western Blotting Substrate (ThermoFisher Scientific, Paisley, UK), and imaged by ChemiDoc™ MP Imaging System (BioRad, Watford, UK).

4.8. Statistical Analysis

Data were normally distributed and therefore analysed using Student's *t*-test to compare between two samples, or one-way ANOVA with post hoc Tukey's test to compare between multiple samples using GraphPad Prism version 6. The details of all statistical analyses are shown in Supplementary Table S1.

Supplementary Materials: The supporting information can be downloaded at: <https://www.mdpi.com/article/10.3390/ijms23010554/s1>.

Author Contributions: T.E.S. and L.N. performed the research and analysed the data with advice from D.V., M.G.P., T.E.S. and I.M.C. All contributed to research direction. All authors wrote and edited the manuscript. All authors have read and agreed to the published version of the manuscript.

Funding: T.E.S. was funded by a Dunhill Medical Trust Programme grant (number R476/0516); L.N. was funded by Action Arthritis and Funds for Women Graduates (number GA-00842).

Institutional Review Board Statement: All experimental procedures and protocols used in this study were reviewed and approved by the Animal Welfare and Ethical Review Body (AWERB) and were conducted within the provisions of the U.K. Home Office Animals (Scientific Procedures) Act 1986 (PF50C7689).

Informed Consent Statement: Not applicable.

Data Availability Statement: Data will be made available upon request.

Acknowledgments: We would like to thank staff in the Disease Modelling Unit for their generous help with these studies.

Conflicts of Interest: The authors declare no conflict of interest.

References

1. Available online: <https://www.who.int/news-room/fact-sheets/detail/dementia> (accessed on 15 October 2021).
2. Prince, M.; Bryce, R.; Albanese, E.; Wimo, A.; Ribeiro, W.; Ferri, C.P. The global prevalence of dementia: A systematic review and metaanalysis. *Alzheimers Dement.* **2013**, *9*, 63–75.e2. [CrossRef]
3. Kumar, A.; Sidhu, J.; Goyal, A.; Tsao, J.W. *Alzheimer Disease*; StatPearls: Treasure Island, FL, USA, 2021.
4. Picanco, L.C.D.S.; Ozela, P.F.; Brito, M.d.F.d.B.; Pinheiro, A.A.; Padilha, E.C.; Braga, F.S.; da Silva, C.H.T.d.P.; Dos Santos, C.B.R.; Rosa, J.M.C.; da Silva Hage-Melim, L.I. Alzheimer's Disease: A Review from the Pathophysiology to Diagnosis, New Perspectives for Pharmacological Treatment. *Curr. Med. Chem.* **2018**, *25*, 3141–3159. [CrossRef] [PubMed]
5. DeTure, M.A.; Dickson, D.W. The neuropathological diagnosis of Alzheimer's disease. *Mol. Neurodegener.* **2019**, *14*, 32. [CrossRef] [PubMed]
6. Selkoe, D.J.; Hardy, J. The amyloid hypothesis of Alzheimer's disease at 25 years. *EMBO Mol. Med.* **2016**, *8*, 595–608. [CrossRef]
7. Dawkins, E.; Small, D.H. Insights into the physiological function of the β -amyloid precursor protein: Beyond Alzheimer's disease. *J. Neurochem.* **2014**, *129*, 756–769. [CrossRef]
8. Haass, C.; Kaether, C.; Thinakaran, G.; Sisodia, S. Trafficking and Proteolytic Processing of APP. *Cold Spring Harb. Perspect. Med.* **2012**, *2*, a006270. [CrossRef] [PubMed]
9. Arnsten, A.F.T.; Datta, D.; Del Tredici, K.; Braak, H. Hypothesis: Tau pathology is an initiating factor in sporadic Alzheimer's disease. *Alzheimer's Dement.* **2020**, *17*, 115–124. [CrossRef] [PubMed]
10. Ballard, C.; Gauthier, S.; Corbett, A.; Brayne, C.; Aarsland, D.; Jones, E. Alzheimer's disease. *Lancet* **2011**, *377*, 1019–1031. [CrossRef]
11. Kametani, F.; Hasegawa, M. Reconsideration of Amyloid Hypothesis and Tau Hypothesis in Alzheimer's Disease. *Front. Neurosci.* **2018**, *12*, 25. [CrossRef]
12. Calsolaro, V.; Edison, P. Neuroinflammation in Alzheimer's disease: Current evidence and future directions. *Alzheimers Dement.* **2016**, *12*, 719–732. [CrossRef] [PubMed]
13. Tanaka, M.; Toldi, J.; Vécsei, L. Exploring the Etiological Links behind Neurodegenerative Diseases: Inflammatory Cytokines and Bioactive Kynurenines. *Int. J. Mol. Sci.* **2020**, *21*, 2431. [CrossRef]
14. Catanesi, M.; d'Angelo, M.; Tupone, M.G.; Benedetti, E.; Giordano, A.; Castelli, V.; Cimini, A. MicroRNAs Dysregulation and Mitochondrial Dysfunction in Neurodegenerative Diseases. *Int. J. Mol. Sci.* **2020**, *21*, 5986. [CrossRef]
15. O'Brien, J.; Hayder, H.; Zayed, Y.; Peng, C. Overview of MicroRNA Biogenesis, Mechanisms of Actions, and Circulation. *Front. Endocrinol.* **2018**, *9*, 402. [CrossRef]
16. Winter, J.; Jung, S.; Keller, S.; Gregory, R.I.; Diederichs, S. Many roads to maturity: MicroRNA biogenesis pathways and their regulation. *Nat. Cell Biol.* **2009**, *11*, 228–234. [CrossRef] [PubMed]

17. Wang, M.; Qin, L.; Tang, B. MicroRNAs in Alzheimer's Disease. *Front. Genet.* **2019**, *10*, 153. [CrossRef] [PubMed]
18. Angelucci, F.; Cechova, K.; Valis, M.; Kuca, K.; Zhang, B.; Hort, J. MicroRNAs in Alzheimer's Disease: Diagnostic Markers or Therapeutic Agents? *Front. Pharmacol.* **2019**, *10*, 665. [CrossRef]
19. Brito, L.M.; Ribeiro-dos-Santos, A.; Vidal, A.F.; de Araújo, G.S. Differential Expression and miRNA–Gene Interactions in Early and Late Mild Cognitive Impairment. *Biology* **2020**, *9*, 251. [CrossRef]
20. Swinger, T.E.; Wheeler, G.; Carmont, V.; Elliott, H.R.; Barter, M.J.; Abu-Elmagd, M.; Donell, S.T.; Boot-Handford, R.P.; Hajhosseini, M.K.; Munsterberg, A.; et al. The expression and function of microRNAs in chondrogenesis and osteoarthritis. *Arthritis Rheum.* **2012**, *64*, 1909–1919. [CrossRef] [PubMed]
21. Hu, S.; Zhao, X.; Mao, G.; Zhang, Z.; Wen, X.; Zhang, C.; Liao, W.; Zhang, Z. MicroRNA-455-3p promotes TGF- β signaling and inhibits osteoarthritis development by directly targeting PAK2. *Exp. Mol. Med.* **2019**, *51*, 1–13. [CrossRef] [PubMed]
22. Kumar, S.; Reddy, P.H. A New Discovery of MicroRNA-455-3p in Alzheimer's Disease. *J. Alzheimers Dis.* **2019**, *72*, S117–S130. [CrossRef] [PubMed]
23. Kumar, S.; Vijayan, M.; Reddy, P.H. MicroRNA-455-3p as a potential peripheral biomarker for Alzheimer's disease. *Hum. Mol. Genet.* **2017**, *26*, 3808–3822. [CrossRef] [PubMed]
24. Kumar, S.; Reddy, P.H. MicroRNA-455-3p as a Potential Biomarker for Alzheimer's Disease: An Update. *Front. Aging Neurosci.* **2018**, *10*, 41. [CrossRef]
25. Kumar, S.; Reddy, A.P.; Yin, X.; Reddy, P.H. Novel MicroRNA-455-3p and its protective effects against abnormal APP processing and amyloid beta toxicity in Alzheimer's disease. *Biochim. Biophys. Acta Mol. Basis Dis.* **2019**, *1865*, 2428–2440. [CrossRef] [PubMed]
26. Inukai, S.; de Lencastre, A.; Turner, M.; Slack, F. Novel microRNAs differentially expressed during aging in the mouse brain. *PLoS ONE* **2012**, *7*, e40028. [CrossRef]
27. Mohammed, C.P.; Rhee, H.; Phee, B.K.; Kim, K.; Kim, H.J.; Lee, H.; Park, J.H.; Jung, J.H.; Kim, J.Y.; Kim, H.C.; et al. miR-204 downregulates EphB2 in aging mouse hippocampal neurons. *Aging Cell* **2016**, *15*, 380–388. [CrossRef]
28. Mohammed, C.P.D.; Park, J.S.; Nam, H.G.; Kim, K. MicroRNAs in brain aging. *Mech. Ageing Dev.* **2017**, *168*, 3–9. [CrossRef]
29. Cao, D.-D.; Li, L.; Chan, W.-Y. MicroRNAs: Key Regulators in the Central Nervous System and Their Implication in Neurological Diseases. *Int. J. Mol. Sci.* **2016**, *17*, 842. [CrossRef]
30. Fitzpatrick, A.L.; Kuller, L.H.; Lopez, O.L.; Diehr, P.; O'Meara, E.S.; Longstreth, W.T., Jr.; Luchsinger, J.A. Midlife and late-life obesity and the risk of dementia: Cardiovascular health study. *Arch. Neurol.* **2009**, *66*, 336–342. [CrossRef]
31. Profenno, L.A.; Porsteinsson, A.P.; Faraone, S.V. Meta-analysis of Alzheimer's disease risk with obesity, diabetes, and related disorders. *Biol. Psychiatry* **2010**, *67*, 505–512. [CrossRef]
32. Atti, A.R.; Valente, S.; Iodice, A.; Caramella, I.; Ferrari, B.; Albert, U.; Mandelli, L.; De Ronchi, D. Metabolic Syndrome, Mild Cognitive Impairment, and Dementia: A Meta-Analysis of Longitudinal Studies. *Am. J. Geriatr. Psychiatry* **2019**, *27*, 625–637. [CrossRef]
33. Borshchev, Y.Y.; Uspensky, Y.P.; Galagudza, M.M. Pathogenetic pathways of cognitive dysfunction and dementia in metabolic syndrome. *Life Sci.* **2019**, *237*, 116932. [CrossRef] [PubMed]
34. Tolppanen, A.M.; Solomon, A.; Soininen, H.; Kivipelto, M. Midlife vascular risk factors and Alzheimer's disease: Evidence from epidemiological studies. *J. Alzheimers Dis.* **2012**, *32*, 531–540. [CrossRef]
35. Cunnane, S.C.; Trushina, E.; Morland, C.; Prigione, A.; Casadesus, G.; Andrews, Z.B.; Beal, M.F.; Bergersen, L.H.; Brinton, R.D.; de la Monte, S.; et al. Brain energy rescue: An emerging therapeutic concept for neurodegenerative disorders of ageing. *Nat. Rev. Drug Discov.* **2020**, *19*, 609–633. [CrossRef] [PubMed]
36. Sim, S.E.; Lim, C.S.; Kim, J.I.; Seo, D.; Chun, H.; Yu, N.K.; Lee, J.; Kang, S.J.; Ko, H.G.; Choi, J.H.; et al. The Brain-Enriched MicroRNA miR-9-3p Regulates Synaptic Plasticity and Memory. *J. Neurosci.* **2016**, *36*, 8641–8652. [CrossRef] [PubMed]
37. Michely, J.; Kraft, S.; Muller, U. miR-12 and miR-124 contribute to defined early phases of long-lasting and transient memory. *Sci. Rep.* **2017**, *7*, 7910. [CrossRef]
38. Lippi, G.; Fernandes, C.C.; Ewell, L.A.; John, D.; Romoli, B.; Curia, G.; Taylor, S.R.; Frady, E.P.; Jensen, A.B.; Liu, J.C.; et al. MicroRNA-101 Regulates Multiple Developmental Programs to Constrain Excitation in Adult Neural Networks. *Neuron* **2016**, *92*, 1337–1351. [CrossRef]
39. Mathew, R.S.; Tatarakis, A.; Rudenko, A.; Johnson-Venkatesh, E.M.; Yang, Y.J.; Murphy, E.A.; Todd, T.P.; Schepers, S.T.; Siuti, N.; Martorell, A.J.; et al. A microRNA negative feedback loop downregulates vesicle transport and inhibits fear memory. *Elife* **2016**, *5*, 463. [CrossRef] [PubMed]
40. Hansen, K.F.; Sakamoto, K.; Aten, S.; Snider, K.H.; Loeser, J.; Hesse, A.M.; Page, C.E.; Pelz, C.; Arthur, J.S.; Impey, S.; et al. Targeted deletion of miR-132/-212 impairs memory and alters the hippocampal transcriptome. *Learn. Mem.* **2016**, *23*, 61–71. [CrossRef]
41. Griffiths, B.B.; Ouyang, Y.B.; Xu, L.; Sun, X.; Giffard, R.G.; Stary, C.M. Postinjury Inhibition of miR-181a Promotes Restoration of Hippocampal CA1 Neurons after Transient Forebrain Ischemia in Rats. *eNeuro* **2019**, *6*. [CrossRef]
42. Zhang, S.F.; Chen, J.C.; Zhang, J.; Xu, J.G. miR-181a involves in the hippocampus-dependent memory formation via targeting PRKAA1. *Sci. Rep.* **2017**, *7*, 8480. [CrossRef]
43. Biundo, F.; Del Prete, D.; Zhang, H.; Arancio, O.; D'Adamo, L. A role for tau in learning, memory and synaptic plasticity. *Sci. Rep.* **2018**, *8*, 3184. [CrossRef]

44. Evans, C.E.; Thomas, R.S.; Freeman, T.J.; Hvoslef-Eide, M.; Good, M.A.; Kidd, E.J. Selective reduction of APP-BACE1 activity improves memory via NMDA-NR2B receptor-mediated mechanisms in aged PDAPP mice. *Neurobiol. Aging* **2019**, *75*, 136–149. [CrossRef] [PubMed]
45. Fukumoto, H.; Takahashi, H.; Tarui, N.; Matsui, J.; Tomita, T.; Hirode, M.; Sagayama, M.; Maeda, R.; Kawamoto, M.; Hirai, K.; et al. A noncompetitive BACE1 inhibitor TAK-070 ameliorates Abeta pathology and behavioral deficits in a mouse model of Alzheimer's disease. *J. Neurosci.* **2010**, *30*, 11157–11166. [CrossRef]
46. Webster, S.J.; Bachstetter, A.D.; Van Eldik, L.J. Comprehensive behavioral characterization of an APP/PS-1 double knock-in mouse model of Alzheimer's disease. *Alzheimers Res. Ther.* **2013**, *5*, 28. [CrossRef]
47. Homolak, J.; Mudrovic, M.; Vukic, B.; Toljan, K. Circadian Rhythm and Alzheimer's Disease. *Med. Sci.* **2018**, *6*, 52. [CrossRef] [PubMed]
48. Hoyles, L.; Pontifex, M.G.; Rodriguez-Ramiro, I.; Anis-Alavi, M.A.; Jelane, K.S.; Snelling, T.; Solito, E.; Fonseca, S.; Carvalho, A.L.; Carding, S.R.; et al. Regulation of blood–brain barrier integrity by microbiome-associated methylamines and cognition by trimethylamine N-oxide. *Microbiome* **2021**, *9*, 235. [CrossRef]
49. Pontifex, M.G.; Martinsen, A.; Saleh, R.N.M.; Harden, G.; Tejera, N.; Müller, M.; Fox, C.; Vauzour, D.; Minihane, A.M. APOE4 genotype exacerbates the impact of menopause on cognition and synaptic plasticity in APOE-TR mice. *FASEB J.* **2021**, *35*, e21583. [CrossRef] [PubMed]
50. Dere, E.; Huston, J.P.; De Souza Silva, M.A. The pharmacology, neuroanatomy and neurogenetics of one-trial object recognition in rodents. *Neurosci. Biobehav. Rev.* **2007**, *31*, 673–704. [CrossRef]



Article

Aggregation of Cystatin C Changes Its Inhibitory Functions on Protease Activities and Amyloid β Fibril Formation

Abdullah Md. Sheikh ^{1,†}, Yasuko Wada ^{2,†}, Shatera Tabassum ¹, Satoshi Inagaki ², Shingo Mitaki ², Shozo Yano ¹ and Atsushi Nagai ^{1,2,*}

¹ Department of Laboratory Medicine, Faculty of Medicine, Shimane University, 89-1 Enya Cho, Izumo 693-8501, Japan; abdullah@med.shimane-u.ac.jp (A.M.S.); tabassum@med.shimane-u.ac.jp (S.T.); syano@med.shimane-u.ac.jp (S.Y.)

² Department of Neurology, Faculty of Medicine, Shimane University, 89-1 Enya Cho, Izumo 693-8501, Japan; wadayasu@med.shimane-u.ac.jp (Y.W.); inasato061009@yahoo.co.jp (S.I.); shingomi@med.shimane-u.ac.jp (S.M.)

* Correspondence: anagai@med.shimane-u.ac.jp; Tel./Fax: +81-0853-20-2198

† Authors contributed equally to this work.

Abstract: Cystatin C (CST3) is an endogenous cysteine protease inhibitor, which is implicated in cerebral amyloid angiopathy (CAA). In CAA, CST3 is found to be aggregated. The purpose of this study is to investigate whether this aggregation could alter the activity of the protein relevant to the molecular pathology of CAA. A system of CST3 protein aggregation was established, and the aggregated protein was characterized. The results showed that CST3 aggregated both at 80 °C without agitation, and at 37 °C with agitation in a time-dependent manner. However, the levels of aggregation were high and appeared earlier at 80 °C. Dot-blot immunoassay for oligomers revealed that CST3 could make oligomeric aggregates at the 37 °C condition. Electron microscopy showed that CST3 could make short fibrillary aggregates at 37 °C. Cathepsin B activity assay demonstrated that aggregated CST3 inhibited the enzyme activity less efficiently at pH 5.5. At 7.4 pH, it lost the inhibitory properties almost completely. In addition, aggregated CST3 did not inhibit A β ₁₋₄₀ fibril formation, rather, it slightly increased it. CST3 immunocytochemistry showed that the protein was positive both in monomeric and aggregated CST3-treated neuronal culture. However, His6 immunocytochemistry revealed that the internalization of exogenous recombinant CST3 by an astrocytoma cell culture was higher when the protein was aggregated compared to its monomeric form. Finally, MTT cell viability assay showed that the aggregated form of CST3 was more toxic than the monomeric form. Thus, our results suggest that aggregation may result in a loss-of-function phenotype of CST3, which is toxic and responsible for cellular degeneration.

Keywords: Cystatin C; aggregation; cathepsin activity; Amyloid β ; neurodegeneration

Citation: Sheikh, A.M.; Wada, Y.; Tabassum, S.; Inagaki, S.; Mitaki, S.; Yano, S.; Nagai, A. Aggregation of Cystatin C Changes Its Inhibitory Functions on Protease Activities and Amyloid β Fibril Formation. *Int. J. Mol. Sci.* **2021**, *22*, 9682. <https://doi.org/10.3390/ijms22189682>

Academic Editors: Masaru Tanaka and Lydia Giménez-Llort

Received: 29 July 2021

Accepted: 1 September 2021

Published: 7 September 2021

Publisher's Note: MDPI stays neutral with regard to jurisdictional claims in published maps and institutional affiliations.



Copyright: © 2021 by the authors. Licensee MDPI, Basel, Switzerland. This article is an open access article distributed under the terms and conditions of the Creative Commons Attribution (CC BY) license (<https://creativecommons.org/licenses/by/4.0/>).

1. Introduction

Cystatin C (CST3) is a cysteine protease inhibitor, which is expressed ubiquitously in every type of cell [1]. It contains 120 amino acids, and its molecular weight is 13 kDa [1]. CST3 is found to be localized in lysosomes [2,3], where it plays an important role in controlling the functions of the organelle by regulating the activity of cysteine protease enzymes including cathepsin B, H, and L [4,5]. It is also localized in the endoplasmic reticulum and Golgi complex, indicating it as a secreted protein [1,6]. In the extracellular space, it is believed to neutralize the activities of proteases that are often released or leaked from the lysosomes of dying or diseased cells [7,8]. The expression of CST3 in the brain is high [9]. In addition, its CSF concentration is about five times higher than that of plasma [10]. Such findings indicate its important role in brain homeostasis. In neuroinflammatory conditions, microglia are demonstrated to secrete cysteine proteases in the extracellular space [11]. Here, CST3 can inhibit the activities of such cysteine proteases,

and thereby regulates the neuroinflammatory conditions. Hence, the dysregulation of such inhibitory effects of CST3 could alter the neuroinflammatory conditions leading to neurodegeneration.

Proper functioning proteins are required for proper functioning cells, tissues, or organs. After release from the ribosome, the unfolded polypeptide chain must adopt a proper three-dimensional structure to perform its function. To perform their functions, sometimes proteins undergo self-assembly such as dimerization or polymerization or combine with other proteins to make a functioning complex for the cells. However, in pathological aggregation, namely, amyloid aggregates, the proteins aggregate in a way that changes their functions [12]. Such pathological aggregation can be the core component of several diseases, including neurodegenerative diseases. For example, amyloid β ($A\beta$) peptide and Tau aggregation are implicated in Alzheimer's disease, and α -synuclein aggregation is related to Parkinson's disease [13,14]. CST3 is also shown to be aggregated in diseases such as cerebral amyloid angiopathy (CAA), where it is deposited on the vessel walls along with $A\beta$ peptide, leading to brain hemorrhage and stroke [15]. In the case of inherited CAA, a mutation (L68Q) in CST3 was identified [16]. L68Q mutation increases its aggregation properties [16,17]. CST3 can bind to $A\beta$ peptide and inhibits its aggregation [18]. It is possible that aggregated CST3 still can bind to $A\beta$ peptide but loses its amyloid inhibition properties, resulting in their co-deposition on the vessels. In addition, deposition might change its protease inhibitory properties and alter the balance of protease activity, which crucially affect the integrity of the vessel wall [7]. Furthermore, in sporadic CAA cases, CST3 without any mutation was found to be deposited on the vessel walls along with $A\beta$, indicating the importance of aggregation for the disease pathology [19].

The misfolding or aggregation of a protein may result in a loss-of-function, or a gain-of-function phenotype, which could alter the cellular functions crucial for the cell viability. In a previous study, we showed that CST3 is localized in Bunina bodies, the inclusion bodies found in the motor neurons of ALS spinal cords [20]. In addition, previous studies showed that the exogenous administration of CST3 can make Bunina body-like intracellular aggregates in the motor neurons of ALS model mice [21]. Since it is found in the inclusion bodies, it is possible that CST3 is aggregated here, and that makes it resistant to degradation. However, it is not known how such aggregation changes the activity of the protein. In a study, it is shown that the CST3 dimer, made by domain swapping, loses its protease inhibitory activity [22]. In CAA or ALS, deposited CST3 could be not only dimers, but also be higher order aggregates. Hence, it is important to characterize CST3 aggregation in terms of its structural changes, conditions that induce aggregation, and changes of activities, especially cathepsin inhibitory activity. Such information could be important for a better understanding of disease pathology such as CAA. Therefore, in this study, we aimed to investigate whether the aggregation of CST3 could change some of its activity.

2. Results

Establishment of a system of CST3 aggregation: Recombinant CST3 (1.3 mg/mL) was incubated at 80 °C without agitation or at 37 °C with agitation. Periodically, CST3 was withdrawn from the incubated samples and the protein aggregation was measured. The results are presented in Figure 1. In the case of the 80 °C condition, the aggregation of protein started from 3 days of incubation and reached a plateau at 6 days (Figure 1A). When CST3 was incubated at 37 °C with agitation, protein aggregation was not observed until 12 days. At 19 days, protein aggregation was increased in this condition, however, that was not as high as at 80 °C without agitation (Figure 1B,C).

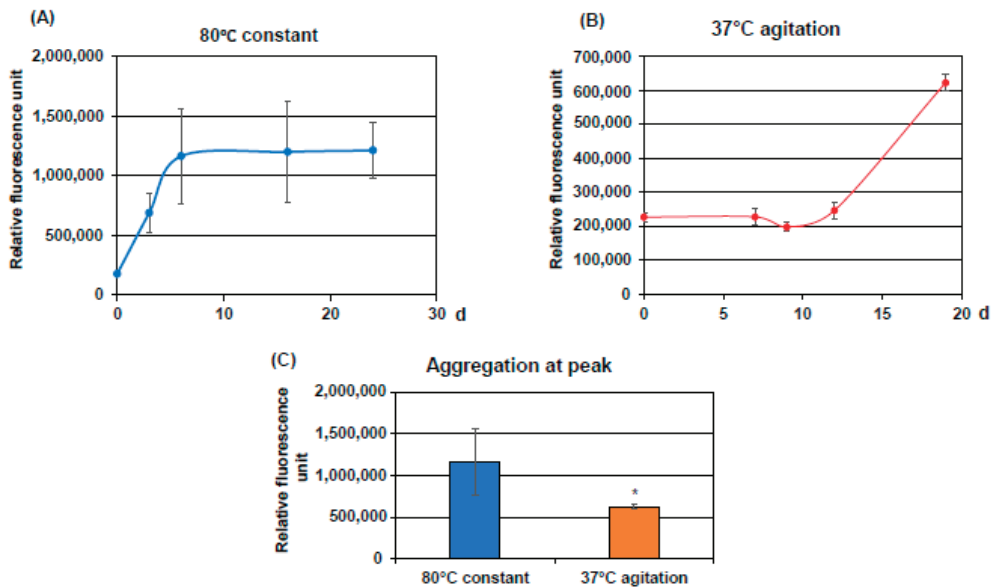


Figure 1. Evaluation of CST3 aggregates: Recombinant CST3 was incubated at 80 °C without agitation or at 37 °C with agitation for indicated times. Aggregation of CST3 was evaluated using an aggregation assay kit, as described in the Materials and Methods. The results were expressed as the average \pm SD of an arbitrary fluorescence unit. (A) shows the fluorescence when CST3 was incubated at 80 °C, and (B) is the fluorescence when CST3 was incubated at 37 °C. (C) shows the aggregated protein levels at the plateau. Statistical significance is denoted as follows.

Characterization aggregated CST3: For characterization, we performed a dot-blot immunoassay using an oligomer conformation-specific antibody. The results showed that the oligomeric CST3 levels were increased in the 37 °C incubation condition compared to that of the 80 °C condition (Figure 2A). Subsequently, the aggregates made at 37 °C were evaluated by Western blotting and electron microscopy. The Western blotting results revealed that CST3 aggregated to several oligomeric species, starting from dimer (Figure 2B). In this condition, CST3 also adopted a fibrillary structure, which was short and broad in morphology (Figure 2C).

Effects of CST3 aggregation on cathepsin B activity: Next, we checked if aggregation changes the function of CST3. Since it is an endogenous cysteine protease inhibitor, we investigated if aggregation changes its inhibitory effects on the activity of a cysteine protease cathepsin B. The cathepsin B activity was measured at pH 5.5 and 7.4 to mimic the conditions of lysosome and extracellular space, respectively. The results showed that the CST3 monomeric form dose-dependently inhibited cathepsin B activity at both the pH 5.5 and 7.4 conditions (Figure 3A,B). In the case of the CST3 aggregated form, the ability of inhibition was decreased at pH 5.5 (Figure 3A). Importantly, at pH 7.4, the aggregated CST3 did not show any inhibitory effects on the cathepsin B activity (Figure 3B).

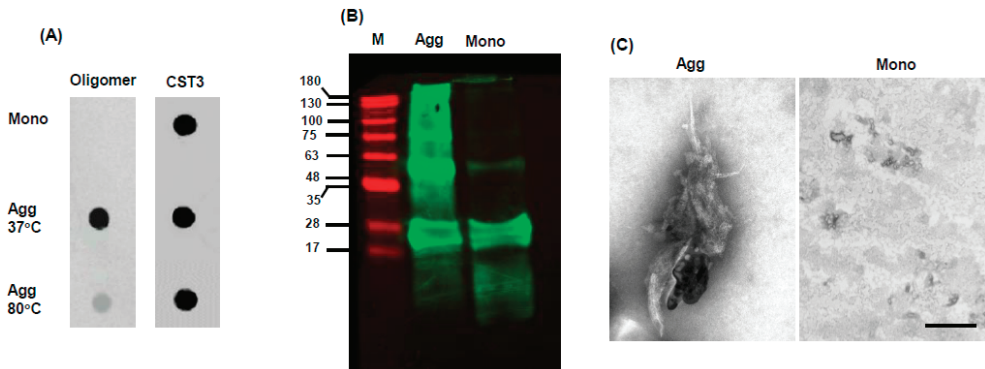


Figure 2. Characterization of CST3 aggregates: For characterization, aggregated CST3 was evaluated by dot-blot immunoassay. After aggregation, the samples were spotted on a nitrocellulose membrane and blotted with an oligomer conformation-specific antibody. (A) shows a representative dot-blot immunoassay data. For loading control, the same membrane was blotted with anti-CST3 IgG. The samples incubated at 37 °C were further evaluated by Western blotting and electron microscopy. Aggregated and monomer samples were separated using a 15% polyacrylamide gel, transferred to a PVDF membrane, and blotted with anti-CST3 IgG. Representative Western blotting data is shown in (B). In (C), electron microscopy photomicrographs of CST3 in monomeric and aggregated forms are shown. Mono = CST3 monomer, Agg = CST3 aggregated at 37 °C. Scale bar = 200 nm.

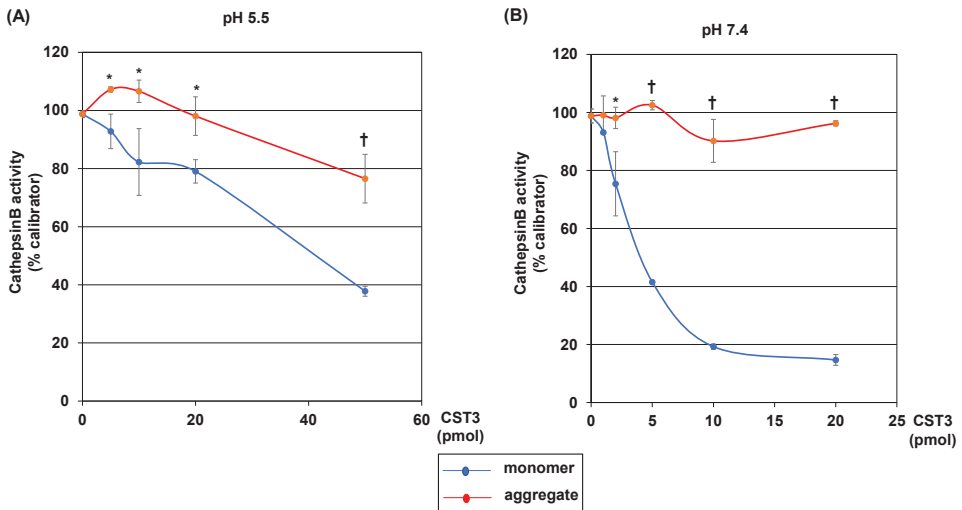


Figure 3. Effects of CST3 aggregation on cathepsin B activity. Cathepsin B activity was measured in the absence or presence of indicated concentrations of non-aggregated or aggregated CST3 at pH 5.5 and 7.4, as described in the Materials and Methods. Cathepsin B activities at pH 5.5 and 7.4 are shown in (A,B), respectively. The data of cathepsin B activity presented here as the average \pm SD of '%calibrator', where cathepsin B activity of one sample in the absence of CST3 was considered as such. Statistical significance is denoted as follows: * $p < 0.01$ vs. corresponding CST3 monomer, and † $p < 0.001$ vs. corresponding CST3 monomer conditions.

Effects of CST3 aggregation on A β fibril formation: Previously, it was demonstrated that CST3 inhibits A β aggregation and protects the neurons from aggregation-induced toxicity [17]. Hence, we checked if aggregation changes such a function of CST3. The incubation of a CST3 monomer with A β ₁₋₄₀ decreased its total fibril levels, as revealed by ThT fluorescence assay. Interestingly, when A β ₁₋₄₀ was incubated with an aggregated form

of CST3, the total fibril levels were not decreased; rather, they slightly but significantly increased (Figure 4). We did not detect an appreciable amount of amyloid fibrils when a CST3 monomer or aggregated forms were incubated alone.

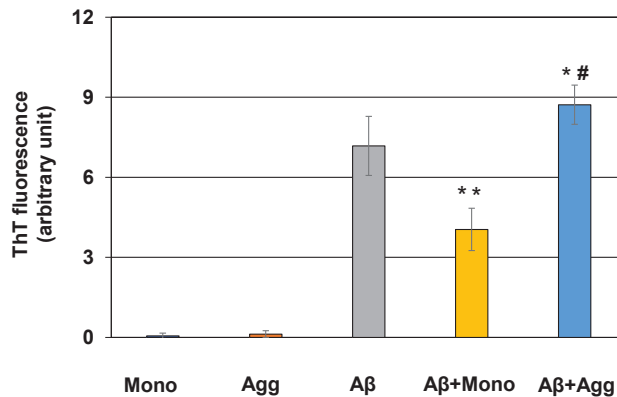


Figure 4. Effects of CST3 aggregation on A β_{1-40} fibril formation. A β_{1-40} (25 μ M) was incubated in the absence or presence of non-aggregated or aggregated CST3 for 48 h, as described in the Materials and Methods. Amyloid fibrils formed after incubation were measured by ThT fluorescence assay. Normalized fluorescence emission values are shown here, and the data are presented as the mean \pm SD of at least three independent experiments. Mono = CST3 monomer, Agg = CST3 aggregated at 37 $^{\circ}$ C. Statistical significance is denoted as follows: * $p < 0.05$ vs. A β_{1-40} , ** $p < 0.005$ vs. A β_{1-40} , # $p < 0.0001$ vs. A β_{1-40} and CST3 monomer condition.

Cellular internalization of CST3: Then, we investigated the cellular internalization of CST3 by immunocytochemistry. After 4 days of incubation with monomeric or aggregated protein, the immunocytochemistry of a neuronal cell culture (NMW7) showed that in both the monomeric and aggregated condition, CST3 was positive inside the cells (Figure 5A). In addition, low levels of immunopositive signals were observed in the neuronal cells without CST3 treatment. Since neuronal cells express CST3, to see the internalization and accumulation of exogenous His6-tagged recombinant CST3 inside the cells, His6 immunocytochemistry was employed. Here, we used an astrocytoma cell line (CCF-STTG1) because of the low levels of endogenous CST3 expression [23]. The results showed that when the cells were incubated with a monomeric form of CST3, His6 was difficult to detect inside the cells. Conversely, when the cells were incubated with an aggregate CST3, most of the cells were found to be His6 positive (Figure 5B).

Effects of CST3 aggregation on cell viability: Finally, we checked the effects of CST3 aggregation on the viability of CCF-STTG1 in culture by MTT assay. The result showed that the aggregated form of CST3 dose-dependently inhibited the viability of CCF-STTG1 cells in culture, whereas the monomeric form of CST3 did not show such effects (Figure 6).

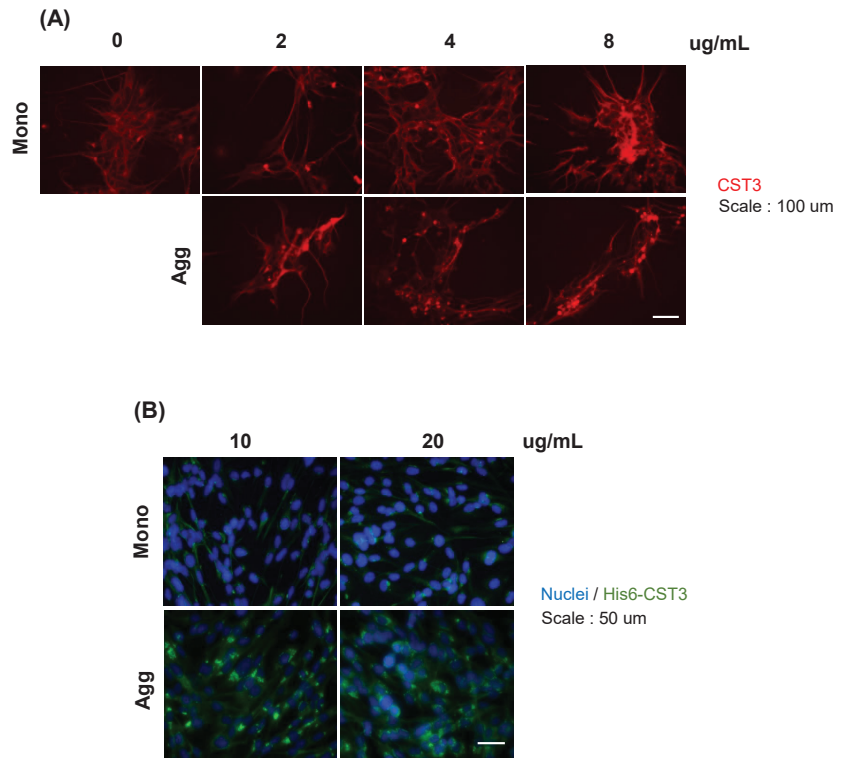


Figure 5. CST3 internalization in neuronal cell culture. (A) Indicated concentrations of recombinant CST3 in non-aggregated or aggregated form were added to a mouse neuronal line and cultured for 4 days. Intracellular CST3 was detected by immunocytochemistry using anti-CST3 IgG (red). (B) A human astrocyte cell line (CCF-STTG1) culture was incubated with indicated concentrations of His6-tagged recombinant non-aggregated and aggregated CST3 for 48 h. After culture, the presence of intracellular CST3 was evaluated by His6 immunocytochemistry (green). Nuclei were stained with Hoechst (blue) Mono = CST3 monomer; Agg = aggregated CST3 at 37 °C.

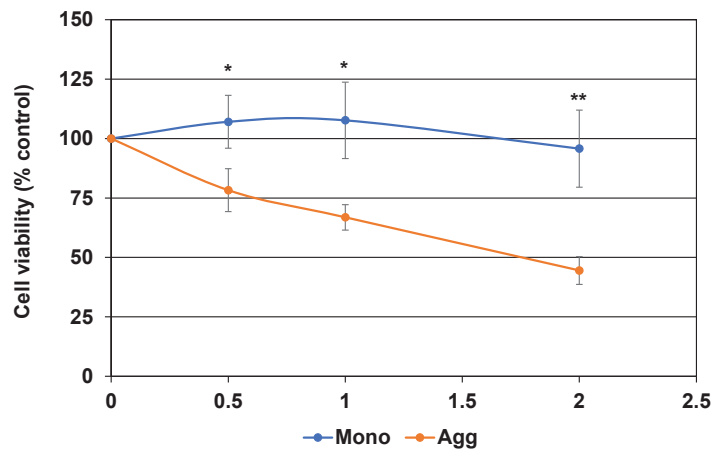


Figure 6. Effects of CST3 aggregation on the viability of a human astrocyte cell line. A human astrocyte cell line culture was treated with indicated concentrations of non-aggregated and aggregated

recombinant CST3 for 48 h. Cell viability after incubation was evaluated by MTT assay, as described in the Materials and Methods. The data was calculated as %control, where cells cultured without CST3 were served as such, and expressed as mean \pm SD of at least three independent experiments. Mono = CST3 monomer, Agg = CST3 aggregated at 37 °C. Statistical significance is denoted as follows; * $p < 0.05$ vs. corresponding aggregated CST3, ** $p < 0.005$ vs. corresponding aggregated CST3 condition.

3. Discussion

In this study we demonstrated that after aggregation, CST3 lost its protease inhibitory activity at physiological pH (7.4) and at pH that is near the lysosomal environment (5.5). It is known that in cerebral and peripheral arteries, CST3 deficiency can induce aneurysmal changes [24–27]. Such changes are largely due to the unchecked activities of proteases such as cathepsins. Consequently, extensive changes of connective tissues and cells of the vessels are seen. In addition, the precise balance of CST3 and proteases is essential for vessel remodeling, and polymorphisms in the gene that alter CST3 levels are found to be associated with pathology such as cerebral small vessel disease [23,28–30]. Aggregated CST3 has a diminished capability to inhibit cathepsin B activity, indicating its reduced function. Moreover, aggregated protein, especially immature aggregates, can interact with cell membranes and make ion channels, leading to the destabilization of the internal environment of the cells [31]. Taken together, the deposition of such aggregated CST3 in the vessel walls during CAA can play an important role in the pathology by altering protease activities and cellular viability. In addition to the vessels, these soluble immature aggregates could also interact with neighboring cells, including neurons and astrocytes. Such interaction of toxic CST3 aggregates could be an independent reason for cellular degeneration, as implied by our cell culture studies.

In CAA, CST3 has been shown to be deposited in the vessel wall along with A β peptide [19]. The ratio of A β and CST3 in the lesion area is about 100:1 [19]. Hence, A β is the primary deposit here, and low level CST3 might try to modulate the course of deposition. A previous study has demonstrated that CST3 can inhibit A β aggregation after binding with the peptide [17], indicating a protective role in the pathology. Since aggregated CST3 did not inhibit A β fibril formation, rather, slightly increasing its levels, such species of the protein could lose its protective effects, resulting in an unchecked deposition of A β . Moreover, a study showed that in the cases of CAA with cerebral hemorrhage, CST3 is most likely to be co-deposited with A β [32], indicating a causal relationship between them. A β used to be deposited in the entire vascular wall, whereas CST3 is positive in the outer media and adventitia layers [32,33]. Similar areas of cathepsins are shown to be positive in cerebral aneurysms [34]. Thus, it is possible that CST3 is deposited in aggregated form, resulting in loss of protease inhibitory activity. Then, combining the effects of unchecked protease activity and A β toxicity cause excessive damage to the vessel wall seen in CAA.

A previous study showed that the oligomeric form of CST3 retains the inhibitory properties of A β aggregation and cathepsin activities [35]. The reason for this discrepancy with our results could be the difference of the preparation procedure of CST3 oligomers. In that study, CST3 samples contain some oligomers, which were separated using membrane filters. Such oligomers were produced by non-domain swapping aggregation and retain their inhibitory properties. A three-dimensional structure analysis showed that CST3 consists of five anti-parallel β -sheets wrapped around a long α -helix. β -sheet 2 and 3 are connected to each other with hairpin loop1 (L1) and β -sheet 4 and 5 with hairpin loop2 (L2). The L1, L2, and N terminal amino acids of CST3 align together and form the motif that inhibits C1 type protease activities [1]. During aggregation by domain swapping, the CST3 monomer unfolded partially, then combined with another molecule by exchanging subdomains, resulting in dimer and other higher order aggregates [1,36]. During the process of oligomerization, the L1 loop present in the canonical CST3 three-dimensional structure disappears, which results in a loss of C1 protease inhibitory activities [1,22,37]. In our aggregation process, prolonged incubation with agitation at 37 °C could induce a

partial unfolding and, consequently, aggregation by domain swapping, which results in loss of cathepsin inhibition properties.

Physical conditions such as heat can alter the aggregation status of protein [38]. At increased temperature, protein adopts an unfolded conformation before being aggregated [38,39]. It is shown that some proteins are aggregation-prone, even in mild heat stress conditions [40]. In this study, we found that CST3 can be aggregated during prolonged incubation at physiological temperature with sufficient agitation, suggesting that CST3 could be an aggregation-prone protein [41]. CST3 can also be aggregated at high temperatures (80 °C). However, it did not adopt an oligomeric structure at this temperature. Hence, it might adopt an amorphous conformation in this condition [42]. In addition, 80 °C is far above the physiological temperature. Thus, we did not pursue further with this temperature. At 37 °C, CST3 clearly showed various sizes of oligomeric species. In addition, some aggregates adopt fibrillary structure, indicating the aggregation-prone properties of CST3.

In culture conditions, including a neuroblastoma cell culture [43,44], CST3 is demonstrated to internalize and localize in the lysosome. In those studies, the monomeric form of CST3 was used to see the internalization. Our study demonstrated that the aggregated form of CST3 can also be internalized more efficiently than its monomeric form. Although we did not investigate the process of internalization, the possible mechanism could be endocytosis, because the size of the aggregates was quite big, as revealed by the electron microscopy. Most of the proteins associated with neurodegenerative diseases have the propensity to make fibrillar aggregate. Such fibrils have the ability to infiltrate into the cells through endocytosis [45]. For endocytosis, several points including membrane properties, membrane receptor-mediated binding, and the monomeric and fibrillar structures of the proteins have been proposed to be important [42–46]. Although we did not elucidate the exact mechanisms, it is possible that aggregated CST3 interacts with cell membranes more robustly than its monomeric form, causing the endocytic internalization efficient. The internalized proteins were found to be distributed in a dot-like pattern, indicating its location in the lysosome. In a previous study, we demonstrated the localization of CST3 in neuronal lysosomes in culture condition and in human brains (20). Hence, the accumulation of aggregated CST3 might alter the lysosomal activities, which could be detrimental for the cells. Indeed, we found that aggregated CST3 is toxic to the cells in culture.

Our study provides an important insight into the functional changes of CST3 after aggregation. However, some limitations of the study should be noted. First, our study used an *in vitro* system to analyze the functional properties of CST3, not animal models or pathological specimens. Since animal models and pathological conditions are far more complex than *in vitro* systems [47], it will be worthwhile to characterize the deposited CST3 in the animal models and pathological conditions such as CAA in respect of structural and functional changes. Second, our study showed that physiological temperature is enough to induce aggregation, even stored at cold conditions can induce its aggregation [48]. Hence, some factors might be involved *in vivo* conditions that keep CST3 in monomeric form. Identification of such factors could be important for a better understanding of the pathology of CST3-related diseases such as CAA and the subsequent identification of potential therapeutic targets for the disease.

4. Conclusions

In conclusion, CST3 aggregated in physiological temperature has altered properties that reduced its protective effects on protease activities and A β aggregation. Such altered properties of CST3 could be important in the pathophysiology of CAA and neurodegenerative diseases such as ALS.

5. Materials and Methods

5.1. Preparation of Recombinant CST3

To prepare recombinant protein, a bacterial expression vector (CST3-pQE32) was generated by inserting the entire coding region of CST3 into a pQE32 expression vector containing His6 tag (Qiagen, Hilden, Germany). Schematic representation of vector generation is shown in Supplemental Figure S1. To generate the vector, the coding sequence of CST3 was PCR amplified using Phusion High-Fidelity DNA polymerase (ThermoFisher, Waltham, MA, USA), where human brain cDNA (Clontech, Mountain View, CA, USA) was used as a template. In addition to cDNA sequence, forward primer contained a SphI and that of reverse primer a HindIII sites at their 5' ends. Then, the PCR product and pQE32 vector were digested with SphI and HindIII (New England BioLab, Ipswich, MA, USA). Digested PCR product ligated with digested pQE32 vector using Ligation High enzyme kit (Toyobo, Osaka, Japan) to prepare CST3-pQE32 vector. The vector was used to transform chemically competent *Escherichia coli* bacteria (JM109; Promega, Madison, WI, USA). Then, CST3 were expressed in transformed JM109 by 0.4 mM Isopropyl β -D-1-thiogalactopyranoside (IPTG) and purified by affinity chromatography using Ni-NTA Superflow columns (Qiagen) according to the manufacturer's instructions.

5.2. Aggregation of CST3

To induce aggregation, recombinant CST3 monomer dissolved in PBS (pH 7.4) (1.3 mg/mL) was incubated at 37 °C with vigorous agitation or at 80 °C without agitation for indicated times.

5.3. Aggregation Assay

Aggregation of the proteins were analyzed using a kit (PROTEOSTAT aggregation assay, Enzo Life Sciences, Farmingdale, NY, USA) according to the manufacturer's instruction. Briefly, 2 μ L of diluted PROTEOSTAT detection reagent was dispensed at the bottom of a well of a 96-well plate. After incubation of the protein at indicated conditions for indicated times, 98 μ L of the protein was taken from the solution and directly added to the well and incubated at room temperature for 15 min in the dark. Then, the generated signal was read using a fluorescence microplate reader with excitation and emission wavelengths at 550 and 600 nm, respectively. Along with the test samples, both positive and negative controls, as well as blanks (1 \times assay buffer alone), were analyzed. The data are presented as the average \pm standard deviation (SD) of an arbitrary fluorescence unit.

5.4. Dot-Blot Oligomer Assay

After aggregation, 2.6 μ g of the proteins were spotted on a nitrocellulose membrane. As a negative control, CST3 monomer samples were used. The membrane was incubated in a blocking solution (2% bovine serum albumin in PBS, 0.5% Tween20) for 1 h. Then, the membrane was blotted with an oligomer-specific antibody (A11, Invitrogen, Waltham, MA, USA, rabbit, 1:1000) diluted in blocking solution for 2 h at room temperature. This antibody specifically reacts with a variety of soluble oligomeric protein aggregates regardless of their amino acid sequence and does not react with monomer species or insoluble fibrils of protein/peptide [49]. To detect immunoreactive protein, an infrared dye conjugated anti-rabbit IgG (Li-COR Biosciences, Lincoln, NE, USA, diluted 5000 times with blocking solution) was added to the membrane, incubated for 1 h at room temperature, and scanned with Odyssey infrared dye scanning system (Li-COR), according to the manufacturer's instructions. After every incubation, the membrane was washed with a wash buffer (0.5% Tween20 in PBS), except after blocking. After stripping, the membrane was also blotted with anti-CST3 antibody (Abcam, Waltham, MA, USA, rabbit, 1:1000), which served as a loading control.

5.5. Electron Microscopy

Electron microscopic analysis of monomeric and aggregated forms of CST3 was performed as described previously [50]. In a brief, 5 μ L of monomeric or aggregated CST3 (1.3 mg/mL) was applied to a carbon coated Formvar grid (Nisshin EM Co., Tokyo, Japan) and incubated for 1 min. After incubation, 1 drop of 0.5% *v/v* glutaraldehyde solution was applied to the grid and incubated again for 1 min. Then, the grid was washed with a few drops of water and dried. Ten microliters of 2% *w/v* uranyl acetate solution were applied to the dried grid and incubated for 2 min. Finally, excess uranyl acetate was soaked with a paper towel, and the grid was air-dried and examined under an EM-002B electron microscope (Topcon, Tokyo, Japan).

5.6. Western Blotting

Western blotting was performed as described previously [51]. In a brief, equal volume of non-reducing Western blotting sample buffer (125 mM Tris HCl, pH 6.8; 20% glycerol; 4% SDS; 0.1% bromophenol blue) was added to monomeric and aggregated CST3, and incubated at 85 °C for 2 min. Then 2 μ g equivalent of monomeric and aggregated proteins were separated by electrophoresis using 15% polyacrylamide gel. After transfer to a PVDF membrane, the membrane was incubated with anti-CST3 IgG (rabbit, Abcam). The Immunoreaction was identified using infrared-fluorophore-conjugated anti-rabbit IgG (Li-COR, diluted 5000 times with blocking solution), and the signals of Immunoreactive proteins were detected using an infrared scanner (Li-COR).

5.7. Cathepsin B Assay

Cathepsin B activity was measured, as described previously [20]. In a brief, 75 μ L reaction mixture was prepared by adding cathepsin B (2.5 μ g/mL, 10 μ L), and indicated concentrations of aggregated or monomeric CST3 to a reaction buffer (final concentrations: 20 mM L-cysteine and 0.13 mM sodium acetate, pH 5.5 or 7.4), mixed and incubated for 5 min at 37 °C. Then, 20 μ L of substrate (Z-Arg-Arg-MCA; 20 μ M, Peptide Institute, Osaka, Japan) was added to the reaction mixtures and incubated for another 1 h at 37 °C. The enzymatic reaction was terminated with 100 μ L of 0.1 M monochloroacetate (pH 4.3), and the levels of released MCA was measured with a multimode microplate reader (DTX880; Beckman coulter, Brea, CA, USA), with excitation and emission wavelengths at 370 nm and 465 nm, respectively.

5.8. A β ₁₋₄₀ Peptide Fibril Formation

For fibril formation, 50 μ L solution of synthetic A β ₁₋₄₀ peptide (Peptide Institute, Osaka, Japan) (25 μ M) in fibril formation buffer (50 mM phosphate buffer pH 7.5 and 100 mM NaCl) was prepared with or without CST3 monomer or aggregates (1.3 μ g). The reaction mixture was incubated at 37 °C without agitation for 48 h, and then the fibril formation reaction was terminated by quickly freezing the samples.

5.9. Assessment of Fibril Levels Using ThT Fluorescence

After incubation, the presence of β -sheet structures in the reaction mixtures were monitored by means of ThT fluorescence spectroscopy. Samples were diluted tenfold with glycine (pH 8.5, 50 mM final concentration) and ThT (5 μ M final concentration). ThT fluorescence was measured using a fluorescence spectrophotometer (F2500 spectrofluorometer, Hitachi, Tokyo, Japan), with excitation and emission wavelengths of 446 and 490 nm, respectively. The normalized fluorescence intensities of the β -sheet amyloids were obtained by subtracting the fluorescence intensity of buffer alone from that of the sample.

5.10. Cell Culture

5.10.1. CCF-STTG1 Culture

A human astrocytoma cell line (CCF-STTG1) was obtained from American Type Culture Collection (ATCC, Manassas, VA, USA) and cultured in RPMI-1640 medium

(ATCC) containing 10% fetal bovine serum (FBS, Gibco, Invitrogen). During stimulations with aggregated or monomeric CST3, FBS concentration was reduced to 1%.

5.10.2. Culture of a Mouse Neuronal Stem Cell Line and Differentiation to Mature Neurons

Neuronal stem cells were isolated from fetus of a wild-type mouse with MRL background at 14.5 days of gestation and a neuronal stem cell line (NMW7) was generated, as described previously [52]. The cell line shows similar morphological, expressional, and differentiation potentials as primary mouse neuronal stem cells. NMW7 was plated in a tissue culture dish in complete media (high glucose DMEM: F12 ham 1:1, 2% FBS, N2 supplement, bFGF 20 ng/mL, and EGF 20 ng/mL). For differentiation, neurospheres were generated by culturing the cells in neurosphere medium (high glucose DMEM: F12 ham 1:1, bFGF 20 ng/mL, EGF 20 ng/mL, N2 supplement, and B27 supplement) for 3 days. Neurospheres containing medium were transferred to poly-L-lysine (PL)-coated dishes, and an equal amount of differentiation medium (DMEM: F12 ham 1:1, B27) was added and cultured. When the neurospheres were attached, the medium was removed; fresh differentiation medium was added and cultured for another 14 days. After differentiation, indicated concentrations of non-aggregated or aggregated recombinant CST3 was added to the medium, and the culture was continued for another 4 days.

5.11. (3-(4,5-Dimethylthiazol-2-yl)-2,5-diphenyltetrazolium Bromide (MTT) Assay

The toxicity of monomeric and aggregated CST3 was evaluated by an MTT cell viability assay, as described previously [24]. Briefly, CCF-STTG1 cells (3×10^3 /well) were seeded into wells of a 96-well plate and cultured for 24 h. The cells were treated with the indicated concentrations of monomeric or aggregated CST3 in 100 μ L DMEM containing 0.5% FBS for 48 h. After incubation, 20 μ L of MTT solution (Sigma Aldrich, St. Louis, MO, USA) (5 mg/mL) was added to the culture medium, and incubation was continued for 3.5 h at 37 °C. Then, the medium was removed carefully, MTT solvent (4 mM HCl, 0.1% Nonidet-P-40 in isopropanol, 150 μ L) was added to the wells, and the plate was incubated at room temperature for 15 min with protection from light. Then, the absorbance was read at 590 nm. The absorbance of the cells culture without CST3 were used as a control.

5.12. Immunocytochemistry

For immunocytochemistry, cells were cultured in appropriate 8-well chamber slides. After culture, CCF-STTG1 or NMW7 cells were fixed with 4% paraformaldehyde in phosphate-buffered saline (PBS) for 15 min and blocked with 5% normal goat serum and 0.1% Triton X-100 in PBS for 30 min. Then, anti-His6 IgG (mouse, 1:50; Roche, Basel, Switzerland) or anti-CST3 IgG (rabbit, 1:200; Abcam) was added to the wells and incubated overnight at 4 °C. Immunoreactive proteins were detected with Texas Red-conjugated goat anti-rabbit IgG (1:200; Santa Cruz Biotechnology, Santa Cruz, CA, USA) or FITC-conjugated goat anti-mouse IgG (1:200; Santa Cruz Biotechnology). The fluorescence signals were visualized using a fluorescence microscope equipped with filters for individual fluorophores (FITC emission filter wavelength 525 nm, Texas red emission filter wavelength 620 nm, Hoechst emission filter wavelength 460 nm) (ECLIPSE E600, NIKON, Tokyo, Japan).

5.13. Statistical Analysis

Numerical data are expressed as means \pm SD of at least three independent experiments. Statistical analysis to compare mean values was performed using one-way ANOVA, followed by Scheffe's post hoc test or Student's T TEST, and *p* value < 0.05 was considered as statistically significant.

Supplementary Materials: The following are available online at <https://www.mdpi.com/article/10.3390/ijms22189682/s1>, Figure S1: Human CST3 coding sequence and schematic design of CST3 expression vector generation; Table S1: CST3 aggregation assay; Table S2: Cathepsin B inhibition assay (pH 5.5); Table S3: Cathepsin B inhibition assay (pH 7.4); Table S4: Effects of CST3 aggregation

on A β 1-40 fibril formation; Table S5: Effects of CST3 aggregation on the viability of a human astrocyte cell line.

Author Contributions: Conceptualization, A.M.S.; Y.W.; and A.N.; methodology, Y.W.; S.T. and A.M.S.; validation, Y.W. and S.T.; formal analysis, A.M.S.; resources, S.Y. and A.N.; data curation, S.I. and S.M.; writing—original draft preparation, A.M.S. and A.N.; writing—review and editing, A.M.S.; S.M.; S.Y. and A.N.; supervision, S.Y.; project administration, A.N.; funding acquisition, S.Y. and A.N. All authors have read and agreed to the published version of the manuscript.

Funding: This research did not receive grants from any funding agencies. The study is entirely supported by internal departmental funding.

Data Availability Statement: All data of this study are shown in the report.

Acknowledgments: We would like to acknowledge and thank the Interdisciplinary Center for Science and research, Organization for Research and Academic Information, Shimane University for their technical expertise and help to efficiently carry out the study.

Conflicts of Interest: All authors declare no conflict of interest.

References

1. Mussap, M.; Plebani, M. Biochemistry and clinical role of human cystatin C. *Crit. Rev. Clin. Lab. Sci.* **2004**, *41*, 467–550. [CrossRef]
2. Yamaze, T.; Mino, S.; Atsuta, I.; Danjo, A.; Kagia, T.; Nishijima, K.; Jang, J.; Kido, M.A.; Tanaka, T. Localization of the endogenous cysteine proteinase Inhibitor, cystatin C, and the cysteine proteinase, cathepsin B, to the junctional epithelium in rat gingiva. *Acta Histochem. Cytochem.* **2005**, *38*, 121–129. [CrossRef]
3. Deng, A.; Irizarry, M.C.; Nitsch, R.M.; Growdon, J.H.; Rebeck, G.W. Elevation of cystatin C in susceptible neurons in Alzheimer's disease. *Am. J. Pathol.* **2001**, *159*, 1061–1068. [CrossRef]
4. Watanabe, S.; Hayakawa, T.; Wakasugi, K.; Yamanaka, K. Cystatin C protects neuronal cells against mutant copper-zinc superoxide dismutase-mediated toxicity. *Cell Death Dis.* **2014**, *5*, e1497. [CrossRef] [PubMed]
5. Abrahamson, M.; Barrett, A.; Salvesen, G.; Grubb, A. Isolation of six cysteine proteinase inhibitors from human urine. Their physicochemical and enzyme kinetic properties and concentrations in biological fluids. *J. Biol. Chem.* **1986**, *261*, 11282–11289. [CrossRef]
6. Zavasnik-Bergant, T.; Bergant, M.; Jaras, M.; Griffiths, G. Different localisation of cystatin C in immature and mature dendritic cells. *Radiol. Oncol.* **2006**, *40*, 183–188.
7. Lutgens, S.P.M.; Cleutjens, K.B.J.M.; Daemen, M.; Heeneman, S. Cathepsin cysteine proteases in cardiovascular disease. *FASEB J.* **2007**, *21*, 3029–3041. [CrossRef]
8. Turk, V.; Stoka, V.; Vasiljeva, O.; Renko, M.; Sun, T.; Turk, B.; Turk, D. Cysteine cathepsins: From structure, function and regulation to new frontiers. *Biochim. Biophys. Acta BBA Proteins Proteom.* **2012**, *1824*, 68–88. [CrossRef]
9. Yasuhara, O.; Hanai, K.; Ohkubo, I.; Sasaki, M.; McGeer, P.L.; Kimura, H. Expression of cystatin C in rat, monkey and human brains. *Brain Res.* **1993**, *628*, 85–92. [CrossRef]
10. Ren, Y.; Zhu, W.; Cui, F.; Yang, F.; Chen, Z.; Ling, L.; Huang, X. Measurement of cystatin C levels in the cerebrospinal fluid of patients with amyotrophic lateral sclerosis. *Int. J. Clin. Exp. Pathol.* **2015**, *8*, 5419–5426.
11. Vidak, E.; Javoršek, U.; Vizovišek, M.; Turk, B. Cysteine cathepsins and their extracellular roles: Shaping the microenvironment. *Cells* **2019**, *8*, 264. [CrossRef]
12. Winklhofer, K.F.; Tatzelt, J.; Haass, C. The two faces of protein misfolding: Gain- and loss-of-function in neurodegenerative diseases. *EMBO J.* **2008**, *27*, 336–349. [CrossRef]
13. Lloret, A.; Fuchsberger, T.; Giraldo, E.; Viña, J. Molecular mechanisms linking amyloid β toxicity and Tau hyperphosphorylation in Alzheimer's disease. *Free Radic. Biol. Med.* **2015**, *83*, 186–191. [CrossRef]
14. Mehra, S.; Sahay, S.; Maji, S.K. α -Synuclein misfolding and aggregation: Implications in Parkinson's disease pathogenesis. *Biochim. Biophys. Acta BBA Proteins Proteom.* **2019**, *1867*, 890–908. [CrossRef]
15. Cohen, D.H.; Feiner, H.; Jensson, O.; Frangione, B. Amyloid fibril in hereditary cerebral hemorrhage with amyloidosis (HCHWA) is related to the gastroentero-pancreatic neuroendocrine protein, gamma trace. *J. Exp. Med.* **1983**, *158*, 623–628. [CrossRef] [PubMed]
16. Palsdottir, A.; Snorraddottir, A.O.; Thorsteinsson, L. Hereditary cystatin C amyloid angiopathy: Genetic, clinical, and pathological aspects. *Brain Pathol.* **2006**, *16*, 55–59. [CrossRef] [PubMed]
17. Abrahamson, M.; Grubb, A. Increased body temperature accelerates aggregation of the Leu-68→Gln mutant cystatin C, the amyloid-forming protein in hereditary cystatin C amyloid angiopathy. *Proc. Natl. Acad. Sci. USA* **1994**, *91*, 1416–1420. [CrossRef] [PubMed]
18. Tizon, B.; Ribe, E.M.; Mi, W.; Troy, C.M.; Levy, E. Cystatin C protects neuronal cells from amyloid- β -induced toxicity. *J. Alzheimer's Dis.* **2010**, *19*, 885–894. [CrossRef] [PubMed]

19. Nagai, A.; Kobayashi, S.; Shimode, K.; Imaoka, K.; Umegae, N.; Fujihara, S.; Nakamura, M. No mutations in cystatin C gene in cerebral amyloid angiopathy with cystatin C deposition. *Mol. Chem. Neuropathol.* **1998**, *33*, 63–78. [CrossRef]
20. Wada, Y.; Nagai, A.; Sheikh, A.M.; Onoda, K.; Terashima, M.; Shiota, Y.; Araki, A.; Yamaguchi, S. Co-localization of cystatin C and prosaposin in cultured neurons and in anterior horn neurons with amyotrophic lateral sclerosis. *J. Neurol. Sci.* **2018**, *384*, 67–74. [CrossRef]
21. Watanabe, S.; Komine, O.; Endo, F.; Wakasugi, K.; Yamanaka, K. Intracerebroventricular administration of Cystatin C ameliorates disease in SOD1-linked amyotrophic lateral sclerosis mice. *J. Neurochem.* **2018**, *145*, 80–89. [CrossRef]
22. Ekiel, I.; Abrahamson, M. Folding-related dimerization of human cystatin, C. *J. Biol. Chem.* **1996**, *271*, 1314–1321. [CrossRef]
23. Mitaki, S.; Nagai, A.; Sheikh, A.M.; Terashima, M.; Isomura, M.; Nabika, T.; Yamaguchi, S. Contribution of cystatin C gene polymorphisms to cerebral white matter lesions. *Cerebrovasc. Dis.* **2011**, *32*, 489–496. [CrossRef]
24. Lindholt, J.S.; Erlandsen, E.J.; Henneberg, E.W. Cystatin C deficiency is associated with the progression of small abdominal aortic aneurysms. *Br. J. Surg.* **2001**, *88*, 1472–1475. [CrossRef]
25. Shi, G.-P.; Sukhova, G.K.; Grubb, A.; Ducharme, A.; Rhode, L.H.; Lee, R.T.; Ridker, P.M.; Libby, P.; Chapman, H.A. Cystatin C deficiency in human atherosclerosis and aortic aneurysms. *J. Clin. Investig.* **1999**, *104*, 1191–1197. [CrossRef]
26. Nishimura, Y.; Honda, K.; Yuzaki, M.; Tajima, K.; Nakamura, R.; Nakanishi, Y.; Kaneko, M.; Agematsu, K.; Nagashima, M. Serum cystatin C level as a biomarker of aortic plaque in patients with an aortic arch aneurysm. *J. Atheroscler. Thromb.* **2021**, *28*, 506–513. [CrossRef]
27. Lv, B.-J.; Lindholt, J.; Cheng, X.; Wang, J.; Shi, G.-P. Plasma cathepsin S and cystatin C levels and risk of abdominal aortic aneurysm: A randomized population-based study. *PLoS ONE* **2012**, *7*, e41813. [CrossRef]
28. Liu, J.; Sukhova, G.K.; Sun, J.-S.; Xu, W.-H.; Libby, P.; Shi, G.-P. Lysosomal cysteine proteases in atherosclerosis. *Arter. Thromb. Vasc. Biol.* **2004**, *24*, 1359–1366. [CrossRef] [PubMed]
29. Yang, S.; Cai, J.; Lu, R.; Wu, J.; Zhang, M.; Zhou, X. Association between serum cystatin C level and total magnetic resonance imaging burden of cerebral small vessel disease in patients with acute lacunar stroke. *J. Stroke Cerebrovasc. Dis.* **2017**, *26*, 186–191. [CrossRef] [PubMed]
30. Maniwa, K.; Yano, S.; Sheikh, A.M.; Onoda, K.; Mitaki, S.; Isomura, M.; Mishima, S.; Yamaguchi, S.; Nabika, T.; Nagai, A. Association between cystatin C gene polymorphism and the prevalence of white matter lesion in elderly healthy subjects. *Sci. Rep.* **2020**, *10*, 1–9. [CrossRef] [PubMed]
31. Lashuel, H.A.; Hartley, D.; Petre, B.M.; Walz, T.; Lansbury, P.T., Jr. Neurodegenerative disease: Amyloid pores from pathogenic mutations. *Nature* **2002**, *418*, 291. [CrossRef] [PubMed]
32. Maruyama, K.; Kametani, F.; Ikeda, S.; Ishihara, T.; Yanagisawa, N. Characterization of amyloid fibril protein from a case of cerebral amyloid angiopathy showing immunohistochemical reactivity for both beta protein and cystatin C. *Neurosci. Lett.* **1992**, *144*, 38–42. [CrossRef]
33. Levy, E.; Jaskolski, M.; Grubb, A. The role of cystatin C in cerebral amyloid angiopathy and stroke: Cell biology and animal models. *Brain Pathol.* **2006**, *16*, 60–70. [CrossRef] [PubMed]
34. Aoki, T.; Kataoka, H.; Ishibashi, R.; Nozaki, K.; Hashimoto, N. Cathepsin B, K, and S are expressed in cerebral aneurysms and promote the progression of cerebral aneurysms. *Stroke* **2008**, *39*, 2603–2610. [CrossRef] [PubMed]
35. Perlenfein, T.J.; Mehlhoff, J.D.; Murphy, R.M. Insights into the mechanism of cystatin C oligomer and amyloid formation and its interaction with beta-amyloid. *J. Biol. Chem.* **2017**, *292*, 11485–11498. [CrossRef] [PubMed]
36. Janowski, R.; Kozak, M.; Jankowska, E.; Grzonka, Z.; Grubb, A.; Abrahamson, M.; Jaskolski, M. Human cystatin C, an amyloidogenic protein, dimerizes through three-dimensional domain swapping. *Nat. Struct. Biol.* **2001**, *8*, 316–320. [CrossRef] [PubMed]
37. Chrabaszczyńska, M.; Sierdzan, A.K.; Rodziewicz-Motowidło, S.; Grubb, A.; Dobson, C.M.; Kumita, J.R.; Kozak, M. Structural characterization of covalently stabilized human cystatin C oligomers. *Int. J. Mol. Sci.* **2020**, *21*, 5860. [CrossRef]
38. Wilkening, A.; Rüb, C.; Sylvester, M.; Voos, W. Analysis of heat-induced protein aggregation in human mitochondria. *J. Biol. Chem.* **2018**, *293*, 11537–11552. [CrossRef]
39. Jahn, T.; Radford, S.E. Folding versus aggregation: Polypeptide conformations on competing pathways. *Arch. Biochem. Biophys.* **2008**, *469*, 100–117. [CrossRef]
40. Jahn, T.; Parker, M.J.; Homans, S.W.; Radford, S. Amyloid formation under physiological conditions proceeds via a native-like folding intermediate. *Nat. Struct. Mol. Biol.* **2006**, *13*, 195–201. [CrossRef]
41. Tsiolaki, P.L.; Louros, N.N.; Hamodrakas, S.J.; Iconomidou, V.A. Exploring the ‘aggregation-prone’ core of human cystatin C: A structural study. *J. Struct. Biol.* **2015**, *191*, 272–280. [CrossRef]
42. Haghghi-Poodeh, S.; Navidpour, L.; Yaghmaei, P.; Ebrahim-Habibi, A. Monocyclic phenolic compounds stabilize human insulin and suppress its amorphous aggregation: In vitro and in vivo study. *Biochem. Biophys. Res. Commun.* **2019**, *518*, 362–367. [CrossRef] [PubMed]
43. Wallin, H.; Bjarnadottir, M.; Vogel, L.K.; Wassélius, J.; Ekström, U.; Abrahamson, M. Cystatins—Extra- and intracellular cysteine protease inhibitors: High-level secretion and uptake of cystatin C in human neuroblastoma cells. *Biochimie* **2010**, *92*, 1625–1634. [CrossRef] [PubMed]
44. Ekström, U.; Wallin, H.; Lorenzo, J.; Holmqvist, B.; Abrahamson, M.; Avilés, F.X. Internalization of cystatin C in human cell lines. *FEBS J.* **2008**, *275*, 4571–4582. [CrossRef]

45. Holmes, B.B.; Diamond, M.I. Cellular mechanisms of protein aggregate propagation. *Curr. Opin. Neurol.* **2012**, *25*, 721–726. [CrossRef]
46. Wesén, E.; Jeffries, G.D.M.; Dzebo, M.M.; Esbjörner, E.K. Endocytic uptake of monomeric amyloid- β peptides is clathrin- and dynamin-independent and results in selective accumulation of A β (1–42) compared to A β (1–40). *Sci. Rep.* **2017**, *7*, 2021. [CrossRef] [PubMed]
47. Beck, A.P.; Meyerholz, D.K. Evolving challenges to model human diseases for translational research. *Cell Tissue Res.* **2020**, *380*, 305–311. [CrossRef]
48. Almy, F.S.; Christopher, M.M.; King, D.P.; Brown, S.A. Evaluation of cystatin c as an endogenous marker of glomerular filtration rate in dogs. *J. Vet. Intern. Med.* **2002**, *16*, 45–51. [CrossRef]
49. Kaye, R.; Head, E.; Thompson, J.L.; McIntire, T.M.; Milton, S.C.; Cotman, C.W.; Glabe, C.G. Common structure of soluble amyloid oligomers implies common mechanism of pathogenesis. *Science* **2003**, *300*, 486–489. [CrossRef]
50. Tabassum, S.; Sheikh, A.M.; Yano, S.; Ikeue, T.; Handa, M.; Nagai, A. A carboxylated Zn-phthalocyanine inhibits fibril formation of Alzheimer's amyloid beta peptide. *FEBS J.* **2015**, *282*, 463–476. [CrossRef] [PubMed]
51. Sheikh, A.M.; Yano, S.; Mitaki, S.; Haque, M.A.; Yamaguchi, S.; Nagai, A. A mesenchymal stem cell line (B10) increases angiogenesis in a rat MCAO model. *Exp. Neurol.* **2019**, *311*, 182–193. [CrossRef] [PubMed]
52. Sheikh, A.; Yano, S.; Tabassum, S.; Omura, K.; Araki, A.; Mitaki, S.; Ito, Y.; Huang, S.; Nagai, A. Alteration of neural stem cell functions in ataxia and male sterility mice: A possible role of β -tubulin glutamylation in neurodegeneration. *Cells* **2021**, *10*, 155. [CrossRef] [PubMed]



Article

Structural and Functional Alterations in Mitochondria-Associated Membranes (MAMs) and in Mitochondria Activate Stress Response Mechanisms in an In Vitro Model of Alzheimer's Disease

Tânia Fernandes ^{1,2,3,4}, Rosa Resende ^{1,2,3}, Diana F. Silva ^{1,2,3}, Ana P. Marques ^{1,2,3}, Armanda E. Santos ^{1,5}, Sandra M. Cardoso ^{1,3,4}, M. Rosário Domingues ⁶, Paula I. Moreira ^{1,3,4,*} and Cláudia F. Pereira ^{1,3,4,*}

- ¹ CNC—Center for Neuroscience and Cell Biology, CIBB—Center for Innovative Biomedicine and Biotechnology, University of Coimbra, 3004-504 Coimbra, Portugal; tfernandes@cnc.uc.pt (T.F.); rresende@cnc.uc.pt (R.R.); dianaffsilva@gmail.com (D.F.S.); apatriciabmarques@gmail.com (A.P.M.); aesantos@ci.uc.pt (A.E.S.); cardoso.sandra.m@gmail.com (S.M.C.)
 - ² IIIUC—Institute for Interdisciplinary Research, University of Coimbra, 3030-789 Coimbra, Portugal
 - ³ CACC—Clinical Academic Center of Coimbra, 3004-561 Coimbra, Portugal
 - ⁴ Faculty of Medicine, University of Coimbra, 3000-548 Coimbra, Portugal
 - ⁵ Laboratory of Biochemistry and Biology, Faculty of Pharmacy, University of Coimbra, 3000-548 Coimbra, Portugal
 - ⁶ Mass Spectrometry Centre, REQUIMTE-LAQV and CESAM, Department of Chemistry, University of Aveiro, 3810-193 Aveiro, Portugal; mrd@ua.pt
- * Correspondence: pimoreira@fmed.uc.pt (P.I.M.); cpereira@fmed.uc.pt (C.F.P.)

Citation: Fernandes, T.; Resende, R.; Silva, D.F.; Marques, A.P.; Santos, A.E.; Cardoso, S.M.; Domingues, M.R.; Moreira, P.I.; Pereira, C.F. Structural and Functional Alterations in Mitochondria-Associated Membranes (MAMs) and in Mitochondria Activate Stress Response Mechanisms in an In Vitro Model of Alzheimer's Disease. *Biomedicines* **2021**, *9*, 881. <https://doi.org/10.3390/biomedicines9080881>

Academic Editor: Masaru Tanaka

Received: 5 July 2021
Accepted: 21 July 2021
Published: 24 July 2021

Publisher's Note: MDPI stays neutral with regard to jurisdictional claims in published maps and institutional affiliations.



Copyright: © 2021 by the authors. Licensee MDPI, Basel, Switzerland. This article is an open access article distributed under the terms and conditions of the Creative Commons Attribution (CC BY) license (<https://creativecommons.org/licenses/by/4.0/>).

Abstract: Alzheimer's disease (AD) is characterized by the accumulation of extracellular plaques composed by amyloid- β ($A\beta$) and intracellular neurofibrillary tangles of hyperphosphorylated tau. AD-related neurodegenerative mechanisms involve early changes of mitochondria-associated endoplasmic reticulum (ER) membranes (MAMs) and impairment of cellular events modulated by these subcellular domains. In this study, we characterized the structural and functional alterations at MAM, mitochondria, and ER/microsomes in a mouse neuroblastoma cell line (N2A) overexpressing the human amyloid precursor protein (APP) with the familial Swedish mutation (APP^{swe}). Proteins levels were determined by Western blot, ER-mitochondria contacts were quantified by transmission electron microscopy, and Ca^{2+} homeostasis and mitochondria function were analyzed using fluorescent probes and Seahorse assays. In this in vitro AD model, we found APP accumulated in MAM and mitochondria, and altered levels of proteins implicated in ER-mitochondria tethering, Ca^{2+} signaling, mitochondrial dynamics, biogenesis and protein import, as well as in the stress response. Moreover, we observed a decreased number of close ER-mitochondria contacts, activation of the ER unfolded protein response, reduced Ca^{2+} transfer from ER to mitochondria, and impaired mitochondrial function. Together, these results demonstrate that several subcellular alterations occur in AD-like neuronal cells, which supports that the defective ER-mitochondria crosstalk is an important player in AD pathophysiology.

Keywords: Alzheimer's disease; subcellular fractions; ER-mitochondria contacts; Ca^{2+} signaling; mitochondrial dysfunction

1. Introduction

Alzheimer's disease (AD) is the most common age-related neurodegenerative disorder affecting more than 47.5 million people worldwide [1]. It is characterized by the accumulation of extracellular neuritic plaques, mainly composed by amyloid β ($A\beta$), and intracellular neurofibrillary tangles mostly formed by hyperphosphorylated tau, as well as by progressive neuronal loss, particularly in the cerebral cortex and hippocampus, which leads to cognitive impairment [2,3]. The familial forms of AD (FAD) are caused by several

mutations, including in the gene that encodes the amyloid precursor protein (APP), whose cleavage by β - and γ -secretases originates the A β peptide [1]. Furthermore, mutations in presenilin-1 (PS1) and presenilin-2 (PS2) that are enzymatic active components of γ -secretase complex were also associated with A β deposition in FAD patients [4]. The major risk factors for sporadic AD (SAD), the most prevalent form of the disease, are aging and the presence of the ϵ 4 allele of apolipoprotein E (ApoE4) that, among other factors, seem to affect MAM function [5].

The disruption of MAM has been implicated in AD physiopathology [4], since it modulates several AD-related features, such as altered lipid and glucose metabolism, aberrant Ca²⁺ homeostasis, increased endoplasmic reticulum (ER) stress, and mitochondrial dysfunction, which occur years before the appearance of the pathological hallmarks of AD [6–8]. MAM are biochemical and physical contact sites between the ER and mitochondria with an intermembrane distance of about 10 to 80 nm [9–11]. This structure that exhibits the features of a lipid raft is dynamic due to the presence of a set of specialized proteins, working as an intracellular signaling platform able to determine cell fate. Indeed, the proteins present in this region regulate numerous cellular processes, such as lipid homeostasis, Ca²⁺ signaling, apoptosis, redox status, proteostasis including autophagy, and the ER stress-induced unfolded protein response (UPR), as well as mitochondrial dynamics and bioenergetics [12–16]. Mitochondria are conserved organelles that play an important role in neuronal cell fate because they regulate both the energy metabolism and cell death pathways. Due to their essential role in energy production, among other things, mitochondrial dysfunction is also considered an early disease feature in vulnerable neurons of the brains of AD patients [17–19].

The main goal of our study was to investigate the structural alterations at MAM using an *in vitro* model of AD, namely the mouse neuroblastoma cell line (N2A) overexpressing the APP familial Swedish mutation (APP^{Swe}). The impact of MAM alterations on several cellular stress responses as well as in mitochondria functioning was also evaluated, including Ca²⁺ transfer from the ER, energetic metabolism and ATP production, dynamics, and biogenesis concomitantly with the analysis of ER stress-induced UPR.

2. Materials and Methods

In order, to study the structural alterations at MAM and the impact of these on cellular stress responses and mitochondria function in AD, we used an *in vitro* cell model. We isolated MAM, microsomes, and mitochondria fractions from N2A-WT and N2A-APP^{Swe} cell lines and protein levels of ER-mitochondria tethers, Ca²⁺ signaling and stress response mediators were determined by Western blot (WB). ER-mitochondria contacts were quantified by transmission electron microscopy, and Ca²⁺ homeostasis and mitochondria function were analyzed using fluorescent probes and Seahorse assays, respectively.

2.1. Cell Culture

The wild-type mouse neuroblastoma cell line N2A (WT) and the N2A-APP^{Swe} cell line, which stably overexpress human Swedish mutant APP KM670/671NL (APP^{Swe}) [20], were maintained in Dulbecco's modified Eagle's medium (DMEM, Sigma-Aldrich, St. Louis, MO, USA, #D5648) supplemented with 10% (*v/v*) fetal bovine serum (FBS) (Gibco, Waltham, MA, USA, #26400-044), 3.7 g/L sodium bicarbonate (Merck, Kenilworth, NJ, USA, S8761), 1% (*v/v*) non-essential amino acids (Merck, #M7145), and 1 mM sodium pyruvate (Merck, #S8636), as previously described [21,22]. Cell culture medium was also supplemented with 1% (*v/v*) penicillin/streptomycin (Gibco, #15140-122) or 0.4 mg/mL geneticin (Gibco, #10131027) for WT or APP^{Swe} cells, respectively. Both cell lines were cultured at 37 °C in a humidified 5% CO₂–95% air atmosphere.

2.2. Subcellular Fractionation

Purification of microsomes, MAM, and crude mitochondria was performed using modifications of the protocols previously described by Wieckowski et al. [23] and Williamson et al. [24].

Cells were harvested and centrifuged at $200\times g$ for 5 min at $4\text{ }^{\circ}\text{C}$. Homogenization of pellets was then performed gently with a glass/teflon homogenizer in isolation buffer, pH 7.4, composed of 250 mM sucrose and 10 mM HEPES for microsomes and MAM isolation, or 225 mM mannitol, 75 mM sucrose, 30 mM Tris-HCl, and 0.1 mM EGTA for crude mitochondria isolation, supplemented with a 1% cocktail of proteases inhibitors (Sigma-Aldrich, #P2714). The suspension was centrifuged eight times at $600\times g$ for 5 min at $4\text{ }^{\circ}\text{C}$ to remove cell debris and nuclei and obtain the total fraction (TF). For microsomes and MAM isolation, the TF was centrifuged at $10,300\times g$ for 10 min at $4\text{ }^{\circ}\text{C}$, resulting in a supernatant (cytosolic and ER/microsomes fraction) and pellet (MAM fraction). The supernatant was centrifuged at $100,000\times g$ for 60 min at $4\text{ }^{\circ}\text{C}$ in a Beckman ultracentrifuge (Indianapolis, IN, USA, model L-100 XP, 90 Ti rotor) to pellet the ER/microsomal fraction that was then resuspended in PBS. For MAM isolation, the pellet resulting from TF centrifugation was resuspended in 1 mL SHM solution (250 mM sucrose and 10 mM HEPES) and centrifuged at $10,300\times g$ for 10 min at $4\text{ }^{\circ}\text{C}$. The resulting pellet was resuspended in 600 μL mannitol buffer A (250 mM mannitol, 0.5 mM EGTA, and 5 mM HEPES, pH 7.4), loaded on top of a 30% (*v/v*) Percoll gradient, and centrifuged for 65 min at $95,000\times g$ in a Beckman ultracentrifuge (Indianapolis, IN, USA, model L-100 XP, SW41 rotor). The upper band (containing the MAM fraction) was collected, diluted in PBS containing 1 mM PMSF, and centrifuged at $6300\times g$ for 10 min at $4\text{ }^{\circ}\text{C}$. The supernatant was centrifuged at $100,000\times g$ for 30 min at $4\text{ }^{\circ}\text{C}$ in a Beckman centrifuge (Indianapolis, IN, USA, model Avanti J-26 XPI, JA 25.15 rotor), and the pellet (MAM purified fraction) was resuspended in PBS containing 1 mM PMSF. To obtain the crude mitochondria fraction, the TF was centrifuged at $7000\times g$ for 10 min at $4\text{ }^{\circ}\text{C}$ in a Beckman centrifuge (model Avanti J-26 XPI, JA 25.15 rotor), the pellet was resuspended in starting buffer (225 mM mannitol, 75 mM sucrose, and 30 mM Tris-HCl, pH 7.4), and centrifuged at $7000\times g$ for 10 min at $4\text{ }^{\circ}\text{C}$. This procedure was repeated five times. The mitochondrial pellet was resuspended in starting buffer, centrifuged at $10,000\times g$ for 10 min at $4\text{ }^{\circ}\text{C}$ in a Beckman centrifuge (model Avanti J-26 XPI, JA 25.15 rotor), and the resulting pellet (crude mitochondrial fraction) was resuspended in MRB buffer (250 mM mannitol, 5 mM HEPES, and 0.5 mM EGTA, pH 7.4). Subcellular fractions purity was analyzed by WB (Supplementary Figure S1).

2.3. Protein Analysis by Western Blot

Protein concentration was determined with the Pierce BCA Protein Assay Kit (Thermo Fisher, Waltham, MA, USA, #23227). Loading buffer was added to samples that were then boiled and denatured. Sample proteins (30–50 μg) were separated using 7.5–15% SDS-PAGE, transferred to a PVDF membrane (Millipore, Burlington, MA, USA), and blocked in 5% (*w/v*) BSA Tris-buffered saline containing 0.1% (*v/v*) Tween-20 (TBS-T). Membranes were incubated with the primary antibody overnight at $4\text{ }^{\circ}\text{C}$ and afterward they were washed with TBS-T and incubated with the secondary antibody at room temperature for 1 h. Membranes were developed using ECF substrate (GE Healthcare, Chicago, IL, USA, #RPN5785) in ChemiDoc Imaging System (Bio-Rad, Hercules, CA, USA), and quantifications were performed with the Bio-Rad Image Lab Software 6.1. Primary and secondary antibodies utilized for WB are summarized in Tables 1 and 2, respectively.

Table 1. Primary antibodies utilized for Western blot.

Primary Antibody	Dilution	Species	Company	Catalog Number	Location
APP	1:4000	Rabbit	Sigma-Aldrich	A8717	St. Louis, MO, USA
β -Actin	1:10,000	Mouse	Sigma-Aldrich	A5316	St. Louis, MO, USA
BiP/GRP78	1:1000	Mouse	BD Transduction	610978	San Jose, CA, USA
DRP1	1:1000	Rabbit	Cell Signaling	8570	Danvers, MA, USA
ERO1 α	1:1000	Mouse	Santa Cruz Biotechnology	sc-100805	Santa Cruz, CA, USA
FIS-1	1:500	Rabbit	Novus Biologicals	NB100-56646	Littleton, CO, USA
Hsp60	1:1000	Mouse	BD Transduction	611563	San Jose, CA, USA
IRE1 α	1:500	Rabbit	Cell Signaling	3294	Danvers, MA, USA
MCU	1:1000	Rabbit	Cell Signaling	14997	Danvers, MA, USA
Mfn1	1:1000	Rabbit	Santa Cruz Biotechnology	sc-50330	Santa Cruz, CA, USA
Mfn2	1:1000	Mouse	Santa Cruz Biotechnology	sc-100560	Santa Cruz, CA, USA
mtTFA	1:1000	Goat	Santa Cruz Biotechnology	sc-23588	Santa Cruz, CA, USA
ND1	1:1000	Goat	Santa Cruz Biotechnology	sc-20493	Santa Cruz, CA, USA
NRF-1	1:1000	Rabbit	Santa Cruz Biotechnology	sc-33771	Santa Cruz, CA, USA
PCNA	1:1000	Mouse	Santa Cruz Biotechnology	sc-25280	Santa Cruz, CA, USA
PERK	1:500	Rabbit	Cell Signaling	3192	Danvers, MA, USA
p-DRP1	1:500	Rabbit	Cell Signaling	3455	Danvers, MA, USA
Sigma1R	1:2000	Goat	Santa Cruz Biotechnology	sc-22948	Santa Cruz, CA, USA
Tom40	1:1000	Mouse	Santa Cruz Biotechnology	sc-365467	Santa Cruz, CA, USA
VDAC1	1:1000	Mouse	Santa Cruz Biotechnology	sc-390996	Santa Cruz, CA, USA

Table 2. Secondary antibodies utilized for Western blot.

Secondary Antibody	Dilution	Species	Company	Catalog Number	Location
IgG (anti-goat)	1:10,000	Rabbit	Santa Cruz Biotechnology	sc-2771	Santa Cruz, CA, USA
IgG (anti-mouse)	1:10,000	Goat	Thermo Fisher	31320	Waltham, MA, USA
IgG (anti-rabbit)	1:20,000	Goat	GE Healthcare	NIF1317	Chicago, IL, USA

2.4. Mitochondria Morphology Analysis by Transmission Electron Microscopy (TEM)

WT and APPswe cells were collected and centrifuged at $1008\times g$ for 5 min to form a pellet. Cells were fixed with 2.5% (*w/v*) glutaraldehyde in 0.1 M sodium cacodylate buffer (pH 7.2) for 2 h. Afterwards, cells were washed in the same buffer and the post-fixation was performed using 1% (*w/v*) osmium tetroxide for 1 h. Then, the cell pellets were rinsed two times with buffer and distilled water and, for contrast enhancement, cells were incubated in 1% (*w/v*) aqueous uranyl acetate during 1 h. After washing with water, cell pellets were embedded in 2% (*w/v*) molten agar and dehydrated in ethanol (30–100%). Then, cell pellets were impregnated and included in Epoxy resin (Fluka Analytical, Charlotte, NC, USA). After polymerization, ultrathin sections were obtained, and observations were carried out on a FEI-Tecnaï G2 Spirit Bio Twin at 100 kV. We analyzed approximately 10 different cells per cell line ($n = 3$) and MAM was considered when the distance between ER and mitochondria, which was measured using the ImageJ program, was ≤ 25 nm. At this distance, Ca^{2+} transfer between both organelles occurs through the $\text{IP}_3\text{R-GRP75-VDAC}$ axis [10]. The number of ER-mitochondria contacts ≤ 25 nm were obtained dividing the number of MAM per number of total mitochondria.

2.5. Mitochondria Morphology Analysis by Confocal Microscopy Using MitoTracker Green

For imaging experiments, cells were cultured on 18 mm glass bottom culture 12-well plate (150,000 cells per well) coated with poly-lysine D and incubated at 37°C in a humidified 5% CO_2 –95% air atmosphere for 24 h. Culture medium was discarded, cells washed in Krebs solution (140 mM NaCl, 5 mM KCl, 1.5 mM CaCl_2 , 1 mM MgCl_2 , 1 mM NaH_2PO_4 , 9.6 mM glucose, 20 mM HEPES; pH 7.4), and loaded with 100 nM MitoTracker Green probe (Invitrogen, Waltham, MA, USA, #M7514) in Krebs solution for 30 min at 37°C in a humidified 5% CO_2 . Then, cells were washed in Krebs solution and incubated with 15 $\mu\text{g}/\text{mL}$ Hoechst 33342 (Molecular Probes) in Krebs solution for 5 min at same conditions. Cells were washed and live images of the cells (608 WT cells and 498 APPswe cells) were captured with the Zeiss LSM 710 Confocal Microscope (Carl Zeiss, Jena, Germany) with $63\times$ oil objective and the fluorescence intensity analyzed using ImageJ software. The value of corrected total cell fluorescence (CTCF) was calculated using the following formula: $\text{CTCF} = \text{integrated density of selected cell} - (\text{area of selected cell} \times \text{mean fluorescence of background readings})$.

2.6. Fluorometric Analysis of Calcium and Mitochondrial Membrane Potential

Intracellular cytosolic Ca^{2+} levels were measured with Fura-2/AM (Invitrogen, #F1221) and mitochondrial Ca^{2+} content was measured with Rhod-2/AM (Invitrogen, #R1244). Cells were cultured in 48-well plates (75,000 cells per well) in triplicate and incubated at 37°C in a humidified 5% CO_2 –95% air atmosphere. The next day, cells were washed with solution A (140 mM NaCl, 2.5 mM KCl, 1 mM MgCl_2 , 20 mM HEPES, 10 mM glucose, and 1.8 mM CaCl_2 , pH 7.4) and incubated for 30 min with 2 μM Fura-2/AM in solution A supplemented with 0.1% (*w/v*) BSA or for 45 min with 10 μM Rhod-2/AM in solution A at 37°C . Cells were rinsed with solution B (140 mM NaCl, 2.5 mM KCl, 1 mM MgCl_2 , 20 mM HEPES, and 10 mM glucose, pH 7.4) and Ca^{2+} levels were measured upon stimulation with 5 μM thapsigargin (Sigma-Aldrich, #T9033) or 100 μM histamine (Sigma-Aldrich, #H7125). The fluorescence signal was measured at 37°C during 10 min (10 in 10 sec) at $\lambda\text{Ex} = 340/380$ nm and $\lambda\text{Em} = 510$ nm for Fura-2/AM and $\lambda\text{Ex} = 552$ nm and $\lambda\text{Em} = 581$ nm for Rhod-2/AM using a plate reader (Fluorimeter SpectraMax Gemini EM, Molecular Devices, San Jose, CA, USA).

Mitochondrial membrane potential ($\Delta\psi\text{m}$) was evaluated using the fluorescent probe TMRE (tetramethylrhodamine ethyl ester perchlorate). Cells were seeded in 96-well plates (25,000 cells per well) in triplicate and incubated at 37°C in a humidified 5% CO_2 –95% air atmosphere for 24 h. Culture medium was discarded and replaced by fresh medium containing 4 μM TMRE (Sigma-Aldrich, #87917) and cells were incubated at 37°C for 30 min. Subsequently, the supernatant was removed, cells were washed using PBS and the

fluorescence signal ($\lambda_{Ex} = 544 \text{ nm}$; $\lambda_{Em} = 590 \text{ nm}$) was measured at 37°C using a plate reader (Fluorimeter SpectraMax Gemini EM, Molecular Devices, San Jose, CA, USA).

The protein content of each well was determined by aspirating the assay buffer, followed by addition of 10 and 20 μL RIPA buffer (250 mM NaCl, 50 mM Tris, 1% Nonidet P-40, 0.5% DOC, and 0.1% SDS) for TMRE and Ca^{2+} assays, respectively. The multi-well plates were placed on a plate shaker at low speed for 10 min and then on ice during 20 min. Finally, 100 and 200 μL BCA assay mix (Invitrogen, #23227) were added for the TMRE and Ca^{2+} assays, respectively. After a 30 min incubation period, absorbance was measured at 562 nm with a Spectrophotometer Spectramax plus 384 (Molecular Devices, San Jose, CA, USA).

2.7. Activity of Mitochondrial Electron Transport Chain and Glycolysis Measured by the Seahorse XFe24 Analyzer

Cells were seeded (50,000 cells per well) in cell culture microplates (5 wells per cell line) provided by the manufacturer and incubated at 37°C in a humidified 5% CO_2 –95% air atmosphere. The next day, cells were washed in unbuffered DMEM (Sigma-Aldrich, #5030) supplemented with 25 mM glucose, 1 mM sodium pyruvate, 0.58 g/L L-glutamine, and 1% (*v/v*) non-essential amino acids for oxygen consumption rate (OCR) assay or in unbuffered glucose-free DMEM for extracellular acidification rate (ECAR) assay. Cells were incubated for 1 h at 37°C in pre-warmed medium with pH adjusted to 7.4 and plates were loaded into a Seahorse XFe24 (Argilent, Santa Clara, CA, USA). OCR was determined under the following conditions: Basal measurements; after 1 μM oligomycin (Alfa Aesar, Karlsruhe, Germany, #J60211) addition; upon injection of 1 μM FCCP (Sigma Chemical, #C2920) and, finally, after a mixture of 2 μM rotenone (Sigma Chemical, #R8875) plus 2 μM antimycin A (Sigma Chemical, #A8674) was injected. Rotenone (a mitochondrial complex I inhibitor) and antimycin A (a mitochondrial complex III inhibitor) inhibit mitochondrial respiration allowing to determine the non-mitochondrial OCR. To calculate the basal mitochondrial OCR, the non-mitochondrial OCR is subtracted from the OCR obtained before the addition of oligomycin (inhibits the mitochondrial ATP synthase). To evaluate the maximal respiratory capacity, we subtracted the non-mitochondrial OCR from the OCR following carbonyl cyanide-4-(trifluoromethoxy) phenyl hydrazone (FCCP) addition (disrupts ATP synthesis by dissipating the proton gradient). To obtain the spare respiratory capacity, we subtracted the basal mitochondrial OCR from the maximal respiratory capacity. The mitochondrial ATP production was assessed after oligomycin addition, by subtracting the non-mitochondrial OCR from the OCR value after oligomycin.

In the ECAR assay, after baseline measurements, the following injections were performed to each well under similar conditions: First, 25 mM glucose, then 1 μM oligomycin, and, finally, an injection of 100 mM 2-deoxyglucose (2DG) provided a non-glycolysis extracellular acidification rate. Cells were first placed in a glucose-free medium and the first injection consisted in 25 mM glucose. The glycolysis rate was obtained by subtracting non-glycolysis ECAR from the ECAR post-glucose. Then, oligomycin was added to the cells to suppress mitochondrial ATP production. The glycolysis capacity was determined by the difference between the post-oligomycin ECAR and post-2-deoxyglucose baseline ECAR. After the assays, buffer was aspirated, 30 μL RIPA buffer was added per well, and protein content was measured using BCA assay mix to determine the protein content per well. In comparison with the basal rates, the % of change was calculated dividing the measured value by the average value of baseline readings and normalized to the total protein content of each well. The OCRs are normalized to the WT cells mean.

2.8. Statistical Analysis

Statistical analysis was performed using the GraphPad Prisma 8.0.2 software (San Diego, CA, USA) and presented as mean \pm standard error of the mean (SEM). All experiments were independent assays. Data were tested for Gaussian distribution using the Shapiro-Wilk test. Differences between the two groups were analyzed using unpaired *t*-test and two-way ANOVA with Sidak post hoc correction for grouped analysis. In case of non-normality distribution, data were analyzed by the Mann-Whitney U-test to compare two groups and Kruskal-Wallis Dunn's correction for multiple comparisons. Statistical significance was considered at $p < 0.05$.

3. Results

3.1. Alterations of ER-Mitochondria Contacts in APPswe Cells

The direct contact between organelles allows the exchange of signals and metabolites that have a role in cell physiology and stress response [25]. The ER-mitochondria contacts are dynamic structures, with the distance between the two membranes ranging from 10 to 80 nm [9,10]. The formation of these contacts requires the presence of tethering proteins inserted in the outer mitochondrial membrane (OMM) that interact with ER membrane-resident proteins. The Ca^{2+} channel, associated with the inositol 1,4,5-trisphosphate receptor (IP₃R) present at ER, interacts with the mitochondrial voltage-dependent anion channel 1 (VDAC1) through the glucose-regulated protein 75 (GRP75) and mitofusin 2 (MFN2), present in both ER and mitochondria homo- and hetero-oligomerizes with the mitochondrial mitofusin 1 (MFN1), to tether both organelles [26–28]. In our study, the ER-mitochondria tethering proteins MFN1 and MFN2 were analyzed by WB in microsomes (heterogenous set of vesicles formed from the ER), mitochondria, and MAM subcellular fractions isolated from WT and APPswe cells. We observed an increase in MFN1 protein levels in MAM fraction ($p < 0.0794$) in APPswe cells when compared with WT cells (Figure 1a,b) and, as expected, this protein was not detected in the microsomes. Furthermore, MFN2 content was significantly decreased in whole-cell extracts and isolated subcellular fractions (microsomes, mitochondria, and MAM) in the APPswe compared with WT cells (total fraction: $p < 0.0001$, microsomes: $p < 0.001$, mitochondria: $p < 0.05$, MAM: $p < 0.05$) (Figure 1a,c). Since this data suggests alterations in ER-mitochondria tethering, we analyzed the contact between both organelles using transmission electron microscopy (TEM) that allows the direct visualization of MAM. Tethers identified in TEM span from 5 to 80 nm. We observed a mild decrease of ER-mitochondria contacts ≤ 25 nm ($p = 0.0656$) (Figure 1d,e) and a significant decrease of mitochondria per cell ($p < 0.001$) (Figure 1f) in APPswe when compared with WT cells. Using the MitoTracker Green probe, we also evaluated the mitochondrial mass/abundance by confocal microscopy. A significant decrease of approximately 25% ($p < 0.0001$) in mitochondria fluorescence intensity was observed in APPswe cells when compared with WT cells (Figure 1g,h). Additionally, we observed a perinuclear localization of mitochondria in APPswe cells, similarly to what has been described for other AD models [29,30]. Altogether these observations indicate a decrease in ER-mitochondria contacts in APPswe cells and, consequently, a possible reduction in the communication between both organelles that affects cell homeostasis.

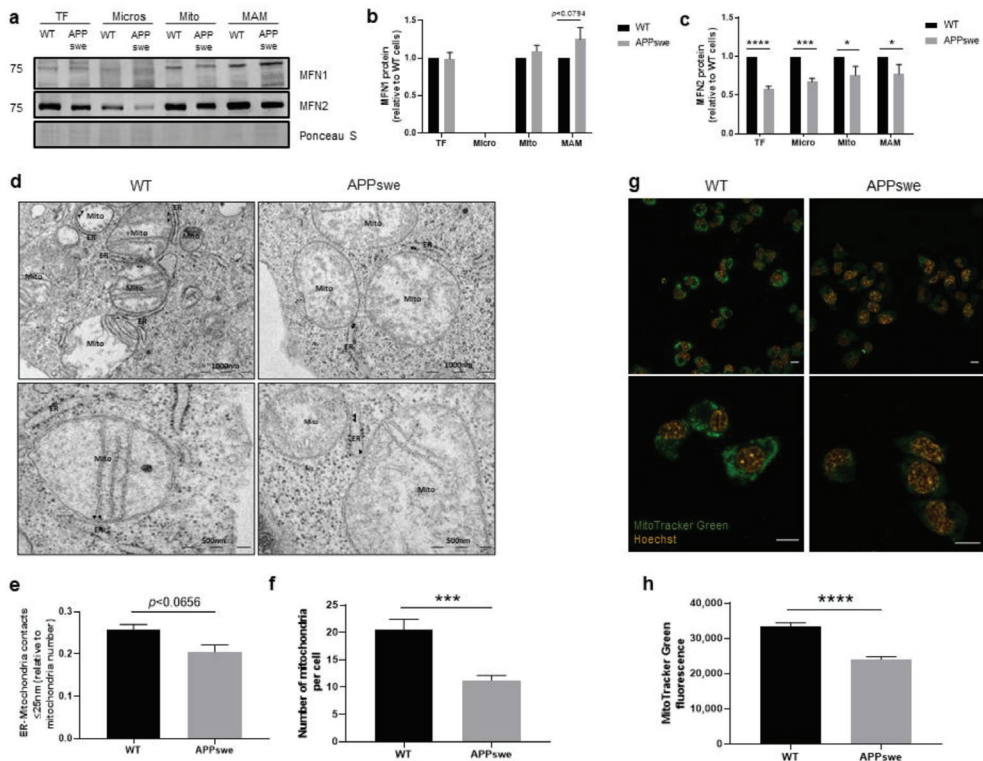


Figure 1. Mitochondria-endoplasmic reticulum (ER) contacts in mouse neuroblastoma cell line (N2A) overexpressing the APP familial Swedish mutation (APPsw) versus wild-type (WT) cells. (a–c) Representative Western blots and quantification of the ER-mitochondria tethering proteins mitofusin 1 (MFN1) and mitofusin 2 (MFN2) in total fraction (TF), microsomes (Micro), mitochondria (Mito), and mitochondrial-associated membranes (MAMs) ($n = 5–9$). (d,e) Representative electron micrographs and quantification of ER-mitochondria contacts (MAM) ≤ 25 nm ($n = 3$). (f) Profile of mitochondria number per cell ($n = 3$). (g,h) Representative image of MitoTracker Green (mitochondria, green) and Hoechst (nucleus, yellow) staining and quantification of corrected total fluorescence intensity (CTCF) of stained cells ($n = 3$). Scale bar represents 10 μ m. Mito—mitochondria, ER—endoplasmic reticulum, arrow heads—MAM. All data presented as mean \pm SEM; *p*-values were obtained by using two-way ANOVA with Sidak’s multiple comparisons test for (b,c), unpaired *t*-test for (f), and non-parametric independent Mann–Whitney U test in (g). * $p \leq 0.05$, *** $p \leq 0.001$, and **** $p \leq 0.0001$ were considered significant.

3.2. Impairment of Ca^{2+} Transfer from ER to Mitochondria in APPsw Cells

Mitochondrial metabolism is versatile and capable to adjust to specific physiological or pathological conditions regulating fundamental cell pathways that range from proliferation to apoptosis [15]. The functional interaction between mitochondria and ER influences mitochondrial Ca^{2+} signaling, which in turn regulates mitochondrial function. Dysregulation of mitochondrial Ca^{2+} and metabolism have been associated with AD development [19,31,32]. Cytosolic Ca^{2+} levels were measured with the Fura-2/AM fluorescent probe following treatment with thapsigargin (TG), which blocks the ability of the cells to pump Ca^{2+} into the ER by inhibiting the sarco/endoplasmic reticulum Ca^{2+} ATPase (SERCA) and depletes ER Ca^{2+} . We observed a significant increase in Ca^{2+} flux from ER to cytosol ($p < 0.01$) in APPsw cells (Figure 2a,b), suggesting a higher ER Ca^{2+} content in these cells in comparison with WT cells. The width of the ER-mitochondria cleft influences Ca^{2+} transfer through the $\text{IP}_3\text{R-GRP75-VDAC}$ complex, which assembles when the distance between both organelles is in the range of 10–25 nm [10]. Since our results show a decrease in

ER-mitochondria contacts ≤ 25 nm in the APPswe cells, we also examined mitochondrial Ca^{2+} levels using the Rhod-2/AM probe. We observed a statistically significant decrease (approximately 50%) in Ca^{2+} flux from ER to mitochondria ($p = 0.05$) in APPswe cells following treatment with histamine that triggers Ca^{2+} release through IP_3R (Figure 2c,d). Then, we analyzed the levels of VDAC1 and mitochondrial Ca^{2+} uniporter (MCU) proteins by WB. VDAC1 is a protein present in the OMM involved in ER-mitochondria tethering by forming a ternary bridging complex with the OMM chaperone GRP75 and IP_3R in the ER, as well as in Ca^{2+} signaling by regulating Ca^{2+} transfer from ER to mitochondria via IP_3R [28,33]. To enter in mitochondrial matrix, Ca^{2+} must cross the MCU located in the inner mitochondrial membrane (IMM) [34]. A significant increase of VDAC1 content in mitochondrial ($p < 0.05$) and MAM ($p < 0.05$) fractions was observed in APPswe cells when compared with WT cells (Figure 2e,g). Furthermore, we detected a significant decrease in MCU levels in APPswe whole-cell extracts ($p < 0.01$) (Figure 2f,i), which was not observed in the mitochondria fraction. Besides that, we also observed a significant increase of sigma-1 receptor (Sig-1R) levels in MAM fraction ($p < 0.05$) (Figure 2f,j), and a significant decrease of glucose-regulated protein 78 (BiP/GRP78) expression in whole-cell extracts ($p < 0.05$) and microsomes ($p < 0.01$) isolated from APPswe cells (Figure 2e,h). Sig-1R is a chaperone that resides mainly at MAM, which is involved in the structural integrity of the MAM and plays a role in the regulation of Ca^{2+} signaling regulation between ER and mitochondria by coupling to the IP_3R . Under ER stress, Sig-1R dissociates from the co-chaperone BiP/GRP78 and acts as a free chaperone to stabilize IP_3Rs , leading to an increased Ca^{2+} transfer from ER to mitochondria that promote ATP production [34,35]. Despite the alterations in ER Ca^{2+} levels and the increased protein levels of VDAC1 and Sig-1R observed in APPswe cells, a decrease in Ca^{2+} flux from ER to mitochondria was found in these cells that can arise from the decrease in ER-mitochondria contacts, as well as due to changes in mitochondria membrane potential.

3.3. Oxygen and Glucose Fluxes in APPswe Cells

Mitochondria have an essential role in the bioenergetic process and are involved in amino acid, lipid, and steroid metabolism, Ca^{2+} homeostasis, ATP production via oxidative phosphorylation (OXPHOS), and apoptosis. Thus, these organelles regulate cellular fate and mitochondrial dysfunction is one of the most prominent features in AD that occurs in the early stage of this disease [17,18,36–38]. Because neuronal survival is dependent on mitochondrial function that, in turn, is affected by Ca^{2+} flux from the ER, which we showed to be decreased in APPswe cells (Figure 2d), we assessed mitochondrial function parameters, namely OCR (Figure 3a), ATP production levels, and mitochondrial membrane potential. We observed that the basal mitochondrial respiration, determined by monitoring ORC in the absence of any inhibitors, was significantly decreased in APPswe cells when compared with WT cells. ($p < 0.01$) (Figure 3b). Additionally, we found that maximal respiratory capacity, which indicates the maximal oxygen consumption rate attained by adding the uncoupler FCCP, was significantly decreased in APPswe cells ($p < 0.001$) (Figure 3c), showing that mitochondria from mutant cells are already working at an increased rate. Accordingly, the spare respiratory capacity, described as the amount of extra ATP that can be produced by OXPHOS in case of a sudden increase in energy demand, was also significantly decreased in APPswe cells when compared with WT cells ($p < 0.001$) (Figure 3d). In the presence of oligomycin, an inhibitor of ATP synthase, mitochondrial oxygen consumption is due to ATP synthase-independent leakage of protons from the intermembrane space to the mitochondrial matrix. Under these conditions, we observed a 30% reduction in ATP production ($p < 0.05$) in APPswe cells (Figure 3e).

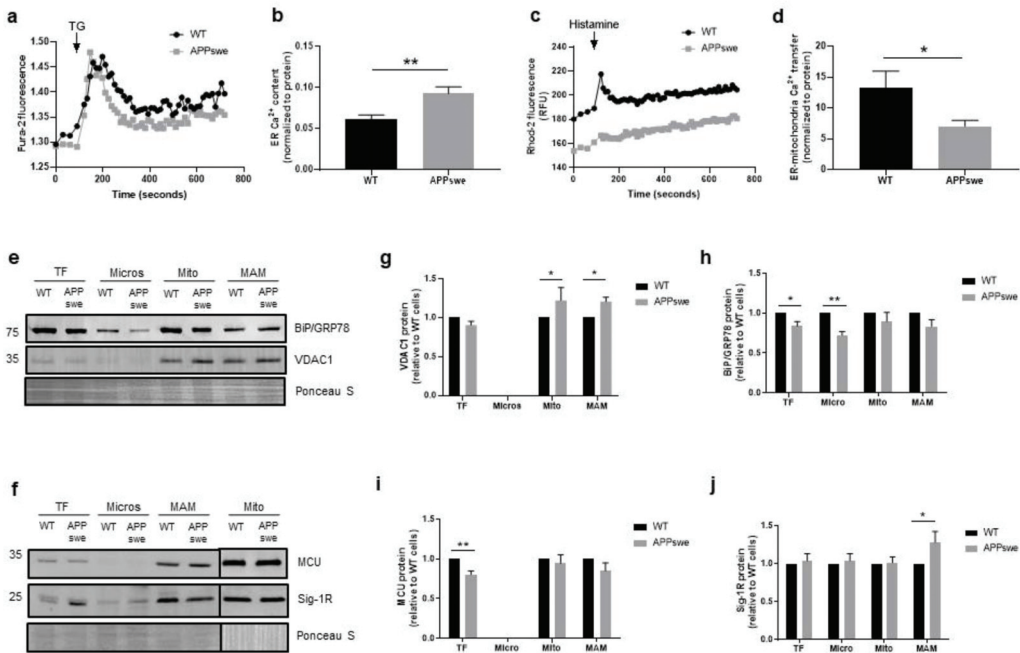


Figure 2. Ca²⁺ transfer from ER to mitochondria in APPswe versus wild-type (WT) N2A cells. (a,c) Representative traces of cytosolic and mitochondrial Ca²⁺ content evaluated with Fura-2 and Rhod-2 probes, respectively. (b,d) Quantification of ER Ca²⁺ content after stimulation with 5 μM thapsigargin (TG) in Ca²⁺-free medium using the Fura-2 probe, and ER-mitochondria Ca²⁺ transfer after stimulation with 100 μM histamine in Ca²⁺-free medium using the Rhod-2 probe. Fura-2 and Rhod-2 results represent the average of five or three independent experiments, respectively, performed in triplicate. (e–j) Representative Western blots and quantification of protein levels of voltage-dependent anion channel 1 (VDAC1) (*n* = 5–9), glucose-regulated protein 78 (BiP/GRP78) (*n* = 5–11), mitochondrial calcium uniporter (MCU) (*n* = 4–8), and sigma-1 receptor (Sig-1R) (*n* = 4–8) proteins in total fraction (TF), microsomes (Micro), mitochondria (Mito), and mitochondrial-associated membranes (MAMs). All data presented as mean ± SEM; *p*-values were obtained by using unpaired *t*-test for (a,c), two-way ANOVA with Sidak’s multiple comparisons test for (g–i), and non-parametric Kruskal-Wallis with Dunn’s multiple comparisons test for (j). * *p* ≤ 0.05 and ** *p* ≤ 0.01 were considered significant.

Since alterations in mitochondrial respiration are associated with changes in mitochondrial membrane potential, we used the TMRE fluorescence probe to assess this mitochondrial parameter. In line with the OCR data, APPswe cells showed mitochondrial membrane depolarization when compared with WT cells (*p* < 0.01) (Figure 3f). Altogether, these results show that mitochondria are significantly impaired in APPswe cells, which suggest a suppression in mitochondrial activity. However, this result might be, at least in part, caused not only by biochemical alterations but by the reduction in mitochondrial mass/abundance that we observed (Figure 1h).

Our studies demonstrated an impairment of mitochondria function that resulted in a decline in the production of ATP via OXPHOS; therefore, we measured glycolysis to study if this pathway could compensate the decrease in ATP synthesis by OXPHOS in APPswe cells. Glycolysis fluxes can be estimated by measuring the pH of cell culture medium since lactic acid, the end-product of anaerobic glycolysis, contributes to its acidification. At the end of the experiments, 2-deoxyglucose (2DG) was added to determine the non-glycolysis acidification rate (Figure 3g). We detected, in APPswe cells, a 40% reduction in glycolysis rate determined by the quantification of the extracellular acidification rate (ECAR) of the surrounding media (*p* < 0.01) (Figure 3h) and a 30% reduction in glycolytic capacity, evaluated by the difference between the post-oligomycin ECAR and the post-2-

deoxyglucose baseline ECAR ($p < 0.01$) (Figure 3i) when compared with WT cells. These results suggest that, in this in vitro AD model, cells present an energy deficit resulting from defects in both mitochondrial respiration and glycolytic pathway.

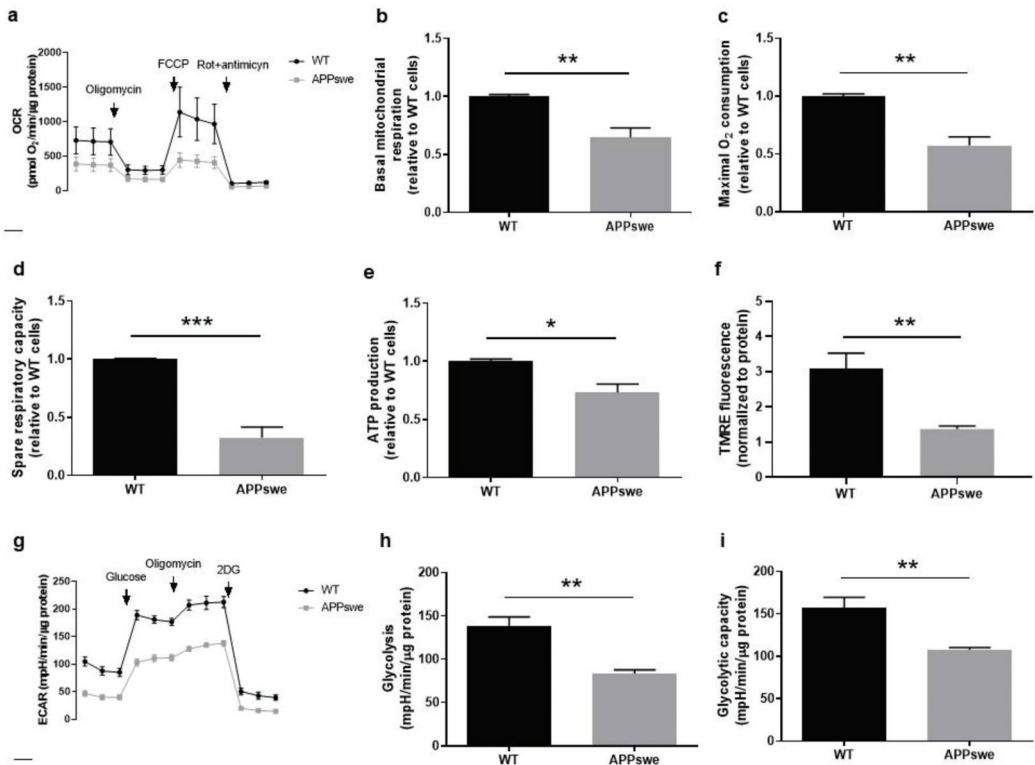


Figure 3. Mitochondrial function and glycolytic activity in APPswe versus wild-type (WT) N2A cells. (a) Representative traces of oxygen consumption rate (OCR) evaluated in WT and APPswe cells by sequential addition of 1 μ M oligomycin, 1 μ M FCCP, and 2 μ M rotenone (Rot) plus 2 μ M antimycin A by Seahorse analysis ($n = 4$). (b–e) Quantification of basal mitochondrial respiration, maximal O₂ consumption, spare respiratory capacity, and ATP production. (f) Quantification of mitochondrial membrane potential using the tetramethylrhodamine ethyl ester perchlorate (TMRE) fluorescence probe ($n = 6$). (g) Representative traces of extracellular acidification rate (ECAR) evaluated in WT and APPswe cells (average $n = 4$) by sequential addition of 25 mM glucose, 1 μ M oligomycin and 100 mM 2-deoxyglucose (2DG) by Seahorse analysis. (h,i) Quantification of glycolysis rate and glycolytic capacity. Experiments were carried out in quintuplicate for (a–e,g–i) and triplicate for (f). All data presented as mean \pm SEM; p -values were obtained by using unpaired t -test. * $p \leq 0.05$, ** $p \leq 0.01$, and *** $p \leq 0.001$ were considered significant.

3.4. Impaired Mitochondrial Dynamics and Biogenesis in APPswe Cells

Mitochondria are dynamic organelles undergoing cycles of fusion (union of two mitochondria) and fission (division of one mitochondrion into two daughter mitochondria) to maintain their shape, distribution, and size. A balanced mitochondrial dynamics is required to ensure a proper mitochondrial function and response to cellular stress [39]. Impaired fusion-fission balance has a key role in mitochondrial dysfunction and can cause neuronal dysregulation, being associated to several neurological disorders [18]. We analyzed by WB the levels of proteins involved in fusion, MFN1 and MFN2, and fission, dynamin-1-like protein (DRP1), and mitochondrial fission 1 (FIS-1). The quantification analysis in total extracts revealed a statistically significant decrease in MFN2 levels ($p < 0.05$) (Figure 4a,d) in the absence of relevant alterations in MFN1, p -DRP1/DRP1 and FIS-1

(Figure 4a–c,e) in APPswe cells when compared with WT cells, suggesting an impaired mitochondrial dynamics in APPswe cells.

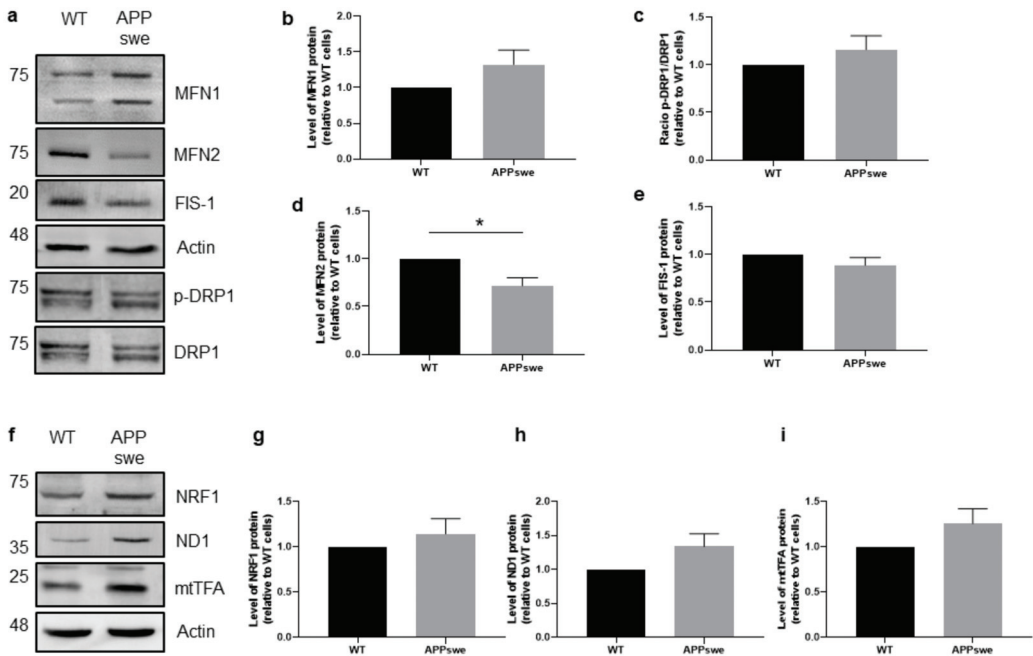


Figure 4. Mitochondrial dynamics and biogenesis in APPswe cells versus wild-type (WT) N2A cells. (a–e) Representative Western blots and quantification of proteins involved in mitochondrial fusion/fission in total fraction: mitofusin 1 (MFN1) ($n = 6$), phospho-dynamic-1-like protein (p -DRP1) ($n = 6$), mitofusin 2 (MFN2) ($n = 6$), and fission-1 (FIS-1) ($n = 5$). (f–i) Representative Western blots and quantification of proteins involved in mitochondrial biogenesis in total fraction: nuclear respiratory factor 1 (NRF1) ($n = 6$), NADH-ubiquinone oxidoreductase chain 1 (ND1) ($n = 6$), and mitochondrial transcription factor A (mtTFA) ($n = 6$). Values were normalized by actin for all proteins, except for p -DRP1 that was normalized by total DRP1. All data presented as mean \pm SEM; p -values were obtained by using unpaired t -test with Welch's correction. * $p \leq 0.05$ was considered significant.

Mitochondrial biogenesis is a process by which mitochondria increase their number/mass [40] contributing to mitochondrial and cellular homeostasis [18,36]. We analyzed the levels of factors that regulate mitochondrial biogenesis, namely nuclear respiratory factor 1 (NRF1), which controls nuclear genes that encode the mitochondrial proteins, NADH-ubiquinone oxidoreductase chain 1 (ND1), which is involved in the transfer of electrons from NADH to the respiratory chain, and the mitochondrial transcription factor A (mtTFA), which drives transcription and replication of mitochondrial DNA. The WB results revealed that the levels of these proteins in total cellular extracts are slightly increased in APPswe cells when compared with WT cells (Figure 4f–h), but the differences are not statistically significant. These observations suggest a compensatory mechanism in APPswe cells to face the decline of mitochondrial function and mass (Figure 1g,h).

3.5. Cellular Stress Responses Are Affected in APPswe Cells

ER is the main compartment involved in protein synthesis and folding as well as Ca^{2+} signaling, and upon stress activates the UPR to restore proteostasis. The UPR activation can be triggered by the accumulation of pathogenic misfolded proteins, disruption of intracellular Ca^{2+} homeostasis, defects in autophagy, oxidative stress, proteasome inhibition, and metabolic or mitochondrial dysfunctions [41,42]. Protein kinase R-like ER kinase

(PERK) and inositol-requiring enzyme 1 α (IRE1 α) are ER stress sensors that are inactive when linked to the chaperone BiP/GRP78 [41]. Upon ER stress, the interaction between BiP/GRP78 and sensor proteins is inhibited and UPR signaling is initiated [42]. PERK is a transmembrane kinase located at ER membrane and its activation inhibits protein synthesis. IRE1 α is a transmembrane kinase and endoribonuclease that regulates the expression of genes involved in protein folding, ER-associated degradation (ERAD), protein quality control, and organelle biogenesis. The ER oxidase 1 (ERO1 α) plays an important role in ER redox potential and its activity is central to maintain cell redox homeostasis, since it oxidizes the active-site cysteines of protein disulfide isomerase (PDI), an essential enzyme that is responsible for the addition of disulfide bonds into newly synthesized proteins. This protein is also involved in Ca²⁺ homeostasis and MAM signaling and its downregulation inhibits mitochondrial Ca²⁺ uptake [43,44]. In the in vitro model of AD used in this study, human APP with the Swedish mutation is overexpressed and A β is generated [20,45], which can induce ER stress and consequently activate the ER stress response [46,47]. Using WB analyses, we observed a significant accumulation of APP in mitochondria ($p < 0.0001$) and MAM fractions ($p < 0.05$) (Figure 5a,b). Due to this evidence, we evaluated UPR activation measuring by WB the protein levels of PERK, IRE1 α , and ERO1 α . A slight increase in PERK levels were detected in total extracts, microsomes, and MAM subcellular fractions (Figure 5c,d) and a significant IRE1 α upregulation was found in MAM fraction ($p < 0.05$) in APP^{swe} cells (Figure 5c,e). Moreover, the content of ERO1 α was significantly decreased in all subcellular fractions (total fraction: $p < 0.0001$, microsomes: $p < 0.05$, mitochondria: $p < 0.0001$, MAM: $p < 0.0001$) obtained from APP^{swe} cells when compared with WT cells (Figure 5f, g), which could lead to the accumulation of misfolded proteins in the ER lumen. Finally, APP^{swe} cells presented a significant increase of proliferating cell nuclear antigen (PCNA) protein levels in all subcellular fractions (total fraction: $p < 0.01$, microsomes: $p < 0.01$, mitochondria: $p < 0.05$, MAM: $p < 0.001$) when compared with WT cells (Figure 5f,h). PCNA is an essential cofactor for DNA replication and repair, thus being a cell lifespan regulator [48]. Together, these results suggest that protein accumulation in APP^{swe} cells, as well as Ca²⁺ deregulation and mitochondrial dysfunction, induce ER stress and activate the UPR, which subsequently upregulates PCNA to maintain cells viability.

The pore translocase of the outer mitochondrial membrane 40 (TOM40) is essential for mitochondrial functioning, since it is required for protein transport into mitochondria, including for the internalization of APP and A β [49]. Accumulation of misfolded and aggregated proteins in the mitochondria matrix activates the mitochondrial UPR, where the chaperone heat shock protein 60 (Hsp60) plays an essential role to preserve protein homeostasis [50]. Our WB analyses revealed a significant increase of TOM40 in mitochondria ($p < 0.0001$) and MAM ($p < 0.001$) fractions (Figure 5f,i) and of Hsp60 in MAM fraction ($p < 0.01$) (Figure 5j,k) in APP^{swe} cells when compared with WT cells. These results suggest that there is an increased transport of APP to mitochondria through the TOM complex, and an accumulation of unfolded/misfolded proteins in this organelle increase the level of the mitochondrial UPR Hsp60 in MAM fraction.

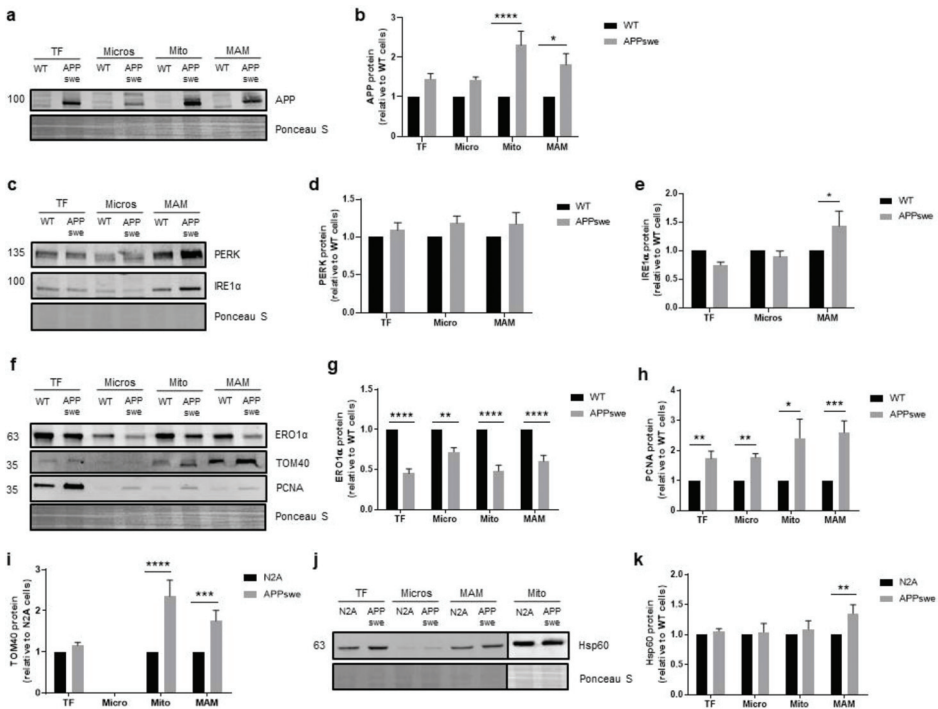


Figure 5. Accumulation of APP and stress responses in APPsw versus wild-type (WT) N2A cells. (a,b). Representative Western blot and quantification of amyloid β precursor protein (APP) (*n* = 4–6) in total fraction (TF), microsomes (Micro), mitochondria (Mito), and mitochondrial-associated membranes (MAMs). (c–e). Representative Western blots and quantification of protein kinase R-like ER kinase (PERK) (*n* = 4–5) and inositol-requiring enzyme 1α (IRE1α) (*n* = 3–6) proteins in TF, Micro, and MAM. (f–i). Representative Western blots and quantification of endoplasmic reticulum oxidase 1 (ERO1α) (*n* = 5–9), proliferating cell nuclear antigen (PCNA) (*n* = 4–10) and outer mitochondrial membrane 40 (TOM40) (*n* = 4–9) proteins in TF, Micro, Mito, and MAM. (j,k). Representative Western blot and quantification for the chaperone heat shock protein 60 (Hsp60) (*n* = 4–10) in TF, Micro, Mito, and MAM. All data presented as mean ± SEM; *p*-values were obtained by using two-way ANOVA with Sidak’s multiple comparisons test for all proteins, except for (h) that was obtained using non-parametric Kruskal-Wallis with Dunn’s multiple comparisons test. * *p* ≤ 0.05, ** *p* ≤ 0.01, *** *p* ≤ 0.001, and **** *p* ≤ 0.0001 were considered significant.

4. Discussion

It has been described that MAM-related functions are perturbed in several neurodegenerative disorders, such as AD, Parkinson’s disease and amyotrophic lateral sclerosis [4]. In AD, an aberrant Ca²⁺ regulation, increased ER stress, alteration in glucose metabolism, and mitochondrial dysfunction have been reported. These alterations may, in part, be attributed to the disruption of the MAM-related functions [6,51,52].

In the present study we characterized the structural and functional alterations in MAM and mitochondria and their effect on stress response mechanisms, in an in vitro model of AD, to support the role of MAM in AD and their potential as therapeutic targets in this disease. Overall, our findings demonstrate: (1) Decreased ER-mitochondria contacts and alteration of MAM’s composition; (2) changes in ER-mitochondria Ca²⁺ transfer; (3) alterations in mitochondrial dynamics and function.

First, we analyzed the structural and functional alterations at MAM in APPsw and WT cells. APPsw cells recapitulate amyloid pathology through increased Aβ generation [20]. ER-mitochondria contacts require the interaction of tethering proteins present in the ER membrane and OMM, such as MFN1 and MFN2 [27]. In APPsw cells, we observed

a slight increase of MFN1 protein levels in mitochondria and MAM fractions (Figure 1a,b) and a decrease of MFN2 levels in all fractions, namely microsomes, mitochondria, and MAM fractions (Figure 1a,c). Previous studies showed that mitochondrial anomalies, oxidative stress, inflammation, and cytoskeletal rearrangements contribute to neurodegeneration in the hippocampus and cortex of a MFN2 KO mouse model [53,54]. Park et al. also found a decrease in MFN2 expression in neuro-2a cells expressing the Swedish mutation of APP [55], and similar observations were also reported in human AD brains [29,56]. A decrease in the number of ER-mitochondria contacts ≤ 25 nm was observed in APP^{swe} cells (Figure 1e), which can be associated with the decreased content of MFN2 (Figure 1a,c). Accordingly, it has been previously found that MFN2 ablation or silencing in mouse embryonic fibroblasts and HeLa cells, respectively, reduce the ER-mitochondria juxtaposition affecting mitochondrial uptake of Ca^{2+} released by the ER [57,58]. The reduction of ER-mitochondria contacts was also reported in senescent cells [59]. We also found a decrease in the number of mitochondria per cell (Figure 1f) and in mitochondrial mass (Figure 1h) in APP^{swe} cells. Jiang et al. observed that neurons of MFN2 knockout mice present a decreased number of mitochondria in the axons and dendrites, changes in mitochondrial morphology, and fragmentation caused by an altered mitochondrial fusion [53]. Possibly, the decrease of ER-mitochondria contacts is associated with the reduction of Ca^{2+} flux, since we observed a decrease in mitochondrial Ca^{2+} levels after histamine stimulation (Figure 2d), despite the accumulation of Ca^{2+} in the ER (Figure 2b). Concerning mitochondrial Ca^{2+} content, discrepancies between studies are found in literature, which may be due to the use of different models of AD (in vitro and in vivo), as well as different in vitro experimental conditions (different models and incubation period, methodologies used to determine these parameters, among others). Other authors demonstrate that mitochondrial Ca^{2+} overload and, consequently, cell death, is induced by $\text{A}\beta$ oligomers [60,61]. Calvo-Rodrigues et al. also reported that $\text{A}\beta$ aggregates are associated with an increase in the cytosolic as well as mitochondrial Ca^{2+} levels via MCU in the APP/PS1 transgenic (Tg) mouse model. The mitochondrial Ca^{2+} overload can induce to the opening of the mitochondrial permeability transition pore (mPTP) and caspases activation, consequently leading to cell death. The same authors reported that blocking MCU with Ru360 prevents the increase of mitochondrial Ca^{2+} levels [31], which is in accordance with a previous study in MCU knockdown HeLa cells that show an inhibition of mitochondrial Ca^{2+} uptake, even in the absence of mitochondrial membrane depolarization [62], suggesting that MCU plays a key role in mitochondrial Ca^{2+} influx. Moreover, human post-mortem AD brains show a downregulation of genes related to mitochondrial influx Ca^{2+} transporter, MCU, and its regulatory subunits, and an upregulation of genes involved in mitochondrial Ca^{2+} efflux pathways, *SLC8B1* (encoding NCLX), suggesting an adaptive mechanism to prevent mitochondrial Ca^{2+} overload [31]. A reduction in mitochondrial Ca^{2+} uptake in *Mfn2*^{-/-} MEFs in response to IP_3 -mediated cytosolic Ca^{2+} transients was also reported [57,58]. Furthermore, MCU expression was reduced by about 50% in *Mfn2*^{-/-} MEFs as compared with control cells [63]. However, other authors suggest that MFN2 knockdown increases ER-mitochondria contacts length and the Ca^{2+} transfer between both organelles [63,64]. In MFN2 knockdown cells, Leal et al. also observed an increase in MFN1 protein expression [64], which can compensate the MFN2 downregulation in terms of energy production and cell viability. The efficiency of ER-mitochondria Ca^{2+} transfer depends not only on the distance between both organelles, but also on the expression level of mitochondrial Ca^{2+} uptake machinery [15] and the mitochondrial membrane potential [65]. We found an increase of VDAC1 (in mitochondria and MAM fraction) (Figure 2e,g) and Sig-1R (in MAM fraction) (Figure 2f,i) levels, together with a decrease of MCU (in total extracts) (Figure 2f,i) and BiP/GRP78 levels (in total extracts and microsomes fraction) (Figure 2e,h) in APP^{swe} cells. VDAC1 regulates ER-mitochondria Ca^{2+} signaling, and $\text{A}\beta$ is capable to upregulate VDAC1 in human neuroblastoma cell line [66]. Its overexpression was also observed in human post-mortem AD brains and in APP Tg mice in an age-dependent manner [66]. Sig-1R resides at the MAM, forms a Ca^{2+} -sensitive chaperone complex with BiP/GRP78,

and associates with IP₃R. Upon IP₃R activation, which decreases Ca²⁺ concentration at MAM, Sig-1R dissociates from BiP/GRP78 in ER periphery, promoting Ca²⁺ signaling into mitochondria via IP₃R [34,67]. Sig-1R up-regulation was found in APPSwe/Lon mouse brains before amyloid deposition, while decreased Sig-1R expression was observed in human post-mortem brain cortical tissue [68]. Sig-1R upregulation can also repress cell death signals in HEK293 and WT cells under ER stress [69]. Despite the decrease of BiP/GRP78 expression in APPSwe cells, we also observed an accumulation of this protein in mitochondria, suggesting that BiP/GRP78 is relocated to the mitochondria (Figure 2e). A previous study shows the translocation of BiP/GRP78 to the mitochondria under ER stress that can be involved in UPR signaling between ER and mitochondria, which regulates cellular Ca²⁺ homeostasis [70]. Simultaneous, decreased BiP/GRP78 and increased in protein ubiquitination levels was observed in the brains of old rodents suggesting an impairment of ER stress response [71,72]. A decreased expression of BiP/GRP78 mRNA was also observed in primary cultures of neurons from mice with a knock-in PS1 mutant allele and in the brains of FAD and SAD patients [73]. However, other authors suggest that BiP/GRP78 expression is increased in “healthy” neurons from the human AD temporal cortex and hippocampus, which do not co-localize with neurofibrillary tangles [74]. An increase in BiP/GRP78 expression levels associated with the accumulation of toxic Aβ peptide was also observed in 2 month-old 3xTg-AD mice [75] and hippocampal cultures [76]. Under thapsigargin-induced ER stress BiP/GRP78 is bound to immature and unfolded APP preventing its translocation to distal compartments, which results in a reduction of Aβ generation because β-/γ-secretases activity is believed to be located in a distal compartment of the ER [77,78]. This evidence suggests that BiP/GRP78 can play a neuroprotective role in the initial phase of AD, but with the progression of the disease its decreased levels can attenuate the UPR signaling pathway resulting in an accumulation of unfolded proteins, namely APP. A reduction in the uptake of Ca²⁺ to mitochondria affects their metabolism contributing to mitochondria dysfunction [15]. Accordingly, we observed a reduction in mitochondrial respiration (Figure 3a–d) and membrane potential (Figure 3f), resulting in a decreased OXPHOS ATP production (Figure 3e) in APPSwe cells. Mitochondrial oxygen consumption of APPSwe cells is altered either under basal conditions and/or when challenged by the mitochondrial modulators, suggesting a less efficient electron transport chain (ETC). Under such conditions, a reduction in mitochondrial membrane potential was observed, hampering the capacity of APPSwe cells to produce ATP, which are in accordance with previous observations made in other models carrying APP mutations [79].

Previously, a reduction in mitochondrial membrane potential in AD fibroblasts after thapsigargin-induced Ca²⁺ stress stimulus [80] and the depolarization of the mitochondrial membrane with FCCP inhibit Ca²⁺ uptake were observed [81]. We also found a decrease in glycolysis rate (Figure 3h) and glycolysis capacity in APPSwe cells (Figure 3i). Glucose withdrawal prevents glycolysis, rendering cells more dependent on OXPHOS to synthesize ATP. A decrease in glycolysis suggests that APPSwe cells are unable to use this pathway to overcome mitochondrial ATP deficits, representing a mal-adaptive response that worsens the cellular energetic status. A similar result was also observed in AD cybrid cell lines that harbor mitochondrial DNA from AD patients platelets [82]. It is described in different cell models that MFN2 depletion changes the cellular metabolic profile, leading to mitochondrial membrane depolarization and decreased cellular oxygen consumption as well as decreased glucose and pyruvate oxidation [83]. Accordingly, a reduction in glucose metabolism was also observed in the neocortex of AD patients that has been correlated with a decreased expression of nuclear and mitochondrial genes that encode proteins of OXPHOS [84]. As previously stated, mitochondria are dynamic organelles that can change morphology and distribution due to fission and fusion events. Mitochondrial fission is regulated by DRP1 and FIS-1 and fusion by MFN1, MFN2, and mitochondrial dynamin like GTPase (OPA1) [85]. Our results obtained in APPSwe cells show an impairment in mitochondrial dynamics due to an unbalance between fusion and fission, particularly in MFN2 levels (Figure 4a–e), as well as a slight increase in mitochondrial biogenesis

(Figure 4f–h) that did not reach statistical significance, which could represent an attempt to improve mitochondrial metabolic capacity reducing the cascade of deleterious events caused by mitochondrial dysfunction. Accordingly, AD fibroblasts also show defects in mitochondrial dynamics and bioenergetics, reduced ATP generation, and Ca^{2+} dysregulation [80]. Furthermore, abnormal mitochondrial distribution and fragmentation were associated to mitochondrial membrane depolarization and decreased ATP production in M17 cells overexpressing APP [86].

The ER-mitochondria contacts are also involved in the ER stress-mediated cell death and UPR, because several ER co-factors and chaperones are present at MAM. Moreover, impairment in the UPR, apoptosis, and misfolded proteins accumulation are common features of AD [87]. In the early phase of ER stress, the cell adapts to stressful conditions through the increase of ER-mitochondria connection, which facilitates mitochondrial Ca^{2+} uptake and ATP production. However, alterations in MAM functional features, such as Ca^{2+} signaling, induce ER stress and UPR activation, so ER-mitochondria communication could also regulate stress responses and the UPR at different levels [33]. Besides the alterations in ER-mitochondria contacts found in our AD cell model, we also observed that UPR markers are present at MAM and the activation of this stress response occurred through the increase of PERK and IRE1 α protein levels (Figure 5c–e). It was previously reported that MFN2 interacts directly with PERK to regulate ER stress-mediated pathways, including UPR, and MFN2 ablation increases PERK activity [88]. PERK is also a member of the MAM that facilitates signals exchanges through these contacts [89] with its upregulation being detected in human post-mortem AD brains [42]. Besides its involvement in UPR, IRE1 α stabilizes IP₃Rs at MAM controlling mitochondrial Ca^{2+} uptake [90]. Under resting conditions, IRE1 α deficiency was shown to trigger mitochondrial and energy metabolism alterations [90]. We also found a decrease in the levels of ERO1 α (Figure 5f,g), which catalyzes disulfide bond formation in ER during protein folding, and loss of its function leads to misfolded proteins accumulation [44]. This protein also plays a key role in ER redox homeostasis. Under ER stress conditions, the pro-apoptotic transcription factor CHOP can activate ERO1 α and promote apoptosis through Ca^{2+} signaling modulation because ERO1 α interacts with IP₃R potentiating Ca^{2+} efflux from ER to mitochondria at MAM [43,91,92]. On the other hand, ERO1 α silencing inhibits ER Ca^{2+} release [43,44]. Therefore, the decrease of ERO1 α that we observed can lead to the loss of ER redox homeostasis increasing ER stress, simultaneously contributing to prevent Ca^{2+} efflux from ER to mitochondria.

We also observed an increase of PCNA levels in APP^{swe} (Figure 5f,h). This nuclear protein is essential for regulation of DNA replication, repair, and epigenetic alterations; however, PCNA has been associated with cellular events through the formation of a complex with many cytosolic proteins involved in the mitogen-activated protein kinase (MAPK) and phosphatidylinositol 3-kinase (PI₃K)/protein kinase B (AKT) signaling pathways demonstrating its involvement in cellular signaling [93]. In mature non-proliferating neutrophils, PCNA is located in the cytosol where it serves as a binding platform for procaspases inhibiting their activation and apoptosis, thus regulating neutrophil survival [48]. Furthermore, in APP^{swe} Tg mice, proliferation markers, such as PCNA, seem to induce cell cycle re-entry [94] and its mRNA levels have been found to be increased in brain tissue from AD patients [95] and in APP human neuroblastoma SH-SY5Y cells [1]. Thus, PCNA is an essential co-factor for DNA replication and repair and appears to be involved in pro-survival pathways in response to cellular stress. In the present AD in vitro model, we also observed an accumulation of PCNA in MAM and mitochondria fractions (Figure 5f), supporting its involvement in cellular stress response.

Internalization of APP and A β peptide by mitochondria was observed in vitro [96,97], in human post-mortem AD brains [29,98,99], as well as in APP-overexpressing mice [96,99,100]. It is described that Hsp60 and TOM40, associated to TOM23, are responsible for APP and A β internalization into mitochondria [96,97,101]. Moreover, accumulation of APP in the TOM complex affects the mitochondrial import of other proteins and, consequently, impairs

mitochondrial functions [102]. As observed in hippocampal neurons of ApoE4 female mice, the increase of the fusion protein MFN1 and TOM40 indicates that the decrease in mitophagy can lead to the accumulation of mitochondrial proteins, due to the accumulation of damaged mitochondria [103]. Immunoblot analyses also revealed that Hsp60 binds to APP and A β , and this interaction seems to be increased in the brain of 3xTg-AD mice and in mitochondria isolated from human AD brain [104]. Furthermore, Hsp60 protein levels were increased by ~50% and ~35%, in mitochondrial fractions isolated from the postmortem frontal cortex of SAD and FAD individuals, respectively [104]. In addition, Hsp60 knockdown attenuates APP and A β translocation to mitochondria in the neural cell line (C17.2) expressing the APP Swedish mutation [101]. In this study, we also observed an increase in TOM40 (in MAM and mitochondria fractions) (Figure 5f,i) and Hsp60 (in MAM fraction) (Figure 5j,k) in APP^{swe} cells, which can contribute to APP accumulation in mitochondria resulting in mitochondrial dysfunction, as previously described.

In conclusion, our results suggest that the overexpression of the familial APP Swedish mutation causes the accumulation of APP in mitochondria and MAM, which can contribute to the structural and functional changes in these subcellular fractions, affecting the response to stress and inducing energy deficits. Together, our findings support the idea that the defective crosstalk between ER and mitochondria, mediated by MAM, plays a key role in AD physiopathology that may represent a relevant therapeutic target in this disorder.

Supplementary Materials: The following are available online at <https://www.mdpi.com/article/10.3390/biomedicines9080881/s1>, Figure S1: Analysis of protein components of subcellular fractions from wild-type (WT) mouse neuroblastoma cell line (N2A).

Author Contributions: Conceptualization: C.F.P., P.I.M. and M.R.D.; methodology: T.F., R.R., D.F.S., A.P.M., A.E.S., C.F.P. and P.I.M.; formal analysis: T.F. and D.F.S.; investigation: T.F.; writing—original draft preparation: T.F.; writing—review and editing: C.F.P., P.I.M. and S.M.C.; funding acquisition: C.F.P., P.I.M. and M.R.D.; supervision: C.F.P., P.I.M. and M.R.D. All authors have read and agreed to the published version of the manuscript.

Funding: This research was supported by the European Regional Development Fund (ERDF), through the Centro 2020 Regional Operational Programme: project CENTRO-01-0145-FEDER-000012-HealthyAging2020, the COMPETE 2020—Operational Programme for Competitiveness and Internationalization, and the Portuguese national funds via FCT—Fundação para a Ciência e a Tecnologia, I.P.: projects POCI-01-0145-FEDER-028214 and POCI-01-0145-FEDER-029369 and UIDB/04539/2020 and UIDP/04539/2020. European Social Fund (Post-Doctoral Researcher Contract SFRH/BPD/101028/2014 to Rosa Resende). Tânia Fernandes is a recipient of the PhD fellow from the FCT (SFRH/BD/148801/2019).

Institutional Review Board Statement: Not applicable.

Informed Consent Statement: Not applicable.

Data Availability Statement: All data are available upon contact of corresponding authors.

Acknowledgments: We are grateful to Mónica Zuzarte (Center for Innovative Biomedicine and Biotechnology CIBB, University of Coimbra, Coimbra, Portugal) for processing samples and acquiring transmission electron microscopy images.

Conflicts of Interest: The authors declare no conflict of interest.

Abbreviations

2DG: 2-deoxyglucose; A β : Amyloid β ; AD: Alzheimer's disease, ApoE4: Apolipoprotein E ϵ 4; APP: Amyloid precursor protein; APP^{swe}: Mouse neuroblastoma cell line overexpressing the human APP with the familial Swedish mutation; BCA: Bicinchoninic acid; BSA: Bovine serum albumin; CTECF: Corrected total cell fluorescence; DMEM: Dulbecco's modified Eagle's medium; DRP1: Dynamin-1-like protein; ECAR: Extracellular acidification rate; ER: Endoplasmic reticulum; ERO1 α : ER oxidase 1; FAD: Familial Alzheimer's disease; FBS: Fetal bovine serum; FCCP: Carbonyl cyanide-4-(trifluoromethoxy) phenyl hydrazone; FIS-1: Mitochondrial fission 1; GRP75: Glucose-regulated

protein 75; GRP78: Glucose-regulated protein 78; Hsp60: Chaperone heat shock protein 60; IMM: Inner mitochondrial membrane; IP3R: Inositol 1,4,5-trisphosphate receptor; IRE1 α : Inositol-requiring enzyme 1 α ; MAM: Mitochondria-associated membrane; MCU: Mitochondrial Ca²⁺ uniporter; MFN 1/2: Mitofusin 1/2; MRB: Mitochondria resuspending buffer; mtTFA: Mitochondrial transcription factor A; N2A: Mouse neuroblastoma cell line; ND1: NADH-ubiquinone oxidoreductase chain 1; NRF1: Nuclear respiratory factor 1; OCR: Oxygen consumption rate; OMM: Outer mitochondrial membrane; OXPHOS: Oxidative phosphorylation; PBS: Phosphate-buffered saline; PCNA: Proliferating cell nuclear antigen; p-DRP1: Phospho-dynamain-1-like protein; PDI: Protein disulfide isomerase; PERK: Protein kinase R-like ER kinase; PMS: Phenylmethylsulfonyl fluoride; PS 1/2: Presenilin-1/2; PVDF: Polyvinylidene fluoride; RIPA: Radioimmunoprecipitation assay buffer; SAD: Sporadic Alzheimer's disease; SDS-PAGE: Sodium dodecyl sulfate polyacrylamide gel electrophoresis; SERCA: Sarco/endoplasmic reticulum Ca²⁺ ATPase; SHM: Sucrose homogenization medium; Sig-1R: Sigma-1 receptor; TBS-T: Tris-buffered saline containing Tween-20; TEM: Transmission electron microscopy; TF: Total fraction; TG: Thapsigargin; TMRE: Tetramethylrhodamine ethyl ester perchlorate; TOM40: Outer mitochondrial membrane 40; UPR: Unfolded protein response; VDAC1: Mitochondrial voltage-dependent anion channel 1; WB: Western blot; WT: Wild-type.

References

- Poirier, Y.; Grimm, A.; Schmitt, K.; Eckert, A. Link between the unfolded protein response and dysregulation of mitochondrial bioenergetics in Alzheimer's disease. *Cell Mol. Life Sci.* **2019**, *76*, 1419–1431. [CrossRef] [PubMed]
- Winblad, B.; Amouyel, P.; Andrieu, S.; Ballard, C.; Brayne, C.; Brodaty, H.; Cedazo-Minguez, A.; Dubois, B.; Edvardsson, D.; Feldman, H.; et al. Defeating Alzheimer's disease and other dementias: A priority for European science and society. *Lancet Neurol.* **2016**, *15*, 455–532. [CrossRef]
- Nelson, P.T.; Abner, E.L.; Schmitt, F.A.; Kryscio, R.J.; Jicha, G.A.; Santacruz, K.; Smith, C.D.; Patel, E.; Markesbery, W.R. Brains with medial temporal lobe neurofibrillary tangles but no neuritic amyloid plaques are a diagnostic dilemma but may have pathogenetic aspects distinct from Alzheimer disease. *J. Neuropathol. Exp. Neurol.* **2009**, *68*, 774–784. [CrossRef] [PubMed]
- Area-Gomez, E.; Schon, E.A. Mitochondria-associated ER membranes and Alzheimer disease. *Curr. Opin. Genet. Dev.* **2016**, *38*, 90–96. [CrossRef]
- Area-Gomez, E.; Schon, E.A. On the pathogenesis of Alzheimer's disease: The MAM hypothesis. *FASEB J.* **2017**, *31*, 864–867. [CrossRef]
- Area-Gomez, E.; de Groof, A.; Bonilla, E.; Montesinos, J.; Tanji, K.; Boldogh, I.; Pon, L.; Schon, E.A. A key role for MAM in mediating mitochondrial dysfunction in Alzheimer disease. *Cell Death Dis.* **2018**, *9*, 335. [CrossRef]
- Ferreiro, E.; Baldeiras, I.; Ferreira, I.L.; Costa, R.O.; Rego, A.C.; Pereira, C.F.; Oliveira, C.R. Mitochondrial- and endoplasmic reticulum-associated oxidative stress in Alzheimer's disease: From pathogenesis to biomarkers. *Int. J. Cell Biol.* **2012**, *2012*, 1–23. [CrossRef]
- Cardoso, S.; Carvalho, C.; Correia, S.C.; Seica, R.M.; Moreira, P.I. Alzheimer's disease: From mitochondrial perturbations to mitochondrial medicine. *Brain Pathol.* **2016**, *26*, 632–647. [CrossRef] [PubMed]
- Simmen, T.; Herrera-Cruz, M.S. Plastic mitochondria-endoplasmic reticulum (ER) contacts use chaperones and tethers to mould their structure and signaling. *Curr. Opin. Cell Biol.* **2018**, *53*, 61–69. [CrossRef] [PubMed]
- Giacomello, M.; Pellegrini, L. The coming of age of the mitochondria–ER contact: A matter of thickness. *Cell Death Differ.* **2016**, *23*, 1417–1427. [CrossRef] [PubMed]
- Wilson, E.L.; Metzakopian, E. ER-mitochondria contact sites in neurodegeneration: Genetic screening approaches to investigate novel disease mechanisms. *Cell Death Differ.* **2021**, *28*, 1804–1821. [CrossRef]
- Bernard-Marissal, N.; Chrast, R.; Schneider, B.L. Endoplasmic reticulum and mitochondria in diseases of motor and sensory neurons: A broken relationship? *Cell Death Dis.* **2018**, *9*, 333. [CrossRef]
- Gordaliza-Alaguero, I.; Cantó, C.; Zorzano, A. Metabolic implications of organelle–mitochondria communication. *EMBO Rep.* **2019**, *20*, 1–27. [CrossRef] [PubMed]
- Van Vliet, A.R.; Verfaillie, T.; Agostinis, P. New functions of mitochondria associated membranes in cellular signaling. *Biochim. Biophys. Acta Mol. Cell Res.* **2014**, *1843*, 2253–2262. [CrossRef]
- Rossi, A.; Pizzo, P.; Filadi, R. Calcium, mitochondria and cell metabolism: A functional triangle in bioenergetics. *Biochim. Biophys. Acta Mol. Cell Res.* **2019**, *1866*, 1068–1078. [CrossRef]
- Brunetti, D.; Catania, A.; Viscomi, C.; Deleidi, M.; Bindoff, L.A.; Ghezzi, D.; Zeviani, M. Role of PITRM1 in mitochondrial dysfunction and neurodegeneration. *Biomedicines* **2021**, *9*, 833. [CrossRef]
- Moreira, P.I.; Carvalho, C.; Zhu, X.; Smith, M.A.; Perry, G. Mitochondrial dysfunction is a trigger of Alzheimer's disease pathophysiology. *Biochim. Biophys. Acta Mol. Basis Dis.* **2010**, *1802*, 2–10. [CrossRef]
- Wang, W.; Zhao, F.; Ma, X.; Perry, G.; Zhu, X. Mitochondria dysfunction in the pathogenesis of Alzheimer's disease: Recent advances. *Mol. Neurodegener.* **2020**, *15*, 30. [CrossRef] [PubMed]

19. Cunnane, S.C.; Trushina, E.; Morland, C.; Prigione, A.; Casadesus, G.; Andrews, Z.B.; Beal, M.F.; Bergersen, L.H.; Brinton, R.D.; de la Monte, S.; et al. Brain energy rescue: An emerging therapeutic concept for neurodegenerative disorders of ageing. *Nat. Rev. Drug Discov.* **2020**, *19*, 609–633. [CrossRef]
20. Thinakaran, G.; Teplow, D.B.; Siman, R.; Greenberg, B.; Sisodia, S.S. Metabolism of the “Swedish” amyloid precursor protein variant in Neuro2a (N2a) cells. *J. Biol. Chem.* **1996**, *271*, 9390–9397. [CrossRef]
21. Cagnin, M.; Ozzano, M.; Bellio, N.; Fiorentino, I.; Follo, C.; Isidoro, C. Dopamine induces apoptosis in APP^{Swe}-expressing Neuro2A cells following Pepstatin-sensitive proteolysis of APP in acid compartments. *Brain Res.* **2012**, *1471*, 102–117. [CrossRef]
22. Resende, R.; Ferreira-Marques, M.; Moreira, P.; Coimbra, J.R.M.; Baptista, S.J.; Isidoro, C.; Salvador, J.A.R.; Dinis, T.C.P.; Pereira, C.F.; Santos, A.E. New BACE1 chimeric peptide inhibitors selectively prevent A β PP- β cleavage decreasing amyloid- β production and accumulation in Alzheimer’s disease models. *J. Alzheimer’s Dis.* **2020**, *76*, 1317–1337. [CrossRef]
23. Wieckowski, M.R.M.R.; Giorgi, C.; Lebiedzinska, M.; Duszynski, J.; Pinton, P. Isolation of mitochondria-associated membranes and mitochondria from animal tissues and cells. *Nat. Protoc.* **2009**, *4*, 1582–1590. [CrossRef]
24. Williamson, C.D.; Wong, D.S.; Bozidis, P.; Zhang, A.; Colberg-Poley, A.M. Isolation of endoplasmic reticulum, mitochondria, and mitochondria-associated membrane and detergent resistant membrane fractions from transfected cells and from human cytomegalovirus-infected primary fibroblasts. In *Current Protocols in Cell Biology*; John Wiley & Sons, Inc.: Hoboken, NJ, USA, 2015; Volume 118, pp. 3–27, ISBN 0471143030.
25. Prinz, W.A.; Toulmay, A.; Balla, T. The functional universe of membrane contact sites. *Nat. Rev. Mol. Cell Biol.* **2020**, *21*, 7–24. [CrossRef] [PubMed]
26. Giorgi, C.; Missiroli, S.; Patergnani, S.; Duszynski, J.; Wieckowski, M.R.; Pinton, P. Mitochondria-associated membranes: Composition, molecular mechanisms, and physiopathological implications. *Antioxid. Redox Signal.* **2015**, *22*, 995–1019. [CrossRef]
27. Herrera-Cruz, M.S.; Simmen, T. Over six decades of discovery and characterization of the architecture at mitochondria-associated membranes (MAMs). *Adv. Exp. Med. Biol.* **2017**, *997*, 13–31. [CrossRef] [PubMed]
28. Raturi, A.; Simmen, T. Where the endoplasmic reticulum and the mitochondrion tie the knot: The mitochondria-associated membrane (MAM). *Biochim. Biophys. Acta Mol. Cell Res.* **2013**, *1833*, 213–224. [CrossRef]
29. Manczak, M.; Calkins, M.J.; Reddy, P.H. Impaired mitochondrial dynamics and abnormal interaction of amyloid beta with mitochondrial protein Drp1 in neurons from patients with Alzheimer’s disease: Implications for neuronal damage. *Hum. Mol. Genet.* **2011**, *20*, 2495–2509. [CrossRef]
30. Manczak, M.; Kandimalla, R.; Yin, X.; Reddy, P.H. Hippocampal mutant APP and amyloid beta-induced cognitive decline, dendritic spine loss, defective autophagy, mitophagy and mitochondrial abnormalities in a mouse model of Alzheimer’s disease. *Hum. Mol. Genet.* **2018**, *27*, 1332–1342. [CrossRef] [PubMed]
31. Calvo-Rodriguez, M.; Hou, S.S.; Snyder, A.C.; Kharitonova, E.K.; Russ, A.N.; Das, S.; Fan, Z.; Muzikansky, A.; Garcia-Alloza, M.; Serrano-Pozo, A.; et al. Increased mitochondrial calcium levels associated with neuronal death in a mouse model of Alzheimer’s disease. *Nat. Commun.* **2020**, *11*, 2146. [CrossRef]
32. Jadiya, P.; Kolmetzky, D.W.; Tomar, D.; Di Meco, A.; Lombardi, A.A.; Lambert, J.P.; Luongo, T.S.; Ludtmann, M.H.; Praticò, D.; Elrod, J.W. Impaired mitochondrial calcium efflux contributes to disease progression in models of Alzheimer’s disease. *Nat. Commun.* **2019**, *10*, 1–14. [CrossRef] [PubMed]
33. Marchi, S.; Patergnani, S.; Missiroli, S.; Morciano, G.; Rimessi, A.; Wieckowski, M.R.; Giorgi, C.; Pinton, P. Mitochondrial and endoplasmic reticulum calcium homeostasis and cell death. *Cell Calcium* **2018**, *69*, 62–72. [CrossRef]
34. Patergnani, S.; Suski, J.M.; Agnoletto, C.; Bononi, A.; Bonora, M.; De Marchi, E.; Giorgi, C.; Marchi, S.; Missiroli, S.; Poletti, F.; et al. Calcium signaling around mitochondria associated membranes (MAMs). *Cell Commun. Signal.* **2011**, *9*, 19. [CrossRef] [PubMed]
35. Weng, T.Y.; Tsai, S.Y.A.; Su, T.P. Roles of Sigma-1 receptors on mitochondrial functions relevant to neurodegenerative diseases. *J. Biomed. Sci.* **2017**, *24*, 1–14. [CrossRef]
36. Picone, P.; Nuzzo, D.; Caruana, L.; Scafidi, V.; Di Carlo, M. Mitochondrial dysfunction: Different routes to Alzheimer’s disease therapy. *Oxid. Med. Cell Longev.* **2014**, *2014*, 1–11. [CrossRef]
37. Carvalho, C.; Cardoso, S.; Correia, S.C.; Santos, R.X.; Santos, M.S.; Baldeiras, I.; Oliveira, C.R.; Moreira, P.I. Metabolic alterations induced by sucrose intake and Alzheimer’s disease promote similar brain mitochondrial abnormalities. *Diabetes* **2012**, *61*, 1234–1242. [CrossRef] [PubMed]
38. Correia, C.S.; Santos, X.R.; Santos, S.M.; Casadesus, G.; LaManna, C.J.; Perry, G.; Smith, A.M.; Moreira, I.P. Mitochondrial abnormalities in a streptozotocin-induced rat model of sporadic Alzheimer’s disease. *Curr. Alzheimer Res.* **2013**, *10*, 406–419. [CrossRef]
39. Tilokani, L.; Nagashima, S.; Paupe, V.; Prudent, J. Mitochondrial dynamics: Overview of molecular mechanisms. *Essays Biochem.* **2018**, *62*, 341–360. [CrossRef] [PubMed]
40. Onyango, I.G.; Lu, J.; Rodova, M.; Lezi, E.; Crafter, A.B.; Swerdlow, R.H. Regulation of neuron mitochondrial biogenesis and relevance to brain health. *Biochim. Biophys. Acta Mol. Basis Dis.* **2010**, *1802*, 228–234. [CrossRef]
41. Gerakis, Y.; Hetz, C. Emerging roles of ER stress in the etiology and pathogenesis of Alzheimer’s disease. *FEBS J.* **2018**, *285*, 995–1011. [CrossRef]
42. Hashimoto, S.; Saido, T.C. Critical review: Involvement of endoplasmic reticulum stress in the aetiology of Alzheimer’s disease. *Open Biol.* **2018**, *8*, 180024. [CrossRef] [PubMed]

43. Anelli, T.; Bergamelli, L.; Margittai, E.; Rimessi, A.; Fagioli, C.; Malgaroli, A.; Pinton, P.; Ripamonti, M.; Rizzuto, R.; Sitia, R. Ero1 α regulates Ca²⁺ fluxes at the endoplasmic reticulum–mitochondria interface (MAM). *Antioxid. Redox Signal.* **2012**, *16*, 1077–1087. [CrossRef]
44. Seervi, M.; Sobhan, P.K.; Joseph, J.; Ann Mathew, K.; Santhoshkumar, T.R. ERO1 α -dependent endoplasmic reticulum-mitochondrial calcium flux contributes to ER stress and mitochondrial permeabilization by procaspase-activating compound-1 (PAC-1). *Cell Death Dis.* **2013**, *4*, 1–14. [CrossRef]
45. Silva, A.; Pereira, M.; Carrascal, M.A.; Brites, G.; Neves, B.; Moreira, P.; Resende, R.; Silva, M.M.; Santos, A.E.; Pereira, C.; et al. Calcium modulation, anti-oxidant and anti-inflammatory effect of skin allergens targeting the Nrf2 signaling pathway in Alzheimer's disease cellular models. *Int. J. Mol. Sci.* **2020**, *21*, 7791. [CrossRef]
46. Costa, R.O.; Ferreira, E.; Martins, I.; Santana, I.; Cardoso, S.M.; Oliveira, C.R.; Pereira, C.M.F. Amyloid β -induced ER stress is enhanced under mitochondrial dysfunction conditions. *Neurobiol. Aging* **2012**, *33*, 824.e5–824.e16. [CrossRef]
47. Fonseca, A.C.R.G.; Ferreira, E.; Oliveira, C.R.; Cardoso, S.M.; Pereira, C.F. Activation of the endoplasmic reticulum stress response by the amyloid-beta 1–40 peptide in brain endothelial cells. *Biochim. Biophys. Acta Mol. Basis Dis.* **2013**, *1832*, 2191–2203. [CrossRef]
48. Witko-Sarsat, V.; Mocek, J.; Bouayad, D.; Tamassia, N.; Ribeil, J.-A.; Candalh, C.; Davezac, N.; Reuter, N.; Mouthon, L.; Hermine, O.; et al. Proliferating cell nuclear antigen acts as a cytoplasmic platform controlling human neutrophil survival. *J. Exp. Med.* **2010**, *207*, 2631–2645. [CrossRef] [PubMed]
49. Gottschalk, W.K.; Lutz, M.W.; He, Y.T.; Saunders, A.M.; Burns, D.K.; Roses, A.D.; Chiba-Falek, O. The broad impact of TOM40 on neurodegenerative diseases in aging. *J. Park. Dis. Alzheimer's Dis.* **2014**, *1*, 1–25. [CrossRef]
50. Campanella, C.; Pace, A.; Bavisotto, C.C.; Marzullo, P.; Gammazza, A.M.; Buscemi, S.; Piccionello, A.P. Heat shock proteins in Alzheimer's disease: Role and targeting. *Int. J. Mol. Sci.* **2018**, *19*, 2603. [CrossRef] [PubMed]
51. Liu, Y.; Zhu, X. Endoplasmic reticulum-mitochondria tethering in neurodegenerative diseases. *Transl. Neurodegener.* **2017**, *6*, 21. [CrossRef] [PubMed]
52. Völgyi, K.; Badics, K.; Sialana, F.J.; Gulyássi, P.; Udvari, E.B.; Kis, V.; Drahos, L.; Lubec, G.; Kékési, K.A.; Juhász, G. Early presymptomatic changes in the proteome of mitochondria-associated membrane in the APP/PS1 mouse model of Alzheimer's disease. *Mol. Neurobiol.* **2018**, *55*, 7839–7857. [CrossRef]
53. Jiang, S.; Nandy, P.; Wang, W.; Ma, X.; Hsia, J.; Wang, C.; Wang, Z.; Niu, M.; Siedlak, S.L.; Torres, S.; et al. Mfn2 ablation causes an oxidative stress response and eventual neuronal death in the hippocampus and cortex. *Mol. Neurodegener.* **2018**, *13*, 5. [CrossRef] [PubMed]
54. Han, S.; Nandy, P.; Austria, Q.; Siedlak, S.L.; Torres, S.; Fujioka, H.; Wang, W.; Zhu, X. Mfn2 ablation in the adult mouse hippocampus and cortex causes neuronal death. *Cells* **2020**, *9*, 116. [CrossRef]
55. Park, J.; Choi, H.; Min, J.S.; Kim, B.; Lee, S.R.; Yun, J.W.; Choi, M.S.; Chang, K.T.; Lee, D.S. Loss of mitofusin 2 links beta-amyloid-mediated mitochondrial fragmentation and Cdk5-induced oxidative stress in neuron cells. *J. Neurochem.* **2015**, *132*, 687–702. [CrossRef]
56. Wang, X.; Su, B.; Zheng, L.; Perry, G.; Smith, M.A.; Zhu, X. The role of abnormal mitochondrial dynamics in the pathogenesis of Alzheimer's disease. *J. Neurochem.* **2009**, *109*, 153–159. [CrossRef]
57. De Brito, O.M.; Scorrano, L. Mitofusin 2 tethers endoplasmic reticulum to mitochondria. *Nature* **2008**, *456*, 605–610. [CrossRef]
58. Naon, D.; Zaninello, M.; Giacomello, M.; Varanita, T.; Grespi, F.; Lakshminarayanan, S.; Serafini, A.; Semenzato, M.; Herkenne, S.; Hernández-Alvarez, M.I.; et al. Critical reappraisal confirms that mitofusin 2 is an endoplasmic reticulum–mitochondria tether. *Proc. Natl. Acad. Sci. USA* **2016**, *113*, 11249–11254. [CrossRef]
59. Janikiewicz, J.; Szymański, J.; Malinska, D.; Patalas-Krawczyk, P.; Michalska, B.; Duszyński, J.; Giorgi, C.; Bonora, M.; Dobrzym, A.; Wieckowski, M.R. Mitochondria-associated membranes in aging and senescence: Structure, function, and dynamics. *Cell Death Dis.* **2018**, *9*, 332. [CrossRef] [PubMed]
60. Esteras, N.; Abramov, A.Y. Mitochondrial calcium deregulation in the mechanism of beta-amyloid and tau pathology. *Cells* **2020**, *9*, 2135. [CrossRef] [PubMed]
61. Sanz-Blasco, S.; Valero, R.A.; Rodríguez-Crespo, I.; Villalobos, C.; Núñez, L. Mitochondrial Ca²⁺ overload underlies A β oligomers neurotoxicity providing an unexpected mechanism of neuroprotection by NSAIDs. *PLoS ONE* **2008**, *3*, e2718. [CrossRef] [PubMed]
62. Mallilankaraman, K.; Cárdenas, C.; Doonan, P.J.; Chandramoorthy, H.C.; Irrinki, K.M.; Golenár, T.; Csordás, G.; Madireddi, P.; Yang, J.; Müller, M.; et al. MCUR1 is an essential component of mitochondrial Ca²⁺ uptake that regulates cellular metabolism. *Nat. Cell Biol.* **2012**, *14*, 1336–1343. [CrossRef]
63. Filadi, R.; Greotti, E.; Turacchio, G.; Luini, A.; Pozzan, T.; Pizzo, P. Mitofusin 2 ablation increases endoplasmic reticulum–mitochondria coupling. *Proc. Natl. Acad. Sci. USA* **2015**, *112*, E2174–E2181. [CrossRef]
64. Leal, N.S.; Schreiner, B.; Pinho, C.M.; Filadi, R.; Wiehager, B.; Karlström, H.; Pizzo, P.; Ankarcrona, M. Mitofusin-2 knockdown increases ER-mitochondria contact and decreases amyloid β -peptide production. *J. Cell. Mol. Med.* **2016**, *20*, 1686–1695. [CrossRef] [PubMed]
65. Finkel, T.; Menazza, S.; Holmström, K.M.; Parks, R.J.; Liu, J.; Sun, J.; Liu, J.; Pan, X.; Murphy, E. The ins and outs of mitochondrial calcium. *Circ. Res.* **2015**, *116*, 1810–1819. [CrossRef] [PubMed]
66. Shoshan-Barmatz, V.; Nahon-Crystal, E.; Shteinifer-Kuzmine, A.; Gupta, R. VDAC1, mitochondrial dysfunction, and Alzheimer's disease. *Pharmacol. Res.* **2018**, *131*, 87–101. [CrossRef] [PubMed]

67. Hayashi, T.; Su, T.-P. Sigma-1 receptor chaperones at the ER-mitochondrion interface regulate Ca²⁺ signaling and cell survival. *Cell* **2007**, *131*, 596–610. [CrossRef]
68. Hedskog, L.; Pinho, C.M.; Filadi, R.; Ronnback, A.; Hertwig, L.; Wiehager, B.; Larssen, P.; Gellhaar, S.; Sandebring, A.; Westerlund, M.; et al. Modulation of the endoplasmic reticulum-mitochondria interface in Alzheimer's disease and related models. *Proc. Natl. Acad. Sci. USA* **2013**, *110*, 7916–7921. [CrossRef] [PubMed]
69. Mitsuda, T.; Omi, T.; Tanimukai, H.; Sakagami, Y.; Tagami, S.; Okochi, M.; Kudo, T.; Takeda, M. Sigma-1Rs are upregulated via PERK/eIF2 α /ATF4 pathway and execute protective function in ER stress. *Biochem. Biophys. Res. Commun.* **2011**, *415*, 519–525. [CrossRef]
70. Sun, F.C.; Wei, S.; Li, C.W.; Chang, Y.S.; Chao, C.C.; Lai, Y.K. Localization of GRP78 to mitochondria under the unfolded protein response. *Biochem. J.* **2006**, *396*, 31–39. [CrossRef]
71. Paz Gavilán, M.; Vela, J.; Castaño, A.; Ramos, B.; del Río, J.C.; Vitorica, J.; Ruano, D. Cellular environment facilitates protein accumulation in aged rat hippocampus. *Neurobiol. Aging* **2006**, *27*, 973–982. [CrossRef] [PubMed]
72. Naidoo, N.; Ferber, M.; Master, M.; Zhu, Y.; Pack, A.I. Aging impairs the unfolded protein response to sleep deprivation and leads to proapoptotic signaling. *J. Neurosci.* **2008**, *28*, 6539–6548. [CrossRef] [PubMed]
73. Katayama, T.; Imaizumi, K.; Sato, N.; Miyoshi, K.; Kudo, T.; Hitomi, J.; Morihara, T.; Yoneda, T.; Gomi, F.; Mori, Y.; et al. Presenilin-1 mutations downregulate the signalling pathway of the unfolded-protein response. *Nat. Cell Biol.* **1999**, *1*, 479–485. [CrossRef]
74. Hoozemans, J.J.M.; Veerhuis, R.; Van Haastert, E.S.; Rozemuller, J.M.; Baas, F.; Eikelenboom, P.; Scheper, W. The unfolded protein response is activated in Alzheimer's disease. *Acta Neuropathol.* **2005**, *110*, 165–172. [CrossRef]
75. Soejima, N.; Ohyagi, Y.; Nakamura, N.; Himeno, E.; Iinuma, K.M.; Sakae, N.; Yamasaki, R.; Tabira, T.; Murakami, K.; Irie, K.; et al. Intracellular accumulation of toxic turn amyloid- β is associated with endoplasmic reticulum stress in Alzheimer's disease. *Curr. Alzheimer Res.* **2013**, *10*, 11–20. [CrossRef]
76. Costa, R.O.; Lacor, P.N.; Ferreira, I.L.; Resende, R.; Auberson, Y.P.; Klein, W.L.; Oliveira, C.R.; Rego, A.C.; Pereira, C.M.F. Endoplasmic reticulum stress occurs downstream of GluN2B subunit of N-methyl-D-aspartate receptor in mature hippocampal cultures treated with amyloid- β oligomers. *Aging Cell* **2012**, *11*, 823–833. [CrossRef] [PubMed]
77. Kudo, T.; Okumura, M.; Imaizumi, K.; Araki, W.; Morihara, T.; Tanimukai, H.; Kamagata, E.; Tabuchi, N.; Kimura, R.; Kanayama, D.; et al. Altered localization of amyloid precursor protein under endoplasmic reticulum stress. *Biochem. Biophys. Res. Commun.* **2006**, *344*, 525–530. [CrossRef]
78. Hoshino, T.; Nakaya, T.; Araki, W.; Suzuki, K.; Suzuki, T.; Mizushima, T. Endoplasmic reticulum chaperones inhibit the production of amyloid- β peptides. *Biochem. J.* **2007**, *402*, 581–589. [CrossRef]
79. Dixit, S.; Fessel, J.P.; Harrison, F.E. Mitochondrial dysfunction in the APP/PSEN1 mouse model of Alzheimer's disease and a novel protective role for ascorbate. *Free Radic. Biol. Med.* **2017**, *112*, 515–523. [CrossRef] [PubMed]
80. Pérez, M.J.; Ponce, D.P.; Aranguiz, A.; Behrens, M.I.; Quintanilla, R.A. Mitochondrial permeability transition pore contributes to mitochondrial dysfunction in fibroblasts of patients with sporadic Alzheimer's disease. *Redox Biol.* **2018**, *19*, 290–300. [CrossRef] [PubMed]
81. Parekh, A.B. Mitochondrial regulation of intracellular Ca²⁺ signaling: More than just simple Ca²⁺ buffers. *Physiology* **2003**, *18*, 252–256. [CrossRef] [PubMed]
82. Silva, D.F.; Selfridge, J.E.; Lu, J.; E, L.; Roy, N.; Hutflles, L.; Burns, J.M.; Michaelis, E.K.; Yan, S.; Cardoso, S.M.; et al. Bioenergetic flux, mitochondrial mass and mitochondrial morphology dynamics in AD and MCI cybrid cell lines. *Hum. Mol. Genet.* **2013**, *22*, 3931–3946. [CrossRef] [PubMed]
83. Schrepfer, E.; Scorrano, L. Mitofusins, from mitochondria to metabolism. *Mol. Cell* **2016**, *61*, 683–694. [CrossRef]
84. García-Escudero, V.; Martín-Maestro, P.; Perry, G.; Avila, J. Deconstructing mitochondrial dysfunction in Alzheimer disease. *Oxid. Med. Cell Longev.* **2013**, *2013*, 1–13. [CrossRef]
85. Wang, X.; Wang, W.; Li, L.; Perry, G.; Lee, H.; Zhu, X. Oxidative stress and mitochondrial dysfunction in Alzheimer's disease. *Biochim. Biophys. Acta Mol. Basis Dis.* **2014**, *1842*, 1240–1247. [CrossRef] [PubMed]
86. Wang, X.; Su, B.; Siedlak, S.L.; Moreira, P.I.; Fujioka, H.; Wang, Y.; Casadesu, G.; Zhu, X. Amyloid- β overproduction causes abnormal mitochondrial dynamics via differential modulation of mitochondrial fission/fusion proteins. *Proc. Natl. Acad. Sci. USA* **2008**, *105*, 19318–19323. [CrossRef] [PubMed]
87. Eysert, F.; Kinoshita, P.F.; Mary, A.; Vaillant-Beuchot, L.; Checler, F.; Chami, M. Molecular dysfunctions of mitochondria-associated membranes (MAMs) in Alzheimer's disease. *Int. J. Mol. Sci.* **2020**, *21*, 9521. [CrossRef] [PubMed]
88. Muñoz, J.P.; Ivanova, S.; Sánchez-Wandelmer, J.; Martínez-Cristóbal, P.; Noguera, E.; Sancho, A.; Díaz-Ramos, A.; Hernández-Alvarez, M.I.; Sebastián, D.; Mauvezin, C.; et al. Mfn2 modulates the UPR and mitochondrial function via repression of PERK. *EMBO J.* **2013**, *32*, 2348–2361. [CrossRef] [PubMed]
89. Verfaillie, T.; Rubio, N.; Garg, A.D.; Bultynck, G.; Rizzuto, R.; Decuypere, J.-P.; Piette, J.; Linehan, C.; Gupta, S.; Samali, A.; et al. PERK is required at the ER-mitochondrial contact sites to convey apoptosis after ROS-based ER stress. *Cell Death Differ.* **2012**, *19*, 1880–1891. [CrossRef]
90. Carreras-Sureda, A.; Jaña, F.; Urra, H.; Durand, S.; Mortenson, D.E.; Sagredo, A.; Bustos, G.; Hazari, Y.; Ramos-Fernández, E.; Sassano, M.L.; et al. Non-canonical function of IRE1 α determines mitochondria-associated endoplasmic reticulum composition to control calcium transfer and bioenergetics. *Nat. Cell Biol.* **2019**, *21*, 755–767. [CrossRef]

91. Pająk, B.; Kania, E.; Orzechowski, A. Killing me softly: Connotations to unfolded protein response and oxidative stress in Alzheimer's disease. *Oxid. Med. Cell Longev.* **2016**, *2016*, 1–17. [CrossRef] [PubMed]
92. Li, G.; Mongillo, M.; Chin, K.-T.; Harding, H.; Ron, D.; Marks, A.R.; Tabas, I. Role of ERO1- α -mediated stimulation of inositol 1,4,5-triphosphate receptor activity in endoplasmic reticulum stress-induced apoptosis. *J. Cell Biol.* **2009**, *186*, 783–792. [CrossRef]
93. Olaisen, C.; Müller, R.; Nedal, A.; Otterlei, M. PCNA-interacting peptides reduce Akt phosphorylation and TLR-mediated cytokine secretion suggesting a role of PCNA in cellular signaling. *Cell Signal.* **2015**, *27*, 1478–1487. [CrossRef]
94. Frade, J.M.; López-Sánchez, N. A novel hypothesis for Alzheimer disease based on neuronal tetraploidy induced by p75 NTR. *Cell Cycle* **2010**, *9*, 1934–1941. [CrossRef]
95. Jensen, H.L.B.; Lillenes, M.S.; Rabano, A.; Günther, C.-C.; Riaz, T.; Kalayou, S.T.; Ulstein, I.D.; Bøhmer, T.; Tønjum, T. Expression of nucleotide excision repair in Alzheimer's disease is higher in brain tissue than in blood. *Neurosci. Lett.* **2018**, *672*, 53–58. [CrossRef]
96. Anandatheerthavarada, H.K.; Biswas, G.; Robin, M.-A.; Avadhani, N.G. Mitochondrial targeting and a novel transmembrane arrest of Alzheimer's amyloid precursor protein impairs mitochondrial function in neuronal cells. *J. Cell Biol.* **2003**, *161*, 41–54. [CrossRef]
97. Hansson Petersen, C.A.; Alikhani, N.; Behbahani, H.; Wiehager, B.; Pavlov, P.F.; Alafuzoff, I.; Leinonen, V.; Ito, A.; Winblad, B.; Glaser, E.; et al. The amyloid-peptide is imported into mitochondria via the TOM import machinery and localized to mitochondrial cristae. *Proc. Natl. Acad. Sci. USA* **2008**, *105*, 13145–13150. [CrossRef] [PubMed]
98. Devi, L.; Prabhu, B.M.; Galati, D.F.; Avadhani, N.G.; Anandatheerthavarada, H.K. Accumulation of amyloid precursor protein in the mitochondrial import channels of human Alzheimer's disease brain is associated with mitochondrial dysfunction. *J. Neurosci.* **2006**, *26*, 9057–9068. [CrossRef] [PubMed]
99. Lustbader, J.W.; Cirilli, M.; Lin, C.; Xu, H.W.; Takuma, K.; Wang, N.; Caspersen, C.; Chen, X.; Pollak, S.; Chaney, M.; et al. ABAD directly links Abeta to mitochondrial toxicity in Alzheimer's disease. *Science* **2004**, *304*, 448–452. [CrossRef] [PubMed]
100. Manczak, M.; Anekonda, T.S.; Henson, E.; Park, B.S.; Quinn, J.; Reddy, P.H. Mitochondria are a direct site of A beta accumulation in Alzheimer's disease neurons: Implications for free radical generation and oxidative damage in disease progression. *Hum. Mol. Genet.* **2006**, *15*, 1437–1449. [CrossRef] [PubMed]
101. Walls, K.C.; Coskun, P.; Gallegos-Perez, J.L.; Zadorian, N.; Freude, K.; Rasool, S.; Blurton-Jones, M.; Green, K.N.; LaFerla, F.M. Swedish Alzheimer mutation induces mitochondrial dysfunction mediated by HSP60 mislocalization of amyloid precursor protein (APP) and beta-amyloid. *J. Biol. Chem.* **2012**, *287*, 30317–30327. [CrossRef]
102. Pavlov, P.F.; Petersen, C.H.; Glaser, E.; Ankarcrana, M. Mitochondrial accumulation of APP and A β : Significance for Alzheimer disease pathogenesis. *J. Cell Mol. Med.* **2009**, *13*, 4137–4145. [CrossRef] [PubMed]
103. Simonovitch, S.; Schmukler, E.; Masliah, E.; Pinkas-Kramarski, R.; Michaelson, D.M. The effects of APOE4 on mitochondrial dynamics and proteins in vivo. *J. Alzheimer's Dis.* **2019**, *70*, 861–875. [CrossRef] [PubMed]
104. Beck, J.S.; Mufson, E.J.; Counts, S.E. Evidence for mitochondrial UPR gene activation in familial and sporadic Alzheimer's disease. *Curr. Alzheimer Res.* **2016**, *13*, 610–614. [CrossRef] [PubMed]



Article

Xenograft of Human Umbilical Mesenchymal Stem Cells Promotes Recovery from Chronic Ischemic Stroke in Rats

Yu-Show Fu ^{1,†}, Chang-Ching Yeh ^{2,3,4,†}, Pei-Ming Chu ⁵, Wen-Hsing Chang ⁶, Maan-Yuh Anya Lin ^{7,8,*} and Yung-Yang Lin ^{9,10,11,12,*}

¹ Department of Anatomy and Cell Biology, School of Medicine, National Yang Ming Chiao Tung University, Taipei 112304, Taiwan; ysfu@nycu.edu.tw

² Department of Obstetrics and Gynecology, Taipei Veterans General Hospital, Taipei 112201, Taiwan; ccye39@gmail.com

³ Department of Obstetrics and Gynecology, National Yang Ming Chiao Tung University, Taipei 112304, Taiwan

⁴ Department of Nurse-Midwifery and Women Health, National Taipei University of Nursing and Health Sciences, Taipei 112303, Taiwan

⁵ Department of Anatomy, School of Medicine, China Medical University, Taichung 404328, Taiwan; pmchu@mail.cmu.edu.tw

⁶ Institute of Anatomy and Cell Biology, School of Medicine, National Yang Ming Chiao Tung University, Taipei 112304, Taiwan; katteken@gmail.com

⁷ Department of Medical Research, Taipei Veterans General Hospital, Taipei 112201, Taiwan

⁸ Department of Pharmacy, National Yang Ming Chiao Tung University, Taipei 112304, Taiwan

⁹ Neurological Institute, Taipei Veterans General Hospital, Taipei 112201, Taiwan

¹⁰ Department of Critical Care Medicine, Taipei Veterans General Hospital, Taipei 112201, Taiwan

¹¹ Institute of Brain Science, National Yang Ming Chiao Tung University, Taipei 112304, Taiwan

¹² Institute of Clinical Medicine, National Yang Ming Chiao Tung University, Taipei 112304, Taiwan

* Correspondence: myalin@nycu.edu.tw (M.-Y.A.L.); yylin@vghtpe.gov.tw (Y.-Y.L.)

† These authors contributed equally to this work.

Citation: Fu, Y.-S.; Yeh, C.-C.; Chu, P.-M.; Chang, W.-H.; Lin, M.-Y.A.; Lin, Y.-Y. Xenograft of Human Umbilical Mesenchymal Stem Cells Promotes Recovery from Chronic Ischemic Stroke in Rats. *Int. J. Mol. Sci.* **2022**, *23*, 3149. <https://doi.org/10.3390/ijms23063149>

Academic Editors: Masaru Tanaka and Lydia Giménez-Llort

Received: 22 February 2022

Accepted: 11 March 2022

Published: 15 March 2022

Publisher's Note: MDPI stays neutral with regard to jurisdictional claims in published maps and institutional affiliations.



Copyright: © 2022 by the authors. Licensee MDPI, Basel, Switzerland. This article is an open access article distributed under the terms and conditions of the Creative Commons Attribution (CC BY) license (<https://creativecommons.org/licenses/by/4.0/>).

Abstract: Stroke is a leading cause of adult disability. In our previous study, transplantation of human umbilical mesenchymal stem cells (HUMSCs) in Wharton's jelly in the acute phase of ischemic stroke promotes recovery in rats. Unfortunately, there is no cure for chronic stroke. Patients with chronic stroke can only be treated with rehabilitation or supportive interventions. This study aimed to investigate the potential of xenograft of HUMSCs for treating chronic stroke in rats. Rats were subjected to 90 min middle cerebral artery occlusion and then reperfusion to mimic ischemic cerebral stroke. On day 14 following stroke, HUMSCs were transplanted into the damaged cerebral cortex. The motor function in rats of the Stroke + HUMSCs group exhibited significant improvement compared to that of the Stroke + Saline group, and the trend persisted until day 56 post stroke. The cerebral cortex changes were tracked using magnetic resonance imaging, showing that cerebral atrophy was found starting on day 7 and was reduced significantly in rats receiving HUMSCs compared to that in the Stroke + Saline group from day 21 to day 56. HUMSCs were found to be existed in the rats' cerebral cortex on day 56, with signs of migration. The grafted HUMSCs did not differentiate into neurons or astrocytes and may release cytokines to improve neuroprotection, decrease inflammation and increase angiogenesis. Our results demonstrate that xeno-transplantation of HUMSCs has therapeutic benefits for chronic ischemic stroke. Most importantly, patients do not need to use their own HUMSCs, which is a gospel thing for clinical patients.

Keywords: chronic stroke; cerebral ischemia; umbilical mesenchymal stem cells; Wharton's jelly; xenograft; transplantation; neuroprotection; angiogenesis; neurologic deficit; MRI

1. Introduction

Stroke is among the leading causes of death and disability in adults [1]. In 2019, over 10 million new cases are reported globally, and over 6 million died due to cerebral stroke [2].

Ischemic stroke incidents comprise nearly 90% of all strokes [1]. The mean survival post stroke is 6 to 7 years, and indeed more than 85% of patients live past the first year post stroke, many with years of enduring disability and neuropsychiatric syndrome [3–6]. Once entering the chronic stage of stroke, the patient's welfare is affected, and significant family and societal burdens are experienced. To date, there are no effective drugs or therapies available for the treatment of chronic stroke; treatment mainly relies on rehabilitation or supportive treatments to prevent extensive tissue loss and further degeneration. Therefore, it is particularly important to identify a new approach in treating chronic ischemic stroke.

Mesenchymal stem cells (MSCs) are among the leading restorative therapy candidates [7,8]. As a part of medical waste after delivery, the umbilical cord can be more easily retrieved than embryos or bone marrow. Based on our previous studies, transplantations of umbilical mesenchymal stem cells in the Wharton's jelly (HUMSCs) into the striatum, spinal cord, cerebral cortex, hippocampus, and cerebellum can effectively treat Parkinson's disease, [9,10] spinal cord injury [11], acute stroke [12], epilepsy [13], and cerebellum atrophy [14]. In addition to central nervous system diseases, we have investigated the feasibility of the HUMSCs transplantation for the treatment of liver fibrosis, peritoneum fibrosis, pulmonary fibrosis, osteoporosis, and diabetes [15–21]. The results demonstrated that xenograft of the HUMSCs did not cause immune reaction or rejection in the host. Therefore, we believe that HUMSCs can be used as transplantation materials for clinical medicine.

In our previously published results, we performed ligation of the middle cerebral artery for 90 min and reperfusion in rats in order to trace the changes in the cerebral cortex with continuous MRI imaging. Severe edema was observed in the cerebral cortex on day 1 to day 2 post stroke. The cerebral cortex exhibits severe atrophy on day 14 post stroke. Therefore, we suspected that it had entered chronic stroke on day 14 after surgery-induced cerebral ischemia and reperfusion. Furthermore, at 24 h post stroke, i.e., the acute stage of stroke, transplantation of HUMSCs into the rat's infarcted region of the cerebral cortex significantly alleviated the level of atrophy in the injured brain region and improved its mobility. The results suggested that HUMSCs transplantation can be applied for the treatment of acute stroke [12]. Currently, there is no cure for chronic stroke. However, on day 14 post stroke, i.e., the chronic stage of stroke, signs of atrophy were already displayed in the cerebral cortex. Whether HUMSCs transplantation performed on day 14 post stroke could still exhibit the treatment effect needs to be further elucidated in this study.

2. Results

2.1. Ischemia–Reperfusion Surgery Causes Cortical Infarction

As shown by MRI images, TTC staining, and Cresyl violet staining, the infarcted cortex of the rats in the Stroke + Saline group were considerably swollen and edematous 1 day post stroke. These images indicated that an ischemia–reperfusion stroke model was successfully established in our experiments (Figure 1B).

2.2. HUMSCs Transplantation Improves Motor Function in Rats with Chronic Stroke

The results of the rotarod test showed that administration of saline, or HUMSCs in the rats' right cortices of the Normal + Saline and Normal + HUMSCs groups caused only a minor change in retention time, without statistical significance. The retention time was significantly reduced to 21–23% of the normal level in the Stroke + Saline and Stroke + HUMSCs groups 1 day post stroke, indicating the mobility was impaired by cerebral ischemia. The situation persisted until day 14 post stroke. On day 21 post stroke, the Stroke + Saline group had a retention time of 27% of the normal level, and the declining trend remained until day 56 post stroke without showing any improvement. On day 7 after stem cell transplantation, i.e., day 21 post stroke, the retention time of the Stroke + HUMSCs group increased to 49%, a significant elevation compared to that in the Stroke + Saline group. The statistical trend sustained until day 56 post stroke. Although the retention time in the Stroke + HUMSCs group increased (from day 21 to day 42), it was not as long as the

time obtained in those of the groups of Normal + Saline and Normal + HUMSCs ($p < 0.05$) (Figure 1C and Supplemental Table S1).

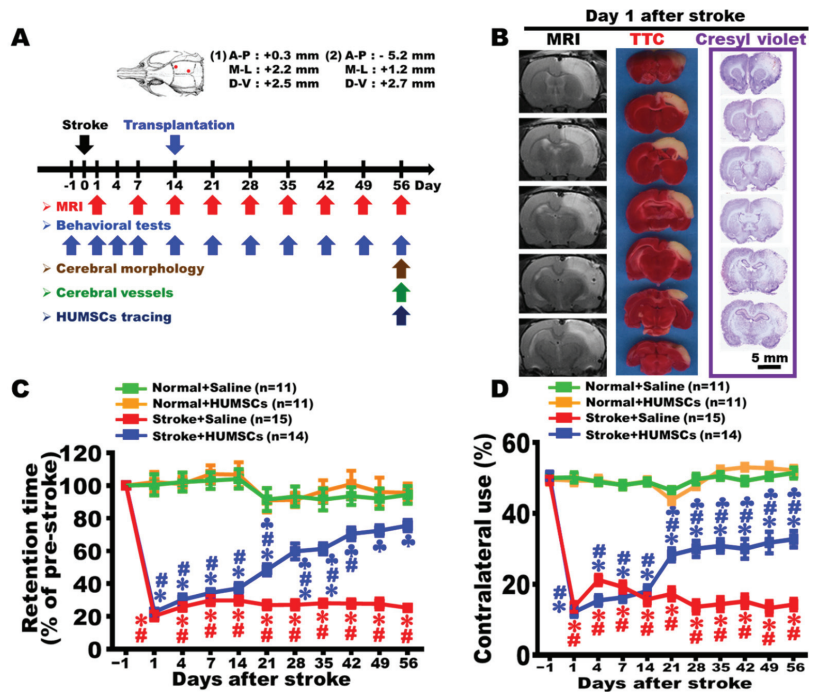


Figure 1. HUMSCs transplantation enhanced motor function in rats with chronic stroke. (A) The diagram shows the time course for various experiments in this study. Representative MRI, TTC-stained, and cresyl violet stained images of rat brains are shown on day 1 after stroke, showing that right cerebral cortices were markedly enlarged (B). The Stroke + HUMSCs group show better functional recovery in the rotarod test (C) and cylinder test (D) than the Stroke + Saline group. Normal + Saline $n = 11$, Normal + HUMSCs $n = 11$, Stroke + Saline $n = 15$, Stroke + HUMSCs $n = 14$. *, vs. the Normal + Saline group at the same day, $p < 0.05$. #, vs. the Normal + HUMSCs group at the same day, $p < 0.05$. ♣, vs. the Stroke + Saline group at the same day, $p < 0.05$.

The quantitative results of the cylinder test showed that the contralateral use of forelimb of the four groups were approximately 50% prior to the surgery, i.e., under normal situation. In the Normal + Saline and Normal + HUMSCs groups, even with injections of saline or HUMSCs into the right cerebral cortex on day 14, contralateral use of forelimb did not statistically change and maintain until day 56 (Figure 1D and Supplemental Table S2).

On day 1 post stroke, the left forelimb activity was substantially reduced compared to pre-stroke, with a percentage of 12–14%, indicating that stroke caused impaired left forelimb activity. The situation remained until day 14 post stroke. On day 21 post stroke, left forelimb use in the Stroke + Saline group was around 17%, which was significantly lower than those of Normal + Saline and Normal + HUMSCs groups. The activity was not improved but sustained until day 56 post stroke ($p < 0.05$) (Figure 1D and Supplemental Table S2). In the Stroke + HUMSCs group, the contralateral use elevated to $28.29 \pm 1.84\%$ on day 7 after transplantation (i.e., day 21 post stroke), which was a significant increase compared to that in the Stroke + Saline group, but was statistically reduced compared to those in Normal + Saline and Normal + HUMSCs groups. The trend remained until day 56 post stroke ($p < 0.05$) (Figure 1D, Supplemental Table S2 and Supplemental Videos S1–S3).

2.3. HUMSCs Transplantation Reduces Brain Atrophy in Rats with Chronic Stroke as Assessed by MRI

The alterations in the infarcted cerebral cortex at different time points were observed using MRI. The results showed that injections of saline, or HUMSCs in the rats' right cortices of the Normal + Saline and Normal + HUMSCs groups did not caused any significant edema or atrophy. The trend remained until day 56 (Figure 2A,B,E,F, and Supplemental Tables S3 and S4).

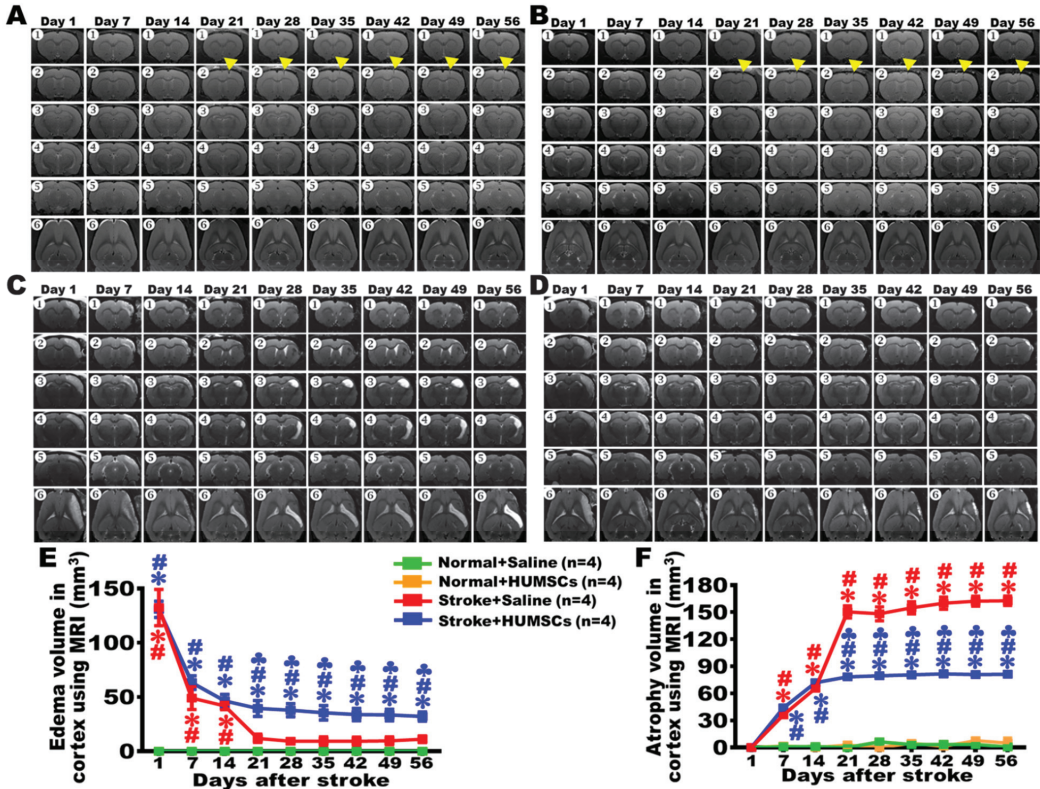


Figure 2. Cortical edema and atrophy examined by MRI. Brain MRI examination was conducted on day 1 (①–⑥), day 7 (①–⑥), day 14 (①–⑥), day 21 (①–⑥), day 28 (①–⑥), day 35 (①–⑥), day 42 (①–⑥), day 49 (①–⑥), and day 56 (①–⑥). Along the rostral–caudal orientation, coronal slices (①–⑤) and horizontal slices (⑥) were taken for monitoring the alterations of brain damages in these rats. MRI slices of the Normal + Saline (A) and Normal + HUMSCs (B) groups did not find significant edema or atrophy areas from day 1 to day 56. MRI slices of the Stroke + Saline group (C) and the Stroke + HUMSCs group (D) were obtained on day 1 post stroke. White areas in the right cerebral cortex were seen, indicating severe inflammation and edema occurred in this region (①–⑥). On day 7 and day 14, there was a reduction in the white edema cortices, but slight atrophy had appeared in the right infarcted area when comparing to the left cerebral cortex (①–⑥). The volumes of edema (E) and atrophy (F) in the right cerebral cortex were quantified post stroke. Atrophy of the infarcted cortex becomes apparent in the Stroke + Saline group but is significantly less severe in the Stroke + HUMSCs group from day 21 to day 56. The results of brain MRI revealed that HUMSCs transplantation alleviated cerebral atrophy in rats with chronic stroke. Normal + Saline $n = 4$, Normal + HUMSCs $n = 4$, Stroke + Saline $n = 4$, Stroke + HUMSCs $n = 4$. *, vs. the Normal + Saline group at the same day, $p < 0.05$. #, vs. the Normal + HUMSCs group at the same day, $p < 0.05$. ♣, vs. the Stroke + Saline group at the same day, $p < 0.05$. ▼ indicates the first injection site.

The Stroke + Saline group displayed a significant white area, suggesting that severe inflammation and edema were present in the cerebral cortex on day 1. The volume of the cortical edema decreased on day 7 and day 14. Since day 21, edema of the injured cerebral cortex markedly reduced, the situation remained until day 56 post stroke. The injured cerebral cortex of the Stroke + Saline group began showing signs of atrophy on day 7 post stroke. From day 21 onwards, the volume of atrophy further increased; the trend sustained until day 56 (Figure 2C,E,F and Supplemental Tables S3 and S4). We postulate that edema areas switched into atrophy areas without treatment; edema areas of the injured cerebral cortex markedly reduced at day 21, at the same time, atrophy area in the Stroke + Saline group was increased. It is worthy of attention that the right lateral ventricle significantly enlarged and showed signs of edema from day 21 to day 56 in the Stroke + Saline group.

The Stroke + HUMSCs group had similar patterns of cerebral cortex edema with the Stroke + Saline group from day 1 to day 14 post stroke. On day 7 after transplantation (day 21 post stroke), the volume of edema and atrophy in the cerebral cortex showed no significant changes compared with those in day 14. However, there was a statistical difference when comparing to that in the Stroke + Saline group at the same time point; the trend remained until day 56. The edema of the right lateral ventricular was also milder than that in the Stroke + Saline group (Figure 2D–F and Supplemental Tables S3 and S4). These results demonstrate that HUMSCs transplantation has a protective role in preventing the infarct cortex from atrophy post stroke.

2.4. HUMSCs Transplantation Preserves Cerebral Cortex in Rats with Chronic Stroke

We likewise used gross appearance and brain sections with cresyl violet staining to determine the therapeutic effect of HUMSCs on the infarct cortex of chronic stroke. On day 56 post stroke, the brains were intact and smooth in the Normal + Saline and Normal + HUMSCs groups. The gross appearance of the Stroke + Saline group had a marked indentation at the right cerebral cortex with extensive cortex atrophy. Although the HUMSCs group had an apparent shrinkage at the right infarcted cerebral cortex, it was less severe than that in the Stroke + Saline group (Figure 3A).

On day 56, cresyl violet staining showed that both of the right and left cerebral cortices were intact in the Normal + Saline and Normal + HUMSCs groups. From the coronal brain sections of the Stroke + Saline group, not only the cerebral cortex had severe atrophy, but the corpus callosum, basal ganglia, and hippocampus also showed signs of atrophy. In addition, brain sections showed an enlarged right lateral ventricle on day 56 post stroke. Although the coronal cerebral sections of the Stroke + HUMSCs group also showed signs of atrophy, these signs were primarily restricted to the regions of the cerebral cortex (Figure 3B). By summing all quantitative data from serial brain sections stained by cresyl violet, it showed that the volume of right cerebral cortex was similar to that of left cerebral cortex in the Normal + Saline and Normal + HUMSCs groups. The overall volumes of right cerebral atrophy were $133.88 \pm 3.90 \text{ mm}^3$ and $89.69 \pm 3.72 \text{ mm}^3$ in the Stroke + Saline and Stroke + HUMSCs groups, respectively. Moreover, the volume of cerebral atrophy in the Stroke + HUMSCs group was also remarkably lower than that in the Stroke + Saline group ($p < 0.05$) (Figure 3C and Supplemental Table S5).

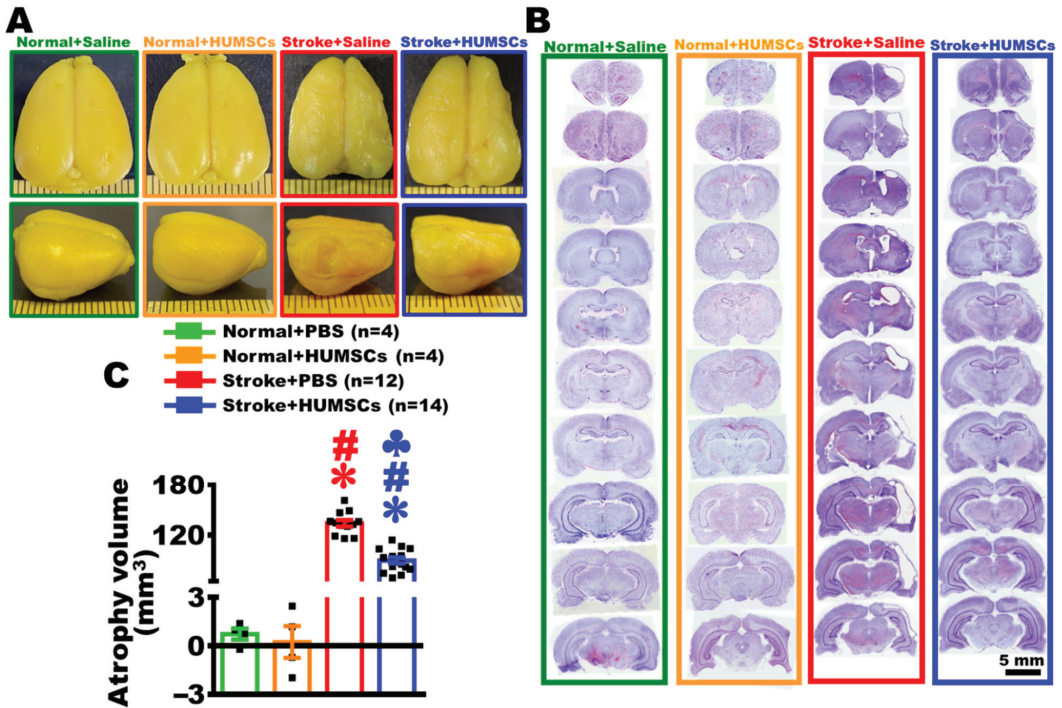


Figure 3. HUMSCs transplantation preserved the cerebral cortex in rats with chronic stroke. On day 56 post stroke, the brains fixed with paraformaldehyde were photographed from a superior (top panel) and a lateral view (bottom panel). The brain of the Stroke + Saline group exhibited more severe atrophy in the cortex than that grafted with HUMSCs (A). Subsequently, the brains of four groups were subjected to serial coronal sections (from bregma +2.52 mm to −5.76 mm) and stained with cresyl violet to observe alterations in the cerebral cortex. The results showed that the brain grafted with HUMSCs had more preserved cortices (B). The volume of atrophy in the infarcted cortex was quantified using the sections stained by cresyl violet, the result indicated the atrophy volume of the Stroke + HUMSCs group was substantially lower than that of the Stroke + Saline group (C). Normal + Saline $n = 4$, Normal + HUMSCs $n = 4$, Stroke + Saline $n = 12$, Stroke + HUMSCs $n = 14$. *, vs. the Normal + Saline group, $p < 0.05$. #, vs. the Normal + HUMSCs group, $p < 0.05$. ♣, vs. the Stroke + Saline group, $p < 0.05$. ■ is the value of individual experiment.

2.5. HUMSCs Transplantation Helps Neuronal Cell Survival in the Infarcted Brain in Rats with Chronic Stroke

On day 56 post stroke, coronal brain sections were subjected to anti-NeuN immunohistochemical staining to observe the alterations of neuronal cells localized at the peripheral regions of the infarcted areas in the cerebral cortex and striatum. The results found that the neuronal cells in the cerebral cortex and striatum exhibited relatively healthy morphology in the Normal + Saline and Normal + HUMSCs groups (Figure 4A(A1–A4) and Figure 4B(B1–B4)). Even with injections of saline or HUMSCs into the right cerebral cortex, the neuronal number in the right cerebral cortex or striatum was not statistically different from that of the contralateral regions in the Normal + Saline and Normal + HUMSCs groups (Figure 4E,F and Supplemental Table S6).

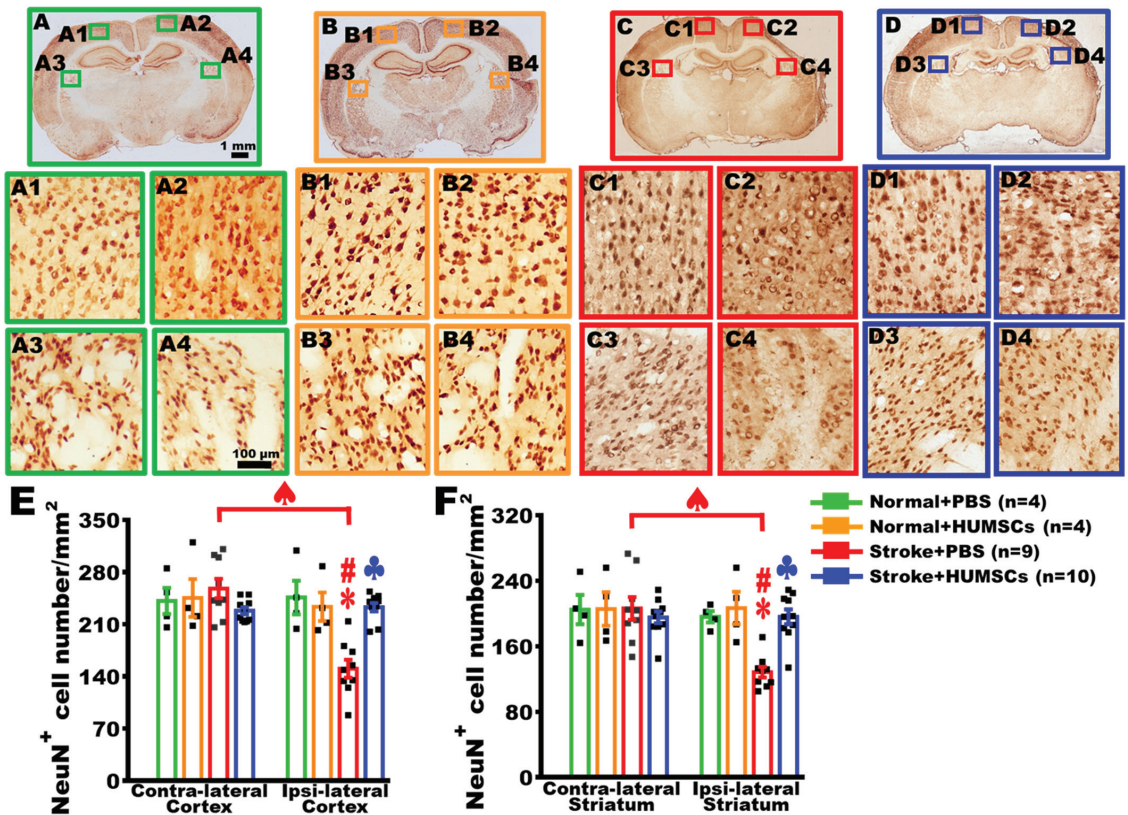


Figure 4. HUMSCs transplantation increased the survival of neuronal cells in the infarcted brain in rats with chronic stroke. On day 56 post stroke, anti-NeuN immunohistochemical staining was applied to observe the number of survived neuronal cells. Brain coronal sections at bregma -1.92 mm are displayed ((A): Normal + Saline group; (B): Normal + HUMSCs group; (C): Stroke + Saline group; (D): Stroke + HUMSCs group). For high magnification, the peripheral region to the infarcted cerebral cortex (A2,B2,C2,D2) or striatum (A4,B4,C4,D4) are shown, as well as undamaged contralateral sides of the cerebral cortex (A1,B1,C1,D1) and striatum (A3,B3,C3,D3). The number of NeuN⁺ cells in the cerebral cortex (E) and striatum (F) was quantified. The results showed that the neuronal cell numbers in the cerebral cortex and striatum peripheral to the damaged brain areas were significantly higher in the Stroke + HUMSCs group than those in the Stroke + Saline group. Normal + Saline $n = 4$, Normal + HUMSCs $n = 4$, Stroke + Saline $n = 9$, Stroke + HUMSCs $n = 10$. *, vs. the ipsilateral region of Normal + Saline group, $p < 0.05$. #, vs. ipsilateral region of the Normal + HUMSCs group, $p < 0.05$. ♣, vs. ipsilateral region of the Stroke + Saline group, $p < 0.05$. ♠, contra-lateral vs. ipsilateral region in the Stroke + Saline group, $p < 0.05$. ■ is the value of individual experiment.

The results showed that the neuronal cells in the cerebral cortex and striatum surrounding the infarcted region exhibited a lighter and relatively loose staining in the Stroke + Saline group (Figure 4C,(C1–C4)). The neuronal number in the infarction cerebral cortex (ipsilateral cortex) of the Stroke + Saline group was significantly lower than those in the Normal + Saline and Normal + HUMSCs groups. Additionally, the number of neuronal cells in the cerebral cortex surrounding the infarcted region was significantly lower than the normal contralateral location ($p < 0.05$). Similarly, the number of neuronal cells in the damaged striatum also statistically decreased when comparing to the normal contralateral side of the brain ($p < 0.05$) (Figure 4E,F and Supplemental Table S6).

In the cerebral cortex and striatum surrounding the infarcted area of the Stroke + HUMSCs group, the numbers of neuronal cells were preserved at a higher level when comparing to those in the ipsilateral regions of Stroke + Saline group ($p < 0.05$). Furthermore, no statistical differences were found in the number of neuronal cells when comparing to the contralateral cerebral cortex and striatum ($p > 0.05$) (Figure 4D(D1–D4),E,F and Supplemental Table S6).

2.6. HUMSCs Transplantation Promotes Angiogenesis in the Infarcted Brain in Rats with Chronic Stroke

On day 56 post stroke, the brains of each group were freshly obtained to observe the distribution of superficial blood vessels of the brain. The qualitative observations showed that the blood vessels with small size were apparent in the Normal + Saline and Normal + HUMSCs groups. In the Stroke + Saline group, the right hemisphere markedly shrunk, with fewer blood vessels found on the surface of the injured cerebral cortex. The vessels with small diameter were observed in the Stroke + HUMSCs group (Figure 5A).

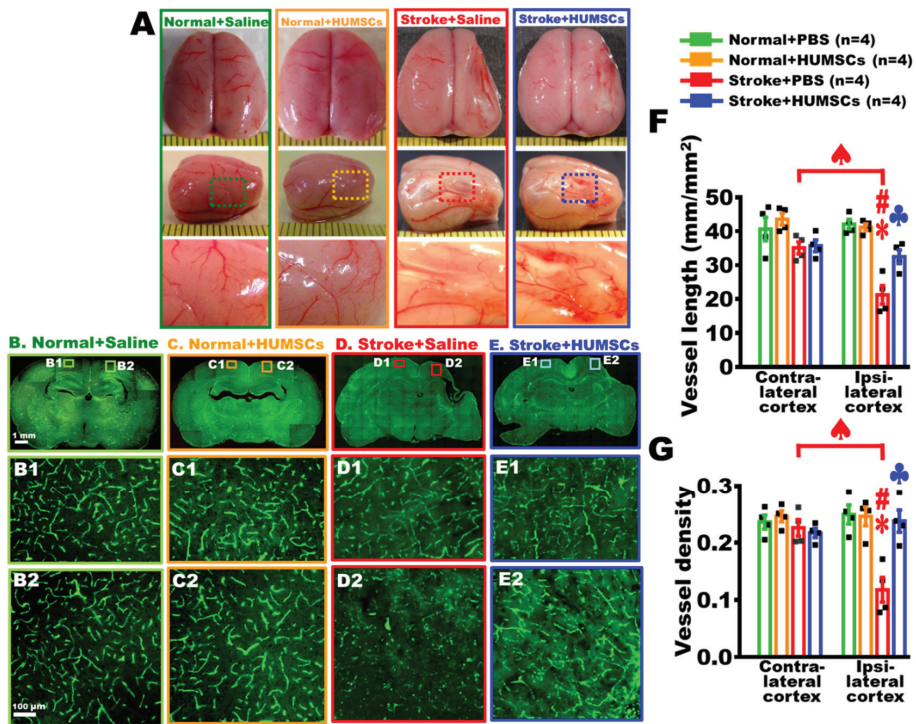


Figure 5. HUMSCs transplantation promoted angiogenesis in the infarcted brain of the rats with chronic stroke. On day 56 post stroke, the brains were photographed from a superior view (top panel) and a lateral view (intermediate panel and high magnification in the bottom panel) to observe the distribution of superficial blood vessels of the cerebral cortex. More blood vessels are observed on the surface of the Stroke + HUMSCs group (A). From coronal brain sections at bregma -2.4 mm, vessels in the contralateral cortex (B1,C1,D1,E1) and ipsilateral cortex (B2,C2,D2,E2) are visualized by fluorescein isothiocyanate-conjugated dextran amine. Boxed areas in the photographs are magnified in the bottom row (B1,B2,C1,C2,D1,D2,E1,E2). The total vessel length per mm² (F) and vessel density (G) in the infarcted region are significantly greater in the cortex of the Stroke + HUMSCs group than those in the Stroke + Saline group. Normal + Saline $n = 4$, Normal + HUMSCs $n = 4$, Stroke + Saline $n = 4$, Stroke + HUMSCs $n = 4$. *, vs. ipsilateral cortex of the Normal + Saline group, $p < 0.05$.

#, vs. ipsilateral cortex of the Normal + HUMSCs group, $p < 0.05$. ♣, vs. ipsilateral cortex of the Stroke + Saline group, $p < 0.05$. ♠, contra-lateral vs. ipsi-lateral cortex in the Stroke + Saline group, $p < 0.05$. ■ is the value of individual experiment.

Additionally, brain sections with perfused by FITC-dextran to quantify vascular distribution near the infarction area. The results showed that blood vessels had a regular reticular pattern in both the right and left cerebral cortices of the Normal + Saline and Normal + HUMSCs groups, as well as in the normal left cerebral cortices of the Stroke + Saline and Stroke + HUMSCs groups (Figure 5B(B1,B2),C(C1,C2),D(D1),E(E1)). The quantitative results indicated that the total vessel lengths were around 43.56 ± 1.73 to 35.09 ± 1.78 mm/per mm², and the vessel density was between 0.25 ± 0.01 to 0.22 ± 0.0 in the normal cerebral cortices of Normal + Saline, Normal + HUMSCs, Stroke + Saline and Stroke + HUMSCs groups (Figure 5F,G and Supplemental Table S7).

In the brain area surrounding the right damaged cerebral cortex of the Stroke + Saline group, the reticular distribution of the brain vessels displayed a destructed pattern, with the total vessel length significantly shortened to 21.25 ± 2.79 mm/per mm² and the vessel density markedly reduced to 0.12 ± 0.02 , which were significantly lower than the normal left contralateral side (Figure 5(D2),F,G and Supplemental Table S7). In the Stroke + HUMSCs group, the number of vessels in the brain area surrounding the right damaged cerebral cortex was higher than that in the Stroke + Saline group, although not as regular or reticular as under normal conditions. There were also many small, thin blood vessels shown (Figure 5(E2),F,G and Supplemental Table S7). The quantitative results showed that the total vessel length and density in the peripheral region surrounding the right damaged cerebral cortex in the Stroke + HUMSCs group were both statistically increased when comparing to those in the corresponding region of the Stroke + Saline group ($p < 0.05$). Furthermore, the total vessel length and density in the ipsilateral cortex of the Stroke + HUMSCs group were similar to those in the Normal + Saline and Normal + HUMSCs groups (Figure 5F,G and Supplemental Table S7). It indicated that HUMSCs may promote angiogenesis in the ischemic cortex of the chronic stroke.

2.7. Engrafted HUMSCs Survive and Migrate in the Infarcted Cortex of Rats with Chronic Stroke

The nucleus of HUMSCs was labeled with bisBenzimide to track their survival and distribution. On day 56, the fluorescence imaging showed that plenty of blue clusters of cells were found at bregma +0.3 mm, i.e., the first site for HUMSCs transplantation, in the Stroke + HUMSCs group. From bregma +0.6 mm to +0.1 mm, there were still many cells in blue fluorescence identified (Figure 6A). At the second transplantation site (bregma −5.2 mm) of the Stroke + HUMSCs group, large clusters of cells could also be found. Similarly, HUMSCs existed in clusters from bregma −4.9 mm to bregma −5.5 mm (Figure 6B).

Anti-human-specific nuclei antigen immunohistochemical staining was further employed to investigate HUMSCs distribution in rats with chronic stroke. The results showed that large clusters of HUMSCs were seen at the first and secondary stem cell transplantation sites of the cerebral cortex in the Stroke + HUMSCs group (at bregma +0.3 mm and −5.2 mm). The number of HUMSCs gradually decreased as the distance away from the implanted sites increased rostrally or caudally (Figure 6C,D). No signal was detected in the cerebral cortex of the Stroke + Saline group (data not shown).

2.8. HUMSCs Does Not Differentiate into Neurons and Astrocytes in Rats with Chronic Stroke

On day 56 post stroke, rat brains were freshly obtained and examined using human NeuN and GFAP primers to elucidate whether the HUMSCs grafted had differentiated into neuronal cells or astrocytes in the cerebral cortex of rats with chronic stroke. The results showed that genes of human NeuN or GFAP were not detected in the cerebral cortex of the Stroke + HUMSCs group, indicating HUMSCs may not have differentiated into neuronal cells or astrocytes. Human glioma cells served as a positive control for human NeuN or human GFAP (Figure 6E).

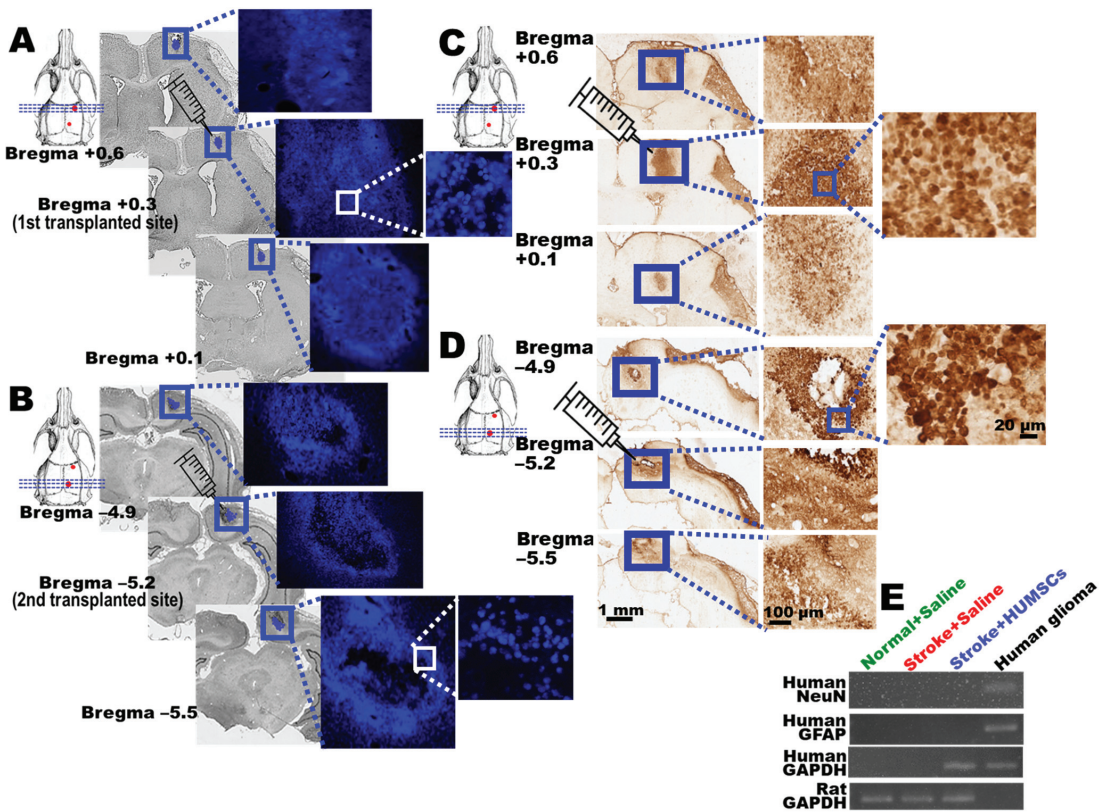


Figure 6. Grafted HUMSCs survived in the infarcted cortex and did not differentiate into neuronal cells or astrocytes. The nucleus of HUMSCs was labeled with bisBenzimide (blue), and the cells were transplanted into the rat’s right cerebral cortex on day 14 post stroke. On day 56, phase-contrast microscopy images of the HUMSCs group are displayed with the section at the first HUMSCs transplantation position of bregma +0.3 mm and its anterior (+0.6 mm) and posterior coronal sections (+0.1 mm). The blue clusters of cells were observed at high magnification (A). The second HUMSCs transplantation position at bregma −5.2 mm and its anterior (bregma −4.9 mm) and posterior (bregma −5.5 mm) coronal brain sections are shown. At high magnification, clusters of cells labeled with bisBenzimide were found (B). Immunostaining for human-specific nucleus antigen demonstrates the aggregation of HUMSCs around the first (C) and secondary (D) transplantation sites at 56 days post stroke. The boxed areas in the left column are magnified in the right column. On day 56 post stroke, the cerebral cortex was subjected to RT-PCR tests to examine whether human NeuN or GFAP could be detected in all the groups. The results showed that the transplanted HUMSCs did not differentiate into neuronal cells or astrocytes (E).

3. Discussion

In the present study, on day 14 post stroke, when significant atrophy was identified in the injured brain region of the SD rats (i.e., the chronic stage of stroke), the infarcted brain tissues were obviously preserved, and the mobility was markedly improved following transplantations of HUMSCs.

The questions about the intervention timing, cell dosage, and route of administration for stem cell therapy on stroke have been in heated discussions [22–26]. HUMSCs (3×10^5 – 1×10^7) were intravenously injected into rats on days 1, 7, 30, and 90 post stroke, and the brain tissue sections were examined on day 140. The results showed that there was

no statistical difference between all the treatment groups and the control group in terms of the cerebral injury volume. However, for the group transplanted with $\geq 3 \times 10^6$ HUMSCs, though the macroscopic morphology of the cerebral cortex did not exhibit a significant change, the mobility was significantly improved compared to that in the control group, suggesting that the amount of HUMSCs transplanted played a crucial role [27]. Another study also evaluated the beneficial treatment effects of 3×10^7 bone marrow mononuclear cells (BMMCs) that were injected via the jugular vein of the rats on days 1, 7, 14, or 30 post stroke. The results showed that the groups transplanted with BMMCs on days 14 or 30 exhibited similar behaviors to that of the control group, suggesting that transplantation performed during the acute phase was superior to the chronic phase [22]. Ishizaka et al. transplanted bone marrow-derived mesenchymal stem cells (BMMSCs) into rats via the internal carotid artery on 1, 4, or 7 days post stroke. The results showed that for the group receiving transplantation on day 7, only a few BMMSCs were found distributed over the brain, and therefore no apparent sensorimotor function recovery was observed in the rats. The results indicated that the reservation of the cerebral cortex was much better compared to that in the control group only in the group receiving transplantation on day 1 [24]. Although the origins of stem cells varied, their results indicated that stem cell transplantation in the acute phase of stroke can reduce neurological deficits and improve functional recovery [12,28–35]. In fact, although some cerebral ischemia patients really survived, they struggled with the impasse of chronic stroke. Currently, there is no cure for chronic stroke. Therefore, it is a therapeutic imperative to find the treatment for chronic stroke.

Given the aforementioned study results, we suspected the number of the survived stem cells in the infarcted brain region plays a critical role in recovery. At the chronic stage of stroke, we suggest that the types or the concentration of the chemotactic factors attracting the stem cells circulating in the blood to the infarcted brain region have relatively decreased or recessed compared to those at the acute stroke stage. Therefore, to treat chronic stroke, direct intra-cerebral transplantation of the stem cells into the brain infarction region might be a more effective treatment approach. The present study's results also demonstrated that a large number of the transplanted HUMSCs survived in the rats' cerebral cortex until day 56 post stroke. However, intra-cerebral implantation is an invasive method which is never recommended to be used in clinical medicine. Therefore, the route of stem cell transplantation may be modified, such as applying stem cells on the surface of the cerebral cortex.

Although the stem cells' types might be different, the treatment mechanisms can be generally categorized into two directions. First, the transplanted stem cells differentiate into neuronal cells to replace the injured or dead neurons [36–38]. Secondly, the transplanted stem cells alter the injured environment via the cytokines secreted. The secreted cytokines might possess the effects of neuroprotection [12,39–41], neuroregeneration [42,43], angiogenesis [12,41–44], or immunomodulation [39,45–47], and thereby repair the damaged tissues or prevent them from further deterioration. From the RT-PCR results of our study, it is suggested that HUMSCs did not directly differentiate into neurons or astrocytes after transplantation into the infarcted cortex of the chronic stroke rats. We suggested that implanted HUMSCs may secrete cytokines to improve neuronal survival, increase angiogenesis and enhance functional recovery. Interestingly, HUMSCs may release different cytokines in response to the pathophysiological microenvironments accordingly [11–15,17]. As demonstrated in our previous study, implanted HUMSCs did not differentiate into neurons but released neuroprotective and growth-associated cytokines, including neutrophil-activating protein-2 (NAP-2), angiopoietin-2, brain-derived neurotrophic factor, CXCL-16, and platelet-derived growth factor-AA in the infarcted cortex of acute ischemia stroke [12]. Instead of differentiating into neurons, astrocytes, or oligodendrocytes, transplanted HUMSCs released neurotrophin-3, NAP-2, basic fibroblast growth factor, glucocorticoid-induced tumor necrosis factor receptor family, and vascular endothelial growth factor receptor-3 in the transected spinal cord [11]. Implanted HUMSCs survived in the epileptic hippocampus and released FGF-6, amphiregulin, glucocorticoid-induced tumor necrosis factors receptor

(GITR), MIP-3 β , and osteoprotegerin [13]. At the same time, human IL-13, GIF, PAI-1, FGF-2, and CXCL-4 were significantly increased in the cerebella of SCA1 mice [14]. Furthermore, without differentiating into alveolar epithelial cells or hepatocytes, HUMSCs grafted into rat fibrotic lung and liver release a considerable amount of human FGF-6 and IGF-1 in lung and human prolactin, leukemia inhibitory factor, and cutaneous T cell-attracting chemokine in livers [15,17].

The therapeutic effect of stem cell species on stroke have also been investigated. Yu et al. administered both auto-adipose derived mesenchymal stem cell (auto-ADMSCs) and allo-ADMSCs in an experimental animal model of stroke to compare their effectiveness. Their results demonstrated that auto-ADMSCs were more effective than allo-ADMSCs to promote recovery and reduce the infarct volume of stroke rats. The improved effects of auto-ADMSCs are likely related to decreased immunological responses, which thereby result in higher survival rates, longer survival times, a wider migratory space, and a lower amount of apoptosis [48]. However, divergent opinions have been raised. Gutiérrez-Fernández et al. suggested that human AD-MSCs and rat AD-MSCs showed equal efficacy in terms of functional recovery and decreased ischemic brain damage in rat [49]. Similarly, autologous and allogeneic cell therapy for ischemic heart disease show a similar improvement in left ventricular ejection fraction in large animal models of myocardial ischemia [50]. HUMSCs were used in this study. The HUMSCs are collected from the umbilical cord, which is generally considered to be a waste after childbirth and can be obtained without invasive techniques. The amount of HUMSCs collected can be amplified greatly in cultures. Moreover, xeno-transplanted HUMSCs are immunologically compatible in recipients [9–20]. Therefore, HUMSCs can serve as an excellent stem cell source for treatment of the chronic stroke in clinical medicine.

In this study, our results showed that on day 56 post stroke, HUMSCs transplanted into the cerebral cortex did not differentiate into neuronal cells or astrocytes. It also showed that an increased number of neuronal cells was preserved, angiogenesis was facilitated, and animal behavior was promoted; therefore, we suggest that the HUMSCs ameliorated and treated chronic stroke by secreting cytokines.

4. Materials and Methods

4.1. Experimental Animals

Sprague Dawley (SD) rats used in the present study were provided by the Laboratory Animal Center of National Yang-Ming University. Rats were housed in transparent polycarbonate (PC) cages (size: 45 × 24 × 20 cm) under a 12/12 h reversed light/dark cycle (lights on from 8:00 a.m. to 8:00 p.m.) and constant temperature (22 ± 2 °C), with bedding changed weekly. The rats were allowed ad libitum access to food and water.

4.2. Procedures of Middle Cerebral Artery Occlusion (MCAO) and Reperfusion

Male Sprague Dawley rats (weighing 280 to 320 g) were used in this study. The rats were anesthetized with Zoletil 20–40 mg/kg and Xylazine 5–10 mg/kg (intraperitoneal injection) and fixed on a stereotaxic frame. We performed MCAO surgery and reperfusion to induce cerebral infarction by ligating the right middle cerebral artery and bilateral common carotid arteries, as previously described [12]. Briefly, a curved, 1 cm skin incision was made vertically by the right orbit, and the temporalis muscle was removed to uncover the junction of the zygomatic arch and the squamous bone, where a 3 mm² burr hole was drilled to expose the middle cerebral artery. The artery was ligated with a 10–0 suture while both common carotid arteries were clamped simultaneously by nontraumatic aneurysm clips for 90 min, after which the ligature and clips were removed to restore blood flow. Subsequently, the incision sites were sutured and disinfected, and the rats were placed on a heating mat until recovery from anesthesia.

4.3. Isolation and Culture of Human Umbilical Mesenchymal Stem Cells (HUMSCs)

The mesenchymal tissue in Wharton's jelly was then diced into cubes 0.5 cm on each side and centrifuged at 250 g for 5 min. After removal of the supernatant fraction, the precipitate that contained mesenchymal tissue was washed with serum-free Dulbecco's Modified Eagle's Medium (DMEM) and centrifuged at 250 g for 5 min. After aspiration of the supernatant fraction, mesenchymal tissue in the precipitate was treated with 0.0125% type I collagenase solution (Sigma-Aldrich, St. Louis, MO, USA) at 37 °C for 18 h, washed, and further digested with 0.025% trypsin at 37 °C for 30 min. The treated umbilical tissue then was cultured until the HUMSCs migration and proliferation. Finally, HUMSCs were stored in liquid nitrogen for later transplantation. HUMSCs were collected between the 10th and 15th passages for transplantation into rats in this study.

4.4. Transplantation of HUMSCs

HUMSCs were transplanted into the right cerebral cortex in rats suffering a stroke. Two transplantation sites were targeted with a stereotaxic instrument: first coordinates for transplantation: AP = −0.3 mm, R/L = +2.2 mm, H = +2.7 mm; second coordinates for transplantation: AP = −5.8 mm, R/L = +1.2 mm, H = + 2.5 mm. On day 14 post stroke, atrophy of the right cerebral cortex was observed. The coordinates were chosen because the two transplantation sites were located at the outer regions of the shrunken cortex. An amount of 5×10^5 HUMSCs were drawn into a glass pipette with a tip diameter of 150–200 µm mounted onto a Hamilton syringe (Hamilton, Reno, NV) attached to a micromanipulator. A total of 5×10^5 HUMSCs were transplanted at each site, and a total of 10^6 cells were administered for each rat. For the stroke group, 5 µL PBS was injected at each location (Figure 1A).

4.5. BisBenzimide-Treated HUMSCs In Vitro

Cultured HUMSCs were treated with 1 µg/mL bisBenzimide (Sigma B2883) for 48 h to label the cell nucleus. Subsequently, HUMSCs were treated with trypsin, collected, and transplanted into the right cerebral cortex at two locations on day 14 post stroke. On day 56 following a stroke, rats were sacrificed and perfused. The brains were obtained and immersed in 30% sucrose buffer until they sunk to the bottom. Protected from light, the samples were subjected to serial cryosectioning. Finally, the sections were observed and photographed using fluorescence microscopy.

4.6. Experimental Groups

There were four groups as follows:

1. Normal + Saline group ($n = 12$): The rats did not receive MCAO and reperfusion, just remove their skulls. On day 14, no treatment was administered except the injection of normal saline into the rat's cerebral cortex.
2. Normal + HUMSCs group ($n = 12$): The rats did not receive MCAO and reperfusion, just remove their skulls. On day 14, HUMSCs were transplanted into the rat's cerebral cortex.
3. Stroke + Saline group ($n = 26$): The rats received MCAO and reperfusion. On day 14 post-MCAO, no treatment was administered except the injection of normal saline into the rat's cerebral cortex.
4. Stroke + HUMSCs group ($n = 26$): The rats received MCAO and reperfusion. HUMSCs were transplanted into the rat's cerebral cortex on day 14 after MCAO.

The four groups were subjected to various assessments at different time points following MCAO (Figure 1A).

4.7. Infarct Cortex Identification

Rats were deeply anesthetized and decapitated. Coronal sections of the brains were sliced at 2 mm, immersed in 2% 2,3,5-triphenyltetrazolium chloride (TTC) (T8877; Sigma), and then fixed with 10% formalin. The infarct area was devoid of red staining.

4.8. Magnetic Resonance Imaging (MRI)

Brain images were acquired using Bruker S300 BioSpec/MedSpec MRI instrument at the Instrumentation Center, National Taiwan University. Normal brain was normally grey; brain images with white signals suggest high water/fluid contains, i.e., brain edema.

The four groups (Normal + Saline, Normal + HUMSCs, Stroke + Saline, and Stroke + HUMSCs groups) were assessed with MRI at nine time points, on days 1, 7, 14, 21, 28, 35, 42, 49, and 56, to continuously monitor the changes in brain damages caused by chronic stroke. Five brain images around bregma +0.48 mm, −0.72 mm, −1.92 mm, −3.12 mm, and −4.32 mm was chosen and summed for quantification. The MRI images of each group were quantified using image processing software Image-Pro Plus to quantify the area of cerebral cortex edema (white areas) in each image. The edema volume of the cerebral cortex was obtained by summing up white area in right cerebral cortex and multiplying the thickness of the section (0.6 mm). Subsequently, the atrophy area of the right cerebral cortex was obtained by subtracting the area of the injured right cerebral cortex from the area of the left (unaffected) cerebral cortex. The atrophy volume of the cerebral cortex was obtained by summing up all areas and multiplying the thickness of the section (0.6 mm).

4.9. Behavioral Test

Two behavioral tests were involved in the present study, including the cylinder test and the rotarod test.

4.10. Cylinder Test

Rats were put in a transparent cylinder (20 cm in diameter × 30 cm in height). A camera was placed toward the bottom of the cylinder for video recording to observe the percentages of each forelimb touching the cylinder wall while standing with hindlimbs. Normal rats generally use each forelimb with a frequency of approximately 50%, suggesting that usage of right and left forelimb are almost symmetrical. In this study, rats suffering a stroke in the right cerebral hemisphere caused locomotor deficits of their left bodies. Hence, the times of touching cylinder wall with left forelimb were divided by the total number of touches using two forelimbs to obtain the frequency of left forelimb usage. The use of impaired contralateral forelimb should significantly decrease in rats with stroke, according to previous studies [12].

4.11. Rotarod Test

Rats were placed on the rotarod with an initial speed of 4 rpm. The speed of the rotarod gradually accelerated to 40 rpm within 5 min. The time that each rat stayed on the rod will be recorded to assess its motor coordination and balance [12]. The retention time of each rat before receiving MCAO was set as a baseline value of 100%. By dividing the retention time obtained post stroke with the retention time obtained before the stroke, the ratio of the retention time in percentage was obtained. Stroke causes impairments of rats' mobility, which is reflected by the reduced duration they stay on the rotarod.

The two behavioral tests of the four groups were performed at 11 time points: 1 day prior to stroke (−1) and days 1, 4, 7, 14, 21, 28, 35, 42, 49, and 56 post stroke.

4.12. Numbering Brain Cryosections

Rats were anesthetized and perfused transcardially with 4% paraformaldehyde. Frozen sections were serially sectioned at 30 μm in a cryostat and stained with cresyl violet and immunocytochemistry staining for light microscopy (Supplemental Figure S1).

4.13. Cresyl Violet Staining

Brain sections were stained with 1% cresyl violet solution for 5 min, followed by passing through a series of increasing alcohol concentrations (50%, 70%, 80%, 90%, 95%, and 100%) for dehydration. Slides were then submerged twice in 100% xylene for 5 min each. Finally, slides were mounted with a mounting medium (Fisher Scientific SP15-500) and photographed under an optical microscope. The area of the normal left cerebral cortex of each section was quantified using the software Image pro-plus. By subtracting the area of the damaged cerebral cortex of the right hemisphere from the area of the normal left cerebral cortex and multiplying by 30 μm (thickness of the tissue section), the atrophy volume of the cerebral cortex was obtained. Subsequently, the total atrophy volume of the entire brain was gained by summing up the volume of all sections stained with cresyl violet.

4.14. Immunohistochemical (IHC) Staining

Brain sections were reacted with primary antibodies of mouse anti-neural nuclei antigen (NeuN) antibody (Millipore, 1:250), mouse anti-ED1 antibody (Millipore, 1:500), or mouse anti-human-specific nuclei antigen antibody (Millipore, 1:100) at 4 °C for 12 h. Subsequently, the secondary antibody of goat anti-mouse IgG-conjugated biotin (Millipore, 1:250) was added and reacted for 1 h at room temperature. Slides were then washed with 0.1 M PBS three times (5 min each), reacted with avidin-biotinylated complex (ABC kit, Vector) for 1 h, washed three times with 0.1 M PBS (5 min each), and developed with DAB. After staining, the slides were mounted with a mounting medium (Fisher Scientific SP15-500) and examined and photographed under an optical microscope.

4.15. Counting the Number of Neuronal Cells

Immunohistochemically stained with anti-NeuN antibody, the number of neuronal cells per mm^2 within the cerebral cortex and striatum in right infarcted brain regions of five brain slides at bregma +0.48 mm, −0.72 mm, −1.92 mm, −3.12 mm, and −4.32 mm was quantified. Four fields ($\times 20$ objective lens) were selected at each brain section. The four areas along the infarcted cortex were chosen for cell counting for the cerebral cortex and the four areas below the corpus callosum were chosen for cell counting for the striatum. Additionally, the numbers of neurons within the normal contralateral regions of the cerebral cortex and striatum were also quantified to serve as a reference.

4.16. Perfusion of the Experimental Animals with Fluorescein Isothiocyanate-Dextran (FITC-dextran)

Following anesthesia, the rats were injected with 0.2 mL fluorescein isothiocyanate-dextran (FITC-dextran; 50 mg/mL, Sigma FD-2000S) through the left ventricle [12]. Two minutes later, rat brain was obtained and placed in 4% paraformaldehyde fixation solution for 24 h. For dehydration, the tissues were then submerged in 30% sucrose until the tissue sunk to the bottom. Subsequently, the brain was covered with cryo-embedding media and fixed on the cryostat for sectioning under −20 °C. The brain tissues were sectioned into 30 μm -thick slices, enabling observation, and brain vessel distribution was photographed using fluorescence microscopy.

Five brain sections at bregma +0.48 mm, −0.72 mm, −1.92 mm, −3.12 mm, and −4.32 mm, labeled with FITC-dextran, were analyzed using Image pro-plus. Along the edges of the infarcted region in the right cerebral cortex, four fields ($\times 20$ objective lens) were selected at each brain section. The four fields next to the infarcted cortex were chosen for green fluorescence counting to measure the total length of FITC-dextran⁺ blood vessels, representing the total length of the blood vessels per mm^2 . In addition, the percentage of FITC-dextran⁺ area was quantified to represent the density of blood vessels. The contralateral cerebral cortex without injury served as a corresponding reference.

4.17. Reverse Transcription-Polymerase Chain Reaction (RT-PCR)

Total RNA of the cerebral cortex was extracted using TRIzol[®] reagent (Invitrogen[®] 15596018). After quantification using a spectrophotometer, a total of 5 µg RNA was subjected to reverse transcription (Invitrogen[®]). Subsequently, 2 µL cDNA was used for PCR with the following primers:

HUMAN RBFOX3:	310 bp
F: 5'-ATCCAGTGGTCGGCGCAGTCTAC-3'	
R: 5'-TACGGGTCGGCAGCTGCCGA-3'	
Human GFAP:	122 bp
F: 5'-CTGGAGAGGAAGATTGAGTCGC-3'	
R: 5'-ACGTCAAGTCCACATGGACCT-3'	
Rat GAPDH:	160 bp
F: 5'-CTCTACCCACGGCAAGTTCAAC-3'	
R: 5'-GGTGAAGACGCCAGTAGACTCCA-3'	
Human GAPDH:	176 bp
F: 5'-TCCTCCACCTTTGACGCT-3'	
R: 5'-CTTCTCTTGTGCTCTTG-3'	

The temperature setting was as follows: denature for 1 min at 95 °C; annealing for 1 min at 59 °C; extension for 1 min at 72 °C. After 35 cycles, the PCR products were analyzed by agarose gel electrophoresis and visualized and photographed with a UV transilluminator.

4.18. Statistical Analysis

All data are presented as the mean ± SEM. Comparisons of the means were performed using one-way ANOVA. Multiple comparisons were further conducted with Tukey's test. $p < 0.05$ was considered statistically significant.

5. Conclusions

HUMSCs transplanted into the cerebral cortex of rats with chronic stroke did not differentiate into neurons or astrocytes. Recovery or preservation of the infarcted region in rats with chronic stroke might be mediated via the cytokines secreted by the transplanted HUMSCs, which protected the neuronal cells and promoted angiogenesis in the infarcted region. These results are important for the design of future clinical trials.

Supplementary Materials: The following supporting information can be downloaded at: <https://www.mdpi.com/article/10.3390/ijms23063149/s1>.

Author Contributions: C.-C.Y., P.-M.C., W.-H.C. and Y.-S.F. for execution and analysis. M.-Y.A.L., Y.-Y.L. and Y.-S.F. for manuscript preparation and supervision. All authors have read and agreed to the published version of the manuscript.

Funding: This research was funded by [Ministry of Science and Technology] grant number [MOST 108-2314-B-075-015] and [Taipei Veterans General Hospital] grant number [V110C-023].

Institutional Review Board Statement: The use of human tissue (umbilical cord) and laboratory animals in this study was approved by the Research Ethics Committee at Taipei Veterans General Hospital (201106014IC and 202006019BC) and the Animal Research Committee of the College of Medicine at National Yang-Ming University (IACUC Approval No 991221 and 2020072).

Informed Consent Statement: Informed consent was obtained from all subjects involved in the study.

Conflicts of Interest: The authors declare no conflict of interest.

References

- Benjamin, E.J.; Blaha, M.J.; Chiuve, S.E.; Cushman, M.; Das, S.R.; Deo, R.; De Ferranti, S.D.; Floyd, J.; Fornage, M.; Gillespie, C. Heart disease and stroke statistics-2017 update: A report from the American Heart Association. *Circulation* **2017**, *135*, e146–e603. [CrossRef] [PubMed]
- World Health Organization. The Top 10 Causes of Death. Available online: <https://www.who.int/news-room/fact-sheets/detail/the-top-10-causes-of-death> (accessed on 9 December 2020).
- Members, W.G.; Lloyd-Jones, D.; Adams, R.J.; Brown, T.M.; Carnethon, M.; Dai, S.; De Simone, G.; Ferguson, T.B.; Ford, E.; Furie, K. Heart disease and stroke statistics—2010 update: A report from the American Heart Association. *Circulation* **2010**, *121*, e46–e215.
- Kowalska, K.; Krzywoszański, L.; Droś, J.; Pasińska, P.; Wilk, A.; Klimkowicz-Mrowiec, A. Early Depression Independently of Other Neuropsychiatric Conditions, Influences Disability and Mortality after Stroke (Research Study-Part of PROPOLIS Study). *Biomedicines* **2020**, *8*, 509. [CrossRef] [PubMed]
- Carrillo-Mora, P.; Pérez-De la Cruz, V.; Estrada-Cortés, B.; Toussaint-González, P.; Martínez-Cortéz, J.A.; Rodríguez-Barragán, M.; Quinzaños-Fresnedo, J.; Rangel-Caballero, F.; Gamboa-Coria, G.; Sánchez-Vázquez, I.; et al. Serum Kynurenines Correlate with Depressive Symptoms and Disability in Poststroke Patients: A Cross-sectional Study. *Neurorehabil. Neural Repair* **2020**, *34*, 936–944. [CrossRef] [PubMed]
- Tanaka, M.; Vécsei, L. Editorial of Special Issue “Crosstalk between Depression, Anxiety, and Dementia: Comorbidity in Behavioral Neurology and Neuropsychiatry”. *Biomedicines* **2021**, *9*, 517. [CrossRef]
- Nishimura, K.; Takata, K. Combination of Drugs and Cell Transplantation: More Beneficial Stem Cell-Based Regenerative Therapies Targeting Neurological Disorders. *Int. J. Mol. Sci.* **2021**, *22*, 9047. [CrossRef]
- Suda, S.; Nito, C.; Yokobori, S.; Sakamoto, Y.; Nakajima, M.; Sowa, K.; Obinata, H.; Sasaki, K.; Savitz, S.I.; Kimura, K. Recent advances in cell-based therapies for ischemic stroke. *Int. J. Mol. Sci.* **2020**, *21*, 6718. [CrossRef]
- Fu, Y.S.; Cheng, Y.C.; Lin, M.Y.A.; Cheng, H.; Chu, P.M.; Chou, S.C.; Shih, Y.H.; Ko, M.H.; Sung, M.S. Conversion of human umbilical cord mesenchymal stem cells in Wharton’s jelly to dopaminergic neurons in vitro: Potential therapeutic application for Parkinsonism. *Stem Cells* **2006**, *24*, 115–124. [CrossRef]
- Ko, T.L.; Fu, Y.Y.; Shin, Y.H.; Lin, Y.H.; Ko, M.H.; Fu, T.W.; Lin, T.Y.; Hsiao, H.S.; Chu, P.M.; Fu, Y.S. A high-efficiency induction of dopaminergic cells from human umbilical mesenchymal stem cells for the treatment of hemiparkinsonian rats. *Cell Transplant.* **2015**, *24*, 2251–2262. [CrossRef]
- Yang, C.C.; Shih, Y.H.; Ko, M.H.; Hsu, S.Y.; Cheng, H.; Fu, Y.S. Transplantation of human umbilical mesenchymal stem cells from Wharton’s jelly after complete transection of the rat spinal cord. *PLoS ONE* **2008**, *3*, e3336. [CrossRef]
- Lin, Y.C.; Ko, T.L.; Shih, Y.H.; Lin, M.Y.A.; Fu, T.W.; Hsiao, H.S.; Hsu, J.Y.C.; Fu, Y.S. Human umbilical mesenchymal stem cells promote recovery after ischemic stroke. *Stroke* **2011**, *42*, 2045–2053. [CrossRef] [PubMed]
- Huang, P.Y.; Shih, Y.H.; Tseng, Y.J.; Ko, T.L.; Fu, Y.S.; Lin, Y.Y. Xenograft of human umbilical mesenchymal stem cells from Wharton’s jelly as a potential therapy for rat pilocarpine-induced epilepsy. *Brain Behav. Immun.* **2016**, *54*, 45–58. [CrossRef] [PubMed]
- Tsai, P.J.; Yeh, C.C.; Huang, W.J.; Min, M.Y.; Huang, T.H.; Ko, T.L.; Huang, P.Y.; Chen, T.H.; Hsu, S.P.; Soong, B.W. Xenografting of human umbilical mesenchymal stem cells from Wharton’s jelly ameliorates mouse spinocerebellar ataxia type 1. *Transl. Neurodegener.* **2019**, *8*, 29. [CrossRef] [PubMed]
- Tsai, P.C.; Fu, T.W.; Chen, Y.M.A.; Ko, T.L.; Chen, T.H.; Shih, Y.H.; Hung, S.C.; Fu, Y.S. The therapeutic potential of human umbilical mesenchymal stem cells from Wharton’s jelly in the treatment of rat liver fibrosis. *Liver Transplant.* **2009**, *15*, 484–495. [CrossRef]
- Fan, Y.P.; Hsia, C.C.; Tseng, K.W.; Liao, C.K.; Fu, T.W.; Ko, T.L.; Chiu, M.M.; Shih, Y.H.; Huang, P.Y.; Chiang, Y.C. The Therapeutic Potential of Human Umbilical Mesenchymal Stem Cells from Wharton’s Jelly in the Treatment of Rat Peritoneal Dialysis-Induced Fibrosis. *Stem Cells Transl. Med.* **2016**, *5*, 235–247. [CrossRef]
- Chu, K.A.; Wang, S.Y.; Yeh, C.C.; Fu, T.W.; Fu, Y.Y.; Ko, T.L.; Chiu, M.M.; Chen, T.H.; Tsai, P.J.; Fu, Y.S. Reversal of bleomycin-induced rat pulmonary fibrosis by a xenograft of human umbilical mesenchymal stem cells from Wharton’s jelly. *Theranostics* **2019**, *9*, 6646–6664. [CrossRef]
- Chu, K.A.; Yeh, C.C.; Kuo, F.H.; Lin, W.R.; Hsu, C.W.; Chen, T.H.; Fu, Y.S. Comparison of reversal of rat pulmonary fibrosis of nintedanib, pirfenidone, and human umbilical mesenchymal stem cells from Wharton’s jelly. *Stem Cell Res. Ther.* **2020**, *11*, 513. [CrossRef]
- Chao, K.C.; Chao, K.F.; Fu, Y.S.; Liu, S.H. Islet-like clusters derived from mesenchymal stem cells in Wharton’s Jelly of the human umbilical cord for transplantation to control type 1 diabetes. *PLoS ONE* **2008**, *3*, e1451. [CrossRef]
- Fu, Y.S.; Lu, C.H.; Chu, K.A.; Yeh, C.C.; Chiang, T.L.; Ko, T.L.; Chiu, M.M.; Chen, C.F. Xenograft of human umbilical mesenchymal stem cells from Wharton’s jelly differentiating into osteocytes and reducing osteoclast activity reverses osteoporosis in ovariectomized rats. *Cell Transplant.* **2018**, *27*, 194–208. [CrossRef]
- Chen, C.F.; Chen, Y.C.; Fu, Y.S.; Tsai, S.W.; Wu, P.K.; Chen, C.M.; Chang, M.C.; Chen, W.M. Characterization of Osteogenesis and Chondrogenesis of Human Decellularized Allogeneic Bone with Mesenchymal Stem Cells Derived from Bone Marrow, Adipose Tissue, and Wharton’s Jelly. *Int. J. Mol. Sci.* **2021**, *22*, 8987. [CrossRef]

22. Dos Santos, A.d.V.; da Costa Reis, J.; Paredes, B.D.; Moraes, L.; Giral-di-Guimarães, A.; Mendez-Otero, R. Therapeutic window for treatment of cortical ischemia with bone marrow-derived cells in rats. *Brain Res.* **2010**, *1306*, 149–158. [CrossRef] [PubMed]
23. Darsalia, V.; Allison, S.J.; Cusulin, C.; Monni, E.; Kuzdas, D.; Kallur, T.; Lindvall, O.; Kokaia, Z. Cell number and timing of transplantation determine survival of human neural stem cell grafts in stroke-damaged rat brain. *J. Cereb. Blood Flow Metab.* **2011**, *31*, 235–242. [CrossRef] [PubMed]
24. Ishizaka, S.; Horie, N.; Satoh, K.; Fukuda, Y.; Nishida, N.; Nagata, I. Intra-arterial cell transplantation provides timing-dependent cell distribution and functional recovery after stroke. *Stroke* **2013**, *44*, 720–726. [CrossRef] [PubMed]
25. Janowski, M.; Lyczek, A.; Engels, C.; Xu, J.; Lukomska, B.; Bulte, J.W.; Walczak, P. Cell size and velocity of injection are major determinants of the safety of intracarotid stem cell transplantation. *J. Cereb. Blood Flow Metab.* **2013**, *33*, 921–927. [CrossRef]
26. Rodríguez-Frutos, B.; Otero-Ortega, L.; Gutiérrez-Fernández, M.; Fuentes, B.; Ramos-Cejudo, J.; Díez-Tejedor, E. Stem Cell Therapy and Administration Routes After Stroke. *Transl. Stroke Res.* **2016**, *7*, 378–387. [CrossRef]
27. Zhang, L.; Li, Y.; Zhang, C.; Chopp, M.; Gosiewska, A.; Hong, K. Delayed administration of human umbilical tissue-derived cells improved neurological functional recovery in a rodent model of focal ischemia. *Stroke* **2011**, *42*, 1437–1444. [CrossRef]
28. Hamblin, M.H.; Lee, J.P. Neural Stem Cells for Early Ischemic Stroke. *Int. J. Mol. Sci.* **2021**, *22*, 7703. [CrossRef]
29. Chen, L.; Zhang, G.; Gu, Y.; Guo, X. Meta-Analysis and Systematic Review of Neural Stem Cells therapy for experimental ischemia stroke in preclinical studies. *Sci. Rep.* **2016**, *6*, 32291. [CrossRef]
30. Cheng, Z.; Wang, L.; Qu, M.; Liang, H.; Li, W.; Li, Y.; Deng, L.; Zhang, Z.; Yang, G.Y. Mesenchymal stem cells attenuate blood-brain barrier leakage after cerebral ischemia in mice. *J. Neuroinflamm.* **2018**, *15*, 135. [CrossRef]
31. Yanar, K.; Molbay, M.; Özyaydin-Goksu, E.; Unek, G.; Cetindağ, E.; Unal, A.; Korgun, E.T. Contribution of Human Trophoblast Progenitor Cells to Neurogenesis in Rat Focal Cerebral Ischemia Model. *Brain Inj.* **2021**, *35*, 850–862. [CrossRef]
32. Qin, M.; Chen, R.; Li, H.; Liang, H.; Xue, Q.; Li, F.; Chen, Y.; Zhang, X. Direct Reprogramming of Human Amniotic Fluid Stem Cells by OCT4 and Application in Repairing of Cerebral Ischemia Damage. *Int. J. Biol. Sci.* **2016**, *12*, 558–568. [CrossRef] [PubMed]
33. Yang, Y.C.; Liu, B.S.; Shen, C.C.; Lin, C.H.; Chiao, M.T.; Cheng, H.C. Transplantation of adipose tissue-derived stem cells for treatment of focal cerebral ischemia. *Curr. Neurovasc. Res.* **2011**, *8*, 1–13. [CrossRef] [PubMed]
34. Grandvuillemin, I.; Garrigue, P.; Ramdani, A.; Boubred, F.; Simeoni, U.; Dignat-George, F.; Sabatier, F.; Guillet, B. Long-Term Recovery After Endothelial Colony-Forming Cells or Human Umbilical Cord Blood Cells Administration in a Rat Model of Neonatal Hypoxic-Ischemic Encephalopathy. *Stem Cells Transl. Med.* **2017**, *6*, 1987–1996. [CrossRef] [PubMed]
35. Wang, F.; Tang, H.; Zhu, J.; Zhang, J.H. Transplanting Mesenchymal Stem Cells for Treatment of Ischemic Stroke. *Cell Transplant.* **2018**, *27*, 1825–1834. [CrossRef] [PubMed]
36. Arvidsson, A.; Collin, T.; Kirik, D.; Kokaia, Z.; Lindvall, O. Neuronal replacement from endogenous precursors in the adult brain after stroke. *Nat. Med.* **2002**, *8*, 963–970. [CrossRef]
37. Boese, A.C.; Le, Q.S.E.; Pham, D.; Hamblin, M.H.; Lee, J.P. Neural stem cell therapy for subacute and chronic ischemic stroke. *Stem Cell Res. Ther.* **2018**, *9*, 154. [CrossRef]
38. Parent, J.M.; Vexler, Z.S.; Gong, C.; Derugin, N.; Ferriero, D.M. Rat forebrain neurogenesis and striatal neuron replacement after focal stroke. *Ann. Neurol.* **2002**, *52*, 802–813. [CrossRef]
39. Gu, N.; Rao, C.; Tian, Y.; Di, Z.; Liu, Z.; Chang, M.; Lei, H. Anti-inflammatory and antiapoptotic effects of mesenchymal stem cells transplantation in rat brain with cerebral ischemia. *J. Stroke Cerebrovasc. Dis.* **2014**, *23*, 2598–2606. [CrossRef]
40. Tian, L.; Zhu, W.; Liu, Y.; Gong, Y.; Lv, A.; Wang, Z.; Ding, X.; Li, S.; Fu, Y.; Lin, Y.; et al. Neural Stem Cells Transfected with Leukemia Inhibitory Factor Promote Neuroprotection in a Rat Model of Cerebral Ischemia. *Neurosci. Bull.* **2019**, *35*, 901–908. [CrossRef]
41. Zhou, L.; Lin, Q.; Wang, P.; Yao, L.; Leong, K.; Tan, Z.; Huang, Z. Enhanced neuroprotective efficacy of bone marrow mesenchymal stem cells co-overexpressing BDNF and VEGF in a rat model of cardiac arrest-induced global cerebral ischemia. *Cell Death Dis.* **2017**, *8*, e2774. [CrossRef]
42. Asgari Taei, A.; Nasoohi, S.; Hassanzadeh, G.; Kadivar, M.; Dargahi, L.; Farahmandfar, M. Enhancement of angiogenesis and neurogenesis by intracerebroventricular injection of secretome from human embryonic stem cell-derived mesenchymal stem cells in ischemic stroke model. *Biomed. Pharmacother.* **2021**, *140*, 111709. [CrossRef] [PubMed]
43. Li, L.; Chu, L.; Ren, C.; Wang, J.; Sun, S.; Li, T.; Yin, Y. Enhanced Migration of Bone Marrow-Derived Mesenchymal Stem Cells with Tetramethylpyrazine and Its Synergistic Effect on Angiogenesis and Neurogenesis After Cerebral Ischemia in Rats. *Stem Cells Dev.* **2019**, *28*, 871–881. [CrossRef] [PubMed]
44. Moon, S.; Chang, M.S.; Koh, S.H.; Choi, Y.K. Repair Mechanisms of the Neurovascular Unit after Ischemic Stroke with a Focus on VEGF. *Int. J. Mol. Sci.* **2021**, *22*, 8543. [CrossRef] [PubMed]
45. Neal, E.G.; Acosta, S.A.; Kaneko, Y.; Ji, X.; Borlongan, C.V. Regulatory T-cells within bone marrow-derived stem cells actively confer immunomodulatory and neuroprotective effects against stroke. *J. Cereb. Blood Flow Metab.* **2019**, *39*, 1750–1758. [CrossRef]
46. Shi, K.; Tian, D.C.; Li, Z.G.; Ducruet, A.F.; Lawton, M.T.; Shi, F.D. Global brain inflammation in stroke. *Lancet Neurol.* **2019**, *18*, 1058–1066. [CrossRef]
47. Xia, Y.; Hu, G.; Chen, Y.; Yuan, J.; Zhang, J.; Wang, S.; Li, Q.; Wang, Y.; Deng, Z. Embryonic Stem Cell Derived Small Extracellular Vesicles Modulate Regulatory T Cells to Protect against Ischemic Stroke. *ACS Nano* **2021**, *15*, 7370–7385. [CrossRef]

48. Yu, Z.; Wenyan, T.; Xuewen, S.; Baixiang, D.; Qian, W.; Zhaoyan, W.; Yinxiang, Y.; Suqing, Q.; Zuo, L. Immunological effects of the intraparenchymal administration of allogeneic and autologous adipose-derived mesenchymal stem cells after the acute phase of middle cerebral artery occlusion in rats. *J. Transl. Med.* **2018**, *16*, 339. [CrossRef]
49. Gutiérrez-Fernández, M.; Rodríguez-Frutos, B.; Ramos-Cejudo, J.; Otero-Ortega, L.; Fuentes, B.; Vallejo-Cremades, M.T.; Sanz-Cuesta, B.E.; Díez-Tejedor, E. Comparison between xenogeneic and allogeneic adipose mesenchymal stem cells in the treatment of acute cerebral infarct: Proof of concept in rats. *J. Transl. Med.* **2015**, *13*, 46. [CrossRef]
50. Jansen of Lorkeers, S.J.; Eding, J.E.; Vesterinen, H.M.; van der Spoel, T.I.; Sena, E.S.; Duckers, H.J.; Doevendans, P.A.; Macleod, M.R.; Chamuleau, S.A. Similar effect of autologous and allogeneic cell therapy for ischemic heart disease: Systematic review and meta-analysis of large animal studies. *Circ. Res.* **2015**, *116*, 80–86. [CrossRef]



Review

The Role of Systemic Filtrating Organs in Aging and Their Potential in Rejuvenation Strategies

Amal Kassab ¹, Nasser Rizk ² and Satya Prakash ^{1,*}

¹ Biomedical Technology and Cell Therapy Research Laboratory, Department of Biomedical Engineering, Faculty of Medicine, McGill University, 3775 University Street, Montreal, QC H3A 2BA, Canada; amal.kassab@mail.mcgill.ca

² Department of Biomedical Sciences, College of Health Sciences-QU-Health, Qatar University, Doha 2713, Qatar; nassirzk@qu.edu.qa

* Correspondence: satya.prakash@mcgill.ca

Abstract: Advances in aging studies brought about by heterochronic parabiosis suggest that aging might be a reversible process that is affected by changes in the systemic milieu of organs and cells. Given the broadness of such a systemic approach, research to date has mainly questioned the involvement of “shared organs” versus “circulating factors”. However, in the absence of a clear understanding of the chronological development of aging and a unified platform to evaluate the successes claimed by specific rejuvenation methods, current literature on this topic remains scattered. Herein, aging is assessed from an engineering standpoint to isolate possible aging potentiators via a juxtaposition between biological and mechanical systems. Such a simplification provides a general framework for future research in the field and examines the involvement of various factors in aging. Based on this simplified overview, the kidney as a filtration organ is clearly implicated, for the first time, with the aging phenomenon, necessitating a re-evaluation of current rejuvenation studies to untangle the extent of its involvement and its possible role as a potentiator in aging. Based on these findings, the review concludes with potential translatable and long-term therapeutics for aging while offering a critical view of rejuvenation methods proposed to date.

Keywords: aging; rejuvenation; kidney; filtration organ; plasma proteomics; heterochronic parabiosis; metabolic pathways; urine proteomics; metal clearance; aging biomarkers

Citation: Kassab, A.; Rizk, N.; Prakash, S. The Role of Systemic Filtrating Organs in Aging and Their Potential in Rejuvenation Strategies.

Int. J. Mol. Sci. **2022**, *23*, 4338.

<https://doi.org/10.3390/ijms23084338>

Academic Editors: Masaru Tanaka and Lydia Giménez-Llort

Received: 28 January 2022

Accepted: 8 April 2022

Published: 14 April 2022

Publisher’s Note: MDPI stays neutral with regard to jurisdictional claims in published maps and institutional affiliations.



Copyright: © 2022 by the authors. Licensee MDPI, Basel, Switzerland. This article is an open access article distributed under the terms and conditions of the Creative Commons Attribution (CC BY) license (<https://creativecommons.org/licenses/by/4.0/>).

1. Introduction

Aging literature has shown remarkable advances over the past two decades and has produced significant milestones that might allow for the first time to view aging as a disease that is not only treatable but also reversible [1–3]. However, these claims remain to date under dispute, as sustainable aging reversal methods are yet to be identified, and in the absence of universally accepted aging biomarkers that successfully isolate healthy aging from disease phenotypes associated with it, its classification as a disease is premature. Thus, although aging is still not officially classified as a disease, it is still a prominent risk factor for a multitude of chronic ones. Admittedly, when it comes to geroscience, it is hard to sum up, findings in the field using clear and comparable metrics, largely since it is very diverse, spanning lifestyle factors [4–7], dietary recommendations [8–12], pharmaceutical interventions [13,14], and young blood plasma transfusions [15], in addition to cell reprogramming agents [16–18]. Additionally, most current literature on the topic ignores the global process of aging, specifically its primary driver and chronological progression, instead of focusing on specific manifestations of it. However, the biggest challenge in assessing current findings on aging is the lack of a common quantifier of biological age. To date, most rejuvenation studies measure the reversibility of some molecular and genetic markers of certain aging-associated chronic diseases or parameters, while the use of systemic cellular and molecular quantifiers of biological aging remains confined to a limited number of studies.

This might be due to the fact that measures of biological aging are themselves diverse and continuously advancing, as some rely on assessing circulating C-reactive protein (CRP), p16^{INK4a}, or telomere attrition, the latter two being also common biomarkers of cellular senescence [19–23]. The most promising biological aging quantifier, however, seems to be DNA methylation, which was presented through several aging “clocks,” such as Horvath’s or Hannum’s, that helped introduce lifespan predicting ones, such as PhenoAge and GrimAge [24,25]. Despite challenges in adopting such methodologies into broader clinical use, as a definite measure of biological age today, the promise of an accurate and precise biological age quantifier is undoubtedly closer than ever, which would be the ultimate judge on the success of any advocated rejuvenation method. Nevertheless, until a unified platform and parameters in geroscience are set, assessing the value of these largely scattered findings remains taxing, especially via well-established scientific methods, such as meta-analysis. More importantly, the effort to bridge these findings to attain a complementary understanding of the systemic phenomenon of aging is becoming increasingly demanding due to the exponential increase of publications in the field.

There are several excellent reviews that detail the recent advances made in all rejuvenation strategies, including quantifiers of biological aging, or age metrics, some of which have already been referenced in the introduction. Therefore, this review attempts to shine a light on a possible systematic aging factor that has been overlooked thus far. Moreover, by critically reviewing the latest findings on aging and rejuvenation strategies, we propose new avenues to address aging and to understand its chronological progression. In the following sections, we start with a juxtaposition between the aging of biological and mechanical fluidic entities. This over-simplification primarily aims to provide an overview of the major systemic causes of aging, in order to break down this phenomenon into main categories that can be targeted and studied. This primary analysis clearly indicates that the filtration system presents a clear gap in aging studies to date. Next, hallmarks of biological aging are discussed, where several milestone publications were able to identify clear aging phenotypes on molecular, cellular, and organismal levels. Nevertheless, no clear understanding of aging progression over time, specifically primary causes and downstream targets, is available to date. Following this analysis and based on the gap in addressing the role of systemic filtration on aging, the role of the kidney specifically on various known aging targets is reviewed, namely the role of the kidney in handling metabolic by-products, metal, circulating aging factors, and plasma clearance. Next, a critical review of present rejuvenation strategies is provided to assess their long-term significance and practicality. Finally, we conclude by exploring possible future rejuvenation avenues that need to be developed to address the complex topic of healthy aging.

2. An Engineering Perspective on Biological Aging

The degradation of physical entities, whether biological or non-biological, over time can be regarded as one of the fundamental natural laws, specifically the second law of thermodynamics. Nevertheless, biological systems are exceptionally resilient due to their built-in maintenance and renewal capabilities that defy non-biological ones in their complexity and efficiency. These systems, however, are far from perfect and eventually exhibit systemic malfunctions that lead to various errors/diseases and finally degrade, leading to death.

However, compared to the vastly diverse and complicated biological systems, mechanical fluidic ones are much simpler and rudimentary, which in a topic as complicated and diverse as aging brings about a much-needed simplicity that can potentially provide a unified platform to assess and measure this process in a more organized and structured manner. The aging of mechanical devices can be ascribed to a set of simple parameters, such as fatigue and stress-induced on moving and load-bearing parts. Additionally, in fluidic systems, the aging of mechanical parts is due to either external environmental exposure or internal corrosion due to a buildup of contaminants within the circulating fluid. These contaminants tend to accumulate over time on internal surfaces, compromising component integrity and eroding their protective and insulating layers due to undesirable

chemical reactions, as shown in Figure 1. Therefore, the most important measures to ensure a long service life of any fluidic system rely on using good quality materials, protecting against external environmental factors, and maintaining a robust and changeable filtration system. Notably, the more complex, and sensitive the fluidic device's components are, the more sophisticated filtration systems become to ensure a secure and safe operation of all internal components.

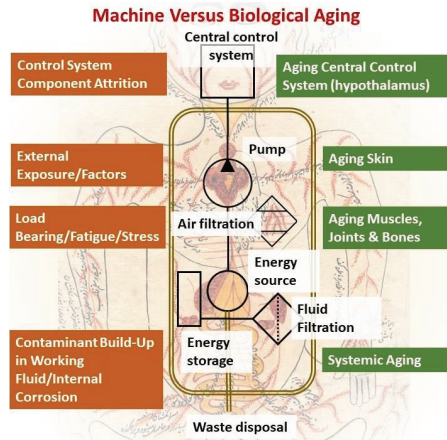


Figure 1. Causes of aging: Juxtaposition between mechanical fluidic and biological systems.

Based on this analogy, external body parts are obviously susceptible to accelerated aging due to environmental stress, such as UV light, heat, cold, and possible reactionary agents [26,27]. On the other hand, moving and load-bearing parts, such as joints, the heart, muscles, and bones are subject to wear and tear [28,29]. This leaves behind the systemic cause of aging, where fluid integrity that is largely controlled by the filtration system is in question. In biological systems, where organ functions are not as clear cut as in their mechanical counterparts, the single most comparable organ in charge of fluid filtration is the kidney, which seems to have the highest burden in protecting the entire system from contaminant build-up. Yet, interestingly, the kidney as an organ has never been considered for its possible role in physiological aging thus far, despite the clear correlation between the functional decline of the kidney and physiological aging in humans.

Reduced kidney function generally starts in the late thirties, which is concomitant with the onset of aging, and continues to degrade over the years; nevertheless, it is not considered an issue from a medical standpoint until the loss of function reaches more than 50% [30,31]. Furthermore, while the effect of the loss of kidney function beyond the critical threshold is well documented, there is no account for the effect of reduced kidney function on the body in general and whether this gradual damage plays a role in the initiation or acceleration of the biological clock. Kidney disease, or the reduction in its functionality beyond 50%, is associated with inflammation, oxidative stress, sympathetic–vagal imbalance, and circadian rhythm, in addition to tissue atrophy, increased protein catabolism, and the activation of the stress resistance response [32], all of which are directly related to aging. Additionally, of the limited chronic diseases known to cause premature biological aging, such as heart failure, obstructive pulmonary disease, rheumatoid arthritis, and HIV, kidney disease is one of the most common [33–37]. Aging hallmarks of these diseases include muscle atrophy, vascular disease, and general frailty [32,35,36], which might be attributed to the sedentary lifestyle that often accompanies chronic diseases. Nevertheless, these diseases also share cellular markers of aging and senescence, namely telomere attrition and p16^{INK4a} accumulation [38].

Of course, correlation alone does not establish causation, especially when considering the complex nature of the aging process and its interpersonal variations. Therefore, a closer re-assessment of aging hallmarks and successful “rejuvenation” methods are warranted to elucidate the possible extent of the kidney’s involvement in aging.

3. Hallmarks of Aging: The Complexity of Cause and Effect

In general, aging hallmarks are consistent on physiological, organ, cellular, and molecular levels. Several review articles have covered aging hallmarks comprehensively [20,39,40], therefore, they will not be detailed herein, rather, the association between these hallmarks will be viewed. Early on, in 2013, Lopez-Otin et al. proposed dividing the hallmarks of aging into primary hallmarks identified as genomic instability, telomere attrition, epigenetic alterations, and impaired proteostasis, as the main initiators of the aging process. This is followed by another set of aging hallmarks as a response, which manifest in deregulated nutrient sensing, mitochondrial dysfunction, and cellular senescence that eventually lead to integrative aging hallmarks such as stem cell exhaustion and altered intercellular communication [39], as shown in Figure 2. This work by Lopez-Otin et al. presents one of the earliest and most comprehensive reviews on aging, with a rare insight into the possible hierarchical and chronological sequence of the aging process that has been the cornerstone of many studies since. The timing of the article also reflects a transitional period in aging research between the two opposing views that regarded this process either as unidirectional or reversible. This might be behind the interpretation that the aging process is fundamentally cellular in nature, and that somatic cell exhaustion is behind the global aging phenomenon that is exacerbated by stem cell exhaustion at its later stages. While this view holds merit in some of its details, it has been challenged by rejuvenation research that has been flourishing at the same time, particularly those pertaining to heterochronic parabiosis, where extracellular factors alone that are devoid of any stem cells were shown to have rejuvenating effects capable of reversing the hallmarks of cellular and molecular aging [41–43]. In other words, extracellular factors might be implicated in renewing or maintaining endogenous cellular repair mechanisms. Thus, experimental evidence that rejuvenation studies provide, may allow for an overview of the aging process’s hierarchy to discern the root cause of the phenomenon, and ultimately address the source of the disease itself.

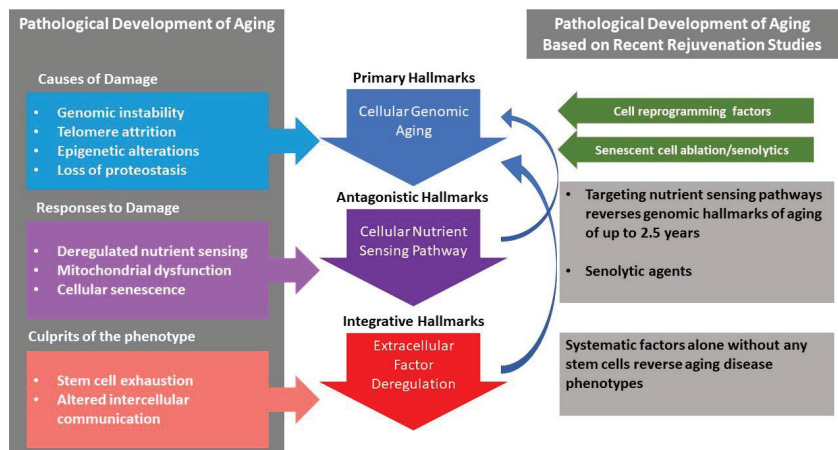


Figure 2. The pathology of aging and the causative relationship between its hallmarks. An illustration of the differences between theoretical assumptions regarding the hierarchical order of the aging process [39] and the various experimental avenues that show the complex relationship between the various hallmarks of aging. These include targeting nutrient sensing pathways [6,7,44–47], circulating factors and young plasma [48–51], senescent cell ablation [52–56] and cell programming factors [57,58].

4. Circulating Factors of Aging and the Kidney

The most obvious drawback of targeting certain “aging” pathways is indeed the complexity and subtle role of the variation of these pathways in different cell types and tissues, which hinders such methods from becoming a widely adaptable and long-term solution for aging. To be clear, while none of the targeted approaches seem to provide a solution to the accumulation of contaminants within the bloodstream, in the absence of a cure for a malfunctioning filtration system, reducing the build-up of metabolic waste with the adoption of a restricted calorie intake, for example, can understandably decelerate the aging process, in addition to the various other factors that add up to achieve the effects observed using such approaches. In this regard, the kidney primarily functions as a purifier of metabolic by-products and a maintainer of plasma mineral homeostasis; additionally, it also filters out small to medium size proteins, all of which have been shown to affect biological aging in one aspect or another.

4.1. Metabolic by-Product Clearance and Kidney-Associated Protein Metabolism

It is known that the estimated glomerular filtration rate (eGFR), which is a measure of serum creatinine levels, reduces gradually with age, even among healthy people [44]. In fact, according to one study in an Italian population, the prevalence of reported kidney disease is merely 3.3% in the group with eGFR < 60 mL/min /1.73 m² [45]. Reduced eGFR is shown to be significantly associated with uric acid, urea, and free ammonia accumulation, particularly citrulline, glycine, and phenylalanine [46]. Based on recent findings, elevated levels of serum uric acid alone, or hyperuricemia, has been linked with gout [47], bone and tissue damage [48], heart disease [49], high blood pressure [50], fatty liver [51], and type 2 diabetes [52], all of which are associated with aging. Therefore, it is worth considering that aging can be defined as an ailment that grows underneath clinically defined disease thresholds, much like contaminant levels within the blood stream. Nevertheless, there are additional metabolic factors involved in reduced kidney function. In a recent study by Chen et al. (2020), comparative blood and urine metabolomics analysis was conducted that identified 32 significantly altered compounds between healthy young and elderly groups [59]. The most noteworthy of which were decreased serum levels of albumin lysyl and essential amino acids, and increased levels of N-acetyl glycoproteins and lipids. On the other hand, urine samples of the elderly had elevated levels of trimethylamine N-oxide, scyllo-inositol, citrate, and ascorbic acid, with decreased levels of amino acids and acetate, among others. Taking into consideration that this is the first age-associated study that compares variations between serum and urine, it provides a rare insight into possible causative factors involved in metabolic changes associated with aging. Nevertheless, the limited number of participants (33 in each group) emphasizes the importance of conducting more comprehensive research in this area based on larger groups of participants in different populations. While there is no doubt that progressive loss of kidney function leads to changes in protein/amino acid exertion, changes in kidney metabolism itself might be implicated in the deregulation of vasoactive compounds and hormones leading to health complications in the elderly [60]. Such changes can be used as possible aging markers, based on urine samples alone, according to a recent study by Teruya et al. (2020) that identified 55 possible metabolic markers, most of which are highly correlated with creatinine [61]. Additionally, age-related changes in kidney-specific transcriptomics can provide additional insight on its role in systemic aging [62].

4.2. Urine Metal Concentration and Aging

Although protein metabolism and its by-product clearance have well-founded effects on aging and age associate diseases in general, the role of mineral homeostasis and the effect of reduced kidney function is less evident. Nevertheless, based on several studies, urine metal clearance increases with age systematically, allowing it to be used as a predictor of biological aging, particularly iron, zinc, and manganese clearance [62,63]. The importance of

increased metal clearance can be demonstrated by the role that some metals play in various organic functions, such as hormone production, blood oxygenation, and enzyme formation.

Iron is one of the most important non-organic elements for a biological system. Iron deficiency has been associated with decreased cognition and functional ability in the elderly, which might be a downstream effect of reduced blood oxygenation [64] that is by far the most important role of iron. The prevalence of anemia increases with age, starting with 17% up to 45% in the nursing home elderly population [65]. On the other hand, the importance of zinc stems from it being an essential component in various biological processes, such as genomic repair [66], growth and reproduction [67], protection against inflammation [68], immunity [69], wound healing, and enzyme synthesis [70], in addition to its important role in maintaining central nervous system function [71]. Additionally, the serum zinc/copper ratio is associated with bone mineral density, which implicates the detrimental effect of reduced serum zinc levels on skeletal health [45]. Finally, when it comes to manganese, unlike iron and zinc, its biological role is limited to trace amounts for various biological functions including enzyme synthesis [46]. Additionally, since it is available in most diets, its excess expression in urine is associated with toxic exposure, which leads to several neurodegenerative diseases [47]. In fact, according to Nwanaji-Enwerem et al. (2020), manganese can be considered an important phenotype as a 1 ng/mL increase in its concentration in urine is associated with a 9.93 year increase in biological age defined by DNA methylation clocks [44].

Most studies on urine metal concentration are presently within the realm of toxicology, however, given the importance of certain metals in biological function, the effect of aging on metal clearance and the specific role those various organs play in the process of their circulation need to be clarified. Presently, based on the limited number of studies on this topic, metal clearance seems to increase with age, which might enforce and/or propagate age-related disease progression, without much evidence supporting its role in the onset of aging.

4.3. Circulating Factors and Plasma Protein Clearance by the Kidney

There have been several extensive studies that undertook the examination of plasma protein variations with age as a result of the rejuvenating effects observed with heterochronic parabiosis. Nevertheless, studies on urine profile variation in connection with age are less common outside of the aim of identifying disease phenotypes as a diagnostic tool.

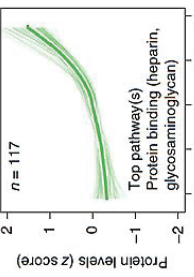
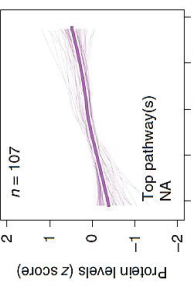
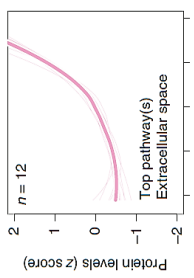
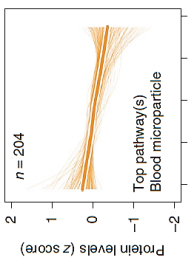
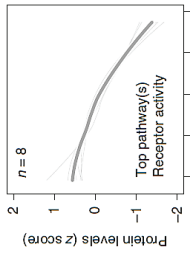
When it comes to plasma protein disparities with aging, one interesting study presented by Lehallier et al. (2019) was able to identify 1379 proteins that changed with age [72]. More importantly, the stratification of changes in these protein concentrations over time provides a rare insight into their association with the aging process itself. The authors remarked that while some groups of proteins seem to be somewhat stable during various life-stages and only start to increase exponentially at the onset of older age (>60 years), other “clusters” accelerate exponentially around mid-age (late 30–40 years), and some tend to increase/decrease linearly with age, as shown in Table 1. This remarkable analysis identifies for the first-time proteins and their associated pathways implicated in the aging process itself versus those that are a product of an aging system and a manifestation of its malfunction. Based on this examination, it is obvious that clusters 3, 4, 7, 8, and to a lesser degree 5, represent proteins involved in the aging process. Specifically, clusters 3, 4, and 7 present proteins that increase/accumulate in the plasma over time, while clusters 5 and 8 decrease with age. Table 1 details the main pathways implicated in these clusters, outlined in the supplementary data provided by Lehallier et al. [72]. Apart from this important and rare global view of plasma protein changes, individually, the most significantly age-associated proteins that are gender-independent can be reduced to, sclerostin (SOST), growth differentiation factor 15 (GDF15), ADP ribosylation factor interacting protein 2 (ARFIP2), motilin (MLN), pleiotrophin (PTN), and scavenger receptor class f member 2 (SCARF2) that increase with age, while the expression of immunoglobulin superfamily

DCC subclass member 4 (IGDCC4) and proto-oncogene tyrosine-protein kinase receptor (RET) decrease over time.

Some of these individual proteins come as a confirmation for the results published by an earlier study in 2018 by Tanaka et al., which presented another plasma proteomic analysis of aging in healthy humans [73]. This investigation identified 197 proteins in connection with aging, 20 of which are negatively associated. The top 10 most significantly affected proteins are GDF15, PTN, a disintegrin and metalloproteinase with thrombospondin motif 5 (ADAMTS5), follitropin (CGA-FSHB), SOST, chordin-like protein 1 (CHRDL1), natriuretic peptides b (NPPB), EGF-containing fibulin-like extracellular matrix protein 1 (EFEMP1), macrophage metalloelastase (MMP12), and cathepsin (CTSV). Additionally, these previously identified circulating plasma factors include the detrimental decrease with age of: growth differentiation factor 11 (GDF11) [74], oxytocin (OXT) [75], tissue inhibitor of metalloproteinase 2 (TIMP2) [76], granulocyte-macrophage colony-stimulating factor (CSF2) [76], growth hormone-releasing hormone (GHRH) [77], apelin (APLN) [78], cadherin 13 (CDH13) [79], extracellular nicotinamide phosphoribosyl transferase (eNAMPT) [80], and thrombospondin-4 (THBS4) [81], in addition to osteocalcin (OCN) [82]. Circulating factors that instead increase with age include small cytokines (CCL2, CCL11 and CCL19) [83], haptoglobin (HP) [83], and β -2 microglobulin (B2M) [84]. In this regard, taking into consideration that old blood seems to have a more damaging effect on organs and tissues than young blood, more emphasis can be dedicated to those that accumulate over time.

When it comes to the general decline in kidney function and its effect on protein clearance, to date, there is only one comparative proteomic analysis of age-associated changes in urine, which included urine samples of 52 healthy men aging 19–54 years [85]. The study identified 259 urinary proteins and analyzed their tissue origin and function, out of which 23 increased and one decreased with age. Although the list of major differentially expressed proteins in urine does not correspond with major ones detected in plasma, however, there seems to be a strong correlation between the molecular weight and the amount of protein clearance with age, which can be associated with increased “leakage”, as the kidney loses its protein retaining ability [85]. Therefore, an investigation into plasma protein molecular weight can elucidate this filtration organ’s role in their signature over time. Table 2 lists major plasma proteins affected by age and their molecular weight. Interestingly, apart from SCARF2, all proteins that increase with age within the bloodstream seem to have a small (< 40 kDa) to medium (40–100 kDa) molecular weight. On the other hand, while some small and medium molecular weight proteins seem to decrease with age, large molecular weight plasma proteins (> 100 kDa) that decrease with age include IGDCC4, RET, and THBS4. Additionally, the tissue origin of urine proteins that significantly correlate with age can be traced back to the gonads and bones, then the liver, the pancreas, the kidneys, the spleen, and the soft tissue, followed by the intestines and the larynx, in descending order [85].

Table 1. Clusters of protein trajectories that reflect changes with age coinciding with the onset of aging, and the top 10 plasma proteins involved in them [72].

Top 10 Plasma Protein Pathways Increasing with Age		Top 10 Plasma Protein Pathways Decreasing with Age	
			
			
Extracellular Region	Chondroitin Sulfate Biosynthesis	Extracellular Space	Transmembrane Receptor Activity
ADAMTS5/ASPN/C10NF1/.../ TREML4/TTN/VEGFA/VIT	CHST19/DCN/BGN/CHST11	ACE2/ADAMTS3/AHSG/AIMP1/.../SPIN1/TF/TNXB/UBB	EGFR/KDR/RET
Extracellular Region Part	Heparan Sulfate Metabolism	Blood Microparticle	Tyrosine Kinase Activity
ADAMTS5/ASPN/.../ TNFSF15/TTN/VEGFA/VIT	DCN/BGN/GPC6/GLCE/H3S3T3A1	AHSG/APOLI7/CFB/.../ IGLL1/TH1H1/PLG/SERPINC1/TF	EGFR/KDR
Extracellular Space	Chondroitin Sulfate Metabolism	Fibrillar Collagen Trimer	Integrin Binding
ADAMTS5/C10NF1/.../ TNFRSF1B/TNFSF15/VEGFA	CHST9/DCN/BGN/GPC6/CHST11	COL11A2/COL1A1/TNXB	ADAMTS13/EGFR/KDR
Proteinaceous Extracellular Matrix	Regulation of IFNG Signaling	Banded Collagen Fibril	Protein Kinase Activity
ADAMTS5/ASPN/CH13L1/.../ TNFRSF11B/VEGFA/VIT	STAT1/SOCS3/PTPN11	COL11A2/COL1A1/TNXB	EGFR/KDR/RET
Glycosaminoglycan binding	Glycosaminoglycan Metabolism	Extracellular Region	Midgut Development
ADAMTS5/CXCL10/GREM2/.../ SRP1/THBS3/VEGFA/VIT	CHST9/DCN/BGN/GPC6/CHST11/GLCE/ H3S3T3A1	ACE2/ADAMTS3/AGER/.../ TMEM132A/TNR/TNXB/UBB	EGFR/RET
Heparin Binding	Interleukin-6 signaling	Extracellular Region Part	Hormone Binding
ADAMTS5/CXCL10/GREM2/.../ SRP1/THBS3/VEGFA	STAT1/SOCS3/PTPN11	ACE2/ADAMTS3/.../ TF/TMEM132A/TNR/TNXB/UBB	EGFR/GHR
Sulfur Compound Binding	Defective B4GALT7, Progeroid	Proteinaceous Extracellular Space	Protein Complex Binding
ADAMTS5/CD34/.../ SRP1/THBS3/VEGFA	DCN/BGN/GPC6	CCDC80/MMP12/PTN	ADAMTS13/CTS/VEGFR/KDR
G-protein Coupled Receptor Binding	Defective B3GAT3	BMP Signaling Pathway	Transmembrane Signaling Receptor Activity
CCL3/CXCL10/CXCL16/.../ NPW/POMC/PPY/RSPO3/SRP1	DCN/BGN/GPC6	CHRDLL1/FSTL3/GDF15	EGFR/GHR/KDR/RET
Chitin Binding	Defective B3GALT6	Response to BMP	Macromolecular Complex Binding
CH13L1/CHIT1/CTBS	DCN/BGN/GPC6	CHRDLL1/FSTL3/GDF15	EGFR/GHR/KDR/RET
Extracellular Matrix	Particulate Exogenous Antigens	Cellular Response to BMP	Protein Tyrosine Kinase Activity
ADAMTS5/ASPN/.../ TIMP4/TNFRSF11B/VEGFA/VIT	CD36/ITGAV	CHRDLL1/FSTL3/GDF15	ADAMTS13/CTS/VEGFR/KDR

On the other hand, investigating the possible association of a number of identified plasma proteins with kidney function may lead to insights into the possible involvement of renal function in a mechanistic way. However, such inferences can only be confirmed via direct investigations to verify their causative association with an aging phenotype. For example, higher serum levels of SOST, one of the proteins that increases with age, is associated with reduced GFR, body mass index, male gender, and diabetes, in addition to heritability [86]. Additionally, a chronic heart failure marker, namely GDF15, correlates with parameters of kidney function [87,88]. Interestingly, β -2 microglobulin, one of the most well-established plasma factors of aging that is associated with inflammation [52], cardiovascular events [53], impaired cognitive function [84], and even tumorigenesis [54], has been shown to directly correlate with GFR [55]. This cellular metabolic product that is normally filtered out directly via the glomerulus, accumulates over time in the system as a function of reduced kidney function, to a point that it can arguably be used as a novel GFR marker [55]. Another circulating factor that has been heavily studied as an aging marker in relation with neural degeneration is eotaxin-1 (CCL-11) [56], which belongs to a chemokine family and is linked to inflammation and allergic reactions [57]. Nevertheless, although increased levels of cytokines and chemokines in plasma are largely regarded as systemic senescence parameters of aging, interestingly, according to one *in vivo* study, cytokine production increases due to induced bilateral nephrectomy, concomitant with decreased cytokine clearance [58]. Additionally, according to several studies, levels of cytokines and chemokines in plasma can be used as markers of kidney disease [89].

Table 2. The molecular weight of plasma proteins that are affected with age.

Plasma Proteins that Increase with Age	Abbreviation	Molecular Weight (kda)	Ref.	Plasma Proteins That Decrease with Age	Abbreviation	Molecular Weight (kda)	Ref.
Motilin	MLN	5.19	[90]	Cadherin-13	CDH13	7.57	[91]
Eotaxin	CCL11	10.73	[92]	Apelin	APLN	8.57	[93]
C-CMotif Chemokine 19	CCL19	10.99	[92]	Osteocalcin	OCN(BGLAP)	10.96	[94]
C-CMotif Chemokine 2	CCL2	11.03	[92]	Somatostatin	GHRH	12.45	[95]
β -2-Microglobulin	B2M	11.73	[96]	Oxytocin-Neurophysin 1	OXT	12.72	[97]
Natriuretic Peptides B	NPPB	14.73	[98]	Granulocyte-Macrophage Colony-Stimulating Factor	CSF2	16.3	[99]
Pleiotrophin	PTN	18.95	[90, 98]	Metalloproteinase Inhibitor 2	TIMP2	24.4	[99]
A Disintegrin And Metalloproteinase with Thrombospondin Motifs 5	ADAMTS5	21.7	[98]	Growth Differentiation Factor 11	GDF11	45.1	[100]
Sclerostin	SOST	24.03	[90, 98]	Extracellular Nicotinamide Phosphoribosyltransferase	eNAMPT	55.53	[101]
Growth Differentiation Factor 15	GDF15	34.15	[90, 98]	Thrombospondin-4	THBS4	96.03	[102]
Cathepsin L2	CTSV	37.33	[98]	Proto-Oncogene Tyrosine-Protein Kinase Receptor Ret	RET	124.39	[90]
Adp Ribosylation Factor Interacting Protein 2	ARFIP2	37.86	[90]	Immunoglobulin Superfamily Dcc Subclass Member 4	IGDCC4	134.23	[90]
Haptoglobin	HP	45.21	[92]				
Chordin-Like Protein 1	CHRDL1	51.18	[98]				
Macrophage Metalloelastase	MMP12	54.01	[98]				
Egf-Containing Fibulin-Like Extracellular Matrix Protein 1	EFEMP1	54.65	[98]				
Scavenger Receptor Class F Member 2	SCARF2	92.4	[90]				

In conclusion, the intertwined role of kidney function into the various hallmarks of aging is clear; however, its causative association with aging requires rigorous investigation in order to elucidate the exact role of this filtration organ on the aging phenotype.

5. Rejuvenation Strategies: Systemic versus Targeted

From an engineering perspective, systemic factors, as those associated with the working fluid and its integrity, seem to hold precedence over other rejuvenation methods, based on the aging analysis presented earlier. Such a view is backed up by several publications on the rejuvenating effects of young plasma on age-related diseases in animal models [89,103–105]. Nevertheless, despite their success, these results are yet to be translated into clinical use, as presently their efficacy hasn't been demonstrated in the limited number of clinical trials conducted thus far [106,107]. Alternatively, assessments of the main drivers of these positive effects led to the discovery of

“circulating rejuvenation factors” in blood plasma [108–110]. Interestingly, investigations from Berkeley University led by Dr. Conboy’s group demonstrated that without the benefits of “shared organs” in heterochronic parabiosis animal models, the effect of young plasma in old animals is different, although still present. In addition, an accelerated aging effect due to old blood is more pronounced than the rejuvenating effects of young blood [111]. More importantly, a recent study by the same group demonstrated that replacing half of the plasma of old mice with a mixture of saline and albumin is sufficient to produce rejuvenating effects that meet, or even exceed, those observed in heterochronic parabiosis [112]. The importance of such findings cannot be underestimated, as it outlines the effect of contaminant buildup in the bloodstream on aging and disease manifestations for the first time. Additionally, it might provide a more translatable clinical solution to plasma transfer, which is riddled with issues of compatibility, possible contamination, and limited resources. What remains to be clarified though is the effect such methods have on the biological clock itself, and how frequent blood “purification” procedures would be required to maintain a youthful/healthy status.

Clinical experience from dialysis patients, as well as the few clinical trials that have tested the concept of plasma exchange with specific components, show that improvements come in a seesaw fashion that is often exhausting and inflicts organismal fatigue that may be detrimental to the general system homeostasis [15,112–114]. This brings back into question the efficacy of highly aggressive intermittent interventions versus a more constant and stable long-term solution and redirects the discussion towards the possible effect of “shared organs” in heterochronic parabiosis models. In particular, it is worth addressing the role of filtration organs such as the kidney, as they are directly implicated in clearing toxic buildup from the blood stream. As such, would a kidney-specific rejuvenation scheme be the ultimate answer to a translatable medical solution for aging? It is clear by now that there is an association between kidney function and some identified plasma circulating factors that are implicated in aging. Nevertheless, it is also worth evaluating the increasing body of targeted rejuvenating agents that have shown promising results, with some managing to turn the aging clock of DNA methylation by 2.5 years [115]; namely, the nutrient-sensing pathway, cell senescence and a senescence-associated secretory phenotype (SASP), in addition to epigenetic interventions.

5.1. Targeting Nutrient-Sensing Pathways

Aging and two of the most prominent chronic diseases mostly associated with it, diabetes and obesity, share the deregulation of nutrient sensing pathways and sporadic low-grade inflammation. A deregulated metabolism has been shown to be a function of the activation of high nutrient-sensing pathways, such as insulin and insulin-like growth factor 1 (IGF-1), that in turn target the forkhead box O transcription factor (FOXO) and mechanistic target of rapamycin (mTOR) complexes. This is accompanied by the downregulation of low nutrient-sensing ones, such as AMP-activated protein kinase (AMPK) and Sirtuins [116]. The effect of these pathways on cellular aging has been solidified by countless studies that stretch back to the earliest rejuvenation investigations based on calorie restriction (CR) [8]. In this regard, it has been demonstrated that blocking one of the pathways or gene targets of IGF-1 or mTOR can be linked with increased energy expenditure, enhanced activity of brown adipose tissue, and improved mitochondrial oxidative metabolism [117]. In fact, these effects have been observed previously in dietary restriction with regards to longevity across all species, which is believed to shift cellular metabolism towards maintenance instead of reproduction and growth [118]. Additionally, mTOR signaling is a key regulator of cell cycle arrest and autophagy [119], which is essential in suppressing the accumulation of senescent cells, making it an interesting target for both senolytic and nutrient-sensing rejuvenation schemes. Moreover, while insulin and IGF-1 pathways are naturally decreased in normal, as well as in accelerated aging, their forced inhibition seems to correlate with longevity and rejuvenation [120].

Other nutrient-sensing pathways have also been investigated heavily in relation to aging, including those that decrease with age, such as Sirtuins that rely on NAD⁺, a critical

coenzyme in metabolism [121]. Pharmacological enhancement of NAD⁺ supplements has shown beneficial effects on a range of metabolic diseases, nevertheless, singling out this pathway has also been linked with increased SASP and tumorigenesis associated with the accumulation of senescent cells and the inflammatory response, all of which contribute to aging [122].

To be sure, nutrient-sensing pathways have been the most well-established avenue thus far when it comes to healthy aging, with several documented clinical trials and data to back up the advantages and trade-offs associated with it. The most promising pharmaceutical interventions targeting these pathways to date are Rapamycin [123], Metformin [124], and Resveratrol [125], to name only a few. Nevertheless, it is important to keep in mind that targeted therapies, especially pharmaceutical interventions that are used continuously, often come with shortcomings that would eventually limit their benefit. This is not surprising, given the complex and intertwined nature of nutrient signaling pathways with those of the cell cycle, apoptosis, and autophagy. Rapamycin for example, which is the most restricted drug within this category, is a known immunosuppressant and used as a part of the chronic regiment of organ transplant patients, which provides an obvious set of drawbacks for its continuous use.

On the other hand, while studies on the possible involvement of Metformin in dementia and memory loss are contradictory [126,127], its role in diminishing the absorption of vitamin B12 resulting in possible nerve damage or anemia, is well documented [128]. Additionally, Metformin is implicated in lactic acidosis and kidney damage, which might be aggravated by reduced kidney function [129,130]. While these risks are not considered a major concern for diabetes patients since their condition is already a risk factor for nerve damage and inflammation, the use of this drug for longevity purposes might be controversial without a proper long-term assessment of its effects. Conversely, Resveratrol is a natural phenol found in many plants, making it a widely available food supplement that has been shown to improve health, including renal and cognitive functions [131] rather than demonstrating tangible effects on the lifespan [125]. More importantly, effective doses used in aging literature far surpass the daily doses available in the market. Thus, as promising as these interventions may be, even the most benign of which, such as caloric restriction, has been found to have conflicting results on different species [132]. Therefore, it is obvious that systemic rather than targeted therapies can be considered as a more sustainable avenue towards rejuvenation, bringing the spotlight towards the organs that are mostly involved in nutrient regulation.

The “filtration” organ that is mostly associated with metabolism is the liver, as it is responsible for regulating most metabolic pathways including glucose, lipids, and insulin sensitivity. Therefore, it is not surprising to consider the aging liver, particularly liver sinusoidal endothelial cells (LSECs), as contributors to biological aging [133]. Additionally, the liver is linked with the production of methyl compounds, that are involved in DNA methylation, one of the main hallmarks and quantifiers of biological aging [134]. Nevertheless, despite the liver’s central role, only a limited number of studies have been dedicated to the full elucidation of its exact role in aging. Thus, more studies are warranted to understand the effect of the liver on aging and rejuvenation. Nonetheless, it is worth noting that, unlike the kidneys, the liver has unique aging characteristics that mostly manifest over the age of 60 [90], by which time, biological aging hallmarks are already set in most populations, which alleviates its direct implication in aging as a causative agent, or limits it to certain age-associated disease phenotypes. On the other hand, the kidney, the organ that escorts the body in its aging journey, and is responsible for clearing metabolic waste from the bloodstream, can also be implicated in metabolism due to its role in vitamin D synthesis [98], the deficiency of which has been shown to participate in aging, metabolism, and age-associated diseases [98,100].

5.2. Senolytic Drugs, the New Pharmacological Focus of Rejuvenation

Although the word senescence is derived from its Latin origin meaning “old”, its implication in propagating the aging process itself has been, up until recently, controversial. This controversy is due to the mostly beneficial views towards senescence, particularly with regards to tissue repair [99], wound healing [95], protection against cancer progression [93], and embryonic development [91]. Therefore, cell senescence was generally regarded as a product of aging, induced by telomere attrition, rather than a possible causative agent. However, a closer examination of the effect of senescent cells on the extracellular milieu, in particular SASP, elucidated the detrimental effects of this phenomenon on aging tissues and organs [101]. The state of proliferation arrest that defines senescent cells is recognized now as a metabolically active state that secretes cytokines, chemokines, proteases, and growth factors that include among others, interleukins (IL-1 β , IL-6, IL-8), TGF β 1, and WNT16B, which propagate senescence across tissues and organs [101]. Markers associated with senescence are cyclin-dependent kinase inhibitors p16^{INK4a} and p21CIP1, which are implicated in cell-cycle arrest [91,101]. This clear senescence marker identification, and the advent of animal models lacking p16^{INK4a} in 2001 by two different groups [94,102], or INK-ATTAC transgenic mice that allow for the elimination of cells over-expressing p16^{INK4a} using a targeted drug [96], permitted a clear demonstration of the major effect of cellular senescence on biological aging. Based on these findings, it is clear that cellular senescence is one of the clearest examples of antagonistic pleiotropy [135,136].

A study conducted by Baker et al. (2016) using INK-ATTAC transgenic mice, was able to show that senescent cell ablation extends the lifespan, delays tumorigenesis, and attenuates age-related diseases. This method, however, caused partial and tissue-selective removal of senescent cells, with varying degrees on different organs [96]. In particular, while this method did not affect the colon and the liver, it had a very noticeable effect on the kidneys, the heart, and the adipose tissue. More importantly, senescent cells appear to have specific effects on different organs rather than a uniform systemic role. In this study, it was shown that it caused a hyper-activation of the local renin–angiotensin–aldosterone system (RAAS), progenitor cell dysfunction, and cardiac Sur2a downregulation in kidney, adipose, and heart tissues of old mice, respectively [96]. This variation in SASP mechanistic action opens speculation on the scope of SASP effect and whether this senescence-associated secretome can differ from one tissue to another, and more importantly, if such tissue-specific extracellular vesicles can be traced back in plasma to their original source, thus defining the extent of specific organ SASP on surrounding tissues, organs, and systems.

Several clinical trials are being performed presently to investigate the therapeutic effect of senescent cell ablation on specific organs and medical conditions, such as the kidney (NCT02848131) and osteoarthritis (NCT03513016). Such pharmaceutical interventions include the use of Dasatinib and Quercetin in a controlled manner and over a short period of time. Although the results obtained thus far seem to be promising, given the important role of cell senescence in general physiological functions, such treatment modalities can be used intermittently to remove the excess accumulation of senescent cells that otherwise would overwhelm the immune system. Nevertheless, the effectiveness and long-term benefits of such an approach remains to be determined.

5.3. Cellular Reprogramming and Genetic Rejuvenation

When it comes to addressing the concept of “rejuvenation” as opposed to healthy aging, cellular reprogramming is the only one to show a significant reversal of cellular aging hallmarks. Therefore, this promising experimental procedure holds amazing promise for future applications, including system and organ-specific rejuvenation. In 2007, Yamanaka factors were identified after the extensive stripping of transcription factors down to four distinct genes: octamer-binding transcription factor 4 (OCT4), Kruppel-like factor 4 (KLF4), SRY (sex-determining region Y)-box 2 (SOX2), and proto-oncogene MYC (C-MYC), that were dubbed OKSM [137]. Concurrently, Yu et al. introduced another set of four reprogramming factors that included OCT3/4, SOX2, NANOG, and LIN-28 [138]. Since then, other

reprogramming agents were presented including micro-RNAs (miRNA) [139,140] and long non-coding RNAs (lncRNA) [141] that aid in the partial reprogramming of somatic cells into different types, otherwise called trans-programming. However, such methods preserve the methylation profile of the original cell, thereby preserving their cellular age profile [139,140]. The importance of cell reprogramming, however, extends beyond aging towards the creation of small organoids that can potentially be harvested and used to treat certain diseases, where preservation of DNA age and methylation are considered beneficial.

Thus far, the major issue that hinders the development of this rejuvenating intervention in a clinical setting is its unpredictability due to the complete reversal of the somatic cell into an induced pluripotent stem cell (iPSC) state. Thus, the manner in which these cells would develop *in vivo* is highly dependent on extracellular conditions and cannot be guaranteed to adopt a restorative or a regenerative role if surrounded by disease phenotypes. Such inferences can be made based on the numerous studies conducted on stem cell organ and tissue regeneration [141–143]. However, the most attractive feature of cell reprogramming is that once differentiated *in vitro* into specific cell types, cells can retain a youthful methylation and transcriptomic profile, although this might require additional treatment to ensure resetting the methylation signature of the cell [144]. However, successful methods of reverting cellular aging markers, including their methylation signature, without the induction of cell de-differentiation, are yet to be accomplished. Regardless, *in vivo* partial rejuvenation was effective using short term induction of Yamanaka factors, which restored DNA damage and ameliorated certain aging hallmarks such as deregulated histone and senescence-associated genes leading to a 20% increase in the lifespan of these animal models [145]. This success though does not diminish the possibility of developing other disease conditions or phenotypes, as more comprehensive research is still needed in this area to ensure its safety and translatability into clinical applications.

6. Future Outlook and Conclusions

Given the clear differences between a biological system and a mechanical one, any comparison must consider the inherent complexity of biological components, particularly when it comes to the diverse roles that each organ plays and the often-overlapping functions within the system in general. As such, an association of a single organ, such as the kidney, with the complex phenomenon of aging can only be taken as a percent involvement instead of an absolute one. Nevertheless, it is obvious, that contaminant build-up in the working fluid is responsible for significant health issues typically associated with aging. Based on such evidence, specific studies designed to isolate the effect of reduced kidney function on aging are warranted, particularly in the absence of such inferences in the field to date. More importantly, establishing rigorous methods to evaluate the percentage role of specific organs in aging might help establish organ-specific intervention methods that can make use of existing therapeutics and rejuvenation techniques in a more translatable manner.

Organ-specific therapeutics, for example, have seen incredible advances over the past decade, with such methods relying on cell reprogramming techniques to provide long-term solutions for a set of chronic diseases. The use of organoids to restore the functionality of some organs, such as the liver, is one of the most promising therapeutic approaches to date [144,146]; although, there are still many challenges that need to be addressed [147]. Organoid and stem cell-based kidney-specific therapeutics are already advancing presently [148,149]. The main challenge that such treatment modalities face is that they are used as a last resort against severe disease conditions, which entails highly toxic cellular microenvironments. However, repurposing these techniques to treat reduced organ function associated with specific age milestones might eventually be more successful in organ and system maintenance in general.

From a biomedical engineering perspective, future interventions can hold some interesting diagnostic and therapeutic solutions. Such designs are still under investigation, however, the need for an implantable diagnostic tool to successfully measure and report the plasma levels of known toxins, hazardous agents, and disease markers, can potentially

help prevent and resolve disease conditions at their early stages [150]. Particularly since, once the symptoms of aging associated diseases manifest, existing therapeutics become increasingly limited. This is particularly important in the context of rejuvenation studies, as aging tends to take hold before any specific disease phenotype is manifested. Further advancements in implantable technology can potentially be actively involved, instead of passively reporting diagnostic data wirelessly [151]. Such devices can potentially remove toxic components in a selective manner and store them until it reaches saturation, only to be removed and replaced with another membrane. This additional filtration mechanism could possibly prevent an extensive list of chronic diseases while providing medical screening and diagnostic tools. Presently though, advances in medical research are far more advanced than their counterparts in biomedical engineering, which is fraught with several challenges and restrictions that hinders their swift development [152]. In particular, implantable devices have to be biocompatible while ensuring an optimum interface with their surrounding tissue and fluids [153]. Tissue build-up is a common problem that such devices face, which causes a reduction in the efficacy of sensors and detectors in an exponential manner [154]. Additionally, other engineering concerns include battery lifecycle [155], degradation over time [151], and information transmissibility [156]. While some of these issues have been addressed by the advent of several biocompatible and non-toxic implantable materials, the design of a completely independent long-term implantable device that relies on implantable *in vivo* energy-harvesting fuel cells is still challenging. Thus, while future medical solutions can be very promising, present biomedical knowledge can successfully tackle aging diseases successfully once efforts are directed towards biological systems maintenance instead of damage control.

In conclusion, we herein attempt to provide a general platform to address aging, where we stress the importance of having standardized biometrics used in rejuvenation studies. Such a platform can potentially allow for the assessment and comparison of any advances made in the field and build upon their success. More importantly, we herein attempt to shine a light on a rejuvenation avenue that has been largely overlooked. The new methodology targets the kidney specifically, which has an aging profile that coincides with overall systemic aging, based on the possible role of filtration organs and contaminant build up on aging. This hypothesis is further examined by reviewing the involvement of the kidney in various known aging factors and after listing existing rejuvenation methods, the possibility of focusing some of these on kidney maintenance becomes very interesting within the context of systemic rejuvenation. The possible involvement of the kidney in aging brings about the need for a large body of research to confirm its direct role in this process. Additionally, once established, numerous rejuvenation methods can be explored in order to maintain the functionality of the kidney as a filtration system or bring about diagnostic or other engineering solutions to aid with the filtration process. However, given that this particular topic has not been explored so far, and in the absence of any direct findings on the possible involvement of the kidney in aging, this presents a major challenge or a limitation in the present review, as this hypothesis hinges on the amazing results presented by Mehdipour et al., (2020), where replacement of plasma with a mixture of saline and albumin was sufficient to produce the same rejuvenation effects observed in heterochronic parabiosis. Additionally, the role of the central nervous system, and in particular the effect of hypothalamus aging on energy homeostasis, hormone balance, circadian rhythm, nutrient sensing dysfunction, stem cell exhaustion, loss of proteostasis, and epigenetic alterations was not discussed [157,158], focusing more on major pathways of rejuvenation studies instead. Thus, it is obvious that several studies are necessary to elucidate the exact role of filtration on aging, but it is our belief that such an approach is indeed warranted and merits further exploration.

Author Contributions: All authors contributed equally in this manuscript. All authors have read and agreed to the published version of the manuscript.

Funding: This work is supported by the research funding granted to Satya Prakash from Canadian Institute of Health Research (CIHR) Fund #201903PJT420512-PS-CFAA-47491.

Institutional Review Board Statement: Not applicable.

Informed Consent Statement: Not applicable.

Data Availability Statement: Not applicable.

Acknowledgments: Data in Table 1 were reproduced with the approval of Lehallier et al. as shown in attached document.

Conflicts of Interest: The authors declare no conflict of interest.

References

1. Mahmoudi, S.; Xu, L.; Brunet, A. Turning back time with emerging rejuvenation strategies. *Nat. Cell Biol.* **2019**, *21*, 32–43. [CrossRef] [PubMed]
2. Katcher, H.L. Towards an evidence-based model of aging. *Curr. Aging Sci.* **2015**, *8*, 46–55. [CrossRef] [PubMed]
3. Campisi, J.; Kapahi, P.; Lithgow, G.J.; Melov, S.; Newman, J.C.; Verdin, E. From discoveries in ageing research to therapeutics for healthy ageing. *Nature* **2019**, *571*, 183–192. [CrossRef] [PubMed]
4. Friedman, S.M. Lifestyle (Medicine) and Healthy Aging. *Clin. Geriatr. Med.* **2020**, *36*, 645–653. [CrossRef]
5. Sellami, M.; Bragazzi, N.L.; Slimani, M.; Hayes, L.; Jabbour, G.; De Giorgio, A.; Dugué, B. The effect of exercise on glucoregulatory hormones: A countermeasure to human aging: Insights from a comprehensive review of the literature. *Int. J. Environ. Res. Public Health* **2019**, *16*, 1709. [CrossRef]
6. Nilsson, M.I.; Tarnopolsky, M.A. Mitochondria and aging—The role of exercise as a countermeasure. *Biology* **2019**, *8*, 40. [CrossRef]
7. Watanabe, M. Smoking: Additional burden on aging and death. *Genes Environ.* **2016**, *38*, 3. [CrossRef]
8. Ottinger, M.A. A Comparative Approach to Metabolic Aspects of Aging: Conserved Mechanisms and Effects of Calorie Restriction and Environment. *Prog. Mol. Biol. Transl. Sci.* **2018**, *155*, 109–127.
9. Brosky, N.T.; Marlatt, K.L.; Most, J.; Erickson, M.L.; Irving, B.A.; Redman, L.M. The Panacea of Human Aging: Calorie Restriction Versus Exercise. *Exerc. Sport Sci. Rev.* **2019**, *47*, 169–175. [CrossRef]
10. Badal, V.D.; Vaccariello, E.D.; Murray, E.R.; Yu, K.E.; Knight, R.; Jeste, D.V.; Nguyen, T.T. The gut microbiome, aging, and longevity: A systematic review. *Nutrients* **2020**, *12*, 3759. [CrossRef]
11. Ottens, F.; Franz, A.; Hoppe, T. Build-UPS and break-downs: Metabolism impacts on proteostasis and aging. *Cell Death Differ.* **2021**, *28*, 505–521. [CrossRef] [PubMed]
12. De Cabo, R.; Mattson, M.P. Effects of Intermittent Fasting on Health, Aging, and Disease. *N. Engl. J. Med.* **2019**, *381*, 2541–2551. [CrossRef] [PubMed]
13. Hillson, O.; Gonzalez, S.; Rallis, C. Prospects of Pharmacological Interventions to Organismal Aging. *Biomol. Concepts* **2018**, *9*, 200–215. [CrossRef] [PubMed]
14. Ros, M.; Carrascosa, J.M. Current nutritional and pharmacological anti-aging interventions. *Biochim. Biophys. Acta-Mol. Basis Dis.* **2020**, *1866*, 165612. [CrossRef]
15. Kheifets, V.; Braithwaite, S.P. Plasma-Based Strategies for Therapeutic Modulation of Brain Aging. *Neurotherapeutics* **2019**, *16*, 675–684. [CrossRef]
16. Goya, R.G.; Lehmann, M.; Chiavellini, P.; Canatelli-Mallat, M.; Hereñú, C.B.; Brown, O.A. Rejuvenation by cell reprogramming: A new horizon in gerontology. *Stem Cell Res. Ther.* **2018**, *9*, 349. [CrossRef]
17. Singh, P.B.; Newman, A.G. Age reprogramming and epigenetic rejuvenation. *Epigenetics Chromatin* **2018**, *11*, 73. [CrossRef]
18. Lehmann, M.; Canatelli-Mallat, M.; Chiavellini, P.; Cónsole, G.M.; Gallardo, M.D.; Goya, R.G. Partial Reprogramming As An Emerging Strategy for Safe Induced Cell Generation and Rejuvenation. *Curr. Gene Ther.* **2019**, *19*, 248–254. [CrossRef]
19. Kuo, C.-L.; Pilling, L.C.; Liu, Z.; Atkins, J.L.; Levine, M.E.; Levine, M.; Kuo, C.-L. Genetic associations for two biological age measures point to distinct aging phenotypes. *Aging Cell* **2021**, *20*, e13376. [CrossRef]
20. Guerville, F.; De Souto Barreto, P.; Ader, I.; Andrieu, S.; Casteilla, L.; Dray, C.; Fazilleau, N.; Guyonnet, S.; Langin, D.; Liblau, R.; et al. Revisiting the Hallmarks of Aging to Identify Markers of Biological Age. *J. Prev. Alzheimer's Dis.* **2020**, *7*, 56–64. [CrossRef]
21. Vandenberg, B.; Brouwers, B.; Hatse, S.; Wildiers, H. P16INK4a: A central player in cellular senescence and a promising aging biomarker in elderly cancer patients. *J. Geriatr. Oncol.* **2011**, *2*, 259–269. [CrossRef]
22. Mensà, E.; Latini, S.; Ramini, D.; Storci, G.; Bonafè, M.; Olivieri, F. The telomere world and aging: Analytical challenges and future perspectives. *Ageing Res. Rev.* **2019**, *50*, 27–42. [CrossRef] [PubMed]
23. Fasching, C.L. Telomere length measurement as a clinical biomarker of aging and disease. *Crit. Rev. Clin. Lab. Sci.* **2018**, *55*, 443–465. [CrossRef] [PubMed]
24. McCrory, C.; Fiorito, G.; Hernandez, B.; Polidoro, S.; O'Halloran, A.M.; Hever, A.; Ni Cheallaigh, C.; Lu, A.T.; Horvath, S.; Vineis, P.; et al. GrimAge outperforms other epigenetic clocks in the prediction of age-related clinical phenotypes and all-cause mortality. *J. Gerontol. Ser. A* **2020**, *76*, 741–749. [CrossRef]

25. Horvath, S.; Raj, K. DNA methylation-based biomarkers and the epigenetic clock theory of ageing. *Nat. Rev. Genet.* **2018**, *19*, 371–384. [CrossRef]
26. Krutmann, J.; Bouloc, A.; Sore, G.; Bernard, B.A.; Passeron, T. The skin aging exposome. *J. Dermatol. Sci.* **2017**, *85*, 152–161. [CrossRef]
27. Zhang, S.; Duan, E. Fighting against Skin Aging: The Way from Bench to Bedside. *Cell Transplant.* **2018**, *27*, 729–738. [CrossRef]
28. Bonewald, L. Use it or lose it to age: A review of bone and muscle communication. *Bone* **2019**, *120*, 212–218. [CrossRef]
29. Carina, V.; Della Bella, E.; Costa, V.; Bellavia, D.; Veronesi, F.; Cepollaro, S.; Fini, M.; Giavaresi, G. Bone's Response to Mechanical Loading in Aging and Osteoporosis: Molecular Mechanisms. *Calcif. Tissue Int.* **2020**, *107*, 301–318. [CrossRef]
30. Sierra, F.; Kohanski, R. *Advances in Geroscience*; Springer: Berlin/Heidelberg, Germany, 2016.
31. Alexander, J.W.; Bennett, L.E.; Breen, T.J. Effect of donor age on outcome of kidney transplantation. A two-year analysis of transplants reported to the United Network for Organ Sharing Registry. *Transplantation* **1994**, *57*, 871–876. [CrossRef]
32. Stenvinkel, P.; Larsson, T.E. Chronic Kidney Disease: A Clinical Model of Premature Aging. *Am. J. Kidney Dis.* **2013**, *62*, 339–351. [CrossRef]
33. Langen, R.C.J.; Gosker, H.R.; Remels, A.H.V.; Schols, A.M.W.J. Triggers and mechanisms of skeletal muscle wasting in chronic obstructive pulmonary disease. *Int. J. Biochem. Cell Biol.* **2013**, *45*, 2245–2256. [CrossRef]
34. Crowson, C.S.; Liang, K.P.; Therneau, T.M.; Kremers, H.M.; Gabriel, S.E. Could accelerated aging explain the excess mortality in patients with seropositive rheumatoid arthritis? *Arthritis Rheum.* **2010**, *62*, 378–382. [CrossRef]
35. Amann, K.; Ritz, E. Cardiovascular abnormalities in ageing and in uraemia—only analogy or shared pathomechanisms? *Nephrol. Dial. Transplant* **1998**, *13* (Suppl. 7), 6–11. [CrossRef]
36. Pathai, S.; Lawn, S.D.; Gilbert, C.E.; McGuinness, D.; McGlynn, L.; Weiss, H.A.; Port, J.; Christ, T.; Barclay, K.; Wood, R.; et al. Accelerated biological ageing in HIV-infected individuals in South Africa: A case-control study. *AIDS* **2013**, *27*, 2375–2384. [CrossRef]
37. Kooman, J.P.; Broers, N.J.H.; Usvyat, L.; Thijssen, S.; van der Sande, F.M.; Cornelis, T.; Levin, N.W.; Leunissen, K.M.L.; Kotanko, P. Out of control: Accelerated aging in uremia. *Nephrol. Dial. Transplant.* **2013**, *28*, 48–54. [CrossRef]
38. Kooman, J.P.; Kotanko, P.; Schols, A.M.W.J.; Shiels, P.G.; Stenvinkel, P. Chronic kidney disease and premature ageing. *Nat. Rev. Nephrol.* **2014**, *10*, 732–742. [CrossRef]
39. López-Otín, C.; Blasco, M.A.; Partridge, L.; Serrano, M.; Kroemer, G. The Hallmarks of Aging. *Cell* **2013**, *153*, 1194–1217. [CrossRef]
40. Aunan, J.R.; Watson, M.M.; Hagland, H.R.; Søreide, K. Molecular and biological hallmarks of ageing. *Br. J. Surg.* **2016**, *103*, e29–e46. [CrossRef]
41. Yates, D. Blood-derived rejuvenation. *Nat. Rev. Neurosci.* **2014**, *15*, 352–353. [CrossRef]
42. Conboy, I.M.; Rando, T.A. Heterochronic parabiosis for the study of the effects of aging on stem cells and their niches. *Cell Cycle* **2012**, *11*, 2260–2267. [CrossRef]
43. Conboy, M.J.; Conboy, I.M.; Rando, T.A. Heterochronic parabiosis: Historical perspective and methodological considerations for studies of aging and longevity. *Aging Cell* **2013**, *12*, 525–530. [CrossRef]
44. Portugal-Nunes, C.; Costa Castanho, T.; Amorim, L.; Silva Moreira, P.; Mariz, J.; Marques, F.; Sousa, N.; Correia Santos, N.; Almeida Palha, J. Iron status is associated with mood, cognition, and functional ability in older adults: A cross-sectional study. *Nutrients* **2020**, *12*, 3594. [CrossRef]
45. Rył, A.; Miazgowski, T.; Szylińska, A.; Turoń-Skrzypińska, A.; Jurewicz, A.; Bohatyrewicz, A.; Rotter, I. Bone health in aging men: Does zinc and cuprum level matter? *Biomolecules* **2021**, *11*, 237. [CrossRef]
46. Parmalee, N.L.; Aschner, M. Manganese and aging. *Neurotoxicology* **2016**, *56*, 262–268. [CrossRef]
47. Gorell, J.M.; Johnson, C.C.; Rybicki, B.A.; Peterson, E.L.; Kortsha, G.X.; Brown, G.G.; Richardson, R.J. Occupational exposures to metals as risk factors for Parkinson's disease. *Neurology* **1997**, *48*, 650–658. [CrossRef]
48. Eriksen, B.O.; Palsson, R.; Ebert, N.; Melsom, T.; van der Giet, M.; Gudnason, V.; Indridason, O.S.; Inker, L.A.; Jenssen, T.G.; Levey, A.S.; et al. GFR in healthy aging: An individual participant data meta-analysis of iohexol clearance in european population-based cohorts. *J. Am. Soc. Nephrol.* **2020**, *31*, 1602–1615. [CrossRef]
49. Cirillo, M.; Laurenzi, M.; Mancini, M.; Zanchetti, A.; Lombardi, C.; De Santo, N.G. Low glomerular filtration in the population: Prevalence, associated disorders, and awareness. *Kidney Int.* **2006**, *70*, 800–806. [CrossRef]
50. Mahbub, M.H.; Yamaguchi, N.; Takahashi, H.; Hase, R.; Yamamoto, H.; Kikuchi, S.; Tanabe, T. Relationship of reduced glomerular filtration rate with alterations in plasma free amino acids and uric acid evaluated in healthy control and hypertensive subjects. *Sci. Rep.* **2019**, *9*, 10252. [CrossRef]
51. Gibson, T. Hyperuricemia, gout and the kidney. *Curr. Opin. Rheumatol.* **2012**, *24*, 127–131. [CrossRef]
52. Nashaat, E.H.; Mohamed, M.M.; Aziz, T.M.; Nakhla, M.W. Serum Beta 2-Microglobulin as a Biomarker of Activity in Ulcerative Colitis. *QJM Int. J. Med.* **2020**, *113*, 10916. [CrossRef]
53. Shi, F.; Sun, L.; Kaptoge, S. Association of beta-2-microglobulin and cardiovascular events and mortality: A systematic review and meta-analysis. *Atherosclerosis* **2021**, *320*, 70–78. [CrossRef] [PubMed]
54. Hyung, J.; Hong, J.Y.; Kim, S.; Ryu, J.S.; Huh, J.; Suh, C. Beta-2 microglobulin as a prognostic factor of primary central nervous system lymphoma. *Blood Res.* **2019**, *54*, 285–288. [CrossRef] [PubMed]
55. Argyropoulos, C.P.; Chen, S.S.; Ng, Y.H.; Roumelioti, M.E.; Shaffi, K.; Singh, P.P.; Tzamaloukas, A.H. Rediscovering Beta-2 microglobulin as a biomarker across the spectrum of kidney diseases. *Front. Med.* **2017**, *4*, 73. [CrossRef] [PubMed]

56. Huber, A.K.; Giles, D.A.; Segal, B.M.; Irani, D.N. An emerging role for eotaxins in neurodegenerative disease. *Clin. Immunol.* **2018**, *189*, 29–33. [CrossRef] [PubMed]
57. Jose, P.J.; Griffiths-Johnson, D.A.; Collins, P.D.; Walsh, D.T.; Moqbel, R.; Totty, N.F.; Truong, O.; Hsuan, J.J.; Williams, T.J. Eotaxin: A potent eosinophil chemoattractant cytokine detected in a guinea pig model of allergic airways inflammation. *J. Exp. Med.* **1994**, *179*, 881–887. [CrossRef] [PubMed]
58. Andres-Hernando, A.; Dursun, B.; Altmann, C.; Ahuja, N.; He, Z.; Bhargava, R.; Edelstein, C.E.; Jani, A.; Hoke, T.S.; Klein, C.; et al. Cytokine production increases and cytokine clearance decreases in mice with bilateral nephrectomy. *Nephrol. Dial. Transplant.* **2012**, *27*, 4339–4347. [CrossRef]
59. Chen, L.; Zhang, J.; Teh, J.P.Y.; Cheon, B.K.; Yang, Y.; Schlundt, J.; Wang, Y.; Conway, P.L. Comparative Blood and Urine Metabolomics Analysis of Healthy Elderly and Young Male Singaporeans. *J. Proteome Res.* **2020**, *19*, 3264–3275. [CrossRef]
60. Garibotto Giacomo, G.; Sofia, A.; Saffioti, S.; Bonanni, A.; Mannucci, I.; Verzola, D. Amino acid and protein metabolism in the human kidney and in patients with chronic kidney disease. *Clin. Nutr.* **2010**, *29*, 424–433. [CrossRef]
61. Teruya, T.; Goga, H.; Yanagida, M. Aging markers in human urine: A comprehensive, non-targeted LC-MS study. *FASEB BioAdvances* **2020**, *2*, 720–733. [CrossRef]
62. Rodwell, G.E.J.; Sonu, R.; Zahn, J.M.; Lund, J.; Wilhelm, J.; Wang, L.; Xiao, W.; Mindrinos, M.; Crane, E.; Segal, E.; et al. A Transcriptional Profile of Aging in the Human Kidney. *PLoS Biol.* **2004**, *2*, e427. [CrossRef]
63. Imelda, M.; Szilvia, A.; Barna, B. Epidemiology of anemia. *Orv. Hetil.* **2020**, *161*, 1569–1573. [CrossRef]
64. Sharif, R.; Thomas, P.; Zalewski, P.; Fenech, M. The role of zinc in genomic stability. *Mutat. Res.-Fundam. Mol. Mech. Mutagen.* **2012**, *733*, 111–121. [CrossRef]
65. Pfrimer, K.; Micheletto, R.F.; Marchini, J.S.; Padovan, G.J.; Moriguti, J.C.; Ferrioli, E. Impact of aging on urinary excretion of iron and zinc. *Nutr. Metab. Insights* **2014**, *7*, 47–50. [CrossRef]
66. Nwanaji-Enwerem, J.C.; Colicino, E.; Specht, A.J.; Gao, X.; Wang, C.; Vokonas, P.; Weisskopf, M.G.; Boyer, E.W.; Baccarelli, A.A.; Schwartz, J. Individual species and cumulative mixture relationships of 24-hour urine metal concentrations with DNA methylation age variables in older men. *Environ. Res.* **2020**, *186*, 109573. [CrossRef]
67. Guo, J.; Xie, J.; Zhou, B.; Găman, M.A.; Kord-Varkaneh, H.; Clark, C.C.T.; Salehi-Sahlabadi, A.; Li, Y.; Han, X.; Hao, Y.; et al. The influence of zinc supplementation on IGF-1 levels in humans: A systematic review and meta-analysis. *J. King Saud Univ.-Sci.* **2020**, *32*, 1824–1830. [CrossRef]
68. Skalny, A.V.; Rink, L.; Ajsuvakova, O.P.; Aschner, M.; Gritsenko, V.A.; Alekseenko, S.I.; Svistunov, A.A.; Petrakis, D.; Spandidos, D.A.; Aaseth, J.; et al. Zinc and respiratory tract infections: Perspectives for COVID-19 (Review). *Int. J. Mol. Med.* **2020**, *46*, 17–26. [CrossRef]
69. Skrajnawska, D.; Bobrowska-Korczak, B. Role of zinc in immune system and anti-cancer defense mechanisms. *Nutrients* **2019**, *11*, 2273. [CrossRef]
70. Cortese-Krott, M.M.; Kulakov, L.; Opländer, C.; Kolb-Bachofen, V.; Kröncke, K.D.; Suschek, C.V. Zinc regulates iNOS-derived nitric oxide formation in endothelial cells. *Redox Biol.* **2014**, *2*, 945–954. [CrossRef]
71. Rychlik, M.; Mlyniec, K. Zinc-mediated Neurotransmission in Alzheimer’s Disease: A Potential Role of the GPR39 in Dementia. *Curr. Neuropharmacol.* **2019**, *18*, 2–13. [CrossRef]
72. Lehallier, B.; Gate, D.; Schaum, N.; Nanasi, T.; Lee, S.E.; Yousef, H.; Moran Losada, P.; Berdnik, D.; Keller, A.; Vergheze, J.; et al. Undulating changes in human plasma proteome profiles across the lifespan. *Nat. Med.* **2019**, *25*, 1843–1850. [CrossRef]
73. Tanaka, T.; Biancotto, A.; Moaddel, R.; Moore, A.Z.; Gonzalez-Freire, M.; Aon, M.A.; Candia, J.; Zhang, P.; Cheung, F.; Fantoni, G.; et al. Plasma proteomic signature of age in healthy humans. *Aging Cell* **2018**, *17*, e12799. [CrossRef]
74. Katsimpardi, L.; Litterman, N.K.; Schein, P.A.; Miller, C.M.; Loffredo, F.S.; Wojtkiewicz, G.R.; Chen, J.W.; Lee, R.T.; Wagers, A.J.; Rubin, L.L. Vascular and neurogenic rejuvenation of the aging mouse brain by young systemic factors. *Science* **2014**, *344*, 630–634. [CrossRef]
75. Elabd, C.; Cousin, W.; Upadhyayula, P.; Chen, R.Y.; Chooljian, M.S.; Li, J.; Kung, S.; Jiang, K.P.; Conboy, I.M. Oxytocin is an age-specific circulating hormone that is necessary for muscle maintenance and regeneration. *Nat. Commun.* **2014**, *5*, 4082. [CrossRef]
76. Castellano, J.M.; Mosher, K.I.; Abbey, R.J.; McBride, A.A.; James, M.L.; Berdnik, D.; Shen, J.C.; Zou, B.; Xie, X.S.; Tingle, M.; et al. Human umbilical cord plasma proteins revitalize hippocampal function in aged mice. *Nature* **2017**, *544*, 488–492. [CrossRef]
77. Thornton, P.L.; Ingram, R.L.; Sonntag, W.E. Chronic [D-Ala²]-growth hormone-releasing hormone administration attenuates age-related deficits in spatial memory. *J. Gerontol. Ser. A Biol. Sci. Med. Sci.* **2000**, *55*, B106–B112. [CrossRef]
78. Vinel, C.; Lukjanenko, L.; Batut, A.; Deleruyelle, S.; Pradère, J.P.; Le Gonidec, S.; Dortignac, A.; Geoffre, N.; Pereira, O.; Karaz, S.; et al. The exerkine apelin reverses age-associated sarcopenia. *Nat. Med.* **2018**, *24*, 1360–1371. [CrossRef]
79. Yang, Y.R.; Kabir, M.H.; Park, J.H.; Park, J.I.; Kang, J.S.; Ju, S.; Shin, Y.J.; Lee, S.M.; Lee, J.; Kim, S.; et al. Plasma proteomic profiling of young and old mice reveals cadherin-13 prevents age-related bone loss. *Aging (Albany N. Y.)* **2020**, *12*, 8652–8668. [CrossRef]
80. Yoshida, M.; Satoh, A.; Lin, J.B.; Mills, K.F.; Sasaki, Y.; Rensing, N.; Wong, M.; Apte, R.S.; Imai, S. Ichi-ro Extracellular Vesicle-Contained eNAMPT Delays Aging and Extends Lifespan in Mice. *Cell Metab.* **2019**, *30*, 329–342.e5. [CrossRef]
81. Gan, K.J.; Südhof, T.C. Specific factors in blood from young but not old mice directly promote synapse formation and NMDA-receptor recruitment. *Proc. Natl. Acad. Sci. USA* **2019**, *116*, 12524–12533. [CrossRef]

82. Khrimian, L.; Obri, A.; Ramos-Brossier, M.; Rousseaud, A.; Moriceau, S.; Nicot, A.S.; Mera, P.; Kosmidis, S.; Karnavas, T.; Saudou, F.; et al. Gpr158 mediates osteocalcin's regulation of cognition. *J. Exp. Med.* **2017**, *214*, 2859–2873. [CrossRef] [PubMed]
83. Villeda, S.A.; Luo, J.; Mosher, K.I.; Zou, B.; Britschgi, M.; Bieri, G.; Stan, T.M.; Fainberg, N.; Ding, Z.; Eggel, A.; et al. The ageing systemic milieu negatively regulates neurogenesis and cognitive function. *Nature* **2011**, *477*, 90–96. [CrossRef] [PubMed]
84. Smith, L.K.; He, Y.; Park, J.S.; Bieri, G.; Snethlage, C.E.; Lin, K.; Gontier, G.; Wabl, R.; Plambeck, K.E.; Udeochu, J.; et al. β 2-microglobulin is a systemic pro-aging factor that impairs cognitive function and neurogenesis. *Nat. Med.* **2015**, *21*, 932–937. [CrossRef] [PubMed]
85. Pastushkova, L.K.; Kononikhin, A.S.; Tiys, E.S.; Dobrokhoto, I.V.; Ivanisenko, V.A.; Nikolaev, E.N.; Larina, I.M.; Popov, I.A. Characteristics of age-dependent changes in urine proteome in healthy men. *Adv. Gerontol.* **2016**, *6*, 123–128. [CrossRef]
86. Kuipers, A.L.; Zhang, Y.; Yu, S.; Kammerer, C.M.; Nestlerode, C.S.; Chu, Y.; Bunker, C.H.; Patrick, A.L.; Wheeler, V.W.; Miljkovic, I.; et al. Relative influence of heritability, environment and genetics on serum sclerostin. *Osteoporos. Int.* **2014**, *25*, 905–912. [CrossRef] [PubMed]
87. Kindstedt, E.; Holm, C.K.; Sulniute, R.; Martinez-Carrasco, I.; Lundmark, R.; Lundberg, P. CCL11, a novel mediator of inflammatory bone resorption. *Sci. Rep.* **2017**, *7*, 5334. [CrossRef]
88. Andreassová, T.; Vránová, J.; Vondráková, D.; Sedláčková, L.; Zákostelská, Z.J.; Neuzil, P.; Málek, F. Role of biomarkers of cardiac remodeling, myofibrosis, and inflammation in assessment of disease severity in euvoletic patients with chronic stable heart failure. *J. Int. Med. Res.* **2020**, *48*, 0300060520947869. [CrossRef]
89. Romanova, Y.; Laikov, A.; Markelova, M.; Khadiullina, R.; Makseev, A.; Hasanova, M.; Rizvanov, A.; Khaiboullina, S.; Salafutdinov, I. Proteomic analysis of human serum from patients with chronic kidney disease. *Biomolecules* **2020**, *10*, 257. [CrossRef]
90. Morsiani, C.; Bacalini, M.G.; Santoro, A.; Garagnani, P.; Collura, S.; D'Errico, A.; de Eguileor, M.; Grazi, G.L.; Cescon, M.; Franceschi, C.; et al. The peculiar aging of human liver: A geroscience perspective within transplant context. *Ageing Res. Rev.* **2019**, *51*, 24–34. [CrossRef]
91. Rhinn, M.; Ritschka, B.; Keyes, W.M. Cellular senescence in development, regeneration and disease. *Development* **2019**, *146*, dev151837. [CrossRef]
92. Krimpenfort, P.; Quon, K.C.; Mooi, W.J.; Loonstra, A.; Berns, A. Loss of p16Ink4a confers susceptibility to metastatic melanoma in mice. *Nature* **2001**, *413*, 83–86. [CrossRef] [PubMed]
93. Lee, S.; Schmitt, C.A. The dynamic nature of senescence in cancer. *Nat. Cell Biol.* **2019**, *21*, 94–101. [CrossRef] [PubMed]
94. Sharpless, N.E.; Bardeesy, N.; Lee, K.H.; Carrasco, D.; Castrillon, D.H.; Aguirre, A.J.; Wu, E.A.; Horner, J.W.; DePinho, R.A. Loss of p16Ink4a with retention of p19 predisposes mice to tumorigenesis. *Nature* **2001**, *413*, 86–91. [CrossRef] [PubMed]
95. Pratsinis, H.; Mavrogonatou, E.; Kletsas, D. Scarless wound healing: From development to senescence. *Adv. Drug Deliv. Rev.* **2019**, *146*, 325–343. [CrossRef] [PubMed]
96. Baker, D.J.; Childs, B.G.; Durik, M.; Wijers, M.E.; Sieben, C.J.; Zhong, J.; Saltness, R.A.; Jeganathan, K.B.; Verzosa, G.C.; Pezeshki, A.; et al. Naturally occurring p16 Ink4a-positive cells shorten healthy lifespan. *Nature* **2016**, *530*, 184–189. [CrossRef]
97. Gallagher, J.C. Vitamin D and Aging. *Endocrinol. Metab. Clin. N. Am.* **2013**, *42*, 319–332. [CrossRef]
98. Kumar, R.; Tebben, P.J.; Thompson, J.R. Vitamin D and the kidney. *Arch. Biochem. Biophys.* **2012**, *523*, 77–86. [CrossRef] [PubMed]
99. Da Silva-Álvarez, S.; Guerra-Varela, J.; Sobrido-Cameán, D.; Quelle, A.; Barreiro-Iglesias, A.; Sánchez, L.; Collado, M. Cell senescence contributes to tissue regeneration in zebrafish. *Ageing Cell* **2020**, *19*, e13052. [CrossRef]
100. Beckett, E. More Than Bone Health: The Many Roles for Vitamin D. *Nutrients* **2020**, *12*, 2388. [CrossRef]
101. McHugh, D.; Gil, J. Senescence and aging: Causes, consequences, and therapeutic avenues. *J. Cell Biol.* **2018**, *217*, 65–77. [CrossRef]
102. Van Deursen, J.M. The role of senescent cells in ageing. *Nature* **2014**, *509*, 439–446. [CrossRef] [PubMed]
103. Villeda, S.A.; Horowitz, A.M. Therapeutic potential of systemic brain rejuvenation strategies for neurodegenerative disease. *FI000Research* **2017**, *6*, 1291. [CrossRef]
104. Kang, J.S.; Yang, Y.R. Circulating plasma factors involved in rejuvenation. *Ageing (Albany N. Y.)* **2020**, *12*, 23394–23408. [CrossRef] [PubMed]
105. Yuan, J.J.; Zhang, Q.; Gong, C.X.; Wang, F.X.; Huang, J.C.; Yang, G.Q.; Liu, L.; Zhou, K.; Xu, R.; Chen, Q.; et al. Young plasma ameliorates aging-related acute brain injury after intracerebral hemorrhage. *Biosci. Rep.* **2019**, *39*, BSR20190537. [CrossRef]
106. Tripathi, S.S.; Kumar, R.; Arya, J.; Rizvi, S.I. Plasma from young rats injected into old rats induce anti-aging effects. *Rejuvenation Res.* **2020**, *24*, 206–212. [CrossRef]
107. Sha, S.J.; Deutsch, G.K.; Tian, L.; Richardson, K.; Coburn, M.; Gaudioso, J.L.; Marcal, T.; Solomon, E.; Boumris, A.; Bet, A.; et al. Safety, Tolerability, and Feasibility of Young Plasma Infusion in the Plasma for Alzheimer Symptom Amelioration Study: A Randomized Clinical Trial. *JAMA Neurol.* **2019**, *76*, 35–40. [CrossRef] [PubMed]
108. VandeVrede, L.; Dale, M.L.; Fields, S.; Frank, M.; Hare, E.; Heuer, H.W.; Keith, K.; Koestler, M.; Ljubenkov, P.A.; McDermott, D.; et al. Open-Label Phase 1 Futility Studies of Salsalate and Young Plasma in Progressive Supranuclear Palsy. *Mov. Disord. Clin. Pract.* **2020**, *7*, 440–447. [CrossRef]
109. Ma, J.; Gao, B.; Zhang, K.; Zhang, Q.; Jia, G.; Li, J.; Li, C.; Yan, L.J.; Cai, Z. Circulating factors in young blood as potential therapeutic agents for age-related neurodegenerative and neurovascular diseases. *Brain Res. Bull.* **2019**, *153*, 15–23. [CrossRef] [PubMed]
110. Rybtsova, N.; Berezina, T.; Kagansky, A.; Rybtsov, S. Can Blood-Circulating Factors Unveil and Delay Your Biological Aging? *Biomedicines* **2020**, *8*, 615. [CrossRef] [PubMed]

111. Rebo, J.; Mehdipour, M.; Gathwala, R.; Causey, K.; Liu, Y.; Conboy, M.J.; Conboy, I.M. A single heterochronic blood exchange reveals rapid inhibition of multiple tissues by old blood. *Nat. Commun.* **2016**, *7*, 13363. [CrossRef]
112. Mehdipour, M.; Skinner, C.; Wong, N.; Lieb, M.; Liu, C.; Etienne, J.; Kato, C.; Kiprof, D.; Conboy, M.J.; Conboy, I.M. Rejuvenation of three germ layers tissues by exchanging old blood plasma with saline-albumin. *Aging (Albany N. Y.)* **2020**, *12*, 8790–8819. [CrossRef] [PubMed]
113. Boada, M.; López, O.; Núñez, L.; Szczepiorkowski, Z.M.; Torres, M.; Grifols, C.; Páez, A. Plasma exchange for Alzheimer's disease Management by Albumin Replacement (AMBAR) trial: Study design and progress. *Alzheimer's Dement. Transl. Res. Clin. Interv.* **2019**, *5*, 61–69. [CrossRef] [PubMed]
114. Relkin, N. Clinical Trials of Intravenous Immunoglobulin for Alzheimer's Disease. *J. Clin. Immunol.* **2014**, *34*, 74–79. [CrossRef] [PubMed]
115. Fahy, G.M.; Brooke, R.T.; Watson, J.P.; Good, Z.; Vasanawala, S.S.; Maecker, H.; Leipold, M.D.; Lin, D.T.S.; Kobor, M.S.; Horvath, S. Reversal of epigenetic aging and immunosenescent trends in humans. *Aging Cell* **2019**, *18*, e13028. [CrossRef]
116. Sogabe, Y.; Seno, H.; Yamamoto, T.; Yamada, Y. Unveiling epigenetic regulation in cancer, aging, and rejuvenation with in vivo reprogramming technology. *Cancer Sci.* **2018**, *109*, 2641–2650. [CrossRef] [PubMed]
117. Kenyon, C.J. The genetics of ageing. *Nature* **2010**, *464*, 504–512. [CrossRef]
118. Shanley, D.P.; Kirkwood, T.B.L. Calorie restriction and aging: A life-history analysis. *Evolution* **2000**, *54*, 740–750. [CrossRef]
119. Zoncu, R.; Efeyan, A.; Sabatini, D.M. mTOR: From growth signal integration to cancer, diabetes and ageing. *Nat. Rev. Mol. Cell Biol.* **2011**, *12*, 21–35. [CrossRef]
120. Pan, H.; Finkel, T. Key proteins and pathways that regulate lifespan. *J. Biol. Chem.* **2017**, *292*, 6452–6460. [CrossRef]
121. Verdin, E. NAD⁺ in aging, metabolism, and neurodegeneration. *Science* **2015**, *350*, 1208–1213. [CrossRef] [PubMed]
122. Mendelsohn, A.R.; Larrick, J.W. Interacting NAD⁺ and Cell Senescence Pathways Complicate Antiaging Therapies. *Rejuvenation Res.* **2019**, *22*, 261–266. [CrossRef]
123. Ehninger, D.; Neff, F.; Xie, K. Longevity, aging and rapamycin. *Cell. Mol. Life Sci.* **2014**, *71*, 4325–4346. [CrossRef] [PubMed]
124. Zajda, A.; Huttunen, K.M.; Sikora, J.; Podsiedlik, M.; Markowicz-Piasecka, M. Is metformin a geroprotector? A peek into the current clinical and experimental data. *Mech. Ageing Dev.* **2020**, *191*, 111350. [CrossRef] [PubMed]
125. Pearson, K.J.; Baur, J.A.; Lewis, K.N.; Peshkin, L.; Price, N.L.; Labinskyy, N.; Swindell, W.R.; Kamara, D.; Minor, R.K.; Perez, E.; et al. Resveratrol Delays Age-Related Deterioration and Mimics Transcriptional Aspects of Dietary Restriction without Extending Life Span. *Cell Metab.* **2008**, *8*, 157–168. [CrossRef] [PubMed]
126. Hsu, C.C.; Wahlqvist, M.L.; Lee, M.S.; Tsai, H.N. Incidence of dementia is increased in type 2 diabetes and reduced by the use of sulfonylureas and metformin. *J. Alzheimer's Dis.* **2011**, *24*, 485–493. [CrossRef]
127. Chin-Hsiao, T. Metformin and the risk of dementia in type 2 diabetes patients. *Aging and Disease.* **2019**, *10*, 37. [CrossRef]
128. Yang, W.; Cai, X.; Wu, H.; Ji, L. Associations between metformin use and vitamin B₁₂ levels, anemia, and neuropathy in patients with diabetes: A meta-analysis. *J. Diabetes* **2019**, *11*, 729–743. [CrossRef]
129. Lalau, J.D.; Kajbaf, F.; Protti, A.; Christensen, M.M.; De Broe, M.E.; Wiernsperger, N. Metformin-associated lactic acidosis (MALA): Moving towards a new paradigm. *Wiley Online Libr.* **2017**, *19*, 1502–1512. [CrossRef]
130. Salvatore, T.; Pafundi, P.C.; Marfella, R.; Sardu, C.; Rinaldi, L.; Monaco, L.; Riccozzi, C.; Imbriani, S.; Nevola, R.; Adinolfi, L.E.; et al. Metformin lactic acidosis: Should we still be afraid? *Diabetes Res. Clin. Pract.* **2019**, *157*, 107879. [CrossRef] [PubMed]
131. Bonkowski, M.S.; Sinclair, D.A. Slowing ageing by design: The rise of NAD⁺ and sirtuin-activating compounds. *Nat. Rev. Mol. Cell Biol.* **2016**, *17*, 679–690. [CrossRef]
132. Liao, C.Y.; Rikke, B.A.; Johnson, T.E.; Diaz, V.; Nelson, J.F. Genetic variation in the murine lifespan response to dietary restriction: From life extension to life shortening. *Aging Cell* **2010**, *9*, 92–95. [CrossRef]
133. Hunt, N.J.; McCourt, P.A.G.; Le Couteur, D.G.; Cogger, V.C. Novel targets for delaying aging: The importance of the liver and advances in drug delivery. *Adv. Drug Deliv. Rev.* **2018**, *135*, 39–49. [CrossRef] [PubMed]
134. Zhou, S.S.; Zhou, Y.M.; Li, D.; Lun, Y.Z. Dietary methyl-consuming compounds and metabolic syndrome. *Hypertens. Res.* **2011**, *34*, 1239–1245. [CrossRef] [PubMed]
135. Schmeer, C.; Kretz, A.; Wengerodt, D.; Stojiljkovic, M.; Witte, O.W. Dissecting Aging and Senescence-Current Concepts and Open Lessons. *Cells* **2019**, *8*, 1446. [CrossRef]
136. Austad, S.N.; Hoffman, J.M. Is antagonistic pleiotropy ubiquitous in aging biology? *Evol. Med. Public Health* **2018**, *2018*, 287–294. [CrossRef] [PubMed]
137. Takahashi, K.; Tanabe, K.; Ohnuki, M.; Narita, M.; Ichisaka, T.; Tomoda, K.; Yamanaka, S. Induction of Pluripotent Stem Cells from Adult Human Fibroblasts by Defined Factors. *Cell* **2007**, *131*, 861–872. [CrossRef]
138. Yu, J.; Vodyanik, M.A.; Smuga-Otto, K.; Antosiewicz-Bourget, J.; Frane, J.L.; Tian, S.; Nie, J.; Jonsdottir, G.A.; Ruotti, V.; Stewart, R.; et al. Induced pluripotent stem cell lines derived from human somatic cells. *Science* **2007**, *318*, 1917–1920. [CrossRef] [PubMed]
139. Yoo, A.S.; Sun, A.X.; Li, L.; Shcheglovitov, A.; Portmann, T.; Li, Y.; Lee-Messer, C.; Dolmetsch, R.E.; Tsien, R.W.; Crabtree, G.R. MicroRNA-mediated conversion of human fibroblasts to neurons. *Nature* **2011**, *476*, 228–231. [CrossRef] [PubMed]
140. Huh, C.J.; Zhang, B.; Victor, M.B.; Dahiya, S.; Batista, L.F.Z.; Horvath, S.; Yoo, A.S. Maintenance of age in human neurons generated by microRNA-based neuronal conversion of fibroblasts. *eLife* **2016**, *5*, e18648. [CrossRef]

141. Kanwal, S.; Guo, X.; Ward, C.; Volpe, G.; Qin, B.; Esteban, M.A.; Bao, X. Role of Long Non-coding RNAs in Reprogramming to Induced Pluripotency. *Genom. Proteom. Bioinform.* **2020**, *18*, 16–25. [CrossRef]
142. Iwamoto, K.; Bundo, M.; Ueda, J.; Oldham, M.C.; Ukai, W.; Hashimoto, E.; Saito, T.; Geschwind, D.H.; Kato, T. Neurons show distinctive DNA methylation profile and higher interindividual variations compared with non-neurons. *Genome Res.* **2011**, *21*, 688–696. [CrossRef] [PubMed]
143. Samoylova, E.M.; Baklaushev, V.P. Cell Reprogramming Preserving Epigenetic Age: Advantages and Limitations. *Biochemistry* **2020**, *85*, 1035–1047. [CrossRef] [PubMed]
144. Lo Sardo, V.; Ferguson, W.; Erikson, G.A.; Topol, E.J.; Baldwin, K.K.; Torkamani, A. Influence of donor age on induced pluripotent stem cells. *Nat. Biotechnol.* **2017**, *35*, 69–74. [CrossRef] [PubMed]
145. Ocampo, A.; Reddy, P.; Martinez-Redondo, P.; Platero-Luengo, A.; Hatanaka, F.; Hishida, T.; Li, M.; Lam, D.; Kurita, M.; Beyret, E.; et al. In Vivo Amelioration of Age-Associated Hallmarks by Partial Reprogramming. *Cell* **2016**, *167*, 1719–1733.e12. [CrossRef] [PubMed]
146. Tepper, O.M.; Galiano, R.D.; Capla, J.M.; Kalka, C.; Gagne, P.J.; Jacobowitz, G.R.; Levine, J.P.; Gurtner, G.C. Human endothelial progenitor cells from type II diabetics exhibit impaired proliferation, adhesion, and incorporation into vascular structures. *Circulation* **2002**, *106*, 2781–2786. [CrossRef] [PubMed]
147. Lee, H.; Son, M.-Y. Current Challenges Associated with the Use of Human Induced Pluripotent Stem Cell-Derived Organoids in Regenerative Medicine. *Int. J. Stem Cells* **2021**, *14*, 9–20. [CrossRef]
148. Hofer, M.; Lutolf, M.P. Engineering organoids. *Nat. Rev. Mater.* **2021**, *6*, 402–420. [CrossRef]
149. Messina, A.; Luce, E.; Hussein, M.; Dubart-Kupperschmitt, A. Pluripotent-Stem-Cell-Derived Hepatic Cells: Hepatocytes and Organoids for Liver Therapy and Regeneration. *Cells* **2020**, *9*, 420. [CrossRef]
150. Li, P.; Lee, G.-H.; Kim, S.Y.; Kwon, S.Y.; Kim, H.-R.; Park, S. From Diagnosis to Treatment: Recent Advances in Patient-Friendly Biosensors and Implantable Devices. *ACS Nano* **2021**, *15*, 1960–2004. [CrossRef]
151. French, P. In-Vivo Microsystems: A Review. *Sensors* **2020**, *20*, 4953. [CrossRef]
152. Jiang, D.; Shi, B.; Ouyang, H.; Fan, Y.; Wang, Z.L.; Chen, Z.M.; Li, Z. A 25-year bibliometric study of implantable energy harvesters and self-powered implantable medical electronics researches. *Mater. Today Energy* **2020**, *16*, 100386. [CrossRef]
153. Singh, R.; Bathaei, M.J.; Istif, E.; Beker, L. A Review of Bioresorbable Implantable Medical Devices: Materials, Fabrication, and Implementation. *Adv. Healthc. Mater.* **2020**, *9*, 2000790. [CrossRef] [PubMed]
154. Hench, L.L.; Ethridge, E.C. Biomaterials-the interfacial problem. *Adv. Biomed. Eng.* **1975**, *5*, 35–150. [CrossRef]
155. Dinis, H.; Mendes, P.M. A comprehensive review of powering methods used in state-of-the-art miniaturized implantable electronic devices. *Biosens. Bioelectron.* **2021**, *172*, 112781. [CrossRef] [PubMed]
156. Teshome, A.K.; Kibret, B.; Lai, D.T.H. A Review of Implant Communication Technology in WBAN: Progress and Challenges. *IEEE Rev. Biomed. Eng.* **2018**, *12*, 88–99. [CrossRef]
157. Masliukov, P.M.; Nozdrachev, A.D. Hypothalamic Regulatory Mechanisms of Aging. *J. Evol. Biochem. Physiol.* **2021**, *57*, 473–491. [CrossRef]
158. Kim, K.; Choe, H.K. Role of hypothalamus in aging and its underlying cellular mechanisms. *Mech. Ageing Dev.* **2019**, *177*, 74–79. [CrossRef]



Article

Peiminine Reduces ARTS-Mediated Degradation of XIAP by Modulating the PINK1/Parkin Pathway to Ameliorate 6-Hydroxydopamine Toxicity and α -Synuclein Accumulation in Parkinson's Disease Models In Vivo and In Vitro

Yu-Ling Hsu ^{1,†}, Huey-Shan Hung ^{1,2,†}, Chia-Wen Tsai ³, Shih-Ping Liu ^{1,2}, Yu-Ting Chiang ¹, Yun-Hua Kuo ⁴, Woei-Cherng Shyu ^{1,2}, Shinn-Zong Lin ⁵ and Ru-Huei Fu ^{1,2,6,*}

- ¹ Graduate Institute of Biomedical Sciences, China Medical University, Taichung 40402, Taiwan; fish38@cgmh.org.tw (Y.-L.H.); hungsh@mail.cmu.edu.tw (H.-S.H.); spliu@mail.cmu.edu.tw (S.-P.L.); tina.chiang831@gmail.com (Y.-T.C.); shyu9423@gmail.com (W.-C.S.)
 - ² Translational Medicine Research Center, China Medical University Hospital, Taichung 40447, Taiwan
 - ³ Department of Nutrition, China Medical University, Taichung 40402, Taiwan; cwtsai@mail.cmu.edu.tw
 - ⁴ Department of Nursing, Taipei Veterans General Hospital, Taipei 12217, Taiwan; yhkuo3@vghtpe.gov.tw
 - ⁵ Bioinnovation Center, Tzu Chi Foundation, Department of Neurosurgery, Buddhist Tzu Chi General Hospital, Tzu Chi University, Hualien 970, Taiwan; shinnzong@yahoo.com.tw
 - ⁶ Department of Psychology, Asia University, Taichung 41354, Taiwan
- * Correspondence: rhfu@mail.cmu.edu.tw; Tel.: +886-422052121-7826
† Co-first author, contributed equally.

Citation: Hsu, Y.-L.; Hung, H.-S.; Tsai, C.-W.; Liu, S.-P.; Chiang, Y.-T.; Kuo, Y.-H.; Shyu, W.-C.; Lin, S.-Z.; Fu, R.-H. Peiminine Reduces ARTS-Mediated Degradation of XIAP by Modulating the PINK1/Parkin Pathway to Ameliorate 6-Hydroxydopamine Toxicity and α -Synuclein Accumulation in Parkinson's Disease Models In Vivo and In Vitro. *Int. J. Mol. Sci.* **2021**, *22*, 10240. <https://doi.org/10.3390/ijms221910240>

Academic Editors: Masaru Tanaka and Lydia Giménez-Llort

Received: 30 July 2021

Accepted: 21 September 2021

Published: 23 September 2021

Publisher's Note: MDPI stays neutral with regard to jurisdictional claims in published maps and institutional affiliations.



Copyright: © 2021 by the authors. Licensee MDPI, Basel, Switzerland. This article is an open access article distributed under the terms and conditions of the Creative Commons Attribution (CC BY) license (<https://creativecommons.org/licenses/by/4.0/>).

Abstract: Parkinson's disease (PD) is a degenerative disease that can cause motor, cognitive, and behavioral disorders. The treatment strategies being developed are based on the typical pathologic features of PD, including the death of dopaminergic (DA) neurons in the substantia nigra of the midbrain and the accumulation of α -synuclein in neurons. Peiminine (PMN) is an extract of *Fritillaria thunbergii* Miq that has antioxidant and anti-neuroinflammatory effects. We used *Caenorhabditis elegans* and SH-SY5Y cell models of PD to evaluate the neuroprotective potential of PMN and address its corresponding mechanism of action. We found that pretreatment with PMN reduced *reactive oxygen species* production and DA neuron degeneration caused by exposure to 6-hydroxydopamine (6-OHDA), and therefore significantly improved the DA-mediated food-sensing behavior of 6-OHDA-exposed worms and prolonged their lifespan. PMN also diminished the accumulation of α -synuclein in transgenic worms and transfected cells. In our study of the mechanism of action, we found that PMN lessened ARTS-mediated degradation of X-linked inhibitor of apoptosis (XIAP) by enhancing the expression of PINK1/parkin. This led to reduced 6-OHDA-induced apoptosis, enhanced activity of the ubiquitin–proteasome system, and increased autophagy, which diminished the accumulation of α -synuclein. The use of small interfering RNA to down-regulate parkin reversed the benefits of PMN in the PD models. Our findings suggest PMN as a candidate compound worthy of further evaluation for the treatment of PD.

Keywords: peiminine; Parkinson's disease; 6-hydroxydopamine; α -synuclein; apoptosis; proteasome; autophagy; parkin; ARTS; XIAP

1. Introduction

Parkinson disease (PD) is a degenerative disease of dopamine neurons caused by environmental or genetic factors that most often occurs in adults older than 60 years. There are currently about 10 million patients with PD worldwide, and the corresponding impacts on the family, economy and medical system are considerable [1]. The detailed pathologic mechanism of PD is still unclear. Loss of dopaminergic (DA) neurons in the substantia nigra compact area of the midbrain is a typical pathologic feature of PD, which results in a lack of dopamine in the basal ganglia and eventually leads to the onset of clinical

symptoms, such as bradykinesia, rigidity, tremors, unstable posture, and cognitive and behavioral problems [2].

Another common and important feature of PD pathology is the accumulation of insoluble cytoplasmic α -synuclein, and the formation of Lewy bodies and Lewy neurites in neurons. Therefore, PD is also known as a synucleinopathy [3]. α -Synuclein contains 140 amino acids and has two forms: free and membrane-bound. It is encoded by the SNCA gene and occupies about 1% of the cytoplasmic protein of brain cells, partly in the mitochondria and nucleus. The main function of α -synuclein may be to regulate the activity of synaptic vesicles, the release of neurotransmitters, and the recycling of synaptic vesicles. In addition, studies have shown that α -synuclein is involved in neuronal Golgi and vesicle transport, membrane structure regulation, lipid metabolism, mitochondrial fusion, DNA repair, and cognitive functions [4]. The structure of α -synuclein is unstable, and the α -helix conformer is easily replaced by a β -sheet. This replacement results in misfolding and aggregation of α -synuclein to form oligomers or fibrils, which may be related to sporadic PD, with the end result being dysregulation of the synaptic, mitochondrial, and protein homeostasis systems; oxidative stress; microtubule damage; and abnormal calcium signaling [5].

Mutants of α -synuclein have been found to be related to familial PD. These include A53T, A30P, E46K, H50Q, and G51D [6]. Overexpression of human wild-type or A53T mutant α -synuclein in animals can lead to the deposition of α -synuclein in brain neurons, causing neurodegenerative toxicity and damage to the dopaminergic system and movement function, and thus can be used as a PD model [7].

The oxidative stress caused by mitochondrial damage, respiratory chain obstruction, and antioxidant enzyme defects reflects the imbalance between the generation of reactive oxygen species (ROS) and the efficiency of cells to detoxify or repair reactive oxygen intermediates, which ultimately leads to protein, lipid, and DNA damage and disturbance of redox signals in cells. These are closely related to the degeneration of DA neurons [8]. One report indicated that excessive ROS in the substantia nigra compact lead to apoptosis of DA neurons [9]. The neurotoxic compound 6-hydroxydopamine (6-OHDA) can enter cells through DA reuptake transporters and produce ROS, which in turn can selectively destroy DA neurons by inducing apoptosis, reducing proteasome activity, and preventing autophagy. 6-OHDA has thus been widely used in various pharmacologic models of PD.

In recent years, important clinical and basic studies have shown that two mitochondrial quality-control mechanisms, autophagy and the ubiquitin-proteasome system (UPS), can help cells resist various types of cellular stress through the PINK1/parkin pathway. The inner mitochondrial membrane protein PINK1 (PTEN-induced kinase 1) is a serine/threonine kinase. Ubiquitin E3 ligase parkin can add ubiquitin to a target protein to promote degradation of the protein by the 26S proteasome. Many proteins are substrates of parkin, such as α -synuclein. It is known that some patients with autosomal-recessive PD have mutations in PINK1 and parkin [10].

In damaged mitochondria, PINK1 accumulates on the outer membrane and then recruits and activates parkin through the phosphorylation of the ubiquitin chain, which causes the degradation of mitochondria through autophagy or mitophagy or degradation of the target protein through the UPS [11,12]. Furthermore, reducing mitochondrial-dependent and mitochondrial-independent apoptosis to increase cell survival can also be achieved by regulating the activity of PINK1 and parkin [13,14].

X-linked inhibitor of apoptosis protein (XIAP), which belongs to the inhibitor of apoptosis family of proteins (IAP), can directly prevent the apoptotic activity of caspase through three baculoviral IAP repeats (BIR domains) [15]. XIAP also has a RING domain, which can act as an ubiquitin E3 ligase to catalyze the ubiquitination of specific substrate proteins and promote their degradation by the proteasome [16]. Moreover, some reports indicate that XIAP can upregulate autophagy [17].

Another protein of interest is ARTS (apoptosis-related protein in the TGF- β signaling pathway). ARTS, which is located in the outer membrane of mitochondria, is a pro-

apoptotic protein. Once stimulated by the apoptotic signal, ARTS quickly translocates to the cytoplasm and binds to XIAP. The antagonized XIAP causes activation of caspase 9, 7, and 3, which leads to apoptosis [18]. ARTS can also act as a modulator of autophagy. Overexpression of ARTS leads to down-regulated autophagy and a lessened capacity for proliferation and migration in vascular smooth muscle cells [19]. Interestingly, ARTS has been proven to be a substrate of parkin. Parkin can reduce neuronal cell apoptosis by promoting the ubiquitination and degradation of ARTS [20]. Some PD patients with mutations of parkin may have augmented neuronal cell apoptosis caused by increased ARTS.

At present, in addition to treatments for alleviating the symptoms of PD, there are no successful treatments to effectively slow down or improve the progress of PD. The aglycone alkaloid peiminine (PMN, Figure 1), which is isolated from the bulbs of *Fritillaria thunbergii* Miq, is a traditional herbal medicine of Southeast Asia, namely zhe bei mu. PMN has been confirmed to have several pharmacologic effects linked to anti-inflammatory and antioxidant activity [21]. For example, Du et al. showed that PMN reduces acute lung injury caused by lipopolysaccharide (LPS) in mice by inhibiting inflammation-related factors and the formation of lipid rafts [22]. Luo et al. indicated that PMN can improve interleukin-1 β (IL-1 β)-induced osteoarthritis in mice by inhibiting the inflammatory response of chondrocytes [23]. Chen et al. revealed that PMN can prevent neuroinflammation and protect DA neurons in the LPS-induced PD model in rat [24]. However, the effectiveness of PMN against PD-related oxidative stress and α -synuclein accumulation has not been evaluated.

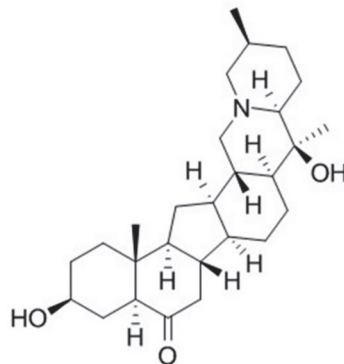


Figure 1. Chemical structure of peiminine (PMN).

In the present study, we first used *Caenorhabditis elegans* as an in vivo model of PD and a platform for evaluating the neuroprotective potential of PMN, because it has DA neurons, humans PD-related orthologous genes, known dopamine-regulated behavior patterns, easy-to-obtain genetically modified strains, low cost, short life cycle, transparent body and other advantages [25–27]. Primary mammalian neurons are terminal mature cells, which cannot be propagated in vitro and have limited use. The use of transformed neuronlike cells can overcome this limitation. The SH-SY5Y neuroblastoma cell line was derived from a metastatic bone tumor biopsy. It expresses tyrosine hydroxylase (TH) and dopamine- β -hydroxylase, which are characteristic of catecholaminergic neurons, and can be differentiated to a more mature neuronlike phenotype by treatment with retinoic acid. Thus, we used the SH-SY5Y cell line as in vitro model to further confirm the neuroprotective ability of PMN and explore its anti-parkinsonism mechanism [28,29].

2. Results

2.1. Toxicity of Peiminine in Worms

The toxicity of PMN in the worm models was evaluated by use of food clearance tests. Compared with the food clearance curve in the untreated group of worms, the curve of the N2, BZ555, NL5901, and DA2123 strains was significantly slowed when 1.25 mM PMN

was added to the culture (Figure 2). Observation with a dissecting microscope showed that the offspring decreased in number and body size (data not shown), which reflects the toxicity of PMN and a significant reduction in *E. coli* consumption. A PMN concentration of 0.25 mM did not significantly affect the food clearance curve of any strain of worms. Therefore, in subsequent experiments, the PMN concentration used to treat worms was set to a maximum of 0.25 mM.

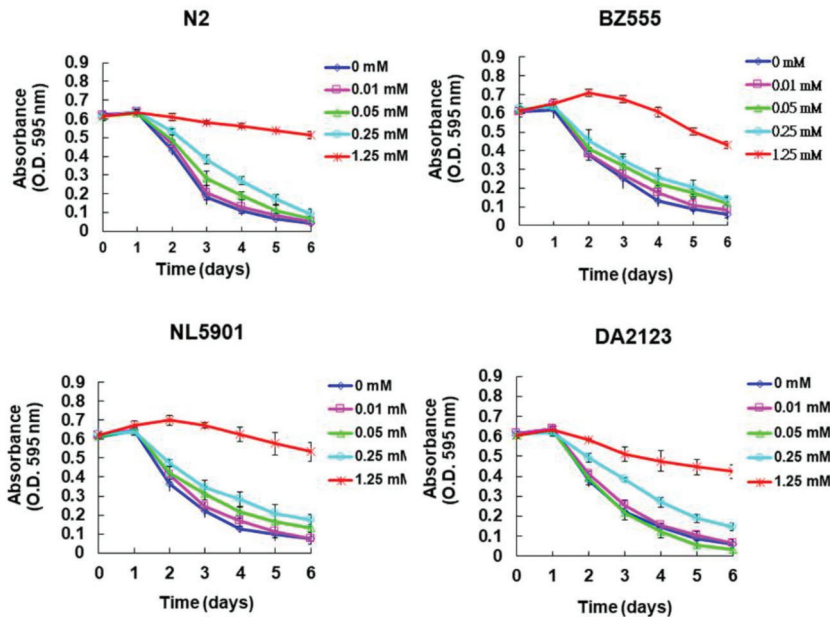


Figure 2. Evaluation of the toxicity of peiminine (PMN) in worms by food clearance test. In 96-well plates, L1 stage worms of four strain were cultured on OP50 *E. coli* (OD $A_{595} = 0.6$) feeding S-medium containing four concentrations of PMN, respectively. Cultivation was continued for 6 days, and the OD value of each group was measured and recorded daily.

2.2. PMN Pretreatment Significantly Reduces Dopaminergic Neuron Degeneration of 6-Hydroxydopamine-Exposed BZ555 Worms

Fluorescence microscopy analysis showed that the GFP expression in the three pairs of DA neurons in the head of 6-OHDA-exposed BZ555 worms was significantly decreased, reflecting the destruction of DA neuron integrity (Figure 3a). PMN pretreatment significantly enhanced the GFP signals (Figure 3a). Using ImageJ software to quantify the fluorescence intensity, we found that the average GFP fluorescence intensity of 6-OHDA-exposed worms was lessened by 57.3% ($p < 0.001$) compared with that in control worms (Figure 3b). PMN pretreatment increased the fluorescence intensity of GFP in 6-OHDA-exposed worms in a dose-dependent manner. The 0.25 mM concentration of PMN raised the fluorescence intensity of DA neurons by 1.8-fold ($p < 0.01$) (Figure 3b).

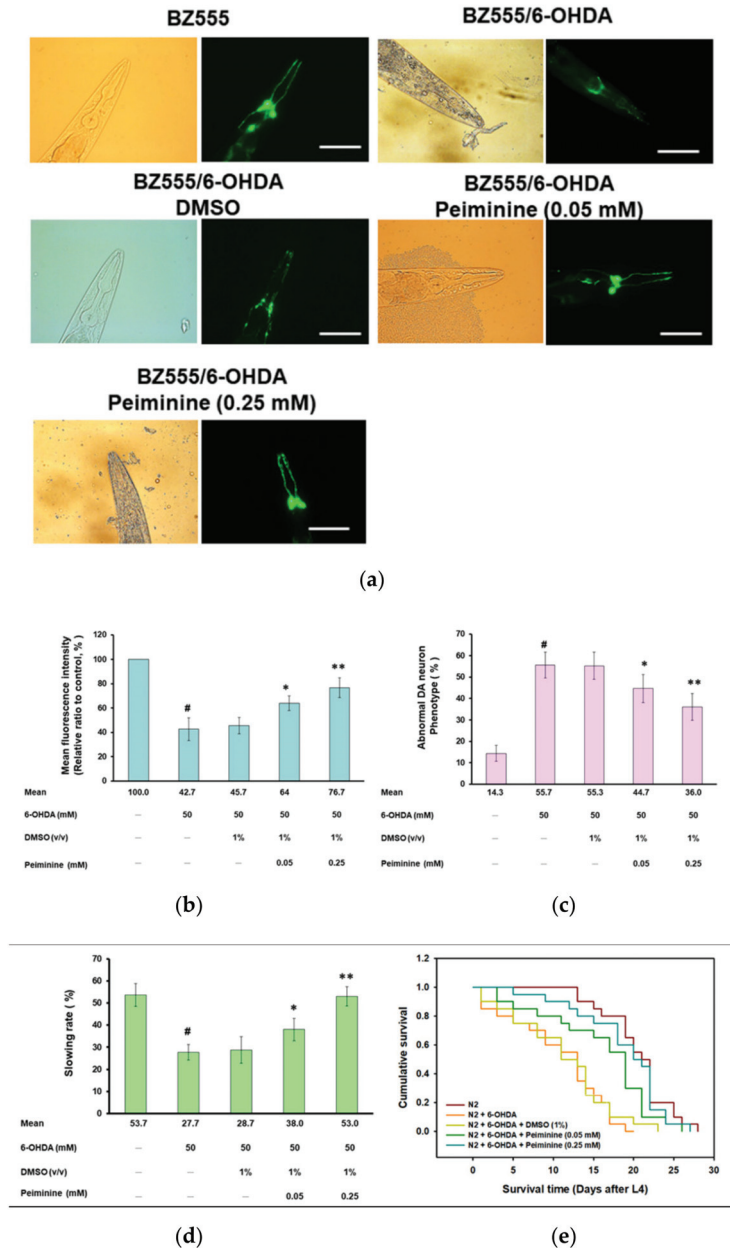


Figure 3. Dopaminergic (DA) neurons degeneration, food-sensing behavior defects, and shortened lifespan of worms caused by 6-hydroxydopamine (6-OHDA) are improved by peiminine (PMN) pretreatment. L1 stage worms were transferred to OP50/NGM plates with or without PMN and grown to the L3 stage, exposed to 6-OHDA for 1 h, and then transferred to OP50/NGM/FUDR plates with or without PMN and cultured for another 3 days before analysis. (a) Representative fluorescence images of GFP expression patterns in head DA neurons of BZ555 worms in each group. Scale bar = 50 μ m. (b) The fluorescence intensity of the GFP image of each group was quantified in (a) using ImageJ software. (c) The DA neuron degeneration phenotype defects of each group in (a)

were scored. The data are represented as a percentage of the total population of worms with defective DA neuron phenotypes. (d) Analysis of the food-sensing behavior of N2 worms in each group. The slowing rate was defined as the percentage decrease in the body bending frequency of worms on the lawn with bacteria compared with without bacteria (20 s on each type of lawn). (e) Cumulative survival curves of N2 worms in each group. In the above experiments, a total of 50 worms were counted in each group. # Indicates a significant difference between 6-OHDA-exposed and control worms (# $p < 0.001$); * Indicates a significant difference between the PMN-pretreated, 6-OHDA-exposed and PMN-untreated, 6-OHDA-exposed groups (* $p < 0.05$, ** $p < 0.01$).

Furthermore, the percentage of abnormal phenotypes in 6-OHDA-exposed worms was significantly higher than in control worms by 3.9-fold ($p < 0.001$) (Figure 3c). Compared with that in the 6-OHDA-exposed worms, the phenotype of DA neuron degeneration was significantly reduced in 6-OHDA-exposed worms pretreated with 0.25 mM PMN by 35.3% ($p < 0.01$) (Figure 3c).

2.3. Food-Sensing Behavioral Defects of 6-OHDA-Exposed Worms Are Restored by PMN Pretreatment

The DA neuron function of worms is reflected in food-sensing behavior. When in contact with food, worms reduce their speed of movement (the frequency of body bending) to increase the efficiency of eating. The results showed that, compared with that on nonbacterial lawns, the bending frequency of wild-type N2 worms decreased by 53.7% ($p < 0.001$) after contact with bacterial lawns (quantified by the “slowing rate”) (Figure 3d). Compared with the control group, 6-OHDA-exposed N2 worms displayed a significant lessening in the slowing rate by 48.4% ($p < 0.001$). PMN dose-dependently increased the slowing rate of worms exposed to 6-OHDA. Compared with the 6-OHDA-exposed worms, the slowing rate of worms pretreated with 0.25 mM PMN increased by 1.9-fold ($p < 0.01$) (Figure 3d). The above results confirm that the damage to DA neurons caused by 6-OHDA can be improved by PMN pretreatment.

2.4. Lifespan of 6-OHDA-Exposed Worms Is Extended by PMN Pretreatment

Patients with PD have a shortened lifespan. As shown in Figure 3e, the lifespan of 6-OHDA-exposed N2 worms was shorter than that of control worms. However, PMN pretreatment could dose-dependently prolong the lifespan of 6-OHDA-exposed worms (Figure 3e). The cumulative survival model of lifespan calculated using the Kaplan–Meier method showed that the average survival time of the 6-OHDA-exposed group was 11.8 ± 1.2 days, while the average survival time of the 0.25 mM PMN-pretreated 6-OHDA-exposed group was 19.8 ± 2.1 days ($p < 0.001$) (Figure 3e). Thus, the shortening of lifespan caused by 6-OHDA was improved by PMN pretreatment.

2.5. Accumulation of Human α -Synuclein in Muscle Cells of NL5901 Worms Is Reduced by PMN Treatment

The aggregation and accumulation of human α -synuclein caused by overexpression or mutation of SNCA is a pathologic feature of PD. We used transgenic worms (NL5901) in which muscle cells express the YFP-fused protein of human α -synuclein for analysis. We found that PMN dose-dependently decreased the YFP fluorescence intensity of muscle cells of worm, which reflected the diminution in α -synuclein accumulation (Figure 4a). The fluorescence intensity of worms treated with 0.25 mM PMN was reduced by 33% compared with that in untreated worms ($p < 0.01$) (Figure 4b).

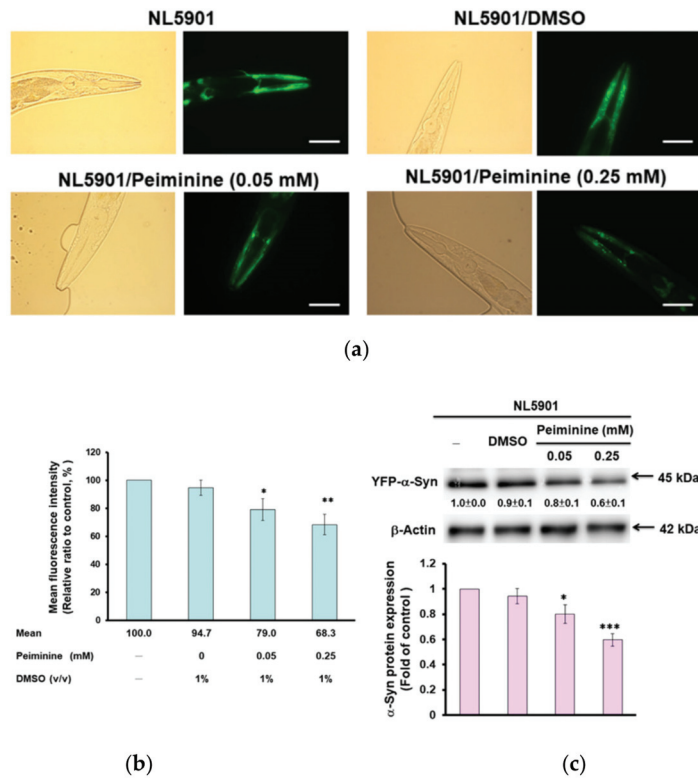


Figure 4. Accumulation of human α -synuclein in muscle cells of NL5901 worms was significantly reduced by treatment with peiminine (PMN). L1 stage NL5901 worms were cultured on OP50/NGM plates with or without PMN for 1 day. The worms were transferred to OP50/NGM/FUDR plates with or without PMN and cultured for 3 days, and then analyzed by fluorescence microscopy. (a) Representative YFP fluorescence images of the accumulation of α -synuclein in the head muscles of worms in each group. Scale bar = 50 μ m. (b) ImageJ software was used to quantify the fluorescence intensity of YFP of each group ($n = 50$) in (a). (c) The protein levels of α -synuclein in each group were analyzed by Western blotting. The loaded internal control is the level of β -actin. The image shows representative data from one of three independent experiments. The relative ratio is expressed as the ratio of the level of α -synuclein in each group to that in the PMN-untreated group. * Indicates a significant difference between the PMN-treated group and the PMN-untreated group (* $p < 0.05$, ** $p < 0.01$, *** $p < 0.001$).

To clarify the reason for the reduced fluorescence intensity of α -synuclein-YFP in NL5901 worms treated with PMN, we performed Western blot analysis. The results indicate that PMN dose-dependently reduced the protein level of α -synuclein and therefore lessened its accumulation (Figure 4c), but did not directly interfere with its aggregation (data not shown). After treatment with 0.25 mM PMN, the level of α -synuclein in muscle cells was diminished by 38% in NL5901 worms compared with untreated worms ($p < 0.001$) (Figure 4c).

2.6. PMN Pretreatment Decreases the Level of Reactive Oxygen Species in 6-OHDA-Exposed N2 Worms and Enhances the Expression of Pink1 and Pdr-1

Our previous studies showed that 6-OHDA exposure will increase the ROS in the worm, thus causing DA neuronal apoptosis and degeneration [30]. Therefore, we wanted to know whether PMN affected the ROS levels in 6-OHDA-exposed worms. Compared

with that in the control group, the ROS level of 6-OHDA-exposed worms was significantly increased by about 2.7-fold ($p < 0.001$) (Figure 5a). PMN diminished the ROS levels of 6-OHDA-exposed worms in a dose-dependent manner. After pretreatment with 0.25 mM PMN, the ROS level was lessened by about 49.2% compared with that in the untreated group ($p < 0.01$) (Figure 5a).

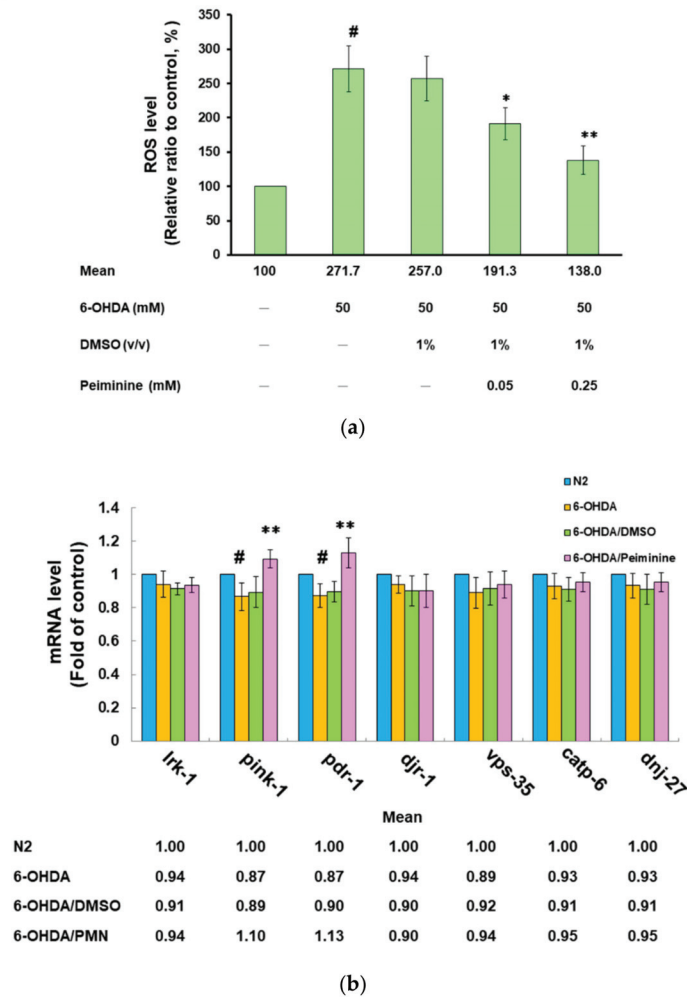


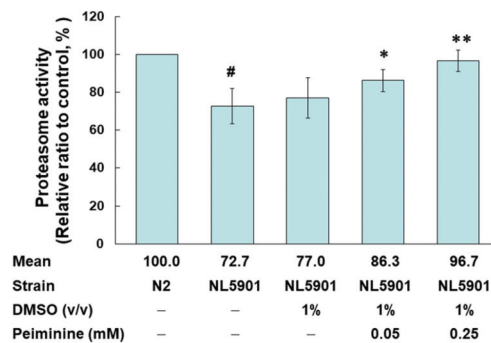
Figure 5. Pretreatment with peiminine (PMN) significantly lessened the level of reactive oxygen species (ROS) in 6-hydroxydopamine (6-OHDA)-exposed N2 worms and augmented the expression of *pink1* and *pdr-1*. L1 stage N2 worms were transferred to OP50/NGM plates with or without PMN and grown to the L3 stage, exposed to 6-OHDA for 1 h, and then transferred to OP50/NGM/FUDR plates with or without PMN and cultured for another 3 days for analysis. (a) Thirty worms randomly selected from each group were transferred to the wells of a 96-well plate, and the 2',7'-dichlorodihydrofluorescein diacetate (H2DCFDA) probe was used to detect the level of intracellular ROS. # Indicates a significant difference between the 6-OHDA-exposed group and the control group (# $p < 0.001$); * Indicates a significant difference between the PMN- pretreated 6-OHDA-exposed group and the PMN-untreated 6-OHDA-exposed group (* $p < 0.05$, ** $p < 0.01$). (b) qPCR was used to quantify the mRNA levels of PD-related homologous genes in worms. # Indicates a

significant difference between the 6-OHDA-exposed group and the control group ([#] $p < 0.05$); * Indicates a significant difference between the PMN-pretreated 6-OHDA-exposed group and the PMN-untreated 6-OHDA-exposed group (** $p < 0.01$).

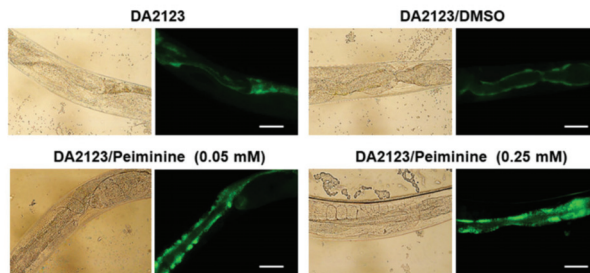
In addition, we analyzed the expression of homologous genes in *C. elegans* that are known to be associated with the pathophysiology of human PD. Using real-time quantitative PCR (qPCR), the expression of *lrk-1/LRRK2*, *djr-1.1/djr-1.2/DJ-1*, *vps-35/VPS35*, *catp-6/ATP13A2*, and *dnj-27/DNAJC10/Hsp40* in the 6-OHDA-exposed group was not significantly different from that in the control group (Figure 5b). However, the level of *pink-1/PINK1* and *pdr-1/PREN/parkin* was slightly reduced ($p < 0.05$). In worms pretreated with 0.25 mM PMN, the mRNA levels of *pink-1* and *pdr-1* were augmented by 1.3-fold ($p < 0.01$), respectively, compared with the PMN-untreated 6-OHDA-exposed group (Figure 5b).

2.7. PMN Treatment Enhances Proteasome Activity, Autophagy, and expression of Pdr-1 in NL5901 Worms

Previous studies have shown that the accumulation of α -synuclein can affect proteasome activity and autophagy, and that increasing the activity of the proteasome and autophagy can improve the cytotoxicity induced by the accumulation of α -synuclein [31]. Therefore, we used the fluorescent substrate of chymotrypsin to evaluate the effect of PMN on the proteasome activity of NL5901 worms. The basal level of proteasome activity in NL5901 worms was decreased by 27.3% compared with activity in N2 worms ($p < 0.01$) (Figure 6a). PMN treatment could enhance proteasome activity in a dose-dependent manner. Compared with the activity of the untreated group, treatment with 0.25 mM PMN increased the proteasome activity of worms 1.3-fold ($p < 0.01$) (Figure 6a).



(a)



(b)

Figure 6. Cont.

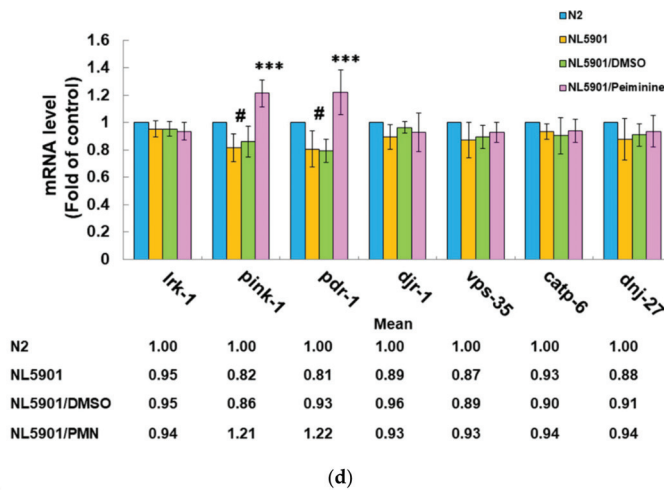
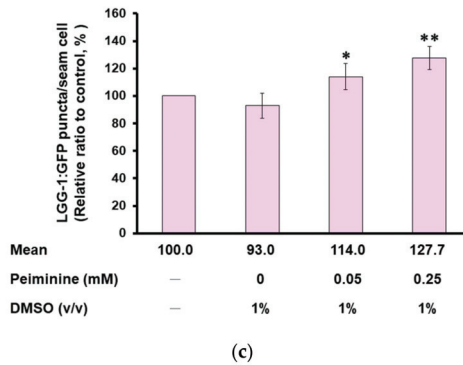


Figure 6. Treatment with peiminine (PMN) enhanced proteasome activity, autophagy, and *pdr-1* expression in NL5901 transgenic worms. (a) L1 stage NL5901 worms were cultured on OP50/NGM plates with or without PMN for 1 day. Worms were then transferred to OP50/NGM/FUDR plates with or without PMN and cultured for 3 days for analysis. The worm extracts of each group were tested for proteasome activity under the same amount of total protein. # Indicates a significant difference between N2 and NL5901 worms (# $p < 0.01$). * Indicates a significant difference between the PMN-treated group and the PMN-untreated group (* $p < 0.05$, ** $p < 0.01$). (b) L1 stage DA2123 worms were cultured on OP50/NGM plates with or without PMN for 1 day. Worms were then transferred to OP50/NGM/FUDR plates with or without PMN and cultured for 3 days for analysis. Representative images of the fluorescence distribution of positive puncta in the seam cells of each group of worm. Scale bar = 10 μ m. (c) The number of positive puncta in the seam cells of DA2123 worms was calculated. At least 20 worms were calculated in each group, and at least 20 seam cells were calculated for each worm. * Indicates a significant difference between the PMN-treated group and the PMN-untreated group (* $p < 0.05$, ** $p < 0.01$). (d) The expression levels of PD-related genes in N2 and PMN-untreated or treated NL5901 worms were quantified by qPCR. # Indicates a significant difference between N2 and NL5901 worms (# $p < 0.05$). * Indicates a significant difference between the PMN-treated group and the untreated group (** $p < 0.001$).

In addition, we used transgenic DA2123 worms expressing LGG-1 (human LC3 homologous protein) fused with GFP derived by the *lgg-1* promoter to evaluate the autophagy activity by counting the number of fluorescent puncta formed in seam cells (Figure 6b).

Compared with the number in untreated worms, the number of LGG-1::GFP puncta increased 1.28-fold ($p < 0.01$) after treatment with 0.25 mM PMN (Figure 6c).

Finally, we used qPCR to determine the expression levels of PD-related genes in N2 and PMN-untreated or treated NL5901 worms. Compared with N2 worms, except for the slightly lower expression of *pink-1* and *pdr-1* ($p < 0.05$), there was no significant difference in the basal level of expression of other genes in NL5901 worms (Figure 6d). After treatment with 0.25 mM PMN, the expression of *pink-1* and *pdr-1* in NL5901 worms was significantly increased by 1.5 fold ($p < 0.001$), respectively, compared with the untreated group (Figure 6d).

2.8. Inhibiting the Expression of *Pdr-1* in Worms Can Reverse the Ability of PMN to Improve PD Pathology

The above experiments showed that PMN can promote the expression of *pdr-1* in worms. Furthermore, we wanted to verify the main mediating role of *pdr-1* by use of RNAi in PMN-pretreated 6-OHDA-exposed BZ555 worms and PMN-treated NL5901 worms. In BZ555 worms, the mRNA expression of *pdr-1* in the *pdr-1* RNAi group was reduced by 71% (No. 1, $p < 0.001$) compared to that in the control RNAi group (Figure 7a). After *pdr-1* down-regulation, GFP fluorescence intensity did not increase in PMN-pretreated 6-OHDA-exposed BZ555 worms compared with that in the PMN-untreated 6-OHDA-exposed group, reflecting that PMN lost the ability to improve DA neuron degeneration (Figure 7b–d).

In NL5901 worms, the expression of *pdr-1* in the *pdr-1* RNAi group was reduced by 76.3% (no. 2, $p < 0.001$) compared with expression in the RNAi control group (Figure 7e). After *pdr-1* down-regulation, YFP fluorescence intensity did not decline in PMN-treated NL5901 worms compared with that in the PMN-untreated group, reflecting that the accumulation of α -synuclein was not improved (Figure 7f,g). In Western blotting analysis, after *pdr-1* was down-regulated, PMN-treated NL5901 worms did not show a lessening in human α -synuclein protein levels compared with the PMN-untreated group (Figure 7h), reflecting that the amount of α -synuclein was not reduced.

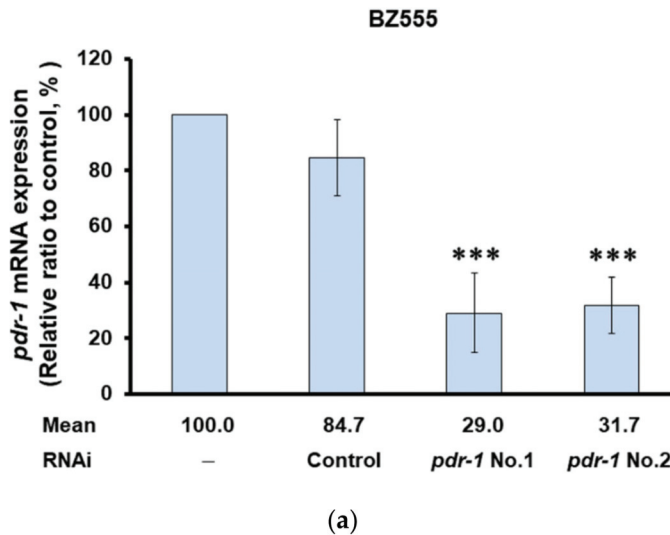
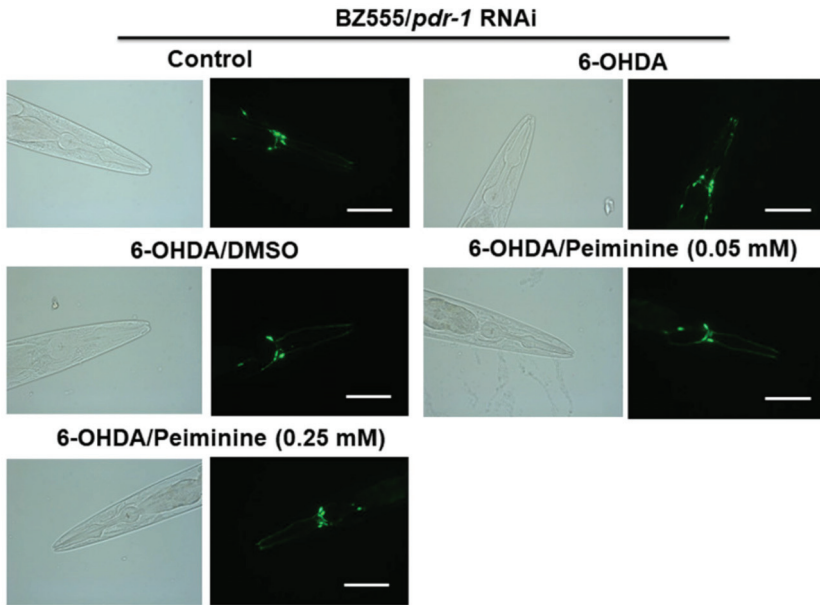
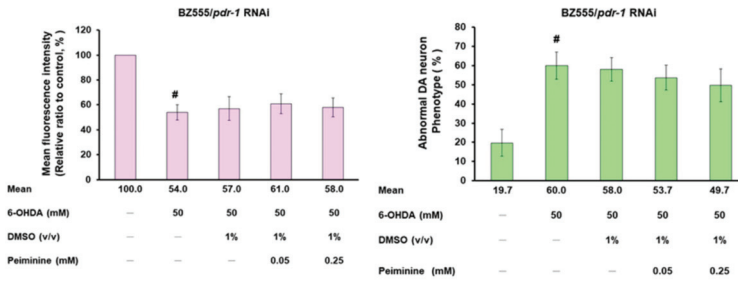


Figure 7. Cont.

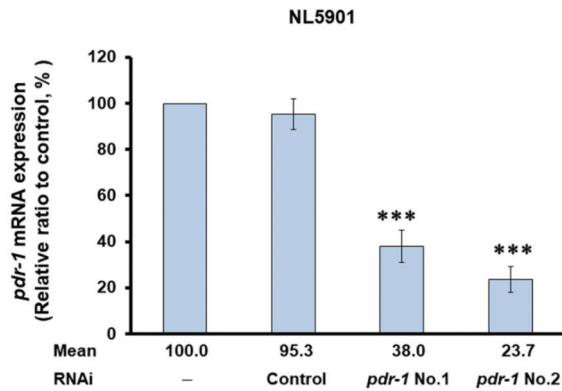


(b)



(c)

(d)



(e)

Figure 7. Cont.

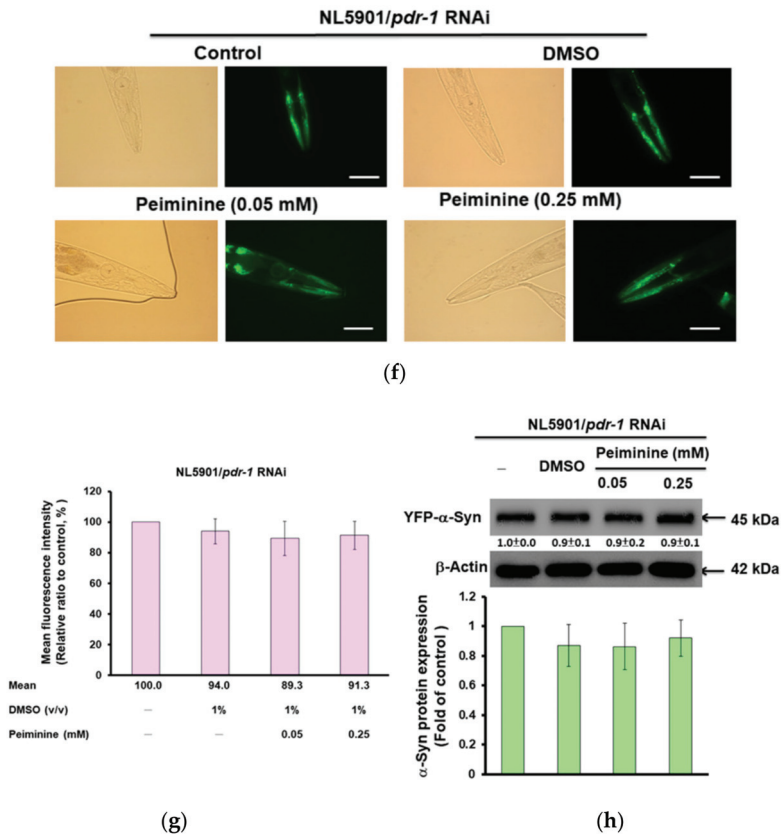


Figure 7. Using RNA interference (RNAi) to down-regulate the mRNA expression of *pdr-1* can abolish the ability of peiminine (PMN) to improve the pathology of Parkinson disease in worm models. In the 6-OHDA-exposed BZ555 model, L1 stage worms were transferred to *pdr-1* RNAi/NGM plates with or without PMN and grown to the L3 stage, exposed to 6-OHDA for 1 h, and then transferred to *pdr-1* RNAi/NGM/FUDR plates with or without PMN and cultured for another 3 days for analysis. In the transgenic NL5901 model, L1 stage worms were cultured on *pdr-1* RNAi/NGM plates with or without PMN for 1 day and then transferred to *pdr-1* RNAi/NGM/FUDR plates with or without PMN and cultured for 3 days. (a) The relative level of *pdr-1* mRNA in *pdr-1* RNAi-treated BZ555 worms was determined by qPCR. * Indicates a significant difference between the *pdr-1* RNAi group and the control RNAi group (** $p < 0.001$). (b) Representative fluorescence images of GFP expression patterns in DA neurons of BZ555 worms in each group. Scale bar = 50 μm . (c) ImageJ software was used to quantify the fluorescence intensity of the GFP image in (b) ($n = 50$). (d) The DA neuron degeneration phenotype defects of each group in (b) were scored. The data are represented as a percentage of the total population of worms with defective DA neuron phenotypes. # Indicates a significant difference between the 6-OHDA-exposed group and the control group (# $p < 0.001$). (e) The relative level of *pdr-1* mRNA in *pdr-1* RNAi-treated NL5901 worms was determined by qPCR. * Indicates a significant difference between the *pdr-1* RNAi group and the control RNAi group (** $p < 0.001$). (f) Representative YFP fluorescence images of the accumulation of α -synuclein in the head muscles of worms in each group. Scale bar = 50 μm . (g) ImageJ software was used to quantify the YFP fluorescence intensity of each group ($n = 50$) in (f). # Indicates a significant difference between the PMN-treated group and the PMN-untreated group (# $p < 0.001$). (h) The protein levels of α -synuclein in each group were analyzed by Western blotting. The loaded internal control is the level of β -actin. The image shows representative data from one of three independent experiments. The relative ratio is represented as the ratio of the level of α -synuclein in each group to that in the PMN-untreated group.

2.9. PMN Treatment Improves the Toxicity of 6-OHDA Exposure and α -Synuclein Overexpression in the SH-SY5Y Cell Line

To further evaluate the efficacy of PMN in improving PD, we used a human SH-SY5Y cell line with 6-OHDA exposure and α -synuclein overexpression. According to the results of the MTT assay, treatment with 4 μ M PMN was not toxic to SH-SY5Y cells (Figure 8). In addition, the viability of 6-OHDA-exposed and α -synuclein-overexpressing cells was reduced by 47% ($p < 0.001$) and 23% ($p < 0.01$), respectively, compared with the control group (Figure 8). When the 6-OHDA-exposed and α -synuclein-overexpressing cells were treated with 1 μ M PMN, their viability was increased 1.7-fold ($p < 0.01$) and 1.3-fold ($p < 0.01$), respectively, compared with the PMN-untreated groups (Figure 8).

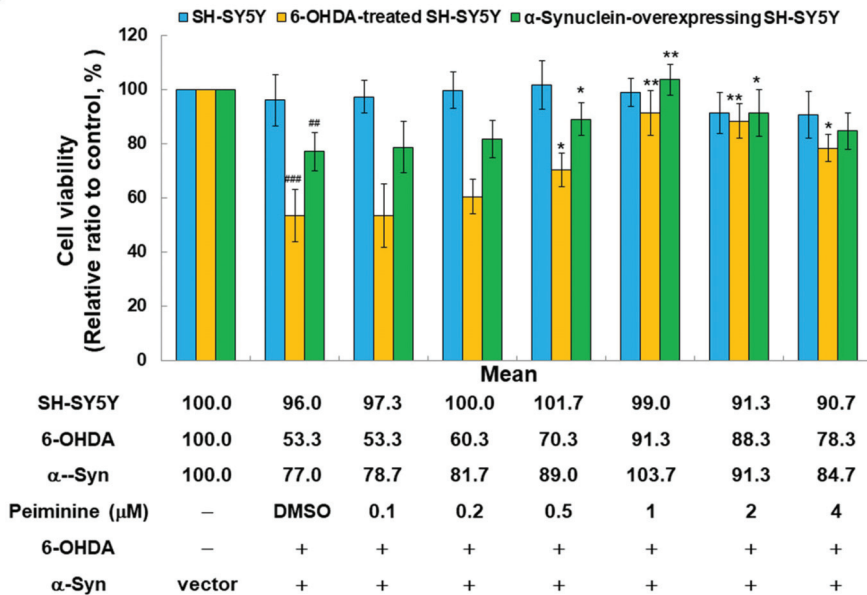
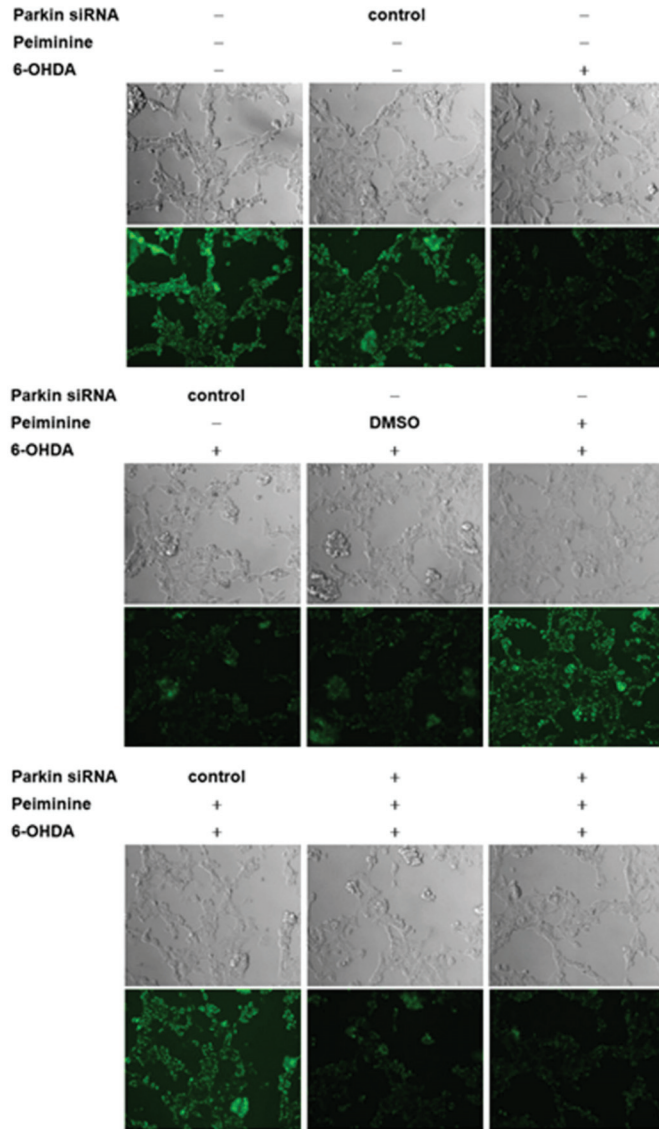


Figure 8. PMN treatment reduces the toxicity of 6-OHDA exposure and α -synuclein overexpression in the SH-SY5Y cell line. Cells were treated with 0.1, 0.2, 0.5, 1, 2, or 4 μ M PMN for 24 h (SH-SY5Y group), followed by 6-OHDA exposure for 18 h (6-OHDA-treated SH-SY5Y group), or α -synuclein-overexpressing cells were treated with PMN for 24 h (α -synuclein-overexpressing SH-SY5Y group), and the cell survival rate was determined by MTT assay. # Indicates a significant difference between the 6-OHDA-exposed group or α -synuclein-overexpressing group and the control group (### $p < 0.01$, #### $p < 0.001$). * Indicates a significant difference between the PMN-treated group and the PMN-untreated group (* $p < 0.05$, ** $p < 0.01$).

2.10. Down-Regulation of Parkin Abolishes the Anti-Apoptotic ability of PMN in 6-OHDA-Exposed SH-SY5Y Cells

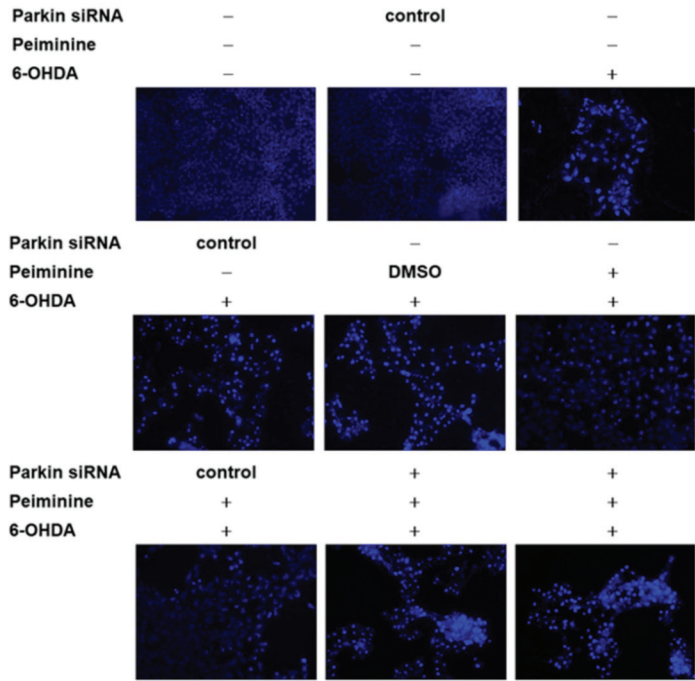
The results of our research in the worm model confirmed that PMN can ameliorate ROS toxicity and DA neuron death caused by 6-OHDA exposure, which may inhibit cell apoptosis by inducing the expression of *pdr-1* (a human parkin homologous gene). We further used the SH-SY5Y cell model to verify this result. DiOC6 and Hoechst 33258 analysis showed that compared with the unexposed group, the 6-OHDA-exposed group had a 44% reduction in mitochondrial membrane potential (MMP, $p < 0.001$) (Figure 9a,c) and 2.1-fold ($p < 0.001$) greater nuclear condensation (Figure 9b,c). To quantify apoptosis, we used Annexin-V-FITC/PI flow cytometry analysis. As shown in Figure 9d, compared with that in the control group, apoptosis was 3.7-fold greater in the 6-OHDA-exposed group ($p < 0.001$). Western blot analysis showed that compared with levels in the control group, the protein levels of PINK1 and parkin were decreased by 47.0% ($p < 0.001$) and 59.7%

($p < 0.001$), respectively, in the 6-OHDA-exposed group. The levels of cleaved caspase 9, caspase 7, caspase 3, and PARP associated with apoptosis were 3.7-fold ($p < 0.001$), 2.5-fold ($p < 0.001$), 3.2-fold ($p < 0.001$), and 9.3-fold ($p < 0.001$) greater, respectively (Figure 10a,b).

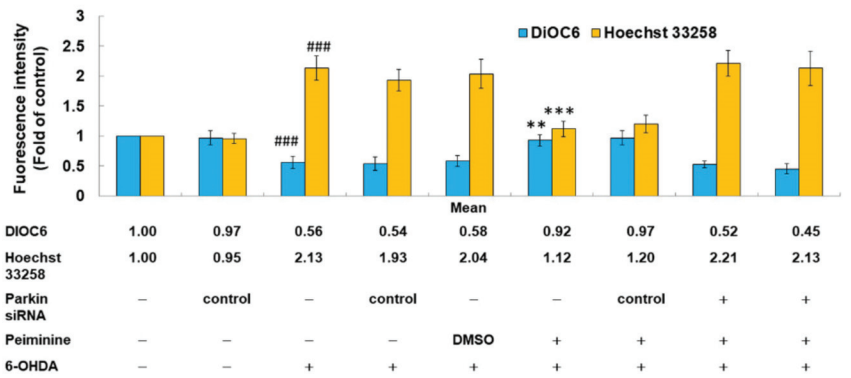


(a)

Figure 9. Cont.



(b)



(c)

Figure 9. Cont.

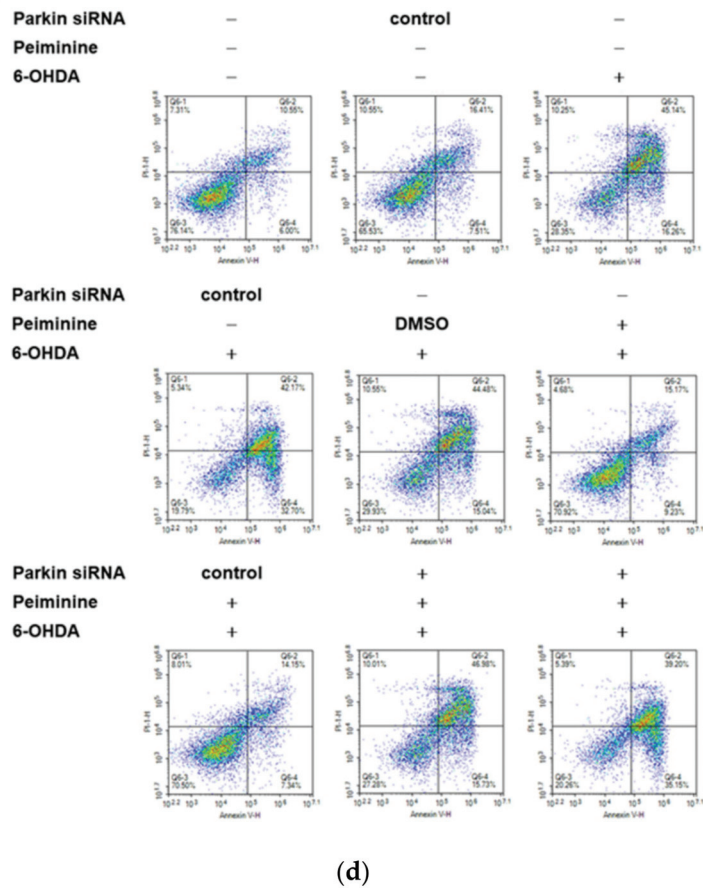
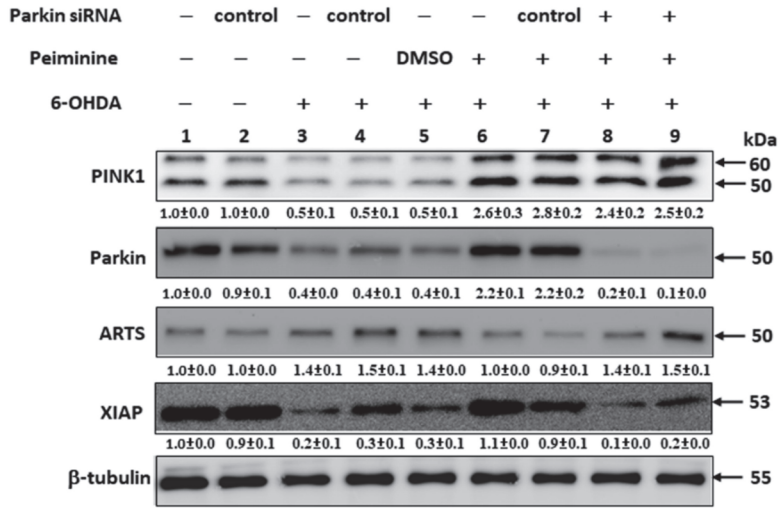


Figure 9. Down-regulation of *parkin* by RNAi can reverse the anti-apoptotic effect of peiminine (PMN) in 6-hydroxydopamine (6-OHDA)-exposed SH-SY5Y cells. SH-SY5Y cells were transfected with control siRNA or *parkin* siRNA for 24 h, and then the transfected cells were treated with 1 μ M PMN or no treatment, respectively. After 24 h, cells were exposed to 100 μ M 6-OHDA for 18 h. (a) DiOC6 (1 μ M) staining was used to evaluate damage to mitochondrial membrane potential (MMP). The representative fluorescence images of each group are shown here. (b) Hoechst 33258 (5 μ g/mL) staining was used to evaluate the ratio of nuclear condensation. The representative fluorescence images of each group are shown here. (c) ImageJ software was employed to analyze the fluorescence intensity of the staining in (a) and (b). The relative fluorescence intensity is indicated as a ratio relative to the control group. # Indicates a significant difference between the 6-OHDA-exposed group and the control group (#### $p < 0.001$). * Indicates a significant difference between the PMN-pretreated 6-OHDA-exposed group and the PMN-untreated 6-OHDA-exposed group (** $p < 0.01$, *** $p < 0.001$).



(a)

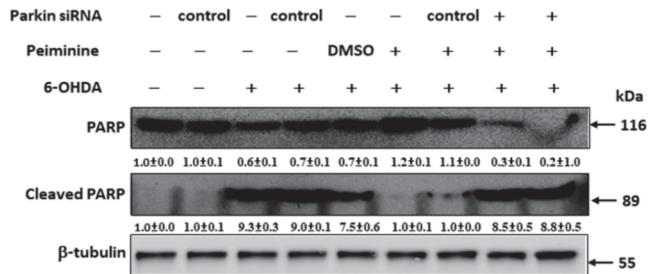
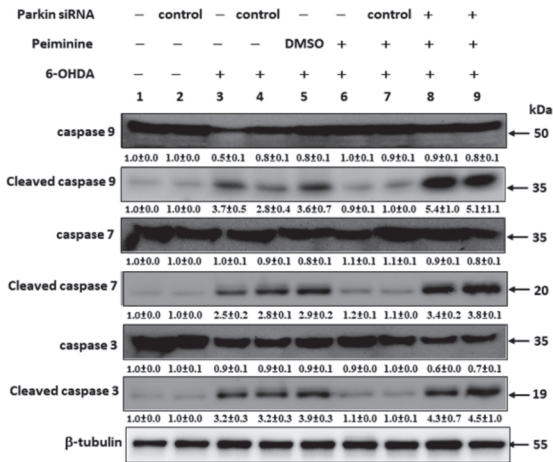


Figure 10. Cont.

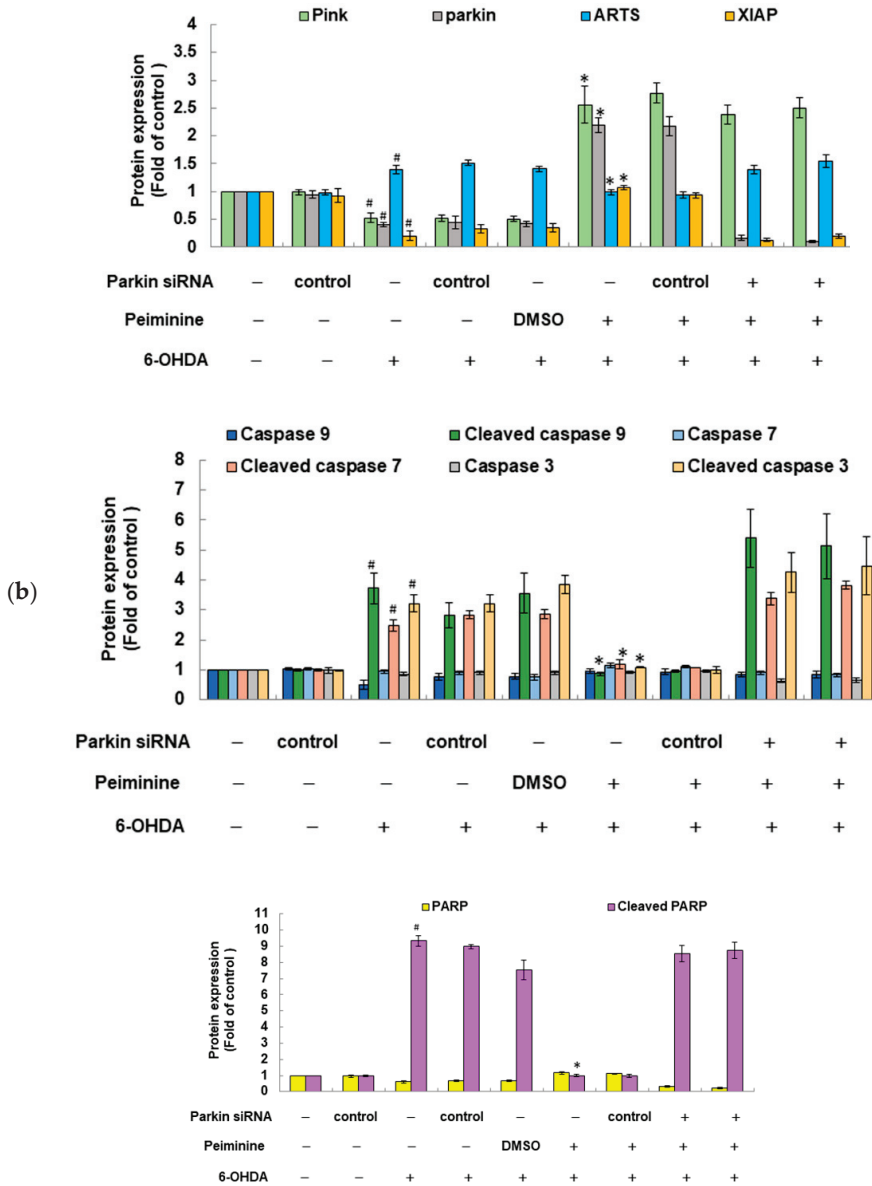


Figure 10. Western blot analysis was used to quantify the levels of PINK1, parkin, ARTS, XIAP, and apoptotic core proteins. SH-SY5Y cells were transfected with control siRNA or *parkin* siRNA for 24 h, and then the transfected cells were treated with 1 μ M PMN or no treatment, respectively. After 24 h, cells were exposed to 100 μ M 6-OHDA for 12 h. (a) Shows representative results from one of three independent experiments. (b) ImageJ software was utilized to quantify the signal intensity of the image in (a). The loaded internal control is the level of β -tubulin. The relative ratio is represented as the ratio of each group to the control group. # Indicates a significant difference between the 6-OHDA-exposed group and the control group ($^{\#} p < 0.001$). * Indicates a significant difference between the PMN-pretreated 6-OHDA-exposed group and PMN-untreated 6-OHDA-exposed group ($^* p < 0.001$).

However, PMN pretreatment significantly lessened the apoptosis of SH-SY5Y cells induced by 6-OHDA. Compared with that of PMN-untreated 6-OHDA-exposed cells, the MMP of 1 μ M PMN-treated 6-OHDA-exposed cells was 1.7-fold greater ($p < 0.01$) (Figure 9a,c). Nuclear condensation was reduced by 47% ($p < 0.001$) (Figure 9b,c), and apoptosis was significantly diminished by 60% ($p < 0.001$) (Figure 9d). In addition, the protein levels of PINK1 and parkin were augmented 4.8-fold ($p < 0.001$) and 5.5-fold ($p < 0.001$), respectively. The levels of cleaved caspase 9, caspase 7, caspase 3, and PARP were reduced by 76% ($p < 0.001$), 52% ($p < 0.001$), 66% ($p < 0.001$), and 89% ($p < 0.001$), respectively (Figure 10a,b). Finally, we used RNAi to inhibit the expression of *parkin* in SH-SY5Y cells. We found that the ability of PMN to reverse 6-OHDA-induced apoptosis was blocked (Figures 9 and 10).

2.11. Down-Regulation of Parkin Can Reverse the Ability of PMN to Enhance Ubiquitin-Proteasome System Activity and Autophagy in α -Synuclein-Overexpressing SH-SY5Y Cells

Since we confirmed in the above experiments that PMN can improve the accumulation of α -synuclein in NL5901 worms, we hypothesized that it may be associated with inducing the expression of *pdr-1* to enhance the UPS and the activity of autophagy. We further used the human α -synuclein-overexpressing SH-SY5Y cell model to verify this result. First, we constructed the pcDNA 3.1-SNCA-Myc plasmid and transfected it into the SH-SY5Y cell line to obtain an α -synuclein-overexpressing cell model [31]. Compared with values in the control group, in α -synuclein-overexpressing cells, the UPS activity and the fluorescence intensity of acidic vesicle organelle staining were decreased by 12% ($p < 0.01$) (Figure 11a) and 39% ($p < 0.001$) (Figure 11b,c), respectively. To quantify the autotrophic defect caused by overexpression of α -synuclein, we used LC3II-based flow cytometry. As shown in Figure 11d, compared with the control group, overexpression of α -synuclein caused a 32% reduction in the autophilic activity of SH-SY5Y cells ($p < 0.01$). Western blot analysis showed that compared with the control group, PINK1 and parkin were reduced by 60% ($p < 0.001$) and 73% ($p < 0.001$) in α -synuclein-overexpressing cells, respectively (Figure 12a,b). The autophagy-related proteins PI3K p100, Atg7, and LC3I/LC3II were lessened by 37% ($p < 0.001$), 62% ($p < 0.001$), and 25% ($p < 0.001$), respectively. There were no significant changes in mTOR or p-mTOR (Figure 12a,b).

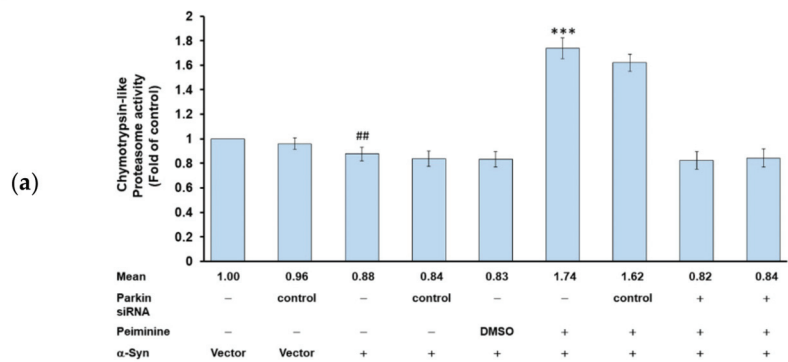


Figure 11. Cont.

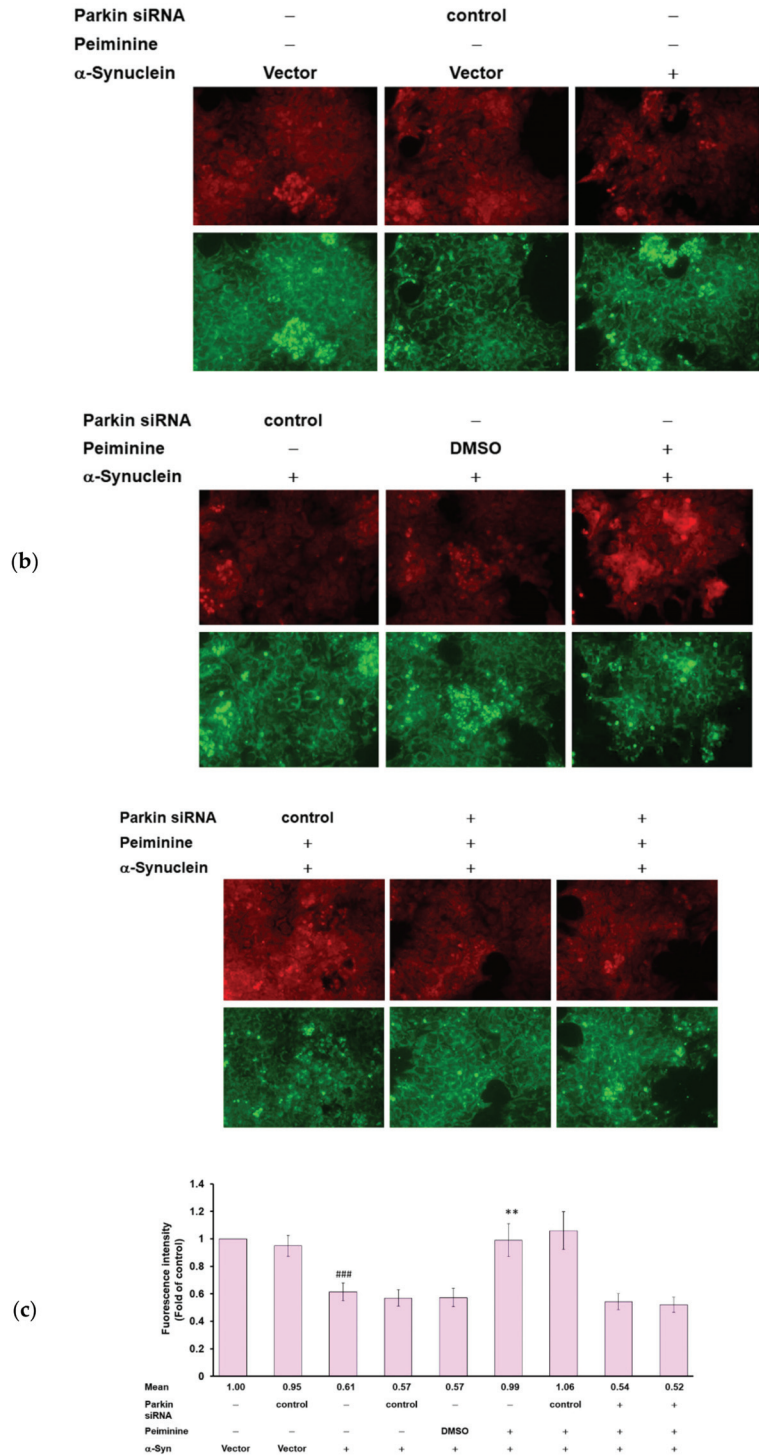


Figure 11. Cont.

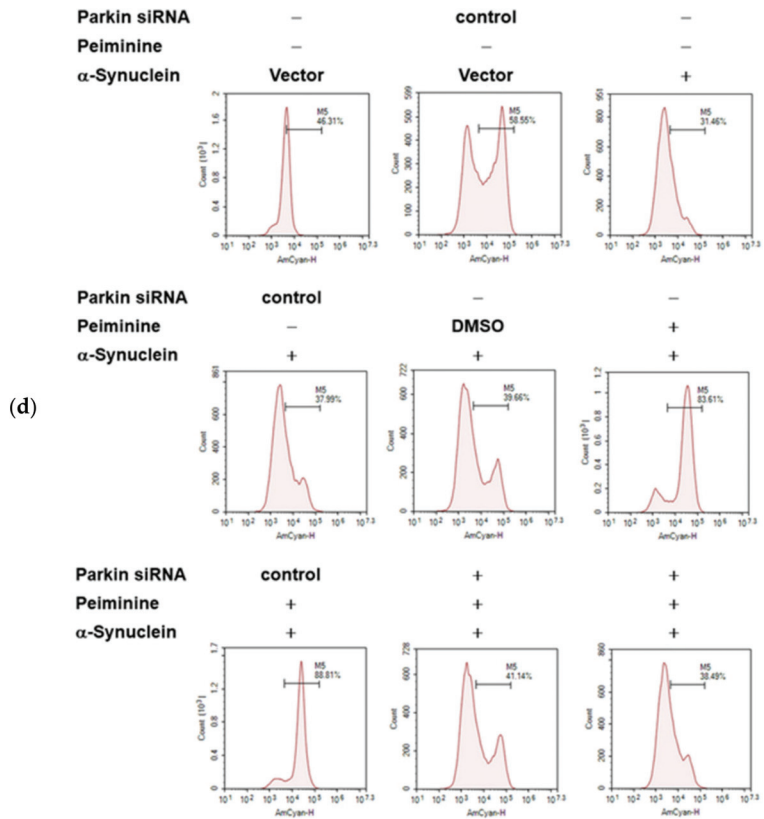


Figure 11. Down-regulation of parkin can abolish the ability of PMN to promote UPS activity and autophagy in α -synuclein-overexpressing SH-SY5Y cells. α -Synuclein-overexpressing SH-SY5Y cells were transfected with control siRNA or *parkin* siRNA for 24 h. Next, the transfected cells were treated with 1 μ M PMN or untreated for 24 h and then analyzed. (a) Suc-Leu-Leu-Val-Tyr-AMC was used as a substrate for measuring proteasome activity. The relative fold of the proteasome activity is represented as the ratio of the activity of each group to the control group. (b) Acridine orange staining was used to evaluate the number of acidic vesicular organelles in cells. The representative fluorescence images of each group are shown here. (c) The fluorescence intensity of the staining in (b) was analyzed by employing ImageJ software. The relative fluorescence intensity is shown as the ratio of the fluorescence intensity of each group to that of the control group. (d) Cells were incubated with the Autophagosome Detection Reagent for 30 min and analyzed by flow cytometry. The results shown above are the standard errors of the average of three independent experiments. # Indicates a significant difference between the α -synuclein-overexpressing group and the control group (## $p < 0.01$, ### $p < 0.001$). * Indicates a significant difference between the PMN-pretreated group and the PMN-untreated group (** $p < 0.01$, *** $p < 0.001$).

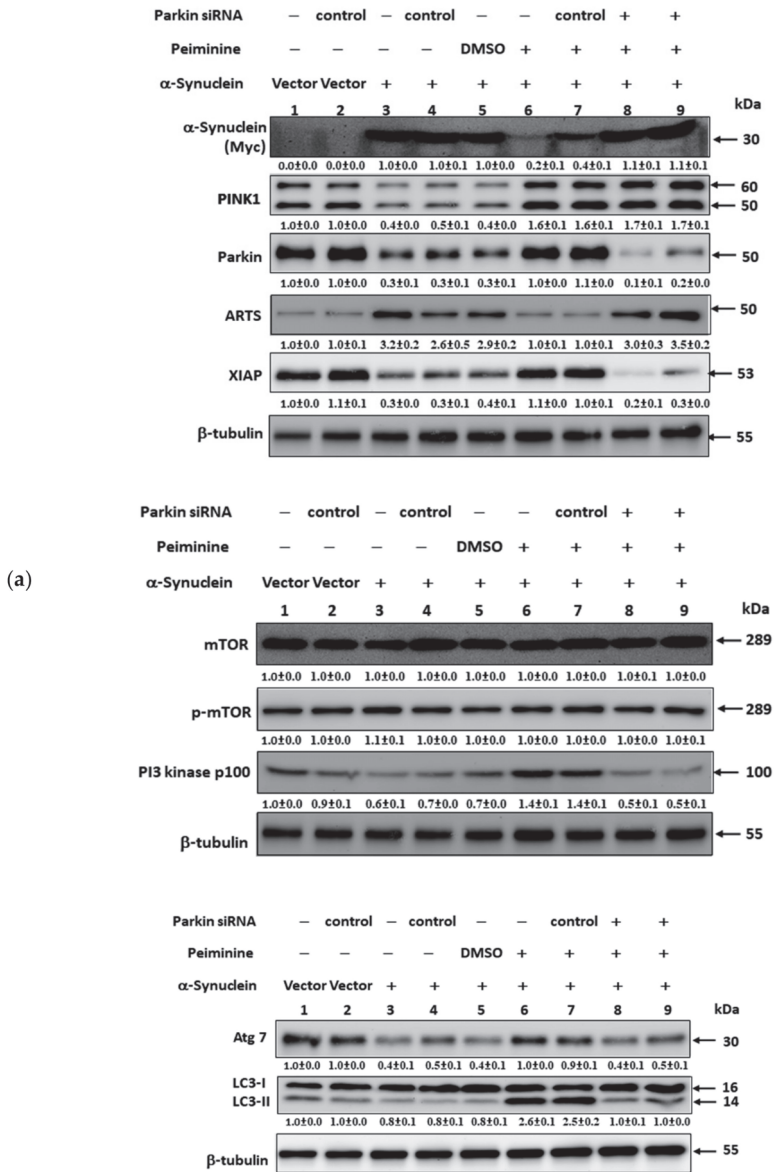


Figure 12. Cont.

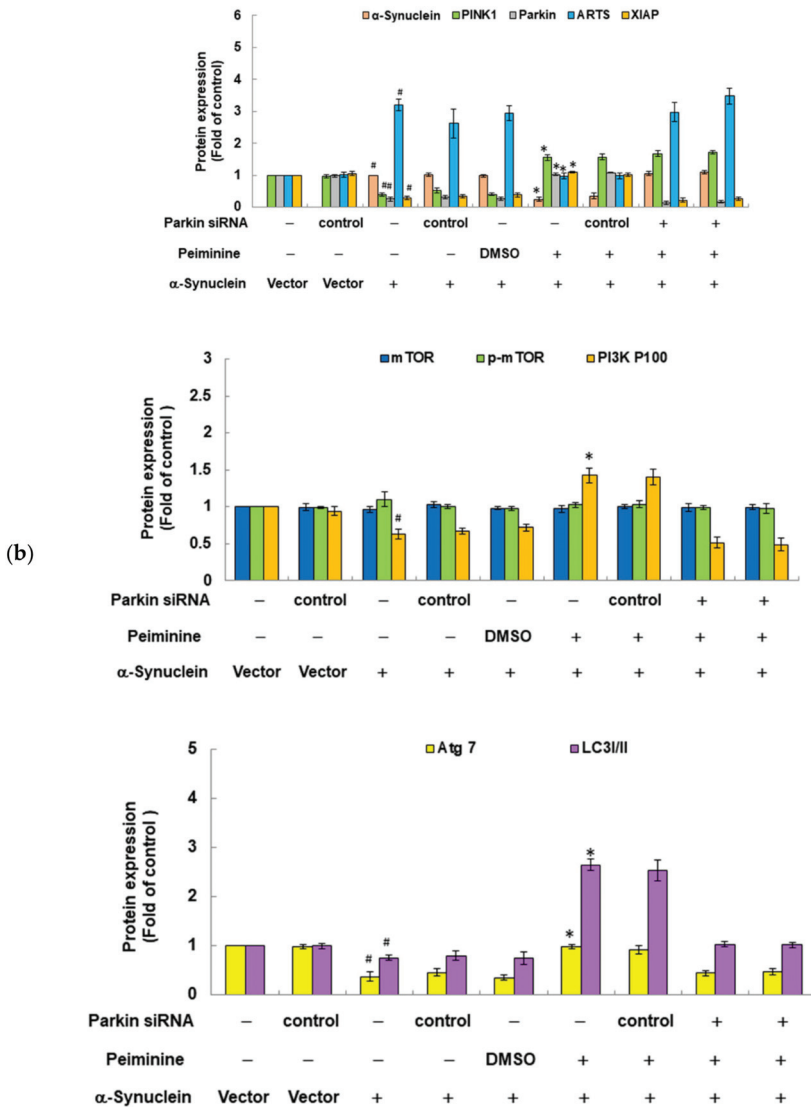


Figure 12. Western blot analysis was used to quantify the protein levels of PINK1, parkin, ARTS, XIAP, and autophagy core proteins. α -Synuclein-overexpressing SH-SY5Y cells were transfected with control siRNA or parkin siRNA for 24 h. Next, the transfected cells were treated with 1 μ M PMN or untreated for 24 h and then analyzed. (a) Shows representative results from one of three independent experiments. (b) ImageJ software was utilized to quantify the signal intensity of the image in (a). The loaded internal control was the level of β -tubulin. The relative ratio is represented as the ratio of each group to the control group. # Indicates a significant difference between the α -synuclein-overexpressing group and the control group (# $p < 0.001$). * Indicates a significant difference between the PMN-treated group and the PMN-untreated group (* $p < 0.001$).

PMN treatment improved the defects in the UPS and autophagy caused by α -synuclein overexpression in SH-SY5Y cells. The results show that compared with the PMN-untreated group, the UPS activity, the fluorescence intensity of acidic vesicular organelle staining, and autophagic activity increased by 2.0-fold ($p < 0.001$) (Figure 11a), 1.6-fold ($p < 0.01$) (Figure 11b,c), and 2.7-fold ($p < 0.001$) (Figure 11d) in the PMN-treated group, respectively. Western blot analysis indicated that in the PMN-treated group compared with the untreated

group, the protein level of PINK1 and parkin increased by 2.9-fold ($p < 0.001$) and 3.8-fold ($p < 0.001$), respectively (Figure 12a,b). The expression of PI3K p100, Atg7, and LC3I/LC3II was augmented by 2.3-fold ($p < 0.001$), 2.6-fold ($p < 0.001$), and 3.5-fold ($p < 0.001$), respectively (Figure 12a,b). There was no significant change in mTOR or p-mTOR (Figure 12a,b). Finally, we used RNAi to down-regulate the expression of *parkin* in α -synuclein-overexpressing cells. The results revealed that the ability of PMN to activate the UPS and autophagy was inhibited (Figures 11 and 12).

2.12. PMN May Contribute to Anti-Parkinson Activity by Up-Regulating Parkin Performance, Leading to a Diminution of Apoptosis-Related Protein in the TGF- β Signaling Pathway (ARTS) and a Rise in X-Linked Inhibitor of Apoptosis (XIAP)

In worm and cell models with 6-OHDA exposure and α -synuclein overexpression, we confirmed that PMN can enhance parkin expression. Parkin is known as an E3 ubiquitin ligase, which can regulate the activity of downstream substrates through selective ubiquitination. Through extensive analysis, we found that one of its substrates, ARTS, may also be involved in the neuroprotective mechanism of PMN. Using Western blot analysis, we showed that ARTS protein expression in 6-OHDA-exposed cells was 1.4-fold ($p < 0.001$) that of control cells (Figure 10). In PMN-treated 6-OHDA-exposed cells, ARTS protein expression was reduced by 29.0% ($p < 0.001$) compared with PMN-untreated 6-OHDA-exposed cells (Figure 10). Using RNAi to down-regulate the expression of parkin in SH-SY5Y cells, we found that the ability of PMN to reverse the 6-OHDA-induced increase in ARTS expression was abolished (Figure 10). In α -synuclein-overexpressing cells, ARTS protein expression increased by 3.2-fold ($p < 0.001$) compared with that in control cells (Figure 12). In α -synuclein-overexpressing cells, the expression of ARTS protein was reduced by 69.0% ($p < 0.001$) in the PMN-treated group compared with the untreated group (Figure 12). RNAi was used to down-regulate the expression of *parkin* in α -synuclein-overexpressing SH-SY5Y cells. We found that the ability of PMN to reverse the increase in ARTS induced by overexpression of α -synuclein was abolished (Figure 12).

Several reports have shown that the function of XIAP, which can regulate apoptosis and promote proteasome activity and autophagy, is inhibited by binding of ARTS [15–17]. We wanted to further analyze whether PMN could affect the level of XIAP. Western blot analysis showed that XIAP protein expression in 6-OHDA-exposed cells was lessened by 79.3% ($p < 0.001$) compared with that in control cells (Figure 10). In PMN-treated 6-OHDA-exposed cells, XIAP protein expression was 5.2-fold ($p < 0.001$) that in PMN-untreated 6-OHDA-exposed cells (Figure 10). Using RNAi to down-regulate the parkin expression of cells, we found that the ability of PMN to reverse 6-OHDA-induced XIAP reduction was abolished (Figure 10). In α -synuclein-overexpressing cells, XIAP protein expression was reduced by 70.3% compared with that in control cells ($p < 0.001$) (Figure 12). In α -synuclein-overexpressing cells, XIAP protein expression in the PMN-treated group was 3.7-fold ($p < 0.001$) that in the untreated group (Figure 12). Using RNAi to down-regulate the *parkin* expression of cells, we found that the ability of PMN to reverse the diminished expression of XIAP induced by overexpression of α -synuclein was abolished (Figure 12).

3. Discussion

Previous studies have shown that PMN has rich biopharmaceutical activities, which can lead to resistance to oxidation, inhibition of inflammation, and blocking of tumor growth [32,33]. Here, we confirmed another activity of PMN: namely, a neuroprotective effect. PMN can inhibit 6-OHDA-induced ROS production, the decline in MMP, and cell apoptosis both in vivo and in vitro, thus preventing DA neuron degeneration and improving DA-related food-sensing behavior and lifespan defects in a worm model. We also showed that PMN can enhance the UPS and autophagy activity, thus reducing the accumulation of α -synuclein. This is the first time that PMN has been shown to have PD pathology-inhibiting features in animal and cell models. We also explored the possible molecular mechanisms of PMN through RNAi experiments. PMN may activate the PINK1 (worm homologous gene *pink1*)/parkin (worm homologous gene *pdr-1*) pathway and

regulate the activity of their downstream substrates, such as enhancing the ubiquitination and degradation of ARTS (worm homologous genes *unc-59* and *unc-61*). This in turn increases the level of XIAP (worm homologous gene *iap*), preventing 6-OHDA-induced apoptosis and excessive accumulation of α -synuclein.

Research has shown that *PINK1* deficiency impairs the differentiation of DA neurons from adult neural stem cells [34] and inhibits the mitophagy and MMP of DA neurons [35]. Knockout of *PINK1* affects the neurotransmission of DA neurons and causes motor dysfunction in *Drosophila* [36]. In *PINK1* knockout mice, the aggregation of abnormal endogenous α -synuclein is increased, which increases the sensitivity of DA neurons to α -synuclein and finally causes degeneration [37]. In addition, *PINK1* knockout mice have less tyrosine hydroxylase in the hippocampus, which changes DA signaling in the hippocampus and causes damage to learning and memory [38]. In aging *PINK1* knockout mice, mitochondrial DNA heteroplasmy in the substantia nigra is increased [39]. Other studies have shown that loss of *PINK1* and overexpression of α -synuclein can lead to a diminution in the length of neurites in midbrain neurons, which may be related to mitochondrial fission and increased Golgi fragmentation [40]. Drp1 is a substrate of *PINK1*, and *PINK1*-mediated phosphorylation of Drp1^{S616} can directly increase mitochondrial fission, independent of parkin and autophagy. Some *PINK1*-related cases of familial and sporadic PD have been shown to have decreased phosphorylation of Drp1^{S616} [41]. Therefore, PMN can enhance the neuroprotective effect by increasing the expression of *PINK1*.

Aging *parkin* knockout mice display dyskinesias, including hindlimb defects and neuronal loss. In the DA neurons of these mice, the internal structure of the mitochondria is abnormal and fragmented [42]. Moreover, loss of parkin function results in an intrastriatal reconfiguration of interneuronal circuits and amplifications of synchronized cortico-striatal oscillations. These changes predispose the animal to an imbalance in striatal outflow [43]. FBP1 and AIMP are substrates of parkin, and both have been found to accumulate in the brains of PD patients. Their function is to transcriptionally activate the deubiquitinase USP29. The substrate for USP29 is myb binding protein 1A (MYBBP1A). In SH-SY5Y cells, knockout of parkin increases the level of AIMP2, leading to the accumulation of USP29 and MYBBP1A, which may be one reason for the pathogenesis of PD [44]. Studies have shown that the expression of parkin in neuronal cells is down-regulated by exogenous α -synuclein, which causes mitochondrial dysfunction [45] and neuroinflammation [46]. Interestingly, oxidative stress induces the post-translational modification of the cysteine of parkin in the substantia nigra of mice and humans, causing it to oxidize with age and gradually become insoluble. This oxidative modification is associated with neuroprotection, including reducing H₂O₂, neutralizing reactive DA metabolites, chelating free radicals in insoluble aggregates, and increasing melanin formation. Therefore, *parkin* mutants may lose the ability to complement this redox effect, which increases oxidative stress and causes DA neurons to age, thereby increasing the risk of PD [47]. Therefore, PMN can prevent neuronal damage and degeneration by improving expression of parkin.

Studies have reported iron deposits in the substantia nigra pars compacta of PD animal models and patients. Thus, the destruction of iron homeostasis may be related to PD. Iron is reported to inhibit the activity of parkin, thereby hindering the degradation of α -synuclein by the proteasome. The resulting aggregated α -synuclein leads to mitochondrial dysfunction and apoptosis in SH-SY5Y cells [48]. Lactoferrin is a transferrin that regulates iron homeostasis. Parkin can bind to lactoferrin and degrade it by ubiquitination to affect iron homeostasis. Elevated levels of lactoferrin and its receptor have been observed in parkin mutant PD [49]. Divalent metal transporter 1 (DMT1) is also a substrate for parkin ubiquitination. α -Synuclein activates p38 mitogen-activated protein kinase (MAPK) to phosphorylate parkin^{S131}, thereby reducing the E3 ubiquitin ligase activity of parkin, leading to high DMT1 levels and abnormal iron accumulation [50]. Some PD patients show S-nitrosylated parkin (SNO-parkin). Studies in SH-SY5Y cells have shown that SNO-parkin lessens the ubiquitination activity for DMT1, leading to high levels of DMT1, thus causing abnormal iron accumulation and neurodegeneration [51]. Interestingly, reducing DMT-1

and iron accumulation may result in augmented iron regulatory protein (IRP)/iron responsive element (IRE) interactions on the 5'UTR of *SNCA* to lower its translation. Therefore, the abnormal increase in iron in the brain of PD patients promotes the development of iron attenuating agents and iron chelators as a new treatment strategy for PD [52]. PMN can upregulate the expression of parkin and may maintain the stable concentration of iron ions in nerve cells and prevent iron and as well as α -synuclein accumulation from causing damage to the cells. In the future, we will further use DA neurons derived from iPS stem cell of PD patient which over express endogenous *SNCA*, to evaluate the efficacy of PMN against α -synucleinopathies.

DA neurons derived from induced pluripotent stem cell lines from patients with *parkin* mutations have mitophagy and autophagy–lysosomal pathway defects [53,54], and the complexity and maturity of neurites is decreased by *parkin* mutations [55]. In the *Drosophila* model, PINK1 or parkin dysfunction can cause PARIS-dependent inhibition of PGC-1 α and its downstream transcription factors NRF1 and TFAM in DA neurons, thereby blocking mitochondrial biogenesis [56]. It is worth noting that VDAC1 is also a substrate of parkin, which can regulate mitophagy and apoptosis. VDAC1 lacking monoubiquitination (K274R) promotes apoptosis by increasing mitochondrial calcium uniporter channel to promote calcium uptake. VDAC1 lacking polyubiquitination (Poly-KR) hinders mitophagy [57]. Recent studies in mouse models and humans have revealed that lack of parkin and PINK1 can cause mitochondrial damage, the release of mitochondrial DNA (mtDNA), and an increase in IL-6 expression, leading to inflammation [58]. In addition, the endoplasmic reticulum-mitochondrial contact site is a key structure for cell function. The site is involved in a large number of cellular processes, including Ca²⁺ signaling and selective degradation of mitochondria. PINK1/parkin is known to be involved in the mediation of this pathway [59]. Therefore, PMN can maintain the function and biogenesis of mitochondria in neuron by increasing the activity of parkin, avoiding its damage and aging.

In addition to our present findings on PMN, other studies have shown that various phytochemicals and plant proteins can overcome defects in PINK1 or parkin or regulate the expression of these genes for neuroprotection. For example, naringenin can improve the expression of PINK1 to diminish cellular oxidative stress and restore MMP, thereby alleviating 6-OHDA-induced toxicity in SH-SY5Y cells and zebrafish models [60]. In an MPTP-induced PD model, ursodeoxycholic acid modulates the PINK1/parkin pathway to improve mitochondrial function, inhibit apoptosis, and enhance autophagy, thus protecting DA neurons against oxidative stress [61]. Celastrol activates mitophagy by enhancing the performance of PINK1, thus preventing DA neuron death [62]. Ginseng protein prevents mitochondrial dysfunction and neurodegeneration by inducing mitochondrial unfolded protein response (UPR^{mt}) in the PINK1-deficient *Drosophila* PD model [63]. Andrographolide can induce parkin-mediated mitophagy to inhibit the activation of NLRP3 inflammasomes in LPS-MPTP mice and microglia and thereby reduce the death of DA neurons [64]. Vasicinone can induce autophagy by enhancing the PINK/parkin pathway to prevent paraquat-induced mitochondrial dysfunction of DA neurons and reduce α -synuclein levels [65].

Our previous report indicated that substrates of parkin are involved in many important cellular physiologic processes, including apoptosis, mitochondrial metabolism, and protein clearance [66]. In this study, we found that the protein expression of ARTS, one of the substrates of parkin, is down-regulated by PMN. By contrast, the protein expression of XAIP, which is inhibited by ARTS binding, is up-regulated by PMN. Both proteins may be related to the mediation of parkin.

ARTS is related to the enhancement of apoptosis induced by TGF- β . When apoptosis occurs, ARTS is located in the mitochondria and is transported to the nucleus. The P loop mutation of ARTS can abolish its ability to activate caspase 3 and induce apoptosis [67]. ARTS is also a polymerizing GTP-binding protein, which can serve as a molecular scaffold. In Lewy bodies, ARTS co-localizes with α -synuclein, which is a main component of the Lewy bodies. Studies have shown that the content of ARTS and α -synuclein in the sub-

stantia nigra of PD patients is increased by more than 10-fold [68]. Studies have also found that overexpression of *Drosophila* ARTS-homologous genes can destroy the integrity of DA neurons in age-dependent dorsal clusters, and that this can be suppressed by increasing parkin co-expression. Conversely, it can also be enhanced by reducing the expression of parkin. This indicates that ARTS accumulation is toxic to DA neurons [69,70]. The ARTS gene is known to be a responsive target gene of p53. p53 binds to reactive DNA elements on the ARTS promoter and promotes its transcription. Inducers of p53 can increase the expression of ARTS, and the blocking of p53 can diminish the expression of ARTS under various stress conditions. These findings indicate that ARTS and p53 act synergistically on apoptosis involving mitochondria [71].

XIAP is a cell survival regulator and the most effective inhibitor of intracellular caspase. The typical apoptotic pathway includes the release of cytochrome *c* and the activation of caspase 9, caspase 7, and caspase 3 in sequence, which causes PARP cleavage and leads to apoptosis [15]. XIAP can inhibit the formation of functional dimers of caspase 9 in apoptotic bodies through the third BIR domain. At the same time, the second BIR domain can block the active sites of activated caspase 3 and caspase 7, thus preventing apoptosis. Studies have shown that specific gene transduction of XIAP in DA neurons can improve neurotoxicity and behavioral damage in MPTP-exposed PD models [72]. A recent study showed that XIAP can be bound by the E3 ligase RING-finger protein 166 (RNF166) and undergo ubiquitination-dependent degradation. 6-OHDA treatment can enhance the expression of RNF166, thus accelerating the activation of caspase and the death of neurons. The down-regulation of RNF166 in cells can activate XIAP and alleviate 6-OHDA-induced cell death [73].

ARTS is known to inhibit XIAP activity, thereby promoting caspase activation [18]. In 6-OHDA-exposed neuronal cells, the level of ARTS will increase. Overexpression of parkin can reduce the level of ARTS and improve apoptosis caused by 6-OHDA [74]. In a healthy brain, ARTS can be degraded by parkin's ubiquitination to maintain low levels and avoid caspase activation. However, in nerve cells containing low or mutated parkin, the activity of parkin to degrade ARTS is reduced or abolished. Finally, XIAP is inhibited by the binding of ARTS, which is sufficient to promote the activation of caspase 9, 7, and 3.

Our data are consistent with these results. 6-OHDA-exposed SH-SY5Y cells displayed augmented expression of ARTS, but reduced expression of XIAP. However, pretreatment with PMN could reverse this result. PMN may promote the ubiquitination and degradation of ARTS by inducing parkin expression. Low levels of ARTS are expected to reduce XIAP inhibition and caspase activation and alleviate the apoptosis caused by 6-OHDA. In addition, we showed that the use of RNAi to down-regulate the expression of parkin could significantly abolish the ability of PMN to reverse 6-OHDA-induced ARTS expression, XIAP inhibition, and caspase activation.

ARTS is also known to be an modulator of autophagy. Overexpression of ARTS reduces autophagy activity [19]. XIAP can be used as a ubiquitin E3 ligase to regulate proteasome activity [16], and it can also upregulate autophagy activity [17]. As for 6-OHDA exposure, α -synuclein-overexpressing SH-SY5Y cells showed augmented levels of ARTS, but lessened levels of XIAP, and pretreatment with PMN could reverse this result. The resulting low level of ARTS could alleviate the damage to nerve cells caused by overexpression of α -synuclein. We also found that the use of RNAi to down-regulate the expression of parkin could considerably abolish the ability of PMN to promote the UPS and autophagy and reduced the accumulation of α -synuclein. In short, PMN decreases ARTS-mediated degradation of XIAP by modulating the PINK1/Parkin pathway, thereby ameliorating 6-hydroxydopamine toxicity and α -synuclein accumulation in PD models of *C. elegans* and SH-SY5Y cell lines. Interestingly, studies have shown that XIAP regulates the level of ARTS by acting as a ubiquitin ligase, thereby providing a potential feedback mechanism to prevent harmful cell apoptosis [75].

The current view of PD comprehends the concept that α -synuclein aggregates can spread from neuron-to-neuron in a prionlike fashion from the peripheral nervous sys-

tem to the brain, via the enteric nervous system [76] or sensory nervous system [77,78]. PMN may also decrease α -synuclein in the peripheral nervous system, enteric nervous system or sensory nervous system by activating UPS and autophagy and downregulate the transneuronal spread of α -synuclein.

In this study, we used *C. elegans* and SH-SY5Y models to verify the effectiveness of PMN in its neuroprotection, but the concentration of PMN used in both models does not reflect the translational correlation with the mammalian model. However, PMN has proven its anti-inflammatory function on lipopolysaccharide-induced acute lung injury mice model, bleomycin-induced acute lung injury rat model, osteoarthritis mice model, and dinitrochlorobenzene-induced atopic dermatitis mice model [22,23,79,80]. Mice were treated with PMN once a day at a dose of 5 mg/kg for 8 weeks. The results showed no obvious toxicity to mice or rats. In addition, the pharmacokinetics, tissue distribution and excretion of PMN on rat model have also been reported [81]. The above information can provide us with a reference for translational research.

Although orthologous gene of SNCA and associated neurodegeneration are not found in *C. elegans*, transgenic worms produced by overexpressing wild-type or mutant human α -synuclein (A53T or A30P) showed degeneration of DA neurons together with loss of the basal slowing response [82]. Therefore, worms can still be used as a platform for preliminary drug development against synucleinopathies.

In conclusion, our experimental data demonstrated that PMN can significantly improve the neurotoxicity induced by 6-OHDA and the accumulation of α -synuclein in a PD model, and may have considerable therapeutic applications in the future. By enhancing the PINK1/parkin pathway, PMN can significantly lessen the expression of ARTS and then promote a rise in XIAP to resist apoptosis and activate the UPS and autophagy. Since *C. elegans* does not have the structure of a mammalian brain, and SH-SY5Y cells are not true DA neurons, in follow-up studies, we will use a unilateral 6-OHDA lesion mouse model, human A53T α -synuclein-overexpressing transgenic mice, and DA neurons derived from iPS cells of PD patient to further evaluate the effectiveness of PMN, especially in terms of pharmacokinetics. Finally, the causes of PD are complex, and mitochondrial dysfunction and chronic inflammation are also important influencing factors. In the future, we hope to use NGS and molecular docking technology to study the improvement effects of PMN on mitochondrial dynamics, mitophagy, and α -synuclein-induced inflammasome activity of microglia. In an aging society, it is important and urgent to establish an effective treatment for PD. PMN may provide an opportunity that is worthy of further research.

4. Materials and Methods

4.1. Chemicals, *C. elegans* Strains and Synchronization

Synthesized PMN (mol. wt. 429.64, 98% purity) was purchased from Rainbow Biotechnology Co. Ltd. (Shilin, Taipei, Taiwan) and dissolved in DMSO as a stock solution (1 M). Other chemicals and culture media were acquired from Sigma-Aldrich (St. Louis, MO, USA) unless otherwise stated. Wild-type Bristol N2 *C. elegans*, transgenic BZ555 strain (Pdat-1::GFP), transgenic N5901 strain (Punc-54:: α -Syn::YFP), transgenic DA2123 strain (Plgg-1::GFP::lgg-1), and *Escherichia coli* strains OP50 and HT115 were obtained from the Caenorhabditis Genetics Center (University of Minnesota, Saint Paul, MN, USA). The general maintenance and synchronization of the worm were carried out using the previously described method [31]. All worms were cultured at 20 °C.

4.2. Food Clearance Assay for Worms

To determine the appropriate treatment concentration of PMN that did not affect the growth of worms, we used the food clearance assay as previously described [83]. First, the PMN was diluted into S-medium to the indicated concentration, and then OP50 *E. coli* that had been allowed to grow overnight was evenly dispersed in PMN/S-medium with an optical density (OD) of 6.6. We loaded 50 μ L of PMN//OP50/S-medium (OD = 0.6) to each well of a 96-well plate, and then added about 10 μ L of medium to contain 20 L1

worms, and finally sealed the plate with a cover plate to prevent evaporation. Once per day, we measured the OD of the culture at 595 nm using a SpectraMax M2 Microplate Reader (Molecular Devices, Silicon Valley, CA, USA) for a total of 6 days. Before OD was measured, each plate was placed on a plate shaker and shaken for 30 s. After the measurement, the number and type of worms in each well were observed simultaneously under the microscope.

4.3. 6-OHDA Exposure and PMN Pretreatment of Worms

We exposed the worms to 6-OHDA according to the previously described method to cause DA neuronal degeneration [83]. First, L1 worms were transferred to OP50/NGM medium without or with different concentrations of PMN and cultured to L3 stage (24 h), and then exposed to 6-OHDA solution (50 mM, containing 10 mM ascorbic acid) for 1 h. During this period, the tube wall was tapped every 10 min to suspend the worms. After treatment, the worms were washed with M9 buffer and transferred to OP50/NGM/5-fluoro-2'-deoxyuridine, 2'-deoxy-5-fluorouridine (FUDR, 0.04 mg/mL) to reduce the generation of offspring. The worms were cultivated for 3 days until they reached the adult stage and were then used in various analyses.

4.4. Quantification of DA Neuron Degeneration in Worms

We used the previously described method to quantitatively analyze the DA neuronal degeneration of the BZ555 worm [83]. The reduction in the GFP signal of the DA neurons represents degeneration of the neurons. The worms were washed 3 times with M9 buffer, and then placed on the agar pad (2%) of a glass slide, anesthetized with sodium azide (100 mM), and then covered with a cover glass. The fluorescence of DA neurons in the head of the worm was imaged with Zeiss Axio Imager A1 fluorescence microscope (Carl Zeiss MicroImaging GmbH, Göttingen, Germany), and ImageJ software (National Institutes of Health, Bethesda, MD, USA) was used to determine fluorescence intensity. In addition, if the dendrites of the DA neurons of a worm showed bubbles or were absent, we recorded that the worm was positive for neurodegeneration of DA neurons.

4.5. Food Sensitivity Behavior Test in Worms

We used the previously described food-sensing behavior test to evaluate the function of DA neurons in worms [83]. To prepare a measurement plate, *E. coli* were spread in a ring on a 9 cm NGM plate with an inner diameter of 1 cm and an outer diameter of 8 cm, and the plates were cultured overnight. N2 adult worms of different treatments were washed with M9 buffer and then dropped into the center of the plate. Five minutes after the transfer, the number of S-shaped movements of each worm on the bacteria-free lawn and the bacterial lawn were measured three times at an interval of 20 s. The slowing rate = (the number of S-shaped movements in the bacteria-free lawn—the number of S-shaped movements in the bacterial lawn)/the number of S-shaped movements in the bacteria-free lawn. In all analyses, each group was anonymously labeled, so that the experimenter was unaware of the treatment of the worm. The average slowing rate of 50 worms was calculated for each group.

4.6. Lifespan Test in Worms

We use the previously described method for the worm lifespan test [83]. L3 stage N2 worms of different treatment groups were transferred to a plate (containing FUDR) for lifespan analysis, and a new plate was replaced every 3 days until all worms died. The number of surviving worms was counted daily. If a worm did not respond to repeated touches of the platinum picker, it was counted as dead. The analysis excluded worms that were removed from the wall and died as a result of dehydration. The survival curve was displayed by using Kaplan–Meier estimator and SPSS software (IBM, Armonk, NY, USA).

4.7. Quantification of Accumulation of Human α -Synuclein in Worm Muscle Cells

We used the previously described method to quantify the accumulation of α -synuclein in the NL5901 worm [83]. The synchronized L1 stage worms were cultured on OP50/NGM plates with or without PMN for 1 day. The worms were then transferred to OP50/NGM/FUDR plates with or without PMN, incubated for 3 days, and then washed with M9 buffer three times. The YFP signal of the worm reflects the accumulation of α -synuclein. The measurement and quantification method of fluorescence intensity is as described in 4.4.

4.8. Analysis of Protein Expression in Worms

We used the previously described method to extract proteins from the worms and perform Western blot analysis [31]. Protein was extracted from frozen worm pellets using Fastprep24 (MP Biomedicals LLC, Solon, OH, USA) and PBS containing protease inhibitors. The extract was boiled with sample buffer containing sodium dodecyl sulfate (SDS) for 10 min and separated by 10% SDS-polyacrylamide gel electrophoresis (SDS-PAGE). The proteins were then transferred to a polyvinylidene fluoride (PVDF) membrane. After reacting with the primary antibody overnight, the position and intensity of human α -synuclein were determined by use of horseradish peroxidase (HRP)-conjugated secondary antibody (PerkinElmer Inc., Boston, MA, USA) and the Amersham enhanced chemiluminescence system (Amersham Biosciences, Piscataway, NJ, USA) and BioSpectrum imaging system (UVP, Upland, CA, United States). Human α -synuclein monoclonal antibody (sc-12767) and β -actin (sc-47778) antibody were purchased from Santa Cruz Biotechnology (Santa Cruz, CA, USA).

4.9. Determination of Reactive Oxygen Species Content in Worms

We used the 2',7'-dichlorodihydrofluorescein diacetate (H2DCFDA) analysis method to quantify the ROS content in worms [31]. Thirty worms were washed 3 times with M9 buffer and transferred to a 96-well plate with 150 μ L PBS per well. We then added 50 μ L of H2DCFDA (150 μ M in PBS) and measured fluorescence at 20 $^{\circ}$ C using a SpectraMax M2 Microplate Reader (Molecular Devices, Silicon Valley, CA, USA) (λ_{ex} = 485; λ_{em} = 520 nm). Fluorescence was measured every 15 min for a total of 150 min.

4.10. Total RNA Extraction and qPCR of Worms

We used the previously described method, using TRIzol reagent (Invitrogen, Carlsbad, CA, USA) and glass beads, to extract total worm RNA and then performed qPCR analysis [31]. The SuperScript one-step RT-PCR kit (Invitrogen), SYBR Green I Master kit (Roche Diagnostics, Indianapolis, IN, USA), and ABI StepOnePlus system (Applied Biosystems, Inc., Foster City, CA, USA) were used according to the manufacturer's instructions. Table 1 lists the primer pairs for this experiment [31]. The comparison $2^{-\Delta\Delta C_t}$ method was used for analysis and the endogenous control was calculated by using *act-1* expression as the fold difference.

4.11. Determination of the Proteasome Activity of Worms

We used the previously described method to determine the proteasome activity (chymotrypsinlike activity) in worms [31]. Worms were first lysed by using a Precellys 24 homogenizer and proteasome activity assay buffer [50 mM Tris-HCl (pH = 7.5), 250 mM sucrose, 2 mM ATP, 5 mM MgCl₂, 1 mM dithiothreitol, and 0.5 mM EDTA]. The lysate was then centrifuged at 10,000 \times g at 4 $^{\circ}$ C for 15 min. For each sample, 25 μ g of total lysate was added to each well of a 96-well microtiter plate, and then the fluorescent substrate Suc-Leu-Leu-Val-Tyr-AMC (Sigma-Aldrich, St. Louis, MO, USA) was added. After the plates were incubated for 1 h at 25 $^{\circ}$ C, the fluorescence was measured with a SpectraMax M2 Microplate Reader (Molecular Devices, Silicon Valley, CA, USA) (λ_{ex} = 380; λ_{em} = 460 nm).

Table 1. Primers for real time PCR [31].

Genes of <i>C. elegans</i> (Human)	Primer Sequences (5'-3')	(Start→End) Size (bp)
Lrk-1 (LRRK1)	Forward: TTTCAACACCCAATCTCCAAC Reverse: TGATACTCGCTTGCCACAC	(1983→2092) 110
Pdr-1 (PRKN)	Forward: TGCTCGTCAACCTCTGTTC Reverse: TCACTTTCTCCTTCCCATCAC	(376→601) 226
Pink-1 (PINK1)	Forward: GAGACGATACCACAAACAC Reverse: GGCATTTCCTCCAAGACTAAC	(882→1158) 277
Djr-1.1 (PARK7)	Forward: CGGATTAGATGGAGCCGAAC Reverse: ATCAGCCCACCAGACTCTAC	(111→305) 195
Djr-1.2 (PARK7)	Forward: GCTTTGATCCTTTTGCCACC Reverse: CTGCCAGTTTGCTACATCC	(19→247) 229
Vps-35 (VPS35)	Forward: AACTCTGCTCAAAACTACTCAC Reverse: CCACAACCTCTTCCCATTC	(1953→2146) 194
Catp-6 (ATP13A3)	Forward: TCACACCATACCAACCTCC Reverse: GTTCCAAGAGTCTTCAGAACC	(3092→3336) 245
Dnj-27 (DNAJC10)	Forward: TCCACTTATGCTCACATTGTC Reverse: TCCACCATCAACTCCACATC	(427→635) 209

4.12. Determination of the Autophagy Activity of Worms

We used the previously described method to observe the autophagy activity in transgenic DA2123 worms (which have a GFP-tagged LGG-1 regulated by the *lgg-1* promoter) [31]. The worms were washed 3 times with M9 buffer, and the LGG-1::GFP-positive puncta area in the outer epidermal seam cells was observed by using a fluorescence microscope. The positive punctate areas of at least 20 seam cells per worm were counted. At least 50 worms were counted in each group.

4.13. RNA Interference of Worm

We used the previously described method to perform RNA interference on worms fed *E. coli* that can express *pdr-1* siRNA [31]. RNase III-resistant *E. coli* (HT115(DE3)) has a *pdr-1*-specific double-stranded RNA expression plasmid (L4440) (Open Biosystems, Huntsville, AL, USA) that can be induced by IPTG. Feeding this *E. coli* to worms can target endogenous *pdr-1* mRNA and promote its specific degradation. In the 6-OHDA-exposed BZ555 model, the L1 worms were transferred to *pdr-1* RNAi/NGM plates with or without PMN and grown to the L3 stage. Next, the worms were exposed to 6-OHDA for 1 h and then cultured in *pdr-1* RNAi/NGM/FUDR plates with or without PMN for 3 days until analyzed. In the transgenic NL5901 model, L1 worms were cultured to *pdr-1* RNAi/NGM plates with or without PMN for 1 day, and then transferred to *pdr-1* RNAi/NGM/FUDR plates with or without PMN and cultured for 4 days until analyzed.

4.14. PMN Pretreatment and 6-OHDA Exposure of SH-SY5Y Cell Line

Human neuroblastoma SH-SY5Y cells (20th generation) were a generous gift from Chia-Wen Tsai (China Medical University, Taichung, Taiwan). We used the previously described method for cell culture [31]. Cells (1.2×10^6) were inoculated on a 35 mm culture dish containing PMN at the specified concentration, allowed to incubate for 24 h, and then exposed to 100 μ M 6-OHDA for 12 h (for Western blotting analysis) or 18 h (for MTT (3-(4,5-dimethylthiazol-2-yl)-2,5-diphenyltetrazolium bromide) assay, mitochondrial membrane potential (MMP) measurement, Hoechst 33258 staining, and Annexin-V FITC and PI staining). DMEM, penicillin-streptomycin, trypsin-EDTA, and fetal bovine serum were purchased from Gibco, ThermoFisher Scientific (Waltham, MA, USA).

4.15. Preparation of SH-SY5Y Cell Line Transiently Overexpressing α -Synuclein

To obtain the SH-SY5Y cell line overexpressing α -synuclein, we first synthesized the SNCA coding sequence (Accession numbers: NM_000345, Genewiz Inc., South Plainfield,

NJ, USA). Then, the sequence was amplified by PCR and cloned into pcDNA3.1(+)-Myc vector (Invitrogen, ThermoFisher Scientific, Carlsbad, CA, USA) using *NheI* and *ApaI* sites via restriction enzymes (New England Biolabs, Beverly, MA, USA). Finally, according to the manufacturer's instructions, Lipofectamine 2000 reagent (Invitrogen) was used to transfect the vector into the SH-SY5Y cell line. Empty pcDNA3.1(+) plasmids were used as the control group. The transfected cells were selected by use of G418 (1.5 mg/mL).

4.16. Immunofluorescence Staining of SH-SY5Y Cells

We used the previously described method for immunofluorescence staining [31]. Briefly, cellular samples grown on poly-L-lysine-coated coverslips were washed and fixed with 4% paraformaldehyde at room temperature for 10 min and then incubated with 0.2% Triton X-100 for 10 min. Next, the samples were soaked in a solution containing 1% BSA and 22.52 mg/mL glycine (dissolved in PBST (PBS + 0.1% Tween 20)) for 30 min. Primary antibody was added and allowed to react overnight at 4 °C. The next day, the sample was washed and placed in PBST containing 1% BSA. Goat anti-mouse IgG secondary antibody-Alexa Fluor 488 conjugate (purchased from Invitrogen) was added at the same time, and the sample was reacted at 25 °C for 1 h. Finally, the sample was washed, the nuclei were stained with DAPI, and the fluorescence was detected using a fluorescence microscope. Myc antibody was purchased from Santa Cruz Biotechnology, Inc. (Santa Cruz, CA, USA).

4.17. Cytotoxicity Analysis of PMN

We used the previously described MTT method to determine cell viability [31]. The SH-SY5Y cells were washed and replaced with fresh medium, and then MTT (5 mg/mL) was added and incubated at 37 °C for 2 h. Next, after washing, the formazan crystals were dissolved with isopropanol and the absorbance was measured at 570 nm using a Microplate Reader (Molecular Devices, Silicon Valley, CA, USA).

4.18. Western Blot Analysis of the SH-SY5Y Cell Line

For Western blot analysis of SH-SY5Y cells, we used the previously described method [31]. SH-SY5Y cells were washed twice with cold PBS and then collected in lysis buffer (25 mM Tris-HCl, 150 mM NaCl, 1% Triton X-100, 10% glycerol, 2 mM EDTA, 1 mM PMSE, 1 µg/mL leupeptin, 1 µg/mL aprotinin, and phosphatase inhibitor). Whole cell lysates were centrifuged at 14,000 × g for 20 min at 4 °C. The protein concentration was measured with Coomassie plus protein assay reagent kit (Pierce, Rockford, IL, USA). The cell protein (50 µg) was then analyzed on 7.5%, 10%, or 12.5% SDS-PAGE gels, as shown in 4.8. Caspase 9 (#9508), cleaved caspase 9 (#20750), caspase 7 (#12827), cleaved caspase 7 (#8438), caspase 3 (#9662), cleaved caspase 3 (#9661), poly-ADP ribose polymerase (PARP) (#9542), cleaved PARP (#5625), mTOR (#2983), p-mTOR (#5536), and Atg7 (#8558) antibodies were from Cell Signaling Technology (Beverly, MA, USA). Monoclonal antibodies to PINK1 (sc-518052), parkin (sc-32282), ARTS, XIAP (sc-55550), PI3 kinase p100 (sc-365404), LC3 (sc-398822), and β-tubulin (sc-166729) were from Santa Cruz Biotechnology, Inc. (Santa Cruz, CA, USA). ARTS antibody (PA5-82767) was from Invitrogen ThermoFisher Scientific. HRP goat anti-rabbit and HRP goat anti-mouse secondary antibodies were from PerkinElmer, Inc. (Boston, MA, USA).

4.19. Measurement of Mitochondrial Membrane Potential in SH-SY5Y Cell Line

For the measurement of MMP of the SH-SY5Y cell line, we used the previously described 3,3'-dihexyloxacarbocyanine iodide (DiOC6) method [31]. The cells were washed with PBS and replaced with fresh medium and exposed to DiOC6 dye (1 µM). Thirty minutes later, the changes in MMP were recorded by use of a fluorescence microscope (green fluorescence) and the fluorescence intensity of the image was quantified by using ImageJ software (National Institutes of Health).

4.20. Staining of Hoechst 33258 in SH-SY5Y Cell Line

For Hoechst 33258 nuclear staining of the SH-SY5Y cell line, we used the previously described method [31]. The cells were washed with PBS and replaced with fresh medium. Cells were then stained with Hoechst 33258 (5 µg/mL) in the dark at 25 °C for 1 h, and changes in chromosome morphology (blue fluorescence) were recorded by using a fluorescence microscope.

4.21. Apoptosis Assay by Flow Cytometry

We used the FITC Annexin-V Apoptosis Detection Kit I (BD Biosciences Pharmingen, San Diego, CA, USA) to perform apoptosis analysis according to the manufacturer's instructions. The cells were collected by trypsinization, washed three times with PBS, and centrifuged at $1500 \times g$ for 5 min at room temperature. Next, the cells were resuspended in 100 µL of $1 \times$ binding buffer (10 mM HEPES/NaOH (pH 7.4), 140 mM NaCl, and 2.5 mM CaCl_2), and then annexin-V FITC and PI were added and the cells stained for 15 min in the dark. Finally, 400 µL of $1 \times$ binding buffer was added and the apoptosis rate was immediately analyzed using a BD LSRII flow cytometer (Becton Dickinson, Heidelberg, Germany). The cell collection gate for each sample contains at least 10,000 events to be collected. Among them, Q2 is a late apoptotic cell, Q4 is an early apoptotic cell, Q3 is a live cell, and Q1 is a dead cell. Apoptosis rate = $(Q2 + Q4)/(Q1 + Q2 + Q3 + Q4) \times 100\%$.

4.22. RNA Interference of SH-SY5Y Cell Line

The sequence of small RNA interference (siRNA) of parkin is as follows: 5'-UUCGCAG GUGACUUUCCUCUGGUCA-3' (Tri-I Biotech Inc, Taipei, Taiwan). We used Lipofectamine 2000 reagent (Invitrogen) for siRNA transfection according to the manufacturer's instructions. In the 6-OHDA exposure experiment, cells were transfected with control siRNA or parkin siRNA for 24 h, then pretreated with 1 µM PMN for 24 h, and finally treated with 100 µM 6-OHDA for 12 h (Western blotting) or 18 h (other analyses). In the SH-SY5Y cell line overexpressing α -synuclein (48 h after transfection), the cells were transfected with control siRNA or parkin siRNA for 24 h, and then treated with 1 mM PMN for 24 h.

4.23. Determination of Proteasome Activity in SH-SY5Y Cell Line

We used the previously described method to measure proteasome activity (chymotrypsinlike activity) in the SH-SY5Y cell line [31]. Cell lysate was incubated with enzyme substrate (Suc-Leu-Leu-Val-Tyr-AMC (Sigma-Aldrich, St. Louis, MO, USA)) at 25 °C for 1 h, and the Microplate Reader (Molecular Devices, Silicon Valley) was used to detect the fluorescence intensity corresponding to the proteasome chymotrypsinlike activity ($\lambda_{\text{ex}} = 380$; $\lambda_{\text{em}} = 460$ nm).

4.24. Acidic Vesicular Organelle Staining in SH-SY5Y Cell Line

We used a method described previously to perform acidic vesicular organelle staining in the SH-SY5Y cell line [31]. After removal of the medium, the cells were washed with PBS, and incubated with acridine orange hydrochloride solution (0.5 µg/mL) at 37 °C for 10 min in the dark. After incubation, the formation of acidic vesicular organelles (red color) was detected under a fluorescence microscope. The fluorescence intensity was quantitatively analyzed by using ImageJ software (National Institutes of Health).

4.25. Determination of Autophilic Activity in SH-SY5Y Cell Line

We used the Autophagy Assay Kit (Sigma-Aldrich) according to the manufacturer's instructions to determine the autophilic activity of the SH-SY5Y cell line. Cells were cultured in 96-well plates to optimal density (1×10^4 cells/well) for the various treatment. The medium was removed from the cells and 100 µL of the autophagosome detection reagent working solution was added (diluting $500 \times$ Autophagosome Detection Reagent in the Stain buffer) to each well. Cells were incubated for 1 h and then washed with the Wash Buffer three times. We measured fluorescence intensity ($\lambda_{\text{ex}} = 360$; $\lambda_{\text{em}} = 520$ nm) using a

Zeiss Axio Imager A1 fluorescence microscope (Carl Zeiss), microplate reader (Molecular Devices), or BD LSRII flow cytometry (Becton Dickinson).

4.26. Statistical Analysis

Statistical analysis was implemented using SAS software (SAS, Institute, Inc, Cary, NC, USA). Each experiment was performed at least three times. Data are expressed as mean \pm standard deviation (SD). We determined statistical significance by employing one-way ANOVA and Tukey's test. Two groups were compared by using Student's *t*-test. *p* values < 0.05 were assumed to indicate statistical significance.

Author Contributions: Conceptualization, C.-W.T., W.-C.S., S.-Z.L., and R.-H.F.; Data curation, Y.-L.H., and R.-H.F.; Formal analysis, Y.-L.H., and R.-H.F.; Funding acquisition, R.-H.F.; Investigation, Y.-L.H., H.-S.H., Y.-T.C., and R.-H.F.; Methodology, H.-S.H., C.-W.T., and S.-P.L.; Project administration, R.-H.F.; Resources, H.-S.H., C.-W.T., S.-P.L., Y.-H.K., W.-C.S., S.-Z.L., and R.-H.F.; Supervision, R.-H.F.; Validation, R.-H.F.; Visualization, Y.-H.K.; Writing—original draft, R.-H.F.; Writing—review and editing, H.-S.H., and R.-H.F. All authors have read and agreed to the published version of the manuscript.

Funding: This research was funded in part by the Ministry of Science and Technology (Taiwan) (MOST 108-2314-B-039-025-), and China Medical University Hospital (DMR-106-076).

Institutional Review Board Statement: Not applicable. For studies not involving humans.

Informed Consent Statement: Not applicable. For studies not involving humans.

Data Availability Statement: All data used and analyzed during the current study are available from the corresponding author on reasonable request.

Acknowledgments: We are thankful to Jennifer Holmes for editing services.

Conflicts of Interest: The authors declare no conflict of interest.

References

1. Tarakad, A.; Jankovic, J. Recent Advances in Understanding and Treatment of Parkinson's Disease. *Fac. Rev.* **2020**, *9*, 6. [CrossRef]
2. Balestrino, R.; Schapira, A.H.V. Parkinson Disease. *Eur. J. Neurol.* **2020**, *27*, 27–42. [CrossRef] [PubMed]
3. Bras, I.C.; Outeiro, T.F. Alpha-Synuclein: Mechanisms of Release and Pathology Progression in Synucleinopathies. *Cells* **2021**, *10*, 375. [CrossRef] [PubMed]
4. Ray, B.; Mahalakshmi, A.M.; Tuladhar, S.; Bhat, A.; Srinivasan, A.; Pellegrino, C.; Kannan, A.; Bolla, S.R.; Chidambaram, S.B.; Sakthar, M.K. "Janus-Faced" Alpha-Synuclein: Role in Parkinson's Disease. *Front. Cell Dev. Biol.* **2021**, *9*, 673395. [CrossRef]
5. He, S.; Zhong, S.; Liu, G.; Yang, J. Alpha-Synuclein: The Interplay of Pathology, Neuroinflammation, and Environmental Factors in Parkinson's Disease. *Neurodegener. Dis.* **2020**, *20*, 55–64. [CrossRef]
6. Stanojlovic, M.; Pallais, J.P.; Kotz, C.M. Inhibition of Orexin/Hypocretin Neurons Ameliorates Elevated Physical Activity and Energy Expenditure in the A53T Mouse Model of Parkinson's Disease. *Int. J. Mol. Sci.* **2021**, *22*, 795. [CrossRef]
7. Nascimento, A.C.; Erustes, A.G.; Reckziegel, P.; Bincoletto, C.; Ureshino, R.P.; Pereira, G.J.S.; Smaili, S.S. Alpha-Synuclein Overexpression Induces Lysosomal Dysfunction and Autophagy Impairment in Human Neuroblastoma SH-SY5Y. *Neurochem. Res.* **2020**, *45*, 2749–2761. [CrossRef] [PubMed]
8. Lee, D.; Jo, M.G.; Kim, S.Y.; Chung, C.G.; Lee, S.B. Dietary Antioxidants and the Mitochondrial Quality Control: Their Potential Roles in Parkinson's Disease Treatment. *Antioxidants* **2020**, *9*, 1056. [CrossRef] [PubMed]
9. Dionisio, P.A.; Amaral, J.D.; Rodrigues, C.M.P. Oxidative Stress and Regulated Cell Death in Parkinson's Disease. *Ageing Res. Rev.* **2021**, *67*, 101263. [CrossRef]
10. Paul, S.; Pickrell, A.M. Hidden Phenotypes of PINK1/Parkin Knockout Mice. *Biochim. Biophys. Acta Gen. Subj.* **2021**, *1865*, 129871. [CrossRef] [PubMed]
11. Tanaka, K. The PINK1-Parkin Axis: An Overview. *Neurosci. Res.* **2020**, *159*, 9–15. [CrossRef]
12. Rakovic, A.; Ziegler, J.; Martensson, C.U.; Prasuhn, J.; Shurkewitsch, K.; Konig, P.; Paulson, H.L.; Klein, C. PINK1-Dependent Mitophagy Is Driven by the UPS and Can Occur Independently of LC3 Conversion. *Cell Death Differ.* **2019**, *26*, 1428–1441. [CrossRef] [PubMed]
13. Arena, G.; Gelmetti, V.; Torosantucci, L.; Vignone, D.; Lamorte, G.; De Rosa, P.; Cilia, E.; Jonas, E.A.; Valente, E.M. PINK1 Protects Against Cell Death Induced by Mitochondrial Depolarization, by Phosphorylating Bcl-xL and Impairing Its Pro-Apoptotic Cleavage. *Cell Death Differ.* **2013**, *20*, 920–930. [CrossRef]

14. Bernardini, J.P.; Brouwer, J.M.; Tan, I.K.; Sandow, J.J.; Huang, S.; Stafford, C.A.; Bankovacki, A.; Riffkin, C.D.; Wardak, A.Z.; Czabotar, P.E.; et al. Parkin Inhibits BAK and BAX Apoptotic Function by Distinct Mechanisms During Mitophagy. *EMBO J.* **2019**, *38*, e99916. [CrossRef]
15. Tu, H.; Costa, M. XIAP's Profile in Human Cancer. *Biomolecules* **2020**, *10*, 1493. [CrossRef] [PubMed]
16. Galban, S.; Duckett, C.S. XIAP as A Ubiquitin Ligase in Cellular Signaling. *Cell Death Differ.* **2010**, *17*, 54–60. [CrossRef]
17. Cheung, C.H.A.; Chang, Y.C.; Lin, T.Y.; Cheng, S.M.; Leung, E. Anti-apoptotic Proteins in the Autophagic World: An Update on Functions of XIAP, Survivin, and BRUCE. *J. Biomed. Sci.* **2020**, *27*, 31. [CrossRef] [PubMed]
18. Shahar, N.; Larisch, S. Inhibiting the Inhibitors: Targeting Anti-Apoptotic Proteins in Cancer and Therapy Resistance. *Drug Resist. Updat.* **2020**, *52*, 100712. [CrossRef] [PubMed]
19. Wang, N.; Xu, F.; Lu, S.; Zhang, N.; Sun, Y. Septin4 as an Autophagy Modulator Regulates Angiotensin-II Mediated VSMCs Proliferation and Migration. *Biochem. Biophys. Res. Commun.* **2020**, *525*, 272–279. [CrossRef]
20. Kemeny, S.; Dery, D.; Loboda, Y.; Rovner, M.; Lev, T.; Zuri, D.; Finberg, J.P.; Larisch, S. Parkin Promotes Degradation of the Mitochondrial Pro-Apoptotic ARTS Protein. *PLoS ONE* **2012**, *7*, e38837. [CrossRef]
21. Li, H.; Hung, A.; Li, M.; Yang, A.W.H. *Fritillariae Thunbergii* Bulbus: Traditional Uses, Phytochemistry, Pharmacodynamics, Pharmacokinetics and Toxicity. *Int. J. Mol. Sci.* **2019**, *20*, 1667. [CrossRef]
22. Du, B.; Cao, L.; Wang, K.; Miu, J.; Yao, L.; Xu, Z.; Song, J. Peiminine Attenuates Acute Lung Injury Induced by LPS Through Inhibiting Lipid Rafts Formation. *Inflammation* **2020**, *43*, 1110–1119. [CrossRef]
23. Luo, Z.; Zheng, B.; Jiang, B.; Xue, X.; Xue, E.; Zhou, Y. Peiminine Inhibits the IL-1beta Induced Inflammatory Response in Mouse Articular Chondrocytes and Ameliorates Murine Osteoarthritis. *Food Funct.* **2019**, *10*, 2198–2208. [CrossRef] [PubMed]
24. Chen, G.; Liu, J.; Jiang, L.; Ran, X.; He, D.; Li, Y.; Huang, B.; Wang, W.; Liu, D.; Fu, S. Peiminine Protects Dopaminergic Neurons from Inflammation-Induced Cell Death by Inhibiting the ERK1/2 and NF-kappaB Signalling Pathways. *Int. J. Mol. Sci.* **2018**, *19*, 821. [CrossRef]
25. Caldwell, K.A.; Willcott, C.W.; Caldwell, G.A. Modeling Neurodegeneration in *Caenorhabditis elegans*. *Dis. Model Mech.* **2020**, *13*, dmm046110. [CrossRef] [PubMed]
26. Brunetti, G.; Di Rosa, G.; Scuto, M.; Leri, M.; Stefani, M.; Schmitz-Linneweber, C.; Calabrese, V.; Saul, N. Healthspan Maintenance and Prevention of Parkinson's-like Phenotypes with Hydroxytyrosol and Oleuropein Aglycone in *C. elegans*. *Int. J. Mol. Sci.* **2020**, *21*, 2588. [CrossRef] [PubMed]
27. Bagoudou, A.F.; Zheng, Y.; Nakabayashi, M.; Rawdkuen, S.; Park, H.Y.; Vattem, D.A.; Sato, K.; Nakamura, S.; Katayama, S. *Glochidion littorale* Leaf Extract Exhibits Neuroprotective Effects in *Caenorhabditis elegans* via DAF-16 Activation. *Molecules* **2021**, *26*, 2958. [CrossRef]
28. Lee, H.S.; Kim, E.N.; Jeong, G.S. Lupenone Protects Neuroblastoma SH-SY5y Cells Against Methamphetamine-Induced Apoptotic Cell Death via PI3K/Akt/mTOR Signaling Pathway. *Int. J. Mol. Sci.* **2020**, *21*, 1617. [CrossRef]
29. Tian, W.; Heo, S.; Kim, D.W.; Kim, I.S.; Ahn, D.; Tae, H.J.; Kim, M.K.; Park, B.Y. Ethanol Extract of *Maclura tricuspidata* Fruit Protects SH-SY5Y Neuroblastoma Cells Against H2O2-Induced Oxidative Damage via Inhibiting MAPK and NF-kappaB Signaling. *Int. J. Mol. Sci.* **2021**, *22*, 6946. [CrossRef]
30. Chen, J.H.; Ou, H.P.; Lin, C.Y.; Lin, F.J.; Wu, C.R.; Chang, S.W.; Tsai, C.W. Carnosic Acid Prevents 6-Hydroxydopamine-Induced Cell Death in SH-SY5Y Cells via Mediation of Glutathione Synthesis. *Chem. Res. Toxicol.* **2012**, *25*, 1893–1901. [CrossRef]
31. Tsai, R.T.; Tsai, C.W.; Liu, S.P.; Gao, J.X.; Kuo, Y.H.; Chao, P.M.; Hung, H.S.; Shyu, W.C.; Lin, S.Z.; Fu, R.H. Maackiain Ameliorates 6-Hydroxydopamine and SNCA Pathologies by Modulating the PINK1/Parkin Pathway in Models of Parkinson's Disease in *Caenorhabditis elegans* and the SH-SY5Y Cell Line. *Int. J. Mol. Sci.* **2020**, *21*, 4455. [CrossRef]
32. Li, J.; Qin, Y.; Wang, W.; Yang, K.; Zhang, M. Peiminine Inhibits the Progression of Colorectal Cancer Through Up-Regulating MiR-760 via Declining the Expression of Long Noncoding RNA LINC00659. *Anticancer Drugs* **2021**, *32*, 148–156. [CrossRef] [PubMed]
33. Morais, M.G.; Saldanha, A.A.; Costa Rodrigues, J.P.; Cotta Mendes, I.; Ferreira, L.M.; Avelar Amado, P.; de Souza Farias, K.; Samudio Santos Zanuncio, V.; Brentan da Silva, D.; Carmo Horta Pinto, F.; et al. Chemical Composition, Antioxidant, Anti-inflammatory and Antinociceptive Activities of the Ethanol Extract of Ripe Fruits of *Solanum lycocarpum* St. Hil. (Solanaceae). *J. Ethnopharmacol.* **2020**, *262*, 113125. [CrossRef] [PubMed]
34. Brown, S.J.; Boussaad, I.; Jarazo, J.; Fitzgerald, J.C.; Antony, P.; Keatinge, M.; Blechman, J.; Schwamborn, J.C.; Kruger, R.; Placzek, M.; et al. PINK1 Deficiency Impairs Adult Neurogenesis of Dopaminergic Neurons. *Sci. Rep.* **2021**, *11*, 6617. [CrossRef]
35. Bus, C.; Zizmare, L.; Feldkaemper, M.; Geisler, S.; Zarani, M.; Schaedler, A.; Klose, F.; Admard, J.; Mageean, C.J.; Arena, G.; et al. Human Dopaminergic Neurons Lacking PINK1 Exhibit Disrupted Dopamine Metabolism Related to Vitamin B6 Co-Factors. *iScience* **2020**, *23*, 101797. [CrossRef]
36. Qiao, J.D.; Mao, Y.L. Knockout of PINK1 Altered the Neural Connectivity of Drosophila Dopamine PPM3 Neurons at Input and Output Sites. *Invert. Neurosci.* **2020**, *20*, 11. [CrossRef]
37. Creed, R.B.; Goldberg, M.S. Enhanced Susceptibility of PINK1 Knockout Rats to Alpha-Synuclein Fibrils. *Neuroscience* **2020**, *437*, 64–75. [CrossRef] [PubMed]
38. Maynard, M.E.; Redell, J.B.; Kobori, N.; Underwood, E.L.; Fischer, T.D.; Hood, K.N.; LaRoche, V.; Waxham, M.N.; Moore, A.N.; Dash, P.K. Loss of PTEN-Induced Kinase 1 (Pink1) Reduces Hippocampal Tyrosine Hydroxylase and Impairs Learning and Memory. *Exp. Neurol.* **2020**, *323*, 113081. [CrossRef]

39. Li, J.; Xue, C.; Gao, Q.; Tan, J.; Wan, Z. Mitochondrial DNA Heteroplasmy Rises in Substantia Nigra of Aged PINK1 KO Mice. *Biochem. Biophys. Res. Commun.* **2020**, *521*, 1024–1029. [CrossRef] [PubMed]
40. Furlong, R.M.; O’Keeffe, G.W.; O’Neill, C.; Sullivan, A.M. Alterations in Alpha-Synuclein and PINK1 Expression Reduce Neurite Length and Induce Mitochondrial Fission and Golgi Fragmentation in Midbrain Neurons. *Neurosci. Lett.* **2020**, *720*, 134777. [CrossRef]
41. Han, H.; Tan, J.; Wang, R.; Wan, H.; He, Y.; Yan, X.; Guo, J.; Gao, Q.; Li, J.; Shang, S.; et al. PINK1 Phosphorylates Drp1(S616) to Regulate Mitophagy-Independent Mitochondrial Dynamics. *EMBO Rep.* **2020**, *21*, e48686. [CrossRef]
42. Noda, S.; Sato, S.; Fukuda, T.; Tada, N.; Uchiyama, Y.; Tanaka, K.; Hattori, N. Loss of Parkin Contributes to Mitochondrial Turnover and Dopaminergic Neuronal Loss in Aged Mice. *Neurobiol. Dis.* **2020**, *136*, 104717. [CrossRef]
43. Baaske, M.K.; Kramer, E.R.; Meka, D.P.; Engler, G.; Engel, A.K.; Moll, C.K.E. Parkin Deficiency Perturbs Striatal Circuit Dynamics. *Neurobiol. Dis.* **2020**, *137*, 104737. [CrossRef]
44. Jo, A.; Lee, Y.; Park, C.H.; Shin, J.H. Deubiquitinase USP29 Governs MYBBP1A in the Brains of Parkinson’s Disease Patients. *J. Clin. Med.* **2019**, *9*, 52. [CrossRef] [PubMed]
45. Wilkaniac, A.; Lenkiewicz, A.M.; Babiec, L.; Murawska, E.; Jesko, H.M.; Cieslik, M.; Culmsee, C.; Adamczyk, A. Exogenous Alpha-Synuclein Evoked Parkin Downregulation Promotes Mitochondrial Dysfunction in Neuronal Cells. Implications for Parkinson’s Disease Pathology. *Front. Aging Neurosci.* **2021**, *13*, 591475. [CrossRef]
46. Yan, Y.Q.; Fang, Y.; Zheng, R.; Pu, J.L.; Zhang, B.R. NLRP3 Inflammasomes in Parkinson’s Disease and Their Regulation by Parkin. *Neuroscience* **2020**, *446*, 323–334. [CrossRef]
47. Tokarew, J.M.; El-Kodsi, D.N.; Lengacher, N.A.; Fehr, T.K.; Nguyen, A.P.; Shutinoski, B.; O’Nuallain, B.; Jin, M.; Khan, J.M.; Ng, A.C.H.; et al. Age-Associated Insolubility of Parkin in Human Midbrain is Linked to Redox Balance and Sequestration of Reactive Dopamine Metabolites. *Acta Neuropathol.* **2021**, *141*, 725–754. [CrossRef] [PubMed]
48. Ganguly, U.; Banerjee, A.; Chakrabarti, S.S.; Kaur, U.; Sen, O.; Cappai, R.; Chakrabarti, S. Interaction of Alpha-synuclein and Parkin in Iron Toxicity on SH-SY5Y Cells: Implications in the Pathogenesis of Parkinson’s Disease. *Biochem. J.* **2020**, *477*, 1109–1122. [CrossRef] [PubMed]
49. Gholkar, A.A.; Schmollinger, S.; Velasquez, E.F.; Lo, Y.C.; Cohn, W.; Capri, J.; Dharmarajan, H.; Deardorff, W.J.; Gao, L.W.; Abdusamad, M.; et al. Regulation of Iron Homeostasis Through Parkin-Mediated Lactoferrin Ubiquitylation. *Biochemistry* **2020**, *59*, 2916–2921. [CrossRef] [PubMed]
50. Bi, M.; Du, X.; Jiao, Q.; Liu, Z.; Jiang, H. Alpha-Synuclein Regulates Iron Homeostasis via Preventing Parkin-Mediated DMT1 Ubiquitylation in Parkinson’s Disease Models. *ACS Chem. Neurosci.* **2020**, *11*, 1682–1691. [CrossRef]
51. Zhong, Y.; Li, X.; Du, X.; Bi, M.; Ma, F.; Xie, J.; Jiang, H. The S-Nitrosylation of Parkin Attenuated the Ubiquitination of Divalent Metal Transporter 1 in MPP(+)-Treated SH-SY5Y Cells. *Sci. Rep.* **2020**, *10*, 15542. [CrossRef]
52. Cahill, C.M.; Lahiri, D.K.; Huang, X.; Rogers, J.T. Amyloid Precursor Protein and Alpha Synuclein Translation, Implications for Iron and Inflammation in Neurodegenerative Diseases. *Biochim. Biophys. Acta.* **2009**, *1790*, 615–628. [CrossRef]
53. Schwartztruber, A.; Boschian, C.; Lopes, F.M.; Myszczyńska, M.A.; New, E.J.; Beyrath, J.; Smeitink, J.; Ferraiuolo, L.; Mortiboys, H. Oxidative Switch Drives Mitophagy Defects in Dopaminergic Parkin Mutant Patient Neurons. *Sci. Rep.* **2020**, *10*, 15485. [CrossRef] [PubMed]
54. Okarmus, J.; Bogtofte, H.; Schmidt, S.I.; Ryding, M.; Garcia-Lopez, S.; Ryan, B.J.; Martinez-Serrano, A.; Hyttel, P.; Meyer, M. Lysosomal Perturbations in Human Dopaminergic Neurons Derived from Induced Pluripotent Stem Cells with PARK2 Mutation. *Sci. Rep.* **2020**, *10*, 10278. [CrossRef] [PubMed]
55. Pu, J.; Gao, T.; Zheng, R.; Fang, Y.; Ruan, Y.; Jin, C.; Shen, T.; Tian, J.; Zhang, B. Parkin Mutation Decreases Neurite Complexity and Maturation in Neurons Derived from Human Fibroblasts. *Brain Res. Bull.* **2020**, *159*, 9–15. [CrossRef] [PubMed]
56. Pirooznia, S.K.; Yuan, C.; Khan, M.R.; Karuppagounder, S.S.; Wang, L.; Xiong, Y.; Kang, S.U.; Lee, Y.; Dawson, V.L.; Dawson, T.M. PARIS Induced Defects in Mitochondrial Biogenesis Drive Dopamine Neuron Loss Under Conditions of Parkin or PINK1 Deficiency. *Mol. Neurodegener.* **2020**, *15*, 17. [CrossRef]
57. Ham, S.J.; Lee, D.; Yoo, H.; Jun, K.; Shin, H.; Chung, J. Decision Between Mitophagy and Apoptosis by Parkin via VDAC1 Ubiquitylation. *Proc. Natl. Acad. Sci. USA* **2020**, *117*, 4281–4291. [CrossRef]
58. Borsche, M.; König, I.R.; Delcambre, S.; Petrucci, S.; Balck, A.; Bruggemann, N.; Zimprich, A.; Wasner, K.; Pereira, S.L.; Avenali, M.; et al. Mitochondrial Damage-Associated Inflammation Highlights Biomarkers in PRKN/PINK1 Parkinsonism. *Brain* **2020**, *143*, 3041–3051. [CrossRef]
59. Barazzuol, L.; Giamogante, F.; Brini, M.; Cali, T. PINK1/Parkin Mediated Mitophagy, Ca(2+) Signalling, and ER-Mitochondria Contacts in Parkinson’s Disease. *Int. J. Mol. Sci.* **2020**, *21*, 1772. [CrossRef] [PubMed]
60. Kesh, S.; Kannan, R.R.; Balakrishnan, A. Naringenin Alleviates 6-Hydroxydopamine Induced Parkinsonism in SHSY5Y Cells and Zebrafish Model. *Comp. Biochem. Physiol. C Toxicol. Pharmacol.* **2021**, *239*, 108893. [CrossRef]
61. Qi, H.; Shen, D.; Jiang, C.; Wang, H.; Chang, M. Ursodeoxycholic Acid Protects Dopaminergic Neurons from Oxidative Stress via Regulating Mitochondrial Function, Autophagy, and Apoptosis in MPTP/MPP(+)-Induced Parkinson’s Disease. *Neurosci. Lett.* **2021**, *741*, 135493. [CrossRef]
62. Lin, M.W.; Lin, C.C.; Chen, Y.H.; Yang, H.B.; Hung, S.Y. Celastrol Inhibits Dopaminergic Neuronal Death of Parkinson’s Disease Through Activating Mitophagy. *Antioxidants* **2019**, *9*, 37. [CrossRef]

63. Liu, M.; Yu, S.; Wang, J.; Qiao, J.; Liu, Y.; Wang, S.; Zhao, Y. Ginseng Protein Protects Against Mitochondrial Dysfunction and Neurodegeneration by Inducing Mitochondrial Unfolded Protein Response in *Drosophila Melanogaster* PINK1 Model of Parkinson's Disease. *J. Ethnopharmacol.* **2020**, *247*, 112213. [CrossRef] [PubMed]
64. Ahmed, S.; Kwatra, M.; Ranjan Panda, S.; Murty, U.S.N.; Naidu, V.G.M. Andrographolide Suppresses NLRP3 Inflammasome Activation in Microglia Through Induction of Parkin-Mediated Mitophagy in In-Vitro and In-Vivo Models of Parkinson Disease. *Brain Behav. Immun.* **2021**, *91*, 142–158. [CrossRef]
65. Huang, C.Y.; Sivalingam, K.; Shibu, M.A.; Liao, P.H.; Ho, T.J.; Kuo, W.W.; Chen, R.J.; Day, C.H.; Viswanadha, V.P.; Ju, D.T. Induction of Autophagy by Vasicinone Protects Neural Cells from Mitochondrial Dysfunction and Attenuates Paraquat-Mediated Parkinson's Disease Associated alpha-Synuclein Levels. *Nutrients* **2020**, *12*, 1707. [CrossRef]
66. Gundogdu, M.; Tadayon, R.; Salzano, G.; Shaw, G.S.; Walden, H. A Mechanistic Review of Parkin Activation. *Biochim. Biophys. Acta Gen. Subj.* **2021**, *1865*, 129894. [CrossRef] [PubMed]
67. Larisch, S.; Yi, Y.; Lotan, R.; Kerner, H.; Eimerl, S.; Tony Parks, W.; Gottfried, Y.; Birkey Refeffy, S.; de Caestecker, M.P.; Danielpour, D.; et al. A Novel Mitochondrial Septin-Like Protein, ARTS, Mediates Apoptosis Dependent on Its P-loop Motif. *Nat. Cell Biol.* **2000**, *2*, 915–921. [CrossRef] [PubMed]
68. Shehadeh, L.; Mitsi, G.; Adi, N.; Bishopric, N.; Papapetropoulos, S. Expression of Lewy Body Protein Septin 4 in Postmortem Brain of Parkinson's Disease and Control Subjects. *Mov. Disord.* **2009**, *24*, 204–210. [CrossRef]
69. Munoz-Soriano, V.; Paricio, N. Overexpression of Septin 4, the *Drosophila* Homologue of Human CDCrel-1, Is Toxic for DopaMinergic Neurons. *Eur. J. Neurosci.* **2007**, *26*, 3150–3158. [CrossRef]
70. Munoz-Soriano, V.; Nieto-Arellano, R.; Paricio, N. Septin 4, the *Drosophila* Ortholog of Human CDCrel-1, Accumulates in Parkin Mutant Brains and Is Functionally Related to the Nedd4 E3 Ubiquitin Ligase. *J. Mol. Neurosci.* **2012**, *48*, 136–143. [CrossRef]
71. Hao, Q.; Chen, J.; Liao, J.; Huang, Y.; Gan, Y.; Larisch, S.; Zeng, S.X.; Lu, H.; Zhou, X. P53 Induces ARTS to Promote Mitochondrial Apoptosis. *Cell Death Dis.* **2021**, *12*, 204. [CrossRef]
72. Crocker, S.J.; Liston, P.; Anisman, H.; Lee, C.J.; Smith, P.D.; Earl, N.; Thompson, C.S.; Park, D.S.; Korneluk, R.G.; Robertson, G.S. Attenuation of MPTP-induced Neurotoxicity and Behavioural Impairment in NSE-XIAP Transgenic Mice. *Neurobiol. Dis.* **2003**, *12*, 150–161. [CrossRef]
73. Oh, C.K.; Choi, Y.K.; Hwang, I.Y.; Ko, Y.U.; Chung, I.K.; Yun, N.; Oh, Y.J. RING-finger Protein 166 Plays a Novel Pro-Apoptotic Role in Neurotoxin-Induced Neurodegeneration via Ubiquitination of XIAP. *Cell Death Dis.* **2020**, *11*, 939. [CrossRef] [PubMed]
74. Fu, R.H.; Huang, L.C.; Lin, C.Y.; Tsai, C.W. Modulation of ARTS and XIAP by Parkin Is Associated with Carnosic Acid Protects SH-SY5Y Cells Against 6-Hydroxydopamine-Induced Apoptosis. *Mol. Neurobiol.* **2018**, *55*, 1786–1794. [CrossRef] [PubMed]
75. Bornstein, B.; Edison, N.; Gottfried, Y.; Lev, T.; Shekhtman, A.; Gonen, H.; Rajalingam, K.; Larisch, S. X-linked Inhibitor of Apoptosis Protein Promotes the Degradation of Its Antagonist, the Pro-Apoptotic ARTS Protein. *Int. J. Biochem. Cell Biol.* **2012**, *44*, 489–495. [CrossRef] [PubMed]
76. Van Den Berge, N.; Ferreira, N.; Gram, H.; Mikkelsen, T.W.; Alstrup, A.K.O.; Casadei, N.; Tsung-Pin, P.; Riess, O.; Nyengaard, J.R.; Tamguney, G.; et al. Evidence for Bidirectional and Trans-Synaptic Parasympathetic and Sympathetic Propagation of Alpha-synuclein in Rats. *Acta Neuropathol.* **2019**, *138*, 535–550. [CrossRef] [PubMed]
77. Ferreira, N.; Goncalves, N.P.; Jan, A.; Jensen, N.M.; van der Laan, A.; Mohseni, S.; Vaegter, C.B.; Jensen, P.H. Trans-Synaptic Spreading of Alpha-Synuclein Pathology Through Sensory Afferents leads to Sensory Nerve Degeneration and Neuropathic pain. *Acta Neuropathol. Commun.* **2021**, *9*, 31. [CrossRef]
78. Ferreira, N.; Gram, H.; Sorrentino, Z.A.; Gregersen, E.; Schmidt, S.I.; Reimer, L.; Betzer, C.; Perez-Gozalbo, C.; Beltoja, M.; Nagaraj, M.; et al. Multiple System Atrophy-Associated Oligodendroglial Protein p25Alpha Stimulates Formation of Novel Alpha-Synuclein Strain With Enhanced Neurodegenerative Potential. *Acta Neuropathol.* **2021**, *142*, 87–115. [CrossRef]
79. Guo, H.; Ji, F.; Liu, B.; Chen, X.; He, J.; Gong, J. Peiminine Ameliorates Bleomycin-Induced Acute Lung Injury in Rats. *Mol. Med. Rep.* **2013**, *7*, 1103–1110. [CrossRef]
80. Lim, J.M.; Lee, B.; Min, J.H.; Kim, E.Y.; Kim, J.H.; Hong, S.; Kim, J.J.; Sohn, Y.; Jung, H.S. Effect of Peiminine on DNCB-Induced atopic Dermatitis by Inhibiting Inflammatory Cytokine Expression in Vivo and in Vitro. *Int. Immunopharmacol.* **2018**, *56*, 135–142. [CrossRef]
81. Chen, L.H.; Zhang, H.M.; Guan, Z.Y.; Zhu, W.F.; Yi, W.J.; Guan, Y.M.; Wang, S.; Liu, H.N. Sex Dependent Pharmacokinetics, Tissue Distribution and Excretion of Peimine and Peiminine in Rats Assessed by Liquid Chromatography-Tandem Mass Spectrometry. *J. Ethnopharmacol.* **2013**, *145*, 77–84. [CrossRef] [PubMed]
82. Duty, S.; Jenner, P. Animal Models of Parkinson's Disease: A Source of Novel Treatments and Clues to the Cause of the Disease. *Br. J. Pharmacol.* **2011**, *164*, 1357–1391. [CrossRef] [PubMed]
83. Fu, R.H.; Wang, Y.C.; Chen, C.S.; Tsai, R.T.; Liu, S.P.; Chang, W.L.; Lin, H.L.; Lu, C.H.; Wei, J.R.; Wang, Z.W.; et al. Acetylcorynoline Attenuates Dopaminergic Neuron Degeneration and Alpha-Synuclein Aggregation in Animal Models of Parkinson's Disease. *Neuropharmacology* **2014**, *82*, 108–120. [CrossRef] [PubMed]



Article

EK100 and Antrodin C Improve Brain Amyloid Pathology in APP/PS1 Transgenic Mice by Promoting Microglial and Perivascular Clearance Pathways

Huey-Jen Tsay^{1,†}, Hui-Kang Liu^{2,3}, Yueh-Hsiung Kuo^{4,5,6,†}, Chuan-Sheng Chiu⁷, Chih-Chiang Liang⁸, Chen-Wei Chung⁹, Chin-Chu Chen¹⁰, Yen-Po Chen¹⁰ and Young-Ji Shiao^{2,3,7,*}

- ¹ Institute of Neuroscience, School of Life Science, National Yang-Ming Chiao Tung University, Taipei 112, Taiwan; hjtsay@ym.edu.tw
 - ² National Research Institute of Chinese Medicine, Ministry of Health and Welfare, Taipei 112, Taiwan; hk.liu@nricm.edu.tw
 - ³ Program in Clinical Drug Development of Chinese Medicine, Taipei Medical University, Taipei 112, Taiwan
 - ⁴ Department of Chinese Pharmaceutical Sciences and Chinese Medicine Resources, China Medical University, Taichung 404, Taiwan; kuoyh@mail.cmu.edu.tw
 - ⁵ Department of Biotechnology, Asia University, Taichung 413, Taiwan
 - ⁶ Chinese Medicine Research Center, China Medical University, Taichung 404, Taiwan
 - ⁷ Institute of Biopharmaceutical Science, National Yang-Ming Chiao Tung University, Taipei 112, Taiwan; vicvic1019@gmail.com
 - ⁸ Institute of Anatomy and Cell Biology, National Yang-Ming Chiao Tung University, Taipei 112, Taiwan; tony0078013@yahoo.com.tw
 - ⁹ Institute of Traditional Medicine, National Yang-Ming Chiao Tung University, Taipei 112, Taiwan; patrick831226@icloud.com
 - ¹⁰ Biotech Research Institute, Grape King Bio Ltd., Taoyuan City 320, Taiwan; gkbioeng@grapeking.com.tw (C.-C.C.); yp.chen@grapeking.com.tw (Y.-P.C.)
- * Correspondence: yshiao@nricm.edu.tw; Tel.: +886-2-28201999 (ext. 4171)
† These authors contributed equally to this work.

Citation: Tsay, H.-J.; Liu, H.-K.; Kuo, Y.-H.; Chiu, C.-S.; Liang, C.-C.; Chung, C.-W.; Chen, C.-C.; Chen, Y.-P.; Shiao, Y.-J. EK100 and Antrodin C Improve Brain Amyloid Pathology in APP/PS1 Transgenic Mice by Promoting Microglial and Perivascular Clearance Pathways. *Int. J. Mol. Sci.* **2021**, *22*, 10413. <https://doi.org/10.3390/ijms221910413>

Academic Editors: Masaru Tanaka and Lydia Giménez-Llort

Received: 8 September 2021
Accepted: 24 September 2021
Published: 27 September 2021

Publisher's Note: MDPI stays neutral with regard to jurisdictional claims in published maps and institutional affiliations.



Copyright: © 2021 by the authors. Licensee MDPI, Basel, Switzerland. This article is an open access article distributed under the terms and conditions of the Creative Commons Attribution (CC BY) license (<https://creativecommons.org/licenses/by/4.0/>).

Abstract: Alzheimer's disease (AD) is characterized by the deposition of β -amyloid peptide ($A\beta$). There are currently no drugs that can successfully treat this disease. This study first explored the anti-inflammatory activity of seven components isolated from *Antrodia cinnamomea* in BV2 cells and selected EK100 and antrodin C for in vivo research. APP^{swe}/PS1^{dE9} mice were treated with EK100 and antrodin C for one month to evaluate the effect of these reagents on AD-like pathology by nesting behavior, immunohistochemistry, and immunoblotting. Ergosterol and ibuprofen were used as control. EK100 and antrodin C improved the nesting behavior of mice, reduced the number and burden of amyloid plaques, reduced the activation of glial cells, and promoted the perivascular deposition of $A\beta$ in the brain of mice. EK100 and antrodin C are significantly different in activating astrocytes, regulating microglia morphology, and promoting plaque-associated microglia to express oxidative enzymes. In contrast, the effects of ibuprofen and ergosterol are relatively small. In addition, EK100 significantly improved hippocampal neurogenesis in APP^{swe}/PS1^{dE9} mice. Our data indicate that EK100 and antrodin C reduce the pathology of AD by reducing amyloid deposits and promoting nesting behavior in APP^{swe}/PS1^{dE9} mice through microglia and perivascular clearance, indicating that EK100 and antrodin C have the potential to be used in AD treatment.

Keywords: Alzheimer's disease; APP^{swe}/PS1^{dE9} transgenic mice; EK100; antrodin C; amyloid plaque; microglia; perivascular clearance

1. Introduction

Alzheimer's disease (AD) is characterized by a progressive decline in cognitive abilities that can ultimately affect daily living activities. Extracellular deposition of β -amyloid ($A\beta$) plaques and intracellular neurofibrillary tangles are considered the main pathological

hallmark. The imbalance between A β production and clearance causes A β to accumulate in the central nervous system (CNS), which in turn induces A β plaque formation, increases neuroinflammation, and alters adult hippocampal neurogenesis [1].

There is increasing evidence that the clearance of A β from the brain in AD is impaired. Therefore, there is an increasing need to study the A β clearance mechanism as a potential target for AD treatment. As we all know, A β can be cleared from the brain in many ways, such as being degraded by proteases, transported through the blood–brain barrier (BBB), and cleared by the flow of interstitial fluid (ISF) and cerebrospinal fluid (CSF) [2]. According to recent studies, two types of perivascular scavenging systems are related to the movement of ISF and CSF, namely intramural peri-arterial drainage (IPAD) and perivascular CSF inflow [2,3]. In IPAD, the parenchymal ISF containing A β exits the brain and enters the cervical lymph nodes along the basement membrane (BM) of capillaries and arterial smooth muscle cells [3]. IPAD failure can cause cerebral amyloid angiopathy (CAA), where A β mainly accumulates in capillaries and arterial smooth muscle cells BM [4]. The development of AD animal models is crucial for elucidating the mechanisms and the etiology of the disease in order to identify efficient therapies. Therefore, animal models overexpressing A β or tau markers were extensively generated [5]. Animal models were first used to understand AD mechanisms, but above all, they were used to test drugs preventing cognitive deficits for therapeutic interventions. However, none of the current developed animal models is able to entirely reproduce the AD pathology, since the deposition of A β and its consequence are not limited to the central nervous system [6–8].

Neuroinflammation can damage neurons and promote A β aggregation, so anti-inflammatory has become the target of AD treatment [9,10]. However, studies have shown that the early activation of M2-like microglia in AD exhibits neuroprotective functions by promoting A β phagocytosis and clearance, but A β -activated M1-like microglia down-regulate A β clearance, thereby promoting A β aggregation and neurodegeneration [11]. It has been proposed that pathologically induced COX-2 activity can induce memory deficits in APP^{swe}/PS1^{dE9} (APP/PS1) transgenic mice [12]. Therefore, the potential beneficial effects of non-steroidal anti-inflammatory drugs (NSAIDs) such as ibuprofen on the treatment of AD have also attracted people's attention [13].

Antrodia cinnamomea (Syn. *Antrodia camphorata*) is a mushroom unique to Taiwan [14] that has been safely used in humans in clinical trials (ClinicalTrials.gov (accessed on 1 September 2021) Identifier:NCT01007656). For a long time, the fruit body of *A. cinnamomea* has been widely used as a traditional medicine for the treatment of many medical diseases [15]. At present, the cultured mycelium of *A. cinnamomea* and its anti-inflammatory components, such as ergosta-7,9(11), 22-trien-3 β -ol (also known as EK100), antrodin C, and antroquinonol can also be used for medicinal purposes. Antroquinonol activates the nuclear factor erythroid-2 related factor-2 (Nrf2)-dependent cellular antioxidant defense system, which has antioxidant and anti-inflammatory effects in peripheral diseases and AD animal models [16].

In this study, six phytosteroids (i.e., EK100, antcin K, eburicoic acid, dehydroeburicoic acid, sulfurenic acid, and dehydrosulfurenic acid) (Figure 1A) and a maleimide derivative (i.e., antrodin C) (Figure 1B) were isolated from the mycelium or fruit body of *Antrodia cinnamomea* for anti-inflammatory research. In order to be used as structural control, ergosterol and ibuprofen were also included in this study (Figure 1A,B).

In previous studies, it was found that EK100 has an anti-inflammatory effect on the liver of chronic alcohol-fed mice [17] and improves brain damage in ischemic stroke through neurogenesis [18]. Ergosterol is an isomer of EK100 (Figure 1B), which has an anti-inflammatory effect on the nitric oxide inhibitory activity in macrophages [19]. Antrodin C (3-isobutyl-4-[4-(3-methyl-2-butenyloxy)phenyl]-1H-pyrrol-1-ol-2,5-dione) has anti-inflammatory activity and can inhibit macrophage nitric oxide production [20]. By activating the Nrf2-dependent cellular antioxidant defense system, it can effectively intervene in diabetes-related cardiovascular diseases [21]. Antcin K, but not EK100, activates peroxisome proliferator-activated receptor (PPAR) α in cell-based transactivation studies [22].

Eburicoic acid and dehydroeburicoic acid-treated mice reduced hyperglycemia, hypertriglyceridemia, hyperinsulinemia, hyperleptinemia, and hypercholesterolemia induced by a high-fat diet [23]. Sulfuric acid showed protective effects on type 1 diabetes and hyperlipidemia in diabetic mice induced by streptozotocin [24]. However, the anti-Alzheimer's disease effect of these compounds has never been studied.

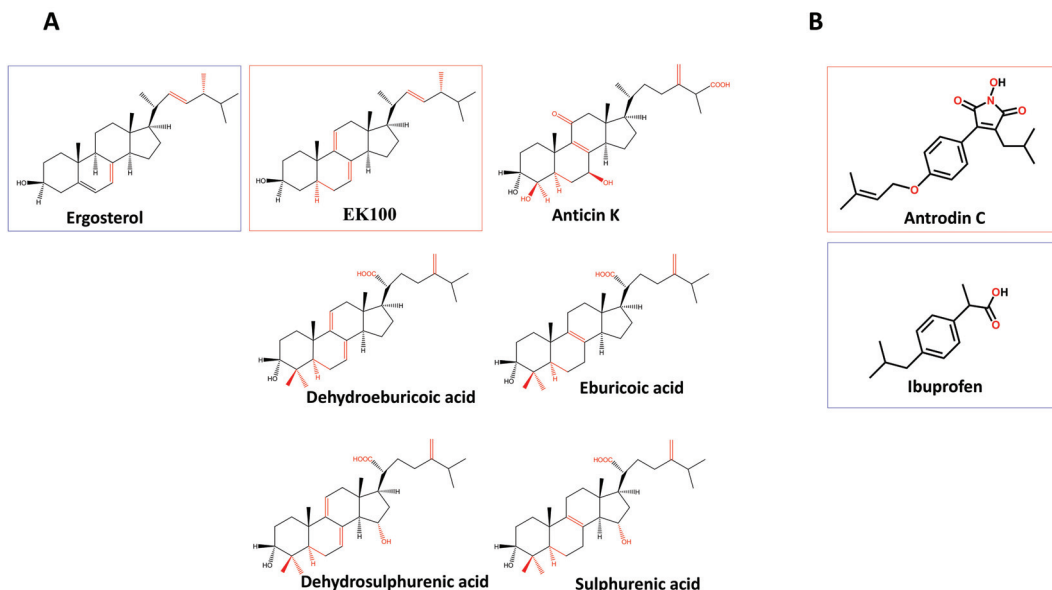


Figure 1. The structure of the compounds used in this study. (A) The structure of EK100 (Ergosta-7,9(11),22-trien-3 β -ol), ergosterol (Ergosta-5,7,22-trien-3 β -ol), anticin K (3 α ,4 β ,7 β -trihydroxy-4 α -methylergosta-8,24(28)-dien-11-on-26-oic acid), dehydroeburicoic acid ((2R)-2-[(3S,5R,10S,13R,14R,17R)-3-hydroxy-4,4,10,13,14-pentamethyl-2,3,5,6,12,15,16,17-octahydro-1H-cyclopenta[a]phenanthren-17-yl]-6-methyl-5-methylideneheptanoic acid), eburicoic acid ((2R)-2-[(3S,5R,10S,13R,14R,17R)-3-hydroxy-4,4,10,13,14-pentamethyl-2,3,5,6,7,11,12,15,16,17-decahydro-1H-cyclopenta[a]phenanthren-17-yl]-6-methyl-5-methylideneheptanoic acid), dehydrosulfurenic acid ((2R)-2-[(3S,5R,10S,13R,14R,15S,17R)-3,15-dihydroxy-4,4,10,13,14-pentamethyl-2,3,5,6,11,12,15,16,17-decahydro-1H-cyclopenta[a]phenanthren-17-yl]-6-methyl-5-methylideneheptanoic acid), and sulfurenic acid ((2R)-2-[(3S,5R,10S,13R,14R,15S,17R)-3,15-dihydroxy-4,4,10,13,14-pentamethyl-2,3,5,6,7,11,12,15,16,17-decahydro-1H-cyclopenta[a]phenanthren-17-yl]-6-methyl-5-methylideneheptanoic acid). (B) The structure of antrodin C (3-isobutyl-4-[4-(3-methyl-2-butenyloxy)phenyl]-1H-pyrrol-1-ol-2,5-dione) and ibuprofen (isobutylphenyl-propionic acid). The red squares indicate the bioactive compounds and the blue squares indicate the control compounds.

APP/PS1 transgenic mice co-expressing Swedish mutant human APP695 and mutant human presenilin 1 (PS1) (in which exon 9 is deleted) [25] exhibit pathological and behavioral changes similar to AD, including amyloid in the brain accumulation of plaques, degeneration of the cholinergic system, and impaired exploratory behavior and spatial memory [26]. As early as 3 to 5 months of age, APP/PS1 mice have increased A β production and plaque formation [27], and impairments in spatial learning and memory are also observed at 6 months of age [28,29]. In order to verify the effects of the four compounds on behavioral disorders in APP/PS1 mice, we focused on species-specific nesting activities, because it is multi-brain-dependent spontaneous [30], which has been considered similar to activities of daily living (ADL) skills [31]. Clinically, ADL disorder is a pathological manifestation of AD [32], and this pathological manifestation also appears in APP/PS1 mice [29]. In addition, it was found that the hippocampal neurogenesis of APP/PS1 mice was damaged at 3 to 6 months of age [33]. Our previous studies have shown that anti-inflammatory effects can promote hippocampal neurogenesis [29], so we hypothesized that the decline in microglia activation may subsequently promote hippocampal neurogenesis.

The purpose of this study is to study the effects of EK100, antrodin C, ergosterol, and ibuprofen on AD-related pathology in APP/PS1 transgenic mice.

2. Results

2.1. EK100 and Antrodin C Confer Anti-Inflammatory Effects on BV2 Microglia

The structure of EK100 and antrodin C as well as their related compounds used in this study are shown in Figure 1.

In order to determine the anti-inflammatory effects of *A. cinnamomea* mycelium components, BV2 cells, a cell line derived from primary mouse microglia cells, were incubated with various concentrations of *A. cinnamomea* mycelium components including ethanol extract (CA-Et) and seven isolated compounds for 30 min, and then, the cells were activated with LPS. Ergosterol (an isomer of EK100) and ibuprofen (a non-steroidal anti-inflammatory drug) were used as controls. The production of nitric oxide in the conditioned medium and the reduction of MTT in the cell were measured after 24 h incubation (Table 1). CA-Et with a non-cytotoxic concentration of 50 µg/mL significantly inhibited the production of nitric oxide in the vehicle-treated control group by 40% ($F(5,12) = 59.70; p < 0.0001, n = 4$). At subtoxic concentrations, antitoxin K, ethylene propionic acid/dehydrobutyric acid mixture, sulfuric acid/dehydrosulfuric acid mixture, and ibuprofen have no anti-inflammatory effects. Compared with the vehicle control, EK100 (20 µM), antrodin C (100 µM), and ergosterol (10 µM) reduced nitric oxide production by 34.0% ($F(3, 16) = 44.97; p < 0.0001, n = 4$), 40.0% ($F(3, 16) = 198.67; p < 0.0001, n = 4$), and 40.2% ($F(3, 12) = 48.87; p < 0.0001, n = 4$), respectively.

Table 1. Anti-inflammatory activity of four reagents on LPS-activated BV2 cells.

	Nitric Oxide	MTT Reduction
Vehicle	25.99 ± 1.14	97.62 ± 1.41
CA-Et		
50 µg/mL	10.55 ± 1.60 ***	101.10 ± 3.39
100 µg/mL	4.77 ± 0.68 ***	100.20 ± 1.54
Anticin K		
50 µM	21.01 ± 0.96	83.36 ± 10.19 **
100 µM	21.16 ± 1.14	89.58 ± 5.50
EA/DEA		
10 µg/mL	24.22 ± 3.17	45.37 ± 3.07 ***
20 µg/mL	16.20 ± 0.49 **	31.94 ± 2.585 ***
SA/DSA		
10 µg/mL	26.26 ± 1.35	73.70 ± 4.31 ***
20 µg/mL	17.46 ± 2.87 *	55.16 ± 2.07 ***
EK100		
10 µM	16.84 ± 1.38 ***	100.9 ± 2.07
20 µM	17.19 ± 1.24 **	96.19 ± 3.14
Antrodin C		
50 µM	18.54 ± 1.83 ***	102.7 ± 3.42
100 µM	15.61 ± 1.01 ***	104.8 ± 2.82
Ergosterol		
5 µM	16.29 ± 1.64 ***	89.14 ± 2.59
10 µM	15.55 ± 1.38 ***	82.30 ± 0.91 **
Ibuprofen		
50 µM	20.27 ± 0.99	103.3 ± 3.56
100 µM	21.80 ± 0.59	101.9 ± 0.63

CA-Et, ethanol extract of *A. cinnamomea* mycelium; EA/DEA, the mixture of eburic acid and dehydroeburic acid; SA/DSA, the mixture of sulfurenic acid and dehydrosulfurenic acid. Significant differences between Vehicle group and reagent-treated groups are indicated by *, $p < 0.05$; **, $p < 0.01$; ***, $p < 0.001$.

2.2. EK100 and Antrodin C Improve Nesting Behavior of APP/PS1 Mice

We chose APP/PS1 transgenic mice (an AD animal model) to check that the effect of two anti-inflammatory components of *A. cinnamomea* (i.e., EK100 and antrodin C) and

two control compounds (i.e., ergosterol and ibuprofen) on AD pathology. APP/PS1 mice (five-month-old, male and female) were orally administered EK100, antrodin C, ergosterol, and ibuprofen ($30 \text{ mg}\cdot\text{kg}^{-1}\cdot\text{day}^{-1}$) or vehicle for 30 days, and body weight were measured weekly. The treatments did not significantly change body weight, indicating that these treatments have no obvious side effect. Nesting behavior involves a wide network of brain regions and has previously been used to assess the activities of daily living (ADL) skills in AD transgenic mice [29]. Compared with wild-type mice, APP/PS1 mice administered vehicle showed defects in nesting behavior, as assessed by nest score (1.33 ± 0.01 vs. 4.88 ± 0.09 , $p < 0.001$, $n = 6$) and unshredded Nestlet (3.77 ± 0.31 vs. 0.87 ± 0.32 , $p < 0.0001$, $n = 6$). The use of EK100, antrodin C, and ibuprofen can significantly restore impaired nesting behavior (3.85 ± 0.57 vs. 1.33 ± 0.01 , $p < 0.01$, $n = 6$, 3.70 ± 0.58 vs. 1.33 ± 0.01 , $p < 0.01$, $n = 6$, 2.50 ± 0.58 vs. 1.33 ± 0.01 , $p < 0.05$, $n = 6$, respectively) (Figure 2). However, ergosterol has no effect on nesting behavior.

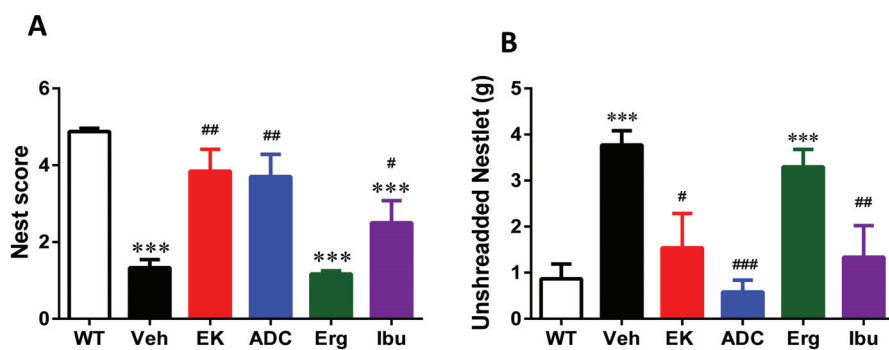


Figure 2. EK100, antrodin C, and ibuprofen ameliorate nesting behavior deficits in APP/PS1 mice. APP/PS1 transgenic mice were orally administered with vehicle (Veh) or EK100 (EK), antrodin C (ADC), ergosterol (Erg), and ibuprofen (Ibu) ($30 \text{ mg}\cdot\text{kg}^{-1}\cdot\text{day}^{-1}$, $n = 6$ each). Nesting tasks were performed at 30 days post administration. The image in wild-type (WT) mice ($n = 6$) is also compared. Bar graphs show the results from the nesting task's nest score (A) and unshredded Nestlet (B) from nesting task. The results are the mean \pm S.E.M. Significant differences between WT group and the other groups are indicated by ***, $p < 0.001$. Significant differences between Veh group and reagent-treated groups are indicated by #, $p < 0.05$; ##, $p < 0.01$; ###, $p < 0.001$.

2.3. EK100 and Antrodin C Reduce the Number and Burden of Amyloid Plaques in the Brains of APP/PS1 Mice

It is known that plaques can be clearly observed in the brains of APP/PS1 mice at 6 months of age [29]. Therefore, the effect of the four compounds on the number and size distribution of plaque were detected by immunostaining with AB10 antibody. The plaque number and burden were calculated using MetaMorph software. The plaque number and burden were significantly reduced after 30-day administration of EK100 or antrodin C. Compared with vehicle-treated mice, EK100 and antrodin C decreased plaque number by 45.4% (170.3 ± 19.04 vs. 272.6 ± 30.89 , $p < 0.05$, $n = 5$) and 43.7% (181.4 ± 19.76 vs. 272.6 ± 30.89 , $p < 0.05$, $n = 5$), respectively (Figure 3A,B; Supplementary Figure S1), and they decreased plaque burden by 37.5% (1.31 ± 0.24 vs. 2.13 ± 0.19 , $p < 0.05$, $n = 5$) and 53.9% (0.98 ± 0.12 vs. 2.13 ± 0.19 , $p < 0.01$, $n = 5$), respectively (Figure 3A,C). In contrast, ergosterol and ibuprofen did not have any significant effect on the number of plaques, and ibuprofen even increased the plaque load by 31.6% (2.80 ± 0.06 vs. 2.13 ± 0.19 , $p < 0.05$, $n = 5$).

Since the decrease in the number of plaques may be due to a decrease in $A\beta$ levels in the brain, we subsequently measured $A\beta$ levels in the hippocampus. However, after all four treatments, there was no significant change in $A\beta$ levels in the hippocampus (Supplementary Figure S2A). In contrast, serum $A\beta_{1-42}$ levels significantly decreased

after the ergosterol and ibuprofen treatment, while serum levels of A β 1-40 significantly increased after antrodin C treatment (Supplementary Figure S2B).

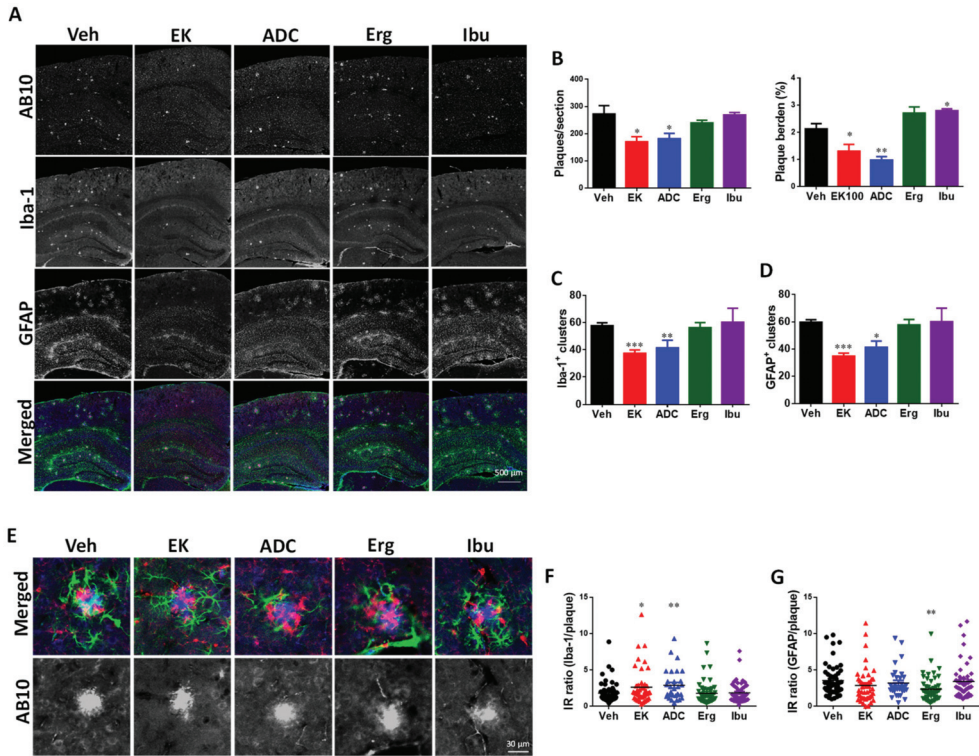


Figure 3. EK100 and antrodin C reduce amyloid plaque load, number of glial clusters, and plaque-related glial activation in APP/PS1 mice. APP/PS1 transgenic mice orally administered vehicle (Veh) or EK100 (EK), antrodin C (ADC), ergosterol (Erg), and ibuprofen (Ibu) ($30 \text{ mg}\cdot\text{kg}^{-1}\cdot\text{day}^{-1}$, each $n = 6$) 1 months, and then amyloid plaques, microglia, and astrocytes were immunostained with AB10, Iba-1, and GFAP antibodies, respectively. (A). The representative fluorescent images of AB10 (blue in the merged panel), Iba-1 (red in the merged panel), and GFAP (green in the merged panel) are shown. Scale bar: $500 \mu\text{m}$. (B–D). The number and burden of AB10-stained plaque (B) and the number of Iba-1⁺ clusters (C) and GFAP⁺ clusters (D) in cerebral hemisphere are counted and shown. The results are the mean \pm S.E.M. Significant differences between the Veh group and reagent-treated groups are indicated by *, $p < 0.05$; **, $p < 0.01$; ***, $p < 0.001$. (E). The representative fluorescent images of glial clusters immunostained with AB10 (blue in the merged panel), Iba-1 (red in the merged panel), and GFAP (green in the merged panel) antibodies are shown. Scale bar: $30 \mu\text{m}$. (F,G). The immunointensity (IR) ratio of Iba-1 to AB10 (F) and GFAP to AB10 (G) are calculated and shown. The results are the mean \pm S.E.M. Significant differences between Veh group and reagent-treated groups are indicated by *, $p < 0.05$; **, $p < 0.01$.

2.4. EK100 and Antrodin C Promote A β Perivascular Deposition in the Brain of APP/PS1 Mice

Since A β in the ISF of the brain can be removed from the brain through the glymphatic perivenous drainage pathway and/or IPAD pathway [34], perivascular A β deposition is detected in both the cortex and hippocampus. We found that the distribution of A β deposits changed from amyloid plaques to A β deposits around blood vessels after treatment with EK100 and antrodin C (Figure 4). The calculation of A β deposition in the perivascular area is expressed as a percentage of the total deposition (Figure 4B). The results showed that EK100 and antrodin C increased the perivascular A β deposition in the cortex by 22.86% (63.97 ± 5.38 vs. 41.12 ± 3.71 , $p < 0.01$, $n = 5$ vs. 6) and 19.89% (61.00 ± 0.84 vs. 41.12 ± 3.713 , $p < 0.01$, $n = 5$ vs. 6), respectively. These changes were found in both

capillaries and arteries (Supplementary Figure S1C). Similarly, EK100 and antrodin C increase the perivascular A β deposition in the hippocampus by 31.67% (76.48 ± 13.05 vs. 44.80 ± 6.52 , $p < 0.05$, $n = 5$ vs. 6) and 28.21% (73.01 ± 4.84 vs. 44.80 ± 6.52 , $p < 0.05$, $n = 5$ vs. 6), respectively.

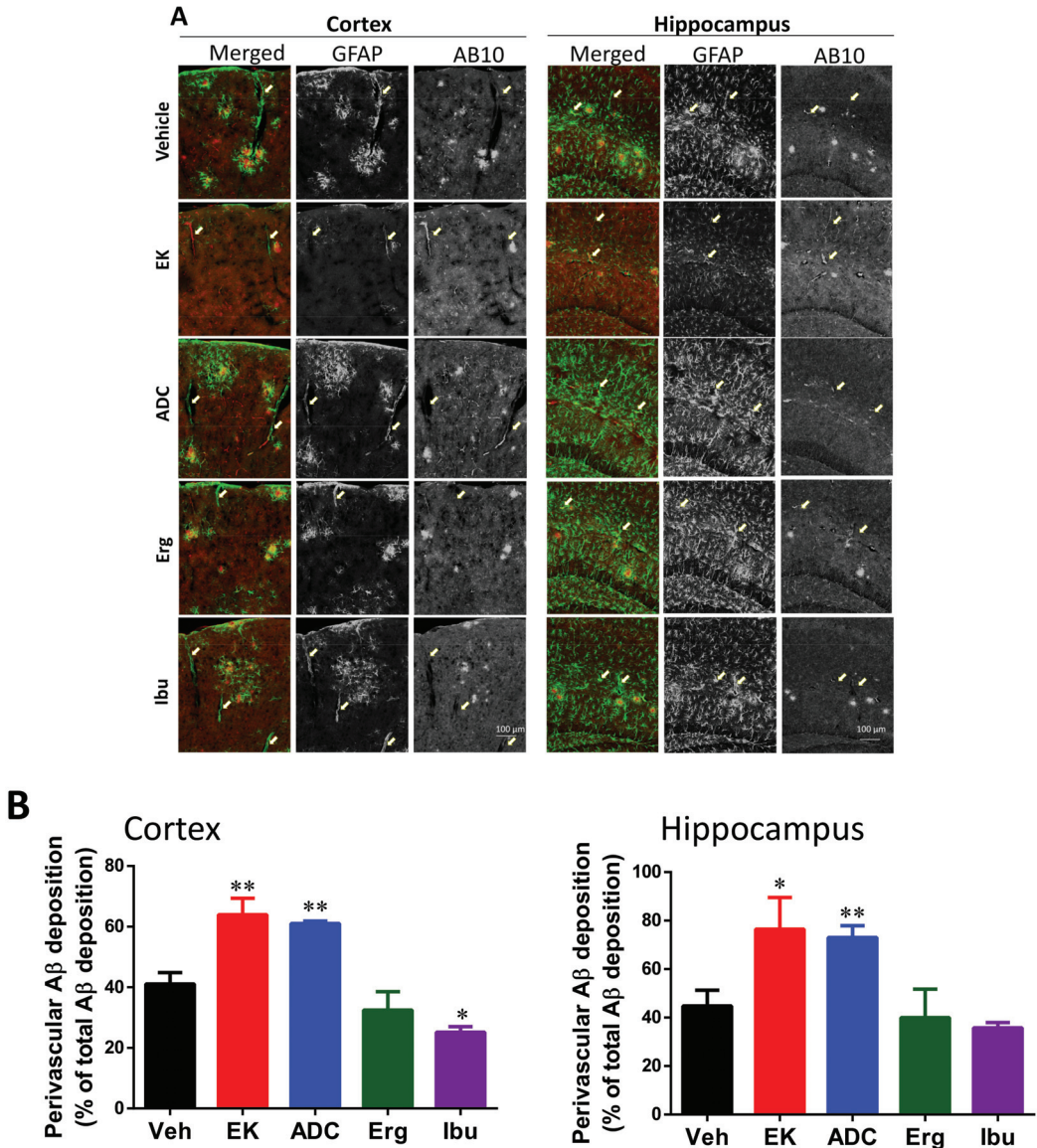


Figure 4. EK100 and antrodin C increase perivascular A β deposition in APP/PS1 mice. APP/PS1 transgenic mice orally administered vehicle (Veh) or EK100 (EK), antrodin C (ADC), ergosterol (Erg), and ibuprofen (Ibu) ($30 \text{ mg}\cdot\text{kg}^{-1}\cdot\text{day}^{-1}$, each $n = 6$) for 1 months, and then astrocytes and microglia were immunostained GFAP and Iba-1 antibodies, respectively. (A) The representative immunostaining images of GFAP and AB10 in the cortex and hippocampus are shown. Scale bar: $100 \mu\text{m}$. Arrows indicate the representative perivascular area. (B) The percentage of perivascular A β deposition to total A β deposition is calculated by MetaMorph image analysis software and shown. The results are the mean \pm S.E.M. Significant differences between the Veh group and the other groups are indicated by *, $p < 0.05$; **, $p < 0.01$.

2.5. EK100 and Antrodin C Reduce the Number of Glial Cluster and Glial Activation in the Brain of APP/PS1 Mice

M2-microglia phagocytosis is another A β clearance pathway. Therefore, changes in the phenotype of microglia may also help reduce amyloid plaques. After 30 days of treatment with EK100 and antrodin C, the number of clusters formed by PAM decrease significantly (Figure 3A,C). Compared with vehicle-treated mice, EK100 treatment reduced the number of clusters formed by PAM by $35.5 \pm 9.6\%$ (37.40 ± 2.50 vs. 57.83 ± 2.07 , $p < 0.001$, $n = 5$). The less effective is that antrodin C treatment reduces the number of clusters containing PAM by $34.2 \pm 18.5\%$ (41.40 ± 5.66 vs. 57.83 ± 2.07 , $p < 0.05$, $n = 5$). In contrast, ergosterol and ibuprofen had no significant effect on the number of clusters formed by PAM.

On the other hand, compared with vehicle-treated mice, EK100 treatment reduced number of clusters formed by PAA by $42.0 \pm 7.9\%$ (34.80 ± 2.11 vs. 59.67 ± 1.84 , $p < 0.0001$, $n = 5$) (Figure 3A,D). The less effective is that antrodin C treatment reduces the number of clusters containing PAA by $34.4 \pm 20.1\%$ (41.20 ± 4.62 vs. 59.67 ± 1.84 , $p < 0.01$, $n = 5$). In contrast, ergosterol and ibuprofen had no significant effect on the number of clusters formed by PAA and PAM.

In order to determine the changes in microglia associated with activated plaques after drug treatment, a scatter plot of the fluorescence intensity of small and medium plaques (<21 pixels) and Iba-1 was drawn (Supplementary Figure S3). Linear regression analysis showed that the slope of the regression equation of EK100, antrodin C, and ibuprofen groups were significantly different from that of the vehicle group. Linear regression for the vehicle group is $y = 0.51x + 0.76$, $R^2 = 0.06$; for the EK100 group is $y = 1.12x + 0.47$, $R^2 = 0.23$ ($p < 0.01$ for different in slope); for the antrodin C group is $y = 1.05x + 3.32$, $R^2 = 0.18$ ($p < 0.01$ for different in slope); for the ergosterol group is $y = 0.84x + 4.47$, $R^2 = 0.21$ ($p = 0.13$ for different in slope); for the ibuprofen group is $y = 0.89x + 0.95$, $R^2 = 0.21$ ($p < 0.01$ for different in slope). This result indicates that EK-100, antrodin C, and ibuprofen, but not ergosterol, changed the relationship between plaque and microglia activation.

In order to determine glial activation associated with plaques after drug treatment, the representative fluorescent images ($n = 34-56$) are captured (Figure 3E). The immunointensity (IR) ratio of Iba-1 to AB10 (Figure 3F) and GFAP to AB10 (Figure 3G) of the captured images are calculated by ImageJ software. The results showed that EK100 and antrodin C increase the IR ratio of Iba-1 to AB10 by 45.12% (2.63 ± 0.36 vs. 1.82 ± 0.20 , $p < 0.05$, $n = 46$ vs. 54) and 59.45% (2.89 ± 0.39 vs. 1.82 ± 0.20 , $p < 0.01$, $n = 30$ vs. 54). On the other hand, EK100 and antrodin C did not change the IR ratio of GFAP to AB10. However, ergosterol decrease the IR ratio of GFAP to AB10 by 35% (2.35 ± 0.23 vs. 3.55 ± 0.29 , $p < 0.05$, $n = 53$).

2.6. EK100 and Antrodin C Reduce Non-Clustered Activation of Glia in the Hippocampus of APP/PS1 Mice

Previously, we found that compared with wild-type mice, APP/PS1 mice had a higher degree of astrocyte reactivity and microglia activation in areas unrelated to plaque [29]. Therefore, the immunoreactivity of the non-clustered glial cells in the hippocampus of each group was compared (Figure 5). The results show that compared with wild-type mice, APP/PS1 mice have a higher degree of glial non-cluster activation. Compared with vehicle-treated mice, EK100 and ibuprofen treatment reduced the IR of non-clustered astrocytes (NCA) in the hippocampal CA1 by 46.7% (9.49 ± 0.42 vs. 17.80 ± 1.98 , $p < 0.01$, $n = 5$ vs. 6) and 47.8% (9.30 ± 0.50 vs. 17.80 ± 1.98 , $p < 0.05$, $n = 5$ vs. 6), respectively (Figure 5A,B). In contrast, antrodin C and ergosterol did not show a significant effect on the IR of NCA in the hippocampus. On the other hand, EK100, antrodin C and ibuprofen treatment reduced the IR of non-clustered microglia (NCM) in hippocampal CA1 by 50.7% (5.87 ± 0.61 vs. 11.90 ± 1.03 , $p < 0.001$, $n = 5$ vs. 6), $54.7 \pm 9.7\%$ (5.14 ± 0.67 vs. 11.90 ± 1.03 , $p < 0.001$, $n = 5$ vs. 6) and 38.1% (7.37 ± 1.37 vs. 11.90 ± 1.03 , $p < 0.05$, $n = 5$ vs. 6), respectively (Figure 5B). In contrast, ergosterol did not show a significant effect on the IR of NCM in the hippocampus. The similar changes were found in CA3 and DG areas.

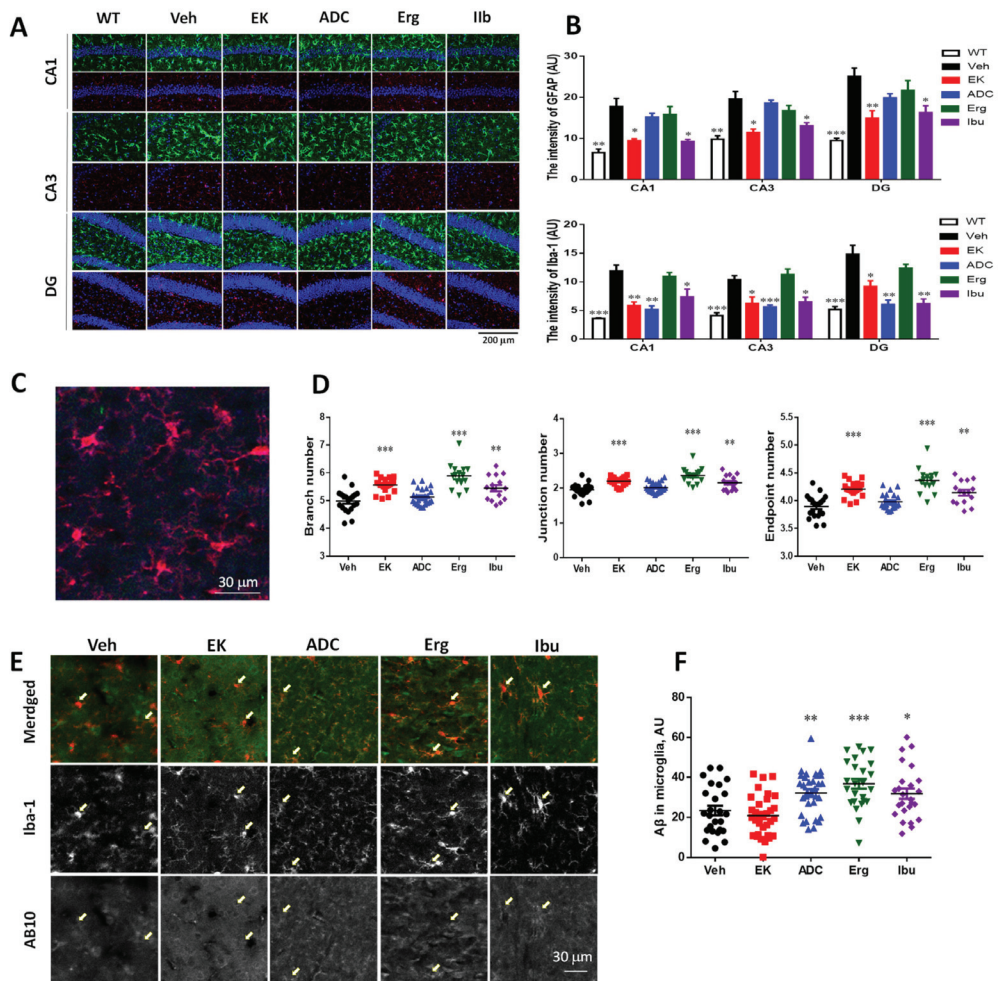


Figure 5. EK100 reduce non-clustered glial activation in APP/PS1 mice. APP/PS1 transgenic mice orally administered vehicle (Veh) or EK100 (EK), antrodin C (ADC), ergosterol (Erg), and ibuprofen (Ibu) ($30 \text{ mg}\cdot\text{kg}^{-1}\cdot\text{day}^{-1}$, each $n = 6$) for 1 month, and then astrocytes and microglia were immunostained with GFAP and Iba-1 antibodies, respectively. (A,B) The representative immunostaining images of GFAP (green) and Iba-1 (red) without being associated with plaque in Cornu Amonis (CA)1, CA3, dentate gurus (DG) are shown in (A). The image in wild-type (WT) mice ($n = 6$) is also compared. Scale bar: $200 \mu\text{m}$. The level of GFAP and Iba-1 in the CA1, CA3, and DG are calculated by MetaMorph image analysis software and shown in (B). The results are the mean \pm S.E.M. Significant differences between the Veh group and the other groups are indicated by *, $p < 0.05$; **, $p < 0.01$; ***, $p < 0.001$. (C,D). The representative image of Iba-1 (red) not associated with plaque is shown in (C). The branch number, junction number, and end point number of Iba-1 immunostained microglia are calculated by FIJI ImageJ software. The results are the mean \pm S.E.M. Significant differences between the Veh group and the other groups are indicated by **, $p < 0.01$; ***, $p < 0.001$. (E,F). The representative immunostaining images of Iba-1 (red) and A β not associated with plaque in the cortex are shown in (E). Arrows indicate the representative microglia. The intracellular A β in microglia are calculated by MetaMorph image analysis software and shown in (F). The results are the mean \pm S.E.M. Significant differences between the Veh group and the other groups are indicated by *, $p < 0.05$; **, $p < 0.01$; ***, $p < 0.001$.

Microglia have different morphological responses to changes in brain physiology, from hyper-ramified form to amoeba form [35]. Since microglia fine-tune the function of neurons and glial through cell-to-cell crosstalk [36], the morphology of microglia can be used as an indicator of a variety of cell functions and dysfunctions in the brain. The skeletal analysis was used for regional analysis of multiple microglia in the region of interest. The results shown that EK100, ergosterol, and ibuprofen increase the number of branches, junctions, and endpoints of microglia (Figure 5C,D). EK100, ergosterol, and ibuprofen treatment increased the branch number of microglia by 11.6% (5.56 ± 0.06 vs. 4.98 ± 0.09 , $p < 0.0001$, $n = 20$), 18.3% ($5.89 \pm 0.12 \pm 0.06$ vs. 4.98 ± 0.09 , $p < 0.0001$, $n = 25$ vs. 20), and 9.4% (5.45 ± 0.11 vs. 4.98 ± 0.09 , $p < 0.0001$, $n = 25$ vs. 20), respectively. The similar changes were found in the intersection number and endpoint number of microglia.

Next, the combined immunostaining of Iba-1 and AB10 was used to check the microglia phagocytosis of A β . The results showed that antrodin C, ergosterol, and ibuprofen, significantly increased the accumulation of A β in microglia by 37.4% (32.18 ± 1.85 vs. 23.42 ± 2.41 , $p < 0.01$, $n = 32$ vs. 25), 57.0% (36.76 ± 2.45 vs. 23.42 ± 2.41 , $p < 0.001$, $n = 25$), and 40.1% (31.82 ± 2.60 vs. 23.42 ± 2.41 , $p < 0.05$, $n = 25$) (Figure 5E,F). On the contrary, EK100 did not alter the accumulation of A β in microglia.

2.7. EK100 and Antrodin C Eliminated Nrf2 Overexpression in the Brain of APP/PS1 Mice

Nrf2 regulates the expression of phase II detoxification enzymes (including HO-1 and NQO-1) as well as antioxidant genes that protect cells from various damages through anti-inflammatory effects, thereby affecting the progression of the disease [37]. Therefore, the expression of HO-1 was detected. Compared with wild-type mice, APP/PS1 mice have increased HO-1 expression (Figure 6A). However, antrodin C and ergosterol significantly promoted the increase of HO-1 expression by 24.3% (0.92 ± 0.04 vs. 0.74 ± 0.03 , $p < 0.001$, $n = 57$ vs. 66) and 24.3% (0.92 ± 0.04 vs. 0.74 ± 0.03 , $p < 0.001$, $n = 64$ vs. 66), respectively (Figure 6B,C). In contrast, EK100 and ibuprofen significantly reduced the expression of HO-1 compared to vehicle therapy by 21.7% (0.58 ± 0.03 vs. 0.74 ± 0.03 , $p < 0.001$, $n = 71$ vs. 66) and 12.2% (0.65 ± 0.03 vs. 0.74 ± 0.03 , $p < 0.01$, $n = 62$ vs. 66), respectively. Both HO-1 and NQO-1 are mainly expressed in microglia and overexpressed in the PAM of APP/PS1 mice (Figure 6A). Antrodin C, ergosterol, and ibuprofen significantly promote the increase of NQO-1 expression by 50% (0.93 ± 0.04 vs. 0.62 ± 0.03 , $p < 0.0001$, $n = 45$ vs. 57), 116% (1.34 ± 0.06 vs. 0.62 ± 0.03 , $p < 0.0001$, $n = 64$ vs. 57), and 53.2% (0.95 ± 0.03 vs. 0.62 ± 0.03 , $p < 0.0001$, $n = 53$ vs. 57), respectively (Figure 6B,C). In contrast, EK100 had no effect on NQO-1 expression compared with vehicle treatment.

Next, we examined the expression of Nrf2 in 6-month-old APP/PS1 mice. We found that APP/PS1 mice have increased Nrf2 expression compared to wild-type mice (Figure 6D,E), and treatment of mice with EK100, antrodin C, and ibuprofen significantly reduced Nrf2 expression by 63.9% (143.4 ± 30.43 vs. 396.8 ± 34.80 , $p < 0.001$, $n = 5$ vs. 6), 73.0% (107.2 ± 11.39 vs. 396.8 ± 34.80 , $p < 0.001$, $n = 5$ vs. 6), and 55% (178.5 ± 14.53 vs. 396.8 ± 34.80 , $p < 0.01$, $n = 5$ vs. 6), respectively. Overexpressed Nrf2 is distributed throughout the brain, but it is not specifically expressed in microglia. We found that compared with wild-type mice, the expression of Nrf2 in neurons of APP/PS1 mice was significantly enhanced by 178.6% ($143,362 \pm 26,766$ vs. $51,447 \pm 7022$, $p < 0.01$, $n = 14$ vs. 10) (Figure 6F,G). After the administration of EK100 and antrodin C, the overexpression of Nrf2 in neurons were decreased by 54.2% ($65,729 \pm 7769$ vs. $143,362 \pm 26,766$, $p < 0.05$, $n = 10$ vs. 14) and 48.2% ($74,224 \pm 9136$ vs. $143,362 \pm 26,766$, $p < 0.05$, $n = 10$ vs. 1), respectively. In contrast, EK100 and antrodin C did not affect the A β content in neurons.

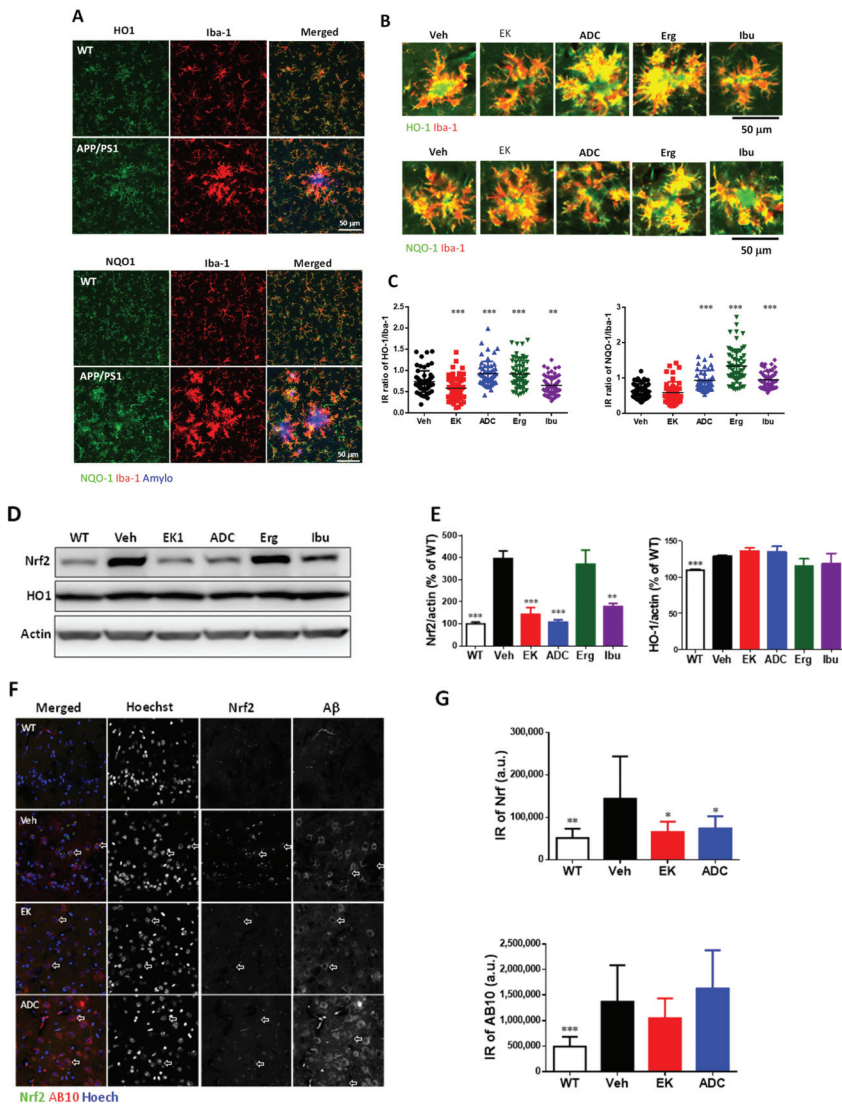


Figure 6. Antrodin C, but not EK100, promotes HO-1 in APP/PS1 mice. (A–E). APP/PS1 transgenic mice orally administered vehicle (Veh) or EK100 (EK), antrodin C (ADC), ergosterol (Erg), and ibuprofen (Ibu) ($30 \text{ mg}\cdot\text{kg}^{-1}\cdot\text{day}^{-1}$, each $n = 6$) for 1 month. The representative images of HO-1 (green in upper panel) and Iba-1 (red) in Iba-1⁺ microglia (red) of WT mice and APP/PS1 transgenic mice are shown in (A). Amyloid plaques were stained with Amylo-Glo (blue). Scale bar: 50 μm . The representative images of HO-1 (green in upper panel) and NQO1 (green in lower panel) in Iba-1⁺ microglia (red) of APP/PS1 transgenic mice are shown in (B). Immunointensity (IR) ratio of HO-1/Iba-1 and NQO-1/Iba-1 are calculated and shown in (C). Representative immunoblots of Nrf2 and HO-1 and β -actin of cortical homogenate are shown in (D). The protein level in wild-type (WT) mice ($n = 6$) is also compared. The ratio of Nrf2 and HO-1 to β -actin is presented as a percentage of the WT group (E). (F,G) APP/PS1 transgenic mice orally administered vehicle (Veh) or EK100 (EK) and antrodin C (ADC) ($30 \text{ mg}\cdot\text{kg}^{-1}\cdot\text{day}^{-1}$, each $n = 6$) for 1 months. The representative images of Nrf2 (green in merged panel) and AB10 (red in merged panel) in neurons of WT mice and APP/PS1 transgenic mice are shown in (F). Nuclei staining using Hoechst 33258 (blue). Scale bar: 20 μm . Immunointensity (IR) of Nrf2 and AB10 were calculated and shown in (G). The results are the mean \pm S.E.M. Significant differences between the Veh group and the other groups are indicated by *, $p < 0.05$; **, $p < 0.01$; ***, $p < 0.001$.

2.8. EK100 Promote Hippocampal Neurogenesis and Dendritic Complexity in the Brain of APP/PS1 Mice

Compared with wild-type mice, the number of BrdU-positive proliferating type 2 progenitor cells and DCX-positive neonatal granule neurons in the subgranular zone (SGZ) of APP/PS1 mice were decreased by 51.3% (6.02 ± 0.74 vs. 12.36 ± 1.08 , $p < 0.001$, $n = 9$ vs. 8) and 34.1% (20.76 ± 1.11 vs. 31.48 ± 2.03 , $p < 0.001$, $n = 9$), respectively, and EK100 restored these decreases by 67.8% (10.10 ± 0.51 vs. 6.02 ± 0.74 , $p < 0.001$, $n = 10$ vs. 9) and 38.9% (28.83 ± 2.41 vs. 20.76 ± 1.11 , $p < 0.001$, $n = 8$ vs. 10) (Figure 7A–D). The number of BrdU- and DCX-double positive neurons was also decreased by 73.8% (3.20 ± 0.48 vs. 8.83 ± 1.01 , $p < 0.001$, $n = 8$ vs. 9), and EK100 restored these decreases by (6.54 \pm 0.55 vs. 3.20 \pm 0.48, $p < 0.001$, $n = 10$ vs. 8).

Since dendritic growth is important for neuron integration in neurogenesis, we further analyzed the dendritic complexity of DCX-positive cells through laminar flow quantitative methods [38]. We found that the vehicle-treated transgenic mice had lower levels of secondary dendritic branches compared to wild-type mice (1.34 ± 0.05 vs. 1.66 ± 0.10 , $p < 0.01$, $n = 10$ vs. 9). EK100 significantly increased the dendritic complexity of secondary dendritic branches by 40.3% (1.88 ± 0.14 vs. 1.34 ± 0.05 , $p < 0.01$, $n = 9$ vs. 10) (Figure 7E,F).

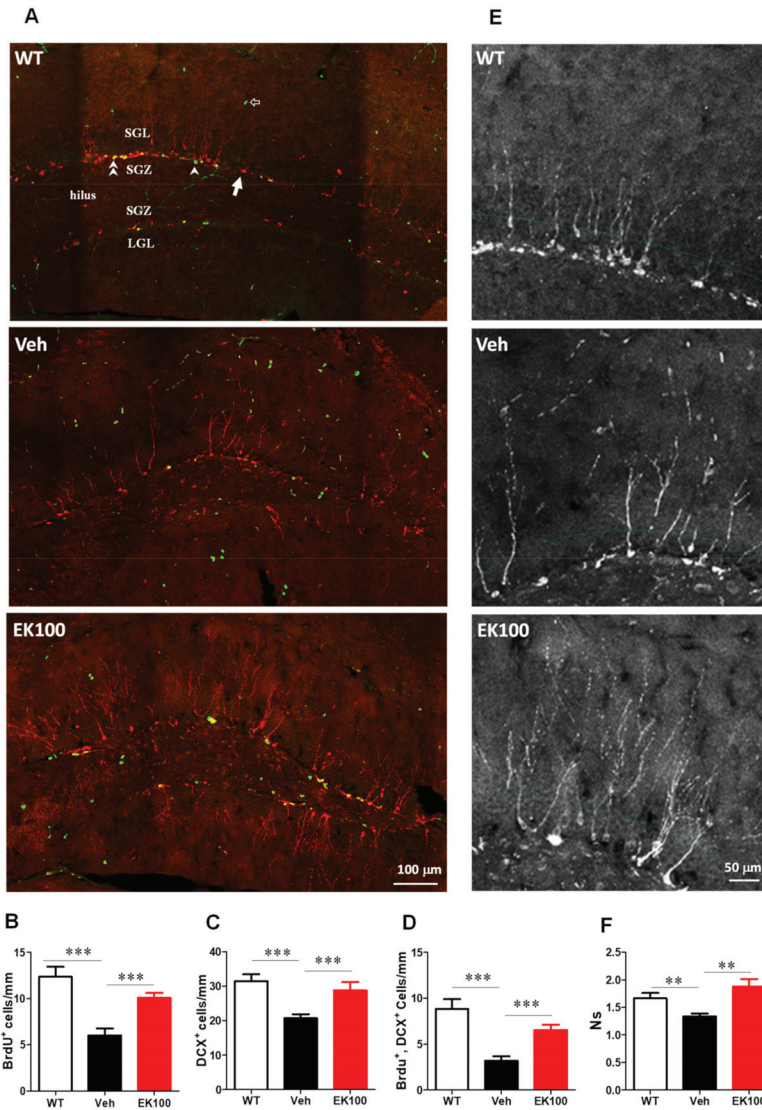


Figure 7. EK100 promotes hippocampal neurogenesis in APP/PS1 mice. APP/PS1 transgenic mice orally administered with vehicle (Veh) or EK100 ($30 \text{ mg} \cdot \text{kg}^{-1} \cdot \text{day}^{-1}$, $n = 6$ each) for 1 month. Wild-type (WT) mice were used as non-transgenic control. Hippocampal neurogenesis was detected by immunohistochemical staining with doublecortin antibody (DCX, red) and BrdU antibody (green). The representative images of the dentate gyrus are shown in (A). Arrow indicated DCX-labeled newly born neuron; arrow head indicates proliferating type 2 neuroprogenitor; double arrow head indicates the newly born neuron immediately after proliferation; hollow arrow indicates proliferating cells other than the neuroprogenitor. ML, molecular layer; UGL, upper blade granular cell layer; SGZ, subgranular zone; LGL, lower blade granular cell layer. Scale bar: 100 μm . Panels B–D show the number/mm SGZ of BrdU positive cells (BrdU⁺, B); DCX-positive cell (DCX⁺, C) and the cells with double labeling (BrdU⁺, DCX⁺, D). (E) The representative immunostaining images of the upper blade dentate gyrus area are shown. Scale bar: 50 μm . Secondary dendrites of the DCX⁺ cells are counted along the middle of granular cell layer (GCL, green dashed line). (F) The dendritic complexity was analyzed by laminar quantification. The branch ratio of secondary dendrites of DCX⁺ cells were shown. Dendrites of DCX⁺ cells are counted along the middle of the GCL. The results are the mean \pm S.E.M. Significant differences between the Veh group and the other groups. **, $p < 0.01$; ***, $p < 0.001$.

3. Discussion

This study shows that two anti-inflammatory compounds, EK100 and antrodin C, selected from components isolated from *A. cinnamomea* mycelium, can reduce AD-like pathological changes in APP/PS1 mice in different ways when administered orally. BV2 cells activated by LPS were used to determine the anti-inflammatory effects of components isolated from *A. cinnamomea* mycelium (including CA-Et, anticin K, eburicoic acid, dehydroeburicoic acid, sulfurenic acid, dehydrosulfurenic acid, EK100, antrodin C, and ergosterol), and ibuprofen (an NSAID control). The results showed that the production of nitric oxide in BV2 cells activated by LPS was significantly inhibited by CA-Et, EK100, antrodin C, and ergosterol, but it was not affected by anticin K, eburicoic acid/dehydroeburicoic acid mixture, sulfurenic acid/dehydrosulfurenic acid mixture, and ibuprofen. Therefore, we examined the effects of EK100, antrodin C, ergosterol, and ibuprofen (an NSAID control) on the pathology of APP/PS1 transgenic mice, including changes in nesting behavior, plaque deposition, perivascular deposition, nerves glial activation, and the Nrf2/HO-1/NQO-1 signaling pathway. Moreover, the effect of EK100 on neurogenesis was also examined.

The results of the animal study are summarized in Table 2. In the behavior test, EK100, antrodin C, and ibuprofen, but not ergosterol, significantly improve the nesting ability of APP/PS1 mice. Among the effects related to A β deposition, EK100 and antrodin C can effectively reduce the number and load of plaques, promote A β deposition around blood vessels, and reduce the accumulation of PAA and PAM. Among the changes in PAM activation, EK100 significantly increased the expression of Iba-1 but did not change the ratios of HO-1/Iba-1 and NQO-1/Iba-1; ADC significantly increased Iba-1 and the HO-1/Iba-1 and NQO-1/Iba-1 ratios; ergosterol significantly increased the ratios of HO-1/Iba-1 and NQO-1/Iba-1 but did not increase the expression of Iba-1; and ibuprofen significantly increased the NQO-1/Iba-1 ratio and reduced the HO-1/Iba-1 ratio without increasing the expression of Iba-1. There are no compounds that can modulate the expression of GFAP in PAA. In the activation of non-plaque-associated glial cells, EK100, antrodin C, and ibuprofen significantly increased the expression of Iba-1 in NCM, while antrodin C, ergosterol, and ibuprofen significantly increased the intracellular accumulation of A β in NCM. On the other hand, EK100, ergosterol, and ibuprofen significantly increased the ramification of NCM, while EK100 and ibuprofen can significantly reduce the expression of GFAP in NCA. In the response of non-plaque-related neurons, EK100, antrodin C, and ibuprofen significantly reduced the expression of Nrf2 in cortical neurons. Finally, EK100 has also been shown to significantly promote hippocampal neurogenesis.

In order to verify the effects of the four compounds on behavioral disorders in APP/PS1 mice, we focused on species-specific nesting activities, because it is multi-brain-dependent spontaneous [30], which has been considered similar to ADL skills [31]. Clinically, ADL disorder is a pathological manifestation of AD [32], and this pathological manifestation also appears in APP/PS1 mice [29]. In this study, we found that EK100, antrodin C, and ibuprofen can alleviate the defects of nesting behavior. These results indicate that the administration of EK100, antrodin C, and ibuprofen may have the potential to restore multiple brain injury in APP/PS1 mice.

Then, we studied the effects of four compounds on amyloid plaque deposition and A β perivascular deposition. EK100 and antrodin C reduced the number of plaques but did not reduce the levels of A β in the hippocampus and serum, indicating that the reduction in the number of plaques was not due to the inhibition of A β production. The use of SH-SY5Y-APP695 cells also confirmed the ineffective inhibition of A β accumulation by EK100 and antrodin C. Therefore, the effect of EK100 and antrodin C on reducing the number of plaques can be attributed to the removal of A β rather than the formation of A β .

Table 2. The effects of four compounds in APP/PS1 mice.

	EK100	ADC	Erg	Ibu	WT
Pathological improvement					
1. Nesting behavior:					
Nesting score	↑	↑	–	↑	↑
Unthreaded nestlet	↓	↓	–	↓	↓
2. A β deposition:					
Plaque number	↓	↓	–	–	ND
Plaque burden	↓	↓	–	↑	ND
Putative A β clearance pathways and neuroprotective effects					
1. Perivascular pathway					
Perivascular A β	↑	↑	–	–	ND
2. PAM/PAA pathway					
Iba-1 ⁺ cluster number	↓	↓	–	–	ND
Iba-1 IR in cluster	↑	↑	–	–	ND
GFAP ⁺ cluster number	↓	↓	–	–	ND
GFAP IR in cluster	–	–	↓	–	ND
HO-1/Iba-1 IR ratio	↓	↑	↑	↓	ND
NQO-1/Iba-1 IR ratio	–	↑	↑	↑	ND
3. NCM/NCA pathway					
Iba-1 IR in HNCM	↓	↓	–	↓	↓
A β IR in HNCM	–	↑	↑	↑	ND
Microglia ramification	↑	–	↑	↑	ND
GFAP IR in HNCA	↓	–	–	↓	↓
4. Neuron protection					
Total Nrf2	↓	↓	–	↓	↓
Neuronal Nrf2	↓	↓	ND	ND	↓
Neurogenesis	↑	ND	ND	ND	↑

ADC, antrodin C; erg, ergosterol; Ibu, Ibuprofen; WT, wild-type mice; A β , amyloid β ; Iba-1, ionized calcium-binding adaptor molecules; GFAP, glial fibrillary acidic protein; PAM, plaque-associated microglia; PAA, plaque-associated astrocytes; HO-1, heme oxygenase-1; NQO-1, NAD(P)H quinone dehydrogenase 1; IR, immunoreactivity; NCM, non-clustered microglia; NCA, non-clustered astrocytes; Nrf2, nuclear factor erythroid-2 related factor 2; ↑, increased; ↓, decreased; –, no effect; ND, not determined.

Recent evidence suggests that impaired clearance may be the driving force behind sporadic AD [39]. Microglia may promote A β clearance through phagocytosis [40]. Although it is obvious that astrocytes and microglia accumulate around amyloid plaques in AD, it is still elusive whether they are mainly attracted by amyloid deposits or only by the plaque-related damaged neurite response [41]. Microglia activation is highly correlated with the accumulation of A β , because activated microglia are found to surround the plaque. Therefore, A β can be cleared by phagocytosis or proteolytic degradation [42]. Studies have shown that limiting the accumulation and phagocytosis of microglia will increase A β deposition, thus highlighting the functional impact of phagocytosis [43].

It is worth noting that EK100, antrodin C, and ibuprofen can effectively improve nesting behavior and inhibiting NCM activation, indicating that these two events are related in APP/PS1 mice. Microglia exhibit a variety of phenotypic states, from pro-inflammatory M1 phenotype to the alternative activation M2 phenotype, especially under chronic inflammatory conditions [44]. In vitro evidence suggests that the phagocytic ability of microglia is inhibited in AD [45]. The activity of M1-like reactive microglia induced by LPS in A β phagocytosis is significantly reduced, and this reduction can be rescued by IL-4 induced activation of M2-like microglia [45]. This phenomenon leads to the hypothesis that the accumulation of A β in AD may be due to changes in the phenotype of microglia. Therefore, the regulation of M2-like reactive microglia by microglia may have potential benefits in the treatment of AD.

Nrf2 is overexpressed in the cerebral cortex neurons of APP/PS1 mice, indicating that the overexpression of Nrf2 may be related to the antioxidant pathway of Nrf2 in neurons, but it has nothing to do with microglia. The overexpression of Nrf2 can be down-regulated by EK100, antrodin C, and ibuprofen, indicating that the overexpression of Nrf2 may be

a feedback effect to protect neurons after the presence of A β . The treatment of EK100, antrodin C, and ibuprofen may overcome the toxicity mediated by A β . Therefore, the feedback effect of Nrf2 can be avoided.

The Nrf2/HO-1/NQO-1 pathway in microglia can regulate the inflammatory function of microglia and inhibit A β accumulation through phagocytosis [46]. The oxidation and anti-oxidation mechanisms are usually balanced by certain known elements, such as Nrf2 and HO-1. The overproduction of reactive oxygen species (ROS) and/or inhibition of antioxidant defense mechanisms may become harmful, which is called oxidative stress [47]. Previous studies reported that despite the presence of oxidative stress, the expression of nuclear Nrf2 in the brains of human AD patients is reduced [48]. However, other studies have shown that the expression of Nrf2 target genes in AD brain is increased. Previous studies have shown that Nrf2 transcripts are significantly reduced in 3-month-old APP/PS1 mice but not found in 6-month-old mice [49]. Fragoulis et al. demonstrated that in the AD mouse model, the administration of methysticin activates the Nrf2 pathway and reduces neuroinflammation, hippocampal oxidative damage, and memory loss [50]. Tanji et al. demonstrated that the expression level of HO-1 in the temporal cortex of AD patients is increased compared with the control group [51]. Other studies have reported increased NQO1 activity and immunoreactivity in the brains of AD patients associated with AD pathology [52]. A reasonable explanation for the differences in these reports is that Nrf2 levels may change during disease progression based on the degree of ROS production. It is now accepted that Nrf2 is up-regulated in the early stages of AD by A β -induced ROS but starts to decrease as the disease progresses [53]. Kanninen et al. used APP/PS1 mice to prove that Nrf2 expression decreases in the later stage [54]. Although the underlying mechanism has not been elucidated, the damage of the Nrf2 pathway may be related to the progression of the disease. Yammzaki et al. found that the expression of Nrf2 increased in APP/PS1 mice [55]. This may be mediated by the A β -mediated phosphorylation of P62, which interacts with Kelch-like ECH-associated protein 1 (Keap1). In addition, cell type-specific Nrf2 expression should be checked [56].

A β clearance can be mediated by microglia. In addition, A β can also be cleared through vascular access [57], the glymphatic system [58], and IPAD [59]. IPAD failure can lead to cerebral amyloid angiopathy (CAA), where A β mainly accumulates in capillaries and arterial smooth muscle cells BM [4]. Therefore, the perivascular deposition of A β was determined. The results showed that EK100 and antrodin C significantly increased the perivascular deposition of A β , indicating that EK100 and antrodin C reduced plaque deposition by promoting the clearance of A β through the perivascular pathway. However, partial failure of these clearance pathways can increase perivascular deposits.

It has been found that antrodin C has anti-inflammatory effects in RAW264.7 macrophages activated by LPS [20] and can effectively interfere with hyperglycemia-induced senescence and apoptosis by activating the HO-1/NQO-1-dependent cellular antioxidant defense system [21]. In our current study, the promotion of HO-1/NQO-1-dependent cellular antioxidant defense was detected in the treatment of antrodin C and ergosterol, but it was not detected during the treatment of EK-100 and ibuprofen. This may help antrodin C to reduce A β burden more than EK100.

EK100 also has anti-inflammatory effects [17] and has been studied to improve ischemic stroke [18]. In our current study, EK100 did not show cellular antioxidant defense that depends on HO-1/NQO-1. Indomethacin was used as a positive control to evaluate the analgesic activity of EK100 in vitro [60]. Our current study uses ibuprofen as an NSAID control and found that EK100 has a similar effect on NCA activation as ibuprofen, which means that the NSAID activity of ibuprofen and EK100 can increase the activation of NCA. In previous studies, it has been found that EK100 and its isomer ergosterol can inhibit LPS-mediated macrophage activation [17]. In our current study, we also found that both of these compounds can inhibit LPS-mediated BV2 microglia activation. However, EK100 (instead of ergosterol) inhibits the activation of non-clustered and clustered microglia,

indicating that A β -mediated activation of microglia is specifically inhibited by EK100 but not affected by ergosterol.

It is speculated that both soluble A β and A β plaques can cause neuroinflammation and subsequent damage to the hippocampal nerves, which then leads to behavioral defects. EK100 can effectively remove plaque, reduce neuroinflammation, increase neurogenesis, and improve behavioral defects. According to this interference, antrodin C may also have the ability to promote neurogenesis.

In this study, we revealed four compounds with anti-inflammatory activity, two of which are structurally similar and exhibit different effects on AD-related pathological changes (including brain A β clearance). However, we cannot determine the precise target of these effects by using APP/PS1 mice as an animal model. In addition, the structure-activity relationship between EK100 and ergosterol and between antrodin C and ibuprofen has not been resolved. The ultimate goal of this study is to reveal the A β clearance promoting activity and the structure-activity relationship of these compounds. The biggest challenge in the future is that we need more technologies and research models, including cell and animal models, to achieve this goal.

4. Materials and Methods

4.1. Reagents

5-Bromo-2'-deoxyuridine (BrdU), formic acid, ergosterol, and ibuprofen were purchased from Sigma-Aldrich (St Louis, MO, USA). General chemicals were purchased from Sigma-Aldrich (St Louis, MO, USA) or Merck (Darmstadt, Germany).

4.2. Extraction, Isolation, Purification, and Structure Determination of Compounds in *A. cinnamomea*

Freeze-dried powder of *A. cinnamomea* of the submerged whole broth (Batch No. MZ-247) was provided by the Biotechnology Center of Grape King Inc., Chung-Li City, Taiwan, Republic of China. The purification procedure of EK100 from *A. cinnamomea* was described previously [61]. In brief, freeze-dried powder of *A. cinnamomea* of the submerged whole broth was extracted three times with methanol at room temperature. The methanol extract was evaporated in vacuum to give a brown residue, which was suspended in H₂O and then partitioned with 1 L of ethyl acetate. The ethyl acetate fraction was chromatographed on silica gel using mixtures of hexane and ethyl acetate of increasing polarity as eluents and further purified with high-performance liquid chromatography (HPLC). Twelve components were identified. EK100 was eluted with 10% ethyl acetate in hexane. The structure of EK100 was elucidated by mass and nuclear magnetic resonance (NMR) spectral data.

The purification procedure of antrodin C from *A. cinnamomea* mycelia was described previously [17]. In brief, the dried and ground mycelium of *A. cinnamomea* was extracted with 95% ethanol. Then, the 95% ethanol extract was concentrated under reduced pressure. The residues are suspended in H₂O and partitioned with *n*-hexane and then ethyl acetate. The ethyl acetate fraction was sequentially chromatographed on silica gel and Sephadex LH-20 columns to obtain antrodin C. The structure of antrodin C was elucidated by mass and NMR spectral data.

The purification procedure of anticin K, dehydroeburicoic acid, eburicoic acid, sulfurenic acid, and dehydrosulfurenic acid from *A. cinnamomea* mycelia was described previously [62]. In brief, dried *A. cinnamomea* fruiting bodies were extracted five times with methanol at 50 °C for 12 h and then concentrated under reduced pressure. The methanol extract was separated by silica gel flash column (70–230 mesh, 15 × 10 cm) with a gradient solvent system of CH₂Cl₂ 100% to methanol 100%, to provide 12 fractions (ACFB.1–ACFB.12). ACFB.3 was purified by preparative HPLC (Cosmosil 5C18-AR-II, 5 μ m, 250 × 20 mm i.d., acetonitrile/H₂O containing 0.1% formic acid, 35:65, flow rate 10 mL/min) to produce anticin K. ACFB.5 was purified by preparative HPLC (Cosmosil 5C18-AR-II, 5 μ m, 250 × 20 mm i.d., acetonitrile/H₂O containing 0.1% formic acid, 65:35,

flow rate 10 mL/min) to produce four subfractions (ACFB.5.1–ACFB.5.4). ACFB.5.2 was further purified by recycled preparative HPLC (Cosmosil 5C18-AR-II, 5 μ m, 250 \times 20 mm i.d., acetonitrile/H₂O containing 0.1% formic acid, 55:45, flow rate 10 mL/min, recycled 8 times) to produce dehydrosulfurenic acid. ACFB.6 was purified by preparative HPLC (Cosmosil 5C18-AR-II, 5 μ m, 250 \times 20 mm i.d., acetonitrile/H₂O containing 0.1% formic acid, 70:30, flow rate 10 mL/min) to produce two subfractions: ACFB.6.1 and ACFB.6.2. ACFB.9 was purified by preparative HPLC (Cosmosil 5C18-AR-II, 5 μ m, 250 \times 20 mm i.d., acetonitrile /H₂O containing 0.1% formic acid, 90:10, flow rate 10 mL/min) to produce dehydroeburicoic acid and eburicoic acid. The structure of the compounds used in this study is shown in Figure 1.

4.3. Cell Culture

BV2 cells, a cell line derived from primary mouse microglia cells, were maintained in Dulbecco's Modified Eagle's Medium (DMEM) supplemented with 10% fetal bovine serum (FBS), 100 U/mL penicillin, and 100 μ g/mL streptomycin. For treatment, the cell medium was replaced with DMEM containing 1% FBS.

4.4. Measurement of Nitric Oxide

For the assessment of the amount of nitric oxide production, the Griess reagent (0.05% *N*-(1-naphthyl)-ethylene-diamine dihydrochloride, 0.5% sulfanilamide, and 1.25% phosphoric acid) was employed. The accumulated nitrite, a stable breakdown product of nitric oxide, can be recorded. The optical density was detected at a wavelength of 540 nm using a microplate reader with NaNO₂ as standard.

4.5. Cell Viability Assay

The reduction of 3-[4,5-dimethylthiazol-2-yl]-2,5-diphenyl-tetrazolium bromide (MTT) was used to evaluate cell viability. Cells were incubated with 0.5 mg·mL⁻¹ MTT for 1 h. The formazan particles were dissolved with DMSO. OD_{600nm} was measured using an ELISA reader.

4.6. Animal Management and Administration

The Institutional Animal Care and Use Committee (IACUC) at the National Research Institution of Chinese Medicine approved the animal protocol (IACUC No: 106-417-4). All experimental procedures involving animals and their care were carried out in accordance with The Guide for the Care and Use of Laboratory Animals published by the United States National Institutes of Health. APP/PS1 was purchased from Jackson Laboratory (No. 005864). The breeding gender ratio was a male with two females in one cage. Experiments were conducted using wild-type siblings and APP/PS1 transgenic C57BL/6J mice. The animals were housed under controlled room temperature (24 \pm 1 $^{\circ}$ C) and humidity (55–65%) with a 12:12 h (07:00–19:00) light–dark cycle. All mice were provided with commercially available rodent normal chow diet and water *ad libitum*.

The dose of EK100 used for humans is typically 7380 mg per day. The mouse dose used was converted from a human-equivalent dose (HED) based on body surface area according to the US Food and Drug Administration formula. Assuming a human weight of 60 kg, the HED for 7380 (mg)/60 (kg) = 123 \times 12.3 = 10 mg/kg; the conversion coefficient of 12.3 is used to account for differences in body surface area between mice and human, as previously described [63]. To investigate the effect of EK100 in CNS, 3 doses (30 mg kg⁻¹ day⁻¹) were applied. EK100, ergosterol, antrodin C, and ibuprofen were dissolved in vehicle (10% Kolliphor EL, 5% ethanol, 85% dextrose solution (5% in water), pH 7.2) to get a final concentration of 3 mg/mL. For studying the therapeutic effect, thirty APP/PS1 mice (5 months of age) were randomly assigned to five groups (*n* = 6, half male and half female) and were administrated by gavage with vehicle, EK100, antrodin C, ergosterol, and ibuprofen (30 mg·kg⁻¹·day⁻¹) for one month. Ergosterol was used as EK100's structural control and ibuprofen was used as an NSAID control. Nesting task was

performed 30 days after drug administration. The animals were sacrificed on the 31st day after drug administration, and then, the A β -related pathological changes were inspected by immunohistochemistry and immunoblotting. For neurogenesis measurement, BrdU was injected intraperitoneally at 50 mg·kg⁻¹·day⁻¹ during the last 7 days.

4.7. Nesting Test

After oral gavage administration for 30 days, mice were assessed for a nesting test as described previously. In brief, two Nestlets (5 g) were placed into cage at 1 h before the dark cycle, and then, the nest score and the weight of unshredded Nestlets were determined after overnight. Nest construction was scored using a six-graded scale [64]. A score of 0 indicates undisturbed Nestlet; 1, Nestlet was disturbed, but nesting material has not been gathered to a nest site in the cage; 2, a flat nest; 3, a cup nest; 4, an incomplete dome and 5, a complete and enclosed dome.

4.8. Tissue Processing

Mice after being anesthetized were sacrificed by transcardial saline perfusion. The mouse brain was removed, and half of the brain was homogenized in homogenization buffer containing 20 mM Tris-HCl (pH 7.4), 320 mM sucrose, 2 mM ethylene diamine tetraacetic acid, 1 mM phenylmethylsulfonyl fluorid, 5 μ g·mL⁻¹ leupeptin, and 5 μ g·mL⁻¹ aprotinin. Another half brain was immersed in 4% formaldehyde overnight at 4 °C and cryoprotected. Then, brain tissue was sectioned into 30 μ m thick sections. Three slides spanning approximately bregma-1.58 to -1.82 in each brain were used for staining and analysis.

4.9. Amylo-Glo Staining

Staining for fibrillary amyloid was performed using Amylo-Glo as described by the manufacturer (Biosensis Inc., Thebarton, South Australia).

4.10. Immunohistochemistry

Immunohistochemistry was performed as described previously [29]. Briefly, sections were blocked in phosphate buffer saline (PBS) containing 1% bovine serum albumin, 3% normal donkey serum, and 0.3% Triton X-100 for 1 h. Then, they were incubated in PBS containing 1% bovine serum albumin, 1% normal donkey serum, 0.3% Triton X-100, and primary antibodies, including mouse monoclonal antibodies to A β 1-16 (AB10, Millipore, MAB5208), glial fibrillary acidic protein (GFAP, Millipore, MAB5804), heme oxygenase 1 (HO-1, Santa Cruz, sc-390991), NAD(P)H quinone dehydrogenase 1 (NQO-1, Santa Cruz, sc-376023), BrdU (Santa Cruz, sc-32323), goat polyclonal antibody to ionized calcium-binding adaptor molecule-1 (Iba-1) antibody (abcam, ab5076), and rabbit polyclonal antibody to anti-Nrf2 antibody (abcam, ab137550), and doublecortin (DCX, abcam, ab18723) overnight at 4 °C. Then, sections were incubated in antibody dilution buffer containing Hoechst33258 (Invitrogen, 2 μ g mL⁻¹), fluorescein isothiocyanate, rhodamine red X-conjugated donkey anti-mouse IgG, rhodamine red X-conjugated donkey anti-rabbit IgG, or Alexa Fluor 647-conjugated donkey anti-goat IgG (Jackson ImmunoResearch, 705-605-147) at room temperature for 2 h. After being washed with PBS containing 0.01% Triton X-100, sections were mounted with Aqua Poly/Mount (Polyscience Inc., Warrington, PA, USA) for microscopic analysis using a Zeiss LSM 780 confocal microscopy (Jena, Germany). Representative confocal images had 10 μ m depth with maximal projection. Quantification of amyloid plaque was performed using ImageJ (<http://imagej.nih.gov/ij/>, accessed on 1 September 2021) software.

Amyloid plaque, astrocytes, and microglia were co-immunostained using anti-A β 1-16 antibody (AB10), anti-GFAP antibody, and anti-Iba-1 antibody, respectively. On amyloid plaque staining, we observed a wide range of plaque size distribution from 2 to 219 pixels using MetaMorph software. To exclude the non-specific staining and the over-size plaque, the plaques with a size range of 11 to 80 pixels were included for observation.

For determining perivascular A β deposition, after merging the images of the GFAP and A β channels into one, the perivascular A β deposition was determined by calculating the positive pixels present in the GFAP vascular mask in the image.

Activated glia is a prominent feature of AD neuropathology, with both reactive astrocytes and activated microglia clustering around amyloid plaques [41]. Therefore, the number of clusters with plaque-associated astrocytes (PAA) and plaque-associated microglia (PAM) were determined by staining with GFAP-antibody and Iba-1-antibody, respectively. The reduced number of clusters with PAM may be related to the reduced number of plaques. To verify the relationship of cluster size with plaque size, the size alteration of the individual plaque-associated microglia cluster was analyzed by scatter plot.

4.11. Skeleton Analysis

The number of branches, junctions, and endpoints of microglia were quantified using FIJI ImageJ software [32]. Briefly, the images of brain sections were transformed to 8-bit format, and the Unsharp Mask and Despeckle were applied to increase contrast and remove noise; then, the images were skeletonized and analyzed using the plug-in AnalyzeSkeleton (2D/3D).

4.12. Quantification of AB10-Stained Plaques

The quantification of AB10-stained plaques was conducted. At least 3 coronal brain sections from each mouse were used for analysis. Each image was adjusted to the threshold for pixel detection (threshold setting for AB10-positive signal is 200). To eliminate background, particle large than 80 pixels (approximately 56 μm^2) less than 20 pixels (approximately 14 μm^2) was excluded.

4.13. Measurement of A β Levels

Two-step sequential extraction of the brain A β using 2% sodium dodecyl sulfate (SDS) and 70% formic acid (FA; Sigma) was processed as described previously [30]. Briefly, cortical homogenate was mixed with an equal volume of 4% SDS in homogenization buffer containing protease inhibitor. Then, the sample was sonicated and centrifuged at $100,000 \times g$ for 60 min at 4 °C. The supernatant was considered an SDS-soluble fraction. The SDS-insoluble pellet was further suspended in 70% FA and centrifuged at $100,000 \times g$ for 60 min at 4 °C. The supernatant was collected and neutralized with 1 M Tris, pH 11. SDS-soluble and SDS-insoluble fractions were stored at -80 °C until sandwich enzyme-linked immunosorbent assay (ELISA) analysis. A β level was measured by a sensitive sandwich ELISA assay using a kit (Invitrogen KHB3481 and KHB3442). The detailed experiments were performed according to the manufacturer's protocol.

4.14. Statistical Analysis

Results are expressed as mean \pm standard error of the mean (S.E.M) and processed for statistical analysis using GraphPad Prism 6 software (La Jolla, CA92037 USA). The parametric data were analyzed by unpaired two-tailed Student's t test or one way analysis of variance (ANOVA) with post hoc multiple comparisons with a Bonferroni test.

5. Conclusions

Our in vitro experiments have shown that EK100, antrodin C, and ergosterol have anti-inflammatory activity by detecting the production of nitric oxide. Ibuprofen is an NSAID that can specifically block the COX-2 enzyme. On the other hand, our in vivo experiments show that EK100 and antrodin C reduce the formation of amyloid plaques in the cortex and hippocampus, which may be due to the glial phagocytosis and perivascular granule pathways in APP/PS1 mice to promote A β clearance. We also showed that EK100 and antrodin C ameliorated behavioral deficits in APP/PS1 mice. EK100 also promotes hippocampal neurogenesis. These findings raise the possibility that EK100 and antrodin C may have the potential to treat AD.

Supplementary Materials: The following are available online at <https://www.mdpi.com/article/10.3390/ijms221910413/s1>.

Author Contributions: C.-S.C., C.-C.L. and C.-W.C. performed the experiments and data analysis, and participated in the drafted manuscript, Y.-H.K. and Y.-P.C. participated in the ferment of *A. cinnamonmea* mycelia. H.-J.T. and C.-C.C. performed the isolation and component identification of *A. cinnamonmea* mycelia. H.-K.L. and Y.-J.S. participated in its design and coordination and helped to draft the manuscript. All authors have read and agreed to the published version of the manuscript.

Funding: The collection, analysis, interpretation of data, and manuscript writing of this study was supported by the Ministry of Science and Technology (MOST 106-2320-B-077-001-MY3).

Institutional Review Board Statement: The Institutional Animal Care and Use Committee (IACUC) at the National Research Institution of Chinese Medicine approved the animal protocol (IACUC No: 106-417-4). All experimental procedures involving animal and their care were carried out in accordance with Guide for the Care and Use of Laboratory Animals published by the United States National Institutes of Health.

Informed Consent Statement: Not applicable.

Acknowledgments: This work was financially supported by the Chinese Medicine Research Center, China Medical University from The Featured Areas Research Center Program within the framework of the Higher Education Sprout Project by the Ministry of Education (MOE) in Taiwan (CMRC-CHM-4); and from the China Medical University grant in Taiwan (CMU108-Z-08); Biotechnology Center, Grape King Bio Ltd. Chung-Li, Taoyuan 320, Taiwan, R.O.C.

Conflicts of Interest: The authors declare no conflict of interest.

References

1. Santos, L.E.; Beckman, D.; Ferreira, S.T. Microglial dysfunction connects depression and Alzheimer's disease. *Brain Behav. Immun.* **2016**, *55*, 151–165. [CrossRef]
2. Van Veluw, S.J.; Hou, S.S.; Calvo-Rodriguez, M.; Arbel-Ornath, M.; Snyder, A.C.; Frosch, M.P.; Greenberg, S.M.; Bacskai, B.J. Vasomotion as a Driving Force for Paravascular Clearance in the Awake Mouse Brain. *Neuron* **2020**, *105*, 549–561. [CrossRef]
3. Bakker, E.N.; Bacskai, B.J.; Arbel-Ornath, M.; Aldea, R.; Bedussi, B.; Morris, A.W.; Weller, R.O.; Carare, R.O. Lymphatic Clearance of the Brain: Perivascular, Paravascular and Significance for Neurodegenerative Diseases. *Cell. Mol. Neurobiol.* **2016**, *36*, 181–194. [CrossRef]
4. Attems, J.; Yamaguchi, H.; Saïdo, T.C.; Thal, D.R. Capillary CAA and perivascular A β -deposition: Two distinct features of Alzheimer's disease pathology. *J. Neurol. Sci.* **2010**, *299*, 155–162. [CrossRef] [PubMed]
5. Vignon, A.; Salvador-Prince, L.; Lehmann, S.; Perrier, V.; Torrent, J. Deconstructing Alzheimer's Disease: How to Bridge the Gap between Experimental Models and the Human Pathology? *Int. J. Mol. Sci.* **2021**, *22*, 8769. [CrossRef] [PubMed]
6. Muntsant, A.; Giménez-Llort, L. Genotype Load Modulates Amyloid Burden and Anxiety-Like Patterns in Male 3xTg-AD Survivors despite Similar Neuro-Immunoendocrine, Synaptic and Cognitive Impairments. *Biomedicines* **2021**, *9*, 715. [CrossRef]
7. Garad, M.; Edelmann, E.; Leßmann, V. Impairment of Spike-Timing-Dependent Plasticity at Schaffer Collateral-CA1 Synapses in Adult APP/PS1 Mice Depends on Proximity of A β Plaques. *Int. J. Mol. Sci.* **2021**, *22*, 1378. [CrossRef]
8. Muntsant, A.; Jiménez-Altayó, F.; Puertas-Umbert, L.; Jiménez-Xarrie, E.; Vila, E.; Giménez-Llort, L. Sex-Dependent End-of-Life Mental and Vascular Scenarios for Compensatory Mechanisms in Mice with Normal and AD-Neurodegenerative Aging. *Biomedicines* **2021**, *9*, 111. [CrossRef]
9. Dong, Y.; Li, X.; Cheng, J.; Hou, L. Drug Development for Alzheimer's Disease: Microglia Induced Neuroinflammation as a Target? *Int. J. Mol. Sci.* **2019**, *20*, 558. [CrossRef]
10. Tanaka, M.; Toldi, J.; Vécsei, L. Exploring the Etiological Links behind Neurodegenerative Diseases: Inflammatory Cytokines and Bioactive Kynurenines. *Int. J. Mol. Sci.* **2020**, *21*, 2431. [CrossRef]
11. Hickman, S.E.; Allison, E.K.; El Khoury, J. Microglial dysfunction and defective beta-amyloid clearance pathways in aging Alzheimer's disease mice. *J. Neurosci.* **2008**, *28*, 8354–8360. [CrossRef] [PubMed]
12. Melnikova, T.; Savonenko, A.; Wang, Q.; Liang, X.; Hand, T.; Wu, L.; Kaufmann, W.E.; Vehmas, A.; Andreasson, K.I. Cyclooxygenase-2 activity promotes cognitive deficits but not increased amyloid burden in a model of Alzheimer's disease in a sex-dimorphic pattern. *Neuroscience* **2006**, *141*, 1149–1162. [CrossRef] [PubMed]
13. Vlad, S.C.; Miller, D.R.; Kowall, N.W.; Felson, D.T. Protective effects of NSAIDs on the development of Alzheimer disease. *Neurology* **2008**, *70*, 1672–1677. [CrossRef] [PubMed]
14. Yue, P.Y.; Wong, Y.Y.; Wong, K.Y.; Tsoi, Y.K.; Leung, K.S. Current evidence for the hepatoprotective activities of the medicinal mushroom *Antrodia cinnamomea*. *Chin. Med.* **2013**, *8*, 21. [CrossRef] [PubMed]

15. Peng, C.C.; Chen, K.C.; Peng, R.Y.; Chyau, C.C.; Su, C.H.; Hsieh-Li, H.M. Antrodia camphorata extract induces replicative senescence in superficial TCC, and inhibits the absolute migration capability in invasive bladder carcinoma cells. *J. Ethnopharmacol.* **2007**, *109*, 93–103. [CrossRef] [PubMed]
16. Chang, W.H.; Chen, M.C.; Cheng, I.H. Antroquinonol Lowers Brain Amyloid-beta Levels and Improves Spatial Learning and Memory in a Transgenic Mouse Model of Alzheimer's Disease. *Sci. Rep.* **2015**, *5*, 15067. [CrossRef] [PubMed]
17. Chang, Y.Y.; Liu, Y.C.; Kuo, Y.H.; Lin, Y.L.; Wu, Y.S.; Chen, J.W.; Chen, Y.C. Effects of antrosterol from Antrodia camphorata submerged whole broth on lipid homeostasis, antioxidation, alcohol clearance, and anti-inflammation in livers of chronic-alcohol fed mice. *J. Ethnopharmacol.* **2017**, *202*, 200–207. [CrossRef] [PubMed]
18. Wang, Y.H.; Chern, C.M.; Liou, K.T.; Kuo, Y.H.; Shen, Y.C. Ergostatrien-7,9(11),22-trien-3beta-ol from Antrodia camphorata ameliorates ischemic stroke brain injury via downregulation of p65NF-kappa-B and caspase 3, and activation of Akt/GSK3/catenin-associated neurogenesis. *Food Funct.* **2019**, *10*, 4725–4738. [CrossRef]
19. Yuan, L.; Zhang, F.; Shen, M.; Jia, S.; Xie, J. Phytosterols Suppress Phagocytosis and Inhibit Inflammatory Mediators via ERK Pathway on LPS-Triggered Inflammatory Responses in RAW264.7 Macrophages and the Correlation with Their Structure. *Foods* **2019**, *8*, 582. [CrossRef] [PubMed]
20. Wu, M.D.; Cheng, M.J.; Wang, B.C.; Yech, Y.J.; Lai, J.T.; Kuo, Y.H.; Yuan, G.F.; Chen, I.S. Maleimide and maleic anhydride derivatives from the mycelia of Antrodia cinnamomea and their nitric oxide inhibitory activities in macrophages. *J. Nat. Prod.* **2008**, *71*, 1258–1261. [CrossRef]
21. Senthil, K.K.J.; Gokila, V.M.; Wang, S.Y. Activation of Nrf2-mediated anti-oxidant genes by antrodin C prevents hyperglycemia-induced senescence and apoptosis in human endothelial cells. *Oncotarget* **2017**, *8*, 96568–96587. [CrossRef]
22. Wang, Y.J.; Lee, S.C.; Hsu, C.H.; Kuo, Y.H.; Yang, C.C.; Lin, F.J. Antcins, triterpenoids from Antrodia cinnamomea, as new agonists for peroxisome proliferator-activated receptor alpha. *J. Food Drug Anal.* **2019**, *27*, 295–304. [CrossRef]
23. Lin, C.H.; Kuo, Y.H. Eburicoic Acid, a Triterpenoid Compound from Antrodia camphorata, Displays Antidiabetic and Anti-hyperlipidemic Effects in Palmitate-Treated C2C12 Myotubes and in High-Fat Diet-Fed Mice. *Int. J. Mol. Sci.* **2017**, *18*, 2314. [CrossRef]
24. Lin, C.H.; Hsiao, L.W.; Kuo, Y.H. Antidiabetic and Antihyperlipidemic Effects of Sulphurenic Acid, a Triterpenoid Compound from Antrodia camphorata, in Streptozotocin-Induced Diabetic Mice. *Int. J. Mol. Sci.* **2019**, *20*, 4897. [CrossRef] [PubMed]
25. Jankowsky, J.L.; Fadale, D.J.; Anderson, J.; Xu, G.M.; Gonzales, V.; Jenkins, N.A.; Copeland, N.G.; Lee, M.K.; Younkin, L.H.; Wagner, S.L.; et al. Mutant presenilins specifically elevate the levels of the 42 residue beta-amyloid peptide in vivo: Evidence for augmentation of a 42-specific gamma secretase. *Hum. Mol. Genet.* **2004**, *13*, 159–170. [CrossRef]
26. Malm, T.; Koistinaho, J.; Kanninen, K. Utilization of APP^{swe}/PS1^{dE9} Transgenic Mice in Research of Alzheimer's Disease: Focus on Gene Therapy and Cell-Based Therapy Applications. *Int. J. Alzheimers Dis.* **2011**, *2011*, 517160. [CrossRef] [PubMed]
27. Volianskis, A.; Kostner, R.; Molgaard, M.; Hass, S.; Jensen, M.S. Episodic memory deficits are not related to altered glutamatergic synaptic transmission and plasticity in the CA1 hippocampus of the APP^{swe}/PS1^{deltaE9}-deleted transgenic mice model of ss-amyloidosis. *Neurobiol. Aging* **2010**, *31*, 1173–1187. [CrossRef] [PubMed]
28. Xiong, H.; Callaghan, D.; Wodzinska, J.; Xu, J.; Premyslova, M.; Liu, Q.Y.; Connelly, J.; Zhang, W. Biochemical and behavioral characterization of the double transgenic mouse model (APP^{swe}/PS1^{dE9}) of Alzheimer's disease. *Neurosci. Bull.* **2011**, *27*, 221–232. [CrossRef] [PubMed]
29. Tzeng, T.T.; Chen, C.C.; Chen, C.C.; Tsay, H.J.; Lee, L.Y.; Chen, W.P.; Shen, C.C. The Cyanthine Diterpenoid and Sesterterpene Constituents of *Hericium erinaceus* Mycelium Ameliorate Alzheimer's Disease-Related Pathologies in APP/PS1 Transgenic Mice. *Int. J. Mol. Sci.* **2018**, *19*, 598. [CrossRef] [PubMed]
30. Deacon, R.M. Assessing nest building in mice. *Nat. Protoc.* **2006**, *1*, 1117–1119. [CrossRef]
31. Jirkof, P. Burrowing and nest building behavior as indicators of well-being in mice. *J. Neurosci. Methods* **2014**, *234*, 139–146. [CrossRef]
32. Woodling, N.S.; Colas, D.; Wang, Q.; Minhas, P.; Panchal, M.; Liang, X.; Mhatre, S.D.; Brown, H.; Ko, N.; Zagol-Ikapitte, I.; et al. Cyclooxygenase inhibition targets neurons to prevent early behavioural decline in Alzheimer's disease model mice. *Brain* **2016**, *139*, 2063–2081. [CrossRef]
33. Hamilton, A.; Holscher, C. The effect of ageing on neurogenesis and oxidative stress in the APP(swe)/PS1(deltaE9) mouse model of Alzheimer's disease. *Brain Res.* **2012**, *1449*, 83–93. [CrossRef] [PubMed]
34. Ghali, M.G.Z.; Marchenko, V.; Yaşargil, M.G.; Ghali, G.Z. Structure and function of the perivascular fluid compartment and vertebral venous plexus: Illuminating a novel theory on mechanisms underlying the pathogenesis of Alzheimer's, cerebral small vessel, and neurodegenerative diseases. *Neurobiol. Dis.* **2020**, *144*, 105022. [CrossRef]
35. Young, K.; Morrison, H. Quantifying Microglia Morphology from Photomicrographs of Immunohistochemistry Prepared Tissue Using ImageJ. *J. Vis. Exp. JoVE* **2018**, *136*, 57648. [CrossRef]
36. Nimmerjahn, A.; Kirchhoff, F.; Helmchen, F. Resting microglial cells are highly dynamic surveillants of brain parenchyma in vivo. *Science* **2005**, *308*, 1314–1318. [CrossRef]
37. Chen, X.L.; Dodd, G.; Thomas, S.; Zhang, X.; Wasserman, M.A.; Rovin, B.H.; Kunsch, C. Activation of Nrf2/ARE pathway protects endothelial cells from oxidant injury and inhibits inflammatory gene expression. *Am. J. Physiol. Heart Circ. Physiol.* **2006**, *290*, 1862–1870. [CrossRef] [PubMed]

38. Rosenzweig, S.; Wojtowicz, J.M. Analyzing dendritic growth in a population of immature neurons in the adult dentate gyrus using laminar quantification of disjointed dendrites. *Front. Neurosci.* **2011**, *5*, 34. [CrossRef]
39. Mawuenyega, K.G.; Sigurdson, W.; Ovod, V.; Munsell, L.; Kasten, T.; Morris, J.C.; Yarasheski, K.E.; Bateman, R.J. Decreased clearance of CNS beta-amyloid in Alzheimer's disease. *Science* **2010**, *330*, 1774. [CrossRef] [PubMed]
40. Baranello, R.J.; Bharani, K.L.; Padmaraju, V.; Chopra, N.; Lahiri, D.K.; Greig, N.H.; Pappolla, M.A.; Sambamurti, K. Amyloid-beta protein clearance and degradation (ABCD) pathways and their role in Alzheimer's disease. *Curr. Alzheimer Res.* **2015**, *12*, 32–46. [CrossRef]
41. Serrano-Pozo, A.; Muzikansky, A.; Gomez-Isla, T.; Growdon, J.H.; Betensky, R.A.; Frosch, M.P.; Hyman, B.T. Differential relationships of reactive astrocytes and microglia to fibrillar amyloid deposits in Alzheimer disease. *J. Neuropathol. Exp. Neurol.* **2013**, *72*, 462–471. [CrossRef]
42. Fu, A.K.; Hung, K.W.; Yuen, M.Y.; Zhou, X.; Mak, D.S.; Chan, I.C.; Cheung, T.H.; Zhang, B.; Fu, W.Y.; Liew, F.Y.; et al. IL-33 ameliorates Alzheimer's disease-like pathology and cognitive decline. *Proc. Natl. Acad. Sci. USA* **2016**, *113*, 2705–2713. [CrossRef]
43. El Khoury, J.; Toft, M.; Hickman, S.E.; Means, T.K.; Terada, K.; Geula, C.; Luster, A.D. Ccr2 deficiency impairs microglial accumulation and accelerates progression of Alzheimer-like disease. *Nat. Med.* **2007**, *13*, 432–438. [CrossRef]
44. Orihuela, R.; McPherson, C.A.; Harry, G.J. Microglial M1/M2 polarization and metabolic states. *Br. J. Pharmacol.* **2016**, *173*, 649–665. [CrossRef]
45. Koenigsnecht-Talboo, J.; Landreth, G.E. Microglial phagocytosis induced by fibrillar beta-amyloid and IgGs are differentially regulated by proinflammatory cytokines. *J. Neurosci.* **2005**, *25*, 8240–8249. [CrossRef] [PubMed]
46. He, X.F.; Xu, J.H.; Li, G.; Li, M.Y.; Li, L.L.; Pei, Z.; Zhang, L.Y.; Hu, X.Q. NLRP3-dependent microglial training impaired the clearance of amyloid-beta and aggravated the cognitive decline in Alzheimer's disease. *Cell Death Dis.* **2020**, *11*, 849. [CrossRef]
47. Zhou, Z.; Liu, C.; Chen, S.; Zhao, H.; Zhou, K.; Wang, W.; Yuan, Y.; Li, Z.; Guo, Y.; Shen, Z.; et al. Activation of the Nrf2/ARE signaling pathway by probucol contributes to inhibiting inflammation and neuronal apoptosis after spinal cord injury. *Oncotarget* **2017**, *8*, 52078–52093. [CrossRef] [PubMed]
48. Ramsey, C.P.; Glass, C.A.; Montgomery, M.B.; Lindl, K.A.; Ritson, G.P.; Chia, L.A.; Hamilton, R.L.; Chu, C.T.; Jordan-Sciutto, K.L. Expression of Nrf2 in neurodegenerative diseases. *J. Neuropathol. Exp. Neurol.* **2007**, *66*, 75–85. [CrossRef]
49. Pedrós, I.; Petrov, D.; Allgaier, M.; Sureda, F.; Barroso, E.; Beas-Zarate, C.; Auladell, C.; Pallàs, M.; Vázquez-Carrera, M.; Casadesús, G.; et al. Early alterations in energy metabolism in the hippocampus of APPsw/PS1dE9 mouse model of Alzheimer's disease. *Biochim. Biophys. Acta* **2014**, *1842*, 1556–1566. [CrossRef] [PubMed]
50. Fragoulis, A.; Siegl, S.; Fendt, M.; Jansen, S.; Soppa, U.; Brandenburg, L.O.; Pufe, T.; Weis, J.; Wruck, C.J. Oral administration of methysticin improves cognitive deficits in a mouse model of Alzheimer's disease. *Redox Biol.* **2017**, *12*, 843–853. [CrossRef]
51. Tanji, K.; Maruyama, A.; Odagiri, S.; Mori, F.; Itoh, K.; Kakita, A.; Takahashi, H.; Wakabayashi, K. Keap1 is localized in neuronal and glial cytoplasmic inclusions in various neurodegenerative diseases. *J. Neuropathol. Exp. Neurol.* **2013**, *72*, 18–28. [CrossRef]
52. SantaCruz, K.S.; Yazlovitskaya, E.; Collins, J.; Johnson, J.; DeCarli, C. Regional NAD(P)H:quinone oxidoreductase activity in Alzheimer's disease. *Neurobiol. Aging* **2004**, *25*, 63–69. [CrossRef]
53. Día, M.; Mesa-Herrera, F.; Marin, R. DHA and Its Elaborated Modulation of Antioxidant Defenses of the Brain: Implications in Aging and AD Neurodegeneration. *Antioxidants* **2021**, *10*, 907. [CrossRef]
54. Kanninen, K.; Malm, T.M.; Jyrkkänen, H.K.; Goldsteins, G.; Keksa-Goldsteine, V.; Tanila, H.; Yamamoto, M.; Ylä-Herttua, S.; Levonen, A.L.; Koistinaho, J. Nuclear factor erythroid 2-related factor 2 protects against beta amyloid. *Mol. Cell Neurosci.* **2008**, *39*, 302–313. [CrossRef] [PubMed]
55. Yamazaki, H.; Tanji, K.; Wakabayashi, K.; Matsuura, S.; Itoh, K. Role of the Keap1/Nrf2 pathway in neurodegenerative diseases. *Pathol. Int.* **2015**, *65*, 210–219. [CrossRef]
56. Licht-Mayer, S.; Wimmer, I.; Traffehn, S.; Metz, I.; Brück, W.; Bauer, J.; Bradl, M.; Lassmann, H. Cell type-specific Nrf2 expression in multiple sclerosis lesions. *Acta Neuropathol.* **2015**, *130*, 263–277. [CrossRef] [PubMed]
57. Zhao, Y.; Wang, S.; Song, X.; Yuan, J.; Qi, D.; Gu, X.; Yin, M.Y.; Han, Z.; Zhu, Y.; Liu, Z. Glial Cell-Based Vascular Mechanisms and Transplantation Therapies in Brain Vessel and Neurodegenerative Diseases. *Front. Cell. Neurosci.* **2021**, *15*, 627682. [CrossRef]
58. Reeves, B.C.; Karimy, J.K.; Kundishora, A.J.; Mestre, H.; Cerci, H.M.; Matouk, C.; Alper, S.L.; Lundgaard, I.; Nedergaard, M.; Kahle, K.T. Glymphatic System Impairment in Alzheimer's Disease and Idiopathic Normal Pressure Hydrocephalus. *Trends Mol. Med.* **2020**, *26*, 285–295. [CrossRef]
59. Greenberg, S.M.; Bacskai, B.J.; Hernandez-Guillamon, M.; Pruzin, J.; Sperling, R.; van Veluw, S.J. Cerebral amyloid angiopathy and Alzheimer disease—one peptide, two pathways. *Nat. Rev. Neurol.* **2020**, *16*, 30–42. [CrossRef]
60. Huang, G.J.; Huang, S.S.; Lin, S.S.; Shao, Y.Y.; Chen, C.C.; Hou, W.C.; Kuo, Y.H. Analgesic effects and the mechanisms of anti-inflammation of ergostatrien-3beta-ol from *Antrodia camphorata* submerged whole broth in mice. *J. Agric. Food Chem.* **2010**, *58*, 7445–7452. [CrossRef] [PubMed]
61. Shao, Y.Y.; Chen, C.C.; Wang, H.Y.; Chiu, H.L.; Hseu, T.H.; Kuo, Y.H. Chemical constituents of *Antrodia camphorata* submerged whole broth. *Nat. Prod. Res.* **2008**, *22*, 1151–1157. [CrossRef]
62. Huang, H.T.; Wang, S.L. Isolation and Identification of Potent Antidiabetic Compounds from *Antrodia cinnamomea*—An Edible Taiwanese Mushroom. *Molecules* **2018**, *23*, 2864. [CrossRef]

63. Chen, Y.M.; Sung, H.C.; Kuo, Y.H.; Hsu, Y.J.; Huang, C.C.; Liang, H.L. The Effects of Ergosta-7,9(11),22-trien-3beta-ol from *Antrodia camphorata* on the Biochemical Profile and Exercise Performance of Mice. *Molecules* **2019**, *24*, 1225. [CrossRef] [PubMed]
64. Hess, S.E.; Rohr, S.; Dufour, B.D.; Gaskill, B.N.; Pajor, E.A.; Garner, J.P. Home improvement: C57BL/6J mice given more naturalistic nesting materials build better nests. *J. Am. Assoc. Lab. Anim. Sci.* **2008**, *47*, 25–31. [PubMed]



Article

Neuron–Microglia Contacts Govern the PGE₂ Tolerance through TLR4-Mediated de Novo Protein Synthesis

Hsing-Chun Kuo^{1,2,3,4}, Kam-Fai Lee⁵, Shiou-Lan Chen⁶, Shu-Chen Chiu⁷, Li-Ya Lee⁸, Wan-Ping Chen⁸, Chin-Chu Chen⁸ and Chun-Hsien Chu^{9,*}

- ¹ Division of Basic Medical Sciences, Department of Nursing, Chang Gung University of Science and Technology, Chiayi 61363, Taiwan; guscsi@gmail.com
 - ² Chang Gung Memorial Hospital, Chiayi 61363, Taiwan
 - ³ Research Center for Food and Cosmetic Safety, College of Human Ecology, Chang Gung University of Science and Technology, Taoyuan 33303, Taiwan
 - ⁴ Chronic Diseases and Health Promotion Research Center, Chang Gung University of Science and Technology, Chiayi 61363, Taiwan
 - ⁵ Department of Pathology, Chang Gung Memorial Hospital, Chiayi 61363, Taiwan; lkf2002@cgmh.org.tw
 - ⁶ Graduate Institute of Medicine, College of Medicine, Kaohsiung Medical University (KMU), Kaohsiung 80708, Taiwan; shioulan@kmu.edu.tw
 - ⁷ National Laboratory Animal Center (NLAC), NARLabs, Tainan 74147, Taiwan; cscsc@narlabs.org.tw
 - ⁸ Grape King Biotechnology Inc (Grape King Bio Ltd.), Zhong-Li, Taoyuan 32542, Taiwan; ly.lee@grapeking.com.tw (L.-Y.L.); wp.chen@grapeking.com.tw (W.-P.C.); gkbioeng@grapeking.com.tw (C.-C.C.)
 - ⁹ Institute of Molecular Medicine, College of Medicine, National Cheng Kung University, Tainan 70456, Taiwan
- * Correspondence: chunhsienchu@gmail.com or chunhsienchu@mail.ncku.edu.tw; Tel.: +886-6-235-3535 (ext. 3592); Fax: +886-6-209-5845

Citation: Kuo, H.-C.; Lee, K.-F.; Chen, S.-L.; Chiu, S.-C.; Lee, L.-Y.; Chen, W.-P.; Chen, C.-C.; Chu, C.-H. Neuron–Microglia Contacts Govern the PGE₂ Tolerance through TLR4-Mediated de Novo Protein Synthesis. *Biomedicines* **2022**, *10*, 419. <https://doi.org/10.3390/biomedicines10020419>

Academic Editors: Masaru Tanaka and Bruno Meloni

Received: 13 November 2021

Accepted: 7 February 2022

Published: 10 February 2022

Publisher's Note: MDPI stays neutral with regard to jurisdictional claims in published maps and institutional affiliations.



Copyright: © 2022 by the authors. Licensee MDPI, Basel, Switzerland. This article is an open access article distributed under the terms and conditions of the Creative Commons Attribution (CC BY) license (<https://creativecommons.org/licenses/by/4.0/>).

Abstract: Cellular and molecular mechanisms of the peripheral immune system (e.g., macrophage and monocyte) in programming endotoxin tolerance (ET) have been well studied. However, regulatory mechanism in development of brain immune tolerance remains unclear. The inducible COX-2/PGE₂ axis in microglia, the primary innate immune cells of the brain, is a pivotal feature in causing inflammation and neuronal injury, both in acute excitotoxic insults and chronic neurodegenerative diseases. This present study investigated the regulatory mechanism of PGE₂ tolerance in microglia. Multiple reconstituted primary brain cells cultures, including neuron–glial (NG), mixed glial (MG), neuron-enriched, and microglia-enriched cultures, were performed and consequently applied to a treatment regimen for ET induction. Our results revealed that the levels of COX-2 mRNA and supernatant PGE₂ in NG cultures, but not in microglia-enriched and MG cultures, were drastically reduced in response to the ET challenge, suggesting that the presence of neurons, rather than astroglia, is required for PGE₂ tolerance in microglia. Furthermore, our data showed that neural contact, instead of its soluble factors, is sufficient for developing microglial PGE₂ tolerance. Simultaneously, this finding determined how neurons regulated microglial PGE₂ tolerance. Moreover, by inhibiting TLR4 activation and de novo protein synthesis by LPS-binding protein (LBP) manipulation and cycloheximide, our data showed that the TLR4 signal and de novo protein synthesis are necessary for microglia to develop PGE₂ tolerance in NG cells under the ET challenge. Altogether, our findings demonstrated that neuron–microglia contacts are indispensable in emerging PGE₂ tolerance through the regulation of TLR4-mediated de novo protein synthesis.

Keywords: PGE₂; COX-2; microglia; endotoxin tolerance; cell–cell contacts; TLR4; de novo protein synthesis; LPS binding protein; innate immune memory; brain immunity

1. Introduction

Microglia, the primary innate immune cells of the brain, maintain the central nervous system (CNS) homeostasis at physiological conditions [1,2]. With their high mobility,

microglia survey, and guard brain microenvironment (surveillance), they can regulate normal development, growth, connection, and functions of the neurons for a lifetime [3]. In response to immune challenge, microglia, as the first defense and inflammatory responder, secrete a wide spectrum and various immunoregulatory factors to protect the neurons against invading pathogens [4]. At the end of the inflammatory process, microglia are back to the status of immune resolution [5]. Conversely, the unresolved inflammation caused by overactivated microglia further damages neurons [6]. However, the immunosuppressive mechanism of microglia in resolving inflammation remains unclear [7].

Recently, many studies have demonstrated the capability of microglia in developing innate immune memory to either enhance (trained immunity) or suppress (immune tolerance) subsequent immune responses [8,9]. In response to the lipopolysaccharide (LPS, glycolipid of the outer cell membrane of Gram-negative bacteria) challenge, activated microglia immediately produce superoxide and TNF- α , followed by the production of IL-1 β , nitrite (NO), prostaglandin E2 (PGE₂), and IL-6 at 24 h [10]. Subsequently, anti-inflammatory cytokines, such as IL-10, are secreted by microglia for neuroinflammation resolution. Under recurrent stimulations with LPS, while microglia decrease (“tolerate”) production of pro-inflammatory mediators (TNF- α , IL-1 β , and PGE₂), they instigate (“sensitize”) the synthesis of anti-inflammatory mediators (IL-10) [11]. In other words, LPS-tolerized microglia become refractory to a subsequent endotoxin challenge referred to as a neuroprotective mechanism, targeted at the prevention of excessive toxic damage from cytokine production. Accordingly, activated microglia are the main target for alleviating neuroinflammation, including immunotolerance and low-grade inflammation, in order to prevent pathogenesis of various neurological and psychiatric disorders [12–14]. Noteworthily, the presence of other brain cells, such as neurons and astroglia, regulates the endotoxin tolerance capacity of microglia in the TNF- α reduction and IL-10 enhancement through M-CSF-mediated ERK signals [11]. In fact, little is known about how other brain cells interact with microglia in shaping their innate immune memory.

Inducible cyclooxygenase-2 (COX-2) catalyzes the first committed step in the synthesis of PGE₂ and subsequently activates its downstream signaling pathways through four E-prostanoid (EP) receptors [15]. Activating PGE₂ signals contributes to the neurotoxic effect of COX-2 in a broad spectrum of neurological disease models in the CNS [16]—from models of cerebral ischemia [17] to models of neurodegeneration and inflammation [18,19]. In addition to the high neural COX-2 activity in acute paradigms of excitotoxicity [20] (e.g., cerebral ischemia [21] and seizures [22]), microglia also show an increase in COX-2 activity and PGE₂ production, causing inflammatory injury in inflammatory paradigms [10,23,24], such as Alzheimer’s disease [24,25], Parkinson’s disease [26], and amyotrophic lateral sclerosis [27]. Thus, the COX-2/PGE₂ axis plays an important role in promoting neuronal injury, both in acute excitotoxic insults and in chronic neurodegenerative diseases [15,16,19]. Nevertheless, regulatory mechanisms for immune suppression (tolerance) of the COX-2/PGE₂ axis in the brain are still unclear. The purpose of this study is to determine the tolerance mechanism of microglial PGE₂ in response to repeated LPS challenges.

2. Materials and Methods

2.1. Animals

Pregnant C57/6J mice ($n = 18$) and their pups ($n = 55$) were purchased from the National Laboratory Animal Center (NLAC) in Tainan, Taiwan. Housing and breeding of the animals were performed humanely and with regard to alleviating suffering following the National Institutes of Health Guide for Care and Use of Laboratory Animals (Institute of Laboratory Animal Resources 1996). All procedures were approved by the National Cheng Kung University (NCKU) Animal Care and Use Committee.

2.2. Reagents

LPS (*E. coli* O111:B4, Cat# 437627, protein contaminants $\leq 2.0\%$, nucleic acid contaminants $\leq 2.5\%$) was obtained from EMD Chemicals, Inc. (Darmstadt, Germany).

Recombinant TLR4 binding protein and cycloheximide were purchased from R&D Systems (Minneapolis, MN, USA) and Sigma-Aldrich (Saint Louis, MO, USA), respectively. Formaldehyde solution was obtained from Sigma-Aldrich (Saint Louis, MO, USA).

2.3. Preparation of Primary Neuron–Glial, Mixed Glial, and Microglia- and Astrocyte-Enriched Cultures

The preparation of mesencephalic neuron–glial cultures was performed from the mesencephalon of embryos at gestation day 14 ± 0.5 of the C57/6J mice ($n = 18$), as previously reported [10,11]. Briefly, after dissection and dissociation of mesencephalic tissues with mild mechanical trituration, cells were seeded to 24-well (5×10^5 cells/well) culture plates precoated with poly-D-lysine (20 $\mu\text{g}/\text{mL}$) and maintained in 0.5 mL/well of MEM medium (10% heat-inactivated fetal bovine serum (FBS), 10% heat-inactivated horse serum (HS), 1 g/L glucose, 2 mM L-glutamine, 1 mM sodium pyruvate, and 0.1 mM nonessential amino acids). Cultures were preserved at 37 °C in a humidified atmosphere of 5% CO₂/95% air. Three days later, 0.5 mL/well of fresh medium was replenished into the cultures. Seven days after seeding, the neuron–glial cultures made up of about 10% microglia, 50% astrocytes, and 40% neurons based on the visual counting of immunostained cells with antibodies against cell-type specific markers: neurons (Neu-N), microglia (OX-42), and astrocytes (GFAP) [28]. The NG cultures were ready for further endotoxin tolerance treatment regimen (Figure 1A). The neuron-enriched culture contained 99% neurons and less than 1% glia. The dividing glial was depleted from neuron–glial cultures 48 h after seeding with 8–10 μM of cytosine β -d-arabinofuranoside (Ara-C; Sigma-Aldrich, St. Louis, MO, USA) for three days.

Primary mixed glial cultures were prepared from whole brains of postnatal day-1 pups ($n = 10$) from the C57BL/6J mice [10,11]. After brain tissue disassociation, the cells were seeded onto 6-well (1×10^6 cells/well) culture plates and maintained in 1 mL/well of DMEM/F-12 medium (10% FBS, 2 mM of L-glutamine, 1 mM of sodium pyruvate, and 0.1 mM of nonessential amino acids). Before reaching confluence, the medium was changed every 3 days. The mixed glial cultures contained about 80% astrocytes and 20% microglia and were used for endotoxin tolerance treatment regimen.

Microglia-enriched cultures were prepared from the whole brains of 1-day-old C57/6J pups ($n = 45$), as previously reported [10,11]. Briefly, after the dissociation of brain tissues, devoid of meninges and blood vessels by mild mechanical trituration, the isolated cells (5×10^7 cells) were seeded in 150 cm² culture flasks in DMEM/F12 medium (10% FBS, 2 mM of L-glutamine, 1 mM of sodium pyruvate, 0.1 mM of nonessential amino acids, 50 U/mL of penicillin, and 50 $\mu\text{g}/\text{mL}$ of streptomycin) and maintained at 37 °C in a humidified atmosphere of 5% CO₂/95% air. Before reaching confluence, the medium was changed 4 days later. Upon reaching confluence (12–14 days), the enriched microglia (99% pure) were obtained by shaking the flasks for 60 min at 180 rpm.

2.4. Cell Treatment

Multiple reconstituted brain cultures, including neuron–glial (NG), mixed glial (MG), microglia-enriched, fixed neurons plus microglia, and neurons plus microglia in Transwell inserts, were pre-incubated with or without LPS (15 ng/mL) for 6 h. After replacing the fresh media and waiting for an additional 6 h, LPS was readed into these cells (Figure 1A). Thus, endotoxin tolerance (ET) treatment regimen included untreated control, LPS (LPS alone treatment), LPS/LPS (twice LPS treatment), and LPS-untreated control groups. The expressions of COX-2 or PGE₂ were measured at 3, 6, and 24 h in these cells by RT-PCR and ELISA, respectively. Furthermore, serum-free medium (no LPS binding protein (LBP)) and the addition of LBP (1 $\mu\text{g}/\text{mL}$) were used to study TLR4's role in the development of microglial PGE₂ tolerance in NG cells. Moreover, treated NG cells with cycloheximide, an inhibitor for protein synthesis, was performed to determine involvement of de novo protein synthesis in PGE₂ tolerance of microglia.

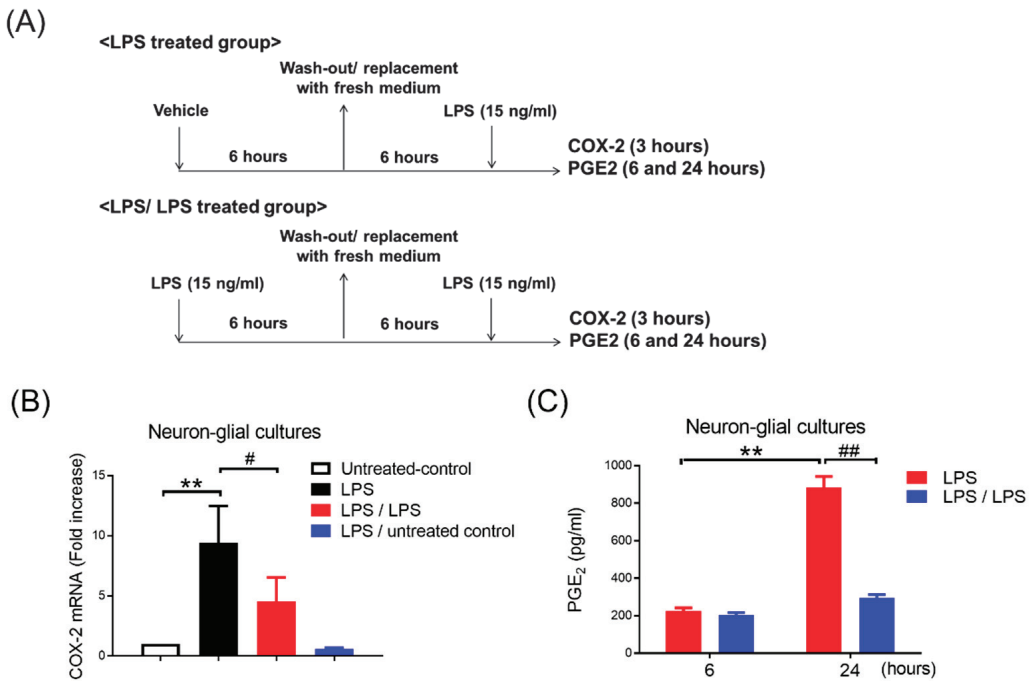


Figure 1. Reduction in COX-2 and PGE₂ expression in neuron–glial cultures in response to endotoxin tolerance. (A) Experimental procedure for the study of PGE₂ production in endotoxin tolerance. Neuron–glial (NG) cultures prepared from E14.5 time-pregnant C56/6J mice were pre-treated with vehicle (LPS-treated group) or LPS (15 ng/mL) (LPS/LPS-treated group) for 6 h. These pre-treated NG cultures were replaced with fresh media. Six hours later, LPS (15 ng/mL) was added to these NG cells. The level of COX-2 gene expression and supernatant PGE₂ production was measured at 3, 6, and 24 h after LPS treatment. (B) After 3 h, the mRNA level of the COX-2 gene was measured in these NG cultures with untreated control, LPS-treated group (LPS), LPS/LPS-treated group (LPS/LPS), and LPS-untreated control group by RT-PCR. Three independent experiments were performed in duplicate. Data are expressed as a percentage of the LPS group (mean ± SEM). ** $p < 0.01$ vs. untreated control; # $p < 0.05$ vs. LPS. (C) A supernatant level of PGE₂ in these cells with LPS-treated (LPS) and LPS/LPS-treated group (LPS/LPS) was detected at 6 and 24 h after LPS treatment by ELISA. Data are expressed as the mean ± SEM from three independent experiments in duplicate, ** $p < 0.01$ vs. 6h, ## $p < 0.01$ vs. LPS.

2.5. Quantitative Real Time-PCR

According to the manufacturer's instruction, the RNeasy Mini Kit (QIAGEN, Valencia, CA, USA) and the MuLV reverse transcriptase (Applied Biosystems, Foster City, CA, USA) were used to isolate the total cellular RNA of cells and synthesize the first-strand cDNA. After reverse transcription reaction, the SYBR-Green Master Mix (Applied Biosystems, Foster City, CA, USA) was used to perform real-time quantitative PCR analysis with the following PCR conditions: hold at 95 °C for 10 min and start 40 cycles at 95 °C for 15 s and 60 °C for 1 min. Data were normalized to a GAPDH expression. Vector NTI Advance 11.5 software (Invitrogen, Waltham, MA, USA) was used to design the primers. The sequences of the primers were the following: mouse COX-2 forward primer 5' -TGA-TAT-GTC-TTC-CAG-CCC-ATT G- 3'; mouse COX-2 reverse primer 5' -AAC-GGA-ACT-AAG-AGG-AGC-AGC- 3'; mouse GAPDH forward primer 5' -TTC-AAC-GGC-ACA-GTC-AAG-GC- 3'; mouse GAPDH reverse primer 5' -GAC-TCC-ACG-ACA-TAC-TCA-GCA-CC- 3'.

2.6. Measurement of PGE₂

PGE₂ in the culture medium was measured with the commercial ELISA kits from R&D Systems (Minneapolis, MN, USA).

2.7. Statistical Analysis

All data are expressed as the mean ± standard error of mean (SEM) and were compared between groups using the Student's *t* test, as well as one-way or two-way analysis of variance (ANOVA) with Bonferroni's multiple comparisons test (Prism 7; GraphPad Software, San Diego, CA, USA). A *p* value of <0.05 was considered statistically significant. *: *p* < 0.05; **: *p* < 0.01; ***: *p* < 0.001.

3. Results

To determine whether endotoxin tolerance (ET) of a microglial COX-2-PGE₂ axis occurred, the ET treatment regimen (as described in Section 2.4; Figure 1A) was performed in primary neuron–glial (NG) cultures, containing 40% neurons, 50% astroglia, and 10% microglia. The expressions of COX-2 mRNA and supernatant PGE₂ were measured at 3, 6, and 24 h in the NG cells by RT-PCR and ELISA, respectively. RT-PCR data showed that the LPS treatment induced mRNA levels of the COX-2 gene in the NG cells (1 vs. 9.41 ± 1.25 , *p* < 0.01, one-way ANOVA, Figure 1B). Conversely, the NG cells received with 6 h LPS pre-incubation had decreased the expression of the subsequent endotoxin-induced COX-2 mRNA by 50% (9.41 ± 1.24 vs. 4.55 ± 0.81 , *p* < 0.05, one-way ANOVA, Figure 1B). Our data indicated that the refractory to up-regulation of COX-2 mRNA occurred in the ET-treated NG cells (Figure 1B). The NG cells with a treatment regimen of saline (untreated control) or the LPS plus untreated control had no effect on the COX-2 induction (Figure 1B). Furthermore, ELISA data revealed that the production of PGE₂ was induced in the supernatant of the LPS-treated NG cells at 24 h (225 ± 16.86 ng/mL vs. 883.67 ± 58.03 ng/mL, *p* < 0.01, two-way ANOVA, Figure 1C). Similar to the expression profile of the COX-2 mRNA, the NG cells with LPS pre-incubation had lower PGE₂ production following subsequent LPS treatment (LPS/LPS) at 24 h in comparison with the NG cells with LPS alone treatment (LPS) (883.67 ± 58.03 ng/mL vs. 294 ± 19.15 ng/mL, *p* < 0.01, two-way ANOVA, Figure 1C). Accordingly, our data indicated that microglia were capable of programming COX-2-PGE₂ axis tolerance in NG cells.

Under the LPS challenge, microglia are the main resource of the brain in producing PGE₂. Then, we determined if the development of PGE₂ reduction also occurred in microglia during the ET challenge. Microglia-enriched cultures were prepared and subjected to the same ET treatment regimen, shown in Figure 1A. Our data showed that the production of PGE₂ in LPS pre-treated microglia (LPS/LPS group) was significantly increased in comparison with the microglia without LPS pre-treatment (LPS group) at 6 h of endotoxin treatment (116.6 ± 46.98 ng/mL vs. 2674.6 ± 680.35 ng/mL, *p* < 0.01, two-way ANOVA, Figure 2A). Meanwhile, similar to the microglia with once LPS treatment, the microglia with LPS pre-treatment produced a certain amount of PGE₂ production at 24 h of endotoxin treatment (2701.2 ± 364.94 ng/mL vs. 2540.2 ± 386.34 ng/mL, Figure 2A). These results suggested that microglia alone failed to develop PGE₂ tolerance during the ET challenge. Furthermore, to determine whether astroglia played a role in PGE₂ reduction in tolerant microglia, the mixed glial cultures containing microglia and astroglia were prepared and applied to the same ET experimental procedure (Figure 1A). Our data revealed that compared to the cells with LPS treatment (LPS group), the pre-treatment of mixed glial (MG) cells with LPS (LPS/LPS group) increased the production of PGE₂ at 6 h (374 ± 78.9 ng/mL vs. 3365.6 ± 495.66 ng/mL, *p* < 0.05, two-way ANOVA, Figure 2B) and failed to show PGE₂ reduction at 24 h after endotoxin treatment (2910.4 ± 624.88 ng/mL vs. 2942.2 ± 1008.49 ng/mL, Figure 2B). The expression profile of PGE₂ in microglia-enriched cultures and MG cells during endotoxin tolerance were similar (Figure 2). In other words, the presence of astroglia was unable to program PGE₂ reduction in tolerant microglia.

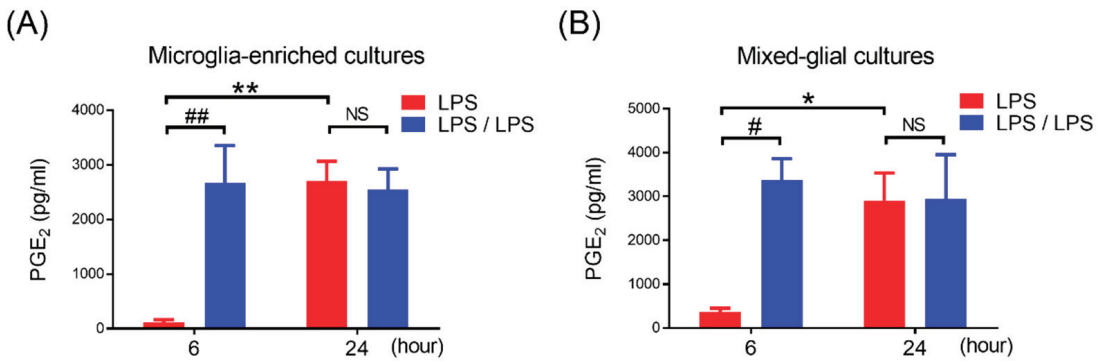


Figure 2. Failure of PGE₂ reduction in microglia-enriched and mixed glia cells with endotoxin tolerance challenge. **(A,B)** A supernatant level of PGE₂ in microglia-enriched cultures **(A)** and mixed glia cultures (MG) containing 80% astroglia and 20% microglia **(B)** in LPS-treated and LPS/LPS-treated regimen were detected at 6 and 24 h after treatment by ELISA. Five independent experiments were performed in duplicate. Data are expressed as the mean \pm SEM, * $p < 0.05$, ** $p < 0.01$ vs. 6H; # $p < 0.05$, ## $p < 0.01$ vs. LPS. NS: no significant differences.

According to Figures 1 and 2, while PGE₂ tolerance occurred in NG cultures, it did not occur in microglia-enriched and MG cultures, implying that the presence of neurons may participate in PGE₂ reduction in tolerant microglia. We further determined whether soluble factors were secreted by neuron-regulated, tolerant microglia for PGE₂ reduction. Thus, the condition media from neuron–glial cells (NGCM) were collected and added into the mixed glial cultures (Figure 3A). After 24 h of incubation, these MG cells were applied to the same ET treatment regimen (Figure 1A). Our data revealed that the incubation of MG cells with NGCM failed to restore the tolerant capacity of microglia in PGE₂ reduction (1822 ± 388.5 ng/mL vs. 1984 ± 268 ng/mL, $p = 0.74$, Student's *t*-test, Figure 3A). Alternatively, by using the Transwell culture system, the microglia in the upper inserts had no direct cell–cell contacts with neurons grown in the lower compartment of the culture plate (Figure 3B, upper panel). However, soluble factors were permeable between the plate's upper and lower compartments (Figure 3B, upper panel). Further, our data showed that the production of PGE₂ in these microglia with either once LPS (LPS group) or twice LPS treatment (LPS/LPS group) were comparable (1010 ± 75.35 ng/mL vs. 1006 ± 112 ng/mL, $p = 0.97$, Student's *t*-test, Figure 3B, bottom panel), suggesting that neural soluble factors were not sufficient for PGE₂ reduction in tolerant microglia. Subsequently, we examined whether physical contact with neurons was involved in PGE₂ reduction in tolerant microglia. Neuron-enriched cultures were fixed with 4% formaldehyde solution and washed out with PBS three times. Although the fixed, dead neurons were unable to produce any soluble factors, they still presented antigen on their cell surface. Microglia were added into the fixed neurons for 24 h of incubation (Figure 3C, upper panel) and applied to the same ET treatment regimen (Figure 1A). Our data showed that PGE₂ reduction occurred in microglia with fixed neurons in response to the ET treatment (4450.66 ± 297.37 ng/mL vs. 2125.33 ± 375.36 ng/mL, $p < 0.01$, two-way ANOVA, Figure 3C, bottom panel). Fixed neurons had no effect on PGE₂ production (Figure 3C, bottom panel). In other words, the loss of PGE₂ tolerance in microglia alone was recovered when it contacted with neurons (Figures 2A and 3C). Moreover, our data indicated that the neuron–microglia contacts were critically involved in the development of the microglial ET capacity on PGE₂ reduction.

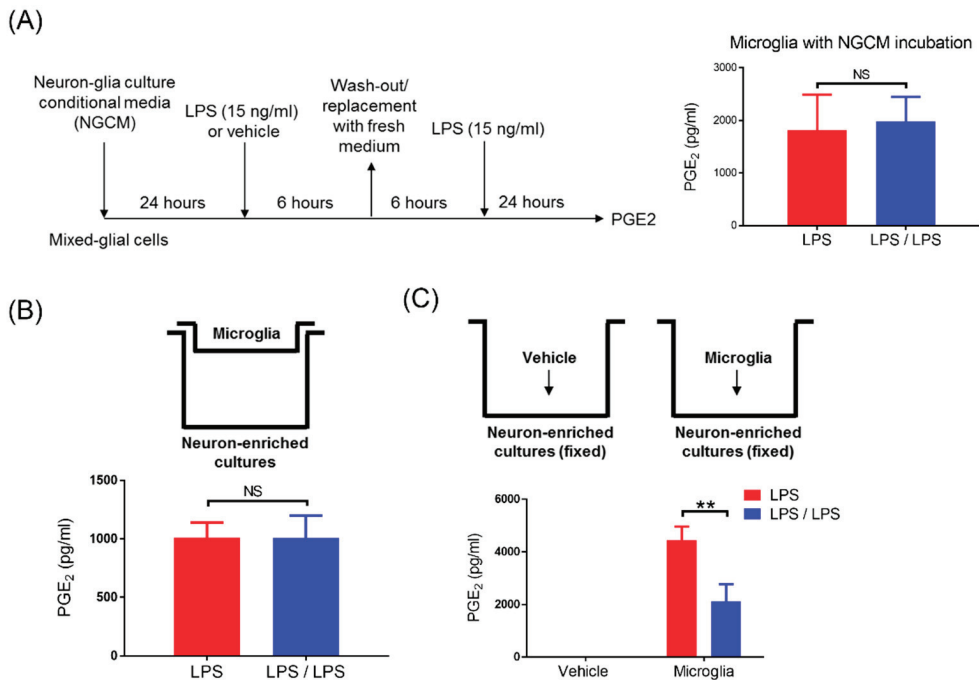


Figure 3. Neural contacts reversed the failure of PGE₂ tolerance in microglia. **(A)** After 24 h incubation with neuron–glial condition media (NGCM), mixed glia (MG) cultures were subjected to the LPS-treated and LPS/LPS-treated regimen, as indicated in the right panel. PGE₂ production in the supernatant of these treated MG cells after 24 h of treatment was measured by ELISA. Data are expressed as the mean ± SEM from three independent experiments in duplicate. NS: no significant differences. **(B)** Microglia were added into Transwell inserts while neurons grew confluent in the lower compartment of the 24-well plate, as indicated in the upper panel. After 24 h of incubation, these cells were applied to the LPS-treated and LPS/LPS-treated regimen. A supernatant level of PGE₂ in these treated cells was detected by ELISA at 24 h of treatment. Data are expressed as the mean ± SEM from three independent experiments in duplicate. NS: no significant differences. **(C)** As indicated in the upper panels, the fixed neuron-enriched cultures were prepared and added with or without microglia. After 24 h of incubation, microglia were applied to the LPS-treated and LPS/LPS-treated regimen. A supernatant level of PGE₂ in these treated microglia was measured by ELISA 24 h after treatment. Three independent experiments were performed in duplicate. Data are expressed as the mean ± SEM, LPS group versus the LPS/LPS group. ** *p* < 0.01. NS: not significant -.

Previous studies demonstrate that the activation of toll-like receptor 4 (TLR4) by LPS is critical for downstream inflammatory [29,30], anti-inflammatory [10], and tolerance responses [31]. Thus, we determined whether the TLR4-derived signal participated in the modulation of microglial PGE₂ tolerance by neurons. Due to LPS-contained hydrophobic multi-acyl chains forming aggregates or micelles in aqueous solutions, the accessory LPS-binding proteins (LBPs) are required to mediate the sensitive recognition of LPS as well as their efficient transfer to the TLR4 [32,33]. After binding to LPS, the TLR4 signaling cascades are activated in the host immune response [30]. Therefore, by using serum-free medium (no LBP) with or without addition of recombinant LBP protein to incubate NG cells, the role of TLR4 signal in PGE tolerance was studied (Figure 4A, left panel). Our data revealed that during the ET treatment, PGE₂ reduction occurred in NG cells at 24 h in the presence of serum medium-contained LBP (100 ± 3.11 vs. 23.79 ± 1.35, *p* < 0.01, two-way ANOVA, Figure 4A, right panel). Conversely, in serum-free media (no LBP), PGE₂ tolerance

disappeared (even higher PGE₂ production) in NG cells at 24 h during the ET challenge (100 ± 17.43 ng/mL vs. 300.53 ± 8.15 ng/mL, $p < 0.01$, two-way ANOVA, Figure 4A, right panel). Furthermore, a recombinant LBP protein was added into serum-free media of NG cultures to confirm whether the TLR4 signal activation was crucial for the development of PGE₂ tolerance. Our results revealed that adding recombinant LBP protein at 1 μ g/mL concentration entirely reversed the failure of PGE₂ tolerance in NG cultures at a serum-free condition (100 ± 2.4 ng/mL vs. 44.02 ± 2.75 ng/mL, $p < 0.01$, two-way ANOVA, Figure 4A, right panel). In addition, our data indicated that the TLR4-derived signal is necessary for PGE₂ tolerance in microglia. Moreover, to determine whether inducing de novo protein synthesis by TLR4 activation was required for programming PGE₂ tolerance, NG cells were treated with a protein synthesis inhibitor cycloheximide at 1 μ g/mL concentration and subsequently applied to the same ET treatment regimen (Figure 4B, left panel). Our data showed that the inhibition of protein synthesis by cycloheximide disrupted the PGE₂ tolerance in NG cells during ET (1882.66 ± 67.62 ng/mL vs. 2394.33 ± 252.02 ng/mL, Figure 4B, right panel). Moreover, our results suggested that the TLR4-dependent de novo protein synthesis participated in neuron-mediated PGE₂ tolerance in microglia.

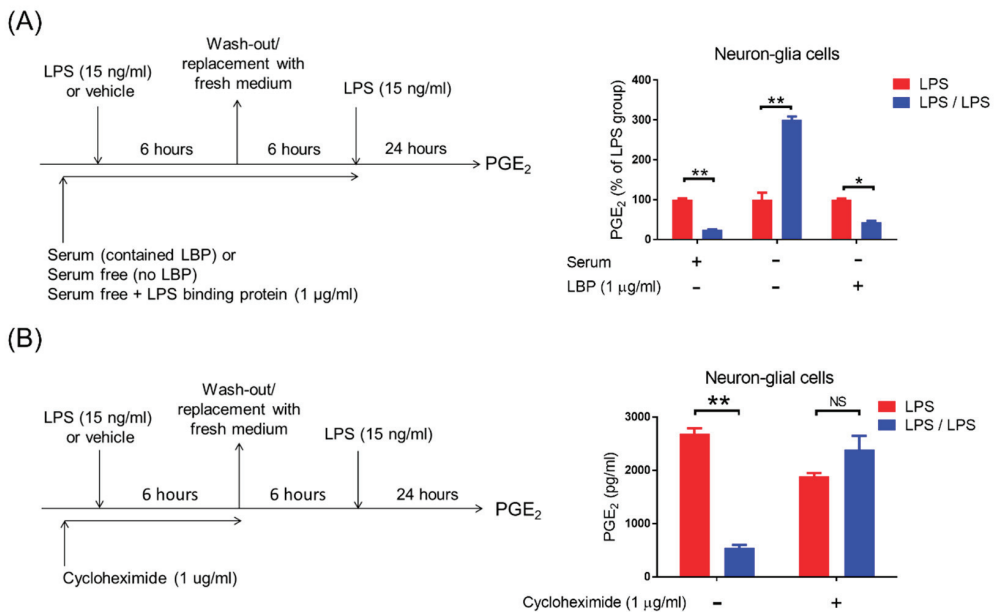


Figure 4. TLR4 signal and de novo protein synthesis is required for the development of PGE₂ tolerance in neuron–glial cells. **(A)** Left panel: Experimental procedure for studying the TLR4’s role in PGE₂ reduction during the endotoxin tolerance challenges. Right panel: Measurement of PGE₂ production in the NG cultures with or without endotoxin tolerance challenge (LPS-treated versus LPS/LPS-treated group) in the conditions of 10% serum medium, serum-free medium, or serum-free plus LBP (1 μ g/mL) at 24 h by ELISA. Data are expressed as the mean \pm SEM from three independent experiments in duplicate, LPS group versus the LPS/LPS group. * $p < 0.05$, ** $p < 0.01$. **(B)** Left panel: Experimental procedure for studying the role of de novo protein synthesis in PGE₂ reduction in response to endotoxin tolerance. Right panel: After treatment with cycloheximide (1 μ g/mL) for 1 h, the NG cultures were applied to the procedure of the endotoxin tolerance challenge (LPS-treated versus LPS/LPS-treated group). PGE₂ level in the supernatant was detected 24 h after treatment by ELISA. Data are expressed as the mean \pm SEM from three independent experiments in duplicate, LPS group versus the LPS/LPS group. ** $p < 0.01$, NS, not significant.

4. Discussion

As the first responder to the immune challenge, microglia secrete a wide spectrum and various inflammatory factors at inflammatory conditions, including IL-1 β , TNF- α , PGE₂, and BDNF, to prevent invading pathogens [34]. However, the uncontrolled and unresolved inflammation induced by microglia can damage the neurons [34]. It is relatively difficult to distinguish the functional role of microglia as either “protective” or “injurious” to the neurons during the neuroinflammatory process. Having a better understanding of heterogenous microglial activation during the inflammatory process, such as the occurrence of microglial endotoxin tolerance, has become a critical issue in developing microglia-based therapy for inflammation-related brain diseases [35,36]. Through using multiple reconstituted brain cell cultures, including neuron–glial, mixed glial, neuron-enriched, and microglia-enriched cultures, the main strength of the current study is to uncover the regulatory mechanisms of microglial PGE₂ tolerance by interacting with other brain cells, such as neurons and astroglia. However, this NG culture system does not contain oligodendrocytes, which are the myelinating cells of the CNS. Interestingly, endotoxin tolerance of PGE₂ occurs in NG cells (Figure 1), implying that oligodendrocytes do not participate in the regulation of PGE₂ tolerance in microglia. Together, this study explored the immune-suppressive mechanism of PGE₂ production mediated by neuron–microglia interactions via TLR4 signal-derived de novo protein synthesis in response to repeated LPS exposure (Figure 5).

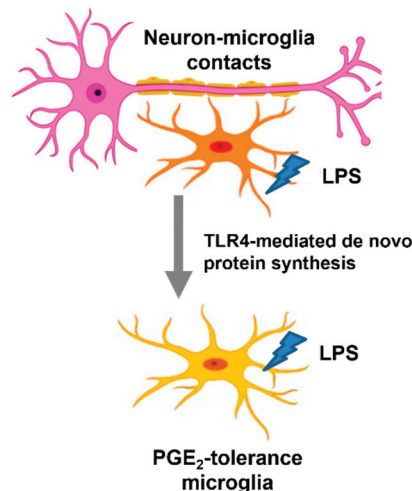


Figure 5. Indispensable role of neuron–microglia contacts for PGE₂ tolerance via TLR4-dependant de novo protein synthesis. Schematic of neuron–microglia contacts alter the immune property of microglia for development of PGE₂ tolerance via TLR4-derived de novo protein synthesis under ET challenge. Without neural contacts, microglia alone or cultured with astroglia or incubated with neural soluble factors fail to show endotoxin tolerance of PGE₂.

In addition to electrical signal transmission, neurons are important immune regulators in restraining immune activation of homeostatic microglia at normal conditions, referred to as immune checkpoint [37,38]. The communications among neurons and microglia are bidirectional and reciprocal through various soluble factors and in receptor–ligand interactions [38,39]. With a volume transmission manner, neurons release the soluble factors out of the synaptic cleft to trigger receptor-mediated signals in microglia [40,41]. The neural soluble factors, such as ATP, glutamate, GABA, CSF-1, and TGF- β , are capable of regulating phagocytosis, motility, and viability of microglia [40,42,43]. On the other hand, many receptor ligands (i.e., CD47, CD200, CD22, and HSP60) on the surface of neurons

directly bind with their corresponding surface receptors on microglia (i.e., CD172a, CD200R, CD45, and TREM2) that represent the classical contact-dependent communications [44–48]. Overall, these humoral or contacts signals from neurons not only lead microglia to prune neural synapses and neurites, and remove the apoptotic neurons during early brain development [45,47], but they also modulate motility, surveillance, and immunity of microglia at inflammatory conditions [44,46,48]. Our data showed that, in response to the ET challenge, microglial PGE₂ tolerance occurred in the presence of neurons (Figure 1), while microglia alone or microglia co-cultured with astroglia failed to develop PGE₂ tolerance (Figure 2). Furthermore, neuron–microglia contacts participate in neuron-mediated PGE₂ tolerance in microglia (Figure 3). Receptor–ligand interactions among neurons and microglia may exert their functions to control microglial PGE₂ tolerance. However, molecular details in neural contacts for microglia ET development remain an open question that will be further investigated.

Toll-like receptors (TLRs) function as the prime cellular sensors in innate immune cells for microbial components. Thus, its activation must be properly controlled by various mechanisms to maintain homeostasis. For instance, the induction of endotoxin tolerance by TLR4-ligand lipopolysaccharide (LPS) is one mechanism to prevent overstimulation from continuous exposure to the same and related danger signals [49]. The activation of the LPS receptor complex induces TLR4 dimerization/oligomerization with rapid activation of the MyD88-dependent signaling and TRIF-dependent signaling pathway, and further triggers various transcription factors, leading to strong production of pro-inflammatory cytokines [50]. Additionally, the activity of the microRNA miR-146a—known to target key elements of the myeloid differentiation factor 88 (MyD88) signaling pathway—including IL-1 receptor-associated kinase (IRAK1), IRAK2, and tumor necrosis factor (TNF) receptor-associated factor 6 (TRAF6), has been reported to establish and sustain tolerance [51]. Our data revealed that TLR4 activation and de novo protein synthesis are required for developing neuron govern PGE₂ tolerance in microglia during ET (Figure 4). It is important to further study the mechanisms underlying neurons that modulate microglial TLR4 activation, its downstream signaling pathways, and de novo protein synthesis to preserve PGE₂ tolerance.

Although the mechanism of ET formation in the brain and cultured brain slices or microglial cells have been reported [52–56], microglial PGE₂ tolerance has not been fully investigated. Dr. Ajmone-Cat and his colleagues have been the first to report that the production of TNF- α , nitric oxide (NO), PGE₂, and 15-deoxy- Δ 12,14-PGJ2 (15d-PGJ2) was measured in primary rat microglial cultures received to one, two, or three consecutive LPS stimulations [53]. The results indicated that the ability of microglial cells to produce NO, TNF- α , and 15d-PGJ2 upon the first LPS challenge rapidly declined after the second and third stimulations, whereas cyclooxygenase-2 and PGE₂ synthesis remained constantly elevated [53]. Further mechanistic studies in the transcription factors nuclear factor kappa B and CREB and the p38 MAPK revealed that the single or multiple LPS stimulations evoke profoundly different signaling pathways [53]. Even if the ET treatment regimens and species are distinct, similar results in this study also showed the failure of PGE₂ tolerance (even having higher PGE₂ production) in mouse microglia-enriched cultures with repeated LPS exposure (Figure 2). Accordingly, these data suggested that the circumstance of the CNS microenvironment, such as the presence of healthy neurons, plays an important regulating role in developing microglial ET [11]. Alternatively, they can determine if neurodegeneration-associated molecular patterns (NAMPs) participate in the disruption of microglial ET and whether its mechanism may provide attracted immune therapeutic targets for neurodegenerative disease.

In this study, we identified a distinct and essential role of non-immune brain cells, i.e., neurons in the development of PGE₂ tolerance in microglia. In the absence of neurons, microglia-enriched and mixed glial cultures failed to form PGE₂ tolerance. Notably, neural contacts program microglial PGE₂ tolerance—not its soluble factors. To the best of our knowledge, our study provides the first evidence that non-immune cells, i.e., neurons,

can influence the capacity of microglial PGE₂. Moreover, this study revealed a novel regulatory role of neuron–microglia contacts in the development of microglial PGE₂.

Author Contributions: H.-C.K. and C.-H.C. designed the research protocol; H.-C.K., K.-F.L., S.-L.C., S.-C.C., L.-Y.L., W.-P.C., C.-C.C. and C.-H.C. performed the research; H.-C.K. and C.-H.C. analyzed the data; H.-C.K. and C.-H.C. wrote the paper; and C.-H.C. supervised the research. All authors have read and agreed to the published version of the manuscript.

Funding: This work was supported by grants MOST 105-2320-B-006-056-MY2, MOST 107-2320-B-006-046-MY3, and MOST 110-2320-B-255-005 -MY3 from the Taiwan Ministry of Science and Technology. This study was supported by grants CMRPF6K0071, CMRPF6K0072, and ZRRPF6L0011 from Chang Gung Memorial Hospital, Chiayi, Taiwan, and Chang Gung University of Science and Technology, Chia-Yi Campus, Taiwan.

Institutional Review Board Statement: The study was conducted according to the guidelines of the Declaration of Helsinki, and approved by the Animal Care and Use Committee of National Cheng Kung University (NCKU) (protocol code 107073 and date of approval: 2018/08/01).

Informed Consent Statement: Not applicable.

Data Availability Statement: All relevant data are within the paper.

Acknowledgments: We thank Jau-Shyong Hong for supporting this work. We thank National Laboratory Animal Center (NLAC), NARLabs, Taiwan, for technical support in contract breeding and testing services.

Conflicts of Interest: The authors declare no conflict of interest.

References

- Li, Q.; Barres, B.A. Microglia and macrophages in brain homeostasis and disease. *Nat. Rev. Immunol.* **2018**, *18*, 225–242. [CrossRef] [PubMed]
- Luo, X.; Chen, S.-D. The changing phenotype of microglia from homeostasis to disease. *Transl. Neurodegener.* **2012**, *1*, 9. [CrossRef]
- Bohlen, C.J.; Friedman, B.A.; Dejanovic, B.; Sheng, M. Microglia in Brain Development, Homeostasis, and Neurodegeneration. *Annu. Rev. Genet.* **2019**, *53*, 263–288. [CrossRef] [PubMed]
- Hoogland, I.C.; Houbolt, C.; van Westerloo, D.J.; van Gool, W.A.; van de Beek, D. Systemic inflammation and microglial activation: Systematic review of animal experiments. *J. Neuroinflamm.* **2015**, *12*, 1–13. [CrossRef]
- Orihuela, R.; McPherson, C.A.; Harry, G.J. Microglial M1/M2 polarization and metabolic states. *Br. J. Pharm.* **2016**, *173*, 649–665. [CrossRef] [PubMed]
- Xu, L.; He, D.; Bai, Y. Microglia-Mediated Inflammation and Neurodegenerative Disease. *Mol. Neurobiol.* **2016**, *53*, 6709–6715. [CrossRef]
- McDonough, A.; Weinstein, J.R. The role of microglia in ischemic preconditioning. *Glia* **2020**, *68*, 455–471. [CrossRef]
- Wendeln, A.-C.; Degenhardt, K.; Kaurani, L.; Gertig, M.; Ulas, T.; Jain, G.; Wagner, J.; Häslner, L.M.; Wild, K.; Skodras, A.; et al. Innate immune memory in the brain shapes neurological disease hallmarks. *Nature* **2018**, *556*, 332–338. [CrossRef]
- Neher, J.J.; Cunningham, C. Priming Microglia for Innate Immune Memory in the Brain. *Trends Immunol.* **2019**, *40*, 358–374. [CrossRef]
- Chu, C.H.; Chen, S.H.; Wang, Q.; Langenbach, R.; Li, H.; Zeldin, D.; Chen, S.L.; Wang, S.; Gao, H.; Lu, R.B.; et al. PGE₂ Inhibits IL-10 Production via EP2-Mediated beta-Arrestin Signaling in Neuroinflammatory Condition. *Mol. Neurobiol.* **2015**, *52*, 587–600. [CrossRef]
- Chu, C.H.; Wang, S.; Li, C.L.; Chen, S.H.; Hu, C.F.; Chung, Y.L.; Chen, S.L.; Wang, Q.; Lu, R.B.; Gao, H.M.; et al. Neurons and astroglia govern microglial endotoxin tolerance through macrophage colony-stimulating factor receptor-mediated ERK1/2 signals. *Brain Behav. Immun.* **2016**, *55*, 260–272. [CrossRef]
- Saccaro, L.F.; Schilliger, Z.; Perroud, N.; Piguët, C. Inflammation, Anxiety, and Stress in Attention-Deficit/Hyperactivity Disorder. *Biomedicines* **2021**, *9*, 1313. [CrossRef] [PubMed]
- Tsay, H.-J.; Liu, H.-K.; Kuo, Y.-H.; Chiu, C.-S.; Liang, C.-C.; Chung, C.-W.; Chen, C.-C.; Chen, Y.-P.; Shiao, Y.-J. EK100 and Antrodin C Improve Brain Amyloid Pathology in APP/PS1 Transgenic Mice by Promoting Microglial and Perivascular Clearance Pathways. *Int. J. Mol. Sci.* **2021**, *22*, 10413. [CrossRef] [PubMed]
- Chen, Y.; Lin, J.; Schlotterer, A.; Kurowski, L.; Hoffmann, S.; Hammad, S.; Dooley, S.; Buchholz, M.; Hu, J.; Fleming, I.; et al. MicroRNA-124 Alleviates Retinal Vasoregression via Regulating Microglial Polarization. *Int. J. Mol. Sci.* **2021**, *22*, 11068. [CrossRef] [PubMed]
- Andreasson, K. Emerging roles of PGE₂ receptors in models of neurological disease. *Prostaglandins Other Lipid Mediat.* **2010**, *91*, 104–112. [CrossRef] [PubMed]

16. Yagami, T.; Koma, H.; Yamamoto, Y. Pathophysiological Roles of Cyclooxygenases and Prostaglandins in the Central Nervous System. *Mol. Neurobiol.* **2016**, *53*, 4754–4771. [CrossRef]
17. Fathali, N.; Ostrowski, R.P.; Lekic, T.; Jadhav, V.; Tong, W.; Tang, J.; Zhang, J.H. Cyclooxygenase-2 inhibition provides lasting protection against neonatal hypoxic-ischemic brain injury. *Crit. Care Med.* **2010**, *38*, 572–578. [CrossRef]
18. Teismann, P. COX-2 in the neurodegenerative process of Parkinson's disease. *Biofactors* **2012**, *38*, 395–397. [CrossRef]
19. Minghetti, L. Cyclooxygenase-2 (COX-2) in Inflammatory and Degenerative Brain Diseases. *J. Neuropathol. Exp. Neurol.* **2004**, *63*, 901–910. [CrossRef]
20. Li, W.; Wu, S.; Hickey, R.W.; Rose, M.E.; Chen, J.; Graham, S.H. Neuronal cyclooxygenase-2 activity and prostaglandins PGE₂, PGD₂, and PGF₂ alpha exacerbate hypoxic neuronal injury in neuron-enriched primary culture. *Neurochem. Res.* **2008**, *33*, 490–499. [CrossRef]
21. Hickey, R.W.; Adelson, P.D.; Johnnides, M.J.; Davis, D.S.; Yu, Z.; Rose, M.E.; Chang, Y.F.; Graham, S.H. Cyclooxygenase-2 activity following traumatic brain injury in the developing rat. *Pediatr. Res.* **2007**, *62*, 271–276. [CrossRef] [PubMed]
22. Rojas, A.; Chen, D.; Ganesh, T.; Varvel, N.H.; Dingleline, R. The COX-2/prostanoid signaling cascades in seizure disorders. *Expert Opin. Ther. Targets* **2019**, *23*, 1–13. [CrossRef] [PubMed]
23. Xia, Q.; Hu, Q.; Wang, H.; Yang, H.; Gao, F.; Ren, H.; Chen, D.; Fu, C.; Zheng, L.; Zhen, X.; et al. Induction of COX-2-PGE₂ synthesis by activation of the MAPK/ERK pathway contributes to neuronal death triggered by TDP-43-depleted microglia. *Cell Death Dis.* **2015**, *6*, e1702. [CrossRef]
24. Hoozemans, J.J.; Veerhuis, R.; Janssen, I.; van Elk, E.J.; Rozemuller, A.J.; Eikelenboom, P. The role of cyclo-oxygenase 1 and 2 activity in prostaglandin E(2) secretion by cultured human adult microglia: Implications for Alzheimer's disease. *Brain Res.* **2002**, *951*, 218–226. [CrossRef]
25. Johansson, J.U.; Woodling, N.S.; Shi, J.; Andreasson, K.I. Inflammatory Cyclooxygenase Activity and PGE₂ Signaling in Models of Alzheimer's Disease. *Curr. Immunol. Rev.* **2015**, *11*, 125–131. [CrossRef]
26. Bartels, A.L.; Leenders, K.L. Cyclooxygenase and neuroinflammation in Parkinson's disease neurodegeneration. *Curr. Neuropharmacol.* **2010**, *8*, 62–68. [CrossRef]
27. Liang, X.; Wang, Q.; Shi, J.; Lokteva, L.; Breyer, R.M.; Montine, T.J.; Andreasson, K. The prostaglandin E₂EP₂ receptor accelerates disease progression and inflammation in a model of amyotrophic lateral sclerosis. *Ann. Neurol.* **2008**, *64*, 304–314. [CrossRef]
28. Liu, B.; Du, L.; Hong, J.S. Naloxone protects rat dopaminergic neurons against inflammatory damage through inhibition of microglia activation and superoxide generation. *J. Pharmacol. Exp. Ther.* **2000**, *293*, 607–617.
29. Qin, L.; Li, G.; Qian, X.; Liu, Y.; Wu, X.; Liu, B.; Hong, J.-S.; Block, M.L. Interactive role of the toll-like receptor 4 and reactive oxygen species in LPS-induced microglia activation. *Glia* **2005**, *52*, 78–84. [CrossRef]
30. Ciesielska, A.; Matyjek, M.; Kwiatkowska, K. TLR4 and CD14 trafficking and its influence on LPS-induced pro-inflammatory signaling. *Cell Mol. Life Sci.* **2021**, *78*, 1233–1261. [CrossRef]
31. Nahid, A.; Satoh, M.; Chan, E.K. MicroRNA in TLR signaling and endotoxin tolerance. *Cell. Mol. Immunol.* **2011**, *8*, 388–403. [CrossRef] [PubMed]
32. Kim, S.J.; Kim, H.M. Dynamic lipopolysaccharide transfer cascade to TLR4/MD2 complex via LBP and CD14. *BMB Rep.* **2017**, *50*, 55–57. [CrossRef]
33. Ryu, J.K.; Kim, S.J.; Rah, S.H.; Kang, J.I.; Jung, H.E.; Lee, D.; Lee, H.K.; Lee, J.O.; Park, B.S.; Yoon, T.Y.; et al. Reconstruction of LPS Transfer Cascade Reveals Structural Determinants within LBP, CD14, and TLR4-MD2 for Efficient LPS Recognition and Transfer. *Immunity* **2017**, *46*, 38–50. [CrossRef]
34. Block, M.L.; Zecca, L.; Hong, J.S. Microglia-mediated neurotoxicity: Uncovering the molecular mechanisms. *Nat. Rev. Neurosci.* **2007**, *8*, 57–69. [CrossRef]
35. Stratoulis, V.; Venero, J.L.; Tremblay, M.E.; Joseph, B. Microglial subtypes: Diversity within the microglial community. *EMBO J.* **2019**, *38*, e101997. [CrossRef] [PubMed]
36. De Schepper, S.; Crowley, G.; Hong, S. Understanding microglial diversity and implications for neuronal function in health and disease. *Dev. Neurobiol.* **2021**, *81*, 507–523. [CrossRef]
37. Deczkowska, A.; Amit, I.; Schwartz, M. Microglial immune checkpoint mechanisms. *Nat. Neurosci.* **2018**, *21*, 779–786. [CrossRef]
38. Szepesi, Z.; Manouchehrian, O.; Bachiller, S.; Deierborg, T. Bidirectional Microglia–Neuron Communication in Health and Disease. *Front. Cell. Neurosci.* **2018**, *12*, 323. [CrossRef] [PubMed]
39. Posfai, B.; Cserep, C.; Orsolits, B.; Denes, A. New Insights into Microglia–Neuron Interactions: A Neuron's Perspective. *Neuroscience* **2019**, *405*, 103–117. [CrossRef]
40. Gomes, F.; Spohr, T.; Martinez, R.; Neto, V.M. Cross-talk between neurons and glia: Highlights on soluble factors. *Braz. J. Med Biol. Res.* **2001**, *34*, 611–620. [CrossRef] [PubMed]
41. Liu, H.; Leak, R.K.; Hu, X. Neurotransmitter receptors on microglia. *Stroke Vasc. Neurol.* **2016**, *1*, 52–58. [CrossRef]
42. Veremeyko, T.; Yung, A.W.; Dukhinova, M.; Strelkova, T.; Ponomarev, E.D. The Role of Neuronal Factors in the Epigenetic Reprogramming of Microglia in the Normal and Diseased Central Nervous System. *Front. Cell. Neurosci.* **2019**, *13*, 453. [CrossRef]
43. Mead, E.L.; Mosley, A.; Eaton, S.; Dobson, L.; Heales, S.J.; Pocock, J.M. Microglial neurotransmitter receptors trigger superoxide production in microglia; consequences for microglial-neuronal interactions. *J. Neurochem.* **2012**, *121*, 287–301. [CrossRef]
44. Lyons, A.; Downer, E.; Crotty, S.; Nolan, Y.; Mills, K.; Lynch, M.A. CD200 Ligand Receptor Interaction Modulates Microglial Activation In Vivo and In Vitro: A Role for IL-4. *J. Neurosci.* **2007**, *27*, 8309–8313. [CrossRef] [PubMed]

45. Lehrman, E.K.; Wilton, D.K.; Litvina, E.Y.; Welsh, C.A.; Chang, S.T.; Frouin, A.; Walker, A.J.; Heller, M.D.; Umemori, H.; Chen, C.; et al. CD47 Protects Synapses from Excess Microglia-Mediated Pruning during Development. *Neuron* **2018**, *100*, 120–134.e6. [CrossRef]
46. Mott, R.T.; Ait-Ghezala, G.; Town, T.; Mori, T.; Vendrame, M.; Zeng, J.; Ehrhart, J.; Mullan, M.; Tan, J. Neuronal expression of CD22: Novel mechanism for inhibiting microglial proinflammatory cytokine production. *Glia* **2004**, *46*, 369–379. [CrossRef] [PubMed]
47. Pluvinage, J.V.; Haney, M.S.; Smith, B.A.H.; Sun, J.; Iram, T.; Bonanno, L.; Li, L.; Lee, D.P.; Morgens, D.W.; Yang, A.C.; et al. CD22 blockade restores homeostatic microglial phagocytosis in ageing brains. *Nature* **2019**, *568*, 187–192. [CrossRef] [PubMed]
48. von Saucken, V.E.; Jay, T.R.; Landreth, G.E. The effect of amyloid on microglia-neuron interactions before plaque onset occurs independently of TREM2 in a mouse model of Alzheimer’s disease. *Neurobiol. Dis.* **2020**, *145*, 105072. [CrossRef]
49. Bohannon, J.K.; Hernandez, A.; Enkhbaatar, P.; Adams, W.L.; Sherwood, E.R. The immunobiology of toll-like receptor 4 agonists: From endotoxin tolerance to immunoadjuvants. *Shock* **2013**, *40*, 451–462. [CrossRef]
50. Hernandez, A.; Bohannon, J.K.; Luan, L.; Fensterheim, B.A.; Guo, Y.; Patil, N.K.; McAdams, C.; Wang, J.; Sherwood, E.R. The role of MyD88- and TRIF-dependent signaling in monophosphoryl lipid A-induced expansion and recruitment of innate immunocytes. *J. Leukoc. Biol.* **2016**, *100*, 1311–1322. [CrossRef]
51. Nahid, M.A.; Pauley, K.M.; Satoh, M.; Chan, E.K. miR-146a is critical for endotoxin-induced tolerance: Implication in Innate Immunity. *J. Biol. Chem.* **2009**, *284*, 34590–34599. [CrossRef] [PubMed]
52. Ajmone-Cat, M.A.; Mancini, M.; De Simone, R.; Cilli, P.; Minghetti, L. Microglial polarization and plasticity: Evidence from organotypic hippocampal slice cultures. *Glia* **2013**, *61*, 1698–1711. [CrossRef] [PubMed]
53. Ajmone-Cat, M.A.; Nicolini, A.; Minghetti, L. Prolonged exposure of microglia to lipopolysaccharide modifies the intracellular signaling pathways and selectively promotes prostaglandin E2 synthesis. *J. Neurochem.* **2003**, *87*, 1193–1203. [CrossRef] [PubMed]
54. Beurel, E.; Jope, R.S. Glycogen synthase kinase-3 regulates inflammatory tolerance in astrocytes. *Neuroscience* **2010**, *169*, 1063–1070. [CrossRef]
55. Schaafsma, W.; Zhang, X.; van Zomeren, K.C.; Jacobs, S.; Georgieva, P.B.; Wolf, S.A.; Kettenmann, H.; Janova, H.; Saiepour, N.; Hanisch, U.K.; et al. Long-lasting pro-inflammatory suppression of microglia by LPS-preconditioning is mediated by RelB-dependent epigenetic silencing. *Brain Behav. Immun.* **2015**, *48*, 205–221. [CrossRef]
56. Chistyakov, D.V.; Astakhova, A.A.; Azbukina, N.V.; Goriainov, S.V.; Chistyakov, V.V.; Sergeeva, M.G. Cellular Model of Endotoxin Tolerance in Astrocytes: Role of Interleukin 10 and Oxylipins. *Cells* **2019**, *8*, 1553. [CrossRef] [PubMed]



Article

In Vitro and In Vivo Effects of SerpinA1 on the Modulation of Transthyretin Proteolysis

Filipa Bezerra ^{1,2}, Christoph Niemietz ³, Hartmut H. J. Schmidt ^{3,†}, Andree Zibert ³, Shuling Guo ⁴, Brett P. Monia ⁴, Paula Gonçalves ¹, Maria João Saraiva ^{1,2} and Maria Rosário Almeida ^{1,2,*}

¹ Molecular Neurobiology Group, i3S-Instituto de Investigação e Inovação em Saúde, IBMC-Instituto de Biologia Molecular e Celular, Universidade do Porto, 4200-135 Porto, Portugal; carla.bezerra@ibmc.up.pt (F.B.); b12458@med.uminho.pt (P.G.); mjsaraiv@ibmc.up.pt (M.J.S.)

² Departamento de Biologia Molecular, ICBAS-Instituto de Ciências Biomédicas Abel Salazar, Universidade do Porto, 4050-313 Porto, Portugal

³ Medizinische Klinik B, Universitätsklinikum Münster, 48149 Münster, Germany; Christoph.Niemietz@taconic.com (C.N.); hepar@ume.de (H.H.J.S.); Andree.Zibert@ukmuenster.de (A.Z.)

⁴ Ionis Pharmaceuticals, Carlsbad, CA 92010, USA; sguo@ionisph.com (S.G.); bmonia@ionisph.com (B.P.M.)

* Correspondence: ralmeida@ibmc.up.pt

† Present address: Universitätsklinikum Essen, Germany.

Abstract: Transthyretin (TTR) proteolysis has been recognized as a complementary mechanism contributing to transthyretin-related amyloidosis (ATTR amyloidosis). Accordingly, amyloid deposits can be composed mainly of full-length TTR or contain a mixture of both cleaved and full-length TTR, particularly in the heart. The fragmentation pattern at Lys48 suggests the involvement of a serine protease, such as plasmin. The most common TTR variant, TTR V30M, is susceptible to plasmin-mediated proteolysis, and the presence of TTR fragments facilitates TTR amyloidogenesis. Recent studies revealed that the serine protease inhibitor, SerpinA1, was differentially expressed in hepatocyte-like cells (HLCs) from ATTR patients. In this work, we evaluated the effects of SerpinA1 on in vitro and in vivo modulation of TTR V30M proteolysis, aggregation, and deposition. We found that plasmin-mediated TTR proteolysis and aggregation are partially inhibited by SerpinA1. Furthermore, in vivo downregulation of SerpinA1 increased TTR levels in mice plasma and deposition in the cardiac tissue of older animals. The presence of TTR fragments was observed in the heart of young and old mice but not in other tissues following SerpinA1 knockdown. Increased proteolytic activity, particularly plasmin activity, was detected in mice plasmas. Overall, our results indicate that SerpinA1 modulates TTR proteolysis and aggregation in vitro and in vivo.

Citation: Bezerra, F.; Niemietz, C.; Schmidt, H.H.J.; Zibert, A.; Guo, S.; Monia, B.P.; Gonçalves, P.; Saraiva, M.J.; Almeida, M.R. In Vitro and In Vivo Effects of SerpinA1 on the Modulation of Transthyretin Proteolysis. *Int. J. Mol. Sci.* **2021**, *22*, 9488. <https://doi.org/10.3390/ijms22179488>

Academic Editor: Masaru Tanaka

Received: 20 July 2021

Accepted: 28 August 2021

Published: 31 August 2021

Keywords: transthyretin; SerpinA1; ATTR amyloidosis; TTR proteolysis; plasmin

Publisher's Note: MDPI stays neutral with regard to jurisdictional claims in published maps and institutional affiliations.



Copyright: © 2021 by the authors. Licensee MDPI, Basel, Switzerland. This article is an open access article distributed under the terms and conditions of the Creative Commons Attribution (CC BY) license (<https://creativecommons.org/licenses/by/4.0/>).

1. Introduction

Transthyretin-related amyloidoses (ATTR amyloidosis) are characterized by extracellular deposition of insoluble TTR amyloid fibrils in several tissues, being polyneuropathy and cardiomyopathy the major clinical manifestations, as reviewed in [1,2]. There are two types of ATTR amyloidoses: hereditary amyloidosis (ATTRm) and wild-type ATTR amyloidosis (ATTRwt) [3]. ATTRm occurs through single-residue substitutions in TTR, mainly producing less stable variants [4–6], whereas ATTRwt is an age-related disorder, affecting 20–25% of the population over 80 years, with predominant cardiac phenotype, characterized by wild-type (WT) TTR amyloid deposits [7,8].

Despite it is widely accepted that tetramer destabilization is a rate-limiting step for the development of amyloid fibrils [9–12], TTR proteolysis has been increasingly recognized as another mechanism driving TTR amyloid formation. Several studies reported the existence of different TTR amyloid deposits in a range of tissues. Thus, amyloid deposits might be composed mainly of full-length TTR (type-B fibrils) or by a mixture of both

cleaved and full-length TTR (type-A fibrils) [13–16]. Type-A fibrils occur in several tissues, particularly in the heart and are related to the development of restrictive cardiomyopathy after liver transplantation, leading to poor clinical outcomes in ATTR V30M patients [17]. The protease responsible for TTR cleavage has not yet been identified. However, the specific fragmentation at Lys48 in the TTR polypeptide suggests that it could be a trypsin-like serine protease [18]. In vitro experiments using recombinant trypsin indicate that several amyloidogenic TTR variants are susceptible to trypsin-mediated proteolysis [19–21]. The process of cleavage and release of the 49–127 TTR fragment, the most frequent fragment detected in fibrils, is faster for the highly amyloidogenic variant, TTR S52P, being the 49–127 C-terminal fragment rapidly incorporated into amyloid fibrils [19,20].

Additionally, in silico studies pointed out plasmin as a plausible pathophysiological candidate protease involved in the process of TTR amyloid formation [22]. Furthermore, the ubiquitous distribution of plasmin, its structural similarities to trypsin [22], and the reported activation of plasminogen activation system (PAS) in other amyloid-related disorders, such as Alzheimer’s disease [23] and immunoglobulin light chain (AL) amyloidosis [24–26] indicate that this protease could have a key role in TTR amyloidogenesis. Indeed, the 49–127 C-terminal TTR fragment was also found in in vitro plasmin-digested TTR S52P samples, suggesting that TTR-digested samples are more prone to aggregate than the non-digested ones [22].

On the other hand, serine protease inhibitors (Serpins), particularly SerpinA1, have also been related to pathological proteinopathies, such as Alzheimer’s disease [27–29]. We hypothesized that SerpinA1 may act as a modulator of TTR proteolysis/fibrillogenesis. SerpinA1 belongs to the clade A serpins, which are classified as antitrypsin-like [30]. SerpinA1 and also SerpinA3 were found to be differentially expressed in ATTRm patients compared to healthy controls [31,32]. The SerpinA1 mRNA was found to be differentially expressed in hepatocyte-like cells (HLCs) from ATTR patients compared to healthy controls and, a high inverse correlation between *SerpinA1* and *TTR* genes was also observed. Upon TTR knockdown in HLCs the correlation was abolished [33]. Recently, it was demonstrated that SerpinA1 knockdown modulates TTR expression in both cellular and animal models, performing an important role in the development of ATTR amyloidosis [34].

In this study, we further explored the role of SerpinA1 on the in vitro and in vivo modulation of plasmin-mediated TTR proteolysis and how this modulation may impact TTR amyloidogenesis to contribute to the development of more targeted therapies for the treatment of ATTR amyloidosis.

2. Results

2.1. SerpinA1 Inhibits In Vitro Plasmin-Mediated Proteolysis of Transthyretin V30M

Previous studies revealed that similarly to TTR S52P, recombinant TTR V30M was also susceptible to plasmin-mediated proteolysis [22]. In addition, amyloid deposits extracted from cardiac and adipose tissue specimens from ATTR V30M patients were composed of a mixture of both cleaved and full-length TTR [13–15]. Thus, we performed in vitro proteolysis experiments to evaluate whether SerpinA1 performs a role on the inhibition of plasmin-mediated TTR V30M proteolysis. Recombinant TTR V30M was incubated with plasmin at 37 °C for 24 h, and the resulting mixture was analyzed by SDS-PAGE and Western blot. Besides the dimeric (~35 kDa) and monomeric (~17 kDa) TTR V30M forms, Western blotting analysis revealed the presence of two different TTR fragments, in contrast to non-digested samples (Figure 1A and Supplementary data Figure S1). These fragments were detected with the commercially available antibody produced and characterized in our lab [35], anti-TTR mutant (Y78F), clone AD7 (Figure 1A) but not with rabbit polyclonal anti-TTR from DAKO (Figure 1B).

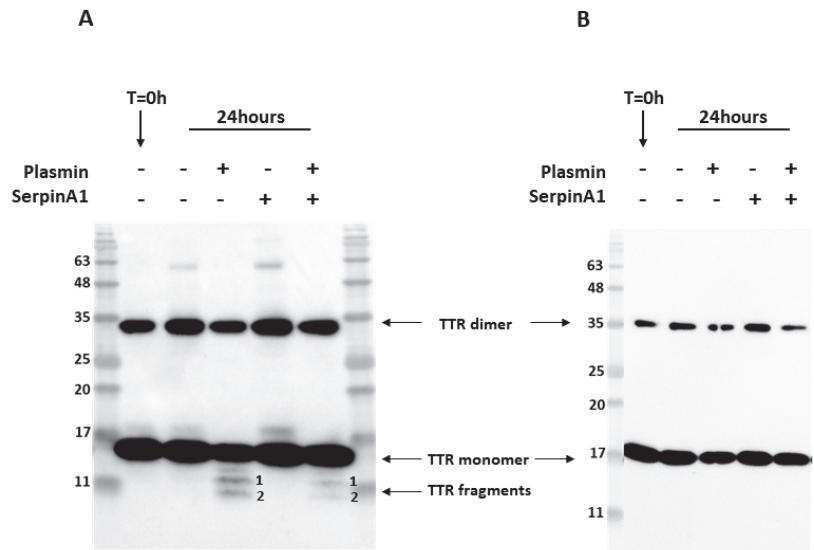


Figure 1. Plasmin cleaves transthyretin V30M, and its activity is inhibited by SerpinA1. Representative images of Western blotting analysis of the three independent in vitro experiments. Western blot was performed using two different antibodies targeting human TTR, mouse anti-TTR mutant (Y78F), clone AD7 (A), and rabbit anti-transthyretin (B). Both antibodies detected dimeric and monomeric TTR forms. However, only the mouse anti-TTR mutant (Y78F) clone AD7 detects TTR fragments (A).

N-terminal sequencing analysis of the TTR fragments firstly observed in Western blotting analysis indicates that band 1 corresponds to a peptide starting at position 49 and band 2 to a peptide starting at the first amino acid of TTR polypeptide chain (Table 1). Furthermore, the bands corresponding to TTR fragments were excised from SDS-PAGE gels and further analyzed by mass spectrometry (MS) analysis after trypsin digestion. These MS experiments revealed that band 1 was composed of the peptides with mass corresponding to the amino acids 81–103, 104–127, 105–126, and 105–127 (Table S1), which along with N-terminal sequencing data, indicated that band 1 should correspond to the TTR fragment 49–127 (Table 1). Band 2 was composed by the peptides with mass corresponding to the amino acids 1–15, 22–34, 35–48, and 36–48 (Table S1). Together with N-terminal sequencing data, our results indicate that band 2 was the TTR fragment 1–48 (Table 1). Intriguingly, the band containing 1–48 N-terminal TTR fragment also revealed the presence of a C-terminal peptide comprising the amino acids 105–127. Since the number of peptide-spectrum matches (PSMs) identified for that peptide group was only two, which was too low compared to the N-terminal peptides, this might indicate that this C-terminal peptide 105–127 was a contaminant.

Table 1. Identification of transthyretin peptides upon plasmin digestion by N-terminal sequencing. Band 1 starts at the amino acid residue 49, whereas band 2 starts at the first amino acid residue in the transthyretin polypeptide chain, indicating that band 1 corresponds to the 49–127 C-terminal fragment and band 2 to the 1–48 N-terminal fragment.

TTR Fragment	Residue Number				
	1	2	3	4	5
#1	T	S	E	S	G
#2	G	P	T	G	T

Following, we investigated the role of the serine protease inhibitor, SerpinA1, as a modulator of plasmin-mediated TTR proteolysis. We found that TTR proteolysis was partially inhibited in the presence of SerpinA1 (Figure 1A and Figure S1). No TTR fragments were observed neither before the assay nor in the absence of plasmin, excluding the influence of TTR auto-proteolysis or degradation. In opposition to TTR V30M, TTR WT was not susceptible to plasmin-mediated proteolysis under the same conditions as presented in supplementary data (Figure S2).

2.2. SerpinA1 Inhibits In Vitro Transthyretin V30M Aggregation upon Plasmin-Mediated Proteolysis

The presence of TTR fragments, particularly the 49–127 C-terminal peptide, was implicated in TTR amyloidogenesis. Studies of in vitro TTR cleavage indicated that this fragment generated upon digestion with trypsin or plasmin was rapidly incorporated into amyloid fibrils, suggesting that TTR proteolysis facilitated the process of TTR aggregation [19–22]. Similarly, in the present work, we investigated the influence of plasmin-mediated proteolysis on the aggregation potential of TTR V30M. Upon 24 h of incubation, both plasmin-digested and non-digested samples were characterized using dynamic light scattering (DLS) analysis (Figure 2). Plasmin-mediated proteolysis facilitates the process of TTR aggregation, as observed by the increase of TTR aggregated species (909.7 nm; 8.1%) along with the decrease of the soluble form (13.15 nm; 75.4%) (Figure 2B), comparatively to non-digested samples, in which TTR was only found in the soluble form (9.228 nm; 98.5%) (Figure 2A). In addition, TTR V30M incubated with SerpinA1 revealed the presence of soluble particles exhibiting a large diameter (23.81 nm, 100%) (Figure 2C), probably indicating the formation of TTR-SerpinA1 complex, as described previously [33]. Samples incubated with both plasmin and SerpinA1 presented less abundant and smaller TTR aggregates (537.7 nm; 4.3%) (Figure 2D), as compared to samples only incubated with plasmin (Figure 2B).

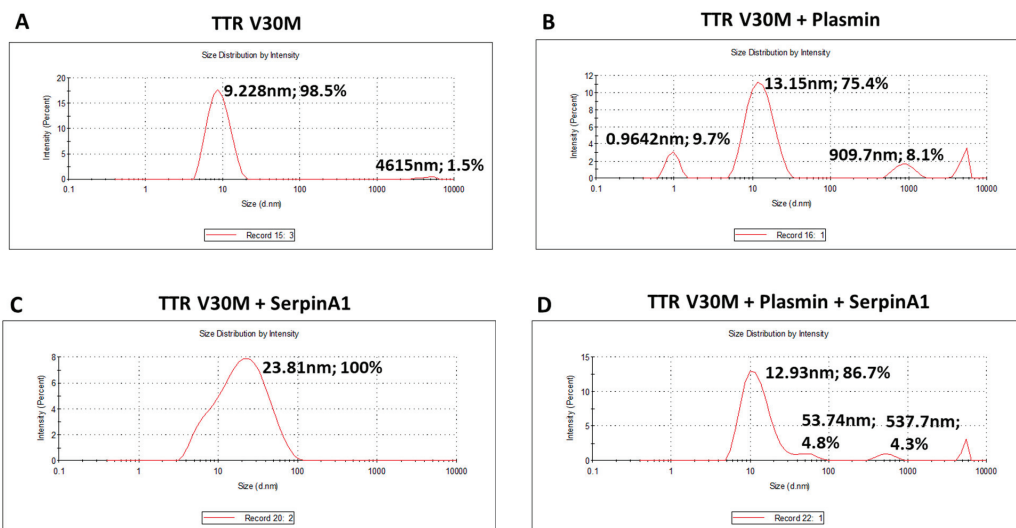


Figure 2. Plasmin enhances the transthyretin V30M aggregation, while SerpinA1 inhibits the process. Dynamic light scattering analysis was performed upon transthyretin V30M incubation at 37 °C for 24 h: (A) alone; (B) with plasmin; (C) with SerpinA1; (D) with plasmin and SerpinA1. The data results from three independent in vitro experiments, each one performed in triplicate.

Besides its function as a serine protease inhibitor, SerpinA1 also functions as an extracellular chaperone and recently, it was reported that SerpinA1 inhibited TTR amyloid formation in vitro [33]. Thus, the same samples were analyzed by thioflavin T (ThT) assays to evaluate the amyloid nature of the formed species. The results demonstrated that plasmin facilitates TTR V30M amyloid formation, as observed by the increased ThT emission fluorescence signals upon plasmin incubation (1086 ± 75.68 vs. 901.3 ± 91.88 in the absence of plasmin) (Figure 3). Moreover, in the presence of plasmin, TTR V30M amyloid formation was significantly inhibited by SerpinA1 (510 ± 60.58 vs. 1086 ± 75.68 in the absence of SerpinA1; $p < 0.05$). SerpinA1 per se seemed to inhibit TTR V30M amyloid formation (613 ± 134 vs. 901.3 ± 91.88 in the absence of SerpinA1) (Figure 3).

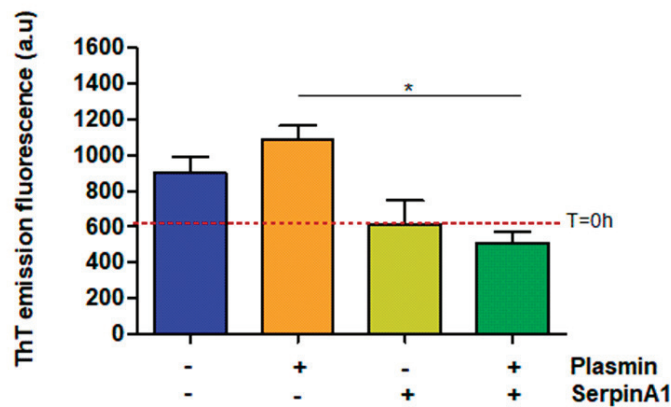


Figure 3. Transthyretin amyloid formation is favored upon plasmin-mediated proteolysis, being partially inhibited by SerpinA1. Thioflavin T experiments were performed upon transthyretin V30M incubation with plasmin and/or SerpinA1, at 37 °C for 24 h. The fluorescence emission signal of thioflavin T of transthyretin V30M at the beginning of the experiment ($t = 0$ h) is represented as the red dotted line around 607. The data results from three independent in vitro experiments ($n = 3$). Statistical analysis was performed using one-way ANOVA with Tukey's multiple comparison as post-test. * $p < 0.05$ in the presence of plasmin/presence of SerpinA1 vs. presence of plasmin/absence of SerpinA1, $q = 6.092$, $df = 3$. Effect size (r) = 0.924, odds ratio = 0.69 for an interval of confidence of 95%.

2.3. SerpinA1 Downregulation Increased Transthyretin Deposition in the Heart of Old Transgenic Mice Carrying Human Transthyretin V30M Mutation

Previous studies reported that SerpinA1 knockdown was accompanied by an increase in TTR mRNA expression, as well as TTR protein levels in HepG2 cells. In collaboration with our group, it was also reported that SerpinA1 knockdown resulted in an increase in TTR mRNA expression in mouse liver, as well as in TTR protein levels in plasmas of transgenic mice carrying human TTR V30M mutation (HM30) [34]. Therefore, we decided to investigate whether SerpinA1 was also specifically downregulated in the mouse heart and whether effects on TTR protein levels could be observed. For that, SerpinA1-specific ASOs were subcutaneously administered to HM30 mice once a week for six weeks. Western blotting analysis (Figure 4A–C), as well as immunohistochemistry (Figure 4D), confirmed that SerpinA1 was effectively downregulated in the heart from younger and older animals (0.018 ± 0.01 vs. 1.0 ± 0.18 in ASO-CTR, $p < 0.0001$). In addition, a significant increase in TTR protein in mice cardiac tissue was observed (1.6 ± 0.18 vs. 1.0 ± 0.14 in ASO-CTR group, $p = 0.020$) (Figure 4E–G).

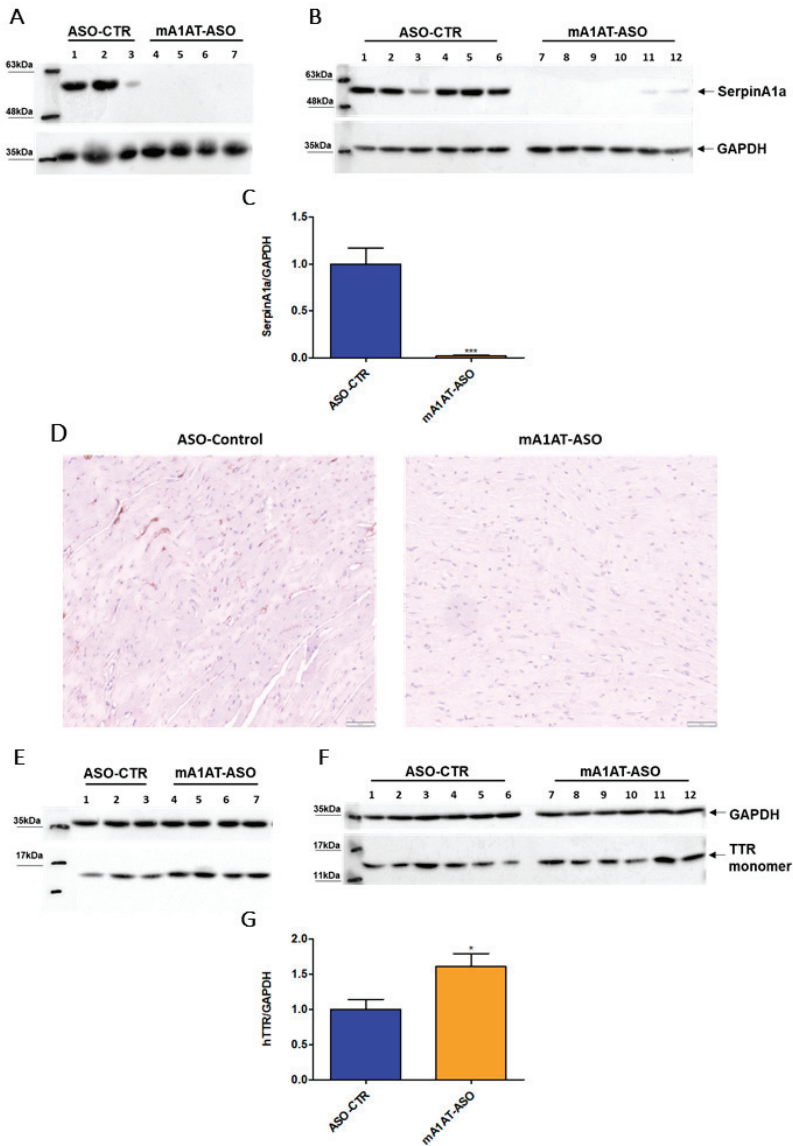


Figure 4. Human transthyretin was found to be increased in the heart of transgenic mice carrying human transthyretin V30M mutation upon SerpinA1 downregulation. Western blotting analysis of SerpinA1 and GAPDH expression in the heart of old (16–21 months, $n = 7$) (A) and young (12–13 months, $n = 12$) (B) mice. Quantification of SerpinA1 expression normalized to GAPDH (loading control protein) of the two pooled experiments (C). Immunohistochemistry data also reveal that SerpinA1 was effectively downregulated in the heart of HM30 mice. Images were captured at 10 \times magnification using Olympus BX50 microscope. Scale bar = 20 μ m (D). Western blotting of TTR and GAPDH expression in mice cardiac tissue of both old (E) and young (F) animals. Bar plot represents the quantification of transthyretin expression normalized to GAPDH of the two pooled in vivo experiments (G). Protein bands were quantified by densitometry using Image J. Statistical analysis was performed using an unpaired t -test. *** $p < 0.0001$ when comparing the SerpinA1/GAPDH ratio between ASO-CTR and mA1AT-ASO, $t = 6.026$, $df = 17$; * $p < 0.05$ when comparing the hTTR/GAPDH ratio between ASO-CTR and mA1AT-ASO, $t = 2.554$, $df = 17$. Calculations were performed for an interval of confidence of 95%.

Our previous data revealed that, along with increased TTR mRNA and protein levels, SerpinA1 knockdown increased in vivo TTR deposition in several tissues, such as dorsal root ganglia (DRGs) and intestine [34]. In this study, we addressed whether TTR deposition was also promoted in mouse cardiac tissue after SerpinA1 downregulation. In younger animals, duodenal TTR deposition was found to be increased upon silencing of SerpinA1 (1.773 ± 0.94 vs. 0.1951 ± 0.04 in ASO-CTR, $p = 0.0087$) (Figure 5, upper panel), and a similar tendency was also observed in older animals (Figure 5, lower panel). Additionally, immunohistochemistry analysis demonstrated that TTR deposition was favored in the heart of older animals upon SerpinA1 downregulation (8.307 ± 0.6697 vs. 3.049 ± 1.269 in ASO-CTR, $p = 0.0106$) (Figure 5, lower panel), comparatively to the younger group (Figure 5, upper panel).

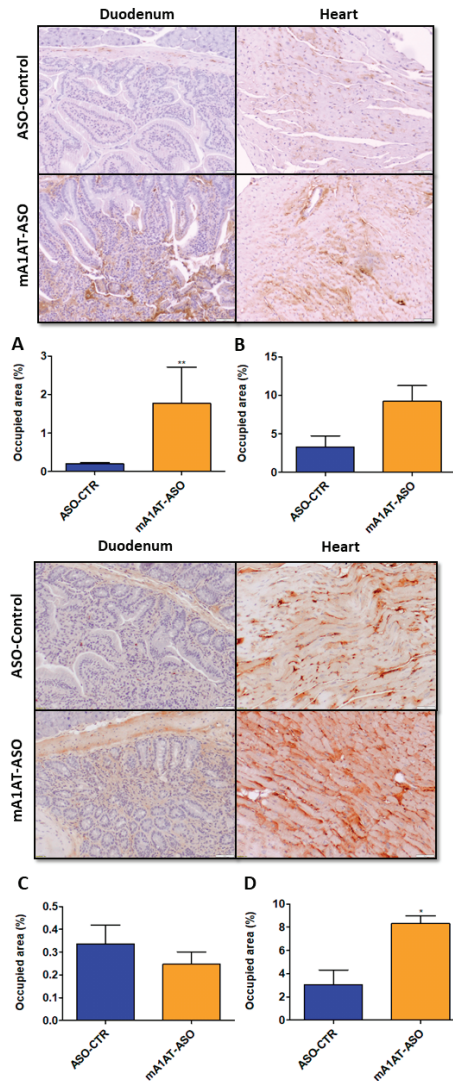


Figure 5. Transthyretin deposition is increased upon SerpinA1 knockdown in the mouse heart of older animals. Representative images of immunohistochemical analysis of mouse heart and duodenum upon the administration of antisense oligonucleotides targeting SerpinA1 to young

(12–13 months, $n = 12$) (upper panel) and old (16–21 months, $n = 7$) (lower panel) animals. Bar plot representation of TTR quantification normalized to the total occupied area in the duodenum (A,C) and heart (B,D) of young (A,B) and old (C,D) mice. Images were captured at $10\times$ magnification using Olympus BX50 microscope and analyzed using Image Pro Plus software. Scale bar = $20\ \mu\text{m}$. Statistical analysis was performed using an unpaired *t*-test. ** $p < 0.01$ comparing TTR deposition in the duodenum of younger animals in ASO-CTR vs. mA1AT-ASO, $t = 3.300$, $df = 10$; * $p < 0.05$ comparing TTR deposition in the heart of younger animals in ASO-CTR vs. mA1AT-ASO, $t = 3.969$, $df = 5$. Calculations were performed for an interval of confidence of 95%.

2.4. Transthyretin Fragments Are Observed in Mouse Cardiac Tissue upon SerpinA1 Downregulation

Based on our experiments of *in vitro* plasmin-mediated proteolysis described above, indicating that SerpinA1 inhibits TTR cleavage, we evaluated the impact of SerpinA1 knockdown on TTR cleavage *in vivo*. Western blotting analysis revealed the presence of a protein band below to the monomeric TTR, corresponding to TTR fragment ($<11\ \text{kDa}$) in mouse cardiac tissue in younger (Figure 6A) and older animals (Figure 6B). Similarly, these fragments were only detected using the antibody anti-TTR mutant (Y78F), clone AD7. In opposition, no TTR fragments were found upon SerpinA1 knockdown neither in other tissues of TTR deposition, such as duodenum (Supplementary data Figure S4A) and stomach (Supplementary data Figure S4B) nor in mice plasmas (Supplementary data Figure S4C).

2.5. SerpinA1 Downregulation Increases Proteolytic Activity, Particularly Plasmin Activity, in Plasmas of Transgenic Mice Carrying Human Transthyretin V30M Mutation

SerpinA1 partially inhibits plasmin-mediated proteolysis *in vitro*. Thus, fluorescence-based enzymatic assays were performed to evaluate the effects of downregulation of SerpinA1 on serine protease activity, namely plasmin activity *in vivo*. In fact, serine protease activity was effectively increased in plasmas of HM30 mice upon SerpinA1 downregulation (12.69 ± 1.746 vs. 9.606 ± 1.675 in ASO-CTR, $p = 0.046$) (Figure 7A) while no proteolytic activity was found in mice heart homogenates (Figure S5). In particular, the activity of plasmin was also found to be increased in mice plasmas after SerpinA1 knockdown (8422 ± 432 vs. 7013 ± 458 in ASO-CTR, $p = 0.040$) (Figure 7B).

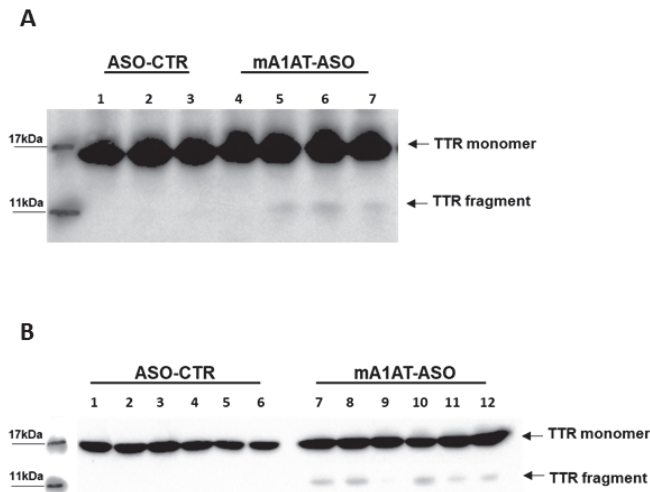


Figure 6. Western blotting analysis revealed the presence of transthyretin fragments upon SerpinA1 downregulation in the heart. Transthyretin fragments were detected in the heart of both older (A) and younger (B) animals.

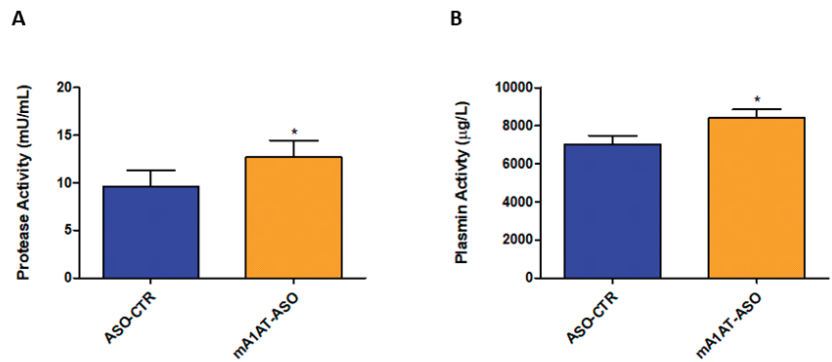


Figure 7. Serine protease activity and, particularly plasmin activity was found to be increased in mice plasmas upon SerpinA1 knockdown. Serine protease activity (A) and plasmin activity (B) were measured in plasma samples of HM30 mice according to the manufacturer’s instructions. Statistical analysis was performed using an unpaired *t*-test. * $p < 0.05$ comparing protease activity between ASO-CTR and mA1AT-ASO, $t = 2.189$, $df = 14$; * $p < 0.05$ comparing plasmin activity between ASO-CTR and mA1AT-ASO, $t = 2.235$, $df = 16$. Calculations were performed for an interval of confidence of 95%.

3. Discussion

Tetramer destabilization is considered the rate-limiting step driving TTR amyloidogenesis. However, TTR proteolysis has been reported as an additional mechanism contributing to TTR amyloid formation [36]. The 49–127 C-terminal fragment is the most frequently encountered in ex vivo amyloid fibrils [13,15], and, the fragmentation pattern at Lys residues indicates the activity of a trypsin-like serine protease [18,37].

Bellotti and collaborators identified three TTR fragments upon in vitro incubation of the highly amyloidogenic TTR S52P with trypsin, being the 49–127 C-terminal fragment more prone to aggregation than the 16–127 and 81–127 C-terminal fragments [19]. A similar pattern of fragmentation was obtained with plasmin, a ubiquitous, widely distributed serine protease related to fibrinolysis [22].

Recently, the serine protease inhibitor, SerpinA1, was implicated in ATTR amyloidogenesis, and we hypothesized that it could also modulate TTR proteolysis. Previous studies by Niemietz et al. demonstrated that SerpinA1 inhibited TTR aggregation both in vitro, in cell culture experiments using hepatocyte-like cells (HLCs), and in vivo, in a study of SerpinA1 knockdown in mice carrying human TTR V30M mutation (HM30) [33,34].

In this study, our aim was to investigate the role of SerpinA1 as an inhibitor of serine proteases and its effect on the in vitro and in vivo modulation of TTR amyloid formation to contribute to a better knowledge of the process and to search for new and more specific therapeutic approaches.

In this sense, we confirmed that TTR V30M, the most frequent TTR variant related to ATTR amyloidosis, was prone to plasmin-mediated proteolysis in vitro and, that the cleaved protein aggregates more rapidly than the non-cleaved TTR V30M. N-terminal sequencing and MS analysis of the bands corresponding to TTR fragments generated by plasmin-mediated proteolysis identified the presence of the peptides 1–48 N-terminal and 49–127 C-terminal. The N-terminal region of the TTR polypeptide chain was enriched in hydrophobic amino acid residues and, importantly, the 26–57 TTR segment, belonging to the aggregation-prone regions (APR), exhibited high amyloid propensity [18]. These APR were protected when the protein was in its native form [38]. However, the destabilization of the native TTR structure induced by the single-point mutation at position 30 might expose those regions to cleavage, and, for that, the fragment 1–48 N-terminal TTR fragment may also be potentially considered highly amyloidogenic. It has been demonstrated that

the 49–127 C-terminal fragment facilitates TTR amyloid formation *in vitro* [19–22], and, accordingly, Dasari et al. recently determined that the proteolytic cleavage of the K48-T49 peptide bond in the CD loop accelerated the formation of small spherical oligomers, which exhibited cytotoxic effects in neuroblastoma SH-SY5Y cells [39]. It was also shown that TTR aggregates generated by full-length or truncated TTR forms exhibited nearly identical molecular structural features, suggesting that TTR proteolysis in the CD loop destabilizes the native TTR tetramer. This destabilization of the TTR tetramer promotes oligomer formation through a similar mechanism of TTR misfolding and aggregation rather than through another molecular mechanism [39].

Marcoux et al. suggested the influence of biomechanical forces, particularly shear stress forces generated by fluid flow, on TTR proteolysis, which could influence the tissue specificity of TTR amyloid deposition. Indeed, a mechano-enzymatic cleavage mechanism for TTR proteolysis was proposed, where tetrameric TTR might be cleaved prior to TTR deposition and, then, due to strong shear stress observed in the heart, the C-terminal fragments would be released being rapidly incorporated into amyloid fibrils. Alternatively, both cleavage and dissociation may occur simultaneously at the heart, where both local shear stress forces and the relevant protease could be present [20]. These shear and interfacial forces are particularly strong in the cardiac tissue [40], which might explain the frequently encountered type-A fibrils in TTR deposits found in the heart. However, the presence of type-A amyloid fibrils in other tissues, such as the vitreous humor and the spinal cord of ATTR V30M patients, indicate that this mechanism would not explain the formation of TTR amyloid deposits based on their tissue-specific location, since these shear stress conditions were not observed neither in the eye nor in the central nervous system [41–43]. Moreover, in a recent study of Suhr et al., 14 out of 15 families with ATTR V30M amyloidosis exhibited a similar amyloid fibril composition within family members, independently of the age-onset disease. These observations indicate that, besides specific tissue/organ characteristics, genetic and/or epigenetic alterations may influence the amyloid fibril composition [44].

Our *in vitro* results using recombinant TTR show that SerpinA1 partially inhibits plasmin-mediated TTR proteolysis and suggest that, in parallel, it can also have an effect on the inhibition of TTR V30M amyloid formation seem to be independent of the presence of plasmin. Interestingly, this effect was compatible with the physical interaction between SerpinA1 and TTR that was recently suggested [33]. In addition, our DLS data indicate the presence of large diameter soluble particles, possibly the SerpinA1-TTR complex. Thus, future studies should be performed to clarify whether SerpinA1 performs an important role as a modulator of TTR proteolysis through its interaction with TTR, avoiding the access of plasmin to its targeting region in the TTR structure.

Our previous studies of SerpinA1 downregulation showed significantly increased TTR serum levels in HM30 mice, as well as in hepatoma cells [34]. Furthermore, SerpinA1 knockdown led to increased TTR deposition in the gastrointestinal tract, as well as in the sciatic nerve and dorsal root ganglia (DRG) of HM30 mice. In this work, we also found increased TTR protein deposits in the heart of older HM30 mice, whereas increased duodenal TTR deposition was found in the younger mice and, the same tendency was also observed in older ages. Moreover, we detected TTR fragments in mouse cardiac tissue upon SerpinA1 downregulation, while no TTR fragments were detected in mice plasmas nor in deposits from other tissues, such as the duodenum and stomach. The absence of fragments in mice plasmas upon SerpinA1 knockdown, as revealed in AD7 immunoblot, might be related to a very low concentration of TTR fragments in plasma and/or to insufficient sensitivity of the method. Additionally, we found increased serine protease activity, particularly plasmin activity, in plasmas upon treatment with ASOs targeting SerpinA1, whereas no proteolytic activity was observed in the heart of HM30 mice (Figure S3).

Despite the increasing interest in TTR proteolysis as a leading mechanism-driving TTR amyloidosis, some questions remain to be answered, namely whether TTR fragmentation

occurs, prior to or after TTR aggregation/deposition and where it occurs. Some authors reported that plasmin degrades amorphous protein aggregates, releasing smaller soluble protein fragments, which were cytotoxic to both endothelial and microglial cells [45]. Trypsin or trypsin-like enzymes directly cleave acid-induced aggregates of full-length TTR V30M and barely cleave native soluble TTR V30M tetramer [46]. Additionally, recent cryo-electron microscopy (cryo-EM) experiments revealed the co-existence of both N-terminal and C-terminal TTR segments in one TTR fibril and, the relative special arrangement of these two segments are compatible with full-length TTR, suggesting that the process of fibril formation precedes TTR proteolysis [47]. In opposition, other studies showed increased proteolytic activity in plasmas from ATTR patients compared to healthy controls, suggesting that TTR proteolysis occurs in the bloodstream prior to TTR aggregation/deposition [31]. Accordingly, our data demonstrating increased protease and plasmin activity in mice plasmas, along with the absence of protease activity in mice hearts, suggest that *in vivo* TTR proteolysis occurs before fibril formation (Figure 7A,B, and supplementary data Figure S5).

In summary, our *in vitro* experiments demonstrate that plasmin cleaves the recombinant TTR V30M proteolytically and promotes its aggregation *in vitro*. Additionally, SerpinA1 partially inhibits the activity of plasmin *in vitro*, which decreases TTR amyloid formation. To investigate the relevance of these findings *in vivo*, SerpinA1 expression was knockdown in HM30 mice. The absence of SerpinA1 favored TTR deposition in mice tissues and increased the serine protease activity, namely plasmin activity in mice plasmas, which was accompanied by the presence of TTR fragments in the mice heart.

This work presents some limitations in particular concerning the knowledge of the detailed mechanism involving SerpinA1 inhibition of plasmin-mediated TTR proteolysis and also the impact of SerpinA1 downregulation in mice carrying TTR WT or carrying non-V30M TTR mutations. Accordingly, future experiments must be performed namely to dissect the molecular mechanisms by which SerpinA1 inhibits plasmin activity through direct interaction with the protease or by the formation of TTR-SerpinA1 complex. Additionally, it would also be interesting to evaluate the role of plasmin on TTR proteolysis using different animal models developing ATTR amyloidosis, such as transgenic mice carrying human A97S mutation [48]. Ultimately, it is important, to investigate plasmin and other extracellular serine proteases activity in TTR V30M patients and patients carrying other TTR amyloidogenic mutations to evaluate whether this activity has tissue-specific effects or is related to disease progression potentiating its interest as a biomarker in ATTR amyloidosis.

Altogether our *in vitro* and *in vivo* results show that plasmin is a plausible protease performing a role on TTR proteolysis and reveal SerpinA1 as an important modulator of the process of TTR cleavage. Our findings might contribute to the development of more effective and targeted therapies for the treatment of ATTR amyloidosis.

4. Materials and Methods

4.1. Reagents

Native human plasmin protein (active), native human SerpinA1 protein (active), protease activity assay kit, plasmin activity assay kit, and recombinant rabbit anti-GAPDH antibody were purchased from Abcam (Cambridge, UK). Mouse monoclonal antibody anti-TTR mutant (Y78F), clone AD7 was from Merck Millipore (Sigma-Merck, Darmstadt, Germany). Rabbit polyclonal anti-human TTR antibody was from DAKO (Hovedstaden, Denmark). Rat monoclonal anti-mouse SerpinA1 antibody was from R&D systems (Minneapolis, MN, USA). Pierce TM High Capacity Endotoxin Removal Resin was from Thermo Scientific (Waltham, MA, USA). GalNAc-AAT ASO (mA1AT-ASO: ACCCAATTCAGAAG-GAAGGA) and GalNAc-Control ASO (ASO-CTR: CCTTCCCTGAAGGTTCTCC) [48] were kindly provided by Ionis Pharmaceuticals (Carlsbad, CA, USA).

4.2. Recombinant Human Transthyretin

TTR V30M and TTR WT were produced using a bacterial expression system and purified as previously described [49]. Recombinant TTR was applied to an affinity chromatography column packed with Pierce TM High Capacity Endotoxin Removal to remove bacterial lipopolysaccharides according to the manufacturer's instructions. TTR was then dialyzed against endotoxin-free phosphate-buffered saline (PBS) (Sigma-Merck, Darmstadt, Germany), concentrated using Vivaspin ultrafiltration units (GE Healthcare, Chicago, IL, USA), and quantified using Bradford protein assay (Bio-Rad, Hercules, CA, USA).

4.3. In Vitro Plasmin-Mediated Proteolysis Assays

TTR variants were firstly filtered through a sterile 0.2 µm inorganic membrane AN-OTOP syringe filter (Whatman, Maidstone, UK) to remove any protein aggregates. Then, TTR (18 µM) was incubated with plasmin (0.4 U) and/or SerpinA1 (2.8 µM) at 37 °C for 24 h, under stagnant conditions. TTR proteolysis was stopped by using phenylmethylsulfonyl fluoride (PMSF) at a final concentration of 1.5 mM and, then TTR samples (500 ng/well) were applied into a 15% polyacrylamide SDS-PAGE. After electrophoresis, proteins were stained with PageBlue™ protein staining solution (Thermo Scientific, Waltham, MA, USA) or transferred onto nitrocellulose membrane using iBlot dry blotting system (Thermo Scientific, Waltham, MA, USA). TTR immunoblot was performed using a commercially available antibody produced in our lab, mouse anti-transsthyretin mutant (Y78F), clone AD7 (1:100) (Sigma-Merck, Darmstadt, Germany). This monoclonal antibody detects glycosylated form of TTR V30M in plasma and acts as a conformational antibody recognizing specific TTR variants, such as G47A, G49A, S50R, and T59K, in particular conditions [28]. Rabbit polyclonal anti-human TTR (1:1000) (DAKO, Hovedstaden, Denmark) was also used. ECL chemiluminescent reagent (Bio-Rad, Hercules, CA, USA) was used as a detection method using Chemidoc apparatus (Bio-Rad, Hercules, CA, USA). Three independent experiments of in vitro plasmin-mediated proteolysis were performed.

4.4. N-Terminal Sequencing Analysis of TTR Fragments

Plasmin-digested TTR V30M samples (15 µg) were loaded into a 15% polyacrylamide SDS-PAGE gel. Samples were then transferred onto a PVDF membrane (Bio-Rad, Hercules, CA, USA) and proteins were further stained with Coomassie blue R-250 (VWR International, Radnor, PA, USA). Membranes were allowed to dry and the bands below to the TTR monomer, corresponding to TTR fragments (band 1 and band 2) were excised for N-terminal sequencing analysis (Edman degradation method) using an ABI Procise Protein Sequencer, an ABI Microgradient Pump System, and an ABI Programmable Absorbance Detector (Applied Biosystems Inc., Waltham, MA, USA).

4.5. Mass Spectrometry Analysis for the Identification of TTR Fragments

Gel bands excised from SDS-PAGE were washed twice with 50% acetonitrile (ACN) in 50 mM triethylammonium bicarbonate (TEAB) with shaking at 1500 rpm for 5 min and further treated with ACN twice. Then, proteins were reduced with 25 mM dithiothreitol (DTT) for 20 min at 56 °C and alkylated with 55 mM iodoacetamide (IAA) for 20 min at room temperature in the dark, followed by the same wash procedure. Proteins were then digested with trypsin (240 ng) in 50 mM TEAB/0.01% surfactant (ProteaseMAX, Promega, Madison, WI, USA) for 60 min at 50 °C. Peptide gel extraction was performed with 2.5% trifluoroacetic acid (TFA) followed by 50% ACN, 0.1% TFA. Samples were dried using Speedvac, resuspended in 10mL 0.1% TFA and cleaned by C18 reverse phase chromatography according to manufacturer's instructions (ZipTip, Sigma-Merck, Darmstadt, Germany).

Sample protein identification and quantification were performed by nano-liquid chromatography mass spectrometry (nano LC-MS/MS), as previously described [50] with a 90 min chromatographic separation run. This equipment was composed of an Ultimate 3000 liquid chromatography system coupled to a Q-Exactive Hybrid Quadrupole-Orbitrap

mass spectrometer (Thermo Scientific, Bremen, Germany). A total of 500 nanograms of each TTR peptide were loaded onto a trapping cartridge (Acclaim PepMap C18 100 Å, 5 mm × 300 µm i.d., 160454, Thermo Scientific, Bremen, Germany) in a mobile phase of 2% ACN, 0.1% FA at 10 µL/min. After 3 min loading, the trap column was switched in-line to a 50 cm × 75 µm inner diameter EASY-Spray column (ES803, PepMap RSLC, C18, 2 µm, Thermo Scientific, Bremen, Germany) at 250 nL/min. The LC separation was achieved by mixing A: 0.1% FA and B: 80% ACN, 0.1% FA with the following gradient: 2 min (2.5% B to 10% B), 50 min (10% B to 35% B), 8 min (35% B to 99% B), and 10 min (hold 99% B). Subsequently, the column was equilibrated with 2.5% B for 17 min. The specific MS parameters were: MS maximum injection time, 100 ms; dd settings: minimum AGC target 7×10^3 , intensity threshold 6.4×10^4 , and dynamic exclusion 20 s. Data acquisition was controlled by Tune 2.11 software (Thermo Scientific, Bremen, Germany). The UniProt database 2020_05 for the Homo sapiens proteome (75069 entries) together with a customized TTR amino acid sequence were considered for protein identification. Protein identification was performed with the Proteome Discoverer software v2.5 (Thermo Scientific, Bremen, Germany). Proteins were quantified by Label-Free Quantification—LFQ, with precursor quantification based on intensity.

4.6. Aggregation Studies: Dynamic Light Scattering and Thioflavin T Assay

DLS measurements were performed at 25 °C using Malvern Zetasizer Nano ZS apparatus (Malvern, Worcestershire, UK). Each sample was measured 3 times, and the values exhibited in the curves were the average distributions from those triplicates. Thioflavin T (ThT) assay was performed in PBS (pH = 7.4) using a 96-well black bottom plate. TTR (12.5 µg) and ThT (30 µM) (Sigma-Merck, Darmstadt, Germany) per well were mixed and the fluorescence was measured at Exc./Em = 450 nm/482 nm using SynergyMx apparatus (BioTek, Winooski, VT, USA).

4.7. Mice

Mice were kept in a controlled temperature room and maintained under a 12 h light/dark period. Transgenic mice carrying human TTR V30M (HM30) were bred as described before [51]. Both younger (12–13 months; $n = 12$) and older (16–21 months; $n = 7$) HM30 mice were subcutaneously (s.c) injected once a week with 5 mg ASO/kg body weight following previous protocols [48]. Animals were euthanized at week 6 of treatment. Plasma and tissue sections were collected and frozen at -80 °C or fixed in formalin for further analysis.

4.8. Determination of SerpinA1 and TTR Protein Levels in Mice Heart

Mouse hearts were homogenized using RIPA lysis and extraction buffer according to the manufacturer's instructions (Santa Cruz Biotechnology, Dallas, TX, USA). Briefly, mouse hearts were homogenized in RIPA buffer using a laboratory homogenizer to disrupt the tissue. Protein homogenates were further frizzed at -80 °C to promote cell lysis, further centrifuged at $21,500 \times g$ for 15 min at 4 °C and, the supernatant containing protein was harvested. Protein was quantified in the heart lysates using Bradford protein assay (BioRad, Hercules, CA, USA), and 50 µg of total protein was loaded into a 10% and 15% polyacrylamide SDS-PAGE to evaluate SerpinA1 and TTR expression, respectively. Gels were then transferred onto nitrocellulose membrane using a wet system and, membranes were incubated overnight with rat monoclonal anti-mouse SerpinA1 antibody (1:1000; R&D systems, Minneapolis, MN, USA), rabbit polyclonal anti-human TTR antibody (1:1000, DAKO) or mouse anti-transferrin mutant (Y78F), clone AD7 (1:100, Sigma-Merck, Darmstadt, Germany). GAPDH was used as a protein loading control, and recombinant rabbit anti-GAPDH antibody was used for immunoblotting (1:100000, Abcam, Cambridge, UK). ECL chemiluminescence reagent (Bio-Rad, Hercules, CA, USA) was used as a detection method using Chemidoc apparatus (Bio-Rad, Hercules, CA, USA). Protein bands were

quantified by densitometry using ImageJ (U. S. National Institutes of Health, Bethesda, MD, USA), and results of protein expression were normalized to GAPDH expression.

4.9. Immunohistochemical Analysis of Tissue TTR Deposition

Paraffin-embedded sections of both duodenal and cardiac tissue were deparaffinized in xylene and rehydrated in descent alcohol series. Antigen retrieval was performed at 95 °C for 15 min using citrate buffer (pH = 6) and, then, endogenous peroxidase activity was quenched in 3% hydrogen peroxide in methanol. Sections were blocked using 10% fetal bovine serum, 1% bovine serum albumin, and 0.5% Triton X-100 in PBS. TTR immunostaining was performed using primary rabbit polyclonal anti-human TTR antibody (1:600, DAKO, Hovedstaden, Denmark) and secondary anti-rabbit antibody (1:200) (Vector, Burlingame, CA, USA). For SerpinA1 staining, primary rat anti-mouse antibody (1:100; R&D systems, Minneapolis, MN, USA) and secondary anti-rat antibody (1:200) (Vector, Burlingame, CA, USA) were used. Tissue slides were developed using 3,3'-diaminobenzidine (DAB) (DAKO, Hovedstaden, Denmark), counterstained with hematoxylin and mounted in Entellan® (Sigma-Merck, Darmstadt, Germany). Images were captured at 10× magnification using Olympus BX50 microscope (Shinjuku, Tokyo, Japan) and analyzed using Image Pro Plus software (Rockville, MD, USA). Results represent the occupied area in pixels corresponding to the substrate reaction color that was further normalized relative to the total image area.

4.10. Protease Activity and Plasmin Activity Fluorescence Measurements

Plasma samples and heart homogenates from HM30 mice were directly used without any dilution. However, protein from heart homogenates was extracted by using RIPA lysis and extraction buffer without supplementation with protease inhibitors. Protease activity assay and plasmin activity assay kits were used according to the manufacturer's instructions. Briefly, mice samples were incubated with FITC-casein substrate in protease activity assay, whereas in the plasmin activity assay, samples were incubated with a synthetic plasmin AMC-substrate. The fluorescence was measured at Ex/Em = 485/530 nm and Ex/Em = 360/450 nm in protease activity assay kit (Abcam, Cambridge, UK) and plasmin activity assay kit (Abcam, Cambridge, UK), respectively, using SynergyMx apparatus (BioTek, Winooski, VT, USA). Both protease and plasmin activities were calculated according to the manufacturer's instructions.

4.11. Statistical Analysis

Statistical analysis was performed by one-way ANOVA (Tukey's multiple comparisons as post-test) and unpaired t-test using GraphPad Prism 5 software (San Diego, CA, USA). Statistical significance was considered when p -value ≤ 0.05 . Results were expressed as mean + standard error of the mean (SEM).

Supplementary Materials: Supplementary Materials can be found at <https://www.mdpi.com/article/10.3390/ijms22179488/s1>.

Author Contributions: Conceived and designed the experiments: F.B., C.N., H.H.J.S., A.Z., M.J.S., M.R.A. Performed the experiments: F.B., P.G. Analyzed the data: F.B., P.G., A.Z., M.J.S., M.R.A. Contributed reagents/materials/analysis tools: S.G., B.P.M., M.J.S., M.R.A. Writing the paper: F.B., A.Z., M.J.S., M.R.A. All authors have read and agreed to the published version of the manuscript.

Funding: This research was funded by COMPETE 2020 of PT2020 through the European Regional Development Fund (ERDF), "NETDIAMOND—New Targets in DIAstolic heart failure: from coMOrbidities to persoNalizeD medicine" project financed by the European Structural and Investment Funds (ESIF), through the Programa Operacional Regional (POCI-01-0145-FEDER-016385) and HEALTH-UNORTE: Setting-up biobanks and regenerative medicine strategies to boost research in cardiovascular, musculoskeletal, neurological, oncological, immunological, and infectious diseases, NORTE-01-0145-FEDER-000039. FB was supported by FCT—Fundação para a Ciência e Tecnologia/MEC—Ministério da Educação e Ciência with a PhD fellowship (SFRH/BD/123674/2016).

Institutional Review Board Statement: All animal experiments were approved by the Portuguese General Veterinarian Board (authorization number 014982 from DGV-Portugal) and animals were kept and used strictly in accordance with National rules and the European Communities Council Directive (86/609/EEC), for the care and handling of laboratory animals.

Informed Consent Statement: Not applicable.

Data Availability Statement: Data are contained within the article or Supplementary Materials.

Acknowledgments: The authors acknowledge technical assistance of Paula Chicau from N-terminal sequencing facility of ITQB Nova, Lisbon, Portugal for N-terminal sequencing experiments and data analysis. The authors also acknowledge to Hugo Osório from Proteomics Unit of i3S (Instituto de Investigação e Inovação em Saúde) for mass spectrometry experiments and analysis.

Conflicts of Interest: The authors declare no conflict of interest.

References

1. Koike, H.; Katsuno, M. Transthyretin Amyloidosis: Update on the Clinical Spectrum, Pathogenesis, and Disease-Modifying Therapies. *Neurol. Ther.* **2020**, *9*, 317–333. [CrossRef] [PubMed]
2. Nativi-Nicolau, J.N.; Karam, C.; Khella, S.; Maurer, M.S. Screening for ATTR amyloidosis in the clinic: Overlapping disorders, misdiagnosis, and multiorgan awareness. *Heart Fail. Rev.* **2021**, 1–9. [CrossRef]
3. Benson, M.D.; Buxbaum, J.N.; Eisenberg, D.S.; Merlini, G.; Saraiva, M.J.M.; Sekijima, Y.; Sipe, J.D.; Westermark, P. Amyloid nomenclature 2018: Recommendations by the International Society of Amyloidosis (ISA) nomenclature committee. *Amyloid Int. J. Exp. Clin. Investig. Off. J. Int. Soc. Amyloidosis* **2018**, *25*, 215–219. [CrossRef]
4. Saraiva, M.J. Transthyretin mutations in health and disease. *Hum. Mutat.* **1995**, *5*, 191–196. [CrossRef]
5. Hurshman Babbes, A.R.; Powers, E.T.; Kelly, J.W. Quantification of the thermodynamically linked quaternary and tertiary structural stabilities of transthyretin and its disease-associated variants: The relationship between stability and amyloidosis. *Biochemistry* **2008**, *47*, 6969–6984. [CrossRef]
6. Sekijima, Y.; Wiseman, R.L.; Matteson, J.; Hammarstrom, P.; Miller, S.R.; Sawkar, A.R.; Balch, W.E.; Kelly, J.W. The biological and chemical basis for tissue-selective amyloid disease. *Cell* **2005**, *121*, 73–85. [CrossRef]
7. Westermark, P.; Bergstrom, J.; Solomon, A.; Murphy, C.; Sletten, K. Transthyretin-derived senile systemic amyloidosis: Clinicopathologic and structural considerations. *Amyloid Int. J. Exp. Clin. Investig. Off. J. Int. Soc. Amyloidosis* **2003**, *10* (Suppl. 1), 48–54. [CrossRef]
8. Sipe, J.D.; Benson, M.D.; Buxbaum, J.N.; Ikeda, S.I.; Merlini, G.; Saraiva, M.J.; Westermark, P. Amyloid fibril proteins and amyloidosis: Chemical identification and clinical classification International Society of Amyloidosis 2016 Nomenclature Guidelines. *Amyloid Int. J. Exp. Clin. Investig. Off. J. Int. Soc. Amyloidosis* **2016**, *23*, 209–213. [CrossRef]
9. McCutchen, S.L.; Colon, W.; Kelly, J.W. Transthyretin mutation Leu-55-Pro significantly alters tetramer stability and increases amyloidogenicity. *Biochemistry* **1993**, *32*, 12119–12127. [CrossRef] [PubMed]
10. Quintas, A.; Vaz, D.C.; Cardoso, I.; Saraiva, M.J.; Brito, R.M. Tetramer dissociation and monomer partial unfolding precedes protofibril formation in amyloidogenic transthyretin variants. *J. Biol. Chem.* **2001**, *276*, 27207–27213. [CrossRef]
11. Si, J.B.; Kim, B.; Kim, J.H. Transthyretin Misfolding, A Fatal Structural Pathogenesis Mechanism. *Int. J. Mol. Sci.* **2021**, *22*, 4429. [CrossRef]
12. Cardoso, I.; Goldsbury, C.S.; Muller, S.A.; Olivieri, V.; Wirtz, S.; Damas, A.M.; Aebi, U.; Saraiva, M.J. Transthyretin fibrillogenesis entails the assembly of monomers: A molecular model for in vitro assembled transthyretin amyloid-like fibrils. *J. Mol. Biol.* **2002**, *317*, 683–695. [CrossRef]
13. Bergstrom, J.; Gustavsson, A.; Hellman, U.; Sletten, K.; Murphy, C.L.; Weiss, D.T.; Solomon, A.; Olofsson, B.O.; Westermark, P. Amyloid deposits in transthyretin-derived amyloidosis: Cleaved transthyretin is associated with distinct amyloid morphology. *J. Pathol.* **2005**, *206*, 224–232. [CrossRef] [PubMed]
14. Ihse, E.; Ybo, A.; Suhr, O.; Lindqvist, P.; Backman, C.; Westermark, P. Amyloid fibril composition is related to the phenotype of hereditary transthyretin V30M amyloidosis. *J. Pathol.* **2008**, *216*, 253–261. [CrossRef]
15. Ihse, E.; Rapezzi, C.; Merlini, G.; Benson, M.D.; Ando, Y.; Suhr, O.B.; Ikeda, S.; Lavatelli, F.; Obici, L.; Quarta, C.C.; et al. Amyloid fibrils containing fragmented ATTR may be the standard fibril composition in ATTR amyloidosis. *Amyloid Int. J. Exp. Clin. Investig. Off. J. Int. Soc. Amyloidosis* **2013**, *20*, 142–150. [CrossRef]
16. Ihse, E.; Suhr, O.B.; Hellman, U.; Westermark, P. Variation in amount of wild-type transthyretin in different fibril and tissue types in ATTR amyloidosis. *J. Mol. Med.* **2011**, *89*, 171–180. [CrossRef]
17. Gustafsson, S.; Ihse, E.; Henein, M.Y.; Westermark, P.; Lindqvist, P.; Suhr, O.B. Amyloid fibril composition as a predictor of development of cardiomyopathy after liver transplantation for hereditary transthyretin amyloidosis. *Transplantation* **2012**, *93*, 1017–1023. [CrossRef]
18. Sant’Anna, R.; Braga, C.; Varejao, N.; Pimenta, K.M.; Grana-Montes, R.; Alves, A.; Cortines, J.; Cordeiro, Y.; Ventura, S.; Foguel, D. The importance of a gatekeeper residue on the aggregation of transthyretin: Implications for transthyretin-related amyloidoses. *J. Biol. Chem.* **2014**, *289*, 28324–28337. [CrossRef]

19. Mangione, P.P.; Porcari, R.; Gillmore, J.D.; Pucci, P.; Monti, M.; Porcari, M.; Giorgetti, S.; Marchese, L.; Raimondi, S.; Serpell, L.C.; et al. Proteolytic cleavage of Ser52Pro variant transthyretin triggers its amyloid fibrillogenesis. *Proc. Natl. Acad. Sci. USA* **2014**, *111*, 1539–1544. [CrossRef]
20. Marcoux, J.; Mangione, P.P.; Porcari, R.; Degiacomi, M.T.; Verona, G.; Taylor, G.W.; Giorgetti, S.; Raimondi, S.; Sanglier-Cianferani, S.; Benesch, J.L.; et al. A novel mechano-enzymatic cleavage mechanism underlies transthyretin amyloidogenesis. *EMBO Mol. Med.* **2015**, *7*, 1337–1349. [CrossRef]
21. Klimtchuk, E.S.; Prokaeva, T.; Frame, N.M.; Abdullahi, H.A.; Spencer, B.; Dasari, S.; Cui, H.; Berk, J.L.; Kurtin, P.J.; Connors, L.H.; et al. Unusual duplication mutation in a surface loop of human transthyretin leads to an aggressive drug-resistant amyloid disease. *Proc. Natl. Acad. Sci. USA* **2018**, *115*, E6428–E6436. [CrossRef]
22. Mangione, P.P.; Verona, G.; Corazza, A.; Marcoux, J.; Canetti, D.; Giorgetti, S.; Raimondi, S.; Stoppini, M.; Esposito, M.; Relini, A.; et al. Plasminogen activation triggers transthyretin amyloidogenesis in vitro. *J. Biol. Chem.* **2018**, *293*, 14192–14199. [CrossRef]
23. Tucker, H.M.; Kihiko-Ehmann, M.; Wright, S.; Rydel, R.E.; Estus, S. Tissue plasminogen activator requires plasminogen to modulate amyloid-beta neurotoxicity and deposition. *J. Neurochem.* **2000**, *75*, 2172–2177. [CrossRef] [PubMed]
24. Mumford, A.D.; O'Donnell, J.; Gillmore, J.D.; Manning, R.A.; Hawkins, P.N.; Laffan, M. Bleeding symptoms and coagulation abnormalities in 337 patients with AL-amyloidosis. *Br. J. Haematol.* **2000**, *110*, 454–460. [CrossRef]
25. Bouma, B.; Maas, C.; Hazenberg, B.P.; Lokhorst, H.M.; Gebbink, M.F. Increased plasmin-alpha2-antiplasmin levels indicate activation of the fibrinolytic system in systemic amyloidosis. *J. Thromb. Haemost. JTH* **2007**, *5*, 1139–1142. [CrossRef] [PubMed]
26. Uchiba, M.; Imamura, T.; Hata, H.; Tatetsu, H.; Yonemura, Y.; Ueda, M.; Wada, Y.; Mitsuya, H.; Ando, Y. Excessive fibrinolysis in AL-amyloidosis is induced by urokinase-type plasminogen activator from bone marrow plasma cells. *Amyloid Int. J. Exp. Clin. Investig. Off. J. Int. Soc. Amyloidosis* **2009**, *16*, 89–93. [CrossRef]
27. Gollin, P.A.; Kalaria, R.N.; Eikelenboom, P.; Rozenmuller, A.; Perry, G. Alpha 1-antitrypsin and alpha 1-antichymotrypsin are in the lesions of Alzheimer's disease. *Neuroreport* **1992**, *3*, 201–203. [CrossRef]
28. Bohrmann, B.; Tjernberg, L.; Kuner, P.; Poli, S.; Levet-Trafit, B.; Naslund, J.; Richards, G.; Huber, W.; Dobeli, H.; Nordstedt, C. Endogenous proteins controlling amyloid beta-peptide polymerization. Possible implications for beta-amyloid formation in the central nervous system and in peripheral tissues. *J. Biol. Chem.* **1999**, *274*, 15990–15995. [CrossRef]
29. Torricelli, C.; Capurro, E.; Santucci, A.; Paffetti, A.; D'Ambrosio, C.; Scaloni, A.; Maioli, E.; Pacini, A. Multiple plasma proteins control atrial natriuretic peptide (ANP) aggregation. *J. Mol. Endocrinol.* **2004**, *33*, 335–341. [CrossRef]
30. Heit, C.; Jackson, B.C.; McAndrews, M.; Wright, M.W.; Thompson, D.C.; Silverman, G.A.; Nebert, D.W.; Vasiliou, V. Update of the human and mouse SERPIN gene superfamily. *Hum. Genom.* **2013**, *7*, 22. [CrossRef] [PubMed]
31. da Costa, G.; Ribeiro-Silva, C.; Ribeiro, R.; Gilberto, S.; Gomes, R.A.; Ferreira, A.; Mateus, E.; Barroso, E.; Coelho, A.V.; Freire, A.P.; et al. Transthyretin Amyloidosis: Chaperone Concentration Changes and Increased Proteolysis in the Pathway to Disease. *PLoS ONE* **2015**, *10*, e0125392. [CrossRef]
32. Chan, G.G.; Koch, C.M.; Connors, L.H. Serum Proteomic Variability Associated with Clinical Phenotype in Familial Transthyretin Amyloidosis (ATTRm). *J. Proteome Res.* **2017**, *16*, 4104–4112. [CrossRef]
33. NIEMIETZ, C.; Fleischhauer, L.; Sandfort, V.; Guttmann, S.; Zibert, A.; Schmidt, H.H. Hepatocyte-like cells reveal novel role of SERPINA1 in transthyretin amyloidosis. *J. Cell Sci.* **2018**, *131*, jcs219824. [CrossRef] [PubMed]
34. NIEMIETZ, C.; Bezerra, F.; Almeida, M.R.; Guo, S.; Monia, B.P.; Saraiva, M.J.; Schutz, P.; Schmidt, H.H.; Zibert, A. SERPINA1 modulates expression of amyloidogenic transthyretin. *Exp. Cell Res.* **2020**, *395*, 112217. [CrossRef]
35. Teixeira, A.C.; Saraiva, M.J. Presence of N-glycosylated transthyretin in plasma of V30M carriers in familial amyloidotic polyneuropathy: An escape from ERAD. *J. Cell. Mol. Med.* **2013**, *17*, 429–435. [CrossRef]
36. Suhr, O.B.; Lundgren, E.; Westermark, P. One mutation, two distinct disease variants: Unravelling the impact of transthyretin amyloid fibril composition. *J. Intern. Med.* **2017**, *281*, 337–347. [CrossRef]
37. Schormann, N.; Murrell, J.R.; Benson, M.D. Tertiary structures of amyloidogenic and non-amyloidogenic transthyretin variants: New model for amyloid fibril formation. *Amyloid Int. J. Exp. Clin. Investig. Off. J. Int. Soc. Amyloidosis* **1998**, *5*, 175–187. [CrossRef] [PubMed]
38. Saelices, L.; Sievers, S.A.; Sawaya, M.R.; Eisenberg, D.S. Crystal structures of amyloidogenic segments of human transthyretin. *Protein Sci. Publ. Protein Soc.* **2018**, *27*, 1295–1303. [CrossRef]
39. Dasari, A.K.R.; Hughes, R.M.; Wi, S.; Hung, I.; Gan, Z.; Kelly, J.W.; Lim, K.H. Transthyretin Aggregation Pathway toward the Formation of Distinct Cytotoxic Oligomers. *Sci. Rep.* **2019**, *9*, 33. [CrossRef] [PubMed]
40. Stoppini, M.; Bellotti, V. Systemic amyloidosis: Lessons from beta2-microglobulin. *J. Biol. Chem.* **2015**, *290*, 9951–9958. [CrossRef]
41. Sandgren, O.; Westermark, P.; Stenkula, S. Relation of vitreous amyloidosis to prealbumin. *Ophthalmic Res.* **1986**, *18*, 98–103. [CrossRef]
42. Liepnieks, J.J.; Wilson, D.L.; Benson, M.D. Biochemical characterization of vitreous and cardiac amyloid in Ile84Ser transthyretin amyloidosis. *Amyloid Int. J. Exp. Clin. Investig. Off. J. Int. Soc. Amyloidosis* **2006**, *13*, 170–177. [CrossRef] [PubMed]
43. Oshima, T.; Kawahara, S.; Ueda, M.; Kawakami, Y.; Tanaka, R.; Okazaki, T.; Misumi, Y.; Obayashi, K.; Yamashita, T.; Ohya, Y.; et al. Changes in pathological and biochemical findings of systemic tissue sites in familial amyloid polyneuropathy more than 10 years after liver transplantation. *J. Neurol. Neurosurg. Psychiatry* **2014**, *85*, 740–746. [CrossRef]
44. Suhr, O.B.; Wixner, J.; Anan, I.; Lundgren, H.E.; Wijayatunga, P.; Westermark, P.; Ihse, E. Amyloid fibril composition within hereditary Val30Met (p. Val50Met) transthyretin amyloidosis families. *PLoS ONE* **2019**, *14*, e0211983. [CrossRef]

45. Constantinescu, P.; Brown, R.A.; Wyatt, A.R.; Ranson, M.; Wilson, M.R. Amorphous protein aggregates stimulate plasminogen activation, leading to release of cytotoxic fragments that are clients for extracellular chaperones. *J. Biol. Chem.* **2017**, *292*, 14425–14437. [CrossRef]
46. Ueda, M.; Okada, M.; Mizuguchi, M.; Kluge-Beckerman, B.; Kanenawa, K.; Isoguchi, A.; Misumi, Y.; Tasaki, M.; Ueda, A.; Kanai, A.; et al. A cell-based high-throughput screening method to directly examine transthyretin amyloid fibril formation at neutral pH. *J. Biol. Chem.* **2019**, *294*, 11259–11275. [CrossRef] [PubMed]
47. Schmidt, M.; Wiese, S.; Adak, V.; Engler, J.; Agarwal, S.; Fritz, G.; Westermark, P.; Zacharias, M.; Fandrich, M. Cryo-EM structure of a transthyretin-derived amyloid fibril from a patient with hereditary ATTR amyloidosis. *Nat. Commun.* **2019**, *10*, 5008. [CrossRef]
48. Guo, S.; Booten, S.L.; Watt, A.; Alvarado, L.; Freier, S.M.; Teckman, J.H.; McCaleb, M.L.; Monia, B.P. Using antisense technology to develop a novel therapy for alpha-1 antitrypsin deficient (AATD) liver disease and to model AATD lung disease. *Rare Dis.* **2014**, *2*, e28511. [CrossRef]
49. Furuya, H.; Saraiva, M.J.; Gawinowicz, M.A.; Alves, I.L.; Costa, P.P.; Sasaki, H.; Goto, I.; Sakaki, Y. Production of recombinant human transthyretin with biological activities toward the understanding of the molecular basis of familial amyloidotic polyneuropathy (FAP). *Biochemistry* **1991**, *30*, 2415–2421. [CrossRef]
50. Osorio, H.; Silva, C.; Ferreira, M.; Gullo, I.; Maximo, V.; Barros, R.; Mendonca, F.; Oliveira, C.; Carneiro, F. Proteomics Analysis of Gastric Cancer Patients with Diabetes Mellitus. *J. Clin. Med.* **2021**, *10*, 407. [CrossRef]
51. Goncalves, N.P.; Moreira, J.; Martins, D.; Vieira, P.; Obici, L.; Merlini, G.; Saraiva, M.; Saraiva, M.J. Differential expression of Cathepsin E in transthyretin amyloidosis: From neuropathology to the immune system. *J. Neuroinflammation* **2017**, *14*, 115. [CrossRef] [PubMed]

Article

Optimization of Neurite Tracing and Further Characterization of Human Monocyte-Derived-Neuronal-like Cells

Alfredo Bellon ^{1,2,*}, Tuna Hasoglu ¹, Mallory Peterson ³, Katherine Gao ⁴, Michael Chen ⁵, Elisabeta Blandin ⁶, Alonso Cortez-Resendiz ¹, Gary A. Clawson ⁷ and Liyi Elliot Hong ⁸

¹ Department of Psychiatry and Behavioral Health, Penn State Hershey Medical Center, Hershey, PA 17033, USA; thasoglu@pennstatehealth.psu.edu (T.H.); acortezresendiz@pennstatehealth.psu.edu (A.C.-R.)

² Department of Pharmacology, Penn State Hershey Medical Center, Hershey, PA 17033, USA

³ Department of Engineering Science and Mechanics, Penn State College of Engineering, State College, Philadelphia, PA 19107, USA; mpeterson1@pennstatehealth.psu.edu

⁴ Department of Psychiatry & Human Behavior, Thomas Jefferson University, Philadelphia, PA 19107, USA; Katherine.c.gao@gmail.com

⁵ Department of Pathology, Lehigh Valley Health Network, 2545 Schoenersville Road, Bethlehem, PA 18017, USA; Michael.Chen@lvhn.org

⁶ Department of Neural & Behavioral Sciences, Penn State Hershey Medical Center, Hershey, PA 17033, USA; emblandin@yahoo.com

⁷ Department of Psychiatry, Penn State University College of Medicine, Gittlen Cancer Research Laboratories, Hershey, PA 17033, USA; gac4gac4@gmail.com

⁸ Department of Psychiatry, Maryland Psychiatric Research Center, University of Maryland School of Medicine, Baltimore, MD 21201, USA; Ehong@som.umaryland.edu

* Correspondence: abellon@pennstatehealth.psu.edu; Tel.: +1-717-531-0003 (ext. 286260); Fax: +1-717-531-5013

Citation: Bellon, A.; Hasoglu, T.; Peterson, M.; Gao, K.; Chen, M.; Blandin, E.; Cortez-Resendiz, A.; Clawson, G.A.; Hong, L.E. Optimization of Neurite Tracing and Further Characterization of Human Monocyte-Derived-Neuronal-like Cells. *Brain Sci.* **2021**, *11*, 1372. <https://doi.org/10.3390/brainsci11111372>

Academic Editors: Masaru Tanaka and Lydia Giménez-Llort

Received: 4 September 2021

Accepted: 14 October 2021

Published: 20 October 2021

Publisher's Note: MDPI stays neutral with regard to jurisdictional claims in published maps and institutional affiliations.



Copyright: © 2021 by the authors. Licensee MDPI, Basel, Switzerland. This article is an open access article distributed under the terms and conditions of the Creative Commons Attribution (CC BY) license (<https://creativecommons.org/licenses/by/4.0/>).

Abstract: Deficits in neuronal structure are consistently associated with neurodevelopmental illnesses such as autism and schizophrenia. Nonetheless, the inability to access neurons from clinical patients has limited the study of early neurostructural changes directly in patients' cells. This obstacle has been circumvented by differentiating stem cells into neurons, although the most used methodologies are time consuming. Therefore, we recently developed a relatively rapid (~20 days) protocol for transdifferentiating human circulating monocytes into neuronal-like cells. These monocyte-derived-neuronal-like cells (MDNCs) express several genes and proteins considered neuronal markers, such as MAP-2 and PSD-95. In addition, these cells conduct electrical activity. We have also previously shown that the structure of MDNCs is comparable with that of human developing neurons (HDNs) after 5 days in culture. Moreover, the neurostructure of MDNCs responds similarly to that of HDNs when exposed to colchicine and dopamine. In this manuscript, we expanded our characterization of MDNCs to include the expression of 12 neuronal genes, including tau. Following, we compared three different tracing approaches (two semi-automated and one automated) that enable tracing using photographs of live cells. This comparison is imperative for determining which neurite tracing method is more efficient in extracting neurostructural data from MDNCs and thus allowing researchers to take advantage of the faster yield provided by these neuronal-like cells. Surprisingly, it was one of the semi-automated methods that was the fastest, consisting of tracing only the longest primary and the longest secondary neurite. This tracing technique also detected more structural deficits. The only automated method tested, Volocity, detected MDNCs but failed to trace the entire neuritic length. Other advantages and disadvantages of the three tracing approaches are also presented and discussed.

Keywords: schizophrenia; autism; stem cells; cytoskeleton; neurite; dendrite; neurodevelopment; biomarker; transdifferentiation and neuronal model

1. Introduction

Neurodevelopmental disorders such as autism and schizophrenia are relatively common alignments [1,2] caused by a complex combination of environmental and genetic factors. Unfortunately, treatment and diagnostic methods for these illnesses remain unsatisfactory. It is therefore not surprising that the search for biomarkers is intense [3–8]. However, a crucial step in the development of biomarkers and improvement of treatment as well as diagnosis for any illness is understanding its pathophysiology.

One of the many challenges researchers face when studying neurodevelopmental disorders is that they are diagnosed once most neurodevelopmental stages have been completed. For instance, schizophrenia is diagnosed in late adolescence or early adulthood. Autism is often recognized earlier in life but still too late to study neuronal processes such as neurite formation, neuronal polarization and pruning of neuronal extensions. These neurodevelopmental processes are of particular importance, as the neuronal structure has been consistently associated with the pathophysiology of schizophrenia and autism [9–13]. It is therefore possible that studying early neurostructural rearrangements directly in cells from patients with autism or schizophrenia would lead to a better understanding of its pathophysiology.

An additional challenge when ascertaining neurodevelopmental disorders is the accessibility of neurons coming directly from clinical patients. This obstacle has been circumvented by several different methods. The collection of olfactory neuroepithelial cells (ONCs) is the only approach presently available that provides access to mature neurons [14]. It also delivers glial, epithelial and neuroprogenitor cells as well as neurons at different stages of differentiation [15,16]. In order to access ONCs, a qualified otorhinolaryngologist has to perform a biopsy of the olfactory mucosa [16]. This invasive procedure has limited the use of ONCs. In addition, concerns have been raised about the reproducibility of data when using olfactory mucosa, as biopsies from the same individual can deliver variable results [15,16]. Another approach that circumvents the limited access of neurons coming directly from patients is the use of mesenchymal stem cells (MSCs). MSCs can be rapidly differentiated into neuronal-like cells *in vitro* [17]. However, the scarce use of MSCs in the study of psychiatric and neurologic disorders appears to be due to difficulties in retrieving MSCs. Obtaining MSCs, often if not always, requires a biopsy [18], which is a surgical procedure that requires consultation with a specialist. There is also another characteristic of MSCs that has determined its fate in research: the fact that MSCs do not trigger an immunological reaction. Such an attribute makes this type of stem cells an excellent tool for cellular transplant [18]. On the other hand, to study neurodevelopmental disorders, the most common stem cells currently used are induced pluripotent stem cells (iPSCs). iPSCs allow researchers to develop different types of neurons with sophisticated neuropils [19]. Even brain organoids that resemble aspects of early brain development can be generated using iPSCs [19]. Unfortunately, generating iPSCs requires altering the cell's genome (reprogramming) [20,21], which can become a confounder when studying illnesses with poorly understood genetic predispositions, such as autism and schizophrenia [22]. iPSCs have also been criticized because of difficulties in reproducibility [23,24]. Moreover, the transformation of somatic cell to differentiated neuron is expensive and time consuming [15]. Not surprisingly, published manuscripts involving iPSCs and neurodevelopmental disorders comprise rather small cohorts. Another emerging methodology consists of directly reprogramming somatic cells, often fibroblasts, directly into neurons [25,26]. This approach, known as induced neurons (iNs), bypasses the need for dedifferentiation but still requires altering the cell's genome [25,26]. The potential confounding effects of reprogramming and the need to show reproducible results when studying neurodevelopmental disorders remain. However, iNs are becoming a promising alternative for regenerative medicine [27]. A faster approach for obtaining neuronal-like cells that completely avoids genetic reprogramming is transdifferentiation of somatic cells.

We have recently developed a methodology for transdifferentiating human circulating monocytes into neuronal-like cells in only 20 days [28]. These monocyte-derived-neuronal-

like cells (MDNCs) express several genes and proteins considered neuronal markers. Among the genes and proteins present in MDNCs are NeuN and PSD-95, considered markers for mature neurons. However, MDNCs also express markers of immature neurons such as nestin. Moreover, these cells are not yet committed to developing into any specific neuronal type and instead express markers for glutamatergic, dopaminergic, GABAergic and serotonergic neurons. Of particular importance for the study of the neuronal structure is the expression of microtubule associated protein 2 (MAP-2) [28], as this protein is a marker for dendrites [29,30]. Tau is another relevant neuronal protein, as it is an axonal marker [29,30]. Immature neuronal extensions that have not yet developed into either axons or dendrites are called neurites [31]. During early stages of neuronal development, MAP-2 is present in all neurites and in the cell soma [29,30]. We have previously shown that MDNCs express MAP-2 in all its extensions as well as in the soma [28]. While expression of tau in MDNCs is still to be proven, the information currently available indicates that MDNCs extend neurites that have not yet developed into either dendrites or axons. However, even at this early stage of neurodevelopment, we have shown that MDNCs conduct electrical activity [28].

In a prior publication, we directly compared the structure of MDNCs with that of human developing neurons (after 5 days in culture) as well as with that of differentiated human neuroblastoma cells [28]. The structure of these three different neuronal cell types was similar [28]. Perhaps more important for the study of schizophrenia and autism is that the structure of MDNCs responds similarly to human neurons and neuroblastoma cells when exposed to dopamine and colchicine [28]. Therefore, MDNCs allow us to study some aspects of the neuronal structure that take place during early development directly in patients' cells that carry the genetic predisposition to illnesses such as schizophrenia and autism. This opens the possibility of starting to unveil the pathophysiology of such neurodevelopmental disorders. While other neurodevelopmental disorders such as attention deficit hyperactivity disorder (ADHD) [32], bipolar disorder [33] and others can also be studied using MDNCs, here we emphasize autism and schizophrenia because deficits in the neuronal structure are consistently found [9–13].

Neurite outgrowth is a key neuronal feature, and therefore characterizing neurites is important for understanding MDNCs' neuronal properties and their application in disease and pharmacology research. Neurites are numerous, and accurate measurements through individual neurite tracing are labor-intensive. Therefore, in order to take advantage of this faster yield of neuronal-like cells, an efficient neurite tracing method is critical for extracting neurostructural data from MDNCs. The current available options can be divided into two general tracing methodologies: automated and semi-automated. Most automated alternatives are similar. They rely on software capable of detecting neurons stained with a fluorochrome. Tagged cells are automatically traced. The output of such softwares is faster than semi-automated methods, as these latter options require the researcher to select the cell to be traced and then identify the beginning and end of the neurite of interest. One of the advantages of semi-automated methods is that researchers have more flexibility when deciding which cells to trace, as they are not bound by the expression of a specific marker. Another advantage is that immunofluorescence or the expression of a fluorescent marker such as green fluorescent protein (GFP) can be avoided. These techniques are not always desirable, as both can lead to cellular damage [34,35].

Postmortem studies indicate that defects in the neuronal structure of patients with neurodevelopmental disorders are subtle [9–13]. Thus, avoiding immunofluorescence or the expression of a fluorescent marker is advantageous, as these techniques could mask inconspicuous defects [34,35]. Another strategy for minimizing structural confounders is using each neuronal-like cell as its own control. For this purpose, cells are identified and photographed before receiving any treatment. Then, after treatment with the compound to be tested and once the desired incubation time has passed, the exact same cells are again identified and photographed. Structural differences in the same cells before and

after treatment are reported. We used this approach to determine the structural effects of colchicine and dopamine on MDNCs [28].

In order to avoid the use of fluorochromes and to utilize each neuronal-like cell as its own control, we decided to test three different neurite tracing approaches. First, we traced each MDNC in its entirety using a semi-automated method. Since this approach is lengthy, we also tested a simplified version in which only the longest primary neurite and longest secondary neurite were traced. Finally, the third and most intriguing alternative was to use an automated method without the addition of a fluorochrome. Automated software are triggered by brightness. Neuronal-like cells appear significantly brighter than the background when pictures are taken using light microscopy, and thus, cell recognition is expected.

The first goal of this study was to compare the expression of several previously unreported neuronal markers between MDNCs, human neuroblastoma cells and THP-1 cells (a human monocytic cell line) to further validate MDNCs as neuronal-like cells. The second and main objective was to determine which of the three neurite tracing methods was faster. We hypothesized that an automated method would be faster than the other two semi-automated approaches. The third and final goal was to establish whether any of the three techniques was better at exposing neurostructural defects, with the expectation that whole-cell tracing of MDNCs would reveal the highest number of structural deficiencies, considering the thoroughness of this approach.

2. Methods

2.1. Cell Culture

All blood donors gave their informed and written consent after receiving a full description of the study. Experiments were approved by the Institutional Review Board (IRB) at Penn State University (Study #00006911). Fresh blood was obtained from healthy individuals. We then followed our transdifferentiation protocol, as previously described [28]. Briefly, fresh blood was separated into its components by Ficoll-Paque (17-1440-03, GE Healthcare, Chicago, IL, USA). A fraction of peripheral blood mononuclear cells (PBMCs) was cultured on fibronectin-coated 25 cm² flasks (13.5 million PBMCs per flask). The remaining PBMCs were used for isolation of CD14+ cells (monocytes) by positive immunomagnetic selection based on the manufacturer protocol (CD14 human microbeads, 130-050-201 Miltenyi Biotec, Auburn, CA, USA). CD14+ cells were cultured on fibronectin-coated wells at a concentration of 180,000 cells per cm². Plastic plates and flasks came from BD Falcon, Glendale, AZ, USA (351146, 353043 and 353109). Human fibronectin from plasma (F2006, Sigma-Aldrich, St. Louis, MO, USA) was used at a concentration of 20 µg/mL, and coating was carried out overnight at 4 °C. Macrophage colony-stimulating factor (M-CSF) from AbCys, Paris, France (300-25) was added to monocytes right before culturing at a final concentration of 50 ng/mL (Figure 1A). All cells were maintained in Dulbecco's modified Eagle medium (DMEM), high glucose, GlutaMAX (61965059, GIBCO, Waltham, MA, USA), in which we added 100 U/mL penicillin; 100 mg/mL streptomycin, 1% nonessential amino acids, 1 mM sodium pyruvate, 10 mM HEPES buffer, (all from Life Technologies, Waltham, MA, USA) and supplemented with 10% fetal bovine serum (FBS) Performance Plus from GIBCO (Waltham, MA, USA). Cell culture medium was then replaced on days 4, 7, 10 and 13, as described in Figure 1. The following chemicals and growth factors were added, as shown in Figure 1: butylated hydroxyanisole (BHA) (B1253, Sigma-Aldrich, St. Louis, MO, USA), retinoic acid (RA) (R2625, Sigma-Aldrich, St. Louis, MO, USA), insulin growth factor-1 (IGF-1) (100-11, PeproTech, Cranbury, NJ, USA) and neurotrophin-3 (NT-3) (450-03-100, Peprotech, Cranbury, NJ, USA). On day 17, cell culture media was not replaced; instead, 25 mM potassium chloride (KCL) was added (P5405, Sigma-Aldrich, St. Louis, MO, USA).

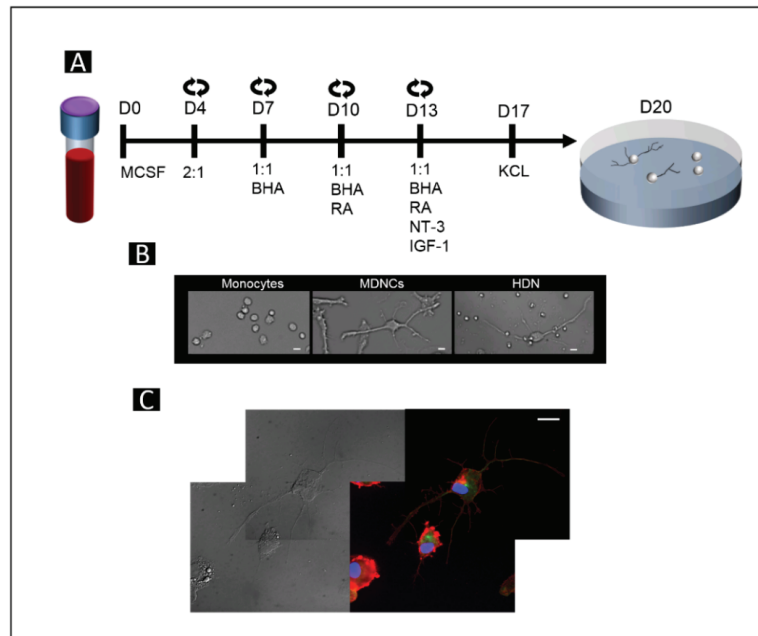


Figure 1. Transdifferentiation of human circulating monocytes into neuronal-like cells. **(A)** Schematic representation of our 20-day protocol for transdifferentiating human circulating monocytes into neuronal-like cells, starting from day zero (D0) with a blood sample and ending on D20 with neuronal-like cells. Circled arrows represent days on which media were changed. Cell cultured media were replaced with new DMEM, together with PBMCs conditioned media, at a rate of either 2:1 or 1:1 (DMEM/PBMCs), depending on the day of culture, as depicted in the diagram. DMEM was supplemented with different chemicals and growth factors depending on the day of culture, as depicted in the diagram. Exact concentrations are described in the Materials and Methods section. **(B)** Light microscopy photographs of monocytes, right after isolation from PBMCs, monocyte-derived-neuronal-like cells (MDNCs) and human developing neurons (HDNs) in culture for 5 days (20× original magnification). **(C)** Light microscopy photographs of MDNCs in parallel with immunostainings showing tubulin in green and actin in red. The cells' nuclei were stained with DAPI in blue (60× original magnification). Scale bar = 20 μm.

Pictures of cells were taken using a Nikon (Melville, NY, USA) Eclipse Ti-S/L 100 inverted microscope equipped with a CoolSNAP Myo, 20 MHz, 2.8 Megapixel, $4.54 \times 4.54 \mu\text{m}$ pixels camera (Melville, NY, USA) and with a Nikon CFI Super flour 20X DIC prism objective (Melville, NY, USA). Pictures were taken immediately after monocyte extraction and on days 20–21 when transdifferentiation was completed (Figure 1B). Pictures of transdifferentiated cells either under control conditions or after treatment with colchicine $0.5 \mu\text{M}$ (Sigma-Aldrich, C9754) were identified via a micro-ruled coverslip (Cellattice CLS5-25D, Nexcelom Bioscience, Lawrence, MA, USA). Only neuronal-like cells with at least one primary neurite longer than 2 times the soma size before treatment were traced.

Immunofluorescence was performed as previously described [28] (f. Briefly, after fixation and permeabilization, cells were stained with 4',6-diamidino-2-phenylindole, dihydrochloride (DAPI, D1306, Thermo Fisher Scientific, Waltham, MA, USA), mouse anti-tubulin (1/100, Invitrogen, Waltham, MA, USA), Alexa Fluor-488 (1/200, Life Technology, Waltham, MA, USA) and rhodamine phalloidin (1/200, Invitrogen, Waltham, MA, USA). Images were visualized with a Leica DMI 6000 microscope (Wetzlar, Germany) equipped with a Micro MAX-1300YHS camera using an HCX PL APO 60X oil objective (Leica, Wetzlar,

Germany). Images were captured using Metamorph Software (Version 7.1.3, Molecular Devices, San Jose, CA, USA).

2.2. Single Cell RNA-Sequencing

We utilized microfluidic single-cell capture and single-cell mRNA sequencing technologies via Fluidigm's C1™ Single-Cell Autoprep System (C1) to explore genome-wide gene expression in 17 cells exposed to our transdifferentiation protocol and for THP-1 cells. We followed the manufacturer's protocol, as previously described [28]. In short, cells were loaded using an integrated fluidic circuit (IFC) chip that allowed capturing a single cell per well. After optical confirmation of cell number at each capture site on the chip, the cells were processed for in-line cell lysis, reverse transcription and cDNA amplification steps. The resulting cDNA was converted to a sequencing library using Illumina's Nextera XT library preparation kit. The *Rapid* mode of Illumina HiSeq 2500 was used to generate sequencing reads of sufficient depth (about 3 million of sequencing reads) per each cell. Demultiplexed sequencing reads passed the default quality filtering of the Illumina CASAVA pipeline (v1.8, Illumina, Inc., San Diego CA, USA) and were then exposed to further quality trimming/filtering using FASTX-Toolkit (v.0.0.13, Hannon Laboratory, Cold Spring Harbor, NY, USA). The filtered reads were aligned to the most recent reference genome (hg38) using Tophat (v2.0.9, Center for Computational Biology, Baltimore, MD, USA) [36] by allowing up to 2 mismatches. After normalization was performed via the median of the geometric means of fragment counts across all libraries, fragments per kilobase per million (FPKM) mapped reads values were calculated using Cuffdiff tool, which is available in Cufflinks version 2.2.1 (Trapnell Lab, Seattle, WA, USA) [37]. Some results from this experiment were reported previously [28], but the expression of all genes presented in this manuscript have never before been reported in MDNCs.

Gene expression for human neuroblastoma cells was obtained from a public database generated by Li et al. [38].

2.3. Statistical Analysis

The non-parametric Mann–Whitney test was used to make pairwise comparisons between MDNCs treated with colchicine versus MDNCs under control conditions. A one-way ANOVA followed by Bonferroni correction was used to make comparisons between the time it took to trace MDNCs using each of the three tracing methods tested. *p* values lower or equal to 0.05 were considered significant.

3. Results

3.1. Neuronal and Monocyte Markers in MDNCs, SH-SY5Y and THP-1 Cells

We compared the expression of 12 neuronal markers between (a) MDNCs; (b) SH-SY5Y cells, a human neuroblastoma cell line commonly used to study neuronal processes; and (c) THP-1 cells, a human monocytic cell line (to serve as negative control). Of the 12 neuronal markers, 7 are involved in synaptic functions, 4 are part of the neuronal structure and one is a gamma-aminobutyric acid (GABA) type A receptor (Table 1). The expression of these 12 genes has never been reported in MDNCs. Expression of these 12 genes in 17 MDNCs was determined by single-cell mRNA sequencing. All 12 neuronal markers were expressed in at least one MDNC, and most genes were expressed in at least 6 MDNCs (Table 2). SH-SY5Y cells also expressed all of these neuronal genes, while they were not expressed in THP-1 cells (Table 2). We then tested whether two markers for monocytes were present in THP-1 cells, MDNCs or SH-SY5Y. As expected, these two monocyte-specific genes were highly expressed by THP-1 cells, whereas they were not expressed by undifferentiated neuroblastoma cells and were barely detectable in differentiated SH-SY5Y cells (Table 2). Only 1 out of the 17 MDNCs showed very low expression of 1 monocyte marker, and none were expressed in the remaining 16 MDNCs (Table 2).

Table 1. Neuronal and monocytic genes and their functions.

Protein	Gene	Identifier	Function	Reference
Neurexin 3	NRXN3	ENSG00000021645	Synapsis	Sudhof 2021 [39]
Synaptosome-associated protein 25	SNAP25	ENSG00000132639	Synapsis	Antonucci et al. 2016 [40]
Synaptic vesicle glycoprotein 2A	SV2A	ENSG00000159164	Synapsis	Nowack et al. 2010 [41]
Vesicle-associated membrane protein 1	VAMP1	ENSG00000139190	Synapsis	Bhattacharya et al. 2002 [42]
SH3 and multiple ankyrin repeat domains 2	SHANK2	ENSG00000162105	Synapsis	Lim et al. 1999 [43]
Synuclein alpha	SNCA	ENSG00000145335	Synapsis	Burre 2015 [44]
Syntaxin 1A	STX1A	ENSG00000106089	Synapsis	Bennett et al. 1992 [45]
Spire type actin nucleation factor 1	SPIRE1	ENSG00000134278	Neuronal structure	Schumacher et al, 2004 [46]
Microtubule-associated protein tau	MAPT	ENSG00000186868	Neuronal structure	Barbier et al. 2019 [47]
Shootin 1	SHTN1 (KIAA1598)	ENSG00000187164	Neuronal structure	Toriyama et al. 2006 [48]
Growth-associated protein 43	GAP43	ENSG00000172020	Neuronal structure	Meiri et al. 1986 [49]
Gamma-aminobutyric acid (GABA) type A receptor subunit beta 3	GABRB3	ENSG00000166206	GABA receptor	Mortensen et al. 2010 [50]
Integrin subunit alpha M CD11B	ITGAM	ENSG00000169896	Immune system	Schmid et al. 2018 [51]
Monocyte chemoattractant protein 1 receptor	CCR2	ENSG00000121807	Immune system	Tu et al. 2020 [52]

Table 2. Expression of 12 neuronal markers and 2 markers for monocytes in THP-1 monocytic cells, SH-SY5Y neuroblastoma cells and 17 MDNCs.

Gene	THP-1	1	2	3	4	5	6	7	8	9	10	11	12	13	14	15	16	17	SH-SY5Y 1*	SH-SY5Y 2*
NRXN3	0	0	0	0.101	3.106	0.04	0.012	0	0.009	0	0.288	0	0	0.062	0.061	0.022	0	0.98	0.01	0.135
SNAP25	0	0	0	0.779	0.167	0.13	0.219	0.401	0	0	0	0	1.19	0.288	0	0	0.171	0	25.06	42.23
SV2A	0	0	0	0.089	0	0	0	0	0	0.127	0.044	0	0	0	0.086	0.171	0	0.055	10.37	6.810
VAMP1	0	0	0	0	0	0.256	0	0	0	0	0.692	0	0	0	0.054	0	0	0	0.942	1.472
SHANK2	0	0	0	0	0	0.132	0.031	0	0.76	0.068	0.929	0	0.059	0	0.223	0.552	0	0.199	0.219	0.229
SNCA	0	5.35	8.08	0	0	0.811	1.12	0	0	0	0	0	276.9	0	0	136.3	1.63	0	3.776	7.513
STX1A	0	0	0	0	0	0	0.028	0	0	0	0	0	0	0	0	0	0	0	8.742	9.759
SPIRE1	0	27.2	58.02	0.292	5.19	0	0.01	0	16.34	0.223	3.37	0	0	17.32	28.61	110.5	2.85	23.25	9.341	6.986
MAPT	0	0.089	0.023	0	0	0.075	0.192	0.024	0.128	0	0.045	0.042	0.028	0	0	0.019	0.032	0.073	1.535	4.176
SHTN1	0	45.73	25.8	4.66	0.27	4.62	2.47	43.59	4.53	16.44	20.04	0	0	1.36	12.95	0.154	0	83.34	2.038	3.827
GAP43	0	0	0	0	0.211	0	0	0	0	0	0	0	0	0	0	0	0	0	62.16	86.84
GABRB3	0	0.324	0.458	0.065	0.254	0.247	0.079	0.095	0.21	0.13	0.06	0.225	0	1.06	0.093	0.901	0.173	0.182	10.25	9.763
ITGAM	14.91	0	0	0	0	0	0	0	0	0	0	0	0.034	0	0	0	0	0	0	0.014
CCR2	24.62	0	0	0	0	0	0	0	0	0	0	0	0	0	0	0	0	0	0	0.078

1 * undifferentiated SH-SY5Y; 2 * differentiated SH-SY5Y; data from Li et al. 2015 [38].

3.2. Whole-Cell Tracing

After 20 days in culture following our protocol [28], transdifferentiated monocytes acquired a neuronal morphology comparable with that of HDNs (Figure 1B). These MDNCs extended neurites with a microtubule-based shaft, as shown in Figure 1C. Colchicine is well-known for its ability to elicit neurite retraction [53,54] via microtubule depolymerization [55]. In a prior publication, we showed that the structure of MDNCs responds similarly to the structure of neuroblastoma cells and that of human neurons in vitro when treated with colchicine 0.5 μ M [28]. While retraction is expected with colchicine 0.5 μ M, minimal to no retraction should occur under control conditions. To determine whether MDNCs exhibited any retraction under control culture conditions, a group of MDNCs was identified and photographed at baseline, meaning at time zero (T0 h). These MDNCs were kept under control conditions for 1 h (T1 h), and pictures of the exact same MDNCs were taken again (Figure 2A). The same procedure was followed to establish whether colchicine elicited pruning of neuronal extensions. In this latter case the 1 h incubation period was carried out in the presence of colchicine 0.5 μ M (Figure 2A).

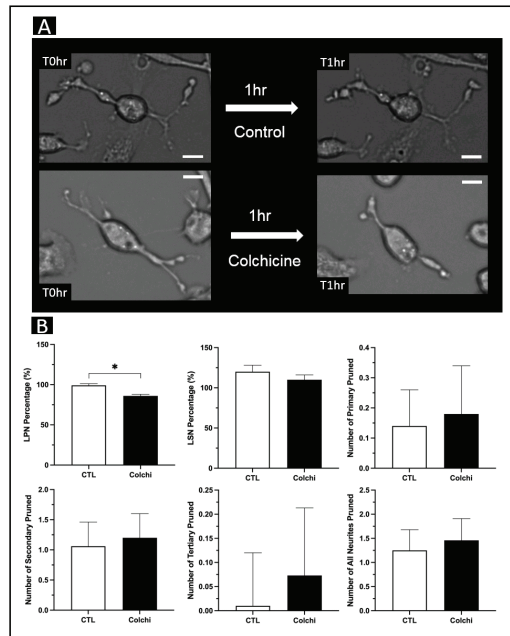


Figure 2. Whole-cell tracing of MDNCs after treatment with colchicine 0.5 μM . (A) Light microscopy photographs of the exact same MDNCs before (T0 h) and after one hour (T1 h) under control conditions or after treatment with colchicine 0.5 μM (20 \times original magnification). Scale bar = 20 μm . (B) Bar graphs comparing MDNCs' structural response to colchicine versus MDNCs under control conditions. Structural parameters include longest primary neurite (LPN), longest secondary neurite (LSN), number of primary neurites, number of secondary neurites, number of tertiary neurites and total number of neurites. Data are presented as mean \pm SEM. Differences were assessed using the non-parametric Mann–Whitney test. For LPN, number of primary, number of secondary, number of tertiary and total number of neurites, $n = 96$ for control and $n = 82$ for colchicine. For LSN, $n = 91$ for control and $n = 75$ for colchicine. * $p = \text{or} < 0.05$.

The principal investigator (PI), who has ample experience tracing cells, traced these four sets of MDNCs, meaning cells that were cultured under control conditions at T0 h and T1 h, as well as cells treated with colchicine at T0 h and T1 h. Since the entire neuropil of each MDNC was traced, we can report differences in the longest primary neurite (LPN), longest secondary neurite (LSN), number of primary neurites, number of secondary neurites, number of tertiary neurites and total number of neurites. MDNCs were traced using a semi-automated software called FIJI (NIH, Bethesda, MD, USA), which is a plugin for ImageJ, an open source image processing program provided by the National Institutes of Health (NIH).

To determine whether there was retraction of LPN or LSN, the percentage of neurite remaining at T1 h was calculated (T1 h/T0 h) for MDNCs cultured under control conditions, as well as cells treated with colchicine 0.5 μM . Then, non-parametric statistical analyses were conducted to establish whether there were differences between control (CTL) and colchicine (Colchi). Whole-cell tracing by the PI evidenced a statistically significant reduction in the percentage of LPN after treatment with colchicine 0.5 μM (CTL, $99 \pm 2\%$; Colchi, $86 \pm 2\%$; $p = 0.0006$), while there were no differences in LSN (CTL, $120 \pm 8\%$; Colchi, $110 \pm 6\%$; $p = 0.22$) (Figure 2B). To establish differences in the number of neurites pruned, we subtracted the number of neurites at T0 h from the number of neurites at T1 h for MDNCs cultured under control conditions as well as for cells treated with colchicine 0.5 μM . Whole-cell tracing did not reveal differences in the number of primary (CTL, 0.14 ± 0.12 ;

Colchi, 0.18 ± 0.16 ; non-parametric analysis $p = 0.48$), secondary (CTL, 1.06 ± 0.4 ; Colchi, 1.2 ± 0.4 ; $p = 0.45$), tertiary (CTL, 0.010 ± 0.11 ; Colchi, 0.073 ± 0.14 ; $p = 0.52$) or total neurites pruned (CTL, 1.25 ± 0.43 ; Colchi, 1.46 ± 0.45 ; $p = 0.27$) (Figure 2B).

3.3. Three Neurite Tracing Approaches

Three neurite tracing approaches were tested by four individuals with research experience (two medical students with previous research experience, one neuroscience graduate student and one laboratory technician). One of the medical students had performed cell tracing before participating in this study, whereas all other participants had no experience in tracing. The tracers were blinded to the treatment condition each of the two groups of MDNCs had received (either CTL or Colchi), and they were unaware of that we were expecting pruning of neuronal extensions with Colchi. Participants were trained on how to use FIJI (NIH, Bethesda, MD, USA), a semi-automated software, and Volocity (Quorum Technologies, Ontario, Canada), an automated software. After training was completed, participants were told to use FIJI for whole-cell tracing, and they were instructed to trace all neurites present in MDNCs for this first tracing method. For the second tracing method, they were again instructed to use FIJI, but this time to trace only the longest primary and longest secondary neurite in each of the MDNCs. This second approach was named the longest neurite method (LN). For the third method, participants processed the photographs of MDNCs for each of the two treatment conditions through Volocity and then confirmed that the MDNCs had been traced. Finally, participants were asked to record the time it took them to trace MDNCs with each of the three tracing methods.

Volocity automatically traces the length and width of the cell, which in the case of neuronal-like cells approximates to the longest primary neurite and the longest secondary neurite. Since two of the three tracing methods tested only provided information on LPN and LSN, we compared the three tracing approaches based on these two neuronal extensions. None of the four individuals encountered any statistically significant difference in LPN after whole-cell tracing (participant 1 (P1), CTL, $95 \pm 2\%$; Colchi, $100 \pm 3\%$; $p = 0.35$; P2, CTL, $100 \pm 5\%$; Colchi, $100 \pm 2\%$; $p = 0.86$; P3, CTL, $100 \pm 2\%$; Colchi, $99 \pm 2\%$, $p = 0.44$; P4, CTL, $99.9 \pm 2.8\%$; Colchi, $100 \pm 4.6\%$; $p = 0.45$) (Figure 3A). Participant 3, however, found colchicine elicited a statistically significant retraction of LSN (P3, CTL, $118 \pm 10.3\%$; Colchi, $88.1 \pm 9.7\%$; $p = 0.004$), while all other participants observed no differences (P1, CTL, $97 \pm 12.4\%$; Colchi, $109.9 \pm 11.3\%$; $p = 0.24$; P2, CTL, $100.6 \pm 9.5\%$; Colchi, $88.9 \pm 6.2\%$; $p = 0.27$; P4, CTL, $104.5 \pm 10\%$; Colchi, $100.1 \pm 7.5\%$; $p = 0.71$) (Figure 3A).

When tracing only longest neurites, one of the participants found colchicine elicited a statistically significant retraction of LPN when compared with MDNCs under control conditions (P2, CTL, $100 \pm 4\%$; Colchi, $90 \pm 2\%$; $p = 0.04$) (Figure 3B). All other participants found no statistical differences in LPN (P1, CTL, $93 \pm 4\%$; Colchi, $92 \pm 3\%$; $p = 0.66$; P3, CTL, $95 \pm 4\%$; Colchi, $100 \pm 3\%$; $p = 0.34$; P4, CTL, $91.7 \pm 2.7\%$; Colchi, $91.4 \pm 3.4\%$; $p = 0.42$). The same participant who found a significant retraction of LSN while tracing the entire cell again encountered retraction elicited by colchicine while tracing only longest neurites (P3, CTL, $143.2 \pm 15.8\%$; Colchi, $84.6 \pm 7\%$; $p = 0.001$) (Figure 3B). Two other participants found no statistical differences in LSN (P1, CTL, $100 \pm 14.9\%$; Colchi, $119.7 \pm 16.3\%$; $p = 0.07$; P2, CTL, $100.7 \pm 7.8\%$; Colchi, $116.2 \pm 17.1\%$; $p = 1.0$), and one participant did not trace LSN (Figure 3B).

The use of Volocity rendered no statistically significant differences in LPN for any of the participants (P1, CTL, $90.2 \pm 5.5\%$; Colchi, $81.4 \pm 11\%$; $p = 0.14$; P2, CTL, $94.6 \pm 9.6\%$; Colchi, $120.7 \pm 17.4\%$; $p = 0.18$; P3, CTL, $95 \pm 6.4\%$; Colchi, $91.7 \pm 5.7\%$, $p = 0.68$; P4, CTL, $116.6 \pm 18.2\%$; Colchi, $92.2 \pm 11.8\%$; $p = 0.27$) (Figure 3C). However, participant 4 found a significant retraction in LSN after treatment with colchicine (P4, CTL, $156.2 \pm 18.4\%$; Colchi, $117 \pm 20.3\%$; $p = 0.05$) (Figure 3C). None of the other participants found statistical differences in LSN while using Volocity (P1, CTL, $202.5 \pm 25.5\%$; Colchi, $182.9 \pm 33.6\%$; $p = 0.27$; P2, CTL, $148.6 \pm 16.1\%$; Colchi, $173 \pm 38.5\%$; $p = 0.99$; P3, CTL, $121.2 \pm 12\%$; Colchi, $119.4 \pm 16.4\%$; $p = 0.31$) (Figure 3C).

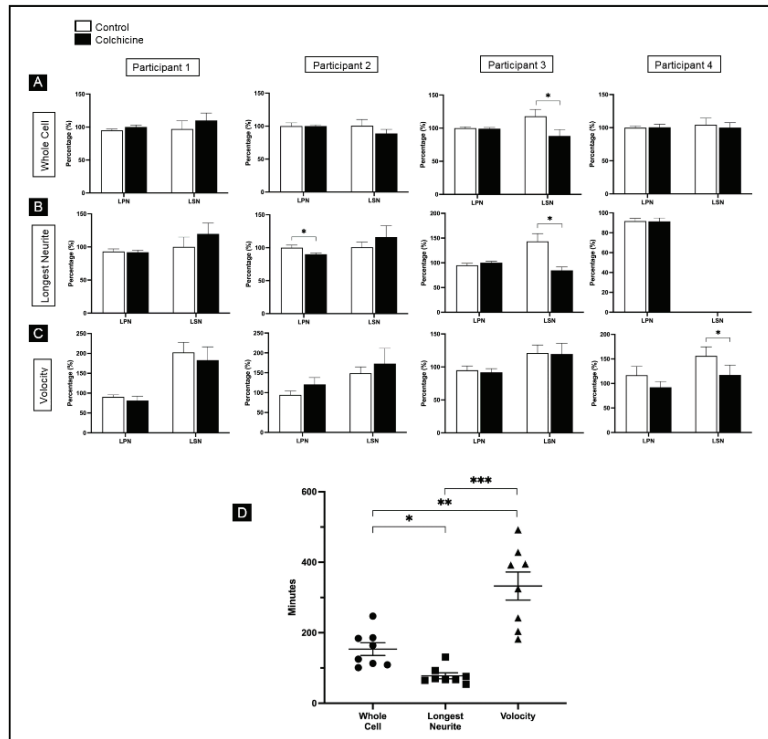


Figure 3. Comparison between three different tracing methods. (A) Bar graphs comparing MDNCs' structural response to colchicine versus MDNCs under control conditions after tracing each MDNC in its entire. Structural parameters include longest primary neurite (LPN) and longest secondary neurite (LSN). Data are presented as mean \pm SEM. Differences were assessed using the non-parametric Mann–Whitney test. Participant 1 (P1): for LPN $n = 37$ for control and $n = 32$ for colchicine; for LSN, $n = 23$ for control and $n = 20$ for colchicine. P2: for LPN $n = 38$ for control and $n = 35$ for colchicine; for LSN, $n = 15$ for control and $n = 19$ for colchicine. P3: for LPN $n = 47$ for control and $n = 34$ for colchicine; for LSN, $n = 41$ for control and $n = 29$ for colchicine. P4: for LPN $n = 51$ for control and $n = 30$ for colchicine; for LSN, $n = 31$ for control and $n = 15$ for colchicine. (B) Bar graphs comparing MDNCs' structural response to colchicine versus MDNCs under control conditions after only tracing LPN and LSN. The statistical assessment and data presentation are the same as in (A). P1: for LPN $n = 39$ for control and $n = 36$ for colchicine; for LSN, $n = 22$ for control and $n = 17$ for colchicine. P2: for LPN $n = 38$ for control and $n = 36$ for colchicine; for LSN, $n = 21$ for control and $n = 17$ for colchicine. P3: for LPN $n = 30$ for control and $n = 35$ for colchicine; for LSN, $n = 28$ for control and $n = 34$ for colchicine. P4: for LPN $n = 42$ for control and $n = 37$ for colchicine; P4 did not trace LSN. (C) Bar graphs comparing MDNCs' structural response to colchicine versus MDNCs under control conditions after tracing MDNCs' length and width using the automated tracing software Velocity. The statistical assessment and data presentation are the same as in (A). P1: for LPN $n = 30$ for control and $n = 26$ for colchicine; for LSN, $n = 30$ for control and $n = 23$ for colchicine. P2: for LPN $n = 25$ for control and $n = 18$ for colchicine; for LSN, $n = 25$ for control and $n = 18$ for colchicine. P3: for LPN $n = 33$ for control and $n = 30$ for colchicine; for LSN, $n = 33$ for control and $n = 30$ for colchicine. P4: for LPN $n = 27$ for control and $n = 24$ for colchicine; for LSN, $n = 27$ for control and $n = 24$ for colchicine. * p or < 0.05 . (D) Dot plot comparing the time in minutes necessary for completing the tracing of all MDNCs (control + colchicine) with each of the three tracing methods: whole cell, longest neurite and Velocity. Data are presented as mean \pm SEM. Differences were assessed using a one-way ANOVA followed by Bonferroni correction. For whole cell, longest neurite and Velocity $n = 8$. * $p < 0.005$, ** $p < 0.002$ and *** $p < 0.00002$.

A one-way ANOVA revealed that the amount of time necessary to complete all tracings was significantly different between each of the three approaches ($F(2, 21) = 25.74$, $p < 0.00001$) (Figure 3D). Bonferroni correction indicated that tracing longest neurites (LN) took less than half of the time needed to trace the whole cell (WC) (LN, 77.8 ± 8.5 min; WC, 153.6 ± 17.9 min; $p = 0.001$), while tracing the entire cell was more efficient than using Volocity (WC, 153.6 ± 17.9 min; V, 332.5 ± 39.9 min; $p = 0.001$) (Figure 3D). Since one of the students did not trace longest secondary neurites when applying the LN approach, we ran another one-way ANOVA excluding that individual's LN data. The results remained significant ($F(2, 19) = 20.81$, $p = 0.00001$).

4. Discussion

We have previously shown that MDNCs conduct electrical activity and express a wide variety of neuronal markers [28]. Here we expanded the list to include 12 neuronal genes: 7 involved in synaptic transmission [39–45], 4 associated with neuronal structure [46–49] and 1 gamma-aminobutyric acid (GABA) receptor [50] (Tables 1 and 2). Several of these genes are implicated in the pathophysiology of neurodevelopmental illnesses. For instance, neurexin 3 has been linked to autism [56], whereas SV2A and VAMP are associated with schizophrenia [57,58]. Another synaptic gene, SNAP-25, has been implicated in the etiology of both illnesses [59,60]. Tau and GAP-43 are essential for the development of neuronal structure [47,49]. While tau is commonly known for its association with Alzheimer's disease, this protein has also been linked to schizophrenia [61]. Similar to tau, GAP-43 is crucial for outgrowth of neuronal extensions [49], and not surprisingly, abnormalities in the expression of GAP-43 have been associated with both schizophrenia [62] and autism [63]. Other proteins relevant for the establishment of neuronal shape during development and often involved in the pathophysiology of schizophrenia, such as MAP-2 [64,65], are also expressed by MDNCs [28]. At the same time, markers for monocytes such as CD11B and CCR2 [51,52] are no longer present in MDNCs (Tables 1 and 2).

Several lines of evidence strongly indicate that deficits in the neuronal structure are implicated in the pathophysiology of autism and schizophrenia [12,13,66–68]. However, the inaccessibility of neurons coming directly from living patients' brains has limited the study of early neurodevelopmental processes that transform neuronal structure. MDNCs not only express a variety of genes crucial in sculpting neuronal shape, but in addition, the structure of MDNCs is comparable with that of human neurons after 5 days in culture and also with that of differentiated human neuroblastoma cells [28]. Moreover, the structure of MDNCs responds similarly to that of neurons and neuroblastoma cells when treated with dopamine and colchicine [28].

MDNCs' ability to reproduce characteristics of the structure of human neurons opens the opportunity for studying these aspects of neurodevelopmental illnesses directly in living patients' cells. This means that MDNCs provide a window into early neurodevelopmental processes in vitro, even when patients are already adults. Nonetheless, in order to maximize the delivery of neurostructural results, it is imperative to determine which neurite tracing method is more efficient in extracting data from MDNCs.

Unfortunately, there is no universal tracing method that can efficiently extract neurostructural data under all research conditions. Instead, experts recommend testing several tracing approaches to determine which is the best suited for each laboratory [69,70]. Currently, there is a plethora of automated tracing methods, but the gold standard continues to be manual tracing via semi-automated approaches [69]. Therefore, here we tested three different tracing approaches: (1) whole-cell tracing, (2) longest neurite tracing and (3) Volocity. The first two are semi-automated and thus require more work, while the third method is completely automated. However, before comparing these three tracing methods, we had to establish the right conditions for comparison. Therefore, the principal investigator, who has ample experience tracing cells, traced two separate groups of MDNCs: one cultured under control conditions and one treated with colchicine $0.5 \mu\text{M}$. This compound is well-known for its capacity to cause neurite retraction via microtubules depolymerization [55]. Further-

more, we have previously shown that colchicine elicits pruning of neuronal extensions in MDNCs in a way similar to what is found in neurons [53] and neuroblastoma cells [54].

Using the more thorough tracing approach—namely, whole-cell tracing—the PI found that colchicine elicited, as expected, a statistically significant retraction of LPN (Figure 2B). None of the other structural parameters revealed statistical differences (Figure 2B). Then, four other individuals, mostly students with research backgrounds, traced the same two groups of MDNCs (control versus colchicine 0.5 μM) using the three different tracing methods. These four participants were blinded to the treatment condition they were tracing. All the statistically significant retractions found by these four participants were, as expected, caused by colchicine (Figure 3A–C). However, relatively few structural differences were found. This is not entirely surprising, as these four individuals had limited experience with tracing, and the differences between the two MDNCs groups were subtle (Figure 2B). It is important to note that the tracing approach that yielded more statistically significant findings was the simplest of all, meaning the approach that only traced the longest primary and longest secondary neurite (Figure 3B).

The most surprising finding was that Volocity, the automated tracing method, was the slowest in delivering structural results (Figure 3D). This delay was not due to lack of recognition of MDNCs, even though these cells were not marked with a fluorochrome. Instead, pictures of MDNCs were live. The difficulties arose because in many instances Volocity did not identify the entire neuritic length. Students, therefore, had to piece together sections of neurites, similar to what other research teams have described using different automated softwares [70]. This task was more time consuming than even tracing the entire cell using a semi-automated approach (Figure 3D). Having MDNCs stained with a fluorochrome would have eliminated the need for reconstruction of the neuritic length. However, given the inherent damage attached to cell fixation and permeabilization [34,35], it is questionable whether the subtle structural differences between control MDNCs and those treated with colchicine would have been observed.

The fastest tracing approach was tracing only the longest primary and longest secondary neurites (Figure 3D). This approach was also the one that yielded more statistically significant differences between treatment conditions (control versus colchicine 0.5 μM) (Figure 3B). We were expecting whole-cell tracing to detect more structural differences, given the precision of this method. However, perhaps the simplicity of tracing only two neurites per MDNC as opposed to delineating the entire neuropil improves accuracy. Given that tracing longest neurites was more accurate and took half the time as tracing the entire cell and a quarter of the time as Volocity (Figure 3D), we recommend this tracing approach for future studies on the structure of MDNCs.

There are other factors that need to be considered when selecting a tracing approach. One is that tracing only the longest neurites neglects other structural parameters. Additionally, Volocity is just one of the many commercially available automated software products. It is possible that other automated applications would recognize the entire structure of MDNCs, even when analyzing photographs of live cells using light microscopy. However, if automated software products become a viable alternative, cost will have to be factored in, as semi-automated methods usually do not bear any cost to the researcher, while most automated software have to be purchased [69,70].

In summary, selecting a tracing method is a complicated process that depends on the specific research conditions to be tested [69,70]. For instance, analyzing neurons in culture (2-dimensional) versus brain slices (3-dimensional) or studying intact neurites versus damaged neurites would each generate its own set of intricacies for which only a couple of tracing approaches would be suitable. It is also essential to determine which aspects of the neuronal structure will be studied, as some tracing paradigms are better at measuring neurite length, while others excel at counting number of extensions [69,70]. Therefore, experts recommend testing different tracing approaches to determine the most efficient method for each laboratory [69,70]. Here, we determined that the most efficient tracing strategy for studying neuritic length in MDNCs is tracing only the longest primary

and longest secondary neurites (Figure 3D). The limitation of this modality is that it does not provide information about the number of neurites or other aspects of the neuropil, such as number or length of tertiary or quaternary neurites. Another limitation of our study is that we only conducted tracing using one automated method among the many currently available [69,70]. Future studies will have to be conducted to determine whether other automated paradigms prove better at extracting neurostructural data from MDNCs.

5. Conclusions

MDNCs express a wide variety of neuronal markers that have been associated with the pathophysiology of autism and schizophrenia. Since MDNCs originate from a blood sample taken directly from patients, these cells carry the genetic susceptibility to the neurodevelopmental illness that the patients are afflicted with. In contrast with rodent neurons in culture or neuronal cell lines such as neuroblastoma cells, MDNCs allow researchers to study directly in patients' cells early neurodevelopmental processes involving changes in neuronal structure. In order to maximize efficiency in studying MDNCs' structure, the best approach is to only trace the longest primary neurite and the longest secondary neurite using FIJI, a semi-automated software made available by the NIH.

Author Contributions: A.B. envisioned and designed this project, wrote the first draft and conducted some of the experiments; T.H. helped with result analysis; M.P. helped with the design of this project; K.G. conducted some experiments and helped write the final draft; M.C., E.B. and A.C.-R. conducted some experiments; G.A.C. conducted some experiments and helped write the final draft; L.E.H. helped design the project and helped write the final draft. All authors have read and agreed to the published version of the manuscript.

Funding: This research received no external funding.

Institutional Review Board Statement: The study was conducted according to the guidelines of the Declaration of Helsinki, and the study was approved by the Institutional Review Board of Penn State Hershey Medical Center (STUDY00006911).

Informed Consent Statement: Informed consent was obtained from all subjects involved in the study.

Data Availability Statement: The data presented in this study are available on request from the corresponding author.

Acknowledgments: The authors would like to thank the Ling and Esther Tan Early Career Professorship endowment given to A.B. We also would like to thank Julia Lesperance for her technical assistance.

Conflicts of Interest: This protocol is patented in the USA (99932556 (B2)) and Europe (2862926 (A1 & B1)). This patent is held by A.B. in collaboration with other authors as well as INSERM and SATT IDF-Innov. The authors report no other financial conflict of interest related to this manuscript.

References

- Christensen, D.L.; Baio, J.; Braun, K.V.N.; Bilder, D.; Charles, J.; Constantino, J.N.; Daniels, J.; Durkin, M.S.; Fitzgerald, R.T.; Kurzius-Spencer, M.; et al. Prevalence and characteristics of autism spectrum disorder among children aged 8 years—Autism and developmental disabilities monitoring network, 11 Sites, United States, 2012. *MMWR Surveill. Summ.* **2016**, *65*, 1–23. [CrossRef]
- Saha, S.; Chant, D.; Welham, J.; McGrath, J. A systematic review of the prevalence of schizophrenia. *PLoS Med.* **2005**, *2*, e141. [CrossRef] [PubMed]
- Tanaka, M.; Tóth, F.; Polyák, H.; Szabó, A.; Mándi, Y.; Vécsei, L. Immune influencers in action: Metabolites and enzymes of the Tryptophan-Kynurenine metabolic pathway. *Biomedicines* **2021**, *9*, 734. [CrossRef] [PubMed]
- Lee, G.A.; Lin, Y.-K.; Lai, J.-H.; Lo, Y.-C.; Yang, Y.-C.S.H.; Ye, S.-Y.; Lee, C.-J.; Wang, C.-C.; Chiang, Y.-H.; Tseng, S.-H. Maternal immune activation causes social behavior deficits and hypomyelination in male rat offspring with an autism-like microbiota profile. *Brain Sci.* **2021**, *11*, 1085. [CrossRef] [PubMed]
- Abuaish, S.; Al-Otaibi, N.; Abujamel, T.; Alzahrani, S.; Alotaibi, S.; AlShawakir, Y.; Aabed, K.; El-Ansary, A. Fecal transplant and *Bifidobacterium* treatments modulate gut *Clostridium* bacteria and rescue social impairment and hippocampal BDNF expression in a rodent model of autism. *Brain Sci.* **2021**, *11*, 1038. [CrossRef] [PubMed]
- Komatsu, H.; Watanabe, E.; Fukuchi, M. Psychiatric neural networks and precision therapeutics by machine learning. *Biomedicines* **2021**, *9*, 403. [CrossRef]

7. Correia, B.; Nani, J.; Ricardo, R.W.; Stanisic, D.; Costa, T.; Hayashi, M.; Tasic, L. Effects of psychostimulants and antipsychotics on serum lipids in an animal model for schizophrenia. *Biomedicines* **2021**, *9*, 235. [CrossRef]
8. Rog, J.; Błażewicz, A.; Juchnowicz, D.; Ludwiczuk, A.; Stelmach, E.; Kozioł, M.; Karakula, M.; Niziński, P.; Karakula-Juchnowicz, H. The role of GPR120 receptor in essential fatty acids metabolism in schizophrenia. *Biomedicines* **2020**, *8*, 243. [CrossRef]
9. Kalus, P.; Muller, T.J.; Zuschratter, W.; Senitz, D. The dendritic architecture of prefrontal pyramidal neurons in schizophrenic patients. *NeuroReport* **2000**, *11*, 3621–3625. [CrossRef]
10. Kalus, P.; Bondzio, J.; Federspiel, A.; Müller, T.J.; Zuschratter, W. Cell-type specific alterations of cortical interneurons in schizophrenic patients. *NeuroReport* **2002**, *13*, 713–717. [CrossRef]
11. Iritani, S.; Kuroki, N.; Niizato, K.; Ikeda, K. Morphological changes in neuropeptide Y-positive fiber in the hippocampal formation of schizophrenics. *Prog. Neuro-Psychopharmacol. Biol. Psychiatry* **2000**, *24*, 241–249. [CrossRef]
12. Martínez-Cerdeño, V. Dendrite and spine modifications in autism and related neurodevelopmental disorders in patients and animal models. *Dev. Neurobiol.* **2017**, *77*, 393–404. [CrossRef]
13. Varghese, M.; Keshav, N.; Jacot-Descombes, S.; Warda, T.; Wicinski, B.; Dickstein, D.L.; Harony-Nicolas, H.; De Rubeis, S.; Drapeau, E.; Buxbaum, J.; et al. Autism spectrum disorder: Neuropathology and animal models. *Acta Neuropathol.* **2017**, *134*, 537–566. [CrossRef] [PubMed]
14. Borgmann-Winter, K.; Rawson, N.; Wang, H.-Y.; MacDonald, M.; Ozdener, M.; Yee, K.; Gomez, G.; Xu, J.; Bryant, B.; Adamek, G.; et al. Human olfactory epithelial cells generated in vitro express diverse neuronal characteristics. *Neuroscience* **2009**, *158*, 642–653. [CrossRef]
15. Borgmann-Winter, K.; Willard, S.L.; Sinclair, D.; Mirza, N.; Turetsky, B.; Berretta, S.; Hahn, C.-G. Translational potential of olfactory mucosa for the study of neuropsychiatric illness. *Transl. Psychiatry* **2015**, *5*, e527. [CrossRef]
16. Féron, F.; Perry, C.; McGrath, J.J.; Mackay-Sim, A. New techniques for biopsy and culture of human olfactory epithelial neurons. *Arch. Otolaryngol. Head Neck Surg.* **1998**, *124*, 861–866. [CrossRef] [PubMed]
17. Woodbury, D.; Schwarz, E.J.; Prockop, D.J.; Black, I.B. Adult rat and human bone marrow stromal cells differentiate into neurons. *J. Neurosci. Res.* **2000**, *61*, 364–370. [CrossRef]
18. Taran, R.; Mamidi, M.K.; Singh, G.; Dutta, S.; Parhar, I.S.; John, J.P.; Bhonde, R.; Pal, R.; Das, A.K. In vitro and in vivo neurogenic potential of mesenchymal stem cells isolated from different sources. *J. Biosci.* **2014**, *39*, 157–169. [CrossRef]
19. Wen, Z.; Christian, K.M.; Song, H.; Ming, G.-L. Modeling psychiatric disorders with patient-derived iPSCs. *Curr. Opin. Neurobiol.* **2016**, *36*, 118–127. [CrossRef]
20. Urbach, A.; Bar-Nur, O.; Daley, G.Q.; Benvenisty, N. Differential modeling of fragile X syndrome by human embryonic stem cells and induced pluripotent stem cells. *Cell Stem Cell* **2010**, *6*, 407–411. [CrossRef]
21. Pera, M.F. Stem cells: The dark side of induced pluripotency. *Nature* **2011**, *471*, 46–47. [CrossRef] [PubMed]
22. Bellin, M.; Marchetto, M.C.; Gage, F.H.; Mummery, C. Induced pluripotent stem cells: The new patient? *Nat. Rev. Mol. Cell Biol.* **2012**, *13*, 713–726. [CrossRef]
23. Hu, B.-Y.; Weick, J.P.; Yu, J.; Ma, L.-X.; Zhang, X.-Q.; Thomson, J.A.; Zhang, S.-C. Neural differentiation of human induced pluripotent stem cells follows developmental principles but with variable potency. *Proc. Natl. Acad. Sci. USA* **2010**, *107*, 4335–4340. [CrossRef]
24. Dolmetsch, R.; Geschwind, D.H. The human brain in a dish: The promise of iPSC-derived neurons. *Cell* **2011**, *145*, 831–834. [CrossRef]
25. Yang, N.; Ng, Y.H.; Pang, Z.; Südhof, T.C.; Wernig, M. Induced neuronal cells: How to make and define a neuron. *Cell Stem Cell* **2011**, *9*, 517–525. [CrossRef]
26. Xu, Z.; Su, S.; Zhou, S.; Yang, W.; Deng, X.; Sun, Y.; Li, L.; Li, Y. How to reprogram human fibroblasts to neurons. *Cell Biosci.* **2020**, *10*, 116. [CrossRef]
27. Zhou, M.; Tao, X.; Sui, M.; Cui, M.; Liu, D.; Wang, B.; Wang, T.; Zheng, Y.; Luo, J.; Mu, Y.; et al. Reprogramming astrocytes to motor neurons by activation of endogenous Ngn2 and Isl1. *Stem Cell Rep.* **2021**, *16*, 1777–1791. [CrossRef]
28. Bellon, A.; Wegener, A.M.-A.; Lescalette, A.R.; Valente, M.; Yang, S.-K.; Gardette, R.; Matricon, J.; Mouaffak, F.; Watts, P.J.; Vimeux, L.; et al. Transdifferentiation of human circulating monocytes into neuronal-like cells in 20 days and without reprogramming. *Front. Mol. Neurosci.* **2018**, *11*, 323. [CrossRef] [PubMed]
29. Kosik, K.; Finch, E. MAP2 and tau segregate into dendritic and axonal domains after the elaboration of morphologically distinct neurites: An immunocytochemical study of cultured rat cerebrum. *J. Neurosci.* **1987**, *7*, 3142–3153. [CrossRef] [PubMed]
30. Dotti, C.G.; A Sullivan, C.; A Banker, G. The establishment of polarity by hippocampal neurons in culture. *J. Neurosci.* **1988**, *8*, 1454–1468. [CrossRef] [PubMed]
31. Dehmelt, L.; Halpain, S. Actin and microtubules in neurite initiation: Are MAPs the missing link? *J. Neurobiol.* **2004**, *58*, 18–33. [CrossRef] [PubMed]
32. Areal, L.B.; Blakely, R.D. Neurobehavioral changes arising from early life dopamine signaling perturbations. *Neurochem. Int.* **2020**, *137*, 104747. [CrossRef] [PubMed]
33. Sanches, M.; Keshavan, M.S.; Brambilla, P.; Soares, J.C. Neurodevelopmental basis of bipolar disorder: A critical appraisal. *Prog. Neuro Psychopharmacol. Biol. Psychiatry* **2008**, *32*, 1617–1627. [CrossRef] [PubMed]
34. Schnell, U.; Dijk, F.; Sjollem, K.A.; Giepmans, B. Immunolabeling artifacts and the need for live-cell imaging. *Nat. Methods* **2012**, *9*, 152–158. [CrossRef]

35. Cheng, R.; Zhang, F.; Li, M.; Wo, X.; Su, Y.-W.; Wang, W. Influence of fixation and permeabilization on the mass density of single cells: A surface plasmon resonance imaging study. *Front. Chem.* **2019**, *7*, 588. [CrossRef]
36. Trapnell, C.; Pachter, L.; Salzberg, S. TopHat: Discovering splice junctions with RNA-Seq. *Bioinformatics* **2009**, *25*, 1105–1111. [CrossRef]
37. Trapnell, C.; A Williams, B.; Pertea, G.; Mortazavi, A.; Kwan, G.; Van Baren, M.J.; Salzberg, S.; Wold, B.J.; Pachter, L. Transcript assembly and quantification by RNA-Seq reveals unannotated transcripts and isoform switching during cell differentiation. *Nat. Biotechnol.* **2010**, *28*, 511–515. [CrossRef]
38. Li, J.; Ma, Z.; Shi, M.; Maly, R.H.; Aoki, H.; Minic, Z.; Phanse, S.; Jin, K.; Wall, D.P.; Zhang, Z.; et al. Identification of Human Neuronal Protein Complexes Reveals Biochemical Activities and Convergent Mechanisms of Action in Autism Spectrum Disorders. *Cell Syst.* **2015**, *1*, 361–374. [CrossRef]
39. Südhof, T.C. The cell biology of synapse formation. *J. Cell Biol.* **2021**, *220*, e202103052. [CrossRef]
40. Antonucci, F.; Corradini, I.; Fossati, G.; Tomasoni, R.; Menna, E.; Matteoli, M. SNAP-25, a known presynaptic protein with emerging postsynaptic functions. *Front. Synaptic Neurosci.* **2016**, *8*, 7. [CrossRef]
41. Nowack, A.; Yao, J.; Custer, K.L.; Bajjalieh, S.M. SV2 regulates neurotransmitter release via multiple mechanisms. *Am. J. Physiol. Physiol.* **2010**, *299*, C960–C967. [CrossRef] [PubMed]
42. Bhattacharya, S.; Stewart, B.; Niemeyer, B.A.; Burgess, R.; McCabe, B.; Lin, P.; Boulianne, G.; O’Kane, C.; Schwarz, T.L. Members of the synaptobrevin/vesicle-associated membrane protein (VAMP) family in *Drosophila* are functionally interchangeable in vivo for neurotransmitter release and cell viability. *Proc. Natl. Acad. Sci. USA* **2002**, *99*, 13867–13872. [CrossRef] [PubMed]
43. Lim, S.; Naisbitt, S.; Yoon, J.; Hwang, J.-I.; Suh, P.-G.; Sheng, M.; Kim, E. Characterization of the shank family of synaptic proteins. Multiple genes, alternative splicing, and differential expression in brain and development. *J. Biol. Chem.* **1999**, *274*, 29510–29518. [CrossRef] [PubMed]
44. Burré, J. The Synaptic Function of α -Synuclein. *J. Park. Dis.* **2015**, *5*, 699–713. [CrossRef]
45. Bennett, M.K.; Calakos, N.; Scheller, R.H. Syntaxin: A synaptic protein implicated in docking of synaptic vesicles at presynaptic active zones. *Science* **1992**, *257*, 255–259. [CrossRef]
46. Schumacher, N.; Borawski, J.M.; Leberfinger, C.B.; Gessler, M.; Kerkhoff, E. Overlapping expression pattern of the actin organizers Spir-1 and formin-2 in the developing mouse nervous system and the adult brain. *Gene Expr. Patterns* **2004**, *4*, 249–255. [CrossRef]
47. Barbier, P.; Zejneli, O.; Martinho, M.; Lasorsa, A.; Belle, V.; Smet-Nocca, C.; Tsvetkov, P.O.; Devred, F.; Landrieu, I. Role of Tau as a microtubule-associated protein: Structural and Functional aspects. *Front. Aging Neurosci.* **2019**, *11*, 204. [CrossRef]
48. Toriyama, M.; Shimada, T.; Kim, K.B.; Mitsuba, M.; Nomura, E.; Katsuta, K.; Sakumura, Y.; Roepstorff, P.; Inagaki, N. Shootin1: A protein involved in the organization of an asymmetric signal for neuronal polarization. *J. Cell Biol.* **2006**, *175*, 147–157. [CrossRef]
49. Meiri, K.F.; Pfenninger, K.H.; Willard, M.B. Growth-associated protein, GAP-43, a polypeptide that is induced when neurons extend axons, is a component of growth cones and corresponds to pp46, a major polypeptide of a subcellular fraction enriched in growth cones. *Proc. Natl. Acad. Sci. USA* **1986**, *83*, 3537–3541. [CrossRef]
50. Mortensen, M.; Ebert, B.; Wafford, K.; Smart, T.G. Distinct activities of GABA agonists at synaptic- and extrasynaptic-type GABA receptors. *J. Physiol.* **2010**, *588*, 1251–1268. [CrossRef] [PubMed]
51. Schmid, M.C.; Khan, S.Q.; Kaneda, M.M.; Pathria, P.; Shepard, R.; Louis, T.L.; Anand, S.; Woo, G.; Leem, C.; Faridi, M.H.; et al. Integrin CD11b activation drives anti-tumor innate immunity. *Nat. Commun.* **2018**, *9*, 5379. [CrossRef]
52. Tu, M.M.; Abdel-Hafiz, H.A.; Jones, R.T.; Jean, A.; Hoff, K.J.; Duex, J.E.; Chauca-Diaz, A.; Costello, J.C.; Dancik, G.M.; Tamburini, B.A.J.; et al. Inhibition of the CCL2 receptor, CCR2, enhances tumor response to immune checkpoint therapy. *Commun. Biol.* **2020**, *3*, 720. [CrossRef]
53. Daniels, M.P. Colchicine inhibition of nerve fiber formation in vitro. *J. Cell Biol.* **1972**, *53*, 164–176. [CrossRef] [PubMed]
54. Brat, D.J.; Brimijoin, S. A paradigm for examining toxicant effects on viability, structure, and axonal transport of neurons in culture. *Mol. Neurobiol.* **1992**, *6*, 125–135. [CrossRef]
55. Drubin, D.; Kobayashi, S.; Kellogg, D.; Kirschner, M. Regulation of microtubule protein levels during cellular morphogenesis in nerve growth factor-treated PC12 cells. *J. Cell Biol.* **1988**, *106*, 1583–1591. [CrossRef]
56. Vaags, A.K.; Lionel, A.C.; Sato, D.; Goodenberger, M.; Stein, Q.; Curran, S.; Ogilvie, C.; Ahn, J.W.; Drmic, I.; Senman, L.; et al. Rare Deletions at the Neurexin 3 Locus in Autism Spectrum Disorder. *Am. J. Hum. Genet.* **2012**, *90*, 133–141. [CrossRef]
57. Onwordi, E.C.; Halff, E.F.; Whitehurst, T.; Mansur, A.; Cotel, M.-C.; Wells, L.; Creaney, H.; Bonsall, D.; Rogdaki, M.; Shatalina, E.; et al. Synaptic density marker SV2A is reduced in schizophrenia patients and unaffected by antipsychotics in rats. *Nat. Commun.* **2020**, *11*, 246. [CrossRef]
58. Halim, N.D.; Weickert, C.S.; McClintock, B.W.; Hyde, T.M.; Weinberger, D.R.; E Kleinman, J.; Lipska, B.K. Presynaptic proteins in the prefrontal cortex of patients with schizophrenia and rats with abnormal prefrontal development. *Mol. Psychiatry* **2003**, *8*, 797–810. [CrossRef]
59. Braid, D.; Guerini, F.R.; Ponzoni, L.; Corradini, I.; De Astis, S.; Pattini, L.; Bolognesi, E.; Benfante, R.; Fornasari, D.; Chiappedi, M.; et al. Association between SNAP-25 gene polymorphisms and cognition in autism: Functional consequences and potential therapeutic strategies. *Transl. Psychiatry* **2015**, *5*, e500. [CrossRef] [PubMed]
60. Corradini, I.; Verderio, C.; Sala, M.; Wilson, M.C.; Matteoli, M. SNAP-25 in neuropsychiatric disorders. *Ann. N. Y. Acad. Sci.* **2009**, *1152*, 93–99. [CrossRef] [PubMed]

61. Demirel, F.; Cetin, I.; Turan, S.; Yildiz, N.; Sağlam, T.; Duran, A. Total Tau and Phosphorylated Tau protein serum levels in patients with schizophrenia compared with controls. *Psychiatr. Q.* **2017**, *88*, 921–928. [CrossRef]
62. Weickert, C.S.; Webster, M.J.; Hyde, T.M.; Herman, M.M.; Bachus, S.E.; Bali, G.; Weinberger, D.R.; Kleinman, J.E. Reduced GAP-43 mRNA in dorsolateral prefrontal cortex of patients with schizophrenia. *Cereb. Cortex* **2001**, *11*, 136–147. [CrossRef] [PubMed]
63. Zikopoulos, V.; Barbas, H. Changes in prefrontal axons may disrupt the network in autism. *J. Neurosci.* **2010**, *30*, 14595–14609. [CrossRef] [PubMed]
64. Arnold, S.E.; Lee, V.M.; Gur, R.E.; Trojanowski, J.Q. Abnormal expression of two microtubule-associated proteins (MAP2 and MAP5) in specific subfields of the hippocampal formation in schizophrenia. *Proc. Natl. Acad. Sci. USA* **1991**, *88*, 10850–10854. [CrossRef] [PubMed]
65. Jones, L.B.; Johnson, N.; Byne, W. Alterations in MAP2 immunocytochemistry in areas 9 and 32 of schizophrenic prefrontal cortex. *Psychiatry Res. Neuroimaging* **2002**, *114*, 137–148. [CrossRef]
66. Bellon, A. New genes associated with schizophrenia in neurite formation: A review of cell culture experiments. *Mol. Psychiatry* **2007**, *12*, 620–629. [CrossRef]
67. Bellon, A.; Krebs, M.-O.; Jay, T.M. Factoring neurotrophins into a neurite-based pathophysiological model of schizophrenia. *Prog. Neurobiol.* **2011**, *94*, 77–90. [CrossRef]
68. Emerelo, V.; Edurand, D.; Lescalette, A.R.; Vrana, K.; Hong, L.E.; Faghihi, M.A.; Ebellon, A. Associating schizophrenia, long non-coding RNAs and neurostructural dynamics. *Front. Mol. Neurosci.* **2015**, *8*, 57. [CrossRef]
69. Donohue, D.E.; Ascoli, G.A. Automated reconstruction of neuronal morphology: An overview. *Brain Res. Rev.* **2011**, *67*, 94–102. [CrossRef]
70. Nguyen, C.; Thompson-Peer, K.L. Comparing automated morphology quantification software on dendrites of uninjured and injured drosophila neurons. *Neuroinformatics* **2021**, 1–15. [CrossRef]

Article

Modulation of Long-Term Potentiation by Gamma Frequency Transcranial Alternating Current Stimulation in Transgenic Mouse Models of Alzheimer's Disease

Won-Hyeong Jeong¹, Wang-In Kim¹, Jin-Won Lee¹, Hyeng-Kyu Park¹, Min-Keun Song², In-Sung Choi¹ and Jae-Young Han^{2,*}

¹ Department of Physical & Rehabilitation Medicine, Chonnam National University Hospital, Gwangju City 61469, Korea; jwhiiii@hanmail.net (W.-H.J.); wangto9@naver.com (W.-I.K.); barksa37@naver.com (J.-W.L.); phk1118@naver.com (H.-K.P.); drchois@hanmail.net (I.-S.C.)

² Department of Physical & Rehabilitation Medicine, Regional Cardiocerebrovascular Center, Center for Aging and Geriatrics, Chonnam National University Medical School & Hospital, Gwangju City 61469, Korea; drsongmk@daum.net

* Correspondence: rmhanjy@hanmail.net; Tel.: +82-62-220-5186

Abstract: Transcranial alternating current stimulation (tACS) is a neuromodulation procedure that is currently studied for the purpose of improving cognitive function in various diseases. A few studies have shown positive effects of tACS in Alzheimer's disease (AD). However, the mechanism underlying tACS has not been established. The purpose of this study was to investigate the mechanism of tACS in five familial AD mutation (5xFAD) mouse models. We prepared twenty 4-month-old mice and divided them into four groups: wild-type mice without stimulation (WT-NT group), wild-type mice with tACS (WT-T group), 5xFAD mice without stimulation (AD-NT group), and 5xFAD mice with tACS (AD-T group). The protocol implemented was as follows: gamma frequency 200 μ A over the bilateral frontal lobe for 20 min over 2 weeks. The following tests were conducted: excitatory postsynaptic potential (EPSP) recording, Western blot analysis (cyclic AMP response element-binding (CREB) proteins, phosphorylated CREB proteins, brain-derived neurotrophic factor, and parvalbumin) to examine the synaptic plasticity. The EPSP was remarkably increased in the AD-T group compared with in the AD-NT group. In the Western blot analysis, the differences among the groups were not significant. Hence, tACS can affect the long-lasting enhancement of synaptic transmission in mice models of AD.

Keywords: transcranial alternating current stimulation; Alzheimer's disease; noninvasive brain stimulation; gamma frequency; long-term potentiation; synaptic plasticity; transgenic mouse model; 5xFAD; excitatory postsynaptic potential; Western blot analysis

Citation: Jeong, W.-H.; Kim, W.-I.; Lee, J.-W.; Park, H.-K.; Song, M.-K.; Choi, I.-S.; Han, J.-Y. Modulation of Long-Term Potentiation by Gamma Frequency Transcranial Alternating Current Stimulation in Transgenic Mouse Models of Alzheimer's Disease. *Brain Sci.* **2021**, *11*, 1532. <https://doi.org/10.3390/brainsci11111532>

Academic Editors: Masaru Tanaka and Lydia Giménez-Llort

Received: 22 October 2021

Accepted: 17 November 2021

Published: 19 November 2021

Publisher's Note: MDPI stays neutral with regard to jurisdictional claims in published maps and institutional affiliations.



Copyright: © 2021 by the authors. Licensee MDPI, Basel, Switzerland. This article is an open access article distributed under the terms and conditions of the Creative Commons Attribution (CC BY) license (<https://creativecommons.org/licenses/by/4.0/>).

1. Introduction

Alzheimer's disease (AD) is a neurological disease characterized by progressive cognitive decline resulting in memory deficit and behavioral changes [1–3]. It is prevalent in a majority of dementia cases. It has been estimated that about 110 million people worldwide will have the disease by 2050 [4]. Today, AD is a global burden, and this trend may continue unless an effective treatment is developed [5]. Currently, pharmacologic treatment is the main therapeutic modality for patients with AD; however, this therapeutic effect has been proven to be insufficient in ameliorating the state of patients affected by the disease. In addition, various side effects have been reported [6–8]. As an alternative to drug therapy, noninvasive brain stimulation (NIBS) has been studied in patients with AD. Previous studies have suggested that repetitive transcranial magnetic stimulation (rTMS) and transcranial direct current stimulation (tDCS) can be used for therapeutic purposes in patients with AD [9–11]. Furthermore, Hausner et al. demonstrated an improvement in the mini-mental state examination (MMSE) score after electroconvulsive treatment in

patients with AD and major depressive disorder (MDD) [12]. Moreover, although there are no noninvasive vagus nerve stimulation (nVNS)-related human studies of AD to date, microglial modulation through nVNS was reported in an animal study (mouse model of AD) [13]. However, according to the studies published so far, cranial electrotherapy stimulation (CES), a type of NIBS, is known to be ineffective in improving cognitive function in the case of AD [14,15].

Recently, as a method of NIBS, transcranial alternating current stimulation (tACS) has been studied in patients with several diseases, including Parkinson's disease and schizophrenia, to improve cognitive function [16,17]. In addition, previous studies showed that tACS can alleviate symptoms in other psychiatric diseases, such as anxiety disorder, MDD, and obsessive-compulsive disorder [18–20]. It is easy to apply in various conditions and a relatively inexpensive tool [21]. Since it is a noninvasive method, it has fewer side effects, including mild headache, nausea, and fatigue [22].

In a previous study using AD transgenic mouse models, neuronal activity, especially gamma frequency oscillations, was found to be impaired in the hippocampus [23]. This condition resulted from the amyloid-beta that alter the excitatory/inhibitory balance of the neuronal network and disrupt the inhibitory interneurons [24,25]. Moreover, tACS can manipulate neuronal oscillations, thereby influencing cognitive processes [26]. Ali et al. showed that tACS is more effective in the entrainment of brain waves using a specific frequency than tDCS, because human brain waves are more similar in form to alternating currents than direct currents [27].

Several studies have investigated the effectiveness of tACS in patients with AD [28–31]. Kehler and Moussavi et al. reported that, in patients with AD, tACS with brain exercise can be more beneficial for cognitive function than brain exercise alone [28,29]. Benussi et al. showed that tACS could enhance memory functions in patients with AD [30]. Dhaynaut et al. reported that tACS may modulate the Tau-related burden in AD measured by positron emission tomography (PET) [31]. Xing et al. suggested a protocol of tACS in patients with AD for a randomized controlled trial that has not yet been completed [32]. However, these studies were limited in terms of identifying the underlying mechanisms of action, because they involved human subjects. In the present study, we conducted a tACS experiment in transgenic mouse models of AD to elucidate its mechanism.

2. Materials and Methods

We first prepared the wild-type C57BL/6 female mice (Damul Science, Daejeon, Korea) and transgenic male mice expressing 5 familial AD mutations (5xFAD) carrying a Swedish double mutation (KM670/671NL) in the amyloid precursor protein (APP) gene. After crossbreeding them, we waited until the mice were 3 weeks old. At this time, only male mice were classified separately and underwent genotyping using polymerase chain reaction (PCR) with ear tissue. In this way, we confirmed the mice as 5xFAD or wild type. We then included twenty 4-month-old mice for the experiments.

2.1. Transcranial Alternating Current Stimulation

We prepared an oscillating-current stimulator (NT Brain 100, CyberMedic Corp., Iksan, Korea). Twenty mice were divided into four groups, with each group consisting of five mice: wild-type mice with no stimulation (WT-NT group), wild-type mice receiving tACS (WT-T group), 5xFAD mice with no stimulation (AD-NT group), and 5xFAD mice receiving tACS (AD-T group). The stimulation group received tACS with a gamma frequency (40 Hz) of 200 μ A over the F3 and F4 (bilateral frontal lobe) areas for 20 min. During stimulation, isoflurane was used to minimize mice movements. tACS was then applied to the precise location. In this manner, the stimulus was implemented 10 times in 2 weeks for five consecutive days with two off days. The AD-NT and WT-NT groups did not undergo stimulation. Instead, they were caged without anesthesia for 20 min, which was equal to the stimulation time.

2.2. Preparation of Brain Tissue

The brain was immediately extracted after the mice were euthanized under anesthesia after 2 weeks of starting the experiment. Artificial cerebrospinal fluid (aCSF) was prepared as follows to maintain osmolarity and pH at the physiological levels: 2.8-mM KCl, 125-mM NaCl, 1.25-mM NaH₂PO₄, 2-mM CaCl₂, 1-mM MgSO₄, and 26-mM NaHCO₃. Furthermore, aCSF and freezing liquid were used to immerse the isolated brains. After placing the brains on a cooling pad, we found the exact location of the hippocampus using various brain landmarks such as the cerebellum and used a rotary slicer and automatic chopper (Mickle Laboratory Engineering Co. Ltd., Gomshall Guildford, UK). The thickness of each sample was about 400 µm. The slices were immersed in aCSF for at least an hour. During this process, oxygen was supplied to stabilized PH with carbogen (mixture of carbon dioxide (5%) and oxygen (95%)).

2.3. Excitatory Postsynaptic Potential (EPSP)

A glass-bottomed recording chamber (Glass cover slip CS-22/40, Warner Instruments, Holliston, MA, USA) filled with aCSF was prepared to record the EPSP in the sliced hippocampus. In this chamber, carbogen was also supplied. Using a nichrome recording electrode (Nickel/Chromium wire, Advent research materials Ltd., Oxford, UK), we recorded the field EPSP (fEPSP) in CA1 of the hippocampal subfield region. During this process, we delivered every pulse at 15-s intervals. For each waveform of fEPSP, the initial slope of the fEPSP was calculated, which showed the postsynaptic response. After adjusting the baseline fEPSP slope (30% of the maximal response), a stimulation was delivered at a high frequency (100 Hz) to the CA3–CA1 hippocampal synapses for long-term potentiation (LTP). The baseline fEPSP slope was recorded for 30 min, and LTP was recorded for 60 min. We analyzed the data using WinLTP software (WinLTP Ltd., Bristol, UK).

2.4. Western Blot Analysis

For protein extraction from the sliced hippocampus, the radioimmunoprecipitation assay buffer and protein inhibitor cocktail were used and centrifuged at 4 °C for 30 min at 15,000 rpm. After the spin down, the upper layer solution (protein) was obtained for protein quantification with the bicinchoninic acid assay. We prepared 10–12% gels and a polyvinylidene fluoride membrane for protein loading and transfer, respectively. The membrane was then incubated for blocking with 5% skim milk for 1 h. Then, using Tris-buffered saline with Tween 20 (TBST), we washed it (3 times). We prepared the diluted primary antibody solution (cyclic AMP response element-binding (CREB) proteins (1:1000), phosphorylated CREB (pCREB) proteins (1:1000), brain-derived neurotrophic factor (BDNF) (1:1000), and parvalbumin (PV) (1:1000)) and incubated them overnight with the membranes (4 °C). The next day, using TBST, we washed the membranes (3 times). We also incubated the diluted secondary antibody solution (rabbit immunoglobulin G (IgG; 1:2000)) with the membrane for one and a half hours. In the same way, we washed the membranes using TBST (3 times). The membranes were incubated in a chemiluminescent substrate for horseradish peroxidase for detection. The Western blot was analyzed using UVITEC Mini HD9 (Alliance UVItec Ltd., Cambridge, UK).

2.5. Statistical Analyses

We used the Kruskal–Wallis test to compare the differences between the AD-NT, AD-T, WT-NT, and WT-T groups. A post hoc analysis was performed by the Bonferroni method. The significance level for multiple comparisons after the Bonferroni method was 0.0083. There was a system that provided a new report of the adjusted *p*-value based on the significance level of 0.05 after Bonferroni correction in the SPSS program, version 27.0 (IBM, SPSS, Armonk, NY, USA). Therefore, we set a statistical significance level of 0.05 based on the adjusted *p*-value. A data analysis was conducted through SPSS, version 27.0 (IBM, SPSS, Armonk, NY, USA).

3. Results

3.1. fEPSP Responses

The fEPSP slope showed the responses of the WT-NT group ($159 \pm 10\%$), WT-T group ($145 \pm 4\%$), the AD-NT group ($123 \pm 3\%$), and the AD-T group ($156 \pm 20\%$). The fEPSP slope was remarkably increased in the AD-T group compared to that in the AD-NT group (p -value = 0.003). In addition, the fEPSP slope was higher in the WT-T group (p -value = 0.001) and WT-NT group (p -value = 0.000) than in the AD-NT group. However, there were no significant differences among the other groups (Figure 1).

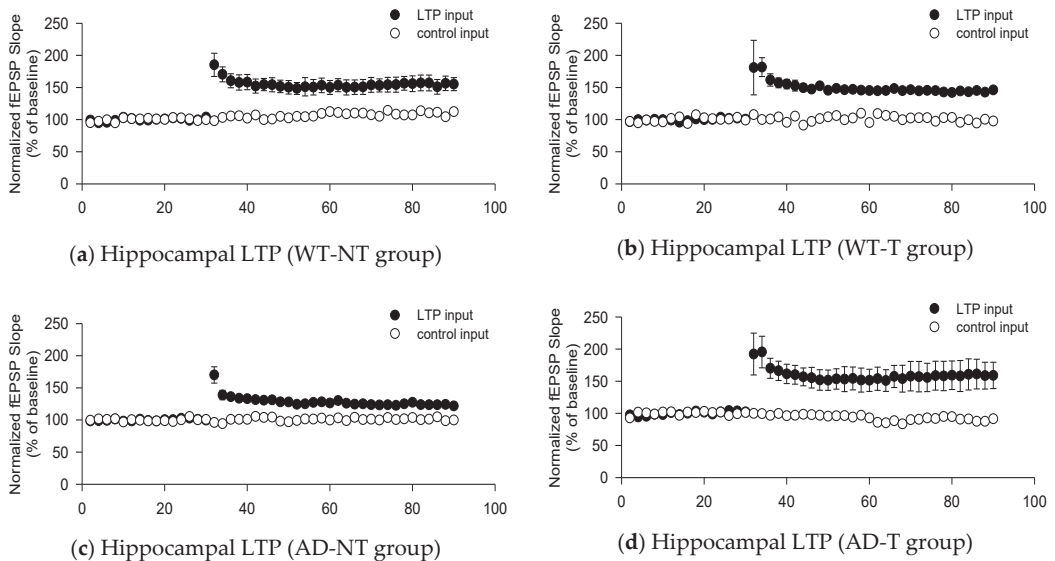


Figure 1. The graphs show the field excitatory postsynaptic potential (fEPSP) responses in each group. High-frequency stimulation are delivered at 30 min for long-term potentiation (LTP). (a) fEPSP in the hippocampal region of wild-type mice that did not receive transcranial alternating current stimulation (tACS). (b) fEPSP in the hippocampal region of wild-type mice that received tACS. (c) fEPSP in the hippocampal region of 5 familial AD mutation (5xFAD) mice that did not receive tACS. (d) fEPSP in the hippocampal region of 5xFAD mice that received tACS. The white dots are the baseline fEPSP slopes, and the black dots are the main results of the fEPSP slope stimulated by high frequency. The fEPSP slope was remarkably increased in the AD-T group (d) compared to that in the AD-NT group (c) (p -value = 0.003). In addition, the fEPSP slope was higher in the WT-T group (b) (p -value = 0.001) and WT-NT group (a) (p -value = 0.000) than in the AD-NT group (c). However, there were no significant differences among the other groups. The data from each group show mean values and standard errors (SE). For statistical analysis, the Kruskal–Wallis test and the Bonferroni method for post hoc analysis were used.

3.2. Protein Level Analyzed by Western Blot Analysis

A Western blot analysis was conducted to examine whether there were any changes in the amount of proteins related to neuroplasticity and gamma oscillation. There were no significant differences in the levels of BDNF, CREB, pCREB, and PV among the groups (Figure 2).

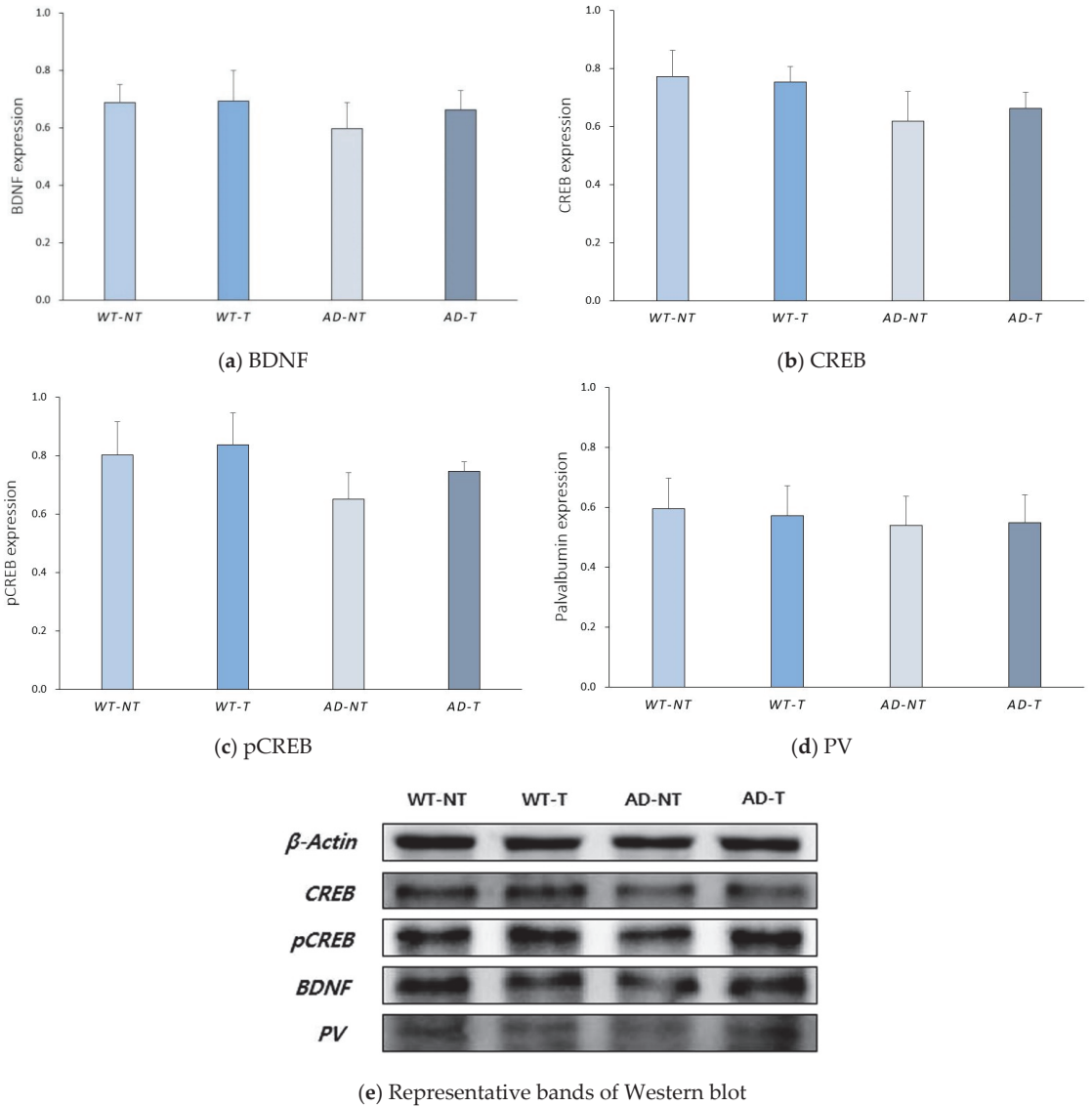


Figure 2. Western blot analysis of brain-derived neurotrophic factor (BDNF), cyclic AMP response element-binding protein (CREB), phosphorylated CREB (pCREB), and parvalbumin (PV). (a) Quantitative BDNF expression level in the WT-NT group (0.69 ± 0.06), the WT-T group (0.69 ± 0.11), the AD-NT group (0.60 ± 0.09), and the AD-T group (0.66 ± 0.07). (b) Quantitative CREB expression level of the WT-NT group (0.77 ± 0.09), the WT-T group (0.75 ± 0.05), the AD-NT group (0.62 ± 0.10), and the AD-T group (0.66 ± 0.06). (c) Quantitative pCREB expression level of the WT-NT group (0.80 ± 0.11), the WT-T group (0.84 ± 0.11), the AD-NT group (0.65 ± 0.09), and the AD-T group (0.75 ± 0.03). (d) Quantitative PV expression level of the WT-NT group (0.60 ± 0.10), the WT-T group (0.57 ± 0.10), the AD-NT group (0.54 ± 0.10), and the AD-T group (0.55 ± 0.09). (e) Representative bands of CREB, pCREB, BDNF, and PV. The data from each group show the mean values and standard errors (SE). A statistical analysis was performed using the Kruskal–Wallis test and the Bonferroni method for post hoc analysis.

4. Discussion

Gamma frequency oscillations are prominent in the hippocampus, which is a major region for the formation of memory [33]. In this region, gamma oscillation can be functionally classified into slow gamma oscillation (25–55 Hz) and fast gamma oscillation (60–100 Hz). Specifically, fast gamma oscillation is related to memory encoding, while slow gamma oscillation is related to memory retrieval [34]. Previous studies have suggested that patients with AD show reduced slow gamma oscillation and the ability to retrieve memory rather than a decreased ability to encode memory [23,35]. Iaccarino et al. showed a reduced hippocampal gamma waveform in transgenic 5xFAD mice and presented an experiment in which amyloid-beta production decreased after using visual stimulation (light flicker) with gamma frequencies [36]. Anthony et al. showed improved memory function and reduced hippocampal amyloid-beta in 5xFAD mice after using auditory tone stimulation with gamma frequencies [37]. In addition, several human studies have suggested that gamma tACS can be a new treatment strategy in patients with AD [28–30].

In this animal study, we investigated the mechanism of tACS in a transgenic mouse model. Oakley et al. reported that, in 5xFAD mice, cognitive function, including working memory, decreased in 4 months due to neurodegeneration [38]. Therefore, we waited until the mice were 4 months old before conducting the tests. We then implemented fEPSP to explore the mechanisms for changes occurring after applying the tACS. Previous studies have shown that high-frequency stimulations of mice's hippocampal CA1 can be used for estimating the degree of synaptic plasticity, such as LTP [39]. LTP is a process in which there is increased synaptic strength, which is the signal transmission between a presynaptic neuron and a postsynaptic neuron. In response to the stimulus, α -amino-3-hydroxy-5-methyl-4-isoxazolepropionate receptor (AMPA) trafficking plays the most decisive part in LTP through mobilizing preexisting AMPARs to the synaptic sites, resulting in increased AMPAR-mediated synaptic responses [40]. BDNF can upregulate the level of AMPAR and increase AMPAR trafficking in the hippocampus [41]. In addition, BDNF can induce LTP by increasing the synaptic response to high-frequency stimulation [42]. Besides the functional modification, BDNF modulates the structure by increasing the dendritic spine and arborization, which enhances the synaptic transmission [43]. In patients with AD, AMPAR is downregulated in an amyloid-beta-dependent manner, and BDNF is downregulated in the hippocampus and cortex, according to a recent meta-analysis [44,45]. Moreover, CREB can modulate the expression of BDNF promoters as a transcriptional factor. However, patients with AD show a decreased level of pCREB (activated form), reducing CREB activity, which is eventually caused by the decreased BDNF downregulation [46]. Hence, we measured the functional changes from an electrophysiological perspective and the amount of protein changes from a molecular perspective to determine the post-treatment effect of tACS. The electrophysiological test we conducted showed that the fEPSP slope was remarkably higher in the AD-T group than in the AD-NT group. However, there were no statistically significant differences between the WT-T and the WT-NT groups, suggesting that applying tACS in AD transgenic mice can increase the degree of synaptic plasticity. In the Western blot analysis, there were no statistically significant differences in the levels of BDNF, CREB, and pCREB among the groups.

In addition to investigating the CREB, pCREB, and BDNF levels, we also investigated the PV levels using the Western blot analysis. PV is a protein that affects the amplitude of the action potential. In addition, a positive PV interneuron is suggested to play an important role in the generation of gamma oscillation [47]. Moreover, Olivier et al. showed that PV can modulate short-term neuroplasticity, which was maintained for up to a few minutes, unlike long-term neuroplasticity [48]. In various mouse models of AD, including the 5xFAD, the density of PV-positive neurons decreased in the hippocampus [49,50]. Hence, we conducted a Western blot analysis of PV to identify whether external gamma oscillation application affected the change in the level of PV; there were no statistically significant differences in the PV levels among the groups.

The application of tACS in the transgenic mouse model could enhance the neuroplasticity at the electrophysiologic level, while the differences were not significant at the protein level. In other words, the synaptic strength was strengthened, but the upregulation of proteins related to neuroplasticity was not very significant.

5. Limitations and Future Directions

The limitation of this study was the lack of behavior tests among the groups, although genotyping identified each mouse type. In addition, compared to the positive results of EPSP, there were no differences among the groups in the Western blot analysis. This might have been the case because the treatment period was as short as 10 times, and this was not long enough to allow the proteins to be sufficiently upregulated. Next, although a nonparametric test was used for the statistical analysis, the small sample size may also have affected the results. Finally, unlike humans, animals move constantly during experiments, so we had no choice but to anesthetize them, because they had to be fixed in place for electrical stimulation. However, it has been reported that exposure to isoflurane for 2 h may be associated with decreased BDNF expression [51]. Furthermore, Sen et al. reported that exposure to isoflurane for 2 h may affect the inactivation of CREB and deteriorate cognitive function [52]. Although the anesthesia time in our experiment was as short as 30 min, its impact should also be considered, because anesthesia was not performed in the WT-NT and AD-NT groups. Therefore, in future studies, animal experiments using anesthetics other than isoflurane will be required when conducting tACS experiments related to AD. Further research will also be needed to explore the most appropriate tACS protocols, including stimulation time, by increasing the sample size.

6. Conclusions

In this study, we confirmed the enhancement of synaptic plasticity in transgenic mice of AD via an electrophysiologic test through the stimulation of gamma tACS in the frontal lobe. These findings support the results in previous human studies that tACS can improve cognitive function in patients with AD. Importantly, we presented the basis for applying tACS, a new treatment method that improves cognitive function in patients with AD. However, since there were no significant differences among the groups in the expressions of the proteins we observed during the Western blot analysis, it is necessary to investigate other pathways related to synaptic plasticity in the future. To the best of our knowledge, since there have been no studies with animal experiments using tACS in AD, further animal studies are needed to identify other unknown mechanisms in the effectiveness of tACS.

Author Contributions: Conceptualization, J.-Y.H. and W.-H.J.; methodology, W.-I.K. and W.-H.J.; formal analysis, W.-H.J. and M.-K.S.; investigation, W.-H.J., J.-W.L. and H.-K.P.; writing—original draft preparation, W.-H.J.; writing—review and editing, J.-Y.H. and I.-S.C.; and funding acquisition, J.-Y.H. All authors have read and agreed to the published version of the manuscript.

Funding: This study was funded by the National Research Foundation of Korea (2019R111A3A01060059).

Institutional Review Board Statement: This study was conducted according to the guidelines of the Declaration of Helsinki and approved by the Institutional Animal Care and Use Committee of the Chonnam National University (approval code: CNUHIACUC-20042).

Data Availability Statement: The data presented in this study are available from the corresponding author upon reasonable request.

Conflicts of Interest: The authors declare no conflict of interest.

References

1. Hooker, K.; Bowman, S.R.; Coehlo, D.P.; Lim, S.R.; Kaye, J.; Guariglia, R.; Li, F. Behavioral change in persons with dementia: Relationships with mental and physical health of caregivers. *J. Gerontol. B Psychol. Sci. Soc. Sci.* **2002**, *57*, P453–P460. [CrossRef] [PubMed]
2. Wilson, R.S.; Segawa, E.; Boyle, P.A.; Anagnos, S.E.; Hize, L.P.; Bennett, D.A. The natural history of cognitive decline in Alzheimer's disease. *Psychol. Aging* **2012**, *27*, 1008–1017. [CrossRef] [PubMed]

3. Jahn, H. Memory loss in Alzheimer's disease. *Dialogues Clin. Neurosci.* **2013**, *15*, 445–454.
4. Prince, M.; Bryce, R.; Albanese, E.; Wimo, A.; Ribeiro, W.; Ferri, C.P. The global prevalence of dementia: A systematic review and metaanalysis. *Alzheimers Dement.* **2013**, *9*, 63–75.e2. [CrossRef]
5. GBD 2016 Dementia Collaborators. Global, regional, and national burden of Alzheimer's disease and other dementias, 1990–2016: A systematic analysis for the Global Burden of Disease Study 2016. *Lancet Neurol.* **2019**, *18*, 88–106. [CrossRef]
6. Briggs, R.; Kennelly, S.P.; O'Neill, D. Drug treatments in Alzheimer's disease. *Clin. Med.* **2016**, *16*, 247–253. [CrossRef] [PubMed]
7. Epperly, T.; Dunay, M.A.; Boice, J.L. Alzheimer Disease: Pharmacologic and Nonpharmacologic Therapies for Cognitive and Functional Symptoms. *Am. Fam. Physician* **2017**, *95*, 771–778.
8. Bishara, D.; Sauer, J.; Taylor, D. The pharmacological management of Alzheimer's disease. *Prog. Neurol. Psychiatry* **2015**, *19*, 9–16. [CrossRef]
9. Chang, C.H.; Lane, H.Y.; Lin, C.H. Brain Stimulation in Alzheimer's Disease. *Front. Psychiatry* **2018**, *9*, 201. [CrossRef]
10. Rajji, T.K. Transcranial Magnetic and Electrical Stimulation in Alzheimer's Disease and Mild Cognitive Impairment: A Review of Randomized Controlled Trials. *Clin. Pharmacol. Ther.* **2019**, *106*, 776–780. [CrossRef]
11. Elder, G.J.; Taylor, J.P. Transcranial magnetic stimulation and transcranial direct current stimulation: Treatments for cognitive and neuropsychiatric symptoms in the neurodegenerative dementias? *Alzheimers Res. Ther.* **2014**, *6*, 74. [CrossRef]
12. Hausner, L.; Damian, M.; Sartorius, A.; Frolich, L. Efficacy and cognitive side effects of electroconvulsive therapy (ECT) in depressed elderly inpatients with coexisting mild cognitive impairment or dementia. *J. Clin. Psychiatry* **2011**, *72*, 91–97. [CrossRef] [PubMed]
13. Kaczmarczyk, R.; Tejera, D.; Simon, B.J.; Heneka, M.T. Microglia modulation through external vagus nerve stimulation in a murine model of Alzheimer's disease. *J. Neurochem.* **2018**, *46*, 76–85. [CrossRef]
14. Scherder, E.J.; Deijen, J.B.; Vreeswijk, S.H.; Sergeant, J.A.; Swaab, D.F. Cranial electrostimulation (CES) in patients with probable Alzheimer's disease. *Behav. Brain Res.* **2002**, *128*, 215–217. [CrossRef]
15. Scherder, E.J.; van Tol, M.J.; Swaab, D.F. High-frequency cranial electrostimulation (CES) in patients with probable Alzheimer's disease. *Am. J. Phys. Med. Rehabil.* **2006**, *85*, 614–618. [CrossRef] [PubMed]
16. Del Felice, A.; Castiglia, L.; Formaggio, E.; Cattelan, M.; Scarpa, B.; Manganotti, P.; Tenconi, E.; Masiero, S. Personalized transcranial alternating current stimulation (tACS) and physical therapy to treat motor and cognitive symptoms in Parkinson's disease: A randomized cross-over trial. *Neuroimage Clin.* **2019**, *22*, 101768. [CrossRef]
17. Mellin, J.M.; Alagapan, S.; Lustenberger, C.; Lugo, C.E.; Alexander, M.L.; Gilmore, J.H.; Jarskog, L.F.; Fröhlich, F. Randomized trial of transcranial alternating current stimulation for treatment of auditory hallucinations in schizophrenia. *Eur. Psychiatry* **2018**, *51*, 25–33. [CrossRef]
18. Clancy, K.J.; Baisley, S.K.; Albizu, A.; Kartvelishvili, N.; Ding, M.; Li, W. Lasting connectivity increase and anxiety reduction via transcranial alternating current stimulation. *Soc. Cogn. Affect. Neurosci.* **2018**, *13*, 1305–1316. [CrossRef]
19. Alexander, M.L.; Alagapan, S.; Lugo, C.E.; Mellin, J.M.; Lustenberger, C.; Rubinow, D.R.; Frohlich, F. Double-blind, randomized pilot clinical trial targeting alpha oscillations with transcranial alternating current stimulation (tACS) for the treatment of major depressive disorder (MDD). *Transl. Psychiatry* **2019**, *9*, 106. [CrossRef]
20. Klimke, A.; Nitsche, M.A.; Maurer, K.; Voss, U. Case Report: Successful Treatment of Therapy-Resistant OCD with Application of Transcranial Alternating Current Stimulation (tACS). *Brain Stimul.* **2016**, *9*, 463–465. [CrossRef]
21. Antal, A.; Paulus, W. Transcranial alternating current stimulation (tACS). *Front. Hum. Neurosci.* **2013**, *7*, 317. [CrossRef] [PubMed]
22. Abd Hamid, A.I.; Gall, C.; Speck, O.; Antal, A.; Sabel, B.A. Effects of alternating current stimulation on the healthy and diseased brain. *Front. Neurosci.* **2015**, *9*, 391. [CrossRef] [PubMed]
23. Klein, A.S.; Donoso, J.R.; Kempter, R.; Schmitz, D.; Beed, P. Early Cortical Changes in Gamma Oscillations in Alzheimer's Disease. *Front. Syst. Neurosci.* **2016**, *10*, 83. [CrossRef]
24. Mably, A.J.; Colgin, L.L. Gamma oscillations in cognitive disorders. *Curr. Opin. Neurobiol.* **2018**, *52*, 182–187. [CrossRef] [PubMed]
25. Palop, J.J.; Chin, J.; Roberson, E.D.; Wang, J.; Thwin, M.T.; Bien-Ly, N.; Yoo, J.; Ho, K.O.; Yu, G.Q.; Kreitzer, A.; et al. Aberrant excitatory neuronal activity and compensatory remodeling of inhibitory hippocampal circuits in mouse models of Alzheimer's disease. *Neuron* **2007**, *55*, 697–711. [CrossRef]
26. Herrmann, C.S.; Rach, S.; Neuling, T.; Strüber, D. Transcranial alternating current stimulation: A review of the underlying mechanisms and modulation of cognitive processes. *Front. Hum. Neurosci.* **2013**, *7*, 279. [CrossRef]
27. Ali, M.M.; Sellers, K.K.; Frohlich, F. Transcranial alternating current stimulation modulates large-scale cortical network activity by network resonance. *J. Neurosci.* **2013**, *33*, 11262–11275. [CrossRef]
28. Kehler, L.; Francisco, C.O.; Uehara, M.A.; Moussavi, Z. The effect of transcranial alternating current stimulation (tACS) on cognitive function in older adults with dementia. In Proceedings of the 42nd Annual International Conference of the IEEE Engineering in Medicine & Biology Society (EMBC), Montreal, QC, Canada, 20–24 July 2020; pp. 3649–3653.
29. Moussavi, Z.; Kimura, K.; Kehler, L.; de Oliveira Francisco, C.; Lithgow, B. A Novel Program to Improve Cognitive Function in Individuals with Dementia Using Transcranial Alternating Current Stimulation (tACS) and Tutored Cognitive Exercises. *Front. Aging* **2021**, *2*, 3. [CrossRef]
30. Benussi, A.; Cantoni, V.; Cotelli, M.S.; Cotelli, M.; Brattini, C.; Datta, A.; Thomas, C.; Santarnecchi, E.; Pascual-Leone, A.; Borroni, B. Exposure to gamma tACS in Alzheimer's disease: A randomized, double-blind, sham-controlled, crossover, pilot study. *Brain Stimul.* **2021**, *14*, 531–540. [CrossRef]

31. Dhaynaut, M.; Pascual-Leone, A.; Santarnecchi, E.; El Fakhri, G. Effects of modulating gamma oscillations via 40 Hz transcranial alternating current stimulation (tACS) on Tau PET imaging in mild to moderate Alzheimer's Disease. *J. Nucl. Med.* **2020**, *61*, 340.
32. Xing, Y.; Wei, P.; Wang, C.; Shan, Y.; Yu, Y.; Qiao, Y.; Xie, B.; Shi, X.; Zhu, Z.; Lu, J.; et al. TRanscranial AlterNating current Stimulation FOR patients with Mild Alzheimer's Disease (TRANSFORM-AD study): Protocol for a randomized controlled clinical trial. *Alzheimers Dement.* **2020**, *6*, e12005. [CrossRef] [PubMed]
33. Colgin, L.L.; Moser, E.I. Gamma oscillations in the hippocampus. *Physiology* **2010**, *25*, 319–329. [CrossRef] [PubMed]
34. Colgin, L.L. Rhythms of the hippocampal network. *Nat. Rev. Neurosci.* **2016**, *17*, 239–249. [CrossRef]
35. Roy, D.S.; Arons, A.; Mitchell, T.I.; Pignatelli, M.; Ryan, T.J.; Tonegawa, S. Memory retrieval by activating engram cells in mouse models of early Alzheimer's disease. *Nature* **2016**, *531*, 508–512. [CrossRef] [PubMed]
36. Iaccarino, H.F.; Singer, A.C.; Martorell, A.J.; Rudenko, A.; Gao, F.; Gillingham, T.Z.; Mathys, H.; Seo, J.; Kritskiy, O.; Abdurrob, F.; et al. Gamma frequency entrainment attenuates amyloid load and modifies microglia. *Nature* **2016**, *540*, 230–235. [CrossRef] [PubMed]
37. Martorell, A.J.; Paulson, A.L.; Suk, H.J.; Abdurrob, F.; Drummond, G.T.; Guan, W.; Young, J.Z.; Kim, D.N.; Kritskiy, O.; Barker, S.J.; et al. Multi-sensory Gamma Stimulation Ameliorates Alzheimer's-Associated Pathology and Improves Cognition. *Cell* **2019**, *177*, 256–271.e22. [CrossRef]
38. Oakley, H.; Cole, S.L.; Logan, S.; Maus, E.; Shao, P.; Craft, J.; Guillozet-Bongaarts, A.; Ohno, M.; Disterhoft, J.; Van Eldik, L.; et al. Intran neuronal beta-amyloid aggregates, neurodegeneration, and neuron loss in transgenic mice with five familial Alzheimer's disease mutations: Potential factors in amyloid plaque formation. *J. Neurosci.* **2006**, *26*, 10129–10140. [CrossRef]
39. Liu, X.J.; Huang, F.S.; Huang, C.; Yang, Z.M.; Feng, X.Z. Analysis of high-frequency stimulation-evoked synaptic plasticity in mouse hippocampal CA1 region. *Sheng Li Xue Bao* **2008**, *60*, 284–291.
40. Park, M. AMPA Receptor Trafficking for Postsynaptic Potentiation. *Front. Cell Neurosci.* **2018**, *12*, 361. [CrossRef]
41. Caldeira, M.V.; Melo, C.V.; Pereira, D.B.; Carvalho, R.; Correia, S.S.; Backos, D.S.; Carvalho, A.L.; Esteban, J.A.; Duarte, C.B. Brain-derived neurotrophic factor regulates the expression and synaptic delivery of alpha-amino-3-hydroxy-5-methyl-4-isoxazole propionic acid receptor subunits in hippocampal neurons. *J. Biol. Chem.* **2007**, *282*, 12619–12628. [CrossRef]
42. Figurov, A.; Pozzo-Miller, L.D.; Olafsson, P.; Wang, T.; Lu, B. Regulation of synaptic responses to high-frequency stimulation and LTP by neurotrophins in the hippocampus. *Nature* **1996**, *381*, 706–709. [CrossRef]
43. Amaral, M.D.; Pozzo-Miller, L. TRPC3 channels are necessary for brain-derived neurotrophic factor to activate a nonselective cationic current and to induce dendritic spine formation. *J. Neurosci.* **2007**, *27*, 5179–5189. [CrossRef]
44. Du, Y.; Wu, H.T.; Qin, X.Y.; Cao, C.; Liu, Y.; Cao, Z.Z.; Cheng, Y. Postmortem Brain, Cerebrospinal Fluid, and Blood Neurotrophic Factor Levels in Alzheimer's Disease: A Systematic Review and Meta-Analysis. *J. Mol. Neurosci.* **2018**, *65*, 289–300. [CrossRef] [PubMed]
45. Zhang, Y.; Guo, O.; Huo, Y.; Wang, G.; Man, H.Y. Amyloid- β Induces AMPA Receptor Ubiquitination and Degradation in Primary Neurons and Human Brains of Alzheimer's Disease. *J. Alzheimers Dis.* **2018**, *62*, 1789–1801. [CrossRef] [PubMed]
46. Keifer, J. Comparative Genomics of the BDNF Gene, Non-Canonical Modes of Transcriptional Regulation, and Neurological Disease. *Mol. Neurobiol.* **2021**, *58*, 2851–2861. [CrossRef]
47. Sohal, V.S.; Zhang, F.; Yizhar, O.; Deisseroth, K. Parvalbumin neurons and gamma rhythms enhance cortical circuit performance. *Nature* **2009**, *459*, 698–702. [CrossRef] [PubMed]
48. Caillard, O.; Moreno, H.; Schwaller, B.; Llano, I.; Celio, M.R.; Marty, A. Role of the calcium-binding protein parvalbumin in short-term synaptic plasticity. *Proc. Natl. Acad. Sci. USA* **2000**, *97*, 13372–13377. [CrossRef]
49. Ali, F.; Baringer, S.L.; Neal, A.; Choi, E.Y.; Kwan, A.C. Parvalbumin-Positive Neuron Loss and Amyloid- β Deposits in the Frontal Cortex of Alzheimer's Disease-Related Mice. *J. Alzheimers Dis.* **2019**, *72*, 1323–1339. [CrossRef]
50. Giesers, N.K.; Wirths, O. Loss of Hippocampal Calretinin and Parvalbumin Interneurons in the 5XFAD Mouse Model of Alzheimer's Disease. *ASN Neuro* **2020**, *12*. [CrossRef]
51. Zhou, C.H.; Zhang, Y.H.; Xue, F.; Xue, S.S.; Chen, Y.C.; Gu, T.; Peng, Z.W.; Wang, H.N. Isoflurane exposure regulates the cell viability and BDNF expression of astrocytes via upregulation of TREK1. *Mol. Med. Rep.* **2017**, *16*, 7305–7314. [CrossRef]
52. Sen, T.; Sen, N. Isoflurane-induced inactivation of CREB through histone deacetylase 4 is responsible for cognitive impairment in developing brain. *Neurobiol. Dis.* **2016**, *96*, 12–21. [CrossRef] [PubMed]



Article

MicroRNA-124 Alleviates Retinal Vasoregression via Regulating Microglial Polarization

Ying Chen ^{1,†}, Jihong Lin ^{1,†}, Andrea Schlotterer ¹, Luke Kurowski ¹, Sigrid Hoffmann ², Seddik Hammad ³, Steven Dooley ³, Malte Buchholz ⁴, Jiong Hu ⁵, Ingrid Fleming ⁵ and Hans-Peter Hammes ^{1,*}

- ¹ 5th Medical Department, Medical Faculty Mannheim, University of Heidelberg, D-68167 Mannheim, Germany; Ying.Chen@medma.uni-heidelberg.de (Y.C.); Jihong.Lin@medma.uni-heidelberg.de (J.L.); Andrea.Schlotterer@medma.uni-heidelberg.de (A.S.); Luke.Kurowski@medma.uni-heidelberg.de (L.K.)
 - ² Center of Medical Research, Medical Faculty Mannheim, University of Heidelberg, D-68167 Mannheim, Germany; Sigrid.Hoffmann@medma.uni-heidelberg.de
 - ³ Molecular Hepatology Section, Department of Medicine II, Medical Faculty Mannheim, University of Heidelberg, D-68167 Mannheim, Germany; Seddik.Hammad@medma.uni-heidelberg.de (S.H.); Steven.Dooley@medma.uni-heidelberg.de (S.D.)
 - ⁴ Department of Gastroenterology and Endocrinology, University Hospital, Philipps-University Marburg, Hans-Meerwein-Str. 3, D-35043 Marburg, Germany; malte.buchholz@staff.uni-marburg.de
 - ⁵ Institute for Vascular Signalling, Center for Molecular Medicine, Goethe University, D-60590 Frankfurt, Germany; Hu@vrc.uni-frankfurt.de (J.H.); Fleming@em.uni-frankfurt.de (I.F.)
- * Correspondence: hp.hammes@umm.de; Tel.: +49-621-383-2663
† These authors contributed equally to this work.

Citation: Chen, Y.; Lin, J.; Schlotterer, A.; Kurowski, L.; Hoffmann, S.; Hammad, S.; Dooley, S.; Buchholz, M.; Hu, J.; Fleming, I.; et al. MicroRNA-124 Alleviates Retinal Vasoregression via Regulating Microglial Polarization. *Int. J. Mol. Sci.* **2021**, *22*, 11068. <https://doi.org/10.3390/ijms222011068>

Academic Editor: Settymio Rossi

Received: 15 September 2021
Accepted: 10 October 2021
Published: 14 October 2021

Publisher's Note: MDPI stays neutral with regard to jurisdictional claims in published maps and institutional affiliations.



Copyright: © 2021 by the authors. Licensee MDPI, Basel, Switzerland. This article is an open access article distributed under the terms and conditions of the Creative Commons Attribution (CC BY) license (<https://creativecommons.org/licenses/by/4.0/>).

Abstract: Microglial activation is implicated in retinal vasoregression of the neurodegenerative ciliopathy-associated disease rat model (i.e., the polycystic kidney disease (PKD) model). microRNA can regulate microglial activation and vascular function, but the effect of microRNA-124 (miR-124) on retinal vasoregression remains unclear. Transgenic PKD and wild-type Sprague Dawley (SD) rats received miR-124 at 8 and 10 weeks of age intravitreally. Retinal glia activation was assessed by immunofluorescent staining and in situ hybridization. Vasoregression and neuroretinal function were evaluated by quantitative retinal morphometry and electroretinography (ERG), respectively. Microglial polarization was determined by immunocytochemistry and qRT-PCR. Microglial motility was examined via transwell migration assays, wound healing assays, and single-cell tracking. Our data showed that miR-124 inhibited glial activation and improved vasoregression, as evidenced by the reduced pericyte loss and decreased acellular capillary formation. In addition, miR-124 improved neuroretinal function. miR-124 shifted microglial polarization in the PKD retina from the pro-inflammatory M1 phenotype to the anti-inflammatory M2 phenotype by suppressing TNF- α , IL-1 β , CCL2, CCL3, MHC-II, and IFN- γ and upregulating Arg1 and IL-10. miR-124 also decreased microglial motility in the migration assays. The transcriptional factor of C/EBP- α -PU.1 signaling, suppressed by miR-124 both in vivo (PKD retina) and in vitro (microglial cells), could serve as a key regulator in microglial activation and polarization. Our data illustrate that miR-124 regulates microglial activation and polarization. miR-124 inhibits pericyte loss and thereby alleviates vasoregression and ameliorates neurovascular function.

Keywords: miR-124; microglia; polarization; vasoregression

1. Introduction

Vasoregression is the primary process of various retinal disorders such as retinal degeneration and diabetic retinopathy (DR). These disorders are characterized by pericyte loss and acellular capillary formation. Microglial activation contributes to vasoregression and neurodegenerative retinopathy [1]. Microglia, Müller cells, and astrocytes comprise the three types of glia cells in the mammalian retina [2,3]. Glial cells play an important

role in cross-communication between neurons and vascular cells (collectively known as neurovascular units (NVUs)), especially in retinal homeostasis, inflammation, and neurodegeneration [4]. In the normal retina, the microglia is quiescent and distributes in the inner plexiform layer with ramified morphology. When exposed to various pathological insults, microglia become activated, change to amoeboid forms, migrate to the site of injury, secrete anti-inflammatory cytokines such as interleukin-10 (IL-10) and Arginase-1 (Arg1), and facilitate the resolution of inflammation and the return of the tissue to homeostasis [5,6]. However, in chronic pathological conditions such as diabetic retinopathy, microglia release excessive pro-inflammatory chemokines, including C-C motif chemokine ligand 2 (CCL2) and CCL3 or cytokines such as tumor necrosis factor- α (TNF- α), interleukin-1 β (IL-1 β), and interferon gamma (IFN- γ), which promote disease progression [4,6,7]. Abnormal microglia activation has also been associated with retinal degenerative diseases, including age-related macular degeneration and hereditary retinopathies [2,4]. The effective modulation of microglial polarization to the anti-inflammatory state could inhibit neurodegenerative disease progression [8,9]. Modulating the state of microglial activation and its response to the inflammatory environment might be an approach to prevent neurovascular change resulting in retinal vasoregression [10,11].

Transgenic PKD rats overexpress the human polycystin-2 gene in retinal photoreceptors, among other tissues [12,13]. They are characterized by abnormal cellular cilia and retinal degenerative phenotypes with severe photoreceptor degeneration, vasoregression, and microglial activation [14]. Microglial activation promotes the expression of immune cytokine CD74, a receptor for the macrophage migration inhibitory factor [15] and the invariant chain of the class II major histocompatibility complex (MHC-II) [16]. CD74 is considered a marker of microglial activation, and it is closely correlated with vasoregression in PKD rats [17]. As a spontaneous neurodegeneration model very similar to human ciliopathy, the PKD rat has been identified as a useful model to study the relationship between neurodegeneration and vasoregression [14,17]. Ciliopathy is a group of human genetic disorders exhibiting major retinal degeneration (rod cone dystrophy and photophobia), sensorineural hearing loss, obesity, and insulin resistance [18].

Given the regulatory role of miRNAs in neurodegeneration, the impact of specific miRNAs needs clarification. miRNAs are involved in many biological processes, while altered expression of miRNAs is associated with the development of many human diseases [19]. miRNA-124 (miR-124) is one of the most abundant miRNAs in the CNS and retina. It regulates physiological neurogenesis and neuronal development [20–22]. The regulatory role of miR-124 in microglial activation has been studied in several disease models of inflammation, and its application was suggested as a promising therapeutic approach [23]. The delivery of miR-124 into a rat model of a spinal cord injury reduced microglia activation and inflammatory cytokine production [24]. Supplementation of miR-124 inhibits the pro-inflammatory activity of Müller cells in a photo-oxidative damage mouse model [25]. miR-124 promotes microglia quiescence in the CNS of an experimental autoimmune encephalomyelitis (EAE) mouse model and represses EAE disease development. In this model, the transcriptional factor protein binding U box (PU.1) and its upstream regulator, CCAAT/enhancer-binding protein- α (C/EBP- α), are involved in miR-124-mediated microglia regulation [26].

However, the effect of miR-124 on retinal vasoregression remains unclear. Our aim was to clarify whether miR-124 regulates retinal microglia activation and subsequently influences retinal vasoregression. We found that miR-124 suppressed retinal microglial activation and polarized microglia to the anti-inflammatory phenotype in the PKD rat. The extensive vasoregression of the PKD retinae and the neuroretinal function were improved by miR-124 introduction. The C/EBP- α /PU.1 signaling pathway was involved in miR-124-mediated retinal microglial activation and polarization.

2. Results

2.1. miR-124 Normalizes Müller Glial Activation in the PKD Retina

To assess miR-124 change in the PKD rat, we performed quantitative RT-PCR. The PKD rat retinae expressed 50% less miR-124 than the SD rats (Figure 1A). To ascertain the localization of miR-124 and to determine whether exogenous miR-124 could influence Müller glial activation, we introduced an miR-124 mimic into the PKD retina and performed in situ hybridization (ISH) combined with immunofluorescent staining. Neither the hybridization signal nor the immunofluorescence signal of glutamine synthetase (GS) in the negative control group of the SD retinae were detectable (Figure 1(Ba)). ISH confirmed the RT-qPCR result that the miR-124 expression was reduced in the PKD retina (Figure 1(Bc)) compared with the expression in the normal SD retina (Figure 1(Bb)). miR-124 was expressed in all layers of the SD retina, predominantly in the photoreceptor layer (PRL) but also in the ganglion cell layer (GCL) and the inner nuclear layer (INL) (Figure 1(Bb)), yet its expression was strikingly decreased in all layers of retinal neurons in the PKD rats (Figure 1(Bc)). Additionally, miR-124 was distributed across the entire retina (Figure 1(Bd,e)), consistent with the Müller cell processes spanning across all retinal layers. The immunofluorescent signal of the Müller glial GS was increased, and the Müller cells showed gliosis in the PKD retinae (arrows in Figure 1(Bc)), while the exogenous miR-124 inhibited GS expression and indicated a reduction of Müller glial activation (arrows in Figure 1(Bd)) [14,17]. The miR-124 inhibitor did not affect Müller glial activation (Figure 1(Be)), indicating that Müller glial activation was inhibited by miR-124.

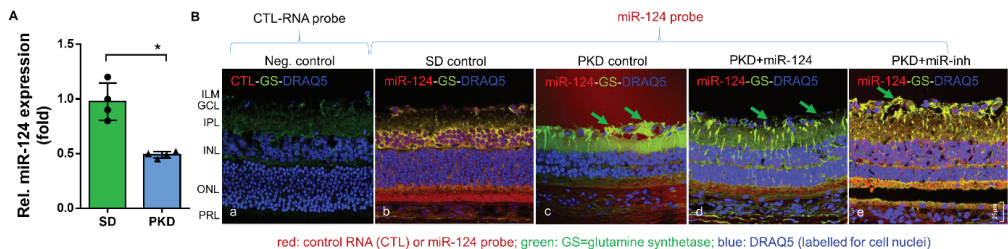


Figure 1. miR-124 expression was reduced in the retinæ of PKD rats and inactivated the Müller glia. (A) Relative expression of miR-124 in the retinæ of SD and PKD rats measured by RT-qPCR using hsp-miR-124-3p specific primers. Data are normalized to the expression of U6 snRNA, exhibited as means \pm SD, $n = 4$. The p value determined by a Student's t test was $* p < 0.05$. (B) ISH combined with fluorescent immunohistochemistry. A control RNA probe (a) or miR-124 probe (b–e) was used to detect paraffin-embedded retinal vertical sections from the SD (a,b) and PKD rats with (d) or without miR-124 (c) or miR-inh (e) injection. The miR-124 probe was labeled with donkey anti-sheep Alexa Fluor 555 (red), the glutamate synthetase (GS) was labeled with chicken anti-rabbit Alexa Fluor 488 (green), and the nuclei were labeled with DRAQ5TM (blue). A section from the SD retina probed with the control miRNA probe (CTL-RNA probe) served as a negative control (a). The images were taken with Leica confocal microscope TCS SP8, and scale bar shown in B, e = 25 μ m.

2.2. miR-124 Decreases the Activation State of Microglia in PKD Retinæ

Neurodegeneration is characterized by a strong microglial activation. To assess whether miR-124 can modify microglial behavior, the expression of the microglial activation marker CD74 was analyzed in the whole-mount retinæ of SD and PKD rats. Microglia are abundant and activated in the entire retina of PKD rats (both in the superficial and deep layer) (Figure 2(Ac,g)) in comparison with the levels in the SD retina (Figure 2(Aa,e)). The delivery of the miR-124 mimic into the PKD retina attenuated microglial activation both in the superficial and the deep layer (Figure 2(Ad,h)). In the deep layer, miR-124 reduced 80% of the activated microglial cell numbers while reducing them 50% in the superficial layer (Figure 2(B,C)) compared with the PKD rat without an miR-124 injection. miR-124 did not influence the microglial activation in the SD rats (Figure 2(Aa,b,e,f)).

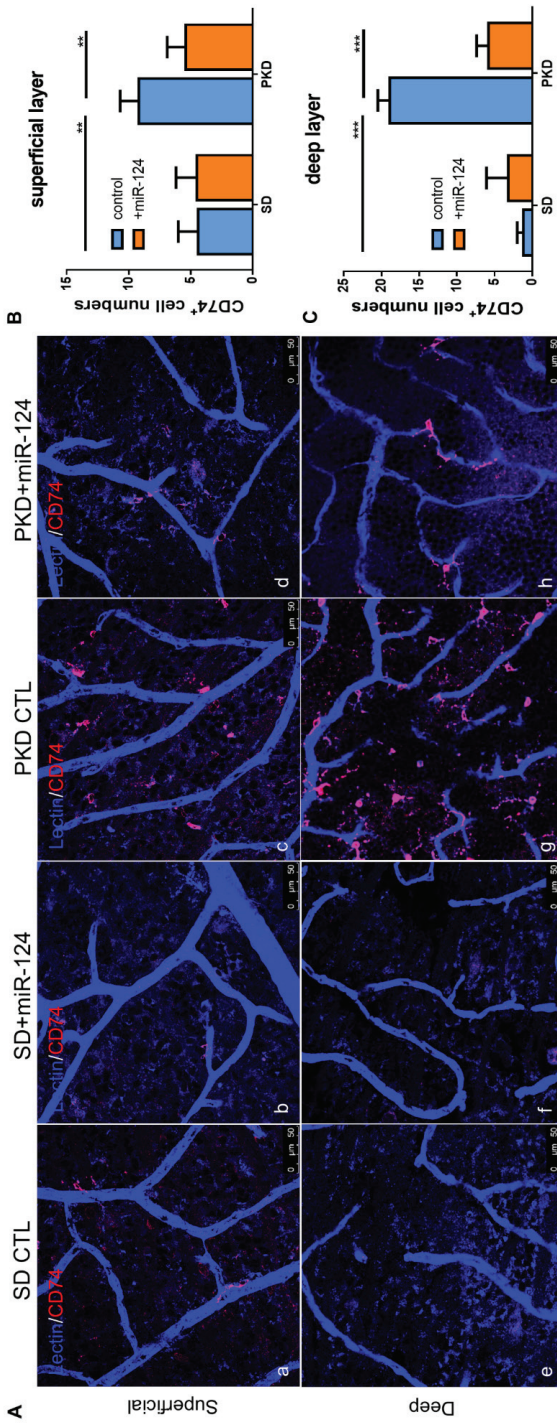


Figure 2. Microglial distribution and activation in SD and PKD retinæ, with whole-mount immunofluorescent staining of CD74 in retinæ from SD (a,b,e,g) and PKD (c,d,g,h) rats treated with either control miRNA (CTL) (a,c,e,g) or an miR-124 mimic (miR-124) (b,d,f,h). Microglia were labeled with CD74 (red). Retinal vessels were labeled with iso-lectin B4 (blue). (A) Representative images of microglial activation (CD74⁺) in the superficial layer (upper panel) and in the deep layer (lower panel). (B) Quantification of the CD74⁺ microglia in the superficial layer (upper panel A). (C) Quantification of the CD74⁺ microglia in the deep layer (lower panel A). The images were taken with a Leica confocal microscope TCS SP8 with scale bars = 50 µm. Data (B,C) are exhibited as means ± SD, *n* = 5. The *p* values were determined by two-way ANOVA with Tukey’s multiple comparisons test were ** *p* < 0.01 and *** *p* < 0.001.

2.3. miR-124 Alleviates Vasoregression of the PKD Retina

To determine whether exogenous miR-124 administered intravitreally could rescue retinal vasoregression, retinal digest preparations of SD and PKD rats treated with an miR-124 mimic, control miRNA (CTL-miR), or miR-124 inhibitor (miR-inh) were analyzed using morphometry. As expected, PKD retinae displayed increased formations of acellular capillaries (ACs) (Figure 3(A,d),B). miR-124 treatment did not affect the low number of ACs in the SD rats (Figure 3(Ab),B). However, it significantly reduced the numbers of AC formation in the PKD retinae (Figure 3(Ae),B). In contrast to miR-124, the inhibitor (miR-inh) did not affect AC formation in both the SD and PKD rats (Figure 3(Ac,f),B). Pericyte numbers were significantly reduced in the retinae from the PKD rats (Figure 3(Aa,d),C). miR-124 also increased the pericyte numbers in the PKD rats (Figure 3(Ab,e),C). Pericyte migration, often found in damaged retinae, was also increased in the PKD retinae and inhibited by miR-124 addition (Figure 3(Ab,e),D). The miRNA inhibitor did not affect pericyte migration (Figure 3(Ac,f),D), which was consistent with the persistent AC formation and pericyte loss under in vivo treatment (Figure 3B–D).

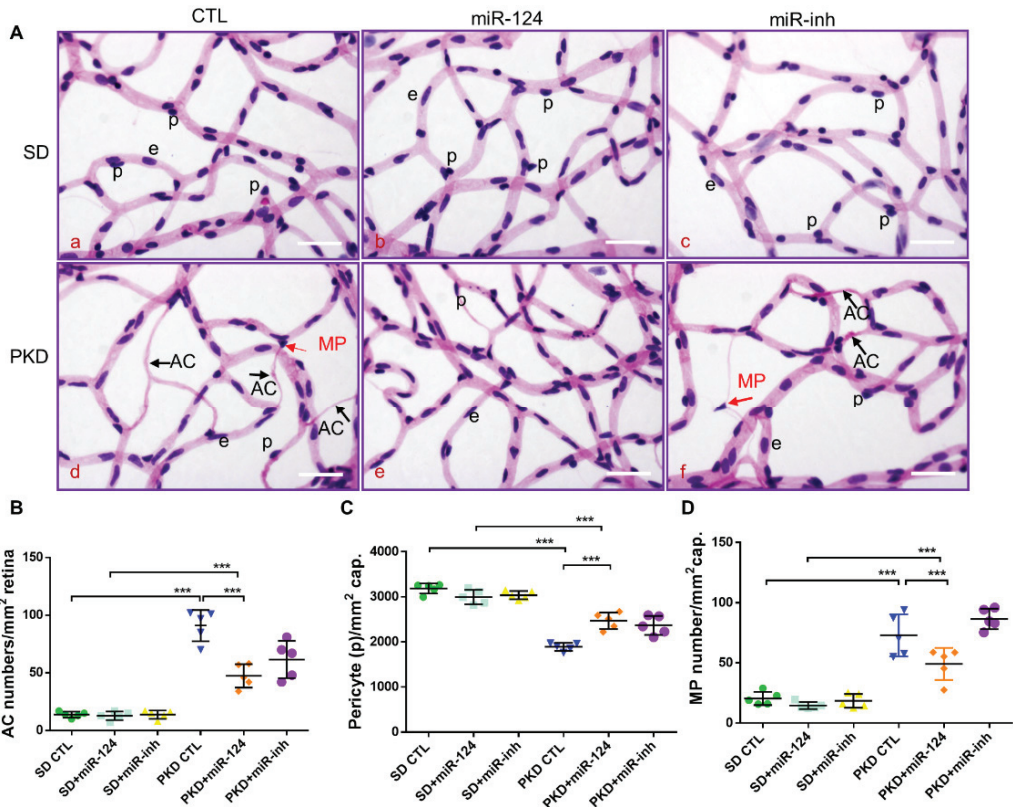


Figure 3. miR-124 ameliorates pericyte loss and reduces vasoregression in PKD retinae. Retinal morphometry was measured in SD and PKD rats treated with or without miR-124. Two-month-old SD and PKD rats were treated with 25 pmol of control microRNA (CTL), an miR-124 mimic, or miR-124 inhibitor (miR-inh) for 4 weeks. (A) Representative images of PAS and hematoxylin-stained retinal vasculature from retinal digest preparation taken by an Olympus BX51 microscope. Black arrows indicate acellular capillaries (ACs), red arrows indicate migrating pericytes (MPs), p = pericyte, e = endothelial cell, and scale bars = 50 μ m. (B–D) Quantification of acellular capillaries (number of ACs/mm² retinal area) (B); quantification of pericytes (number of pericytes/mm² retinal area) (C); and quantification of migrating pericytes (number of MP/mm² retinal area) (D) were analyzed using CellF software from Olympus. (B–D) $n = 5$ and $*** p < 0.001$ (one-way ANOVA with Tukey’s multiple comparisons test).

2.4. miR-124 Improves Retinal Function in Neurodegeneration

Given that miR-124 mitigated PKD Müller glial activation and retinal vasoregression, which are the successors of neurodegeneration, we assessed the effect of miR-124 on neuroretinal function using electroretinography (ERG). The a-wave amplitude reflects the function of the photoreceptors, while the b-wave amplitude represents the function of the bipolar cells and Müller cells. In the PKD retina, both the functions of photoreceptors (Figure 4A) and of bipolar cells and Müller cells (Figure 4B) were reduced compared with the SD retina. Photoreceptor function of the PKD rat was not improved by miR-124 mimic administration (Figure 4A). However, after 4 weeks of treatment with the miR-124 mimic, the response to light of the inner retinal neurons of the PKD rat was significantly recovered to the level present in the SD control (Figure 4B). Altogether, miR-124 not only regulated Müller glia activation and microglial activity but also rescued vasoregression and neuroretinal functions of the PKD rat.

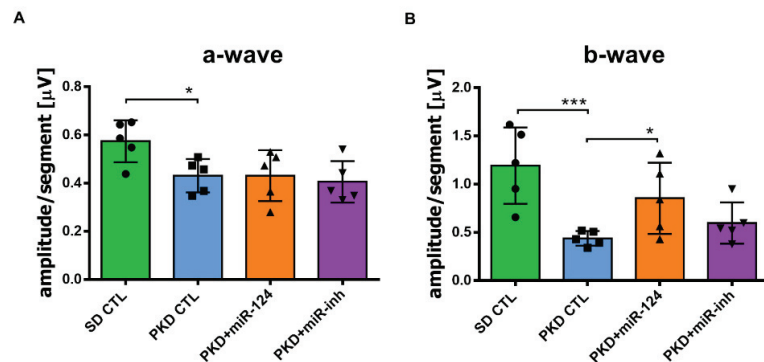


Figure 4. miR-124 ameliorated neuroretinal function in the PKD rats. The neuroretinal function was measured via electroretinography (ERG) in the SD and PKD rats. SD and PKD rats were intravitreally administrated with 25 pmol of the control miRNA (CTL), miR-124 mimic, or miR-124 inhibitor (miR-inh) at week 8 and week 10, respectively. ERG was performed at week 12. Data are presented as means \pm SD, $n = 5$. The p values were determined by one-way ANOVA with Tukey's multiple comparisons test, where * $p < 0.05$ and *** $p < 0.001$. (A) Represented a-wave amplitudes in ERG. (B) Represented b-wave amplitudes in ERG.

2.5. miR-124 Inhibits the Migratory Capability of Microglia

Given that migration is a key feature during microglial surveillance and an important characteristic of microglial activation [4,27], we investigated the effect of miR-124 on the migratory capability of mouse BV2 microglia and rat primary microglia. Via a transwell migration assay, 24 h after transfection, the number of BV2 cells that migrated to the lower transwell chamber was effectively inhibited by 50% in the group transfected with the miR-124 mimic compared with the control miRNA (CTL-miR) (Figure 5A,B). A wound healing assay (WHA), which is used to measure the cell moving speed, confirmed our findings. Twenty-four hours after transfection, the miR-124 mimic transfected rat primary microglial cells traveled much slower than the CTL-miRNA or miR-124 inhibitor transfected control cells (Figure 5C,D). Similar results for the WHA were observed in mouse microglia BV2 cells (data not shown). The single-cell mobility was assessed by live cell imaging techniques, accomplished with an Incucyte S3 phase contrast system and analyzed with the TimeLapse Analyzer (TLA) program. The average migrating distance (AMD, in μm) of miR-124 transfected BV2 cells was significantly shorter ($p < 0.05$) than the non-transfected control group (Neg-CTL) and shorter than the CTL-miRNA and miR-124 inhibitor groups (Figure 5E,F), indicating that microglial motility was inhibited by miR-124's introduction.

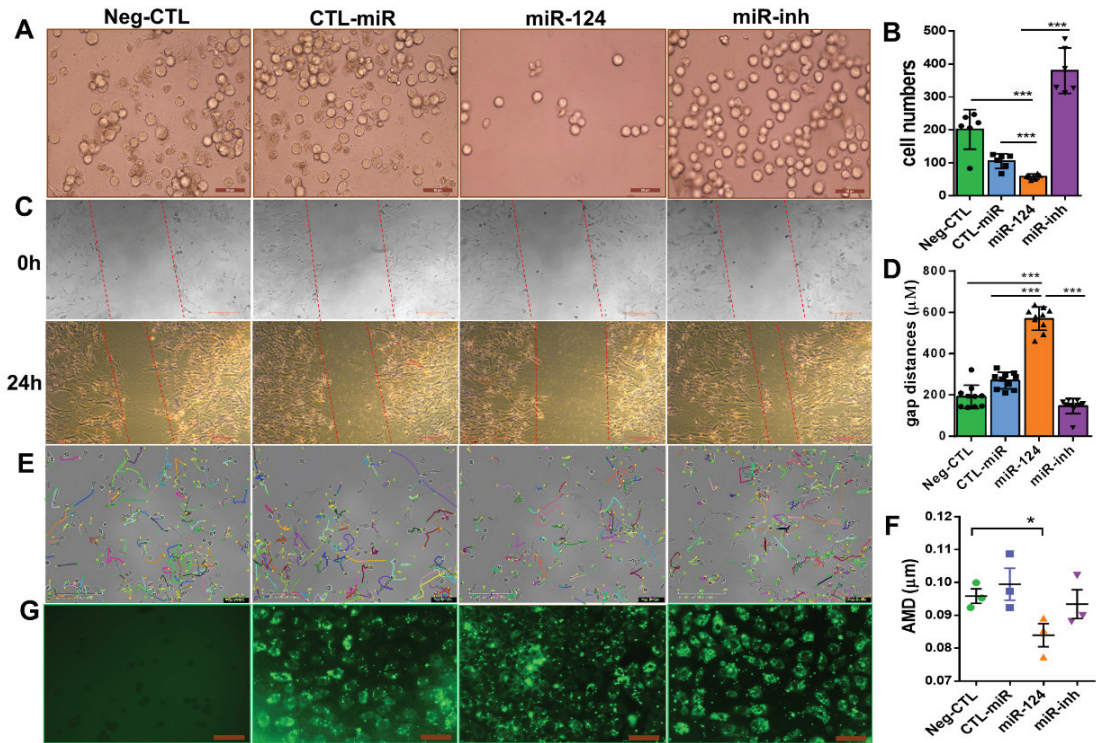


Figure 5. miR-24 reduced microglial cell motility. BV2 microglial cells (A,E,G) and rat primary microglial cells (C) were transfected with Lipofectamine 2000 Transfection Reagent as a negative control (Neg-CTL), control microRNA (CTL-miR), microRNA-124 (miR-124), and miR-124 inhibitor (miR-inh) for 24 h (A,C,E,G). (A) Images of transwell migration assays taken with a Zeiss Axio Observer Z1 microscope, where the scale bars = 50 µm. (B) Quantification showed that the migrating cells moved downward well with the serum-free medium after 24 h. (C) Images of wound healing assays with rat primary microglial cells at time point 0 h (upper panel) and end time point 24 h (low panel), with scale bars = 200 µm. (D) Quantification of the gap sizes from the 24 h-panel of (C). (E) Tracking of single BV2 cell movement. After 24 h of transfection, cells were applied to live cell imaging with an Incucyte S3 phase contrast microscope. Images of three fields per well were taken at 30-min intervals, and cell tracking was monitored for 10 h. Tracks of individual cells are shown in different colors, where the scale bars = 200 µm. (F) Quantification of the average migration distance (AMD in µm) of a single cell was analyzed with the TimeLapse Analyzer (TLA). Three fields each of 100 cells were analyzed, where $n = 3$ and $* p < 0.05$ (one-way ANOVA with Tukey’s multiple comparisons test). (G) Transfection evidence of BV2 cells with FAM-conjugated control miRNA, an miR-124 mimic, or miR-124 inhibitor observed using a Zeiss Axio Observer Z1 phase-contrast fluorescent microscope, with scale bars = 100 µm. (B) $n = 5$. (D) $n = 10$ and $*** p < 0.001$ (one-way ANOVA with Tukey’s multiple comparisons test).

To evaluate the transfection efficiency and to position miR-24 in the microglial cells, an FAM-labeled miR-24 mimic, control miRNA (CTL-miR), or miRNA inhibitor (miR-inh) were transfected into the microglial cells. The 24-h transfection efficiency in each experimental group of BV2 cells was similar in green fluorescence intensity (Figure 5G).

2.6. miR-24 Modulates the Polarization of Microglia to an Anti-Inflammatory Phenotype

To identify whether miR-24 could influence the microglia response to inflammation, the expressions of pro-inflammatory M1 and anti-inflammatory M2 mediators or specific secreted cytokines were evaluated by RT-qPCR in the retinæ of SD and PKD rats treated with the miR-24 mimic for 4 weeks. In the PKD retinæ, miR-24 reduced the expression of pro-inflammatory cytokines (TNF- α , IL-1 β , and IFN- γ), chemokines (CCL2 and CCL3),

MHC-II, CD74, and TGF- β 1, whereas it promoted the expression of the M2 marker Arg1 and anti-inflammatory cytokine IL-10 (Figure 6A). The fact was that the expression of pro-inflammatory chemokines CCL2 and CCL3 was suppressed by miR-124 was also confirmed at the protein level by ICC (Figure 6 B–E). These data supported the capability of miR-124 to shift microglia to the anti-inflammatory phenotype.

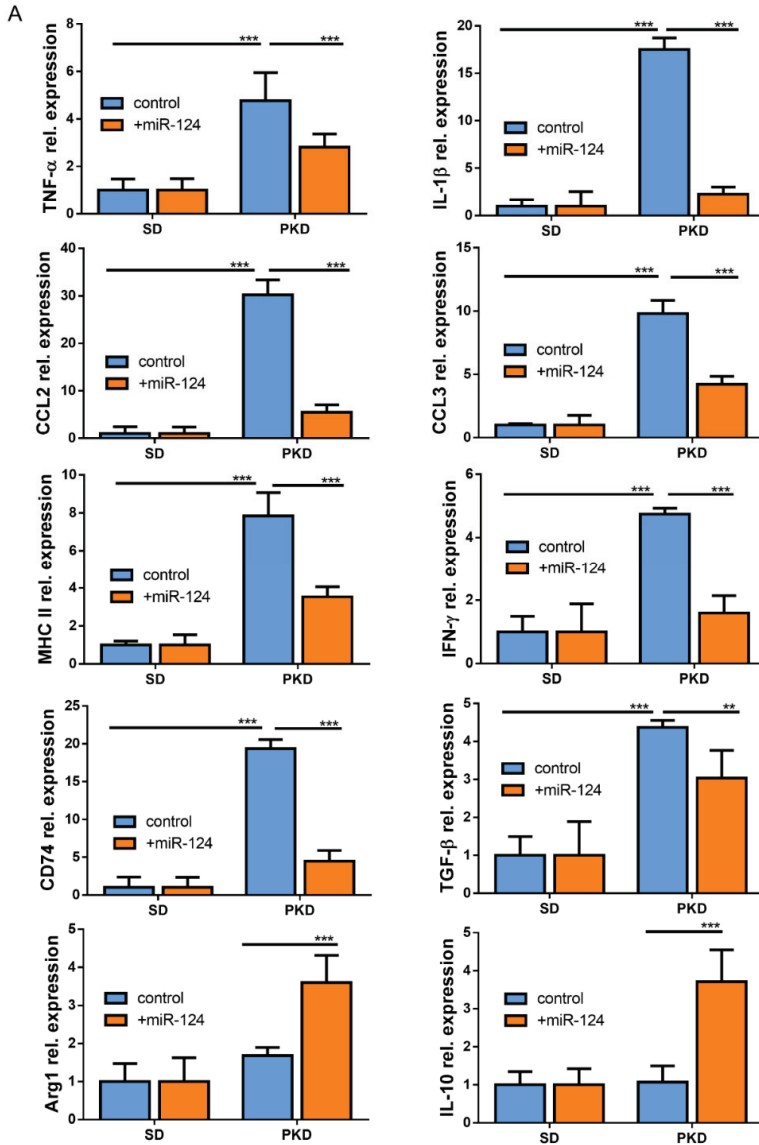


Figure 6. Cont.

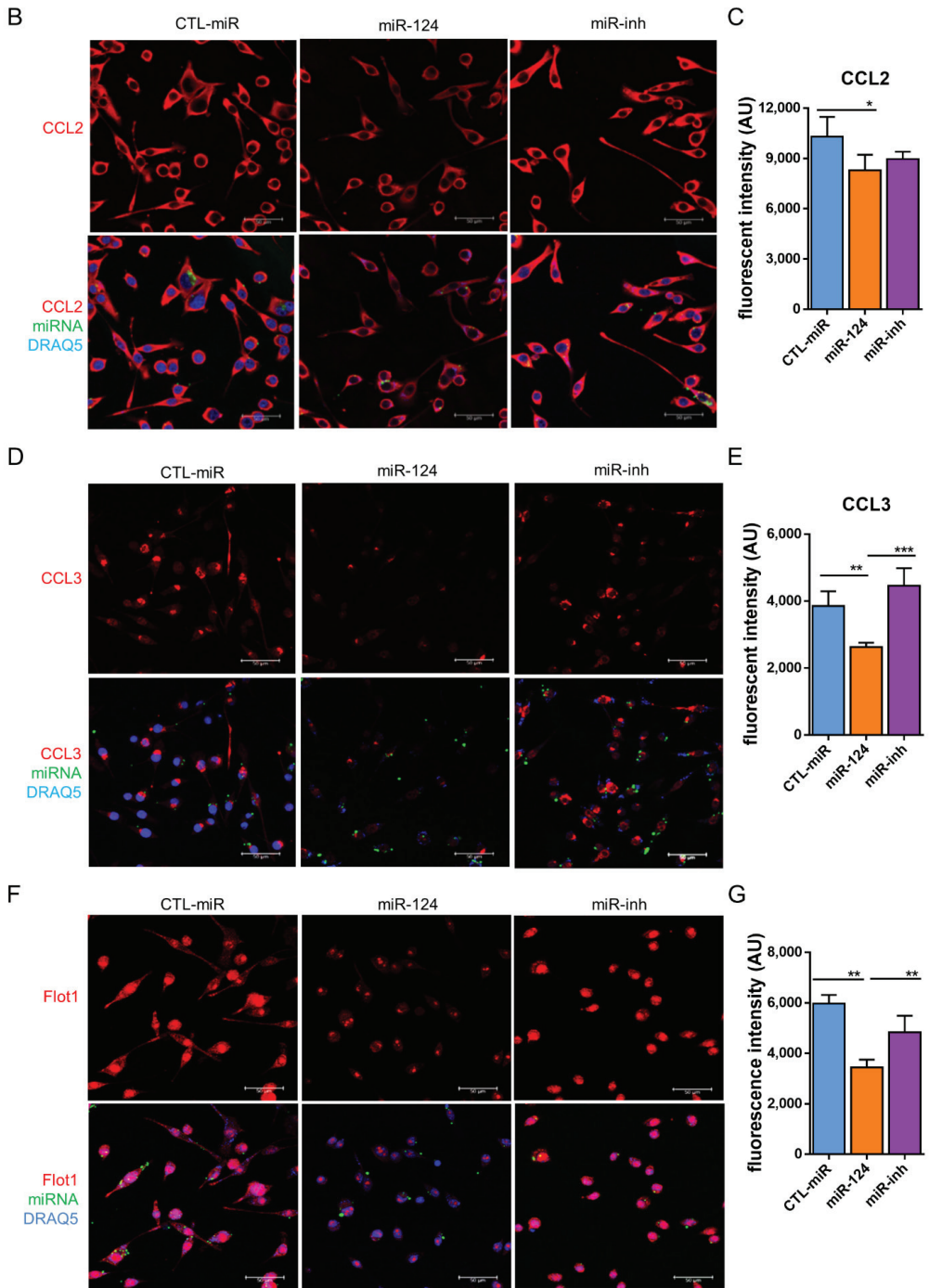


Figure 6. miR-124 reduced expression of pro-inflammatory cytokines in the PKD rat. (A) Quantitative M1 and M2 gene expressions in SD and PKD rats treated with or without the miR-124 mimic. RT-qPCR was performed to evaluate the genes

specially expressed in the M1 state (TNF- α , IL-1 β , IFN- γ , CCL2, CCL3, MHC-II, CD74, and TGF- β) and M2 state (Arg1 and IL-10). The expression of the house-keeping gene, rat Gapdh, was used as a control. Relative gene expression (fold versus Gapdh) was calculated using the $\Delta\Delta$ CT method. (B,D,F) Representative images of fluorescent immunocytochemistry (ICC) of CCL2 (B), CCL3 (D), and Flot1 (F) in BV2 cells. BV2 cells were transfected with FAM-labeled miR-124 or an miR-124 inhibitor (miR-inh) (green) for 24 h. Antibodies of CCL2, CCL3, and Flot1 were labeled with Alexa Fluor 555 (red), and the nuclei were labeled with DRAQ5TM (blue). Images were taken using a Leica confocal microscope TCS SP8, with scale bars = 50 μ m. (C,E,G) Quantification of CCL2 (C), CCL3 (E), and Flot1 (G) expressions from ICC fluorescence intensity using Image J software. Data are shown in arbitrary units (AU). (A,C,E,G) $n = 5$, * $p < 0.05$, ** $p < 0.01$, and *** $p < 0.001$ (two-way ANOVA with Tukey's multiple comparisons test).

Flotillin 1 (Flot1) is a target of miR-124 and an important protein in lipid raft formation [28]. To further investigate the mechanism of miR-124 on the anti-inflammatory phenotype of microglia, we examined the expression of Flot1 in BV2 microglial cells using ICC. The expression of Flot1 was inhibited by about 40% in miR-124-transfected BV2 cells compared with the control miRNA or miR-124 inhibitor treated groups (Figure 6F,G). We concluded that miR-124-induced Flot1 reduction might have interfered with lipid raft-mediated inflammatory signal transduction, which inhibited pro-inflammatory signals and promoted anti-inflammatory signals to the microglia.

2.7. miR-124 Downregulates the Transcription Factors C/EBP- α /PU.1

Next, we explored the possible mechanisms underlying the above observations. It has been reported that miR-124 promotes microglia quiescence in CNS and downregulates PU.1 in bone marrow-derived macrophages (BMDMs) [26]. The expression of C/EBP- α , a master transcription factor which is a target of miR-124, as well as its downstream transcription factor PU.1 was detected both in vitro (BV2 cells) and in vivo (PKD retinae). PU.1 expression was downregulated in the miR-124 mimic-transfected BV2 cells but not in the control miRNA- or miR-124 inhibitor-transfected groups ($p < 0.01$, Figure 7A,B). To confirm the in vitro experiment, we examined the PU.1 protein expression by western blotting in samples of the SD and PKD retinae. PU.1 suppression was observed in the miR-124 mimic-treated PKD retina by western blot analysis but not in the control miRNA- or miRNA inhibitor-treated PKD or in the control SD retinae ($p < 0.01$, Figure 7C,D). The mRNA of PU.1, known as the Spi1 (Spi-1 Proto-Oncogene) gene, in comparison with the level in the SD retina, was 7.1-fold higher in the PKD retina, which was, however, neutralized to about 56.3% expression in the control miRNA-treated groups through miR-124 mimic introduction (Figure 7E). C/EBP- α expression was reduced in the miR-124-transfected BV2 cells by 50% on the protein level (Figure 7F,G) and by 45% on the mRNA level (Figure 7H). These data indicated that C/EBP- α /PU.1 signaling was involved in the miR-124 dependent regulation of microglial activation and polarization.

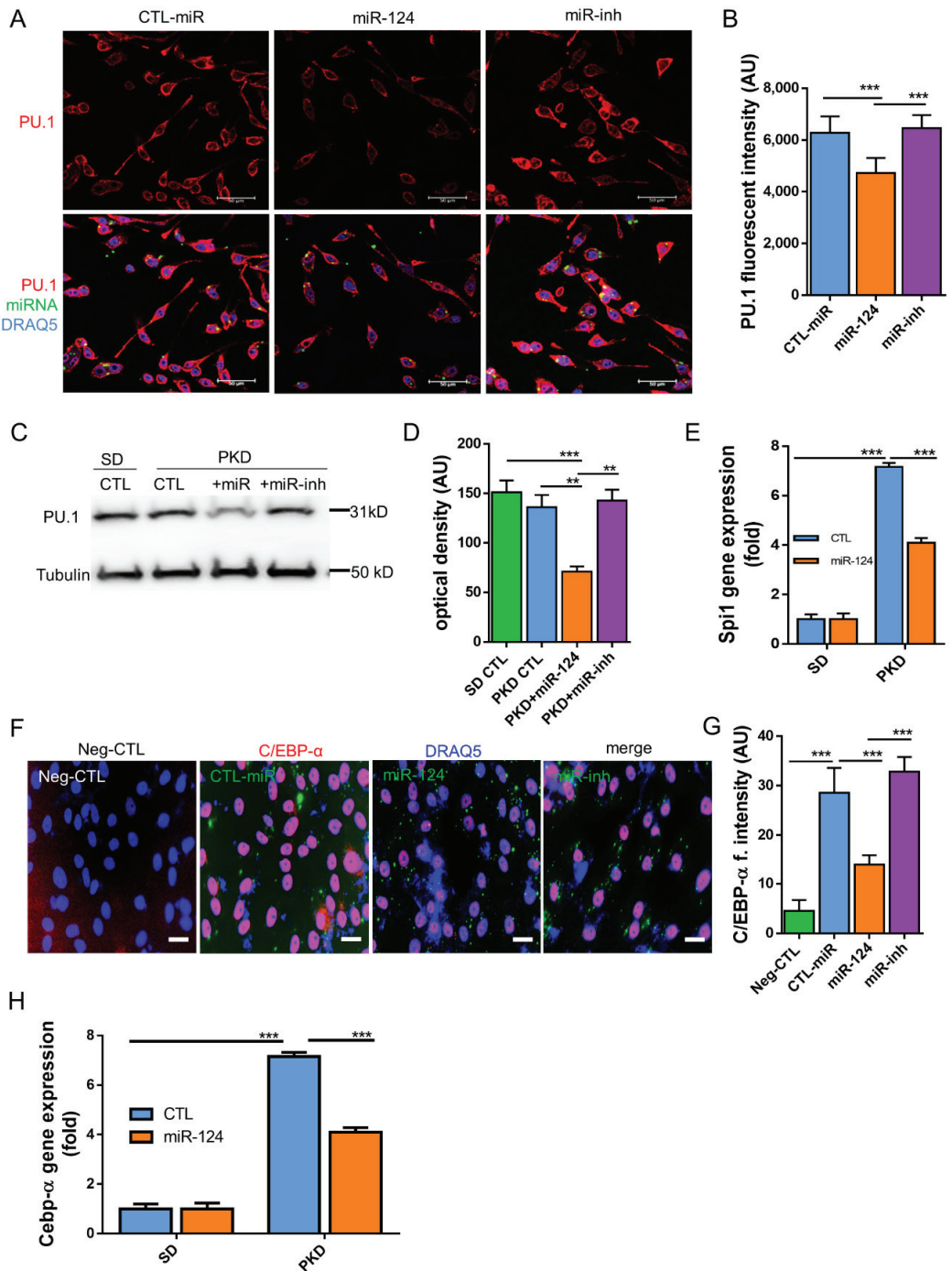


Figure 7. miR-124 regulated the expression of PU.1 and C/EBP-α in microglial cells and in PKD retinæ. (A,F) Immunocytochemistry (ICC) of PU.1 and C/EBP-α expression in BV2 cells. BV2 cells were transfected with an miR-124 mimic (miR-124),

control miRNA (CTL-miR), or miR-124 inhibitor (miR-inh). Cells transfected with only Lipofectamine 2000 Transfection Reagent were used as a negative control (Neg-CTL). PU.1 (A) and C/EBP- α (F) were detected using an Alexa 555-labeled secondary antibody (red), miRNA localization was visualized by FITC (green), and cell nuclei were labeled with DRAQ5TM (blue). Images were taken using a Leica confocal microscope TCS SP8, with scale bars = 50 μ m. (B,G) Quantification of ICC fluorescence from PU.1 (B) and C/EBP- α (G). (C) Western blot detection of PU.1 in the lysates of SD and PKD retinae, where 10 μ g of total protein preparation from retina tissue was separated in 4–20% SDS-PAGE gel, and an anti-PU.1 antibody 1:1000 dilution was used for detection. Protein expression of α -Tubulin was used as an internal control. (D) Quantification of western blots by optical intensity. Data are represented as means \pm SEM. (E,H) Gene expression of Spi1 (PU.1) and Cebp- α in miR-124 mimic- or control miRNA-treated retinae of SD and PKD rats was evaluated by RT-qPCR. The rat Gapdh gene was used as a housekeeping control. The immunostaining density was quantified with Image J software (B,G). Data are shown as the mean fluorescent intensity of five images of each condition, where $n = 5$, ** $p < 0.01$, and *** $p < 0.001$ (one-way ANOVA with Tukey's multiple comparisons test) (A–H).

3. Discussion

In the present study, we investigated the role of miR-124 in retinal vasoregression. Our results demonstrated that the administration of miR-124 in the PKD model of retinal degeneration reduced the activation of Müller glia and microglia as well as microglial motility. The administration of miR-124 downregulated the expression of pro-inflammatory mediators and redirected the response of microglia toward the anti-inflammatory phenotype. The downregulation of the transcription factor PU.1 and its upstream regulator C/EBP- α were associated with microglial modulation. With the replacement of miR-124, pericyte loss and acellular capillary formation were inhibited, and retinal vasoregression was subsequently alleviated.

In comparison with the expression of Müller cells and photoreceptor cells in the SD retina, the level of miR-124 was markedly reduced in the PKD retina. This was likely a consequence of the destroyed photoreceptors in the PKD rats, as the photoreceptor layer is the main source of miR-124, and PKD rats develop severe neurodegeneration between birth and 3 months [14]. We replaced miR-124 in the PKD retina by intravitreal injection. miR-124 expression was inversely correlated with Müller glial and microglial activation. As an important member of the retinal NVU, Müller glia mediate the signal transduction and molecule transport between neurons and vessels mainly through supporting and protecting photoreceptors and neuronal functions [3,29]. Müller glia undergo reactivation and dysfunction under pathological conditions, such as the ciliopathy model of the PKD rat retina [30]. Our results confirmed that the Müller glia underwent gliosis in the PKD rats and their activation was suppressed by miR-124's introduction. These results indicating that miR-124 inhibited microglial activation and recruitment support our hypothesis that miR-124 is an important modulator of microglia and Müller glia and that it contributes to retinal vasoregression. Upon administration of miR-124, microglial production of M1 markers was reduced, while M2 marker expression was increased in the retina of the PKD rat. This indicates that miR-124 shifts microglia to the anti-inflammatory phenotype. The switch of microglia to the anti-inflammation state may be the important determinant of further disease dynamics. In a spinal cord injury (SCI) mouse model, the viability of microglia was improved when the M1 markers were downregulated and the M2 markers were upregulated [31], supporting the proposed concept. In a mouse model of focal cerebral ischemia, miR-124 shifted the pro-inflammatory microglia and macrophages toward the anti-inflammatory phenotype and induced neuroprotection and functional improvement [32]. Our study demonstrated that miR-124 supports the anti-inflammatory phenotype of microglia in the retina and shifts the retinal microglia toward healing, despite the persistence of the primary insult. The replacement of miR-124 decreased the vasoregression phenotype by increasing the number of pericytes and reducing the extent of acellular capillaries. Müller glial function (b-wave ERG) in PKD rats was rescued by the replacement of miR-124; however, the photoreceptor function (a-wave ERG) could not be recovered. This indicates that miR-124's mediating of anti-inflammatory microglial function is mainly accomplished through regulating glial activation. The outer retinal degeneration caused mainly by photoreceptor death beginning early in a PKD rat's life

is irreversible. Considering the reciprocal interaction between microglia and Müller glia cells [33,34], as well as by identifying that microglial activation is associated with pericyte loss and capillary formation in the PKD model [17], we speculated that miR-124-regulated vasoregression and Müller glial function was most probably mediated by microglia. When the miR-124 level was sufficient, the microglia were deactivated and polarized to the M2 state. In contrast, when miR-124 was absent in diseased circumstances, the microglia were overactivated and secreted pro-inflammatory molecules, causing vascular cell loss and damaging NVU function.

To elucidate the potentially involved mechanisms by which miR-124 mediated microglial activation and polarization, the transcription factor PU.1 and its upstream regulator C/EBP- α were investigated. C/EBP- α /PU.1 signaling is a key regulator of the miR-124-mediated immune response in the EAE model and CNS inflammation. Overexpression of miR-124 downregulates C/EBP- α /PU.1 expression in macrophages and promotes microglia quiescence [26]. PU.1 is constitutively expressed by peripheral macrophages and brain microglia [35,36]. Its effect in modulating microglia development and activation has been widely explored in neurodegenerative diseases [37–39]. Zhou et al. demonstrated that PU.1 is essential for microglial activation in a mouse model of traumatic injury-induced neurodegeneration [39]. When PU.1 expression was downregulated with siRNA, the viability and phagocytotic function of human brain microglia were decreased [37]. In our study, PU.1 was highly expressed in the PKD retina relative to the SD retina. However, after miR-124 replacement, PU.1 expression was reduced in the PKD retina both at the mRNA and protein level. The *in vitro* study confirmed that the PU.1 expression in microglial cells was decreased by miR-124 transfection. As shown in an *in silico* analysis, PU.1 is not a direct target of miR-124; rather, it is regulated through the upstream transcription regulator C/EBP- α , a direct binding target of miR-124 [26]. We identified that the expression of C/EBP- α in BV2 cells was also inhibited after the transfection of the miR-124 mimic. PU.1 not only regulates macrophage and microglia activation but is, together with C/EBP- α , also an essential transcription factor for inflammatory polarization [40,41]. In a study on Alzheimer's disease, downregulation of PU.1 in BV2 cells suppressed the expression of pro-inflammatory genes, such as CCL2 and IL-1 β , as well as Aif1 (also known as Iba1), a molecular marker of microglia [37]. In another study with BMDM, miR-150-induced PU.1 downregulation inhibited the expression of pro-inflammatory cytokines and shifted the macrophage polarization toward the M2 state [42]. In a recent study of EAE mice, CNS microglia switched toward the M2 phenotype after BSYS (a traditional Chinese medicine) treatment. Concurrently, the upregulation of miR-124, but reduction of C/EBP- α /PU.1, were observed *in vivo* [43]. Thus, we assumed that miR-124 supplementation reduced C/EBP- α /PU.1 signaling, which regulated the expression of inflammatory associated genes and subsequently mediated microglial activation and polarization.

In the present study, we found that Flot1 expression was markedly reduced in miR-124 mimic-transfected BV2 cells. Flot1 was identified as a direct target of miR-124 [28]. As a pivotal lipid raft protein, Flot1 is involved in vesicular trafficking and signal transduction [44,45]. Lipid rafts regulate signaling cascades according to the changes of protein-protein interaction by intra- or extracellular stimuli [46]. For instance, upon TNF- α stimulation, excessive TNF receptors (TNFRs) were recruited to lipid rafts and elicited the TNF- α induced inflammation [47]. Dysregulated lipid raft formation and abnormal signaling may lead to the onset of neurodegenerative diseases, including Alzheimer's disease and Parkinson's disease [48]. We speculate that TNF- α stimulation was inhibited in the miR-124-treated microglial cells. Concurrently, the disruption of lipid rafts due to Flot1 suppression led to restricted translocation of TNFRs to lipid rafts and consequently to disturbed TNF- α -induced inflammatory responses of the microglia. Flot1 regulates the migration of many cancer cells [28,45,49] and immune cells [50]. Ludwig et al. demonstrated that Flot1 deficiency impairs the migration of neutrophil and the recruitment of immune cells to inflammatory sites [50]. Whether Flot1 downregulation correlates with the migration inhibition of microglia through miR-124 requires further investigation.

Another direct target of miR-124 is the chemokine CCL2 [25]. CCL2 is a potent chemoattractant of microglia and macrophages secreted by Müller cells and thus regulates microglial activation, migration, and recruitment to the position of retinal injury [51,52]. In this study, we identified that the expression of CCL2 was negatively correlated with the level of miR-124 in the PKD retina and BV2 cells, indicating that CCL2 was implicated in the miR-124-regulated microglial activation and inflammatory response. miR-124 inversely regulating CCL2-mediated inflammation has been described in a photo-oxidative damage (PD) mouse model of a degenerating retina [25]. This 5-day PD acute retina degeneration model, combined with our discoveries in the chronic PKD environment, indicates that the replacement of miR-124 modulates the retinal degeneration at least partially with CCL2.

In summary, in the PKD retina, photoreceptor damage causes a reduction of miR-124, resulting in abnormal activation of Müller- and micro-glia and a subsequent increase in vasoregression. After the miR-124 was replaced, Müller glia activation was inhibited, which directed its effector—the microglia—to inactivation, but the anti-inflammatory property was correlated with C/EBP- α /PU.1 regulation. Hence, miR-124 alleviated vasoregression and improved the neuroretinal function.

In conclusion, our study demonstrates that miR-124 inhibits microglial activation and motility, promotes microglial polarization to the anti-inflammatory phenotype (M2 state), and thus decreases vasoregression and improves neuroretinal function in the PKD retina. Introduction of miR-124 as an early medical intervention to instruct microglia to shift to an anti-inflammatory phenotype is of great importance in maintaining retinal neurovascular function before entering advanced disease states.

4. Materials and Methods

4.1. Rat and Intravitreal Injection

The transgenic PKD rat model was generated at the Center of Medical Research of the Medical Faculty Mannheim at the University of Heidelberg [12]. The animals were held in a 12-h light and dark cycle with free access to food and water. The rats received intravitreal injections of 25 pmol of the miR-124 mimic (miR-124), control miRNA (CTL-miR), or miR-124-inhibitor (miR-inh) at week 8 and week 10 and were sacrificed at week 12. The eyes were enucleated and stored in 4% formalin or frozen at -80°C . The wild-type SD rats were used as a control. The animal experiments were carried out in compliance with the statement of Association for Research in Vision and Ophthalmology (ARVO) and approved by the local governmental authorities (animal license numbers G-150/16, Regierungspräsidium, Karlsruhe, Germany).

4.2. Retinal Digest Preparation and Quantitative Morphometry

The vascular preparation of rat eyes was obtained by trypsin digestion as described previously [53,54]. Briefly, the rat eyes were fixed in 4% formalin overnight. Then, the retina was separated from the eyecup. After brief washing with distilled water, the retina was digested in a 0.2 mol/L Tris-HCl (pH 7.4) buffer with 3% trypsin for 3 h. The extra tissues between capillaries were washed away with water drops. The retinal vascular net was dried on a glass slide and stained with Periodic Acid Schiff's reagent (PAS) and hematoxylin.

Ten randomly selected areas were imaged with an Olympus BX51 Microscope under $400\times$ magnification, and the retinal quantitative morphometry was carried out using an image analysis system of Cell^F (Olympus Opticals, Hamburg, Germany). Quantification of pericytes (PCs) or migrating pericytes (MPs) was calculated as the cell number relative to the retinal capillary area (cell number/ mm^2 capillary area), while quantification of the acellular capillaries was calculated as the number relative to the retinal area (AC number/ mm^2 retina area), according to the established methods and morphology definition described previously [55–57].

4.3. miRNA In Situ Hybridization (ISH) and Fluorescent Immunohistochemistry

The formalin-fixed and paraffin-embedded retinal samples were cut into 6- μ m thick sections using SuperFrost Plus™ (Thermo Fisher Scientific, Waltham, MA, USA) slides. The tissue sections were baked at 60 °C for 45 min, rehydrated in a gradient ethanol (100%, 95%, 80%, or 70%) each for 5 min, and briefly washed in a PBS buffer for 2 min. After denaturing the miRNA by heating at 90 °C for 4 min, the slides were treated with 20 μ g/mL proteinase K at 37 °C for 10 min. The tissues were hybridized with an 80-nM Digoxigenin (DIG)-labeled miRCURY LNA miR-124 Detection Probe (Qiagen, Hilden, Germany) or scrambled miRNA probes (Qiagen) at 53 °C for 1 h. The slides were washed in 5 \times SSC, 2 \times SSC, and 0.2 \times SSC buffers at 45 °C for 5 min. After an additional wash in a 0.2 \times SSC solution at room temperature, the samples were blocked with 3% BSA containing 0.1% Tween-20 in PBS in a humidity chamber at room temperature for 20 min. Then, the tissues were incubated with sheep anti-digoxigenin (Roche, cat#11333089001, 1:800) and rabbit anti-glutamine synthetase (anti-GS) (Sigma, St. Louis, MO, USA, cat#G2781, 1:100) antibodies at 4 °C overnight. After being washed twice with PBS-T (0.1% Tween-20 in PBS), donkey anti-sheep Alexa Fluor 555 (Invitrogen, Waltham, MA, USA, cat#A21436, 1:200) and chicken anti-rabbit Alexa Fluor 488 (Invitrogen, cat#21441, 1:200) were added onto the samples at room temperature for 1 h, and the nuclei were stained with DRAQ5™ (Invitrogen, cat#65-0880, 1:1000) for 10 min. The images were acquired with a Leica TCS SP8 confocal microscope (Leica Microsystems, Wetzlar, Germany) under constant exposure time and gain for all specimens, including negative scrambled miRNA controls.

4.4. Primary Culture of Rat Microglia

The primary microglial cells were isolated from the male homo-PKD rats at 3 months of age using magnetic beads from Neural Tissue Dissociation Kit-Postnatal Neurons (Miltenyi Biotec, cat#130-094-802, Bergisch Gladbach, Germany) according to the manufacturer's instructions. The isolated retina was immersed in 6 mL of Dulbecco's phosphate buffered saline (D-PBS) (Sigma, Taufkirchen/Munich, Germany) and then digested with Enzyme mix 1 (buffer with enzyme P) for 15 min at 37 °C and Enzyme mix 2 for 10 min. The retinal tissue was then dissociated by pipetting the whole solution up and down around 10 times. The cell suspension was loaded onto a MACS SmartStrainer (70 μ m) (Miltenyi Biotec). After centrifugation at 1200 rpm for 5 min, the cells were collected and labeled with rabbit anti-CD74 antibody (Santa Cruz, cat#SC-20082, 1:100, Heidelberg, Germany) for 1 hour at room temperature. After sorting with anti-rabbit magnetic beads, the CD74⁺ cells were harvested and seeded in fibronectin-coated T25 flasks and cultured in a MACS Neuro medium (Miltenyi Biotec, cat#130-093-570) in a humidified incubator at 37 °C with 5% CO₂.

4.5. Cell Line Cultivation and Transfection

The mouse microglia BV2 cell line was cultured in a DMEM medium containing 10% fetal bovine serum (FBS) (Invitrogen, cat#A4766801) supplemented with 100 U/mL penicillin and 100 μ g/mL streptomycin (Invitrogen). In the 24-well cell culture format, 1 μ L of 20 μ M miRCURY LNA miR-124-3p mimic (Qiagen, cat#471256-001, sequence: 5'-UAAGGCACGCGGUGAAUGCC-3'), miRCURY LNA control miRNA mimic (Qiagen, cat#479903-001, sequence: 5'-GAUGGCAUUCGAUCAGUUCUA-3'), or miR-124 inhibitor (Qiagen cat#4102198-001, sequence 5'-GCATTCACCGCGTGCCTTA-3') was transfected into the cells using a Lipofectamine 2000 Transfection Reagent (Invitrogen, cat#11668-027) according to the manufacturer's instructions. Each miRNA mimic had a fluorescein labeled form (FAM), allowing observation after introduction.

4.6. Analysis of mRNA and miRNA Expression

The total RNA was extracted from the retinae with a TRIzol Reagent (Invitrogen, Waltham, MA, USA) according to the manufacturer's instructions. For the messenger RNA (mRNA) quantification of the protein-encoding genes, 1 μ g of RNA was reverse transcribed

to first strand complementary DNA (cDNA) using a QuantiTect Reverse Transcription Kit (cat#205310, Qiagen, Hilden, Germany). The mRNA levels were determined using a real-time quantitative polymerase chain reaction (RT-qPCR) performed in a StepOne Plus Real-Time PCR system (Applied Biosystems, Waltham, MA, USA). Reactions were performed in a MicroAmp Optical 96-well Reaction Plate (Thermo Fisher Scientific, Dreieich, Germany) with the following steps: 50 °C for 2 min, 95 °C for 10 min, and then 40 cycles of 95 °C for 15 s and 60 °C for 1 min per cycle. Rat gene glyceraldehyde-3-phosphate dehydrogenase (Gapdh) was used as the internal control. The relative expression of each gene was normalized and calculated using the $\Delta\Delta C_t$ method. The catalogue numbers of the primers are listed in Table 1.

Table 1. List of primers used in this study.

Gene Name	Reference Number *
Arg1	Rn00567522_m1
CCL2	Rn00580555_m1
CCL3	Rn01464736_g1
CD74	Rn00565062_m1
Cebp- α	Rn00560963_s1
IL-1 β	Rn00580432_m1
IL-10	Rn00563409_m1
IFN- γ	Rn00594078_m1
Gapdh	Rn99999916_s1
MHC-II	Rn01428452_m1
Spi1/PU.1	Rn01513815_m1
TGF- β 1	Rn00572010_m1
TNF- α	Rn01525859_g1

* All primers were from Thermo Fisher Scientific.

Reverse transcription for the miRNA was performed using a miRCURY LNA RT-Kit (Qiagen, cat#339340) with 10 ng total RNA. Quantitative evaluation of miR-124 expression was detected using a miRCURY LNA SYBR PCR Kit (Qiagen, cat#339345) according to the manufacturer's instructions. As the sequences of mature miR-124 in humans, mice, and rats are completely identical [58], we used the hsp-miR-124-3p Primer Set (Qiagen, cat#YP00206026) in this study. The expression of miRNA was normalized to U6 small nuclear RNA (snRNA).

4.7. Whole Mount Immunohistochemistry

After separation from the eyecup, the whole-mount retina was blocked and permeabilized in PBS with 1% BSA and 0.5% Triton X-100 for 2 h at room temperature. Following brief washing with PBS, the retina was incubated with biotin-conjugated iso-lectin B4 antibody (Sigma, cat#L1240, 1:100) and anti-CD74 antibody (Santa Cruz, cat#SC-20082, 1:100) at 4 °C overnight. The secondary antibodies of porcine anti-rabbit TRITC (DAKO, Glostrup, Denmark, cat#R0156, 1:200) and streptavidin Alexa Fluor[®] 633 (Invitrogen, cat#S21375, 1:500) were incubated at room temperature for 1 hour in the dark. All images were scanned using a Leica TCS SP8 confocal microscope. The microglia were defined as expressing CD74 and quantified in 10 randomly selected fields (400 \times magnification) from superficial and deep vascular retinal layers.

4.8. Immunocytochemistry (ICC)

After transfection for 24 h, the cells were re-seeded on the coverslips in a 24-well cell culture plate of 50–60% confluency. The cells were fixed with 4% formalin for 10 min and blocked in PBS with 1% BSA and 0.5% Triton X-100 for 30 min at room temperature. Then, the cells were incubated with primary antibodies against CCL2 (Millipore, Burlington, MA, USA, cat#MABN712, 1:100), CCL3 (Acris, cat#PP038P2, 1:100), PU.1 (Abcam, Cambridge, UK, cat#ab88082, 1:100), or Flot1 (Abcam, cat#ab41927, 1:100) at 4 °C overnight. Secondary

antibodies, namely Alexa Fluor 555 donkey anti-mouse (Life technologies, Carlsbad, CA, USA, Ref: A31570) and Alexa Fluor 555 donkey anti-rabbit (Life technologies, Ref: A31572), were applied at a 1:200 dilution for 1 hour at room temperature in the dark. The nuclei were stained with DRAQ5TM at a 1:1000 dilution for 30 min at room temperature. After washing with PBS three times, the slides were mounted with a fluorescence-preserving VECTASHIELD[®] HardSetTM Antifade Mounting Medium (Vector Laboratories, cat#H-1400). The images were taken with a Leica TCS SP8 confocal microscope.

4.9. Western Blot

A frozen retina from a SD or PKD rat was homogenized in a 100- μ L lysis buffer containing 0.1% SDS, 1% TritonX 100, 0.5% deoxycholate, 25 mmol/L HEPES pH 7.3, 10 mmol/L EDTA, 125 mmol/L NaCl, 10 mmol/L NaF, 10 mmol/L Na₄P₂P₂, and 2 mmol/L of orthovanadate and protease inhibitor. After centrifugation at 14,000 rpm at 4 °C for 20 min, the supernatant was harvested. The protein concentration was determined with Bio-Rad Protein Assay Dye Reagent Concentrate (BIO-RAD, Hercules, CA, USA, cat#500-0006). Ten μ g of protein was separated in 4–20% serial TGXTM SDS-polyacrylamide gel (BIO-RAD, cat#456-1096). The proteins were transferred onto a 0.2- μ m PVDF membrane using the Bio-Rad Trans-Blot Turbo Transfer System (BIO-RAD). The membrane was then blocked with 5% non-fat milk in PBS with 0.1% Tween 20 and incubated with primary antibodies at a 1:1000 dilution of anti-PU.1 antibody (Abcam, cat#ab88082) or anti-alpha Tubulin antibody (Abcam, cat#ab4074) at 4 °C overnight. After incubation with the Horseradish Peroxidase (HRP)-conjugated secondary antibody goat anti-mouse (DAKO, cat#P0447) and goat anti-rabbit (DAKO, cat#P0448) at a 1:2000 dilution at room temperature for 1 h, the immunoreactivity was visualized with Enhanced Chemiluminescence Substrate (Western Lighting ECL Pro, PerkinElmer). The Fusion SL system (Peqlab) was used for imaging and the densitometry was measured using Image J software.

4.10. Transwell Migration Assay

A total of 10⁵ BV2 cells were seeded in a Transwell[®] (Biocompare, Germany) with an 8- μ m pore size for the polyester membrane in the 24-well cell culture plate, and 100 μ L of Opti-medium with a transfection reagent and the miRNA or control miRNA were added to the cells, with the downside of the well containing only 750 μ L of Opti-medium. After 24 h of incubation at 37 °C, the cells still inside the Transwell membrane were removed with cotton sticks, and the cells that migrated to the lower side of the transwell were photographed and counted.

4.11. Wound Healing Assay

A scratch was made in the 24-well cell culture plate with confluent primary microglial cells, and the Opti-medium with a transfection complex (Lipofectamine 2000 addition with the miR-124 or control miRNA) was added. Images were taken at time points of 0 h and 24 h with a Leica DM IRB microscope, and at the end point, the cells were stained with Giemsa solution (cat#T862.1 ROTH, Berlin, Germany). The wound sizes were quantified with Image J software.

4.12. Live Cell Imaging and Time Lapse Analysis

After transfection for 24 h, the BV2 cells were reseeded in a new 24-well cell culture plate with a density of 4 \times 10⁴ per well. Four hours later, the culture medium was changed to a serum-free medium, and live cell imaging was started with the Incucyte S3 system (Essen Biosciences). Phase contrast images were taken at 30-min intervals for 20 h, videos were exported in an uncompressed AVI format, and cell moving distances were analyzed by the Timelapse Analyzer program. The average migration distance (AMD) of each single cell was measured and expressed in micrometers. In all, 100 cells were analyzed per imaging field, and an average of 3 fields for each experimental condition was shown.

4.13. Electroretinography (ERG)

The neuroretinal function was measured by multifocal electroretinography under photopic conditions as previously described [59]. The RETImap system was utilized for the measurement (Roland Consult, Brandenburg an der Havel, Germany).

4.14. Statistical Analysis

Data are presented as means \pm SD or means \pm SEM. A Student's t-test or one-way or two-way analysis of variance (ANOVA) with Tukey's multiple comparisons test was used to determine the statistical differences between the experimental groups (Prism, GraphPad Software, San Diego, CA, USA), and a *p* value < 0.05 was considered statistically significant.

Author Contributions: Y.C. designed the *in vitro* experiments of the research and carried out whole-mount immunofluorescence, microglial quantification, RT-qPCR, and western blotting; J.L. and H.-P.H. designed the *in vivo* experiments of the research and analyzed the data, including retinal quantitative morphometry and ISH; S.H. (Seddik Hammad), S.D., and M.B. facilitated the live cell imaging analysis; A.S. and L.K. executed the paraffin sections for ISH and immunohistochemistry; S.H. (Sigrid Hoffmann) developed the transgenic PKD rats; Y.C., J.L., and H.-P.H. drafted the work; I.F., J.H., A.S., and H.-P.H. revised the manuscript critically for important intellectual content. All authors have read and agreed to the published version of the manuscript.

Funding: This research work was funded by the EYEnovative Prize 2014 (Novartis Ophthalmologie Förderpreis, Novartis Pharma GmbH). Y.C. was funded by German Research Foundation (DFG: Deutsche Forschungsgemeinschaft, LI 3384/2-1). J.L., A.S. and H.-P.H. were funded by DFG (SFB 1118, project 236360313). L.K. and H.-P.H. were supported by DFG GRK 1874-2 DIAMICOM. Seddik Hammad and S.D. were supported by the BMBF (German Federal Ministry of Education and Research) Project LiSyM (Grants PTJ-FKZ: 031 L0043). I.F. was funded by DFG grant (SFB 834/3 B13, project ID: 75732319).

Institutional Review Board Statement: The study was conducted according to the guidelines of the Declaration of Helsinki. The animal experiments were carried out in compliance with the statement of the Association for Research in Vision and Ophthalmology (ARVO) and approved by the local governmental authorities (animal license number G-150/16, Regierungspräsidium, Karlsruhe, Germany).

Informed Consent Statement: Not applicable.

Acknowledgments: We thank Chun Zhang and Hua Su for critical discussion of the results. We thank Bettina Kraenzlin and Ina Schaefer from the Core Facility of the Medical Faculty Mannheim at the University of Heidelberg. We also thank Nadine Dietrich and Fortunata Tina Jung for their technical support. The graphical abstract was created with BioRender.com.

Conflicts of Interest: The authors declare no conflict of interest.

Abbreviations

Arg1	Arginase-1
BMDMs	Bone marrow-derived macrophages
BSYS	Bu Shen Yi Sui capsule
CCL2	C-C motif chemokine ligand 2
CCL3	C-C motif chemokine ligand 3
CD74	Major histocompatibility complex, class II invariant chain
C/EBP- α	CCAAT/enhancer-binding protein- α
CNS	Central nervous system
DR	Diabetic retinopathy
EAE	Experimental autoimmune encephalomyelitis
ERG	Electroretinography GCL ganglion cell layer
Flot1	Flottilin-1
Gapdh	Glyceraldehyde 3-phosphate dehydrogenase

GS	Glutamine synthetase
IFN- γ	Interferon gamma
IL-1 β	Interleukin-1 β
IL-10	Interleukin-10
ILM	Inner limiting membrane
INL	Inner nuclear layer
IPL	Inner plexiform layer
MHC-II	Major histocompatibility complex class II molecule
miR-124	MicroRNA-124
miR-inh	MicroRNA-124 inhibitor
NVU	Neurovascular unit
OLM	Outer limiting membrane
ONL	Outer nuclear layer
OPL	Outer plexiform layer
PD	Photo-oxidative damage
PKD	Polycystic kidney disease
PU.1	Protein binding U box
SCI	Spinal cord injury
SD	Sprague Dawley
Spi1	Salmonella Pathogenicity Island 1 (gene name of PU.1)
TNF- α	Tumor necrosis factor- α
TNFR	TNF receptor

References

- Hammes, H.P.; Feng, Y.; Pfister, F.; Brownlee, M. Diabetic retinopathy: Targeting vasoregression. *Diabetes* **2011**, *60*, 9–16. [CrossRef]
- Karlstetter, M.; Scholz, R.; Rutar, M.; Wong, W.T.; Provis, J.M.; Langmann, T. Retinal microglia: Just bystander or target for therapy? *Prog. Retin. Eye Res.* **2015**, *45*, 30–57. [CrossRef]
- Vecino, E.; Rodriguez, F.D.; Ruzafa, N.; Pereiro, X.; Sharma, S.C. Glia-neuron interactions in the mammalian retina. *Prog. Retin. Eye Res.* **2016**, *51*, 1–40. [CrossRef]
- Rashid, K.; Akhtar-Schaefer, I.; Langmann, T. Microglia in Retinal Degeneration. *Front. Immunol.* **2019**, *10*, 1975. [CrossRef] [PubMed]
- Bellver-Landete, V.; Bretheau, F.; Mailhot, B.; Vallieres, N.; Lessard, M.; Janelle, M.E.; Vernoux, N.; Tremblay, M.E.; Fuehrmann, T.; Shoichet, M.S.; et al. Microglia are an essential component of the neuroprotective scar that forms after spinal cord injury. *Nat. Commun.* **2019**, *10*, 518. [CrossRef] [PubMed]
- Gupta, N.; Shyamasundar, S.; Patnala, R.; Karthikeyan, A.; Arumugam, T.V.; Ling, E.A.; Dheen, S.T. Recent progress in therapeutic strategies for microglia-mediated neuroinflammation in neuropathologies. *Expert Opin. Ther. Targets* **2018**, *22*, 765–781. [CrossRef]
- Zhao, H.; Garton, T.; Keep, R.F.; Hua, Y.; Xi, G. Microglia/Macrophage Polarization After Experimental Intracerebral Hemorrhage. *Transl. Stroke Res.* **2015**, *6*, 407–409. [CrossRef] [PubMed]
- Jiang, C.T.; Wu, W.F.; Deng, Y.H.; Ge, J.W. Modulators of microglia activation and polarization in ischemic stroke (Review). *Mol. Med. Rep.* **2020**, *21*, 2006–2018. [CrossRef]
- Yao, K.; Zu, H.B. Microglial polarization: Novel therapeutic mechanism against Alzheimer’s disease. *Inflammopharmacology* **2020**, *28*, 95–110. [CrossRef]
- Arroba, A.I.; Valverde, A.M. Modulation of microglia in the retina: New insights into diabetic retinopathy. *Acta Diabetol.* **2017**, *54*, 527–533. [CrossRef] [PubMed]
- Lull, M.E.; Block, M.L. Microglial activation and chronic neurodegeneration. *Neurotherapeutics* **2010**, *7*, 354–365. [CrossRef]
- Gallagher, A.R.; Hoffmann, S.; Brown, N.; Cedzich, A.; Meruvu, S.; Podlich, D.; Feng, Y.; Konecke, V.; de Vries, U.; Hammes, H.P.; et al. A truncated polycystin-2 protein causes polycystic kidney disease and retinal degeneration in transgenic rats. *J. Am. Soc. Nephrol.* **2006**, *17*, 2719–2730. [CrossRef]
- Yoder, B.K. Role of primary cilia in the pathogenesis of polycystic kidney disease. *J. Am. Soc. Nephrol.* **2007**, *18*, 1381–1388. [CrossRef] [PubMed]
- Feng, Y.; Wang, Y.; Stock, O.; Pfister, F.; Tanimoto, N.; Seeliger, M.W.; Hillebrands, J.L.; Hoffmann, S.; Wolburg, H.; Gretz, N.; et al. Vasoregression linked to neuronal damage in the rat with defect of polycystin-2. *PLoS ONE* **2009**, *4*, e7328. [CrossRef]
- Herrero, L.J.; Sheng, K.C.; Jian, P.; Taylor, A.; Her, Z.; Herring, B.L.; Chow, A.; Leo, Y.S.; Hickey, M.J.; Morand, E.F.; et al. Macrophage migration inhibitory factor receptor CD74 mediates alphavirus-induced arthritis and myositis in murine models of alphavirus infection. *Arthritis Rheum.* **2013**, *65*, 2724–2736.
- Benedek, G.; Meza-Romero, R.; Andrew, S.; Leng, L.; Burrows, G.G.; Bourdette, D.; Offner, H.; Bucala, R.; Vandenbark, A.A. Partial MHC class II constructs inhibit MIF/CD74 binding and downstream effects. *Eur. J. Immunol.* **2013**, *43*, 1309–1321. [CrossRef]

17. Lin, J.; Hu, J.; Schlotterer, A.; Wang, J.; Kolibabka, M.; Awwad, K.; Dietrich, N.; Breitschopf, K.; Wohlfart, P.; Kannt, A.; et al. Protective effect of Soluble Epoxide Hydrolase Inhibition in Retinal Vasculopathy associated with Polycystic Kidney Disease. *Theranostics* **2020**, *10*, 7857–7871. [CrossRef]
18. McConnachie, D.J.; Stow, J.L.; Mallett, A.J. Ciliopathies and the Kidney: A Review. *Am. J. Kidney Dis* **2021**, *77*, 410–419. [CrossRef]
19. Ardekani, A.M.; Naeini, M.M. The Role of MicroRNAs in Human Diseases. *Avicenna J. Med. Biotechnol.* **2010**, *2*, 161–179. [PubMed]
20. Karali, M.; Persico, M.; Mutarelli, M.; Carissimo, A.; Pizzo, M.; Singh Marwah, V.; Ambrosio, C.; Pinelli, M.; Carrella, D.; Ferrari, S.; et al. High-resolution analysis of the human retina miRNome reveals isomiR variations and novel microRNAs. *Nucleic Acids Res.* **2016**, *44*, 1525–1540. [CrossRef] [PubMed]
21. Lagos-Quintana, M.; Rauhut, R.; Yalcin, A.; Meyer, J.; Lendeckel, W.; Tuschl, T. Identification of tissue-specific microRNAs from mouse. *Curr. Biol.* **2002**, *12*, 735–739. [CrossRef]
22. Sanuki, R.; Onishi, A.; Koike, C.; Muramatsu, R.; Watanabe, S.; Muranishi, Y.; Irie, S.; Uneo, S.; Koyasu, T.; Matsui, R.; et al. miR-124a is required for hippocampal axogenesis and retinal cone survival through Lhx2 suppression. *Nat. Neurosci.* **2011**, *14*, 1125–1134. [CrossRef] [PubMed]
23. Nakamachi, Y.; Ohnuma, K.; Uto, K.; Noguchi, Y.; Saegusa, J.; Kawano, S. MicroRNA-124 inhibits the progression of adjuvant-induced arthritis in rats. *Ann. Rheum. Dis.* **2016**, *75*, 601–608. [CrossRef] [PubMed]
24. Louw, A.M.; Kolar, M.K.; Novikova, L.N.; Kingham, P.J.; Wiberg, M.; Kjems, J.; Novikov, L.N. Chitosan polyplex mediated delivery of miRNA-124 reduces activation of microglial cells in vitro and in rat models of spinal cord injury. *Nanomedicine* **2016**, *12*, 643–653. [CrossRef] [PubMed]
25. Chu-Tan, J.A.; Rutar, M.; Saxena, K.; Aggio-Bruce, R.; Essex, R.W.; Valter, K.; Jiao, H.; Fernando, N.; Wooff, Y.; Madigan, M.C.; et al. MicroRNA-124 Dysregulation is Associated With Retinal Inflammation and Photoreceptor Death in the Degenerating Retina. *Investig. Ophthalmol. Vis. Sci.* **2018**, *59*, 4094–4105. [CrossRef] [PubMed]
26. Ponomarev, E.D.; Veremeyko, T.; Barteneva, N.; Krichevsky, A.M.; Weiner, H.L. MicroRNA-124 promotes microglia quiescence and suppresses EAE by deactivating macrophages via the C/EBP- α -PU.1 pathway. *Nat. Med.* **2011**, *17*, 64–70. [CrossRef]
27. Chen, M.; Xu, H. Parainflammation, chronic inflammation, and age-related macular degeneration. *J. Leukoc. Biol.* **2015**, *98*, 713–725. [CrossRef]
28. Li, L.; Luo, J.; Wang, B.; Wang, D.; Xie, X.; Yuan, L.; Guo, J.; Xi, S.; Gao, J.; Lin, X.; et al. MicroRNA-124 targets flotillin-1 to regulate proliferation and migration in breast cancer. *Mol. Cancer* **2013**, *12*, 163. [CrossRef]
29. Goldman, D. Muller glial cell reprogramming and retina regeneration. *Nat. Rev. Neurosci.* **2014**, *15*, 431–442. [CrossRef]
30. Vogler, S.; Pannicke, T.; Hollborn, M.; Grosche, A.; Busch, S.; Hoffmann, S.; Wiedemann, P.; Reichenbach, A.; Hammes, H.P.; Bringmann, A. Muller cell reactivity in response to photoreceptor degeneration in rats with defective polycystin-2. *PLoS ONE* **2014**, *8*, e61631. [CrossRef]
31. Yang, Z.; Xu, J.; Zhu, R.; Liu, L. Down-Regulation of miRNA-128 Contributes to Neuropathic Pain Following Spinal Cord Injury via Activation of P38. *Med. Sci. Monit.* **2017**, *23*, 405–411. [CrossRef] [PubMed]
32. Hamzei Taj, S.; Kho, W.; Riou, A.; Wiedermann, D.; Hoehn, M. MiRNA-124 induces neuroprotection and functional improvement after focal cerebral ischemia. *Biomaterials* **2016**, *91*, 151–165. [CrossRef] [PubMed]
33. Reichenbach, A.; Bringmann, A. Glia of the human retina. *Glia* **2020**, *68*, 768–796. [CrossRef] [PubMed]
34. Wang, M.; Wong, W.T. Microglia-Muller cell interactions in the retina. *Adv. Exp. Med. Biol.* **2014**, *801*, 333–338. [PubMed]
35. Smith, A.M.; Gibbons, H.M.; Oldfield, R.L.; Bergin, P.M.; Mee, E.W.; Faull, R.L.; Dragunow, M. The transcription factor PU.1 is critical for viability and function of human brain microglia. *Glia* **2013**, *61*, 929–942. [CrossRef]
36. Walton, M.R.; Gibbons, H.; MacGibbon, G.A.; Sirimanne, E.; Saura, J.; Gluckman, P.D.; Dragunow, M. PU.1 expression in microglia. *J. Neuroimmunol.* **2000**, *104*, 109–115. [CrossRef]
37. Pimenova, A.A.; Herbinet, M.; Gupta, I.; Machlovi, S.I.; Bowles, K.R.; Marcora, E.; Goate, A.M. Alzheimer’s-associated PU.1 expression levels regulate microglial inflammatory response. *Neurobiol. Dis.* **2021**, *148*, 105217. [CrossRef] [PubMed]
38. Rustenhoven, J.; Smith, A.M.; Smyth, L.C.; Jansson, D.; Scotter, E.L.; Swanson, M.E.V.; Aalderink, M.; Coppieters, N.; Narayan, P.; Handley, R.; et al. PU.1 regulates Alzheimer’s disease-associated genes in primary human microglia. *Mol. Neurodegener.* **2018**, *13*, 44. [CrossRef] [PubMed]
39. Zhou, N.; Liu, K.; Sun, Y.; Cao, Y.; Yang, J. Transcriptional mechanism of IRF8 and PU.1 governs microglial activation in neurodegenerative condition. *Protein Cell* **2019**, *10*, 87–103. [CrossRef] [PubMed]
40. Juhas, U.; Ryba-Stanislawowska, M.; Szargiej, P.; Mysliwska, J. Different pathways of macrophage activation and polarization. *Postepy Hig. Med. Dosw.* **2015**, *69*, 496–502. [CrossRef]
41. Lawrence, T.; Natoli, G. Transcriptional regulation of macrophage polarization: Enabling diversity with identity. *Nat. Rev. Immunol.* **2011**, *11*, 750–761. [CrossRef]
42. Shakerian, L.; Ghorbani, S.; Talebi, F.; Noorbakhsh, F. MicroRNA-150 targets PU.1 and regulates macrophage differentiation and function in experimental autoimmune encephalomyelitis. *J. Neuroimmunol.* **2018**, *323*, 167–174. [CrossRef]
43. Zha, Z.; Gao, Y.F.; Ji, J.; Sun, Y.Q.; Li, J.L.; Qi, F.; Zhang, N.; Jin, L.Y.; Xue, B.; Yang, T.; et al. Bu Shen Yi Sui Capsule Alleviates Neuroinflammation and Demyelination by Promoting Microglia toward M2 Polarization, Which Correlates with Changes in miR-124 and miR-155 in Experimental Autoimmune Encephalomyelitis. *Oxid. Med. Cell Longev.* **2021**, *2021*, 5521503. [CrossRef]

44. Cremona, M.L.; Matthies, H.J.; Pau, K.; Bowton, E.; Speed, N.; Lute, B.J.; Anderson, M.; Sen, N.; Robertson, S.D.; Vaughan, R.A.; et al. Flotillin-1 is essential for PKC-triggered endocytosis and membrane microdomain localization of DAT. *Nat. Neurosci.* **2011**, *14*, 469–477. [CrossRef]
45. Song, L.; Gong, H.; Lin, C.; Wang, C.; Liu, L.; Wu, J.; Li, M.; Li, J. Flotillin-1 promotes tumor necrosis factor- α receptor signaling and activation of NF- κ B in esophageal squamous cell carcinoma cells. *Gastroenterology* **2012**, *143*, 995–1005.e12. [CrossRef]
46. Simons, K.; Toomre, D. Lipid rafts and signal transduction. *Nat. Rev. Mol. Cell Biol.* **2000**, *1*, 31–39. [CrossRef] [PubMed]
47. Legler, D.F.; Micheau, O.; Doucey, M.A.; Tschopp, J.; Bron, C. Recruitment of TNF receptor 1 to lipid rafts is essential for TNF α -mediated NF- κ B activation. *Immunity* **2003**, *18*, 655–664. [CrossRef]
48. Sonnino, S.; Aureli, M.; Grassi, S.; Mauri, L.; Prioni, S.; Prinetti, A. Lipid rafts in neurodegeneration and neuroprotection. *Mol. Neurobiol.* **2014**, *50*, 130–148. [CrossRef]
49. Lin, C.; Wu, Z.; Lin, X.; Yu, C.; Shi, T.; Zeng, Y.; Wang, X.; Li, J.; Song, L. Knockdown of FLOT1 impairs cell proliferation and tumorigenicity in breast cancer through upregulation of FOXO3a. *Clin. Cancer Res.* **2011**, *17*, 3089–3099. [CrossRef] [PubMed]
50. Ludwig, A.; Otto, G.P.; Riento, K.; Hams, E.; Fallon, P.G.; Nichols, B.J. Flotillin microdomains interact with the cortical cytoskeleton to control uropod formation and neutrophil recruitment. *J. Cell Biol.* **2010**, *191*, 771–781. [CrossRef] [PubMed]
51. Feng, C.; Wang, X.; Liu, T.; Zhang, M.; Xu, G.; Ni, Y. Expression of CCL2 and its receptor in activation and migration of microglia and monocytes induced by photoreceptor apoptosis. *Mol. Vis.* **2017**, *23*, 765–777. [PubMed]
52. Rutar, M.; Natoli, R.; Valter, K.; Provis, J.M. Early focal expression of the chemokine Ccl2 by Muller cells during exposure to damage-inducing bright continuous light. *Investig. Ophthalmol. Vis. Sci.* **2011**, *52*, 2379–2388. [CrossRef] [PubMed]
53. Hammes, H.P.; Martin, S.; Federlin, K.; Geisen, K.; Brownlee, M. Aminoguanidine treatment inhibits the development of experimental diabetic retinopathy. *Proc. Natl. Acad. Sci. USA* **1991**, *88*, 11555–11558. [CrossRef] [PubMed]
54. Lin, J.; Bierhaus, A.; Bugert, P.; Dietrich, N.; Feng, Y.; Vom Hagen, F.; Nawroth, P.; Brownlee, M.; Hammes, H.P. Effect of R-(+)- α -lipoic acid on experimental diabetic retinopathy. *Diabetologia* **2006**, *49*, 1089–1096. [CrossRef]
55. Armulik, A.; Abramsson, A.; Betsholtz, C. Endothelial/pericyte interactions. *Circ. Res.* **2005**, *97*, 512–523. [CrossRef]
56. Dietrich, N.; Hammes, H.P. Retinal digest preparation: A method to study diabetic retinopathy. *Methods Mol. Biol.* **2012**, *933*, 291–302.
57. Pfister, F.; Feng, Y.; vom Hagen, F.; Hoffmann, S.; Molema, G.; Hillebrands, J.L.; Shani, M.; Deutsch, U.; Hammes, H.P. Pericyte migration: A novel mechanism of pericyte loss in experimental diabetic retinopathy. *Diabetes* **2008**, *57*, 2495–2502. [CrossRef]
58. Qin, Z.; Wang, P.Y.; Su, D.F.; Liu, X. miRNA-124 in Immune System and Immune Disorders. *Front. Immunol.* **2016**, *7*, 406. [CrossRef]
59. Dutescu, R.M.; Skosyrski, S.; Kociok, N.; Semkova, I.; Mergler, S.; Atorf, J.; Joussen, A.M.; Strauss, O.; Kremers, J. Multifocal ERG recordings under visual control of the stimulated fundus in mice. *Investig. Ophthalmol. Vis. Sci.* **2013**, *54*, 2582–2589. [CrossRef]



Article

Combined Therapy of Vitamin D3-Tolerogenic Dendritic Cells and Interferon- β in a Preclinical Model of Multiple Sclerosis

Bibiana Quirant-Sánchez ^{1,2,†}, María José Mansilla ^{1,2,†}, Juan Navarro-Barruso ^{1,2}, Silvia Presas-Rodríguez ^{3,4}, Aina Teniente-Serra ^{1,2}, Federico Fondelli ^{1,2}, Cristina Ramo-Tello ^{3,4,*} and Eva Martínez-Cáceres ^{1,2,*}

- ¹ Immunology Division, LCMN, Germans Trias i Pujol University Hospital and Research Institute, Campus Can Ruti, 08916 Badalona, Spain; bquirant.germanstrias@gencat.cat (B.Q.-S.); mjmansilla@igtp.cat (M.J.M.); juan_navarro@outlook.com (J.N.-B.); ateniente.germanstrias@gencat.cat (A.T.-S.); ffondelli@igtp.cat (F.F.)
 - ² Department of Cellular Biology, Physiology and Immunology, Campus Bellaterra, Universitat Autònoma de Barcelona, 08193 Cerdanyola del Vallès, Spain
 - ³ Multiple Sclerosis Unit, Department of Neurosciences, Germans Trias i Pujol University Hospital, 08916 Badalona, Spain; spresas@igtp.cat
 - ⁴ Department of Medicine, Campus Bellaterra, Universitat Autònoma de Barcelona, 08193 Cerdanyola del Vallès, Spain
- * Correspondence: cramot.germanstrias@gencat.cat or cramot@gmail.com (C.R.-T.); emmartinez.germanstrias@gencat.cat (E.M.-C.); Tel.: +34-93-497-8433 (C.R.-T.); +34-93-497-8666 (E.M.-C.)
- † These authors equally contributed to the study.

Citation: Quirant-Sánchez, B.; Mansilla, M.J.; Navarro-Barruso, J.; Presas-Rodríguez, S.; Teniente-Serra, A.; Fondelli, F.; Ramo-Tello, C.; Martínez-Cáceres, E. Combined Therapy of Vitamin D3-Tolerogenic Dendritic Cells and Interferon- β in a Preclinical Model of Multiple Sclerosis. *Biomedicines* **2021**, *9*, 1758. <https://doi.org/10.3390/biomedicines9121758>

Academic Editors: Masaru Tanaka and Lydia Giménez-Llort

Received: 22 September 2021
Accepted: 20 November 2021
Published: 24 November 2021

Publisher's Note: MDPI stays neutral with regard to jurisdictional claims in published maps and institutional affiliations.



Copyright: © 2021 by the authors. Licensee MDPI, Basel, Switzerland. This article is an open access article distributed under the terms and conditions of the Creative Commons Attribution (CC BY) license (<https://creativecommons.org/licenses/by/4.0/>).

Abstract: Autologous antigen-specific therapies based on tolerogenic dendritic cells (tolDC) offer the possibility to treat autoimmune diseases by restoring homeostasis and targeting specifically autoreactive responses. Here, we explore the hypothesis that systemic inflammation occurring in autoimmune diseases, such as multiple sclerosis (MS), can generate a disease-specific environment able to alter the functionality of tolDC. In this context in fact, a combined therapy of tolDC with an immunomodulatory treatment could potentiate the beneficial effect of this antigen-specific cell therapy. For this purpose, we analyzed the efficacy of a combined therapy based on the use of vitamin D3 (VitD3)-tolDC plus interferon beta (IFN-beta) in MS. VitD3-tolDC were generated from healthy donors and MS patients and co-cultured with allogeneic peripheral blood mononuclear cells, in the presence or absence of IFN-beta. In vitro, VitD3-tolDC treatment reduced the percentage of activated T cells and allogeneic proliferation, whereas VitD3-tolDC+IFN-beta treatment enhanced the suppressive ability of VitD3-tolDC and, additionally, induced a shift towards a Th2 profile. To determine the clinical benefit of the combined therapy, C57BL/6-experimental autoimmune encephalomyelitis (EAE)-induced mice were treated with antigen-specific VitD3-tolDC and/or IFN-beta. Treatment of EAE mice with combined therapy ameliorated the disease course compared to each monotherapy. These results suggest that a combined therapy based on antigen-specific VitD3-tolDC and IFN-beta may represent a promising strategy for MS patients.

Keywords: combined therapy; antigen-specific therapies; immunomodulatory; multiple sclerosis

1. Introduction

Tolerance is a state of unresponsiveness of the immune system towards antigens that can elicit an immune response. It is a mechanism primarily aimed to avoid the reactivity of the immune system against “self” tissues. Indeed, when tolerance towards self-antigens is lost, autoimmune diseases, such as multiple sclerosis (MS), can develop [1].

MS is the most common multifocal inflammatory demyelinating disease of the central nervous system (CNS). Diagnosis of MS is based on clinical, radiological, and laboratory criteria (oligoclonal bands in the cerebrospinal fluid). Currently, available therapies for MS exert their effects through immunomodulatory or immunosuppressive functions. These treatments are focused on reducing the activity of the disease and slowing its progression, but it is a disease that has no cure [2].

MS is considered an immune-mediated disease. Extensively reported in both healthy individuals and MS patients is the presence of circulating myelin-specific autoreactive T cells. However, the specific mechanisms causing their activation and infiltration of CNS, resulting in wide systemic inflammation and neurodegeneration, are still unknown [3–5]. In MS patients, altered and dysfunctional regulatory T cells (Treg), monocytes and dendritic cells (DC), have been described [6,7]. In this scenario, DC are pivotal regulators of the immune response, able to induce T cell priming and differentiation [5], control T effector cells and promote Treg differentiation in the periphery. The presence of dysfunctional Treg [3], DC [5] and altered cytokine production may facilitate the activation and arrival of autoreactive T cells into the CNS [3,8,9].

Recombinant interferon beta (IFN-beta) is one of the most prescribed treatments for relapsing-remitting MS (RRMS) patients. This is due to its multi-level immunomodulatory and anti-inflammatory functionality: the inhibition of Th1 response, reduction in T cell expansion, decrease in costimulatory and MHC class-II molecules expression, induction of Th2 cytokine profile, and blockage of immune cells entry into the CNS [10–13]. Because of the long experience using IFN-beta for treating MS patients and its wide immunomodulatory effects, we aim to demonstrate that the combination of myelin-specific vitamin D3 tolerogenic dendritic cells (VitD3-tolDC) with IFN-beta could improve the therapeutic effect of myelin-specific VitD3-tolDC.

Antigen-specific cell-based tolerogenic therapies (CTT) are promising therapeutic strategies [14–16] that, in contrast to the currently available immunomodulatory or immunosuppressive drugs, have the potential to restore self-tolerance by suppressing the autoreactive T cell clones [17–21]. In this context, our research group has developed an autologous cell-based tolerogenic product consisting of monocyte-derived tolerogenic DC generated in the presence of vitamin D3 (VitD3-tolDC) and loaded with a pool of myelin peptides [22]. Preclinical data in experimental autoimmune encephalomyelitis (EAE) demonstrated that the treatment with antigen-specific VitD3-tolDC is able to abrogate disease progression when they were administrated to mice with clinical symptoms of the disease [23–25]. Currently, two harmonized phase I clinical trials using autologous myelin-specific VitD3-tolDC therapy in patients with active forms of MS are ongoing in Spain and Belgium [22,26].

However, the potent inflammatory processes taking place in MS patients may influence the phenotype and functionality of the VitD3-tolDC administrated. In order to get an efficient translation of this therapy to the clinic, we hypothesize that the combination of antigen-specific VitD3-tolDC with an immunomodulatory drug, could act synergically by restoring an appropriate immune environment, potentiating the antigen-specific tolerogenic effect of VitD3-tolDC.

2. Materials and Methods

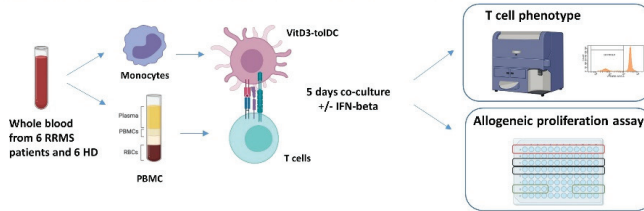
An overview of the experimental strategy is represented in Figure 1.

2.1. Sample Collection

Monocyte-derived dendritic cells (MDDC) differentiation was performed from 6 buffy coat samples obtained following standard operating procedures for blood donation, provided by the Banc de Sang i Teixits (Barcelona, Spain). In addition, 40 mL of peripheral blood samples from 6 Relapsing Remitting MS patients (RRMS) from the MS unit of the Germans Trias i Pujol Hospital (Spain) were collected in lithium heparin tubes and processed as detailed below. Patients selected did not receive any treatment during at least the previous two months (Supplementary Table S1). The study was approved by the Ethical Committee of Germans Trias i Pujol Hospital and all subjects gave their informed consent according to the Declaration of Helsinki.

Overview of the experimental strategy

In vitro studies with blood samples of HD and RRMS patients



In vivo studies in the EAE model

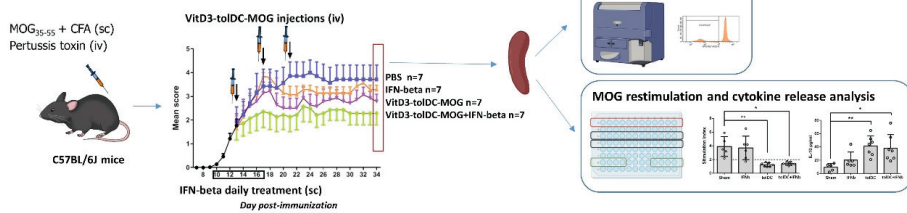


Figure 1. Overview of the experimental strategy. Two experimental approaches were used to investigate the effect of the combined VitD3-tolDC plus IFN-beta therapy in MS. In vitro studies: we performed in vitro co-cultures of VitD3-tolDC plus PBMC of RRMS patients and of HD ($n = 6$ /group) in presence/absence of IFN-beta. After 5 days of culture, the phenotype of cultured T cells and the induction of allogeneic proliferation by different concentrations of VitD3-tolDC in presence/absence of IFN-beta were analyzed (see Methods for a more detailed explanation); in vivo studies: EAE was induced to C57BL/6J mice. Mice were treated subcutaneously (sc) with IFN-beta (from day 10 to 17 post-immunization, (pi)) and /or intravenously (iv) with antigen-specific VitD3-tolDC (VitD3-tolDC-MOG) (on days 13, 17 and 21 pi) ($n = 7$ /group). Clinical scores were recorded daily. Splenocytes of mice ($n = 7$ /group) were analyzed to evaluate antigen-specific proliferation (ex-vivo restimulation with MOG antigen), secretion of cytokines and percentage of regulatory T cells (Treg). * $p < 0.05$, ** $p < 0.01$.

2.2. Monocyte Isolation

To isolate monocytes from RRMS patients, peripheral mononuclear cells (PBMC) from 40 mL whole blood samples were obtained by ficoll-hypaque gradient (Rafer, Zaragoza, Spain) and positive selection of CD14⁺ cells was performed using the EasySep uman CD14 Positive Selection kit (StemCell Technologies, Vancouver, BC, Canada) following the manufacturer's instructions. In the case of buffy coats, a depletion of T lymphocytes (CD3⁺ cells) was performed incubating samples with RosetteSep Human CD3 Depletion Cocktail (StemCell Technologies) before ficoll-hypaque gradient separation due to the high number of cells present in the buffy coat samples.

Samples were incubated with 7-amino-actinomycin D (7-AAD) (BD Biosciences, San José, CA, USA) and annexin V-PE (Immunotools, Friesoythe; Germany) for 20 min at 4 °C in darkness to analyze the viability of monocytes. In addition, perfect count microspheres (Cytognos S.L, Salamanca, Spain) were added to each sample and acquired in a flow cytometer (FACS Canto II, BD Biosciences) to determine the number of viable monocytes obtained.

2.3. The Generation of Vitamin D3-Tolerogenic Dendritic Cells

Monocytes were cultured for 6 days in X-VIVO 15 medium (Lonza, Basel, Switzerland) supplemented with 100 U/mL penicillin (Reig Jofre, Sant Joan Despi, Spain) and 100 µg/mL streptomycin (Normon, Tres Cantos, Spain) + 2 nM L-Glu (Sigma-Aldrich, St Louis, MI, USA) + 2% human AB serum, in the presence of 200 U/mL granulocyte-macrophage colony-stimulating factor (Peprotech, London, UK) and 250 U/mL interleukin 4 (Peprotech) for 6 days, as previously reported [27]. VitD3-tolDC and mDC were treated on day 4 with a maturation cocktail of cytokines containing 1000 U/mL tumor necrosis factor alpha

(Peprotech), 1000 U/mL IL-1 β (Peprotech) and 1 μ M prostaglandin E2 (Pfizer, New York, NY, USA). While mDC did not receive any additional stimuli, VitD3-tolDC were obtained by adding 1 nM vitamin D3 (Calcijex, Abbott, Chicago, IL, USA) on days 0 and 4. On day 6, cells were harvested after 30 min of incubation with accutase (Invitrogen, San Diego, CA, USA) and washed twice. Cell viability and count were determined by flow cytometry (as mentioned above). Functional and phenotypical characterizations were performed as previously reported [27]. Briefly, to determine the stimulatory capacity of DC, either 5000 immature DC (iDC), mature DC (mDC), or VitD3-tolDC, were incubated in X-VIVO 15 medium with 1×10^5 allogeneic PBMC. Six replicated wells of each condition were performed. Allogeneic proliferative assays were performed for 5 days at 37 °C in a 5% CO₂ atmosphere. During the last 18 h, 1 μ Ci of [3H]-methylthymidine (PerkinElmer, Waltham, MA, USA) was added to each well. Cells were harvested onto glass fiber filters, and [3H]-methylthymidine incorporation was measured in a β -scintillation counter (Trilux, Wallac, Ramsey, MN, USA).

2.4. Allogeneic Proliferative Response

PBMC were isolated from whole blood by ficoll-density gradient centrifugation. Cell viability and counts were performed following the protocol described above.

MDDC were harvested on day 6 of differentiation and co-cultured with allogenic PBMC (2×10^5 PBMC co-cultured with 5×10^3 MDDC) for 5 days in supplemented X-VIVO 15 medium, in the presence or absence of 10 IU/mL IFN- β 1a (Rebif[®], Merck Serono Darmstadt, Germany).

PBMC were co-cultured with different percentages of VitD3-tolDC: (a) 5.10^3 VitD3-tolDC (100% VitD3-tolDC) condition; (b) $3,75.10^3$ VitD3-tolDC and $1,25.10^3$ mDC (75% VitD3-tolDC) condition; (c) $2,5.10^3$ VitD3-tolDC and $2,5.10^3$ mDC (50% VitD3-tolDC) condition; and (d) $1,25.10^3$ VitD3-tolDC and $3,75.10^3$ mDC (25% VitD3-tolDC) condition, in the presence/absence of 10 IU/mL of IFN- β . After 5 days of culture, proliferation of PBMC was analyzed by [3H]-methyl-thymidine incorporation. The values of PBMC co-cultured with 5.10^3 mDC were used as positive control.

2.5. Phenotype

2.5.1. The Phenotype of Monocyte-Derived Dendritic Cells

Cells from each culture condition were incubated with monoclonal antibodies for 20 min at room temperature in the dark. The following monoclonal antibodies were used: CD11c PE-Cy7, CD14 V450, CD83 APC, CD86 FITC and HLA-DR V500 (BD Bioscience). At least 10,000 CD11c+ cells of each condition were acquired on a FACS Canto II flow cytometer (BD Biosciences).

2.5.2. The Phenotype of Peripheral Blood Mononuclear Cells

After 5 days of culture, PBMC co-cultured with mature DC (mDC), VitD3-tolDC (100% VitD3-tolDC) and 50% VitD3-tolDC (50% VitD3-tolDC + 50% mDC) in the presence and absence of IFN- β were harvested and stained using CD3-V450, CD4-PerCP-Cy5.5, CD45RA PE-Cy7, CCR7 PE, CD38 APC, CD8 APC-H7, HLA-DR V500 (BD Bioscience), CD183 AF488, CD196 BV605 and CD45 AF700 (Biolegend, San Diego, CA, USA) for T cell analysis; and CD4 PerCP-Cy5.5, CD25 PE, CCR4 PE-Cy7, CD127 AF647, CD45RO APC-H7, CD3 V450, HLA-DR V500 (BD Biosciences) and CD45 AF700 (Biolegend) for Treg analysis. Monoclonal antibodies were incubated for 20 min at room temperature and protected from the light. Samples were washed and a total of 50,000 CD3+ events were acquired on an LSR Fortessa flow cytometer (BD Biosciences). Both panels were analyzed using FACSDiva software (BD Biosciences). The gating strategy used to analyze the desired T cell subpopulations was previously reported [28].

2.5.3. The Phenotype of Splenocytes from C57BL/6J Mice

The percentage of Treg from ex vivo splenocytes was analyzed following the manufacturer's instructions. Briefly, 5×10^5 splenocytes were stained with anti-CD3, CD4, CD25 and intracellular FoxP3 (all from BD Pharmingen, San Diego, CA, USA), and analyzed in a FACS Canto II and FACS Diva software (BD Biosciences).

2.6. Animals

Female C57BL/6J mice, 8–10 weeks old, were purchased from Envigo Rms Spain SL (Sant Feliu de Codines, Barcelona, Spain) and housed at the Comparative Medicine and Bioimage Centre of Catalonia (CMCiB) under standard light- and climate-controlled conditions, with standard chow diet and water provided ad libitum.

2.7. Bone Marrow-Derived Dendritic Cells Generation

BMDC were generated following the protocol previously described by Mansilla et al. in 2015 and 2016 [24,25]. Briefly, progenitor bone marrow cells were obtained from C57BL/6 donor mice and cultured in RPMI medium containing 1000 IU/mL of murine GM-CSF (Peprotech). VitD3-tolDC were generated by adding 1 nM $1\alpha, 25$ -dihydroxyvitamin D3 (Kern Pharma, Terrassa, Spain) for 8 days. On day 7, 0.1 mg/mL lipopolysaccharide (LPS; Sigma-Aldrich) was added to the culture medium of mDC and VitD3-tolDC. After 22–24 h of LPS stimulation, DC were pulsed with 10 μ M the peptide 35-55 of myelin oligodendrocyte glycoprotein (MOG₃₅₋₅₅) for 18 h. Finally, VitD3-tolDC-MOG were cryopreserved in aliquots of 10^7 cells and stored in liquid nitrogen until use.

VitD3-tolDC were characterized by analyzing their phenotype (the reduction in the expression of the co-stimulatory molecules CD80 and CD40; as well as MHC II) and functionality (suppression of T cell proliferation in co-cultures of DC with allogeneic splenocytes) to ensure their correct production.

2.8. Induction of EAE and Clinical Follow-Up

For EAE induction, mice were anesthetized with ketamine/xylazine at 50 and 5 mg/kg body weight, respectively, and then immunized subcutaneously with 100 μ g of MOG₃₅₋₅₅ (YRSPFSRVVHLYRNGK) (Immunostep, Salamanca, Spain), emulsified in an equal volume (1:1) of Freund's complete adjuvant containing 4 mg/mL of *Mycobacterium tuberculosis* (strain H37RA, Difco, Detroit, MI, USA). In addition, 250 ng of pertussis toxin (Sigma Chemical, St. Louis, MO, USA) was injected intravenously (iv) at day 0 and 2. All animals were weighed and examined daily for welfare and clinical signs. Clinical evaluation was performed in a blinded manner by two different observers according to the following criteria: 0, asymptomatic; 0.5, loss of distal half of tail tone; 1, loss of entire tail tone; 1.5, hind limb weakness; 2, hind limb paralysis; 2.5, hind limb paraplegia; 3, forelimb weakness; 4, quadriparesis; 4.5, severe quadriparesis; 5, quadriplegia; and 6, death. Endpoint criteria were established to minimize suffering and ensure animal welfare.

2.9. In Vivo Treatment of EAE Mice

C57BL/6-EAE induced mice were treated daily from day 10 to 17 post-immunization (pi) with IFN-beta (5000 IU of IFN-beta1a, subcutaneous, sc) and/or on day 13, 17 and 21pi with VitD3-tolDC-MOG (1×10^6 cells, iv) ($n = 7$ mice/group) and monitored for 34 days. The vehicle group received 200 μ L of both sc and iv administration of PBS.

2.10. Antigen-Specific T Cell Reactivity and Cytokine Secretion

Mice were euthanized on day 34 pi, and splenocytes from the vehicle (PBS), VitD3-tolDC-MOG, IFN-beta, or VitD3-tolDC-MOG+ IFN-beta groups were cultured in a 96-well plate at 2×10^5 cells/well in 200 μ L of supplemented RPMI containing 5 μ M MOG₃₅₋₅₅, 5 μ M of phytohemagglutinin (PHA) (Sigma-Aldrich) (positive control) or culture medium (negative control). After 48 h of culture, 50 μ L of supernatant of each well was collected and stored for cytokine release detection, and 1 μ Ci/well of [³H]-thymidine (PerkinElmer)

was added for the last 18 h of culture. The stimulation index (SI) for each stimulus was calculated as the mean counts per minute (cpm) of antigen-stimulated cultures divided by the mean cpm of the non-stimulated cultures.

The secretion of IL-2, IL-4, IL-6, IFN- γ , TNF- α , IL-17, and IL-10 cytokines were quantified in the culture supernatants using the BD cytometric bead array mouse Th1/Th2/Th17 cytokine kit (BD Biosciences) and an LRS Fortessa cytometer (BD Biosciences) according to the manufacturer's instructions.

2.11. Statistical Analysis

Statistical analyses were performed using GraphPad Prism version 6.0 for Windows (La Jolla, CA, USA). Parametric and nonparametric tests were used depending on the normality distribution of the variables. To compare data from two groups, Mann–Whitney U or t tests were applied. When more than two groups were compared, non-parametric one-way ANOVA (Kruskal–Wallis) followed by Dunnett's multiple comparisons tests were applied. Differences were considered statistically significant when $p < 0.05$. Data were expressed as the mean \pm standard deviation (SD) values unless otherwise stated.

3. Results

3.1. The Combination of VitD3-tolDC and IFN-Beta Treatment Enhances the Suppressive Ability of VitD3-tolDC and IFN-Beta Monotherapies

First, the optimal concentration of IFN-beta to evaluate the anti-proliferative property of this cytokine on peripheral PBMC cultures was analyzed. To do so, 0.2×10^6 PBMC stimulated to proliferate with mitogens (25 ng/mL PMA+ 250 ng/mL Ionomycin), were cultured in presence of 10 or 100 IU/mL of IFN-beta. After 5 days of culture, the inhibition of proliferation was measured compared to the reference condition (PBMC stimulated with mitogens without IFN-beta treatment). Our results showed a suppression of $29.39 \pm 13.58\%$ (10 IU/mL of IFN-beta) and of $18.60 \pm 9.67\%$ (100 IU/mL of IFN-beta) ($n = 3$ for each condition). Based on these results, a concentration of 10 IU/mL of IFN-beta was selected to evaluate the IFN-beta effect on the immune function.

The ability of VitD3-tolDC to suppress allogeneic PBMC proliferation was evaluated for VitD3-tolDC generated from RRMS patients and HD ($n = 6$ for each group). VitD3-tolDC induced a suppression of allogeneic proliferation of $54.73 \pm 9.90\%$ in PBMC of RRMS patients and of $56.14 \pm 18.43\%$ in PBMC of HD in relation to the reference control mDC. On the other side, no statistical differences were observed in the suppressive capability among VitD3-tolDC generated from RRMS patients and HD (Table 1).

Table 1. Percentage of inhibition of allogeneic proliferation in relapsing-remitting multiple sclerosis (RRMS) patients and healthy donors (HD) depending on the treatment.

Condition	RRMS Patients ($n = 6$)		HD ($n = 6$)		p -Value
	Mean (%)	SD	Mean (%)	SD	
100%VitD3-tolDC	54.73	9.90	56.14	18.43	0.87
100%VitD3-tolDC + IFN-beta	64.87	8.28	61.14	16.17	0.62
75%VitD3-tolDC: 25%mDC	42.63	23.95	49.29	8.81	0.51
75%VitD3-tolDC: 25%mDC + IFN-beta	57.05	20.09	65.29	12.97	0.39
50%VitD3-tolDC: mDC	21.00	16.00	36.29	10.44	0.14
50%VitD3-tolDC: mDC + IFN-beta	25.00	19.00	45.71	19.54	0.16
25%VitD3-tolDC: 75%mDC	12.00	17.00	19.23	13.99	0.25
25%VitD3-tolDC: 75%mDC + IFN-beta	28.00	6.78	40.86	13.83	0.10

IFN-beta = interferon-beta; Mdc = mature dendritic cells; VitD3-tolDC = vitamin-D3 tolerogenic dendritic cells.

Then, PBMC were co-cultured with different percentages of VitD3-tolDC, as specified in Methods (Section 2.4), in the presence/absence of 10 IU/mL of IFN-beta. The percentage of inhibition of allogeneic proliferation, in relation to the reference control (mDC) was analyzed. Results obtained show a dose dependent suppressive effect of VitD3-tolDC. Addition of 10 IU/mL IFN-beta increased the suppressive effect of VitD3-tolDC (Figure 2 and Table 1).

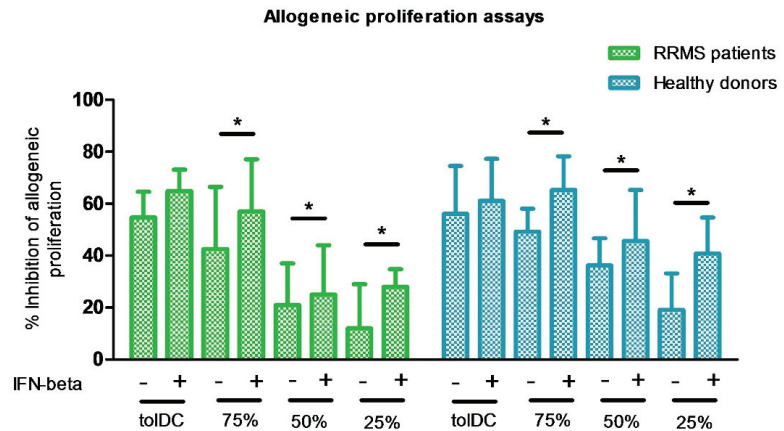


Figure 2. Dose-dependent reduction of allogeneic proliferation of PBMC, cultured with different percentages of VitD3-tolDC in presence/absence of IFN-beta. Suppressive ability of VitD3-tolDC on allogeneic PBMC from RRMS patients (green) and HD (blue) is represented as the percentage of proliferation compared to mature DC (mDC) stimulus. Different percentages of VitD3-tolDC and mDC are represented: 100% (100% VitD3-tolDC), 75% (75% VitD3-tolDC + 25% mDC), 50% (50% VitD3-tolDC + 50% mDC) and 25% (25% VitD3-tolDC + 75% mDC) in presence/absence of IFN-beta. Error bars correspond to SEM; * $p < 0.05$.

3.2. Treatment with VitD3-tolDC Reduces the Activation of T Lymphocytes from RRMS Patients

To further investigate the *in vitro* effect of VitD3-tolDC and IFN-beta combined therapy on lymphocytes, the phenotype of PBMC co-cultured for 5 days with two concentrations of VitD3-tolDC (100% VitD3-tolDC and 50% VitD3-tolDC) in the presence/absence of IFN-beta was determined and compared to the reference condition (mDC). As shown in Figure 3, the presence of 100% VitD3-tolDC in PBMC cultures, reduced the percentage of activated CD4+ and CD8+ T cells (HLA-DR+ CD38+ T lymphocytes) in both, RRMS patients and HD, compared to the reference condition (mDC) ($p < 0.05$), except for activated CD4+ T cells from HD ($p = 0.050$) ($n = 6$ for each group) (Table 2). However, no differences in phenotype were observed with the addition of IFN-beta to PBMC cultures in any of the culture conditions, except for activated CD8+ T cell in HD (Figure 3 and Table 2).

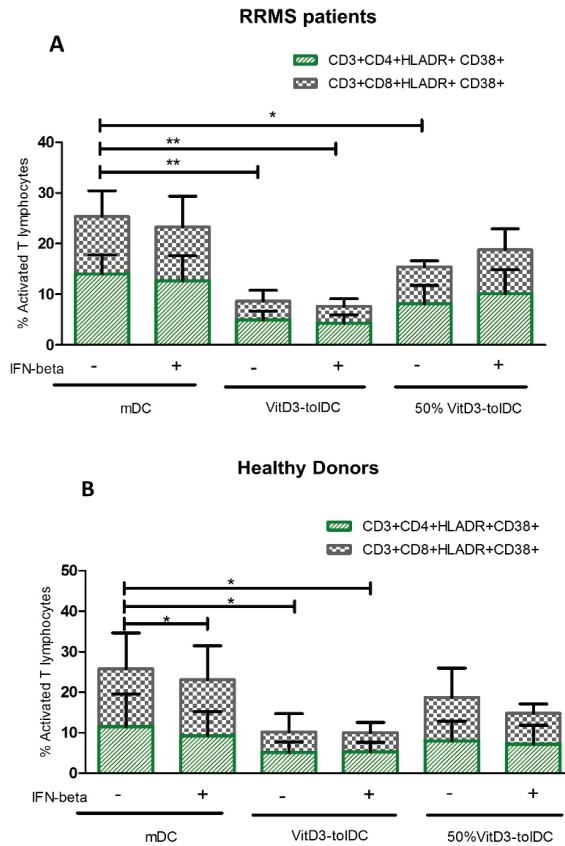


Figure 3. VitD3-tolDC reduce the activation of T lymphocytes in RRMS patients and HD. The percentage of activated CD4 + lymphocytes (CD3+CD4+HLA-DR+CD38+) (green) and CD8+ lymphocytes (CD3+CD8+HLA-DR+CD38+) (gray) in co-cultures of PBMC with mature DC (mDC), (100% VitD3-tolDC) or (50%VitD3-tolDC), in presence/absence of IFN-beta was analyzed in relapsing-remitting multiple sclerosis (RRMS) patients (A) and healthy donors (HD) (B) (n = 6 each group). Data represent the relative percentage of each lymphocyte subpopulation in relation to total percentages of CD4+ or CD8+ T cells. Error bars correspond to SEM; * p < 0.05, ** p < 0.01.

Table 2. Percentage of activated CD4+ and CD8+ T cells depending on the therapy.

Condition	RRMS n = 6			HD n = 6		p-Value	
	Mean (%)	SD	p-Value	Mean (%)	SD		
CD4 Activated lymphocytes **	mDC	14.03	3.73	-	11.50	8.11	-
	mDC + IFN-beta	12.68	4.92	0.604	9.28	5.95	0.514
	100%VitD3-tolDC	4.95	1.71	0.003	5.16	2.60	0.050
	100%VitD3-tolDC + IFN-beta	4.27	1.68	0.003	5.25	2.42	0.060
	50% VitD3-tolDC	8.13	3.58	0.020	8.01	4.85	0.310
CD8 Activated lymphocytes *	50% VitD3-tolDC + IFN-beta	10.10	4.77	0.150	7.21	4.63	0.210
	mDC	11.33	5.11	-	14.33	8.82	-
	mDC + IFN-beta	10.60	6.07	0.825	13.83	8.37	0.028
	100%VitD3-tolDC	3.72	2.12	0.007	5.07	4.50	0.040
	100%VitD3-tolDC + IFN-beta	3.33	1.56	0.004	4.75	2.55	0.020
50% VitD3-tolDC	7.28	1.21	0.087	10.70	7.27	0.450	
50% VitD3-tolDC + IFN-beta	8.70	4.11	0.340	7.62	2.26	0.100	

CD4 Activated lymphocytes = CD4+HLA-DR+ CD38+ T lymphocytes; CD8 activated lymphocytes = CD8+HLA-DR+ CD38+ T lymphocytes. HD: healthy donors; IFN-beta: interferon-beta; mDC: mature dendritic cells; RRMS: relapsing-remitting multiple sclerosis; SD: standard deviation; VitD3-tolDC: vitamin D3 tolerogenic dendritic cells. Statistically significant p values are marked in bold. * p < 0.05, ** p < 0.01.

No statistical differences were found in the analysis of the maturation stages (naïve, central memory, effector memory and effector compartments) of either CD4+ or CD8+ T cells (Supplementary Table S2) in the different culture conditions analyzed.

3.3. VitD3-tolDC+IFN-Beta Culture Induces the Differentiation of Th2 Lymphocytes

The effect of VitD3-tolDC in presence/absence of IFN-beta on different functional stages of lymphocytes was studied. Percentages of Th1 (CD3+ CD4+ CXCR3+ CCR6-), Th2 (CD3+ CD4+ CXCR3- CCR6-), Th17 (CD3+ CD4+ CXCR3- CCR6+) and Treg (CD4+ CD25+ CCR4+ CD45RO+) cells were analyzed in PBMC cultures from RRMS patients and HD, after 5 days of co-culture. A representative experiment is shown in Figure 4.

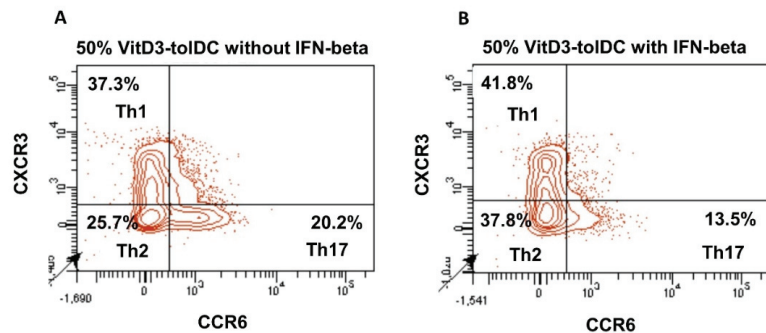


Figure 4. Immunomodulatory effect of VitD3-tolDC with/without IFN-beta on T lymphocytes. Representative example of changes in the relative percentages of Th1, Th2 and Th17 lymphocytes in relation to total CD4+ T lymphocytes, after 5 days co-culture of 50% VitD3-tolDC in absence (A) or presence (B) of IFN-beta.

As shown in Figure 5, we observed a significant increase in the percentage of Th2 lymphocytes when PBMC were co-cultured with 100%VitD3-tolDC+IFN-beta or 50%VitD3-tolDC+IFN-beta, compared to the reference condition (mDC) ($p < 0.05$), either in RRMS patients (Figure 5A) or HD (Figure 5B). In contrast, no significant differences were found when PBMC were co-cultured only with 100%VitD3-tolDC or 50%VitD3-tolDC (without IFN-beta) compared to mDC, either in RRMS patients or HD (Figure 5 and Supplementary Table S2).

When analyzing Th17 cells in RRMS patients, we only observed a significant reduction in this subpopulation when IFN-beta was added to PBMC co-cultured with 100%VitD3-tolDC ($p < 0.05$) (Figure 5A and Supplementary Table S2). In contrast, in HD, this decrease in Th17 cells was only significant when IFN-beta was added to PBMC co-cultured with mDC or 50%VitD3-tolDC ($p < 0.05$) (Figure 5B and Supplementary Table S2).

No differences in the percentage of Th1 and Treg were found in any of the different culture conditions analyzed (Supplementary Table S2).

3.4. Antigen-Specific VitD3-tolDC Administration in Combination with IFN-Beta Treatment Improves EAE Clinical Signs

To investigate the *in vivo* efficacy of the administration of antigen-specific VitD3-tolDC in combination with IFN-beta treatment, VitD3-induced tolerogenic bone marrow DC loaded with the peptide 35-55 of myelin oligodendrocyte glycoprotein (MOG₃₅₋₅₅) were generated VitD3-tolDC-MOG and administrated to mice with clinical signs of EAE under IFN-beta treatment. The clinical follow-up of mice receiving the combined therapy was compared to mice treated only with VitD3-tolDC-MOG, IFN-beta or vehicle (PBS). As shown in Figure 6A, while the treatment with IFN-beta did not significantly improve the disease severity of EAE mice compared to the vehicle group (mean clinical score at day 34 pi: 3.29 ± 0.49 for IFN-beta group and 3.71 ± 1.60 for PBS treated mice), the

administration of antigen-specific VitD3-tolDC-MOG, both alone or in combination with IFN-beta treatment, caused an important reduction in the severity of the disease (mean clinical score at day 34 pi: 2.79 ± 0.81 for the VitD3-tolDC-MOG group and 2.29 ± 1.29 for the VitD3-tolDC-MOG+IFN-beta treated mice; $p < 0.001$ for both groups). Indeed, the beneficial effect of VitD3-tolDC-MOG therapy was significantly higher when this cell therapy was administered in combination with IFN-beta than alone ($p < 0.05$) (Figure 6A).

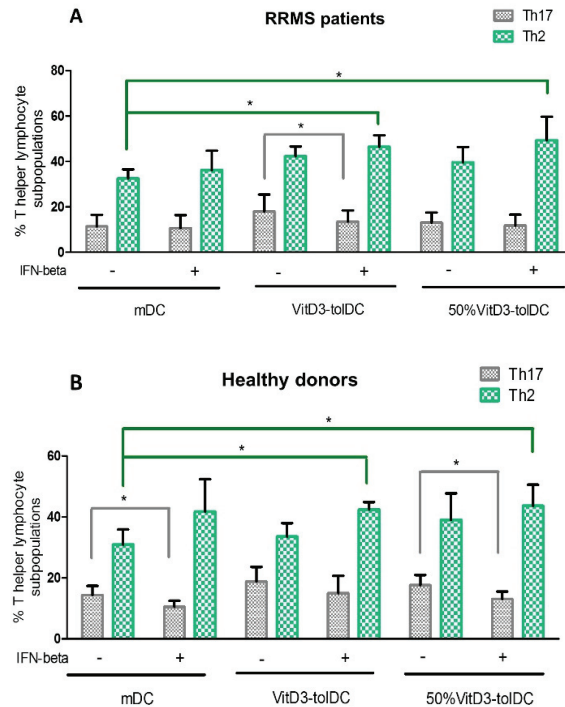


Figure 5. Effect of VitD3-tolDC in presence/absence of IFN-beta on the differentiation of Th2 and Th17 cells. Percentage of Th2 (CD3+ CD4+ CXCR3- CCR6-) lymphocytes (green) and Th17 (CD3+ CD4+ CXCR3- CCR6+) lymphocytes (gray) from (A) relapsing-remitting multiple sclerosis (RRMS) patients ($n = 6$) and (B) healthy donors (HD) ($n = 6$). The percentages of Th2 and Th17 lymphocyte subpopulations were analyzed on PBMC co-cultured with mature DC (mDC), 100%VitD3-tolDC or 50%VitD3-tolDC, in presence/absence of IFN-beta after 5 days of culture. Data represent the relative percentage of each lymphocyte subpopulation in relation to total CD4+ T cells. Error bars correspond to SEM; * $p < 0.05$.

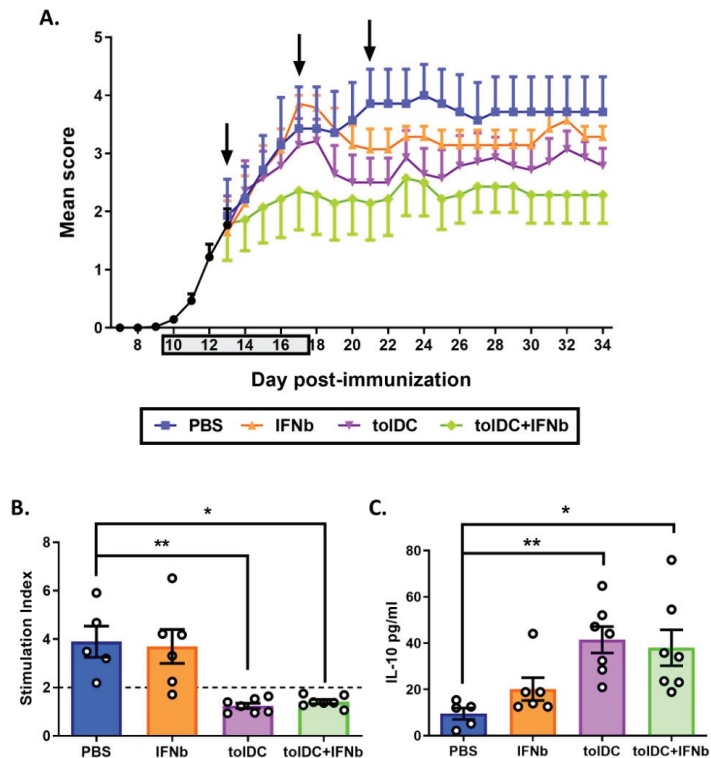


Figure 6. Combined therapy of antigen-specific VitD3-tolDC-MOG+IFN-beta ameliorates clinical signs of EAE. **(A)** Representation of daily mean clinical score of mice treated with vehicle (PBS) (blue), IFN-beta (IFNβ) [5000IU] (orange), VitD3-tolDC-MOG [1×10^6 cells] (tolDC) (violet) or VitD3-tolDC-MOG+IFN-beta (tolDC+IFNβ) (green) ($n = 7$ /group) for 34 days of follow-up. Gray square in the X axis and arrows indicate daily treatment period with IFN-beta (from day 10 to 17 post-immunization, pi) and VitD3-tolDC-MOG administration (days 13, 17 and 21 pi), respectively. **(B)** Analysis of antigen-specific T cell reactivity to MOC₃₅₋₅₅ in splenocytes from mice treated with vehicle (PBS), IFN-beta (IFNβ), VitD3-tolDC-MOG (tolDC) or VitD3-tolDC-MOG+IFN-beta (tolDC+IFNβ) on day 34 pi. **(C)** Level of IL-10 in the supernatant of re-stimulated splenocytes with MOC₃₅₋₅₅ antigen from each group of mice. Errors bars correspond to SEM. * $p < 0.05$, ** $p < 0.01$.

3.5. VitD3-tolDC-MOG Treatment Reduces Antigen-Specific T Cell Reactivity

Mice treated solely with VitD3-tolDC-MOG or with the combination of VitD3-tolDC-MOG+IFN-beta exhibited reduced antigen-specific T cell reactivity compared to both, vehicle and IFN-beta group ($p < 0.01$ and $p < 0.05$, respectively) (Figure 6B). In contrast, the administration of IFN-beta alone, did not decrease T cell proliferation against MOG (Figure 6B). Moreover, when cytokine secretion profile of splenocytes re-stimulated with MOC₃₅₋₅₅ antigen was analyzed, an increased IL-10 secretion was detected in the two groups of mice treated with VitD3-tolDC-MOG (VitD3-tolDC-MOG: $p < 0.01$ and VitD3-tolDC-MOG+IFN-beta: $p < 0.05$), but it was not enhanced by IFN-beta administration, neither in mice treated with IFN-beta vs. the vehicle group, nor mice receiving VitD3-tolDC-MOG+IFN-beta vs. the VitD3-tolDC-MOG group (Figure 6C). Regarding the ex vivo percentage of Treg in the spleen (in relation to total CD4⁺ splenocytes), no differences were found between any of the groups (data not shown).

4. Discussion

Despite the substantial advances in the understanding of MS pathology, none of the currently existing therapies are able to stop the course of the disease by inducing a long-term remission [18,29,30]. Nowadays, available treatments are based on a continuous dependence on nonspecific immunosuppressive or immunomodulatory drugs [31–41], exposing patients to potentially serious adverse effects, that may compromise their safety and adherence to therapy [42–46]. Fortunately, during the last decade, the increase in the knowledge of immune regulatory mechanisms has offered the possibility to claim antigen-specific CTT as a potential strategy to restore immune tolerance in patients with autoimmune diseases avoiding undesirable and potentially dangerous side effects [47–49].

Due to the complexity of MS pathology, a therapeutic approach based on a combination of treatments targeting different pathways involved in the induction and maintenance of tolerance may be required to fully control autoimmunity [50–54]. In this regard, several murine studies have demonstrated that administration of immunosuppressive drugs, such as dexamethasone or rapamycin, potentiate the regulatory effect of tolDC by prolonging allograft survival or by being beneficial in treating different autoimmune diseases [55–60]. In our approach, we evaluated the effect of combined VitD3-tolDC and IFN-beta treatment in the EAE model as well as using co-cultures of peripheral blood lymphocytes from MS patients. Our results showed that the combined therapy had an enhanced effect compared to each monotherapy in the above-mentioned models. Furthermore, we identified which lymphocyte subpopulations and functional subsets were specifically affected by VitD3-tolDC+IFN-beta treatment.

Here, the *in vitro* experiments using MS and HD samples showed that VitD3-tolDC induces a decrease in CD4+ and CD8+ T cells activation. These results are in accordance with our previous studies reporting a strong antigen-specific hypo-responsiveness mediated by a down-modulation of genes involved in cell cycle and pro-inflammatory immune response [27,60]. Moreover, we found a low level of antigen-specific T cell reactivity in splenocytes from EAE mice treated with VitD3-tolDC-MOG, both in the presence and absence of IFN-beta treatment. In this regard, and in agreement with our previous data [24], splenocytes from EAE mice treated with VitD3-tolDC-MOG exhibited inhibition of antigen-specific T cell reactivity and an increase of IL-10 secretion when re-stimulated with MOG₃₅₋₅₅ antigen. Consequently, *in vivo* results suggest that VitD3-tolDC are inducing a complex immunoregulation mediated by IL-10 that reduces T cell activation [25].

On the other hand, IFN-beta is a commonly used first-line treatment for RRMS patients, which exerts multiple immunomodulatory functions. It has been reported that IFN-beta treatment reduces Th1 and Th17 cells, the main players initiating and perpetuating the autoimmune attack in MS [61–63]. In this study, *in vitro* human studies with IFN-beta revealed a decrease in the percentage of Th17 cells, although it was not possible to detect changes in the percentage of Th1 lymphocytes after 5 days of co-culture. When VitD3-tolDC were combined with IFN-beta, *in vitro* results revealed that IFN-beta treatment contributes to the T cell hypo-responsiveness produced by VitD3-tolDC therapy, with the induction of an anti-inflammatory effect caused by a Th17 decrease, as well by an induction of Th2 lymphocytes.

In the EAE *in vivo* experiments, although the monotherapy with IFN-beta in mice with clinical signs of EAE was not sufficient to induce a significant reduction of EAE severity, when IFN-beta was combined with antigen-specific VitD3-tolDC-MOG, it was able to potentiate the beneficial effect of these therapeutic cells. Altogether, these results suggest that IFN-beta treatment triggers an anti-inflammatory effect that synergizes together with the tolerogenic functionality of VitD3-tolDC-MOG. As a result, the combined therapy resulted in a powerful clinical effect, significantly reducing EAE disease severity. In fact, in our aggressive EAE model, the efficacy of the combined treatment was so potent that it allowed mice to reach only hind limb paralysis, while mice not receiving treatment (PBS group) or mice treated with IFN-beta or VitD3-tolDC-MOG monotherapies, exhibited different grades of hind limb and forelimb motor alteration.

However, in spite of the presence of *in vitro* and *in vivo* evidence demonstrating that VitD3-tolDC are sufficient to decrease T cell proliferation and abrogate EAE disease progression [23,24], the translation of this CTT to the clinical context remains complex due to the chronic inflammatory context of the patients that may affect their functionality [9,18]. In this context and from the abovementioned results, we postulate that the unspecific anti-inflammatory effect of IFN-beta treatment, which has been used for a long time to treat non-aggressive RRMS, could enhance the antigen-specific efficacy of VitD3-tolDC contributing to restore the immune homeostasis.

Our study has focused on the clinical and immunological effect of the combined treatment of VitD3-tolDC with IFN-beta. However, no analysis on the influence of the combined therapy on demyelination was assessed. Future studies should determine if the combination therapy would also induce a decrease in demyelination, what would strongly support the relevance of the combined therapy as a long-term therapeutic strategy for MS patients. In this context, future studies should be addressed to analyze the mechanisms involved in the synergic effect of the combined therapies of VitD3-tolDC plus IFN-beta, as well as with other immunomodulatory or immunosuppressive treatments that have appeared in recent years in the multiple sclerosis arena.

Altogether, our results demonstrate that antigen-specific VitD3-tolDC is an effective therapy able to reduce autoreactive T cell activation. Moreover, the combination of VitD3-tolDC-MOG with IFN-beta treatment resulted in a stronger anti-inflammatory effect and an increased clinical beneficial effect in EAE, suggesting that a combined therapy of antigen-specific cells and immunomodulatory drugs may be a promising new strategy for the treatment of MS patients.

Supplementary Materials: The following are available online at <https://www.mdpi.com/article/10.3390/biomedicines9121758/s1>.

Author Contributions: Conceptualization: B.Q.-S., M.J.M. and E.M.-C.; Formal analysis: B.Q.-S. and M.J.M.; Investigation: B.Q.-S. and J.N.-B. performed the cell cultures and B.Q.-S. and M.J.M. developed the mouse experimental model experiments, and S.P.-R. and C.R.-T. recruited patients; Methodology: B.Q.-S., M.J.M. and E.M.-C.; Supervision: E.M.-C. and C.R.-T.; Writing—original draft, B.Q.-S. and M.J.M.; Writing—review and editing, B.Q.-S., M.J.M., F.F., A.T.-S., J.N.-B., S.P.-R., C.R.-T. and E.M.-C. All authors have read and agreed to the published version of the manuscript.

Funding: This work has received funding from the European Union’s Horizon 2020 research and Innovation programme under grant agreement n° 779316 (ReStoRe) and has been feasible thanks to the resources provided by projects PI16/01737, PI17/01521 and PI20/01313 integrated in the Plan Nacional de I+D+I and co-supported by the ISCIII-Subdirección General de Evaluación and the Fondo Europeo de Desarrollo Regional (FEDER); and by a grant from Fundación Salud 2000 (Madrid, España). M.J.M. is beneficiary of a Sara Borrell contract from the ISCIII and the FEDER (CD19/00209). F.F. holds a PhD fellowship from the INsTRuCT Consortium focused on developing innovative myeloid regulatory cell (MRC)-based immunotherapies, which receive an Innovative Training Network subsidy from the European Union Horizon 2020 Programme.

Institutional Review Board Statement: This study was reviewed and approved by the Germans Trias i Pujol Hospital Ethical Committee. Animal experiments were carried out in strict accordance with EU and governmental regulations (Generalitat de Catalunya, Decret 214/97 30th July). The Ethics Committee on Animal Experimentation of the “Germans Trias i Pujol” Research Institute approved all procedures described in this study (protocol number: 9469).

Informed Consent Statement: The participants provided their written informed consent to participate in this study.

Acknowledgments: We want to thank Marco A. Fernández-Sanmartín from the IGTP Flow Cytometry Platform his support. We acknowledge all patients who participated in this study for their collaboration, and the nurses from the Multiple Sclerosis Unit from the Germans Trias i Pujol Hospital for their nursing care. We also thank Susi Soler for technical assistance.

Conflicts of Interest: The authors declare no conflict of interest.

References

- Theofilopoulos, A.N.; Kono, D.H.; Baccala, R. The multiple pathways to autoimmunity. *Nat. Immunol.* **2017**, *18*, 716–724. [CrossRef] [PubMed]
- Mansilla, M.J.; Presas-Rodríguez, S.; Teniente-Serra, A.; González-Larreategui, I.; Quirant-Sánchez, B.; Fondelli, F.; Djedovic, N.; Iwaszkiewicz-Grześ, D.; Chwojncki, K.; Miljković, Đ.; et al. Paving the way towards an effective treatment for multiple sclerosis: Advances in cell therapy. *Cell. Mol. Immunol.* **2021**, *18*, 1353–1374. [CrossRef]
- Goverman, J. Autoimmune T cell responses in the central nervous system. *Nat. Rev. Immunol.* **2009**, *9*, 393–407. [CrossRef]
- Machado-Santos, J.; Saji, E.; Tröschner, A.; Paunovic, M.; Liblau, R.; Gabriely, G.; Bien, C.G.; Bauer, J.; Lassmann, H. The compartmentalized inflammatory response in the multiple sclerosis brain is composed of tissue-resident CD8+ T lymphocytes and B cells. *Brain* **2018**, *141*, 2066–2082. [CrossRef]
- Xie, Z.-X.; Zhang, H.; Wu, X.-J.; Zhu, J.; Ma, D.-H.; Jin, T. Role of the Immunogenic and Tolerogenic Subsets of Dendritic Cells in Multiple Sclerosis. *Mediat. Inflamm.* **2015**, *2015*, 1–20. [CrossRef] [PubMed]
- Carlström, K.E.; Ewing, E.; Granqvist, M.; Gyllenberg, A.; Aeinehband, S.; Enoksson, S.L.; Checa, A.; Badam, T.V.S.; Huang, J.; Gomez-Cabrero, D.; et al. Therapeutic efficacy of dimethyl fumarate in relapsing-remitting multiple sclerosis associates with ROS pathway in monocytes. *Nat. Commun.* **2019**, *10*, 3081. [CrossRef]
- Nuyts, A.; Lee, W.; Bashir-Dar, R.; Berneman, Z.; Cools, N. Dendritic cells in multiple sclerosis: Key players in the immunopathogenesis, key players for new cellular immunotherapies? *Mult. Scler. J.* **2013**, *19*, 995–1002. [CrossRef]
- Mbongue, J.; Nicholas, D.; Firek, A.; Langridge, W. The Role of Dendritic Cells in Tissue-Specific Autoimmunity. *J. Immunol. Res.* **2014**, *2014*, 857143. [CrossRef]
- Morante-Palacios, O.; Fondelli, F.; Ballestar, E.; Martínez-Cáceres, E.M. Tolerogenic Dendritic Cells in Autoimmunity and Inflammatory Diseases. *Trends Immunol.* **2021**, *42*, 59–75. [CrossRef] [PubMed]
- Axtell, R.C.; Raman, C.; Steinman, L. Type I interferons: Beneficial in Th1 and detrimental in Th17 autoimmunity. *Clin. Rev. Allergy Immunol.* **2013**, *44*, 114–120. [CrossRef] [PubMed]
- Hirovani, M.; Niino, M.; Fukazawa, T.; Yaguchi, H.; Nakamura, M.; Kikuchi, S.; Sasaki, H. Decreased interferon- α production in response to CpG DNA dysregulates cytokine responses in patients with multiple sclerosis. *Clin. Immunol.* **2012**, *143*, 145–151. [CrossRef]
- Kim, M.J.; Lim, J.Y.; Park, S.A.; Park, S.I.; Kim, W.S.; Ryu, C.H.; Jeun, S.S. Effective combination of methylprednisolone and interferon β -secreting mesenchymal stem cells in a model of multiple sclerosis. *J. Neuroimmunol.* **2018**, *314*, 81–88. [CrossRef] [PubMed]
- González, L.F.; Acuña, E.; Arellano, G.; Morales, P.; Sotomayor, P.; Oyarzun-Ampuero, F.; Naves, R. Intranasal delivery of interferon- β -loaded nanoparticles induces control of neuroinflammation in a preclinical model of multiple sclerosis: A promising simple, effective, non-invasive, and low-cost therapy. *J. Control. Release* **2021**, *331*, 443–459. [CrossRef]
- Ten Brinke, A.; Hilkens, C.M.; Cools, N.; Geissler, E.K.; Hutchinson, J.A.; Lombardi, G.; Lord, P.; Sawitzki, B.; Trzonkowski, P.; Van Ham, S.M.; et al. Clinical Use of Tolerogenic Dendritic Cells-Harmonization Approach in European Collaborative Effort. *Mediat. Inflamm.* **2015**, *2015*, 471719. [CrossRef] [PubMed]
- Phillips, B.E.; Garciafigueroa, Y.; Engman, C.; Trucco, M.; Giannoukakis, N. Tolerogenic Dendritic Cells and T-Regulatory Cells at the Clinical Trials Crossroad for the Treatment of Autoimmune Disease; Emphasis on Type 1 Diabetes Therapy. *Front. Immunol.* **2019**, *10*, 148. [CrossRef] [PubMed]
- Bell, G.M.; Anderson, A.E.; Diboll, J.; Reece, R.; Eltherington, O.; Harry, R.A.; Fouweather, T.; MacDonald, C.; Chadwick, T.; McColl, E.; et al. Autologous tolerogenic dendritic cells for rheumatoid and inflammatory arthritis. *Ann. Rheum. Dis.* **2017**, *76*, 227–234. [CrossRef] [PubMed]
- Fousteri, G.; Jofra, T.; Di Fonte, R. Combination of an Antigen-Specific Therapy and an Immunomodulatory Treatment to Simultaneous Block Recurrent Autoimmunity and Alloreactivity in Non-Obese Diabetic Mice. *PLoS ONE* **2015**, *10*, e0127631. [CrossRef]
- Northrup, L.; Christopher, M.A.; Sullivan, B.P.; Berkland, C. Combining antigen and immunomodulators: Emerging trends in antigen-specific immunotherapy for autoimmunity. *Adv. Drug Deliv. Rev.* **2016**, *98*, 86–98. [CrossRef]
- Flórez-Grau, G.; Zubizarreta, I.; Cabezón, R.; Villoslada, P.; Benitez-Ribas, D. Tolerogenic Dendritic Cells as a Promising Antigen-Specific Therapy in the Treatment of Multiple Sclerosis and Neuromyelitis Optica from Preclinical to Clinical Trials. *Front. Immunol.* **2018**, *31*, 1169. [CrossRef]
- Torkildsen, Ø.; Myhr, K.M.; Bø, L. Disease-modifying treatments for multiple sclerosis—a review of approved medications. *Eur. J. Neurol.* **2016**, *23*, 18–27. [CrossRef]
- Pardo, G.; Jones, D.E. The sequence of disease-modifying therapies in relapsing multiple sclerosis: Safety and immunologic considerations. *J. Neurol.* **2017**, *264*, 2351–2374. [CrossRef]
- Willekens, B.L.; Presas-Rodríguez, S.; Mansilla, M.J.; Derdelinckx, J.; Lee, W.-P.; Nijs, G.; De Laere, M.; Wens, I.; Cras, P.; Parizel, P.; et al. Tolerogenic dendritic cell-based treatment for multiple sclerosis (MS): A harmonised study protocol for two phase I clinical trials comparing intradermal and intranodal cell administration. *BMJ Open* **2019**, *9*, e030309. [CrossRef]
- Derdelinckx, J.; Mansilla, M.J.; De Laere, M.; Lee, W.P.; Navarro-Barriuso, J.; Wens, I.; Nkansah, I.; Daans, J.; De Reu, H.; Jolanta Keliris, A.; et al. Clinical and immunological control of experimental autoimmune encephalomyelitis by tolerogenic dendritic cells loaded with MOG-encoding mRNA. *J. Neuroinflamm.* **2019**, *16*, 167. [CrossRef] [PubMed]

24. Mansilla, M.J.; Sellès-Moreno, C.; Fàbregas-Puig, S. Beneficial Effect of Tolerogenic Dendritic Cells Pulsed with MOG Autoantigen in Experimental Autoimmune Encephalomyelitis. *CNS Neurosci. Ther.* **2015**, *21*, 222–230. [CrossRef]
25. Mansilla, M.J.; Contreras-Cardone, R.; Navarro-Barriuso, J. Cryopreserved vitamin D3-tolerogenic dendritic cells pulsed with autoantigens as a potential therapy for multiple sclerosis patients. *J. Neuroinflamm.* **2016**, *13*, 113. [CrossRef] [PubMed]
26. Ten Brinke, A.; Martínez-Llordella, M.; Cools, N. Ways Forward for Tolerance-Inducing Cellular Therapies- an FAACCT Perspective. *Front. Immunol.* **2019**, *10*, 181. [CrossRef]
27. Navarro-Barriuso, J.; Mansilla, M.J.; Quirant-Sánchez, B.; Ardiaca-Martínez, A.; Teniente-Serra, A.; Presas-Rodríguez, S.; Ten Brinke, A.; Ramo-Tello, C.; Martínez-Cáceres, E.M. MAP7 and MUCL1 Are Biomarkers of Vitamin D3-Induced Tolerogenic Dendritic Cells in Multiple Sclerosis Patients. *Front. Immunol.* **2019**, *19*, 10. [CrossRef] [PubMed]
28. Quirant-Sánchez, B.; Hervás-García, J.V.; Teniente-Serra, A.; Brieva, L.; Moral-Torres, E.; Cano, A.; Munteis, E.; Mansilla, M.J.; Presas-Rodríguez, S.; Navarro-Barriuso, J.; et al. Predicting therapeutic response to fingolimod treatment in multiple sclerosis patients. *CNS Neurosci. Ther.* **2018**, *24*, 1175–1184. [CrossRef]
29. Apostolopoulos, V.; Matsoukas, J. Advances in Multiple Sclerosis Research-Series I. *Brain Sci.* **2020**, *10*, 795. [CrossRef] [PubMed]
30. Reich, D.S.; Lucchinetti, C.F.; Calabresi, P.A. Multiple Sclerosis. *N. Engl. J. Med.* **2018**, *378*, 169–180. [CrossRef]
31. Polman, C.H.; O'Connor, P.W.; Havrdova, E.; Hutchinson, M.; Kappos, L.; Miller, D.H.; Phillips, J.T.; Lublin, F.D.; Giovannoni, G.; Wajgt, A.; et al. A randomized, placebo-controlled trial of natalizumab for relapsing multiple sclerosis. *N. Engl. J. Med.* **2006**, *354*, 899–910. [CrossRef] [PubMed]
32. Hauser, S.L.; Waubant, E.; Arnold, D.L. B-cell depletion with rituximab in relapsing-remitting multiple sclerosis. *N. Engl. J. Med.* **2008**, *358*, 676–688. [CrossRef]
33. Giovannoni, G.; Comi, G.; Cook, S.; Rammohan, K.; Rieckmann, P.; Soelberg Sørensen, P.; Vermersch, P.; Chang, P.; Hamlett, A.; Musch, B.; et al. A placebo-controlled trial of oral cladribine for relapsing multiple sclerosis. *N. Engl. J. Med.* **2010**, *362*, 416–426. [CrossRef]
34. Kappos, L.; Radue, E.W.; O'Connor, P.; Polman, C.; Hohlfeld, R.; Calabresi, P.; Selmaj, K.; Agoropoulou, C.; Leyk, M.; Zhang-Auberson, L.; et al. A placebo-controlled trial of oral fingolimod in relapsing multiple sclerosis. *N. Engl. J. Med.* **2010**, *362*, 387–401. [CrossRef] [PubMed]
35. O'Connor, P.; Wolinsky, J.S.; Confavreux, C.; Comi, G.; Kappos, L.; Olsson, T.P.; Benzerdjeb, H.; Truffinet, P.; Wang, L.; Miller, A.; et al. Randomized trial of oral teriflunomide for relapsing multiple sclerosis. *N. Engl. J. Med.* **2011**, *365*, 1293–1303. [CrossRef] [PubMed]
36. Cohen, J.A.; Coles, A.J.; Arnold, D.L.; Confavreux, C.; Fox, E.J.; Hartung, H.P.; Havrdova, E.; Selmaj, K.W.; Weiner, H.L.; Fisher, E.; et al. Alemtuzumab versus interferon beta 1a as first-line treatment for patients with relapsing-remitting multiple sclerosis: A randomised controlled phase 3 trial. *Lancet* **2012**, *380*, 1819–1828. [CrossRef]
37. Calabresi, P.A.; Radue, E.W.; Goodin, D.; Jeffery, D.; Rammohan, K.W.; Reeder, A.T.; Vollmer, T.; Agius, M.A.; Kappos, L.; Stites, T.; et al. Safety and efficacy of fingolimod in patients with relapsing-remitting multiple sclerosis (FREEDOMS II): A double-blind, randomised, placebo-controlled, phase 3 trial. *Lancet Neurol.* **2014**, *13*, 545–556. [CrossRef]
38. Wang, Q.; Chuikov, S.; Taitano, S.; Wu, Q.; Rastogi, A.; Tuck, S.J.; Corey, J.M.; Lundy, S.K.; Mao-Draayer, Y. Dimethyl Fumarate Protects Neural Stem/Progenitor Cells and Neurons from Oxidative Damage through Nrf2-ERK1/2 MAPK Pathway. *Int. J. Mol. Sci.* **2015**, *16*, 13885–13907. [CrossRef]
39. Hauser, S.L.; Bar-Or, A.; Comi, G. Ocrelizumab versus interferon beta-1a in relapsing multiple sclerosis. *N. Engl. J. Med.* **2017**, *376*, 221–234. [CrossRef] [PubMed]
40. Mansilla, M.J.; Navarro-Barriuso, J.; Presas-Rodríguez, S.; Teniente-Serra, A.; Quirant-Sánchez, B.; Ramo-Tello, C.; Martínez-Cáceres, E.M. Optimal response to dimethyl fumarate is mediated by a reduction of Th1-like Th17 cells after 3 months of treatment. *CNS Neurosci. Ther.* **2019**, *25*, 995–1005. [CrossRef]
41. Hauser, S.L.; Cree, B.A.C. Treatment of Multiple Sclerosis: A Review. *Am. J. Med.* **2020**, *133*, 1380–1390.e2. [CrossRef]
42. Kolb-Mäurer, A.; Goebeler, M.; Mäurer, M. Cutaneous Adverse Events Associated with Interferon-β Treatment of Multiple Sclerosis. *Int. J. Mol. Sci.* **2015**, *16*, 14951–14960. [CrossRef]
43. Berger, J.R.; Cree, B.A.; Greenberg, B.; Hemmer, B.; Ward, B.J.; Dong, V.M.; Merschhemke, M. Progressive multifocal leukoencephalopathy after fingolimod treatment. *Neurology* **2018**, *90*, e1815–e1821. [CrossRef]
44. Mills, E.A.; Mao-Draayer, Y. Aging and lymphocyte changes by immunomodulatory therapies impact PML risk in multiple sclerosis patients. *Mult. Scler. J.* **2018**, *24*, 1014–1022. [CrossRef]
45. Ryerson, L.Z.; Foley, J.; Chang, I.; Kister, I.; Cutter, G.; Metzger, R.R.; Goldberg, J.D.; Li, X.; Riddle, E.; Smirnakis, K.; et al. Risk of natalizumab-associated PML in patients with MS is reduced with extended interval dosing. *Neurology* **2019**, *93*, e1452–e1462. [CrossRef]
46. Focosi, D.; Tuccori, M.; Maggi, F. Progressive multifocal leukoencephalopathy and anti-CD20 monoclonal antibodies: What do we know after 20 years of rituximab. *Rev. Med. Virol.* **2019**, *29*, e2077. [CrossRef]
47. Medaer, R.; Stinissen, P.; Truyen, L.; Raus, J.; Zhang, J. Depletion of myelin-basic-protein autoreactive T cells by T-cell vaccination: Pilot trial in multiple sclerosis. *Lancet* **1995**, *346*, 807–808. [CrossRef]
48. Hu, J.; Wan, Y. Tolerogenic dendritic cells and their potential applications. *Immunology* **2011**, *132*, 307–314. [CrossRef] [PubMed]

49. Lutterotti, A.; Yousef, S.; Sputtek, A.; Stürner, K.H.; Stellmann, J.P.; Breiden, P.; Reinhardt, S.; Schulze, C.; Bester, M.; Heesen, C.; et al. Antigen-specific tolerance by autologous myelin peptide-coupled cells: A phase 1 trial in multiple sclerosis. *Sci. Transl. Med.* **2013**, *5*, 188ra75. [CrossRef]
50. Calabresi, P.A.; Wilterdink, J.L.; Rogg, J.M.; Mills, P.; Webb, A.; Whartenby, K.A. An open-label trial of combination therapy with interferon beta-1a and oral methotrexate in MS. *Neurology* **2002**, *58*, 314–317. [CrossRef] [PubMed]
51. Pulicken, M.; Bash, C.N.; Costello, K.; Said, A.; Cuffari, C.; Wilterdink, J.L.; Rogg, J.M.; Mills, P.; Calabresi, P.A. Optimization of the safety and efficacy of interferon beta 1b and azathioprine combination therapy in multiple sclerosis. *Mult. Scler. J.* **2005**, *11*, 169–174. [CrossRef] [PubMed]
52. Jeffery, D.R.; Chepuri, N.; Durden, D.; Burdette, J. A pilot trial of combination therapy with mitoxantrone and interferon beta-1b using monthly gadolinium-enhanced magnetic resonance imaging. *Mult. Scler. J.* **2005**, *11*, 296–301. [CrossRef]
53. Rudick, R.A.; Stuart, W.H.; Calabresi, P.A.; Confavreux, C.; Galetta, S.L.; Radue, E.W.; Lublin, F.D.; Weinstock-Guttman, B.; Wynn, D.R.; Lynn, F.; et al. Natalizumab plus interferon beta-1a for relapsing multiple sclerosis. *N. Engl. J. Med.* **2006**, *354*, 911–923. [CrossRef] [PubMed]
54. Lublin, F.D.; Cofield, S.S.; Cutter, G.R.; Conwit, R.; Narayana, P.A.; Nelson, F.; Salter, A.R.; Gustafson, T.; Wolinsky, J.S.; CombiRx Investigators. Randomized study combining interferon and glatiramer acetate in multiple sclerosis. *Ann. Neurol.* **2013**, *73*, 327–340. [CrossRef]
55. Macedo, C.; Turquist, H.; Metes, D.; Thomson, A.W. Immunoregulatory properties of rapamycin-conditioned monocyte-derived dendritic cells and their role in transplantation. *Transplant. Res.* **2012**, *1*, 16. [CrossRef]
56. Suwandi, J.S.; Toes, R.E.; Nikolic, T.; Roep, B.O. Inducing tissue specific tolerance in autoimmune disease with tolerogenic dendritic cells. *Clin. Exp. Rheumatol.* **2015**, *33*, S97–S103.
57. Nguyen-Pham, T.N.; Jung, S.H.; Vo, M.C.; Thanh-Tran, H.T.; Lee, Y.K.; Lee, H.J.; Choi, N.R.; Hoang, M.D.; Kim, H.J.; Lee, J.J. Lenalidomide Synergistically Enhances the Effect of Dendritic Cell Vaccination in a Model of Murine Multiple Myeloma. *J. Immunother.* **2015**, *38*, 330–339. [CrossRef]
58. Zhou, Y.; Shan, J.; Guo, Y.; Li, S.; Long, D.; Li, Y.; Feng, L. Effects of Adoptive Transfer of Tolerogenic Dendritic Cells on Allograft Survival in Organ Transplantation Models: An Overview of Systematic Reviews. *J. Immunol. Res.* **2016**, *2016*, 5730674. [CrossRef]
59. Dáňová, K.; Grohová, A.; Strnadová, P.; Funda, D.P.; Šumník, Z.; Lebl, J.; Cinek, O.; Průhová, Š.; Koloušková, S.; Obermannová, B.; et al. Tolerogenic Dendritic Cells from Poorly Compensated Type 1 Diabetes Patients Have Decreased Ability To Induce Stable Antigen-Specific T Cell Hyporesponsiveness and Generation of Suppressive Regulatory T Cells. *J. Immunol.* **2017**, *198*, 729–740. [CrossRef]
60. Grau-López, L.; Granada, M.L.; Raich-Regué, D.; Naranjo-Gómez, M.; Borràs-Serres, F.E.; Martínez-Cáceres, E.; Ramo-Tello, C. Regulatory role of vitamin D in T-cell reactivity against myelin peptides in relapsing-remitting multiple sclerosis patients. *BMC Neurol.* **2012**, *12*, 103. [CrossRef] [PubMed]
61. Ramgolam, V.S.; Sha, Y.; Jin, J.; Zhang, X.; Markovic-Plese, S. IFN-beta inhibits human Th17 cell differentiation. *J. Immunol.* **2009**, *183*, 5418–5427. [CrossRef] [PubMed]
62. Trinschek, B.; Luessi, F.; Gross, C.C.; Wiendl, H.; Jonuleit, H. Interferon-Beta Therapy of Multiple Sclerosis Patients Improves the Responsiveness of T Cells for Immune Suppression by Regulatory T Cells. *Int. J. Mol. Sci.* **2015**, *16*, 16330–16346. [CrossRef] [PubMed]
63. Tanaka, M.; Vécsei, L. Monitoring the Redox Status in Multiple Sclerosis. *Biomedicines* **2020**, *8*, 406. [CrossRef] [PubMed]



Review

Neurogenic Inflammation: The Participant in Migraine and Recent Advancements in Translational Research

Eleonóra Spekker¹, Masaru Tanaka^{1,2}, Ágnes Szabó² and László Vécsei^{1,2,*}

¹ Neuroscience Research Group, Hungarian Academy of Sciences, University of Szeged (MTA-SZTE), H-6725 Szeged, Hungary; spekker.eleonora@med.u-szeged.hu (E.S.); tanaka.masaru.1@med.u-szeged.hu (M.T.)

² Interdisciplinary Excellence Centre, Department of Neurology, Albert Szent-Györgyi Medical School, University of Szeged, H-6725 Szeged, Hungary; szabo.agnes.4@med.u-szeged.hu

* Correspondence: vecsei.laszlo@med.u-szeged.hu; Tel.: +36-62-545-351; Fax: +36-62-545-597

Abstract: Migraine is a primary headache disorder characterized by a unilateral, throbbing, pulsing headache, which lasts for hours to days, and the pain can interfere with daily activities. It exhibits various symptoms, such as nausea, vomiting, sensitivity to light, sound, and odors, and physical activity consistently contributes to worsening pain. Despite the intensive research, little is still known about the pathomechanism of migraine. It is widely accepted that migraine involves activation and sensitization of the trigeminovascular system. It leads to the release of several pro-inflammatory neuropeptides and neurotransmitters and causes a cascade of inflammatory tissue responses, including vasodilation, plasma extravasation secondary to capillary leakage, edema, and mast cell degranulation. Convincing evidence obtained in rodent models suggests that neurogenic inflammation is assumed to contribute to the development of a migraine attack. Chemical stimulation of the dura mater triggers activation and sensitization of the trigeminal system and causes numerous molecular and behavioral changes; therefore, this is a relevant animal model of acute migraine. This narrative review discusses the emerging evidence supporting the involvement of neurogenic inflammation and neuropeptides in the pathophysiology of migraine, presenting the most recent advances in preclinical research and the novel therapeutic approaches to the disease.

Keywords: primary headache; migraine; trigeminal system; neuropeptides; neurogenic inflammation; animal model; inflammatory soup; dura mater; immune system; migraine treatment

Citation: Spekker, E.; Tanaka, M.; Szabó, Á.; Vécsei, L. Neurogenic Inflammation: The Participant in Migraine and Recent Advancements in Translational Research. *Biomedicines* **2022**, *10*, 76. <https://doi.org/10.3390/biomedicines10010076>

Academic Editor: Marco Segatto

Received: 2 November 2021

Accepted: 27 December 2021

Published: 30 December 2021

Publisher's Note: MDPI stays neutral with regard to jurisdictional claims in published maps and institutional affiliations.



Copyright: © 2021 by the authors. Licensee MDPI, Basel, Switzerland. This article is an open access article distributed under the terms and conditions of the Creative Commons Attribution (CC BY) license (<https://creativecommons.org/licenses/by/4.0/>).

1. Introduction

Migraine is a common neurological condition as the third most prevalent disease worldwide [1]. According to the Global Burden of Disease Study 2016, migraine is the second leading cause of disability [2]. The prevalence of migraine is 14.7%, and it is three times more common in women than men; in addition, women are less responsive to treatment [3]. Moreover, as migraine is a chronic episodic disorder that predominantly affects the working sector of a population, it thus has high social costs [4]. Migraine is ascribed to complicated, multifactorial conditions that give rise to substantial variations among patients and single patient responses to treatments [5]. Clinically, migraine can cause a variety of symptoms besides recurrent headaches, such as allodynia, photo- and phonophobia, and decreased daily activity, which can last from 4 to 72 h without treatment [6]. Due to its own pathogenesis and the fact that no other cause can be associated with the development of the disease, migraine belongs to the family of primary headache disorders [7].

The clinical course of migraine can be divided into different stages: the prodrome phase, a possible aura, followed by the headache, and the recovery stage (postdrome). The prodrome phase typically occurs up to a few days before the headache attack, and changes in well-being and behavior are experienced, while fatigue and impaired concentration occur as frequent complaints [8]. In 25% of the migraineurs, a temporary dysfunction of

the central nervous system (CNS), the aura phenomenon, occurs [9]. The most common symptoms are visual (e.g., visual field disturbances), but sensory or speech disturbances and rarely motor symptoms can also be observed [6,10–12]. The typical aura appears before or at the beginning of the headache and lasts up to one hour. The headache in migraineurs is moderate or strong and throbbing, lasting 4–72 h, and is associated with sensitivity to light/sound and nausea/vomiting. Physical activity worsens the symptoms, and thus, the migraineurs seek rest (Figure 1A).

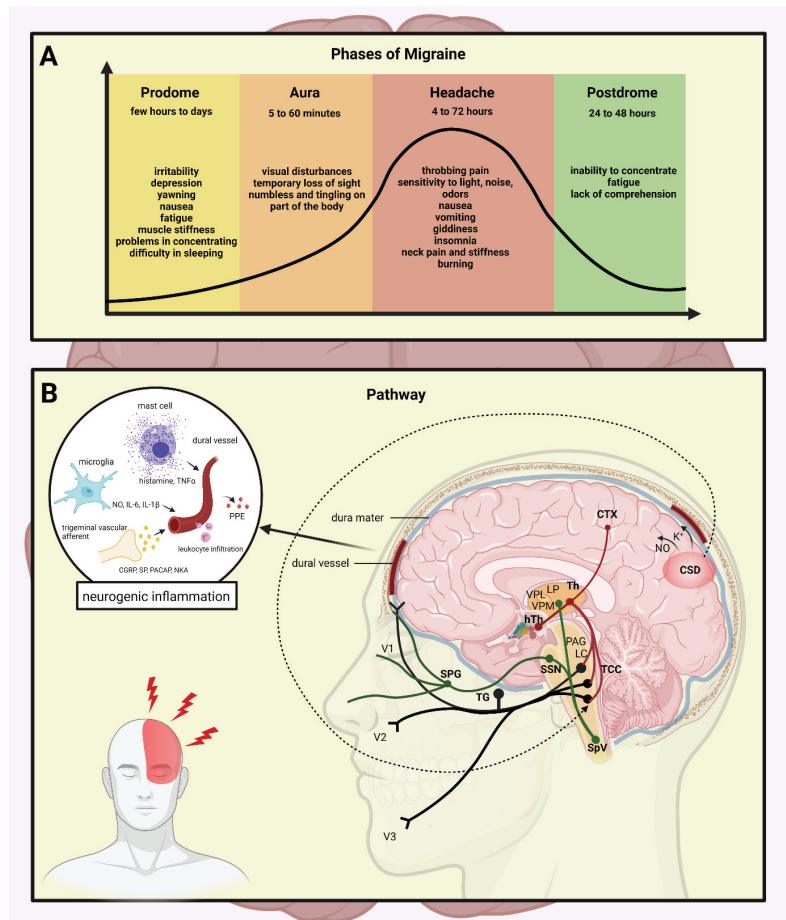


Figure 1. The stages and the pathways of migraine. (A) The stages of migraine attack: the prodrome phase, a possible aura, followed by the headache, and subsequently the postdrome. A strong headache is frequently accompanied with nausea, vomiting, and sensitivity to light, which lasts 4 to 72 h. (B) Mechanisms and structures involved in the pathogenesis of migraine: CTX, cortex; NO, nitric-oxide; CSD, cortical spreading depression; Th, thalamus; hTh, hypothalamus; LP, lateral posterior nucleus; VPM, ventral posteromedial nucleus; VPL, ventral posterolateral nucleus; PAG, periaqueductal grey matter; LC, locus coeruleus; TCC, trigeminocervical complex; SSN, superior salivatory nucleus; SpV, spinal trigeminal nucleus caudalis; TG, trigeminal ganglion; SPG, sphenopalatine ganglion; V1, ophthalmic nerve; V2, maxillary nerve; V3, mandibular nerve; CGRP, calcitonin gene-related peptide; SP, substance P; PACAP, pituitary adenylate cyclase-activating polypeptide; NKA, neurokinin A; PPE, plasma protein extravasation; TNF α , tumour necrosis factor alpha; IL, interleukin.

Despite intensive research, the pathomechanism of migraine is still unclear; however, activation and sensitization of the trigeminal system (TS) is essential during the attacks [13]. The TS is responsible for processing painful stimuli from the cortical area; during its activation, neurotransmitters, such as calcitonin gene-related peptide (CGRP), substance P (SP), pituitary adenylate cyclase-activating polypeptide (PACAP), and neurokinin A (NKA), are released both at the peripheral and central arm of the primary sensory neurons [14]. The neuropeptide release can induce mast cell degranulation and plasma extravasation, leading to neurogenic inflammation (NI) [15]. In the meantime, activation of the second-order neurons occurs in the caudal trigeminal nucleus (TNC) and their axons ascend to terminate in the thalamus, and the nociceptive information is projected to the primary somatosensory cortex [16]. Recent neuroimaging studies revealed other regions of the CNS (e.g., cerebellum, insula, pulvinar) that might play a role in the modulation of pain sensation [17,18] (Figure 1B).

In the 1950s, Ray and Wolff developed the first theory about the pathomechanism of migraine. They believed that migraine pain was caused by extracranial vasodilation, while intracranial vasospasm was responsible for aura symptoms [19]. At that time, this theory was in line with the pharmacological observations that the potent vasodilator amyl nitrate aborted the aura phase; meanwhile, ergotamine with vasoconstrictive properties decreased the headache [20]. Since vascular changes do not explain all the symptoms experienced during migraine attacks, new theories emerged regarding the pathomechanism of migraine.

The most widely accepted theory is focusing on the so-called cortical spreading depression (CSD) first described by Leao and Morison [21], which may be the equivalent of the aura phenomenon [22] playing a role in the development of migraine attacks [23]. During CSD, depolarization following an excitatory wave across the cerebral cortex changes cerebral blood supply, increases tissue metabolism, and releases amino acids and nitric oxide in the cortex, which activates nerves running in the dura, thus dilating the dural vessels, leading to sterile inflammation [24]. Under experimental conditions, CSD can activate secondary trigeminal nociceptors [25], suggesting that susceptibility to CSD might be responsible for the appearance of the attack.

Weiller and colleagues observed that the dorsolateral pons and the dorsal midbrain involving the nuclei nucleus raphe magnus (NRM), nucleus raphe dorsalis (DR), locus coeruleus (LC), and the periaqueductal grey matter (PAG) are activated during a migraine attack, which persists even after triptan treatment [26]. These nuclei can influence TNC activity, and they are involved in the transmission of pain. Brainstem serotonergic (NRM and PAG) and adrenergic (LC) nuclei contribute to the activation of the trigeminovascular system [27]. These brainstem areas, in addition to the trigeminovascular system, have a bidirectional connection with thalamus and hypothalamus. The thalamus has a role in integrating nociceptive inputs in migraine and pain sensation. The hypothalamus has direct connections with many structures involved in pain processing, including the nucleus tractus solitarius, rostral ventromedial medulla, PAG, and NRM [28–30]. It is hypothesized that the altered function of these brainstem migraine generators also plays a major role in attack development.

Nowadays, the most accepted concept is that migraine is a neurovascular disorder, which originates in the CNS, causing hypersensitivity to the peripheral trigeminal nerve fibers that innervate the vessels of the meninges.

This narrative review discusses the processes underlying the pathomechanism of migraine, focusing on the role of neuropeptides and neurogenic inflammation. Furthermore, it emphasizes the importance of preclinical translational research, which has led to current understanding of migraine and summarizes the novel potential therapeutic options for migraine.

2. Dura Mater in Migraine

The dura mater, its vasculature supply, and the cerebral blood vessels are the only structures containing nociceptive nerve fibers [31]. The role of dura mater in migraine pain was widely examined. Ray and Wolff found that electrical stimulation of dural and cerebral vessels can cause nausea and the perception of headache-like pain in humans [19]. The dura mater is the outermost layer of the meninges and is located directly underneath the skull and vertebral column bones. The three branches of the trigeminal nerve (ophthalmic (V1), maxillary (V2), and mandibular (V3)) innervate the face and head region [32]. Dowgjallo and Grzybowski were the first to find the origin of meningeal nerve fibers in the trigeminal ganglion (TG) [33,34]. The tentorial nerve (a branch of the ophthalmic nerve) innervates most of the supratentorial dura; this nerve supplies the falx cerebri, calvarial dura, and superior surface of the tentorium cerebelli, forming a dense plexus with the arteries that form the vascular intracranial pain-sensitive structures [35]. The afferents innervating intracranial structures are collectively referred to as the trigeminovascular system [36,37]. Strassmann described that peripheral trigeminovascular neurons become mechanically hypersensitive to dural stimulation, which explains the pulsation and intensification of headache in case of cough or bending [38]. Furthermore, Burstein et al. observed that stimulation of the dura causes prolonged sensitization of central trigeminovascular neurons in the spinal trigeminal nucleus [39]. Several studies have shown peptidergic trigeminal afferents to innervate the dura mater [40–42].

3. Neuropeptides and Neurotransmitters

Meningeal nerve fibers are immunoreactive for CGRP, SP, NKA, neuropeptide Y (NPY), and vasoactive intestinal peptide (VIP), among others [43]. CGRP plays multiple roles in neurogenic inflammation [44]. In pharmacological and immunological experiments, antagonism of CGRP supported that CGRP is indirectly involved in plasma extravasation, which is primarily caused by SP and NKA [45]. Together with SP, CGRP can trigger mast cell degranulation to release proinflammatory and inflammatory compounds [46]. Beside these, dural mast cells and satellite glia express the CGRP receptor [47]. It is suggested that satellite glia and neurons are involved in a positive feedback loop of CGRP synthesis and release, maintaining increased inflammation and sensitization [48].

SP is widely distributed in the central and peripheral nervous systems of vertebrates [49]. In the CNS, it is present in the dorsal root ganglion, spinal cord, hippocampus, cortex, basal ganglia, hypothalamus, amygdala, and TNC [50,51] and has a role in the neurotransmission of pain and noxious stimuli in the spinal cord [52]. It has been described in numerous cell-type SP products, e.g., macrophages, eosinophils, lymphocytes, and dendritic cells [53,54]. The SP-induced release of inflammatory mediators, such as cytokines, oxygen radicals, and histamine, enhances tissue damage and stimulates further recruitment of leukocytes, thereby enhancing the inflammatory response [55]. SP induces local vasodilation and changes the vascular permeability, thereby increasing the delivery and accumulation of leukocytes into tissues to express local immune responses [56]. SP often co-expresses with other transmitter molecules, like CGRP and glutamate in the TG and trigeminal nucleus caudalis [57,58]. During the headache phase of migraine, a significant increase in plasma SP and CGRP levels is demonstrated [59].

Moreover, PACAP is found in several structures that are relevant to the pathomechanism of migraine, e.g., in the dura mater, the cerebral vessels [60], the TG [61], the TNC [62], and the cervical spinal cord [63]. It was recently found that PACAP is co-expressed with CGRP in some dural nerve fibers [64]. PACAP plays a role in neuromodulation, neurogenic inflammation, and nociception [65], and in addition, it is involved in the higher-order processing of pain in brain regions such as the thalamus and the amygdala [66,67]. PACAP is also relevant in the central sensitization and emotional load of pain [68]. Zhang and colleagues found that following inflammation in sensory neurons, PACAP is upregulated [69]. Meningeal sensory fibers can release neuropeptides from their peripheral endings in the meninges, where they can evoke components of neurogenic inflammation [64].

VIP is widely distributed in the central and peripheral nervous systems [70]. VIP plays as potent vasodilators, acting on the smooth muscle cells in arterioles [71]. VIP can modulate mast cell degranulation and the production of proinflammatory cytokines, such as interleukins, including IL-6 and IL-8 [72]. In a clinical study, during the interictal period of chronic migraine, higher VIP levels have been reported in peripheral venous blood than in control subjects [73]. Pellesi et al. observed that as opposed to shorter vasodilation, prolonged VIP-mediated vasodilation causes more headaches [74]. Together, VIP may contribute to migraine pain through vasodilation and dural mast cell degranulation.

Transient receptor potential vanilloid-1 receptor (TRPV1), a nonselective cation channel, is a molecular component of pain detection and modulation [75]. TRPV1 receptors are present in the human TG [76] and trigeminal afferents, which innervate the dura mater [77]. In addition to excessive heat, various exogenous and endogenous triggering factors can directly activate or sensitize TRPV1 [78]. TRPV1 activation leads to the release of neuropeptides, such as SP and CGRP, which can cause vasodilation and initiate neurogenic inflammation within the meninges [79]. TRPV1 activation and/or sensitization can enhance inflammatory responses via the expression and release of other inflammatory mediators.

Histamine plays a role in migraine; it can modulate neurogenic inflammation and nociceptive sensitization [80]. During a migraine attack, elevated levels of a histamine precursor histidine were found in plasma and cerebrospinal fluid (CSF) [81], and the histamine levels of the plasma were increased both ictally and interictally in migraine patients [80]. The release of SP contributes to local vasodilation, induces histamine release from mast cells, and produces flare and further activates other sensory nerve endings [82]. C-fibers are known to be activated by histamine and are responsible for the neuropeptide release. Nerve fibers, which contain histamine, have been found in the superficial laminae of the dorsal horn, an essential site for nociceptive transmission [83]. In inflammatory conditions, histamine can mediate the release of SP and glutamate [84] (Table 1).

Table 1. Neuropeptides and neurotransmitters and their role in migraine and neurogenic inflammation.

Neuropeptides/ Neurotransmitters	Receptors	Migraine/Neurogenic Inflammation-Related Functions	References
CGRP	CLR, RAMP1	craniocervical vasodilation, peripheral and central sensitization, neuron-glia interaction, involved plasma extravasation, mast cell degranulation,	Asghar et al., 2011 [44], Holzer, 1998 [45], Ottosson and Edvinsson, 1997 [46], Lennerz et al., 2008 [47], Raddant and Russo, 2011 [48]
SP	NK1	craniocervical vasodilation, plasma protein extravasation, cytokines, oxygen radicals, and histamine release	Hökfelt et al., 1975 [49], Ribeiro-da-Silva and Hökfelt, 2000 [50], Snijdelaar et al., 2000 [51], Graefe and Mohiuddin, 2021 [52], Killingsworth et al., 1997 [53], Weinstock et al., 1988 [54], Holzer and Holzer-Petsche, 1997 [55], Pernow, 1983 [56], Gibbins et al., 1985 [57], Battaglia and Rustioni, 1988 [58], Malhotra, 2016 [59]
PACAP	PAC1, VPAC1, VPAC2	craniocervical vasodilation, peripheral and central sensitization	Jansen-Olesen and Hougaard Pedersen, 2018 [60], Eftekhari et al., 2013 [61], Nielsen et al., 1998 [62], Jansen-Olesen et al., 2014 [63], Uddman et al., 2002 [64], Hashimoto et al., 2006 [65], Martin et al., 2003 [66], Missig et al., 2014 [67], Kaiser and Russo, 2013 [68], Zhang et al., 1998 [69]

Table 1. Cont.

Neuropeptides/ Neurotransmitters	Receptors	Migraine/Neurogenic Inflammation-Related Functions	References
VIP	VPAC1, VPAC2	craniocervical vasodilation, mast cell degranulation, IL-6 and IL-8 production	Kilinc et al., 2015 [70], Ohhashi et al., 1983 [71], Kakurai et al., 2001 [72], Cernuda-Morollón et al., 2014 [73], Pellesi et al., 2020 [74]
-	TRPV1	vasodilation, peripheral and central sensitization, neuropeptide release (SP, CGRP) initiate neurogenic inflammation	Caterina et al., 2000 [75], Quartu et al., 2016 [76], Dux et al., 2020 [77], Bevan et al., 2014 [78], Meents et al., 2010 [79]
histamine	H ₁₋₄ R	vasodilation, mediate SP and glutamate release	Yuan and Silberstein, 2018 [80], Castillo et al., 1995 [81], Heatley et al., 1982 [82], Foreman et al., 1983 [83], Rosa and Fantozzi, 2013 [84]

4. Neurogenic Inflammation

The localized form of inflammation is neuroinflammation, which occurs in both the peripheral and CNSs. The main features of NI are the increased vascular permeability, leukocyte infiltration, glial cell activation, and increased production of inflammatory mediators, such as cytokines and chemokines [85]. NI increases the permeability of the blood to the brain barrier, thus allowing an increased influx of peripheral immune cells into the CNS [86] (Figure 2A).

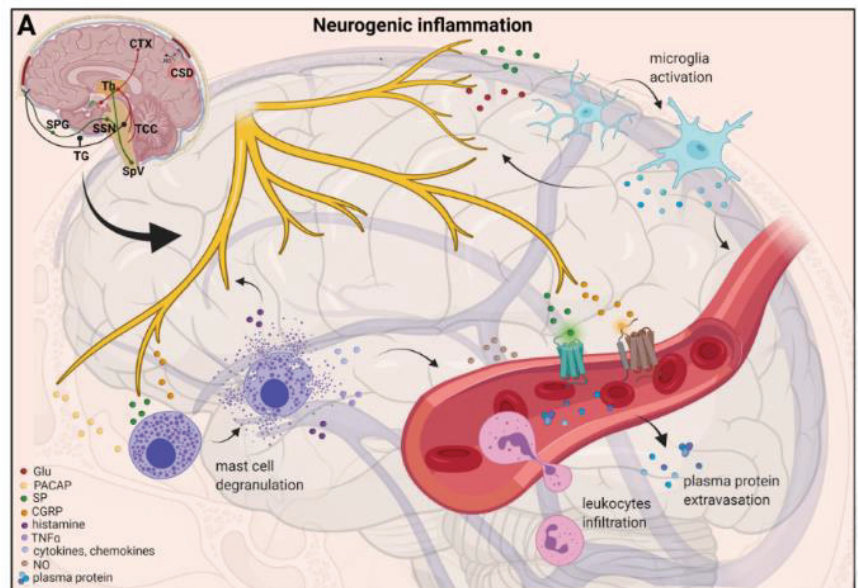


Figure 2. Cont.

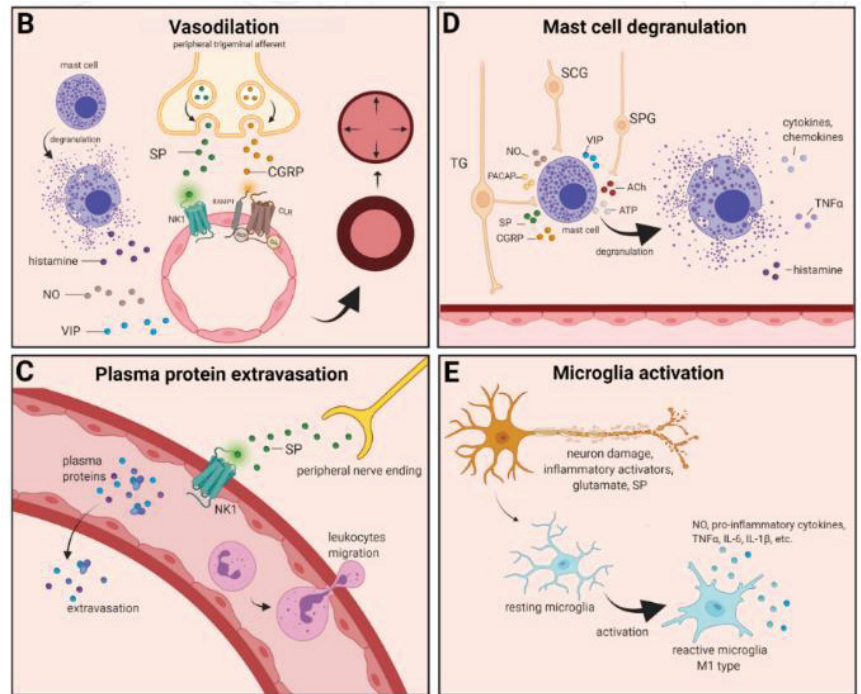


Figure 2. Neurogenic inflammation and its main features. (A) Stimulation of the trigeminal nerve causes the release of neuropeptides, including CGRP, SP, NO, VIP, and 5-HT, leading to neurogenic inflammation, which has four main features: the increased vascular permeability, leukocyte infiltration, glial cell activation, and increased production of inflammatory mediators, such as cytokines and chemokines. (B) Vasoactive peptides, such as CGRP and SP, bind their receptors on smooth muscle of dural vessels and cause vasodilation. The released neuropeptides induce mast cell degranulation, resulting in the release of histamine, which leads endothelium-dependent vasodilation. (C) Binding of the released SP to the NK1 receptors expressed on the microvascular blood vessels disrupts the membrane and causes plasma protein leakage and leukocyte extravasation. (D) Mast cells are in close association with neurons, especially in the dura, where they can be activated following trigeminal nerve and cervical or sphenopalatine ganglion stimulation. Release of neuropeptides causes mast cell degranulation, which leads to release of histamine and serotonin and selectively can cause the release of pro-inflammatory cytokines, such as TNF- α , IL-1, and IL-6. (E) Under the influence of inflammatory stimuli, microglia can become reactive microglia. Microglia activation leads to the production of inflammatory mediators and cytotoxic mediators.

The concept of NI was introduced by the experiment of Goltz and Bayliss, in which skin vasodilation was observed during electrical stimulation of the dorsal horn, which could not be linked to the immune system [87,88]. Dalessio was the first who hypothesized a connection between NI and migraine and believed that a headache is a result of vasodilation of cranial vessels associated with local inflammation [89]. This theory was later reworked by Moskowitz, who believed that upon activation, the neuropeptide release from trigeminal neurons has a role in increasing vascular permeability and vasodilation [90].

There are several theories concerning the mechanism of NI. Hormonal fluctuations or cortical spreading depression can initiate two types of processes: activating the TS to trigger the liberation of neuropeptides from the peripheral trigeminal afferents and/or degranulating the mast cells that can lead to the release of neuropeptides by activating and sensitizing the nociceptors [91]. In rats, Bolay and colleagues demonstrated that after local electrical stimulation of the cerebral cortex, CSD is generated, and it can trigger trigeminal activation,

which causes meningeal inflammation occurring after the CSD disappearance [92]. Both CGRP and SP play an important role in the development of NI. Released peptides, such as CGRP, bind to its receptor on smooth muscle cells, eliciting a vasodilatory response, thereby increasing meningeal blood flow in the dural vasculature. In contrast to CGRP, binding of the released SP to the NK1 receptors expressed on the microvascular blood vessels disrupts the membrane and causes plasma protein leakage. Both neuropeptides can induce mast cell degranulation through their specific receptors and further sensitize meningeal nociceptors [91]. The meningeal nerve fibers also contain neurotransmitters (e.g., glutamate, serotonin) and hormones (e.g., prostaglandins) that can affect the activation and release of neuropeptides, causing neurogenic inflammation [89]. Moreover, several cell types (e.g., endothelial cells, mast cells, and dendritic cells) can release tumor necrosis factor alpha (TNF α), interleukins, nerve-growth factor (NGF), and VIP, also causing plasma protein extravasation (PPE) [93,94], which is a key characteristic of NI. In addition, neuronal nitric oxide synthase (nNOS) enzyme can be detected in the trigeminal nerve endings, the dural mastocytes, and also the TNC and the TG [95], which catalyzes the synthesis of retrograde signaling molecule nitric oxide (NO). NO has a major role in mediating many aspects of inflammatory responses; NO can affect the release of various inflammatory mediators from cells participating in inflammatory responses (e.g., leukocytes, macrophages, mast cells, endothelial cells, and platelets) [96]. Through its retrograde signaling action, astrocytes can influence the release of CGRP, SP, and glutamate [97,98]. Beside this, bradykinin and histamine induce NO release from vascular endothelial cells, suggesting a strong interaction between NO and inflammation [99]. The inflammation can lead to CGRP release from the activated primary afferent neurons, which force satellite glial cells to release NO. NO can induce nNOS, which can be considered a significant marker of the sensitization process of the TS. TRPV channels permit afferent nerves to detect thermal, mechanical, and chemical stimuli, thereby regulating NI and nociception [100]. TRPV1 was identified in dorsal root ganglion (DRG), TG neurons, and spinal and peripheral nerve terminals [101]. Inflammatory mediators remarkably up-regulate TRPV1 through activation of phospholipase C (PLC) and protein kinase A (PKA) and protein kinase C (PKC) signaling pathways [102–105]. Increased TRPV1 expression in peripheral nociceptors contributes to maintaining inflammatory hyperalgesia [101]. In an experimental injury model, Vergnolle et al. demonstrated that a decrease in osmolarity of extracellular fluid could induce neurogenic inflammation, which TRPV4 can mediate [106]. Furthermore, plasma and cerebrospinal fluid levels of neuropeptides, histamine, proteases, and pro-inflammatory cytokines (e.g., TNF α , IL-1 β) are elevated during migraine attacks [107,108], suggesting that neuroimmune interactions contribute to migraine pathogenesis.

4.1. Vasodilation

There are various cell types in blood vessels that both release and respond to numerous mediators that can contribute to migraine; this includes growth factors, cytokines, adenosine triphosphate (ATP), and NO [109–112]. In the central system, NO may be involved in the regulation of cerebral blood flow and neurotransmission [59]. NO can stimulate the release of neuropeptides and causes neurogenic vasodilation [113]. In addition to NO, NGF also increases the expression of CGRP and enhances the production and release of neuropeptides, including SP and CGRP, in sensory neurons [114]. CGRP, a potent vasodilator, is released from intracranial afferents during migraine attacks. This vasodilatory effect of CGRP is mediated by its action on CGRP receptors, which stimulates the adenylyl cyclase and increases cyclic adenosine monophosphate (cAMP), thus producing potent vasodilation via the direct relaxation of vascular smooth muscle [115,116]. In response to prolonged noxious stimuli, SP is released from trigeminal sensory nerve fibers around dural blood vessels, leading to endothelium-dependent vasodilation [82]. VIP also contributes to neurogenic inflammation by inducing vasodilation [117] (Figure 2B).

4.2. Plasma Protein Extravasation

Another critical feature of neurogenic inflammation is PPE. Based on preclinical studies, the neurogenic PPE plays a role in the pathogenesis of migraine [118]. In several studies, following electrical stimulation of the trigeminal neurons or intravenous capsaicin, the peripheral nerve endings in the dural vasculature released SP, which caused plasma protein leakage and vasodilation through the NK-1 receptors [119]. Transduction of the SP signal through the NK1 receptor occurs via G protein signaling and the secondary messenger cAMP, ultimately leading to the regulation of ion channels, enzyme activity, and alterations in gene expression [120]. SP can indirectly influence plasma extravasation by activating mast cell degranulation, which results in histamine release [83]. In addition, NKA is able to induce plasma protein efflux and activate inflammatory cells [121] (Figure 2C).

4.3. Mast Cell Degranulation

It is well known that dural mast cells play a role in the pathophysiology of migraine [122]. Meningeal mast cells are in close association with neurons, especially in the dura, where they can be activated following trigeminal nerve and cervical or sphenopalatine ganglion stimulation [123]. The release of neuropeptides, such as CGRP, PACAP, and SP, from meningeal nociceptors can cause the degranulation of mast cells [124], resulting in the release of histamine and serotonin and selectively can cause the release of pro-inflammatory cytokines, such as TNF- α , IL-1, and IL-6 [125–127]. The plasma and CSF levels of these mediators (e.g., CGRP, TNF α , and IL-1 β) are enhanced during migraine attacks [104]. VIP promotes degranulation of mast cells [128], similar to the effects of SP [83]. It was found that CSD can induce intracranial mast cell degranulation and promote the activation of meningeal nociceptors [129,130]. Besides these, according to several studies, mast cells can be activated by acute stress [123,131,132], which is known to precipitate or exacerbate migraines [133,134]. Based on these findings, mast cells in themselves may promote a cascade of associated inflammatory events resulting in trigeminovascular activation (Figure 2D).

4.4. Microglia Activation

Microglia appears in the CNS and can exert neuroprotective and neurotoxic effects as well. Under the influence of inflammatory stimuli, microglia can become efficient mobile effector cells [135]. Microglia activation leads the production of inflammatory mediators and cytotoxic mediators (e.g., NO, reactive oxygen species, prostaglandins) [136,137], which might disrupt the integrity of the blood brain barrier, thereby allowing leukocyte migration into the brain [138]. Microglia express receptors for neurotransmitters, such as glutamate, gamma-aminobutyric acid, noradrenaline, purines, and dopamine [139]. It has been described that activation of ion channels is related to the activation of microglia; therefore, neurotransmitters probably influence microglia function [140]. Glutamate leads to neuronal death but is also an activation signal for microglia [141]. Activation of glutamate receptors causes the release of TNF- α , which, with microglia-derived Fas ligand, leads to neurotoxicity [142]. Besides this, Off signals from neurons appear important in maintaining tissue homeostasis and limiting microglia activity under inflammatory conditions, presumably preventing damage to intact parts of the brain [143]. Endothelin B-receptor-mediated regulation of astrocytic activation was reported to improve brain disorders, such as neuropathic pain [144]. SP also directly activates microglia and astrocytes and contributes to microglial activation [145,146], initiating signaling via the nuclear factor kappa B pathway, leading to pro-inflammatory cytokines production [147] (Figure 2E).

4.5. Cytokines, Chemokines

Cytokines are small proteins produced by most cells in the body, which possess multiple biologic activities to promote cell-cell interaction [148]. There is evidence that cytokines play an important role in several physiological and pathological settings, such as immunology, inflammation, and pain. [149]. The most important pro-inflammatory cytokines include IL-1, IL-6, and TNF α , and the key chemokine is IL-8 [149]. Cytokines

and chemokines are released by neurons, microglia, astrocytes, macrophages, and T cells, and these factors might activate nociceptive neurons [150]. $\text{TNF}\alpha$ can trigger tissue edema and immune cell infiltration [151] and can influence the reactivity of signal nociceptors to the brain and increase blood levels during headaches, playing a crucial role in the genesis of migraine [152]. Cytokines are considered to be pain mediators in neurovascular inflammation, which generates migraine pain [153]. They can induce sterile inflammation of meningeal blood vessels in migraines [154]. Besides this, elevated levels of chemokines can stimulate the activation of trigeminal nerves and the release of vasoactive peptides; thereby, they can induce inflammation [155]. Based on these, cytokines and chemokines might contribute to migraine.

5. Animal Models of Neurogenic Inflammation

Developing animal models of human illnesses is a challenging task for translational research, but it is indispensable to understanding pathomechanism, searching for biomarkers, and engineering novel treatment [156–164]. Migraine research is no exception. Chemical activation of meningeal trigeminal nociceptors is possible in animal experiments. The use of Complete Freund's adjuvant (CFA, dried and inactivated *Mycobacterium tuberculosis* in mineral oil) or inflammatory soup (IS, a standard mixture of histamine, serotonin, bradykinin, and prostaglandin E2) on the surface of the dura mater is a useful method for inducing trigeminal activation and sensitization and developing neurogenic inflammation in rats [165–167]. It has been shown that trigeminal brainstem neurons have been sensitive to both subarachnoid superfusion and topical IS administration [37,168]. Lukács et al. demonstrated that the application of CFA or IS onto the dural surface can induce changes in the expression of phosphorylated extracellular signal-regulated kinase $\frac{1}{2}$ (pERK1/2), IL-1 β , and CGRP-positive nerve fibers in the TG [167]. Similar to the previous experiment, Laborc et al. used topical administration of IS or CFA on the dura mater to examine the activation pattern that is caused by chemical stimulation, and they found that application of IS on the dura mater induces short-term c-Fos activation, while CFA did not cause any difference in the number of c-Fos-positive cells between the CFA-treated and control groups. Whereas short survival times were used, the authors believe this may have been the reason that the CFA did not prove effective [169]. Spekker et al. found that IS was able to cause sterile neurogenic inflammation in the dura mater and increased the area covered by CGRP and TRPV1 immunoreactive fibers and the number of neuronal nitric oxide synthase (nNOS)-positive cells in the TNC, and pretreatment with sumatriptan or kynurenic acid (KYNA) could modulate the changes caused by IS. Sumatriptan probably acted through the 5-HT_{1B/1D} receptors, while KYNA possibly acted predominantly by inhibiting the glutamate system and thereby blocking sensitization processes, which is important in migraine [170]. Furthermore, Wieseler and colleagues observed an increase in the level of IL-1 β and $\text{TNF}\alpha$, and the microglial/macrophage activation marker CD11b in Sp5C after IS was administered bilaterally through supradural catheters in freely moving rats [171].

In addition to morphological changes, IS can also influence animal behavior. Oshinsky and Gomonchareonsiri used IS treatment three times per week for up to four weeks, and they demonstrated that repeated infusions of IS over weeks induced a long-lasting decrease in periorbital pressure thresholds [172]. Melo-Carrillo and colleagues described that repeated infusion of IS increased the resting and freezing behavior and decreased the locomotor activity [173]. These observations are consistent with decreased routine physical activity and lack of exercise due to migraine-induced pain in migraine patients [174]. Moreover, they found a specific ipsilateral facial grooming behavior, which may be related to the unilateral nature of migraine. In an animal model of intracranial pain, Malick et al. showed that simultaneous chemical and mechanical stimulation of the dura mater not only increases the number of Fos-positive neurons in the medullary dorsal horn but can reduce the appetite of the rats. [175]. Wieseler et al. experienced facial and hind paw allodynia and after two IS infusions [176]. In a novel large animal model of recurrent migraine, repeated

chemical stimulation of the dura mater reduced locomotor behavior, which may mimic a decrease in routine physical activity in people with headaches. In addition, increased scratches and slow movements were observed; these may reflect pain localized to the head area [177] (Figure 3). Based on these experiments, it can be said that dural application of IS triggers activation and sensitization of the trigeminal system. Therefore, this is a relevant animal model of acute migraine.

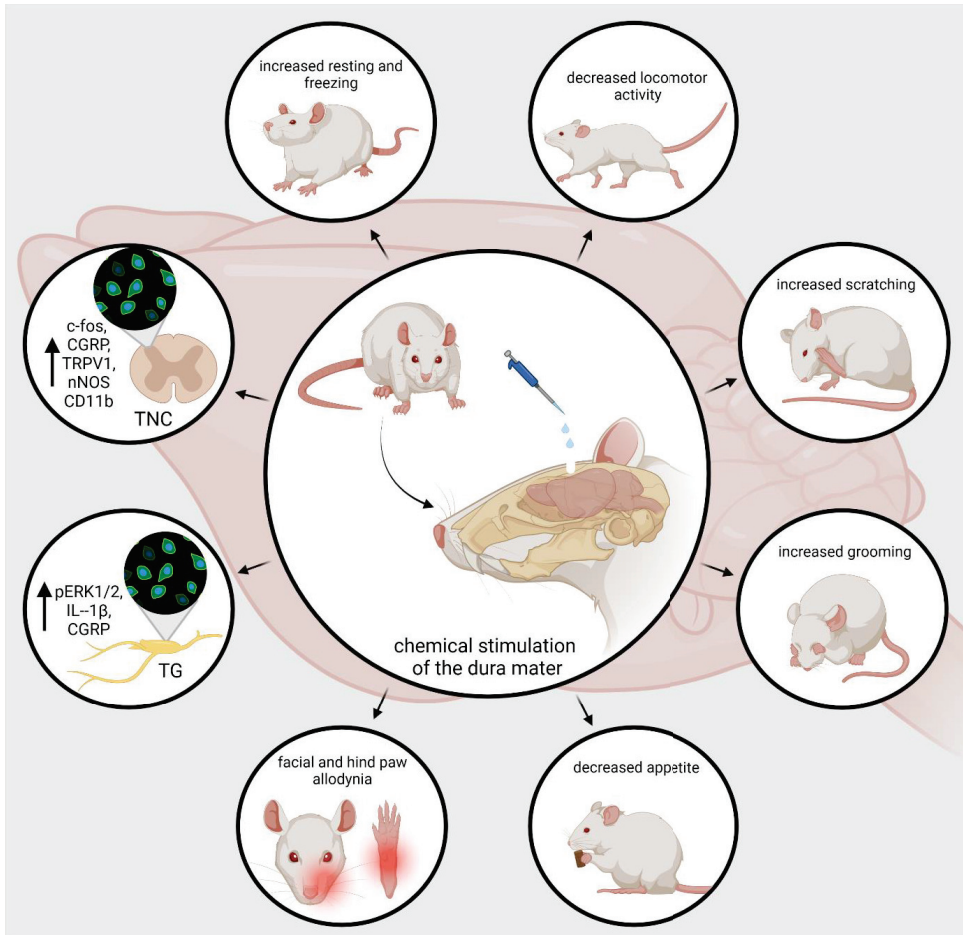


Figure 3. nNOS, pERK, ILs, increase the resting and freezing behavior, and decrease the appetite and locomotor activity of the animals. In addition, it can enhance grooming and scratching behavior and elicit mechanical and thermal hypersensitivity. CGRP, calcitonin gene-related peptide; TRPV1, transient receptor potential vanilloid receptor; nNOS, neuronal nitric-oxide synthase; IL, interleukins; pERK, phosphorylated extracellular signal-regulated kinase.

6. Current Treatments and Advances in Preclinical Research

Triptans are widely used to relieve migraine attacks; acting as agonists on 5-hydroxytryptamine receptors (5-HT_{1B/1D}), they can cause the constriction of dilated cranial arteries and the inhibition of CGRP release [178]. In an animal model of migraine, after electrical stimulation of the TG, sumatriptan attenuates PPE by preventing the release of CGRP [179]. In knockout mice and guinea pigs, it has been shown that 5-HT_{1D} receptors have a role in the inhibition of neuropeptide release, thereby modifying the dural neurogenic inflammatory

response [180]. The use of triptans is limited by their vasoconstrictive properties. As triptans are not effective in everyone, they often lead to medication overuse, triggering migraine to become chronic (Table 2).

Table 2. Current treatments and advances in preclinical research.

Drug Class	Drug	Target	FDA Approved
NSAIDs	Acetylsalicylic acid	COX1–2	yes
	Ibuprofen		yes
	Diclofenac potassium		yes
Triptans	Paracetamol	5-HT _{1D} receptor	yes
	Sumatriptan		yes
	Zolmitriptan		yes
	Almotriptan		yes
	Rizatriptan		yes
	Frovatriptan		yes
	Naratriptan		yes
	Eletriptan		5-HT _{1B/1D} receptor
Ditans	Lasmiditan	5-HT _{1F} receptor	yes
Gepants	Ubrogepant	CGRP receptor	yes
	Rimegepant		yes
	Atogepant		no
	Vazegepant		no
Ergot alkaloids	Ergotamine tartrate	α -adrenergic receptor, 5-HT receptors	yes
CGRP/CGRP receptor monoclonal antibody	Erenumab	CGRP receptor	yes
	Eptinezumab	CGRP ligand	yes
	Fremanezumab		yes
	Galcenezumab		yes
NK1R antagonists	Aprepitant	NK1 receptor	yes
PACAP/PAC1 receptor monoclonal antibody	ALD1910	PACAP38	no
	AMG-301	PAC1 receptor	no
Endocannabinoids	2-Arachidonoylglycerol	CB1 receptor	no
	Anandamide	CB1 receptor	no

Ditans target the 5-HT_{1F} receptor, which is expressed in the cortex, the hypothalamus, the trigeminal ganglia, the locus coeruleus, the middle cerebral artery, and the upper cervical cord. Lasmiditan is the first drug approved for clinical use. Contrary to triptans, Lasmiditan does not cause vasoconstriction. The activation of 5-HT_{1F} receptor inhibits the release of CGRP and probably SP from the peripheral trigeminal endings of the dura and acts on the trigeminal nucleus caudalis or the thalamus [181].

Besides triptans and ditans, acute treatments of migraine headaches, i.e., ergot alkaloids and nonsteroidal anti-inflammatory agents (NSAIDs), may decrease the neurogenic inflammatory response [182]. NSAIDs have anti-inflammatory, analgesic, and anti-pyretic properties. Their primary effect is to block the enzyme cyclooxygenase and hence mitigate prostaglandin synthesis from arachidonic acid [183]. Both acetaminophen and ibuprofen, which can reduce pain intensity, can also be used in children. Magnesium pretreatment increases the effectiveness of these treatments and reduces the frequency of pain [184]. Er-

gotamine has been recommended to abort migraine attacks by eliminating the constriction of dilated cranial blood vessels and carotid arteriovenous anastomoses, reducing CGRP release from perivascular trigeminal nerve endings, and inhibit the nociceptive transmission on peripheral and central ends of trigeminal sensory nerves [185].

An alternative treatment strategy is the use of CGRP-blocking monoclonal antibodies. Monoclonal antibodies have a number of positive properties: (1) a long half-life, (2) long duration of action, and (3) high specificity [186]. Four monoclonal antibodies are currently developing for migraine prevention: three against CGRP and one against the CGRP receptor. The safety and tolerability of these antibodies are promising; no clinically significant change in vitals, ECGs, or hepatic enzymes was observed. Blocking of CGRP function by monoclonal antibodies has demonstrated efficacy in the prevention of migraine with minimal side effects in multiple Phase II and III clinical trials [187].

Another alternative approach to treating the migraine attack by limiting neurogenic inflammatory vasodilation is the blockade of CGRP receptors by selective antagonists. Gepants were designed to treat acute migraines [188]. These bind to CGRP receptors and reverse CGRP-induced vasodilation but were not vasoconstrictors per se [189]. Based on these, gepants may be an alternative if triptans are contraindicated. Currently, two gepants (Ubrogепant, Rimegepant) are available on the market, but several are in development.

In gene-knockout studies, the hypothesis the tachykinins are the primary mediators of the PPE component of NI has been strengthened [190,191]. Following topical application of capsaicin to the ear, the PPE was decreased in Tac1-deficient mice compared to wild-type mice [192]. Following activation of the trigeminal system by chemical, mechanical, or electrical stimulation, tachykinin Receptor 1 (TACR1) antagonists seem to be adequate to blocking dural PPE [193]. However, lanepitant, a selective TACR1 antagonist, has no significant effect on migraine-associated symptoms [194]; moreover, it was found ineffective in a migraine prevention study [195]. The only currently available and clinically approved NK1 receptor antagonist is aprepitant, which is used as an antiemetic to chemotherapy-induced nausea in cancer patients [196].

In animal models, blockage of TRPV1 receptors was effective to reverse inflammatory pain; however, TRPV1 antagonists produce some serious side effects, e.g., hyperthermia [197]. Clinical data suggest that TRPV1 antagonists might be effective as therapeutic options for certain conditions, such as migraine and pain related to several types of diseases. Hopefully, current clinical trials with TRPV1 receptor antagonists and future studies provide an answer as to the role of TRPV1 in inflammatory and neuropathic pain syndromes.

The anti-nociceptive effects of endocannabinoids are thought to be mediated mainly through the activation of cannabinoid receptor type 1 (CB1) [198]. Localization of CB1 receptors along the trigeminal tract and trigeminal afferents [199,200] suggests that the endocannabinoid system can modulate the neurogenic-induced migraine [201]. Clinical data suggested that in migraine patients, the endocannabinoid levels are lower [202,203]. In animal models of migraine, endocannabinoids can reduce neurogenic inflammation. Akerman et al. reported that capsaicin-induced vasodilation is less after intravenous administration of anandamide (AEA); in addition, AEA significantly prevented CGRP- and NO-induced vasodilation in the dura [204]. In a previous study, Nagy-Grócz and colleagues observed that NTG and AEA alone or combined treatment of them affects 5-HTT expression, which points out a possible interaction between the serotonergic and endocannabinoid system on the NTG-induced trigeminal activation and sensitization phenomenon, which are essential during migraine attacks [205]. These results raise the possibility that the AEA has a CB1 receptor-mediated inhibitory effect on neurogenic vasodilation of trigeminal blood vessels. Based on these, anandamide may be a potential therapeutic target for migraine. Besides these, the presence of CB1 receptors in the brain makes them a target for the treatment of migraine, blocking not only peripheral but also central nociceptive traffic and reducing CSD. CB2 receptors in immune cells may be targeted to reduce the inflammatory component associated with migraine.

PACAP and its G-protein-coupled receptors, pituitary adenylate cyclase 1 receptor (PAC1) and vasoactive intestinal peptide receptor 1/2 (VPAC1/2), are involved in various biological processes. Activation of PACAP receptors has an essential role in the pathophysiology of primary headache disorders, and PACAP plays an excitatory role in migraine [206]. There are two pharmacology options to inhibit PACAP: PAC1 receptor antagonists/antibodies directed against the receptor or antibodies directed against the peptide PACAP [207]. Studies of the PAC1 receptor antagonist PACAP (6–38) have proved that antagonism of this receptor may be beneficial even during migraine progression [208]. PACAP38 and PAC1 receptor blockade are promising antimigraine therapies, but results from clinical trials are needed to confirm their efficacy and side effect profile.

The tryptophan-kynurenine metabolic pathway (KP) is gaining growing attention in search of potential biomarkers and possible therapeutic targets in various illnesses, including migraine [209,210]. KYNA is a neuroactive metabolite of the KP, which affects several glutamate receptors, playing a relevant role in pain processing and neuroinflammation [181]. KYNA may block the activation of trigeminal neurons, affect the migraine generators, and modulate the generation of CSD [209,211]. An abnormal decrease or increase in the KYNA level can cause an imbalance in the neurotransmitter systems, and it is associated with several neurodegenerative and neuropsychiatric disorders [212–215]. Based on human and animal data, the KP is downregulated under different headaches; thus, possibly less KYNA is produced [216]. It is consistent with the theory of hyperactive NMDA receptors, which play a key role in the development of central sensitization [217] and thus in migraine pathophysiology. In an NTG-induced rodent model of migraine, Nagy-Grócz et al. demonstrated a decrease in the expression of KP enzymes after NTG administration in rat TNC [218]. Interferons can control the transcription expression of indoleamine 2,3-dioxygenase (IDO), kynurenine 3-monooxygenase (KMO), and kynureninase (KYNU); therefore, the pro-inflammatory cytokines may affect the kynurenine pathway [219]. It is difficult for KYNA to cross the blood-brain barrier (BBB); therefore, synthetic KYNA analogs may provide an additional alternative for synthesizing compounds that have neuroprotective effects comparable to KYNA that can cross the BBB effectively. Preclinical studies have shown the effectiveness of KYNA analogs in animal models of dural stimulation [220,221]. Further preclinical studies are required to understand the role of KYNA analogs in migraine and clinical studies that assess their effectiveness in acute or prophylactic treatment (Figure 4).

In animal models of chronic pain and inflammation and several clinical trials, palmitoylethanolamide (PEA), endogenous fatty acid amide, has been influential on various pain states [222–224]. In a pilot study, for patients suffering from migraine with aura, ultra-micronized PEA treatment has been shown effective and safe [225]. Based on these, PEA is a new therapeutic option in the treatment of pain and inflammatory conditions.

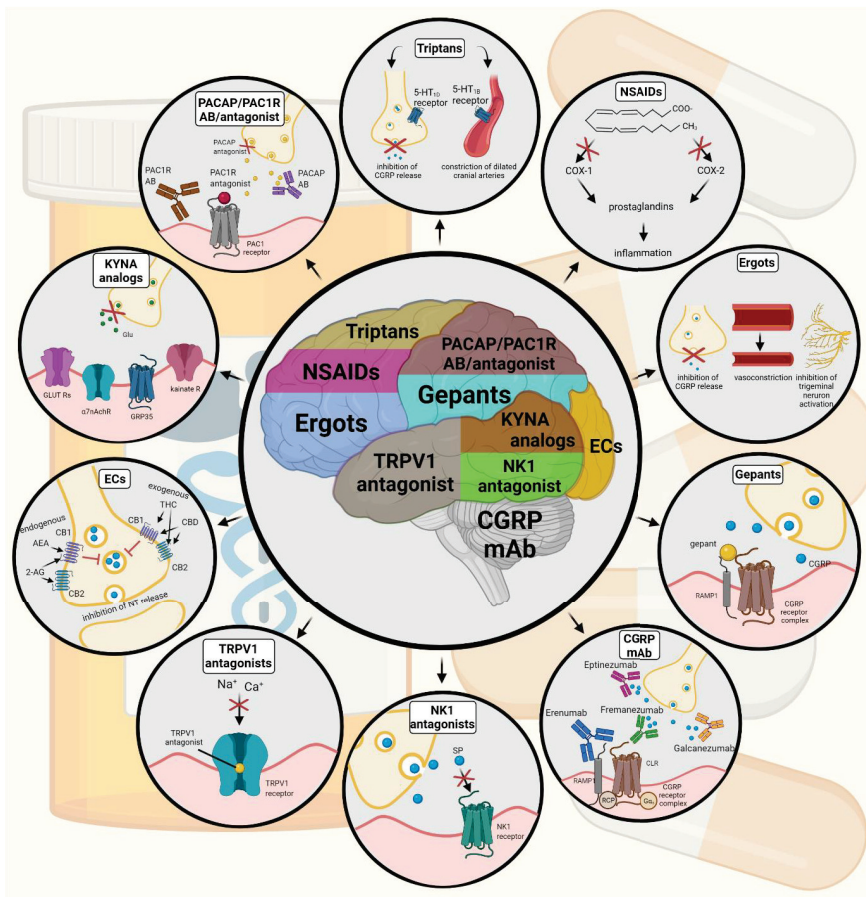


Figure 4. Possible treatments of neurogenic inflammation and migraine. NSAIDs, non-steroidal anti-inflammatory drugs; 5-HT, serotonin; CGRP, calcitonin gene-related peptide; COX, cyclooxygenase; Ab, antibody; NK1, neurokinin 1; TRPV1, transient receptor potential vanilloid receptor; SP, substance P; EC, endocannabinoids; AEA, anandamide; 2-AG, 2-arachidonoylglycerol; CB, cannabinoid receptor; THC, tetrahydrocannabinol; CBD, cannabidiol; NT, neurotransmitter; GLUT R, glutamate receptors; $\alpha 7$ AchR, alpha-7 nicotinic receptor; GPR35, G protein-coupled receptor 35; PACAP, pituitary adenylate cyclase-activating polypeptide; PAC1R, pituitary adenylate cyclase 1 receptor.

7. Conclusions and Future Perspective

Migraines impose a tremendous negative impact on quality of life; nevertheless, antimigraine pharmacotherapy provides limited success in efficacy and tolerability. Migraineurs and patients with chronic pain helplessly seek alternative or complementary treatments, such as biofeedback, botox, yoga, acupuncture, acupressure, and music therapy, among others [226]. The biggest challenge in antimigraine research may lie in complex multifactorial pathogenesis of migraine headache, which is precipitated by intertwining genetic, endocrine, metabolic, and/or environmental factors, and thus, the exact pathology leading to migraine attack remains poorly understood. This review article focuses on that migraine headache is a reflection of neurogenic inflammation in the activation and sensitization of trigeminovascular afferent nerves, which project to the second-order neurons in the brainstem. The local release of neuropeptides and neurotransmitters can not only cause the dilation of meningeal vessels but also induce neuroinflammation. Animal models

of migraine support this hypothesis that neurogenic inflammation plays a crucial role in the sensitization process that leads to enhanced responsiveness of target tissues. However, clinical study remains to be conducted. Understanding the signal transduction and regulation of neuropeptides, including CGRP, SP, or neurokinin A, may open an approach to discovery of new targets leading to the prevention of neurogenic inflammation.

Moreover, NI can be initiated by chronic stress, diet, hormonal fluctuations, or CSD. The NI-triggering factors may become a possible interventional target preventing the initiation of neuroinflammatory cascade. Immune reactions can also participate in NI. However, little is known about the interaction of the immune system in NI. Understanding the mechanism of NI trigger is essential in migraine research. Migraine headache is frequently observed in patients with cardiovascular diseases, respiratory diseases, psychiatric diseases, and restless legs syndrome. The disturbance of the serotonergic nervous system, the sympathetic nervous system, and the hypothalamic-pituitary-adrenal axis links migraine to mood disorders and obesity. Thus, identifying predisposing factors precipitating to the NI trigger may be a potential clue for a novel approach of migraine treatment.

Identification and usage of specific disease biomarkers can be suitable to guide the treatment and monitor the improvement or worsening of migraine symptoms during the treatment. MicroRNAs (miRs) may be useful as biomarkers of several diseases, including pain conditions and migraine in both adults and children. Deregulation of miRNAs has recently been described in migraine patients during attacks and pain-free periods [227]. In addition, significant levels of some miRs have been demonstrated in the serum of migraine children and adolescents without aura [228], suggesting that they are involved in the pathogenetic mechanisms of migraine, further enhancing the role of these miRs in the pathophysiology of migraine and their potential use as potential biomarkers.

We are untangling the puzzle of the mechanisms behind migraine attacks. However, finding the initial cause and effective treatment remains far away. The translational animal research currently tows forward the field of migraine research and may successfully serve as a savior of migraineurs in the future.

Author Contributions: Conceptualization, E.S.; writing—original draft preparation, E.S.; writing—review and editing, E.S., M.T., Á.S. and L.V.; visualization, E.S.; supervision, L.V.; project administration, L.V.; funding acquisition, M.T. and L.V. All authors have read and agreed to the published version of the manuscript.

Funding: The authors are funded by the Economic Development and Innovation Operational Programme [GINOP 2.3.2-15-2016-00034; GINOP 2.3.2-15-2016-00048], National Research, Development and Innovation Office [NKFIH-1279-2/2020 TKP 2020], TUDFO/47138-1/2019-ITM, and National Scientific Research Fund [OTKA138125].

Institutional Review Board Statement: Not applicable.

Informed Consent Statement: Not applicable.

Acknowledgments: All figures were created with BioRender.com.

Conflicts of Interest: The authors have no other relevant affiliations or financial involvement with any organization or entity with a financial interest in or financial conflict with the subject matter or materials discussed in the manuscript apart from those disclosed.

Abbreviations

α 7AChR	alpha-7 nicotinic receptor
2-AG	2-arachidonoylglycerol
AEA	anandamide
ATP	adenosine triphosphate
cAMP	cyclic adenosine monophosphate
CB1	cannabinoid receptor type 1
CBD	cannabidiol

CFA	Complete Freund's adjuvant
CGRP	calcitonin gene-related peptide
CNS	central nervous system
CSD	cortical spreading depression
CSF	cerebrospinal fluid
DR	nucleus raphe dorsalis
DRG	dorsal root ganglion
GLUT R	glutamate receptors
GPR35	G protein-coupled receptor 35
5-HT _{1B/1D}	5-hydroxytryptamine receptors
IDO	indoleamine 2,3-dioxygenase
IS	inflammatory soup
KMO	kynurenine 3-monooxygenase
KP	tryptophan-kynurenine metabolic pathway
KYNA	kynurenic acid
KYNU	kynureninase
LC	locus coeruleus
miRs	microRNAs
NGF	nerve-growth factor
NI	neurogenic inflammation
NK1	neurokinin 1
NKA	neurokinin A
nNOS	neuronal nitric oxide synthase
NO	nitric oxide
NPY	neuropeptide Y
NRM	nucleus raphe magnus
NSAIDs	nonsteroidal anti-inflammatory agents
NT	neurotransmitter
PAC1R	pituitary adenylate cyclase 1 receptor
PACAP	pituitary adenylate cyclase-activating polypeptide
PAG	the periaqueductal grey matter
PEA	palmitoylethanolamide
pERK	phosphorylated extracellular signal-regulated kinase
PKA	protein kinase A
PKC	protein kinase C
PLC	phospholipase C
PPE	plasma protein extravasation
SP	substance P
TACR1	tachykinin Receptor 1
TG	trigeminal ganglion
THC	tetrahydrokannabinol
TNC	caudal trigeminal nucleus
TNF α	tumor necrosis factor alpha
TRPV1	transient receptor potential vanilloid-1 receptor
TS	trigeminal system
VIP	vasoactive intestinal peptide
VPAC1/2	vasoactive intestinal peptide receptor 1/2

References

- Steiner, T.J.; Stovner, L.J.; Vos, T. GBD 2015: Migraine is the third cause of disability in under 50s. *J. Headache Pain* **2016**, *17*, 104. [CrossRef] [PubMed]
- GBD 2016 Disease and Injury Incidence and Prevalence Collaborators. Global, regional, and national incidence, prevalence, and years lived with disability for 328 diseases and injuries for 195 countries, 1990–2016: A systematic analysis for the Global Burden of Disease Study 2016. *Lancet* **2017**, *390*, 1211–1259. [CrossRef]
- Gazerani, P.; Cairns, B.E. Sex-Specific Pharmacotherapy for Migraine: A Narrative Review. *Front. Neurosci.* **2020**, *14*, 222. [CrossRef] [PubMed]
- Cerbo, R.; Pesare, M.; Aurilia, C.; Rondelli, V.; Barbanti, P. Socio-economic costs of migraine. *J. Headache Pain* **2001**, *2*, s15–s19. [CrossRef]

5. Mayans, L.; Walling, A. Acute Migraine Headache: Treatment Strategies. *Am. Fam. Physician* **2018**, *97*, 243–251.
6. Headache Classification Committee of the International Headache Society (IHS). The International Classification of Headache Disorders, 3rd edition (beta version). *Cephalalgia*. **2013**, *33*, 629–808. [CrossRef]
7. Headache Classification Subcommittee of the International Headache Society. The International Classification of Headache Disorders: 2nd edition. *Cephalalgia* **2004**, *24* (Suppl. S1), 9–160. [CrossRef]
8. Giffin, N.J.; Ruggiero, L.; Lipton, R.B.; Silberstein, S.D.; Tvedskov, J.F.; Olesen, J.; Altman, J.; Goadsby, P.J.; Macrae, A. Premonitory symptoms in migraine: An electronic diary study. *Neurology* **2003**, *60*, 935–940. [CrossRef]
9. Lai, J.; Dilli, E. Migraine Aura: Updates in Pathophysiology and Management. *Curr. Neurol. Neurosci. Rep.* **2020**, *20*, 17. [CrossRef] [PubMed]
10. van Dongen, R.M.; Haan, J. Symptoms related to the visual system in migraine. *F1000Research* **2019**, *8*, F1000. [CrossRef]
11. Pescador Ruschel, M.A.; De Jesus, O. Migraine Headache. In *StatPearls*; StatPearls Publishing: Treasure Island, FL, USA. Available online: <https://www.ncbi.nlm.nih.gov/books/NBK560787/> (accessed on 27 October 2021).
12. Chen, P.K.; Wang, S.J. Non-headache symptoms in migraine patients. *F1000Research* **2018**, *7*, 188. [CrossRef] [PubMed]
13. Goadsby, P.J.; Holland, P.R.; Martins-Oliveira, M.; Hoffmann, J.; Schankin, C.; Akerman, S. Pathophysiology of Migraine: A Disorder of Sensory Processing. *Physiol. Rev.* **2017**, *97*, 553–622. [CrossRef] [PubMed]
14. Edvinsson, L. Tracing neural connections to pain pathways with relevance to primary headaches. *Cephalalgia* **2011**, *31*, 737–747. [CrossRef]
15. Fusco, B.M.; Barzoi, G.; Agrò, F. Repeated intranasal capsaicin applications to treat chronic migraine. *Br. J. Anaesth* **2003**, *90*, 812. [CrossRef]
16. Cross, S.A. Pathophysiology of pain. *Mayo. Clin. Proc.* **1994**, *69*, 375–383. [CrossRef]
17. Matharu, M.S.; Bartsch, T.; Ward, N.; Frackowiak, R.S.; Weiner, R.; Goadsby, P.J. Central neuromodulation in chronic migraine patients with suboccipital stimulators: A PET study. *Brain* **2004**, *127 Pt 1*, 220–230. [CrossRef]
18. Vincent, M.; Hadjikhani, N. The cerebellum and migraine. *Headache* **2007**, *47*, 820–833. [CrossRef]
19. Ray, B.S.; Wolff, H.G. Experimental studies on headache: Pain sensitive structures of the head and their significance in headache. *Headache Arch. Surg.* **1940**, *41*, 813–856. [CrossRef]
20. Tunis, M.M.; Wolff, H.G. Studies on headache; long-term observations of the reactivity of the cranial arteries in subjects with vascular headache of the migraine type. *AMA Arch. Neurol. Psychiatry* **1953**, *70*, 551–557. [CrossRef]
21. Leao, A.A.P.; Morison, R.S. Propagation of spreading cortical depression. *J. Neurophysiol.* **1945**, *8*, 33–45. [CrossRef]
22. Ayata, C. Cortical spreading depression triggers migraine attack: Pro. *Headache* **2010**, *50*, 725–730. [CrossRef]
23. Lauritzen, M. Pathophysiology of the migraine aura. The spreading depression theory. *Brain* **1994**, *117*, 199–210. [CrossRef]
24. Olesen, J.; Goadsby, P.J. Synthesis of migraine mechanisms. In *The Headaches*, 2nd ed.; Olesen, J., Tfelt-Hansen, P., Welch, K.M.A., Eds.; Lippincott Williams & Wilkins: Philadelphia, PA, USA, 2000; pp. 331–336.
25. Moskowitz, M.A. Defining a pathway to discovery from bench to bedside: The trigeminovascular system and sensitization. *Headache* **2008**, *48*, 688–690. [CrossRef] [PubMed]
26. Weiller, C.; May, A.; Limmroth, V.; Jüptner, M.; Kaube, H.; Schayck, R.V.; Coenen, H.H.; Diener, H.C. Brain stem activation in spontaneous human migraine attacks. *Nat. Med.* **1995**, *1*, 658–660. [CrossRef]
27. Edvinsson, L.; Goadsby, P.J. Neuropeptides in the Cerebral Circulation: Relevance to Headache. *Cephalalgia* **1995**, *15*, 272–276. [CrossRef] [PubMed]
28. Akerman, S.; Holland, P.R.; Goadsby, P.J. Diencephalic and brainstem mechanisms in migraine. *Nat. Rev. Neurosci.* **2011**, *12*, 570–584. [CrossRef]
29. Fleetwood-Walker, S.M.; Hope, P.J.; Mitchell, R. Antinociceptive actions of descending dopaminergic tracts on cat and rat dorsal horn somatosensory neurones. *J. Physiol.* **1988**, *399*, 335–348. [CrossRef]
30. Settle, M. The hypothalamus. *Neonatal Netw.* **2000**, *19*, 9–14. [CrossRef]
31. Witten, A.; Marotta, D.; Cohen-Gadol, A. Developmental innervation of cranial dura mater and migraine headache: A narrative literature review. *Headache* **2021**, *61*, 569–575. [CrossRef] [PubMed]
32. Rozen, T.; Swidan, S.Z. Elevation of CSF tumor necrosis factor alpha levels in new daily persistent headache and treatment refractory chronic migraine. *Headache* **2007**, *47*, 1050–1055. [CrossRef]
33. Dowgjallo, N. Über die Nerven der harten Hirnhaut des Menschen und einiger Säuger. *Z. Anat. Entwickl. Gesch.* **1929**, *89*, 453–466. [CrossRef]
34. Grzybowski, J. L'innervation de la dure-mère crânienne chez l'homme. *Arch. Anat. Histol. Embryol.* **1931**, *14*, 387–428.
35. Penfield, W.; McNaughton, F. Dural headache and innervation of the dura mater. *Arch. Neuropsych.* **1940**, *44*, 43–75. [CrossRef]
36. Steiger, H.J.; Meakin, C.J. The meningeal representation in the trigeminal ganglion—an experimental study in the cat. *Headache* **1984**, *24*, 305–309. [CrossRef] [PubMed]
37. Uddman, R.; Hara, H.; Edvinsson, L. Neuronal pathways to the rat middle meningeal artery revealed by retrograde tracing and immunocytochemistry. *J. Auton. Nerv. Syst.* **1989**, *26*, 69–75. [CrossRef]
38. Strassman, A.M.; Raymond, S.A.; Burstein, R. Sensitization of meningeal sensory neurons and the origin of headaches. *Nature* **1996**, *384*, 560–564. [CrossRef] [PubMed]
39. Burstein, R.; Yamamura, H.; Malick, A.; Strassman, A.M. Chemical stimulation of the intracranial dura induces enhanced responses to facial stimulation in brain stem trigeminal neurons. *J. Neurophysiol.* **1998**, *79*, 964–982. [CrossRef] [PubMed]

40. Amenta, F.; Sancesario, G.; Ferrante, F.; Cavallotti, C. Acetylcholinesterase-containing nerve fibers in the dura mater of guinea pig, mouse, and rat. *J. Neural. Transm.* **1980**, *47*, 237–242. [CrossRef] [PubMed]
41. Schueler, M.; Neuhuber, W.L.; De Col, R.; Messlinger, K. Innervation of rat and human dura mater and pericranial tissues in the parieto-temporal region by meningeal afferents. *Headache* **2014**, *54*, 996–1009. [CrossRef]
42. Ebersberger, A.; Averbeck, B.; Messlinger, K.; Reeh, P.W. Release of substance P, calcitonin gene-related peptide and prostaglandin E2 from rat dura mater encephali following electrical and chemical stimulation in vitro. *Neuroscience* **1999**, *89*, 901–907. [CrossRef]
43. Lv, X.; Wu, Z.; Li, Y. Innervation of the cerebral dura mater. *Neuroradiol. J.* **2014**, *27*, 293–298. [CrossRef]
44. Asghar, M.S.; Hansen, A.E.; Amin, F.M.; van der Geest, R.J.; Koning, P.V.; Larsson, H.B.; Olesen, J.; Ashina, M. Evidence for a vascular factor in migraine. *Ann. Neurol.* **2011**, *69*, 635–645. [CrossRef]
45. Holzer, P. Neurogenic vasodilatation and plasma leakage in the skin. *Gen. Pharmacol.* **1998**, *30*, 5–11. [CrossRef]
46. Ottosson, A.; Edvinsson, L. Release of histamine from dural mast cells by substance P and calcitonin gene-related peptide. *Cephalalgia* **1997**, *17*, 166–174. [CrossRef]
47. Lennerz, J.K.; Rühle, V.; Ceppa, E.P.; Neuhuber, W.L.; Bunnett, N.W.; Grady, E.F.; Messlinger, K. Calcitonin receptor-like receptor (CLR), receptor activity-modifying protein 1 (RAMP1), and calcitonin gene-related peptide (CGRP) immunoreactivity in the rat trigeminovascular system: Differences between peripheral and central CGRP receptor distribution. *J. Comp. Neurol.* **2008**, *507*, 1277–1299. [CrossRef]
48. Raddant, A.C.; Russo, A.F. Calcitonin gene-related peptide in migraine: Intersection of peripheral inflammation and central modulation. *Expert Rev. Mol. Med.* **2011**, *13*, e36. [CrossRef] [PubMed]
49. Hökfelt, T.; Kellerth, J.O.; Nilsson, G.; Pernow, B. Substance p: Localization in the central nervous system and in some primary sensory neurons. *Science* **1975**, *190*, 889–890. [CrossRef] [PubMed]
50. Ribeiro-da-Silva, A.; Hökfelt, T. Neuroanatomical localisation of Substance P in the CNS and sensory neurons. *Neuropeptides* **2000**, *34*, 256–271. [CrossRef] [PubMed]
51. Snijsdelaar, D.G.; Dirksen, R.; Slappendel, R.; Crul, B.J. Substance P. *Eur. J. Pain* **2000**, *4*, 121–135. [CrossRef] [PubMed]
52. Graefe, S.; Mohiuddin, S.S. Biochemistry, Substance P. In *StatPearls*; StatPearls Publishing: Treasure Island, FL, USA. Available online: <https://www.ncbi.nlm.nih.gov/books/NBK554583/> (accessed on 27 October 2021).
53. Killingsworth, C.R.; Shore, S.A.; Alessandrini, F.; Dey, R.D.; Paulauskis, J.D. Rat alveolar macrophages express preprotachykinin gene-1 mRNA-encoding tachykinins. *Am. J. Physiol.* **1997**, *273*, L1073–L1081. [CrossRef] [PubMed]
54. Weinstock, J.V.; Blum, A.; Walder, J.; Walder, R. Eosinophils from granulomas in murine schistosomiasis mansoni produce substance P. *J. Immunol.* **1988**, *141*, 961–966.
55. Holzer, P.; Holzer-Petsche, U. Tachykinins in the gut. Part II. Roles in neural excitation, secretion and inflammation. *Pharmacol. Ther.* **1997**, *73*, 219–263. [CrossRef]
56. Pernow, B. Substance P. *Pharmacol. Rev.* **1983**, *35*, 85–141.
57. Gibbins, I.L.; Furness, J.B.; Costa, M.; MacIntyre, I.; Hillyard, C.J.; Girgis, S. Co-localization of calcitonin gene-related peptide-like immunoreactivity with substance P in cutaneous, vascular and visceral sensory neurons of guinea pigs. *Neurosci. Lett.* **1985**, *57*, 125–130. [CrossRef]
58. Battaglia, G.; Rustioni, A. Coexistence of glutamate and substance P in dorsal root ganglion neurons of the rat and monkey. *J. Comp. Neurol.* **1988**, *277*, 302–312. [CrossRef] [PubMed]
59. Malhotra, R. Understanding migraine: Potential role of neurogenic inflammation. *Ann. Indian Acad. Neurol.* **2016**, *19*, 175–182. [CrossRef]
60. Jansen-Olesen, I.; Hougaard Pedersen, S. PACAP and its receptors in cranial arteries and mast cells. *J. Headache Pain* **2018**, *19*, 16. [CrossRef] [PubMed]
61. Eftekhari, S.; Warfvinge, K.; Blixt, F.W.; Edvinsson, L. Differentiation of nerve fibers storing CGRP and CGRP receptors in the peripheral trigeminovascular system. *J. Pain* **2013**, *14*, 1289–1303. [CrossRef] [PubMed]
62. Nielsen, H.S.; Hannibal, J.; Fahrenkrug, J. Embryonic expression of pituitary adenylate cyclase-activating polypeptide in sensory and autonomic ganglia and in spinal cord of the rat. *J. Comp. Neurol.* **1998**, *394*, 403–415. [CrossRef]
63. Jansen-Olesen, I.; Baun, M.; Amrutkar, D.V.; Ramachandran, R.; Christophersen, D.V.; Olesen, J. PACAP-38 but not VIP induces release of CGRP from trigeminal nucleus caudalis via a receptor distinct from the PAC1 receptor. *Neuropeptides* **2014**, *48*, 53–64. [CrossRef] [PubMed]
64. Uddman, R.; Tajti, J.; Hou, M.; Sundler, F.; Edvinsson, L. Neuropeptide expression in the human trigeminal nucleus caudalis and in the cervical spinal cord C1 and C2. *Cephalalgia* **2002**, *22*, 112–116. [CrossRef]
65. Hashimoto, H.; Shintani, N.; Baba, A. New insights into the central PACAPergic system from the phenotypes in PACAP- and PACAP receptor-knockout mice. *Ann. N. Y. Acad. Sci.* **2006**, *1070*, 75–89. [CrossRef] [PubMed]
66. Martin, M.; Otto, C.; Santamarta, M.T.; Torrecilla, M.; Pineda, J.; Schütz, G.; Maldonado, R. Morphine withdrawal is modified in pituitary adenylate cyclase-activating polypeptide type I-receptor-deficient mice. *Brain Res. Mol. Brain Res.* **2003**, *110*, 109–118. [CrossRef]
67. Missig, G.; Roman, C.W.; Vizzard, M.A.; Braas, K.M.; Hammack, S.E.; May, V. Parabrachial nucleus (PbN) pituitary adenylate cyclase activating polypeptide (PACAP) signaling in the amygdala: Implication for the sensory and behavioral effects of pain. *Neuropharmacology* **2014**, *86*, 38–48. [CrossRef]
68. Kaiser, E.A.; Russo, A.F. CGRP and migraine: Could PACAP play a role too? *Neuropeptides* **2013**, *47*, 451–461. [CrossRef] [PubMed]

69. Zhang, Y.; Danielsen, N.; Sundler, F.; Mulder, H. Pituitary adenylate cyclase-activating peptide is upregulated in sensory neurons by inflammation. *Neuroreport* **1998**, *9*, 2833–2836. [CrossRef]
70. Kilinc, E.; Firat, T.; Tore, F.; Kiyani, A.; Kukner, A.; Tunçel, N. Vasoactive Intestinal peptide modulates c-Fos activity in the trigeminal nucleus and dura mater mast cells in sympathectomized rats. *J. Neurosci. Res.* **2015**, *93*, 644–650. [CrossRef]
71. Ohhashi, T.; Olschowka, J.A.; Jacobowitz, D.M. Vasoactive intestinal peptide inhibitory innervation in bovine mesenteric lymphatics. A histochemical and pharmacological study. *Circ. Res.* **1983**, *53*, 535–538. [CrossRef]
72. Kakurai, M.; Fujita, N.; Murata, S.; Furukawa, Y.; Demitsu, T.; Nakagawa, H. Vasoactive intestinal peptide regulates its receptor expression and functions of human keratinocytes via type I vasoactive intestinal peptide receptors. *J. Invest. Dermatol.* **2001**, *116*, 743–749. [CrossRef]
73. Cernuda-Morollón, E.; Martínez-Cambor, P.; Ramón, C.; Larrosa, D.; Serrano-Pertierra, E.; Pascual, J. CGRP and VIP levels as predictors of efficacy of Onabotulinumtoxin type A in chronic migraine. *Headache* **2014**, *54*, 987–995. [CrossRef]
74. Pellesi, L.; Al-Karagholi, M.A.; Chaudhry, B.A.; Lopez, C.L.; Snellman, J.; Hannibal, J.; Amin, F.M.; Ashina, M. Two-hour infusion of vasoactive intestinal polypeptide induces delayed headache and extracranial vasodilation in healthy volunteers. *Cephalalgia* **2020**, *40*, 1212–1223. [CrossRef] [PubMed]
75. Caterina, M.J.; Leffler, A.; Malmberg, A.B.; Martin, W.J.; Trafton, J.; Petersen-Zeit, K.R.; Koltzenburg, M.; Basbaum, A.I.; Julius, D. Impaired nociception and pain sensation in mice lacking the capsaicin receptor. *Science* **2000**, *288*, 306–313. [CrossRef] [PubMed]
76. Quartu, M.; Serra, M.P.; Boi, M.; Poddighe, L.; Picci, C.; Demontis, R.; Del Fiacco, M. TRPV1 receptor in the human trigeminal ganglion and spinal nucleus: Immunohistochemical localization and comparison with the neuropeptides CGRP and SP. *J. Anat.* **2016**, *229*, 755–767. [CrossRef] [PubMed]
77. Dux, M.; Rosta, J.; Messlinger, K. TRP Channels in the Focus of Trigeminal Nociceptor Sensitization Contributing to Primary Headaches. *Int. J. Mol. Sci.* **2020**, *21*, 342. [CrossRef] [PubMed]
78. Bevan, S.; Quallo, T.; Andersson, D.A. TRPV1. *Handb. Exp. Pharmacol.* **2014**, *222*, 207–245. [CrossRef]
79. Meents, J.E.; Neeb, L.; Reuter, U. TRPV1 in migraine pathophysiology. *Trends Mol. Med.* **2010**, *16*, 153–159. [CrossRef]
80. Yuan, H.; Silberstein, S.D. Histamine and Migraine. *Headache* **2018**, *58*, 184–193. [CrossRef]
81. Castillo, J.; Martínez, F.; Corredera, E.; Lema, M.; Noya, M. Migraña e histamina: Determinación de histidina en plasma y líquido cefalorraquídeo durante crisis de migraña [Migraine and histamine: Determining histidine in plasma and cerebrospinal fluid during migraine attacks]. *Rev. Neurol.* **1995**, *23*, 749–751.
82. Heatley, R.V.; Denburg, J.A.; Bayer, N.; Bienenstock, J. Increased plasma histamine levels in migraine patients. *Clin. Allergy* **1982**, *12*, 145–149. [CrossRef]
83. Foreman, J.C.; Jordan, C.C.; Oehme, P.; Renner, H. Structure-activity relationships for some substance P-related peptides that cause wheal and flare reactions in human skin. *J. Physiol.* **1983**, *335*, 449–465. [CrossRef] [PubMed]
84. Rosa, A.C.; Fantozzi, R. The role of histamine in neurogenic inflammation. *Br. J. Pharmacol.* **2013**, *170*, 38–45. [CrossRef] [PubMed]
85. Goadsby, P.J.; Knight, Y.E.; Hoskin, K.L.; Butler, P. Stimulation of an intracranial trigeminally-innervated structure selectively increases cerebral blood flow. *Brain Res.* **1997**, *751*, 247–252. [CrossRef]
86. Ji, R.R.; Xu, Z.Z.; Gao, Y.J. Emerging targets in neuroinflammation-driven chronic pain. *Nat. Rev. Drug Discov.* **2014**, *13*, 533–548. [CrossRef]
87. Goltz, F. Über gefässerweiternde nerven. *Pflueger Arch. Ges. Physiol.* **1874**, *9*, 185. [CrossRef]
88. Bayliss, W.M. On the origin from the spinal cord of the vaso-dilator fibres of the hind-limb, and on the nature of these fibres. *J. Physiol.* **1901**, *26*, 173–209. [CrossRef]
89. Dalessio, D.J. Vascular permeability and vasoactive substances: Their relationship to migraine. *Adv. Neurol.* **1974**, *4*, 395–401.
90. Moskowitz, M.A. The neurobiology of vascular head pain. *Ann. Neurol.* **1984**, *16*, 157–168. [CrossRef]
91. Ramachandran, R. Neurogenic inflammation and its role in migraine. *Semin. Immunopathol.* **2018**, *40*, 301–314. [CrossRef]
92. Bolay, H.; Reuter, U.; Dunn, A.K.; Huang, Z.; Boas, D.A.; Moskowitz, M.A. Intrinsic brain activity triggers trigeminal meningeal afferents in a migraine model. *Nat. Med.* **2002**, *8*, 136–142. [CrossRef]
93. Xanthos, D.N.; Sandkühler, J. Neurogenic neuroinflammation: Inflammatory CNS reactions in response to neuronal activity. *Nat. Rev. Neurosci.* **2014**, *15*, 43–53. [CrossRef]
94. Tajti, J.; Szok, D.; Majláth, Z.; Tuka, B.; Csáti, A.; Vécsei, L. Migraine and neuropeptides. *Neuropeptides* **2015**, *52*, 19–30. [CrossRef] [PubMed]
95. Berger, R.J.; Zuccarello, M.; Keller, J.T. Nitric oxide synthase immunoreactivity in the rat dura mater. *Neuroreport* **1994**, *5*, 519–521. [CrossRef]
96. Wallace, J.L. Nitric oxide as a regulator of inflammatory processes. *Mem. Inst. Oswaldo Cruz* **2005**, *100* (Suppl. 1), 5–9. [CrossRef] [PubMed]
97. Bellamy, J.; Bowen, E.J.; Russo, A.F.; Durham, P.L. Nitric oxide regulation of calcitonin gene-related peptide gene expression in rat trigeminal ganglia neurons. *Eur. J. Neurosci.* **2006**, *23*, 2057–2066. [CrossRef]
98. Strecker, T.; Dux, M.; Messlinger, K. Increase in meningeal blood flow by nitric oxide–interaction with calcitonin gene-related peptide receptor and prostaglandin synthesis inhibition. *Cephalalgia* **2002**, *22*, 233–241. [CrossRef] [PubMed]
99. Leston, J.M. Anatomie fonctionnelle du nerf trijumeau [Functional anatomy of the trigeminal nerve]. *Neurochirurgie* **2009**, *55*, 99–112. (In French) [CrossRef] [PubMed]
100. Pedersen, S.F.; Owsianik, G.; Nilius, B. TRP channels: An overview. *Cell Calcium* **2005**, *38*, 233–252. [CrossRef] [PubMed]

101. Planells-Cases, R.; Garcia-Sanz, N.; Morenilla-Palao, C.; Ferrer-Montiel, A. Functional aspects and mechanisms of TRPV1 involvement in neurogenic inflammation that leads to thermal hyperalgesia. *Pflugers Arch.* **2005**, *451*, 151–159. [CrossRef]
102. Bhave, G.; Zhu, W.; Wang, H.; Brasier, D.J.; Oxford, G.S.; Gereau, R.W., Iv. cAMP-dependent protein kinase regulates desensitization of the capsaicin receptor (VR1) by direct phosphorylation. *Neuron* **2002**, *35*, 721–731. [CrossRef]
103. Crandall, M.; Kwash, J.; Yu, W.; White, G. Activation of protein kinase C sensitizes human VR1 to capsaicin and to moderate decreases in pH at physiological temperatures in *Xenopus oocytes*. *Pain* **2002**, *98*, 109–117. [CrossRef]
104. Premkumar, L.S.; Ahern, G.P. Induction of vanilloid receptor channel activity by protein kinase C. *Nature* **2000**, *408*, 985–990. [CrossRef] [PubMed]
105. Vellani, V.; Mapplebeck, S.; Moriondo, A.; Davis, J.B.; McNaughton, P.A. Protein kinase C activation potentiates gating of the vanilloid receptor VR1 by capsaicin, protons, heat and anandamide. *J. Physiol.* **2001**, *534 Pt 3*, 813–825. [CrossRef]
106. Vergnolle, N.; Cenac, N.; Altier, C.; Cellars, L.; Chapman, K.; Zamponi, G.W.; Materazzi, S.; Nassini, R.; Liedtke, W.; Cattaruzza, F.; et al. A role for transient receptor potential vanilloid 4 in toxicity-induced neurogenic inflammation. *Br. J. Pharmacol.* **2010**, *159*, 1161–1173. [CrossRef] [PubMed]
107. Perini, F.; D'Andrea, G.; Galloni, E.; Pignatelli, F.; Billo, G.; Alba, S.; Bussone, G.; Toso, V. Plasma cytokine levels in migraineurs and controls. *Headache* **2005**, *45*, 926–931. [CrossRef]
108. Sarchielli, P.; Alberti, A.; Baldi, A.; Coppola, F.; Rossi, C.; Pierguidi, L.; Floridi, A.; Calabresi, P. Proinflammatory cytokines, adhesion molecules, and lymphocyte integrin expression in the internal jugular blood of migraine patients without aura assessed ictally. *Headache* **2006**, *46*, 200–207. [CrossRef] [PubMed]
109. Jacobs, B.; Dussor, G. Neurovascular contributions to migraine: Moving beyond vasodilation. *Neuroscience* **2016**, *338*, 130–144. [CrossRef] [PubMed]
110. Breier, G.; Risau, W. The role of vascular endothelial growth factor in blood vessel formation. *Trends Cell Biol.* **1996**, *6*, 454–456. [CrossRef]
111. Palmer, R.M.; Ashton, D.S.; Moncada, S. Vascular endothelial cells synthesize nitric oxide from L-arginine. *Nature* **1988**, *333*, 664–666. [CrossRef] [PubMed]
112. Mantovani, A.; Sozzani, S.; Introna, M. Endothelial activation by cytokines. *Ann. N. Y. Acad. Sci.* **1997**, *832*, 93–116. [CrossRef]
113. Yonehara, N.; Yoshimura, M. Effect of nitric oxide on substance P release from the peripheral endings of primary afferent neurons. *Neurosci. Lett.* **1999**, *271*, 199–201. [CrossRef]
114. Price, T.J.; Louria, M.D.; Candelario-Soto, D.; Dussor, G.O.; Jeske, N.A.; Patwardhan, A.M.; Diogenes, A.; Trott, A.A.; Hargreaves, K.M.; Flores, C.M. Treatment of trigeminal ganglion neurons in vitro with NGF, GDNF or BDNF: Effects on neuronal survival, neurochemical properties and TRPV1-mediated neuropeptide secretion. *BMC Neurosci.* **2005**, *6*, 4. [CrossRef]
115. Miyoshi, H.; Nakaya, Y. Calcitonin gene-related peptide activates the K⁺ channels of vascular smooth muscle cells via adenylate cyclase. *Basic Res. Cardiol.* **1995**, *90*, 332–336. [CrossRef] [PubMed]
116. Hanko, J.; Hardebo, J.E.; Kährström, J.; Owman, C.; Sundler, F. Calcitonin gene-related peptide is present in mammalian cerebrovascular nerve fibres and dilates pial and peripheral arteries. *Neurosci. Lett.* **1985**, *57*, 91–95. [CrossRef]
117. Wilkins, B.W.; Chung, L.H.; Tublitz, N.J.; Wong, B.J.; Minson, C.T. Mechanisms of vasoactive intestinal peptide-mediated vasodilation in human skin. *J. Appl. Physiol. (1985)* **2004**, *97*, 1291–1298. [CrossRef]
118. Williamson, D.J.; Hargreaves, R.J. Neurogenic inflammation in the context of migraine. *Microsc. Res. Tech.* **2001**, *53*, 167–178. [CrossRef] [PubMed]
119. Markowitz, S.; Saito, K.; Moskowitz, M.A. Neurogenically mediated plasma extravasation in dura mater: Effect of ergot alkaloids. A possible mechanism of action in vascular headache. *Cephalalgia* **1988**, *8*, 83–91. [CrossRef] [PubMed]
120. Lundy, F.T.; Linden, G.J. Neuropeptides and neurogenic mechanisms in oral and periodontal inflammation. *Crit. Rev. Oral Biol. Med.* **2004**, *15*, 82–98. [CrossRef]
121. De Swert, K.O.; Joos, G.F. Extending the understanding of sensory neuropeptides. *Eur. J. Pharmacol.* **2006**, *533*, 171–181. [CrossRef]
122. Koyuncu Irmak, D.; Kilinc, E.; Tore, F. Shared Fate of Meningeal Mast Cells and Sensory Neurons in Migraine. *Front. Cell Neurosci.* **2019**, *13*, 136. [CrossRef]
123. Theoharides, T.C.; Spanos, C.; Pang, X.; Alferes, L.; Ligris, K.; Letourneau, R.; Rozniecki, J.J.; Webster, E.; Chrousos, G.P. Stress-induced intracranial mast cell degranulation: A corticotropin-releasing hormone-mediated effect. *Endocrinology* **1995**, *136*, 5745–5750. [CrossRef]
124. Rozniecki, J.J.; Dimitriadou, V.; Lambrecht-Hall, M.; Pang, X.; Theoharides, T.C. Morphological and functional demonstration of rat dura mater mast cell-neuron interactions in vitro and in vivo. *Brain Res.* **1999**, *849*, 1–15. [CrossRef]
125. Theoharides, T.C.; Donelan, J.; Kandere-Grzybowska, K.; Konstantinidou, A. The role of mast cells in migraine pathophysiology. *Brain Res. Brain Res. Rev.* **2005**, *49*, 65–76. [CrossRef] [PubMed]
126. Schwartz, L.B. Mediators of human mast cells and human mast cell subsets. *Ann. Allergy* **1987**, *58*, 226–235.
127. Aich, A.; Afrin, L.B.; Gupta, K. Mast Cell-Mediated Mechanisms of Nociception. *Int. J. Mol. Sci.* **2015**, *16*, 29069–29092. [CrossRef]
128. Theoharides, T.C.; Alysandratos, K.D.; Angelidou, A.; Delivanis, D.A.; Sismanopoulos, N.; Zhang, B.; Asadi, S.; Vasiadi, M.; Weng, Z.; Miniati, A.; et al. Mast cells and inflammation. *Biochim. Biophys. Acta.* **2012**, *1822*, 21–33. [CrossRef] [PubMed]
129. Karatas, H.; Erdener, S.E.; Gursoy-Ozdemir, Y.; Lule, S.; Eren-Kocak, E.; Sen, Z.D.; Dalkara, T. Spreading depression triggers headache by activating neuronal Panx1 channels. *Science* **2013**, *339*, 1092–1095. [CrossRef]

130. Zhao, J.; Levy, D. Modulation of intracranial meningeal nociceptor activity by cortical spreading depression: A reassessment. *J. Neurophysiol.* **2015**, *113*, 2778–2785. [CrossRef] [PubMed]
131. Kempuraj, D.; Selvakumar, G.P.; Thangavel, R.; Ahmed, M.E.; Zaheer, S.; Raikwar, S.P.; Iyer, S.S.; Bhagavan, S.M.; Beladakere-Ramaswamy, S.; Zaheer, A. Mast Cell Activation in Brain Injury, Stress, and Post-traumatic Stress Disorder and Alzheimer's Disease Pathogenesis. *Front. Neurosci.* **2017**, *11*, 703. [CrossRef]
132. Baldwin, A.L. Mast cell activation by stress. *Methods Mol. Biol.* **2006**, *315*, 349–360. [CrossRef] [PubMed]
133. Sauro, K.M.; Becker, W.J. The stress and migraine interaction. *Headache* **2009**, *49*, 1378–1386. [CrossRef] [PubMed]
134. Radat, F. Stress et migraine [Stress and migraine]. *Rev. Neurol (Paris)* **2013**, *169*, 406–412. [CrossRef]
135. Davalos, D.; Grutzendler, J.; Yang, G.; Kim, J.V.; Zuo, Y.; Jung, S.; Littman, D.R.; Dustin, M.L.; Gan, W.B. ATP mediates rapid microglial response to local brain injury in vivo. *Nat. Neurosci.* **2005**, *8*, 752–758. [CrossRef]
136. Hanisch, U.K.; Kettenmann, H. Microglia: Active sensor and versatile effector cells in the normal and pathologic brain. *Nat. Neurosci.* **2007**, *10*, 1387–1394. [CrossRef]
137. Colton, C.A.; Gilbert, D.L. Production of superoxide anions by a CNS macrophage, the microglia. *FEBS Lett.* **1987**, *223*, 284–288. [CrossRef]
138. de Vries, H.E.; Blom-Roosemalen, M.C.; van Oosten, M.; de Boer, A.G.; van Berkel, T.J.; Breimer, D.D.; Kuiper, J. The influence of cytokines on the integrity of the blood-brain barrier in vitro. *J. Neuroimmunol.* **1996**, *64*, 37–43. [CrossRef]
139. Färber, K.; Kettenmann, H. Physiology of microglial cells. *Brain Res. Brain Res. Rev.* **2005**, *48*, 133–143. [CrossRef]
140. Pannasch, U.; Färber, K.; Nolte, C.; Blonski, M.; Yan Chiu, S.; Messing, A.; Kettenmann, H. The potassium channels Kv1.5 and Kv1.3 modulate distinct functions of microglia. *Mol. Cell Neurosci.* **2006**, *33*, 401–411. [CrossRef] [PubMed]
141. Pocock, J.M.; Kettenmann, H. Neurotransmitter receptors on microglia. *Trends Neurosci.* **2007**, *30*, 527–535. [CrossRef] [PubMed]
142. Taylor, D.L.; Jones, F.; Kubota, E.S.; Pocock, J.M. Stimulation of microglial metabotropic glutamate receptor mGlu2 triggers tumor necrosis factor alpha-induced neurotoxicity in concert with microglial-derived Fas ligand. *J. Neurosci.* **2005**, *25*, 2952–2964. [CrossRef]
143. Biber, K.; Neumann, H.; Inoue, K.; Boddeke, H.W. Neuronal 'On' and 'Off' signals control microglia. *Trends Neurosci.* **2007**, *30*, 596–602. [CrossRef]
144. Koyama, Y. Endothelin ET_B Receptor-Mediated Astrocytic Activation: Pathological Roles in Brain Disorders. *Int. J. Mol. Sci.* **2021**, *22*, 4333. [CrossRef] [PubMed]
145. Fiebich, B.L.; Schleicher, S.; Butcher, R.D.; Craig, A.; Lieb, K. The neuropeptide substance P activates p38 mitogen-activated protein kinase resulting in IL-6 expression independently from NF-kappa B. *J. Immunol.* **2000**, *165*, 5606–5611. [CrossRef]
146. Lin, R.C. Reactive astrocytes express substance-P immunoreactivity in the adult forebrain after injury. *Neuroreport* **1995**, *7*, 310–312. [CrossRef]
147. Carthew, H.L.; Ziebell, J.M.; Vink, R. Substance P-induced changes in cell genesis following diffuse traumatic brain injury. *Neuroscience* **2012**, *214*, 78–83. [CrossRef]
148. Bruno, P.P.; Carpino, F.; Carpino, G.; Zicari, A. An overview on immune system and migraine. *Eur. Rev. Med. Pharmacol. Sci.* **2007**, *11*, 245–248.
149. Turner, M.D.; Nedjai, B.; Hurst, T.; Pennington, D.J. Cytokines and chemokines: At the crossroads of cell signalling and inflammatory disease. *Biochim. Biophys. Acta.* **2014**, *1843*, 2563–2582. [CrossRef]
150. Edvinsson, L.; Haanes, K.A.; Warfvinge, K. Does inflammation have a role in migraine? *Nat. Rev. Neurol.* **2019**, *15*, 483–490. [CrossRef]
151. Roach, D.R.; Bean, A.G.; Demangel, C.; France, M.P.; Briscoe, H.; Britton, W.J. TNF regulates chemokine induction essential for cell recruitment, granuloma formation, and clearance of mycobacterial infection. *J. Immunol.* **2002**, *168*, 4620–4627. [CrossRef] [PubMed]
152. Conti, P.; D'Ovidio, C.; Conti, C.; Gallenga, C.E.; Lauritano, D.; Caraffa, A.; Kritas, S.K.; Ronconi, G. Progression in migraine: Role of mast cells and pro-inflammatory and anti-inflammatory cytokines. *Eur. J. Pharmacol.* **2019**, *844*, 87–94. [CrossRef] [PubMed]
153. Empl, M.; Sostak, P.; Riedel, M.; Schwarz, M.; Müller, N.; Förderreuther, S.; Straube, A. Decreased sTNF-RI in migraine patients? *Cephalalgia* **2003**, *23*, 55–58. [CrossRef] [PubMed]
154. Mueller, L.; Gupta, A.K.; Stein, T.P. Deficiency of tumor necrosis factor alpha in a subclass of menstrual migraineurs. *Headache* **2001**, *41*, 129–137. [CrossRef] [PubMed]
155. Christopherson, K., II; Hromas, R. Chemokine regulation of normal and pathologic immune responses. *Stem Cells* **2001**, *19*, 388–396. [CrossRef] [PubMed]
156. Tsay, H.J.; Liu, H.K.; Kuo, Y.H.; Chiu, C.S.; Liang, C.C.; Chung, C.W.; Chen, C.C.; Chen, Y.P.; Shiao, Y.J. EK100 and Antro-din C Improve Brain Amyloid Pathology in APP/PS1 Transgenic Mice by Promoting Microglial and Perivascular Clearance Pathways. *Int. J. Mol. Sci.* **2021**, *22*, 10413. [CrossRef] [PubMed]
157. Lam, S.; Hartmann, N.; Benfeitas, R.; Zhang, C.; Arif, M.; Turkez, H.; Uhlén, M.; Englert, C.; Knight, R.; Mardinoglu, A. Systems Analysis Reveals Ageing-Related Perturbations in Retinoids and Sex Hormones in Alzheimer's and Parkinson's Diseases. *Biomedicines* **2021**, *9*, 1310. [CrossRef] [PubMed]

158. Hsu, Y.L.; Hung, H.S.; Tsai, C.W.; Liu, S.P.; Chiang, Y.T.; Kuo, Y.H.; Shyu, W.C.; Lin, S.Z.; Fu, R.H. Peiminine Reduces ARTS-Mediated Degradation of XIAP by Modulating the PINK1/Parkin Pathway to Ameliorate 6-Hydroxydopamine Toxicity and α -Synuclein Accumulation in Parkinson's Disease Models In Vivo and In Vitro. *Int. J. Mol. Sci.* **2021**, *22*, 10240. [CrossRef] [PubMed]
159. Smagin, D.A.; Kovalenko, I.L.; Galyamina, A.G.; Belozertseva, I.V.; Tamkovich, N.V.; Baranov, K.O.; Kudryavtseva, N.N. Chronic Lithium Treatment Affects Anxious Behaviors and the Expression of Serotonergic Genes in Midbrain Raphe Nuclei of Defeated Male Mice. *Biomedicines* **2021**, *9*, 1293. [CrossRef]
160. Bezerra, F.; Niemietz, C.; Schmidt, H.H.J.; Zibert, A.; Guo, S.; Monia, B.P.; Gonçalves, P.; Saraiva, M.J.; Almeida, M.R. In Vitro and In Vivo Effects of SerpinA1 on the Modulation of Transthyretin Proteolysis. *Int. J. Mol. Sci.* **2021**, *22*, 9488. [CrossRef]
161. Lee, G.A.; Lin, Y.K.; Lai, J.H.; Lo, Y.C.; Yang, Y.S.H.; Ye, S.Y.; Lee, C.J.; Wang, C.C.; Chiang, Y.H.; Tseng, S.H. Maternal Immune Activation Causes Social Behavior Deficits and Hypomyelination in Male Rat Offspring with an Autism-Like Microbiota Profile. *Brain Sci.* **2021**, *11*, 1085. [CrossRef]
162. Garro-Martínez, E.; Fullana, M.N.; Florensa-Zanuy, E.; Senserrich, J.; Paz, V.; Ruiz-Bronchal, E.; Adell, A.; Castro, E.; Díaz, Á.; Pazos, Á.; et al. mTOR Knockdown in the Infralimbic Cortex Evokes a Depressive-Like State in Mouse. *Int. J. Mol. Sci.* **2021**, *22*, 8671. [CrossRef]
163. Santana-Santana, M.; Bayascas, J.R.; Giménez-Llort, L. Sex-Dependent Signatures, Time Frames and Longitudinal Fine-Tuning of the Marble Burying Test in Normal and AD-Pathological Aging Mice. *Biomedicines* **2021**, *9*, 994. [CrossRef]
164. Abuaish, S.; Al-Otaibi, N.M.; Abujamel, T.S.; Alzahrani, S.A.; Alotaibi, S.M.; AlShawakir, Y.A.; Aabed, K.; El-Ansary, A. Fecal Transplant and Bifidobacterium Treatments Modulate Gut Clostridium Bacteria and Rescue Social Impairment and Hippocampal BDNF Expression in a Rodent Model of Autism. *Brain Sci.* **2021**, *11*, 1038. [CrossRef] [PubMed]
165. Phebus, L.A.; Johnson, K.W. Dural inflammation model of migraine pain. *Curr. Protoc. Neurosci.* **2001**, *Chapter 9*, Unit9.1. [CrossRef]
166. Andreou, A.P.; Summ, O.; Charbit, A.R.; Romero-Reyes, M.; Goadsby, P.J. Animal models of headache: From bedside to bench and back to bedside. *Expert Rev. Neurother.* **2010**, *10*, 389–411. [CrossRef] [PubMed]
167. Lukács, M.; Haanes, K.A.; Majláth, Z.; Tajti, J.; Vécsei, L.; Warfvinge, K.; Edvinsson, L. Dural administration of inflammatory soup or Complete Freund's Adjuvant induces activation and inflammatory response in the rat trigeminal ganglion. *J. Headache Pain* **2015**, *16*, 564. [CrossRef] [PubMed]
168. Ebersberger, A.; Ringkamp, M.; Reeh, P.W.; Handwerker, H.O. Recordings from brain stem neurons responding to chemical stimulation of the subarachnoid space. *J. Neurophysiol.* **1997**, *77*, 3122–3133. [CrossRef] [PubMed]
169. Laborc, K.F.; Spekker, E.; Bohár, Z.; Szűcs, M.; Nagy-Grócz, G.; Fejes-Szabó, A.; Vécsei, L.; Párdutz, Á. Trigeminal activation patterns evoked by chemical stimulation of the dura mater in rats. *J. Headache Pain* **2020**, *21*, 101. [CrossRef] [PubMed]
170. Spekker, E.; Laborc, K.F.; Bohár, Z.; Nagy-Grócz, G.; Fejes-Szabó, A.; Szűcs, M.; Vécsei, L.; Párdutz, Á. Effect of dural inflammatory soup application on activation and sensitization markers in the caudal trigeminal nucleus of the rat and the modulatory effects of sumatriptan and kynurenic acid. *J. Headache Pain* **2021**, *22*, 17. [CrossRef]
171. Wieseler, J.; Ellis, A.; McFadden, A.; Stone, K.; Brown, K.; Cady, S.; Bastos, L.F.; Sprunger, D.; Rezvani, N.; Johnson, K.; et al. Supradural inflammatory soup in awake and freely moving rats induces facial allodynia that is blocked by putative immune modulators. *Brain Res.* **2017**, *1664*, 87–94. [CrossRef]
172. Oshinsky, M.L.; Gomonchareonsiri, S. Episodic dural stimulation in awake rats: A model for recurrent headache. *Headache* **2007**, *47*, 1026–1036. [CrossRef]
173. Melo-Carrillo, A.; Lopez-Avila, A. A chronic animal model of migraine, induced by repeated meningeal nociception, characterized by a behavioral and pharmacological approach. *Cephalalgia* **2013**, *33*, 1096–1105. [CrossRef]
174. Ferrari, M.D. Migraine. *Lancet* **1998**, *351*, 1043–1051. [CrossRef]
175. Malick, A.; Jakubowski, M.; Elmquist, J.K.; Saper, C.B.; Burstein, R. A neurohistochemical blueprint for pain-induced loss of appetite. *Proc. Natl. Acad. Sci. USA* **2001**, *98*, 9930–9935. [CrossRef] [PubMed]
176. Wieseler, J.; Ellis, A.; Sprunger, D.; Brown, K.; McFadden, A.; Mahoney, J.; Rezvani, N.; Maier, S.F.; Watkins, L.R. A novel method for modeling facial allodynia associated with migraine in awake and freely moving rats. *J. Neurosci. Methods* **2010**, *185*, 236–245. [CrossRef]
177. Chen, N.; Su, W.; Cui, S.H.; Guo, J.; Duan, J.C.; Li, H.X.; He, L. A novel large animal model of recurrent migraine established by repeated administration of inflammatory soup into the dura mater of the rhesus monkey. *Neural Regen. Res.* **2019**, *14*, 100–106. [CrossRef] [PubMed]
178. Saxena, P.R.; De Vries, P.; Villalón, C.M. 5-HT₁-like receptors: A time to bid goodbye. *Trends Pharmacol. Sci.* **1998**, *19*, 311–316. [CrossRef]
179. Buzzi, M.G.; Moskowitz, M.A. The antimigraine drug, sumatriptan (GR43175), selectively blocks neurogenic plasma extravasation from blood vessels in dura mater. *Br. J. Pharmacol.* **1990**, *99*, 202–206. [CrossRef]
180. Cutrer, F.M.; Yu, X.J.; Ayata, G.; Moskowitz, M.A.; Waeber, C. Effects of PNU-109,291, a selective 5-HT_{1D} receptor agonist, on electrically induced dural plasma extravasation and capsaicin-evoked c-fos immunoreactivity within trigeminal nucleus caudalis. *Neuropharmacology* **1999**, *38*, 1043–1053. [CrossRef]
181. Tanaka, M.; Török, N.; Vécsei, L. Are 5-HT₁ receptor agonists effective anti-migraine drugs? *Expert Opin. Pharmacother.* **2021**, *22*, 1221–1225. [CrossRef]

182. Moskowitz, M.A. Neurogenic versus vascular mechanisms of sumatriptan and ergot alkaloids in migraine. *Trends Pharmacol. Sci.* **1992**, *13*, 307–311. [CrossRef]
183. Pardutz, A.; Schoenen, J. NSAIDs in the Acute Treatment of Migraine: A Review of Clinical and Experimental Data. *Pharmaceuticals* **2010**, *3*, 1966–1987. [CrossRef]
184. Gallelli, L.; Avenoso, T.; Falcone, D.; Palleria, C.; Peltrone, F.; Esposito, M.; De Sarro, G.; Carotenuto, M.; Guidetti, V. Effects of acetaminophen and ibuprofen in children with migraine receiving preventive treatment with magnesium. *Headache* **2014**, *54*, 313–324. [CrossRef]
185. Goadsby, P.J.; Lipton, R.B.; Ferrari, M.D. Migraine—current understanding and treatment. *N. Engl. J. Med.* **2002**, *346*, 257–270. [CrossRef]
186. Tso, A.R.; Goadsby, P.J. Anti-CGRP Monoclonal Antibodies: The Next Era of Migraine Prevention? *Curr. Treat. Options Neurol.* **2017**, *19*, 27. [CrossRef] [PubMed]
187. Yuan, H.; Lauritsen, C.G.; Kaiser, E.A.; Silberstein, S.D. CGRP Monoclonal Antibodies for Migraine: Rationale and Progress. *BioDrugs* **2017**, *31*, 487–501. [CrossRef]
188. Negro, A.; Martelletti, P. Novel synthetic treatment options for migraine. *Expert Opin. Pharmacother.* **2021**, *22*, 907–922. [CrossRef]
189. Olesen, J.; Diener, H.C.; Husstedt, I.W.; Goadsby, P.J.; Hall, D.; Meier, U.; Pollentier, S.; Lesko, L.M. Calcitonin gene-related peptide receptor antagonist BIBN 4096 BS for the acute treatment of migraine. *N. Engl. J. Med.* **2004**, *350*, 1104–1110. [CrossRef]
190. Peroutka, S.J. Neurogenic inflammation and migraine: Implications for the therapeutics. *Mol. Interv.* **2005**, *5*, 304–311. [CrossRef] [PubMed]
191. Zimmer, A.; Zimmer, A.M.; Baffi, J.; Usdin, T.; Reynolds, K.; König, M.; Palkovits, M.; Mezey, E. Hypoalgesia in mice with a targeted deletion of the tachykinin 1 gene. *Proc. Natl. Acad. Sci. USA* **1998**, *95*, 2630–2635. [CrossRef] [PubMed]
192. Cao, Y.Q.; Mantyh, P.W.; Carlson, E.J.; Gillespie, A.M.; Epstein, C.J.; Basbaum, A.I. Primary afferent tachykinins are required to experience moderate to intense pain. *Nature* **1998**, *392*, 390–394. [CrossRef]
193. Lee, W.S.; Moussaoui, S.M.; Moskowitz, M.A. Blockade by oral or parenteral RPR 100893 (a non-peptide NK1 receptor antagonist) of neurogenic plasma protein extravasation within guinea-pig dura mater and conjunctiva. *Br. J. Pharmacol.* **1994**, *112*, 920–924. [CrossRef]
194. Goldstein, D.J.; Wang, O.; Saper, J.R.; Stoltz, R.; Silberstein, S.D.; Mathew, N.T. Ineffectiveness of neurokinin-1 antagonist in acute migraine: A crossover study. *Cephalalgia* **1997**, *17*, 785–790. [CrossRef] [PubMed]
195. Goldstein, D.J.; Offen, W.W.; Klein, E.G.; Phebus, L.A.; Hipskind, P.; Johnson, K.W.; Ryan, R.E., Jr. Lanepitant, an NK-1 antagonist, in migraine prevention. *Cephalalgia* **2001**, *21*, 102–106. [CrossRef] [PubMed]
196. Herrstedt, J.; Muss, H.B.; Warr, D.G.; Hesketh, P.J.; Eisenberg, P.D.; Raftopoulos, H.; Grunberg, S.M.; Gabriel, M.; Rodgers, A.; Hustad, C.M.; et al. Efficacy and tolerability of aprepitant for the prevention of chemotherapy-induced nausea and emesis over multiple cycles of moderately emetogenic chemotherapy. *Cancer* **2005**, *104*, 1548–1555. [CrossRef]
197. Jara-Oseguera, A.; Simon, S.A.; Rosenbaum, T. TRPV1: On the road to pain relief. *Curr. Mol. Pharmacol.* **2008**, *1*, 255–269. [CrossRef] [PubMed]
198. Leimuranta, P.; Khiroug, L.; Giniatullin, R. Emerging Role of (Endo)Cannabinoids in Migraine. *Front. Pharmacol.* **2018**, *9*, 420. [CrossRef]
199. Tsou, K.; Brown, S.; Sañudo-Peña, M.C.; Mackie, K.; Walker, J.M. Immunohistochemical distribution of cannabinoid CB1 receptors in the rat central nervous system. *Neuroscience* **1998**, *83*, 393–411. [CrossRef]
200. Matsuda, L.A.; Lolait, S.J.; Brownstein, M.J.; Young, A.C.; Bonner, T.I. Structure of a cannabinoid receptor and functional expression of the cloned cDNA. *Nature* **1990**, *346*, 561–564. [CrossRef] [PubMed]
201. Russo, E.B. Clinical endocannabinoid deficiency (CECD): Can this concept explain therapeutic benefits of cannabis in migraine, fibromyalgia, irritable bowel syndrome and other treatment-resistant conditions? *Neuro. Endocrinol. Lett.* **2004**, *25*, 31–39.
202. Greco, R.; Demartini, C.; Zanaboni, A.M.; Piomelli, D.; Tassorelli, C. Endocannabinoid System and Migraine Pain: An Update. *Front. Neurosci.* **2018**, *12*, 172. [CrossRef]
203. Cupini, L.M.; Bari, M.; Battista, N.; Argiró, G.; Finazzi-Agró, A.; Calabresi, P.; Maccarrone, M. Biochemical changes in endocannabinoid system are expressed in platelets of female but not male migraineurs. *Cephalalgia* **2006**, *26*, 277–281. [CrossRef]
204. Akerman, S.; Kaube, H.; Goadsby, P.J. Anandamide is able to inhibit trigeminal neurons using an in vivo model of trigeminovascular-mediated nociception. *J. Pharmacol. Exp. Ther.* **2004**, *309*, 56–63. [CrossRef]
205. Nagy-Grócz, G.; Bohár, Z.; Fejes-Szabó, A.; Laborc, K.F.; Spekker, E.; Tar, L.; Vécsei, L.; Párdutz, Á. Nitroglycerin increases serotonin transporter expression in rat spinal cord but anandamide modulated this effect. *J. Chem. Neuroanat.* **2017**, *85*, 13–20. [CrossRef] [PubMed]
206. Tajti, J.; Tuka, B.; Botz, B.; Helyes, Z.; Vécsei, L. Role of pituitary adenylate cyclase-activating polypeptide in nociception and migraine. *CNS Neurol. Disord. Drug Targets* **2015**, *14*, 540–553. [CrossRef]
207. Rubio-Beltrán, E.; Correnti, E.; Deen, M. PACAP38 and PAC1 receptor blockade: A new target for headache? *J. Headache Pain* **2018**, *19*, 64. [CrossRef] [PubMed]
208. Tanaka, M.; Vécsei, L. Monitoring the kynurenine system: Concentrations, ratios or what else? *Adv. Clin. Exp. Med.* **2021**, *30*, 775–778. [CrossRef] [PubMed]
209. Török, N.; Tanaka, M.; Vécsei, L. Searching for Peripheral Biomarkers in Neurodegenerative Diseases: The Tryptophan-Kynurenine Metabolic Pathway. *Int. J. Mol. Sci.* **2020**, *21*, 9338. [CrossRef]

210. Liao, C.; de Molliens, M.P.; Schneebeli, S.T.; Brewer, M.; Song, G.; Chatenet, D.; Braas, K.M.; May, V.; Li, J. Targeting the PAC1 Receptor for Neurological and Metabolic Disorders. *Curr. Top. Med. Chem.* **2019**, *19*, 1399–1417. [CrossRef]
211. Fejes, A.; Párdutz, Á.; Toldi, J.; Vécsei, L. Kynurenine metabolites and migraine: Experimental studies and therapeutic perspectives. *Curr. Neuropharmacol.* **2011**, *9*, 376–387. [CrossRef]
212. Tajti, J.; Majlath, Z.; Szok, D.; Csati, A.; Toldi, J.; Fülöp, F.; Vécsei, L. Novel kynurenic acid analogues in the treatment of migraine and neurodegenerative disorders: Preclinical studies and pharmaceutical design. *Curr. Pharm. Des.* **2015**, *21*, 2250–2258. [CrossRef]
213. Tanaka, M.; Toldi, J.; Vécsei, L. Exploring the Etiological Links behind Neurodegenerative Diseases: Inflammatory Cytokines and Bioactive Kynurenines. *Int. J. Mol. Sci.* **2020**, *21*, 2431. [CrossRef]
214. Tanaka, M.; Tóth, F.; Polyák, H.; Szabó, Á.; Mándi, Y.; Vécsei, L. Immune Influencers in Action: Metabolites and Enzymes of the Tryptophan-Kynurenine Metabolic Pathway. *Biomedicines* **2021**, *9*, 734. [CrossRef]
215. Tanaka, M.; Török, N.; Tóth, F.; Szabó, Á.; Vécsei, L. Co-Players in Chronic Pain: Neuroinflammation and the Tryptophan-Kynurenine Metabolic Pathway. *Biomedicines* **2021**, *9*, 897. [CrossRef]
216. Curto, M.; Lionetto, L.; Negro, A.; Capi, M.; Fazio, F.; Giamberardino, M.A.; Simmaco, M.; Nicoletti, F.; Martelletti, P. Altered kynurenine pathway metabolites in serum of chronic migraine patients. *J. Headache Pain* **2015**, *17*, 47. [CrossRef]
217. Sarchielli, P.; Di Filippo, M.; Nardi, K.; Calabresi, P. Sensitization, glutamate, and the link between migraine and fibromyalgia. *Curr. Pain Headache Rep.* **2007**, *11*, 343–351. [CrossRef]
218. Nagy-Grócz, G.; Laborc, K.F.; Veres, G.; Bajtai, A.; Bohár, Z.; Zádori, D.; Fejes-Szabó, A.; Spekker, E.; Vécsei, L.; Párdutz, Á. The Effect of Systemic Nitroglycerin Administration on the Kynurenine Pathway in the Rat. *Front. Neurol.* **2017**, *14*, 278. [CrossRef]
219. Mándi, Y.; Vécsei, L. The kynurenine system and immunoregulation. *J. Neural Trans.* **2012**, *119*, 197–209. [CrossRef] [PubMed]
220. Lukács, M.; Tajti, J.; Fülöp, F.; Toldi, J.; Edvinsson, L.; Vécsei, L. Migraine, Neurogenic Inflammation, Drug Development - Pharmacochimical Aspects. *Curr. Med. Chem.* **2017**, *24*, 3649–3665. [CrossRef] [PubMed]
221. Jovanovic, F.; Candido, K.D.; Knezevic, N.N. The Role of the Kynurenine Signaling Pathway in Different Chronic Pain Conditions and Potential Use of Therapeutic Agents. *Int. J. Mol. Sci.* **2020**, *21*, 6045. [CrossRef] [PubMed]
222. Hesselink, J.M.K. New targets in pain, non-neuronal cells, and the role of palmitoylethanolamide. *Open Pain J.* **2012**, *5*, 2–23. [CrossRef]
223. Chirchiglia, D.; Paventi, S.; Seminara, P.; Cione, E.; Gallelli, L. N-Palmitoyl Ethanol Amide Pharmacological Treatment in Patients With Nonsurgical Lumbar Radiculopathy. *J. Clin. Pharmacol.* **2018**, *58*, 733–739. [CrossRef] [PubMed]
224. Chirchiglia, D.; Della Torre, A.; Signorelli, F.; Volpentesta, G.; Guzzi, G.; Stroschio, C.A.; Deodato, F.; Gabriele, D.; Lavano, A. Administration of palmitoylethanolamide in combination with topiramate in the preventive treatment of nummular headache. *Int. Med. Case Rep. J.* **2016**, *18*, 193–195. [CrossRef] [PubMed]
225. Chirchiglia, D.; Cione, E.; Caroleo, M.C.; Wang, M.; Di Mizio, G.; Faedda, N.; Giacolini, T.; Siviglia, S.; Guidetti, V.; Gallelli, L. Effects of Add-On Ultramicronized N-Palmitol Ethanol Amide in Patients Suffering of Migraine With Aura: A Pilot Study. *Front. Neurol.* **2018**, *17*, 674. [CrossRef] [PubMed]
226. Karakurum Göksel, B. The Use of Complementary and Alternative Medicine in Patients with Migraine. *Noro. Psikiyatri Arsivi* **2013**, *50* (Suppl. 1), S41–S46. [CrossRef] [PubMed]
227. Tafuri, E.; Santovito, D.; de Nardis, V.; Marcantonio, P.; Paganelli, C.; Affaitati, G.; Bucci, M.; Mezzetti, A.; Giamberardino, M.A.; Cipollone, F. MicroRNA profiling in migraine without aura: Pilot study. *Ann. Med.* **2015**, *47*, 468–473. [CrossRef] [PubMed]
228. Gallelli, L.; Cione, E.; Peltrone, F.; Siviglia, S.; Verano, A.; Chirchiglia, D.; Zampogna, S.; Guidetti, V.; Sammartino, L.; Montana, A.; et al. Hsa-miR-34a-5p and hsa-miR-375 as Biomarkers for Monitoring the Effects of Drug Treatment for Migraine Pain in Children and Adolescents: A Pilot Study. *J. Clin. Med.* **2019**, *27*, 928. [CrossRef] [PubMed]



Article

The Class I HDAC Inhibitor, MS-275, Prevents Oxaliplatin-Induced Chronic Neuropathy and Potentiates Its Antiproliferative Activity in Mice

Sylvain Lamoine ^{1,†}, MéliSSa Cumenal ^{1,†}, David A. Barriere ¹, Vanessa Pereira ¹, Mathilde Fereyrolles ¹, Laëtitia Prival ¹, Julie Barbier ¹, Ludivine Boudieu ¹, Emilie Brasset ², Benjamin Bertin ², Yoan Renaud ², Elisabeth Miot-Noirault ³, Marie-Ange Civiale ⁴, David Balayssac ^{1,5}, Youssef Aissouni ¹, Alain Eschalier ^{1,6} and Jérôme Busserolles ^{1,*}

- ¹ UMR 1107 Inserm/UCA, CHU Clermont-Ferrand, Université Clermont Auvergne, Neuro-Dol, 63000 Clermont-Ferrand, France; sylvain.lamoine@uca.fr (S.L.); melissa.cumenal@ucalgary.ca (M.C.); david.a.barriere@gmail.com (D.A.B.); vanesp_63@hotmail.com (V.P.); mathilde.fereyrolles@ans-biotech.com (M.F.); laetitia.prival@uca.fr (L.P.); julie.barbier@uca.fr (J.B.); lboudieu@chu-clermontferrand.fr (L.B.); david.balayssac@uca.fr (D.B.); youssef.aissouni@inserm.fr (Y.A.); alain.eschalier@uca.fr (A.E.)
 - ² iGRéD, CNRS, INSERM, Faculté de Médecine, Université Clermont Auvergne, 63000 Clermont-Ferrand, France; emilie.brasset@uca.fr (E.B.); benjamin.bertin@uca.fr (B.B.); yoan.renaud@uca.fr (Y.R.)
 - ³ UMR 1240 INSERM IMoST, Université Clermont Auvergne, 58 Rue Montalembert, 63000 Clermont-Ferrand, France; elisabeth.noirault@uca.fr
 - ⁴ ACCePPT—AutomédiCation aCcompagnement Pluriprofessionnel Patient, Université Clermont Auvergne, 63000 Clermont-Ferrand, France; marie-ange.civiale@uca.fr
 - ⁵ CHU Clermont-Ferrand, Délégation à la Recherche Clinique et à l'Innovation, 63000 Clermont-Ferrand, France
 - ⁶ Institut Analgesia, Faculté de Médecine, BP38, 63001 Clermont-Ferrand, France
- * Correspondence: jerome.busserolles@uca.fr; Tel.: +33-(0)-4-7317-8235; Fax: +33-(0)-4-7327-7162
† These authors contributed equally to the work.

Citation: Lamoine, S.; Cumenal, M.; Barriere, D.A.; Pereira, V.; Fereyrolles, M.; Prival, L.; Barbier, J.; Boudieu, L.; Brasset, E.; Bertin, B.; et al. The Class I HDAC Inhibitor, MS-275, Prevents Oxaliplatin-Induced Chronic Neuropathy and Potentiates Its Antiproliferative Activity in Mice. *Int. J. Mol. Sci.* **2022**, *23*, 98. <https://doi.org/10.3390/ijms23010098>

Academic Editors: Masaru Tanaka and Lydia Giménez-Llort

Received: 4 November 2021
Accepted: 17 December 2021
Published: 22 December 2021

Publisher's Note: MDPI stays neutral with regard to jurisdictional claims in published maps and institutional affiliations.



Copyright: © 2021 by the authors. Licensee MDPI, Basel, Switzerland. This article is an open access article distributed under the terms and conditions of the Creative Commons Attribution (CC BY) license (<https://creativecommons.org/licenses/by/4.0/>).

Abstract: Oxaliplatin, the first-line chemotherapeutic agent against colorectal cancer (CRC), induces peripheral neuropathies, which can lead to dose limitation and treatment discontinuation. Downregulation of potassium channels, which involves histone deacetylase (HDAC) activity, has been identified as an important tuner of acute oxaliplatin-induced hypersensitivity. MS-275, a class I histone deacetylase inhibitor (HDACi), prevents acute oxaliplatin-induced peripheral neuropathy (OIPN). Moreover, MS-275 exerts anti-tumor activity in several types of cancers, including CRC. We thus hypothesized that MS-275 could exert both a preventive effect against OIPN and potentially a synergistic effect combined with oxaliplatin against CRC development. We first used RNAseq to assess transcriptional changes occurring in DRG neurons from mice treated by repeated injection of oxaliplatin. Moreover, we assessed the effects of MS-275 on chronic oxaliplatin-induced peripheral neuropathy development in vivo on *APC^{Min/+}* mice and on cancer progression when combined with oxaliplatin, both in vivo on *APC^{Min/+}* mice and in a mouse model of an orthotopic allograft of the CT26 cell line as well as in vitro in T84 and HT29 human CRC cell lines. We found 741 differentially expressed genes (DEGs) between oxaliplatin- and vehicle-treated animals. While acute OIPN is known as a channelopathy involving HDAC activity, chronic OIPN exerts weak ion channel transcriptional changes and no HDAC expression changes in peripheral neurons from OIPN mice. However, MS-275 prevents the development of sensory neuropathic symptoms induced by repeated oxaliplatin administration in *APC^{Min/+}* mice. Moreover, combined with oxaliplatin, MS-275 also exerts synergistic antiproliferative and increased survival effects in CT26-bearing mice. Consistently, combined drug associations exert synergic apoptotic and cell death effects in both T84 and HT29 human CRC cell lines. Our results strongly suggest combining oxaliplatin and MS-275 administration in CRC patients in order to potentiate the antiproliferative action of chemotherapy, while preventing its neurotoxic effect.

Keywords: colorectal cancer; oxaliplatin; peripheral neuropathy; histone deacetylase inhibitor; MS-275; *APC^{Min/+}* mice; T84 cells; HT29 cells; CT26 cells; orthotopic model of colorectal cancer

1. Introduction

Oxaliplatin, in combination with 5-fluorouracil, is a standard treatment option for primary and metastasized colorectal cancer [1], which induces a peripheral neuropathy, known to be uniquely due to oxaliplatin [2], which can lead to dose limitation and treatment discontinuation [2,3]. Oxaliplatin-induced peripheral neuropathy (OIPN) is characterized by paresthesias and dysesthesias, which can be triggered or exacerbated by cold exposure as soon as after the first infusion of the drug in 90% of patients [2,4]. These neuropathic symptoms do not always completely resolve between treatment cycles [2], and 30–50% of patients suffer from chronic OIPN [5]. Currently, none of the drugs used for prevention or treatment of OIPN have been shown to be sufficiently effective to be routinely incorporated into clinical practice [6,7], and strategies to control neuropathy rely essentially on modifications of dosage and infusion scheme, thus decreasing the chances of survival [8]. Moreover, cumulative doses of chemotherapy are probably not a predictive factor of chemotherapy-induced neuropathy (CIPN) [9], suggesting that modifications of dosage and infusion scheme might not affect the development of neuropathic symptoms in cancer survivors.

Evidence has shown that oxaliplatin causes ion channel expression modulations in dorsal root ganglia (DRG) neurons [10–16], which are thought to contribute to acute peripheral hypersensitivity. Most dysregulated genes encode for ion channels involved in cold and mechanical perception, including members of the transient receptor potential (TRP), the two-pore potassium channels (K2P) and the voltage-dependent potassium (Kv) families. We recently demonstrated that oxaliplatin-mediated downregulation of K⁺ channels of the K2P and Kv families involves a transcription factor known as the neuron-restrictive silencer factor (NRSF), and its epigenetic corepressors, class I histone deacetylases (HDACs) [17]. Furthermore, the class I HDAC inhibitor, MS-275, exerted a preventive effect against both neuropathy and K⁺ channels downregulation after a single-dose of administered oxaliplatin [17]. Whether sustained peripheral epigenetic events are involved in OIPN chronicization is not known. Oxaliplatin-induced chronic neuropathy is rather thought to be caused by platinum accumulation in DRG neurons [18–20], leading to morphologic and functional changes in DRG neurons. Mitochondrial toxicity, as well as satellite glial cell activation in DRG, favoring the development of neuroinflammation, could also contribute to chronic OIPN establishment [21,22]. Besides—or as a consequence of peripheral sensitization—cumulative evidence suggests that spinal neuronal plasticity plays a critical role in the persistence of OIPN [23,24]; with the mechanisms still poorly defined. In the present study, we used repeated oxaliplatin administration and analyzed whole transcriptomic changes that occur in DRG neurons from OIPN mice as compared with vehicle-treated animals.

Since we observed a preventive effect of MS-275 against acute OIPN development, we wondered whether this molecule would be able to exert a preventive effect against chronic OIPN. Furthermore, HDAC inhibitors are promising therapeutic molecules against several pathological states, including cancer [25]. Several class I HDACs—HDAC1, 2, 3—and eight isoforms have been involved in colorectal cancer [26,27]. In a recent meta-analysis, the expression level of HDAC1 in colorectal cancer was found to be higher and closely associated with tumor stage and tumor grade than that in noncancerous tissue. In addition, patients with low HDAC1 expression showed better overall survival than did those with high HDAC1 expression in gastrointestinal malignancy [26]. HDAC3, another class I HDAC isoform, was found to be upregulated in 52.1% of colorectal tumor tissue specimens [28].

In this context, we hypothesized that MS-275 could exert both a preventive effect against OIPN and potentially a synergistic effect combined with oxaliplatin against CRC development. Thus, we assessed the effects of MS-275 on chronic OIPN development and on cancer progression when combined to oxaliplatin both in vitro on different human colorectal cancer cell lines and in vivo on mice models of colorectal cancer.

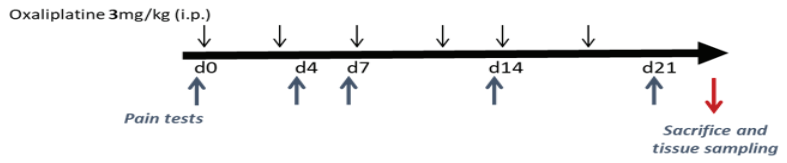
2. Results

2.1. Transcriptomic Changes Observed in DRG Neurons from Mice Treated with Repeated Oxaliplatin Administration

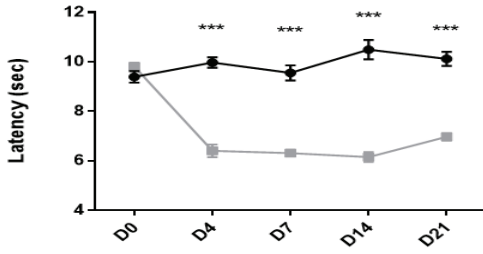
Prolonged oxaliplatin treatment is known to induce persistent peripheral neuropathy that particularly affects extremities. We evaluated the development of these symptoms in C57Bl/6J mice administered with a clinically relevant dose of oxaliplatin (3 mg/kg, i.p.) twice per week for 3 weeks (Figure 1A). Cold and mechanical hypersensitivity develop from day 4 and persisted until the end of the experiment (day 21) in oxaliplatin-treated mice, as evaluated using the paw immersion test (Figure 1B, Supplementary Table S1) and von Frey test, respectively (Figure 1C, Supplementary Table S1).

We then performed a comparative RNAseq analysis in DRG neurons of oxaliplatin- and vehicle-treated animals at end-point of the experiment. We found 741 differentially expressed genes (DEGs) between oxaliplatin- and vehicle-treated animals. Respectively, 342 and 399 genes were up- and downregulated in OIPN DRG neurons as compared to control animals (Figure 1D,E. For full list of upregulated and downregulated genes following oxaliplatin treatment, see Supplementary data S1 and S2, respectively). Of note, while acute OIPN is known as a channelopathy, including transcriptional variation of a variety of ion channels involved in cold and pain perception, only a discrete number of ion channels (GIRK1 and Kv3.3) showed distinct mRNA levels in DRG neurons between OIPN and sham animals at day 21. We previously showed an increase in HDAC3 expression in DRG neurons from mice administered with a single dose of oxaliplatin [17]. However, in the present work, we failed to observe any transcriptional differences of class I HDACs (HDAC1, HDAC2, and HDAC3) in mice treated with repeated dose of vehicle or oxaliplatin. However, several genes encoding for methyl transferase (Setd1b, Mettl8, kmt2d) were found to be downregulated, and genes associated to histone deacetylase complex such as Sap301 [29] and Banp [30] were upregulated in DRG neurons from oxaliplatin-treated animals (see supplementary data S1). As DRGs are a heterogeneous tissue containing the cell bodies of peripheral nerves, epithelial cells, fibroblasts, glial cells, and immune cells, DEGs discovered following treatment with oxaliplatin cannot be unequivocally assigned to sensory neurons alone. We thus performed CTEN, a web-based analytical platform using a highly expressed, cell-specific gene database to identify enriched cell types from transcriptomic data [31] to gain insights into cell-specific effects of oxaliplatin (Figure 2A). We also performed GO-enrichment analysis to further elucidate potential biological functions (Figure 2B) and cellular components (Figure 2C) associated with the 741 overlapping DEGs. For molecular functions, the overlapping DEGs were mainly associated with axogenesis, axon development, myelin sheath, and actin and filament organization. Cellular organelles (Golgi, endoplasmic reticulum, and mitochondria) component genes were also significantly differentially expressed.

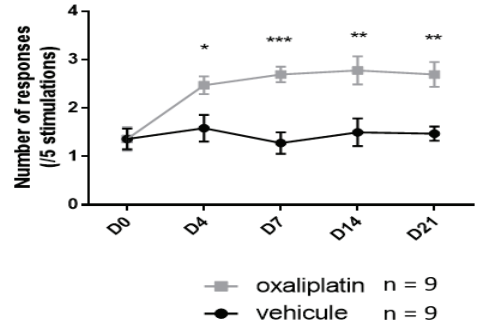
A



B



C



D

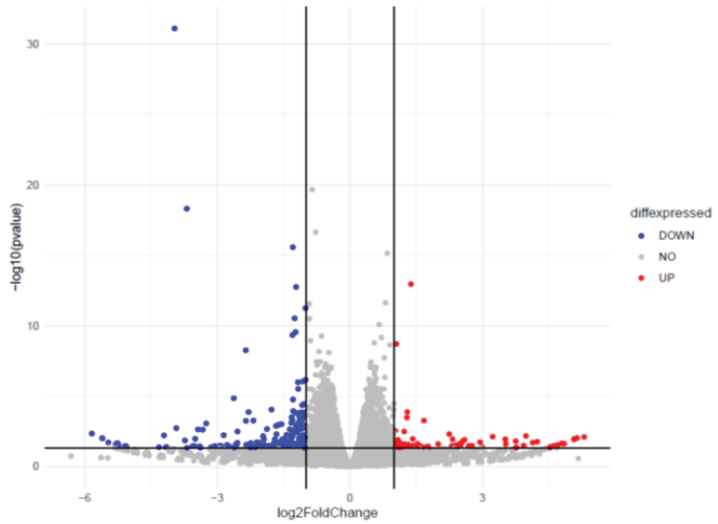


Figure 1. Cont.

E

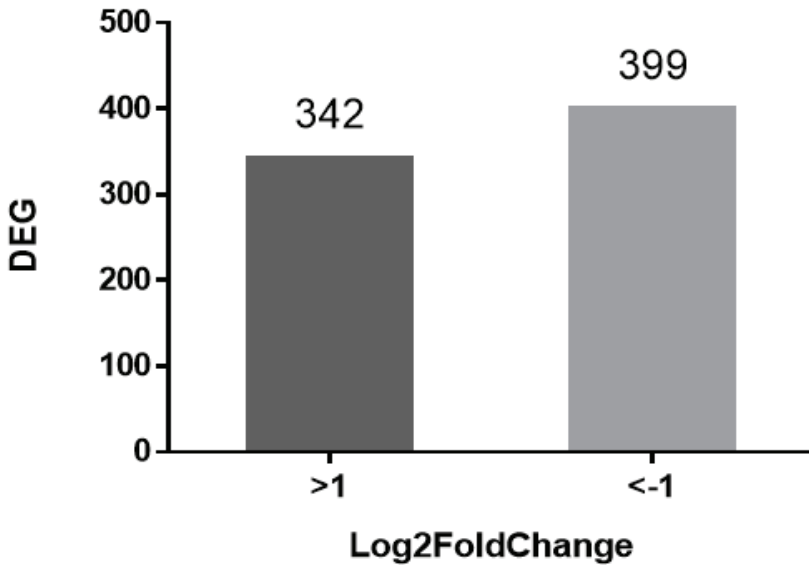


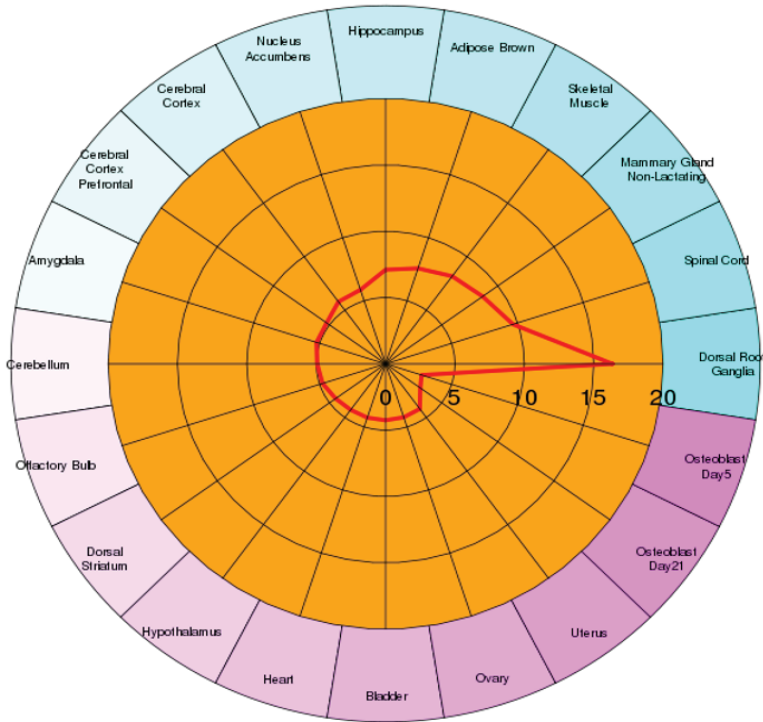
Figure 1. Analysis of DEG in mouse lumbar dorsal root ganglia L4 to L6 following repeated oxaliplatin administration. (A) Experimental design: C57Bl/6J mice received oxaliplatin (3 mg/kg, i.p.) or vehicle (Glucose 5%) twice a week for 3 weeks. Both thermal cold (B) and mechanical (C) pain hypersensitivity developed as soon as after day 4 in oxaliplatin treated group. Values are mean \pm SEM (n = nine per group). Statistical analysis was performed using a two-way repeated measure analysis of variance (RM ANOVA), detailed in Supplementary Table S1, and a Tukey's multi-comparisons post hoc test; *, $p < 0.05$, **, $p < 0.01$, ***, $p < 0.001$, vehicle *versus* oxaliplatin. (D) Volcano plot of all DEGs following oxaliplatin administration showing the most highly upregulated (log2fold change > 1) or downregulated (log2fold change < -1) genes. Only genes with $\text{Padj} < 0.05$ and log2fold change greater than 1 or smaller than -1 were used for further analysis. (E) Oxaliplatin administration caused the upregulation of 342 DEGs and the downregulation of 399 DEGs.

2.2. MS-275 Prevents Oxaliplatin-Induced Chronic Neuropathy in Mice

We recently showed that the class I HDAC inhibitor, MS-275, significantly prevented pain symptoms induced after a single oxaliplatin injection in mice [17]. Moreover, it is increasingly recognized that histone modifications play a crucial role in cancer initiation and progression, including in CRC [32]. In vitro experiments and animal models have shown anti-tumor activities of HDAC inhibitors [33]. Thus, we hypothesized that MS-275 would potentially exert beneficial effects, both against neuropathic symptoms induced by oxaliplatin and against colorectal cancer progression. For that, we evaluated the development of these symptoms in mice administered with oxaliplatin (3 mg/kg, i.p.) twice per week for 3 weeks with or without MS-275 (15mg/kg) administered by oral gavage half an hour before each oxaliplatin injection (Figure 3A). We first assessed the effect of oxaliplatin and MS-275 on $APC^{Min/+}$ mice, a model of intestinal neoplasia, and on the C57BL/6J background [34]. Cold hypersensitivity developed in oxaliplatin-treated $APC^{Min/+}$ mice (Figure 3B, Supplementary Table S1) from day 4 after the first injection as evidenced by the significant decrease in tail withdrawal latency in response to a noxious cold stimulation (10 °C). Mechanical hypersensitivity was also observed with a similar time course in oxaliplatin-treated animals (Figure 3C, Supplementary Table S1). MS-275 administration significantly prevented both cold (Figure 3B) (two-way ANOVA analysis: treatment effect

($p < 0.0001$); time effect ($p = 0.0004$), interaction ($p = 0.0174$) and mechanical hypersensitivities (Figure 3C) (two-way ANOVA analysis: oxaliplatin effect (two-way ANOVA analysis: treatment effect ($p = 0.0002$); MS-275 effect ($p < 0.0001$), interaction ($p = 0.0035$)) induced by oxaliplatin.

A



B

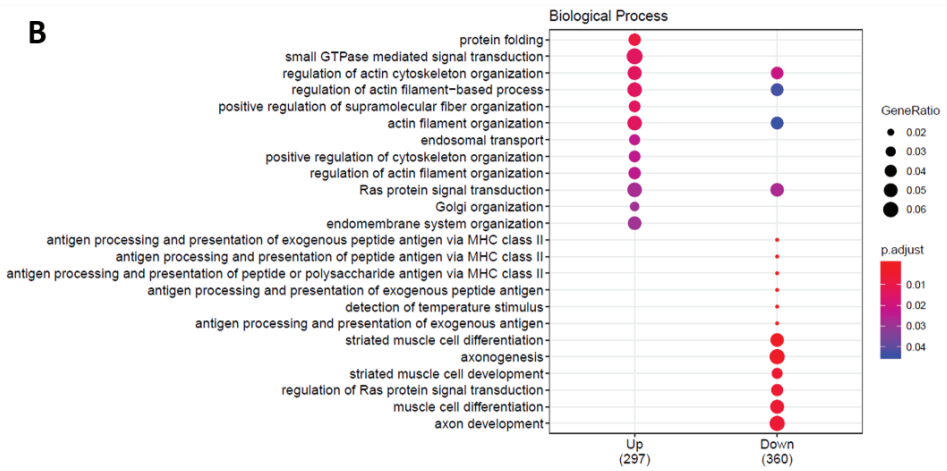


Figure 2. Cont.

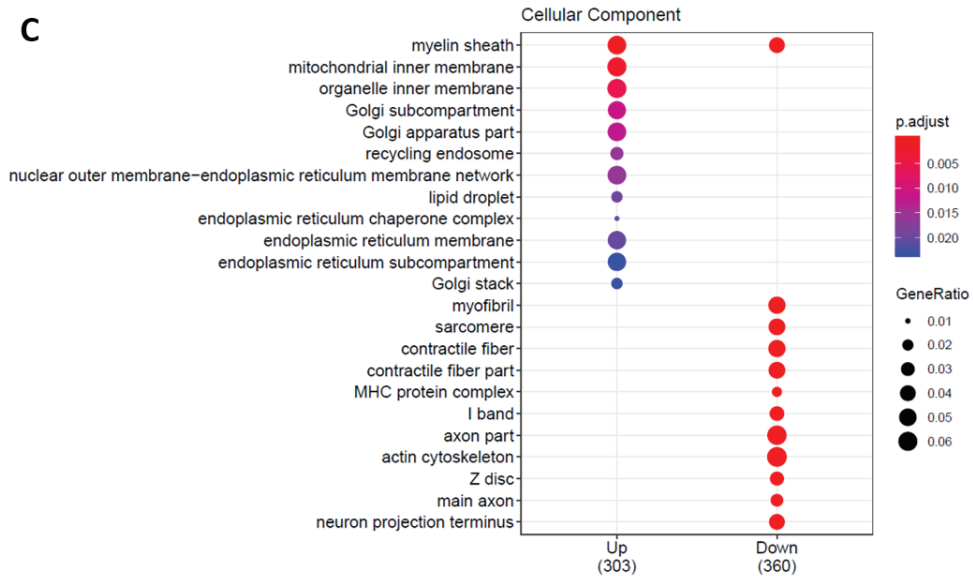


Figure 2. Cell type specific effect of oxaliplatin and enrichment analysis of the overlapping DEGs. (A) Cell type enrichment analysis (CTEN) of DEG in lumbar dorsal root ganglia L3 to L5 following repeated oxaliplatin administration. CTEN was performed using the CTen tool. The score is generated using one-sided, Fisher's exact test for enrichment and it is shown as the $-\log_{10}$ of the Benjamini-Hochberg (BH) adjusted P values. Scores > 20 optimally minimize the false positive rate. (B,C) illustrate the GO enrichment analysis results: (B) biological process, (C) cellular components.

2.3. General and Hematologic Toxicity Profile of Oxaliplatin and MS-275 Combination

The body weight of animals was monitored twice per week during all experimental procedures. Oxaliplatin slowed down body weight gain in *APC^{Min/+}*. Oxaliplatin-treated animals had significant lower body weight at end point (D21). On the contrary, MS-275 did not affect this parameter and did not worsen this oxaliplatin side effect (Figure 3D, Supplementary Table S1) (two-way ANOVA analysis: treatment effect ($p = 0.0143$); time effect ($p < 0.0001$), interaction ($p < 0.0001$)).

Hematologic toxicity represents a known adverse side effect of several anticancer chemotherapeutic agents. Consistently, we observed a significant erythropenia at end point (day 21 after the first infusion) in oxaliplatin-treated animals as compared with control animals (Figure 3E, Supplementary Table S1). Noteworthy, MS-275 did not demonstrate any effect on red blood cells and had no additional effect when combined with oxaliplatin (Figure 3E) (two-way ANOVA analysis: oxaliplatin effect ($p < 0.0001$); MS-275 effect ($p = 0.7926$), interaction ($p = 0.0805$)). On the contrary, MS-275 is known to exert lymphocytopenia, neutropenia and thrombocytopenia [35]. In our experimental conditions, MS-275 significantly decreased white blood cells counts in *APC^{Min/+}* as compared with control mice (Figure 3F, Supplementary Table S1). Oxaliplatin did not exert any effect on white blood cells and did not have any synergic effect with MS-275 on this parameter (Figure 3F) (two-way ANOVA analysis: oxaliplatin effect ($p = 0.5441$); MS-275 effect ($p < 0.0001$), interaction ($p = 0.6229$)). None of the drugs, whether used alone or in combination, affected the number of thrombocytes (Figure 3G, Supplementary Table S1) (two-way ANOVA analysis: oxaliplatin effect ($p = 0.5638$); MS-275 effect ($p = 0.6911$), interaction ($p = 0.9272$)). These results suggest that co-administration of MS-275 and oxaliplatin would have additive, but not synergic, hematological toxicities that should be taken into consideration since in chemotherapy-treated patients, white blood cell count is an important marker for the continuation of the treatment.

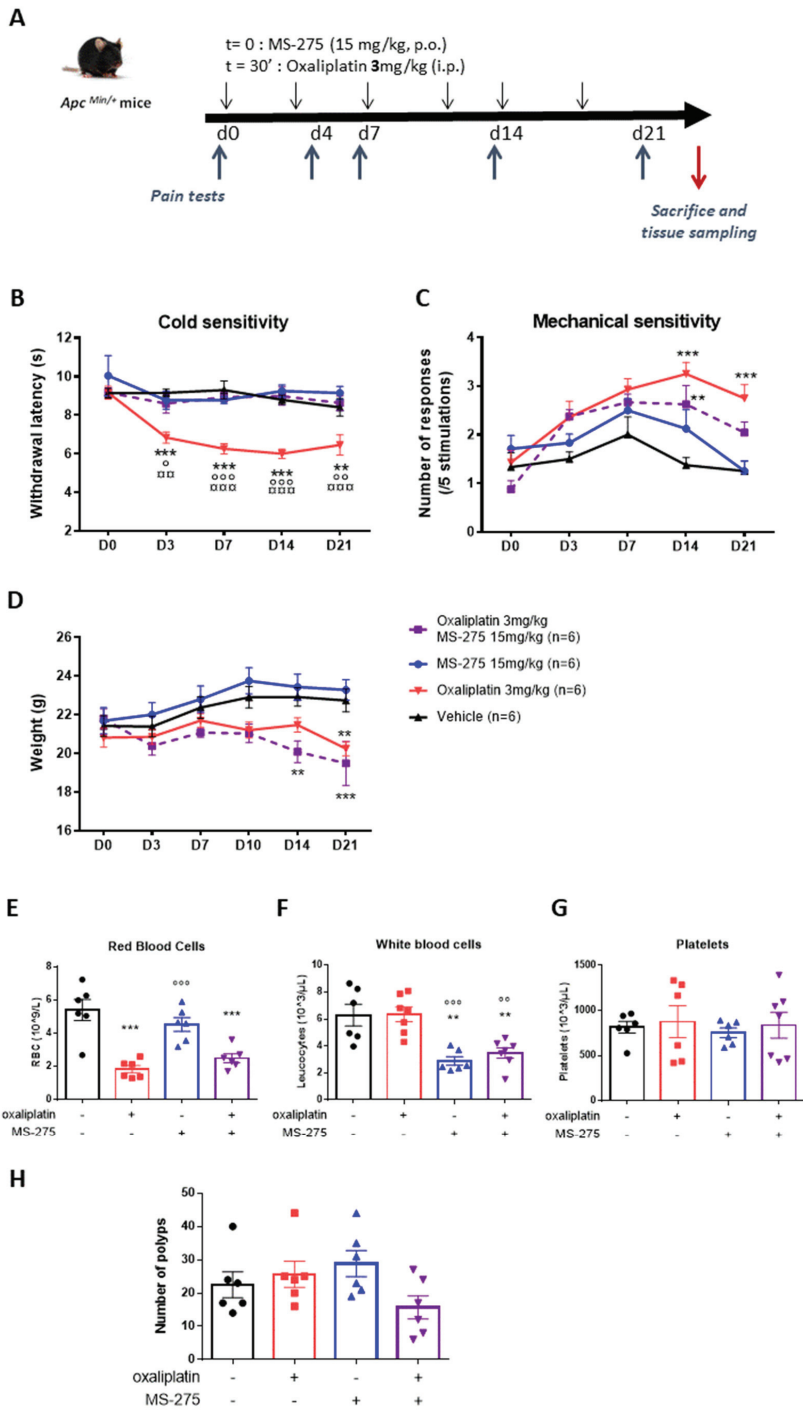


Figure 3. MS-275 prevents oxaliplatin-induced chronic neuropathic pain in *APC^{Min/+}* mice. **(A)** Experimental design: *APC^{Min/+}* mice received oxaliplatin (3 mg/kg, i.p.) or vehicle (Glucose 5%) twice a week for 3 weeks. MS-275 (15 mg/kg, p.o.) was administered half an hour before each oxaliplatin

injection. MS-275 significantly prevented cold (B) and mechanical (C) pain hypersensitivity induced by oxaliplatin administration. Values are mean \pm SEM (n = 5/7 per group). Statistical analysis was performed using a two-way repeated measure analysis of variance (RM ANOVA), detailed in Supplementary Table S1, and a Tukey's multi-comparisons post hoc test; **, $p < 0.01$, ***, $p < 0.001$, vehicle versus oxaliplatin; □□, $p < 0.01$, □□□, $p < 0.001$, oxaliplatin versus MS-275; °, $p < 0.05$, °°, $p < 0.01$, °°°, $p < 0.001$, oxaliplatin versus oxaliplatin + MS-275. General and hematologic toxicity profile of oxaliplatin and MS-275 combination. The body weight of animals was monitored twice a week during all the experimental procedure (D). Effect of oxaliplatin and/or MS-275 treatment on hematological parameters, red blood counts (E), white blood counts (F) and platelets counts (G) was done at end point (D21). Number of polyps in $APC^{Min/+}$ at end-point (H). Values are mean \pm SEM (n = 6/7 per group). Statistical analysis was performed using a two-way analysis of variance, detailed in Supplementary Table S1, and a Tukey's multi-comparisons post hoc test; **, $p < 0.01$, ***, $p < 0.001$, versus the vehicle group; ° $p < 0.05$, °°, $p < 0.01$, °°°, $p < 0.001$, versus the oxaliplatin group.

2.4. MS-275 and Oxaliplatin Antiproliferative Effects in Familial Adenomatous Polyposis (FAP) Mice and in CT26 Tumor-Bearing Mice

$APC^{Min/+}$ mice harbor a germline mutation in the *Apc* gene at codon 850 that leads to a truncation of the protein [34]. In $APC^{Min/+}$ mice, adenomas begin to develop in infancy, with death occurring at 16–20 weeks due to chronic intestinal hemorrhage [36]. We assessed the effect of the drugs on the number of polyps in $APC^{Min/+}$ mice at necropsy. The dose of oxaliplatin used (3 mg/kg, i.p.), while inducing strong neuropathic adverse effects, failed to impact polyposis in this model of FAP (Figure 3H, Supplementary Table S1). MS-275 also failed to significantly decrease the number of polyps in $APC^{Min/+}$ as well, but a significant interaction was detected using the two-way ANOVA analysis (two-way ANOVA analysis: oxaliplatin effect ($p = 0.2037$); MS-275 effect ($p = 0.6351$), interaction ($p = 0.0443$)), suggesting a synergistic effect of combined drugs treatment in this model.

Additionally, we used a mouse model of an orthotopic allograft of the CT26 cell line (mouse colorectal cancer cells) that was stably transfected with the luciferase gene. This model consists of grafting a piece of tumor onto the caecum of animals [37] and to follow tumor progression using bioluminescence (Figure 4A). As shown in Figure 4B (Supplementary Table S1), animals receiving the vehicle treatment show a rapid tumor growth that is hampered in the mice treated with oxaliplatin from day 7 after the start of treatment. MS-275, either alone or combined with oxaliplatin, also strongly slowed cancer progression in this model (two-way repeated measure ANOVA analysis: treatment effect ($p = 0.0005$); time effect ($p < 0.0001$), interaction ($p < 0.0001$)). Bioluminescence results are shown until D10 because of the occurrence of death events at D12 in the vehicle group, in which 100% animals died before D23 (Figure 4C, Supplementary Table S1). Oxaliplatin improves the survival of the mice since 50% of the treated animals are still alive at the end of the treatment and 30% at the end of the follow-up on D40 ($p = 0.0064$). MS-275 alone also significantly improves mice survival since 66% of animals were still alive after end of treatment and 50% at D40 ($p = 0.0019$). Drugs association demonstrated an increased benefit for survival, as shown by their synergistic effect on mean and median survival (Figure 4 and Table S1).

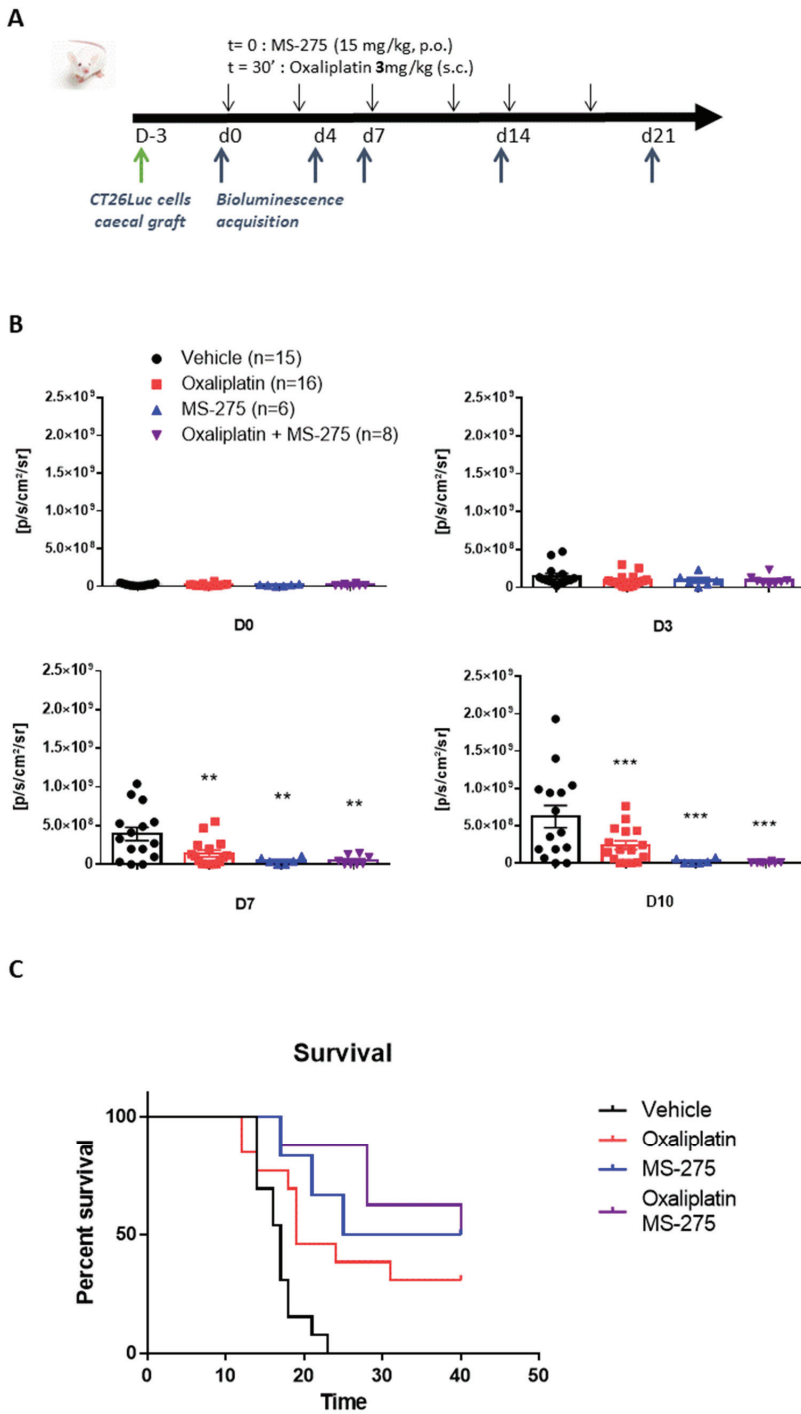


Figure 4. Oxaliplatin and MS-275 exert synergic antitumoral effect in a mouse model of orthotopic CRC.

(A) Experimental design: BALB/c AnN mice, randomized for treatment, were treated 3 days after graft with oxaliplatin (3 mg/kg i.p.) and/or MS-275 (15 mg/kg, p.o.), twice a week for three weeks. MS-275 was administered half an hour before each oxaliplatin injection. (B) MS-275, either alone or combined with oxaliplatin strongly slowed cancer progression in this model. Bioluminescence results are shown until D10 because of the occurrence of death events at D12 in the vehicle group in which 100% animals died before D23 (Figure 4C). Statistical analysis was performed using a two-way analysis of variance, detailed in Supplementary Table S1, and a Tukey's multi-comparisons post hoc test: **, $p < 0.01$, ***, $p < 0.001$, versus the vehicle group. (C) Oxaliplatin and MS-275 improves the survival of mice, and drugs association demonstrated an increased benefit for survival as shown by their synergistic effect on mean and median survival (Table S1). Statistical analysis was performed using Kruskal–Wallis test, detailed in Supplementary Table S1, and a Dunn's multi-comparisons post hoc test; **, $p < 0.01$, versus vehicle.

2.5. MS-275 and Oxaliplatin Effects on Human Cancer Cell Viability

The combined effect of oxaliplatin and MS-275 was monitored on the viability of two human colon cancer cell lines, T84 and HT29, using the MTT test. Oxaliplatin (1 to 64 μM) exerted a dose-dependent effect, decreasing both cell line viabilities (Figure 5A,B). MS-275 (1 to 25 μM) also significantly decreased HT29 viability in a dose-dependent manner (Figure 5B, Supplementary Table S1). In contrast, it failed to affect T84 cell viability, except at the highest dose tested (25 μM) (Figure 5A, Supplementary Table S1). A recent report found large variation in maximal plasma concentrations from 4 to $53.1 \pm 92.4 \mu\text{M}$ after MS-275 administration in humans [38], whereas therapeutically achievable concentrations of oxaliplatin have been reported to be around 5–10 μM [39]. For subsequent analysis, we chose concentrations in the upper range, but these are still therapeutically achievable concentrations for both drugs. The combined effect of MS-275 (2.5 μM) and oxaliplatin (16 μM) was assessed on T84 and HT29 cell viability (Figure 5C,D). In T84 cells, two-way ANOVA analysis made on cell viability data reveals an oxaliplatin effect ($p < 0.0001$), MS-275 effect ($p = 0.9492$), interaction ($p = 0.1667$) (Figure 5C, Supplementary Table S1). In HT29 cells, two-way ANOVA analysis made on cell viability data reveals an oxaliplatin effect ($p < 0.0001$), MS-275 effect ($p < 0.0001$), and interaction ($p = 0.0001$), (Figure 5D, Supplementary Table S1).

2.6. MS-275 and Oxaliplatin Effects on Human Cancer Cells Cycle

To investigate the cytostatic effect of both drugs, cell cycle analysis was performed using PI incorporation, followed by flow cytometry analysis (Figure 5E,F). Oxaliplatin exerted an S-phase delay accompanied by a G0/G1 phase reduction on both T84 and HT29 cell lines. As previously shown on the HCT116 cell line, MS-275 induced a G0/G1 blockade and a strong S-phase reduction at a dose of 2.5 μM in both cell lines (Figure 5E,F). Combined treatment resulted in a significant reduction of G0/G1 phase in T84 cells (Figure 5E, Supplementary Table S1), while it significantly decreased the S phase and increased the G2/M phase in HT29 cells (Figure 5F, Supplementary Table S1). It is known that the cytostatic action of oxaliplatin is mediated through a G2/M blockade in T84 and HT29 cell lines after 72 h of treatment [20]. In our case, only 48 h of treatment were completed, and this earlier stage could explain the S-phase delay observed after oxaliplatin treatment. However, the addition of MS-275 to oxaliplatin seems to accelerate the oxaliplatin cytostatic effect, resulting in a G2/M blockade on HT29 cells (Figure 5F).

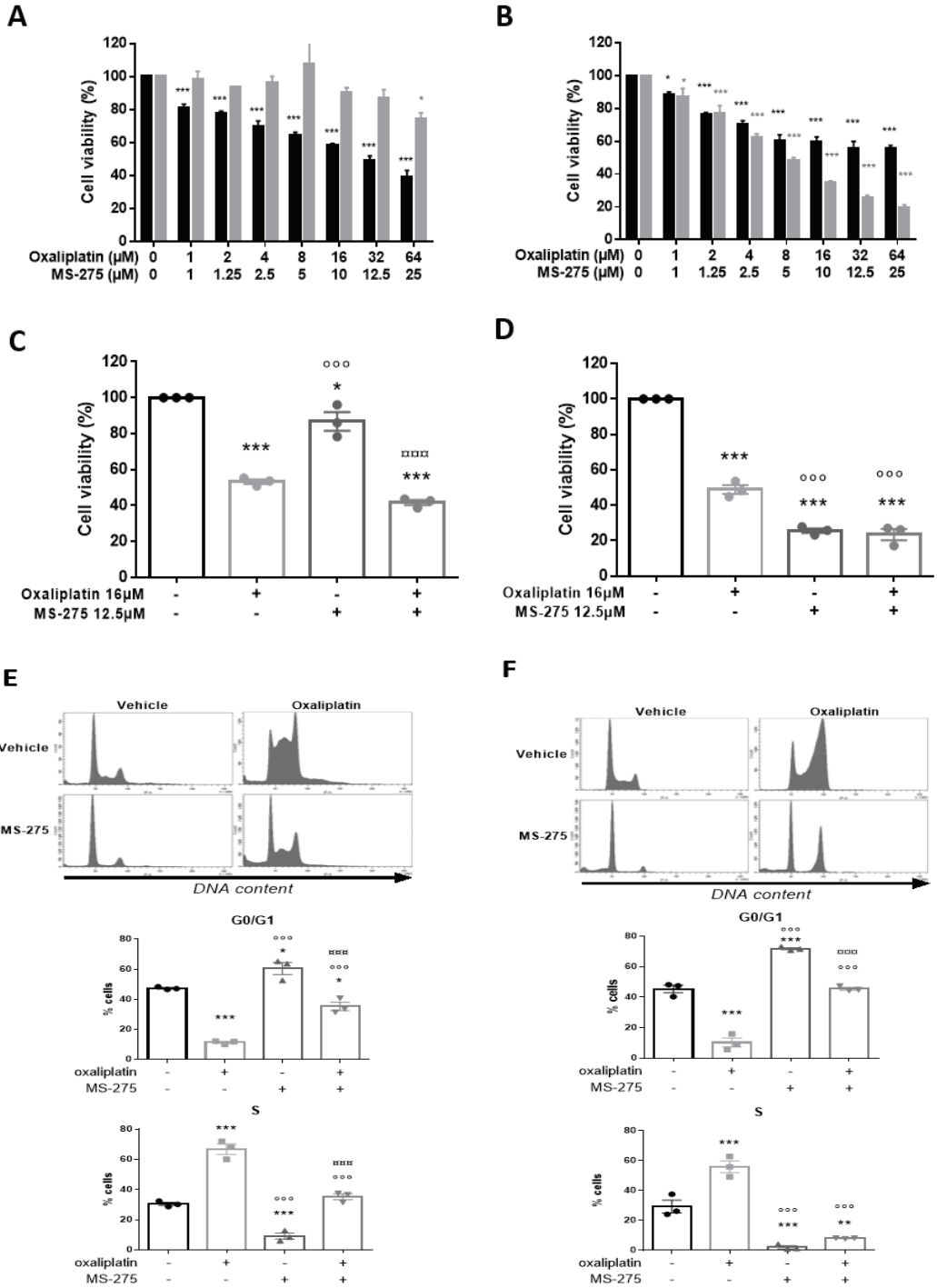


Figure 5. Cont.

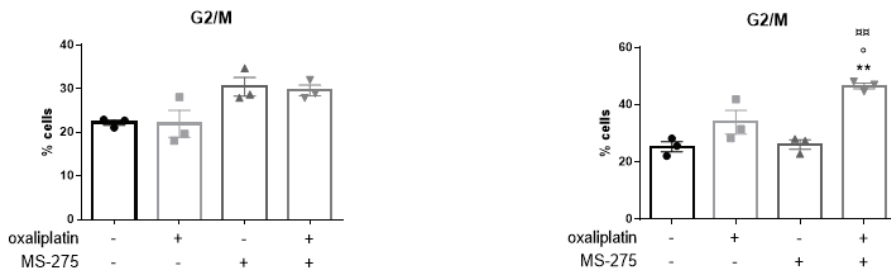


Figure 5. Oxaliplatin and MS-275 effects on in human colon cancer cell lines viability and cell cycle. Oxaliplatin dose-dependently inhibited survival of T84 (A) and HT29 (B) colorectal cancer cells as measured by inhibition of mitochondrial dehydrogenase activity (MTT assay). MS-275 dose-dependently inhibited survival HT29 cells (B) while significantly decreasing T84 cell viability only at the highest dose tested (B). Combined effect of oxaliplatin (16 µM) and MS-275 (2.5 µM) on T84 (C) and on HT29 (D) cell viability and on T84 (E) and HT29 (F) cells cycles. The average results from at least three independent experiments are presented. Values are expressed as mean \pm SEM. Statistical analysis was performed using two-way ANOVA, detailed in Supplementary Table S1, with Tukey's multi-comparisons post-hoc test; * for $p < 0.05$; ** $p < 0.01$; *** $p < 0.001$, versus the vehicle group; ° for $p < 0.05$, °°° for $p < 0.001$, versus the oxaliplatin group; °° for $p < 0.01$, °°° for $p < 0.001$, versus the MS-275 group.

2.7. Oxaliplatin and MS-275 Act Synergistically to Induce Apoptosis In Vitro

Oxaliplatin is known to disrupt cell proliferation by induction of apoptosis and cell cycle inhibition, through DNA adduct formation [40]. In order to assess the effects of oxaliplatin and MS-275 to trigger apoptosis and cell death, Annexin V and propidium iodide (PI) staining were performed on T84 and HT29 cell lines, followed by flow cytometry analysis (Figure 6). In T84 cells, oxaliplatin (16 µM) significantly induced apoptosis, while MS-275 (2.5 µM) had no effect (two-way ANOVA analysis: oxaliplatin effect ($p = 0.0004$); MS-275 effect ($p = 0.5484$), interaction ($p = 0.9226$)) (Figure 6B, Supplementary Table S1). When MS-275 was used at higher concentration (12.5 µM), it significantly induced apoptosis and exerted a synergic effect with oxaliplatin on this parameter (two-way ANOVA analysis: oxaliplatin effect ($p = 0.0003$); MS-275 effect ($p = 0.0002$), interaction ($p = 0.6639$)) (C, Supplementary Table S1). Oxaliplatin (16 µM) and MS-275, only at the highest dose (12.5 µM), induced a significant cell death effect in T84 cells. A synergic effect was observed on this parameter when oxaliplatin (16 µM) was co-administered with MS-275 (2.5 µM) (two-way ANOVA analysis: oxaliplatin effect ($p = 0.0004$); MS-275 effect ($P < 0.0001$), interaction ($p = 0.3297$)) (Figure 6C, Supplementary Table S1) or with MS-275 (12.5 µM) (two-way ANOVA analysis: oxaliplatin effect ($p = 0.0004$); MS-275 effect ($p < 0.0001$), interaction ($p = 0.3297$)) (E, Supplementary Table S1). In the HT29 cell line, oxaliplatin (16 µM) and MS-275 (2.5 µM) had a weak apoptosis inducing effect but demonstrated a synergic effect (two-way ANOVA analysis: oxaliplatin effect ($p = 0.0020$); MS-275 effect ($p = 0.0002$), interaction ($p = 0.3784$)) (Figure 6E). The same pattern was observed when oxaliplatin (16 µM) was co-administered with a higher MS-275 concentration (12.5 µM) (two-way ANOVA analysis: oxaliplatin effect ($p = 0.2046$); MS-275 effect ($p = 0.0077$), interaction ($p = 0.8588$)). Both oxaliplatin and MS-275 significantly induce cell death, and we found a synergic effect of these drugs on this parameter in HT29 cells either with MS-275 at 2.5 µM ((two-way ANOVA analysis: oxaliplatin effect ($p < 0.0001$); MS-275 effect ($p < 0.0001$), interaction ($p = 0.0027$)) (Figure 6F, Supplementary Table S1) or with higher MS-275 concentration (12.5 µM) (two-way ANOVA analysis: oxaliplatin effect ($p = 0.0063$); MS-275 effect ($p < 0.0001$), interaction ($p = 0.3287$)) (Supplementary Figure S1F, Supplementary Table S1).

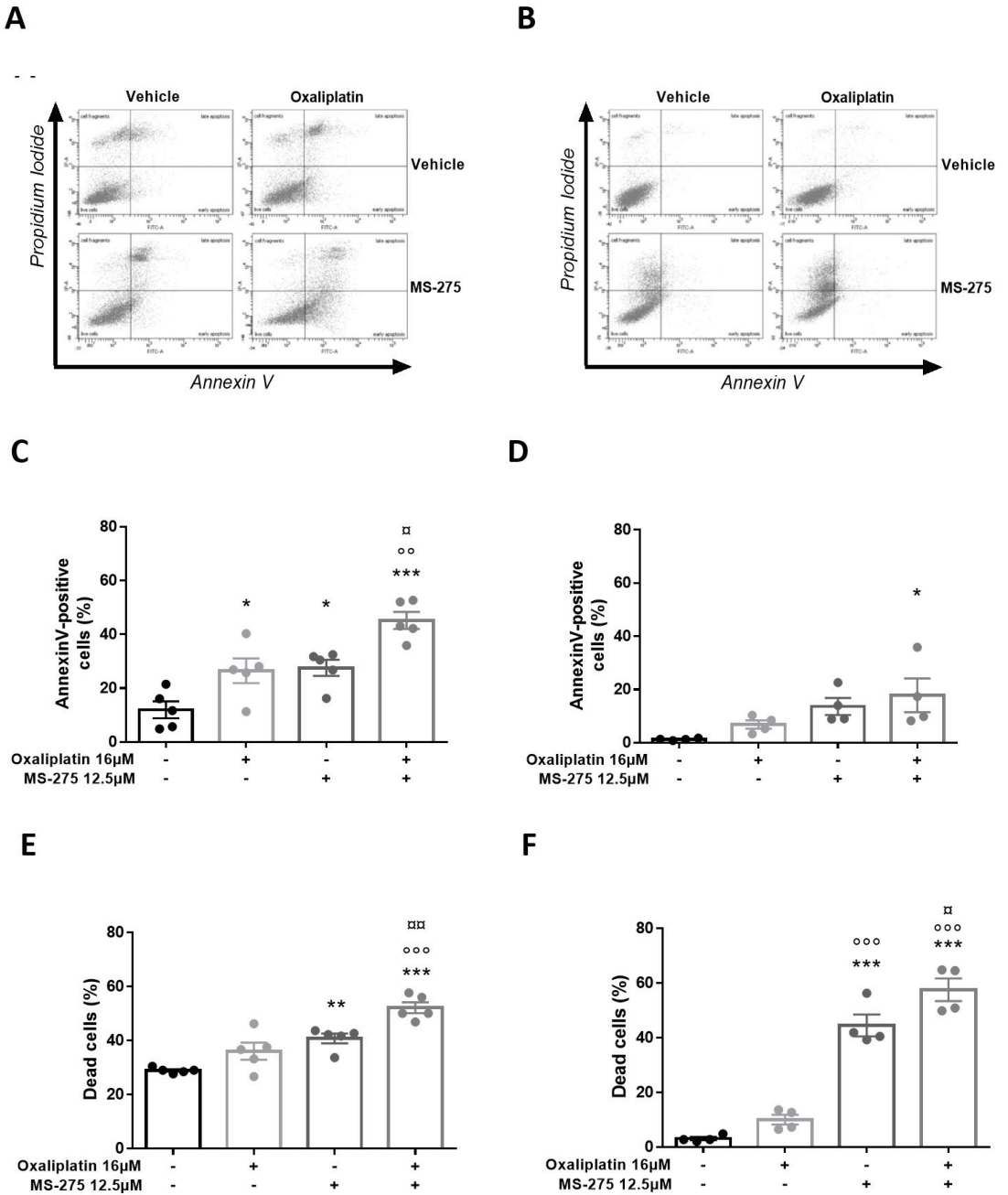


Figure 6. Oxaliplatin and MS-275 effects on apoptosis and cell death in T84 and HT29 cells. Annexin V and Propidium Iodide (PI) staining was performed on T84 (A) and HT29 (D) cell lines followed by flow cytometry analysis. Effects of oxaliplatin (16 μM) with or without MS-275 (2.5 μM) on T84 apoptosis (B) and cell death (C) and on HT29 apoptosis (E) and cell death (F). The average results from

at least three independent experiments are presented. Values are expressed as mean \pm SEM. Statistical analysis was performed using two-way ANOVA, detailed in Supplementary Table S1, with Tukey's multi-comparisons post-hoc test; * for $p < 0.05$; ** for 0.01; *** $p < 0.001$, versus the vehicle group; °° for $p < 0.01$, °°° for $p < 0.001$, versus the oxaliplatin group; □ for $p < 0.05$, □□ for $p < 0.01$, versus the MS-275 group.

3. Discussion

The results obtained in the present study demonstrate that the class I HDAC inhibitor MS-275 prevents the development of sensory neuropathic symptoms induced by repeated oxaliplatin administration in mice. MS-275 also exerts antiproliferative effects in defined in vitro and in vivo CRC models.

While acute neuropathic pain symptoms induced by oxaliplatin-based chemotherapy could be due to changes in ion channel gene expression in DRG neurons, chronic neurotoxicity that occurs with cumulative dosing of oxaliplatin is rather known to involve nuclear DNA damage, mitochondrial damage, overload oxidative stress, glia activation and neuroinflammation [41]. The transcriptomic analysis that we performed on DRG neurons from C57Bl/6J mice treated with repeated oxaliplatin administration is more likely in line with the results obtained by Starobova et al. [42] since oxaliplatin treatment affected mainly neuronal genes in our conditions. No gene coding for depolarizing ion channels was increased and only very few potassium channels-encoding genes were downregulated in chronic OIPN mice DRG neurons, among them being Kv3.3. Oxaliplatin-mediated downregulation of K^+ channels of the K2P and Kv families we previously observed [17] should thus be transient. On the contrary, while Kv3.3 mRNA was not decreased in acute OIPN animals [17], this K^+ channel has recently been shown to be downregulated in DRG neurons from oxaliplatin-treated $APC^{Pirc/+}$ rats after repeated oxaliplatin treatment cessation [43]. Our results are thus in line with and suggest the involvement of Kv3.3 downregulation in sustained occurrence of sensory symptoms induced by repeated oxaliplatin injections. In addition, no overexpression of NRSF and HDAC3, or epigenetic factors involved in K^+ channel downregulation [17], was observed in DRG neurons from chronic oxaliplatin-treated animals. These results suggest that HDAC inhibition might not be effective once OIPN has set in. MS-275 has already been shown to prevent the development of persistent mechanical hypersensitivity after trigeminal nerve injury [44] and to produce analgesia in sciatic nerve injury models [45]. In these later conditions, drug treatment did not affect already-established neuropathic pain after spinal nerve transection, suggesting that histone acetylation might be specifically involved in the emergence of hypersensitivity. Since MS-275 significantly prevented oxaliplatin-induced acute neuropathy [17], we hypothesized that this molecule could also act as a preventive therapeutic drug in a "programmed" chronic oxaliplatin-induced neuropathic condition. We effectively demonstrate that MS-275 prevents oxaliplatin-induced chronic sensory neuropathic symptoms development in $APC^{Min/+}$ mice. Denk et al. [45] stated that MS-275 likely exerted its effect centrally within the spinal cord in models of traumatic nerve injury and antiretroviral drug-induced peripheral neuropathy. Our recently published data suggest that MS-275 acts by preventing peripheral sensitization induced by a single dose of oxaliplatin [17]. In the present study, MS-275 was administered using a systemic route. We suspect a peripheral action as a key element in the prevention of chronic OIPN development. However, we cannot rule out an additional central effect of the drug.

Safety of anticancer drug associations represent a matter of concern. The hematologic toxicity of oxaliplatin was reported to be mild to moderate, even when associated with 5FU-FA [46]. After oxaliplatin infusion, up to 40% of blood platinum is found in erythrocytes [47], where it is able to form adducts with hemoglobin that may be associated with toxic effects, such as anemia [48]. We observed an important and significant drop of erythrocytes after three weeks of oxaliplatin treatment at the cumulative dose of 18 mg/kg in $APC^{Min/+}$ mice. This drug was reported to significantly affect RBC count at a higher cumulative dose (30 mg/kg) in C57Bl/6J mice [49]. This suggests that, as shown for neuropathy [43],

hematological toxicity may be enhanced in cancer conditions, and it reinforces the need for preclinical studies in experimental models of cancer. MS-275 is known to induce a dose-dependent decrease of thrombocytes and leucocytes both in human [50] and in rodents [51]. In our experimental conditions, MS-275 did not affect RBC nor thrombocytes count, but it significantly decreased white blood cells counts in *APC^{Min/+}* mice. Of note, the association of MS-275 with oxaliplatin did not worsen the hematological toxicities induced by individual drugs, and MS-275 did not increase oxaliplatin-induced reduced weight gain. The overall safety of combined drug administration seems acceptable, suggesting a possible association of MS-275 with oxaliplatin in humans to prevent oxaliplatin-induced neuropathy, but close monitoring will be needed regarding the hematological impact of individual drugs.

The next question was to evaluate the combined effects of MS-275 and oxaliplatin on CRC development. While oxaliplatin, at a dose that induces neuropathic symptoms, and MS-275 did not individually significantly decreased the total number of polyps in *APC^{Min/+}* mice, we observed a significant synergistic effect of oxaliplatin and MS-275 co-administration. It is known that loss of APC function leads to increased expression of HDAC2 in intestinal epithelial cells and tumors [52]. Inhibition of the enzymatic activity of class I HDACs and induction of HDAC2 degradation with valproic acid has previously been shown to reduce the number and sizes of intestinal adenomas in *APC^{Min/+}* mice [52]. We hypothesized that the lack of effect of MS-275 in our conditions could rely on the dose used, and/or on the different inhibitory profile of valproic acid and MS-275 on the different HDAC isoforms. Using the same dose regimen, both oxaliplatin and MS-275 exert antiproliferative effects, and combined-drug administration significantly impedes tumor progression and increases overall survival in an orthotopic graft tumor-bearing mouse model. These results are consistent with recent data obtained *in vitro* and *in vivo* in a transplant study in which female BALB/c mice received subcutaneous injection of CT26 cells [53]. CT26 was derived from an undifferentiated colorectal carcinoma induced in a BALB/c mouse by repeated intrarectal instillations of N-nitroso-N-methylurethan and was shown to be modestly immunogenic [54]. In addition to acting on tumor cells, MS-275 also acted on host cells in the immune system [55], which could account for additional benefit when combined with oxaliplatin in this model. When tested on human CRC cells, both drugs, individually, demonstrated different antiproliferative profile depending on the cell line. Although efficient in both T84 and HT29 cells, oxaliplatin exerted improved efficacy in the T84 cell line. Organic cation transporter 3 (OCT3) is an interesting target for oxaliplatin resistance because of its implication on oxaliplatin transport and efficacy [56]. The expression of OCT3, which is known to be weaker in HT29 than in T84 cells, has been shown to be correlated with platinum accumulation in these cells and with oxaliplatin cytotoxicity [56], which can sustain our results. MS-275 has previously been shown to be less effective in p53 null cells [57]. Consistently, we observed that T84 cells, that do not express p53 [58] demonstrated a strong resistance, whereas HT29, which expresses p53, was highly sensitive toward the antiproliferative effect of MS-275. HT29 was previously shown to be a responder to MS-275, which might increase the adhesive properties of these cells, thus preventing their metastatic spread and immune escape [59]. On the contrary, T84 cells can thus be considered as a weak or non-responder, as it has been shown for other CRC cell lines for which MS-275 induced downregulation of genes involved in cell adhesion [59]. Whether such genes regulation also occurs in T84 cells will be of interest in order to define biomarkers to predict the response to MS-275. Whatever the sensitivity of these cell lines toward oxaliplatin and MS-275, combined drug associations result in synergistic apoptotic and cell death effects. These results are concordant with those obtained in HCT116 cells in which MS-275 has been shown to enhance apoptosis induced by oxaliplatin [53]. At the highest doses tested, apoptosis accounts for more than 67% and 86% of the cell death effect of MS-275 solely or MS-275 and oxaliplatin combined, respectively in T84 cells, while it accounts for only 30% and 31% of these effects in HT29 cells. Of note, MS-275 was proposed to promote mainly caspase-dependent cell death in p53+ cells, whereas,

in p53- cells, caspase inhibition switches the mode of cell death to a mainly non-caspase-dependent one [57]. HDACi are epigenetic drugs that enhance protein acetylation and thereby influence a large number of cellular functions. Global assays and analyses revealed that HDACi promote an induction of replicative stress and DNA damage [60], and that they disrupt functional EMT/MET protein expression signatures and trigger apoptosis of cultured cancer cells [61]. MS-275 induced autophagy has also been involved in human colon cancer cell death (HCT116) [62], and could thus be differently involved in both cell lines in our conditions. It is increasingly recognized that HDACi sensitize tumor cells to chemotherapeutics, causing replication stress and DNA damage [8–10]. Combined application of irinotecan and entinostat synergistically kills CRC cells *in vitro* and *in vivo*, and the induction of acetyl-p53-BAK complexes inducing MOMP upon RS C-terminal hyperacetylation of p53 is an absolute requirement for apoptosis induction by irinotecan and entinostat [63]. More work is needed to understand the mechanisms involved in the beneficial effects observed with MS-275 and oxaliplatin association in our conditions. Future work will include experiments helping to obtain more information on the potential of both drugs to induce replicative stress and DNA damage at different time points.

4. Methods

4.1. Animals and Models

Procedures were evaluated by a regional ethics committee (CEMEA Auvergne) before approval by the French Ministry of Research and Education (project N° APAFIS#21980) under the European 2010/63/ UE directive. Animal studies are reported in compliance with the ARRIVE 2.0 guidelines [64]. All efforts were taken at each stage of the experiments to limit the numbers of animals used and any discomfort to which they might be exposed, especially in pain experiments.

Experiments were performed using 20–25g C57BL/6J and *Apc^{Min/+}* male mice and female BALBc/AnN mice. *Apc^{Min/+}* mice were a gift from Dr. Mathilde Bonnet (UMR U1071 Inserm, Clermont-Ferrand, FRANCE). All mice were housed in grouped cages in a temperature-controlled environment with food and water *ad libitum*. Behavioral experiments were conducted in a quiet room, blind to the treatment, by the same experimenter taking care to avoid or minimize any discomfort of the animals.

For the mouse allograft colorectal cancer model, 5 female BALBc/AnN mice under isoflurane anesthesia were subcutaneously injected in their right flank with 0.5×10^6 CT26 cells, stably transfected with the Luciferase gene. Mice were housed and monitored until tumors reached a sufficient size (1000–2000 mm²) to perform grafts. Mice were then sacrificed, tumors were sampled, and 25 mm² grafts were sized up in DMEM medium on ice. “Recipient mice” were incised along 1 cm in the lower abdomen, under isoflurane anesthesia. Caecum was then exteriorized, on a sterile compress soaked with 0.9% NaCl solution, and slightly damaged using a 26G needle. Grafts were then apposed on the damaged region, to promote tumor attachment, and were maintained on it using 7.0 absorbable suture filament. Caecum was then replaced in the abdomen and muscles, and skin was sutured using 4.0 non-absorbable filament. Mice, randomized for treatment, were treated 3 days after graft (oxaliplatin 3 mg/kg *s.c.* and/or MS-275 *p.o.*, twice a week for three weeks). Tumor progression was monitored twice per week by bioluminescence. Mice were injected with luciferin (*i.p.*; 150 µL/mouse of a 25 mg mL⁻¹ solution) 5 min before bioluminescence acquisition, were anesthetized with isoflurane, and then the acquisition was realized on an IVIS spectrum (UMR 1240, Clermont-Ferrand, France).

4.2. Materials

The following drugs were used: oxaliplatin (Leancare Ltd., Flintshire, UK) and MS-275 (Selleck Chemicals, Houston TX, USA) solutions were prepared directly before experiments in 5% glucose solution for oxaliplatin and in 0.9% (*w/v*) NaCl solution for MS-275. Oxaliplatin (3 mg kg⁻¹, *i.p.*) was administered twice per week for three weeks. MS-275 (15 mg kg⁻¹, *p.o.*) was administered half an hour before each oxaliplatin injection. The

administration route of oxaliplatin changed (from i.p. to s.c.) in the graft model to avoid direct contact of the drug with the tumor.

4.3. Evaluation of Pain Thresholds

Cold thermal nociceptive responsiveness was assessed using the cold water (10 °C) paw immersion test. The paw of the animal was immersed in the temperature-controlled water bath until withdrawal was observed (cutoff time: 30 s). Two separate withdrawal latency time determinations were averaged.

Mechanical pain hypersensitivity was assessed using a 0.6 g bending force calibrated Von Frey hair filament, applied perpendicular to the plantar surface of the hind paw until it bent. Scores were expressed, averaging results from the left and right paws, as a number of responses elicited by five consecutive stimulations by a given filament was averaged between the left and right paw.

4.4. Hematological Analysis

Blood samples of animals were collected intraorbitally in a heparin tube and were kept at 4 °C until the count. Full blood counts were realized at the Biological Center of the University Hospital Center of Clermont-Ferrand, France.

4.5. RNA Sequencing

To investigate global mRNA changes, we used RNA sequencing analysis on L4-L5-L6 DRGs from mice treated with oxaliplatin (3 mg kg⁻¹, i.p.) or vehicle twice per week for 3 weeks. At the end of the experiment (D21), mice were terminally anesthetized and L4-L5-L6 DRGs were quickly harvested, snap frozen in liquid nitrogen, and stored at −80 °C until use. Total RNA of L4-L5-L6 DRGs was extracted using RNeasy Micro Kit (Qiagen, Hilden, Germany) according to the manufacturer's protocol. Thereafter, rRNA was removed using Illumina® Ribo-Zero Plus rRNA Depletion Kit (Epicentre, Illumina, San Diego, CA, USA). RNA integrity and concentration were obtained using 2100 Bioanalyzer instrument (Agilent Technologies, Santa Clara, CA, USA) and were sent to Fasteris (<https://www.fasteris.com> (accessed on 6 September 2017)) for RNA sequencing. Libraries were prepared using the Illumina TruSeq stranded protocol, and an SBS-based sequencing was achieved using HiSeq 2500 platform (Illumina). Analysis was performed in different steps: splice junction mapping (TopHat2), counting (HTSeq-count), filtering, normalization (edgeR, DESeq and DESeq2) and differential analysis (edgeR, DESeq and DESeq2) were performed by Benjamin Bertin and Yoan Renaud (GreD, Clermont-Ferrand, France).

4.6. Bioinformatics Analysis

Quality control of sequencing was evaluated using FastQC software. High-quality reads were mapped to the *Mus musculus* mm9 reference genome using bowtie2 with default parameters [65]. Reads per gene were counted using HTSeq-count [66].

Normalization and differential gene expression analysis were performed using DESeq2 [67] from the SARTools package [68]. Only genes with an adjusted *p*-value of <0.05 were considered as differentially expressed between the two conditions. GO and KEGG enrichment analyses were performed using the R package clusterProfiler from Bioconductor [69].

Significantly enriched GO terms were selected, respectively, according to a *p* value <0.01. The gene ontology study was performed using R package ClusterProfiler (v 4.2.0). Volcano plot was generated using R package ggplot2 (v 3.3.5). Cell Type enrichment analysis (CTen) was performed using <http://sbi.jp/influenza-x/cten> (accessed on 6 September 2017) web application.

4.7. Cell Culture

The CT26 (ATCC, CRL-2638) cell line was purchased from LGC Standards (France), HT29 (ATCC, HTB-38) and T84 (ATCC, CCL-248) cell lines were a kind gift from Dr. Mathilde Bonnet (UMR 1071 Inserm, Clermont-Ferrand, France). Cell lines were grown in

DMEM (CT26, HT29) or DMEM/F-12 (T84) complete medium. Cells were maintained in a humidified atmosphere at 37 °C and 5% CO₂. All drugs tested in vitro were dissolved in 100% dimethyl sulfoxide (DMSO, Sigma-Aldrich, Saint Quentin Fallavier, France) solution.

4.8. Cell Viability Analysis

Cell viability was assessed using 3-(4,5-Dimethylthiazol-2-yl)-2,5-diphenyltetrazolium bromide (MTT) (Life Technologies, France), according to the manufacturer's instructions. Briefly, 7500 cells were plated in a 96-well plate and treated for 48 h with oxaliplatin and/or MS-275. The optical density was read at 562 nm using an Epoch microplate spectrophotometer (BioTek, Winooski, FL, USA).

4.9. Apoptosis Analysis

Cells were seeded at 225×10^3 cells in a 6-well plate and were treated for 48 h with oxaliplatin and/or MS-275. Briefly, the medium was removed and kept, and the cells were rinsed with PBS, trypsinized, and added to the medium. After centrifugation (10 min, 200 g), cells were homogenized in 100 µL of Binding Buffer and were stained with 5 µL propidium iodide (PI) and 1 µL Annexin V-FITC (Annexin V-FITC kit Beckman Coulter, Indianapolis, IN, USA) for 15 min at 4 °C in the dark. Afterward, 400 µL of binding buffer was added, and apoptosis was analyzed by flow cytometry at CICS (Centre Imagerie Cellulaire Santé) Core Facility (Clermont-Auvergne University, France) using the LSR II flow cytometer (BD Biosciences, San Jose, CA, USA). Quantification was performed with the BD FACS Diva software version 6.1.3.

4.10. Cell Cycle Analysis

Cells were plated and treated as described above. Cells were collected, washed in ice-cold PBS, and fixed in 70% ice-cold ethanol for 30 min at 4 °C. After fixation, cells were washed with ice-cold PBS and were pelleted. Cells were resuspended with 1 mL of RNase A-PI solution (500 and 50 µg/mL, separately) and were stained for 30 min at 4 °C in the dark. Cell cycle analysis was performed as described above, except for the quantification that was performed with the ModFit LT software (Verity Software House, Topsham, ME, USA) version 3.0.

4.11. Statistical Analysis

Results were expressed as mean \pm standard error of the mean. Data were analyzed using GraphPad Prism software (GraphPad software, La Jolla, CA, USA) version 7.0. The specific tests used are indicated within the text of the figure legends, and power analysis for all the tests is provided as a Supplementary Table S1.

5. Conclusions

The well-tolerated epigenetic drug MS-275 was tested in phase III clinical trials for the treatment of various tumor entities [70]. Our results strongly suggest the interest for combining oxaliplatin and MS-275 administration in CRC patients in order to potentiate the antiproliferative action of the chemotherapy while minimizing the neurotoxic effects of the platinum drug.

Supplementary Materials: The following are available online at <https://www.mdpi.com/article/10.3390/ijms23010098/s1>

Author Contributions: S.L., M.C. and Y.A. conducted the experiments, analyzed the data, and participated in the preparation of the manuscript. J.B. (Julie Barbier), L.P., M.F., L.B., D.A.B. and V.P. participated in the experiments. D.B. and E.M.-N. were associated with the design and analysis of the research. M.-A.C. was involved in hematological experiments. E.B., Y.R. and B.B. were involved in bioinformatics analysis. J.B. (Jérôme Busserolles), A.E. and E.B. designed the research, supervised the project, participated in data analysis, and wrote the paper. All authors have read and agreed to the published version of the manuscript.

Funding: This project was funded by the Regional Council of Auvergne (Conseil Régional d’Auvergne) together with the European Fund for Regional Economic Development (FEDER), the University of Clermont Auvergne and the French government through the program “Investissements d’Avenir” (I-Site CAP 20-25).

Institutional Review Board Statement: Animal procedures were evaluated by a regional ethics committee (CEMEA Auvergne) before approval by the French Ministry of Research and Education (project N° APAFIS#21980) under the European 2010/63/ UE directive.

Informed Consent Statement: Not applicable.

Acknowledgments: We would like to thank Mathilde BONNET (M2iSH, Clermont-Ferrand, France) who provided us with HT29 and T84 cells and *APC^{Min/+}* mice, Claire SZCZEPANIAK, Christelle BLAVIGNAC and Lorraine NOVAIS-GAMEIRO (Center for Medical Cell Imaging (CICS), University of Clermont Auvergne) for their technical assistance with flow cytometry, and Arnaud BRIAT and Elodie JOUBERTON for technical assistance concerning the bioluminescence study.

Conflicts of Interest: The authors declare no conflict of interest.

References

1. Carrato, A. Adjuvant treatment of colorectal cancer. *Gastrointest Cancer Res.* **2008**, *2* (Suppl. 4), S42–S46. [PubMed]
2. Pachman, D.R.; Qin, R.; Seisler, D.K.; Smith, E.M.; Beutler, A.S.; Ta, L.E.; Lafky, J.M.; Wagner-Johnston, N.D.; Ruddy, K.J.; Dakhil, S.R.; et al. Clinical Course of Oxaliplatin-Induced Neuropathy: Results From the Randomized Phase III Trial N08CB (Alliance). *J. Clin. Oncol.* **2015**, *33*, 3416–3422. [CrossRef] [PubMed]
3. Argyriou, A.A.; Polychronopoulos, P.; Iconomou, G.; Chroni, E.; Kalofonos, H.P. A review on oxaliplatin-induced peripheral nerve damage. *Cancer Treat. Rev.* **2008**, *34*, 368–377. [CrossRef] [PubMed]
4. Grothey, A. Clinical Management of Oxaliplatin-Associated Neurotoxicity. *Clin. Color. Cancer* **2005**, *5* (Suppl. 1), S38–S46. [CrossRef]
5. Beijers, A.J.; Mols, F.; Tjan-Heijnen, V.C.; Faber, C.G.; van de Poll-Franse, L.V.; Vreugdenhil, G. Peripheral neuropathy in colorectal cancer survivors: The influence of oxaliplatin administration. Results from the population-based PROFILES registry. *Acta Oncol.* **2015**, *54*, 463–469. [CrossRef]
6. Hershman, D.L.; Lacchetti, C.; Dworkin, R.H.; Lavoie Smith, E.M.; Bleeker, J.; Cavaletti, G.; Chauhan, C.; Gavin, P.; Lavino, A.; Lustberg, M.B.; et al. Prevention and Management of Chemotherapy-Induced Peripheral Neuropathy in Survivors of Adult Cancers: American Society of Clinical Oncology Clinical Practice Guideline. *J. Clin. Oncol.* **2014**, *32*, 1941–1967. [CrossRef]
7. Loprinzi, C.L.; Lacchetti, C.; Bleeker, J.; Cavaletti, G.; Chauhan, C.; Hertz, D.L.; Kelley, M.R.; Lavino, A.; Lustberg, M.B.; Paice, J.A.; et al. Prevention and Management of Chemotherapy-Induced Peripheral Neuropathy in Survivors of Adult Cancers: ASCO Guideline Update. *J. Clin. Oncol.* **2020**, *38*, 3325–3348. [CrossRef]
8. Gent, P.; Massey, K. An overview of chemotherapy-induced peripheral sensory neuropathy, focusing on oxaliplatin. *Int. J. Palliat. Nurs.* **2001**, *7*, 354–359. [CrossRef]
9. Molassiotis, A.; Cheng, H.L.; Lopez, V.; Au, J.S.K.; Chan, A.; Bandla, A.; Leung, K.T.; Li, Y.C.; Wong, K.H.; Suen, L.K.P.; et al. Are we mis-estimating chemotherapy-induced peripheral neuropathy? Analysis of assessment methodologies from a prospective, multinational, longitudinal cohort study of patients receiving neurotoxic chemotherapy. *BMC Cancer* **2019**, *19*, 132. [CrossRef]
10. Grolleau, F.; Gamelin, L.; Boisdron-Celle, M.; Lapiet, B.; Pelhate, M.; Gamelin, E. A possible explanation for a neurotoxic effect of the anticancer agent oxaliplatin on neuronal voltage-gated sodium channels. *J. Neurophysiol.* **2001**, *85*, 2293–2297. [CrossRef]
11. Gauchan, P.; Andoh, T.; Kato, A.; Kuraishi, Y. Involvement of increased expression of transient receptor potential melastatin 8 in oxaliplatin-induced cold allodynia in mice. *Neurosci. Lett.* **2009**, *458*, 93–95. [CrossRef]
12. Nassini, R.; Gees, M.; Harrison, S.; De Siena, G.; Materazzi, S.; Moretto, N.; Failli, P.; Preti, D.; Marchetti, N.; Cavazzini, A.; et al. Oxaliplatin elicits mechanical and cold allodynia in rodents via TRPA1 receptor stimulation. *Pain* **2011**, *152*, 1621–1631. [CrossRef]
13. Zhao, M.; Isami, K.; Nakamura, S.; Shirakawa, H.; Nakagawa, T.; Kaneko, S. Acute Cold Hypersensitivity Characteristically Induced by Oxaliplatin is Caused by the Enhanced Responsiveness of TRPA1 in Mice. *Mol. Pain* **2012**, *8*, 55. [CrossRef]
14. Trevisan, G.; Materazzi, S.; Fusi, C.; Altomare, A.; Aldini, G.; Lodovici, M.; Patacchini, R.; Geppetti, P.; Nassini, R. Novel Therapeutic Strategy to Prevent Chemotherapy-Induced Persistent Sensory Neuropathy By TRPA1 Blockade. *Cancer Res.* **2013**, *73*, 3120–3131. [CrossRef]
15. Pereira, V.; Busserolles, J.; Christin, M.; Devilliers, M.; Poupon, L.; Legha, W.; Alloui, A.; Aissouni, Y.; Bourinet, E.; Lesage, F.; et al. Role of the TREK2 potassium channel in cold and warm thermosensation and in pain perception. *Pain* **2014**, *155*, 2534–2544. [CrossRef]
16. Descoeur, J.; Pereira, V.; Pizzoccaro, A.; Francois, A.; Ling, B.; Maffre, V.; Couette, B.; Busserolles, J.; Courteix, C.; Noel, J.; et al. Oxaliplatin-induced cold hypersensitivity is due to remodelling of ion channel expression in nociceptors. *EMBO Mol. Med.* **2011**, *3*, 266–278. [CrossRef]

17. Pereira, V.; Lamoine, S.; Cuménil, M.; Lollignier, S.; Aissouni, Y.; Pizzoccaro, A.; Prival, L.; Balayssac, D.; Eschalier, A.; Bourinet, E.; et al. Epigenetics Involvement in Oxaliplatin-Induced Potassium Channel Transcriptional Downregulation and Hypersensitivity. *Mol. Neurobiol.* **2021**, *58*, 3575–3587. [CrossRef]
18. Cavaletti, G.; Tredici, G.; Petruccioli, M.G.; Dondè, E.; Tredici, P.; Marmioli, P.; Minoia, C.; Ronchi, A.; Bayssas, M.; Etienne, G.G. Effects of different schedules of oxaliplatin treatment on the peripheral nervous system of the rat. *Eur. J. Cancer* **2001**, *37*, 2457–2463. [CrossRef]
19. Jamieson, S.M.; Liu, J.; Connor, B.; McKeage, M. Oxaliplatin causes selective atrophy of a subpopulation of dorsal root ganglion neurons without inducing cell loss. *Cancer Chemother. Pharmacol.* **2005**, *56*, 391–399. [CrossRef]
20. Xiao, W.; Zheng, H.; Bennett, G. Characterization of oxaliplatin-induced chronic painful peripheral neuropathy in the rat and comparison with the neuropathy induced by paclitaxel. *Neuroscience* **2012**, *203*, 194–206. [CrossRef]
21. Zheng, H.; Xiao, W.H.; Bennett, G.J. Functional deficits in peripheral nerve mitochondria in rats with paclitaxel- and oxaliplatin-evoked painful peripheral neuropathy. *Exp. Neurol.* **2011**, *232*, 154–161. [CrossRef]
22. Warwick, R.; Hanani, M. The contribution of satellite glial cells to chemotherapy-induced neuropathic pain. *Eur. J. Pain* **2013**, *17*, 571–580. [CrossRef]
23. Ferrier, J.; Bayet-Robert, M.; Pereira, B.; Daulhac, L.; Eschalier, A.; Pezet, D.; Moulinoux, J.-P.; Balayssac, D. A Polyamine-Deficient Diet Prevents Oxaliplatin-Induced Acute Cold and Mechanical Hypersensitivity in Rats. *PLoS ONE* **2013**, *8*, e77828. [CrossRef]
24. Yamamoto, S.; Ushio, S.; Egashira, N.; Kawashiri, T.; Mitsuyasu, S.; Higuchi, H.; Ozawa, N.; Masuguchi, K.; Ono, Y.; Masuda, S. Excessive spinal glutamate transmission is involved in oxaliplatin-induced mechanical allodynia: A possibility for riluzole as a prophylactic drug. *Sci. Rep.* **2017**, *7*, 9661. [CrossRef]
25. Falkenberg, K.J.; Johnstone, R.W. Histone deacetylases and their inhibitors in cancer, neurological diseases and immune disorders. *Nat. Rev. Drug Discov.* **2014**, *13*, 673–691. [CrossRef]
26. Cao, L.-L.; Yue, Z.; Liu, L.; Pei, L.; Yin, Y.; Qin, L.; Zhao, J.; Liu, H.; Wang, H.; Jia, M. The expression of histone deacetylase HDAC1 correlates with the progression and prognosis of gastrointestinal malignancy. *Oncotarget* **2017**, *8*, 39241–39253. [CrossRef]
27. Nemati, M.; Ajami, N.; Estiar, M.A.; Rezapour, S.; Gavvani, R.R.; Hashemzadeh, S.; Kafil, H.S.; Sakhinia, E. Deregulated expression of HDAC3 in colorectal cancer and its clinical significance. *Adv. Clin. Exp. Med.* **2018**, *27*, 305–311. [CrossRef]
28. He, P.; Li, K.; Li, S.-B.; Hu, T.-T.; Guan, M.; Sun, F.-Y.; Liu, W.-W. Upregulation of AKAP12 with HDAC3 depletion suppresses the progression and migration of colorectal cancer. *Int. J. Oncol.* **2018**, *52*, 1305–1316. [CrossRef]
29. Banks, C.A.S.; Zhang, Y.; Miah, S.; Hao, Y.; Adams, M.K.; Wen, Z.; Thornton, J.L.; Florens, L.; Washburn, M.P. Integrative Modeling of a Sin3/HDAC Complex Sub-structure. *Cell Rep.* **2020**, *31*, 107516. [CrossRef]
30. Rampalli, S.; Pavithra, L.; Bhatt, A.; Kundu, T.K.; Chattopadhyay, S. Tumor suppressor SMAR1 mediates cyclin D1 repression by recruitment of the SIN3/histone deacetylase 1 complex. *Mol. Cell Biol.* **2005**, *25*, 8415–8429. [CrossRef]
31. Shoemaker, J.E.; Lopes, T.J.S.; Ghosh, S.; Matsuo, Y.; Kawaoka, Y.; Kitano, H. CTen: A web-based platform for identifying enriched cell types from heterogeneous microarray data. *BMC Genom.* **2012**, *13*, 460. [CrossRef] [PubMed]
32. Vaipopoulos, A.G.; Athanasoula, K.C.; Papavassiliou, A.G. Epigenetic modifications in colorectal cancer: Molecular insights and therapeutic challenges. *Biochim. Biophys. Acta (BBA) Mol. Basis Dis.* **2014**, *1842*, 971–980. [CrossRef]
33. Ikehata, M.; Ogawa, M.; Yamada, Y.; Ueda, K.; Iwakawa, S. Different Effects of Epigenetic Modifiers on the Cytotoxicity Induced by 5-Fluorouracil, Irinotecan or Oxaliplatin in Colon Cancer Cells. *Biol. Pharm. Bull.* **2014**, *37*, 67–73. [CrossRef] [PubMed]
34. Moser, A.R.; Pitot, H.C.; Dove, W.F. A dominant mutation that predisposes to multiple intestinal neoplasia in the mouse. *Science* **1990**, *247*, 322–324. [CrossRef] [PubMed]
35. Fraczek, J.; Vanhaecke, T.; Rogiers, V. Toxicological and metabolic considerations for histone deacetylase inhibitors. *Expert Opin. Drug Metab. Toxicol.* **2013**, *9*, 441–457. [CrossRef] [PubMed]
36. Shoemaker, A.R.; Moser, A.R.; Dove, W.F. N-ethyl-N-nitrosourea treatment of multiple intestinal neoplasia (Min) mice: Age-related effects on the formation of intestinal adenomas, cystic crypts, and epidermoid cysts. *Cancer Res.* **1995**, *55*, 4479–4485. [PubMed]
37. Tseng, W.; Leong, X.; Engleman, E. Orthotopic Mouse Model of Colorectal Cancer. *J. Vis. Exp.* **2007**, *15*, e484. [CrossRef] [PubMed]
38. Connolly, R.M.; Rudek, M.A.; Piekarz, R. Entinostat: A promising treatment option for patients with advanced breast cancer. *Futur. Oncol.* **2017**, *13*, 1137–1148. [CrossRef]
39. Ehrsson, H.; Wallin, I.; Yachnin, J. Pharmacokinetics of Oxaliplatin in Humans. *Med. Oncol.* **2002**, *19*, 261–266. [CrossRef]
40. Arango, D.; Wilson, A.J.; Shi, Q.; Corner, G.A.; Aranes, M.J.; Nicholas, C.; Lesser, M.; Mariadason, J.M.; Augenlicht, L.H. Molecular mechanisms of action and prediction of response to oxaliplatin in colorectal cancer cells. *Br. J. Cancer* **2004**, *91*, 1931–1946. [CrossRef]
41. Kang, L.; Tian, Y.; Xu, S.; Chen, H. Oxaliplatin-induced peripheral neuropathy: Clinical features, mechanisms, prevention and treatment. *J. Neurol.* **2020**, *268*, 3269–3282. [CrossRef]
42. Starobova, H.; Mueller, A.; Deuis, J.R.; Carter, D.A.; Vetter, I. Inflammatory and Neuropathic Gene Expression Signatures of Chemotherapy-Induced Neuropathy Induced by Vincristine, Cisplatin, and Oxaliplatin in C57BL/6J Mice. *J. Pain* **2020**, *21*, 182–194. [CrossRef]
43. Housley, S.N.; Nardelli, P.; Carrasco, D.I.; Rotterman, T.M.; Pfahl, E.; Matyunina, L.V.; McDonald, J.F.; Cope, T.C. Cancer Exacerbates Chemotherapy-Induced Sensory Neuropathy. *Cancer Res.* **2020**, *80*, 2940–2955. [CrossRef]

44. Danaher, R.J.; Zhang, L.; Donley, C.J.; A Laungani, N.A.; Hui, S.E.; Miller, C.S.; Westlund, K.N. Histone deacetylase inhibitors prevent persistent hypersensitivity in an orofacial neuropathic pain model. *Mol. Pain* **2018**, *14*, 1745691620968771. [CrossRef]
45. Denk, F.; Huang, W.; Sidders, B.; Bithell, A.; Crow, M.; Grist, J.; Sharma, S.; Ziemek, D.; Rice, A.S.; Buckley, N.J.; et al. HDAC inhibitors attenuate the development of hypersensitivity in models of neuropathic pain. *Pain* **2013**, *154*, 1668–1679. [CrossRef]
46. Raymond, E.; Chaney, S.G.; Taamma, A.; Cvitkovic, E. Oxaliplatin: A review of preclinical and clinical studies. *Ann. Oncol.* **1998**, *9*, 1053–1071. [CrossRef]
47. Pendyala, L.; Creaven, P.J. In vitro cytotoxicity, protein binding, red blood cell partitioning, and biotransformation of oxaliplatin. *Cancer Res.* **1993**, *53*, 5970–5976.
48. Garufi, C.; Vaglio, S.; Brienza, S.; Conti, L.; D’Attino, R.M.; Girelli, G.; Terzoli, E. Immuno-hemolytic anemia following oxaliplatin administration. *Ann. Oncol.* **2000**, *11*, 497. [CrossRef]
49. Lees, J.G.; White, D.; Keating, B.A.; Barkl-Luke, M.E.; Makker, P.G.S.; Goldstein, D.; Moalem-Taylor, G. Oxaliplatin-induced haematological toxicity and splenomegaly in mice. *PLoS ONE* **2020**, *15*, e0238164. [CrossRef]
50. Gojo, I.; Jiemjit, A.; Trepel, J.B.; Sparreboom, A.; Figg, W.D.; Rollins, S.; Tidwell, M.L.; Greer, J.; Chung, E.J.; Lee, M.-J.; et al. Phase 1 and pharmacologic study of MS-275, a histone deacetylase inhibitor, in adults with refractory and relapsed acute leukemias. *Blood* **2007**, *109*, 2781–2790. [CrossRef]
51. Fournel, M.; Trachy-Bourget, M.-C.; Yan, P.T.; Kalita, A.; Bonfils, C.; Beaulieu, C.; Frechette, S.; Leit, S.; Abou-Khalil, E.; Woo, S.-H.; et al. Sulfonamide anilides, a novel class of histone deacetylase inhibitors, are antiproliferative against human tumors. *Cancer Res.* **2002**, *62*, 4325–4330. [PubMed]
52. Zhu, P.; Huber, E.M.; Kiefer, F.; Göttlicher, M. Specific and Redundant Functions of Histone Deacetylases in Regulation of Cell Cycle and Apoptosis. *Cell Cycle* **2004**, *3*, 1240–1242. [CrossRef] [PubMed]
53. Lees, A.; McIntyre, A.J.; Crawford, N.T.; Falcone, F.; McCann, C.; Holohan, C.; Quinn, G.P.; Roberts, J.Z.; Sessler, T.; Gallagher, P.F.; et al. The pseudo-caspase FLIP(L) regulates cell fate following p53 activation. *Proc. Natl. Acad. Sci. USA* **2020**, *117*, 17808–17819. [CrossRef] [PubMed]
54. Belnap, L.P.; Cleveland, P.H.; Colmerauer, M.E.; Barone, R.M.; Pilch, Y.H. Immunogenicity of chemically induced murine colon cancers. *Cancer Res.* **1979**, *39*, 1174–1179.
55. Kim, K.; Skora, A.D.; Li, Z.; Liu, Q.; Tam, A.J.; Blosser, R.L.; Diaz, L.A., Jr.; Papadopoulos, N.; Kinzler, K.W.; Vogelstein, B.; et al. Eradication of metastatic mouse cancers resistant to immune checkpoint blockade by suppression of myeloid-derived cells. *Proc. Natl. Acad. Sci. USA* **2014**, *111*, 11774–11779. [CrossRef]
56. Yokoo, S.; Masuda, S.; Yonezawa, A.; Terada, T.; Katsura, T.; Inui, K.-I. Significance of Organic Cation Transporter 3 (SLC22A3) Expression for the Cytotoxic Effect of Oxaliplatin in Colorectal Cancer. *Drug Metab. Dispos.* **2008**, *36*, 2299–2306. [CrossRef]
57. Sonnemann, J.; Marx, C.; Becker, S.; Wittig, S.; Palani, C.D.; Krämer, O.H.; Beck, J.F. p53-dependent and p53-independent anticancer effects of different histone deacetylase inhibitors. *Br. J. Cancer* **2014**, *110*, 656–667. [CrossRef]
58. Liu, Y.; Bodmer, W.F. Analysis of P53 mutations and their expression in 56 colorectal cancer cell lines. *Proc. Natl. Acad. Sci. USA* **2006**, *103*, 976–981. [CrossRef]
59. Haendler, B.; Bracker, T.U.; Sommer, A.; Fichtner, I.; Faus, H.; Hess-Stumpp, H. Efficacy of MS-275, a selective inhibitor of class I histone deacetylases, in human colon cancer models. *Int. J. Oncol.* **2009**, *35*, 909–920. [CrossRef]
60. Kiweler, N.; Wünsch, D.; Wirth, M.; Mahendrarajah, N.; Schneider, G.; Stauber, R.H.; Brenner, W.; Butter, F.; Krämer, O.H. Histone deacetylase inhibitors dysregulate DNA repair proteins and antagonize metastasis-associated processes. *J. Cancer Res. Clin. Oncol.* **2020**, *146*, 343–356. [CrossRef]
61. Kiweler, N.; Brill, B.; Wirth, M.; Breuksch, I.; Laguna, T.; Dietrich, C.; Strand, S.; Schneider, G.; Groner, B.; Butter, F.; et al. The histone deacetylases HDAC1 and HDAC2 are required for the growth and survival of renal carcinoma cells. *Arch. Toxicol.* **2018**, *92*, 2227–2243. [CrossRef]
62. Zhan, Y.; Gong, K.; Chen, C.; Wang, H.; Li, W. P38 MAP kinase functions as a switch in MS-275-induced reactive oxygen species-dependent autophagy and apoptosis in Human colon Cancer cells. *Free. Radic. Biol. Med.* **2012**, *53*, 532–543. [CrossRef]
63. Marx, C.; Sonnemann, J.; Beyer, M.; Maddocks, O.D.K.; Lilla, S.; Hauzenberger, I.; Pié-Staffa, A.; Siniuk, K.; Nunna, S.; Marx-Blümel, L.; et al. Mechanistic insights into p53-regulated cytotoxicity of combined entinostat and irinotecan against colorectal cancer cells. *Mol. Oncol.* **2021**, *15*, 3404–3429. [CrossRef]
64. Percie du Sert, N.; Hurst, V.; Ahluwalia, A.; Alam, S.; Avey, M.T.; Baker, M.; Browne, W.J.; Clark, A.; Cuthill, I.C.; Dirnagl, U.; et al. The ARRIVE guidelines 2.0: Updated guidelines for reporting animal research. *PLoS Biol.* **2020**, *18*, e3000410.
65. Langmead, B.; Salzberg, S.L. Fast gapped-read alignment with Bowtie 2. *Nat. Methods* **2012**, *9*, 357–359. [CrossRef]
66. Anders, S.; Pyl, P.T.; Huber, W. HTSeq—A Python framework to work with high-throughput sequencing data. *Bioinformatics* **2015**, *31*, 166–169. [CrossRef]
67. Love, M.I.; Huber, W.; Anders, S. Moderated estimation of fold change and dispersion for RNA-seq data with DESeq2. *Genome Biol.* **2014**, *15*, 550. [CrossRef]
68. Varet, H.; Brillet-Gueguen, L.; Coppee, J.Y.; Dillies, M.A. SARTools: A DESeq2- and EdgeR-Based R Pipeline for Comprehensive Differential Analysis of RNA-Seq Data. *PLoS ONE* **2016**, *11*, e0157022. [CrossRef]

69. Yu, G.; Wang, L.-G.; Han, Y.; He, Q.-Y. clusterProfiler: An R Package for Comparing Biological Themes Among Gene Clusters. *OMICS J. Integr. Biol.* **2012**, *16*, 284–287. [CrossRef]
70. Eckschlager, T.; Plch, J.; Stiborova, M.; Hrabeta, J. Histone Deacetylase Inhibitors as Anticancer Drugs. *Int. J. Mol. Sci.* **2017**, *18*, 1414. [CrossRef]



Review

Cerebellar and Striatal Implications in Autism Spectrum Disorders: From Clinical Observations to Animal Models

Mathieu Thabault ^{1,†}, Valentine Turpin ^{1,†}, Alexandre Maisterrena ¹, Mohamed Jaber ^{1,2}, Matthieu Egloff ^{1,2,†} and Laurie Galvan ^{1,*}

¹ Laboratoire de Neurosciences Expérimentales et Cliniques, Institut National de la Santé et de la Recherche Médicale, Université de Poitiers, 86073 Poitiers, France; mathieu.thabault@univ-poitiers.fr (M.T.); valentine.turpin@univ-poitiers.fr (V.T.); alexandre.maisterrena@univ-poitiers.fr (A.M.); mohamed.jaber@univ-poitiers.fr (M.J.); matthieu.egloff@univ-poitiers.fr (M.E.)

² Centre Hospitalier Universitaire de Poitiers, 86021 Poitiers, France

* Correspondence: laurie.galvan@univ-poitiers.fr

† These authors contributed equally to this work.

Abstract: Autism spectrum disorders (ASD) are complex conditions that stem from a combination of genetic, epigenetic and environmental influences during early pre- and postnatal childhood. The review focuses on the cerebellum and the striatum, two structures involved in motor, sensory, cognitive and social functions altered in ASD. We summarize clinical and fundamental studies highlighting the importance of these two structures in ASD. We further discuss the relation between cellular and molecular alterations with the observed behavior at the social, cognitive, motor and gait levels. Functional correlates regarding neuronal activity are also detailed wherever possible, and sexual dimorphism is explored pointing to the need to apprehend ASD in both sexes, as findings can be dramatically different at both quantitative and qualitative levels. The review focuses also on a set of three recent papers from our laboratory where we explored motor and gait function in various genetic and environmental ASD animal models. We report that motor and gait behaviors can constitute an early and quantitative window to the disease, as they often correlate with the severity of social impairments and loss of cerebellar Purkinje cells. The review ends with suggestions as to the main obstacles that need to be surpassed before an appropriate management of the disease can be proposed.

Keywords: ASD; cerebellum; striatum; epigenetics; motricity; autism

Citation: Thabault, M.; Turpin, V.; Maisterrena, A.; Jaber, M.; Egloff, M.; Galvan, L. Cerebellar and Striatal Implications in Autism Spectrum Disorders: From Clinical Observations to Animal Models. *Int. J. Mol. Sci.* **2022**, *23*, 2294. <https://doi.org/10.3390/ijms23042294>

Academic Editors: Masaru Tanaka and Lydia Giménez-Llort

Received: 14 January 2022

Accepted: 8 February 2022

Published: 18 February 2022

Publisher's Note: MDPI stays neutral with regard to jurisdictional claims in published maps and institutional affiliations.



Copyright: © 2022 by the authors. Licensee MDPI, Basel, Switzerland. This article is an open access article distributed under the terms and conditions of the Creative Commons Attribution (CC BY) license (<https://creativecommons.org/licenses/by/4.0/>).

1. Introduction

Autism spectrum disorder (ASD) is a neurodevelopmental condition manifested by early onset of (i) persistent deficits in communication and social interactions and (ii) restricted patterns of behaviors, activities or interests (DSM5). The severity range of each symptom, and the fact that other abnormalities can accompany ASD, led to the “spectrum” umbrella term. Comorbidities vary among patients, but the most common ones are: sleep disorders (up to 80%), intellectual deficits (45%), epilepsy (up to 30%) and, interestingly, motor abnormalities (79%) [1]. The WHO considers that ASD affects 1 in 160 children worldwide following a ratio of 3 boys for 1 girl [2], suggesting male susceptibility. To this day, the diagnosis age ranges from infant to adult, depending on the severity of the symptoms and the social environment.

The etiology of ASD is still uncertain, but evidence has strongly linked genetic, epigenetic and environmental factors to it. The gathered knowledge in this domain is interdependent with technological advances. The possibility to collect and analyze broad genetic information for the past ten years has led to breakthroughs. The first pieces of evidence of genetic involvement in ASD were the case studies of monozygotic twins. These twins displayed a 60% probability to share the same ASD diagnosis, whereas dizygotic

twins' probability was at 10% [3–5]. More importantly, the incidence of having an ASD child is proportional to the child's shared genomic percentage with an ASD parent or sibling [6–8]. The advancement of sequencing technics led to the possibility of analyzing the patient's whole genome, which helped identify more than 1200 susceptibility genes (SFARI gene, <https://www.sfari.org/resource/sfari-gene/>, accessed on 14 September 2021). These genes can be broadly categorized into two families, involving either chromatin modeling or synapse formation [9].

Perinatal factors have been identified as increasing ASD incidence, including maternal infection and maternal toxin exposure. A 2016 meta-analysis of more than 40,000 ASD cases highlighted an increased risk of ASD in children whose mother had a viral infection during pregnancy, leading to hospitalization [10]. One hypothesis underlying this observation is that maternal immune regulation leads to increased production of inflammatory cytokines. There is not a consensus about how the cytokines could reach the fetus brain. They could reach it by disrupting the brain–blood barrier (BBB) [11] or by the actions of proinflammatory cytokines able to cross the BBB (for review, see [12]). Several pharmacological agents are also responsible for increasing ASD incidence in children exposed during prenatal development. For instance, valproic acid (VPA) is widely used as an antiepileptic drug and a mood stabilizer. It has various effects, from inhibiting the histone deacetylase [13] to the GABA signaling potentiation [14]. Pregnant women under VPA medication are four to five times more likely to have an ASD child even when VPA was taken at the lowest doses [15] (for review, see [16] and Table 1). We will focus on the VPA as an environmental model of ASD in this review event, though; others have been described as the phthalic acid ester exposition (for review, see [17]).

Some of the mutations and perinatal factors increasing ASD incidence have led to the generation of corresponding animal models, with some showing good face validity compared to clinical conditions. However, not all ASD symptoms can be reproduced in rodents. For example, while social interaction and motor stereotypy can be robustly observed and scored in rodents using various and complementary behavioral tests, cognitive stereotypy and intellectual disability cannot be adequately assessed. Speech deficits are also a symptom in patients, which cannot be directly translated in the mouse models. The closest feature that can be measured is ultrasonic vocalizations (USVs). USVs are used by pups separated from their mother or littermates, by juveniles when playing and by adults during social interactions or mating. Although their exact significance is unclear, many different USVs parameters were modified in ASD mice compared to wild type. *Shank1*^{-/-} pups emitted less isolation-induced USV with a shift in frequencies than control mice [18], but not *Shank3*^{-/-} pups, where other parameters were modified [19]. Additionally, no difference in the number of USVs emitted by pups was found between the *Frm1*^{-/-} mice and wild type but rather a change in specific frequency [20]. Thus, it seems challenging to observe consistent and robust USV changes through different ASD mouse models.

Since 1943 and the first description of autistic features by Leo Kanner [21], followed almost concomitantly in 1944 by Hans Asperger [22], motor and cognitive impairments have been within the core of ASD symptoms. Currently, studies focus more on cognitive aspects of ASD and the corresponding physiopathology and brain regions [23,24]. The notion linking ASD to a focal cerebral dysfunction has drastically evolved toward a consensus of cerebral multi-regional reorganization during development. We will focus this review on two complex brain areas involving sensory and motor functions: the cerebellum and the striatum.

Table 1. Various outcomes in various animal models of valproic acid administration during development in relation with species, dose and age. This table recapitulates the different VPA models and their phenotypes. IP: Intraperitoneal injection, USV: Ultrasonic vocalizations, DIR and D2R: D1 dopamine receptor and D2 dopamine receptor, PC: Purkinje cells, MOR: Mu opioid receptor, PV: Parvalbumin interneurons, mPFC: median Prefrontal cortex, GABAP3: GABA receptor subunit p3.

Species	Treated Animal	Periodicity	Dose	Age of Treatment	Phenotype
Xenopus [13]	Embryo	24 h exposition of the eggs	<ul style="list-style-type: none"> • 1 mM • 2.5 mM • 5 mM 	Stage 8 embryo	<ul style="list-style-type: none"> • 5 mM: loss of anterior structures and shortening of anterior-posterior axis in 88% of embryos
C57BL/6j mice [25]	Pregnant female	One IP injection	450 mg/kg	E12.5	<ul style="list-style-type: none"> • <input checked="" type="checkbox"/> Eye-opening delay • <input checked="" type="checkbox"/> Time to climb the wire and the grid • <input checked="" type="checkbox"/> Immobility in males • <input checked="" type="checkbox"/> Crossing in males • <input checked="" type="checkbox"/> Grooming duration • <input checked="" type="checkbox"/> Rearing in males • <input checked="" type="checkbox"/> Sociability index in males • <input checked="" type="checkbox"/> Errors during challenging beam test • <input checked="" type="checkbox"/> Gait abnormality • <input checked="" type="checkbox"/> PC number in Crus 1/2 and M1/M2
C57BL/6j mice [16]	Pregnant female	One IP injection	600 mg/kg	E12	<ul style="list-style-type: none"> • <input checked="" type="checkbox"/> PC density in young mice at P13 • <input checked="" type="checkbox"/> PC number in males at P40
C57BL/6j mice [26]	Pregnant female	One oral administration	600 mg/kg	E12	<ul style="list-style-type: none"> • <input checked="" type="checkbox"/> PV expression level but not PV neurons • <input checked="" type="checkbox"/> mPFC volume • <input checked="" type="checkbox"/> KCNC1 mRNA level in forebrain • <input checked="" type="checkbox"/> Kv3.1b mRNA level in forebrain • <input checked="" type="checkbox"/> HCN1 mRNA level in forebrain
CD-1 and GFAP-eGFP mice [27]	Pregnant female	One IP injection	500 mg/kg	E12.5	<ul style="list-style-type: none"> • <input checked="" type="checkbox"/> CB+ cells CB intensity and GABAP3 intensity in lobule X at P8 • <input checked="" type="checkbox"/> Expression of GABP3 in ependymal glial cells • <input checked="" type="checkbox"/> Disrupted GABAP3 expression through development

Table 1. Cont.

Species	Treated Animal	Periodicity	Dose	Age of Treatment	Phenotype
FVB/NJ mice [28]	Pregnant female	One IP injection	400 mg/kg	E11.5 or E12.75	<p>E11.5</p> <ul style="list-style-type: none"> ☒ MOR1 expression in caudal striatum at P14 ☒ Abnormal cell aggregation into striosomal patch <p>E12.75</p> <ul style="list-style-type: none"> ☒ MOR1 expression in caudal striatum at P14 ☒ CB number rich matrix in rostral in the ventro-medial striatum at P14 ☒ Abnormal cell aggregation into striosomal patch ☒ FOXP2+ cell in layer 5 (S1 cortex) and layer 6 (S2 cortex) ☒ Corticostriatal synapse in rostral striatum ☒ Number, duration, peak frequency and peak amplitude in USV
Long Evans rats [29]	Pregnant female	One IP injection	600 mg/kg	E12.5	<ul style="list-style-type: none"> ☒ PC number in vermis, anterior, posterior lobes ☒ Granule layer volume in vermis, anterior, posterior lobes
Long Evans rats [30]	Pregnant female	One oral administration	800 mg/kg	E12	<ul style="list-style-type: none"> ☒ Brain weight ☒ Errors in T-maze ☒ Deficits in females in skilled reaching but improvement in male ☒ Time in open arms in elevated plus maze ☒ Dendritic branching in male ☒ Dendritic length; decrease spine density, decrease cortical thickness
Sprague-Dawley rats [31]	Pregnant female	Two oral administrations	800 mg/kg	E10 and E12	<ul style="list-style-type: none"> ☒ Body weight between P21 and P28, ☒ brain weight ☒ Body length ☒ Purkinje cell size in all ten lobules ☒ Number of calbindin positive PC in all ten vermal lobules ☒ Primary dendrite thickness. ☒ Time to righting ☒ Length in limb stride ☒ Time to complete static beam and number of errors and of failed attempts

Table 1. Cont.

Species	Treated Animal	Periodicity	Dose	Age of Treatment	Phenotype
Wistar rats [32]	Young rat	Daily intragastric administration	200 mg/kg	<ul style="list-style-type: none"> • 1 month • 3 months • 6 months • 9 months • 12 months 	<ul style="list-style-type: none"> • <input checked="" type="checkbox"/> Swelling of perikarya and dendritic process • <input checked="" type="checkbox"/> Abnormalities of mitochondria • 9 and 12 months: severe degenerative changes • <input checked="" type="checkbox"/> Swollen Bergmann astrocytes
Wistar rats [33]	Pregnant female	One IP injection	500 mg/kg	E12.5	<ul style="list-style-type: none"> • <input checked="" type="checkbox"/> Social play behavior and sociability in 3-CT • <input checked="" type="checkbox"/> Social discrimination ability • <input checked="" type="checkbox"/> D2R expression in Nucleus accumbens • <input checked="" type="checkbox"/> DIR expression in Nucleus accumbens • <input checked="" type="checkbox"/> Resting potential in MSNs • <input checked="" type="checkbox"/> Altered action potential discharge pattern in MSN

2. Cerebellar Involvement in ASD

2.1. Structure and Function of the Cerebellum

All vertebrates have a cerebellum, although not all have a cortex [34]. The cerebellum might have first emerged in fish, providing computational analysis of sensory feedback from their lateral lines and hair cells on their skin that help them detect their environment [35]. The primary role of the cerebellum has long been linked to coordination and control of movement. Its implication in higher function has first been proposed by Leiner, following the observation in higher primates of an enlargement of the cerebellum that paralleled that of the frontal cortex during phylogenetic evolution [36]. A few years later, Middleton and Strike provided anatomical evidence of cerebellar and basal ganglia involvement in higher cognitive function [37]. Since then, many studies highlighted the eminent role of the cerebellum in cognitive and emotional function, and that was attributed to its connections with cortical and subcortical centers [38,39]. In addition, extensive connections between the cerebellum and frontal associative cortical areas suggest a critical role in treating sensory motor information from visual, auditory and sensory input, as well as a role in memory, language processing and planification [40].

Although relatively simple in its general structure, as well as afferent and efferent projections and cellular organization, the anatomy of the cerebellum can be difficult to describe. This is mainly due to three factors: (i) the structure/function of the cerebellum is quite different depending on whether one is considering the anteroposterior or parasagittal plans; (ii) each part of the cerebellum can have several names depending on the user and the current trend; (iii), not all authors agree on what each part encompasses. When viewed from the anteroposterior axis, the cerebellum is formed from three lobes: the vestibulocerebellum, the posterior cerebellum and the anterior cerebellum, which are separated by deep fissures. Each lobe is constituted by lobules numbered I to X, giving the cerebellum its folded shape. The vestibulocerebellum (also called lobule X) comprises a median nodule and flocculus lateral ones. It is directly connected to the vestibular nuclei within the brainstem and receives projections from the auditory nerve. Most of the efferent projections from the cerebellum originate from four deep cerebellar nuclei within the vestibulocerebellum that receive projections from collateral fibers, parallel fibers and Purkinje cells (PC). This is the oldest part of the cerebellum phylogenetically, and it is shared among all vertebrates. It handles perception of self-motion and spatial orientation through the auditory system of the head's position and motion. The anterior lobe is composed of lobules I–V and includes the medial vermis part. It receives proprioceptive information from the body and limbs, as well as from the visual and auditory systems. It sends projections toward the cortex and the spinal cord, modulating the descending motor system. The anterior lobe is responsible for balance, posture and consequent movement adjustments in time and space. The posterior lobe is composed of lobules VI–IX. This lobe constitutes the cerebellar hemispheres and is the most recent and evolved part of the cerebellum. It is only present in higher mammals and is particularly enlarged in the human species. The posterior lobe receives projections exclusively from the cerebellar cortex and sends projections to the ventrolateral part of the thalamus. It is thought to be implicated in movement planification, motor learning, timing, language processing and emotional, cognitive and social functions.

From a parasagittal perspective, the central part of the cerebellum is constituted by the vermis, followed by the paravermis and ending laterally by the cerebral hemispheres, which constitute the most significant part in the primate's cerebellum. Each lobule can have a different function and set of projections, depending on its parasagittal plan. Of interest to us here are crus I and crus II that constitute the lateral parts of lobules VI and VII, respectively, within the posterior lobe and that are affected in ASD. Crus I and crus II are homologous in human and non-human primates. However, rodent crus I corresponds to crus I and crus II in primates [41], while rodent crus II may be homologous to HVIIIB.

At the cellular level, the cerebellar cortex is organized into three layers that are, from the surface to the white matter: (i) the molecular layer, a cell-poor layer containing stellate and basket cells as well as PC dendrites connected to parallel fiber axons from granule

cells and to climbing fibers. The climbing fiber axons are also found in the granular layer, (ii) the PC layer, a thin single cell layer and (iii) the granule cell layer containing what is thought to constitute more than 50% of whole nerve cells within the brain (up to 10^{11} neurons) [42]. Granule cells receive projections from mossy fibers originating from the vestibular nuclei. In turn, they project excitatory parallel fibers to PC dendrites within the molecular layer, each parallel fiber contacting 100 PC. Each PC receives an approximate number of 150,000 synapses from parallel fibers and projections emanating from a single climbing fiber [43] originating from the inferior olive. The PC are large neurons with flat and rich dendritic arborization. Their inhibitory GABAergic axon projects through the granular layer to the vestibular nuclei and constitutes the sole efferent projection from the cerebellar cortex (Figure 1).

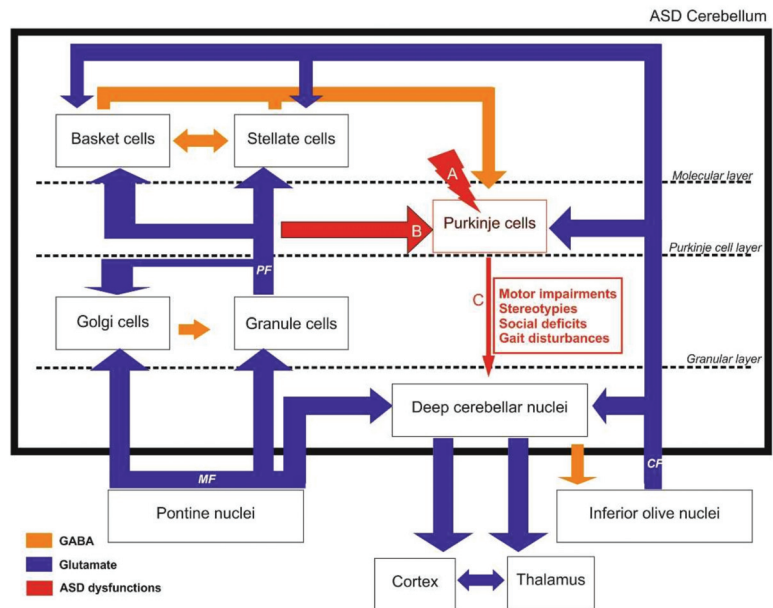


Figure 1. The cerebellum is involved in both motor and social impairments reported in ASD. Dysfunctional Purkinje cells (PC) seem to be at the center of these impairments as they represent the sole output of the cerebellum and receive inputs from both inhibitory and excitatory cells. PC dysfunctions are reported in ASD clinical settings and in animal models (A, B, C). PC intrinsic changes (A) such as reduced PC density was shown in *Fmr1* KO mice [44], *TSC2f*^{-/-} mice [45], *Mecp2* deficient mice [46], VPA mice [47], polyI:C mice [48] and *Shank3* $\Delta C/\Delta C$ mice [49], with regional lobular differences between males and females. Low PC numbers associated with a decrease in soma size and an increase in ectopic PC number were also reported in VPA rats [50], especially in lobule VII hemispheres (crus I and II) that are involved in sensorimotoricity. Impaired inputs from granule cells through parallel fibers (B) were also reported. For instance, the mGluR-long term depression (LTD) was altered at the PF-PC synapse in both PC-specific *Grip1/2* KO mice and *Fmr1* KO mice [51,52]. Furthermore, PC abnormal dendritic branching and reduced density of dendritic spines were found to impair synapse formation in VPA rats [53,54] and in *Fmr1* KO mice [44,51]. Outputs from PC onto deep cerebellar nuclei (C) are also impacted, as PC firing pattern is impaired in mice lacking Calbindin, with decreased complex spike duration and pause, as well as decreased simple high spike firing rate [55]. In the *Shank2* KO mice, an increased irregularity in simple spike PC firing accompanied by increased inhibition was only found in the posterior cerebellum [56]. Altogether, these PC-focused alterations would lead to dysfunctional cerebellar loop up to the thalamus and cortex leading to both motor and cognitive impairments. MF: Mossy fibers, CF: climbing fibers, PF: parallel fibers.

The various functions of the cerebellum that have been described to date, whether motor or cognitive, seem to converge toward a peculiar capacity of the cerebellum to estimate and keep track of time. James Albus proposed that the anatomy and physiology of the cerebellum both point toward a pattern-recognition data processing that allows the handling and storage of information based on trial (intent) and error (action) and that this is achieved by weakening the synaptic weights rather than by strengthening them [36,57]. Clumsiness and deficits in motor coordination and manual dexterity, abnormal balance gait and posture are all dependent on the cerebellar function and are affected in ASD [58–60]. These deficits can be detected even in the first months of life, with affected babies exhibiting difficulties positioning their body when carried, hypotonia and uncoordinated movements.

Based on the existing knowledge of the sensory motor role of the cerebellum and suspecting its implication in psychiatric disorders, Dow and Moruzzi developed test batteries early in 1958 on patients with various psychiatric disorders. They reported severe cerebellar-type impairments in what was referred to as patients suffering from autistic and Asperger syndromes [61]. Since then, a growing number of papers have reported substantial implications of the cerebellum in motor and non-motor deficits in ASD. From this aspect, the severity of cerebellar injury in premature infants is predictive of the severity of ASD symptoms in adult age [62]. Indeed, there are three cerebellar-related deficits reported in ASD patients based on imaging and post-mortem histological observations: (i) a decrease in the number of PC, (ii) reduced cerebellar volume and (iii) disrupted circuitry between the cerebellum and connecting brain areas, such as the thalamus, the pons and the cortex [63,64]. As PC are inhibitory, this, in turn, leads to hypersensitivity of cerebellar target areas [65,66].

2.2. Anatomical Evidence of Cerebellar Involvement in ASD

The involvement of cerebellum in the ASD context is also supported by genetic evidence. Indeed, 38 genes, whose expression is enriched in the cerebellum, were identified as ASD-linked susceptibility genes [25]. Several studies showed that ASD patients displayed hypoplasia (−12% [67,68], for review, see [63]). Using magnetic resonance imaging (MRI) in both adult ASD and healthy patients, Murakami et al. reported a reduced size of both vermis and hemispheres in ASD patients without and with mild mental retardation [67]. This alteration is not always found in ASD mouse models and could be due to the spectrum of the disease or the heterogeneous way of assessing it at the levels of (i) methodology (stereology vs. MRI), (ii) diversity of genetic background of ASD animals, (iii) animal age and (iv) gender (for review, see [69]). A decrease in cerebellar volume has also been reported in multiple genetic pathologies related to ASD, including fragile X syndrome (FXS) [70,71], Rett syndrome [70–72], the Phelan–McDermid syndrome, including *Shank3* deletion [73,74] (SH3 and multiple ankyrin repeat domains 2), and *NLGN4* (Neurologin-4) associated non-syndromic X-linked ASD [46]. Decreases in cerebellar volume can also be observed in corresponding animal models, such as the *Fmr1* Knock-out (KO) [44] and *Nlgn4* KO [75] mice models (Table 2).

Table 2. Cerebellar dysfunctions in ASD. This table recapitulates cerebellar dysfunctions found in patients and animal models.

	Children			Teenagers	Adults	Animal Models
	<5 years old	5 to 14 years old	14 to 21 years old	>21 years old		
Anatomical impairment	Global cerebellar volume	• N/A	• N/A	• N/A	• Hypoplasia [55,56]	• No consistent changes [57] <input checked="" type="checkbox"/> Fmr1KO [64] and Nlgn4KO ⁻ [65] = Shank3 ^{ΔC/ΔC} , VPA and Poly I:C models [25,66,67]
	White matter (WM) changes	• <input checked="" type="checkbox"/> WM [68,69]	• No change [69] • Local thickening in boys [70,71]	• No change [69]	• N/A	• N/A
Connectivity	• N/A	• <input checked="" type="checkbox"/> in the right Crus I and left inferior parietal lobule [76]	• <input checked="" type="checkbox"/> in the right Crus I and left inferior parietal lobule [76]	• <input checked="" type="checkbox"/> in right Crus I and left mPFC [77]	• <input checked="" type="checkbox"/> in at least 30 mouse lines for Crus I/II projections [78] • <input checked="" type="checkbox"/> PC firing in left mPFC when right crus I is inhibited [76]	
	• <input checked="" type="checkbox"/> Right during motor task [72] • <input checked="" type="checkbox"/> in the left supplementary motor areas [72] • Global right overconnectivity [73]					
Cellular correlates	Purkinje cell (PC)	• <input checked="" type="checkbox"/> axon numbers [79]	• <input checked="" type="checkbox"/> axon numbers [79]	• <input checked="" type="checkbox"/> PC density [80]	• <input checked="" type="checkbox"/> PC density [51,80–82] • <input checked="" type="checkbox"/> soma size & ectopic PC in molecular layer [81,82]	• <input checked="" type="checkbox"/> PC density [25,66,67,83] • <input checked="" type="checkbox"/> PC density [63] • <input checked="" type="checkbox"/> PC arborization in LPS rats [84] • <input checked="" type="checkbox"/> Dendritic spine density in VPA rats [30]
	Bergmann cells	• N/A	• N/A	• N/A	• Activated/reactivated in PC loss area [51,85]	• <input checked="" type="checkbox"/> Increased ectopic PC in VPA rats [29,30] • Activated/reactive in PC loss area in Fmr1 ^{-/-} [64] and VPA rat [32]
Microglia	• N/A	• High global microglial activation [85]			• No changes in poly I:C mice [67]	• No changes in poly I:C mice [67]
Neurotransmission	Glutamate	• N/A	• <input checked="" type="checkbox"/> AMPA-R density [86] • <input checked="" type="checkbox"/> glutamate & glutamate metabolite levels [87]	• <input checked="" type="checkbox"/> AMPA-R density [86] • <input checked="" type="checkbox"/> glutamate & its metabolite levels [87]	• <input checked="" type="checkbox"/> AMPA-R density [86] • <input checked="" type="checkbox"/> levels of EAAT1/2 [88]	• Impaired mGluR LTD [89–91] • <input checked="" type="checkbox"/> mGluR5 expression in Gripl1/2-PC, Fmr1 ^{-/-} and Shank2 ^{-/-} [90,92–94] • <input checked="" type="checkbox"/> mGluR5 expression in Shank3 ^{ΔC/ΔC} [66]
	GABA	• <input checked="" type="checkbox"/> GABA-A β3 level [95]	• <input checked="" type="checkbox"/> GABA-A β3 level [95]	• <input checked="" type="checkbox"/> GABA-A β3 level [95]	• <input checked="" type="checkbox"/> GABA-A α, GABA-B R1 density, GAD65/67 levels [96,97] • <input checked="" type="checkbox"/> GABA-A β3 level [95]	• Abnormal PC firing pattern in Calbindin deficient mice [98] • <input checked="" type="checkbox"/> GABA-A p3 levels in VPA model [27] • <input checked="" type="checkbox"/> GABA-A β1 & β2 levels in Fmr1 KO [99]

N/A: not applicable.

PC loss has been consistently described in ASD patient brains, and cerebellar hypoplasia was found in most cases [49,62,63,75]. In our previous articles, three ASD mice models (Shank3^{ΔC/ΔC} [49], VPA [47] and polyinosinic:polycytidylic acid (poly I:C) [48]) displayed no global changes in cerebellum size, although they did show PC loss predominantly in crus I and II. Beyond the cell count, cerebellar connectivity is also affected in ASD, and white and gray matter abnormalities have been observed by voxel-based morphometry. Analysis of cerebellar white matter in low- and high-functioning ASD young male children shows a significant increase in white matter volume compared to a typical children group [77]. That characteristic has been robustly used as a prediction for ASD diagnosis in this same study. A specific change in cerebellar white matter is typical in 2–3-year-old ASD children, which is not observed in older ASD children and adolescents [78]. A few studies have investigated fiber tracts and myelin differences in ASD patients using diffusion tensor imaging (DTI), revealing changes in white matter structure and projections. The evaluation of white matter in male ASD children (6–12 years old) shows a thickening of the left cerebellar peduncle and of both middle cerebellar peduncles compared to typical children [76]. Interestingly, motor-related structures were also affected, such as the left putamen and the corticocortical pathway [76]. Considering motor deficits in ASD, another study assessed, contingently, motor function and DTI in ASD children (5–14 years old, twelve males and one female) compared to a non-ASD control age group [100]. In this study, ASD children displayed the poorest motor function scores (manual dexterity, ball skills and balance) compared to neurotypical children. Additionally, these motor deficits were correlated with a decrease in fractional anisotropy (white matter microstructural integrity index) bilaterally in the superior cerebellar peduncle [100], the efferent cerebellar tract to the midbrain being mainly composed of the cerebellothalamic tract. Taken together, these white matter analyses reveal an alteration of cerebellar motor pathways in ASD.

Lateralization of functional connectivity patterns is modified in ASD, revealing changes in functional topography. Noonan et al. assessed the functional connectivity of ASD brains by asking adult patients to perform a memory task while undergoing an MRI. They selected high functioning ASD adult males who showed the lowest score at general word recognition and source recognition performance compared to a control group. Although ASD and control groups showed no differences in functional connectivity in the left hemisphere, ASD patients showed greater connectivity in the right hemisphere, including the right supplementary motor areas and the cerebellum [101]. This right overconnected lateralization of the ASD cerebellum was also observed in ASD children and adolescents [81]. Interestingly, the performance of a simple motor task (self-paced button press with the dominant thumb) by young ASD adults and control patients while being imaged revealed that the magnitude of activation of the ipsilateral anterior cerebellum is strongly increased in ASD patients [68]. Moreover, the authors found that contralateral and posterior cerebellar regions that are not generally associated with simple motor tasks were abnormally active in ASD patients [68].

Consequently, based on the over-recruitment of crus I and II in ASD patients, as well as in cerebral regions involved in both cognitive and motor tasks, these regions might be essential for understanding the behavior impairments in ASD patients. From this aspect, MRI analysis in young children showed that ASD children with repetitive movements had a negative correlation with cerebellar vermis area of lobule VI and VII (crus I and II) [82]. Evidence from 10-year-old ASD children revealed higher functional connectivity between the right crus I and the left inferior parietal lobule than neurotypical children [102]. This connectivity is not the only one impaired in ASD. Similar observations were reported regarding projections originating from the right crus I to the left mPFC in ASD patients [79] and in 30 out of 94 ASD mice models [83]. Consequently, chemogenetics-specific inhibition of PC in the right crus I in the tuberous sclerosis complex 1 (Tsc1) ASD mouse model led to increased firing in the left mPFC associated with improved sociability behavior, inflexibility and motor stereotypies [80]. This pathway is polysynaptic, as it anatomically relays on the ventral medial thalamus. In the Tsc1 ASD mouse models, the optogenetic inhibition

of these specific thalamic neurons was sufficient to prevent both social impairments and repetitive behavior [83].

The posterior cerebellar circuits allow the processing and integration of multisensory information, including visual, proprioceptive and somatosensory, which may be reduced in ASD patients. This raises the hypothesis of compensating mechanisms in ASD patients regarding their sensory forward control deficits in prehension, gait and postural control. When high-functioning ASD children have been asked to perform a simple motor task, such as a “grip”, they displayed an increase in the grip to load force, suggesting temporal dyscoordination. Since Vilensky’s study in the 1980s, ASD patients’ walking features have been highly investigated, and a dozen differences were found, such as increased stance duration, reduced stride length, toe striking and increased angular motions [103]. Interestingly, these features are also modified in some ASD mice models. ASD patients seem to slow down their movements in relation to task difficulty and need more practice than typical individuals. These deficits in complex social motor skills could be associated with social and imitation impairments and over-reliance on proprioceptive feedback in motor control and learning (for review, see [104]).

2.3. Cellular Correlates

The PC number decreases from 35 to 95% in ASD patients [49,63,75,84], and their soma size and, consequently, their density [29,84], are affected too. Differences in the extent of the reported decreases seem to result from a high variability both in subjects and methods. One of the pioneer post-mortem studies found PC loss and ectopic PCs within the molecular layer only in adults, whereas PC inclusions were described in a sole child case [30]. In parallel, fewer axons were found in PCs from ASD children (male and female, 3.6–13.3 years old) using diffusion MRI tractography [31]. These findings highlight age as a crucial parameter in ASD cellular consequences. The spectrum of symptoms in this disorder might account for the difficulty in obtaining homogenous results in both patients and animal models. This is even the case with genetic mouse models of ASD, where different cellular outcomes have been reported. For instance, PC density was reduced in both *Fmr1* KO mice (C57BL/6J, P30) [44] and mice with a specific deletion of the tuberous sclerosis complex 2 (*TSC2*) [45], whereas an increase was observed in *Mecp2*-deficient mice [46]. In our study, *Shank3^{Δc/Δc}* mice displayed an extensive loss of PC in both crus I and II, but only in males [49]. While gait was disrupted only in males, deficits in social novelty were observed in both sexes. In environmental ASD models, our previous studies showed PC loss in both crus II and 7cb in males and PM in females, with poly I:C prenatal insult [48]. In the VPA mouse model (E12.5; 450 mg/kg) (Table 1), PC number was reduced in crus I in males and crus II in females [47]. This sex-specific reduction was correlated with behavioral tests assessing sociability and motor impairments. Sexual dimorphism was also found in another study that reported PC decrease only in VPA males in the cerebellar lobules VI, VIII, IX and the paramedian one [16]. Clinical studies also established correlations between sex and regional-specific PC loss. For instance, Skefos et al. found that ASD male patients (7–56 years old) exhibited a 21% decrease in regional volume-weighted mean compared to females (4–21 years old). Only males presented a reduction in PC in the lobule X of the flocculonodular lobe. The posterolateral region seems to be the most affected, specifically the lobule VII hemispheres, which are crucial sensorimotor areas with reciprocal interaction with the PFC and the posterior parietal cortex [105] (Table 2).

Differences between males and females in ASD seem to find their origin in the brain masculinization during brain development, a critical period that puts males at risk regarding neurodevelopmental disorders. During the second postnatal week, arachidonic acid and estradiol production peak. It has been shown that inflammation or nonsteroidal anti-inflammatory drugs (NSAIDs) result in impaired play behavior in males [106]. Even though it is still assumed that the cerebellum is not sexually dimorphic, as opposed to the preoptic area, for example, specific subregions such as lobules VI and VII have been demonstrated to represent a particular sexual orientation dimorphism related to emotion and

sensation [106]. In the cerebellum, prostaglandins stimulate aromatase and local estradiol production. PCs respond to prostaglandin E2 (PGE2) and 17-estradiol (E2) levels. Indeed, E2 induced BDNF expression at physiological levels and promoted PC dendritic growth, spinogenesis and synaptogenesis during neonatal life. High E2 levels stop dendritic growth and reduce excitatory synapses number [89,106]. Given that E2 is the primary hormone in females, this raises the hypothesis that E2 could protect females from environmental insults, whether toxic, pharmacologic or immune. Indeed, only male rats exposed to LPS or PGE2 during the second postnatal week displayed reduced PC arborization and impaired juvenile social play behavior [107] (Table 1).

Unfortunately, not all studies separate male and female groups; many use only males, and some studies even pool the data from both sexes, undermining sex differences. For instance, rats (male and female pooled) prenatally exposed to a single VPA dose exhibited a reduced number of neurons in the cerebellum, abnormal dendritic branching and reduced density dendritic spines affecting axonal projections of PC [53,54]. Double-dose VPA-exposed rats (male and female pooled, E10 and E12 800 mg/kg) exhibited an increased number of ectopic PCs correlated with a 21% reduction in soma size compared to control ones in all ten vermal lobules. While lobules IV and VIc were both affected in decreased PC soma size (30 and 39%, respectively) and PC number (55 and 36%, respectively), lobule VII seemed to be less affected, with only a 9% decrease. In the same study, VPA gestational exposure induced a reduction in Calbindin across all ten vermal lobules. Only 65% of vermal PC were Calbindin positive compared to control animals that were 90% PC Calbindin positive [50]. In this model, Calbindin-positive PC dendrites were shorter and showed reduced branching complexity, in accordance with a previously reported slight increase in spine length and volume in Calbindin KO mice [85], suggesting that a lack of Calbindin could lead to impaired spine morphology, hence reducing synapse formation. Interestingly, no significant changes were observed in the Parvalbumin KO mice. Nonetheless, double transgenic KO mice for the two EF-hand type Ca^{2+} binding proteins (Calbindin and Parvalbumin (PV)) showed significant differences in PC spine morphology compared to wild type [85]. Synapse establishment is a crucial process for PC to engage in cognitive and motor tasks. It has been known that mutations of genes coding for SHANK are impaired in autistic patients [32]. These mutations lead to fewer mature dendritic spines due to impaired spine induction and morphology. In detail, this leads to reduced mature glutamatergic synapses, which would affect cognitive functions. Studies on the male Fmr1 KO mouse model also showed dendritic impairments in the cerebellum, with PC exhibiting longer and immature dendritic spines [44,88]. The eye-blink conditioning, a behavior managed by the cerebellum and mainly the interpositus nucleus, was impaired in both Fmr1 KO and PC-specific Fmr1 KO mice [88] (Table 1). Although eye-blink conditioning was impaired in FXS patients [88,108], repeated training led to improvements in adult patients [108].

Bergmann cells are cerebellar astrocytes that are crucial for PC dendritic formation and maintenance. Post-mortem analysis of six male ASD patients revealed that these cells were activated and reactive in cerebellar areas where PC were reduced [64,90]. This was also observed in VPA rats [86] and Fmr1 KO mice [44]. The microglia oversee the proper neuronal development and have been demonstrated to be involved in synaptic density, spatial localization, morphology, process retraction and thickening, resulting in synaptic pruning. The co-activation of microglia and astroglia seems to correlate with degenerating PC, granule cells and axons. Indeed, post-mortem analysis of ASD patients' cerebellum (male and female, 5–44 years old) showed a pattern of high microglial activation compared to control tissues [90]. However, in our study, no change in microglia was found in the poly I:C animals (P45) [48]. Since microglia are known to be activated during a specific time window, a more detailed investigation of the timing of these processes is needed. In addition, microglia and astroglia activation in post-mortem samples could be an independent event that may not be linked to ASD but rather to traumatic cause of death (listed in [90]). PCs seem to be at the center of the gliosis found in ASD patients and animal models through

auto-toxic mechanisms, independent of adaptative immunity. Indeed, markers found in the perineural compartment of PCs raise the hypothesis of complement system involvement in immunopathogenic means, similarly to what is reported in neurodegenerative disorders. These findings indicate that cerebellar abnormalities found in ASD patients could be due not only to prenatal developmental insults but also to glia-mediated chronic neuroinflammatory processes persisting throughout life.

Other cerebellar cell types, such as basket and stellate cells, seem to be preserved in ASD patients [109]. These observations reinforce the hypothesis that PC density loss could be due to an insult during late prenatal periods, when PCs and inferior olivary neurons establish their connections [105]. Only one study found a decreased granule cell number in ASD patients [90], but findings in this cellular population rarely constitute a perfect match through animal models of various cerebellar pathologies.

2.4. Neurotransmission Systems Implicated

Glutamate and GABA have consistently been reported to be the most affected neurotransmission systems in ASD. The nature of motor and cognitive impairments in ASD points toward an excitatory/inhibitory imbalance within the cerebellum (for review, see [87]). The GABA–glutamate imbalance was thought to be responsible only for seizures occurring in some schizophrenic and ASD patients, but recent evidence has proven a wider array of pathologies [51]. For instance, glutamate has been extensively related to neurogenesis, synaptogenesis and neuronal maintenance in relation with emotional behavior acquisition. The cerebellum contains various AMPA, NMDA and kainate glutamate receptors. Using microarrays, autoradiography and western blot on post-mortem patient samples, Purcell et al. compared markers of glutamatergic neurotransmission in ASD subjects (5–54 years old) and neurotypical ones (2.4–53 years old) and reported a decreased AMPA receptors (AMPA) density in patients' cerebellum [110]. Since glutamatergic interacting proteins 1/2 (Grip1/2) regulate AMPAR trafficking and synaptic strength, PC–AMPA signaling in ASD was recently examined in a PC-specific knockout mouse model. The specific loss of expression of Grip1/2 in PC resulted in an increased repetitive self-grooming in 3-month-old male mice and impaired mGluR long-term depression (LTD) at the parallel fiber (PF)–PC synapses [51]. In addition, mGluR5 and Arc were increased in a possible attempt to compensate for AMPAR inefficient recycling in the absence of Grip 1/2 [51]. However, no PC loss was found in this animal model [109]. Both excitatory amino acid transporter 1 (EAAT1) and 2 (EAAT2) mRNA and proteins were increased in ASD patients [87]. The EAAT1 and 2 are mainly expressed by Bergmann astroglia in the cerebellum, which is highly activated in ASD patients. The glutamatergic extracellular concentrations are thus suspected to be abnormally elevated in ASD subjects, resulting in an imbalance in excitation/inhibition. This may implicate a glutamate-mediated strong activation of PCs, which in turn would lead to cerebellar inhibition. Interestingly, the precursor of the glutamate synthesis, glutamine, is also upregulated in the left cerebellum of ASD patients [52]. However, a few studies did not report any increase in the ASD glutamatergic system. For instance, DeVito et al. used proton magnetic resonance spectroscopic imaging (1H MRSI) to detect various low-molecular-weight metabolites in vivo in young male ASD patients (6–17 years old) and control subjects (6–16 years old) [111]. Among the studied metabolites, both N-acetyl aspartate and glutamine were reduced in the cerebellum of ASD patients compared to controls, suggesting not only neuronal loss or dysfunction but also reduced levels of glutamate. These results suggest widespread reductions in gray matter neuronal integrity and a dysfunction of cerebellar glutamatergic neurons in ASD patients. However, it is to be noted that no females were used in this study, contrary to the work from Hassan et al. [52]. This is of relevance, as the menstrual cycle influences women's neurotransmitter levels across cortical regions [112]. Further studies with a larger cohort, including sex, age and menstrual cycle parameters, are required to determine parameters influencing the glutamate and glutamine levels in the ASD cerebellum [113]. Glutamatergic transmission is also modified in ASD animal models. Shank2-deficient mice

(Shank2^{-/-}) displayed abnormal and repetitive behaviors, as well as autism-like social deficit behaviors [114]. The cerebellar synaptosomes from these mice had fewer AMPA receptor subunits (GluA1 and GluA2) than control without affecting dendritic arborization and postsynaptic density. Electrophysiological recordings in these animals revealed deficits in long-term potentiation (LTP) in PF-PC [114]. In line with these findings, mice with a Shank2 deletion restricted to PC (*Pcp2-Cre;Shank2^{fl/fl}* mice) displayed an interesting phenotype that only partially related to ASD symptomatology [98]. Indeed, social behavior and repetitive behaviors were not observed in this mouse line, as these transgenic mice showed mainly motor coordination impairments and increased anxiety. The PC lacking Shank2 protein (*Pcp2-Cre;Shank2^{fl/fl}* mice) displayed fewer miniature excitatory postsynaptic currents (mEPSC) and fewer GluA1, GluA2, GluN2C, VGluT1 and GluD2 protein levels than control [98]. Specific loss of the TSC1 in the PC (*L7Cre;Tsc1^{lox/1}* and *L7Cre;Tsc1^{lox/lox}*) results in ASD behaviors [96]. Indeed, mice carrying this mutation displayed an increase in stereotypic movements, abnormal behavior and changes in PC electrophysiological properties. PC lacking Tsc1 had a decrease in action potential frequency and EPSCs, but not IPSCs. This modification led to a decrease in the Excitation:Inhibition (E:I) ratio in mutant mice compared to control [96].

GABA has been studied to a lesser extent in the cerebellum compared to glutamate. Indeed, even though PC generate a GABAergic output, their cerebellar inputs are mainly glutamatergic, except for interneurons regulating PCs' firing pattern. Interestingly, Calbindin reduction in mice resulted in abnormal firing patterns in PC, such as decreased complex spike duration and pause and simple high spike firing rate [55]. These findings suggest that GABAergic inputs on the PC could be partially dependent on Calbindin levels. Lower densities of the two GABA receptor subtypes—GABA-A and GABA-B—have been found in ASD individuals. The GABA-A receptor is known for its fast inhibitory action, whereas GABA-B receptor activation results in excitatory/inhibitory regulation. The subunits GABA-A α protein levels and GABA-B R1 receptor density and levels of glutamic acid decarboxylase (GAD) 65 and 67 proteins, in charge of glutamate to GABA conversion, were all found to be decreased in the cerebella of ASD patients [97,115]. Furthermore, ASD children (5–15 years) showed increased GABA concentration in their plasma [116]. GABA ρ 3 is a subunit of the GABA-A receptor, with a high affinity for GABA, providing the receptor with low desensitization upon activation. The GABA ρ 3-composed GABA-A receptor plays an important role in regulating GABAergic transmission during the postnatal development of the cerebellum [27]. In the VPA model, GABA ρ 3 is decreased by 43% in the lobule X [99], in charge of the gaze coordination. Importantly, GABA ρ 3 level linearly increases during typical development, but not in the VPA model, as it chronically decreases at each studied time point (P4: -54%, P30: -83%) [99]. A significant reduction of GABA-A β 1 and GABA-A β 2 levels were also observed in the cerebellum of *Fmr1* KO mice. Interestingly, the decrease in GABA-A β 1 mRNA is only observed in the cerebellum, whereas GABA-A β 2 mRNA levels also drop in the cortex, hippocampus and diencephalon [117]. In this mouse model, the administration of a GABA-A (Diazepam) or GABA-B (STX209) agonists results in the improvement of several behavioral deficits and a partial rescue at the molecular level [95,118] (Table 2).

Excitatory/inhibitory imbalance is one of the major hypotheses explaining ASD symptoms. Of interest is the finding that both ASD patients and ASD mouse models (FMRP) displayed surprising GABA dysregulations and glutamate receptor subunit changes, even in *post-mortem* cerebella of ASD subjects, without FXS or FMRP being downregulated, which was associated with increased levels of mGluR5 and decreased levels in GABA-A β 3 subunits [92]. *Fmr1* KO mouse models confirmed these findings, as PSD-95 (Postsynaptic Density protein 95) and mGluR5 were found to be increased in the cerebellum [93,94,119]. In our study, mGluR5 levels were reduced in the cerebellum of Shank3^{AC/AC} males [49]. These findings suggest that mGluR5 plays a crucial role in the synaptic targeting and postsynaptic assembly of the Shank3 scaffolding complex. Drug therapies targeting this protein could be of interest, as the administration of 3-Cyano-N-(1,3diphenyl-1H-pyrazole-

5-yl) benzamide, which increases mGluR5 activity, was shown to alleviate functional and behavioral ASD defects [91]. In another study, the *Fmr1* KO mouse model showed abnormal presynaptic vesicle dynamics and increased LTD induction at the PF-PC synapse [88]. Other models, such as *Shank2* KO mice and specific *patDP/+* mutant mice, also showed impaired LTD associated with dysfunctional intrinsic plasticity [56]. The latter is based on findings in ASD patients with mutations in 15q11-q13, a genetic region involved in GABA A β 3 subunits and two other subunit candidate genes for ASD [120]. The *patDp/+* mice mutants within the cerebellum exhibited impairments in motor coordination, learning, eye-blink conditioning, along with abnormal climbing fiber elimination of the PCs [56]. In the *Shank2* KO mice, an increased irregularity in simple spike PC firing, accompanied by increased inhibition, was only found in the posterior cerebellum, possibly underlying cognitive impairments in this model. mGluR1 receptors are expressed by PC mediating LTD plasticity with parallel fiber [121]. In the postnatal developing cerebellum, the mGluR1 activating pathway is involved in axon pruning [122]. The inactivation of this receptor in mice (*mGluR1^{-/-}*) leads to a lack of motor coordination [123]. Even though the role of these receptors is crucial in glutamatergic transmission in the cerebellum, there is yet no direct evidence of mGluR1 dysfunction in ASD. In conclusion, there is an imbalance of the excitation/inhibition inputs in the cerebellum of ASD animal models and patients, with a significant reduction in GABA amount due to a reduction of its synthesizing enzymes GAD65 and GAD67. This is accompanied by a decrease in GABA receptors' activity, causing an increase in the activity of mGluR5. The mGluR signaling has been shown to be involved in GABA-A receptor stabilization at the synaptic membrane [124] in a healthy context. This may underly the fact that mGluR dysfunctions in ASD are often linked to GABA-A dysregulations. However, it appears that a reduction of the activity of mGluR5 can also lead to social deficits. Pharmacological treatments in animal models indicate that either activating the GABAergic system or inactivating the mGluR5 receptor may be of interest in managing some of the ASD symptoms where a reduced activity of the GABAergic system is reported. In the case of a decrease in mGluR5 levels or activity, the activation of mGluR5 reduces social deficits by restoring the excitation/inhibition balance.

2.5. Evidence from Our Previous Work

We have recently set up a series of studies on environmental and genetic animal models of ASD [47–49]. Our choice of the models was based mainly on their reported strong construct and face validity, as they were known to replicate both the etiology of the disease and at least some of its cardinal behavioral symptoms. The predictive value of animal models is hard to achieve, especially when no known treatment for the corresponding illness is available, which is the case for ASD. Our main aims when starting these studies were: (i) to determine whether different animal models of the same pathology would yield a spectrum of behavioral and cellular outcomes, mirroring the large and variable range of ASD symptoms in clinical settings, i.e., whether the nature (motor, social, gait) and the severity of the symptoms are variables depending on the etiology of the disease; (ii) to determine whether we can replicate the sexual dimorphism reported in clinical settings, as ASD affects three times more males than females [2], and again, whether sexual dimorphism is observed whatever the animal model and with the same proportion; (iii) to determine whether motor and gait deficits are observed in all animal models and whether they are correlated with the severity of social deficits. All experiments were performed within a relatively short timeframe (4 years in total), in the same laboratory and animal facility, using the same behavioral and bench equipment and software. For this, we have chosen two environmental animal models: the VPA and the poly I:C, a maternal immune activation (MIA) animal model and a genetic animal model bearing a *Shank3* deletion. All three animal models showed major motor and gait deficits that were more pronounced in males than in females, but to a variable extent.

VPA animal models were obtained by injecting the drug i.p. at 400 mg/kg to pregnant females at E12.5 [47,125] (Table 1). In this model, we have found that the male offspring, but not females, expressed severe social deficits. However, both sexes showed motor coordination and gait deficits that were more pronounced in males than in females in their severity and variety. Cellular consequences accompanied these differential social and behavioral phenotypes. We reported a decrease in the number of PC found in the crus I cerebellar subregion in males and in crus II in females. In addition, only males showed a reduction in the number of neurons within the motor cortex. No neuronal decrease was found in the striatal region. Of interest is the finding that the severity of motor and gait disturbances was directly and strongly correlated to deficits in social behavior, as mice that had the most motor coordination deficits were the ones that had major social deficits and the highest decrease in PC within the cerebellar cortices.

In order to induce MIA, pregnant mice received a single i.p. injection of poly I:C (20 mg/kg, a double-stranded RNA analog polyinosinic:polycytidylic acid, which presents strong construct and face validity toward ASD and is the preferred MIA paradigm compared to direct injection of viruses [48,126]. Mice that received a Poly I:C injection at the prenatal age of 12.5, inducing an MIA phenotype, showed less dramatic social and motor behavior alterations than those following VPA injection [48]. Only males showed deficits in social behavior and motor coordination. Of interest is that neither gait nor walking skills were affected in either males or females. A reduced number of PC in the cerebellum was found to be more widespread and within distinct lobules in males than in females.

The Shank3^{Δc/Δc} mice that we have used for our studies are those with C-terminal 508 deletion in the Shank3 gene following a frameshift in exon 21, which includes the homer-binding site in the sterile alpha motif domain. Consequently, there is a partial or total loss of the major naturally occurring isoforms of Shank3 proteins in heterozygotes and homozygotes, respectively [127]. This mutation has a strong construct validity, as it mimics a human mutation, which is not the case for several other Shank3 mutations in mice [127]. In homozygote animals, we reported significant impairments in social novelty preference, stereotyped behavior and gait. These were accompanied by a decreased number of PC in restricted cerebellar sub-regions and decreased cerebellar expression of mGluR5. Heterozygote mice showed impairments only in social novelty preference, grooming and decreased mGluR5 expression, but to a much lesser extent than in homozygote mice. All reported deficits were more pronounced in males than in females (Table 2).

Several elements of conclusion can be drawn for our studies: (i) The severity of ASD phenotypes, whether behavioral, cellular or molecular, varies from one animal model to another. This recapitulates in some way the spectrum of the disease, where variability may be due to its etiology, i.e., to what initially caused it. In our study, the VPA model yielded the most robust and severe phenotypes at all explored behavioral and cellular levels. (ii) Females are globally less affected than males in all the paradigms explored, whatever the treatment or the mutation. This is in line with clinical settings, where ASD is reported to be present three times more in males than in females. Notably, females showed no social deficits but still exhibited motor and gait alterations. In addition, the decrease in the number of PC was found in different sub lobules in females than in males. This suggests that ASD may be expressed differently in relation to sexual dimorphism. Thus, the proportion of affected ASD females may be higher than previously suspected if one also investigates motor and gait behavior. Such behaviors may be of relevance to implement in clinical exploration to help diagnose the disease. (iii) When the phenotypes explored are robust, as with the VPA animal model, the magnitude of social deficits can be correlated to both motor and gait deficits and PC cell number. In line with the previous conclusion, this further suggests that exploring motor and gait deficits may constitute an objective, early and quantitative diagnosis tool in ASD.

3. Striatal Involvement in ASD

3.1. Anatomical Evidence of Striatal Involvement in ASD

The basal ganglia are a group of subcortical nuclei involved primarily in motor skills. The term “Basal Ganglia” refers to the striatum and the globus pallidus, while the substantia nigra (mesencephalon), the subthalamic nuclei (diencephalon) and the pons are related nuclei [128]. The basal ganglia and their related nuclei can be split into three groups: input nuclei receiving incoming information from different cerebral areas, output nuclei sending basal ganglia information to the thalamus and intrinsic nuclei located in between, playing the role of a relay. The striatum is the largest subcortical structure and the only input nucleus of the basal ganglia (Figure 2). Although it has been remarkably conserved through the evolution of the vertebrate lineage for 530 million years, the striatum enhanced its role from primarily motor relay in amniotes to a complex circuitry capable of motor control (action selection), dealing with emotions and motivational state in mammals [129,130]. In primates and humans, the striatum is formed by the caudate and the putamen, separated by the internal capsule in the dorsal part and the nucleus accumbens in the ventral part. For the rest of the mammals, the striatum is divided into two parts: the dorsal and ventral striatum. The dorsal striatum receives inputs from the sensory and motor cortices, the insular cortex and the orbital cortex on its lateral part (i.e., on the putamen in primates and humans) and the visual cortex, the anterior cingulate cortex, the ventral hippocampus and the amygdala on its medial part (i.e., on the caudate). The nucleus accumbens receives inputs from prelimbic and infralimbic cortices, the amygdala, the hypothalamus and the ventral hippocampus. This input organization leads to each territory’s specializations from the motor to associative and cognitive mechanisms, from dorsolateral to dorsomedial and ventral striatum [129,130].

In the late 20th century, several studies took an interest in symptoms and brain structures other than the cardinal ones by studying the link between ASD and the cerebellum, as we discussed before. First evidence of the involvement of the striatum in the physiopathology of ASD was obtained from imaging studies [131–133]. Studies over the last decades highlighted anatomical differences between ASD and non-ASD subjects regarding the striatum and reported a wide range of modifications and inconsistencies. On the one hand, only the putamen and nucleus accumbens volumes appear to increase by, respectively, 22% and 34% in ASD patient brain compared to age-matched controls. The caudate volume was not significantly different between groups [84]. On the other hand, all the striatum, i.e., the caudate, was found to be more prominent in ASD patient brains than age-matched controls in magnetic resonance imaging studies [134–136]. Thus, the larger right caudate volume seems to be positively correlated with repetitive and stereotyped behavior [134–136] and negatively correlated with insistence on sameness [135]. Interestingly, neuroanatomical changes of the striatum are also found in animal models of ASD but can be different from one model to another: *Neurologin3* Knock-In (B6/129F2 strain, 15 weeks of age), *Shank3*^{-/-} (B6/SV129 strain, 22–23 weeks of age) and *Cntnap2*^{-/-} (C57BL/6J strain, 8–9 weeks of age) transgenic mice, for example, have bigger striatum than control littermates [69], while *16p11*^{+/-} mice (B6/129F2 strain 32–35 weeks of age) have a bigger nucleus accumbens [137]. Idiopathic models of ASD, such as the BTBR mice (C57BL/6J strain, 11 weeks of age) show a reduction of their striatal volume [138]. Although no modification of the global striatal volume has been reported in FVB/NJ mice exposed in utero to valproic acid (VPA) (National Laboratory Animal Center, Taipei, Taiwan), the balance between striosomes and the matrix is reported to be impaired at postnatal day 8 (P8) depending on the time of the VPA administration. These two compartments receive different cortical inputs: the matrix compartment receives inputs from the cortical sensorimotor areas, while the striosomal compartment receives inputs from prelimbic and insular cortices. The authors reported that both striosomal and matrix areas were affected and could be linked with both social and motor impairments in ASD, highlighting the heterogeneous nature of the disease [28] (Table 2). These differences align with the inconsistencies reported in humans and reflect the large scale of striatal neuroanatomical changes. More generally, all three parts of the

striatum are involved in functions that are altered in one way or another in ASD. The dorsolateral striatum has been linked to motor stereotypies in a large range of species, from rodents [139] to monkeys [140], and to insensitivity to reward devaluation [141]. The dorsomedial striatum has been linked to executive dysfunctions and abnormal reactivity [142], and the nucleus accumbens has been linked to the inability to process and respond to social cues [33].

Taken together, these sets of results indicate that all three striatal parts are affected in ASD patient brains and animal models of ASD, reinforcing the link between the striatum and ASD symptoms.

3.2. Cellular Consequences Correlates

Despite increasing their volume, the numerical density of neurons is reported to decrease by 15% in the nucleus accumbens and 13% in the putamen in patients diagnosed with ASD and comorbidities [84]. These findings need to be more thoroughly replicated, as 7 out of 14 patients included in the study (50%) were diagnosed with seizure, and death was seizure related for 5 of them. Similar variations in striatal cellular alterations were also found in ASD animal models. In VPA mice and rats, no drastic striatal neuronal loss has been described. A recent paper strongly suggested that the lack of PV staining observed in the striatum of VPA mouse model should not be attributed to cell loss but rather to a decrease in PV protein contents within the interneurons, as the cell can still be observed using another marker (Vicia Villosa lectin, VVA) [26,143]. Nevertheless, the general cellular organization within the striatum appears to be disturbed, with an impaired aggregation of striosomal cells into cell clusters [28] (see Table 1). This could cause (or enhance) an imbalance between sensorimotor and cognitive inputs on the striatum, leading to social and motor impairments.

Representing more than 95% of the striatal neuronal population, medium spiny neurons (MSNs) are the striatum's main neuronal population and are the striatum's only output. They are segregated into at least two subtypes according to their axonal projection patterns: striatonigral MSNs, or direct pathway MSNs, expressing dopamine receptor D1 (RD1) and striatopallidal MSNs, or indirect pathway MSNs, expressing dopamine receptor D2 (RD2) [129,144]. All MSNs share a similar morphology and exhibit similar properties, except for excitability, which appears to be increased in DRD2-expressing MSN [145]. Male and female 5-week-old Shank3^{B-/-} MSNs exhibit increased neuronal complexity, increased total dendritic length and surface area, but a lower spine density compared to Shank3^{B+/+} littermates [146]. At the age of 2–4 months, a reduced MSNs spine density is also found in Shank3^{B-/-} mice, in both males and females, only in DRD2-expressing MSNs [147]. This is particularly relevant to human findings, where regional quantification revealed that RD2, but not RD1, was significantly more expressed in both caudate and putamen of 4–20-year-old ASD male patients, with multiple ethnicities and non-comorbidities-related death [148] (Table 2).

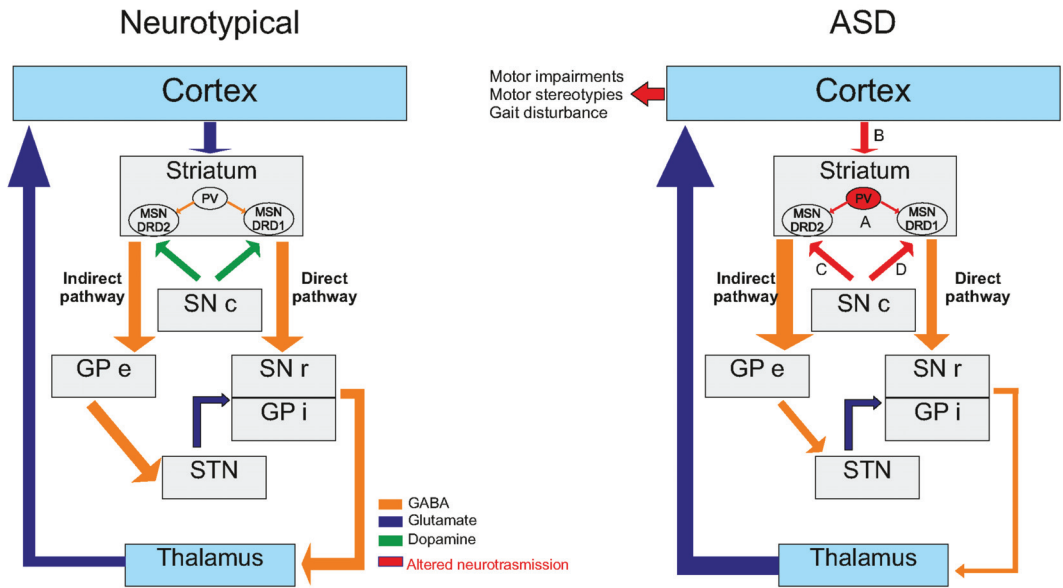


Figure 2. Basal ganglia modifications in ASD. Basal ganglia network is shown to be deeply affected in ASD models. The main alterations are found at 4 points of interest (A,B,C,D). Striatal local inhibition mediated by PV interneurons. (A) is altered in some ASD models like *Shank1*^{-/-} and *Shank3B*^{-/-} mice [149], VPA mice [26] or *Cntnap2*^{-/-} mice [143]. Responsible of feed-forward inhibition, alteration of these interneurons may lead to altered MSNs' functionality. Interestingly, corticostriatal pathway (B) is widely described as altered in ASD models. For instance, in *Ngn1*^{-/-} mice, *Ngn3*^{-/-} mice, *Shank3*^{-/-} mice [150] or *Shank2*^{-/-} rats [151], alterations of the glutamatergic transmission onto MSNs are reported. Thus, alterations of plasticity were also highlighted in *Shank3e4-22*^{-/-} mice [91]. However, the dichotomy between direct and indirect pathway allows to highlight some pathway-specific alteration. On the one hand, some alterations were found to be specific of the indirect pathway (C), like an increase of DRD2 expression in the striatum, leading to a dopaminergic imbalance in favor of the indirect pathway [148,152]. On the other hand, some alterations were found to be specific to the direct pathway (D) as alteration of synaptic transmission has been highlighted in DRD1 MSNs but not DRD2 in *NL3-cKO* mice [153]. Thus, in *Nlgn1*^{-/-} mice, the AMPA/NMDA ratio was found to be reduced specifically in direct pathway MSNs [154], leading to an altered response.

The striatal interneurons are responsible for local inputs and regulation, which play a major role in the striatum's functionality. A conjoint depletion of the PV fast-spiking and cholinergic interneurons in the dorsal striatum leads to autism-like behavior in male mice [155], but not in females, suggesting that interneurons, including cholinergic interneurons, could be involved in ASD pathophysiology and could take part in the reported sexual dimorphism in ASD patients and animal models [47–49]. The central role of cholinergic interneurons is further highlighted, as they are also involved in other brain pathologies. For instance, they have been directly linked to Tourette's syndrome or attention deficit hyperactivity disorder [156] and motor stereotypies, as a lesion of these cells in the dorsal striatum significantly prolonged their duration [157,158]. A significant increase in the stereotyped behavior was also found in mice (*C57BL/6*, 6–21 weeks) with a loss of MeCP2 in somatostatin-expressing interneurons, including in the striatum [159]. Nevertheless, there is no available information regarding the involvement of striatal somatostatin-expressing interneurons in ASD pathophysiology.

The striatal PV fast-spiking interneurons, responsible for gamma oscillations and feed-forward inhibition onto MSNs, are important in the excitatory/inhibitory balance [129,160]. The inactivation of the PV gene in mice leads to reduced social interactions, reduced ultrasonic vocalizations and repetitive and stereotyped patterns of behavior [161]. This ASD-like phenotype of PV^{-/-} mice is also directly correlated with brain morphological abnormalities similar to those reported in patients. This is accompanied by functional disturbances, as PV^{-/-} fast-spiking interneurons exhibit a lower excitatory post-synaptic current facilitation, i.e., a lower excitatory synaptic plasticity [161]. Interestingly, these striatal PV fast-spiking interneurons are not only related to ASD-like mechanisms when targeted but are commonly affected in ASD models. PV expression levels are reduced in the striatum of Shank1^{-/-} and Shank3^{B^{-/-}} mice, the two mice models of ASD, without a loss of PV interneurons [149]. Similar findings are reported in VPA mice [26] or Cntnap2^{-/-} mice [143]. Given that PV^{-/-} mice ASD-like phenotype is strongly relevant to human ASD core symptoms and related abnormalities and that PV fast-spiking interneurons are affected in a wide range of ASD models, a PV hypothesis of ASD has been formulated recently [162] (Table 3).

Glial cells, including astrocytes and microglia, are now well known to influence synapse formation and function, as astrocytes, for example, can make contact with multiple neurons and express receptors and ion channels that are also expressed in neurons [163]. The role of astrocytes in ASD pathophysiology has been demonstrated by re-expressing Mecp2 in whole-brain astrocytes in Mecp2^{-/-} mice (C57BL/6 strain, 4–8 weeks of age), leading to the recovery of motor symptoms [164]. However, no striatum-specific astroglial changes in Shank3^{+/ Δ C} and Cntnap2^{-/-} male mice (C57BL/6J strain, 5–6 months of age) were reported [165]. The overexpression of the eukaryotic translation initiation factor 4E (eIF4E) in macrophages in mice, i.e., in microglia in the central nervous system, leads to elevated protein synthesis and abnormal morphology of microglia, as well as an increase in their size and number within the striatum of both males and females (C57BL/6 strain, 2–6 weeks of age). This overexpression of eIF4E in microglia has no phenotypic consequences in females, but it causes ASD-like phenotype in male mice [166], suggesting that microglial impairment could cause ASD with a sexual polarity. Thus, a significant increase in the size and number of microglial cells in the striatum has been reported in Pten^{+/-} and Fmr1^{-/-} mice [166]. These two models exhibit core ASD features, such as social deficits [167,168] and repetitive behavior [169,170], suggesting that microglia could also be impaired due to ASD.

3.3. Neurotransmission Systems Implicated

In the early 2000s, John Rubenstein and Michael Merzenich formulated the excitation/inhibition (E/I) imbalance hypothesis of ASD, suggesting that the pathophysiology of ASD and their related comorbidities may reflect a disturbance in such a balance [87]. Even though their work focused only on the cortical networks, it may be easily extended to striatal networks, as the striatum receives major excitatory inputs from cortical areas and major inhibitory inputs from the local interneurons network [142]. Added to the dopaminergic and serotonergic neuromodulations, this would lead to a balance within the striatum, which is essential for its functioning. Another argument suggests an E/I imbalance in the striatum is found in the numerous genes involved in ASD pathophysiology. According to the SFARI database, nearly one-third of genes (68 out of 213) used to model ASD in mice directly concern synaptic establishment, strength and/or transmission or are associated with receptors in pre- and/or post-synaptic compartments. Most of these genes are expressed in the striatum, although not exclusively.

Table 3. Striatal dysfunctions in ASD. This table sums up the striatal dysfunctions identified in patients and animal models of ASD.

	Children			Teenagers	Adults	Animal Models		
	<5 yo	5 to 14 yo	14 to 21 yo	>21 yo				
Anatomical impairment	•	•	<input checked="" type="checkbox"/> Volume of putamen and nucleus accumbens but not of the caudate [82]	•	•	<input checked="" type="checkbox"/> Striatal volume in cntnap2 ko mice [57] <input checked="" type="checkbox"/> Striatal volume in bibr mice [137]		
		N/A	•	<input checked="" type="checkbox"/> Volume of putamen, accumbens & caudate [133–136]	•	•	<input checked="" type="checkbox"/> Striatal volume in vpa exposed mice [28]	
Matrix/striosome organization	•	N/A	•	•	N/A	•	<input checked="" type="checkbox"/> Impaired balance in vpa exposed mice [28]	
Cellular correlates	•	N/A	•	•	•	•	<input checked="" type="checkbox"/> Neuronal complexity; <input checked="" type="checkbox"/> dendritic length and surface area, <input checked="" type="checkbox"/> Spine density in Shank3B KO mice [146]	
	•	N/A	•	•	•	•	<input checked="" type="checkbox"/> Spine density in DRD2-expressing msns in Shank3B ^{-/-} mice [147] <input checked="" type="checkbox"/> ePSCs [155] <input checked="" type="checkbox"/> PV expression [26,143] <input checked="" type="checkbox"/> No cell loss [143–156]	
Astrocyte	•	N/A	•	•	•	•	•	No striatum-specific changes in shank3 ^{+/δc} or cntnap2 ko mice [160]
Microglia	•	N/A	•	•	•	•	•	<input checked="" type="checkbox"/> Size and number of microglial cells [161]
Neurotransmission	•	N/A	•	•	•	•	•	<input checked="" type="checkbox"/> sEPSCs amplitude and frequency [171] <input checked="" type="checkbox"/> NMDA/AMPA ratio [170] & <input checked="" type="checkbox"/> NMDA-R function [172]
	•	N/A	•	•	•	•	•	<input checked="" type="checkbox"/> AMPA mediated mEPSCs amplitude & frequency, no defect in paired-pulse ratio [146] <input checked="" type="checkbox"/> NMDA/AMPA ratio but no changes in mEPSCs amplitude or frequency [173]
GABA	•	N/A	•	•	•	•	•	<input checked="" type="checkbox"/> Abnormal distribution and <input checked="" type="checkbox"/> expression of mGluR5 in MSNs in [119] <input checked="" type="checkbox"/> mIPSCs amplitude [171]
Dopamine	•	N/A	•	•	•	•	•	<input checked="" type="checkbox"/> mIPSCs frequency in ventral DRD1-expressing MSNs only [174] <input checked="" type="checkbox"/> sIPSCs & mIPSCs frequency in Fmr1 KO mice [175]
	•	N/A	•	•	•	•	•	<input checked="" type="checkbox"/> DAT level in BTBR and Fmr1 KO mice [176]

N/A: not applicable.

Both ionotropic and metabotropic receptors mediate the glutamatergic responses in the striatum and are differentially expressed throughout the striatal territories at the pre- or post-synaptic compartments. While metabotropic receptors are involved in long-term synaptic plasticity, the ionotropic receptors, i.e., AMPA-R and NMDA-R, are responsible for the neurotransmission itself in the striatum [172,177]. In ASD, alterations of the glutamatergic transmission are reported in several models, such as *Nlgn1*^{-/-} mice, *Ngln3*^{-/-} mice, *Shank3*^{-/-} mice [150] or *Shank2*^{-/-} rats [151]. In *Nlgn1*^{-/-} mice (C57BL/6 strain, P15-P38), the NMDA/AMPA ratio is reported to be decreased in the dorsal striatum and can be restored to WT levels with the application of D-Cycloserine (DCS), a co-activator of NMDA-R. This rescue of NMDA-R function also lowers the increased grooming behavior observed in *Nlgn1*^{-/-} mice [178]. Interestingly, in the same mice that are 2–3 weeks old, the NMDA/AMPA ratio is reduced in the direct pathway (DRD1-expressing MSNs) but not in the indirect pathway (DRD2-expressing MSNs) and is directly driven by a decrease in GluN2A-containing NMDA-R currents. However, the strength of the synapse, measured by input/output curves, as well as the short-term plasticity, are not reported to be impaired in KO mice compared to WT littermates [154]. Such a dichotomy between direct and indirect pathway has also been described regarding endocannabinoid (CB)-mediated LTD in a model of selective loss of TSC1 in either DRD1-expressing MSNs or DRD2-expressing MSNs (C57BL/6 strain, P40 to P50) [179]. Here, the authors highlighted impairments of CB-mediated LTD in TSC1^{-/-} DRD1-expressing MSNs but not in DRD2-expressing MSNs. In *Fmr1*^{-/-} mice (C57BL/6J, males only, adult), a loss of LTD has been described in ventral MSNs, without any CB1-R functional alteration [173]. These findings suggest that impairments of glutamatergic neurotransmission and plasticity are directly linked to the neuromodulation system specificity in ASD.

In another neuroligin model of ASD (R451C-NL3 male mice, B6/J strain, 2 months), a high-frequency stimulation (HFS) protocol failed to induce LTD in R451C-NL3 mice, while it did do so in WT littermates. Furthermore, the application of quinpirole to activate D2 receptors, known to be involved in the establishment of LTD during HFS protocol, did not prevent the induction of LTD in the dorsal striatum of mutated mice [180]. Male and female *Shank3B*^{-/-} mice (C57BL/6 strain, 5 weeks) exhibited a lower MSNs population spike amplitude than control and reduced miniature AMPA-mediated post-synaptic currents (mEPSCs) amplitude, suggesting a reduction of the post-synaptic response on available synapses [146]. *Shank3B*^{-/-} MSNs also exhibited a reduced mEPSCs frequency, but there were no defects in the paired-pulse ratio, suggesting that the number of functional synapses is decreased. These findings indicate that cortico-striatal impairments are occurring at the post-synaptic, i.e., striatal disturbances. In another *Shank3* mouse model (*Shank3*^{e4-9} mice, C57BL/6 strain, 3–4 weeks), the NMDA/AMPA ratio significantly decreased at glutamatergic synapses on MSNs from both *Shank3*^{e4-9/+} and KO mice compared to WT. Nevertheless, no difference in mEPSCs amplitude or frequency has been highlighted [181]. However, in another mouse model of ASD (eIF4E overexpressing mice, males only, 2–6 months), increased mEPSCs amplitude but not frequency has been highlighted [182]. The authors suggested that the increased expression of this translation initiation factor may lead to exaggerated cap-dependent protein synthesis, such as mGluR5 pathway, as it has been described in the hippocampus of *Fmr1*^{-/-y} mice (C57BL/6J, males only, 3–6 weeks). Considering that no AMPA-mediated disturbances have been reported in several models and that mGluR5 are involved in the potentiation of NMDA response, these findings suggest that the disturbances at glutamatergic synapses are due to decreased NMDA-R function. The mGluR5 receptors are mainly involved in the potentiation of NMDA responses in striatal MSNs and are reported to be abnormally distributed and accumulated in striatal MSNs in *Shank3*^{e4-22-/-} mice (C57BL/6 strain, 2–5 months). These same mice's MSNs also exhibit enhanced excitability and a loss of plasticity through impairments of high-frequency stimulation (HFS)-induced LTD. All this information suggests that mGluR5 receptors could be dysfunctional and involved in electrophysiological changes observed at excitatory synapses on striatal MSNs in mice models of ASD. To further test

such a hypothesis, the authors proposed a pharmacological enhancement of mGluR5 with 3-cyano-N-(1,3-diphenyl-1H-pyrazole-5-yl)-benzamide (CDPPB) and showed that it restores Shank3^{ex4-22-/-} MSNs normal excitability and plasticity, as well as behavioral ASD-like behavior [91]. In Shank3 Δ 11^{-/-} mice (C57BL/6 strain, 3 months), pharmacological enhancement of mGluR5 with CDPPB leads to a total recovery of NMDA receptor functions, compared to WT littermates [91].

Although GABAergic transmission is crucial for proper striatal function, this transmission is far less studied in an ASD context. The first apparent involvement of the GABAergic transmission in ASD pathophysiology is following the knock-out of either GABA-A receptor subunit α 5 or β 3 in mice that leads to ASD-like phenotype [171,174]. In Chd8^{+/-} mice (C57BL/6 strain, males only, 6–8 weeks), the MSNs of the ventral striatum exhibited decreased miniature inhibitory postsynaptic currents (mIPSC) amplitude, compared to WT littermates, while no changes were observed in mIPSC frequency. The authors also report increased spontaneous excitatory postsynaptic currents (sEPSC) amplitude and frequency but no changes in mEPSCs [175]. This suggests that the observed enhancement of the excitatory transmission is partly allowed by a local decrease in inhibitory transmission. In the NL3-cKO mice (C57BL/6 strain, males only, 4–6 weeks), a reduction in the mIPSC frequency, but not amplitude, is reported in ventral striatum D1-MSNs only. The authors also report no changes in the paired-pulse ratio of evoked IPSCs or short-term plasticity and no changes in excitatory transmission. Added to a significant decrease in inhibition/excitation ratio, measured by the ratio between GABA receptor-mediated inhibition and AMPA receptor-mediated excitation, this suggests that the GABAergic alterations observed in inhibition of D1-MSNs of the ventral striatum could be responsible for a shift of balance between synaptic excitation and inhibition [153]. Little is known regarding the implication of dorsal striatum GABAergic transmission in ASD. To date, the most comprehensive study on that topic concerns the Fmr1^{-/-} mouse model, in which extensive GABAergic disturbances have been reported [183]. In this study, the authors found that dorsal striatal MSNs of Fmr1^{-/-} mice (C57BL/6 strain, 2–3 months) have a higher sIPSCs and mIPSCs frequency than WT littermates, but no changes were found in sIPSCs and mIPSCs amplitude and kinetic properties. In addition, the paired-pulse ratio of evoked IPSCs is lower in Fmr1^{-/-} mice than WT littermates at 50 ms interstimulus interval, but not at 80 ms interstimulus interval. Taken together, these findings suggest that alterations may occur in pre-synaptic neurons, but in an action-potential-independent manner.

Post-mortem analysis of striata of ASD young patients revealed an increase in RD2 mRNA within MSNs in both the caudate and putamen using radioisotopic in situ hybridization histochemistry [148]. This suggested a dopaminergic imbalance in favor of the indirect pathways in ASD patients [152]. This may support dopaminergic targeted therapeutics that are currently used to manage ASD-related symptoms, such as irritability or aggression. Indeed, treatments with D2 antagonists result in improved sociality (under risperidone) [184] and a decrease in stereotypy scores (under aripiprazole) [185]. Interestingly, it seems that the direct pathway is only dysfunctional when activated during a task. A study in young ASD adults using PET (¹¹C)raclopride, a D2-antagonist) simultaneously with magnetic resonance scanning during an incentive task revealed a decrease in phasic dopaminergic release in the putamen and caudate nucleus, suggesting an impairment in the learning and goal-directed reinforcement [186]. The dopaminergic content is not extensively studied in ASD due to the result disparateness among animal models, especially regarding the striatal dopaminergic content, tyrosine hydroxylase staining and dopaminergic transporter (DAT) levels (for review, see [176]). Dysfunction in the striatal direct pathway in ASD animal models leads to deficits in social interactions and an increase in grooming [153,187,188]. Optogenetic stimulation of the nigrostriatal pathway (ii) was shown to reduce the preference for the social target in the 3-chamberts test (3-CT) with an increase in rearing but no change in grooming or digging behaviors. The stimulation also caused an increase in p-ERK1/2 and p-CAMKII α levels in the dorsal caudate nucleus-putamen (CPu) [187]. The indirect pathway seems to be not as affected as the direct pathway in ASD mouse

models, but studies on early life stress in D2R^{+/-} heterozygous mice showed that these mice display ASD-like phenotype [188] (Table 3).

Alterations in the dopaminergic and glutamatergic systems have been found in several animal models of ASD. For example, a diminution of DAT level is observed in the BTBR mice and Fmr1 KO mice models [188]. It is also interesting to note that in both models, there is an increase in tyrosine hydroxylase-positive neurons (TH+) coupling with VGlut1+ neurons [188] due to the existence of a strong link between VGlut1 and mGluR5 [189]. The inactivation of adenylyl cyclase 5 (AC5), an effector of the D2R and mGluR3 receptor in the striatum, induces ASD-like behaviors in mice [190]. Interestingly, mGluR3 has an antagonistic effect on mGluR5, mirroring the interrelation between D1R and D2R. In the case of WT mice, either the activation of mGluR5 (with DHPG) or the inactivation of mGluR3 (with LY341495) is sufficient to induce ASD-like behaviors [190], as is the inactivation of either GluA1 or GluN2B.

4. Epigenetic Alterations in the Brain of ASD Animal Models

Interactions between specific genes and environmental factors play an essential role in the development of ASD, acting directly or indirectly on the transmission and transduction systems detailed above [191]. Environmental factors can affect gene expression without causing changes in the DNA sequence, but by acting via epigenetic mechanisms: DNA methylation, histone modifications or post-transcriptional regulation by non-coding RNAs. Thus, the exposure to environmental factors can cause changes in the expression of critical genes in a crucial period of embryonic and fetal development, resulting in an increased risk of inducing ASD [192]. This is a significant focus of current research, specifically in deciphering the link between environmental insults that occur very early in life and a pathological phenotype that is only observed later in childhood or even adulthood. Epigenetic modifications may be essential molecular mechanisms that can translate early aggressions into lasting brain pathologies that could even be transmitted to the descendants. The best-characterized epigenetic modification is DNA cytosine methylation [193]. This mechanism is already known to be involved in neurodevelopmental disorders, such as Prader Willy/Angelman or Fragile X syndromes, which are major causes of ASD with intellectual disability that have been known for a long time in humans [194]. Methylated cytosines are mainly localized at CpG islands, corresponding to regions of the genome enriched in GC and essentially present in the promoter regions of genes. The primary known function of cytosine methylation at these islands is to repress transcription of the downstream gene(s) [195]. However, there are many exceptions, and the mechanism by which DNA methylation regulates transcription may be specific to different contexts, such as gene content, locus and time of development. Furthermore, DNA methylation is thought to be more abundant in gene bodies, where it probably plays a primary role in fine alternative splicing and expression regulation [196].

In the mouse prefrontal cortex, significant reconfiguration of the methylome occurs throughout synaptogenesis from fetus to young adult [197]. This is thought to be a critical process in defining the molecular identity of neurons [197]. In humans, DNA methylation alterations in the cortex and anterior cingulate gyrus have been observed in patients with ASD [198]. The differentially methylated genes were primarily related to microglial cell specification and synaptic pruning during brain development [198]. More recently, Nardone et al. refined these observations more selectively on neurons after FACS cell sorting of the prefrontal cortex. In doing so, they identified differences in DNA-specific methylation profiles in neuronal nuclei affecting genes related to synaptic, GABAergic and immune processes [199]. This is the first characterization of neuron-specific DNA methylation changes in ASD and is consistent with observations by Lister et al. in mice that showed a specific distribution of methylation in neurons that appeared very different from other tissues, with as many methylated cytosines outside of GC-rich regions as in CpG islands [197]. Epigenetic changes in specific brain structures other than the cortex have only rarely been reported. Notably, the differences in methylation and acetylation

of lysine 27 of histone 3 (H3K27) in the cerebellum have been detected in autistic patients compared to controls [200]. Furthermore, in the developing human prefrontal cortex, the 3D organization of chromatin forms loops around synapse-related genes, allowing the regulation of their expression [201]. The formation of these loops is probably regulated by DNA methylation [196]. Other yet unresolved functions of DNA methylation likely play major roles in brain development and neurodevelopmental disorders such as ASD.

Regarding transmission systems, the GABA and Glutamate pathways have already been linked to epigenetic changes. Indeed, an increase in glutamate concentration was identified in the blood of ASD patients compared to healthy subjects [201]. This increase in glutamate metabolism, which could be associated with ASD in children, could be genetic in origin and under epigenetic control. Similarly, the alterations in synaptic physiology in PV interneurons previously described may be related to a deficiency in genes encoding GABA-related enzymes, which alters neuronal GABA content [202].

Concerning the link between epigenetics and environmental insults known to increase the risk of ASD, Richetto et al. [203] showed that maternal infections mimicked by poly I:C injection result in persistent changes in DNA methylation. These changes are visible in many different genomic regions and are related to the timing of prenatal infection. Indeed, late prenatal infection during pregnancy induced methylation changes in significant genes of GABAergic cell development, while early prenatal infection seemed to affect mainly the WNT signaling pathway, involved in the nervous system development [203]. These epigenetic mechanisms have been suggested to be involved in maintaining the long-term effects of prenatal insults, as well as maintaining the cellular dysfunctions they generate [203,204].

In addition, a growing body of evidence proposes the gut microbiota as a likely key player modulating the effect of environmental factors on brain function. This could occur through changes in the immune system and epigenetic machinery. Changes in microbiota composition have been found in patients with behavioral disorders and autism spectrum disorders [205], adding further complexity to the already multifactorial pathogenic mechanisms associated with neurodevelopmental and psychiatric disorders. Epigenetic changes in ASD could notably be induced by metabolites produced by an abnormal gut microbiota [206].

5. Conclusions and Future Direction

Although we better understand the implication of the cerebellum and the striatum in ASD, further studies are needed on at least two aspects. First, more knowledge should be gathered on a widespread population of ASD patients without gender or age bias. This means systematically including women and middle-aged and senior ASD patients that are often left out of clinical studies. The state of the brain and its maturation are both sex- and age-dependent. Second, there is an urgent need to focus on developing effective treatments to alleviate ASD symptoms, and knowledge of cellular and molecular correlates of the disease is key to help in this research avenue. Motor social and cognitive functions are common features between the cerebellum and the striatum, which are only two synapses away from each other. A better and more thorough assessment of the corresponding interconnections may lead to breakthroughs in this field.

Author Contributions: Writing—original draft preparation, M.T., V.T., A.M., M.E., M.J. and L.G.; writing—review and editing, M.J., L.G.; visualization, L.G. All authors have read and agreed to the published version of the manuscript.

Funding: M.T. and V.T. are partially funded through “Région Nouvelle Aquitaine”.

Institutional Review Board Statement: Not applicable.

Informed Consent Statement: Not applicable.

Conflicts of Interest: The authors declare no conflict of interest.

References

1. Lai, M.C.; Lombardo, M.V.; Baron-Cohen, S. Autism. *Lancet* **2014**, *383*, 896–910. [CrossRef]
2. Loomes, R.; Hull, L.; Mandy, W.P.L. What Is the Male-to-Female Ratio in Autism Spectrum Disorder? A Systematic Review and Meta-Analysis. *J. Am. Acad. Child Adolesc. Psychiatry* **2017**, *56*, 466–474. [CrossRef] [PubMed]
3. Liu, J.; Nyholt, D.R.; Magnussen, P.; Parano, E.; Pavone, P.; Geschwind, D.; Lord, C.; Iversen, P.; Hoh, J.; Autism Genetic Resource Exchange Consortium; et al. A Genomewide Screen for Autism Susceptibility Loci. *Am. J. Hum. Genet.* **2001**, *69*, 327–340. [CrossRef] [PubMed]
4. Folstein, S.E.; Rutter, M.L. Autism: Familial aggregation and genetic implications. *J. Autism Dev. Disord.* **1988**, *18*, 3–30. [CrossRef] [PubMed]
5. Bailey, W.; Popovich, B.; Jones, K.L. Monozygotic twins discordant for Russell-Silver syndrome. *Am. J. Med. Genet.* **1995**, *58*, 101–105. [CrossRef]
6. Sandin, S.; Lichtenstein, P.; Kuja-Halkola, R.; Larsson, H.; Hultman, C.M.; Reichenberg, A. The familial risk of autism. *JAMA-J. Am. Med. Assoc.* **2014**, *311*, 1770–1777. [CrossRef]
7. Constantino, J.N.; Zhang, Y.; Frazier, T.; Abbacchi, A.M.; Law, P. Sibling recurrence and the genetic epidemiology of autism. *Am. J. Psychiatry* **2010**, *167*, 1349–1356. [CrossRef]
8. Risch, N.; Hoffmann, T.J.; Anderson, M.; Croen, L.A.; Grether, J.K.; Windham, G.C. Familial recurrence of autism spectrum disorder: Evaluating genetic and environmental contributions. *Am. J. Psychiatry* **2014**, *171*, 1206–1213. [CrossRef]
9. De Rubeis, S.; He, X.; Goldberg, A.P.; Poultney, C.S.; Samocha, K.; Cicek, A.E.; Kou, Y.; Liu, L.; Fromer, M.; Walker, S.; et al. Synaptic, transcriptional and chromatin genes disrupted in autism. *Nature* **2014**, *515*, 209–215. [CrossRef]
10. Jiang, H.Y.; Xu, L.L.; Shao, L.; Xia, R.M.; Yu, Z.H.; Ling, Z.X.; Yang, F.; Deng, M.; Ruan, B. Maternal infection during pregnancy and risk of autism spectrum disorders: A systematic review and meta-analysis. *Brain Behav. Immun.* **2016**, *58*, 165–172. [CrossRef]
11. Shigemoto-Mogami, Y.; Hoshikawa, K.; Sato, K. Activated microglia disrupt the blood-brain barrier and induce chemokines and cytokines in a rat in vitro model. *Front. Cell. Neurosci.* **2018**, *12*, 494. [CrossRef] [PubMed]
12. Zawadzka, A.; Cieřlik, M.; Adamczyk, A. The Role of Maternal Immune Activation in the Pathogenesis of Autism: A Review of the Evidence, Proposed Mechanisms and Implications for Treatment. *Int. J. Mol. Sci.* **2021**, *22*, 11561. [CrossRef]
13. Phiel, C.J.; Zhang, F.; Huang, E.Y.; Guenther, M.G.; Lazar, M.A.; Klein, P.S. Histone Deacetylase is a Direct Target of Valproic Acid, a Potent Anticonvulsant, Mood Stabilizer, and Teratogen. *J. Biol. Chem.* **2001**, *276*, 36734–36741. [CrossRef] [PubMed]
14. Löscher, W. Basic pharmacology of valproate: A review after 35 years of clinical use for the treatment of epilepsy. *CNS Drugs* **2002**, *16*, 669–694. [CrossRef] [PubMed]
15. Coste, J.; Blotiere, P.O.; Miranda, S.; Mikaeloff, Y.; Peyre, H.; Ramus, F.; Zureik, M.; Weill, A.; Dray-Spira, R. Risk of early neurodevelopmental disorders associated with in utero exposure to valproate and other antiepileptic drugs: A nationwide cohort study in France. *Sci. Rep.* **2020**, *10*. [CrossRef] [PubMed]
16. Roux, S.; Bailly, Y.; Bossu, J.L. Regional and sex-dependent alterations in Purkinje cell density in the valproate mouse model of autism. *Neuroreport* **2019**, *30*, 82–88. [CrossRef]
17. Morová, M.; Krřková, L. Autistic-Like Traits in Laboratory Rodents Exposed to Phthalic Acid Esters During Early Development – an Animal Model of Autism? *Physiol. Res.* **2021**, *70*, 345–361. [CrossRef]
18. Wöhr, M.; Roullet, F.I.; Hung, A.Y.; Sheng, M.; Crawley, J.N. Communication impairments in mice lacking shank1: Reduced levels of ultrasonic vocalizations and scent marking behavior. *PLoS ONE* **2011**, *6*, e0020631. [CrossRef]
19. Yang, M.; Bozdagi, O.; Scattoni, M.L.; Wöhr, M.; Roullet, F.I.; Katz, A.M.; Abrams, D.N.; Kalikhman, D.; Simon, H.; Woldeyohannes, L.; et al. Reduced excitatory neurotransmission and mild Autism-Relevant phenotypes in adolescent shank3 null mutant mice. *J. Neurosci.* **2012**, *32*, 6525–6541. [CrossRef]
20. Roy, S.; Watkins, N.; Heck, D. Comprehensive Analysis of Ultrasonic Vocalizations in a Mouse Model of Fragile X Syndrome Reveals Limited, Call Type Specific Deficits. *PLoS ONE* **2012**, *7*, e44816. [CrossRef]
21. Kanner, L. Autistic Disturbances of affective contact. *Nerv. Child* **1943**, *2*, 217–250.
22. Asperger, H. Die „Autistischen Psychopathen“ im Kindesalter. *Arch. Psychiatr. Nervenkrankh.* **1944**, *117*, 76–136. [CrossRef]
23. Amaral, D.G.; Schumann, C.M.; Nordahl, C.W. Neuroanatomy of autism. *Trends Neurosci.* **2008**, *31*, 137–145. [CrossRef] [PubMed]
24. American Psychiatric Association. *Diagnostic and Statistical Manual of Mental Disorders*; American Psychiatric Association: Washington, DC, USA, 2013; ISBN 0-89042-555-8.
25. Sarnat, H.B.; Netsky, M.G. When does a ganglion become a brain? Evolutionary origin of the central nervous system. *Semin. Pediatr. Neurol.* **2002**, *9*, 240–253. [CrossRef] [PubMed]
26. Dianne, M. Broussard What Do. In *The Cerebellum*; Wiley Online Books; Wiley: Hoboken, NJ, USA, 2013; pp. 213–214, ISBN 9781118730133.
27. Leiner, H.C.; Leiner, A.L.; Dow, R.S. Does the Cerebellum Contribute to Mental Skills? *Behav. Neurosci.* **1986**, *100*, 443–454. [CrossRef] [PubMed]
28. Middleton, F.A.; Strick, P.L. Anatomical evidence for cerebellar and basal ganglia involvement in higher cognitive function. *Science* **1994**, *266*, 458–461. [CrossRef]
29. Allen, G.; Buxton, R.B.; Wong, E.C.; Courchesne, E. Attentional activation of the cerebellum independent of motor involvement. *Science* **1997**, *275*, 1940–1943. [CrossRef]

30. Leroi, I.; O'Hearn, E.; Marsh, L.; Lyketsos, C.G.; Rosenblatt, A.; Ross, C.A.; Brandt, J.; Margolis, R.L. Psychopathology in Patients With Degenerative Cerebellar Diseases: A Comparison to Huntington's Disease. *Am. J. Psychiatry* **2002**, *159*, 1306–1314. [CrossRef]
31. Ramnani, N.; Behrens, T.E.J.; Johansen-Berg, H.; Richter, M.C.; Pinsk, M.A.; Andersson, J.L.R.; Rudebeck, P.; Ciccirelli, O.; Richter, W.; Thompson, A.J.; et al. The Evolution of Prefrontal Inputs to the Cortico-pontine System: Diffusion Imaging Evidence from Macaque Monkeys and Humans. *Cereb. Cortex* **2006**, *16*, 811–818. [CrossRef]
32. Sugihara, I. Crus I in the Rodent Cerebellum: Its Homology to Crus I and II in the Primate Cerebellum and Its Anatomical Uniqueness among Neighboring Lobules. *Cerebellum* **2018**, *17*, 49–55. [CrossRef]
33. Braitenberg, V.; Atwood, R.P. Morphological observations on the cerebellar cortex. *J. Comp. Neurol.* **1958**, *109*, 1–33. [CrossRef] [PubMed]
34. Eccles, J.C. An instruction-selection theory of learning in the cerebellar cortex. *Brain Res.* **1977**, *127*, 327–352. [CrossRef]
35. Ellegood, J.; Pacey, L.K.; Hampson, D.R.; Lerch, J.P.; Henkelman, R.M. Anatomical phenotyping in a mouse model of fragile X syndrome with magnetic resonance imaging. *Neuroimage* **2010**, *53*, 1023–1029. [CrossRef] [PubMed]
36. Reith, R.M.; McKenna, J.; Wu, H.; Hashmi, S.S.; Cho, S.H.; Dash, P.K.; Gambello, M.J. Loss of Tsc2 in Purkinje cells is associated with autistic-like behavior in a mouse model of tuberous sclerosis complex. *Neurobiol. Dis.* **2013**, *51*, 93–103. [CrossRef]
37. Varghese, M.; Keshav, N.; Jacot-Descombes, S.; Warda, T.; Wicinski, B.; Dickstein, D.L.; Harony-Nicolas, H.; De Rubeis, S.; Drapeau, E.; Buxbaum, J.D.; et al. Autism spectrum disorder: Neuropathology and animal models. *Acta Neuropathol.* **2017**, *134*, 537–566. [CrossRef]
38. Al Sagheer, T.; Haida, O.; Balbous, A.; Francheteau, M.; Matas, E.; Fernagut, P.O.; Jaber, M. Motor impairments correlate with social deficits and restricted neuronal loss in an environmental model of autism. *Int. J. Neuropsychopharmacol.* **2018**, *21*, 871–882. [CrossRef]
39. Haida, O.; Al Sagheer, T.; Balbous, A.; Francheteau, M.; Matas, E.; Soria, F.; Fernagut, P.O.; Jaber, M. Sex-dependent behavioral deficits and neuropathology in a maternal immune activation model of autism. *Transl. Psychiatry* **2019**, *9*. [CrossRef]
40. Matas, E.; Maisterrena, A.; Thabault, M.; Balado, E.; Francheteau, M.; Balbous, A.; Galvan, L.; Jaber, M. Major motor and gait deficits with sexual dimorphism in a Shank3 mutant mouse model. *Mol. Autism* **2021**, *12*. [CrossRef]
41. Main, S.L.; Kulesza, R.J. Repeated prenatal exposure to valproic acid results in cerebellar hypoplasia and ataxia. *Neuroscience* **2017**, *340*, 34–47. [CrossRef]
42. Mejias, R.; Chiu, S.L.; Han, M.; Rose, R.; Gil-Infante, A.; Zhao, Y.; Huganir, R.L.; Wang, T. Purkinje cell-specific Grip1/2 knockout mice show increased repetitive self-grooming and enhanced mGluR5 signaling in cerebellum. *Neurobiol. Dis.* **2019**, *132*. [CrossRef]
43. Hassan, T.H.; Abdelrahman, H.M.; Abdel Fattah, N.R.; El-Masry, N.M.; Hashim, H.M.; El-Gerby, K.M.; Abdel Fattah, N.R. Blood and brain glutamate levels in children with autistic disorder. *Res. Autism Spectr. Disord.* **2013**, *7*, 541–548. [CrossRef]
44. Ingram, J.L.; Peckham, S.M.; Tisdale, B.; Rodier, P.M. Prenatal exposure of rats to valproic acid reproduces the cerebellar anomalies associated with autism. *Neurotoxicol. Teratol.* **2000**, *22*, 319–324. [CrossRef]
45. Mychasiuk, R.; Richards, S.; Nakahashi, A.; Kolb, B.; Gibb, R. Effects of rat prenatal exposure to valproic acid on behaviour and neuro-anatomy. *Dev. Neurosci.* **2012**, *34*, 268–276. [CrossRef] [PubMed]
46. Servais, L.; Bearzatto, B.; Schwaller, B.; Dumont, M.; De Saedeleer, C.; Dan, B.; Barski, J.J.; Schiffmann, S.N.; Cheron, G. Mono- and dual-frequency fast cerebellar oscillation in mice lacking parvalbumin and/or calbindin D-28k. *Eur. J. Neurosci.* **2005**, *22*, 861–870. [CrossRef] [PubMed]
47. Piochon, C.; Kloth, A.D.; Grasselli, G.; Titley, H.K.; Nakayama, H.; Hashimoto, K.; Wan, V.; Simmons, D.H.; Eissa, T.; Nakatani, J.; et al. Cerebellar plasticity and motor learning deficits in a copy-number variation mouse model of autism. *Nat. Commun.* **2014**, *5*. [CrossRef] [PubMed]
48. Albus, J.S. A theory of cerebellar function. *Math. Biosci.* **1971**, *10*, 25–61. [CrossRef]
49. Kemper, T.L.; Bauman, M.L. The contribution of neuropathologic studies to the understanding of autism. *Neurol. Clin.* **1993**, *11*, 175–187. [CrossRef]
50. Ghaziuddin, M.; Butler, E.; Tsai, L.; Ghaziuddin, N. Is clumsiness a marker for Asperger syndrome? *J. Intellect. Disabil. Res.* **2008**, *38*, 519–527. [CrossRef]
51. Gowen, E.; Hamilton, A. Motor abilities in autism: A review using a computational context. *J. Autism Dev. Disord.* **2013**, *43*, 323–344. [CrossRef]
52. Maudsley, H. Reviews and Notices. *BMJ* **1867**, *1*, 540–541. [CrossRef]
53. Limperopoulos, C.; Bassan, H.; Gauvreau, K.; Robertson, R.L.; Sullivan, N.R.; Benson, C.B.; Avery, L.; Stewart, J.; Soul, J.S.; Ringer, S.A.; et al. Does cerebellar injury in premature infants contribute to the high prevalence of long-term cognitive, learning, and behavioral disability in survivors? *Pediatrics* **2007**, *120*, 584–593. [CrossRef] [PubMed]
54. Courchesne, E. Brainstem, cerebellar and limbic neuroanatomical abnormalities in autism. *Curr. Opin. Neurobiol.* **1997**, *7*, 269–278. [CrossRef]
55. Bailey, A.; Luthert, P.; Dean, A.; Harding, B.; Janota, I.; Montgomery, M.; Rutter, M.; Lantos, P. A clinicopathological study of autism. In *The Science of Mental Health: Volume 2: Autism*; Routledge: New York, NY, USA, 2013; Volume 121, pp. 141–157, ISBN 9781136800818.
56. Baron-Cohen, S.; Ashwin, E.; Ashwin, C.; Tavassoli, T.; Chakrabarti, B. Talent in autism: Hyper-systemizing, hyper-attention to detail and sensory hypersensitivity. *Philos. Trans. R. Soc. B Biol. Sci.* **2009**, *364*, 1377–1383. [CrossRef] [PubMed]

57. Phillips, J.R.; Hewedi, D.H.; Eissa, A.M.; Moustafa, A.A. The Cerebellum and Psychiatric Disorders. *Front. Public Health* **2015**, *3*. [CrossRef]
58. Arnett, A.B.; Wang, T.; Eichler, E.E.; Bernier, R.A. Reflections on the genetics-first approach to advancements in molecular genetic and neurobiological research on neurodevelopmental disorders. *J. Neurodev. Disord.* **2021**, *13*, 24. [CrossRef] [PubMed]
59. Murakami, J.W.; Courchesne, E.; Press, G.A.; Yeung-Courchesne, R.; Hesselink, J.R. Reduced Cerebellar Hemisphere Size and Its Relationship to Verbal Hypoplasia in Autism. *Arch. Neurol.* **1989**, *46*, 689–694. [CrossRef]
60. Allen, G.; Müller, R.A.; Courchesne, E. Cerebellar function in autism: Functional magnetic resonance image activation during a simple motor task. *Biol. Psychiatry* **2004**, *56*, 269–278. [CrossRef]
61. Ellegood, J.; Crawley, J.N. Behavioral and Neuroanatomical Phenotypes in Mouse Models of Autism. *Neurotherapeutics* **2015**, *12*, 521–533. [CrossRef]
62. Dum, R.P.; Strick, P.L. An unfolded map of the cerebellar dentate nucleus and its projections to the cerebral cortex. *J. Neurophysiol.* **2003**, *89*, 634–639. [CrossRef]
63. Peter, S.; De Zeeuw, C.I.; Boeckers, T.M.; Schmeisser, M.J. Cerebellar and striatal pathologies in mouse models of autism spectrum disorder. In *Advances in Anatomy Embryology and Cell Biology*; Springer: New York, NY, USA, 2017; Volume 224, pp. 103–119.
64. Belichenko, N.P.; Belichenko, P.V.; Hong, H.L.; Mobley, W.C.; Francke, U. Comparative Study of Brain Morphology in Mecp2 Mutant Mouse Models of Rett Syndrome. *J. Comp. Neurol.* **2008**, *508*, 184–195. [CrossRef]
65. Aldinger, K.A.; Kogan, J.; Kimonis, V.; Fernandez, B.; Horn, D.; Klopocki, E.; Chung, B.; Toutain, A.; Weksberg, R.; Millen, K.J.; et al. Cerebellar and posterior fossa malformations in patients with autism-associated chromosome 22q13 terminal deletion. *Am. J. Med. Genet. Part A* **2013**, *161*, 131–136. [CrossRef] [PubMed]
66. Srivastava, S.; Scherrer, B.; Prohl, A.K.; Filip-Dhima, R.; Kapur, K.; Kolevzon, A.; Buxbaum, J.D.; Berry-Kravis, E.; Soorya, L.; Thurm, A.; et al. Volumetric Analysis of the Basal Ganglia and Cerebellar Structures in Patients with Phelan-McDermid Syndrome. *Pediatr. Neurol.* **2019**, *90*, 37–43. [CrossRef] [PubMed]
67. Jamain, S.; Radyushkin, K.; Hammerschmidt, K.; Granon, S.; Boretius, S.; Varoqueaux, F.; Ramanantsoa, N.; Gallego, J.; Ronnenberg, A.; Winter, D.; et al. Reduced social interaction and ultrasonic communication in a mouse model of monogenic heritable autism. *Proc. Natl. Acad. Sci. USA* **2008**, *105*, 1710–1715. [CrossRef] [PubMed]
68. Akshoomoff, N.; Lord, C.; Lincoln, A.J.; Courchesne, R.Y.; Carper, R.A.; Townsend, J.; Courchesne, E. Outcome classification of preschool children with autism spectrum disorders using MRI brain measures. *J. Am. Acad. Child Adolesc. Psychiatry* **2004**, *43*, 349–357. [CrossRef] [PubMed]
69. Courchesne, E.; Karns, C.M.; Davis, H.R.; Ziccardi, R.; Carper, R.A.; Tigue, Z.D.; Chisum, H.J.; Moses, P.; Pierce, K.; Lord, C.; et al. Unusual brain growth patterns in early life in patients with autistic disorder: An MRI study. *Neurology* **2001**, *57*, 245–254. [CrossRef] [PubMed]
70. Brito, A.R.; Vasconcelos, M.M.; Domingues, R.C.; Hygino Da Cruz, L.C.; Rodrigues, L.D.S.; Gasparetto, E.L.; Calçada, C.A.B.P. Diffusion tensor imaging findings in school-aged autistic children. *J. Neuroimaging* **2009**, *19*, 337–343. [CrossRef]
71. Hanaie, R.; Mohri, I.; Kagitani-Shimono, K.; Tachibana, M.; Azuma, J.; Matsuzaki, J.; Watanabe, Y.; Fujita, N.; Taniike, M. Altered Microstructural Connectivity of the Superior Cerebellar Peduncle is Related to Motor Dysfunction in Children with Autistic Spectrum Disorders. *Cerebellum* **2013**, *12*, 645–656. [CrossRef]
72. Noonan, S.K.; Haist, F.; Müller, R.A. Aberrant functional connectivity in autism: Evidence from low-frequency BOLD signal fluctuations. *Brain Res.* **2009**, *1262*, 48–63. [CrossRef]
73. Khan, A.J.; Nair, A.; Keown, C.L.; Datko, M.C.; Lincoln, A.J.; Müller, R.A. Cerebro-cerebellar resting-state functional connectivity in children and adolescents with autism spectrum disorder. *Biol. Psychiatry* **2015**, *78*, 625–634. [CrossRef]
74. Pierce, K.; Courchesne, E. Evidence for a cerebellar role in reduced exploration and stereotyped behavior in autism. *Biol. Psychiatry* **2001**, *49*, 655–664. [CrossRef]
75. Stoodley, C.J.; Valera, E.M.; Schmahmann, J.D. Functional topography of the cerebellum for motor and cognitive tasks: An fMRI study. *Neuroimage* **2012**, *59*, 1560–1570. [CrossRef] [PubMed]
76. Gilbert, S.J.; Bird, G.; Brindley, R.; Frith, C.D.; Burgess, P.W. Atypical recruitment of medial prefrontal cortex in autism spectrum disorders: An fMRI study of two executive function tasks. *Neuropsychologia* **2008**, *46*. [CrossRef] [PubMed]
77. Kelly, E.; Meng, F.; Fujita, H.; Morgado, F.; Kazemi, Y.; Rice, L.C.; Ren, C.; Escamilla, C.O.; Gibson, J.M.; Sajadi, S.; et al. Regulation of autism-relevant behaviors by cerebellar–prefrontal cortical circuits. *Nat. Neurosci.* **2020**, *23*, 1102–1110. [CrossRef]
78. Stoodley, C.J.; D’Mello, A.M.; Ellegood, J.; Jakkamsetti, V.; Liu, P.; Nebel, M.B.; Gibson, J.M.; Kelly, E.; Meng, F.; Cano, C.A.; et al. Altered cerebellar connectivity in autism and cerebellar-mediated rescue of autism-related behaviors in mice. *Nat. Neurosci.* **2017**, *20*, 1744–1751. [CrossRef]
79. Vilensky, J.A. Gait Disturbances in Patients with Autistic Behavior. *Arch. Neurol.* **1981**, *38*. [CrossRef] [PubMed]
80. Mosconi, M.W.; Wang, Z.; Schmitt, L.M.; Tsai, P.; Sweeney, J.A. The role of cerebellar circuitry alterations in the pathophysiology of autism spectrum disorders. *Front. Neurosci.* **2015**, *9*, 296. [CrossRef] [PubMed]
81. Wegiel, J.; Flory, M.; Kuchna, I.; Nowicki, K.; Ma, S.Y.; Imaki, H.; Wegiel, J.; Cohen, I.L.; London, E.; Wisniewski, T.; et al. Stereological study of the neuronal number and volume of 38 brain subdivisions of subjects diagnosed with autism reveals significant alterations restricted to the striatum, amygdala and cerebellum. *Acta Neuropathol. Commun.* **2014**, *2*. [CrossRef]
82. Fatemi, S.H.; Halt, A.R.; Realmuto, G.; Earle, J.; Kist, D.A.; Thuras, P.; Merz, A. Purkinje Cell Size Is Reduced in Cerebellum of Patients with Autism. *Cell. Mol. Neurobiol.* **2002**, *22*, 171–175. [CrossRef]

83. Bailey, A. A clinicopathological study of autism. *Brain* **1998**, *121*, 889–905. [CrossRef]
84. Jeong, J.-W.; Tiwari, V.N.; Behen, M.E.; Chugani, H.T.; Chugani, D.C. In vivo detection of reduced Purkinje cell fibers with diffusion MRI tractography in children with autistic spectrum disorders. *Front. Hum. Neurosci.* **2014**, *8*, 110. [CrossRef]
85. Skefos, J.; Cummings, C.; Enzer, K.; Holiday, J.; Weed, K.; Levy, E.; Yuce, T.; Kemper, T.; Bauman, M. Regional alterations in Purkinje cell density in patients with autism. *PLoS ONE* **2014**, *9*, e0081255. [CrossRef] [PubMed]
86. McCarthy, M.M.; Wright, C.L. Convergence of Sex Differences and the Neuroimmune System in Autism Spectrum Disorder. *Biol. Psychiatry* **2017**, *81*, 402–410. [CrossRef] [PubMed]
87. Haraguchi, S.; Sasahara, K.; Shikimi, H.; Honda, S.I.; Harada, N.; Tsutsui, K. Estradiol promotes purkinje dendritic growth, spinogenesis, and synaptogenesis during neonatal life by inducing the expression of BDNF. *Cerebellum* **2012**, *11*, 416–417. [CrossRef]
88. Hoffman, J.F.; Wright, C.L.; McCarthy, M.M. A critical period in purkinje cell development is mediated by local estradiol synthesis, disrupted by inflammation, and has enduring consequences only for males. *J. Neurosci.* **2016**, *36*, 10039–10049. [CrossRef] [PubMed]
89. Vecellio, M.; Schwaller, B.; Meyer, M.; Hunziker, W.; Celio, M.R. Alterations in Purkinje cell spines of calbindin D-28 k and parvalbumin knock-out mice. *Eur. J. Neurosci.* **2000**, *12*, 945–954. [CrossRef]
90. Leblond, C.S.; Nava, C.; Polge, A.; Gauthier, J.; Huguet, G.; Lumbroso, S.; Giuliano, F.; Stordeur, C.; Depienne, C.; Mouzat, K.; et al. Meta-analysis of SHANK Mutations in Autism Spectrum Disorders: A Gradient of Severity in Cognitive Impairments. *PLoS Genet.* **2014**, *10*, e1004580. [CrossRef]
91. Koekkoek, S.K.E.; Yamaguchi, K.; Milojkovic, B.A.; Dortland, B.R.; Ruigrok, T.J.H.; Maex, R.; De Graaf, W.; Smit, A.E.; VanderWerf, F.; Bakker, C.E.; et al. Deletion of FMR1 in Purkinje cells enhances parallel fiber LTD, enlarges spines, and attenuates cerebellar eyelid conditioning in Fragile X syndrome. *Neuron* **2005**, *47*, 339–352. [CrossRef]
92. Tobia, M.J.; Woodruff-Pak, D.S. Delay Eyeblink Classical Conditioning is Impaired in Fragile X Syndrome. *Behav. Neurosci.* **2009**, *123*, 665. [CrossRef]
93. Vargas, D.L.; Nascimbene, C.; Krishnan, C.; Zimmerman, A.W.; Pardo, C.A. Neuroglial activation and neuroinflammation in the brain of patients with autism. *Ann. Neurol.* **2005**, *57*, 67–81. [CrossRef]
94. Sobaniec-Lotowska, M.E. Ultrastructure of Purkinje cell perikarya and their dendritic processes in the rat cerebellar cortex in experimental encephalopathy induced by chronic application of valproate. *Int. J. Exp. Pathol.* **2001**, *82*, 337–348. [CrossRef]
95. Whitney, E.R.; Kemper, T.L.; Rosene, D.L.; Bauman, M.L.; Blatt, G.J. Density of cerebellar basket and stellate cells in autism: Evidence for a late developmental loss of Purkinje cells. *J. Neurosci. Res.* **2009**, *87*, 2245–2254. [CrossRef] [PubMed]
96. Rubenstein, J.L.R.; Merzenich, M.M. Model of autism: Increased ratio of excitation/inhibition in key neural systems. *Genes Brain Behav.* **2003**, *2*, 255–267. [CrossRef] [PubMed]
97. Purcell, A.E.; Jeon, O.H.; Zimmerman, A.W.; Blue, M.E.; Pevsner, J. Postmortem brain abnormalities of the glutamate neurotransmitter system in autism. *Neurology* **2001**, *57*, 1618–1628. [CrossRef] [PubMed]
98. DeVito, T.J.; Drost, D.J.; Neufeld, R.W.J.; Rajakumar, N.; Pavlosky, W.; Williamson, P.; Nicolson, R. Evidence for Cortical Dysfunction in Autism: A Proton Magnetic Resonance Spectroscopic Imaging Study. *Biol. Psychiatry* **2007**, *61*, 465–473. [CrossRef]
99. Neill Epperson, C.; Haga, K.; Mason, G.F.; Sellers, E.; Gueorguieva, R.; Zhang, W.; Weiss, E.; Rothman, D.L.; Krystal, J.H. Cortical gamma-aminobutyric acid levels across the menstrual cycle in healthy women and those with premenstrual dysphoric disorder: A proton magnetic resonance spectroscopy study. *Arch. Gen. Psychiatry* **2002**, *59*, 851–858. [CrossRef]
100. Dickinson, A.; Jones, M.; Milne, E. Measuring neural excitation and inhibition in autism: Different approaches, different findings and different interpretations. *Brain Res.* **2016**, *1648*, 277–289. [CrossRef]
101. Peter, S.; Ten Brinke, M.M.; Stedehouder, J.; Reinelt, C.M.; Wu, B.; Zhou, H.; Zhou, K.; Boele, H.J.; Kushner, S.A.; Lee, M.G.; et al. Dysfunctional cerebellar Purkinje cells contribute to autism-like behaviour in Shank2-deficient mice. *Nat. Commun.* **2016**, *7*. [CrossRef]
102. Ha, S.; Lee, D.; Cho, Y.S.; Chung, C.; Yoo, Y.E.; Kim, J.; Lee, J.; Kim, W.; Kim, H.; Bae, Y.; et al. Cerebellar shank2 regulates excitatory synapse density, motor coordination, and specific repetitive and anxiety-like behaviors. *J. Neurosci.* **2016**, *36*, 12129–12143. [CrossRef]
103. Tsai, P.T.; Hull, C.; Chu, Y.; Greene-Colozzi, E.; Sadowski, A.R.; Leech, J.M.; Steinberg, J.; Crawley, J.N.; Regehr, W.G.; Sahin, M. Autistic-like behaviour and cerebellar dysfunction in Purkinje cell Tsc1 mutant mice. *Nature* **2012**, *488*, 647–651. [CrossRef]
104. Fatemi, S.H.; Halt, A.R.; Stary, J.M.; Kanodia, R.; Schulz, S.C.; Realmuto, G.R. Glutamic acid decarboxylase 65 and 67 kDa proteins are reduced in autistic parietal and cerebellar cortices. *Biol. Psychiatry* **2002**, *52*, 805–810. [CrossRef]
105. Yip, J.; Soghomonian, J.-J.; Blatt, G.J. Increased GAD67 mRNA expression in cerebellar interneurons in autism: Implications for Purkinje cell dysfunction. *J. Neurosci. Res.* **2008**, *86*. [CrossRef] [PubMed]
106. Dhossche, D.; Applegate, H.; Abraham, A.; Maertens, P.; Bland, L.; Bencsath, A.; Martinez, J. Elevated plasma gamma-aminobutyric acid (GABA) levels in autistic youngsters: Stimulus for a GABA hypothesis of autism. *Med. Sci. Monit.* **2002**, *8*, PR1–PR6. [PubMed]
107. Pétriz, A.; Reyes-Haro, D.; González-González, M.A.; Miledi, R.; Martínez-Torres, A. GABA ρ subunits confer a bicuculline-insensitive component to GFAP+ cells of cerebellum. *Proc. Natl. Acad. Sci. USA* **2014**, *111*, 17522–17527. [CrossRef]
108. Varman, D.R.; Soria-Ortiz, M.B.; Martínez-Torres, A.; Reyes-Haro, D. GABA ρ 3 expression in lobule X of the cerebellum is reduced in the valproate model of autism. *Neurosci. Lett.* **2018**, *687*, 158–163. [CrossRef] [PubMed]

109. Hong, A.; Zhang, A.; Ke, Y.; El Idrissi, A.; Shen, C.H. Downregulation of GABA(A) β subunits is transcriptionally controlled by Fmr1p. *J. Mol. Neurosci.* **2012**, *46*, 272–275. [CrossRef]
110. Heulens, I.; D’Hulst, C.; Van Dam, D.; De Deyn, P.P.; Kooy, R.F. Pharmacological treatment of fragile X syndrome with GABAergic drugs in a knockout mouse model. *Behav. Brain Res.* **2012**, *229*, 244–249. [CrossRef]
111. Henderson, C.; Wijetunge, L.; Kinoshita, M.N.; Shumway, M.; Hammond, R.S.; Postma, F.R.; Brynczka, C.; Rush, R.; Thomas, A.; Paylor, R.; et al. Reversal of disease-related pathologies in the fragile X mouse model by selective activation of GABAB receptors with arbaclofen. *Sci. Transl. Med.* **2012**, *4*. [CrossRef]
112. Fatemi, S.H.; Folsom, T.D.; Kneeland, R.E.; Liesch, S.B. Metabotropic glutamate Receptor 5 upregulation in children with autism is associated with underexpression of both fragile X mental retardation protein and GABA A receptor beta 3 in adults with autism. *Anat. Rec.* **2011**, *294*, 1635–1645. [CrossRef]
113. Muddashetty, R.S.; Kelić, S.; Gross, C.; Xu, M.; Bassell, G.J. Dysregulated metabotropic glutamate receptor-dependent translation of AMPA receptor and postsynaptic density-95 mRNAs at synapses in a mouse model of fragile X syndrome. *J. Neurosci.* **2007**, *27*, 5338–5348. [CrossRef]
114. Bear, M.F.; Huber, K.M.; Warren, S.T. The mGluR theory of fragile X mental retardation. *Trends Neurosci.* **2004**, *27*, 370–377. [CrossRef]
115. Fatemi, S.H.; Aldinger, K.A.; Ashwood, P.; Bauman, M.L.; Blaha, C.D.; Blatt, G.J.; Chauhan, A.; Chauhan, V.; Dager, S.R.; Dickson, P.E.; et al. Consensus paper: Pathological role of the cerebellum in Autism. *Cerebellum* **2012**, *11*, 777–807. [CrossRef] [PubMed]
116. Vicidomini, C.; Ponzoni, L.; Lim, D.; Schmeisser, M.J.; Reim, D.; Morello, N.; Orellana, D.; Tozzi, A.; Durante, V.; Scalmani, P.; et al. Pharmacological enhancement of mGlu5 receptors rescues behavioral deficits in SHANK3 knock-out mice. *Mol. Psychiatry* **2017**, *22*, 689–702. [CrossRef] [PubMed]
117. Blatt, G.J. GABAergic Cerebellar System In Autism: A Neuropathological And Developmental Perspective. *Int. Rev. Neurobiol.* **2005**, *71*, 167–178. [PubMed]
118. Ito, M.; Sakurai, M.; Tongroach, P. Climbing fibre induced depression of both mossy fibre responsiveness and glutamate sensitivity of cerebellar Purkinje cells. *J. Physiol.* **1982**, *324*, 113–134. [CrossRef] [PubMed]
119. Kano, M.; Hashimoto, K.; Kurihara, H.; Watanabe, M.; Inoue, Y.; Aiba, A.; Tonegawa, S. Persistent multiple climbing fiber innervation of cerebellar Purkinje cells in mice lacking mGluR1. *Neuron* **1997**, *18*, 71–79. [CrossRef]
120. Ichise, T.; Kano, M.; Hashimoto, K.; Yanagihara, D.; Nakao, K.; Shigemoto, R.; Katsuki, M.; Aiba, A. mGluR1 in cerebellar Purkinje cells essential for long-term depression, synapse elimination, and motor coordination. *Science* **2000**, *288*, 1832–1835. [CrossRef]
121. Bannai, H.; Niwa, F.; Sherwood, M.W.; Shrivastava, A.N.; Arizono, M.; Miyamoto, A.; Sugiura, K.; Lévi, S.; Triller, A.; Mikoshiba, K. Bidirectional Control of Synaptic GABAAR Clustering by Glutamate and Calcium. *Cell Rep.* **2015**, *13*, 2768. [CrossRef]
122. Nicolini, C.; Fahnestock, M. The valproic acid-induced rodent model of autism. *Exp. Neurol.* **2018**, *299*, 217–227. [CrossRef]
123. Shi, L.; Smith, S.E.P.; Malkova, N.; Tse, D.; Su, Y.; Patterson, P.H. Activation of the maternal immune system alters cerebellar development in the offspring. *Brain Behav. Immun.* **2009**, *23*, 116–123. [CrossRef]
124. Kouser, M.; Speed, H.E.; Dewey, C.M.; Reimers, J.M.; Widman, A.J.; Gupta, N.; Liu, S.; Jaramillo, T.C.; Bangash, M.; Xiao, B.; et al. Loss of predominant shank3 isoforms results in hippocampus-dependent impairments in behavior and synaptic transmission. *J. Neurosci.* **2013**, *33*, 18448–18468. [CrossRef]
125. Lanciego, J.L.; Luquin, N.; Obeso, J.A. Functional neuroanatomy of the basal ganglia. *Cold Spring Harb. Perspect. Med.* **2012**, *2*. [CrossRef] [PubMed]
126. Kreitzer, A.C. Physiology and Pharmacology of Striatal Neurons. *Annu. Rev. Neurosci.* **2009**, *32*, 127–147. [CrossRef] [PubMed]
127. Subramanian, K.; Brandenburg, C.; Orsati, F.; Soghomonian, J.J.; Hussman, J.P.; Blatt, G.J. Basal ganglia and autism—A translational perspective. *Autism Res.* **2017**, *10*, 1751–1775. [CrossRef] [PubMed]
128. Creasey, H.; Rumsey, J.M.; Schwartz, M.; Duara, R.; Rapoport, J.L.; Rapoport, S.I. Brain Morphometry in Autistic Men as Measured by Volumetric Computed Tomography. *Arch. Neurol.* **1986**, *43*, 669–672. [CrossRef] [PubMed]
129. Aylward, E.H.; Schwartz, J.; Machlin, S.; Pearl, G. Bicaudate Ratio as a Measure of Caudate Volume on MR Images. *Am. J. Neuroradiol.* **1991**, *12*, 1217–1222.
130. Reiss, A.L.; Faruque, F.; Naidu, S.; Abrams, M.; Beaty, T.; Bryan, R.N.; Moser, H. Neuroanatomy of Rett syndrome: A volumetric imaging study. *Ann. Neurol.* **1993**, *34*, 227–234. [CrossRef]
131. Hollander, E.; Anagnostou, E.; Chaplin, W.; Esposito, K.; Haznedar, M.M.; Licalzi, E.; Wasserman, S.; Soorya, L.; Buchsbaum, M. Striatal volume on magnetic resonance imaging and repetitive behaviors in autism. *Biol. Psychiatry* **2005**, *58*, 226–232. [CrossRef]
132. Langen, M.; Schnack, H.G.; Nederveen, H.; Bos, D.; Lahuis, B.E.; de Jonge, M.V.; van Engeland, H.; Durston, S. Changes in the Developmental Trajectories of Striatum in Autism. *Biol. Psychiatry* **2009**, *66*, 327–333. [CrossRef]
133. Rojas, D.C.; Peterson, E.; Winterrowd, E.; Reite, M.L.; Rogers, S.J.; Tregellas, J.R. Regional gray matter volumetric changes in autism associated with social and repetitive behavior symptoms. *BMC Psychiatry* **2006**, *6*, 56. [CrossRef]
134. Portmann, T.; Yang, M.; Mao, R.; Panagiotakos, G.; Ellegood, J.; Dolen, G.; Bader, P.L.; Grueter, B.A.; Goold, C.; Fisher, E.; et al. Behavioral abnormalities and circuit defects in the basal ganglia of a mouse model of 16p11.2 deletion syndrome. *Cell Rep.* **2014**, *7*, 1077–1092. [CrossRef]
135. Ellegood, J.; Anagnostou, E.; Babineau, B.A.; Crawley, J.N.; Lin, L.; Genestine, M.; Dicicco-Bloom, E.; Lai, J.K.Y.; Foster, J.A.; Peñagarikano, O.; et al. Clustering autism: Using neuroanatomical differences in 26 mouse models to gain insight into the heterogeneity. *Mol. Psychiatry* **2015**, *20*, 118–125. [CrossRef]

136. Kuo, H.Y.; Liu, F.C. Valproic acid induces aberrant development of striatal compartments and corticostriatal pathways in a mouse model of autism spectrum disorder. *FASEB J.* **2017**, *31*, 4458–4471. [CrossRef]
137. Ashkenazi, S.L.; Polis, B.; David, O.; Morris, G. Striatal cholinergic interneurons exert inhibition on competing default behaviours controlled by the nucleus accumbens and dorsolateral striatum. *Eur. J. Neurosci.* **2021**, *53*, 2078–2089. [CrossRef] [PubMed]
138. Tu, Z.; Zhao, H.; Li, B.; Sen, Y.; Lu, W.; Yongjin, T.; Zhujun, L.; Dazhang, B.; Caijuan, L.; Yingqi, L.; et al. CRISPR/Cas9-mediated disruption of SHANK3 in monkey leads to drug-treatable autism-like symptoms. *Hum. Mol. Genet.* **2019**, *28*, 561–571. [CrossRef] [PubMed]
139. Lingawi, N.W.; Balleine, B.W. Amygdala central nucleus interacts with dorsolateral striatum to regulate the acquisition of habits. *J. Neurosci.* **2012**, *32*, 1073–1081. [CrossRef] [PubMed]
140. Fuccillo, M.V. Striatal circuits as a common node for autism pathophysiology. *Front. Neurosci.* **2016**, *10*. [CrossRef] [PubMed]
141. Schiavi, S.; Iezzi, D.; Manduca, A.; Leone, S.; Melancia, F.; Carbone, C.; Petrella, M.; Mannaioni, G.; Masi, A.; Trezza, V. Reward-Related Behavioral, Neurochemical and Electrophysiological Changes in a Rat Model of Autism Based on Prenatal Exposure to Valproic Acid. *Front. Cell. Neurosci.* **2019**, *13*, 1–14. [CrossRef] [PubMed]
142. Lauber, E.; Filice, F.; Schwaller, B. Prenatal valproate exposure differentially affects parvalbumin-expressing neurons and related circuits in the cortex and striatum of mice. *Front. Mol. Neurosci.* **2016**, *9*, 1–16. [CrossRef] [PubMed]
143. Lauber, E.; Filice, F.; Schwaller, B. Dysregulation of Parvalbumin Expression in the *Cntnap2*^{-/-} Mouse Model of Autism Spectrum Disorder. *Front. Mol. Neurosci.* **2018**, *11*. [CrossRef] [PubMed]
144. Jaber, M.; Robinson, S.W.; Missale, C.; Caron, M.G. Dopamine receptors and brain function. *Neuropharmacology* **1996**, *35*, 1503–1519. [CrossRef]
145. Kreitzer, A.C.; Malenka, R.C. Endocannabinoid-mediated rescue of striatal LTD and motor deficits in Parkinson's disease models. *Nature* **2007**, *445*, 643–647. [CrossRef]
146. Peça, J.; Feliciano, C.; Ting, J.T.; Wang, W.; Wells, M.F.; Venkatraman, T.N.; Lascola, C.D.; Fu, Z.; Feng, G. Shank3 mutant mice display autistic-like behaviours and striatal dysfunction. *Nature* **2011**, *472*, 437–442. [CrossRef] [PubMed]
147. Wang, W.; Li, C.; Chen, Q.; Van Der Goes, M.S.; Hawrot, J.; Yao, A.Y.; Gao, X.; Lu, C.; Zang, Y.; Zhang, Q.; et al. Striatopallidal dysfunction underlies repetitive behavior in Shank3-deficient model of autism. *J. Clin. Investig.* **2017**, *127*, 1978–1990. [CrossRef] [PubMed]
148. Brandenburg, C.; Soghomonian, J.J.; Zhang, K.; Sulkaj, I.; Randolph, B.; Kachadoorian, M.; Blatt, G.J. Increased Dopamine Type 2 Gene Expression in the Dorsal Striatum in Individuals with Autism Spectrum Disorder Suggests Alterations in Indirect Pathway Signaling and Circuitry. *Front. Cell. Neurosci.* **2020**, *14*, 1–13. [CrossRef] [PubMed]
149. Filice, F.; Janickova, L.; Henzi, T.; Bilella, A.; Schwaller, B. The Parvalbumin Hypothesis of Autism Spectrum Disorder. *Front. Cell. Neurosci.* **2020**, *14*, 1–24. [CrossRef]
150. Li, W.; Pozzo-Miller, L. Dysfunction of the corticostriatal pathway in autism spectrum disorders. *J. Neurosci. Res.* **2020**, *98*, 2130–2147. [CrossRef]
151. Modi, M.E.; Brooks, J.M.; Guilmette, E.R.; Beyna, M.; Graf, R.; Reim, D.; Schmeisser, M.J.; Boeckers, T.M.; O'Donnell, P.; Buhl, D.L. Hyperactivity and hypermotivation associated with increased striatal *mgur1* signaling in a Shank2 rat model of autism. *Front. Mol. Neurosci.* **2018**, *11*, 1–17. [CrossRef]
152. Provenzano, G.; Zunino, G.; Genovesi, S.; Sgado, P.; Bozzi, Y. Mutant mouse models of autism spectrum disorders. *Dis. Markers* **2012**, *33*, 225–239. [CrossRef]
153. Rothwell, P.E.; Fuccillo, M.V.; Maxeiner, S.; Hayton, S.J.; Gokce, O.; Lim, B.K.; Fowler, S.C.; Malenka, R.C.; Südhof, T.C. Autism-associated *neuroligin-3* mutations commonly impair striatal circuits to boost repetitive behaviors. *Cell* **2014**, *158*, 198–212. [CrossRef]
154. Espinosa, F.; Xuan, Z.; Liu, S.; Powell, C.M. Neuroligin 1 modulates striatal glutamatergic neurotransmission in a pathway and NMDAR subunit-specific manner. *Front. Synaptic Neurosci.* **2015**, *7*, 1–16. [CrossRef]
155. Rapanelli, M.; Frick, L.R.; Xu, M.; Groman, S.M.; Jindachomthong, K.; Tamamaki, N.; Tanahira, C.; Taylor, J.R.; Pittenger, C. Targeted Interneuron Depletion in the Dorsal Striatum Produces Autism-like Behavioral Abnormalities in Male but Not Female Mice. *Biol. Psychiatry* **2017**, *82*, 194–203. [CrossRef] [PubMed]
156. Poppi, L.A.; Ho-Nguyen, K.T.; Shi, A.; Daut, C.T.; Tischfield, M.A. Recurrent Implication of Striatal Cholinergic Interneurons in a Range of Neurodevelopmental, Neurodegenerative, and Neuropsychiatric Disorders. *Cells* **2021**, *10*, 907. [CrossRef]
157. Aliane, V.; Pérez, S.; Bohren, Y.; Deniau, J.M.; Kemel, M.L. Key role of striatal cholinergic interneurons in processes leading to arrest of motor stereotypies. *Brain* **2011**, *134*, 110–118. [CrossRef] [PubMed]
158. Xu, M.; Kobets, A.; Du, J.C.; Lenington, J.; Li, L.; Banasr, M.; Duman, R.S.; Vaccarino, F.M.; DiLeone, R.J.; Pittenger, C. Targeted ablation of cholinergic interneurons in the dorsolateral striatum produces behavioral manifestations of tourette syndrome. *Proc. Natl. Acad. Sci. USA* **2015**, *112*, 893–898. [CrossRef] [PubMed]
159. Ito-Ishida, A.; Ure, K.; Chen, H.; Swann, J.W.; Zoghbi, H.Y. Loss of MeCP2 in Parvalbumin- and Somatostatin-Expressing Neurons in Mice Leads to Distinct Rett Syndrome-like Phenotypes. *Neuron* **2015**, *88*, 651–658. [CrossRef]
160. Owen, S.F.; Berke, J.D.; Kreitzer, A.C. Fast-Spiking Interneurons Supply Feedforward Control of Bursting, Calcium, and Plasticity for Efficient Learning. *Cell* **2018**, *172*, 683–695. [CrossRef]

161. Wöhr, M.; Orduz, D.; Gregory, P.; Moreno, H.; Khan, U.; Vörckel, K.J.; Wolfer, D.P.; Welzl, H.; Gall, D.; Schiffmann, S.N.; et al. Lack of parvalbumin in mice leads to behavioral deficits relevant to all human autism core symptoms and related neural morphofunctional abnormalities. *Transl. Psychiatry* **2015**, *5*, e525. [CrossRef]
162. Filice, F.; Vörckel, K.J.; Sungur, A.Ö.; Wöhr, M.; Schwaller, B. Reduction in parvalbumin expression not loss of the parvalbumin-expressing GABA interneuron subpopulation in genetic parvalbumin and shank mouse models of autism. *Mol. Brain* **2016**, *9*, 1–17. [CrossRef]
163. Petrelli, F.; Pucci, L.; Bezzi, P. Astrocytes and microglia and their potential link with autism spectrum disorders. *Front. Cell. Neurosci.* **2016**, *10*, 1–8. [CrossRef]
164. Lioy, D.T.; Garg, S.K.; Monaghan, C.E.; Raber, J.; Foust, K.D.; Kaspar, B.K.; Hirrlinger, P.G.; Kirchhoff, F.; Bissonnette, J.M.; Ballas, N.; et al. A role for glia in the progression of Rett-syndrome. *Nature* **2011**, *475*, 497–500. [CrossRef]
165. Cope, E.C.; Briones, B.A.; Brockett, A.T.; Martinez, S.; Vigneron, P.A.; Opendak, M.; Wang, S.S.H.; Gould, E. Immature neurons and radial glia, but not astrocytes or microglia, are altered in adult Cntnap2 and Shank3 mice, models of autism. *eNeuro* **2016**, *3*. [CrossRef]
166. Xu, Z.X.; Kim, G.H.; Tan, J.W.; Riso, A.E.; Sun, Y.; Xu, E.Y.; Liao, G.Y.; Xu, H.; Lee, S.H.; Do, N.Y.; et al. Elevated protein synthesis in microglia causes autism-like synaptic and behavioral aberrations. *Nat. Commun.* **2020**, *11*. [CrossRef] [PubMed]
167. Mineur, Y.S.; Huynh, L.X.; Crusio, W.E. Social behavior deficits in the Fmr1 mutant mouse. *Behav. Brain Res.* **2006**, *168*, 172–175. [CrossRef] [PubMed]
168. Clipperton-Allen, A.E.; Page, D.T. Pten haploinsufficient mice show broad brain overgrowth but selective impairments in autism-relevant behavioral tests. *Hum. Mol. Genet.* **2014**, *23*, 3490–3505. [CrossRef] [PubMed]
169. Clipperton-Allen, A.E.; Page, D.T. Decreased aggression and increased repetitive behavior in Pten haploinsufficient mice. *Genes Brain Behav.* **2015**, *14*, 145–157. [CrossRef]
170. Kazdoba, T.M.; Leach, P.T.; Silverman, J.L.; Crawley, J.N. Modeling fragile X syndrome in the Fmr1 knockout mouse. *Intractable Rare Dis. Res.* **2014**, *3*, 118–133. [CrossRef]
171. Ravenscroft, P.; Brochie, J. NMDA receptors in the basal ganglia. *J. Anat.* **2000**, *196*, 577–585. [CrossRef]
172. Stefani, A.; Chen, Q.; Flores-Hernandez, J.; Jiao, Y.; Reiner, A.; Surmeier, D.J. Physiological and molecular properties of AMPA/kainate receptors expressed by striatal medium spiny neurons. *Dev. Neurosci.* **1998**, *20*, 242–252. [CrossRef]
173. Blundell, J.; Blaiss, C.A.; Etherton, M.R.; Espinosa, F.; Tabuchi, K.; Walz, C.; Bolliger, M.F.; Südhof, T.C.; Powell, C.M. Neuroigin-1 deletion results in impaired spatial memory and increased repetitive behavior. *J. Neurosci.* **2010**, *30*, 2115–2129. [CrossRef]
174. Benthall, K.N.; Cording, K.R.; Agopyan-Mitu, A.H.C.W.; Wong, C.D.; Chen, E.Y.; Bateup, H.S. Loss of Tsc1 from striatal direct pathway neurons impairs endocannabinoid-LTD and enhances motor routine learning. *Cell Rep.* **2021**, *36*. [CrossRef]
175. Jung, K.M.; Sepers, M.; Henstridge, C.M.; Lassalle, O.; Neuhofer, D.; Martin, H.; Frick, A.; Dipatrizio, N.V.; MacKie, K.; et al. Uncoupling of the endocannabinoid signalling complex in a mouse model of fragile X syndrome. *Nat. Commun.* **2012**, *3*. [CrossRef] [PubMed]
176. Martella, G.; Meringolo, M.; Trobiani, L.; De Jaco, A.; Pisani, A.; Bonsi, P. The R451C-Neuroigin 3 mutation hampers the expression of long-term synaptic depression in the dorsal striatum. *Eur. J. Neurosci.* **2017**, *47*, 701–708. [CrossRef] [PubMed]
177. Jaramillo, T.C.; Speed, H.E.; Xuan, Z.; Reimers, J.M.; Liu, S.; Powell, C.M. Altered Striatal Synaptic Function and Abnormal Behaviour in Shank3 Exon4-9 Deletion Mouse Model of Autism. *Autism Res.* **2016**, *9*, 350–375. [CrossRef] [PubMed]
178. Santini, E.; Huynh, T.N.; MacAskill, A.F.; Carter, A.G.; Pierre, P.; Ruggero, D.; Kaphzan, H.; Klann, E. Exaggerated translation causes synaptic and behavioural aberrations associated with autism. *Nature* **2013**, *493*, 411–415. [CrossRef]
179. Zurek, A.A.; Kemp, S.W.P.; Aga, Z.; Walker, S.; Milenkovic, M.; Ramsey, A.J.; Sibille, E.; Scherer, S.W.; Orser, B.A. α 5GABAA receptor deficiency causes autism-like behaviors. *Ann. Clin. Transl. Neurol.* **2016**, *3*, 392–398. [CrossRef] [PubMed]
180. DeLorey, T.M. GABRB3 Gene Deficient Mice: A Potential Model of Autism Spectrum Disorder. *Int. Rev. Neurobiol.* **2005**, *71*, 359–382. [CrossRef]
181. Platt, R.J.; Zhou, Y.; Slaymaker, I.M.; Shetty, A.S.; Weisbach, N.R.; Kim, J.A.; Sharma, J.; Desai, M.; Sood, S.; Kempton, H.R.; et al. Chd8 Mutation Leads to Autistic-like Behaviors and Impaired Striatal Circuits. *Cell Rep.* **2017**, *19*, 335–350. [CrossRef]
182. Centunze, D.; Rossi, S.; Mercaldo, V.; Napoli, I.; Ciotti, M.T.; De Chiara, V.; Musella, A.; Prosperetti, C.; Calabresi, P.; Bernardi, G.; et al. Abnormal Striatal GABA Transmission in the Mouse Model for the Fragile X Syndrome. *Biol. Psychiatry* **2008**, *63*, 963–973. [CrossRef]
183. Aman, M.; Rettiganti, M.; Nagaraja, H.N.; Hollway, J.A.; Mccracken, J.; Mcdougale, C.J.; Tierney, E.; Scahill, L.; Arnold, L.E.; Hellings, J.; et al. Tolerability, Safety, and Benefits of Risperidone in Children and Adolescents with Autism: 21-Month Follow-up after 8-Week Placebo-Controlled Trial. *J. Child Adolesc. Psychopharmacol.* **2015**, *25*, 482. [CrossRef]
184. Aman, M.G.; Kasper, W.; Manos, G.; Mathew, S.; Marcus, R.; Owen, R.; Mankoski, R. Line-item analysis of the Aberrant Behavior Checklist: Results from two studies of aripiprazole in the treatment of irritability associated with autistic disorder. *J. Child Adolesc. Psychopharmacol.* **2010**, *20*, 415–422. [CrossRef]
185. Zürcher, N.R.; Walsh, E.C.; Phillips, R.D.; Cernasov, P.M.; Tseng, C.E.J.; Dharanikota, A.; Smith, E.; Li, Z.; Kinard, J.L.; Bizzell, J.C.; et al. A simultaneous [11C]raclopride positron emission tomography and functional magnetic resonance imaging investigation of striatal dopamine binding in autism. *Transl. Psychiatry* **2021**, *11*, 33. [CrossRef] [PubMed]
186. Kosillo, P.; Bateup, H.S. Dopaminergic Dysregulation in Syndromic Autism Spectrum Disorders: Insights from Genetic Mouse Models. *Front. Neural Circuits* **2021**, *15*. [CrossRef] [PubMed]

187. Shonesy, B.C.; Parrish, W.P.; Haddad, H.K.; Stephenson, J.R.; Báldi, R.; Bluett, R.J.; Marks, C.R.; Centanni, S.W.; Folkes, O.M.; Spiess, K.; et al. Role of Striatal Direct Pathway 2-Arachidonoylglycerol Signaling in Sociability and Repetitive Behavior. *Biol. Psychiatry* **2018**, *84*, 304–315. [CrossRef] [PubMed]
188. Lee, Y.; Han, P.-L. Early-Life Stress in D2 Heterozygous Mice Promotes Autistic-like Behaviors through the Downregulation of the BDNF-TrkB Pathway in the Dorsal Striatum. *Exp. Neurobiol.* **2019**, *28*, 337–351. [CrossRef] [PubMed]
189. Morel, L.; Higashimori, H.; Tolman, M.; Yang, Y. VGluT1+ Neuronal Glutamatergic signaling regulates postnatal developmental maturation of cortical protoplasmic astroglia. *J. Neurosci.* **2014**, *34*, 10950–10962. [CrossRef] [PubMed]
190. Kim, H.; Lee, Y.; Park, J.Y.; Kim, J.E.; Kim, T.K.; Choi, J.; Lee, J.E.; Lee, E.H.; Kim, D.; Kim, K.S.; et al. Loss of Adenylyl Cyclase Type-5 in the Dorsal Striatum Produces Autistic-Like Behaviors. *Mol. Neurobiol.* **2017**, *54*, 7994–8008. [CrossRef]
191. Herbert, M.R. Contributions of the environment and environmentally vulnerable physiology to autism spectrum disorders. *Curr. Opin. Neurol.* **2010**, *23*, 103–110. [CrossRef]
192. Perera, F.; Herbstman, J. Prenatal environmental exposures, epigenetics, and disease. *Reprod. Toxicol.* **2011**, *31*, 363–373. [CrossRef]
193. Wu, X.; Zhang, Y. TET-mediated active DNA demethylation: Mechanism, function and beyond. *Nat. Rev. Genet.* **2017**, *18*, 517–534. [CrossRef]
194. Jiang, Y.; Tsai, T.F.; Bressler, J.; Beaudet, A.L. Imprinting in Angelman and Prader-Willi syndromes. *Curr. Opin. Genet. Dev.* **1998**, *8*, 334–342. [CrossRef]
195. Deaton, A.M.; Bird, A. CpG islands and the regulation of transcription. *Genes Dev.* **2011**, *25*, 1010–1022. [CrossRef] [PubMed]
196. Tremblay, M.W.; Jiang, Y. DNA Methylation and Susceptibility to Autism Spectrum Disorder. *Annu. Rev. Med.* **2019**, *70*, 151–166. [CrossRef] [PubMed]
197. Lister, R.; Mukamel, E.A.; Nery, J.R.; Urich, M.; Puddifoot, C.A.; Johnson, N.D.; Lucero, J.; Huang, Y.; Dwork, A.J.; Matthew, D.; et al. Global Epigenomic Reconfiguration During Mammalian Brain Development. *Science* **2013**, *341*, 1–21. [CrossRef]
198. Nardone, S.; Sharan Sams, D.; Reuveni, E.; Getselter, D.; Oron, O.; Karpuj, M.; Elliott, E. DNA methylation analysis of the autistic brain reveals multiple dysregulated biological pathways. *Transl. Psychiatry* **2014**, *4*, e433. [CrossRef] [PubMed]
199. Nardone, S.; Sams, D.S.; Zito, A.; Reuveni, E.; Elliott, E. Dysregulation of cortical neuron DNA methylation profile in autism spectrum disorder. *Cereb. Cortex* **2017**, *27*, 5739–5754. [CrossRef]
200. Sun, W.; Poschmann, J.; Cruz-Herrera del Rosario, R.; Parikshak, N.N.; Hajan, H.S.; Kumar, V.; Ramasamy, R.; Belgard, T.G.; Elangovan, B.; Wong, C.C.Y.; et al. Histone Acetylome-wide Association Study of Autism Spectrum Disorder. *Cell* **2016**, *167*. [CrossRef] [PubMed]
201. Won, H.; de la Torre-Ubieta, L.; Stein, J.L.; Parikshak, N.N.; Huang, J.; Opland, C.K.; Gandal, M.J.; Sutton, G.J.; Hormozdiari, F.; Lu, D.; et al. Chromosome conformation elucidates regulatory relationships in developing human brain. *Nature* **2016**, *538*. [CrossRef]
202. Steullet, P.; Cabungcal, J.H.; Monin, A.; Dwir, D.; O'Donnell, P.; Cuenod, M.; Do, K.Q. Redox dysregulation, neuroinflammation, and NMDA receptor hypofunction: A “central hub” in schizophrenia pathophysiology? *Schizophr. Res.* **2016**, *176*, 41–51. [CrossRef]
203. Richetto, J.; Massart, R.; Weber-Stadlbauer, U.; Szyf, M.; Riva, M.A.; Meyer, U. Genome-wide DNA Methylation Changes in a Mouse Model of Infection-Mediated Neurodevelopmental Disorders. *Biol. Psychiatry* **2017**, *81*, 265–276. [CrossRef]
204. Basil, P.; Li, Q.; Dempster, E.L.; Mill, J.; Sham, P.C.; Wong, C.C.Y.; McAlonan, G.M. Prenatal maternal immune activation causes epigenetic differences in adolescent mouse brain. *Transl. Psychiatry* **2014**, *4*. [CrossRef]
205. Dinan, T.G.; Cryan, J.F. Brain–gut–microbiota axis—Mood, metabolism and behaviour. *Nat. Rev. Gastroenterol. Hepatol.* **2017**, *14*, 69–70. [CrossRef] [PubMed]
206. Sabit, H.; Tombuloglu, H.; Rehman, S.; Almandil, N.B.; Cevik, E.; Abdel-Ghany, S.; Rashwan, S.; Abasiyanik, M.F.; Yee Waye, M.M. Gut microbiota metabolites in autistic children: An epigenetic perspective. *Heliyon* **2021**, *7*, e06105. [CrossRef] [PubMed]

Article

Maternal Immune Activation Causes Social Behavior Deficits and Hypomyelination in Male Rat Offspring with an Autism-Like Microbiota Profile

Gilbert Aaron Lee^{1,2}, Yen-Kuang Lin³, Jing-Huei Lai^{4,5}, Yu-Chun Lo⁶, Yu-Chen S. H. Yang⁷, Syuan-You Ye¹, Chia-Jung Lee^{8,9}, Ching-Chiung Wang¹⁰, Yung-Hsiao Chiang^{4,5,11,12} and Sung-Hui Tseng^{13,14,*}

¹ Department of Medical Research, Taipei Medical University Hospital, Taipei 110, Taiwan; gilbertlee@tmu.edu.tw (G.A.L.); yoyoyei330@gmail.com (S.-Y.Y.)

² Department of Microbiology and Immunology, School of Medicine, College of Medicine, Taipei Medical University, Taipei 110, Taiwan

³ Graduate Institute of Athletics and Coaching Science, National Taiwan Sport University, Taoyuan 333, Taiwan; robbinlin@ntsu.edu.tw

⁴ Core Laboratory of Neuroscience, Office of R&D, Taipei Medical University, Taipei 110, Taiwan; M105095006@tmu.edu.tw (J.-H.L.); ychiang@tmu.edu.tw (Y.-H.C.)

⁵ Center for Neurotrauma and Neuroregeneration, Taipei Medical University, Taipei 110, Taiwan

⁶ PhD Program for Neural Regenerative Medicine, College of Medical Science and Technology, Taipei Medical University, Taipei 110, Taiwan; aricalo@tmu.edu.tw

⁷ Joint Biobank, Office of Human Research, Taipei Medical University, Taipei 110, Taiwan; can_0131@tmu.edu.tw

⁸ PhD Program for Clinical Drug Discovery of Herbal Medicine, College of Pharmacy, Taipei Medical University, Taipei 110, Taiwan; cjlee@tmu.edu.tw

⁹ Graduate Institute of Pharmacognosy Science, College of Pharmacy, Taipei Medical University, Taipei 110, Taiwan

¹⁰ Department of Pharmaceutical Sciences, Taipei Medical University, Taipei 110, Taiwan; crystal@tmu.edu.tw

¹¹ Department of Surgery, College of Medicine, Taipei Medical University, Taipei 110, Taiwan

¹² Graduate Institute of Neural Regenerative Medicine, College of Medical Science and Technology, Taipei Medical University, Taipei 110, Taiwan

¹³ Department of Physical Medicine and Rehabilitation, School of Medicine, College of Medicine, Taipei Medical University, No. 250 Wu Hsing Street, Taipei 110, Taiwan

¹⁴ Department of Physical Medicine and Rehabilitation, Taipei Medical University Hospital, Taipei 110, Taiwan

* Correspondence: m003089010@tmu.edu.tw; Tel.: +886-970405336

Citation: Lee, G.A.; Lin, Y.-K.; Lai, J.-H.; Lo, Y.-C.; Yang, Y.-C.S.H.; Ye, S.-Y.; Lee, C.-J.; Wang, C.-C.; Chiang, Y.-H.; Tseng, S.-H. Maternal Immune Activation Causes Social Behavior Deficits and Hypomyelination in Male Rat Offspring with an Autism-Like Microbiota Profile. *Brain Sci.* **2021**, *11*, 1085. <https://doi.org/10.3390/brainsci11081085>

Academic Editor: Masaru Tanaka

Received: 16 July 2021

Accepted: 16 August 2021

Published: 18 August 2021

Publisher's Note: MDPI stays neutral with regard to jurisdictional claims in published maps and institutional affiliations.



Copyright: © 2021 by the authors. Licensee MDPI, Basel, Switzerland. This article is an open access article distributed under the terms and conditions of the Creative Commons Attribution (CC BY) license (<https://creativecommons.org/licenses/by/4.0/>).

Abstract: Maternal immune activation (MIA) increases the risk of autism spectrum disorder (ASD) in offspring. Microbial dysbiosis is associated with ASD symptoms. However, the alterations in the brain–gut–microbiota axis in lipopolysaccharide (LPS)-induced MIA offspring remain unclear. Here, we examined the social behavior, anxiety-like and repetitive behavior, microbiota profile, and myelination levels in LPS-induced MIA rat offspring. Compared with control offspring, MIA male rat offspring spent less time in an active social interaction with stranger rats, displayed more anxiety-like and repetitive behavior, and had more hypomyelination in the prefrontal cortex and thalamic nucleus. A fecal microbiota analysis revealed that MIA offspring had a higher abundance of *Alistipes*, *Fusobacterium*, and *Ruminococcus* and a lower abundance of *Coprococcus*, *Erysipelotrichaies*, and *Actinobacteria* than control offspring, which is consistent with that of humans with ASD. The least absolute shrinkage and selection operator (LASSO) method was applied to determine the relative importance of the microbiota, which indicated that the abundance of *Alistipes* and *Actinobacteria* was the most relevant for the profile of defective social behavior, whereas *Fusobacterium* and *Coprococcus* was associated with anxiety-like and repetitive behavior. In summary, LPS-induced MIA offspring showed an abnormal brain–gut–microbiota axis with social behavior deficits, anxiety-like and repetitive behavior, hypomyelination, and an ASD-like microbiota profile.

Keywords: autism spectrum disorder; lipopolysaccharide; maternal immune activation; microbiota; three-chamber test; myelination; brain–gut–microbiota axis; social behavior deficits

1. Introduction

Maternal immune activation (MIA) has been linked to an increased risk of neurodevelopmental psychiatric disorders in offspring [1,2]. Animal models of MIA have been developed by activating the immune system with immunogens during pregnancy and then observing the development of defective behaviors in offspring with autism-like behavior [3]. MIA generates inflammatory cytokines to which the fetus is exposed during mid-gestation, possibly affecting fetal brain development [4]. Furthermore, the presence of inflammatory molecules and cytokines can affect central nervous system development [5] and adversely affect neuron survival [6].

Gut microbiota plays a critical role in regulating host physiology, metabolism, nutrition, and brain function [7]. Microbial dysbiosis is correlated with various adverse consequences, including behavioral abnormalities, neuropathology, immune dysfunction, and deficient gastrointestinal integrity [7]. The prenatal environment affects the microbiome of offspring [8]. Microbial dysbiosis is associated with the symptoms of autism spectrum disorder (ASD), including impaired social communication and repetitive behaviors [9]. However, how prenatal infection affects the brain–gut–microbiota axis, which regulates behavioral phenotypes, remains unclear.

Maternal lipopolysaccharide (LPS) exposure causes reproductive, behavioral, and neurochemical abnormalities in offspring [10]. LPS, an endotoxin, activates immune cells to release proinflammatory cytokines, which induce maternal cytokine responses and may increase the risk of atypical brain development [11]. Prenatal LPS treatment causes social behavior deficits in male offspring [9,12]. Pregnant rats injected with intraperitoneal LPS on gestation day (GD) 9.5 were demonstrated to induce the most relevant long-term neuropathological consequences in offspring [13,14]. However, the microbiota changes have not been quantified in these MIA offspring.

In this study, we investigated the relationship between microbiota and ASD-related behavior and demonstrated brain myelination changes in MIA offspring. Furthermore, we used the least absolute shrinkage and selection operator (LASSO) method to determine the most relevant microbiota genera associated with ASD-related behaviors. Taken together, we demonstrated that an abnormal brain–gut–microbiota axis with phenotypes includes a social behavior deficit, anxiety-like and repetitive behavior, hypomyelination, and dysbiosis microbiota in MIA offspring; thus, providing a link between maternal infection and the etiopathogenesis of ASD.

2. Materials and Methods

2.1. LPS-Induced MIA Rat Model

All animal procedures were approved by the Animal Care and Use Committees of Taipei Medical University. Eight-week-old Wistar female rats (BioLASCO, Taipei, Taiwan) in their first pregnancy were used in this study. Female rats were mated overnight with male rats with mating experience and were checked for the presence of a vaginal plug the subsequent morning to confirm mating. Pregnant rats were housed individually and allowed to raise their own litters until weaning. On GD 9.5, 500 µg/kg LPS (*Escherichia coli* O127:B8) or phosphate-buffered saline (PBS) was injected intraperitoneally into pregnant rats. Litters were left undisturbed until weaning at postnatal day 21. Offspring were housed in same-sex cages containing three rats until the end of the experiments. All animals were housed in temperature-controlled rooms under a 12 h light/dark cycle with ad libitum access to water and same food. All behavioral testing was performed during rats' light cycle between 9 a.m. and 5 p.m. The experiments were performed in accordance with guidelines by the International Council for Laboratory Animal Science (ICLAS) for the care and use of laboratory animals for experiments.

2.2. Three-Chamber Test

The three-chamber social interaction test was adapted from a previous study [15]. Stranger rats were age- and sex-matched with the testing rats. The body weights of stranger

rats at 5 and 7 weeks were 130 and 195 g, respectively. Stranger rat was placed in the right-side chamber of three-chambered apparatus (Deep Brain Tech, Taiwan) to test the social interaction between stranger and the test rat during a 10 min test session (Figure 1B). The left chamber remained empty. The sociability score, used to measure the social preference of test rat was defined as the time spent in the social region of the central space near stranger rat during test session (Figure 1B). Test rat's behavior was recorded using a camera (The Imaging Source, DFK 33UP1300, Bremen, Germany). OptiMouse software was used to calculate the total time spent by rats in three zones of the central space (nonsocial, center, and social regions) in a three-chambered apparatus (Figure 1B).

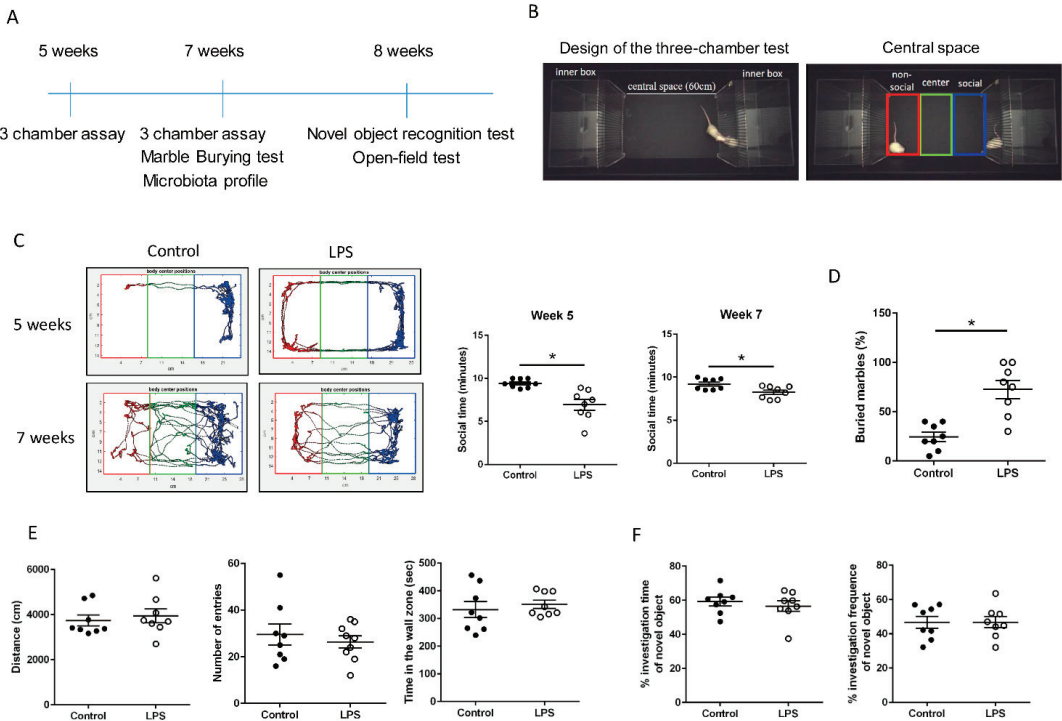


Figure 1. Maternal lipopolysaccharide (LPS) stimulation caused social behavior deficits and anxiety-like and repetitive behavior in male offspring. (A) Timeline for behavioral experiments. The age of the rats in weeks is indicated on the timeline. (B) Design of the three-chamber test apparatus for rats. The apparatus contained three parts: two side chambers and one central space. The length of the central space was 60 cm. The right-side chamber housed the stranger rat. The test rat was placed in the central space and allowed to freely interact with the stranger rat. The central space was divided into three regions: social, center, and nonsocial. (C) Quantification of time spent in the social region. The social behavior of 5- and 7-week-old maternal immune activation (MIA) and control offspring was detected using a three-chamber apparatus. Their tracks in the central space of the three-chamber apparatus are indicated, with the nonsocial region indicated in red, the center region in green, and the social region in blue. * $p < 0.05$ ($n = 8$ per group). (D) Percentage of buried marbles in the MIA and control offspring. * $p < 0.05$ ($n = 8$ per group) (E) Locomotor activity evaluation was performed in 7-week-old MIA and control male offspring using the open-field test ($n = 8$ per group). (F) The NOR test was performed on 7-week-old MIA and control male offspring ($n = 8$ per group). All data are presented as mean \pm SEM.

2.3. Marble-Burying Test

The marble-burying test was used to examine the test rat's anxiety-like and repetitive behavior. A clean cage ($22 \times 45 \times 20 \text{ cm}^3$) was prepared with a 4 cm corncob bedding material containing 20 embedded marbles. After 30 min, the number of marbles that remained buried in the corncob bedding was recorded.

2.4. Novel Object Recognition Test

Recognition memory was evaluated using the novel object recognition (NOR) test, which was used to compare the amount of time a rat spent investigating a novel object versus a familiar object. The familiar object was a plastic square block, and the novel object was a plastic V-shaped block. First, rats were habituated to an open-field Plexiglas arena ($60 \times 60 \times 100 \text{ cm}^3$) for 10 min. After habituation, the rats were allowed to explore two identical familiar objects for 10 min during the familiarization phase. After a 24 h intertrial interval, one familiar object was replaced with a novel object, and the rats were returned to the arena and allowed to explore the two objects. A preference index, which measured the time spent by the test rat exploring the novel object over the familiar one, was calculated as a percentage using the following equation: $((\text{Time N} - \text{Time F}) / (\text{Time N} + \text{Time F})) \times 100$, where F and N represent the time spent near the familiar and novel objects, respectively.

2.5. Open-Field Test

Using an open-field test, we evaluated the general motor activity and anxiety-related exploratory activity in the MIA and control rats. Rats were first habituated to an open-field Plexiglas arena ($60 \times 60 \times 100 \text{ cm}^3$) for 10 min. Their locomotor activity and anxiety-like behavior were monitored for 10 min using open-field tests and recorded using an EthoVision system. General locomotor activity was defined as the total distance traveled in the open field. Anxiety-like behavior was measured based on the number of entries and retention times in the wall zone of the open field. The center of the open field was defined as a $30 \times 30\text{-cm}^2$ area in the geometric center of the arena. The wall zone was defined as a peripheral zone 5 cm from all four sides.

2.6. 16S rRNA Gene Sequencing and Next-Generation Sequencing

The stool samples of the rats were purified using the QIAamp Fast DNA Stool Mini Kit (QIAGEN, Germany). Library preparation was conducted following the protocol of 16S ribosomal RNA gene amplicons for the Illumina MiSeq system. Sequence reads were deposited in the European Nucleotide Archive (accession number: PRJEB28574). Universal primers (341F and 805R) were used to amplify the V3–V4 region of bacterial 16S rRNA genes; they were first removed from demultiplexed, paired reads using Cutadapt (v1.12; DOI:10.14806/ej.17.1.200). The filtered reads were then processed using the DADA2 package (v1.3.5) in R (v3.3.3) [16], following the workflow described by Callahan et al. [17], but without the rarefying procedure. Briefly, the forward and reverse reads were filtered and trimmed based on the read quality score and read length. Dereplication was then performed to merge identical reads, and the reads were then subjected to the denoising algorithm DADA2; the reads alternated between error rate estimation and sample composition inference until they converge into a consistent solution. Finally, paired reads with ≥ 20 -bp overlap were merged, and chimeras were removed. A list of V3–V4 sequence variants found in the samples, which were inferred with DADA2, and the frequency of each sequence variant in each sample were obtained. Taxonomy assignment was performed using the SILVA database (v128) [18] for reference with a minimum bootstrap confidence of 80. Multiple sequence alignment of variants was performed using DECIPHER (v2.2.0) and the phylogenetic tree was constructed from the alignment using phangorn (v2.2.0) [19]. The count table, taxonomy assignment results, and phylogenetic tree were consolidated into a phyloseq object, and community analyses were performed using phyloseq (v1.19.1) [20]. The alpha-diversity indices were calculated using the estimated richness function of the phyloseq package. Data from the treatment and control groups

were compared using the Wilcoxon–Mann–Whitney test (at $\alpha = 0.05$). UniFrac distances were calculated using the GUniFrac package (v1.1) to assess community dissimilarity between the groups [21]. Principal coordinate analysis ordination on UniFrac distances was performed, and the *adonis* and *betadisper* functions from the *vegan* package (v2.4; <https://CRAN.R-project.org/package=vegan>, accessed on 24 August 2017) were used to analyze the dissimilarity of composition among the groups and the homogeneity of dispersion, respectively. *Vegan* is R package which provides tools for descriptive community ecology. It includes functions of diversity analysis, community ordination, and dissimilarity analysis. *Adonis* and *Betadisper* are the sister functions of *Vegan* package. *Adonis* analyzes and partitions the sum of squares using distance matrices. It can be seen as an ANOVA using distance matrices (analogous to MANOVA—multivariate analysis of variance). Therefore, it could test if two or more groups have similar compositions. *Betadisper* first calculates the average distance of group members to the group centroid in multivariate space (generated by a distance matrix). Then, an ANOVA is conducted to test if the dispersions (variances) of groups are different.

2.7. LASSO Method

In the LASSO algorithm, the feature importance was ranked in the framework of general linear models. Specifically, Tibshirani's LASSO method was adopted (Tibshirani, 1996). LASSO arises from a constrained form of ordinary least squares regression, where the sum of the absolute values of the regression coefficients is constrained to be smaller than a specified parameter. The LASSO procedure offers extensive capabilities for customizing the selection with a wide variety of selection and stopping criteria, such as the Akaike information criterion (AIC).

2.8. Immunohistochemistry

The rats were euthanized and transcardially perfused with 25 mL of PBS and 4% paraformaldehyde. Whole brains were fixed with 4% paraformaldehyde for approximately 3 days. Paraformaldehyde-fixed 2 mm coronal slices were embedded in paraffin and cut into 5 μ m thick sections, which were deparaffinized and rehydrated using a graded series of ethanol solutions. The sections then underwent an antigen retrieval process and were stained using horseradish peroxidase anti-myelin basic protein (MBP) antibody (BioLegend, catalog number 808405). Next, 3,3'-diaminobenzidine and hematoxylin staining was performed on sections by using the Chemicon IHC Select system (Millipore, catalog number DAB050). The sections were observed through microscopy (Olympus/Bx43). The MBP-positive area was calculated from sections by using HistoQuest tissue analysis software V2.0 (TissueGnostics, Vienna, Austria).

2.9. Statistical Analysis

Unpaired *t*-test were performed for behavioral data analyses using GraphPad Prism software. Error bars represent the standard error of mean. Microbiota enrichment analysis between the groups was conducted using the linear discriminant analysis (LDA) effect size (LEfSe) method. Data were compared using the Kruskal–Wallis and Wilcoxon tests; differences were considered significant at $p \leq 0.05$ and a logarithmic LDA score of ≥ 2 [22]. Data were visualized as cladograms created using GraPhlAn [23].

3. Results

3.1. Maternal LPS Stimulation Causes Social Behavior Deficits and Anxiety-Like and Repetitive Behavior in MIA Male Offspring

No significant alterations in reproductive parameters were found in female rats exposed to prenatal LPS treatment (LPS-treated group) or PBS treatment (control group). The number of pups born in each litter, the parturition day, or individual bodyweight of offspring at 5 and 7 weeks showed no significant difference between prenatal LPS and PBS treatments (data not shown). To test whether MIA offspring began displaying social

behavior deficits before or after sexual maturity, we examined their social behavior at 5 and 7 weeks. We used OptiMouse software to track the movement of rats in our three-chamber apparatus during the social behavior tests. Male offspring from the prenatal LPS-treated group spent less time in the social region of the central space in the three-chamber apparatus than those from the PBS-treated control group at both 5 and 7 weeks (Figure 1B,C), whereas female offspring had a normal social behavior (data not shown). Thus, male MIA offspring displayed social behavior deficits before and after sexual maturity. MIA male offspring also buried more marbles than the control male offspring (Figure 1D), which indicates anxiety-like and repetitive behavior. MIA and control male offspring had no differences in the total distance moved, number of entries, or time spent in the wall zone of the open-field assay (Figure 1E). Male offspring from the LPS group demonstrated a similar preference for the novel object compared with male offspring from the control group (Figure 1F). Taken together, the results revealed that locomotor activity and cognition were similar in LPS and control groups.

3.2. Fecal Microbiome Profile in Male MIA Offspring Is Similar to That of Patients with ASD

The gut microbiota profile in ASD was determined by identifying fecal microbiota through 16S rRNA gene sequencing and next-generation sequencing [24]. We observed that the fecal microbiota of prenatal LPS-treated male offspring had slightly, but not significantly, higher alpha diversity than that of the control offspring (Figure 2A). An unweighted and weighted UniFrac principal coordinate analysis indicated that the fecal microbiota profile of male MIA offspring was significantly different from that of PBS-treated male offspring (Figure 2B). A significant increase in *Fusobacteria* abundance and decrease in *Actinobacteria* abundance at the phylum level of microbial composition was observed in MIA offspring compared with that in control offspring (Figure 3 and Table 1). Compared with control offspring, MIA male offspring had a significantly increased abundance of *Fusobacteriaceae* and *Rikenellaceae* families (Figure 4A), and significantly decreased abundance of *Micrococcaceae*, *Staphylococcaceae*, *Aerococcaceae*, *Corynebacteriaceae*, and *Erysipelotrichaceae* families (Figure 4B). At the genus level, compared with control offspring, MIA male offspring had significantly increased *Ruminococcus_1*, *Fusobacterium*, *Acetatifactor*, *Alistipes*, and *DNF00809* (Figure 4C), and significantly decreased *Coprococcus_3*, *Rothia*, *Sellimonas*, *Staphylococcus*, *Aerococcus*, *Corynebacterium_1*, *Candidatus_Stoquefichus*, and *Blautia* (Figure 4D).

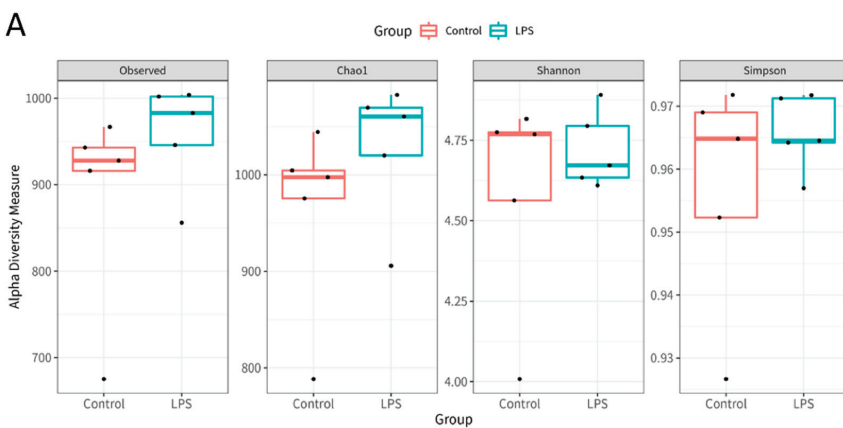


Figure 2. Cont.

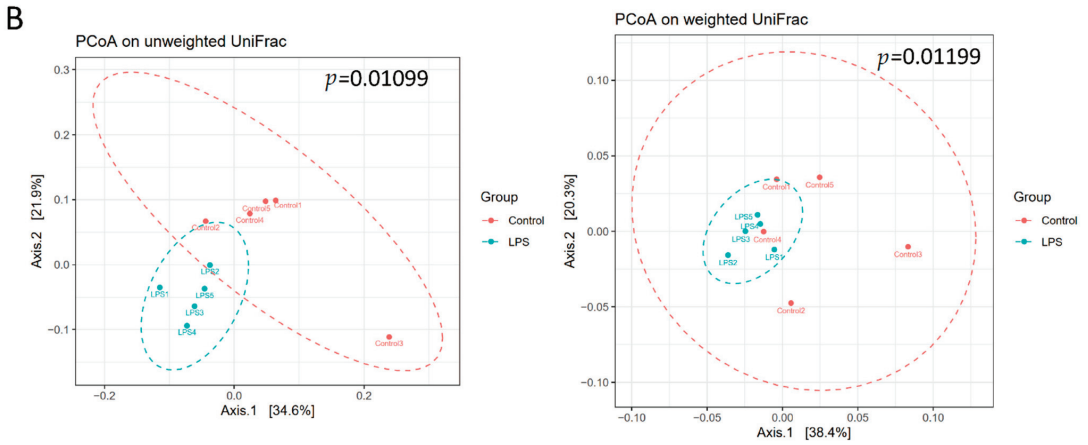


Figure 2. Fecal microbiome distribution in male maternal immune activation (MIA) offspring. The feces of prenatal lipopolysaccharide (LPS)-stimulated male offspring (LPS group) and control rats were prepared for fecal microbiome profiling through high-throughput sequencing of the 16s rRNA gene on the Illumina MiSeq system. (A) Alpha diversity of MIA offspring (LPS) and controls. (B) Principal coordinate analysis plot based on unweighted or weighted UniFrac distance of omeprazole MIA offspring and control samples. A significant difference in beta diversity was evaluated using permutational multivariate analysis of variance (vegan:adonis, 1000 permutations), and beta dispersion was quantified using a betadisper (vegan:betadisper, 1000 permutations). Both indices achieved adonis $p < 0.05$ and betadisper $p > 0.05$.

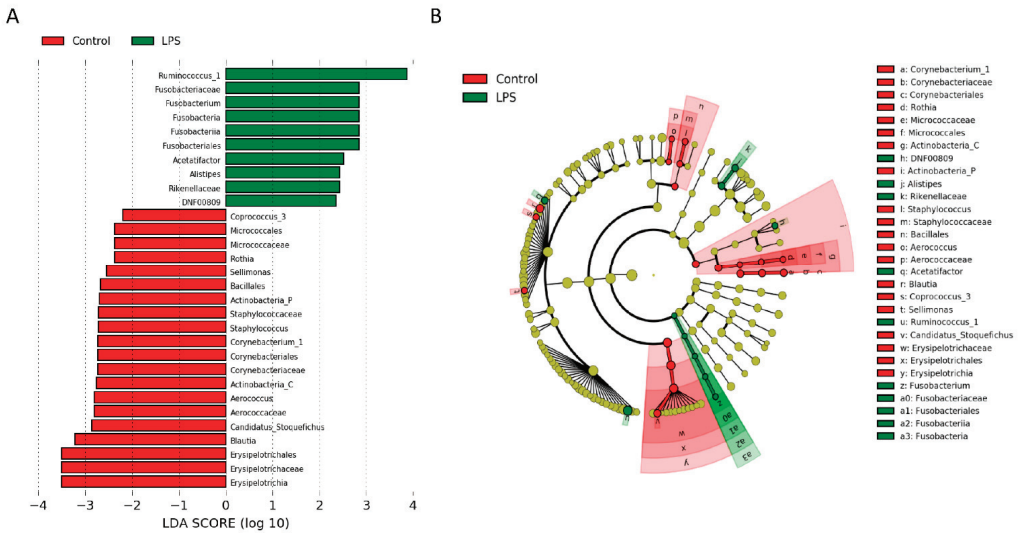


Figure 3. Fecal microbiota was changed in male MIA offspring. (A) Linear discriminant analysis (LDA) effect size analysis of gut microbiota changed in MIA offspring (lipopolysaccharide (LPS)) and control rats. Significant biomarkers were defined as taxa with an LDA score (log10) of ≥ 2 . (B) Significant taxa differences in MIA offspring (LPS) are highlighted on the cladogram.

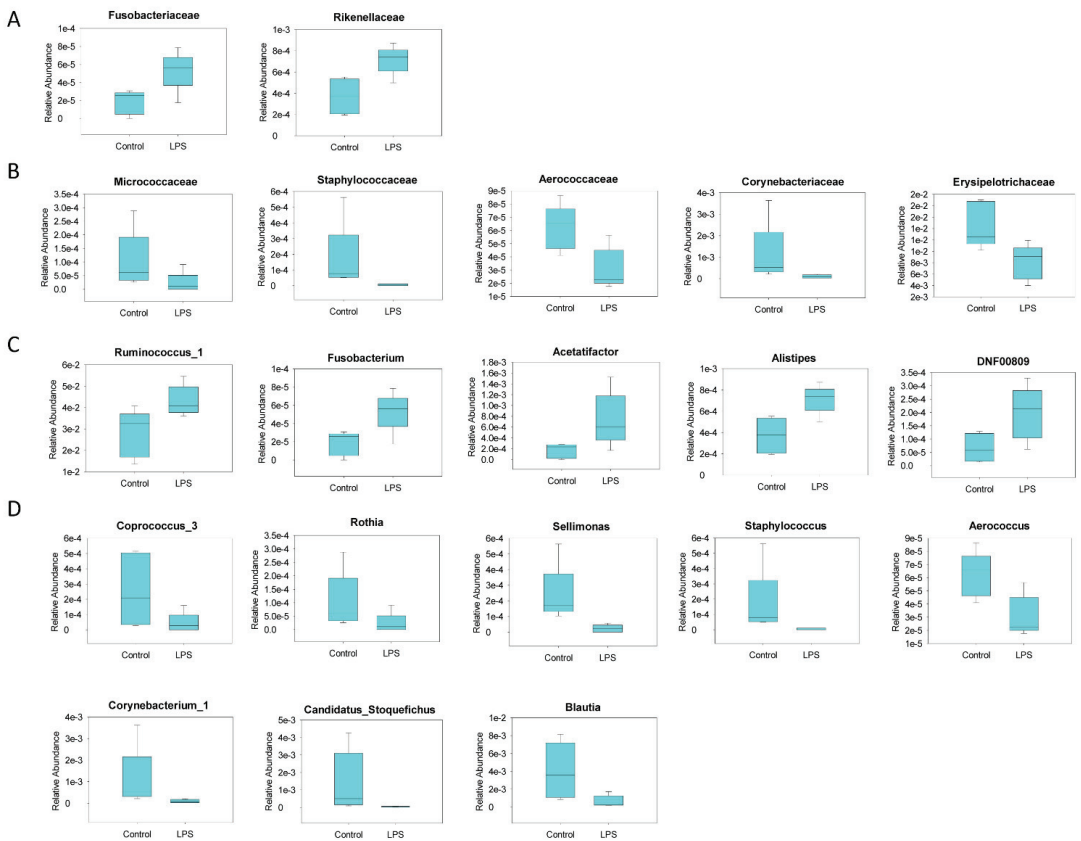


Figure 4. Fecal microbiota at the family and genus levels with significant changes in abundance in maternal immune activation (MIA) offspring. A significant (A) increase and (B) decrease in bacteria at the family level in MIA offspring (lipopolysaccharide (LPS)) compared with control rats. Similarly, significant increase (C) and decrease (D) in bacteria at the genus level were observed in MIA offspring (LPS) compared with control rats. $n = 5$ per group. All data had LDA scores ≥ 2 . Relative abundance indicates number of reads of targeted microbes per sample/total number of reads per sample.

3.3. Association of Fecal Microbiome Profile with Social Behavior and Anxiety-Like and Repetitive Behavior in MIA Male Offspring

The increased abundance of *Alistipes*, *Fusobacterium*, and *Ruminococcus* and decreased abundance of *Coprococcus* [25–27], *Erysipelotrichaceae*, and *Actinobacteria* in LPS-induced MIA offspring were consistent with that of humans with ASD [28–30]. Next, we determined the association of ASD-related microbiota (increased or decreased amount of microbiota in the LPS group) with the level of the social behavior deficit and with anxiety-like and repetitive behavior by using the LASSO method. The LASSO procedure offers extensive capabilities to build a model that can determine the coefficient progression of selected microbiota with the profile of the indicated phenotypes (social behavior time and the percentage of buried marbles). The AIC method was applied to determine which microbiota profile was the best fit for the model that could reflect the profile of social behavior time and anxiety-like and repetitive behavior. Figure 5A indicates that the AIC values of *Alistipes* and phylum *Actinobacteria* were the smallest in terms of the information loss; thus, the abundance of *Alistipes* and phylum *Actinobacteria* had a higher association level with the profile of defective social behavior than the other microbiota, and *Fusobacterium* and *Coprococcus* had a higher association level with the profile of buried marble percentage based on AIC (Figure 5B).

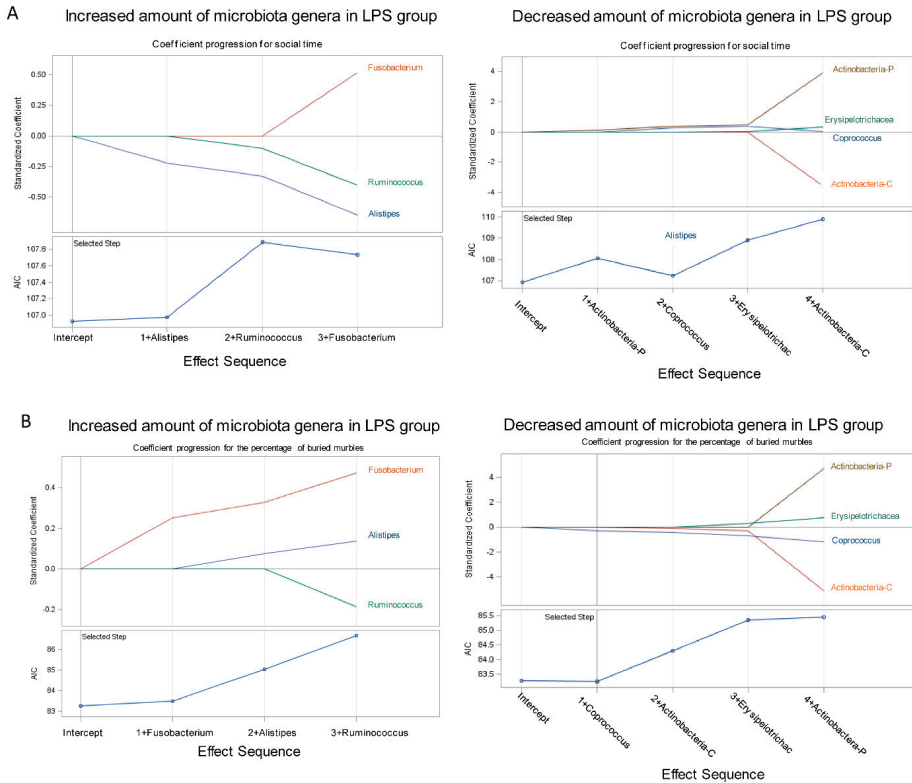


Figure 5. Feature importance of bacterial species for social behavior deficit and anxiety-like and repetitive behavior. (A) Standardized coefficients of the effects selected (the increased or decreased amount of microbiota genera in the lipopolysaccharide (LPS) group) with social time or (B) the percentage of buried marble at a given step of the stepwise method are plotted as a function of the step number. The coefficients plot displays the values of the estimates for each model at each iteration step. The effect was added into the model in an order of its relative importance measured with AIC. The plot labels the added effects at each step. The vertical axis of plot shows standardized estimates that can track the change of AIC for each successive model. Each colored line visualizes the evolution of values for a particular effect. The AIC plots show the relative importance of the effects selected (microbiota species) at steps of the selection process when effects entered the model. Actinobacteria-P indicates the relative amount of phylum *Actinobacteria*. Actinobacteria-C indicates the relative amount of class *Actinobacteria*.

3.4. Maternal LPS Stimulation Causes Hypomyelination in the Prefrontal Cortex and Thalamus Nucleus in MIA Male Offspring

Prenatal LPS stimulation at gestation days 15 and 16 causes abnormal myelination in the cortical and limbic brain regions in offspring [31]. In our study, prenatal LPS stimulation at gestation day 9.5 resulted in a significantly decreased MBP⁺ area in the prefrontal cortex (Figure 6A) and thalamic nucleus (Figure 6B) of the male MIA offspring (LPS group) than in control offspring by immunohistochemistry staining. In other words, maternal LPS stimulation caused hypomyelination in the prefrontal cortex and thalamic nucleus of adult male offspring.

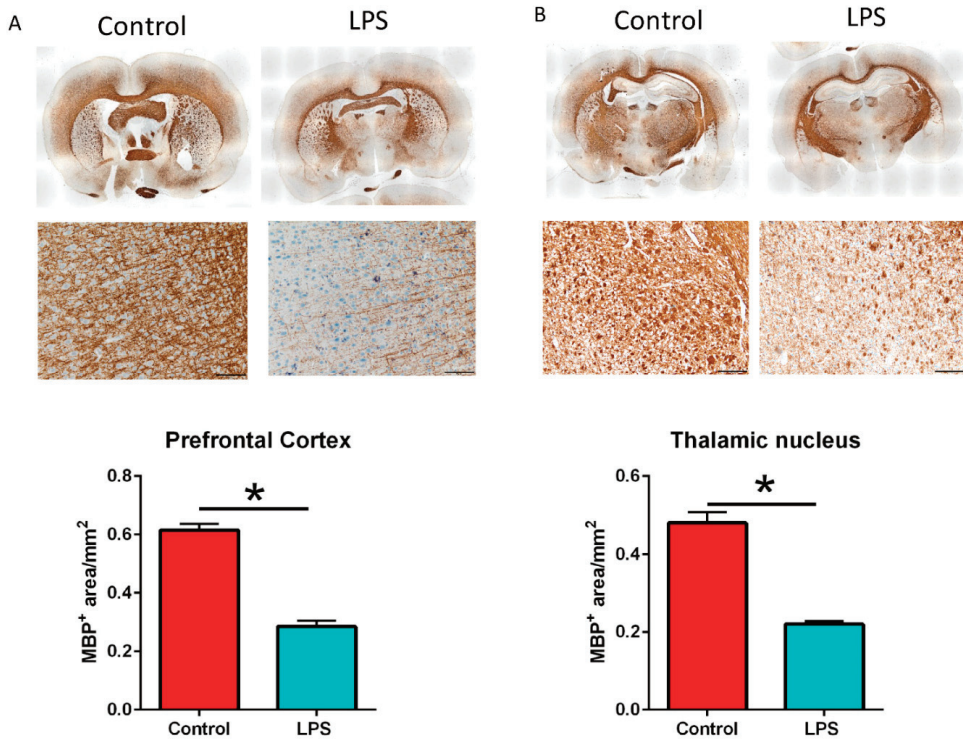


Figure 6. Myelin basic protein (MBP) expression level in the prefrontal cortex and thalamic nucleus in maternal immune activation (MIA) male offspring. (A) The MBP expression level in the prefrontal cortex and (B) thalamic nucleus of control and MIA offspring (lipopolysaccharide—(LPS) group) was detected with immunohistochemistry staining. The MBP expression level in whole brain slices are shown in the upper pictures. The MBP expression level in prefrontal cortex and thalamic nucleus are shown in the lower pictures. The quantification of the MBP⁺ area in the prefrontal cortex and thalamic nucleus is shown in the bar graph. * $p < 0.05$ ($n = 4$ per group). All data are presented as mean \pm SEM. Scale bar, 100 μ m.

Table 1. Phylum-level microbiome composition in the feces of control and maternal immune activation male offspring. The relative abundance of microbiomes in phylum level from the feces of control and LPS MIA offspring were obtained from 16S rRNA gene sequencing data. The significant difference of group was statistically calculated by U-test. SD: standard deviation.

Phylum	Control		LPS		U-Test
	Mean	SD	Mean	SD	
Actinobacteria	1.7×10^{-3}	1.3×10^{-3}	8×10^{-4}	1.0×10^{-4}	0.01
Bacteroidetes	5.8×10^{-1}	4.0×10^{-2}	6×10^{-1}	1.0×10^{-2}	0.2
Deferribacteres	2.0×10^{-4}	2.0×10^{-4}	4×10^{-4}	1.0×10^{-4}	0.2
Firmicutes	3.8×10^{-1}	3.4×10^{-2}	3.6×10^{-1}	1.0×10^{-2}	0.149
Fusobacteria	1.8×10^{-5}	1.3×10^{-5}	5.3×10^{-5}	2.2×10^{-5}	0.03
Patescibacteria	4.4×10^{-3}	4.8×10^{-3}	5.7×10^{-3}	3.7×10^{-3}	0.037
Proteobacteria	1.1×10^{-2}	3.7×10^{-3}	8.2×10^{-3}	4.4×10^{-3}	0.105
Tenericutes	8.0×10^{-4}	1.8×10^{-3}	4.2×10^{-3}	9.5×10^{-3}	0.416
Verrucomicrobia	5.2×10^{-3}	1.1×10^{-2}	6.7×10^{-6}	1.0×10^{-5}	0.086

4. Discussion

MIA causes an altered brain–gut–microbiota profile in male offspring, with autism-like phenotypes. In this study, we demonstrated that prenatal LPS stimulation caused altered social behavior and anxiety-like and repetitive behavior in male offspring, as revealed by our three-chamber test and marble-burying test, respectively. The NOR test and open-field assay demonstrated that MIA male offspring had a behavior profile similar to that of control offspring, indicating normal recognition memory and locomotor activity. MIA-induced hypomyelination in the prefrontal cortex and thalamic nucleus and altered microbiota profile provided evidence to show that LPS stimulation in the gestation stage causes altered brain–gut–microbiota axis phenotypes in offspring.

Patients with ASD have alterations in the gut microbiota composition compared with individuals without ASD [7,9]. In the present study, the gut microbiota diversity in male MIA offspring with ASD phenotypes was similar to the fecal microbiota profiles of children with ASD, such as a significant increase in *Ruminococcus*, *Fusobacterium*, and *Alistipes* [25–27]. We also observed a significant reduction in *Coprococcus*, *Erysipelotrichaies*, and *Actinobacteria*, which is consistent with the results of previous studies [28–30]. Compared with children without ASD, multiple microbiota species are elevated or reduced in children with ASD who have complex neurodevelopmental disorders involving disruptions in language and social behavior, restricted interests, and repetitive behaviors [9]. Microbiota transfer therapies have reported an improvement in ASD behavioral symptoms [32,33], suggesting that correcting the altered microbiota profile is a promising treatment strategy for ASD. Among the various changed microbiota species in MIA offspring, we demonstrated that the abundance of *Alistipes* and *Actinobacteria* was associated with the profile of social behavior, and *Fusobacterium* and *Coprococcus* was associated with the profile of anxiety-like and repetitive behavior; this suggests that *Alistipes*, *Actinobacteria*, *Fusobacterium*, and *Coprococcus* may be microbiome biomarkers or treatment targets for ASD.

MIA animal models are unique experimental tools for overcoming the limitations of epidemiological studies, such as the longitudinal evaluation of neurobiological processes from gestation to adulthood. Maternal exposure to LPS induces hypomyelination in the internal capsule and in newborn rats [34]. Maternal valproic acid stimulation causes hypomyelination of the prefrontal cortex and has been associated with social behavior deficit [35]. Poly I:C-induced MIA stimulation also causes a disruption in the myelin structure and a weakened thalamocortical connection in offspring [36]. In the present study, prenatal LPS-induced MIA caused the following changes in adult offspring: social behavior deficit, anxiety-like and repetitive behavior, ASD-related microbiota, and hypomyelination in the prefrontal cortex and thalamic nucleus. Prenatal LPS stimulation causes the inflammatory responses in brain of MIA offspring. The elevated levels of inflammatory cytokine (TNF- α and IL-1 β) in the gestational stage are associated with behavioral impairment and hypomyelination [34,37]. The activation of an inflammatory reaction, including pro-inflammatory and anti-inflammatory cytokines, is associated with ASD [38–41]. In addition, poly I:C-induced MIA increases TNF- α and IL-1 β expression in the colon of MIA offspring with an altered microbiota profile [42]. These results suggest that maternal LPS stimulation might impart an inflammatory reaction that is associated with an altered brain–gut–microbiota axis. Together, these findings suggest that MIA stress alters the brain–gut–microbiota axis leading to an inflammatory reaction, defective myelination and abnormal microbiota in offspring in ASD-related behavior deficits.

The most commonly used MIA animal models are prenatal poly I:C and LPS stimulation in pregnant animals. Poly I:C is a synthetic analogue of the viral double-strand RNA which activates Toll-like receptors (TLR)-3, whereas LPS is an endotoxin from Gram-negative bacteria which activates TLR-4 [43]. Prenatal poly I:C stimulation can alter the MIA microbiota profile in MIA offspring with a behavior impairment [29,42,44,45]. However, the link of an altered microbiota and social behavior impairment remains unclear in the LPS-induced MIA animal model. A previous study demonstrated several different effects of poly I:C and LPS prenatal stimulation on the behavior, development, and

inflammatory response in pregnant mice and their offspring [46]. For example, prenatal LPS stimulation caused a decrease in the astrocytic marker (GFAP) and neuronal marker (NeuN) expression level in offspring at GD18, whereas GFAP and NeuN expression levels were not altered in the poly I:C-induced MIA model [46]. In addition, plasma cytokine IL-2, IL-5, IL-6, and inflammatory marker mGluR5 were significantly increased in the brain of poly I:C-induced MIA offspring, but not in LPS-induced MIA offspring [46]. In this study, we found that human ASD-related *Ruminococcus* are increased in the LPS-induced MIA model, whereas *Ruminococcus* are decreased in the poly I:C-induced MIA model [29]. Taken together, different prenatal stimulation sources (virus or bacteria) may induce a differential profile of brain cell markers and microbiota profile in MIA offspring.

The prevalence of ASD is higher in males, with an approximate male-to-female ratio of 3:1 [47]. In this study, our MIA female offspring had normal social behavior when compared to the control group. In addition, sex may affect the microbiota profile [48]. For example, *Coprococcus* was less present in the microbiota profile of male mice compared to female mice [49]. These data were consistent to our study, revealing a decreased number of *Coprococcus* in the microbiota profile of male rats compared to female rats (data not shown). A human study showed that healthy males possess higher levels of *Fusobacterium* than females [50]. In an ASD predominantly male cohort study (18 males and 2 females), ASD children had decreased *Coprococcus* than the healthy subjects [28]. Another study showed that ASD patients with constipation (25 male and 5 female subjects) had increased *Fusobacterium* compared with healthy subjects [26]. Taken together, this evidence suggests that the differences in microbiota profiles between male and female subjects may be correlated to the altered microbiota profiles of ASD patients.

5. Conclusions

In the present study, LPS-induced MIA offspring displayed altered brain–gut–microbiota axis phenotypes, including social behavior deficits, anxiety-like and repetitive behavior, a human ASD-like microbiota profile (higher abundance of *Alistipes*, *Fusobacterium*, and *Ruminococcus* and a lower abundance of *Coprococcus*, *Erysipelotrichaies*, and *Actinobacteria* than control offspring), and hypomyelination in the prefrontal cortex and thalamic nucleus. An abundance of *Alistipes* and *Actinobacteria* was the most relevant for the profile of defective social behavior, whereas the abundance of *Fusobacterium* and *Coprococcus* was associated with anxiety-like and repetitive behavior. These potential ASD-related microbiomes require further studies to prove their direct association to ASD-related behavior, such as fecal transplantation or target microbiome transplantation therapy. The relative mechanisms of ASD etiopathogenesis still remain unknown and further studies are needed to prove the cause–effect relations between microbiome dysbiosis and ASD. Our findings provide insights into the relationship between maternal infection and the etiopathogenesis of ASD with an abnormal brain–gut–microbiota axis.

Author Contributions: Conceptualization, G.A.L. and S.-H.T.; methodology, G.A.L. and Y.-K.L.; software, G.A.L.; validation, G.A.L.; formal analysis, Y.-K.L. and Y.-C.S.H.Y.; investigation, S.-Y.Y., J.-H.L. and Y.-C.L.; resources, S.-Y.Y., C.-J.L., C.-C.W. and Y.-H.C.; data curation, G.A.L.; writing—original draft preparation, G.A.L.; writing—review and editing, G.A.L.; visualization, G.A.L.; supervision, S.-H.T.; project administration, S.-H.T.; funding acquisition, S.-H.T. All authors have read and agreed to the published version of the manuscript.

Funding: This research was funded by the Taipei Medical University (grant number TMU A00000952) and the Taipei Medical University Hospital (grant number 110TMU-TMUH-09).

Institutional Review Board Statement: All animal procedures were approved by the Animal Care and Use Committees of Taipei Medical University (LAC-2019-0109).

Data Availability Statement: The datasets used and/or analyzed during the current study are available from the corresponding author on reasonable request.

Acknowledgments: This manuscript was edited by Wallace Academic Editing. We would like to acknowledge the support provided by the Core Laboratory of Human Microbiome, Taipei Medical University.

Conflicts of Interest: The authors declare no conflict of interest.

References

1. Atladottir, H.O.; Thorsen, P.; Ostergaard, L.; Schendel, D.E.; Lemcke, S.; Abdallah, M.; Parner, E.T. Maternal infection requiring hospitalization during pregnancy and autism spectrum disorders. *J. Autism Dev. Disord.* **2010**, *40*, 1423–1430. [CrossRef]
2. Ciaranello, A.L.; Ciaranello, R.D. The neurobiology of infantile autism. *Annu. Rev. Neurosci.* **1995**, *18*, 101–128. [CrossRef] [PubMed]
3. Careaga, M.; Murai, T.; Bauman, M.D. Maternal Immune Activation and Autism Spectrum Disorder: From Rodents to Nonhuman and Human Primates. *Biol. Psychiatry* **2017**, *81*, 391–401. [CrossRef] [PubMed]
4. Dahlgren, J.; Samuelsson, A.M.; Jansson, T.; Holmang, A. Interleukin-6 in the maternal circulation reaches the rat fetus in mid-gestation. *Pediatr. Res.* **2006**, *60*, 147–151. [CrossRef]
5. Boksa, P. Effects of prenatal infection on brain development and behavior: A review of findings from animal models. *Brain Behav. Immun.* **2010**, *24*, 881–897. [CrossRef]
6. Qiu, Z.; Sweeney, D.D.; Netzeband, J.G.; Gruol, D.L. Chronic interleukin-6 alters NMDA receptor-mediated membrane responses and enhances neurotoxicity in developing CNS neurons. *J. Neurosci.* **1998**, *18*, 10445–10456. [CrossRef]
7. Vuong, H.E.; Hsiao, E.Y. Emerging Roles for the Gut Microbiome in Autism Spectrum Disorder. *Biol. Psychiatry* **2017**, *81*, 411–423. [CrossRef] [PubMed]
8. Conway, F.; Brown, A.S. Maternal Immune Activation and Related Factors in the Risk of Offspring Psychiatric Disorders. *Front. Psychiatry* **2019**, *10*, 430. [CrossRef]
9. Rosenfeld, C.S. Microbiome Disturbances and Autism Spectrum Disorders. *Drug Metab. Dispos.* **2015**, *43*, 1557–1571. [CrossRef]
10. Golan, H.M.; Lev, V.; Hallak, M.; Sorokin, Y.; Huleihel, M. Specific neurodevelopmental damage in mice offspring following maternal inflammation during pregnancy. *Neuropharmacology* **2005**, *48*, 903–917. [CrossRef] [PubMed]
11. Jonakait, G.M. The effects of maternal inflammation on neuronal development: Possible mechanisms. *Int. J. Dev. Neurosci.* **2007**, *25*, 415–425. [CrossRef]
12. Kirsten, T.B.; Taricano, M.; Maiorka, P.C.; Palermo-Neto, J.; Bernardi, M.M. Prenatal lipopolysaccharide reduces social behavior in male offspring. *Neuroimmunomodulation* **2010**, *17*, 240–251. [CrossRef] [PubMed]
13. Meyer, U.; Yee, B.K.; Feldon, J. The neurodevelopmental impact of prenatal infections at different times of pregnancy: The earlier the worse? *Neuroscientist* **2007**, *13*, 241–256. [CrossRef] [PubMed]
14. Meyer, U.; Nyffeler, M.; Engler, A.; Urwyler, A.; Schedlowski, M.; Knuesel, I.; Yee, B.K.; Feldon, J. The time of prenatal immune challenge determines the specificity of inflammation-mediated brain and behavioral pathology. *J. Neurosci.* **2006**, *26*, 4752–4762. [CrossRef]
15. Wu, H.F.; Chen, P.S.; Hsu, Y.T.; Lee, C.W.; Wang, T.F.; Chen, Y.J.; Lin, H.C. D-Cycloserine Ameliorates Autism-Like Deficits by Removing GluA2-Containing AMPA Receptors in a Valproic Acid-Induced Rat Model. *Mol. Neurobiol.* **2018**, *55*, 4811–4824. [CrossRef]
16. Callahan, B.J.; McMurdie, P.J.; Rosen, M.J.; Han, A.W.; Johnson, A.J.; Holmes, S.P. DADA2: High-resolution sample inference from Illumina amplicon data. *Nat. Methods* **2016**, *13*, 581–583. [CrossRef] [PubMed]
17. Callahan, B.J.; Sankaran, K.; Fukuyama, J.A.; McMurdie, P.J.; Holmes, S.P. Bioconductor Workflow for Microbiome Data Analysis: From raw reads to community analyses. *F1000Research* **2016**, *5*, 1492. [CrossRef]
18. Quast, C.; Pruesse, E.; Yilmaz, P.; Gerken, J.; Schweer, T.; Yarza, P.; Peplies, J.; Glockner, F.O. The SILVA ribosomal RNA gene database project: Improved data processing and web-based tools. *Nucleic Acids Res.* **2013**, *41*, D590–D596. [CrossRef] [PubMed]
19. Schliep, K.P. phangorn: Phylogenetic analysis in R. *Bioinformatics* **2011**, *27*, 592–593. [CrossRef]
20. McMurdie, P.J.; Holmes, S. phyloseq: An R package for reproducible interactive analysis and graphics of microbiome census data. *PLoS ONE* **2013**, *8*, e61217. [CrossRef]
21. Chen, J.; Bittinger, K.; Charlson, E.S.; Hoffmann, C.; Lewis, J.; Wu, G.D.; Collman, R.G.; Bushman, F.D.; Li, H.Z. Associating microbiome composition with environmental covariates using generalized UniFrac distances. *Bioinformatics* **2012**, *28*, 2106–2113. [CrossRef]
22. Segata, N.; Izard, J.; Waldron, L.; Gevers, D.; Miropolsky, L.; Garrett, W.S.; Huttenhower, C. Metagenomic biomarker discovery and explanation. *Genome Biol.* **2011**, *12*, R60. [CrossRef] [PubMed]
23. Asnicar, F.; Weingart, G.; Tickle, T.L.; Huttenhower, C.; Segata, N. Compact graphical representation of phylogenetic data and metadata with GraPhlAn. *PeerJ* **2015**, *3*, e1029. [CrossRef] [PubMed]
24. Zierer, J.; Jackson, M.A.; Kastenmuller, G.; Mangino, M.; Long, T.; Telenti, A.; Mohny, R.P.; Small, K.S.; Bell, J.T.; Steves, C.J.; et al. The fecal metabolome as a functional readout of the gut microbiome. *Nat. Genet.* **2018**, *50*, 790–795. [CrossRef] [PubMed]
25. De Angelis, M.; Piccolo, M.; Vannini, L.; Siragusa, S.; De Giacomo, A.; Serrazanetti, D.I.; Cristofori, F.; Guerzoni, M.E.; Gobetti, M.; Francavilla, R. Fecal microbiota and metabolome of children with autism and pervasive developmental disorder not otherwise specified. *PLoS ONE* **2013**, *8*, e76993. [CrossRef]

26. Liu, S.; Li, E.; Sun, Z.; Fu, D.; Duan, G.; Jiang, M.; Yu, Y.; Mei, L.; Yang, P.; Tang, Y.; et al. Altered gut microbiota and short chain fatty acids in Chinese children with autism spectrum disorder. *Sci. Rep.* **2019**, *9*, 287. [CrossRef] [PubMed]
27. Wang, L.; Christophersen, C.T.; Sorich, M.J.; Gerber, J.P.; Angley, M.T.; Conlon, M.A. Increased abundance of *Sutterella* spp. and *Ruminococcus torques* in feces of children with autism spectrum disorder. *Mol. Autism* **2013**, *4*, 42. [CrossRef]
28. Krajmalnik-Brown, R.; Lozupone, C.; Kang, D.W.; Adams, J.B. Gut bacteria in children with autism spectrum disorders: Challenges and promise of studying how a complex community influences a complex disease. *Microb. Ecol. Health Dis.* **2015**, *26*, 26914. [CrossRef]
29. Hsiao, E.Y.; McBride, S.W.; Hsien, S.; Sharon, G.; Hyde, E.R.; McCue, T.; Codelli, J.A.; Chow, J.; Reisman, S.E.; Petrosino, J.F.; et al. Microbiota modulate behavioral and physiological abnormalities associated with neurodevelopmental disorders. *Cell* **2013**, *155*, 1451–1463. [CrossRef]
30. Finegold, S.M.; Dowd, S.E.; Gontcharova, V.; Liu, C.; Henley, K.E.; Wolcott, R.D.; Youn, E.; Summanen, P.H.; Granpeesheh, D.; Dixon, D.; et al. Pyrosequencing study of fecal microflora of autistic and control children. *Anaerobe* **2010**, *16*, 444–453. [CrossRef]
31. Wischhof, L.; Irrsack, E.; Osorio, C.; Koch, M. Prenatal LPS-exposure—A neurodevelopmental rat model of schizophrenia—differentially affects cognitive functions, myelination and parvalbumin expression in male and female offspring. *Prog. Neuropsychopharmacol. Biol. Psychiatry* **2015**, *57*, 17–30. [CrossRef]
32. Kang, D.W.; Adams, J.B.; Gregory, A.C.; Borody, T.; Chittick, L.; Fasano, A.; Khoruts, A.; Geis, E.; Maldonado, J.; McDonough-Means, S.; et al. Microbiota Transfer Therapy alters gut ecosystem and improves gastrointestinal and autism symptoms: An open-label study. *Microbiome* **2017**, *5*, 10. [CrossRef]
33. Abuaish, S.; Al-Otaibi, N.M.; Abujaamel, T.S.; Alzahrani, S.A.; Alotaibi, S.M.; AlShawakir, Y.A.; Aabed, K.; El-Ansary, A. Fecal Transplant and Bifidobacterium Treatments Modulate Gut Clostridium Bacteria and Rescue Social Impairment and Hippocampal BDNF Expression in a Rodent Model of Autism. *Brain Sci.* **2021**, *11*, 1038. [CrossRef]
34. Rousset, C.I.; Chalou, S.; Cantagrel, S.; Bodard, S.; Andres, C.; Gressens, P.; Saliba, E. Maternal exposure to LPS induces hypomyelination in the internal capsule and programmed cell death in the deep gray matter in newborn rats. *Pediatr. Res.* **2006**, *59*, 428–433. [CrossRef] [PubMed]
35. Graciarena, M.; Seiffe, A.; Nait-Oumesmar, B.; Depino, A.M. Hypomyelination and Oligodendroglial Alterations in a Mouse Model of Autism Spectrum Disorder. *Front. Cell. Neurosci.* **2018**, *12*, 517. [CrossRef] [PubMed]
36. Kreitz, S.; Zambon, A.; Ronovsky, M.; Budinsky, L.; Helbich, T.H.; Sideromenos, S.; Ivan, C.; Konerth, L.; Wank, I.; Berger, A.; et al. Maternal immune activation during pregnancy impacts on brain structure and function in the adult offspring. *Brain Behav. Immun.* **2020**, *83*, 56–67. [CrossRef] [PubMed]
37. Simoes, L.R.; Sangiogo, G.; Tashiro, M.H.; Generoso, J.S.; Faller, C.J.; Domingui, D.; Mastella, G.A.; Scaini, G.; Giridharan, V.V.; Michels, M.; et al. Maternal immune activation induced by lipopolysaccharide triggers immune response in pregnant mother and fetus, and induces behavioral impairment in adult rats. *J. Psychiatr. Res.* **2018**, *100*, 71–83. [CrossRef] [PubMed]
38. Tanaka, M.; Toth, F.; Polyak, H.; Szabo, A.; Mandi, Y.; Vecsei, L. Immune Influencers in Action: Metabolites and Enzymes of the Tryptophan-Kynurenine Metabolic Pathway. *Biomedicines* **2021**, *9*, 734. [CrossRef] [PubMed]
39. Masi, A.; Quintana, D.S.; Glozier, N.; Lloyd, A.R.; Hickie, I.B.; Guastella, A.J. Cytokine aberrations in autism spectrum disorder: A systematic review and meta-analysis. *Mol. Psychiatry* **2015**, *20*, 440–446. [CrossRef]
40. Saghazadeh, A.; Ataieina, B.; Keynejad, K.; Abdolalizadeh, A.; Hirbod-Mobarakeh, A.; Rezaei, N. A meta-analysis of pro-inflammatory cytokines in autism spectrum disorders: Effects of age, gender, and latitude. *J. Psychiatr. Res.* **2019**, *115*, 90–102. [CrossRef] [PubMed]
41. Molloy, C.A.; Morrow, A.L.; Meinzen-Derr, J.; Schleifer, K.; Dienger, K.; Manning-Courtney, P.; Altaye, M.; Wills-Karp, M. Elevated cytokine levels in children with autism spectrum disorder. *J. Neuroimmunol.* **2006**, *172*, 198–205. [CrossRef]
42. Li, W.; Chen, M.; Feng, X.; Song, M.; Shao, M.; Yang, Y.; Zhang, L.; Liu, Q.; Lv, L.; Su, X. Maternal immune activation alters adult behavior, intestinal integrity, gut microbiota and the gut inflammation. *Brain Behav.* **2021**, *11*, e02133. [CrossRef]
43. Maelfait, J.; Vercammen, E.; Janssens, S.; Schotte, P.; Haegman, M.; Magez, S.; Beyaert, R. Stimulation of Toll-like receptor 3 and 4 induces interleukin-1 β maturation by caspase-8. *J. Exp. Med.* **2008**, *205*, 1967–1973. [CrossRef] [PubMed]
44. Li, Y.; Dugyala, S.R.; Ptacek, T.S.; Gilmore, J.H.; Frohlich, F. Maternal Immune Activation Alters Adult Behavior, Gut Microbiome and Juvenile Brain Oscillations in Ferrets. *eNeuro* **2018**, *5*. [CrossRef]
45. Roussin, L.; Prince, N.; Perez-Pardo, P.; Kraneveld, A.D.; Rabot, S.; Naudon, L. Role of the Gut Microbiota in the Pathophysiology of Autism Spectrum Disorder: Clinical and Preclinical Evidence. *Microorganisms* **2020**, *8*, 1369. [CrossRef]
46. Arsenaault, D.; St-Amour, I.; Cisbani, G.; Rousseau, L.S.; Cicchetti, F. The different effects of LPS and poly I:C prenatal immune challenges on the behavior, development and inflammatory responses in pregnant mice and their offspring. *Brain Behav. Immun.* **2014**, *38*, 77–90. [CrossRef] [PubMed]
47. Loomes, R.; Hull, L.; Mandy, W.P.L. What Is the Male-to-Female Ratio in Autism Spectrum Disorder? A Systematic Review and Meta-Analysis. *J. Am. Acad. Child Adolesc. Psychiatry* **2017**, *56*, 466–474. [CrossRef] [PubMed]
48. Kim, Y.S.; Unno, T.; Kim, B.Y.; Park, M.S. Sex Differences in Gut Microbiota. *World J. Men's Health* **2020**, *38*, 48–60. [CrossRef] [PubMed]

49. Org, E.; Mehrabian, M.; Parks, B.W.; Shipkova, P.; Liu, X.; Drake, T.A.; Lusi, A.J. Sex differences and hormonal effects on gut microbiota composition in mice. *Gut Microbes* **2016**, *7*, 313–322. [CrossRef] [PubMed]
50. Takagi, T.; Naito, Y.; Inoue, R.; Kashiwagi, S.; Uchiyama, K.; Mizushima, K.; Tsuchiya, S.; Dohi, O.; Yoshida, N.; Kamada, K.; et al. Differences in gut microbiota associated with age, sex, and stool consistency in healthy Japanese subjects. *J. Gastroenterol.* **2019**, *54*, 53–63. [CrossRef] [PubMed]

Article

Fecal Transplant and *Bifidobacterium* Treatments Modulate Gut *Clostridium* Bacteria and Rescue Social Impairment and Hippocampal BDNF Expression in a Rodent Model of Autism

Sameera Abuaiash ^{1,†}, Norah M. Al-Otaibi ^{2,†}, Turki S. Abujamel ^{3,4}, Saleha Ahmad Alzahrani ²,
Sohailah Masoud Alotaibi ², Yasser A. AlShawakir ⁵, Kawther Aabed ^{2,*} and Afaf El-Ansary ⁶

- ¹ Department of Basic Sciences, College of Medicine, Princess Nourah Bint Abdulrahman University, P.O. Box 84428, Riyadh 11671, Saudi Arabia; syabuaiash@pnu.edu.sa
 - ² Department of Biology, College of Science, Princess Nourah Bint Abdulrahman University, P.O. Box 84428, Riyadh 11671, Saudi Arabia; noramajd22@gmail.com (N.M.A.-O.); salehah1416@gmail.com (S.A.A.); sohailah1997@gmail.com (S.M.A.)
 - ³ Vaccines and Immunotherapy Unit, King Fahd Medical Research Center, King Abdulaziz University, Jeddah 21589, Saudi Arabia; tabujamel@kau.edu.sa
 - ⁴ Department of Medical Laboratory Technology, Faculty of Applied Medical Sciences, King Abdulaziz University, Jeddah 21589, Saudi Arabia
 - ⁵ Prince Naif for Health Research Center, King Saud University, P.O. Box 7805, Riyadh 11472, Saudi Arabia; yalshawakir@ksu.edu.sa
 - ⁶ Central Laboratory, Female Center for Medical Studies and Scientific Section, King Saud University, P.O. Box 22452, Riyadh 11472, Saudi Arabia; elansary@ksu.edu.sa
- * Correspondence: kfated@pnu.edu.sa
† Authors contributed equally to this work.

Citation: Abuaiash, S.; Al-Otaibi, N.M.; Abujamel, T.S.; Alzahrani, S.A.; Alotaibi, S.M.; AlShawakir, Y.A.; Aabed, K.; El-Ansary, A. Fecal Transplant and *Bifidobacterium* Treatments Modulate Gut *Clostridium* Bacteria and Rescue Social Impairment and Hippocampal BDNF Expression in a Rodent Model of Autism. *Brain Sci.* **2021**, *11*, 1038. <https://doi.org/10.3390/brainsci11081038>

Academic Editors: Masaru Tanaka and Lydia Giménez-Llort

Received: 6 July 2021
Accepted: 4 August 2021
Published: 5 August 2021

Publisher's Note: MDPI stays neutral with regard to jurisdictional claims in published maps and institutional affiliations.



Copyright: © 2021 by the authors. Licensee MDPI, Basel, Switzerland. This article is an open access article distributed under the terms and conditions of the Creative Commons Attribution (CC BY) license (<https://creativecommons.org/licenses/by/4.0/>).

Abstract: Autism is associated with gastrointestinal dysfunction and gut microbiota dysbiosis, including an overall increase in *Clostridium*. Modulation of the gut microbiota is suggested to improve autistic symptoms. In this study, we explored the implementation of two different interventions that target the microbiota in a rodent model of autism and their effects on social behavior: the levels of different fecal *Clostridium* spp., and hippocampal transcript levels. Autism was induced in young Sprague Dawley male rats using oral gavage of propionic acid (PPA) for three days, while controls received saline. PPA-treated animals were divided to receive either saline, fecal transplant from healthy donor rats, or *Bifidobacterium* for 22 days, while controls continued to receive saline. We found that PPA attenuated social interaction in animals, which was rescued by the two interventions. PPA-treated animals had a significantly increased abundance of fecal *C. perfringens* with a concomitant decrease in *Clostridium* cluster IV, and exhibited high hippocampal *Bdnf* expression compared to controls. Fecal microbiota transplantation or *Bifidobacterium* treatment restored the balance of fecal *Clostridium* spp. and normalized the level of *Bdnf* expression. These findings highlight the involvement of the gut–brain axis in the etiology of autism and propose possible interventions in a preclinical model of autism.

Keywords: autism spectrum disorder; microbiota; propionic acid; *Clostridium perfringens*; *Clostridium* cluster IV; fecal transplant; *Bifidobacterium*; hippocampus; BDNF

1. Introduction

Autism spectrum disorder (ASD) is a complex neurodevelopmental disorder that disturbs brain development. The reported incidence of ASD has increased dramatically over the past decade to 1 in 54 births, with males having a higher prevalence than females with a ratio of 4:1 [1]. The etiological mechanisms of ASD remain unclear, although the heterogeneity between patient cohorts supports a complex interaction between environmental and genetic factors [2]. One factor that has received much attention in these past few years is gut microbiota dysbiosis as an underlying link to understanding ASD etiology.

Clinical data show an imbalance in the microbiota of autistic individuals compared to neurotypical ones. Studies suggest a significant imbalance between the *Bacteroidetes* and *Firmicutes* phyla in ASD [3–5]. For example, children with ASD exhibited less diverse microbiota with lower *Bifidobacterium* and *Firmicutes* and higher *Lactobacillus*, *Clostridium*, *Bacteroidetes*, *Desulfovibrio*, *Sarcina*, and *Caloramator* levels compared to children without ASD [3].

The *Clostridium* genus is a predominant cluster of gut microbiota and classified as anaerobic, Gram-positive, rod-shaped, and spore-forming bacteria. More recently, following the sequencing of 16S rRNA, the diversity between *Clostridium* spp. became more noteworthy, as more than 200 variants of *Clostridium* spp. were recognized. Depending on their species and strains, the *Clostridium* may exert many benefits or potential risks to the host's health [6]. For instance, *Clostridium* clusters XIVa and IV, which have a great potential acting as probiotics, were reduced in autistic children [7]. *Clostridium* clusters XIVa and IV play a key role in the normalization of germ-free (GF) mice gut microbiota [8]. Besides, cellular components of *Clostridium* cluster XIVa and IV and their metabolites (e.g., butyrate, secondary bile acids) can exert anti-inflammatory effects and increase gut immune tolerance [9,10]. On the other hand, autistic children with gastrointestinal symptoms had a significantly higher abundance of *Clostridium perfringens* [11,12]. Indeed, *C. perfringens* are virulent bacteria that simulate gastrointestinal dysfunction through the production of more than 20 toxins, as well as antimicrobial and drying-resistant spores [13].

The gut–brain axis consists of a communication network that includes the vagal nerve, microbial metabolites, gut hormones, and the endocrine and immune systems, which control the gut process and link it to the brain [14,15]. Illustrating the role of microbiota in the gut–brain axis has been demonstrated in GF mice. These mice revealed abnormalities in hippocampal gene expression and deficits in behavior that were more significant in male mice [16]. ASD-like symptoms in these mice ameliorated after restoring the gut microbial community [17]. In addition, behavior abnormality symptoms in GF mice were partially alleviated after fecal matter transplant and fully ameliorated by the ingestion of probiotics [18].

The production of short-chain fatty acids, such as propionic acid (PPA), by the gut *Clostridia* and *Desulfovibrio*, is suggested to play a role in developing ASD [19]. PPA is a by-product of the digestion of high carbohydrate foods by gut bacteria fermentation. In addition, PPA is used as a preservative in refined food products [19]. Interestingly, reports of increased severity of ASD symptoms were associated with the consumption of either food source, while eliminating these products was associated with improvement of symptoms [20,21]. In support of the suggested role of PPA in ASD etiology, PPA treatments, including subcutaneous, intragastric gavage, intraperitoneal, or intracerebroventricular, have induced autistic-like features in rodent models of ASD, including behavioral and physiological traits [22].

Abnormalities in the hippocampal structure and neurobiology have been observed in both autistic human and ASD animal models. For example, autistic individuals were reported to have reduced neuronal dendritic branching compared to non-autistic individuals [23]. Moreover, PPA treatment reduced the thickness of the granular layer of the dentate gyrus of the hippocampus, reduced the total number of synaptic vesicles, and induced dendritic spine loss in vitro [22,24,25]. Brain-derived neurotrophic factor (BDNF) is well known for its role in brain development and plasticity. Serum BDNF levels have been reported to be higher in autistic individuals [26]. BDNF levels in the brain of animal models of autism have shown unclear results ranging from no change, increase, or decrease [27–29]. Interestingly, BDNF transcript levels have been shown to be regulated by gut microbiota and short-chain fatty acids [30,31]. BDNF levels are also known to be regulated by methyl-CpG binding protein 2 (MeCP2). The MeCP2 gene is mutated in several neurodevelopmental disorders, including autism, and its protein is known to repress BDNF transcriptionally [32].

In this study, we evaluated social behavior impairment and the modulation of fecal *Clostridium* spp. levels, specifically *Clostridium* cluster XIVa and IV and *C. perfringens* in a rodent model of autism induced by oral PPA treatment. We also examined hippocampal *Bdnf* and *Mecp2* transcript levels along with solute carrier family 17, member 7 (*Slc17a7*) and glutamate decarboxylase 1 (*Gad1*) transcript levels as markers of glutamatergic and GABAergic neurons. Finally, we implemented an intervention treatment using either a fecal transplant or probiotic treatment of *Bifidobacterium*, which showed rescuing effects on social behavior, fecal *Clostridium* levels, and hippocampal *Bdnf* transcript levels in this PPA-induced animal model of autism. This study might highlight the benefits of modulating gut microbiota through different interventional modalities and its link to molecular neurobiology in the context of autism.

2. Materials and Methods

2.1. Animals

Twenty-eight Sprague Dawley male rats weighing 80–120 g and aged approximately 28 days old were acquired from in-house breeding from different litters from the Center for Laboratory Animals and Experimental Surgery at King Saud University (Riyadh, Saudi Arabia). Animals were housed in groups of 3–4 animals per cage at 21 ± 1 °C and exposed to 12:12 h light–dark cycle and had access to food and water ad libitum. The Ethics Committee approved all procedures for Animal Research of King Saud University, Riyadh (IRB No: KSU-SE-19-61) and the Research Ethics Committee of Princess Nourah bint Abdulrahman University, Riyadh (IRB No.19-0103).

2.2. Experimental Design

On the first day of testing, rats were designated to receive either 1 mL oral saline (control $n = 7$) or an oral dose of 250 mg/kg PPA ($n = 21$) dissolved in distilled water for three days [33]. Later, the PPA-treated animals were divided to receive either saline (PPA $n = 7$), fecal transplant (FT $n = 7$), or *Bifidobacteria* (BF $n = 7$) for 22 days. For the fecal transplant group, 1 g of pooled fecal samples from healthy donor rats was suspended in 10 mL of sterile phosphate-buffered saline (PBS, pH 7.4; Gibco™, Thermo Fisher Scientific Inc, Waltham, MA, USA) by vortexing. The homogenized solution was later filtered twice through a sterilized metal sieve. Fecal transplantation was performed by oral gavage of the fecal filtrate at a dose of 1 g/kg [34]. For the *Bifidobacteria* (BF)-treated group, powder from 1 capsule of *Bifidobacterium longum* BB536 (Bifido GI balance, Life Extension), which contains 2×10^9 colony forming units (CFU) per 25 mg, was dissolved in 1 mL sterile PBS. Animals were given 0.5 mL daily (1×10^9 CFU) by oral gavage [35]. The control animals continued to receive oral saline for 22 days. Freshly evacuated fecal pellets were collected weekly into sterile microtubes and stored at -80 °C until later assayed. After the last day of treatment, animals were handled daily for 2 min for a week. Behavioral testing was conducted, and a day later, animals were euthanized, and their brains were harvested and dissected (Figure 1).

2.3. Social Behavior

Social behavior was assessed using the three-chamber social test, a commonly used test to evaluate social impairments in animal models of autism [36,37]. An 80 cm \times 40 cm \times 40 cm clear rectangular plexiglass box that was divided into three chambers with walls with 15 cm \times 15 cm doors with removable sliders in order to allow the animals to pass through was used for the test. The three-chamber box was cleaned with 70% ethanol, dried with paper towels, and then let to air dry between trials. The animals were transferred to the testing room one hour before the test for acclimatization. Animals were picked from the cage and placed individually in the center chamber and were allowed to explore for 5 min while the two doorways of the box were closed. Following this habituation period, both doors were opened immediately, and a novel same-sex conspecific rat with similar body weight was placed in one of the two perforated holding containers that were

located on either side of the box. The subject rat was allowed to explore all three chambers freely for 10 min. The conspecific rat position was alternated between animals to avoid side preference. The test was recorded using an HD camcorder (Legria, Canon, Tokyo, Japan). Videos were later analyzed to code behaviors using BORIS 7.9.16 software [38] with examiners who were blind to animal treatments. Time of social interaction, which was defined by the orientation towards and investigation of the cup holding the conspecific animal by the focal animal through sniffing or rearing against it, was obtained. Moreover, time spent in each chamber was analyzed, and the percent of time spent in the social chamber (containing the conspecific rat) relative to the non-social chamber (containing the empty holding container) and the center chamber was calculated. Time spent immobile (bouts of no movements) was also recorded.

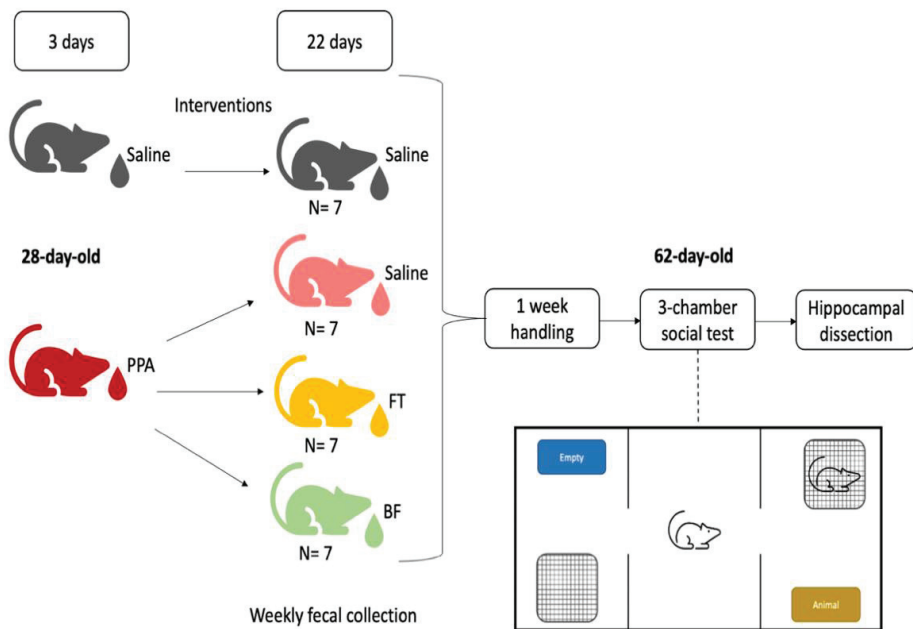


Figure 1. Study experimental design. Animals either received propionic acid (PPA) or saline for three days, after which PPA animals were treated with either saline, fecal transplant (FT), or Bifidobacterium (BF) for 22 days. Later, animals were evaluated for sociability using the 3-chamber social test and sacrificed a day later, their brains collected, and the hippocampi dissected out.

2.4. DNA Extraction and Microbial Quantitative Real-Time PCR

Metagenomic DNA was extracted from day 11 and day 22 fecal samples ($n = 5/\text{group}$) using the QIAamp DNA soil Kit (Qiagen, Hilden, Germany) according to the manufacturer's instructions. The final DNA concentration and purity were quantified by a spectrophotometer (Nanodrop, Thermo Fisher Scientific Inc., Waltham, MA, USA) and samples were stored at $-20\text{ }^{\circ}\text{C}$ until further use. Quantification of microbiota was carried out by qPCR using 7500 Real-Time PCR System (Applied Biosystems, Thermo Fisher Scientific Inc., Waltham, MA, USA). Each PCR reaction was set up in a total volume of $25\text{ }\mu\text{L}$ per reaction using 50 ng of fecal DNA, which was added to a reaction mixture containing $1\text{ }\mu\text{M}$ of each primer and $2\times$ SYBR[®] master mix (Applied Biosystems). qPCR cycling conditions were performed according to the manufacturer's recommendation (Applied Biosystems). PCR reactions were performed in duplicate. Target gene ΔCt values were calculated against the Ct value of the universal bacterial 16S rRNA. The fold change of the three experimental

groups from the control saline group was calculated by computing $2^{-\Delta\Delta Ct}$. The primers used in the current study are listed in Table 1.

Table 1. List of primer sequences.

Gene	Forward Primer	Reverse Primer
Fecal Targets		
Universal Bacterial 16S rRNA [39]	5'-GTGSTGCAYGGYGTGTCGTC-3'	5'-ACGTCRTCCMCACCTTCCTC-3'
<i>Clostridium perfringens</i> [40]	5'-GGGGTTTCAACACCTCC-3'	5'-GCAAGGGATGTCAAGTGT-3'
<i>Clostridium</i> cluster IV [41]	5'-GACGCCGCGTGAAGGA-3'	5'-AGCCCCAGCCTTTCACATC-3'
<i>Clostridium</i> cluster XIVa [41]	5'-GACGCCGCGTGAAGGA-3'	5'-AGCCCCAGCCTTTCACATC-3'
Brain Targets		
<i>ActinB</i>	5'-TTTGAGACCTTCAACACCCC-3'	5'-CTGCTGCCTTCCTTGGATG-3'
18S rRNA	5'-ATGGTAGTCGCCGTGCCA-3'	5'-CTGCTGCCTTCCTTGGATG-3'
<i>Gapdh</i>	5'-ACATCAAATGGGGTGTATGCT-3'	5'-GTGGTTCACACCCATCACAA-3'
<i>Bdnf</i>	5'-AAAACCATAAAGGACGCGACTT-3'	5'-AAAGAGCAGAGGAGGCTCCAA-3'
<i>Mecp2</i>	5'-CAAACAGCGACGTTCCATCA-3'	5'-TGTTAAGCTTTCGCGTCCAA-3'
<i>Slc17a7</i>	5'-CCTTAGAACGGAGTCGGCTG-3'	5'-AAGATCCCGAAGCTGCCATA-3'
<i>Gad1</i>	5'-ACTGGCCTGAAGATCTGTG-3'	5'-CCGTTCTTAGCTGGAAGCAG-3'

2.5. Brain Collection and RNA Extraction

On the last day of the study, animals were euthanized by inhalation of an overdose of sevoflurane, and the animals were decapitated using a rodent guillotine. The brain was rapidly removed from the skull and placed on a cold metal dissecting plate placed onto ice. The brain was freshly dissected to collect hippocampal tissues from both hemispheres. Hippocampi were placed into 1.5 mL Eppendorf tubes, flash frozen on dry ice, and stored at $-80\text{ }^{\circ}\text{C}$.

Brain tissue was homogenized in lysis buffer by passing it through a 20-gauge needle attached to a sterilized plastic syringe at least ten times or until a homogeneous lysate was achieved. RNA was extracted using the Allprep DNA/RNA Micro Kit (Qiagen, Hilden, Germany) according to manufacturer's instructions. Quantification and purity of the RNA were assessed with a spectrophotometer (Genova nano, Jenway, Cole-Parmer Ltd., Staffordshire, UK). RNA (0.5 μg) was converted into cDNA using the High-Capacity cDNA Conversion Kit (Applied Biosystems, Thermo Fisher Scientific Inc., Waltham, MA, USA) according to manufacturer's instructions.

2.6. Hippocampal Gene Expression Analysis by Quantitative Real-Time Reverse Transcriptase-Polymerase Chain Reaction (qRT-PCR)

The expression patterns of 4 genes (*Bdnf*, *Mecp2*, *Slc17a7*, and *Gad1*) and three housekeeping genes (*ActinB*, *18S rRNA*, and *Gapdh*) were quantified ($n = 5/\text{group}$) and analyzed using QuantStudio 5 Real-Time PCR (Applied Biosystems) with HOT FIREPol SolisGreen qPCR Mix (Solis Biodyne, Tartu, Estonia). The reaction was set up following the manufacturing instructions. Samples were run in triplicates, and the average cycle threshold (Ct) values were calculated. Target gene ΔCt values were calculated using the geometric mean of the three housekeeping genes. The fold change of the three experimental groups from the control saline group was calculated by computing $2^{-\Delta\Delta Ct}$. Primers (Table 1) were designed according to GenBank sequence information at the National Center for Biotechnology Information (NCBI; www.ncbi.nlm.nih.gov).

2.7. Statistical Analysis

Prism version 9.1.1 was used for data analysis and visualization; the results were expressed as mean \pm SE. The data were checked for normality using the Shapiro–Wilk test. Two-way ANOVA followed by Fisher's least significant difference post hoc test was used to analyze data for interaction duration in the 3-chamber social test. One-way ANOVA

followed by Fisher's least significant difference post hoc test was used to analyze data for percent of time spent in the social chamber, fold change in *Clostridium perfringens* on day 11, fold change in *Clostridium* cluster IV, fold change in *Clostridium* cluster XIVa on day 22, and fold change in hippocampal gene expression. Kruskal–Wallis non-parametric test followed by uncorrected Dunn's test for multiple comparisons was used to analyze *Clostridium* cluster IV and *Clostridium* cluster XIVa data on day 11, and *Clostridium perfringens* on day 22.

3. Results

3.1. Social Behavior

The different treatments differentially affected the time spent interacting with the two holding containers ($F(3, 47) = 3.240, p = 0.03$; Figure 2A). Overall, animals spent more time interacting with the conspecific animal ($F(1, 47) = 10.67, p = 0.002$). Specifically, saline control animals spent significantly more time interacting with the conspecific animal than time spent with the empty holding container (Fisher's LSD: $p = 0.02$). On the other hand, PPA animals did not show a significant difference in time spent interacting with the conspecific animal and the empty holding container (Fisher's LSD: $p = 0.61$). PPA animals also spent significantly less time interacting with the conspecific animal than saline control animals (Fisher's LSD: $p = 0.01$). FT-treated animals did not show a significant difference between time spent interacting with the conspecific animal and the empty holding container (Fisher's LSD: $p = 0.14$). However, FT-treated animals showed a trend of more time spent interacting with the conspecific animal compared to PPA-treated animals (Fisher's LSD: $p = 0.06$). BF-treated animals spent significantly more time interacting with the conspecific animal compared to time spent with the empty holding container (Fisher's LSD: $p = 0.03$). Moreover, BF-treated animals spent significantly more time interacting with the conspecific animal than PPA-treated animals (Fisher's LSD: $p = 0.005$).

Similarly, the different treatments significantly affected the percentage of time spent in the social chamber relative to the other chambers ($F(3, 23) = 4.46, p = 0.01$; Figure 2B). Specifically, PPA treatment significantly reduced the percentage of time spent in the social chamber when compared to control saline animals (Fisher's LSD: $p = 0.005$). FT treatment increased the percentage of time spent in the social chamber compared to PPA treatment, but it did not reach statistical significance (Fisher's LSD: $p = 0.15$). On the other hand, BF treatment significantly increased the percentage of time spent in the social chamber compared to PPA treatment (Fisher's LSD: $p = 0.006$).

In addition, we found a main effect of treatment on time spent immobile (bouts of no movements) by animals ($F(3, 23) = 4.182, p = 0.02$; Figure 2C). Specifically, PPA treatment increased the immobility of animals compared to saline (Fisher's LSD: $p = 0.008$), which was rescued by the two interventions (FT: Fisher's LSD: $p = 0.04$; BF: Fisher's LSD: $p = 0.004$).

3.2. Fecal *Clostridium* Bacteria Levels

On day 11, the different treatments affected the levels of *Clostridium perfringens* ($F(3, 11) = 5.94, p = 0.01$; Figure 3A), with the PPA animals exhibiting higher levels compared to all groups (Fisher's LSD: control saline $p = 0.004$; FT $p = 0.009$; BF $p = 0.003$). *Clostridium* cluster IV levels (Figure 3B) were significantly different between the different treatment groups ($X^2(3) = 11, p = 0.01$), with PPA animals exhibiting significantly lower levels compared to the other groups (uncorrected Dunn's tests: control saline $p = 0.007$; FT $p = 0.02$; BF $p = 0.003$). *Clostridium* cluster XIVa levels (Figure 3B) were comparable among the different treatment groups ($X^2(3) = 3.17, p = 0.36$).

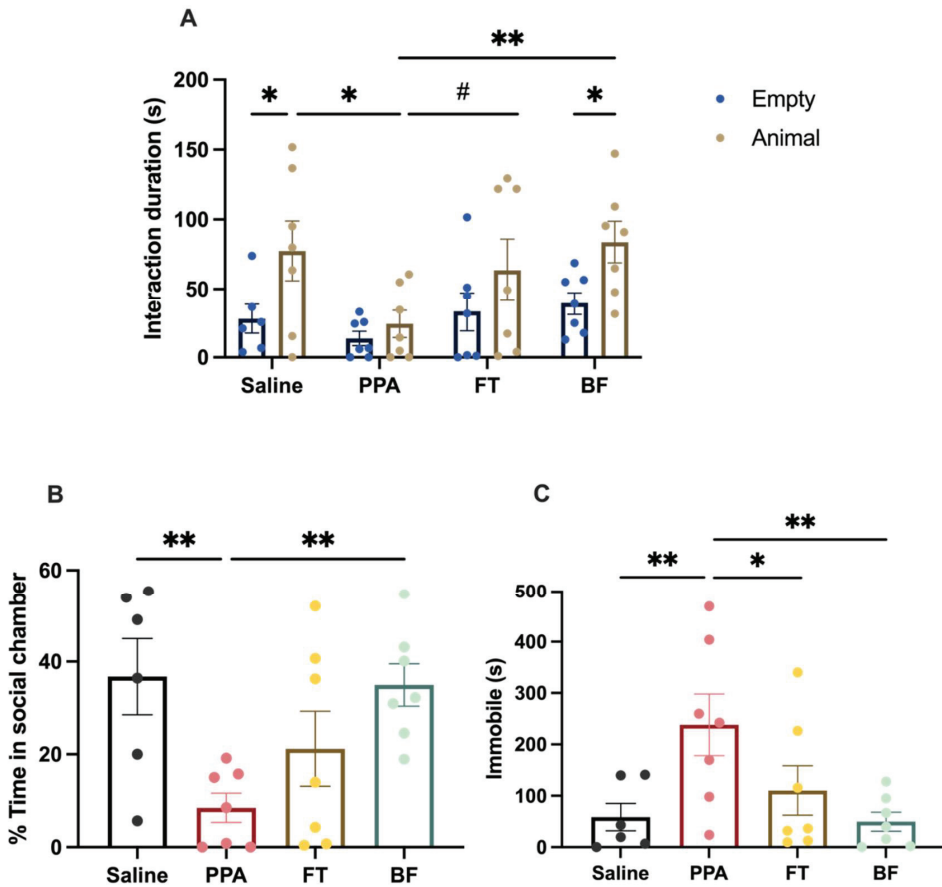


Figure 2. Social interaction in the three-chamber social test following saline ($n = 6$) and propionic acid (PPA) ($n = 7$) treatments, and fecal transplant (FT) ($n = 7$) and Bifidobacterium (BF) interventions ($n = 7$): (A) time spent by focal animals interacting with the conspecific animal and the empty holding box during the three-chamber social test; (B) percentage of time spent in the social chamber relative to other chambers; (C) time spent immobile during the test. Data presented are means \pm standard error. Significant two-way and one-way ANOVAs were followed by multiple comparisons by Fisher's least significance difference ** $p \leq 0.01$, * $p \leq 0.05$, # $p = 0.06$.

On day 22, only Clostridium cluster IV levels (Figure 3E) were significantly different between the different treatment groups ($F(3, 16) = 3.269$, $p = 0.05$). BF-treated animals had significantly lower Clostridium cluster IV levels than control saline (Fisher's LSD: $p = 0.03$) and PPA-treated animals (Fisher's LSD: $p = 0.01$). There were no differences in the levels of Clostridium perfringens (Figure 3D) and Clostridium cluster XIVa (Figure 3E).

The radar plot shows that, after 11 days of the different treatments, PPA-treated animals show a divergent pattern of levels of the three bacteria compared to the control and the FT and BF intervention treatments, which show comparable levels to the control animals (Figure 4A). On the last day of the treatments (day 22), the patterns of the levels of the three bacteria were similar (Figure 4B).

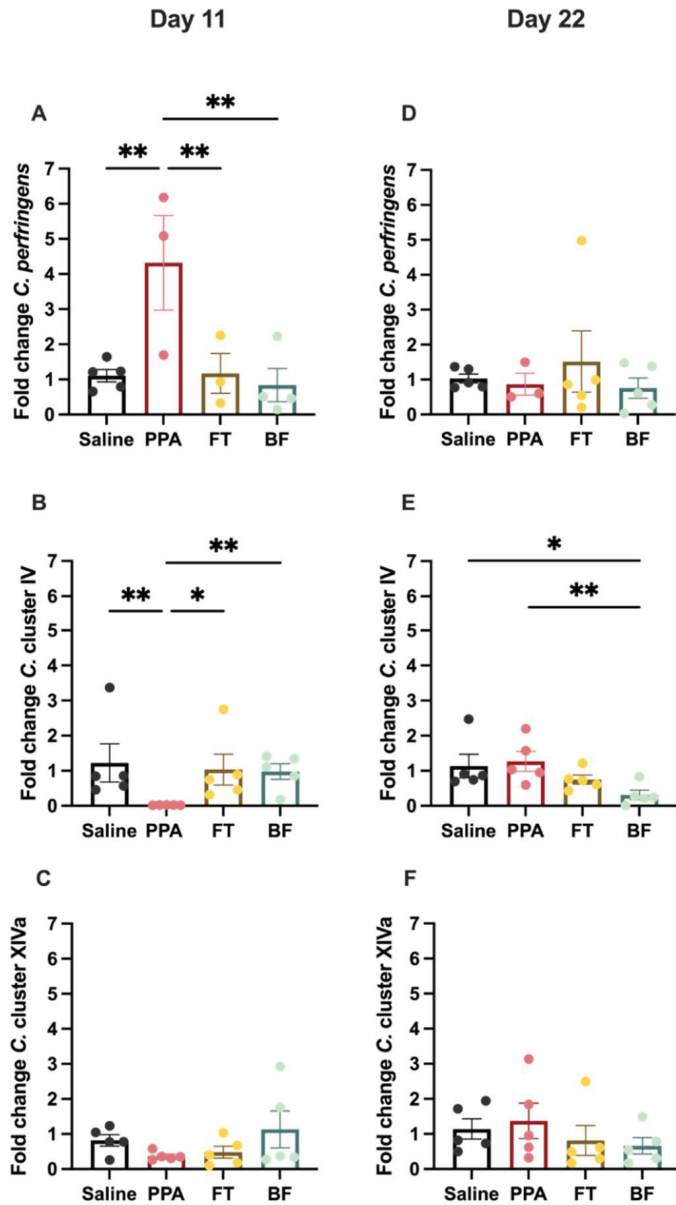


Figure 3. Levels of fecal *Clostridium* bacteria following saline ($n = 5$) and propionic acid (PPA) ($n = 3-5$) treatments, and fecal transplant (FT) ($n = 3-5$) and *Bifidobacterium* (BF) ($n = 4-5$) interventions at day 11 and at the last day of the intervention (day 22): (A) *Clostridium perfringens*; (B) *Clostridium* cluster IV; (C) *Clostridium* cluster XIVa at 11 days; (D) *Clostridium perfringens*; (E) *Clostridium* cluster IV; (F) *Clostridium* cluster XIVa at 22 days. Data presented are means \pm standard error of $2^{-\Delta\Delta C_t}$ values. Significant one-way ANOVA was followed by multiple comparisons by Fisher's least significance difference or Kruskal–Wallis followed by uncorrected Dunn's test. ** $p \leq 0.01$, * $p \leq 0.05$.

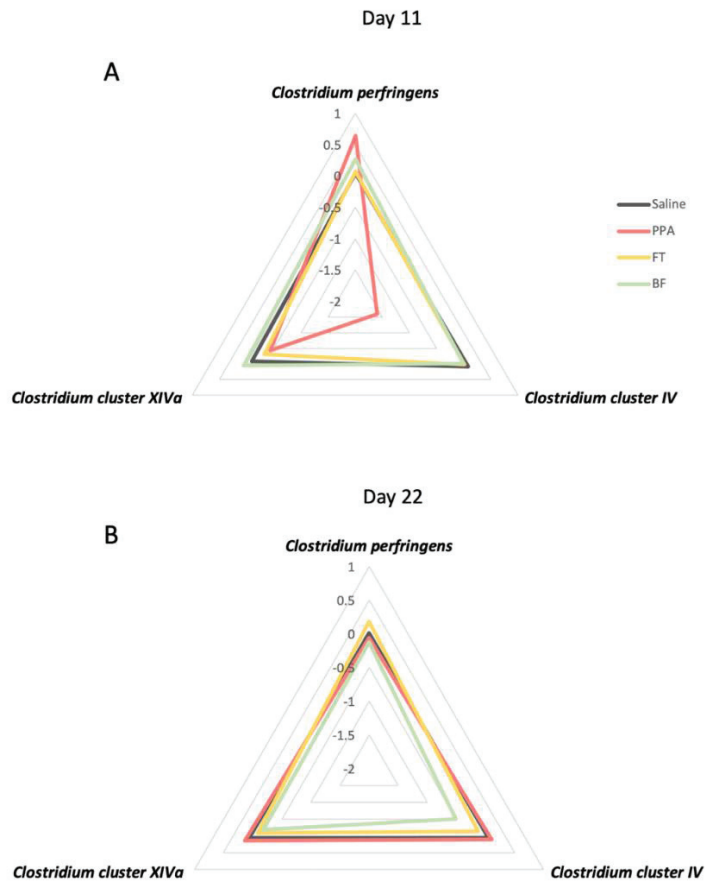


Figure 4. Radar plots of the patterns of fecal *Clostridium* bacteria levels following propionic acid (PPA) treatment and fecal transplant (FT) and *Bifidobacterium* (BF) interventions at day 11 and 22 of the intervention: (A) levels of *Clostridium perfringens*, *Clostridium* cluster IV, and *Clostridium* cluster XIVa at 11 days; (B) levels of *Clostridium perfringens*, *Clostridium* cluster IV, and *Clostridium* cluster XIVa at 22 days. Data presented as log-transformed means of $2^{-\Delta\Delta C_t}$ values.

3.3. Hippocampal Gene Expression

Transcript levels of hippocampal *Bdnf* (Figure 5A) were significantly different between the different treatment groups ($F(3, 16) = 4.14, p = 0.02$). PPA-treated animals exhibited significantly higher levels than the controls (Fisher's LSD $p = 0.008$) and FT-treated animals (Fisher's LSD: $p = 0.007$). PPA animals also showed a trend of an increase in *Bdnf* transcript levels compared to BF-treated animals (Fisher's LSD: $p = 0.07$). In addition, *Mecp2* transcript levels (Figure 5B) were different between the different treatment groups ($F(3, 16) = 4.14, p = 0.02$), with FT-treated animals exhibiting higher levels compared to all other groups (Fisher's LSD: saline $p = 0.01$; PPA $p = 0.03$; BF $p = 0.01$). Transcript levels of hippocampal *Slc17a7* (Figure 5C) showed a trend of differences among the different treatment groups ($F(3, 16) = 2.82, p = 0.07$). FT-treated animals exhibited higher transcript levels than all other groups (Fisher's LSD: saline $p = 0.03$; PPA $p = 0.06$; BF $p = 0.02$). *Gad1* transcript levels (Figure 5D) did not significantly differ among the different treatment groups ($F(3, 16) = 1.68, p = 0.21$).

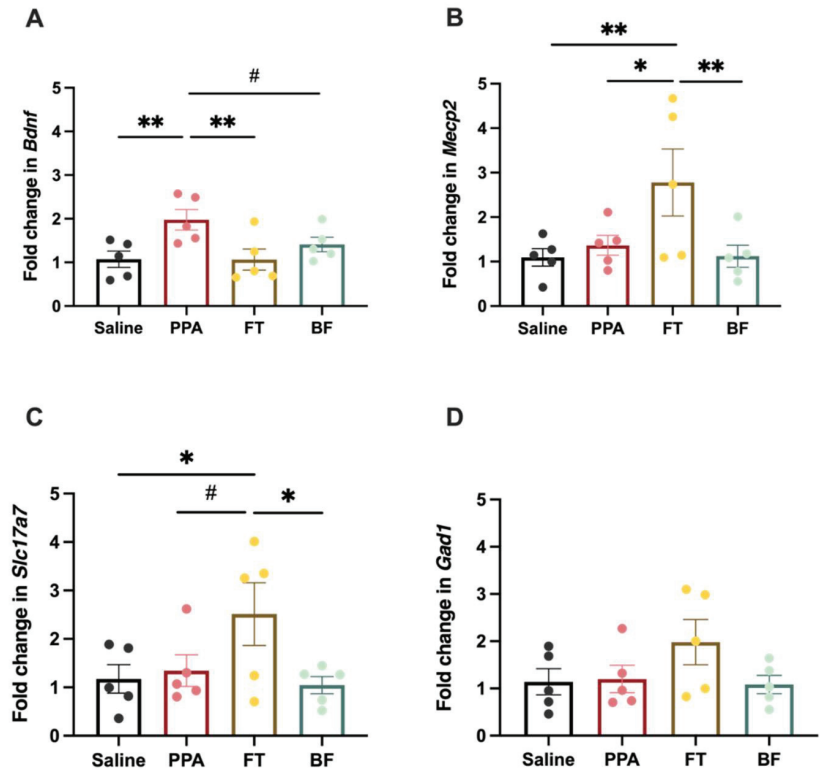


Figure 5. Fold change in hippocampal transcript levels following saline ($n = 5$) and propionic acid (PPA) ($n = 5$) treatments, and fecal transplant (FT) ($n = 5$) and *Bifidobacterium* (BF) ($n = 5$) interventions: (A) brain-derived neurotrophic factor (*Bdnf*); (B) methyl-CpG binding protein 2 (*Mecp2*); (C) solute carrier family 17, member 7 (*Slc17a7*); (D) glutamate decarboxylase 1 (*Gad1*). Data presented are means \pm standard error of $2^{-\Delta\Delta C_t}$ values. Significant one-way ANOVA was followed by multiple comparisons by Fisher's least significance difference ** $p \leq 0.01$, * $p \leq 0.05$, # $p = 0.06$.

4. Discussion

ASD is a neurodevelopmental disorder that shows an association with differential gut microbiota diversity and metabolites [3–5]. Consequently, there are several attempts of interventional treatments to modulate the gut microbiota in order to manage ASD symptoms [42]. In this study, we implemented an interventional paradigm using either fecal microbiota transplantation or probiotic treatment using *Bifidobacterium* in an animal model of autism induced by oral PPA treatment. We found that the implemented interventions successfully improved the social behavior impairment observed in PPA-treated animals. PPA treatment induced a transient increase and decrease in fecal levels of the harmful *Clostridium perfringens* and the probiotic acting *Clostridium* cluster IV, respectively. Finally, the PPA-treated animals exhibited significantly higher hippocampal *Bdnf* transcript levels that were normalized in the two intervention groups.

Given the strong evidence highlighting the link between neurological diseases and gastrointestinal health, including ASD, a number of interventional methods targeting the gut microbiota have been explored. These interventions include administering fecal transplants, probiotics, or prebiotics [42]. A fecal transplant, or fecal microbiota transplant, defined as administering a fecal solution containing microbiota from a healthy donor to a patient [43], has been reported to improve gastrointestinal and behavioral symptoms and increase gut bacterial abundance and diversity in autistic children [44]. *Bifidobacterium*

forms a significant fraction of the human microbiome and is significantly reduced in both autistic individuals and autistic children, while the supplementation of *B. longum* along with other probiotics was found to improve the severity of ASD and reduce gastrointestinal symptoms [45–47]. *B. longum* BB536 has been added to many dairy-based products, including infant formula, and is suggested to have multiple health benefits [48]. This study implemented both interventions for three weeks following PPA treatment in order to explore their possible benefit in restoring social behavior, fecal *Clostridium* spp. levels, and hippocampal transcript levels.

First, we evaluated the effects of PPA treatment on social behavior using the three-chamber social test, which utilizes the innate preference of rodents to interact with social stimuli over an inanimate object, and has been applied extensively to assess social impairment in rodent models of autism [36,37]. We found that PPA treatment induced a social behavior deficit, indicated by the loss of the preference to interact with a social stimulus (conspecific animal) (Figure 2A,B). These results indicate long-lasting (>4 weeks) effects of the initial 3-day treatment of PPA. This is in parallel with other studies using PPA treatment, which also report social impairment measured more than four weeks after the initial PPA treatment [22,49–51]. PPA animals also exhibited an increased immobility time compared to the control animals (Figure 2C), which might indicate an increased anxiety-like behavior, which is a behavioral feature of ASD models [27,49]. However, validated tests of anxiety need to be performed in future studies to better assess anxiety-like behavior in this model of autism.

Overall, the interventional treatments showed a rescue of the impaired social behavior that was observed in PPA-treated animals (Figure 2). Fecal transplant treatment post-autism-induction improved social behavior; however, the change in behavior did not reach significance. Others have also reported a non-significant trend of improvement of social behavior after fecal transplant treatment from healthy human donors in a maternal immune activation rodent model of autism [52]. It has been suggested that prolonged fecal transplant treatment could be required in order to achieve profound remission in some patients with inflammatory bowel disease [53]. Clinical studies reporting improved ASD symptoms after fecal transplant treatment have typically used a course of treatment that is 7–8 weeks or more [54–56]. On the other hand, *B. longum* treatment significantly improved the social behavior in PPA-treated animals. Multiple studies in humans and animal models have reported beneficial effects of *Bifidobacterium* administration on different behavioral outcomes, such as anxiety and depression [57–60]. There are limited studies examining the impact of *Bifidobacterium* treatment on social behavior. One study has found an increased interaction in mice with an aggressive mouse in a model of chronic social defeat stress after *Bifidobacterium* treatment [61]. Some evidence suggests that *Bifidobacterium* mediates its effects through vagal signaling [62]. Further, others have shown that *Bifidobacterium* administration might rescue behavioral deficits by increasing the synthesis of 5-hydroxytryptamine in vitro and serotonin in the brain [58]. Our interventional treatments show promising results in ameliorating social behavior impairments induced by PPA treatment.

Clostridium is the predominant cluster of commensal bacteria in human and animal intestines, with several species with a wide range of effects [63]. In the present study, after two weeks of the treatment administration, we found that the abundance of *C. perfringens* was significantly elevated in PPA-treated animals compared to the controls (Figure 3A). These findings align with many reports of detecting *C. perfringens* in autistic patients [11,12,64]. It has been previously confirmed that high detection rates of *C. perfringens* and toxins in autistic children are associated with gastrointestinal troubles [12]. Specifically, *C. perfringens* containing the beta-2 toxin gene are found significantly more frequently in autistic individuals compared to controls [11,12,64]. To our knowledge, no studies have examined the effects of the beta-2 toxin on the brain; however, another toxin produced by *C. perfringens* (epsilon) has been reported to induce neural injury in rats and can bind to glial cells and the myelin

sheaths of neurons [65–67]. More studies examining the effects of the beta-2 toxin on the brain could shed light on its relevance to ASD etiology.

We also found that PPA-treated rats showed a significant decrease in the abundance of *Clostridium* cluster IV compared to controls (Figure 3B). At the same time, there was no significant difference in the levels of *Clostridium* cluster XIVa (Figure 3C). In a previous study, cultured bacteria from fecal samples obtained from PPA-treated golden hamsters showed *Clostridia* growth, which was absent in the control animals [68]. In addition, treatment of these animals with a probiotic containing a mixture of bacteria, including *Bifidobacteria*, inhibited *Clostridia* growth. More recently, *Clostridium* cluster IV and XIVa reduction have been reported in autistic children [7]. *Clostridium* cluster IV accounts for 16–25% of the fecal microbiota and consists of essential members, including *C. leptum*, *Faecalibacterium prausnitzii* (*F. prausnitzii*), *C. sporosphaeroides*, and *C. cellulosi* [69–71]. The health benefits from *Clostridium* cluster IV are attributed to its anti-inflammatory action that inhibits nuclear factor-kappa B (NF- κ B) activation and IL-8 production [72]. In addition, these clusters are butyrate-producing bacteria, a short-chain fatty acid that is reportedly reduced in autistic individuals [73]. Butyrate plays a role in maintaining the integrity of the gut epithelial barrier by upregulating the expression of the tight junction-associated protein [74]. Moreover, sodium butyrate administration in an autistic rodent model improves social behavior [75].

These differential *Clostridia* levels observed in PPA-treated animals were only transiently observed after approximately two weeks of treatment and were not observed at the terminal time point of treatment (22 days). It appears that PPA-treated animals recovered this transient imbalance in the *Clostridia* levels by the end of the treatment course (Figures 3 and 4). At the first time point, animals in this study were aged around 42 days old and still considered juveniles [76], a developmental period mainly examined in the literature for autism-related microbiota differences [46,77,78]. At the last time point in this study, animals were aged around 52 days, a period in which animals reached sexual maturity and adolescence [76]. Studies have shown that the gut microbiota of rodents changes after puberty and that sex hormones mediate that change in the microbiota [79,80]. Although we did not find effects of PPA treatment at the later time point, we cannot exclude differential effects on other gut microorganisms. A future study will examine the microbiome in this model of autism.

We found that fecal transplant and *B. longum* treatments following PPA treatment were able to normalize *C. perfringens* and cluster IV levels at day 11 of treatment. On day 22, we found that *B. longum*-treated animals had significantly reduced levels of *C. cluster IV* compared to control animals and PPA-treated animals. Fecal transplantation has been used previously in autistic children and was found to increase the abundance of *Bifidobacterium*, *Prevotella*, and *Desulfovibrio* [54,55]. In addition, fecal transplantation has been successfully used to treat recurrent *C. difficile* infection [81], another pathogenic *Clostridium* spp. Our results show beneficial effects of fecal transplant in reducing the pathogenic *C. perfringens* abundance seen in PPA-treated animals. The effects of *Bifidobacterium* treatment in our study are supported by evidence indicating the suppression of *C. perfringens* in vivo and in vitro by *Bifidobacterium* [82,83]. Moreover, *B. longum* BB536 production of acetate during carbohydrate digestion was found to stimulate butyrate-producing bacteria in vitro [84], which could be a mechanism through which it increased *Clostridium* cluster IV abundance after PPA treatment in our study. Our findings highlight the importance of examining different species of *Clostridium* in the context of autism and how they respond to different interventions.

We finally examined the effects of PPA treatment on transcript expression of *Bdnf*, *Mecp2*, *Slc17a7*, and *Gad1* in the hippocampus. ASD affects the structure and function of several brain regions, including the hippocampus. Studies have reported a decreased dendritic complexity and thickness of the hippocampus in humans and animal models that could be related to behavioral abnormalities associated with ASD [22–25]. The hippocampus connection with the amygdala plays an important role in mediating social interactions as well [85]. We found that PPA treatment alone has significantly increased the expression of *Bdnf* in the hippocampus (Figure 5A). This increase was restored to control levels in

both intervention treatment groups (Figure 5A). Studies of animal models of autism have reported increased BDNF protein and mRNA levels in fetal brains [29,86]. In addition, several clinical studies have reported significantly higher levels of BDNF in the serum of autistic individuals [26]. However, others using the subcutaneous injection of PPA in rats have reported a significant reduction in the protein levels of BDNF in the hippocampus in juvenile animals [27]. Interestingly, a study using a transgenic model of autism (*Shank1* knock-out) reported an increase in *Bdnf* transcript levels in *Shank1* knock-out animals only after an object recognition task and not at baseline, and levels were negatively correlated with object recognition memory [87]. In this study, we have measured the transcript levels in animals after performing the social test during which animals are acquiring information about their environment and learning, which could have influenced the levels of the *Bdnf* transcript, unmasking differences that would not have been recorded at baseline. In addition, some reports indicate that BDNF is upregulated by NF- κ B, a primary protein in the neuroinflammatory cascade [88]. Neuroinflammation and enhanced NF- κ B levels is a feature that has been reported by many studies of autism [89]. Consequently, the increase in *Bdnf* transcript levels might act as a compensatory mechanism downstream of the neuroinflammation that has been reported previously in the PPA model of autism [19,22]. Our study is limited in just measuring transcript levels and not protein levels, especially given the differential function of the pro-BDNF form (precursor uncleaved BDNF) and the mature form of BDNF in neuronal function [90]. In fact, one study has reported an altered balance in the pro-BDNF/BDNF ratio in autistic human brains [90]. More studies should closely examine the role BDNF plays in the etiology of autism and the relevance of its increased levels in the serum to its function in the brain.

We did not observe any effects of PPA treatment on the other transcripts. However, the fecal transplant treatment has significantly increased the transcript levels of *Mecp2* and *Slc17a7* compared to all other groups (Figure 5B,C). Reduced MeCP2 levels have been found in the pre-frontal cortex of autistic individuals and animal models of autism [91,92], which we did not find in the hippocampus in our model. Fecal transplant treatment might have restored the levels of *Bdnf* transcript by increasing the MeCP2 levels. MeCP2 protein is a known transcriptional suppressor of BDNF [32]. There are no previous reports linking the fecal transplant to the modulation of MeCP2 levels. It is not clear the mechanism by which fecal transplant treatment induced this increase in MeCP2 levels. Examining differential microbiome metabolome in response to the fecal transplant in this model could shed light on possible factors contributing to this effect. The alteration in mice microbiome using GF and specific-pathogen-free mice has recently been reported to influence the expression of several genes involved in the neural excitation–inhibition balance, including *Bdnf* and *Slc17a7* in different brain regions [93]. Previous work has indicated increased glutamate and decreased GABA in the brains of PPA-treated animals [68,94], which is not replicated in this study by measuring *Slc17a7* and *Gad1* transcript levels as markers of the excitation–inhibition balance. The increase observed in *Slc17a7* by fecal transplant treatment without an increase in *Gad1* levels might suggest that there is increased excitatory signaling, which could explain the lack of full recovery of social impairment of this interventional treatment. Further examination of glutamate and GABA levels after fecal transplantation should be considered in order to fully understand its effects on the excitation–inhibition balance in the hippocampus in this model. Overall, our hippocampal transcript results implicate the alteration in *Bdnf* transcript levels in the neuropathology of autism induced by PPA administration, and its modulation by different microbiota-directed interventions, which is possibly associated with social behavioral improvement observed after the interventions.

5. Conclusions

This study explored the implementation of two interventional treatments, fecal transplantation and probiotic treatment using *Bifidobacterium*, that targeted the microbiota of an animal model of autism. We demonstrated that orally administering PPA, a short-chain fatty acid produced by gut microbiota and commonly elevated in autistic children, induced

social impairments in animals, which was normalized by the interventions. In addition, here, we examined the differential modulation of harmful and beneficial *Clostridium* spp. in response to PPA induction of autism, rather than examining the overall genus *Clostridium*, which is generally reported in the literature. The interventional treatments restored the imbalance observed in *C. perfringens* and cluster IV after PPA treatment. Finally, we report that the impairment in social behavior and imbalanced *clostridium* spp. induced by PPA treatment was associated with augmented *Bdnf* transcript levels in the hippocampus. The two interventional therapies were successful in reducing the abnormal increase in *Bdnf* levels in the hippocampus. These findings propose targeting the microbiota as a potential intervention in autism and provide possible underlying mechanisms of action in a preclinical model of autism.

Author Contributions: Conceptualization, S.A., T.S.A., K.A. and A.E.-A.; methodology, S.A., N.M.A.-O., T.S.A., K.A. and A.E.-A.; formal analysis, S.A.; investigation, S.A., N.M.A.-O., S.A.A., S.M.A. and Y.A.A.; data curation, S.A.; writing—original draft preparation, S.A., N.M.A.-O.; writing—review and editing, S.A., N.M.A.-O., T.S.A., K.A. and A.E.-A.; visualization, S.A.; supervision, K.A. and A.E.-A.; project administration, K.A.; funding acquisition, K.A. All authors have read and agreed to the published version of the manuscript.

Funding: This research project was funded by the Deanship of Scientific Research, Princess Nourah bint Abdulrahman University, through the Research Groups Program, Grant no. (RGP-1441-0027).

Institutional Review Board Statement: The study was conducted according to the guidelines of the Declaration of Helsinki, and approved by the Ethics Committee approved all procedures for Animal Research of King Saud University, Riyadh (IRB No: KSU-SE-19-61) and the Research Ethics Committee of Princess Nourah bint Abdulrahman University, Riyadh (IRB No.19-0103).

Data Availability Statement: The data presented in this study are available on request from the corresponding author.

Acknowledgments: We would like to thank the Health Sciences Research Centre (HSRC) for their technical support.

Conflicts of Interest: The authors declare no conflict of interest. The funders had no role in the design of the study; in the collection, analyses, or interpretation of data; in the writing of the manuscript, or in the decision to publish the results.

References

1. Maenner, M.J.; Shaw, K.A.; Baio, J.; Washington, A.; Patrick, M.; DiRienzo, M.; Christensen, D.L.; Wiggins, L.D.; Pettygrove, S.; Andrews, J.G.; et al. Prevalence of Autism Spectrum Disorder Among Children Aged 8 Years—Autism and Developmental Disabilities Monitoring Network, 11 Sites, United States, 2016. *MMWR Surveill. Summ.* **2020**, *69*, 1–12. [CrossRef] [PubMed]
2. Hallmayer, J.; Cleveland, S.; Torres, A.; Phillips, J.; Cohen, B.; Torigoe, T.; Miller, J.; Fedele, A.; Collins, J.; Smith, K.; et al. Genetic heritability and shared environmental factors among twin pairs with autism. *Arch. Gen. Psychiatry* **2011**, *68*, 1095–1102. [CrossRef] [PubMed]
3. De Angelis, M.; Piccolo, M.; Vannini, L.; Siragusa, S.; De Giacomo, A.; Serrazanetti, D.I.; Cristofori, F.; Guerzoni, M.E.; Gobetti, M.; Francavilla, R. Fecal Microbiota and Metabolome of Children with Autism and Pervasive Developmental Disorder Not Otherwise Specified. *PLoS ONE* **2013**, *8*, e76993. [CrossRef] [PubMed]
4. Finegold, S.M.; Downes, J.; Summanen, P.H. Microbiology of regressive autism. *Anaerobe* **2012**, *18*, 260–262. [CrossRef] [PubMed]
5. Adams, J.B.; Johansen, L.J.; Powell, L.D.; Quig, D.; Rubin, R.A. Gastrointestinal flora and gastrointestinal status in children with autism—comparisons to typical children and correlation with autism severity. *BMC Gastroenterol.* **2011**, *11*, 22. [CrossRef]
6. Madigan, M.T.; Bender, K.S.; Buckley, D.H.; Sattley, M.; Stahl, D.A. *Brock Biology of Microorganisms*, 15th ed.; Pearson: New York, NY, USA, 2019.
7. Zou, R.; Wang, Y.; Duan, M.; Guo, M.; Zhang, Q.; Zheng, H. Dysbiosis of Gut Fungal Microbiota in Children with Autism Spectrum Disorders. *J. Autism Dev. Disord.* **2020**, *51*, 267–275. [CrossRef]
8. Momose, Y.; Maruyama, A.; Iwasaki, T.; Miyamoto, Y.; Itoh, K. 16S rRNA gene sequence-based analysis of clostridia related to conversion of germfree mice to the normal state. *J. Appl. Microbiol.* **2009**, *107*, 2088–2097. [CrossRef] [PubMed]
9. Umesaki, Y.; Setoyama, H.; Matsumoto, S.; Imaoka, A.; Itoh, K. Differential roles of segmented filamentous bacteria and clostridia in development of the intestinal immune system. *Infect. Immun.* **1999**, *67*, 3504–3511. [CrossRef]
10. Atarashi, K.; Tanoue, T.; Oshima, K.; Suda, W.; Nagano, Y.; Nishikawa, H.; Fukuda, S.; Saito, T.; Narushima, S.; Hase, K.; et al. Treg induction by a rationally selected mixture of Clostridia strains from the human microbiota. *Nature* **2013**, *500*, 232–236. [CrossRef]

11. Alshammari, M.K.; AlKhulaifi, M.M.; Al Farraj, D.A.; Somily, A.M.; Albarrag, A.M. Incidence of Clostridium perfringens and its toxin genes in the gut of children with autism spectrum disorder. *Anaerobe* **2020**, *61*, 102114. [CrossRef]
12. Finegold, S.M.; Summanen, P.H.; Downes, J.; Corbett, K.; Komoriya, T. Detection of Clostridium perfringens toxin genes in the gut microbiota of autistic children. *Anaerobe* **2017**, *45*, 133–137. [CrossRef]
13. Revitt-Mills, S.A.; Rood, J.I.; Adams, V. Clostridium perfringens extracellular toxins and enzymes: 20 and counting. *Microbiol. Aust.* **2015**, *36*, 114. [CrossRef]
14. Brookes, S.J.H.; Spencer, N.J.; Costa, M.; Zagorodnyuk, V.P. Extrinsic primary afferent signalling in the gut. *Nat. Rev. Gastroenterol. Hepatol.* **2013**, *10*, 286–296. [CrossRef] [PubMed]
15. Mayer, E.A.; Tillisch, K.; Gupta, A. Gut/brain axis and the microbiota. *J. Clin. invest.* **2015**, *125*, 926–938. [CrossRef] [PubMed]
16. Clarke, G.; Grenham, S.; Scully, P.; Fitzgerald, P.; Moloney, R.D.; Shanahan, F.; Dinan, T.G.; Cryan, J.F. The microbiome-gut-brain axis during early life regulates the hippocampal serotonergic system in a sex-dependent manner. *Mol. Psychiatry* **2013**, *18*, 666–673. [CrossRef]
17. Desbonnet, L.; Clarke, G.; Shanahan, F.; Dinan, T.G.; Cryan, J.F. Microbiota is essential for social development in the mouse. *Mol. Psychiatry* **2014**, *19*, 146–148. [CrossRef]
18. Sudo, N.; Chida, Y.; Aiba, Y.; Sonoda, J.; Oyama, N.; Yu, X.N.; Kubo, C.; Koga, Y. Postnatal microbial colonization programs the hypothalamic-pituitary-adrenal system for stress response in mice. *J. Physiol.* **2004**, *558*, 263–275. [CrossRef] [PubMed]
19. Shultz, S.R.; MacFabe, D.F. Propionic Acid Animal Model of Autism. In *Comprehensive Guide to Autism*; Springer: New York, NY, USA, 2014; pp. 1755–1778. [CrossRef]
20. Horvath, K.; Papadimitriou, J.C.; Rabszty, A.; Drachenberg, C.; Tildon, J.T. Gastrointestinal abnormalities in children with autistic disorder. *J. Pediatr.* **1999**, *135*, 559–563. [CrossRef]
21. Jyonouchi, H.; Sun, S.; Itokazu, N. Innate Immunity Associated with Inflammatory Responses and Cytokine Production against Common Dietary Proteins in Patients with Autism Spectrum Disorder. *Neuropsychobiology* **2002**, *46*, 76–84. [CrossRef]
22. Choi, J.; Lee, S.; Won, J.; Jin, Y.; Hong, Y.; Hur, T.-Y.; Kim, J.-H.; Lee, S.-R.; Hong, Y. Pathophysiological and neurobehavioral characteristics of a propionic acid-mediated autism-like rat model. *PLoS ONE* **2018**, *13*, e0192925. [CrossRef]
23. Raymond, G.V.; Bauman, M.L.; Kemper, T.L. Hippocampus in autism: A Golgi analysis. *Acta Neuropathol.* **1995**, *91*, 117–119. [CrossRef]
24. Choi, H.; Kim, I.S.; Mun, J.Y. Propionic acid induces dendritic spine loss by MAPK/ERK signaling and dysregulation of autophagic flux. *Mol. Brain* **2020**, *13*, 86. [CrossRef]
25. Lobzhanidze, G.; Japaridze, N.; Lordkipanidze, T.; Rzayev, F.; MacFabe, D.; Zhvania, M. Behavioural and brain ultrastructural changes following the systemic administration of propionic acid in adolescent male rats. Further development of a rodent model of autism. *Int. J. Dev. Neurosci.* **2020**, *80*, 139–156. [CrossRef]
26. Armeanu, R.; Makkonen, M.; Crespi, B. Meta-Analysis of BDNF Levels in Autism. *Cell. Mol. Neurobiol.* **2017**, *37*, 949–954. [CrossRef] [PubMed]
27. Alò, R.; Olivito, I.; Fazzari, G.; Zizza, M.; Di Vito, A.; Avolio, E.; Mandalà, M.; Bruno, R.; Barni, T.; Canonaco, M.; et al. Correlation of distinct behaviors to the modified expression of cerebral Shank1,3 and BDNF in two autistic animal models. *Behav. Brain Res.* **2021**, *404*, 113165. [CrossRef]
28. Win-Shwe, T.-T.; Nway, N.C.; Imai, M.; Lwin, T.-T.; Mar, O.; Watanabe, H. Social behavior, neuroimmune markers and glutamic acid decarboxylase levels in a rat model of valproic acid-induced autism. *J. Toxicol. Sci.* **2018**, *43*, 631–643. [CrossRef] [PubMed]
29. Almeida, L.E.F.; Roby, C.D.; Krueger, B.K. Increased BDNF expression in fetal brain in the valproic acid model of autism. *Mol. Cell. Neurosci.* **2014**, *59*, 57–62. [CrossRef]
30. Maqsood, R.; Stone, T.W. The Gut-Brain Axis, BDNF, NMDA and CNS Disorders. *Neurochem. Res.* **2016**, *41*, 2819–2835. [CrossRef] [PubMed]
31. Barichello, T.; Generoso, J.S.; Simões, L.R.; Faller, C.J.; Ceretta, R.A.; Petronilho, F.; Lopes-Borges, J.; Valvassori, S.S.; Quevedo, J. Sodium Butyrate Prevents Memory Impairment by Re-establishing BDNF and GDNF Expression in Experimental Pneumococcal Meningitis. *Mol. Neurobiol.* **2015**, *52*, 734–740. [CrossRef]
32. Qiu, Z. Deciphering MECP2-associated disorders: Disrupted circuits and the hope for repair. *Curr. Opin. Neurobiol.* **2018**, *48*, 30–36. [CrossRef]
33. El-Ansary, A.K.; Bacha, A.B.; Kotb, M. Etiology of autistic features: The persisting neurotoxic effects of propionic acid. *J. Neuroinflamm.* **2012**, *9*, 74. [CrossRef]
34. Yan, Z.-X.; Gao, X.-J.; Li, T.; Wei, B.; Wang, P.-P.; Yang, Y.; Yan, R. Fecal Microbiota Transplantation in Experimental Ulcerative Colitis Reveals Associated Gut Microbial and Host Metabolic Reprogramming. *Appl. Environ. Microbiol.* **2018**, *84*, e00434-18. [CrossRef] [PubMed]
35. Javed, N.H.; Alsahly, M.B.; Khubchandani, J. Oral Feeding of Probiotic Bifidobacterium infantis : Colonic Morphological Changes in Rat Model of TNBS-Induced Colitis. *Scientifica* **2016**, *2016*, 9572596. [CrossRef]
36. Schwartz, J.J.; Careaga, M.; Onore, C.E.; Rushakoff, J.A.; Berman, R.F.; Ashwood, P. Maternal immune activation and strain specific interactions in the development of autism-like behaviors in mice. *Transl. Psychiatry* **2013**, *3*, e240. [CrossRef] [PubMed]
37. Lo, S.-C.; Scaearce-Levie, K.; Sheng, M. Characterization of Social Behaviors in caspase-3 deficient mice. *Sci. Rep.* **2016**, *6*, 18335. [CrossRef] [PubMed]

38. Friard, O.; Gamba, M. BORIS : A free, versatile open-source event-logging software for video/audio coding and live observations. *Methods Ecol. Evol.* **2016**, *7*, 1325–1330. [CrossRef]
39. Maeda, H.; Fujimoto, C.; Haruki, Y.; Maeda, T.; Koikeguchi, S.; Petelin, M.; Arai, H.; Tanimoto, I.; Nishimura, F.; Takashiba, S. Quantitative real-time PCR using TaqMan and SYBR Green for *Actinobacillus actinomycetemcomitans*, *Porphyromonas gingivalis*, *Prevotella intermedia*, tetQ gene and total bacteria. *FEMS Immunol. Med. Microbiol.* **2003**, *39*, 81–86. [CrossRef]
40. Nagpal, R.; Ogata, K.; Tsuji, H.; Matsuda, K.; Takahashi, T.; Nomoto, K.; Suzuki, Y.; Kawashima, K.; Nagata, S.; Yamashiro, Y. Sensitive quantification of *Clostridium perfringens* in human feces by quantitative real-time PCR targeting alpha-toxin and enterotoxin genes. *BMC Microbiol.* **2015**, *15*, 219. [CrossRef]
41. Mayeur, C.; Gratadoux, J.-J.; Bridonneau, C.; Chegdani, F.; Larroque, B.; Kapel, N.; Corcos, O.; Thomas, M.; Joly, F. Faecal D/L Lactate Ratio Is a Metabolic Signature of Microbiota Imbalance in Patients with Short Bowel Syndrome. *PLoS ONE* **2013**, *8*, e54335. [CrossRef] [PubMed]
42. Garcia-Gutierrez, E.; Narbad, A.; Rodríguez, J.M. Autism Spectrum Disorder Associated With Gut Microbiota at Immune, Metabolomic, and Neuroactive Level. *Front. Neurosci.* **2020**, *14*, 1072. [CrossRef]
43. Vendrik, K.E.W.; Ooijevaar, R.E.; De Jong, P.R.C.; Laman, J.D.; van Oosten, B.W.; Van Hilten, J.J.; Ducarmon, Q.R.; Keller, J.J.; Kuijper, E.J.; Contarino, M.F. Fecal Microbiota Transplantation in Neurological Disorders. *Front. Cell. Infect. Microbiol.* **2020**, *10*, 98. [CrossRef] [PubMed]
44. Martínez-González, A.E.; Andreo-Martínez, P. Probiotics, prebiotics and fecal microbiota transplantation in autism: A systematic review. *Rev. Psiquiatr. Salud Ment.* **2020**, *13*, 150–164. [CrossRef]
45. Wang, L.; Christophersen, C.T.; Sorich, M.J.; Gerber, J.P.; Angley, M.T.; Conlon, M.A. Low Relative Abundances of the Mucolytic Bacterium *Akkermansia muciniphila* and *Bifidobacterium* spp. in Feces of Children with Autism. *Appl. Environ. Microbiol.* **2011**, *77*, 6718–6721. [CrossRef] [PubMed]
46. Coretti, L.; Paparo, L.; Riccio, M.P.; Amato, F.; Cuomo, M.; Natale, A.; Borrelli, L.; Corrado, G.; De Caro, C.; Comegna, M.; et al. Gut Microbiota Features in Young Children With Autism Spectrum Disorders. *Front. Microbiol.* **2018**, *9*, 3146. [CrossRef] [PubMed]
47. Shaaban, S.Y.; El Gendy, Y.G.; Mehanna, N.S.; El-Senousy, W.M.; El-Feki, H.S.A.; Saad, K.; El-Asheer, O.M. The role of probiotics in children with autism spectrum disorder: A prospective, open-label study. *Nutr. Neurosci.* **2018**, *21*, 676–681. [CrossRef] [PubMed]
48. Wong, C.B.; Odamaki, T.; Xiao, J. Beneficial effects of *Bifidobacterium longum* subsp. *longum* BB536 on human health: Modulation of gut microbiome as the principal action. *J. Funct. Foods* **2019**, *54*, 506–519. [CrossRef]
49. Mirza, R.; Sharma, B. Selective modulator of peroxisome proliferator-activated receptor- α protects propionic acid induced autism-like phenotypes in rats. *Life Sci.* **2018**, *214*, 106–117. [CrossRef]
50. Paudel, R.; Raj, K.; Gupta, Y.K.; Singh, S. Oxiracetam and Zinc Ameliorates Autism-Like Symptoms in Propionic Acid Model of Rats. *Neurotox. Res.* **2020**, *37*, 815–826. [CrossRef]
51. Daghestani, M.H.; Selim, M.E.; Abd-Elhakim, Y.M.; Said, E.N.; El-Hameed, N.E.A.; Khalil, S.R.; El-Tawil, O.S. The role of apitoxin in alleviating propionic acid-induced neurobehavioral impairments in rat pups: The expression pattern of Reelin gene. *Biomed. Pharmacother.* **2017**, *93*, 48–56. [CrossRef]
52. Chen, K.; Fu, Y.; Wang, Y.; Liao, L.; Xu, H.; Zhang, A.; Zhang, J.; Fan, L.; Ren, J.; Fang, B. Therapeutic Effects of the In Vitro Cultured Human Gut Microbiota as Transplants on Altering Gut Microbiota and Improving Symptoms Associated with Autism Spectrum Disorder. *Microb. Ecol.* **2020**, *80*, 475–486. [CrossRef]
53. Borody, T.J.; Khoruts, A. Fecal microbiota transplantation and emerging applications. *Nat. Rev. Gastroenterol. Hepatol.* **2012**, *9*, 88–96. [CrossRef]
54. Kang, D.-W.; Adams, J.B.; Gregory, A.C.; Borody, T.; Chittick, L.; Fasano, A.; Khoruts, A.; Geis, E.; Maldonado, J.; McDonough-Means, S.; et al. Microbiota Transfer Therapy alters gut ecosystem and improves gastrointestinal and autism symptoms: An open-label study. *Microbiome* **2017**, *5*, 10. [CrossRef]
55. Kang, D.-W.; Adams, J.B.; Coleman, D.M.; Pollard, E.L.; Maldonado, J.; McDonough-Means, S.; Caporaso, J.G.; Krajmalnik-Brown, R. Long-term benefit of Microbiota Transfer Therapy on autism symptoms and gut microbiota. *Sci. Rep.* **2019**, *9*, 5821. [CrossRef] [PubMed]
56. Zhao, H.; Gao, X.; Xi, L.; Shi, Y.; Peng, L.; Wang, C.; Zou, L.; Yang, Y. Mofecal microbiota transplantation for children with autism spectrum disorder. *Gastrointest. Endosc.* **2019**, *89*, AB512–AB513. [CrossRef]
57. Desbonnet, L.; Garrett, L.; Clarke, G.; Kiely, B.; Cryan, J.F.; Dinan, T.G. Effects of the probiotic *Bifidobacterium infantis* in the maternal separation model of depression. *Neuroscience* **2010**, *170*, 1179–1188. [CrossRef]
58. Tian, P.; Wang, G.; Zhao, J.; Zhang, H.; Chen, W. *Bifidobacterium* with the role of 5-hydroxytryptophan synthesis regulation alleviates the symptom of depression and related microbiota dysbiosis. *J. Nutr. Biochem.* **2019**, *66*, 43–51. [CrossRef] [PubMed]
59. Li, N.; Wang, Q.; Wang, Y.; Sun, A.; Lin, Y.; Jin, Y.; Li, X. Oral Probiotics Ameliorate the Behavioral Deficits Induced by Chronic Mild Stress in Mice via the Gut Microbiota-Inflammation Axis. *Front. Behav. Neurosci.* **2018**, *12*, 266. [CrossRef] [PubMed]
60. Messaoudi, M.; LaLonde, R.; Violle, N.; Javelot, H.; Desor, D.; Nejdí, A.; Bisson, J.-F.; Rougeot, C.; Pichelin, M.; Cazaubiel, M.; et al. Assessment of psychotropic-like properties of a probiotic formulation (*Lactobacillus helveticus* Rand *Bifidobacterium longum* R0175) in rats and human subjects. *Br. J. Nutr.* **2011**, *105*, 755–764. [CrossRef]
61. Yang, C.; Fujita, Y.; Ren, Q.; Ma, M.; Dong, C.; Hashimoto, K. *Bifidobacterium* in the gut microbiota confer resilience to chronic social defeat stress in mice. *Sci. Rep.* **2017**, *7*, 45942. [CrossRef] [PubMed]

62. Bercik, P.; Denou, E.; Collins, J.; Jackson, W.; Lu, J.; Jury, J.; Deng, Y.; Blennerhassett, P.; Macri, J.; McCoy, K.D.; et al. The Intestinal Microbiota Affect Central Levels of Brain-Derived Neurotrophic Factor and Behavior in Mice. *Gastroenterology* **2011**, *141*, 599–609.e3. [CrossRef] [PubMed]
63. Guo, P.; Zhang, K.; Ma, X.; He, P. Clostridium species as probiotics: Potentials and challenges. *J. Anim. Sci. Biotechnol.* **2020**, *11*, 24. [CrossRef]
64. Góra, B.; Gofron, Z.; Grosiak, M.; Aptekorz, M.; Kazek, B.; Kocelak, P.; Radosz-Komoniewska, H.; Chudek, J.; Martirosian, G. Toxin profile of fecal Clostridium perfringens strains isolated from children with autism spectrum disorders. *Anaerobe* **2018**, *51*, 73–77. [CrossRef]
65. Soler-Jover, A.; Dorca, J.; Popoff, M.R.; Gibert, M.; Saura, J.; Tusell, J.M.; Serratos, J.; Blasi, J.; Martín-Satué, M. Distribution of Clostridium perfringens epsilon toxin in the brains of acutely intoxicated mice and its effect upon glial cells. *Toxicon* **2007**, *50*, 530–540. [CrossRef] [PubMed]
66. Dorca-Arévalo, J.; Soler-Jover, A.; Gibert, M.; Popoff, M.R.; Martín-Satué, M.; Blasi, J. Binding of ϵ -toxin from Clostridium perfringens in the nervous system. *Vet. Microbiol.* **2008**, *131*, 14–25. [CrossRef]
67. Finnie, J.W.; Blumbergs, P.C.; Manavis, J. Neuronal Damage Produced in Rat Brains by Clostridium perfringens Type D Epsilon Toxin. *J. Comp. Pathol.* **1999**, *120*, 415–420. [CrossRef]
68. El-Ansary, A.; Ben Bacha, A.; Bjørklund, G.; Al-Orf, N.; Bhat, R.S.; Moubayed, N.; Abed, K. Probiotic treatment reduces the autistic-like excitation/inhibition imbalance in juvenile hamsters induced by orally administered propionic acid and clindamycin. *Metab. Brain Dis.* **2018**, *33*, 1155–1164. [CrossRef] [PubMed]
69. Sghir, A.; Gramet, G.; Suau, A.; Rochet, V.; Pochart, P.; Dore, J. Quantification of bacterial groups within human fecal flora by oligonucleotide probe hybridization. *Appl. Environ. Microbiol.* **2000**, *66*, 2263–2266. [CrossRef]
70. Pryde, S.E.; Duncan, S.H.; Hold, G.L.; Stewart, C.S.; Flint, H.J. The microbiology of butyrate formation in the human colon. *FEMS Microbiol. Lett.* **2002**, *217*, 133–139. [CrossRef] [PubMed]
71. Lay, C.; Rigottier-Gois, L.; Holmström, K.; Rajilic-Stojanovic, M.; Vaughan, E.E.; de Vos, W.M.; Collins, M.D.; Thiel, R.; Namsolleck, P.; Blaut, M.; et al. Colonic microbiota signatures across five northern European countries. *Appl. Environ. Microbiol.* **2005**, *71*, 4153–4155. [CrossRef]
72. Sokol, H.; Pigneur, B.; Watterlot, L.; Lakhdari, O.; Bermúdez-Humarán, L.G.; Gratadoux, J.-J.; Blugeon, S.; Bridonneau, C.; Furet, J.-P.; Corthier, G.; et al. Faecalibacterium prausnitzii is an anti-inflammatory commensal bacterium identified by gut microbiota analysis of Crohn disease patients. *Proc. Natl. Acad. Sci. USA* **2008**, *105*, 16731–16736. [CrossRef] [PubMed]
73. Liu, S.; Li, E.; Sun, Z.; Fu, D.; Duan, G.; Jiang, M.; Yu, Y.; Mei, L.; Yang, P.; Tang, Y.; et al. Altered gut microbiota and short chain fatty acids in Chinese children with autism spectrum disorder. *Sci. Rep.* **2019**, *9*, 287. [CrossRef] [PubMed]
74. Peng, L.; Li, Z.-R.; Green, R.S.; Holzman, I.R.; Lin, J. Butyrate Enhances the Intestinal Barrier by Facilitating Tight Junction Assembly via Activation of AMP-Activated Protein Kinase in Caco-2 Cell Monolayers. *J. Nutr.* **2009**, *139*, 1619–1625. [CrossRef] [PubMed]
75. Kratsman, N.; Getselter, D.; Elliott, E. Sodium butyrate attenuates social behavior deficits and modifies the transcription of inhibitory/excitatory genes in the frontal cortex of an autism model. *Neuropharmacology* **2016**, *102*, 136–145. [CrossRef] [PubMed]
76. Sengupta, P. The Laboratory Rat: Relating Its Age With Human's. *Int. J. Prev. Med.* **2013**, *4*, 624–630. [PubMed]
77. de Theije, C.G.M.; Wopereis, H.; Ramadan, M.; van Eijndthoven, T.; Lambert, J.; Knol, J.; Garssen, J.; Kraneveld, A.D.; Oozeer, R. Altered gut microbiota and activity in a murine model of autism spectrum disorders. *Brain. Behav. Immun.* **2014**, *37*, 197–206. [CrossRef] [PubMed]
78. Hsiao, E.Y.; McBride, S.W.; Hsien, S.; Sharon, G.; Hyde, E.R.; McCue, T.; Codelli, J.A.; Chow, J.; Reisman, S.E.; Petrosino, J.F.; et al. Microbiota Modulate Behavioral and Physiological Abnormalities Associated with Neurodevelopmental Disorders. *Cell* **2013**, *155*, 1451–1463. [CrossRef]
79. Yurkovetskiy, L.; Burrows, M.; Khan, A.A.; Graham, L.; Volchkov, P.; Becker, L.; Antonopoulos, D.; Umesaki, Y.; Chervonsky, A.V. Gender Bias in Autoimmunity Is Influenced by Microbiota. *Immunity* **2013**, *39*, 400–412. [CrossRef] [PubMed]
80. Org, E.; Mehrabian, M.; Parks, B.W.; Shipkova, P.; Liu, X.; Drake, T.A.; Lusa, A.J. Sex differences and hormonal effects on gut microbiota composition in mice. *Gut Microbes* **2016**, *7*, 313–322. [CrossRef]
81. Krajčiček, E.; Fischer, M.; Allegretti, J.R.; Kelly, C.R. Nuts and Bolts of Fecal Microbiota Transplantation. *Clin. Gastroenterol. Hepatol.* **2019**, *17*, 345–352. [CrossRef]
82. Kullen, M.J.; Khil, J.; Busta, F.F.; Gallaher, D.D.; Brady, L.J. Carbohydrate source and bifidobacteria influence the growth of Clostridium perfringens in vivo and in vitro. *Nutr. Res.* **1998**, *18*, 1889–1897. [CrossRef]
83. Morishita, Y.; Owada, T.; Ozaki, A.; Mizutani, T. Galactooligosaccharide in combination with Bifidobacterium and Bacteroides affects the population of Clostridium perfringens in the intestine of gnotobiotic mice. *Nutr. Res.* **2002**, *22*, 1333–1341. [CrossRef]
84. Falony, G.; Vlachou, A.; Verbrugghe, K.; De Vuyst, L. Cross-Feeding between Bifidobacterium longum BB536 and Acetate-Converting, Butyrate-Producing Colon Bacteria during Growth on Oligofructose. *Appl. Environ. Microbiol.* **2006**, *72*, 7835–7841. [CrossRef] [PubMed]
85. Felix-Ortiz, A.C.; Tye, K.M. Amygdala Inputs to the Ventral Hippocampus Bidirectionally Modulate Social Behavior. *J. Neurosci.* **2014**, *34*, 586–595. [CrossRef] [PubMed]

86. Hwang, S.-R.; Kim, C.-Y.; Shin, K.-M.; Jo, J.-H.; Kim, H.-A.; Heo, Y. Altered Expression Levels of Neurodevelopmental Proteins in Fetal Brains of BTBR T+ tf /J Mice with Autism-Like Behavioral Characteristics. *J. Toxicol. Environ. Health Part A* **2015**, *78*, 516–523. [CrossRef]
87. Sungur, A.Ö.; Jochner, M.C.E.; Harb, H.; Kılıç, A.; Garn, H.; Schwarting, R.K.W.; Wöhr, M. Aberrant cognitive phenotypes and altered hippocampal BDNF expression related to epigenetic modifications in mice lacking the post-synaptic scaffolding protein SHANK1: Implications for autism spectrum disorder. *Hippocampus* **2017**, *27*, 906–919. [CrossRef]
88. Lima Giacobbo, B.; Doorduyn, J.; Klein, H.C.; Dierckx, R.A.J.O.; Bromberg, E.; de Vries, E.F.J. Brain-Derived Neurotrophic Factor in Brain Disorders: Focus on Neuroinflammation. *Mol. Neurobiol.* **2019**, *56*, 3295–3312. [CrossRef] [PubMed]
89. Liao, X.; Li, Y. Nuclear Factor Kappa B in Autism Spectrum Disorder: A Systematic Review. *Pharmacol. Res.* **2020**, *159*, 104918. [CrossRef]
90. Garcia, K.L.P.; Yu, G.; Nicolini, C.; Michalski, B.; Garzon, D.J.; Chiu, V.S.; Tongiorgi, E.; Szatmari, P.; Fahnestock, M. Altered Balance of Proteolytic Isoforms of Pro-Brain-Derived Neurotrophic Factor in Autism. *J. Neuropathol. Exp. Neurol.* **2012**, *71*, 289–297. [CrossRef]
91. Nagarajan, R.; Hogart, A.; Gweye, Y.; Martin, M.R.; LaSalle, J.M. Reduced MeCP2 Expression is Frequent in Autism Frontal Cortex and Correlates with Aberrant MECP2 Promoter Methylation. *Epigenetics* **2006**, *1*, 172–182. [CrossRef]
92. Kim, K.C.; Choi, C.S.; Kim, J.-W.; Han, S.-H.; Cheong, J.H.; Ryu, J.H.; Shin, C.Y. MeCP2 Modulates Sex Differences in the Postsynaptic Development of the Valproate Animal Model of Autism. *Mol. Neurobiol.* **2016**, *53*, 40–56. [CrossRef]
93. Philip, V.; Newton, D.F.; Oh, H.; Collins, S.M.; Bercik, P.; Sibille, E. Transcriptional markers of excitation-inhibition balance in germ-free mice show region-specific dysregulation and rescue after bacterial colonization. *J. Psychiatr. Res.* **2021**, *135*, 248–255. [CrossRef] [PubMed]
94. El-Ansary, A.; Al-Salem, H.S.; Asma, A.; Al-Dbass, A. Glutamate excitotoxicity induced by orally administered propionic acid, a short chain fatty acid can be ameliorated by bee pollen. *Lipids Health Dis.* **2017**, *16*, 96. [CrossRef] [PubMed]



Review

Sleep Disturbance and Metabolic Dysfunction: The Roles of Adipokines

Zhikui Wei ^{1,*}, You Chen ² and Raghu P. Upender ¹

¹ Department of Neurology, Vanderbilt University Medical Center, Nashville, TN 37232, USA; raghu.p.upender@vumc.org

² Department of Biomedical Informatics, Vanderbilt University Medical Center, Nashville, TN 37232, USA; You.chen@vumc.org

* Correspondence: zhikui.wei@vumc.org; Tel.: +1-(615)-936-0060; Fax: +1-(615)-936-0223

Abstract: Adipokines are a growing group of peptide or protein hormones that play important roles in whole body metabolism and metabolic diseases. Sleep is an integral component of energy metabolism, and sleep disturbance has been implicated in a wide range of metabolic disorders. Accumulating evidence suggests that adipokines may play a role in mediating the close association between sleep disorders and systemic metabolic derangements. In this review, we briefly summarize a group of selected adipokines and their identified function in metabolism. Moreover, we provide a balanced overview of these adipokines and their roles in sleep physiology and sleep disorders from recent human and animal studies. These studies collectively demonstrate that the functions of adipokine in sleep physiology and disorders could be largely twofold: (1) adipokines have multifaceted roles in sleep physiology and sleep disorders, and (2) sleep disturbance can in turn affect adipokine functions that likely contribute to systemic metabolic derangements.

Keywords: adipokine; cardiometabolic disease; metabolic syndrome; sleep disorder; obstructive sleep apnea

Citation: Wei, Z.; Chen, Y.; Upender, R.P. Sleep Disturbance and Metabolic Dysfunction: The Roles of Adipokines. *Int. J. Mol. Sci.* **2022**, *23*, 1706. <https://doi.org/10.3390/ijms23031706>

Academic Editor: Cristiano Fava

Received: 13 December 2021

Accepted: 29 January 2022

Published: 1 February 2022

Publisher's Note: MDPI stays neutral with regard to jurisdictional claims in published maps and institutional affiliations.



Copyright: © 2022 by the authors. Licensee MDPI, Basel, Switzerland. This article is an open access article distributed under the terms and conditions of the Creative Commons Attribution (CC BY) license (<https://creativecommons.org/licenses/by/4.0/>).

1. Introduction

Adipokines (also known as adipocytokines) are secreted peptides and proteins produced by adipose tissue. They comprise an ever-expanding group of proteins, exemplified by leptin and adiponectin, that play diverse roles in whole body energy metabolism [1]. Adipokines are from different protein families and are produced by diverse cell types, including fat cells, immune cells, and other cells within and outside of the adipose tissue [1]. Studies on adipokines have revealed the importance of adipose tissue as a metabolically active tissue/organ in mediating crosstalk among different tissues and organs [2]. Meanwhile, they have also deepened our understanding of the complex interplay between different physiologic or pathological processes such as metabolism, inflammation, and cardiovascular diseases [2].

Sleep disturbance has been implicated in a wide range of metabolic disorders contributing to significant morbidity and mortality [3]. This has been studied extensively in epidemiological studies in the context of the modern epidemic of metabolic syndrome, a cluster of medical conditions that include central obesity, systemic hypertension, insulin resistance, and dyslipidemia. For example, prospective longitudinal studies in children have shown a temporal relationship between short sleep time and the development of obesity, suggesting a possible causal relationship [4]. In adults, sleep disorders are associated with glucose intolerance, insulin resistance, and a predisposition to type 2 diabetes [5]. Short sleep duration also increases the risk of obesity, hypertension, coronary artery disease, and stroke, and all of which cause morbidity and mortality [6,7].

While the associations between sleep disturbance and metabolic disorders have been repeatedly shown, the underlying mechanisms remain poorly understood. Accumulating

evidence suggests that adipokines may provide the link between sleep disturbances and systemic metabolic derangements. This review aims to provide a brief discussion of representative adipokines and their major metabolic functions. Further, we aim to provide a balanced discussion of emerging evidence from both human and animal studies on the role of adipokines in sleep physiology and sleep disorders. These studies collectively demonstrate that the functions of adipokines in sleep physiology and disorders could be largely twofold: (1) adipokines have multifaceted roles in sleep physiology and sleep disorders, and (2) sleep disturbance can in turn affect adipokine functions that are important in systemic metabolic derangements.

2. Adipokines in Sleep Physiology and Disorders

Currently, more than 600 adipokines with various biological activities have been described in humans [1]. A common classification scheme roughly divides adipokines into proinflammatory or anti-inflammatory groups [8,9]. It is shown that obesity is associated with the upregulation of proinflammatory adipokines and the downregulation of anti-inflammatory adipokines, leading to the development of chronic low-grade inflammation [8]. This model of pathogenesis was thought to be important in several disease processes, including type 2 diabetes, cardiovascular diseases, dermatological diseases, and osteoarthritis [8–11]. Comparatively, the roles of adipokines in sleep physiology and sleep disorders are less understood. Recent literature indicates that some adipokines, such as leptin, have direct roles in sleep physiology and sleep disorders. Other adipokines are mainly described as mediators of the metabolic dysfunction of sleep disturbance, including insufficient sleep and obstructive sleep apnea. A selected group of adipokines with demonstrated roles in human sleep physiology and sleep disorders are reviewed below.

2.1. Leptin

Leptin is by far the most intensely studied adipokine concerning sleep physiology and sleep disorders (Table 1). Leptin is a peptide hormone produced mainly in the white adipose tissue. Its major function is to regulate whole body energy metabolism by balancing the central pathways that regulate satiety and feeding. It binds to surface Ob receptors (OBRs) in the hypothalamus and activates signaling pathways to regulate satiety and feeding. More specifically, it can activate the JAK-STAT signaling to increase the expression of anorexigenic peptides such as POMC and CART and inhibit the expression of orexigenic neuropeptides NPY and AgRP to decrease appetite [12]. In addition, it also plays important functions in reproductive health, glycemic control, and bone metabolism (Figure 1A, Table 2) [13].

Table 1. Adipokines and their functions in sleep and sleep disorders.

Adipokine	Functions in Sleep and Sleep Disorders
Leptin	<ul style="list-style-type: none"> • ↓ in short sleep and obesity (Children) • Nonlinear relationship with sleep time (Adults) • ↑ in OSAS and correlated with AHI (Adults) • Improved sleep quality in adults with obesity and DM2 or anorexia (Adults) • Associated with compensatory response in upper airway obstruction in obese women (Adults) • Serum levels have diurnal rhythmicity (Adults)

Table 1. Cont.

Adipokine	Functions in Sleep and Sleep Disorders
Adiponectin	<ul style="list-style-type: none"> • ↓ in short sleep and obesity (Children) • Variable relationship with sleep time modified by other factors (Adults)
Chemerin	<ul style="list-style-type: none"> • ↑ in OSAS and obesity (adults) • Correlated with AHI and mean SaO₂ in adults with OSAS (Adults) • Useful as a biomarker for OSAS (Adults)
Vaspin	<ul style="list-style-type: none"> • Variable changes in OSAS (Adults) • Serum levels have diurnal rhythmicity (Adults)
Omentin	<ul style="list-style-type: none"> • Variable changes in OSAS (Adults)
Visfatin	<ul style="list-style-type: none"> • ↑ in narcolepsy (Adults) • Positively correlated with sleep latency in OSAS (Adults) • Negatively correlated with total sleep time, stage 2 sleep, and REM sleep in OSAS (Adults) • Serum levels have diurnal rhythmicity (Adults)

List of symbols and abbreviations: ↓: Decreased circulating levels; ↑: Increased circulating levels; AHI: apnea hypopnea index; DM2: diabetes mellitus type 2; OSAS: obstructive sleep apnea syndrome; REM: rapid eye movement (a sleep stage).

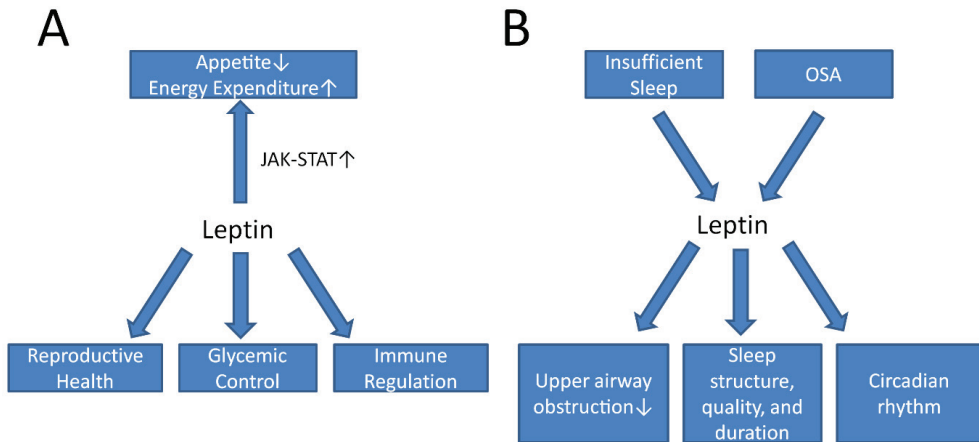


Figure 1. An illustration showing the metabolic and sleep functions of leptin. (A) Leptin activates JAK-STAT pathways to decrease appetite and increase energy expenditure centrally. It also has important functions in reproductive health, glycemic control, and immune regulation. (B) Insufficient sleep and OSA can both influence leptin levels in the serum. Leptin, in turn, can reduce upper airway obstruction in sleep and improve sleep parameters such as sleep structure, quality, and duration. Leptin may also play a role in circadian rhythms. Abbreviations: JAK, Janus kinase; OSA, obstructive sleep apnea; STAT, signal transducer and activator of transcription.

Table 2. Adipokines and their major molecular pathways and metabolic functions.

Adipokine	Receptor	Major Signaling Pathway	Major Metabolic Functions
Leptin	Ob receptors (OBRs)	JAK-STAT(↑), POMC and CART (↑), NPY and AgRP (↓)	Promote satiety, decrease feeding, improve reproductive health
Adiponectin	AdipoR1, AdipoR2, T-cadherin	AMPK (↑), PPARα(↑), interaction with PI3K/Akt signaling via APPL1, gluconeogenic genes (↓)	Decrease hepatic glucose production, increase fatty acid oxidation, improve insulin sensitivity, improve cardiovascular health
Chemerin	CMKLR1, GPR1, CCr12	MAPK(↑), ERK1/2 (↑), PI3K-Akt (↑)	Regulate adipogenesis, angiogenesis, and inflammation, decrease glucose production
Vaspin	Unknown	Akt (↑), NF-κB(↓), POMC (↑), NPY(↓)	Improve insulin sensitivity, reduce endothelial inflammation, reduce food intake
Omentin	Unknown	Akt (↑), NF-κB (↓)	Reduce endothelial inflammation, improve insulin sensitivity
Visfatin	Unknown	Syntaxin 4(↑), HNF4α(↑), HNF1β(↑), ERK1/2 (↑)	Regulate NAD production, insulin secretion, and beta-cell function; Increase endothelial dysfunction

List of symbols and abbreviations: ↓: Decreased activity; ↑: Increased activity; AdipoR1/2, adiponectin receptors 1/2; AgRP, agouti-related peptide; AMPK, AMP-activated protein kinase; APPL1, adaptor protein phosphotyrosine interacting with PH domain and leucine zipper 1; CART, cocaine and amphetamine regulated transcript; CMKLR1, chemerin chemokine-like receptor 1; ERK1/2, extracellular signal-regulated kinase1/2; GPR1, G protein-coupled receptor 1; HNF1β, hepatocyte nuclear factor-1 β; HNF4α, hepatocyte nuclear factor-4α; JAK, Janus kinase; MAPK, mitogen-activated protein kinase; NAD, nicotinamide adenine dinucleotide; NF-κB, nuclear factor κ B; NPY, neuropeptide Y; OBR, ob (leptin) receptor; PI3K, phosphoinositide 3-kinase; POMC, pro-opiomelanocortin; STAT, signal transducer and activator of transcription.

A number of large population studies have established the importance of leptin in sleep and metabolic functions. The Beijing Child and Adolescent Metabolic Syndrome Study (BCAMS) showed that poor sleep is associated with higher body mass index (BMI), fasting glucose, insulin, and Homeostatic Model Assessment for Insulin Resistance (HOMA-IR) among 3166 school children aged 6–12 [14]. These associations disappeared after adjusting for leptin, underscoring leptin as a potential link between poor sleep and metabolic derangements [14]. Using two cohort studies, involving children in Project Viva ($n = 655$) and adolescents in the Cleveland Children's Sleep & Health Study ($n = 502$), Boeke et al. showed that chronic insufficient sleep was associated with reduced levels of leptin in girls at age 7 and the association was stronger among girls with greater adiposity [15]. Shorter sleep was also associated with lower leptin levels in adolescent males [15]. These results demonstrated a positive relationship between leptin and sleep time, which were inversely correlated with obesity in the pediatric population.

In adults, the relationship between leptin, sleep time, and BMI is more variable. The Wisconsin Sleep Cohort Study included 1024 participants aged 30–60 and showed a U-shaped curvilinear relationship between sleep duration and BMI, where short sleep duration (<8 h) was associated with reduced leptin, elevated ghrelin, and increased BMI [16]. In a sample of postmenopausal women ($n = 769$, median age 63 years), individuals reporting shorter sleep duration (<6 h) were associated with lower leptin levels, higher energy intake, and lower diet quality [17]. The Quebec Family Study also demonstrated a cross-sectional association between short sleep duration, reduced leptin, and increased adiposity in a sample of 323 men and 417 women aged 21–64 [18]. In contrast, the Cleveland Family Study (CFS) ($n = 561$) showed an increased fasting level of leptin with a reduction in total sleep time and a decrease in rapid eye movement (REM) sleep [19]. The discrepancies in leptin changes associated with short sleep time could be in part due to different characteristics of patient populations (e.g., age, BMI, and prevalence of diabetes and obesity) and different methods of sleep measurement (e.g., polysomnography vs. self-report sleep time). These

studies suggest that leptin may have a nonlinear relationship associated with short sleep time modified by other factors such as age, gender, and comorbidities in adults.

Studies involving experimental conditions of sleep, i.e., sleep restriction or sleep loss, provide additional insights into the function of leptin in sleep. Earlier studies involving healthy men showed total sleep loss or sleep restriction attenuated the amplitudes of the diurnal rhythm of leptin [20]. Sleep restriction was also shown to be associated with decreased leptin, increased ghrelin, and increased hunger and appetite in healthy young men [21]. In contrast, subsequent studies showed that acute sleep deprivation or sleep restriction significantly increased morning leptin in healthy women and women with obesity [22,23], as well as in a group of healthy young men and women [24]. These findings suggest there is possibly a gender-dimorphic difference in leptin changes associated with sleep deprivation. Another source of complexity comes from the activation of the stress response, which may be the cause of appetite increase and hormonal changes, not the sleep loss per se [24]. Additionally, caloric intake could also play a role in affecting the leptin changes associated with sleep loss [25].

There is a particular interest in looking at the roles of leptin in sleep disorders among different patient populations with metabolic dysfunction. In a cross-sectional study by Hirota et al. [26], leptin was shown to be positively associated with sleep quality among patients with obesity and type 2 diabetes, but not in nonobese diabetic patients. Interestingly, among patients with anorexia (mean BMI = 13.3) higher levels of leptin and IGF-1 were also associated with longer and deeper sleep [27]. In a group of overweight/obese postmenopausal women, changes in self-reported sleep measures during a 1-year moderate intensity physical activity intervention were not associated with weight loss, nor did it affect ghrelin and leptin levels [28]. Serum leptin levels were associated with BMI in both patients with obstructive sleep apnea syndrome (OSAS) and normal controls. However, only in patients with OSAS, leptin also correlated with the apnea hypopnea index (AHI) [29]. Male patients with OSAS treated with continuous positive airway pressure (CPAP) also showed a significant decrease in leptin levels after 8 weeks of treatment without changes in BMI [30]. These studies indicated that leptin may play a role in ameliorating poor sleep quality and sleep disordered breathing among patients with metabolic derangements, and treatment of sleep disorders such as OSAS can in turn impact leptin as well.

Considerable research has been performed on the relationship between circadian dyssynchrony and metabolic disturbance. Some evidence, particularly those from studies on shift workers, indicates that leptin may also play an important role in mediating the metabolic changes in patients with circadian misalignment/dyssynchrony [31–33]. It is noteworthy that leptin expression and serum concentration show circadian rhythmicity, and such circadian changes are more significant in non-obese subjects than obese subjects [31]. Leptin expression is also regulated significantly by behavior cycles, i.e., feeding and sleep, independent of circadian rhythm [32]. Using a 10-day circadian misalignment protocol, Scheer et al. showed that circadian misalignment is associated with decreased leptin, increased glucose and insulin levels, an increase in mean arterial blood pressure, and reduced sleep efficiency [32]. In shift workers such as resident physicians, it was shown that women shift workers with excessive daytime sleepiness have lower levels of leptin than those without sleepiness. Further, the disruption of the normal diurnal sleep pattern and long working hours are also associated with unfavorable lipid profiles and reduced consumption of healthy foods that predispose shift workers to obesity and other metabolic disorders [33]. These studies indicate that leptin may contribute to the development of metabolic dysfunction in shift workers with circadian dyssynchrony.

Studies involving lab animals provide insights into the mechanisms of leptin in sleep physiology. Studies in ob/ob mice (which are genetically deficient in leptin) showed that leptin deficiency reduced ventilatory response to CO₂ challenges [34] and disrupted sleep architecture and diurnal rhythmicity [35]. Db/Db mice, which are genetically deficient in leptin receptors, demonstrated an increased total sleep time, increased sleep fragmentation, attenuated sleep diurnal rhythmicity, and reduced compensation for acute sleep

deprivation [36]. Systemic infusion of leptin in ob/ob mice reversed hypoventilation and reduced the response to CO₂ challenges [37]. Using ob/ob mice, Yao et al. determined that leptin acts on the forebrain, possibly the dorsomedial hypothalamus, to relieve upper airway obstructions in sleep apnea, and it acts on the hindbrain, possibly the nucleus of the solitary tract, to upregulate ventilatory control [38]. In humans and diet-induced obese (DIO) mice, leptin administered systemically has not been shown to have similar effects in those in ob/ob and Db/Db mice, possibly due to the inhibition of the blood brain barrier [39]. Interestingly, leptin given intranasally significantly improved hypopnea during REM sleep and improved ventilation during REM and non-REM sleep in DIO mice. These effects were independent of the metabolic actions of leptin [39]. Further, leptin concentration was significantly associated with increased compensatory responses to upper airway obstruction in sleep in obese women, and the associations were independent of BMI, waist to hip ratio, neck circumference, and sagittal girth [40]. These findings suggest the leptin likely augments the neurocircuitry to improve disordered breathing in obstructive sleep apnea.

In summary, leptin has been shown to have significant roles in sleep physiology and sleep disorders (Figure 1B). Leptin may represent a component of an important neurocircuitry that can improve hypopnea and reduce upper airway obstruction during sleep. It may have additional functions in regulating sleep structure, duration, and quality, as well as circadian rhythmicity. Additionally, leptin has been shown to link insufficient sleep to increased BMI, fasting glucose, and other metabolic dysfunctions in the pediatric population, though this relationship is less consistent in adult studies. Lastly, leptin can contribute to the metabolic dysfunction in circadian dyssynchrony as well.

2.2. Adiponectin

Adiponectin is an adipocyte-specific adipokine with the highest expression of the mature adipocytes. It serves as a critical messenger to mediate the crosstalk between adipose tissue and other metabolic tissues and organs [41]. Functionally, adiponectin binds to surface receptors adipoR1 and adipoR2 and activates downstream signaling pathways such as AMPK and PPAR α to increase glucose uptake and fatty acid oxidation (Table 2) [41]. It can also suppress hepatic glucose production via the interaction of the APPL1 and insulin signaling pathway as well as the suppression of gluconeogenic gene expression (Table 2) [41]. In addition, numerous studies have demonstrated its important roles in cardiovascular diseases [41].

Adiponectin plays important roles in sleep physiology and disorders (Table 1). The BCAMS study showed that short sleep duration was associated with decreased levels of the high molecular weight (HMW) adiponectin, but not the full-length adiponectin, among children from 6–12 years old [14]. HMW adiponectin is considered the bioactive component of adiponectin and possesses beneficial effects such as insulin-sensitizing and anti-inflammatory actions [41]. Studies involving smaller cohorts have also shown decreased total adiponectin with reduced sleep time in children [42,43]. Similarly, in a cross-sectional observational study, adiponectin levels were higher in lean Saudi adolescent female subjects (62 lean and 64 obese) aged 14–18 years and increased proportionally to the duration of sleep [43]. These studies indicate that the adiponectin level is positively associated with sleep time in the pediatric population.

In adults, the relationship of adiponectin and sleep varies depending on multiple factors including age, sex, ethnicity, and comorbidities. A study involving six healthy male subjects indicated that adiponectin did not have independent changes in response to the circadian rhythm of sleep [44]. In a group of healthy Japanese male subjects, adiponectin concentration was found to be positively correlated with sleep duration, and the association was found to be stronger in an older age group (>55 years) [45]. Adiponectin levels were also lower in a group of patients with severe OSAS [46]. A recent study also showed that improvement in sleep quality is associated with increased serum adiponectin levels and improved indices of glycemic control [47]. Conversely, chronic sleep deprivation was

associated with higher adiponectin levels in a cross-section study among patients with metabolic diseases, after adjusting for age, sex, BMI, hypertension, menopause, and exercise levels [48]. This may reflect a compensatory effect of adiponectin in sleep deprivation among patients with metabolic syndrome [48]. A study involving sleep restriction showed that sleep restriction (five nights of 4 h in bed) led to reduced levels of adiponectin in Caucasian women but an increased level in African American women, with no effect on the adiponectin levels in men, indicating the effect of sleep loss on adiponectin could be sex- and ethnicity-specific [23].

Studies involving lab animals show additional insights into the regulation of adiponectin in sleep. Sleep-deprived 30-day-old male Wistar rats had a reduced expression of adiponectin in retroperitoneal fat without affecting the serum level of adiponectin [49]. Sleep fragmentation during late gestation of mother mice induces epigenetic changes resulting in a long-lasting reduction in adiponectin expression in male offspring mice at 21 weeks when the mother experienced sleep fragmentation for five days [50]. These studies indicate that sleep restriction can have both short-term and long-term effects on the expression of adiponectin.

2.3. Chemerin

Chemerin is a newly discovered adipokine shown to have various roles in inflammation, angiogenesis, adipogenesis, and whole body energy homeostasis [51]. Chemerin is highly expressed in the white adipose tissue, liver, and lungs [51]. Chemerin binds to surface receptors CMKLR1 and GPR1 and activates downstream signaling pathways including the MAPK, ERK1/2, and PI3K-Akt pathways to regulate adipogenesis, angiogenesis, and inflammation (Table 2) [51]. In addition, chemerin also regulates glucose metabolism via actions on insulin secretion and the suppression of hepatic glucose production [51].

Previous research shows that chemerin may also play an important role in metabolic and sleep disorders. The nocturnal area under the curve (AUC) levels of chemerin were higher among obese/overweight adolescent females than normal weight controls but not in adolescent males, suggesting a gender-dimorphic effect of chemerin in adolescents [52]. Feng et al. showed that serum chemerin levels were significantly elevated in patients with OSAS compared to controls [53]. Serum chemerin levels were also shown to be an independent determinant of OSAS and correlated with the severity of OSAS [53]. Studies by Xu et al. showed that chemerin was higher before and after sleep among patients with severe OSAS compared with the control group after adjusting for BMI [54]. Additionally, chemerin level after sleep was associated with mean SaO₂%, although plasma chemerin levels were mainly determined by BMI rather than hypoxia during sleep [54]. These studies indicate that chemerin is elevated in proportion to OSAS severity and may be useful as a biomarker for OSAS, as its level correlated with the severity of OSAS (Table 1).

2.4. Vaspin

Vaspin is a visceral adipose tissue-derived serine protein inhibitor. In humans, elevated vaspin levels are associated with higher BMI and insulin resistance [55]. Vaspin improves insulin sensitivity in adipose tissue by enhancing Akt signaling [55]. It also reduces endothelial cell inflammation via multiple actions, including reducing the activation of NF- κ B [55]. Centrally, vaspin reduces the expression of NPY and increases the expression of POMC to decrease food intake (Table 2) [55].

Regarding its role in sleep disorders, studies by Kiskac showed that vaspin was lower in patients with severe OSAS (AHI > 30, $n = 34$) compared to age-matched healthy volunteers ($n = 25$) [56]. In contrast, Pan et al. showed the level of vaspin was markedly increased in the group with obstructive sleep apnea-hypopnea syndrome (OSAHS) compared with healthy controls and positively associated with clinical measures of insulin resistance, including fasting blood glucose, insulin levels, and HOMA-IR [57]. Similarly, in studies by Xu et al., patients with severe OSAS had higher levels of vaspin compared to the control group after adjusting for the BMI, and the levels of vaspin were not associated with any measured sleep parameters [54]. Interestingly, studies by Zhuang showed that healthy

male Wistar rats exposed to chronic intermittent hypoxia had higher vaspin mRNA and protein levels in the visceral adipose tissue [58]. It is possible that vaspin is elevated in OSAS secondary to insulin resistance and chronic intermittent hypoxia; however, the exact relationship between vaspin and OSAS warrants further investigation.

2.5. Omentin

Omentin is an adipokine expressed in the visceral adipose tissue, including omentum, epicardial fat, and a wide range of other tissues and cells [59]. Omentin has been shown to decrease TNF- α and CRP-induced NF- κ b activation and modulate eNOS activity in endothelial cells [60]. Omentin also has been shown to have an insulin sensitizing effect and to promote insulin-stimulated glucose transport via Akt activation in adipocytes in vitro (Table 2) [59].

Regarding its role in sleep (Table 1), studies by Zirlik showed that omentin was increased among 10 patients with newly diagnosed OSAS compared to controls, and CPAP treatment for 3 months reduced the omentin levels toward the levels of the control group [61]. A subsequent study involving 46 newly diagnosed patients with OSAS and 35 controls showed that omentin levels were much higher among patients with OSAS, and its levels correlated with age in patients with OSAS [62]. In contrast, Wang et al. showed that omentin levels were significantly lower among patients with OSAS ($n = 192$) than the healthy controls ($n = 144$). The concentration of omentin was also inversely correlated with AHI among patients with OSAS [63]. A study by Uygur et al. showed omentin levels were significantly lower among patients with OSAS ($n = 96$) when compared with non-apneic controls ($n = 31$), and the levels of omentin were lower among patients with severe OSAS than those with mild/moderate forms of OSAS [64]. Further, they showed that effective treatment with CPAP for 3 months reversed the levels of omentin to the levels of controls [64]. A subsequent study by Zhang et al. showed that the omentin levels were reduced among 30 patients with obesity and severe OSAS compared with healthy controls ($n = 20$) and were associated with sleep parameters such as AHI and SpO₂ [65]. These studies indicate that omentin is differentially regulated among patients with OSAS, and the direction of change varies among different studies, which could be due to various factors including sample size, patient population, and methodology [66].

2.6. Visfatin

Visfatin is an adipokine that is enriched in the human visceral adipose tissue [67]. It is mainly secreted by the macrophages in the adipose tissue rather than by adipocytes [67]. Visfatin is an essential enzyme in nicotinamide adenine dinucleotide (NAD) production and regulates insulin secretion (via actions on syntaxin 4, HNF4a, HNF1b), insulin signaling (via activations on insulin receptor and ERK1/2), and beta-cell function [67]. Visfatin is also shown to be a proinflammatory cytokine and is increased in unstable coronary plaques and involved in endothelial dysfunction, implicating important roles in cardiovascular diseases [67].

In sleep disorders (Table 1), visfatin was shown to be elevated in patients with narcolepsy ($n = 56$) when compared with age- and BMI-matched controls ($n = 39$), mainly driven by HLA DR2-positive narcolepsy patients [68]. Among patients with OSAS, levels of visfatin were positively correlated with sleep latency and negatively correlated with total sleep time, percentage of stage 2 sleep, and REM sleep [69]. Indeed, results from the CFS study showed that there was a 14% increase in visfatin for each hour of reduction in total sleep time and a 31% increase in visfatin for every hour of reduction in REM sleep [19]. Studies by Benedict showed that visfatin levels also displayed a diurnal rhythm in humans, and sleep loss also induced a rhythm phase shift of visfatin that was positively correlated with postprandial glucose levels due to the sleep loss [70]. These studies suggest that visfatin plays a role in regulating sleep structure, and sleep can also regulate whole body inflammation and insulin resistance through adipokines such as visfatin (Table 2).

3. Conclusions

In this review, we have briefly summarized recent work on representative adipokines and their roles in sleep physiology and disorders. These studies collectively have shown that the functions of adipokines in sleep physiology and disorders could be largely twofold (Figure 2). First, adipokines have multi-faceted roles in sleep physiology and sleep disorders (Table 1). Adipokines such as leptin and visfatin can regulate various aspects of sleep, including latency, duration, quality, and/or structure. Leptin has also been shown to alleviate upper airway obstruction and improve hypoventilation in obese states. This is unique among the adipokines studied to date. Second, adipokines can mediate the metabolic dysfunction associated with sleep disturbance and sleep disorders. Their levels can be differentially regulated in the setting of sleep deprivation, circadian dyssynchrony, and obstructive sleep apnea, contributing to systemic metabolic derangements. Adipokines have been shown to have important roles in the metabolic dysfunction associated with obesity [8]. Given the large overlap between metabolic diseases and sleep disturbance/disorders, adipokines are likely an important mechanism that link poor sleep to systemic metabolic dysfunction. Future large scale prospective studies and additional mechanistic studies of adipokines in sleep physiology and sleep disorders are needed to further clarify the complex interplay between sleep and metabolic function mediated by adipokines.

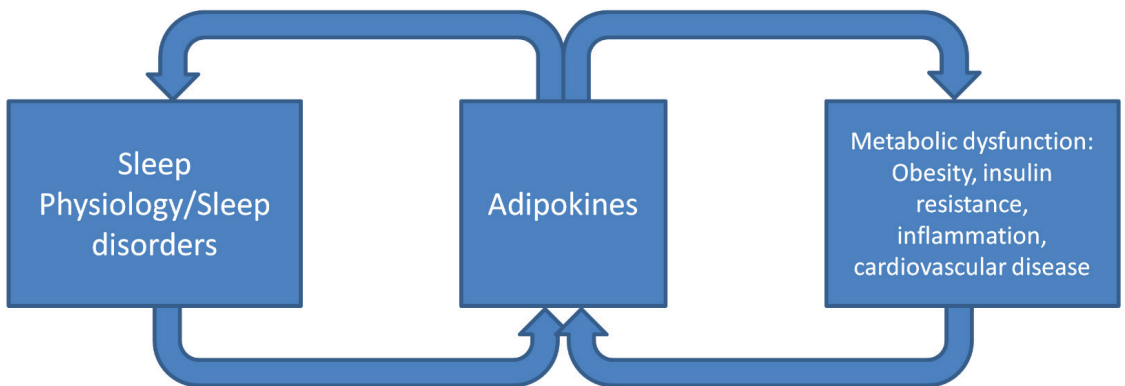


Figure 2. A proposed model of adipokine function in sleep physiology/disorders and metabolic dysfunction. Adipokines have multi-faceted roles in regulating the various aspects of sleep physiology and disorders, which can in turn affect adipokines and their functions, which contribute to systemic metabolic dysfunction.

Author Contributions: Conceptualization, investigation, and original draft preparation, Z.W.; investigation, Y.C.; writing—reviewing and editing, Y.C. and R.P.U. All authors have read and agreed to the published version of the manuscript.

Funding: This study was partially supported by the National Library of Medicine of the National Institutes of Health (award number: R01LM012854). The content of this study is solely the authors' responsibility; it does not necessarily represent the National Institutes of Health's official views.

Institutional Review Board Statement: Not applicable.

Informed Consent Statement: Not applicable.

Data Availability Statement: Not applicable.

Conflicts of Interest: The authors declare no conflict of interest.

Abbreviations

AdipoR1/2	adiponectin receptors 1/2
AgRP	agouti-related peptide
AHI	apnea hypopnea index
AMPK	AMP-activated protein kinase
APPL1	adaptor protein phosphotyrosine interacting with PH domain and leucine zipper 1
AUC	area under the curve
BCAMS	the Beijing child and adolescent metabolic syndrome study
BMI	body mass index
CART	cocaine and amphetamine regulated transcript
CCR2	C-C motif chemokine receptor like 2
CFS	the Cleveland family study
CMKLR1	chemerin chemokine-like receptor 1
CPAP	continuous positive airway pressure
CRH	corticotropin-releasing hormone
CRP	C-reactive protein
DIO	diet-induced obesity
DM2	diabetes mellitus type 2
eNOS	endothelial nitric oxide synthase
ERK1/2	extracellular signal-regulated kinase
GPR1	G protein coupled receptor 1
HLA-DR	human leukocyte antigen-DR isotype
HMW	high molecular weight
HNF1 β	hepatocyte nuclear factor-1 β
HNF4 α	hepatocyte nuclear factor-4 α
HOMA-IR	homeostatic model assessment for insulin resistance
HTN	hypertension
IGF1	insulin-like growth factor 1
JAK	Janus kinase
LH	luteinizing hormone
MAPK	mitogen-activated protein kinase
NAD	nicotinamide adenine dinucleotide
NF- κ B	nuclear factor κ B
NPY	neuropeptide Y
OBR	obstructive sleep apnea syndrome
OSAHS	obstructive sleep apnea hypopnea syndrome
OSAS	obstructive sleep apnea syndrome
PI3K	phosphoinositide 3-kinase
POMC	pro-opiomelanocortin
PPAR α	peroxisome proliferator-activated receptor- α
REM	rapid eye movement
STAT	signal transducer and activator of transcription
TNF- α	tumor necrosis factor- α

References

1. Lehr, S.; Hartwig, S.; Sell, H. Adipokines: A treasure trove for the discovery of biomarkers for metabolic disorders. *Proteom. Clin. Appl.* **2012**, *6*, 91–101. [CrossRef] [PubMed]
2. Funcke, J.B.; Scherer, P.E. Beyond adiponectin and leptin: Adipose tissue-derived mediators of inter-organ communication. *J. Lipid Res.* **2019**, *60*, 1648–1684. [CrossRef]
3. Grandner, M.A. Sleep, Health, and Society. *Sleep Med. Clin.* **2017**, *12*, 1–22. [CrossRef]
4. Ruan, H.; Xun, P.; Cai, W.; He, K.; Tang, Q. Habitual Sleep Duration and Risk of Childhood Obesity: Systematic Review and Dose-response Meta-analysis of Prospective Cohort Studies. *Sci. Rep.* **2015**, *5*, 16160. [CrossRef]
5. Spiegel, K.; Tasali, E.; Leproult, R.; Van Cauter, E. Effects of poor and short sleep on glucose metabolism and obesity risk. *Nat. Rev. Endocrinol.* **2009**, *5*, 253–261. [CrossRef] [PubMed]
6. Cappuccio, F.P.; Miller, M.A. Sleep and Cardio-Metabolic Disease. *Curr. Cardiol. Rep.* **2017**, *19*, 110. [CrossRef]
7. Primack, C. Obesity and Sleep. *Nurs. Clin. N. Am.* **2021**, *56*, 565–572. [CrossRef] [PubMed]

8. Ouchi, N.; Parker, J.L.; Lugus, J.J.; Walsh, K. Adipokines in inflammation and metabolic disease. *Nat. Rev. Immunol.* **2011**, *11*, 85–97. [CrossRef]
9. Kovács, D.; Fazekas, F.; Oláh, A.; Törőcsik, D. Adipokines in the Skin and in Dermatological Diseases. *Int. J. Mol. Sci.* **2020**, *21*, 9048. [CrossRef]
10. Burhans, M.S.; Hagman, D.K.; Kuzma, J.N.; Schmidt, K.A.; Kratz, M. Contribution of Adipose Tissue Inflammation to the Development of Type 2 Diabetes Mellitus. *Compr. Physiol.* **2018**, *9*, 1–58. [CrossRef]
11. Azamar-Llamas, D.; Hernández-Molina, G.; Ramos-Avalos, B.; Furuzawa-Carballeda, J. Adipokine Contribution to the Pathogenesis of Osteoarthritis. *Mediat. Inflamm.* **2017**, *2017*, 5468023. [CrossRef] [PubMed]
12. Zhang, F.; Chen, Y.; Heiman, M.; Dimarchi, R. Leptin: Structure, function and biology. *Vitam. Horm.* **2005**, *71*, 345–372. [CrossRef] [PubMed]
13. Park, H.K.; Ahima, R.S. Physiology of leptin: Energy homeostasis, neuroendocrine function and metabolism. *Metabolism* **2015**, *64*, 24–34. [CrossRef]
14. Li, L.; Fu, J.; Yu, X.T.; Li, G.; Xu, L.; Yin, J.; Cheng, H.; Hou, D.; Zhao, X.; Gao, S.; et al. Sleep Duration and Cardiometabolic Risk Among Chinese School-aged Children: Do Adipokines Play a Mediating Role? *Sleep* **2017**, *40*, zsx042. [CrossRef] [PubMed]
15. Boeke, C.E.; Storfer-Isser, A.; Redline, S.; Taveras, E.M. Childhood sleep duration and quality in relation to leptin concentration in two cohort studies. *Sleep* **2014**, *37*, 613–620. [CrossRef]
16. Taheri, S.; Lin, L.; Austin, D.; Young, T.; Mignot, E. Short sleep duration is associated with reduced leptin, elevated ghrelin, and increased body mass index. *PLoS Med.* **2004**, *1*, e62. [CrossRef]
17. Stern, J.H.; Grant, A.S.; Thomson, C.A.; Tinker, L.; Hale, L.; Brennan, K.M.; Woods, N.F.; Chen, Z. Short sleep duration is associated with decreased serum leptin, increased energy intake and decreased diet quality in postmenopausal women. *Obesity* **2014**, *22*, E55–E61. [CrossRef]
18. Chaput, J.P.; Després, J.P.; Bouchard, C.; Tremblay, A. Short sleep duration is associated with reduced leptin levels and increased adiposity: Results from the Quebec family study. *Obesity* **2007**, *15*, 253–261. [CrossRef]
19. Hayes, A.L.; Xu, F.; Babineau, D.; Patel, S.R. Sleep duration and circulating adipokine levels. *Sleep* **2011**, *34*, 147–152. [CrossRef]
20. Mullington, J.M.; Chan, J.L.; Van Dongen, H.P.; Szuba, M.P.; Samaras, J.; Price, N.J.; Meier-Ewert, H.K.; Dinges, D.F.; Mantzoros, C.S. Sleep loss reduces diurnal rhythm amplitude of leptin in healthy men. *J. Neuroendocrinol.* **2003**, *15*, 851–854. [CrossRef]
21. Spiegel, K.; Tasali, E.; Penev, P.; Van Cauter, E. Brief communication: Sleep curtailment in healthy young men is associated with decreased leptin levels, elevated ghrelin levels, and increased hunger and appetite. *Ann. Intern. Med.* **2004**, *141*, 846–850. [CrossRef]
22. Omisade, A.; Buxton, O.M.; Rusak, B. Impact of a acute sleep restriction on cortisol and leptin levels in young women. *Physiol. Behav.* **2010**, *99*, 651–656. [CrossRef]
23. Simpson, N.S.; Banks, S.; Dinges, D.F. Sleep restriction is associated with increased morning plasma leptin concentrations, especially in women. *Biol. Res. Nurs.* **2010**, *12*, 47–53. [CrossRef]
24. Pejovic, S.; Vgontzas, A.N.; Basta, M.; Tsaousoglou, M.; Zoumakis, E.; Vgontzas, A.; Bixler, E.O.; Chrousos, G.P. Leptin and hunger levels in young healthy adults after one night of sleep loss. *J. Sleep Res.* **2010**, *19*, 552–558. [CrossRef] [PubMed]
25. Reynolds, A.C.; Dorrian, J.; Liu, P.Y.; Van Dongen, H.P.; Wittert, G.A.; Harmer, L.J.; Banks, S. Impact of five nights of sleep restriction on glucose metabolism, leptin and testosterone in young adult men. *PLoS ONE* **2012**, *7*, e41218. [CrossRef]
26. Hirota, T.; Morioka, T.; Yoda, K.; Toi, N.; Hayashi, N.; Maruo, S.; Yamazaki, Y.; Kurajoh, M.; Motoyama, K.; Yamada, S.; et al. Positive association of plasma leptin with sleep quality in obese type 2 diabetes patients. *J. Diabetes Investig.* **2018**, *9*, 1100–1105. [CrossRef] [PubMed]
27. Lindberg, N.; Virkkunen, M.; Tani, P.; Appelberg, B.; Rimón, R.; Porkka-Heiskanen, T. Growth hormone-insulin-like growth factor-1 axis, leptin and sleep in anorexia nervosa patients. *Neuropsychobiology* **2003**, *47*, 78–85. [CrossRef]
28. Littman, A.J.; Vitiello, M.V.; Foster-Schubert, K.; Ulrich, C.M.; Tworoger, S.S.; Potter, J.D.; Weigle, D.S.; McTiernan, A. Sleep, ghrelin, leptin and changes in body weight during a 1-year moderate-intensity physical activity intervention. *Int J. Obes.* **2007**, *31*, 466–475. [CrossRef]
29. Ciftci, T.U.; Kokturk, O.; Bukan, N.; Bilgihan, A. Leptin and ghrelin levels in patients with obstructive sleep apnea syndrome. *Respiration* **2005**, *72*, 395–401. [CrossRef]
30. Harsch, I.A.; Koebnick, C.; Wallaschofski, H.; Schahin, S.P.; Hahn, E.G.; Ficker, J.H.; Lohmann, T.; Konturek, P.C. Resistin levels in patients with obstructive sleep apnoea syndrome—the link to subclinical inflammation? *Med. Sci. Monit.* **2004**, *10*, CR510–CR515.
31. Radić, R.; Nikolić, V.; Karner, I.; Kosović, P.; Kurbel, S.; Selthofer, R.; Curković, M. Circadian rhythm of blood leptin level in obese and non-obese people. *Coll. Antropol.* **2003**, *27*, 555–561. [PubMed]
32. Scheer, F.A.; Hilton, M.F.; Mantzoros, C.S.; Shea, S.A. Adverse metabolic and cardiovascular consequences of circadian misalignment. *Proc. Natl. Acad. Sci. USA* **2009**, *106*, 4453–4458. [CrossRef] [PubMed]
33. Mota, M.C.; Waterhouse, J.; De-Souza, D.A.; Rossato, L.T.; Silva, C.M.; Araujo, M.B.; Tufik, S.; De Mello, M.T.; Crispim, C.A. Sleep pattern is associated with adipokine levels and nutritional markers in resident physicians. *Chronobiol. Int.* **2014**, *31*, 1130–1138. [CrossRef]
34. Tankersley, C.; Kleeberger, S.; Russ, B.; Schwartz, A.; Smith, P. Modified control of breathing in genetically obese (ob/ob) mice. *J. Appl. Physiol.* **1996**, *81*, 716–723. [CrossRef] [PubMed]

35. Laposky, A.D.; Shelton, J.; Bass, J.; Dugovic, C.; Perrino, N.; Turek, F.W. Altered sleep regulation in leptin-deficient mice. *Am. J. Physiol. Regul. Integr. Comp. Physiol.* **2006**, *290*, R894–R903. [CrossRef]
36. Laposky, A.D.; Bradley, M.A.; Williams, D.L.; Bass, J.; Turek, F.W. Sleep-wake regulation is altered in leptin-resistant (db/db) genetically obese and diabetic mice. *Am. J. Physiol. Regul. Integr. Comp. Physiol.* **2008**, *295*, R2059–R2066. [CrossRef]
37. O'Donnell, C.P.; Schaub, C.D.; Haines, A.S.; Berkowitz, D.E.; Tankersley, C.G.; Schwartz, A.R.; Smith, P.L. Leptin prevents respiratory depression in obesity. *Am. J. Respir. Crit. Care Med.* **1999**, *159*, 1477–1484. [CrossRef]
38. Yao, Q.; Pho, H.; Kirkness, J.; Ladenheim, E.E.; Bi, S.; Moran, T.H.; Fuller, D.D.; Schwartz, A.R.; Polotsky, V.Y. Localizing Effects of Leptin on Upper Airway and Respiratory Control during Sleep. *Sleep* **2016**, *39*, 1097–1106. [CrossRef]
39. Berger, S.; Pho, H.; Fleury-Curado, T.; Bevans-Fonti, S.; Younas, H.; Shin, M.K.; Jun, J.C.; Anokye-Danso, F.; Ahima, R.S.; Enquist, L.W.; et al. Intranasal Leptin Relieves Sleep-disordered Breathing in Mice with Diet-induced Obesity. *Am. J. Respir. Crit. Care Med.* **2019**, *199*, 773–783. [CrossRef]
40. Shapiro, S.D.; Chin, C.H.; Kirkness, J.P.; McGinley, B.M.; Patil, S.P.; Polotsky, V.Y.; Biselli, P.J.; Smith, P.L.; Schneider, H.; Schwartz, A.R. Leptin and the control of pharyngeal patency during sleep in severe obesity. *J. Appl. Physiol.* **2014**, *116*, 1334–1341. [CrossRef]
41. Wang, Z.V.; Scherer, P.E. Adiponectin, the past two decades. *J. Mol. Cell Biol.* **2016**, *8*, 93–100. [CrossRef] [PubMed]
42. Hitze, B.; Bosity-Westphal, A.; Bielfeldt, F.; Settler, U.; Plachta-Danielzik, S.; Pfeuffer, M.; Schrezenmeier, J.; Mönig, H.; Müller, M.J. Determinants and impact of sleep duration in children and adolescents: Data of the Kiel Obesity Prevention Study. *Eur. J. Clin. Nutr.* **2009**, *63*, 739–746. [CrossRef] [PubMed]
43. Al-Disi, D.; Al-Daghri, N.; Khanam, L.; Al-Othman, A.; Al-Saif, M.; Sabico, S.; Chrousos, G. Subjective sleep duration and quality influence diet composition and circulating adipocytokines and ghrelin levels in teen-age girls. *Endocr. J.* **2010**, *57*, 915–923. [CrossRef]
44. Shea, S.A.; Hilton, M.F.; Orlova, C.; Ayers, R.T.; Mantzoros, C.S. Independent circadian and sleep/wake regulation of adipokines and glucose in humans. *J. Clin. Endocrinol. Metab.* **2005**, *90*, 2537–2544. [CrossRef] [PubMed]
45. Kotani, K.; Sakane, N.; Saiga, K.; Kato, M.; Ishida, K.; Kato, Y.; Kurozawa, Y. Serum adiponectin levels and lifestyle factors in Japanese men. *Heart Vessel.* **2007**, *22*, 291–296. [CrossRef]
46. Bingol, Z.; Karaayvaz, E.B.; Telci, A.; Bilge, A.K.; Okumus, G.; Kiyan, E. Leptin and adiponectin levels in obstructive sleep apnea phenotypes. *Biomark. Med.* **2019**, *13*, 865–874. [CrossRef]
47. Magnusdottir, S.; Thomas, R.J.; Hilmisson, H. Can improvements in sleep quality positively affect serum adiponectin-levels in patients with obstructive sleep apnea? *Sleep Med.* **2021**, *84*, 324–333. [CrossRef]
48. Oliveira, R.F.; Daniele, T.M.D.C.; Façanha, C.F.S.; Forti, A.C.E.; Bruin, P.F.C.; Bruin, V.M.S. Adiponectin levels and sleep deprivation in patients with endocrine metabolic disorders. *Rev. Assoc. Med. Bras.* **2018**, *64*, 1122–1128. [CrossRef]
49. De Mattos, A.B.; Pinto, M.J.; Oliveira, C.; Biz, C.; Ribeiro, E.B.; Do Nascimento, C.M.; Andersen, M.L.; Tufik, S.; Oyama, L.M. Dietary fish oil did not prevent sleep deprived rats from a reduction in adipose tissue adiponectin gene expression. *Lipids Health Dis.* **2008**, *7*, 43. [CrossRef]
50. Khalyfa, A.; Mutskov, V.; Carreras, A.; Khalyfa, A.A.; Hakim, F.; Gozal, D. Sleep fragmentation during late gestation induces metabolic perturbations and epigenetic changes in adiponectin gene expression in male adult offspring mice. *Diabetes* **2014**, *63*, 3230–3241. [CrossRef]
51. Helfer, G.; Wu, Q.F. Chemerin: A multifaceted adipokine involved in metabolic disorders. *J. Endocrinol.* **2018**, *238*, R79–R94. [CrossRef] [PubMed]
52. Daxer, J.; Hertztrich, T.; Zhao, Y.Y.; Vogel, M.; Hiemisch, A.; Scheuermann, K.; Körner, A.; Kratzsch, J.; Kiess, W.; Quante, M. Nocturnal levels of chemerin and progranulin in adolescents: Influence of sex, body mass index, glucose metabolism and sleep. *J. Pediatr. Endocrinol. Metab.* **2017**, *30*, 57–61. [CrossRef] [PubMed]
53. Feng, X.; Li, P.; Zhou, C.; Jia, X.; Kang, J. Elevated levels of serum chemerin in patients with obstructive sleep apnea syndrome. *Biomarkers* **2012**, *17*, 248–253. [CrossRef] [PubMed]
54. Xu, T.; Lin, Y.; Sun, S.; Zhang, Q. Changes in four plasma adipokines before and after sleep in OSAS patients. *Clin. Respir. J.* **2017**, *11*, 968–974. [CrossRef] [PubMed]
55. Weiner, J.; Zieger, K.; Pippel, J.; Heiker, J.T. Molecular Mechanisms of Vaspin Action-From Adipose Tissue to Skin and Bone, from Blood Vessels to the Brain. *Adv. Exp. Med. Biol.* **2019**, *1111*, 159–188. [CrossRef] [PubMed]
56. Kiskac, M.; Zorlu, M.; Akkoyunlu, M.E.; Kilic, E.; Karatoprak, C.; Cakirca, M.; Yavuz, E.; Ardic, C.; Camli, A.A.; Cikrikcioglu, M.; et al. Vaspin and lipocalin-2 levels in severe obstructive sleep apnea. *J. Thorac. Dis.* **2014**, *6*, 720–725. [CrossRef] [PubMed]
57. Pan, Z.; Zhuang, X.; Li, X.; Huang, S.; Zhang, L.; Lou, F.; Chen, S.; Ni, Y. Significance of vaspin in obstructive sleep apnea-hypopnea syndrome. *Exp. Ther. Med.* **2016**, *11*, 841–845. [CrossRef] [PubMed]
58. Zhuang, X.; Ni, Y.; Jiang, D.; Pu, Y.; Liu, X.; Chen, S.; Sun, F.; Sun, A.; Pan, Z. Vaspin as a Risk Factor of Insulin Resistance in Obstructive Sleep Apnea-Hypopnea Syndrome in an Animal Model. *Clin. Lab.* **2015**, *61*, 883–889. [CrossRef]
59. Tan, B.K.; Adya, R.; Randeve, H.S. Omentin: A novel link between inflammation, diabesity, and cardiovascular disease. *Trends Cardiovasc. Med.* **2010**, *20*, 143–148. [CrossRef]
60. Watanabe, T.; Watanabe-Kominato, K.; Takahashi, Y.; Kojima, M.; Watanabe, R. Adipose Tissue-Derived Omentin-1 Function and Regulation. *Compr. Physiol.* **2017**, *7*, 765–781. [CrossRef]
61. Zirlik, S.; Hildner, K.M.; Targosz, A.; Neurath, M.F.; Fuchs, F.S.; Brzozowski, T.; Konturek, P.C. Melatonin and omentin: Influence factors in the obstructive sleep apnoea syndrome? *J. Physiol. Pharmacol.* **2013**, *64*, 353–360.

62. Kurt, O.K.; Tosun, M.; Alcelik, A.; Yilmaz, B.; Talay, F. Serum omentin levels in patients with obstructive sleep apnea. *Sleep Breath.* **2014**, *18*, 391–395. [CrossRef]
63. Wang, Q.; Feng, X.; Zhou, C.; Li, P.; Kang, J. Decreased levels of serum omentin-1 in patients with obstructive sleep apnoea syndrome. *Ann. Clin. Biochem.* **2013**, *50*, 230–235. [CrossRef]
64. Uygur, F.; Tanrıverdi, H.; Can, M.; Erboyl, F.; Altınsoy, B.; Atalay, F.; Ornek, T.; Damar, M.; Kokturk, F.; Tor, M. Association between continuous positive airway pressure and circulating omentin levels in patients with obstructive sleep apnoea. *Sleep Breath.* **2016**, *20*, 939–945. [CrossRef]
65. Zhang, D.M.; Pang, X.L.; Huang, R.; Gong, F.Y.; Zhong, X.; Xiao, Y. Adiponectin, Omentin, Ghrelin, and Visfatin Levels in Obese Patients with Severe Obstructive Sleep Apnea. *Biomed. Res. Int.* **2018**, *2018*, 3410135. [CrossRef] [PubMed]
66. Zhou, Y.; Zhang, B.; Hao, C.; Huang, X.; Li, X.; Huang, Y.; Luo, Z. Omentin-A Novel Adipokine in Respiratory Diseases. *Int. J. Mol. Sci.* **2017**, *19*, 73. [CrossRef] [PubMed]
67. Saggi-Rosa, P.; Oliveira, C.S.; Giuffrida, F.M.; Reis, A.F. Visfatin, glucose metabolism and vascular disease: A review of evidence. *Diabetol. Metab. Syndr.* **2010**, *2*, 21. [CrossRef] [PubMed]
68. Dahmen, N.; Manderscheid, N.; Helfrich, J.; Musholt, P.B.; Forst, T.; Pfützner, A.; Engel, A. Elevated peripheral visfatin levels in narcoleptic patients. *PLoS ONE* **2008**, *3*, e2980. [CrossRef]
69. Trakada, G.; Steiropoulos, P.; Nena, E.; Gkioka, T.; Kouliatsis, G.; Pataka, A.; Sotiriou, I.; Anevlaivis, S.; Papanas, N.; Bouros, D. Plasma visfatin levels in severe obstructive sleep apnea-hypopnea syndrome. *Sleep Breath.* **2009**, *13*, 349–355. [CrossRef]
70. Benedict, C.; Shostak, A.; Lange, T.; Brooks, S.J.; Schiöth, H.B.; Schultes, B.; Born, J.; Oster, H.; Hallschmid, M. Diurnal rhythm of circulating nicotinamide phosphoribosyltransferase (Nampt/visfatin/PBEF): Impact of sleep loss and relation to glucose metabolism. *J. Clin. Endocrinol. Metab.* **2012**, *97*, E218–E222. [CrossRef]



Article

mTOR Knockdown in the Infralimbic Cortex Evokes A Depressive-like State in Mouse

Emilio Garro-Martínez ^{1,2,3,†}, Maria Neus Fullana ^{1,4,5}, Eva Florensa-Zanuy ^{1,2,3}, Julia Senserrich ^{1,2,3}, Verónica Paz ^{1,4,5}, Esther Ruiz-Bronchal ^{1,4,5}, Albert Adell ^{1,2}, Elena Castro ^{1,2,3}, Álvaro Díaz ^{1,2,3}, Ángel Pazos ^{1,2,3}, Analía Bortolozzi ^{1,4,5} and Fuencisla Pilar-Cuéllar ^{1,2,3,*}

- ¹ Centro de Investigación Biomédica en Red de Salud Mental (CIBERSAM), Instituto de Salud Carlos III, 28029 Madrid, Spain; egamarrone@gmail.com (E.G.-M.); mneusfl@gmail.com (M.N.F.); florensa@unican.es (E.F.-Z.); senserrich@unican.es (J.S.); veronica.paz@iibb.csic.es (V.P.); esther.ruiz@iibb.csic.es (E.R.-B.); adella@unican.es (A.A.); castroe@unican.es (E.C.); diazma@unican.es (Á.D.); pazosa@unican.es (Á.P.); analia.bortolozzi@iibb.csic.es (A.B.)
 - ² Instituto de Biomedicina y Biotecnología de Cantabria (IBBTec), Universidad de Cantabria-CSIC-SODERCAN, 39011 Santander, Spain
 - ³ Departamento de Fisiología y Farmacología, Universidad de Cantabria, 39011 Santander, Spain
 - ⁴ Departamento de Neuroscience and Experimental Therapeutics, Instituto de Investigaciones Biomédicas de Barcelona (IIBB-CSIC), 08036 Barcelona, Spain
 - ⁵ Systems Neuropharmacology Group, Instituto de Investigaciones Biomédicas August Pi i Sunyer (IDIBAPS), 08036 Barcelona, Spain
- * Correspondence: pilarmf@unican.es; Tel.: +34-942-206860
† Present address: Emilio Garro-Martínez, Department of Integrative Medical Biology (IMB), Umeå Universitet, 901 87 Umeå, Sweden.

Citation: Garro-Martínez, E.; Fullana, M.N.; Florensa-Zanuy, E.; Senserrich, J.; Paz, V.; Ruiz-Bronchal, E.; Adell, A.; Castro, E.; Díaz, Á.; Pazos, Á.; et al. mTOR Knockdown in the Infralimbic Cortex Evokes A Depressive-like State in Mouse. *Int. J. Mol. Sci.* **2021**, *22*, 8671. <https://doi.org/10.3390/ijms22168671>

Academic Editor: Masaru Tanaka

Received: 14 July 2021

Accepted: 9 August 2021

Published: 12 August 2021

Publisher's Note: MDPI stays neutral with regard to jurisdictional claims in published maps and institutional affiliations.



Copyright: © 2021 by the authors. Licensee MDPI, Basel, Switzerland. This article is an open access article distributed under the terms and conditions of the Creative Commons Attribution (CC BY) license (<https://creativecommons.org/licenses/by/4.0/>).

Abstract: Fast and sustained antidepressant effects of ketamine identified the mammalian target of rapamycin (mTOR) signaling pathway as the main modulator of its antidepressant effects. Thus, mTOR signaling has become integral for the preclinical evaluation of novel compounds to treat depression. However, causality between mTOR and depression has yet to be determined. To address this, we knocked down mTOR expression in mice using an acute intracerebral infusion of small interfering RNAs (siRNA) in the infralimbic (IL) or prelimbic (PrL) cortices of the medial prefrontal cortex (mPFC), and evaluated depressive- and anxious-like behaviors. mTOR knockdown in IL, but not PrL, cortex produced a robust depressive-like phenotype in mice, as assessed in the forced swimming test (FST) and the tail suspension test (TST). This phenotype was associated with significant reductions of mTOR mRNA and protein levels 48 h post-infusion. In parallel, decreased brain-derived neurotrophic factor (BDNF) expression was found bilaterally in both IL and PrL cortices along with a dysregulation of serotonin (5-HT) and glutamate (Glu) release in the dorsal raphe nucleus (DRN). Overall, our results demonstrate causality between mTOR expression in the IL cortex and depressive-like behaviors, but not in anxiety.

Keywords: mTOR; infralimbic cortex; behavioral despair; BDNF; neurotransmitter

1. Introduction

Major depressive disorder (MDD) is a chronic, recurrent, and multifactorial psychiatric disorder that places the subject's life at risk and has become the leading cause of disability worldwide in terms of disease [1]. MDD is characterized by a series of physiological, psychological, and behavioral symptoms such as depressed mood, sleep or appetite disturbances, loss of interest and pleasure, or the impairment of executive functions, among others.

As the neurobiological basis of this pathology is still unknown, several hypotheses have been proposed to date. One of the most relevant is the neurotrophic/neuroplastic hypothesis of depression, which postulates that a reduction in neurotrophic factors (such

as the brain-derived neurotrophic factor, BDNF), in brain areas such as the hippocampus and the prefrontal cortex, underlies the neuronal atrophy associated with this disease in preclinical [2–4] and clinical studies [5,6]. In addition, increased hippocampal BDNF levels were associated with antidepressant response in human studies [5], as well as in preclinical studies after chronic treatment with classic antidepressant drugs [7–13], or after acute treatment using fast-acting antidepressants such as ketamine [14–18].

The fast antidepressant effect of ketamine, an *N*-methyl-D-aspartate (NMDA) receptor antagonist, has been attributed to the activation of the mammalian target of rapamycin (mTOR) signaling pathway in rat [14,19]. mTOR is a serine/threonine-protein kinase that was first described in yeast as the pharmacological target of rapamycin [20]. In mammals, there are two different complexes, mTORC1 and mTORC2 [21], which control various aspects of cell physiology. In the central nervous system, the activation of mTORC1 triggers the phosphorylation of several effectors such as the ribosomal protein S6 kinase 1 (p70S6K), or the eukaryotic translation initiation factor 4E-binding protein (4E-BP1) [22], inducing protein translation. These proteins are located in the neuronal soma and dendrites, specifically in the synapses, where they colocalize with the postsynaptic density protein-95 (PSD-95), suggesting a postsynaptic location of the pathway [23]. Following activation of the mTOR pathway, there is an increased synthesis of proteins such as PSD-95, the GluA1 subunit of the AMPA receptor, and presynaptic proteins such as synapsin 1 or the activity-regulated cytoskeleton-associated protein (Arc) [14,24,25]. These proteins participate in synaptic plasticity processes such as the formation, maturation, and function of new dendritic spines [14], memory processes [22], or long-term potentiation (LTP) [23,26], which are impaired in MDD.

Mental disorders are defined as “connectopathies” with a complex pathological mechanism at the level of circuits and their communication [27]. Neuroimaging studies in MDD patients show functional and structural connectivity disruptions in the cingulate cortex, the hippocampus, and the prefrontal cortex, among others [28,29]. The ventral anterior cingulate cortex (vACC, Brodman area 25, Cg25) has a special interest since clinical studies reported functional hyperactivity of this area in MDD patients [28–30]. Likewise, a moderate small interfering RNAs (siRNA)-induced reduction of astrocytic GLAST and GLT-1 expression in the mouse infralimbic cortex (IL, rodent counterpart to human vACC), markedly increased local glutamatergic neurotransmission and evoked a depressive-like phenotype [31,32]. Moreover, different preclinical studies support the importance of the IL cortex in the antidepressant-like effects induced by deep brain stimulation (DBS) [33–36], (2*R*,6*R*)-hydroxynorketamine [37], ketamine, or optogenetic stimulation [38]. The activation of the IL cortex reverses changes in the dorsal raphe nucleus (DRN) of animals subjected to the chronic social defeat depression model [34], reinforcing the critical role of this brain area and its outputs to the midbrain in the regulation of emotion and stress responses.

Previous studies have reported the downregulation of the mTOR signaling pathway in postmortem human brain samples from subjects with MDD [39], as well as in PFC, hippocampus, and amygdala of several animal models of depression including the olfactory bulbectomy, chronic unpredictable stress (CUS), and chronic corticosterone exposure [40–44]. In order to examine the role of the mTOR pathway in the IL cortex as a neurobiological substrate in MDD, we evaluated in this study the effects of the mTOR knockdown in mouse IL cortex on the anxious- and depressive-like behavior, the expression of synaptic plasticity markers as the brain-derived neurotrophic factor (BDNF) using *in situ* hybridization, and used *in vivo* microdialysis to explore the evoked adaptive changes in cortico-subcortical circuits leading to the emergence of a depressive-like phenotype.

2. Results

2.1. Acute Unilateral mTOR Silencing in the Infralimbic Cortex Induces a Depressive- but Not Anxiety-like Behavior

We examined the role of mTOR knockdown in mPFC on depressive- and anxiety-like behavior by a single unilateral intracerebral infusion selectively into the IL or PrL cortices. mTOR-siRNA infusion (40 µg/µL siRNA pool) into the IL cortex evoked a

depressive-like behavior measured in the FST and TST, 24 and 48 h post-infusion, respectively (Figure 1A,B). The immobility times were significantly higher compared to the control groups in the FST (mTOR-siRNAs: 173.0 ± 6.2 s vs. aCSF: 149.2 ± 5.2 s, $p < 0.01$), and in the TST (mTOR-siRNAs: 187.7 ± 6.3 s vs. aCSF: 155.2 ± 7.4 s, $p < 0.01$). The observed increase in immobility time was not due to an overall reduction in locomotor activity, as the total distance traveled in the open field was similar between both groups (Figure 1C). In addition, we evaluated the total time spent within the central area of the arena to preliminary study putative anxiety-related behaviors using the open-field test paradigm. No differences were observed between the groups (Figure 1D).

The infusion of mTOR-siRNAs in the PrL cortex (Figure 1E–H) did not produce changes in any of the tests used to evaluate depressive- or anxiety-like behaviors. Likewise, a comparable behavioral profile was observed after intra-IL NS-siRNA infusion compared to control mice receiving intra-IL aCSF (Figure S1).

Thus, the unilateral acute infusion of mTOR-siRNA in the IL cortex induces a depressive-like behavior, as evidenced by the increased behavioral despair.

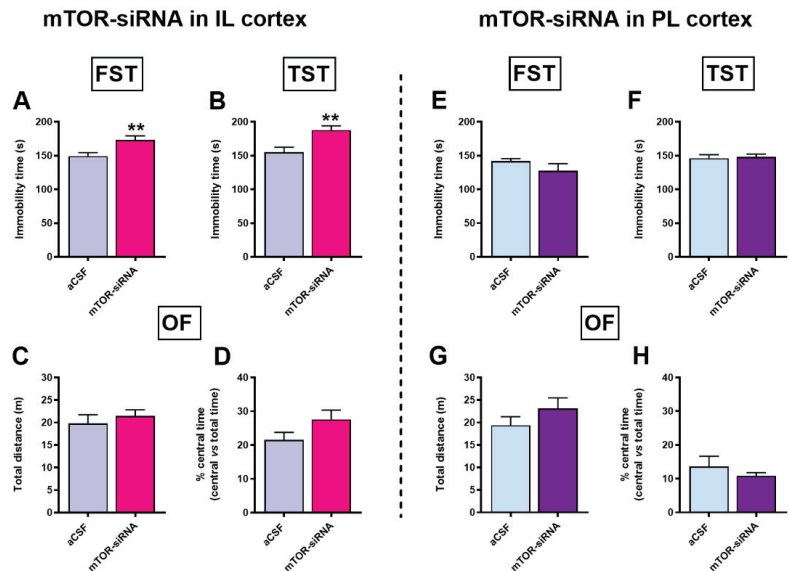


Figure 1. Acute mTOR knockdown in the infralimbic, but not in the prelimbic cortex, induces a depressive-, but not anxious-like behavior. Depressive-like responses were examined using (A) forced swimming test and (B) tail suspension test, respectively, 24 h and 48 h after unilateral mTOR-siRNA infusion in the IL cortex. No changes were observed in (C) locomotion or (D) anxiety-related behavior in intra-IL mTOR knockdown mice evaluated in the open-field test 24 h after siRNA infusion. (E–H) No behavioral changes were observed when mTOR was knocked down in the PrL cortex. Results are presented as mean \pm S.E.M. Unpaired Student's *t*-test, ** $p < 0.01$. $n = 7$ –9 animals per group. aCSF: artificial cerebrospinal fluid; IL: infralimbic; PrL: prelimbic; FST: forced swimming test; TST: tail suspension test; OF: open-field test; siRNA: small interfering RNA.

2.2. Intra-Infralimbic mTOR-siRNA Infusion Reduces mTOR mRNA Expression and Protein Levels

The mTOR downregulation was confirmed using *in situ* hybridization (Figure 2A–E) and immunohistochemistry (Figure 2F–W) procedures. mTOR-siRNA infusion in the IL cortex significantly reduced mTOR mRNA expression in the IL (two-tailed unpaired *t*-test, $t_8 = 2.315$; $p < 0.05$) (Figure 2A,E), but not in the PrL cortex (Figure 2B,E).

In parallel, we found that intra-IL mTOR-siRNA infusion induced a significant reduction of mTOR protein levels locally in the IL cortex (Figure 2F,L–O) compared to control

mice (Figure 2H–K) (two-tailed unpaired *t*-test, $t_8 = 2.524$; $p < 0.05$), without affecting mTOR expression in the PrL cortex (Figure 2G,P–W).

The unilateral infusion of mTOR-siRNA in the IL cortex induces a reduction in mTOR mRNA and protein levels in the ipsilateral side 48 h after siRNA infusion.

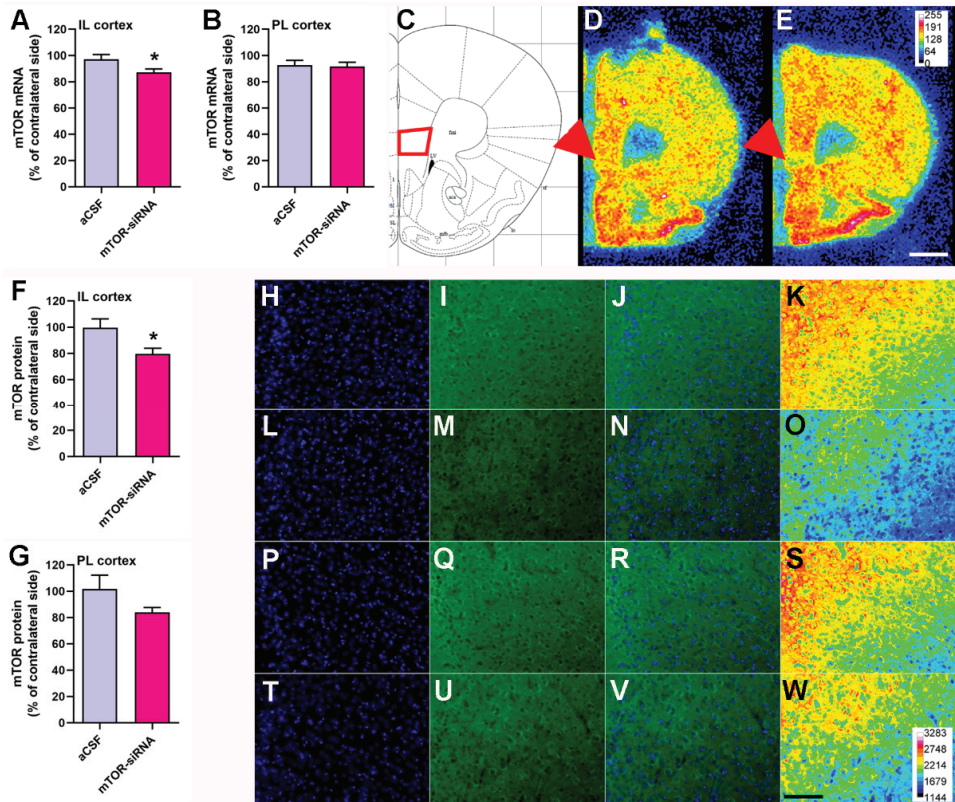


Figure 2. mTOR downregulation after intracerebral administration of siRNAs targeting mTOR in the infralimbic cortex (C). mTOR levels in (A,F), the IL, and (B,G) the PrL cortex were evaluated by (A–E) in situ hybridization, and (F–W) mTOR protein expression by immunofluorescence, after unilateral infusion into the IL cortex. Data are expressed as mean \pm S.E.M. Unpaired Student’s *t*-test, * $p < 0.05$. $n = 4$ –5 animals per group. Representative coronal brain sections containing IL cortex showing mTOR mRNA expression in (D) aCSF-infused and (E) mTOR-siRNA-infused mice as assessed by in situ hybridization. Representative immunofluorescent images of the mTOR protein levels in (H–K) the IL and (P–S) the PrL cortex of vehicle-infused mice, and in (L–O) the IL and (T–W) the PrL cortex of mTOR-siRNA-infused mice. Images show (H,L,P,T) DAPI, (I,M,Q,U) mTOR, (J,N,R,V) merged, and (K,O,S,W) heat-map image. Scale bar in E: 1 mm. Scale bar in W: 100 μ m. Heat-map calibration bar in E and W showing the intensity values. aCSF: artificial cerebrospinal fluid; IL: infralimbic; PrL: prelimbic; siRNA: small interfering RNA.

2.3. Reduced BDNF mRNA Expression in Medial Prefrontal Cortex after mTOR Knockdown in Infralimbic Cortex

Given that brain BDNF levels are critical in the neurobiology of MDD, as well as in the antidepressant effects [45,46], we also examined the BDNF expression in the intra-IL mTOR knockdown mice. Moreover, as the mTOR-siRNA was infused in the IL cortex unilaterally, we also considered the brain side as a variable. mTOR knockdown in the IL cortex produced a significant reduction of BDNF mRNA expression in both brain sides (ipsi- and contralateral IL cortices) (Figure 3B,C), and in the ipsilateral PrL cortex (Figure 3B,D) 48 h post-infusion. Two-way ANOVA analyzing the effect of the treatment and the brain

side factors revealed a significant effect of treatment on the BDNF expression in the IL cortex ($F(1,16) = 26.41, p < 0.001$) (Figure 3C), and in the PrL cortex ($F(1,16) = 13.65, p < 0.01$) (Figure 3D).

The unilateral infusion of mTOR-siRNA in the IL cortex induces a bilateral reduction in BDNF mRNA levels in the IL cortex, and in the ipsilateral side in the PrL cortex.

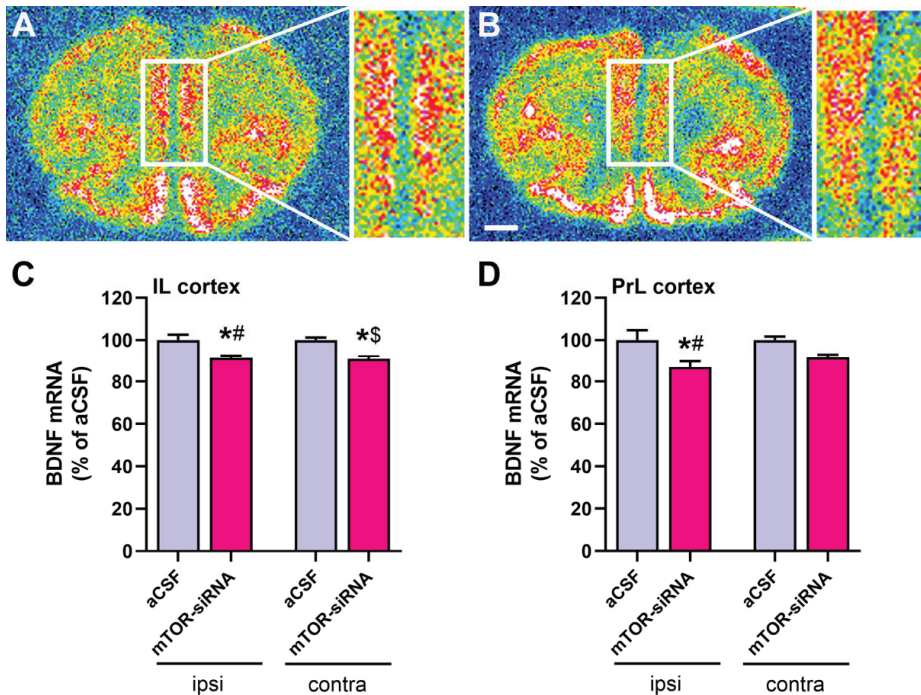


Figure 3. mTOR knockdown in infralimbic cortex reduces BDNF transcription in medial prefrontal cortex. Representative coronal brain sections showing BDNF mRNA expression in (A) aCSF-treated and (B) mTOR-siRNA-treated mice, as assessed by in situ hybridization. Effect of local mTOR-siRNAs infusion in the IL cortex on BDNF mRNA expression in the mPFC: (C) IL and (D) PrL areas. Data are expressed as mean \pm S.E.M. Two-way ANOVA followed by a Bonferroni post hoc test, * $p < 0.05$ compared to their respective aCSF group; # $p < 0.05$ compared to the contralateral aCSF group; \$ $p < 0.05$ compared to the ipsilateral aCSF group. $n = 5$ animals per group. Scale bar: 1 mm. aCSF: artificial cerebrospinal fluid; BDNF: brain-derived neurotrophic factor; contra: contralateral to the infusion site; ipsi: ipsilateral to the infusion site; IL: infralimbic; PrL: prelimbic; siRNA: small interfering RNA.

2.4. Extracellular Serotonin and Glutamate Levels in Dorsal Raphe Nucleus after mTOR Knockdown in Infralimbic Cortex

Glutamatergic projections from the IL cortex regulate the 5-HTergic neuronal activity in the DRN, and alterations of the IL-DRN circuitry function are implicated in depressive-like behaviors [31,38,47]. Therefore, extracellular 5-HT and glutamate levels were assessed in the DRN of mice after acute mTOR knockdown in the IL cortex using in vivo microdialysis procedures. mTOR knockdown in the IL cortex did not alter the extracellular basal levels of 5-HT and glutamate in the DRN compared to control animals (Figure 4A,B). The local administration of the depolarizing agent veratridine (50 μ M) in the DRN revealed opposite effects on presynaptic releasable pools of 5-HT and glutamate since extracellular levels of 5-HT were lower (Figure 4C), while those of glutamate were higher (Figure 4D) in the IL cortex of mTOR knockdown animals compared to control mice. Two-way ANOVA showed a significant effect of time ($F(9,72) = 12.71, p < 0.001$) for 5-HT, whereas significant effects of

mTOR siRNAs ($F(1,8) = 18.57, p < 0.01$), time ($F(9,72) = 8.00, p < 0.001$), and interaction of both factors ($F(9,72) = 2.62, p < 0.05$) were found for glutamate.

The local application of the AMPA receptor antagonist NBQX (100 μM) in the DRN of IL-mTOR silenced mice did not modify the extracellular 5-HT levels in DRN (Figure 4E) while it reduced the DRN glutamate levels (Figure 4F). Two-way ANOVA revealed a significant effect of time ($F(9,72) = 2.33, p < 0.05$) for 5-HT, and a significant effect of mTOR-siRNAs ($F(1,8) = 10.66, p < 0.05$) and the interaction of both factors ($F(9,72) = 3.250, p < 0.01$) for glutamate.

The unilateral infusion of mTOR-siRNA in the IL cortex induces the dysregulation in the serotonergic and glutamatergic neurotransmission in the DRN.

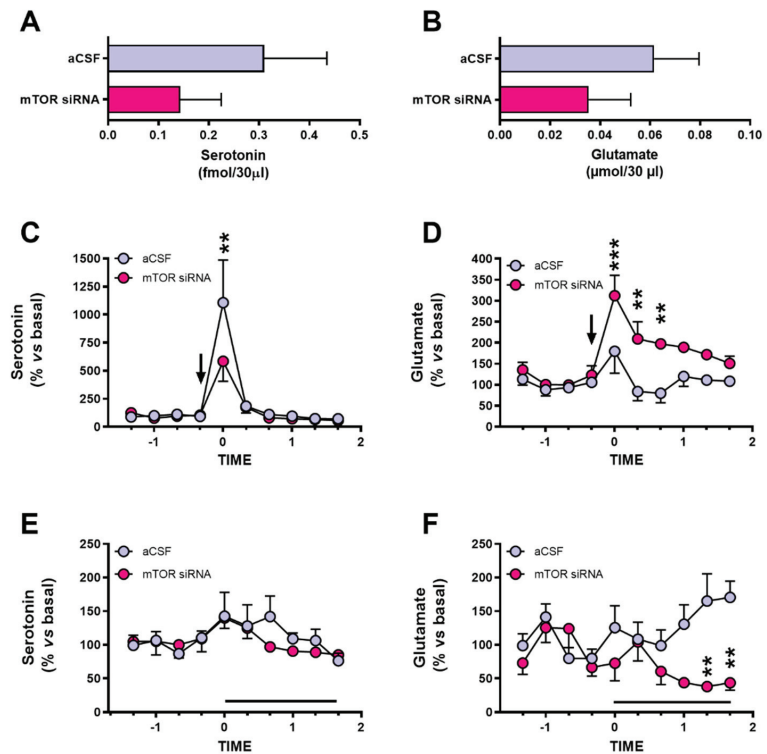


Figure 4. Dysregulation of extracellular serotonin and glutamate neurotransmitters in the dorsal raphe nucleus after acute infralimbic-mTOR knockdown in mice. Baseline extracellular values of (A) serotonin and (B) glutamate in DRN. The effects of local 50 μM veratridine on extracellular (C) serotonin and (D) glutamate levels, and intra-DRN 100 μM NBQX infusion on extracellular (E) 5-HT and (F) glutamate levels in control and mTOR-siRNAs mice. Data are represented as mean \pm SEM. Two-way ANOVA followed by Bonferroni post hoc test (** $p < 0.01$, *** $p < 0.001$). $n = 4$ –5 animals per experimental group. 5-HT: serotonin; aCSF: artificial cerebrospinal fluid; NBQX: 2,3-dihydroxy-6-nitro-7-sulfamoyl-benzo(f)quinoxaline; siRNA: small interfering RNA.

3. Discussion

Herein, we demonstrated that acute mTOR knockdown in the IL cortex, induced by the intracerebral administration of mTOR-siRNA, elicited a depressive-like state in mice, which was maintained for at least 48 h without affecting anxiety-like behavior. The acute mTOR downregulation in the IL cortex leads to reduced BDNF mRNA levels in mPFC, together with impaired 5-HT and glutamate neurotransmission in the DRN, disturbances linked to neuropathophysiology of depression, as reported in preclinical [31,36,48,49] and

clinical [50] studies. Our findings highlight the importance of mTOR signaling in the IL cortex for adequate mPFC-DRN circuit functioning.

In the present mouse model, a single unilateral mTOR-siRNA dose in the IL cortex was sufficient to reduce mTOR expression (mRNA and protein), ultimately inducing a depressive-phenotype, and this is in line with the lower mTOR protein levels found in the mPFC of patients with MDD [39]. In addition, the overexpression of the mTOR negative regulator REDD1 (regulated in development and DNA damage responses-1) in mPFC was associated with depressive-like behavior in rats [41]. Moreover, the long-term oral administration of mTOR inhibitors (i.e., rapamycin) in rodents also induced a depressive-like state characterized by behavioral despair [51,52] and anhedonia [51]. In line with these observations, pilot studies in our lab using subchronic mTOR siRNA infusion showed both behavioral despair and anhedonia in mice (data not shown). However, neither the subchronic [51] nor the acute [51,53,54] systemic administration of rapamycin in rat induced depressive-like effects. It is worth mentioning that some authors reported an antidepressant-like effect of acute systemic rapamycin administration, but this effect was observed in animal models of neurological pathologies as epilepsy [51,54], tuberous sclerosis complex [55], and Parkinson's disease [56]. The behavioral discrepancies between our study and others might be due to the use of a genetic approach (mTOR-siRNA) compared with the pharmacological inhibition of mTOR (rapamycin), and/or the local (infralimbic cortex) versus the systemic administration, respectively. This marked behavioral effect following siRNAs unilateral infusion is in line with previous studies using this genetic approach [31].

We also failed to find any effect of the acute mTOR silencing in the IL cortex when preliminarily analyzing *state* anxiety using the open-field test. This finding contrasts with the anxiety-like behavior elicited by the chronic administration of mTOR inhibitors [52] and the overexpression of the mTOR inhibitor REDD1 in mPFC [41]. Besides, a single prenatal administration of rapamycin in mice induced increased anxiety in the adult offspring [57]. The appearance of anxiety in these studies compared to the lack of effect observed in our study could be due (1) to the systemic administration of mTOR inhibitors (compared to our local knockdown), (2) to the use of a wider battery of behavioral tests (including the elevated plus maze) [41,52], or (3) to the temporal appearance of this behavior, as some authors study the long-term behavioral effect [41,52,57] (compared to our acute studies). Overall, our data and those from previous reports reflect the complex and region-dependent effects of mTOR inhibition in the behavioral readouts, opening a new field of study in the treatment of depressive-related behaviors.

The importance of mTOR in the IL cortex in the neurobiology of depression could be complemented with the fact that the infusion of drugs as ketamine [38] and (2R,6R)-hydroxynorketamine [37] in this area in the rodent brain induce an antidepressant-like effect mediated by mTOR pathway activation. Moreover, this antidepressant-like effect is blocked by rapamycin infusion into the mPFC [14,37,58]. Ketamine administration in patients resistant to conventional antidepressant treatments induces a rapid improvement of depressive symptoms 2 h after administration that is maintained for up to 2 weeks [59–61]. However, preclinical studies indicate a lack of effect of rapamycin on the inhibition of the antidepressant-like effect of ketamine [62]. Moreover, a recent clinical study describes that the administration of rapamycin prolongs the antidepressant effect of ketamine [63], indicating that there is still a lot of work to be done to clarify the role of this signaling pathway in the mechanism of action of fast-acting antidepressant drugs.

The depressive-like behavior present after the acute mTOR-siRNAs infusion into the IL cortex correlates with the downregulation of BDNF expression in both ipsilateral IL and PrL cortices, as well as in the contralateral IL cortex. The BDNF downregulation observed in both the IL and PrL cortices may account for the neuronal network interaction of both areas [64,65]. Interestingly, a recent study reported a similar reduction of BDNF expression after the acute knockdown of the astrocytic glutamate transporter (GLAST/GLT-1) in the IL cortex of mice [31], associated also with a depressive-like phenotype. Several clinical

and preclinical reports point to an impairment in neurotrophic factors, mainly BDNF, as the causal role of the atrophy observed in brain areas as PFC or hippocampus in patients diagnosed with major depression [66]. In this regard, BDNF levels are decreased in the post-mortem PFC samples from depressed patients [6,67,68], and in the PFC and hippocampus of rodent models of depression exposed to different types of stress [3,69].

The mPFC exerts top-down control over several limbic regions and brainstem nuclei, which, in turn, influence different aspects such as cognition and emotion, mental processes compromised in major depressive disorder. The outputs to the DRN are important to modulate the harmful effects of uncontrollable stress [70]. Therefore, the mPFC-DRN connection was analyzed in the present study, determining the extracellular levels of serotonin and glutamate in the DRN by *in vivo* microdialysis after acute mTOR-siRNAs infusion into the IL cortex, in parallel to the depressive-like behavior. Recent studies in depression-like mouse models reported an enhancement of the activity of the glutamatergic output from the IL cortex, leading to the inhibition of the serotonergic neurons in the DRN [31,71,72]. In contrast, our results did not show significant changes in serotonin or glutamate basal levels, in line with previous reports in other animal models of depression in relevant areas as the mPFC [49,73].

After the local infusion of the depolarizing agent veratridine, opposite changes were detected in the serotonin and glutamate levels in DRN with a significant decrease or increase, respectively, suggesting that the reduction of mTOR in the IL cortex may affect the readily releasable pool (RRP) of perisomatic serotonin neurons and glutamatergic terminals in the DRN. Rapamycin-mediated mTOR inhibition induces the depletion of synaptic vesicles from monoamine presynaptic terminals in the striatum in a macroautophagy-dependent manner [74]. In addition, a lower serotonin release promoted by veratridine in the infralimbic mTOR knockdown animals is similar to previous reports in animal models of depression as the olfactory bulbectomy [36], chronic corticosterone administration [49], and genetic models of depression as the conditional β -catenin knockout in GLAST-expressing cells [49]. This lower stimulation-induced neurotransmitter release [75] might be associated with an impaired ability to cope with stressful situations [76].

The increased glutamate release following veratridine observed in the animals after acute mTOR-siRNAs knockdown was also described after acute stress in the mPFC [77,78] or the amygdala [79]. Furthermore, the inactivation of mTORC1 in cultured glutamatergic hippocampal neurons is associated with an increased rate of spontaneous and asynchronous glutamate release [80]. In this sense, an enhancement of glutamatergic output activity from the IL cortex, causing inhibition of the serotonergic neurons mediated by GABAergic interneurons in the DRN, has been reported in mouse models of depression [31,71,72]. Moreover, the inactivation of the mPFC using muscimol is associated with the impairment of information processing, resulting in altered serotonergic activity and its behavioral consequences [70].

Regarding the effects of the local infusion of NBQX in DRN, the serotonin levels were not modified as previously described [81]. The reduction of glutamate extracellular levels following local AMPA inhibition does not have a straightforward explanation, since, to date, AMPA receptors have not been described in presynaptic localization in glutamatergic terminals. However, it has been reported an inhibitory role of AMPA receptors, leading to the presynaptic inhibition of GABAergic transmission in cerebellar cells, which may be mediated by G-protein-linked mechanisms [82].

Finally, some potential limitations could be considered. First, the use of only one behavioral test to preliminarily analyze the state anxiety may hinder a wider effect on anxiety of the acute infusion of mTOR-siRNA in the IL cortex. A second limitation is the lack of knowledge regarding the duration of the depressive-like effect of a single infusion of mTOR-siRNA into this cortical area. Finally, and associated with the latter, is the issue of whether the silencing of mTOR in the IL cortex for a longer period would have been able to induce other changes in the depressive-like behavior manifestations, such as the

appearance of anhedonia. In this sense, further investigations will be needed to broaden the current data.

4. Materials and Methods

4.1. Animals

Male C57BL/6J mice (2–3 months old, 25–30 g, Charles River, Lyon, France) were housed under controlled conditions (22 ± 1 °C; 12 h light/dark cycle) with food and water available ad libitum, unless otherwise stated. All procedures involving the use of mice and their care followed the principles of the ARRIVE guidelines were carried out with the previous approval of the Animal Care Committee of the Universidad de Cantabria and according to the Spanish legislation and the European Communities Council Directive on “Protection of Animals Used in Experimental and Other Scientific Purposes” (86/609/EEC) (ref. No.: PL05-17).

4.2. siRNAs

Two unmodified siRNAs against mTOR (mTOR-siRNAs) (GenBank accession #NM_020009.2) which specific sequences are: mTOR-siRNA1 sense: gaaggucagaggauuaaTT, antisense: uaaauccucagugaccuucTT; and mTOR-siRNA2 sense: acccggcgugaucauaaTT, antisense: uuauugaucacgcccgguTT, were co-administered (Microsynth; Balgach, Switzerland). A non-sense siRNA (NS-siRNAs, sense: aguacugcuuacgacggTT, antisense: ccguaucgaaagcaguacuTT) with no homology to the mouse genome was used as a negative control (nLife Therapeutics, S.L. (La Coruña, Spain) as described (International patent application PCT/EP2011/056270)). In the intracerebral infusion, 40 µg (20 µg of each) of siRNAs were diluted in artificial cerebrospinal fluid (aCSF: 125 mM NaCl, 2.5 mM KCl, 1.18 mM MgCl₂, 1.26 mM CaCl₂, containing glucose 5%). aCSF was infused to control animals.

4.3. Drugs and Reagents

Veratridine and 2,3-dihydroxy-6-nitro-7-sulfamoyl-benzo(f)quinoxaline (NBQX) were purchased from Tocris Bioscience (UK). Veratridine (50 µM) [31,83] and NBQX (100 µM) [84,85], were infused through the intracerebral probe into the DRN of the animals.

[³³P]α-dATP (2′ deoxyadenosine 5′-(α-thio) triphosphate at a specific activity of >2500 Ci/mmol was purchased from Perkin Elmer and GTPγS (10 µM) and used for the mTOR and BDNF in situ hybridization studies.

4.4. Acute Intracerebral siRNA Infusion

Mice were anesthetized with pentobarbital (40 mg/kg; i.p.) [31,49,86] and a single dose of the specific mTOR pool (40 µg/µL; 20 µg of each sequence) of siRNAs was stereotaxically and unilaterally infused [31], using a perfusion pump at 0.2 µL/min, in the infralimbic cortex (IL; coordinates in mm: anteroposterior-AP, +2.0; mediolateral-ML, -0.2 and dorsoventral-DV, -3.4), or the prelimbic cortex (PrL; AP, +2.0; ML, -0.2; DV, -2.0). The local infusion of this siRNA dose does not induce off-target effects [31,86,87]. A different set of animals was used for microdialysis studies. After siRNAs infusion, a microdialysis probe was implanted in the dorsal raphe nucleus (DRN) (Figure 5).

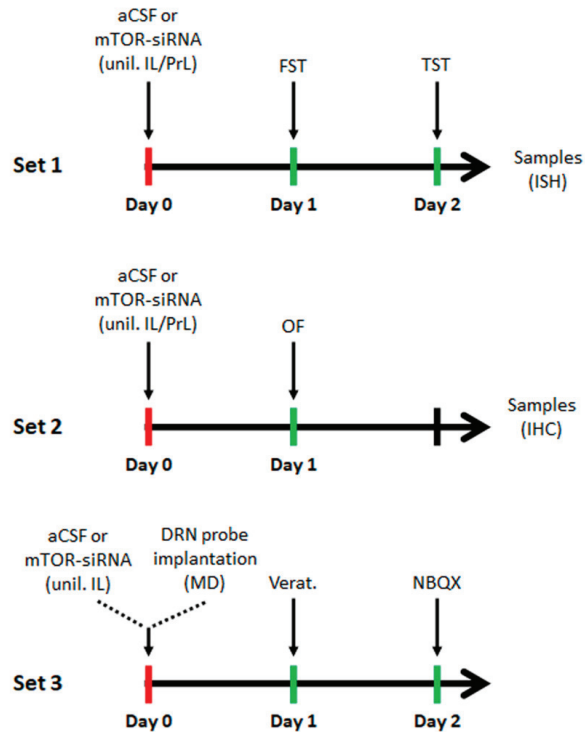


Figure 5. Experimental schedule of the different experimental procedures performed in this study. mTOR-siRNA or vehicle (aCSF) was unilaterally infused in the IL or PrL cortices for the behavioral experiments (sets 1 and 2), and in the IL cortex for the microdialysis studies (set 3). Samples were collected 48 h post-infusion (2 h after the last behavioral test for set 1). aCSF: artificial cerebrospinal fluid; siRNA: small interfering RNA; unil.: unilateral infusion; IL: infralimbic cortex; PrL: prelimbic cortex; DRN: dorsal raphe nucleus; FST: forced swimming test; TST: tail suspension test; OF: open-field test; ISH: in situ hybridization; IHC: immunohistochemistry; MD: microdialysis; Verat.: vetridine; NBQX: 2,3-dihydroxy-6-nitro-7-sulfamoyl-benzo(f)quinoxaline.

4.5. Behavioral Studies

All behavioral tests were performed between 10:00 a.m. and 3:00 p.m. by an experimenter blind to treatments. Mice were habituated for at least 1 h before testing. For the acute siRNAs treatment, animals were evaluated in two behavioral paradigms including the forced swimming test (FST) and the tail suspension test (TST), 24 and 48 h, respectively, after the single unilateral intracerebral infusion of mTOR-siRNAs or aCSF. In another animal cohort, the locomotor activity was assessed in the open-field test (OF) 24 h after the siRNAs or aCSF infusion (Figure 5).

4.5.1. Forced Swimming Test (FST)

Mice were placed in cylinder tanks (30 × 20 cm) filled with water at 25 °C for a 6 min session, and the last 4 min were recorded. The time spent immobile was scored. At the end of the test, animals were immediately removed from the tank, dried off with a paper towel, and returned to their home cages [88].

4.5.2. Tail Suspension Test (TST)

Mice were suspended 30 cm above the bench using adhesive tape placed approximately 1 cm from the tip of the tail. The total duration of immobility during a 6 min test was recorded using a video camera (Smart, Panlab) [87].

4.5.3. Open-Field Test (OF)

Motor activity was measured in four Plexiglas open-field boxes 35 × 35 × 40 cm indirectly illuminated (25–40 luxes) to avoid reflection and shadows. The floor of the open field was covered with an interchangeable opaque plastic base that was replaced for each animal. Motor activity and the total time spent within the central area of the arena, to evaluate anxiety, were recorded for 15 min by a camera connected to a computer (Videotrack, View Point, Lyon, France) [87].

4.6. *In situ* Hybridization

Mice were killed by pentobarbital overdose and brains were rapidly removed, frozen on dry ice, and stored at -80°C . Coronal tissue sections containing mPFC (14 μm thick) were cut using a microtome-cryostat (HM500-OM, Microm, Walldorf, Germany), thaw-mounted onto 3-aminopropyltriethoxysilane (Sigma-Aldrich, St. Louis, MO, USA)-coated slides, and kept at -80°C until use. The oligoprobes used were: mTOR/4721-4766 (NM_020009) and BDNF/1188-1238 (NM_007540), respectively (Göttingen, Germany). Oligoprobes (2 pmol) were 3'-end labeled with [^{33}P]-dATP (>2500 Ci/mmol; DuPont-NEN, Boston, MA, USA) using terminal deoxynucleotidyl transferase (TdT, Calbiochem, La Jolla, CA, USA), and the sections were incubated overnight with the labeled probes. Sections were then washed, air-dried, and exposed to films (Biomax MR, Kodak, Madrid, Spain) together with 14C microscaler (Amersham, Buckinghamshire, UK) at 4°C for 3 weeks. Films were analyzed and relative optical densities (ROD) were obtained using a computer-assisted image analyzer (MCID, Mering, Germany), as previously described [87,89]. The slide background and nonspecific densities were subtracted. ROD was evaluated in 2–3 duplicate adjacent sections from each mouse and averaged to obtain individual values along the anteroposterior axis.

4.7. mTOR Immunofluorescence

Animals were deeply anesthetized with sodium pentobarbital (40 mg/kg, i.p.) and transcardially perfused with 4% paraformaldehyde [90]. Brains were post-fixed for 4 h at 4°C and cryoprotected with 30% sucrose in PBS. Free-floating coronal brain sections (40 μm thick) were processed for immunohistochemical experiments as follows. Sections were washed in PBS, blocked with a blocking solution (PBS containing 0.3% Triton-X-100 and 2% normal donkey serum) for 1 h at room temperature, and incubated with the primary antibody rabbit anti-mTOR (1:800, Cell Signaling Technology, Leiden, The Netherlands) in PBS and 2% normal donkey serum, overnight at 4°C . After, sections were washed and incubated with the secondary donkey anti-rabbit Alexa Fluor 488 antibody (Invitrogen, Waltham, MA, USA) for 2 h at room temperature. After washing, sections were incubated with DAPI 1:1000 in PBS for 5 min and mounted using Vectashield. The fluorescent signal was detected using a Zeiss Axio Imager M1 fluorescence microscope, 12 bits B&W camera (AxioCam MRm). Cubes: GFP (Ex. 470/40–Em. 525/50). Objective: x40/NA 0.75. The relative immunoreactivity was measured as the mean densitometric measurement of the IL and PrL areas in silenced and control groups. The staining intensity was measured using the software ImageJ 1.52S (NIH, Bethesda, MD, USA). The image density was obtained by subtracting the density in the nonspecific condition (without primary antibody).

4.8. Intracerebral Microdialysis

Extracellular serotonin (5-HT) and glutamate (Glu) concentrations in DRN were measured by *in vivo* microdialysis, as previously described [31]. Briefly, one concentric dialysis probe (Cuprophane; 1.5-mm long) was implanted into the DRN (coordinates in mm:

AP, -4.5 ; ML, 1.0 ; DV, -4.2 , with a lateral angle of 20°) of pentobarbital-anesthetized mice. Microdialysis experiments were conducted 24 h (for intra-DRN infusion of veratridine; day 1) and 48 h (for intra-DRN infusion of NBQX; day 2) after surgery in freely moving mice by continuously perfusing probes with artificial cerebrospinal fluid (aCSF, containing $1 \mu\text{M}$ citalopram) at a rate of $1.64 \mu\text{L}/\text{min}$. After a 180 min stabilization period, dialysate samples of $30 \mu\text{L}$ were collected every 20 min, six 20 min fractions were collected to obtain basal values (expressed as the concentration of neurotransmitter in the $30 \mu\text{L}$ sample), and another six samples after the local infusion of $50 \mu\text{M}$ veratridine (day 1) and $100 \mu\text{M}$ NBQX (day 2). 5-HT and Glu were determined by HPLC, as previously described [91]. The neurotransmitter levels (% vs. basal) were determined for every time point for each animal and the mean of the experimental groups was compared for 5-HT and Glu contents. The absolute basal levels of 5-HT (fmol/sample) and Glu ($\mu\text{mol}/\text{sample}$) were also compared among groups. After the experiments, mice were sacrificed, and brain tissue was processed according to standard procedures (cresyl violet staining) to verify the correct placement of the dialysis probe.

4.9. Statistical Analysis

Results are expressed as mean \pm standard error of the mean (S.E.M.). The statistical analysis of the results was performed using Student's *t*-test or two-way ANOVA, followed by the Bonferroni post hoc test. Graphs and statistical analyses were done using the GraphPad Prism software, version 6.1 (GraphPad Software Inc., San Diego, CA, USA). The level of significance was set at $p < 0.05$. The number of animals used in each experimental group is indicated in the Results section and Figure legends.

5. Conclusions

The present study demonstrates the causal link between mTOR expression in the infralimbic cortex and depressive-like state, with no clear implication in state anxiety-like behavior, at least in the open-field test. Here we demonstrate how an acute unilateral infusion of mTOR-siRNA into the infralimbic cortex, that induces a reduction of mTOR mRNA and protein expression in this area, is able to promote pro-depressive behavioral effects, accompanied with BDNF mRNA downregulation in the medial prefrontal cortex and an impairment of the serotonergic and glutamatergic neurotransmission in the ventromedial prefrontal cortex-dorsal raphe nucleus (vmPFC-DRN) pathway. These data support the importance of the mTOR pathway in the infralimbic cortex in the control of brainstem nuclei and the development of depressive-like behavioral despair. Our data are in accordance with previous findings on the importance of the mTOR pathway in major depression. Future experiments would be of interest to determine whether a sustained elimination of mTOR in the infralimbic cortex is able to promote a more pronounced behavioral phenotype (e.g., anhedonia).

Supplementary Materials: The following are available online at <https://www.mdpi.com/article/10.3390/ijms22168671/s1>.

Author Contributions: Conceptualization, A.B. and F.P.-C.; methodology, E.G.-M., M.N.F., E.F.-Z., J.S., V.P., E.R.-B. and A.A.; validation, M.N.F.; formal analysis, E.G.-M., A.A. and F.P.-C.; investigation, E.G.-M., M.N.F., E.F.-Z., J.S., V.P. and E.R.-B.; resources, Á.P., A.B. and F.P.-C.; data curation, E.G.-M., A.B. and F.P.-C.; writing—original draft preparation, E.G.-M., A.B. and F.P.-C.; writing—review and editing, A.A., Á.D., E.C. and F.P.-C.; supervision, A.B. and F.P.-C.; project administration, F.P.-C. and Á.P.; funding acquisition, Á.P. and A.B. All authors have read and agreed to the published version of the manuscript.

Funding: This research was funded by grants of the Ministerio de Economía y Competitividad (SAF2011-25020 and SAF2015-67457-R MINECO); Ministerio de Ciencia, Innovación y Universidades (RTI2018-097534-B-I00); Ministerio de Ciencia e Innovación (PID2019-105136RB-I00); and the European Regional Development Fund (ERDF), UE; Instituto de Salud Carlos III (PI19/00170), and Centro de Investigación Biomédica en Red de Salud Mental (CIBERSAM).

Institutional Review Board Statement: The study was conducted according to the guidelines of the Declaration of Helsinki, the Spanish legislation and the European Communities Council Directive on “Protection of Animals Used in Experimental and Other Scientific Purposes” (86/609/EEC), and approved by the Animal Care Committee of the Universidad de Cantabria and the Consejería de Medio Rural, Pesca y Alimentación of the Gobierno de Cantabria (protocol code: PI-05-17, 3/7/2017).

Informed Consent Statement: Not applicable.

Data Availability Statement: The data presented in this study are available on request from the corresponding author.

Acknowledgments: E.G.-M. is a recipient of a fellowship of the Ministerio de Economía y Competitividad. M.N.F. is a recipient of a fellowship from the Ministerio de Educación, Cultura y Deporte. E.F.-Z. was supported by a predoctoral fellowship from the Universidad de Cantabria (Spain). We greatly acknowledge the technical assistance of Víctor Campa in the acquisition of the immunohistochemical images.

Conflicts of Interest: The authors declare no conflict of interest.

References

1. WHO. 2018. Available online: <https://www.who.int/news-room/fact-sheets/detail/depression> (accessed on 30 July 2019).
2. Duman, R.S.; Heninger, G.R.; Nestler, E.J. A molecular and cellular theory of depression. *Arch. Gen. Psychiatry* **1997**, *54*, 597–606. [CrossRef]
3. Duman, R.S.; Monteggia, L.M. A neurotrophic model for stress-related mood disorders. *Biol. Psychiatry* **2006**, *59*, 1116–1127. [CrossRef]
4. Duman, R.S.; Aghajanian, G.K.; Sanacora, G.; Krystal, J.H. Synaptic plasticity and depression: New insights from stress and rapid-acting antidepressants. *Nat. Med.* **2016**, *22*, 238–249. [CrossRef] [PubMed]
5. Chen, B.; Dowlatshahi, D.; MacQueen, G.M.; Wang, J.F.; Young, L.T. Increased hippocampal BDNF immunoreactivity in subjects treated with antidepressant medication. *Biol. Psychiatry* **2001**, *50*, 260–265. [CrossRef]
6. Karege, F.; Vaudan, G.; Schwald, M.; Perroud, N.; La Harpe, R. Neurotrophin levels in postmortem brains of suicide victims and the effects of antemortem diagnosis and psychotropic drugs. *Brain Res. Mol. Brain Res.* **2005**, *136*, 29–37. [CrossRef] [PubMed]
7. Nibuya, M.; Morinobu, S.; Duman, R.S. Regulation of BDNF and trkB mRNA in rat brain by chronic electroconvulsive seizure and antidepressant drug treatments. *J. Neurosci.* **1995**, *15*, 7539–7547. [CrossRef]
8. Nibuya, M.; Nestler, E.J.; Duman, R.S. Chronic antidepressant administration increases the expression of cAMP response element binding protein (CREB) in rat hippocampus. *J. Neurosci.* **1996**, *16*, 2365–2372. [CrossRef]
9. Dwivedi, Y.; Rizavi, H.S.; Pandey, G.N. Antidepressants reverse corticosterone-mediated decrease in brain-derived neurotrophic factor expression: Differential regulation of specific exons by antidepressants and corticosterone. *Neuroscience* **2006**, *139*, 1017–1029. [CrossRef]
10. Calabrese, F.; Molteni, R.; Maj, P.F.; Cattaneo, A.; Gennarelli, M.; Racagni, G.; Riva, M.A. Chronic duloxetine treatment induces specific changes in the expression of BDNF transcripts and in the subcellular localization of the neurotrophin protein. *Neuropsychopharmacology* **2007**, *32*, 2351–2359. [CrossRef]
11. Balu, D.T.; Hoshaw, B.A.; Malberg, J.E.; Rosenzweig-Lipson, S.; Schechter, L.E.; Lucki, I. Differential regulation of central BDNF protein levels by antidepressant and non-antidepressant drug treatments. *Brain Res.* **2008**, *1211*, 37–43. [CrossRef]
12. Zhang, Y.; Gu, F.; Chen, J.; Dong, W. Chronic antidepressant administration alleviates frontal and hippocampal BDNF deficits in CUMS rat. *Brain Res.* **2010**, *1366*, 141–148. [CrossRef]
13. Bath, K.G.; Jing, D.Q.; Dincheva, I.; Neeb, C.C.; Pattwell, S.S.; Chao, M.V.; Lee, F.S.; Ninan, I. BDNF Val66Met impairs fluoxetine-induced enhancement of adult hippocampus plasticity. *Neuropsychopharmacology* **2012**, *37*, 1297–1304. [CrossRef]
14. Li, N.; Lee, B.; Liu, R.J.; Banasr, M.; Dwyer, J.M.; Iwata, M.; Li, X.Y.; Aghajanian, G.; Duman, R.S. mTOR-dependent synapse formation underlies the rapid antidepressant effects of NMDA antagonists. *Science* **2010**, *329*, 959–964. [CrossRef] [PubMed]
15. Liu, R.J.; Lee, F.S.; Li, X.Y.; Bambico, F.; Duman, R.S.; Aghajanian, G.K. Brain-derived neurotrophic factor Val66Met allele impairs basal and ketamine-stimulated synaptogenesis in prefrontal cortex. *Biol. Psychiatry* **2012**, *71*, 996–1005. [CrossRef]
16. Lepack, A.E.; Fuchikami, M.; Dwyer, J.M.; Banasr, M.; Duman, R.S. BDNF release is required for the behavioral actions of ketamine. *Int. J. Neuropsychopharmacol.* **2014**, *18*, 33. [CrossRef] [PubMed]
17. Choi, M.; Lee, S.H.; Chang, H.L.; Son, H. Hippocampal VEGF is necessary for antidepressant-like behaviors but not sufficient for antidepressant-like effects of ketamine in rats. *Biochim. Biophys. Acta* **2016**, *1862*, 1247–1254. [CrossRef]
18. Lepack, A.E.; Bang, E.; Lee, B.; Dwyer, J.M.; Duman, R.S. Fast-acting antidepressants rapidly stimulate ERK signaling and BDNF release in primary neuronal cultures. *Neuropharmacology* **2016**, *111*, 242–252. [CrossRef] [PubMed]
19. Li, N.; Liu, R.J.; Dwyer, J.M.; Banasr, M.; Lee, B.; Son, H.; Li, X.Y.; Aghajanian, G.; Duman, R.S. Glutamate N-methyl-D-aspartate receptor antagonists rapidly reverse behavioral and synaptic deficits caused by chronic stress exposure. *Biol. Psychiatry* **2011**, *69*, 754–761. [CrossRef] [PubMed]

20. Heitman, J.; Movva, N.R.; Hall, M.N. Targets for cell cycle arrest by the immunosuppressant rapamycin in yeast. *Science* **1991**, *253*, 905–909. [CrossRef] [PubMed]
21. Guertin, D.A.; Sabatini, D.M. Defining the role of mTOR in cancer. *Cancer Cell* **2007**, *12*, 9–22. [CrossRef]
22. Hoeffler, C.A.; Klann, E. mTOR signaling: At the crossroads of plasticity, memory and disease. *Trends Neurosci.* **2010**, *33*, 67–75. [CrossRef] [PubMed]
23. Tang, S.J.; Reis, G.; Kang, H.; Gingras, A.C.; Sonenberg, N.; Schuman, E.M. A rapamycin-sensitive signaling pathway contributes to long-term synaptic plasticity in the hippocampus. *Proc. Natl. Acad. Sci. USA* **2002**, *99*, 467–472. [CrossRef] [PubMed]
24. Gong, R.; Park, C.S.; Abbassi, N.R.; Tang, S.J. Roles of glutamate receptors and the mammalian target of rapamycin (mTOR) signaling pathway in activity-dependent dendritic protein synthesis in hippocampal neurons. *J. Biol. Chem.* **2006**, *281*, 18802–18815. [CrossRef]
25. Duman, R.S.; Voleti, B. Signaling pathways underlying the pathophysiology and treatment of depression: Novel mechanisms for rapid-acting agents. *Trends Neurosci.* **2012**, *35*, 47–56. [CrossRef]
26. Cammalleri, M.; Lutjens, R.; Berton, F.; King, A.R.; Simpson, C.; Francesconi, W.; Sanna, P.P. Time-restricted role for dendritic activation of the mTOR-p70S6K pathway in the induction of late-phase long-term potentiation in the CA1. *Proc. Natl. Acad. Sci. USA* **2003**, *100*, 14368–14373. [CrossRef] [PubMed]
27. Bargmann, C.I.; Lieberman, J.A. What the BRAIN Initiative means for psychiatry. *Am. J. Psychiatry* **2014**, *171*, 1038–1040. [CrossRef]
28. Mayberg, H.S. Targeted electrode-based modulation of neural circuits for depression. *J. Clin. Investig.* **2009**, *119*, 717–725. [CrossRef]
29. Savitz, J.B.; Drevets, W.C. Imaging phenotypes of major depressive disorder: Genetic correlates. *Neuroscience* **2009**, *164*, 300–330. [CrossRef]
30. Mayberg, H.S.; Lozano, A.M.; Voon, V.; McNeely, H.E.; Seminowicz, D.; Hamani, C.; Schwab, J.M.; Kennedy, S.H. Deep brain stimulation for treatment-resistant depression. *Neuron* **2005**, *45*, 651–660. [CrossRef]
31. Fullana, M.N.; Ruiz-Bronchal, E.; Ferrés-Coy, A.; Juárez-Escoto, E.; Artigas, F.; Bortolozzi, A. Regionally selective knockdown of astroglial glutamate transporters in infralimbic cortex induces a depressive phenotype in mice. *Glia* **2019**, *67*, 1122–1137. [CrossRef]
32. Fullana, N.; Gasull-Camós, J.; Tarrés-Gatius, M.; Castañé, A.; Bortolozzi, A.; Artigas, F. Astrocyte control of glutamatergic activity: Downstream effects on serotonergic function and emotional behavior. *Neuropharmacology* **2020**, *166*, 107914. [CrossRef]
33. Hamani, C.; Diwan, M.; Macedo, C.E.; Brandão, M.L.; Shumake, J.; Gonzalez-Lima, F.; Raymond, R.; Lozano, A.M.; Fletcher, P.J.; Nobrega, J.N. Antidepressant-like effects of medial prefrontal cortex deep brain stimulation in rats. *Biol. Psychiatry* **2010**, *67*, 117–124. [CrossRef] [PubMed]
34. Veerakumar, A.; Challis, C.; Gupta, P.; Da, J.; Upadhyay, A.; Beck, S.G.; Berton, O. Antidepressant-like effects of cortical deep brain stimulation coincide with pro-neuroplastic adaptations of serotonin systems. *Biol. Psychiatry* **2014**, *76*, 203–212. [CrossRef] [PubMed]
35. Jiménez-Sánchez, L.; Castañé, A.; Pérez-Caballero, L.; Grifoll-Escoda, M.; López-Gil, X.; Campa, L.; Galofré, M.; Berrocoso, E.; Adell, A. Activation of AMPA Receptors Mediates the Antidepressant Action of Deep Brain Stimulation of the Infralimbic Prefrontal Cortex. *Cereb. Cortex* **2016**, *26*, 2778–2789. [CrossRef]
36. Jiménez-Sánchez, L.; Linge, R.; Campa, L.; Valdizán, E.M.; Pazos, Á.; Díaz, Á.; Adell, A. Behavioral, neurochemical and molecular changes after acute deep brain stimulation of the infralimbic prefrontal cortex. *Neuropharmacology* **2016**, *108*, 91–102. [CrossRef] [PubMed]
37. Fukumoto, K.; Fogaça, M.V.; Liu, R.J.; Duman, C.; Kato, T.; Li, X.Y.; Duman, R.S. Activity-dependent brain-derived neurotrophic factor signalling is required for the antidepressant actions of (2R,6R)-hydroxynorketamine. *Proc. Natl. Acad. Sci. USA* **2019**, *116*, 297–302. [CrossRef]
38. Fuchikami, M.; Thomas, A.; Liu, R.; Wohleb, E.S.; Land, B.B.; DiLeone, R.J.; Aghajanian, G.K.; Duman, R.S. Optogenetic stimulation of infralimbic PFC reproduces ketamine's rapid and sustained antidepressant actions. *Proc. Natl. Acad. Sci. USA* **2015**, *112*, 8106–8111. [CrossRef]
39. Jernigan, C.S.; Goswami, D.B.; Austin, M.C.; Iyo, A.H.; Chandran, A.; Stockmeier, C.A.; Karolewicz, B. The mTOR signaling pathway in the prefrontal cortex is compromised in major depressive disorder. *Prog. Neuropsychopharmacol. Biol. Psychiatry* **2011**, *35*, 1774–1779. [CrossRef]
40. Chandran, A.; Iyo, A.H.; Jernigan, C.S.; Legutko, B.; Austin, M.C.; Karolewicz, B. Reduced phosphorylation of the mTOR signaling pathway components in the amygdala of rats exposed to chronic stress. *Prog. Neuropsychopharmacol. Biol. Psychiatry* **2013**, *40*, 240–245. [CrossRef]
41. Ota, K.T.; Liu, R.J.; Voleti, B.; Maldonado-Aviles, J.G.; Duric, V.; Iwata, M.; Duthiel, S.; Duman, C.; Boike, S.; Lewis, D.A.; et al. REDD1 is essential for stress-induced synaptic loss and depressive behavior. *Nat. Med.* **2014**, *20*, 531–535. [CrossRef]
42. Wu, R.; Zhang, H.; Xue, W.; Zou, Z.; Lu, C.; Xia, B.; Wang, W.; Chen, G. Transgenerational impairment of hippocampal Akt-mTOR signaling and behavioral deficits in the offspring of mice that experience postpartum depression-like illness. *Prog. Neuropsychopharmacol. Biol. Psychiatry* **2017**, *73*, 11–18. [CrossRef]

43. Wang, X.; Zou, Z.; Shen, Q.; Huang, Z.; Chen, J.; Tang, J.; Xue, W.; Tao, W.; Wu, H.; Wang, D.; et al. Involvement of NMDA-AKT-mTOR Signaling in Rapid Antidepressant-like Activity of Chaihu-jia-Longgu-Muli-tang on Olfactory Bulbectomized Mice. *Front. Pharmacol.* **2019**, *9*, 1537. [CrossRef]
44. Olescowicz, G.; Sampaio, T.B.; de Paula Nascimento-Castro, C.; Brocardo, P.S.; Gil-Mohapel, J.; Rodrigues, A.L.S. Protective Effects of Agmatine Against Corticosterone-Induced Impairment on Hippocampal mTOR Signaling and Cell Death. *Neurotox. Res.* **2020**, *38*, 319–329. [CrossRef]
45. Molendijk, M.L.; Bus, B.A.; Spinhoven, P.; Penninx, B.W.; Kenis, G.; Prickaerts, J.; Voshaar, R.C.; Elzinga, B.M. Serum levels of brain-derived neurotrophic factor in major depressive disorder: State-trait issues, clinical features and pharmacological treatment. *Mol. Psychiatry* **2011**, *16*, 1088–1095. [CrossRef]
46. Kreinin, A.; Lisson, S.; Neshet, E.; Schneider, J.; Bergman, J.; Farhat, K.; Farah, J.; Lejbkiewicz, F.; Yadid, G.; Raskin, L.; et al. Blood BDNF level is gender specific in severe depression. *PLoS ONE* **2015**, *10*, e0127643. [CrossRef] [PubMed]
47. Challis, C.; Berton, O. Top-Down Control of Serotonin Systems by the Prefrontal Cortex: A Path toward Restored Socioemotional Function in Depression. *ACS Chem. Neurosci.* **2015**, *6*, 1040–1054. [CrossRef]
48. Popoli, M.; Yan, Z.; McEwen, B.S.; Sanacora, G. The stressed synapse: The impact of stress and glucocorticoids on glutamate transmission. *Nat. Rev. Neurosci.* **2011**, *13*, 22–37. [CrossRef] [PubMed]
49. Garro-Martínez, E.; Vidal, R.; Adell, A.; Díaz, Á.; Castro, E.; Amigó, J.; Gutiérrez-Lanza, R.; Florensa-Zanuy, E.; Gómez-Acero, L.; Taketo, M.M.; et al. β -Catenin Role in the Vulnerability/Resilience to Stress-Related Disorders Is Associated to Changes in the Serotonergic System. *Mol. Neurobiol.* **2020**, *57*, 1704–1715. [CrossRef] [PubMed]
50. Malhi, G.S.; Mann, J.J. Depression. *Lancet* **2018**, *392*, 2299–2312. [CrossRef]
51. Russo, E.; Citraro, R.; Donato, G.; Camastra, C.; Iuliano, R.; Cuzzocrea, S.; Constanti, A.; De Sarro, G. mTOR inhibition modulates epileptogenesis, seizures and depressive behavior in a genetic rat model of absence epilepsy. *Neuropharmacology* **2013**, *69*, 25–36. [CrossRef]
52. Russo, E.; Leo, A.; Crupi, R.; Aiello, R.; Lippio, P.; Spiga, R.; Chimirri, S.; Citraro, R.; Cuzzocrea, S.; Constanti, A.; et al. Everolimus improves memory and learning while worsening depressive- and anxiety-like behavior in an animal model of depression. *J. Psychiatr. Res.* **2016**, *78*, 1–10. [CrossRef]
53. Cleary, C.; Linde, J.A.; Hiscock, K.M.; Hadas, I.; Belmaker, R.H.; Agam, G.; Flaisher-Grinberg, S.; Einat, H. Antidepressant-like effects of rapamycin in animal models: Implications for mTOR inhibition as a new target for treatment of affective disorders. *Brain Res. Bull.* **2008**, *76*, 469–473. [CrossRef] [PubMed]
54. Russo, E.; Andreozzi, F.; Iuliano, R.; Dattilo, V.; Procopio, T.; Fiume, G.; Mimmi, S.; Perrotti, N.; Citraro, R.; Sesti, G.; et al. Early molecular and behavioral response to lipopolysaccharide in the WAG/Rij rat model of absence epilepsy and depressive-like behavior, involves interplay between AMPK, AKT/mTOR pathways and neuroinflammatory cytokine release. *Brain Behav. Immun.* **2014**, *42*, 157–168. [CrossRef]
55. Cambiaghi, M.; Cursi, M.; Magri, L.; Castoldi, V.; Comi, G.; Minicucci, F.; Galli, R.; Leocani, L. Behavioural and EEG effects of chronic rapamycin treatment in a mouse model of tuberous sclerosis complex. *Neuropharmacology* **2013**, *67*, 1–7. [CrossRef]
56. Masini, D.; Bonito-Oliva, A.; Bertho, M.; Fisone, G. Inhibition of mTORC1 Signaling Reverts Cognitive and Affective Deficits in a Mouse Model of Parkinson's Disease. *Front. Neurol.* **2018**, *9*, 208. [CrossRef] [PubMed]
57. Tsai, P.T.; Greene-Colozzi, E.; Goto, J.; Anderl, S.; Kwiatkowski, D.J.; Sahin, M. Prenatal rapamycin results in early and late behavioral abnormalities in wildtype C57BL/6 mice. *Behav. Genet.* **2013**, *43*, 51–59. [CrossRef]
58. Yang, C.; Ren, Q.; Qu, Y.; Zhang, J.C.; Ma, M.; Dong, C.; Hashimoto, K. Mechanistic Target of Rapamycin-Independent Antidepressant Effects of (R)-Ketamine in a Social Defeat Stress Model. *Biol. Psychiatry* **2017**, *83*, 18–28. [CrossRef] [PubMed]
59. Berman, R.M.; Cappiello, A.; Anand, A.; Oren, D.A.; Heninger, G.R.; Charney, D.S.; Krystal, J.H. Antidepressant effects of ketamine in depressed patients. *Biol. Psychiatry* **2000**, *47*, 351–354. [CrossRef]
60. Zarate, C.A., Jr.; Singh, J.B.; Carlson, P.J.; Brutsche, N.E.; Ameli, R.; Luckenbaugh, D.A.; Charney, D.S.; Manji, H.K. A randomized trial of an N-methyl-D-aspartate antagonist in treatment-resistant major depression. *Arch. Gen. Psychiatry* **2006**, *63*, 856–864. [CrossRef]
61. Murrrough, J.W.; Perez, A.M.; Pillemer, S.; Stern, J.; Parides, M.K.; aan het Rot, M.; Collins, K.A.; Mathew, S.J.; Charney, D.S.; Iosifescu, D.V. Rapid and Longer-Term Antidepressant Effects of Repeated Ketamine Infusions in Treatment-Resistant Major Depression. *Biol. Psychiatry* **2013**, *74*, 250–256. [CrossRef]
62. Autry, A.E.; Adachi, M.; Nosyreva, E.; Na, E.S.; Los, M.F.; Cheng, P.F.; Kavalali, E.T.; Monteggia, L.M. NMDA receptor blockade at rest triggers rapid behavioural antidepressant responses. *Nature* **2011**, *475*, 91–95. [CrossRef] [PubMed]
63. Abdallah, C.G.; Averill, L.A.; Gueorguieva, R.; Goktas, S.; Purohit, P.; Ranganathan, M.; Sherif, M.; Ahn, K.H.; D'Souza, D.C.; Formica, R.; et al. Modulation of the antidepressant effects of ketamine by the mTORC1 inhibitor rapamycin. *Neuropsychopharmacology* **2020**, *45*, 990–997. [CrossRef] [PubMed]
64. Jones, B.F.; Groenewegen, H.J.; Witter, M.P. Intrinsic connections of the cingulate cortex in the rat suggest the existence of multiple functionally segregated networks. *Neuroscience* **2005**, *133*, 193–207. [CrossRef] [PubMed]
65. Van Aerde, K.I.; Heistek, T.S.; Mansvelder, H.D. Prelimbic and infralimbic prefrontal cortex interact during fast network oscillations. *PLoS ONE* **2008**, *3*, e2725. [CrossRef]
66. Deyama, S.; Duman, R.S. Neurotrophic mechanisms underlying the rapid and sustained antidepressant actions of ketamine. *Pharmacol. Biochem. Behav.* **2020**, *188*, 172837. [CrossRef]

67. Dwivedi, Y.; Rizavi, H.S.; Conley, R.R.; Roberts, R.C.; Tamminga, C.A.; Pandey, G.N. Altered gene expression of brain-derived neurotrophic factor and receptor tyrosine kinase B in postmortem brain of suicide subjects. *Arch. Gen. Psychiatry* **2003**, *60*, 804–815. [CrossRef]
68. Qi, X.R.; Zhao, J.; Liu, J.; Fang, H.; Swaab, D.F.; Zhou, J.N. Abnormal retinoid and TrkB signaling in the prefrontal cortex in mood disorders. *Cereb. Cortex* **2015**, *25*, 75–83. [CrossRef]
69. Krishnan, V.; Nestler, E.J. Linking molecules to mood: New insight into the biology of depression. *Am. J. Psychiatry* **2010**, *167*, 1305–1320. [CrossRef]
70. Amat, J.; Baratta, M.V.; Paul, E.; Bland, S.T.; Watkins, L.R.; Maier, S.F. Medial prefrontal cortex determines how stressor controllability affects behavior and dorsal raphe nucleus. *Nat. Neurosci.* **2005**, *8*, 365–371. [CrossRef]
71. Challis, C.; Boulden, J.; Veerakumar, A.; Espallergues, J.; Vassoler, F.M.; Pierce, R.C.; Beck, S.G.; Berton, O. Raphe GABAergic neurons mediate the acquisition of avoidance after social defeat. *J. Neurosci.* **2013**, *33*, 13978–13988. [CrossRef]
72. Challis, C.; Beck, S.G.; Berton, O. Optogenetic modulation of descending prefrontocortical inputs to the dorsal raphe bidirectionally bias socioaffective choices after social defeat. *Front. Behav. Neurosci.* **2014**, *17*, 43. [CrossRef]
73. Linge, R.; Jiménez-Sánchez, L.; Campa, L.; Pilar-Cuéllar, F.; Vidal, R.; Pazos, A.; Adell, A.; Díaz, Á. Cannabidiol induces rapid-acting antidepressant-like effects and enhances cortical 5-HT/glutamate neurotransmission: Role of 5-HT1A receptors. *Neuropharmacology* **2016**, *103*, 16–26. [CrossRef] [PubMed]
74. Hernandez, D.; Torres, C.A.; Setlik, W.; Cebrián, C.; Mosharov, E.V.; Tang, G.; Cheng, H.C.; Kholodilov, N.; Yarygina, O.; Burke, R.E.; et al. Regulation of presynaptic neurotransmission by macroautophagy. *Neuron* **2012**, *74*, 277–284. [CrossRef] [PubMed]
75. Saitoh, A.; Yamaguchi, K.; Tatsumi, Y.; Murasawa, H.; Nakatani, A.; Hirose, N.; Yamada, M.; Yamada, M.; Kamei, J. Effects of milnacipran and fluvoxamine on hyperemotional behaviors and the loss of tryptophan hydroxylase-positive cells in olfactory bulbectomized rats. *Psychopharmacology (Berl.)* **2007**, *191*, 857–865. [CrossRef] [PubMed]
76. Aksoz, E.; Aksoz, T.; Bilge, S.S.; Ilkaya, F.; Celik, S.; Diren, H.B. Antidepressant-like effects of echo-planar magnetic resonance imaging in mice determined using the forced swimming test. *Brain Res.* **2008**, *1236*, 194–199. [CrossRef] [PubMed]
77. Bagley, J.; Moghaddam, B. Temporal dynamics of glutamate efflux in the prefrontal cortex and in the hippocampus following repeated stress: Effects of pretreatment with saline or diazepam. *Neuroscience* **1997**, *77*, 65–73. [CrossRef]
78. Treccani, G.; Musazzi, L.; Perego, C.; Milanese, M.; Nava, N.; Bonifacino, T.; Lamanna, J.; Malgaroli, A.; Drago, F.; Racagni, G.; et al. Acute stress rapidly increases the readily releasable pool of glutamate vesicles in prefrontal and frontal cortex through non-genomic action of corticosterone. *Mol. Psychiatry* **2014**, *19*, 401. [CrossRef]
79. Reznikov, L.R.; Grillo, C.A.; Piroli, G.G.; Pasumarthi, R.K.; Reagan, L.P.; Fadel, J. Acute stress-mediated increases in extracellular glutamate levels in the rat amygdala: Differential effects of antidepressant treatment. *Eur. J. Neurosci.* **2007**, *25*, 3109–3114. [CrossRef]
80. McCabe, M.P.; Cullen, E.R.; Barrows, C.M.; Shore, A.N.; Tooke, K.I.; Laprade, K.A.; Stafford, J.M.; Weston, M.C. Genetic inactivation of mTORC1 or mTORC2 in neurons reveals distinct functions in glutamatergic synaptic transmission. *Elife* **2019**, *9*, e51440. [CrossRef]
81. Nishitani, N.; Nagayasu, K.; Asaoka, N.; Yamashiro, M.; Shirakawa, H.; Nakagawa, T.; Kaneko, S. Raphe AMPA receptors and nicotinic acetylcholine receptors mediate ketamine-induced serotonin release in the rat prefrontal cortex. *Int. J. Neuropsychopharmacol.* **2014**, *17*, 1321–1326. [CrossRef]
82. Satake, S.; Saitow, F.; Yamada, J.; Konishi, S. Synaptic activation of AMPA receptors inhibits GABA release from cerebellar interneurons. *Nat. Neurosci.* **2000**, *3*, 551–558. [CrossRef]
83. Pavia-Collado, R.; Cópola-Segovia, V.; Miquel-Rio, L.; Alarcón-Aris, D.; Rodríguez-Aller, R.; Torres-López, M.; Paz, V.; Ruiz-Bronchal, E.; Campa, L.; Artigas, F.; et al. Intracerebral Administration of a Ligand-ASO Conjugate Selectively Reduces α -Synuclein Accumulation in Monoamine Neurons of Double Mutant Human A30P*A53T* α -Synuclein Transgenic Mice. *Int. J. Mol. Sci.* **2021**, *22*, 2939. [CrossRef] [PubMed]
84. Fukumoto, K.; Iijima, M.; Chaki, S. The Antidepressant Effects of an mGlu2/3 Receptor Antagonist and Ketamine Require AMPA Receptor Stimulation in the mPFC and Subsequent Activation of the 5-HT Neurons in the DRN. *Neuropsychopharmacology* **2016**, *41*, 1046–1056. [CrossRef]
85. Hettinger, J.C.; Lee, H.; Bu, G.; Holtzman, D.M.; Cirrito, J.R. AMPA-ergic regulation of amyloid- β levels in an Alzheimer's disease mouse model. *Mol. Neurodegener.* **2018**, *13*, 22. [CrossRef]
86. Ferrés-Coy, A.; Pilar-Cuellar, F.; Vidal, R.; Paz, V.; Masana, M.; Cortés, R.; Carmona, M.C.; Campa, L.; Pazos, A.; Montefeltro, A.; et al. RNAi-mediated serotonin transporter suppression rapidly increases serotonergic neurotransmission and hippocampal neurogenesis. *Transl. Psychiatry* **2013**, *3*, e211. [CrossRef]
87. Ferrés-Coy, A.; Galofré, M.; Pilar-Cuellar, F.; Vidal, R.; Paz, V.; Ruiz-Bronchal, E.; Campa, L.; Pazos, Á.; Caso, J.R.; Leza, J.C.; et al. Therapeutic antidepressant potential of a conjugated siRNA silencing the serotonin transporter after intranasal administration. *Mol. Psychiatry* **2016**, *21*, 328–338. [CrossRef]
88. Vidal, R.; Garro-Martínez, E.; Díaz, Á.; Castro, E.; Florensa-Zanuy, E.; Taketo, M.M.; Pazos, Á.; Pilar-Cuellar, F. Targeting β -Catenin in GLAST-Expressing Cells: Impact on Anxiety and Depression-Related Behavior and Hippocampal Proliferation. *Mol. Neurobiol.* **2019**, *56*, 553–566. [CrossRef]

89. Bortolozzi, A.; Castañé, A.; Semakova, J.; Santana, N.; Alvarado, G.; Cortés, R.; Ferrés-Coy, A.; Fernández, G.; Carmona, M.C.; Toth, M.; et al. Selective siRNA-mediated suppression of 5-HT_{1A} autoreceptors evokes strong anti-depressant-like effects. *Mol. Psychiatry* **2012**, *17*, 612–623. [CrossRef]
90. Pilar-Cuéllar, F.; Vidal, R.; Díaz, Á.; Garro-Martínez, E.; Linge, R.; Castro, E.; Haberzettl, R.; Fink, H.; Bert, B.; Brosda, J.; et al. Enhanced Stress Response in 5-HT_{1A}R Overexpressing Mice: Altered HPA Function and Hippocampal Long-Term Potentiation. *ACS Chem. Neurosci.* **2017**, *8*, 2393–2401. [CrossRef]
91. López-Gil, X.; Babot, Z.; Amargós-Bosch, M.; Suñol, C.; Artigas, F.; Adell, A. Clozapine and haloperidol differently suppress the MK-801-increased glutamatergic and serotonergic transmission in the medial prefrontal cortex of the rat. *Neuropsychopharmacology* **2007**, *32*, 2087–2097. [CrossRef]

MDPI
St. Alban-Anlage 66
4052 Basel
Switzerland
www.mdpi.com

MDPI Books Editorial Office
E-mail: books@mdpi.com
www.mdpi.com/books



Disclaimer/Publisher's Note: The statements, opinions and data contained in all publications are solely those of the individual author(s) and contributor(s) and not of MDPI and/or the editor(s). MDPI and/or the editor(s) disclaim responsibility for any injury to people or property resulting from any ideas, methods, instructions or products referred to in the content.



Academic Open
Access Publishing

[mdpi.com](https://www.mdpi.com)

ISBN 978-3-0365-9657-0